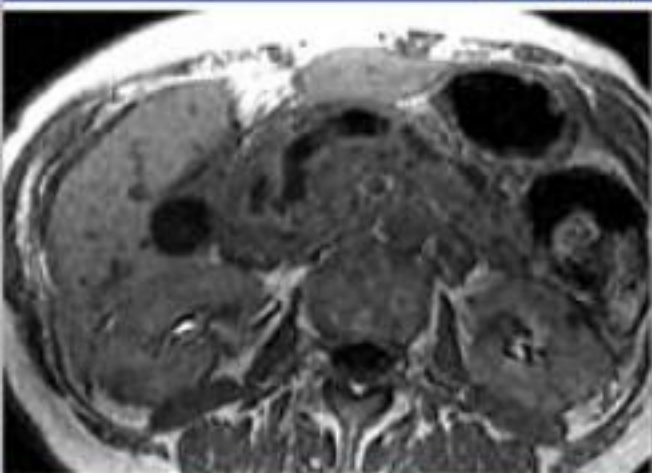
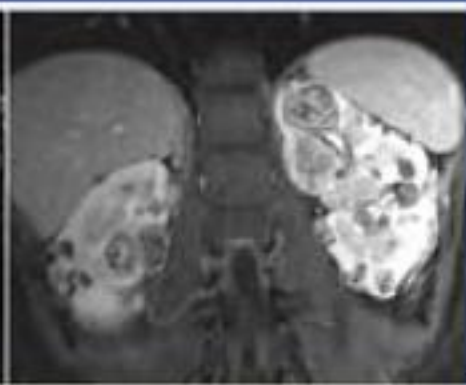
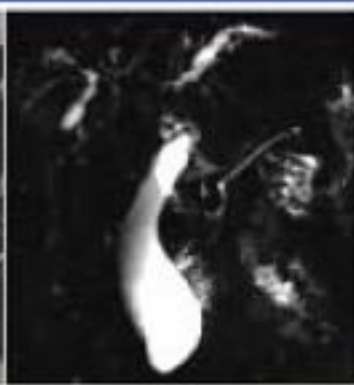


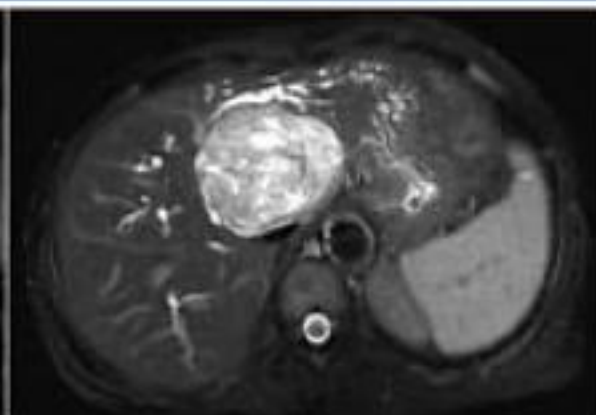
Fundamentals of



Body MRI



Christopher G. Roth



Fundamentals of **Body MRI**

Fundamentals of Body MRI

Christopher G. Roth, MD

Vice Chairman
Methodist Division
Department of Radiology
Thomas Jefferson University
Philadelphia, Pennsylvania

ELSEVIER
SAUNDERS

1600 John F. Kennedy Blvd.
Ste 1800
Philadelphia, PA 19103-2899

FUNDAMENTALS OF BODY MRI

ISBN: 978-1-4160-5183-1

Copyright © 2012 by Saunders, an imprint of Elsevier Inc.

All rights reserved. No part of this publication may be reproduced or transmitted in any form or by any means, electronic or mechanical, including photocopying, recording, or any information storage and retrieval system, without permission in writing from the publisher. Details on how to seek permission, further information about the Publisher's permissions policies and our arrangements with organizations such as the Copyright Clearance Center and the Copyright Licensing Agency, can be found at our website: www.elsevier.com/permissions.

This book and the individual contributions contained in it are protected under copyright by the Publisher (other than as may be noted herein).

Notices

Knowledge and best practice in this field are constantly changing. As new research and experience broaden our understanding, changes in research methods, professional practices, or medical treatment may become necessary.

Practitioners and researchers must always rely on their own experience and knowledge in evaluating and using any information, methods, compounds, or experiments described herein. In using such information or methods they should be mindful of their own safety and the safety of others, including parties for whom they have a professional responsibility.

With respect to any drug or pharmaceutical products identified, readers are advised to check the most current information provided (i) on procedures featured or (ii) by the manufacturer of each product to be administered, to verify the recommended dose or formula, the method and duration of administration, and contraindications. It is the responsibility of practitioners, relying on their own experience and knowledge of their patients, to make diagnoses, to determine dosages and the best treatment for each individual patient, and to take all appropriate safety precautions.

To the fullest extent of the law, neither the Publisher nor the authors, contributors, or editors, assume any liability for any injury and/or damage to persons or property as a matter of products liability, negligence or otherwise, or from any use or operation of any methods, products, instructions, or ideas contained in the material herein.

International Standard Book Number 978-1-4160-5183-1

Acquisitions Editor: Don Scholz
Editorial Assistant: David Mack
Publishing Services Manager: Pat Joiner-Myers
Design Direction: Steven Stave
Marketing Manager: Cara Jespersen

Printed in the United States of America

Last digit is the print number: 9 8 7 6 5 4 3 2 1

Working together to grow
libraries in developing countries

www.elsevier.com | www.bookaid.org | www.sabre.org

ELSEVIER

BOOK AID
International

Sabre Foundation

I dedicate this book to my family ...

... to my grandparents whose spiritual will to pursue intellectual advancement provided me role models and confidence to pursue my own education and intellectual enrichment.

... to my mother whose support and academic and professional achievements served as my inspiration.

... to my father whose support, intellectual curiosity, encouragement, and literary exploits helped guide me through my academic and literary endeavors.

... to my fiancée, Stephanie, whose unconditional love and support provided me the sustenance I needed to complete this work.

... I dedicate this book to our future.



Contributor

Sandeep Deshmukh, MD
Clinical Assistant Professor
Methodist Division
Department of Radiology
Thomas Jefferson University
Philadelphia, Pennsylvania
MRI of the Pancreaticobiliary System



Preface

I wrote this book rebelling against a number of trends in medical literature—a tendency to write exclusively in the passive tense, a predilection for the encyclopedic method, a distaste for visual aids (e.g., diagrams, tables), and an aversion to the basic science behind the scenes of our clinical practice. Some of these trends are easier to avoid than others. Tackling the science of body MRI and composing a basic introduction to MRI physics was definitely the most difficult. Once you pull at the thread, there is no end to the unraveling; in MRI physics, each of the many abstract concepts are predicated on multiple others, inviting an endless series of interconnected explanations, and I feel like an inhabitant in the M. C. Escher lithograph, “Relativity” (depicting a network of impossibly interconnected staircases constructed in different dimensions). I sacrificed comprehensiveness in this regard for a concise, common sense approach to MRI physics and introductory concepts in Chapter 1 with the liberal use of visual aids and sparing use of abstract concepts and equations.

In the clinical chapters (Chapters 2 to 5), I resisted the encyclopedic style in favor of a reader-oriented approach, where possible. Most of the text is arranged by the imaging

appearance, which is more in sync with the reader’s perspective than the encyclopedic style of organizing by disease entity. This format more closely mirrors the reader’s experience at the workstation, providing a useful reference for a problematic case or imaging pattern and facilitating differential diagnoses. Hopefully, abstention from the passive tense further enhances the readability of this text.

In writing a “fundamentals” text, my goal was to provide a stepping stone to a comfort level with body MRI—both technically and clinically. My intent was to provide in-depth useful information and commentary on the bread-and-butter material accounting for most of what is seen in clinical practice, deferring on the more advanced applications and exotic diseases. Advanced body MRI applications, such as prostate, breast, and cardiovascular MRI, were consciously excluded. For these topics, I refer you to many worthy texts and review articles.¹⁻⁹

This book has been long overdue—as one of the most complex fields in radiology, body MRI needs a “fundamentals” text. It’s my hope that this book fulfills this need and it was my honor and privilege to write it.

Christopher G. Roth

-
1. Siegelman ES. *Body MRI*. Philadelphia: Saunders, 2005.
 2. Semelka RC. *Abdominal-Pelvic MRI*, 2nd ed. Hoboken, NJ: Wiley-Liss, 2006.
 3. Lee VS. *Cardiovascular MRI: Physical Principles to Practical Protocols*. Philadelphia: Lippincott Williams & Wilkins, 2006.
 4. Bogaert J, Dymarkowski S, Taylor AM. *Clinical Cardiac MRI*. Berlin: Springer, 2005.
 5. Kwong RY. *Cardiovascular Magnetic Resonance Imaging*. Totowa, NJ: Humana Press, 2008.
 6. Morris EA, Liberman L. *Breast MRI*. New York: Springer, 2005.
 7. Hendrick RE. *Breast MRI: Fundamentals and Technical Aspects*. Secaucus, NJ: Springer Science and Business Media, 2008.
 8. Bard RL. *Dynamic Contrast-Enhanced MRI Atlas of Prostate Cancer*. Berlin: Springer, 2009.
 9. Verma S, Rajesh A. A clinically relevant approach to imaging prostate cancer: Review. *AJR Am J Roentgenol* 196:S1-S10, 2011.



Acknowledgments

Without the guidance and support of my mentors, this work would not have been possible. I credit the visionary leadership of our chair—Vijay Rao—for the fertile clinical and academic environment of our department in which I was able to compose this work.

I largely owe my interest, aptitude, and understanding of MRI to Don Mitchell. His book, *MRI Principles*, attracted me to MRI and TJU for fellowship training and provided the foundation of my understanding of MRI physics. With his own unique brand of mentorship, George Holland also endowed me with a deeper appreciation and understanding of body MRI.

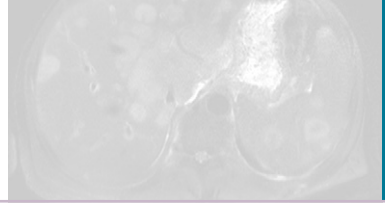
I'd be remiss not to acknowledge the diligence, efficiency, and industriousness of Angelique Burke, who assisted me with printing and reprinting and collating drafts during the revision process. I'd also be remiss in not acknowledging the countless technologists

who generated the images that I display in my book, although there are too many to name individually.

Without the help of my friend and colleague Sandeep Deshmukh, this book would be fodder for future generations of radiologists. With his help in finishing the last written (MRI of the Pancreaticobiliary System) chapter, I was able to complete the work in a reasonable timeframe and bring the project to fruition.

I owe the privilege of writing this book to my friend Rob Ward, whose recommendation ultimately landed me this opportunity. I also owe him gratitude for suggesting the unique reader-oriented organization of the chapters and other helpful suggestions along the way. Without his friendship and insight, this would not have been possible.

Christopher G. Roth



Introduction to Body MRI

MAGNETIC RESONANCE IMAGING: WHAT IS THE OBJECTIVE?

Magnetic resonance imaging (MRI) exploits the inherent magnetism in the protons that constitute the human body in a creative way by manipulating them with radiofrequency (Rf) energy in the presence of a strong magnetic field. This manipulation induces the protons to emit energy, which is detected and reconstructed into an image. The human body—not ostensibly magnetic—is effectively magnetized by a strong magnet. Once magnetized, Rf energy shifts magnetized protons to a higher energy state. Subsequently, the protons release this energy in the process of returning to their original low-energy state. The released energy is detected in a specialized receiver (referred to as a *coil* in MRI parlance). With this information, ultimately images with spatial and molecular information are reconstructed without harmful effects to the patient (such as ionizing radiation).

MAGNETISM: HOW IS THE HUMAN BODY MAGNETIZED?

The process of magnetizing the human body actually involves only select magnetically active nuclei (Fig. 1-1). The term *magnetically active nuclei* refers to those nuclei with unpaired protons or neutrons. These magnetically active nuclei harbor a net charge—the requisite property for interaction with a magnetic field (although neutrons have no actual net charge, the distribution of component charges is not uniform).

This interaction involves two phenomena—magnetic alignment and spin, or angular momentum. *Magnetic alignment* describes the tendency of the magnetically active nucleus (or “magnetic moment,” or “spin”)—a miniature magnet itself—to align along the orientation of an external magnetic field (Fig. 1-2). The alignment of these magnetic moments is quantized into one of two energy states: (1) parallel to (or

“spin up”) or (2) anti-parallel to (or “spin down”) to the magnetic field.

The second phenomenon—*spin*, or angular momentum—describes the propensity of a nucleus with net charge to oscillate like a gyroscope (or “precess”) in the presence of a magnetic field (Fig. 1-3). The rate of precession is nucleus-specific and defined by a variable known as the *gyromagnetic ratio* (γ).

Resonance capitalizes on nuclear precession in MRI. Energy absorption by a precessing nucleus exposed to oscillating energy of equal frequency defines *resonance*. By altering the oscillating frequency, only specific nuclei are selected and energized, establishing the spectroscopic basis of MRI.

MRI is founded on these two nuclear phenomena—spin and magnetic moment—occurring only in nuclei with net charge and applicable only to few nuclei in the human body (see Fig. 1-1). Among the biologically occurring magnetically active nuclei, it is the hydrogen nucleus (^1H) that serves as the substrate for MRI because of its large magnetic moment (proportional to the magnetic resonance [MR] “signal,” or emitted energy converted to visual images) and abundance in the human body (i.e., fat and water molecules).

THE COMPONENTS

The Magnet

The heart of the MRI apparatus is the magnet, or main magnetic field—referred to as B_0 . Without a strong external magnetic field, the body’s protons align themselves randomly, yielding no net magnetization and, therefore, no potential signal to convert to an image when subjected to Rf energy. The vector sum of the randomly aligned proton magnetic poles is zero—they cancel each other out. In the presence of a strong magnetic field— B_0 —protons align themselves parallel and anti-parallel to the magnetic field (see Fig. 1-2).¹ Because more protons align parallel versus anti-parallel to the

Element	Protons	Neutrons	Nuclear Spin	Gyromagnetic Ratio (MHz/T)	Natural Abundance (%)	Angular Momentum (MHz)
¹ H (Protium)	1	0	1/2	42.5774	99.985	63.8646
² H (Deuterium)	1	1	1	6.53896	0.015	9.8036
³ He	2	1	1/2	32.436	0.000138	48.6540
¹² C	6	6	0	0	98.90	0
¹³ C	6	7	1/2	10.7084	1.10	16.0621
¹⁴ N	7	7	1	3.07770	99.634	4.6164
¹⁵ N	7	8	1/2	4.3173	0.366	6.4759
¹⁶ O	8	8	0	0	99.762	0
¹⁷ O	8	9	5/2	5.7743	0.038	8.6614
²³ Na	11	12	3/2	11.2686	100	16.9029
³¹ P	15	16	1/2	17.2514	100	25.8771

FIGURE 1-1. Biologically relevant nuclei.

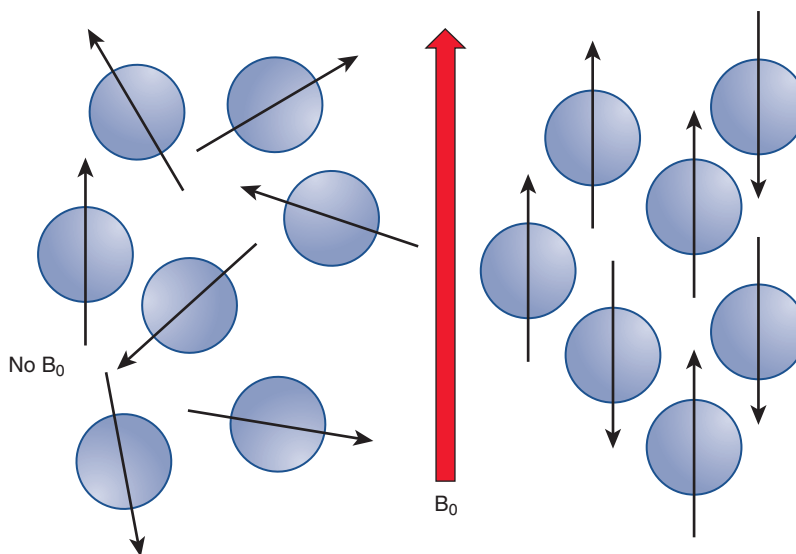


FIGURE 1-2. Proton alignment with and without a magnetic field. Left, Randomly oriented protons in the absence of a magnetic field. Right, Protons oriented parallel and anti-parallel to the magnetic field.

magnetic field, a net magnetic vector (NMV) is created from the protons in an external magnetic field (Fig. 1-4). This magnetic vector, representing net magnetism, is the basis for creating MR images—the sine qua non of MRI. Creating this magnetism explains the need for a strong magnetic field. The stronger the magnetic field, the greater the discrepancy between parallel and anti-parallel spins, with fewer aligning anti-parallel in the higher energy state. The result is

a larger NMV—the currency used to fashion MR images.

Whereas different types of commercially used magnets exist, the superconducting type is most clinically relevant to body MRI. Body MRI applications require high magnetic field strength (at least 1.0 Tesla and optimally 1.5 Tesla) in order to image rapidly with adequate signal-to-noise ratio (SNR). Resistive magnets top out at 0.5 Tesla and permanent magnets are also generally

manufactured at lower magnetic field strengths (≤ 0.7 Tesla) not optimized for body MRI applications. Conceptually, the superconducting magnet is a large solenoid composed of superconducting wire (i.e., niobium-titanium or niobium-tin), which is supercooled (with liquid helium or nitrogen) (Fig. 1-5).² Superconducting wire cooled appropriately permits the flow of electric current with virtually no resistance. By virtue of the thumb rule (officially Ampere's Law), the result is a magnetic field oriented along the axis of the solenoid (B_0).

Rf System

Another key component of the MRI apparatus is the Rf transmitter system that generates

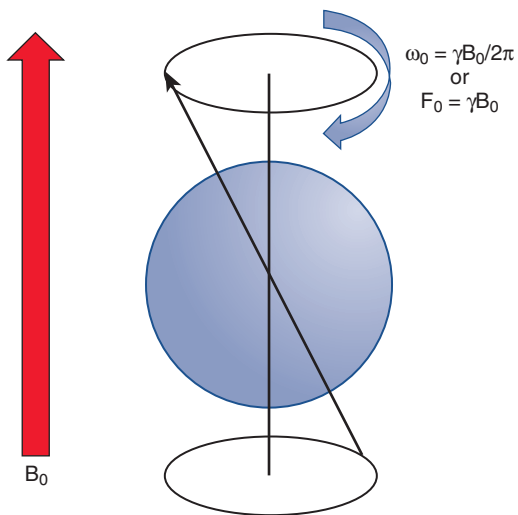


FIGURE 1-3. The concept of a nuclear spin.

the Rf pulse exciting the magnetized protons. Four components constitute the Rf transmitter system: the frequency synthesizer, the digital envelope of Rfs, a high-power amplifier, and an antenna in the form of a “coil.” The net effect is generation of an Rf pulse to excite the magnetized protons by exploiting MR.

In order to explain this process and the concept of MR, a basic understanding of nuclear physics and magnetism is necessary. As mentioned earlier, protons in a magnetic field become aligned, and the body becomes magnetized. In addition to aligning parallel or anti-parallel to B_0 , the protons rotate—or precess—around their magnetic axis, referred to as *magnetic spin* (see Fig. 1-3). The angular momentum (ω_0) and, accordingly, the frequency of precession (f_0) vary according to the strength of the magnetic field (B_0) and the gyromagnetic ratio (γ), which is a function of the specific properties of the nucleus—expressed by the Larmor equation:

$$\omega_0 = \gamma B_0 / 2\pi$$

which simplifies to

$$f_0 = \gamma B_0$$

Magnetic spins precessing at the frequency of the Rf pulse will absorb energy and move to the higher energy state. Thereafter, excited protons “relax,” emitting the absorbed energy and returning to their original low-energy state. The emitted Rf energy constitutes the signal that

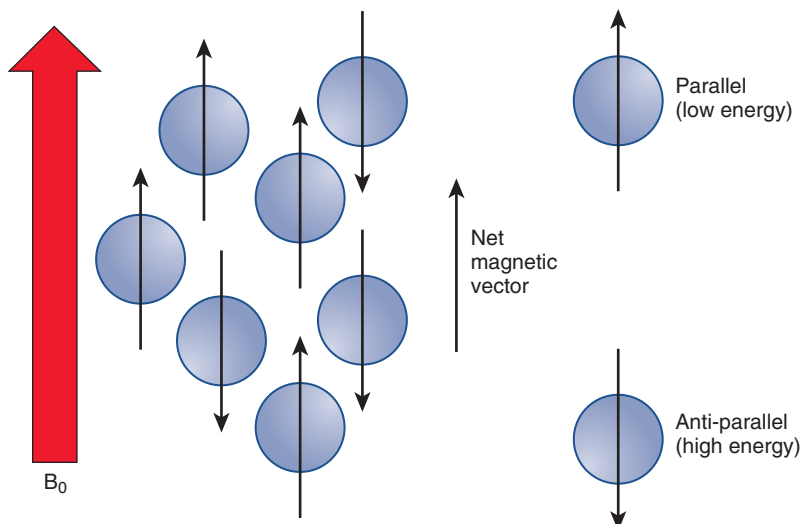


FIGURE 1-4. The net magnetic vector (NMV) concept.

ultimately generates an MR image. Conceptually, the NMV is aligned parallel to B_0 preceding the Rf excitation pulse. The Rf excitation pulse shifts spins into the higher energy state and the NMV away from the longitudinal axis of B_0 into the transverse plane. So, initially, the NMV is longitudinal—parallel to B_0 —and tilted by the Rf excitation pulse away from B_0 into the transverse plane (Fig. 1-6). The transverse component of the spin vector ultimately constitutes the MR signal.³

The Gradient System

A gradient system (a spatially varying magnetic field superimposed on spatially uniform B_0)

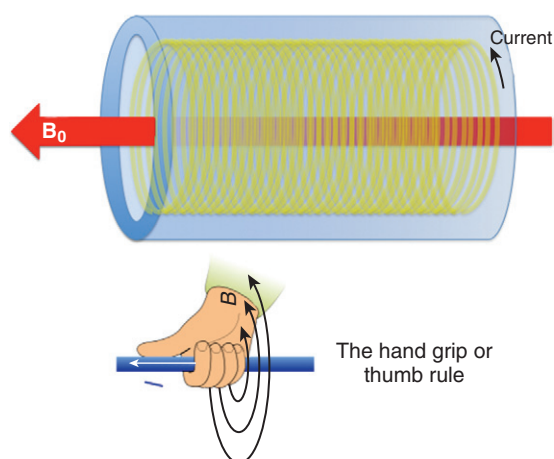


FIGURE 1-5. Schematic of a superconducting magnet.

distorts the magnetic environment in order to selectively excite a region—or slice—of tissue at a time to facilitate image generation and to send spatial information into the excited volume of protons. The gradient system includes three separate gradients each designed for its designated orthogonal plane: x, y, and z (Fig. 1-7). Each gradient is a coil through which current passes to induce changes in B_0 . Each gradient induces a linear variation in the main magnetic field (B_0) along its respective axis. In other words, a gradient alters the B_0 along a scale such that the magnetic field strength at one end of the gradient is stronger than the other (see Fig. 1-7).

The z—or slice-select—gradient (G_z or G_s) establishes the environment in which a specific slice of protons is excited. By varying the magnetic field strength along the axis of B_0 , the slice-select gradient concordantly varies the precessional frequency of the protons along the B_0 axis. Consequently, an Rf pulse emitted with a narrow range of frequencies excites only a thin slice of protons (Fig. 1-8). The narrow range of frequencies included in the Rf pulse—the transmit bandwidth—thereby determines the thickness of the excited slice protons. This slice of excited protons ultimately constitutes the MR image.

X- and y-gradients incorporate additional spatial information into the excited slice of protons, allowing the emitted MR energy to be converted into an MR image. The gradients

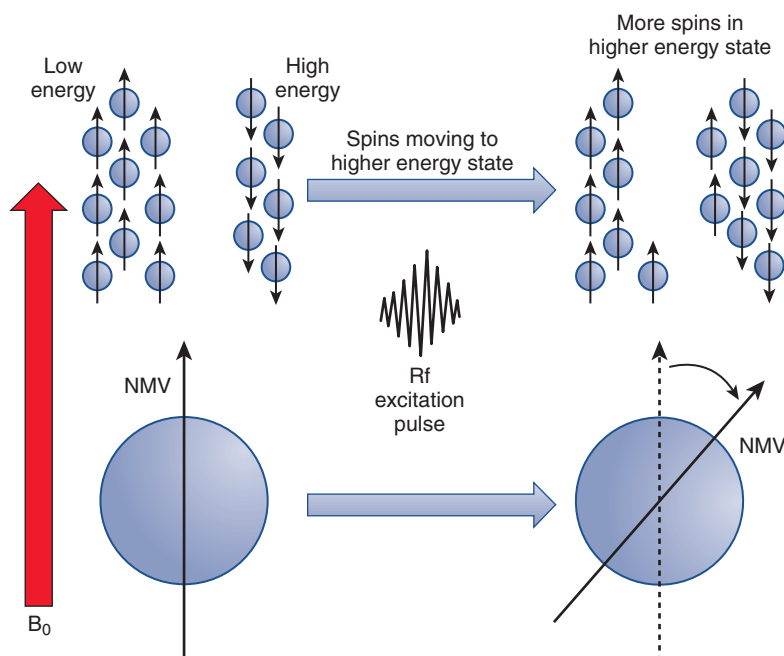


FIGURE 1-6. Net magnetic vector (NMV) tilted by the radiofrequency (Rf) excitation pulse.

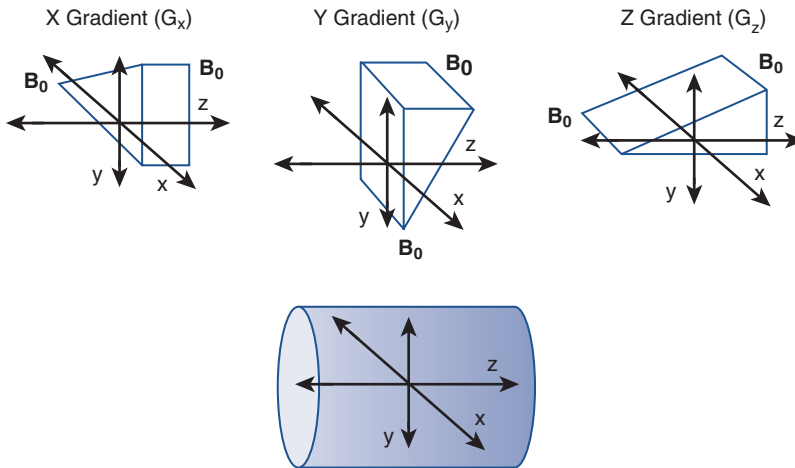


FIGURE 1-7. Schematic of a magnetic field gradient.

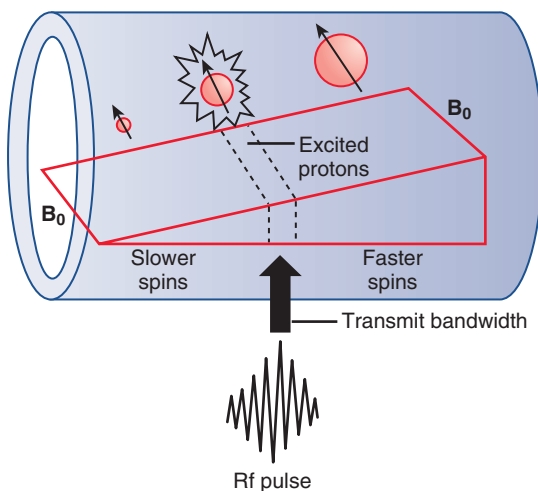


FIGURE 1-8. Slice-select gradient and the radiofrequency (Rf) pulse.

are applied in axes orthogonal to the slice-select gradient. The x-gradient—or frequency-encoding gradient or readout gradient (G_x or G_f)—applied perpendicular to B_0 —functions analogously to the slice-select gradient. By orchestrating a gradient magnetic field, spins vary in precessional frequency along a spectrum from one end of the excited slice of protons to the other (Fig. 1-9). Because spins precessing at different frequencies results in destructive interference, which reduces the emitted signal, the frequency-encoding gradient is applied in two separate phases, or lobes—the dephasing and rephasing lobes (Fig. 1-10).

The y-gradient—or phase-encoding gradient (G_y or G_p)—encodes spatial information into the excited slice of protons along the final

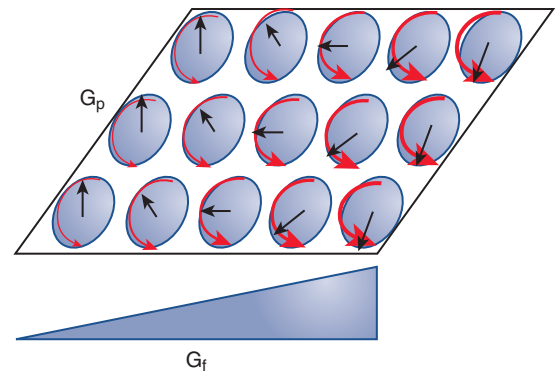


FIGURE 1-9. The frequency-encoding gradient.

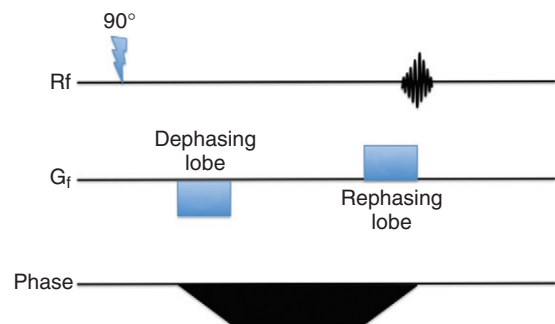


FIGURE 1-10. Frequency-encoding gradient scheme.

orthogonal axis. Applied briefly, the phase-encoding gradient induces a magnetic field gradient along the final orthogonal axis such that spins at one end transiently spin faster than spins at the opposite end (Fig. 1-11). Thereafter, when turned off, the spins retain their differential phase varying across the phase-encoding direction. This phase variation constitutes the spatial information along the phase-encoding

axis, which is incorporated into the emitted resonance signal.

This complex sequence of Rf energy and magnetic field gradients is precisely timed to accomplish the feat of coaxing a coherent emission of resonance energy from a specific slice or volume of protons that can be received by a specialized antenna, or coil (Fig. 1-12). Variations on this basic theme constitute the different pulse sequences used in MRI—such as spin-echo (SE), fast spin-echo (FSE), single-shot fast spin-echo (SSFSE), gradient-echo (GE), steady-state free precession (SSFP), and echo planar imaging (EPI).⁴ For a brief discussion of different pulse sequences, refer to the upcoming section in this chapter; for more detail on this subject, refer to texts dedicated to MRI physics—*MRI Principles*, D. G. Mitchell; *MRI Basic Principles and Applications*, M. A. Brown and R. C. Semelka; *The MRI Manual*, R. B. Lufkin; *MRI The Basics*, R. H. Hashemi, W. G. Bradley Jr., and C. J. Lisanti;

and *MRI in Practice*, C. Westbrook and C. Kaut.⁵⁻⁹

The Receiver System

The next pertinent hardware component is the system designed to receive or capture the emitted resonance energy. To review, the components discussed to this point include the main magnetic field (B_0), the Rf transmitter system, and the gradient magnetic field system. The receiver system includes a receiver coil, a receiver amplifier, and an analog-to-digital converter (ADC). A component of the Rf system previously mentioned—the transmit coil—often doubles as the receiver coil. In other words, some coils are send-receive coils—they perform the dual function of emitting the Rf excitation pulse and receiving the emitted resonance signal. Body—abdominal and pelvic—MRI applications demand the use of a dedicated torso coil. Although these devices vary from manufacturer to manufacturer and from device to device, torso coils are designed to closely encircle the body to enhance reception of the emitted resonance energy. Most torso coils take advantage of the phased-array configuration, combining multiple coil elements into a single coil device, which facilitates the reception of signal and the performance of parallel imaging (discussed later).

Because the amplitude of the received signal is so miniscule (on the order of nanovolts or microvolts), a signal amplifier is a requisite component of the receiver system. The ADC

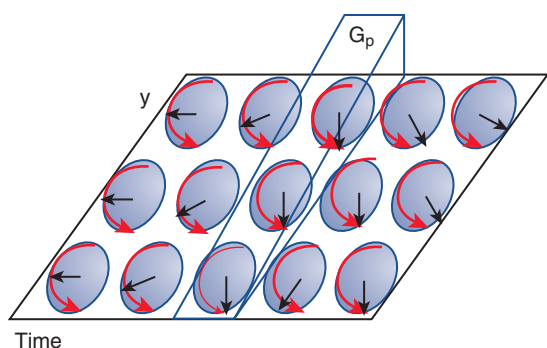


FIGURE 1-11. The phase-encoding gradient.

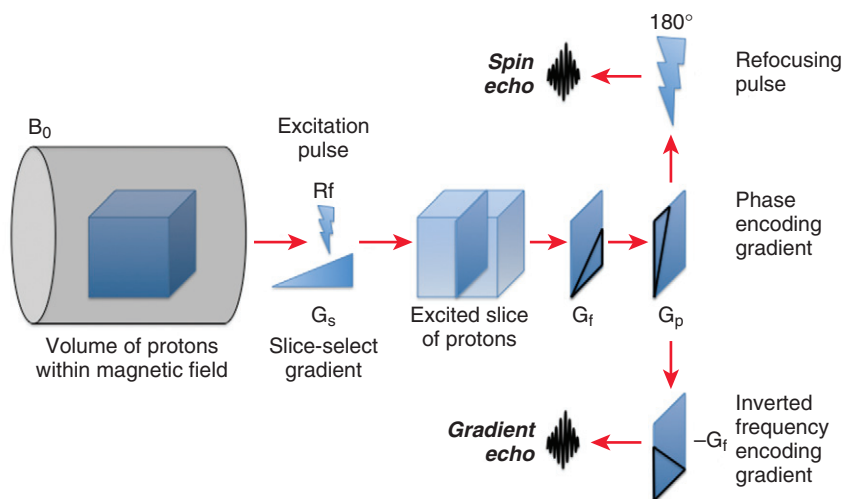


FIGURE 1-12. Basic pulse sequence schematic.

converts the received analog signal into digital data to be processed into image data.

K Space and the Fourier Transform

The final phase of the process involves decoding this digitized data into the visual medium of an MR image. This process happens on a computer storing the digital data and empowered with the mystical Fourier transform.¹⁰ The digital data resides in an abstract formulation known as *k* space. K space is a metaphysical construct serving as the repository for the raw (pre-Fourier transform-deciphered) data with frequency and phase coordinates (Fig. 1-13). The difficulty in understanding *k* space arises from the lack of a visual frame of reference; K-space data bear no direct resemblance to image data. Instead of spatial coordinates, *k*-space data plot along frequency and phase coordinates (in cycles/meter). Dividing *k* space into peripheral versus central regions facilitates understanding its place in image formation.

The echoes acquired for each slice of raw data plot into a corresponding *k* space map for that particular slice. K-space coordinates correspond to the frequency and phase-encoding gradient strengths at which the signal is obtained. Central points in *k* space represent the data acquired with the weakest gradients. Conversely, the periphery of *k* space coincides with signal obtained with the strongest gradients. Stronger gradients discriminate fine detail at the expense of signal loss due to dephasing. Weaker gradients fail to discriminate fine detail, but preserve signal. Central *k*-space plots image contrast information; peripheral *k*-space plots image detail information. Increasing *k*-space plotting density expands the field of view (FOV);

increasing *k*-space plotting area augments spatial resolution.

Each point in *k* space contains information from the entire excited cohort of protons. The number and distribution of *k*-space coordinates set by the pulse sequence dictate the time required for signal acquisition or “*k*-space filling.” K-space filling follows a trajectory determined by the spatial encoding scheme, which varies by pulse sequence. The trajectory begins at the origin of *k* space and is deflected peripherally by spatial gradients. For example, consider a simple GE pulse sequence in which the strongest negative phase-encoding gradient is applied first (Fig. 1-14A). At time zero—the Rf excitation pulse—the journey through *k* space begins at the origin— k_{x0} , k_{y0} . The strong negative phase-encoding gradient transports *k* space sampling trajectory to point $k_x, 0$, k_y -max (maximally negative phase-encoding gradient strength with no frequency-encoding gradient). Thereafter, frequency-encoding gradient dephasing and rephasing yield data points (the readout) transversely across that line of *k* space horizontally, at the end of which a single line of *k* space has been filled. At the next Rf excitation pulse, the journey begins at the *k*-space origin again to be deflected to the next, slightly less negative, line in *k* space by a slightly weaker phase-encoding gradient. Frequency-encoding fills this line in the same fashion and the process is repeated for each line in *k* space until *k* space is filled. The scheme exemplifies cartesian *k*-space filling, which rigidly follows a coordinate system in *k* space. Noncartesian *k* space trajectory schemes include radial, PROPELLER (Periodically Rotated Overlapping Parallel Lines with Enhanced Reconstruction), and

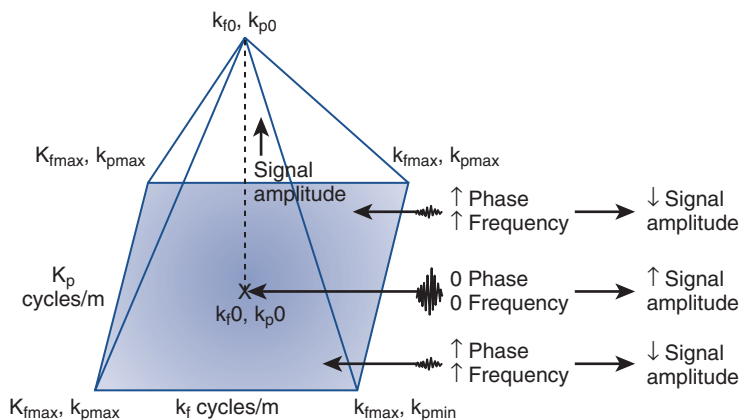


FIGURE 1-13. K-space.

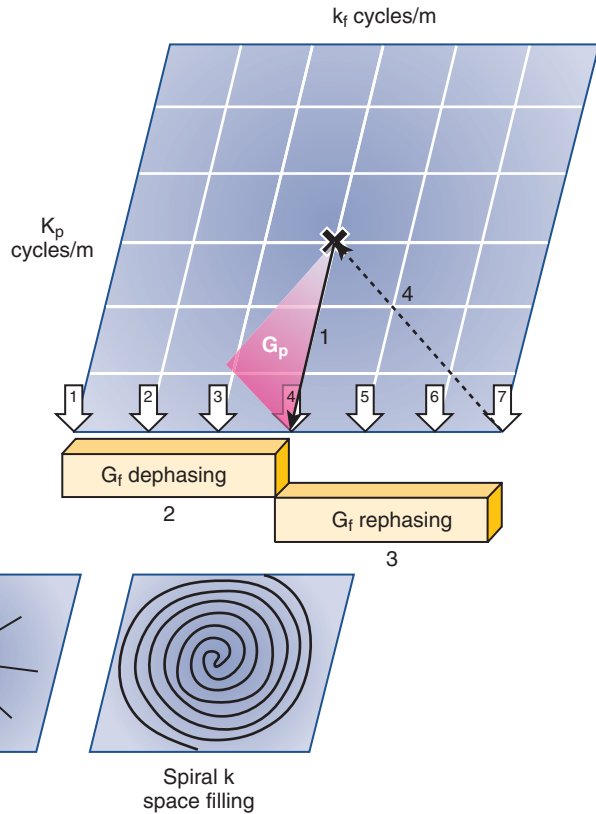
Following the initial excitation pulse,

Step 1: phase encoding gradient (G_p) deflects the potential signal to point $k_{x0}, k_{y\max}$

Step 2: frequency encoding (G_f) dephasing gradient deflects k space trajectory to point $k_{x\max}, k_{y\max}$

Step 3: frequency encoding (G_f) rephasing gradient applied with opposite polarity drives trajectory to $k_{x\max}, k_{y\max}$ during which time readout datapoints 1–7 are collected

Step 4: the next radiofrequency excitation pulse deflects the trajectory back to the origin of k space



A

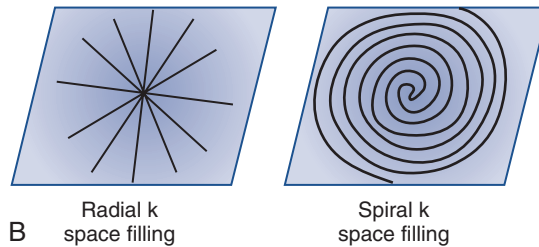


FIGURE 1-14. A, Basic (gradient echo) Cartesian k-space trajectory. B, Examples of noncartesian k-space trajectory schemes.

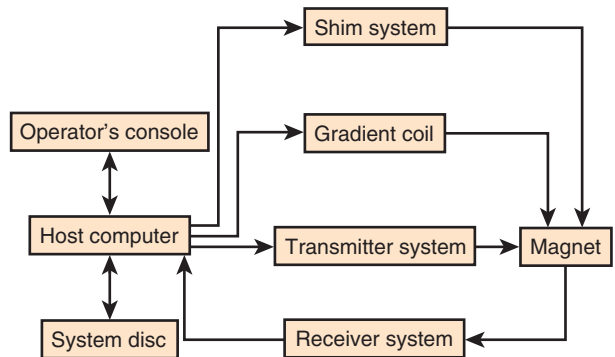


FIGURE 1-15. Magnetic resonance imaging (MRI) system schematic.

spiral k-space trajectories (see Fig. 1-14B). These k-space filling techniques involve combining gradients during the readout to fill k space in novel, potentially more efficient ways.

The purpose of the Fourier transform is to translate the k-space data in the frequency and phase domain into image data with spatial coordinates. The Fourier transform “solves” k space for pixel data. The numeric value assigned to each Fourier transform–solved pixel corresponds to the MR signal amplitude, or signal.

Operator’s Console

On the user’s (technologist’s) side, the main component is the operator’s console. The operator’s console is the portal of entry into the main system computer, which subsequently executes instructions from the operator’s console to the system hardware and channels incoming image data to the operator’s console and storage module (Fig. 1-15). This is the computer that the technologist uses to select the imaging protocol and the sequence parameters and that receives the image data decoded by the Fourier transform for review by the technologist.

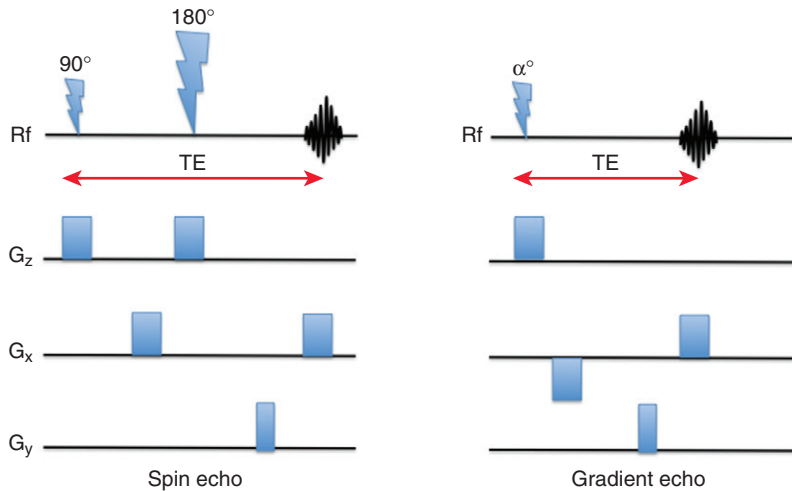


FIGURE 1-16. Spin-echo and gradient-echo pulse sequences. TE, time to excitation.

PULSE SEQUENCES

The process of filling k space depends on the pulse sequence chosen. Two major types of pulse sequences dominate body MRI and MRI in general: (1) SE and (2) GE sequences. The presence or absence of a “refocusing pulse” characterizes the SE and GE sequences, respectively. These two pulse sequences represent different approaches to the problem of generating signal after the initial Rf excitation pulse. The frequency-encoding gradient dephases the excited spins (i.e., destructive interference), which must be rephased in order to yield signal—referred to as an *echo* of the original Rf excitation pulse, reverberating at time TE (time to excitation) after the Rf excitation pulse. Of course, these pulse sequences usually need to be repeated multiple times in order to acquire enough data to fill k space for a single image. The interval between Rf excitation pulses is referred to as *TR* (*time to repetition*).

In the SE pulse sequence experiment, the excited spins are inverted by a 180° refocusing pulse prior to a rephasing lobe of the frequency-encoding gradient of equal polarity (Fig. 1-16). In the GE experiment, the refocusing pulse is omitted and a frequency-encoding rephasing lobe of reversed polarity reestablishes phase coherence. Advantages and disadvantages of each technique must be acknowledged when devising MRI protocols.¹¹

The implementation of a refocusing pulse furnishes SE sequences with two distinctive attributes: (1) increased imaging time and (2) resistance to artifacts. By flipping the spins

180° , the refocusing pulse inverts the phase difference between spins so that spins ahead in phase become equally behind in phase after the refocusing pulse. Therefore, in a time period equal to the time period preceding the refocusing pulse, the spins will be aligned. Consequently, the duration of echo generation in an SE pulse sequence (TE) is generally twice the time preceding the refocusing pulse, which incurs the passage of a significant amount of time compared with a GE pulse sequence.

However, the benefits outweigh this disadvantage under many circumstances. Spins dephase not only as a consequence of the frequency-encoding gradient but also because of magnetic field inhomogeneities and inherent microenvironmental factors (spin-spin interactions)—known as $T2^*$ decay. The 180° refocusing pulse corrects for these dephasing artifacts at the cost of image acquisition time. In the end, spectral considerations dictate the use of these two types of pulse sequences. The increased time required to obtain T2-weighted sequences demands a longer acquisition time (which is discussed in more detail later), conforming to the specifications of the SE sequence. Meanwhile, T1-weighted sequences benefit from shorter acquisition times, which also minimize $T2^*$ artifacts, favoring the use of GE sequences.

Practically speaking, modifications of the prototypic SE and GE sequences already described are implemented in modern-day body MRI protocols. These sequences have been adapted to acquire multiple echoes with a single excitation pulse, rather than the single-echo scenario

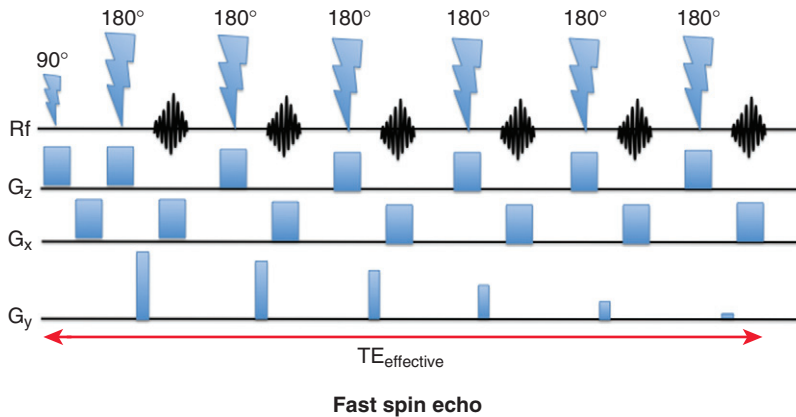


FIGURE 1-17. Multiecho spin-echo and gradient-echo pulse sequence diagrams. TE, time to excitation.

previously described, in order to save time. In the case of the SE sequence, multiple refocusing pulses follow the Rf excitation pulse, each producing an echo (Fig. 1-17). The extreme example of this multiecho technique is the SSFSE sequence in which all echoes necessary to fill k space for a given image are acquired after a single excitation pulse. Consequently, the SSFSE sequence robustly corrects susceptibility artifact and minimizes acquisition time. The FSE sequence includes at least two and less than all of the refocusing pulses and echoes necessary to fill k space; acquisition time and susceptibility artifact resistance of an FSE sequence are greater than a conventional SE sequence and less than an SSFSE sequence.

GE sequences have also been adapted as multiecho sequences to minimize acquisition time (see Fig. 1-17). Another pulse sequence modification frequently adapted to GE sequences in body MRI is three-dimensional (3-D) imaging. The basic premise of a 3-D pulse sequence is the excitation of a volume of tissue instead of a slice. Rather than covering the region of interest (ROI) with individual contiguous slices, the ROI is covered with a single volume. Instead of acquiring multiple images independently, the 3-D technique acquires the volume data set all at once. During 3-D image acquisition, the rephasing lobe of the slice-select gradient serves as a phase-encoding gradient in the slice axis, thereby encoding z-axis spatial information into the excited volume. While the two-dimensional (2-D) approach preempts the problem of spatially localizing along the z-axis by preselecting targeted tissue, the 3-D approach adds another gradient, adding another dimension to k space and the Fourier transform. The 3-D Fourier

transform “solves” the 3-D k-space data in the same way as the 2-D Fourier transform previously described for each individual slice while using the z-axis phase-encoded data to partition the information along the slice axis.

Using 3-D k-space filling techniques, each Rf pulse excites the entire volume of tissue (rather than a single slice), magnifying SNR compared with 2-D techniques. In 3-D pulse sequences, each voxel of tissue benefits from every excitation pulse in the entire sequence, whereas voxels in 2-D schemes receive only slice-selective excitation pulses (none from the other slices in the prescribed ROI). Consequently, 3-D sequences yield higher SNRs, permitting the partition of the data into smaller fragments, or voxels, generating higher spatial resolution and image detail.

Other GE sequence types used in body MRI include SSFP and EPI sequences. The SSFP sequence is a specialized sequence in which an equilibrium quantity of transverse and longitudinal magnetization is maintained in a steady state. Tissue contrast—to be discussed in greater detail—is T2-/T1-weighted. The EPI sequence is a GE sequence that acquires all the data necessary to fill k space with 1 Rf excitation pulse. In body MRI, the EPI sequence is commandeered for diffusion-weighted imaging (DWI). An additional gradient applied in two phases—with sensitizing and desensitizing lobes—favors signal from static tissue, which phases and dephases from the diffusion gradient, yielding no net phase shift. Moving—or diffusing—tissue unpredictably experiences the diffusion gradient, resulting in some degree of dephasing and proportionally negating signal. The DWI sequence is T2-weighted—an exception to the GE rule in body MRI.

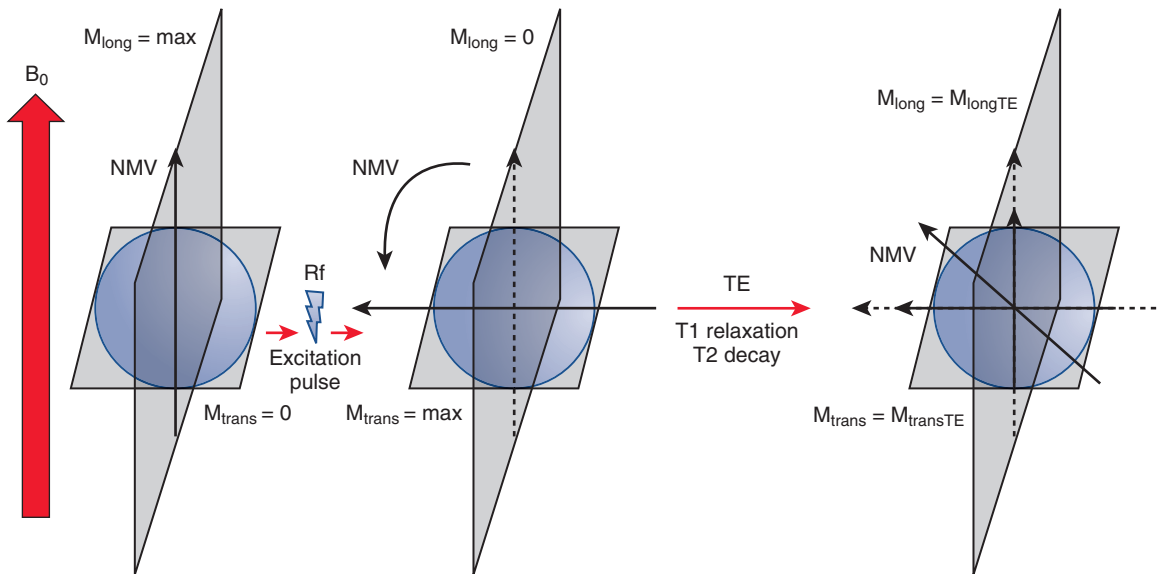


FIGURE 1-18. Rf excitation and T1 recovery and T2 decay. NMV, net magnetic vector; TE, time to excitation.

TISSUE CONTRAST

One of the remarkable qualities of MRI is the ability to render spectroscopic images. The behavior of a proton in a magnetic field varies depending on its unique microenvironment. For all intents and purposes, the protons relevant to MR imaging are hydrogen (^1H) protons. ^1H protons in fat and water behave differently; different fat protons in the same fat molecule behave differently; and free water protons in liquid form versus bound water protons in solid tissue (such as visceral organs) behave differently. These differences are exploited in MRI with the use of targeted pulse sequences with characteristic parameters.

T1- and T2-weighting are the main pulse sequence strategies employed to yield spectroscopic information, or tissue contrast.¹² T1-weighting enhances the differences in T1 values between tissues, whereas T2-weighting enhances the differences in T2 values between tissues. In order to understand these concepts, consider the proton spin magnetic moment initially parallel to B_0 and subsequently tilted perpendicular to B_0 into the transverse plane by the Rf excitation pulse (Fig. 1-18). At this point, the longitudinal component of the vector is minimized and the transverse component is maximized. Immediately thereafter, spins lose transverse and regain longitudinal magnetization according to their unique microenvironment. Regaining, or recovering, longitudinal magnetization is referred to as *T1 relaxation*

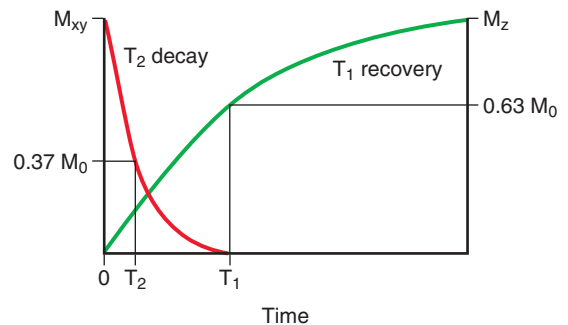


FIGURE 1-19. T1 and T2 relaxation curves and values for different tissues.

(or spin-lattice relaxation); the T1 relaxation time is the time to recover 63% of the original longitudinal magnetization after an Rf excitation pulse. Decaying transverse magnetization is T2 relaxation (or spin-spin relaxation) and the T2 value of a tissue corresponds to the time elapsed after 63% of the original transverse magnetization has decayed. The (oversimplified) premise that spins are simple vectors of magnetization that are tipped into the transverse plane and reorient parallel to the longitudinal plane suggests that these processes occur at equal rates. However, premise fails. Whereas these values usually approximate that rule—that is, spins with long T2 values also have long T1 values—they do not always directly follow one another. T2 decay generally outpaces T1 recovery and the T1 relaxation rate of a proton defines the potential upper limit of the T2 decay time (Fig. 1-19).

T1 (msec)

Tissue	0.5T	1.5T	3.0T
Free Water	>4000	>4000	>4000
Muscle	560	870	898
Fat	192	200	382
Liver	395	570	809
Spleen	760	1025	1328

FIGURE 1-20. T1 values at different magnetic field strengths.

The T1 value of a proton defines its ability to release energy and return to its original state. The T1 is a function of the proton microenvironment, or lattice, and the magnetic field strength. T1 values decrease with greater structural organization and increase with increasing magnetic field strength. This is another counterintuitive principle—stronger magnetic field strength would seem to draw spins back to equilibrium faster. Suspend that notion and remember that T1 relaxation depends on the internal structure of the proton. A stronger magnetic field overwhelms the facilitating effects of a proton's structure, and T1 values for all spins generally increase and converge with increasing field strength (Fig. 1-20).

T2 values are not affected by magnetic field strength. T2 values also decrease with structural organization facilitating the dissipation of energy. The T2 value measures the length of time that transverse magnetization remains coherent. In other words, after the Rf excitation pulse, the NMV is deflected into the transverse plane, at which time all spins are in phase. Eventually, spins dephase because some precess faster than others owing to local differences in the magnetic microenvironment—hence, the term *spin-spin relaxation*. Other factors affect transverse magnetization in addition to intrinsic T2 decay, referred to as *T2** (*T2 star*) decay. Factors that induce *T2** decay include heterogeneity of the local magnetic field and heterogeneity of tissue chemical shifts (or susceptibility artifact). While transverse magnetization undergoes *T2** decay during GE sequences, the operational mechanism of transverse magnetization decay in spin echo imaging is T2 decay, since

the refocusing pulse in an SE sequence eliminates *T2** effects. Therefore, the term *T2 contrast* applies to SE imaging, whereas *T2* contrast* is reserved for GE sequences.

The TR and TE of a pulse sequence are manipulated to favor signal from protons with either short T1 values or long T2 values. Colloquially speaking, when favoring short T1 values, the pulse sequence is “T1-weighted,” and when favoring long T2 values, the pulse sequence is “T2-weighted.” Actually the T1-weighted pulse sequence is short-T1-value-weighted and the T2-weighted pulse sequence is long-T2-value-weighted; for obvious reasons, the more succinct “T1-weighted” and “T2-weighted” designations suffice.

In order to understand how to isolate signal from protons with short T1 values versus protons with long T2 values, consider the following experiment. In order to receive signal from all protons in a substance, the TE is set to zero to negate spin-spin (T2) relaxation and the TR is maximized to ensure that all spins have fully recovered longitudinal magnetization. Under these circumstances, all spins yield signal regardless of their T1 and T2 values (Fig. 1-21). Therefore, signal generated from this pulse sequence represents a map of proton density—hence, the designation *proton density (PD)*. Using the PD pulse sequence as a starting point, decreasing the TR below the T1 relaxation rates of spins with long T1 values diminishes the signal contribution from these spins (Fig. 1-22A). After the Rf excitation pulse, these spins incompletely recover longitudinal magnetization before the next Rf excitation pulse. Therefore, the longitudinal magnetization

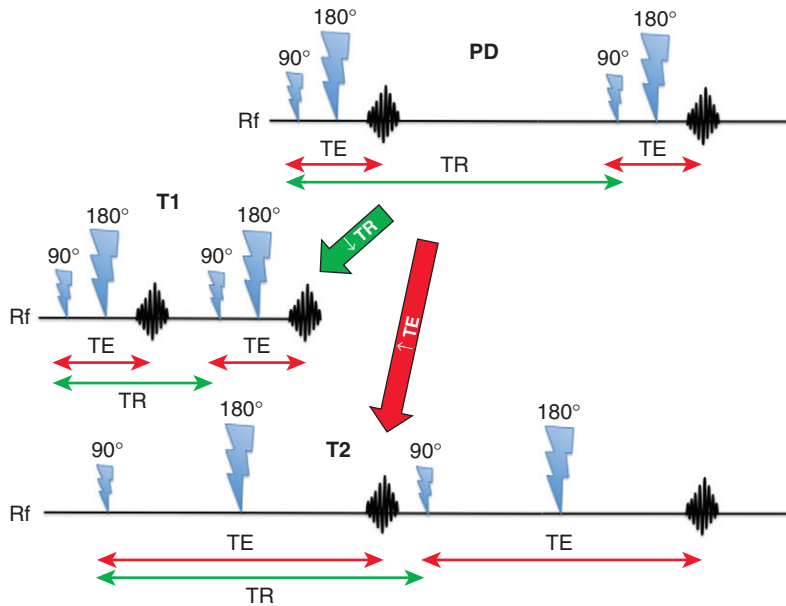


FIGURE 1-21. Pulse sequence schemes: PDW, T1W, T2W. PD, proton density; TE, time to excitation; TR, time to repetition.

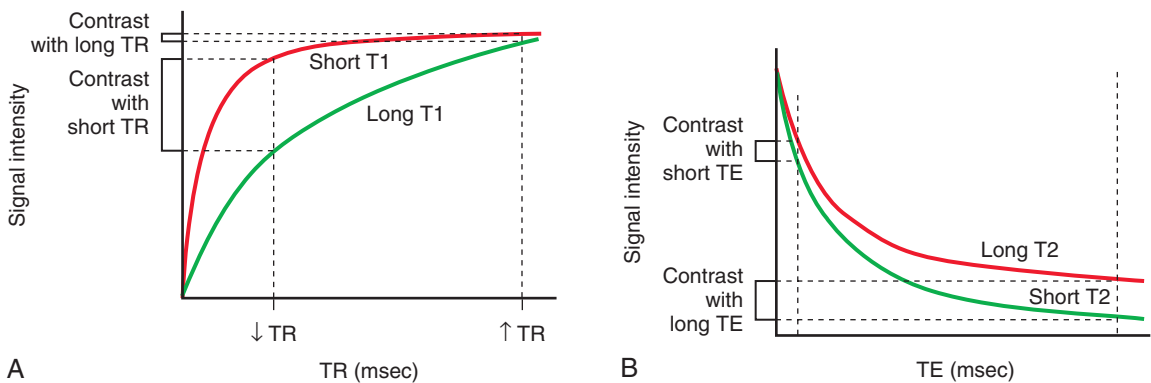


FIGURE 1-22. A, T1 contrast mechanism. B, T2 contrast mechanism. TR, time to repetition. TE, time to excitation.

converted to transverse magnetization by successive Rf excitation pulses is continuously diminished for spins with long T1 values, effectively eliminating the signal contribution of these spins to the resulting image and isolating the signal from spins with short T1 values (T1-weighting).

Parenthetically, another method of achieving T1-weighting involves modifying the *flip angle* (FA). The FA refers to the degree of deflection of NMV away from B_0 by the Rf excitation pulse. SE pulse sequences conventionally fix FA at 90° and T1-weighting relies on the TR. However, GE sequences generally employ lower FAs and commonly rely on FA to modify T1-weighting. Increasing the FA increases the amount of—and time for—longitudinal magnetization to be recovered before the next Rf excitation pulse.

Only spins with short T1 values recover enough longitudinal magnetization to be excited into the transverse plane and avoid saturation. Incomplete, fractional longitudinal magnetization recovery is repeated mathematically. In other words, if initial longitudinal magnetization equals L and the TR occurs when only half of L has recovered, then

After the first Rf pulse, longitudinal magnetization = $\frac{1}{2} L$

After the second Rf pulse, longitudinal magnetization = $\frac{1}{4} L$

After the third Rf pulse, longitudinal magnetization = $\frac{1}{8} L$

and so on.

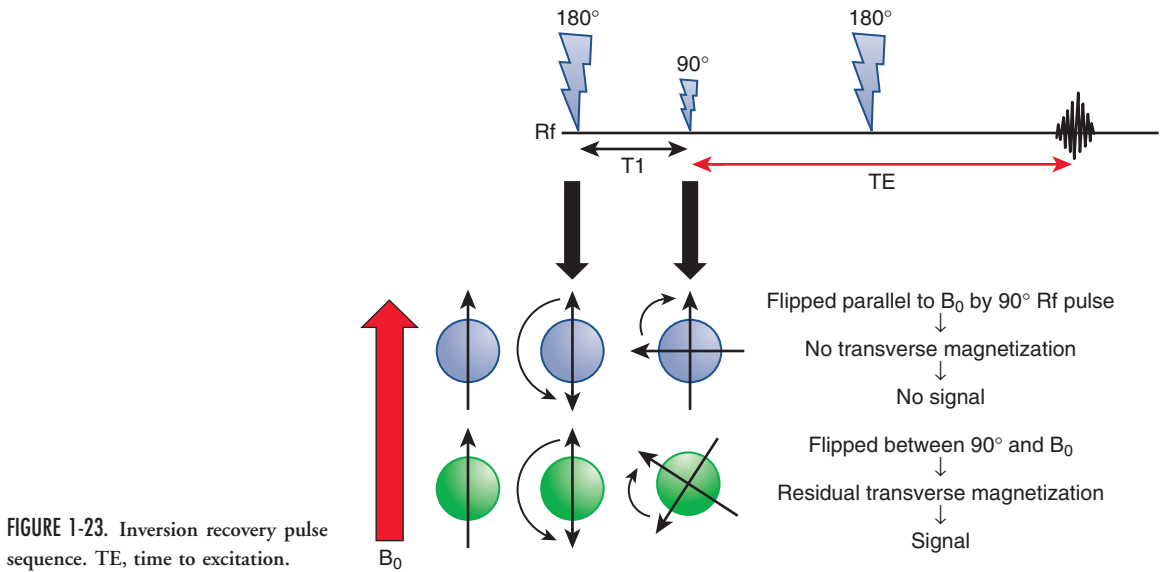


FIGURE 1-23. Inversion recovery pulse sequence. TE, time to excitation.

This sequence of events exemplifies saturation. Because longitudinal magnetization is analogous to potential energy, the decremental impact on longitudinal magnetization translates to vanishing signal potential.

Starting with the PD sequence template with minimal TE and maximal TR, increasing the TE favors signal from spins with long T2 values. Spins with short T2 values experience rapid loss of transverse magnetization with little to no residual signal at the time the echo is sampled (TE) (see Fig. 1-22B). Maintaining a long TR ensures that spins with long T1 values (which usually characterize spins with long T2 values) will not be saturated. This pulse sequence scheme—T2-weighting—therefore ensures that signal yield primarily results from spins with long T2 values.

A few pulse sequence modifications bear consideration in order to explain the ability to selectively image protons in body MRI: the spectrally selective pulse, the inversion pulse, and chemical shift. The *spectrally selective pulse* most commonly manifests in body MRI as the “fat-saturation pulse” or “fat-suppression pulse.” This is an Rf pulse set to the resonant frequency of fat followed by a spoiler gradient, which dephases the excited fat protons, eliminating their transverse magnetization. Thereafter, the Rf excitation pulse is applied in the absence of signal contribution from fat protons.

The *inversion pulse* serves as an alternative to the spectrally selective pulse as a method of

eliminating signal from fat. The inversion pulse deflects all protons 180° preceding the 90° Rf excitation pulse, which is timed to occur when fat protons are at the 90° position; this time interval is referred to as the *inversion time (TI)* (Fig. 1-23). Consequently, the fat protons are tilted to the 0° position, yielding no signal. The short T1 value of fat protons expedites their T1 recovery ahead of most other protons, which are at some value between 180° and 90° at the time of the Rf excitation pulse. Therefore, longitudinal magnetization is an intermediate value, which results in relatively lower SNRs for inversion recovery sequences. This type of inversion recovery pulse sequence is known as the *STIR (short tau inversion recovery) sequence*. Changing the TI targets protons with different T1 relaxation rates. For example, a long TI is applied to eliminate signal from water protons, which have a long T1 value, so that the 90° Rf excitation pulse reverts them to the 0° position. This technique is usually applied to brain imaging, and is known as the *FLAIR (fluid attenuation inversion recovery) sequence*.

Chemical shift refers to the difference (or shift) in precessional frequency between different proton species, such as water and fat, which is a function of the proton microenvironment (remember the Larmor equation expressing the precessional frequency incorporates the nucleus-specific gyromagnetic ratio). At some point, spins with different rates of precession rotate out-of-phase with one another (180° apart). If the TE occurs at this timepoint,

destructive interference ensues negating signal. The most popular practical application of this phenomenon is fat-water chemical shift imaging—colloquially referred to as *in- and out-of-phase imaging*. This technique is necessarily applied to a GE pulse sequence (the 180° refocusing pulse in an SE sequence eliminates chemical shift). Echoes are timed to coincide with out-of-phase and in-phase timepoints of the relevant spins (Fig. 1-24). In the case of fat and water protons at 1.5 Tesla, water protons precess an additional 360° in 4.4 msec. Therefore, after an Rf excitation pulse, echoes acquired at 2.2 msec and 4.4 msec are out-of-phase and in-phase, respectively. Coexistent fat and water protons deprive signal from the imaging voxel in out-of-phase images and both contribute signal to the imaging voxel in in-phase images (Fig. 1-25).

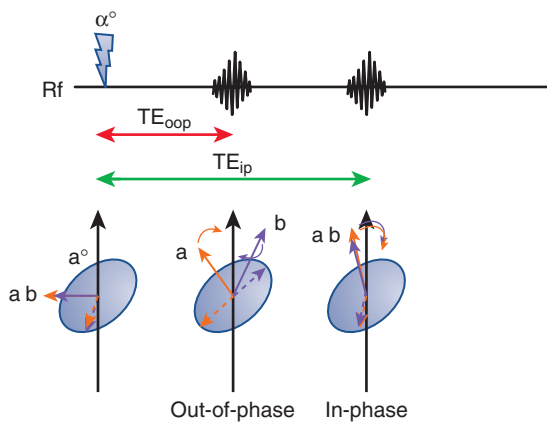


FIGURE 1-24. Chemical shift imaging. Rf, radiofrequency; TE, time to excitation.

To summarize, a number of physical phenomena and parameter manipulations empower MRI to exploit the unique behavior of different protons in the presence of a magnetic field. Decreasing the TR isolates signal from protons with short T1 values, whereas increasing the TE isolates signal from protons with long T2 values. T1- and T2-weighted sequence design follows these parameter prescriptions. In the case of GE sequences, T1-weighting involves increasing the FA to favor signal from spins with long T1 values. Fat saturation techniques supplement pulse sequences to eliminate signal from lipid protons, isolating signal from the remaining protons. Spectrally selective and inversion recovery techniques are commonly used methods. Fat-water chemical shift imaging is used to identify the coexistence of these protons by synchronizing echoes with the out-of-phase and in-phase precessional timepoints.

THE PULSE SEQUENCE SCHEME

Body MRI pulse sequences fall into two main categories: T1- and T2-weighted sequences (Fig. 1-26). Each pulse sequence is designed with a tissue-specific objective in mind, which necessitates a familiarity of the different tissues encountered (see Fig. 1-26). The two major categories of protons encountered in body MRI—water and fat protons—require further subdivision to generate a rational pulse sequence scheme. Water protons split into two major categories: bound water and free water protons. Bound (intracellular) water protons exist in solid

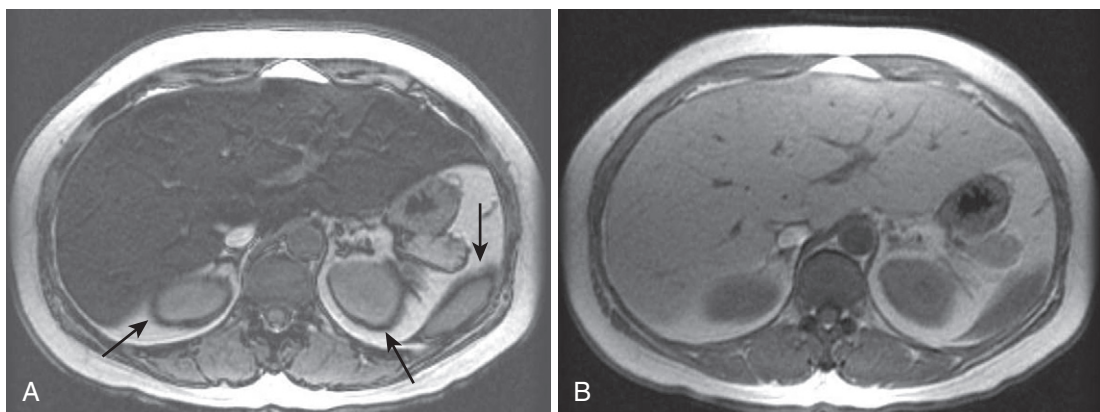


FIGURE 1-25. Out-of-phase imaging shows microscopic fat. The marked signal loss in the liver on the out-of-phase image (A) compared with the in-phase image (B) indicates the presence of microscopic fat. The etched appearance at the fat-water interfaces (arrows) on the out-of-phase image is referred to as “India ink” artifact.

	Pulse Sequence	Application	Sequence Type	Other
T1	Out-of-phase	Microscopic fat	GRE	India ink artifact
	In-phase	Susceptibility artifact (iron, metal, etc.)	GRE	Acquired with OOP as single dual-echo acquisition
	Pre-contrast	Paramagnetic substances (blood, melanin, etc.)	(3-D) GRE	Optimally with fat suppression
	Dynamic post-contrast	Solid tissue and vascular structures	(3-D) GRE	Same as above
	Delayed post-contrast	Extracellular space (fibrous tissue, inflammation)	GRE	Same as above
T2	Moderately T2-weighted	Bound Water (malignant lesions)	FSE	Optimally with fat suppression, TE ≈ 80
	Heavily T2-weighted	Free Water (fluid)	SSFSE	TE ≈ 180
	MRCP	Free water only	SSFSE	TE > 500

FIGURE 1-26. Body MRI pulse sequences. FSE, fast spin-echo; GRE, gradient-recalled echo; MRCP, magnetic resonance cholangiopancreatography; OOP, out of phase; SSFSE, single-shot fast spin-echo; TE, time to excitation.

tissues bound in close proximity to large molecules, such as protein. Free (extracellular) water protons exist in solution (e.g., bile, urine, cerebrospinal fluid). Fat protons experience a similar distribution—macroscopic (or extracellular) fat versus microscopic (or intracellular) fat. Macroscopic fat occurs in subcutaneous, retroperitoneal, and intraperitoneal distributions and in certain types of tumors, such as angiomyolipoma, dermoid cyst, and myelolipoma. Microscopic fat infiltrates solid organs (such as the liver) and certain tumors (such as hepatic adenomas and renal cell carcinoma).

A third category includes substances with magnetic susceptibility. *Magnetic susceptibility* describes the tendency of a substance to become magnetized in a magnetic field. Magnetism is denoted by the Greek symbol χ . Substances not magnetizable—diamagnetic—have χ values less than or equal to zero—which characterizes most of the tissues of the human body. Paramagnetic substances are weakly magnetic and have χ values greater than zero, but less than superparamagnetic substances with χ values 100 to 1000 times stronger. At the far end of the spectrum, ferromagnetic materials have the highest χ value. Paramagnetic substances enhance the efficiency of T1 and T2 relaxation. These substances have unpaired electrons that facilitate proton relaxation—usually in aqueous solution.

Relevant paramagnetic substances include methemoglobin (present in hemorrhage), melanin, protein, and gadolinium. Concentrated gadolinium—typically used as an intravenous injection—is an example of a relevant superparamagnetic substance. Iron, cobalt, and nickel are examples of ferromagnetic substances.

MRI pulse sequences each generally target one or more of these substances. Although protocols vary between different institutions, body parts, and manufacturers, a general tissue-based pulse sequence scheme transcends provincial differences, providing a universally applicable system. T1-weighted sequences usually include an in- and out-of-phase sequence, a pre- and postcontrast dynamic sequence and a delayed postcontrast sequence. T2-weighted sequences include moderately T2-weighted, heavily T2-weighted, and extremely heavily T2-weighted (or MRCP [magnetic resonance cholangiopancreatography] or MRU [magnetic resonance urography]) sequences.

T1-weighted sequences evoke signal from substances with short T1 values, such as fat and protons experiencing paramagnetic effects (e.g., protons in protein-rich organs such as the pancreas and liver). Sequence-specific attributes, such as fat saturation and chemical shift, confer greater specificity, isolating or highlighting individual proton species.

In- and out-of-phase images are usually acquired simultaneously in a single pulse sequence with two different TEs. The data are subsequently separated into two image sets covering the same anatomy. The out-of-phase sequence is T1-weighted sequence with sensitivity to microscopic fat—“the microscopic fat sequence.” Wherever fat and water protons coexist, destructive interference and signal loss ensue (see Fig. 1-25). These images distinguish themselves with the unique “India ink” artifact, alluding to the etched appearance at the interface between water-rich substances and fat (see Fig. 1-25)—another manifestation of destructive interference.

The in-phase sequence is T1-weighted with sensitivity to susceptibility artifact—“the susceptibility sequence.” Whereas most T1-weighted sequences in body imaging are GE sequences and inherently possess sensitivity to susceptibility artifact, the in-phase sequence benefits from a relatively long TE and a reference standard in the form of its cohort—the out-of-phase sequence. Susceptibility artifact is induced by substances with drastically different χ values from the substances around them and most commonly arises from metallic substances, such as surgical hardware and iron—manifesting signal loss. Because of the doubled TE, the in-phase sequence exaggerates susceptibility artifact compared with the out-of-phase sequence (Fig. 1-27). The appearance ranges from modest signal loss, such as in the case of depositional iron disease, to a dramatic signal void, in the case of embolization coils and metallic surgical devices.

The dynamic sequence involves multiphase repetition of the same sequence before and multiple times after intravenous gadolinium administration (Fig. 1-28). This sequence is designed to detect enhancement, or the paramagnetic effect of gadolinium. The sequence parameters are adjusted to detect the T1-shortening effects of administered gadolinium. In order to select for substances only experiencing the paramagnetic effects of gadolinium, fat, the dominant substance with a short T1 value, is selectively removed with a spectrally selective pulse. Therefore, on the precontrast set of images before gadolinium is administered, paramagnetic substances other than gadolinium—methemoglobin (blood), melanin, and protein—are conspicuous (Fig. 1-29) and this sequence is appropriately termed the *paramagnetic sequence*.

After injecting gadolinium (usually administered as an extracellular agent), vascular structures followed by perfused tissues followed by interstitial spaces enhance, according to the sequential delivery of gadolinium to the different compartments of the extracellular space. The postcontrast phases of the dynamic sequence usually include an arterial phase, a portal venous phase, and occasionally, a venous phase. In addition to rendering its respective vascular network, each phase of this sequence confirms viable tissue by demonstrating an increase in signal compared with the precontrast phase. Therefore, this multiphase sequence is referred to as the *vascular, or solid/viable tissue sequence*.

The delayed postcontrast sequence usually mirrors the parameters of the dynamic sequence. The timing of the delayed sequence most closely approximates the delivery of contrast to the interstitium. The dynamic sequence precedes delivery of gadolinium to the interstitium and exhibits no enhancement. Consequently, fibrous tissue and interstitial edema (i.e., associated with inflammation) enhance preferentially on the delayed phase (Fig. 1-30)—hence, the designation *interstitial sequence*.

Whereas T1-weighted sequences used in body MRI are usually GE sequences, the T2-weighted sequences are mostly SE-based sequences, removing consideration of chemical shift and susceptibility phenomena. The need to attain higher TE values for T2-weighting increases acquisition time, imposing prohibitive susceptibility artifact, decreasing SNR, and increasing breathhold demands on GE images. SE sequences are better adapted to the needs of T2-weighting for most applications. T2-weighted SE pulse sequences used in body MRI benefit from the refocusing pulse, which eliminates potentially prohibitive susceptibility artifact and also helps to preserve SNR.

T2-weighted sequences differ chiefly in their targeted water molecule—free water versus bound water. The main difference between these sequences is the TE. A relatively lower TE is adapted to identify differences in bound water content between solid tissues. Increasingly higher TE values more selectively isolate signal from free water protons and eliminate signal from solid tissues.

The moderately T2-weighted sequence approximates the T2 values of solid organs, such as the liver. The typical TE value of a moderately

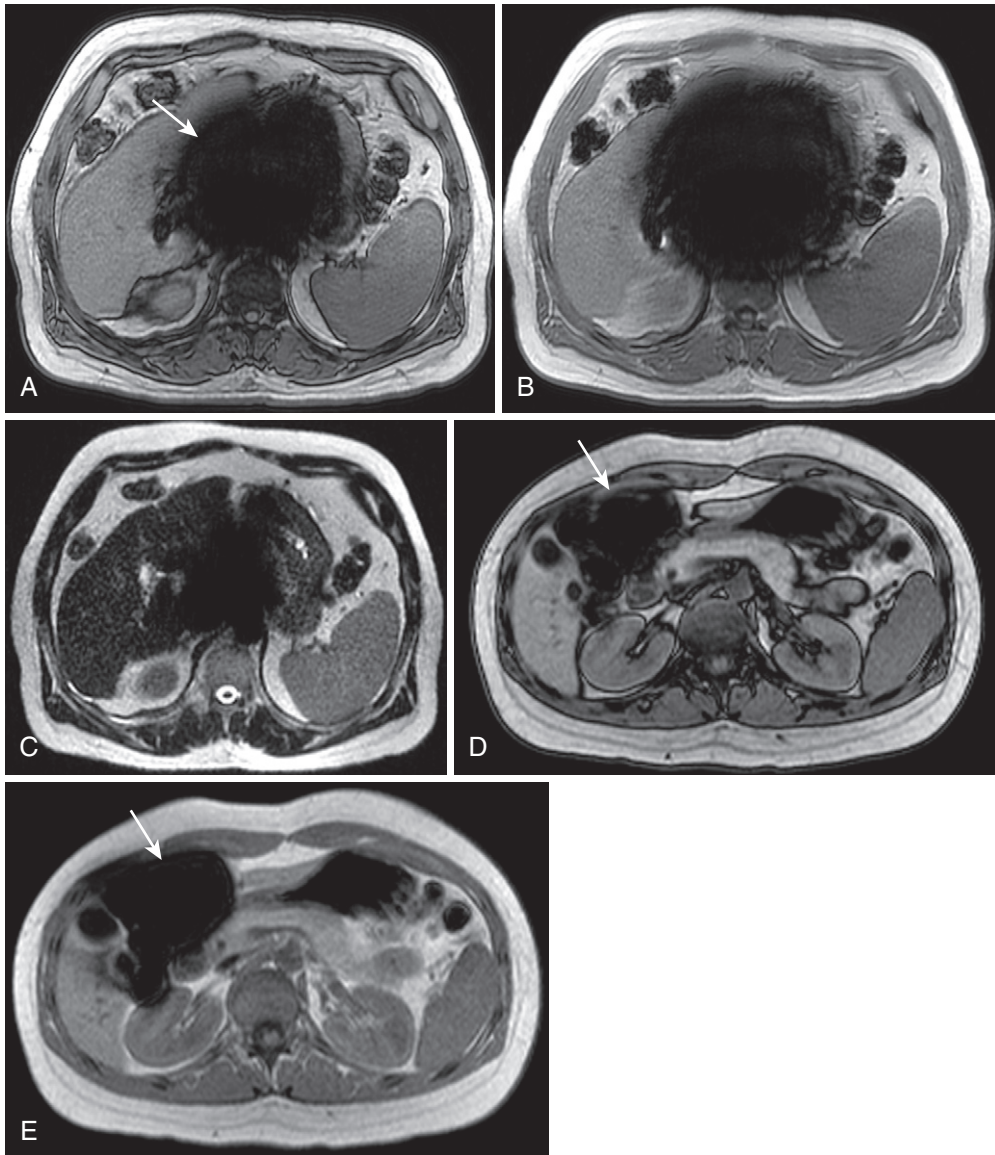


FIGURE 1-27. In-phase imaging shows susceptibility artifact. The magnification or “blooming” of the central signal void (*arrow*) from embolization coils on the in-phase image (B) compared with the out-of-phase image (A) is a function of the longer time to excitation (TE). C, The artifact on the corresponding single-shot fast spin-echo (SSFSE) image is better controlled owing to the refocusing pulses (despite the much longer TE). D, Susceptibility artifact also arises from endogenous structures, such as gas-containing bowel, as seen in the out-of-phase image (*arrow*) in a different patient. E, Blooming (*arrow*) is evidence on the susceptibility (in-phase) image.

T2-weighted sequence used in abdominal imaging is 80 msec. This value optimizes the contrast between substances of different bound water content, such as normal parenchymal tissue and neoplasms, which typically harbor higher water content. The addition of fat suppression augments tissue contrast by improving the dynamic range, which increases the visible discrepancy between tissues with different quantities of bound water (Fig. 1-31). The bound water specificity justifies the name *bound water sequence*.

The heavily T2-weighted sequence employs a higher TE (~180 msec). By increasing the TE value to this level, the transverse magnetization of solid tissues with bound water decays significantly, whereas free water maintains transverse magnetization (Fig. 1-32) (free water T2 = ~180 msec at 1.5 Tesla). Contrast between solid tissues with different bound water content decays compared with the moderately T2-weighted sequence, potentially obscuring solid lesions (prompting the name *lesion suppression sequence*). Because SNR depends

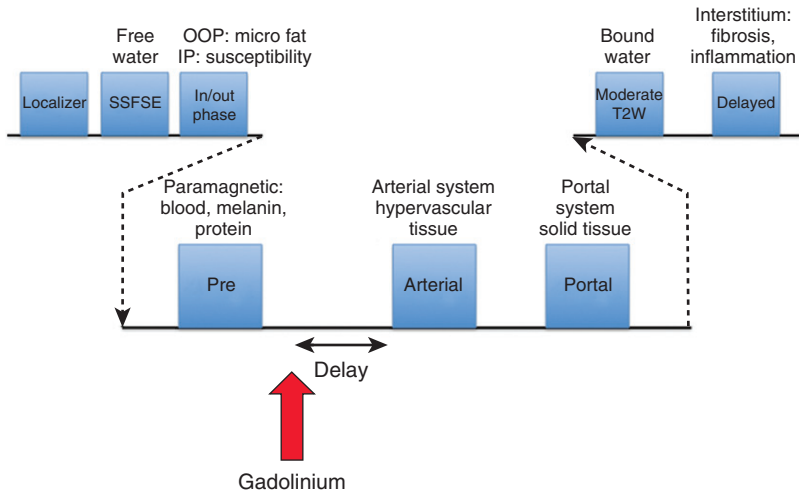


FIGURE 1-28. Dynamic pulse sequence schematic. IP, in phase; OOP, out of phase; SSFSE, single-shot fast spin-echo.

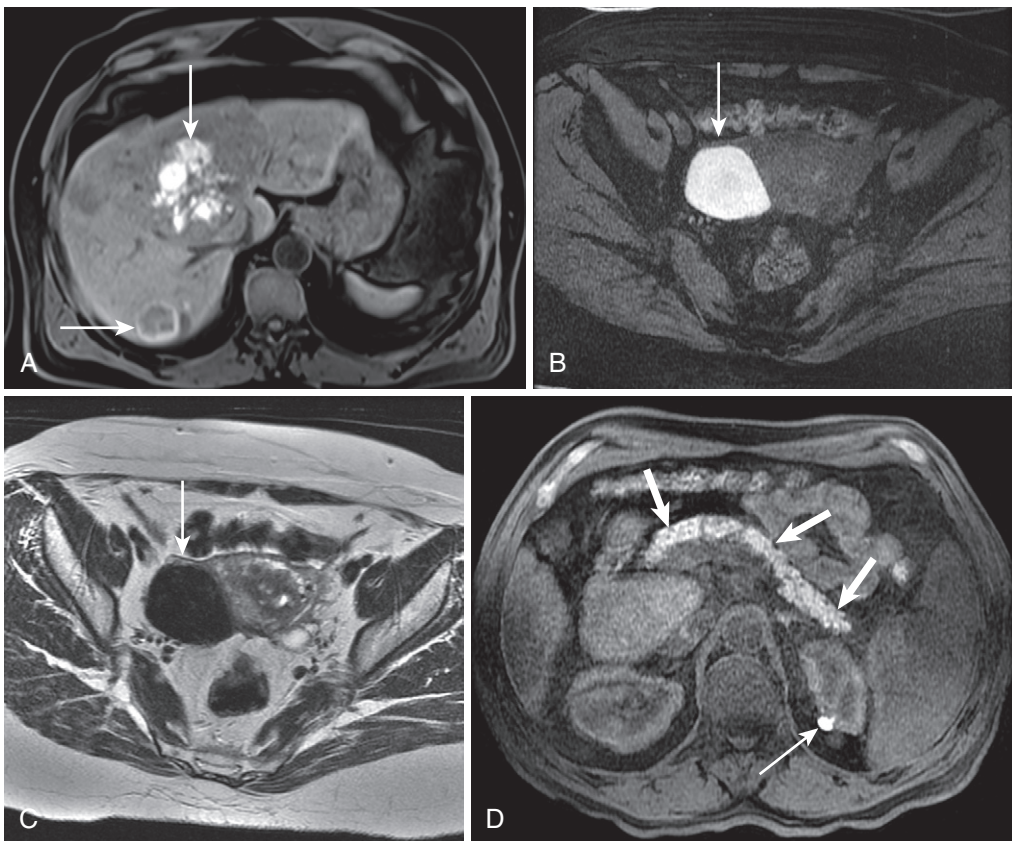


FIGURE 1-29. Precontrast imaging shows paramagnetic substance. A, The precontrast fat-suppressed (paramagnetic) image in a patient with metastatic uveal melanoma shows multiple, variably hyperintense lesions (*arrows*) reflecting variable melanotic content. B, A paramagnetic image in a patient with pelvic pain shows a large, irregularly shaped lesion with significant paramagnetism (*arrow*) due to hemorrhage. C, Marked hypointensity on the T2-weighted image characterizes the concentrated blood products found in an endometrioma (*arrow*). D, A paramagnetic image in a different patient shows the paramagnetic effects of a small left renal hemorrhagic cyst (*thin arrow*) and enzymatic proteins in the pancreas (*thick arrows*), causing these structures to be relatively hyperintense.

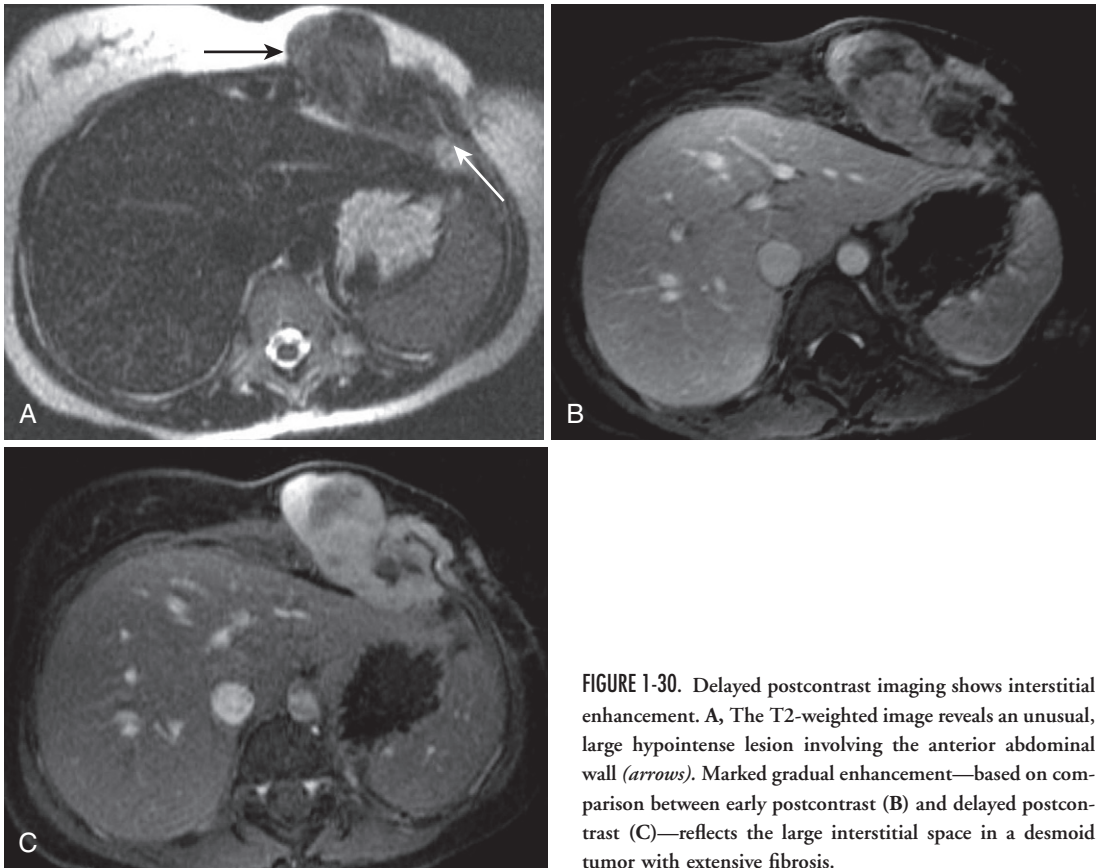


FIGURE 1-30. Delayed postcontrast imaging shows interstitial enhancement. **A**, The T2-weighted image reveals an unusual, large hypointense lesion involving the anterior abdominal wall (*arrows*). Marked gradual enhancement—based on comparison between early postcontrast (**B**) and delayed postcontrast (**C**)—reflects the large interstitial space in a desmoid tumor with extensive fibrosis.

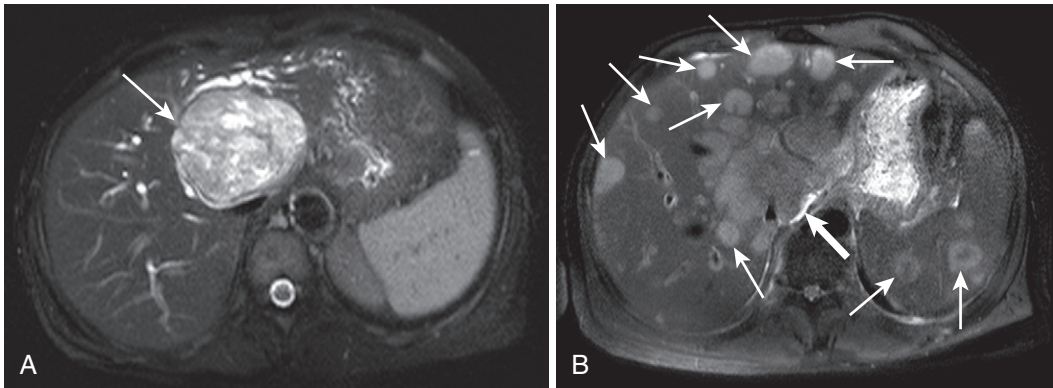


FIGURE 1-31. Moderately T2-weighted imaging shows bound water tissue contrast. **A**, The moderately T2-weighted image in a patient with a hepatic schwannoma (*arrow*) expresses the high water content often seen in schwannomas. Note the relatively higher tissue water content of the spleen compared with the liver—reflected by relative hyperintensity—serving as an indication of the tissue contrast of the bound water sequence. **B**, Even the relatively unhydrated lymphomatous lesions (*thin arrows*) with periportal lymphadenopathy (*thick arrow*) in a different patient with disseminated lymphoma are conspicuous on the bound water sequence owing to the high tissue contrast.

on transverse magnetization, which decays rapidly with increasing TE, the heavily T2-weighted sequence is relatively signal-starved. Consequently, this sequence usually avoids fat-suppression—which has the secondary effect of decreasing SNR. By relatively

isolating free water protons, this sequence deserves the title *free water sequence*.

Dramatically increasing the TE results in extreme T2-weighting and T2 decay of all substances except free water protons—a *water-only sequence*. This technique is applied to

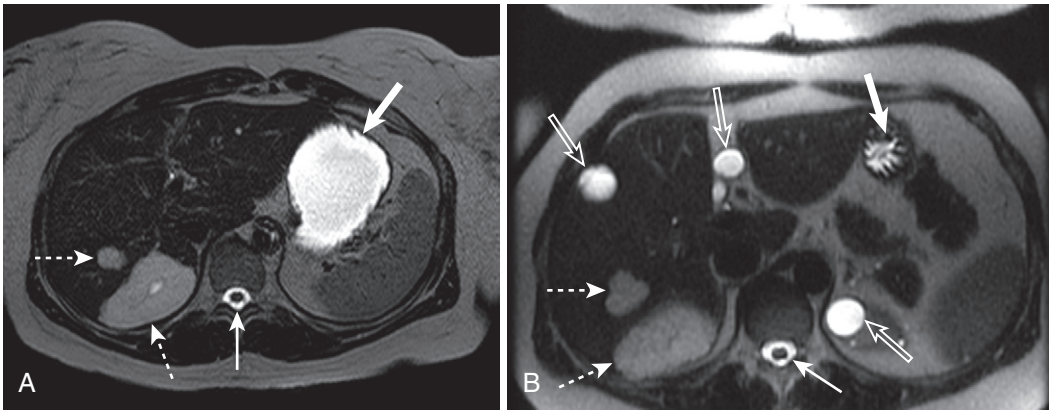


FIGURE 1-32. Heavily T2-weighted imaging shows free water. A and B, The heavily T2-weighted images depict free water protons preferentially, at the expense of solid tissue contrast. Solid tissues with bound water molecules, such as the liver, lack signal, whereas structures with free water exhibit marked hyperintensity proportional to their water content. Pure free water molecules found in cerebrospinal fluid (*arrows*), gastrointestinal contents (*thick arrows*), gallbladder (*open arrow*), and simple renal and hepatic cysts define maximum signal intensity, whereas lesions with intermediate free water content, such as hemangiomas (*dashed arrows*) appear moderately hyperintense.

imaging structures containing free water molecules, such as the biliary system (MRCP) and the urinary system (MRU).

OPTIMIZING BODY MRI

The torso poses many unique problems to the prospect of obtaining MR images. In addition to artifacts encountered universally in MRI applications, such as magnetic field heterogeneity, chemical shift artifact, and Rf artifact, body MRI encounters additional obstacles. Unlike most other body parts, continuous physiologic motion, variable quantities of paramagnetic substances, and variable patient body habitus frequently complicate the process. Addressing these issues greatly improves image quality.

Motion

Motion artifact is a layered topic complicating every examination, especially in the abdomen. Motion induces a phase shift in a proton during the application of a magnetic field gradient. There is no implicit correction algorithm in k space or the Fourier transform for the phase shift induced by motion. Phase shift induced by the phase-encoding gradient is indistinguishable from phase shift induced by motion. Consequently, the Fourier transform spatially misregisters moving protons.

Motion from bulk patient motion, cardiac pulsation, respiratory motion, bowel peristalsis, and blood flow separates into two broad

categories, based on the physical explanation for the artifact encountered—view-to-view phase errors and within-view phase errors.¹⁵ The term *view* refers to echo and *within-view phase errors* occur during the acquisition of the echo, whereas *view-to-view phase errors* arise because of motion between the acquisition of successive echoes.

Within-view phase errors arise because a moving proton fails to be rephased by applied gradients. Magnetic gradients in MR imaging are often applied in separate dephasing and rephasing lobes with a net phase shift of zero in order to reestablish spin phase coherence, as previously discussed. The unpredictable phase shift accumulated by the moving spin is not addressed with this technique and the acquired phase shift is assumed to have been induced by the phase-encoding gradient and spatially mapped accordingly (Figs. 1-33 and 1-34). View-to-view phase errors result from signal amplitude variations resulting from motion between echoes, which results from bulk motion (see Fig. 1-34). Considering a single voxel, when the signal amplitude varies from echo to echo because motion transports different spins into the voxel between echoes view-to-view phase errors occur. This happens under the circumstances of direct motion and pulsatile vascular flow. Physically replacing spins of different species explains the basis for this error in the case of direct motion. The variable replacement of unpredictably saturated spins with inconstant velocity explains this problem in pulsatile vascular flow.

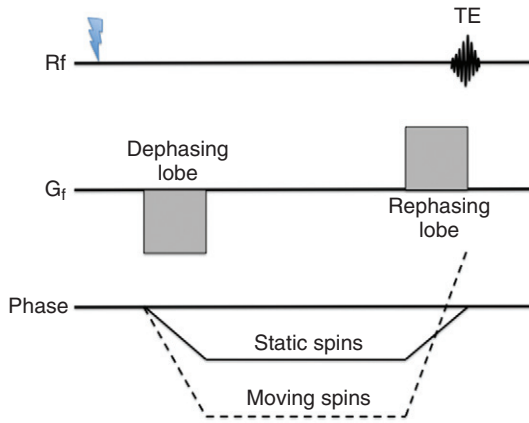


FIGURE 1-33. Within-view motion artifact. Rf, radiofrequency; TE, time to excitation.

Most of the strategies employed in body MRI to correct motion artifact minimize acquisition time. Acquisition time depends on multiple parameters (Fig. 1-35) and is expressed in the form of the equation:

$$T = \frac{TR \times G_p \times NEX}{ETL \times R}$$

where T is the acquisition time, TR is the repetition time, G_p is the number of phase-encoding steps, NEX is the number of excitations, ETL is the echo train length, and R is the acceleration factor (in parallel imaging).¹⁴ The TR is usually already minimized and optimized to the pulse sequence and not amenable to modification. The NEX is usually already minimized. The other parameters in the equation offer the most potential utility in minimizing acquisition time. Because G_p contributes to acquisition time and G_f does not, the smaller of the transverse axes

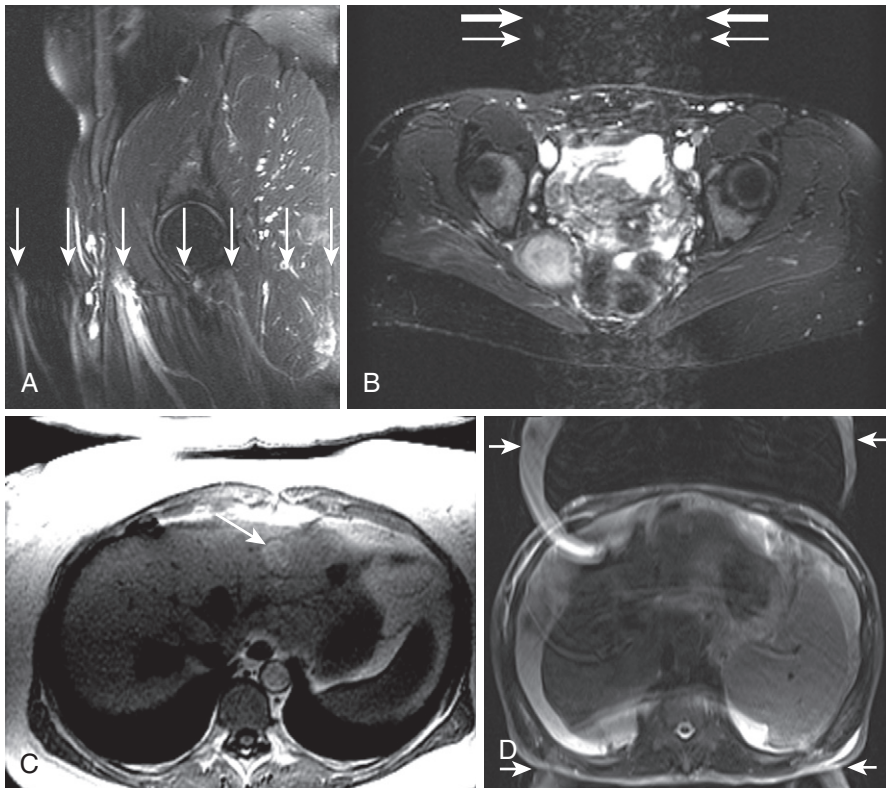


FIGURE 1-34. Motion artifact. A, The sagittal T2-weighted fat-suppressed image shows the effects of motion during image acquisition with phase misregistration of protons in the iliac vessels (*arrows*) portrayed by periodic superimposition across the phase axis—ghosting. B, The same phenomenon (*thin arrows*) occurs along the phase-encoding axis on the corresponding axial image, which is accompanied by phase misregistration of bowel loops due to peristaltic motion (*thick arrows*). C, Occasionally, this artifact simulates a pathologic lesion (*arrow*). The appearance of this pseudolesion (the pulsatile ghost of the aorta) on multiple contiguous images and absence on other sequences resistant to artifact disclose the artifactual etiology. D, Bulk motion from breathing also causes phase-encoding errors reflected by ghosting (*arrows*).

Motion artifact correction	Parameter adjusted	Tradeoffs
Rectangular FOV	Decreased phase FOV (less phase encoding steps acquired)	Phase wraparound (see Fig. 1-37A)
Phase encoding resolution	Decreasing phase matrix (y and z axes—z with 3D technique)	Decreased spatial resolution (decrease phase FOV first)
Fast spin echo	Increasing echo train length (more echoes acquired per excitation pulse)	Increased image blur
Parallel imaging	Decreasing phase encoding (parallel imaging substitutes for phase encoding steps)	Decreased SNR, central wraparound (see Fig. 1-37C)
Respiratory triggering	Segmenting acquisition according to expiratory phase	Increased overall acquisition time
Phase compensation (ROPE)	Reordering the acquisition of echoes according to the phase encoding gradient	Decreased spatial resolution and fine detail
Navigator pulse	Selective pulse targeting diaphragmatic motion	Increased acquisition time
Tissue saturation	Spectral or inversion pulse (usually targeted to hyperintense fat)	Decreased SNR, slightly increased acquisition time
Signal averaging	Increasing signal averages	Increased acquisition time
Gradient moment nulling	Frequency encoding gradient	Increased acquisition time, increased TE

FIGURE 1-35. Strategies to minimize motion artifact. FOV, field of view; ROPE, respiratory-ordered phase encoding; SNR, signal-to-noise ratio; TE, time to excitation.

of the patient (usually anteroposterior) is assigned to the phase-encoding gradient. Careful attention to crop the phase-encoding FOV by reducing the phase-encoding matrix (number of phase-encoding lines) and include only relevant anatomy (and not air surrounding the patient) yields dividends in image acquisition time. Eliminating phase-encoding steps covering air directly reduces scan time (Fig. 1-36). Converting the default square FOV (equal x and y dimensions) to an asymmetrical phase-encoding minimized construct is termed *rectangular FOV*.

Overminimizing the FOV threatens the possibility of wraparound artifact, however (Fig. 1-37).¹⁵ Spatial mapping of received MR signal plots along a periodic spectrum from 0° to 360° in the phase-encoding axis. Spins outside the prescribed phase FOV do not fall within the 0° to 360° phase range. Instead, consider these spins to have phases of either 360 + a° or 0 - b° phase, which plots to the 0 + a° and 360 - b° phase locations, respectively, at the upper and lower margins of the image. Although not problematic when wraparound artifact is superimposed over superfluous anatomy, superimposition over important structures is clearly problematic. The solution is to increase the phase FOV. When implementing parallel

imaging, the problem is exacerbated by the fact that wraparound artifact plots centrally rather than at the periphery of the image (see Fig. 1-37). For this reason, parallel imaging demands greater attention to FOV considerations. Although theoretically wraparound artifact also plagues the frequency-encoding axis when sampled frequencies outside the sampled range are plotted into k space, digital filters eliminate these unwanted frequencies, obviating this problem.

Increasing the ETL also reduces scan time by economizing the utility of each Rf excitation pulse. For each applied Rf excitation pulse, the ETL defines the number of echoes acquired. With increasing ETL, the pulse sequence repetition decreases, resulting in decreased overall scan time. The SSFSE sequence exemplifies the utility of this technique by acquiring all echoes after a single Rf excitation pulse.

Image blur is a potential unwanted side effect of long echo-train imaging. Each successive echo sampled during an echo train possesses a progressively longer TE. When combined to form a single image, the effect of the variable TE is suboptimal edge detection, or blur. The echo with the weakest phase-encoding gradient defines the effective TE (TE_{eff})—understandable,

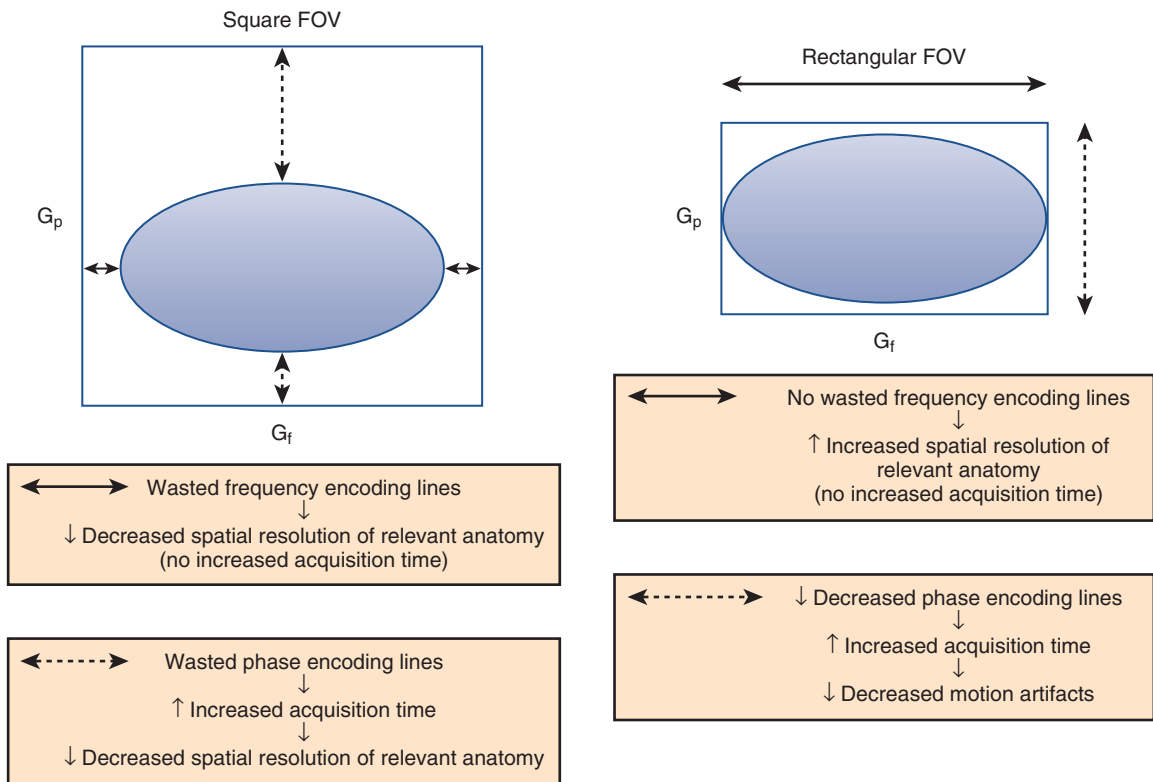


FIGURE 1-36. Rectangular field of view (FOV).

because the weakest gradient defines tissue contrast. Acquiring echoes after the TE_{eff} contributes to blur. For this reason, ETL and TE adjustments follow one another proportionally to minimize blur artifact.

Parallel imaging is the MR counterpart to multidetector-to-multidetector computed tomography (CT) technology (relative to single-slice CT) by maximizing the utility and functionality of the detector system. Parallel imaging uses the differential spatial profiles of the phased array coil elements to reduce k space filling. Undersampled, aliasing k space is unwrapped with mathematical equations using the various spatially dependent coil element sensitivities. The relative amount of coil spatial sensitivity information replacing unwrapping aliased k space is expressed through the coefficient R. Increasing R decreases SNR according to the following equation:

$$SNR = 1/(g \times \sqrt{R}).$$

The geometry factor, g, measures the aliasing unwrapping proficiency of the coil arrangement.

The acceleration factor R applied to parallel imaging describes the proportion of phase-encoding k-space lines filled per Rf excitation pulse. So, an acceleration factor of 2 means that only half of the phase-encoding lines of k space must be filled using the echoes obtained from the pulse sequence. R defines the theoretical upper limit by which acquisition time is reduced (practically speaking, the time saving is generally significantly less).

As a last resort, decreasing spatial resolution in the slice and phase axes diminishes scan time. By decreasing the image matrix in the phase-encoding direction, fewer phase-encoding steps are acquired, decreasing acquisition time, according to the previous equation. Obtaining fewer slices translates to adding the sum of the acquisition time equation together fewer times (i.e., 15 slices instead of 20 means acquisition time $\times 15$ instead of 20).

Alternatively, using physiologic monitoring to determine relatively motionless phases of the cardiac/respiratory cycles, pulse sequences are acquired in fragments during these quiescent phases and subsequently spliced together. This technique involves cardiac or respiratory

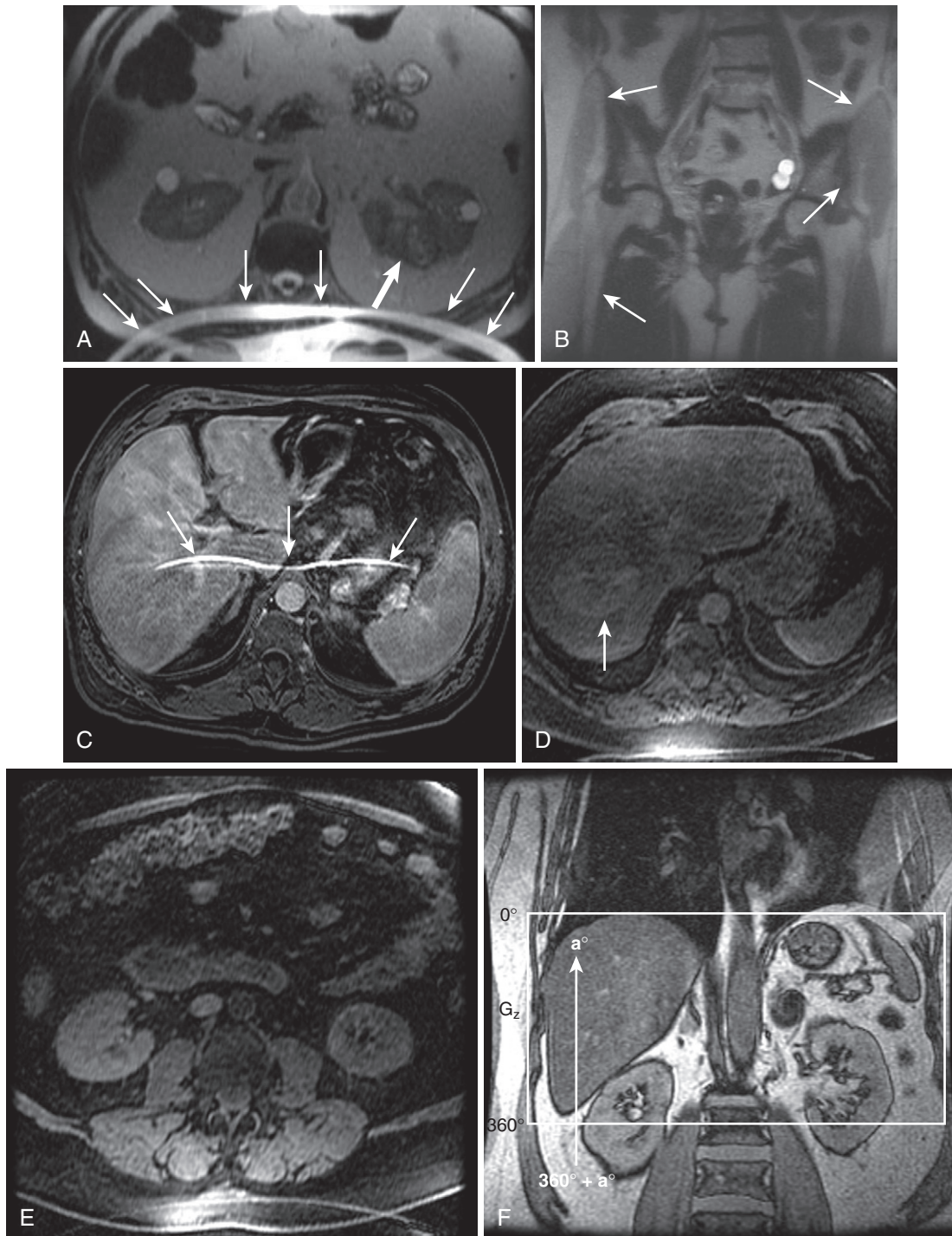


FIGURE 1-37. Wraparound artifact. **A**, The axial T2-weighted image focused on the kidneys demonstrates two-dimensional (2-D) wrap-around artifact (*thin arrows*) because the prescribed field of view (FOV) excludes the anterior abdominal wall (not assigned 0° – 360° phase), causing it to alias—or wraparound—to an anatomically incorrect spatial location. However, the relevant finding—the left renal cell carcinoma (RCC; *thick arrow*)—is not obscured by this artifact. **B**, Wraparound artifact occurs in any acquisition plane, exemplified by the coronal image with right-to-left phase encoding and wraparound artifact (*arrows*). **C**, With parallel imaging, wraparound artifact appears in the middle of the image (*arrows*), forcing prescription of larger FOVs. An apparent enhancing mass in the liver (*arrow*) on the three-dimensional (3-D) postcontrast image (**D**) in a different patient resembles the transverse appearance of the kidney more inferiorly positioned (**E**). This example illustrates wraparound artifact occurring along the second phase-encoding axis in a 3-D acquisition—the slice direction. **F**, *Arrows* outside the volume plotted on the coronal image correspond to tissue prone to 3-D aliasing.

monitoring to trigger each phase of the acquisition. 3-D MRCP and FSE T2-weighted and inversion recovery sequences occasionally employ respiratory triggering (Fig. 1-38). Cardiac monitoring, although integral to chest and cardiac imaging, is rarely employed in abdominal imaging.

Methods of controlling for respiratory motion include respiratory triggering using a bellows (wrapped around the patient's torso designed to detect the inspiratory and expiratory phases) and navigator pulse triggering. The respiratory bellows approach offers two possibilities. Either image acquisition is triggered to occur during the relatively quiescent expiratory phase only, or phase encoding steps are arranged so that central k-space steps are acquired during the quiescent expiratory phase and peripheral k-space steps are acquired during inspiration—known as respiratory compensation or respiratory-ordered phase encoding (ROPE). Since central k-space corresponds to image signal, perceived motion artifact is reduced.

The navigatory system involves a “navigator pulse,” a vertically-oriented column of echoes targeted to the diaphragm to detect diaphragmatic motion. Practically speaking, this sequence maps out diaphragmatic excursion so that image acquisition is timed to occur only

when diaphragmatic motion is minimal (i.e., expiration).

Reducing the signal intensity of tissues contributing to visible motion artifact is another viable strategy for minimizing motion artifact. Spatially and spectrally selective saturation techniques both accomplish this objective in different ways. Spatially selective Rf excitation pulse applied to the vascular inflow outside the image volume followed by a spoiler gradient inducing dephasing eliminates signal from flowing blood, thereby eliminating ghost artifact. Spectrally selective saturation pulses generally target hyperintense fat—especially copious in the abdominal wall—potentially ghosting across the phase-encoding axis.

Another method of reducing signal intensity from tissues contributing to motion artifact involves increasing the signal intensity of tissues relative to artifact. Although counterintuitive, increasing the number of signal averages (NEX) increases the signal intensity of tissues relative to motion artifact, which is not reproducible and not equally intensified compared with body tissues. Of course, while downsizing motion artifact, this technique actually increases the chances of motion artifact and increases the acquisition time.

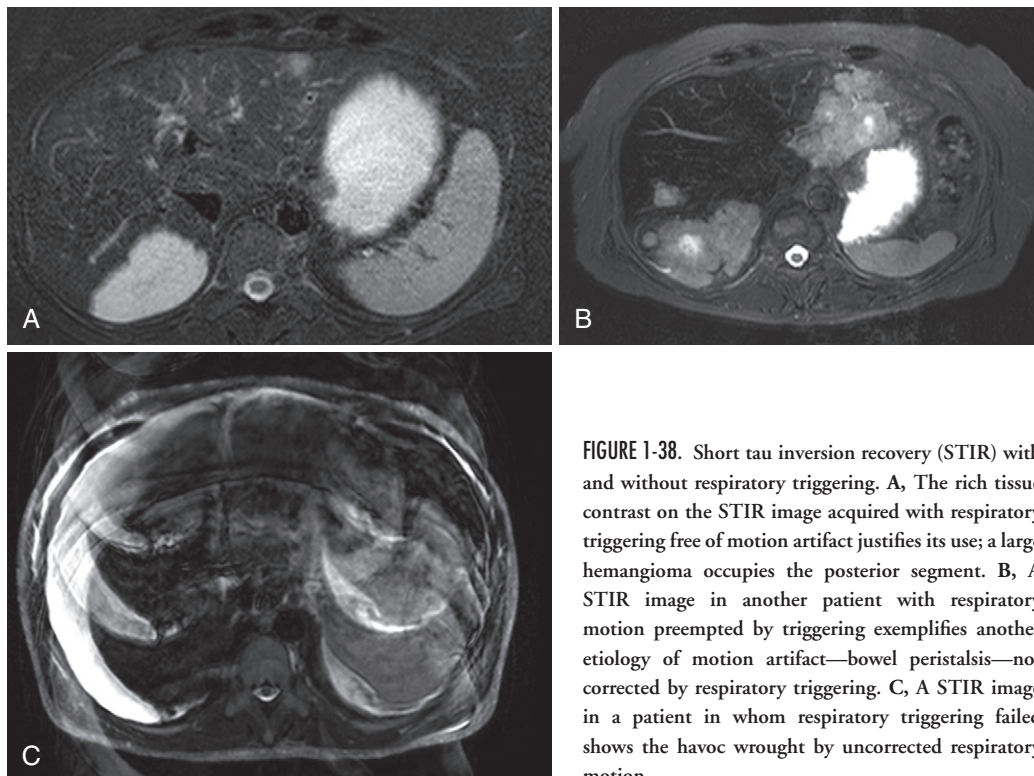


FIGURE 1-38. Short tau inversion recovery (STIR) with and without respiratory triggering. **A**, The rich tissue contrast on the STIR image acquired with respiratory triggering free of motion artifact justifies its use; a large hemangioma occupies the posterior segment. **B**, A STIR image in another patient with respiratory motion preempted by triggering exemplifies another etiology of motion artifact—bowel peristalsis—not corrected by respiratory triggering. **C**, A STIR image in a patient in whom respiratory triggering failed shows the havoc wrought by uncorrected respiratory motion.

Gradient moment nulling (GMN) addresses within-view phase errors and involves manipulation of the magnetic gradient to result in successful rephasing of both static and moving spins. Adding lobes to the standard unipolar dephasing and rephasing lobes of the frequency encoding gradient increases the chances of successful rephasing of static and moving spins (Fig. 1-39).

Susceptibility Artifact

Decreasing scan time dovetails with a problem often arising in body MRI—susceptibility artifact—managed by decreasing scan time. Because most body tissues are diamagnetic (not very magnetizable), proximity to substances with highly magnetic properties—ferromagnetic—induces susceptibility artifact. *Susceptibility artifact* in MRI is defined as signal incoherence generated by the intermingling of substances with discrepant capacities to be magnetized (measured by χ , susceptibility). In the setting of the diamagnetic human body with little to no inherent magnetism to distort the magnetic field, highly magnetic substances with induced magnetic fields of their own corrupt the homogeneity of B_0 . Because protons precess

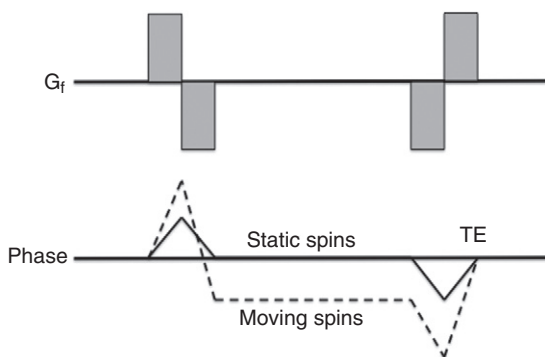


FIGURE 1-39. Gradient moment nulling. TE, time to excitation.

at rates based on the strength of the magnetic field, this magnetic field heterogeneity results in unpredictably random precessional frequencies. Consequently, protons dephase (T_2^*) and signal loss ensues. Because the degree of this random dephasing process is proportional to the time elapsed before the echo, minimizing the echo time minimizes susceptibility artifact (Fig. 1-40).

The problem of susceptibility artifact poses the greatest challenge in the context of surgical hardware and embolization coils (see Fig. 1-27). Surgical clips are generally not highly ferromagnetic and susceptibility artifact is not prohibitively severe. Whereas all pulse sequences experience susceptibility artifact in some measure, the dynamic sequence is most amenable to corrective measures. The FSE and SSFSE sequences inherently address susceptibility artifact through the application of multiple 180° refocusing pulses. The in- and out-of-phase sequence is not subject to corrective measures because the approach to the susceptibility problem centers on lowering the TE (otherwise the desired chemical shift properties are sacrificed). The shorter the TE, the less time elapses during which spin dephasing occurs owing to magnetic susceptibility.

Whereas the dynamic sequence TE is usually set to minimum, a number of adjustments lower the potential minimum TE. For example, fractional echo sampling decreases the time during which the echo reception occurs, decreasing the TE by that incremental amount (Fig. 1-41). This involves sampling slightly more than half of the echo, thereby filling slightly more than half of k space in the frequency dimension. Because of the symmetry of k space, the remainder is interpolated. The time saving is counterbalanced by a reduction in SNR (usually not problematic in inherently SNR-rich 3-D acquisitions). In order to take advantage of this technique, another competing parameter modification must be disabled—partial Fourier

Parameter adjusted	Effect
Minimize TE	Less time for susceptibility artifact to occur
Fractional echo sampling	Decreased TE, decreased SNR
Increased receiver bandwidth	Faster echo sampling → decreased TE, decreased SNR
Eliminate fat saturation	Preclude variable fat saturation

FIGURE 1-40. Strategies to minimize susceptibility artifact. SNR, signal-to-noise ratio; TE, time to excitation.

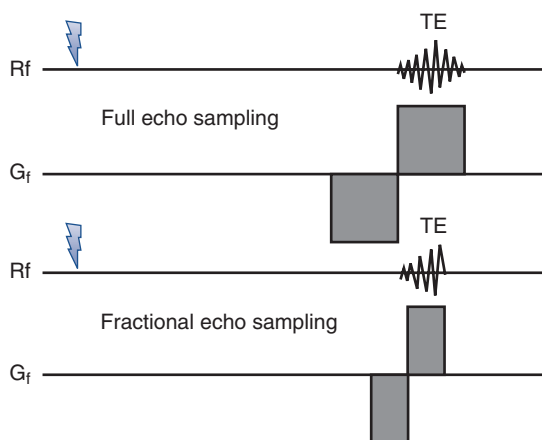


FIGURE 1-41. Fractional echo sampling. Rf, radiofrequency; TE, time to excitation.

acquisition. Whereas fractional echo sampling involves filling k space partially in the frequency domain, partial Fourier acquisition involves partial k -space filling in the phase domain. These techniques are generally mutually exclusive owing to SNR reduction.

Another method to minimize TE and susceptibility artifact accomplishes the same feat of decreased echo sampling time—increasing the receiver (or receiver) bandwidth. The receiver bandwidth defines the rate at which the echo is sampled by the receiver. Increased receiver bandwidth samples faster with a greater range of sampled frequencies, which includes more noise and less relevant signal-generated frequencies. So, although time is saved, thereby decreasing the TE, SNR is compromised (generally not prohibitively with 3-D sequences) (Fig. 1-42).

By altering spin precessional frequencies, susceptibility artifact also wreaks havoc on spectrally selective Rf pulses, such as fat saturation (in addition to inducing signal loss due to spin dephasing). Therefore, consider eliminating fat suppression on the dynamic sequence in the setting of susceptibility artifact. The fat suppression Rf excitation pulse depends on reliably predictable precessional fat proton frequency. Variable precessional frequencies result in incomplete fat proton excitation and subsequently incomplete dephasing by the ensuing spoiler gradient.

MRI SAFETY

MRI incurs a number of potential hazards to patients and employees if proper care and adherence to established guidelines is not considered.

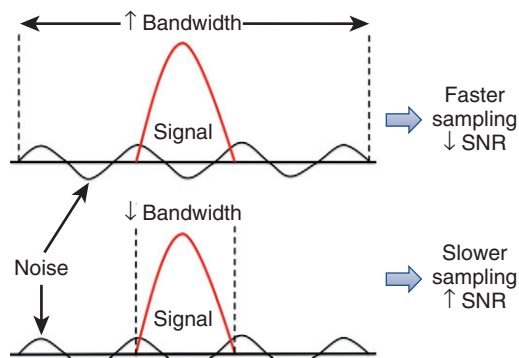


FIGURE 1-42. Receiver bandwidth. SNR, signal-to-noise ratio.

Potential problems arise from the magnetic field, the cryogenics, the gradient coils, the Rf transmitter, contrast agents, and the configuration of the MR system itself—claustrophobia (Fig. 1-43). In order to preempt at least most of these problems, careful screening must be undertaken. Ideally, screening begins at the referring physician's office. Realistically, this never happens. Redundancy of screening at the time of scheduling, registration, and immediately before scanning minimizes the risk of complications. Documenting and guiding the execution of the screening process with a screening form are critical (Fig. 1-44).

Patient safety concerns arising from the magnetic field are twofold—complications arising from the static magnetic field and from induced time-varying magnetic fields.^{16,17} According to the latest guidelines generated by the U.S. Food and Drug Administration (FDA), clinical MR systems with static magnetic fields up to 8 Tesla pose no significant biologic effects to adults. MR systems in routine clinical practice range up to 3 Tesla.

The most prevalent threat due to the static magnetic field is the attractive force on ferromagnetic objects. B_0 in a 1.5-Tesla magnet is 15,000 times as strong as the earth's magnetic force. The attraction to ferromagnetic objects is proportionally stronger and metallic objects experience projectile behavior in proximity to B_0 . The attractive force increases exponentially with proximity to B_0 —half the distance quadruples the attractive force. The likelihood of this phenomenon is a function of the fringe field, extending centrifugally away from the bore of the magnet (Fig. 1-45). The fringe field does not respect normal structural elements, such as ceilings, walls, and doors, and the fringe field must be contained by passive and/or active shielding.

Static Magnetic Field	Gradient Coil System	Radiofrequency Transmitter System	Cryogenics	Contrast Agents	Patient Factors
Projectile effect	Acoustic noise	Energy deposition (SAR)	Quenching	Nephrogenic systemic fibrosis	Claustrophobia
Implanted device failure	Peripheral stimulation	Conduction effects		Contrast-induced nephropathy (rare)	Discomfort
Implanted device torque	Visual stimulatory effects			Acute reactions	

FIGURE 1-43. MRI safety issues.

The goal of shielding is to minimize the fringe field so that the perimeter of potential harmful effects is reduced. Passive shielding involves enveloping the magnet within material that counteracts B_0 ; active shielding passes current through coils on the exterior of the magnet, generating a magnetic field that opposes B_0 . By containing the fringe field, shielding eliminates the interference with devices such as pacemakers and video monitors, which safely operate below field strengths of 0.5 mT and 0.1 mT, respectively. Accordingly, access below the fringe field strength at 0.5 mT, or 5 gauss (1 Tesla = 104 gauss), must be vigilantly guarded to prevent untoward accidents (see Fig. 1-45). The term *5-gauss line* communicates the presence of this invisible barrier that MR personnel observe to protect patients (with pacemakers) from magnetic field effects. The American College of Radiology (ACR) promotes the concept of static field safety zones.¹⁸ Zones 1 through 4 describe increased levels of vigilance and stringency to access in order to prevent inadvertent exposure to the fringe field (Fig. 1-46).

Because of the number of devices that are potentially incompatible with a strong magnetic field, vigilance is warranted (for a comprehensive MRI compatibility, see “The List” at www.mrisafety.com). Generally contraindicated devices include pacemakers, cochlear implants, and intraorbital metallic foreign bodies. Most other artificially implanted or inserted devices or objects usually incur no risk from the static magnetic field, including frequently encountered shrapnel, heart valves, inferior vena cava filters, and orthopedic

implants. Recently implanted devices, such as vascular stents, deserve caution and exposure to the magnetic field is generally delayed for 6 weeks to allow for the ingrowth of granulation tissue to prevent deflection and migration. Whereas almost all of these artificial devices pose no health risk, most induce at least some degree of susceptibility artifact and appropriate measures address this problem, as previously discussed.

The gradient coils, used to generate the magnetic field gradients for spatial localization, engender time-varying magnetic fields (TVMFs). TVMFs induce electric current in conductive media, according to Faraday’s Law of Induction. The potential clinical manifestations reflect peripheral nerve stimulation—including muscular contractions and cutaneous sensory disturbances—and retinal phosphene stimulation, inducing visual disturbances. FDA limits TVMFs to 6 T/sec and sequences with the fastest gradient-switching needs, such as echo planar imaging, incur the greatest risk.

TVMFs pose another serious risk—burns. Conducting materials, such as monitoring cables, permit the flow of current induced by TVMFs, which is facilitated in the setting of a loop configuration (which increases inductance and therefore current). Ohmic heating—the dissipation of heat by a conductor transmitting current—ensues, potentially resulting in burns. All looped devices—including leg crossing—must be eliminated to minimize the risk of this complication.

The other side effect of passing current through the gradient coils is acoustic noise.¹⁹ Rapid gradient switching in the presence of a strong magnetic field generates the loud noise

MAGNETIC RESONANCE (MR) PROCEDURE SCREENING FORM FOR PATIENTS

Date ____/____/____ Patient Number _____

Name _____ Age _____ Height _____ Weight _____
Last name First name Middle Initial

Date of Birth ____/____/____ Male Female Body Part to be Examined _____
month day year

Address _____ Telephone (home) (____) ____-____

City _____ Telephone (work) (____) ____-____

State _____ Zip Code _____

Reason for MRI and/or Symptoms _____

Referring Physician _____ Telephone (____) ____-____

1. Have you had prior surgery or an operation (e.g., arthroscopy, endoscopy, etc.) of any kind? No Yes

If yes, please indicate the date and type of surgery:

Date ____/____/____ Type of surgery _____

Date ____/____/____ Type of surgery _____

2. Have you had a prior diagnostic imaging study or examination (MRI, CT, Ultrasound, X-ray, etc.)? No Yes

If yes, please list: Body part Date Facility

MRI _____/____/____ _____

CT/CAT Scan _____/____/____ _____

X-Ray _____/____/____ _____

Ultrasound _____/____/____ _____

Nuclear Medicine _____/____/____ _____

Other _____/____/____ _____

3. Have you experienced any problem related to a previous MRI examination or MR procedure? No Yes

If yes, please describe: _____

4. Have you had an injury to the eye involving a metallic object or fragment (e.g., metallic slivers, shavings, foreign body, etc.)? No Yes

If yes, please describe: _____

5. Have you ever been injured by a metallic object or foreign body (e.g., BB, bullet, shrapnel, etc.)? No Yes

If yes, please describe: _____

6. Are you currently taking or have you recently taken any medication or drug? No Yes

If yes, please list: _____

7. Are you allergic to any medication? No Yes

If yes, please list: _____

8. Do you have a history of asthma, allergic reaction, respiratory disease, or reaction to a contrast medium or dye used for an MRI, CT, or X-ray examination? No Yes

9. Do you have anemia or any disease(s) that affects your blood, a history of renal (kidney) disease, renal (kidney) failure, renal (kidney) transplant, high blood pressure (hypertension), liver (hepatic) disease or seizures? No Yes

If yes, please describe: _____

For female patients:

10. Date of last menstrual period: ____/____/____ Post menopausal? No Yes

11. Are you pregnant or experiencing a late menstrual period? No Yes


12. Are you taking oral contraceptives or receiving hormonal treatment? No Yes

13. Are you taking any type of fertility medication or having fertility treatments? No Yes

If yes, please describe: _____

14. Are you currently breastfeeding? No Yes

FIGURE 1-44. MRI screening form.

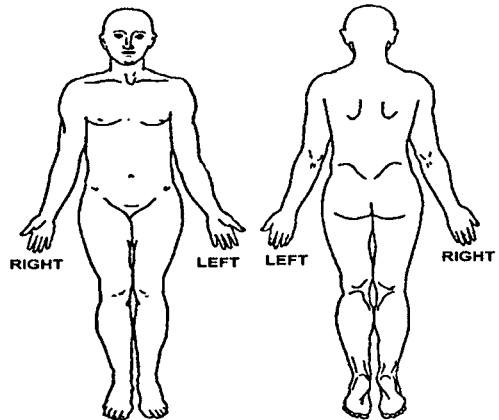


WARNING: Certain implants, devices, or objects may be hazardous to you and/or may interfere with the MR procedure (i.e., MRI, MR angiography, functional MRI, MR spectroscopy). Do not enter the MR system room or MR environment if you have any question or concern regarding an implant, device, or object. Consult the MRI Technologist or Radiologist **BEFORE** entering the MR system room. The MR system magnet is **ALWAYS** on.

Please indicate if you have any of the following:

- Yes No Aneurysm clip(s)
- Yes No Cardiac pacemaker
- Yes No Implanted cardioverter defibrillator (ICD)
- Yes No Electronic implant or device
- Yes No Magnetically-activated implant or device
- Yes No Neurostimulation system
- Yes No Spinal cord stimulator
- Yes No Internal electrodes or wires
- Yes No Bone growth/bone fusion stimulator
- Yes No Cochlear, otologic, or other ear implant
- Yes No Insulin or other infusion pump
- Yes No Implanted drug infusion device
- Yes No Any type of prosthesis (eye, penile, etc.)
- Yes No Heart valve prosthesis
- Yes No Eyelid spring or wire
- Yes No Artificial or prosthetic limb
- Yes No Metallic stent, filter, or coil
- Yes No Shunt (spinal or intraventricular)
- Yes No Vascular access port and/or catheter
- Yes No Radiation seeds or implants
- Yes No Swan-Ganz or thermodilution catheter
- Yes No Medication patch (Nicotine, Nitroglycerine)
- Yes No Any metallic fragment or foreign body
- Yes No Wire mesh implant
- Yes No Tissue expander (e.g., breast)
- Yes No Surgical staples, clips, or metallic sutures
- Yes No Joint replacement (hip, knee, etc.)
- Yes No Bone/joint pin, screw, nail, wire, plate, etc.
- Yes No IUD, diaphragm, or pessary
- Yes No Dentures or partial plates
- Yes No Tattoo or permanent makeup
- Yes No Body piercing jewelry
- Yes No Hearing aid
- Yes No *(Remove before entering MR system room)*
- Yes No Other implant _____
- Yes No Breathing problem or motion disorder
- Yes No Claustrophobia

Please mark on the figure(s) below the location of any implant or metal inside of or on your body.





IMPORTANT INSTRUCTIONS

Before entering the MR environment or MR system room, you must remove **all** metallic objects including hearing aids, dentures, partial plates, keys, beeper, cell phone, eyeglasses, hair pins, barrettes, jewelry, body piercing jewelry, watch, safety pins, paperclips, money clip, credit cards, bank cards, magnetic strip cards, coins, pens, pocket knife, nail clipper, tools, clothing with metal fasteners, & clothing with metallic threads.

Please consult the MRI Technologist or Radiologist if you have any question or concern **BEFORE** you enter the MR system room.

NOTE: You may be advised or required to wear earplugs or other hearing protection during the MR procedure to prevent possible problems or hazards related to acoustic noise.

I attest that the above information is correct to the best of my knowledge. I read and understand the contents of this form and had the opportunity to ask questions regarding the information on this form and regarding the MR procedure that I am about to undergo.

Signature of Person Completing Form: _____ Date ____/____/____
Signature

Form Completed By: Patient Relative Nurse _____
Print name Relationship to patient

Form Information Reviewed By: _____
Print name Signature

MRI Technologist Nurse Radiologist Other _____

FIGURE 1-44, cont'd

experienced by the patient during scanning. Ear plugs or MR-compatible earphones mitigate this problem.

The deposition of energy by the transmitted Rf energy (i.e., Rf excitation pulse, refocusing pulse) potentially imposes harmful biologic effects. This quantity is measured by specific absorption rate (SAR), expressed in Watts/kilogram. Patient weight and pulse sequence parameters figure most prominently into this calculation. The FDA imposes SAR limits based on an increase of 1°C in core body temperature (e.g., 4 W/kg for whole body exposure), and most modern MR systems calculate SAR before each pulse sequence, avoiding excessive SAR levels.

One of the most potentially lethal risks in MRI is quenching. *Quenching* refers to the abrupt heating of the cryogen, converting from liquid to gaseous form. Helium in gaseous form supplants oxygen, threatening suffocation, and critically elevates pressure, potentially preventing entrance to the magnet room. Quenching risks to the patient include asphyxiation, tympanic

membrane rupture (due to pressure effects), and hypothermia.

Intravenous gadolinium formulations (Fig. 1-47)²⁰ pose potentially harmful—even lethal—effects, albeit extremely rare (Fig. 1-48). Minor complications include headaches, nausea, vomiting, rash, and hypotension. The overall incidence of adverse reactions approximates 0.2%.²¹⁻²³ Most reactions fall into the acute category and the vast majority are minor and treated conservatively with observation. Chronic reactions include contrast-induced nephropathy (CIN) and nephrogenic systemic fibrosis (NSF). CIN occurs much less commonly after gadolinium administration than with iodinated contrast materials. Risk factors for CIN include diabetes mellitus, renal insufficiency, intravascular volume depletion, reduced cardiac output, and concomitant nephrotoxins.

Between 200 and 300 cases of NSF have been reported worldwide. Originally dubbed “nephrogenic fibrosing dermopathy” (NFD) in the 1990s, skeletal muscle, lung, myocardium, and liver involvement superimposed on preeminent skin manifestations prompted the name change to NSF. More cases of NSF have been reported after the use of gadodiamide (Omniscan) and gadoversetamide (OptiMARK) compared with other contrast agents, and the use of newer agents, such as gadoxetate disodium (Eovist) and gadobenate dimeglumine (Multihance), with greater relaxivity and decreased dosing potentially reduces the risk of NSF. The calculated glomerular filtration rate (GFR) establishes the risk category of gadolinium administration—normal: $GFR > 60 \text{ mL/min/1.73 m}^2 = \text{no risk}$; mild-moderate renal insufficiency: $30 < GFR < 60 \text{ mL/min/1.73 m}^2 = \text{minimal if any risk}$; severe renal insufficiency: $GFR < 30 \text{ mL/min/1.73 m}^2 =$

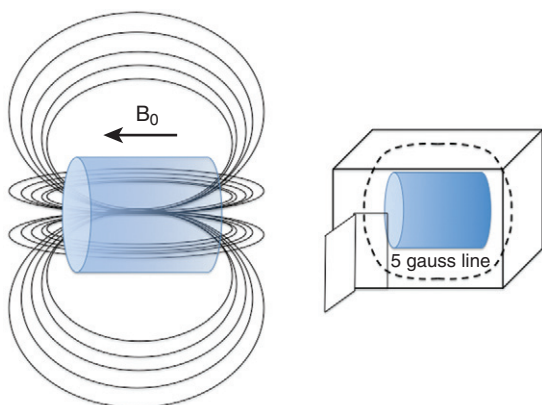


FIGURE 1-45. The fringe field.

Zone	Access	Environment	Details
1	General public	Outside MR facility	
2	Patients undergoing screening, paperwork, etc.	Reception, patient dressing and holding areas, etc.	Supervised by MR personnel; interception of ferromagnetic objects; venue for patient screening
3	MR personnel and screened patients	Control room, computer room, etc.	Restricted access; includes all areas with fringe field >5 gauss
4	MR personnel and screened patients	Scanner room	Labeled as hazardous

FIGURE 1-46. American College of Radiology (ACR) magnetic resonance (MR) safety zones.

Brand Name	Chemical Name	Structure	Ionicity	Clearance, T (hours)	Relaxivity
Magnevist	Gadopentetate dimeglumine (Gd-DTPA)	Linear	Ionic	Renal, 1.6	4.3
Prohance	Gadoteridol (Gd-HP-DO3A)	Macro-cyclic	Non-ionic	Renal, 1.57	4.4
Omniscan	Gadodiamide (Gd-DTPA-BMA)	Linear	Non-ionic	Renal, 1.3	4.6
OptiMARK	Gadoversetamide (Gd-DTPA-BMEA)	Linear	Non-ionic	Renal, 1.73	5.2
Multihance	Gadobenate dimeglumine (Gd-BOPTA)	Linear	Non-ionic	Renal (96%)/hepatic (4%), up to 2 hrs	6.7
Eovist	Gadoxetate disodium (Gd-EOB-DTPA)	Linear	Ionic	Renal (50%)/hepatic (50%), 0.95	8.7

FIGURE 1-47. Gadolinium formulations.

A c c u t e	Mild <ul style="list-style-type: none"> • Nausea • Vomiting • Cough • Warmth • Headache • Dizziness • Shaking • Taste alteration • Itching • Pallor • Flushing • Chills • Sweats • Rash/hives • Nasal congestion • Eye/face swelling • Anxiety 	Moderate <ul style="list-style-type: none"> • Generalized or diffuse erythema • Dyspnea • Bronchospasm • Wheezing • Mild hypotension/hypertension • Tachycardia/bradycardia 	Severe <ul style="list-style-type: none"> • Laryngeal edema • Unresponsiveness • Cardiopulmonary arrest • Convulsions • Profound hypotension • Arrhythmias
	C h r o n i c	<ul style="list-style-type: none"> • Contrast-induced nephropathy (CIN) • Nephrogenic systemic fibrosis (NSF) 	

FIGURE 1-48. Adverse reactions to gadolinium agents.

potential risk. Based on this scheme, gadolinium aversion in patients with GFR less than 30 is recommended.

Another circumstance in which gadolinium administration is not recommended is pregnancy.²⁴ Gadolinium passes across the placenta, entering the fetal circulation, and is excreted by the fetal kidneys into the amniotic fluid, where it potentially dissociates threatening harmful effects. However, the risk to the fetus/embryo is unknown, relegating gadolinium use in pregnancy to the class C drug category. The (theoretical) risk-benefit ratio recommends gadolinium abstinence during pregnancy.

MRI imposes no known biologic effects on the fetus. However, the theoretical risk of subjecting dividing cells undergoing organogenesis

to electromagnetic fields prompts circumspection, especially during the first trimester. The decision to scan a pregnant patient reduces to a risk-benefit analysis. Whereas the risk is unknown and theoretical, the benefit should be tangible to justify the study. For example, in cases of suspected appendicitis, MRI threatens less fetal harm than the effects of ionizing radiation incurred during CT scanning, justifying the use of MRI in this potentially life-threatening circumstance.²⁵

SUMMARY

Although MRI avoids ionizing radiation present in other imaging modalities and employs contrast media with less risk of serious

complications, a finite risk of complications exists. Careful, redundant screening minimizes unnecessary exposure to patients at elevated risk of complications, such as patients with implanted electronic devices or foreign bodies and patients with severe renal insufficiency.

The process of obtaining images in MRI involves a complex interplay of multiple components with specific functions. MRI presupposes a strong magnetic field, on the order of 15,000 times the strength of the earth's magnetic field, in order to prime protons for perturbations inducing them to release energy ultimately converted to images. An Rf transmitter emits the necessary energy tuned to the frequency of precessing protons, which deflect to a higher energy state momentarily and subsequently release energy received by a specialized receiver coil. Gradient coils inducing magnetic field gradients during this process encode spatial information into this released energy, which is then deposited in k space and decoded by the Fourier transform.

An almost infinite number of parameters and pulse sequence variations complicate body MRI. A rational approach dividing conventional pulse sequences into T1-weighted and T2-weighted sequences simplifies the confusing nomenclature and myriad of vendor-specific options. Articulating the tissue-specific directive of each pulse sequence facilitates understanding body MRI (see Fig. 1-26). The tissue-specific objective must be preserved in confronting the various artifacts in body MRI in order to maintain the integrity of the pulse sequence. Motion and susceptibility artifact most frequently plague MR image acquisition and are handled most efficiently and practically with time-saving maneuvers.

Condensing the physical principles of (body) MRI into this brief synopsis inevitably trivializes its complexity and the time and effort required to master it. Truly understanding this densely rich specialty mandates a multifaceted approach involving learning the basic physics and clinical applications, analyzing image quality and artifacts, learning from and interacting with the technologists, and appreciating the specific utility of each pulse sequence.

References

- Pooley RA. AAPM/RSNA Physics Tutorial for Residents: Fundamental physics of MR imaging. *Radiographics* 25:1087-1099, 2005.
- Pavlicek W. MR instrumentation and image formation. *Radiographics* 7:809-814, 1987.
- Fullerton GD. Magnetic resonance imaging signal concepts. *Radiographics* 7:579-596, 1987.
- Bitar R, Leung G, Perng R, et al. MR pulse sequences: What every radiologist wants to know but is afraid to ask. *Radiographics* 30:513-537, 2010.
- Mitchell DG. *MRI Principles*, 2nd ed. Philadelphia: Saunders, 2004.
- Brown MA, Semelka RC. *MRI Basic Principles and Applications*, 4th ed. Hoboken, NJ: John Wiley & Sons, 2010.
- Lufkin RB. *The MRI Manual*, 2nd ed. St. Louis: Mosby, 1997.
- Hashemi RH, Bradley Jr WG, Lisanti CJ. *MRI the Basics*, 2nd ed. Philadelphia: Lippincott Williams & Wilkins, 2004.
- Westbrook C, Kaut C. *MRI in Practice*, 3rd ed. Oxford: Blackwell, 2005.
- Gallagher TA, Nemeth AJ, Haccin-Bey L. Pictorial essay: An introduction to the Fourier transform: Relationship to MRI. *AJR Am J Roentgenol* 190:1396-1405, 2008.
- Bitar R, Leung G, Perng R, et al. MR pulse sequences: What every radiologist wants to know but is afraid to ask. *Radiographics* 26:513-537, 2006.
- Plewes DB. The AAPM/RSNA Physics Tutorial for Residents: Contrast mechanisms in spin-echo MR imaging. *Radiographics* 14:1389-1404, 1994.
- Yang RK, Roth CG, Ward RJ, et al. Optimizing abdominal MR imaging: Approaches to common problems. *Radiographics* 30:185-199, 2010.
- Glockner JF, Houchun HH, Stanley BS, et al. Parallel MR imaging: A user's guide. *Radiographics* 25:1279-1297, 2005.
- Arena L, Morehouse HT, Safir J. MR imaging artifacts that simulate disease: How to recognize and eliminate them. *Radiographics* 15:1373-1394, 1995.
- Zhuo J, Gullapalli RP. AAPM/RSNA Physics Tutorial for Residents: MR artifacts, safety, and quality control. *Radiographics* 26:275-297, 2006.
- Price RP. The AAPM/RSNA Physics Tutorial for Residents: MR imaging safety considerations. *Radiographics* 19:1641-1651, 1999.
- Kanal E, Barkovich AJ, Bell C, et al. ACR Guidance Document for Safe MR Practices: 2007. *AJR Am J Roentgenol* 188:1-27, 2007.
- Heverhagen JT. Noise measurement and estimation in MR imaging experiments. *Radiology* 245:638-639, 2007.
- Bellin M-F. MR contrast agents, the old and the new. *Eur J Radiol* 60:314-323, 2006.
- Abujudeh HH, Kosaraju VK, Kaewlai R. Acute adverse reactions to gadopentetate dimeglumine and gadobenate dimeglumine: Experience with 32,659 injections. *AJR Am J Roentgenol* 194:430-434, 2010.
- Hunt CH, Hartman RP, Hesley GK. Frequency and severity of adverse effects of iodinated and gadolinium contrast materials: Retrospective review of 456,930 doses. *AJR Am J Roentgenol* 193:1124-1127, 2009.
- Li A, Wong CS, Wong MK, et al. Acute adverse reactions to magnetic resonance contrast media—gadolinium chelates. *Br J Radiol* 79:368-371, 2006.
- Patel SF, Reede DL, Katz DS, et al. Imaging the pregnant patient for nonobstetric conditions: Algorithm and radiation dose considerations. *Radiographics* 27:1705-1722, 2007.
- Cobben LP, Haans L, Blickman JG, et al. MRI for clinically suspected appendicitis during pregnancy. *AJR Am J Roentgenol* 183:671-675, 2004.



MRI of the Liver

INTRODUCTION

Magnetic resonance imaging (MRI) is the most comprehensive and definitive noninvasive modality for evaluating the liver. A combination of enhancement characteristics and exquisite tissue contrast allows for characterization of liver lesions. Unique artifacts—such as susceptibility and chemical shift—allow for sensitive detection of hepatic iron and lipid deposition, respectively. Common indications for liver MRI include liver lesion characterization, hepatic steatosis quantification and surveillance, liver surveillance in patients with risk factors for hepatocellular carcinoma (HCC), metastatic workup in patients diagnosed with cancer, and further investigation for patients with abnormal liver enzymes of unknown etiology (Table 2-1).

TECHNIQUE

The need to achieve high spatial resolution promptly—within a breathhold—demands rapid imaging capabilities. Because signal-to-noise ratio (SNR) is the rate-limiting step, scanners yielding more SNR scan faster. Because SNR increases roughly proportionally to magnetic field strength, high-field systems are capable of shorter acquisition times compared with their low-field counterparts, minimizing motion artifact while preserving SNR. Practically speaking, 1.0 Tesla defines the threshold below which abdominal imaging suffers from prohibitively low SNR and long acquisition times promoting (breathing) motion artifact (Fig. 2-1). With diminishing field strength, image quality declines generally below acceptable levels (Fig. 2-2; see also Fig. 2-1).

A quality examination demands a coil dedicated to the region of interest (ROI)—an abdominal phased array torso coil, which is wrapped around the abdomen. The body coil built into the gantry of the magnetic resonance (MR) system is a suboptimal alternative yielding less signal commensurate with the increased

distance from the patient and ROI. Most torso coils afford the use of parallel imaging (MRI's counterpart to multidetector computed tomography [CT]) to further lower acquisition times. Acquisition times drop in proportion to the parallel imaging factor—a measure of the degree of parallel imaging incorporated into the pulse sequence—facilitating breathholding (although SNR also drops).

Intravenous gadolinium is routinely administered unless contraindicated by a previously documented reaction to gadolinium or a significant risk of nephrogenic systemic fibrosis (NSF) in cases of severe renal failure (glomerular filtration rate [GFR] < 30 mL/min). With lesser degrees of renal insufficiency (GFR 30–60 mL/min), gadolinium formulations with higher relaxivity permit a lower dose, theoretically minimizing the risk of NSF (Table 2-2). The standard dose is 0.1 mmol/kg; smaller doses (0.5–0.7 mmol/kg) of agents with greater relaxivity are administered in patients with renal insufficiency.

Dynamic imaging—repetitive imaging of the same ROI before and repeatedly after gadolinium—depicts the duality of hepatic blood supply and detects underlying lesions with aberrant blood supply. Dynamic imaging relies on reproducible, rapid contrast delivery best achieved by power injecting (2–3 mL/sec). Timing the acquisition of the arterial phase images is critical and multiple techniques serve to gauge the arrival of contrast into the arterial system to accurately time the arterial phase of the examination (Fig. 2-3). The timing bolus is the time-tested and least technically sensitive method. After an injection of a small volume of contrast (2–3 mL), a T1-weighted gradient-echo (GE) image is obtained at the level of the abdominal aorta until enhancement is detected—defining the onset of the arterial phase. The application of superior and inferior saturation pulses removes pseudoenhancement of the aorta and inferior vena cava (IVC), respectively, due to the inflow effect.

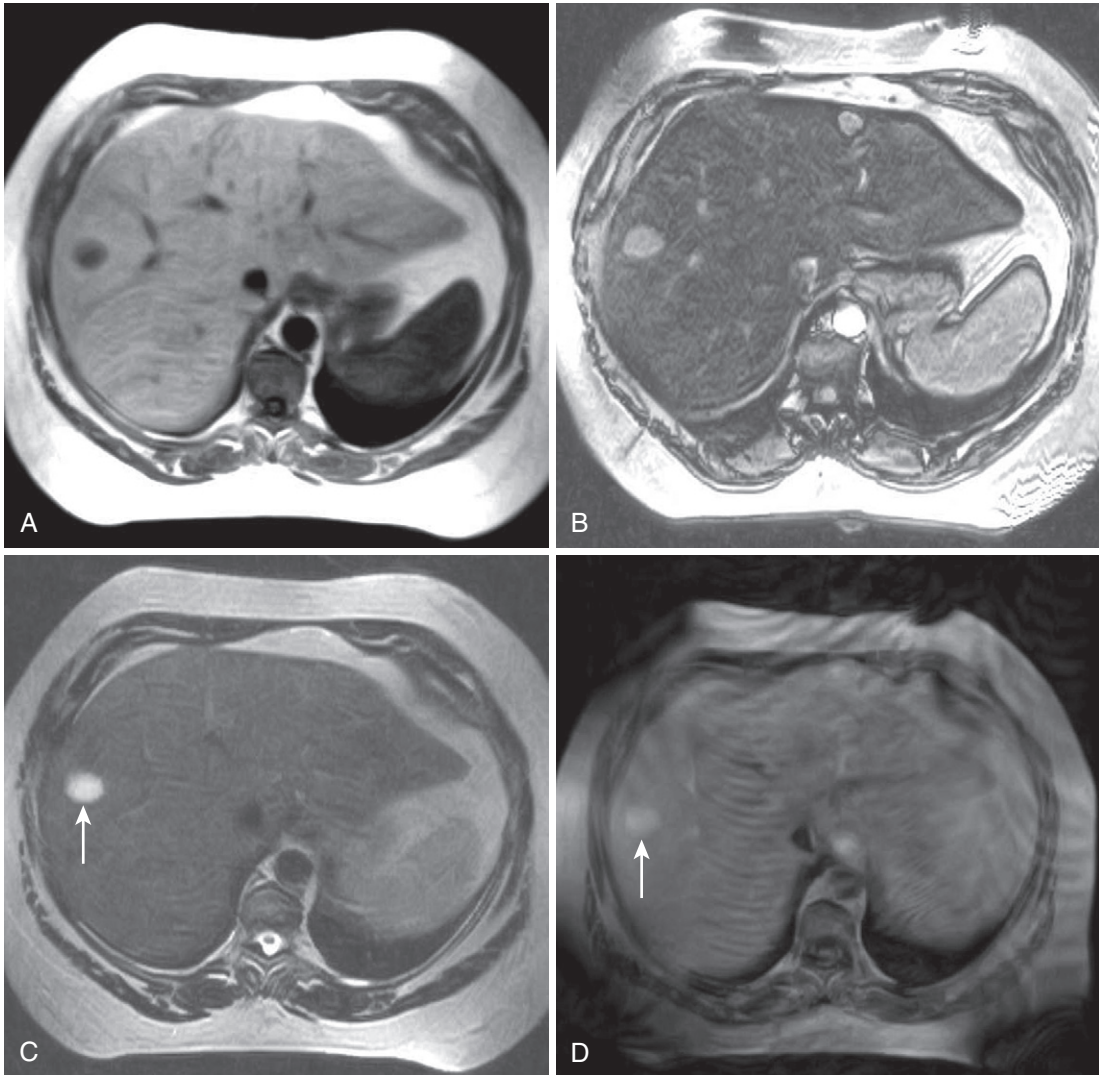


FIGURE 2-1. Liver magnetic resonance imaging (MRI) obtained on a 0.3-Tesla system. Axial in-phase (A) and out-of-phase (B) images display relatively markedly diminished signal throughout the liver on the out-of-phase image compared with the in-phase image, indicating fatty infiltration. The axial T2-weighted image (C) reveals a small hyperintense lesion (*arrow* in C and D), which enhances as seen on the delayed T1-weighted gradient echo image (D), degraded by low signal-to-noise ratio and breathing motion artifact.

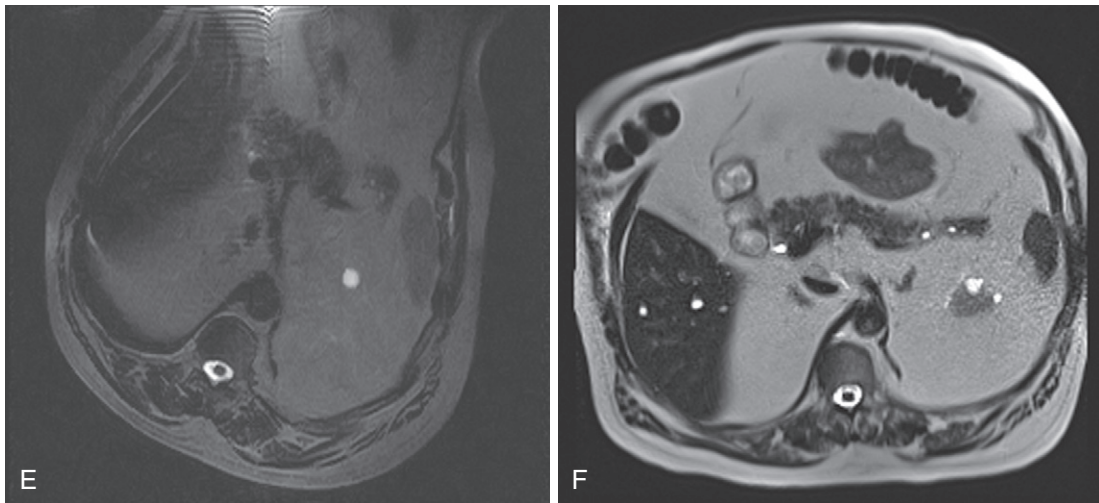


FIGURE 2-1, cont'd Axial T2-weighted image obtained on a different patient on a 0.3-Tesla system (E) demonstrates prohibitive artifact distorting the image beyond diagnostic utility compared with the corresponding image (F) from a follow-up study performed on a 1.5-Tesla short-bore, open-configuration system.

TABLE 2-1. Common Indications for Liver Magnetic Resonance Imaging

Indication	Imaging Objective	Details
Liver lesion characterization	Definitive lesion diagnosis (usually detected on CT, US)	
Known or suspected metastasis	Exclude or detect metastases from gastrointestinal, pancreatic breast, melanoma, or other primary tumors	
Elevated LFTs	Exclude or detect biliary obstruction and potential obstructing mass or stones, parenchymal disease due to inflammation or underlying lesions	
Chronic liver disease/cirrhosis	Exclude or detect hepatocellular carcinoma, evaluate vascular structures for patency, assess for portal hypertension, assess degree of cirrhosis	
Portal venous patency	Identify normal enhancement and absence of filling defect, recanalization or collateralization	Consider ↑ dose gadolinium, SSFP
Hepatic steatosis	Quantify degree of steatosis, assess for development of cirrhosis	Consider spectroscopy
Iron deposition	Liver iron quantification; involvement of pancreas, spleen, bone marrow, myocardium	Specific protocol for Fe quantification
Response to treatment	Identification of residual/recurrent viable tumor after percutaneous, intra-arterial, or systemic therapy	
Hepatocellular carcinoma	Assess size, multifocality and vascular invasion	Correlate with alpha-fetoprotein levels
Cholangiocarcinoma	Assess size, extent of biliary involvement, lobar atrophy, lymphadenopathy, vascular invasion	

CT, computed tomography; LFTs, liver function tests; SSFP, steady state free precession; US, ultrasound.

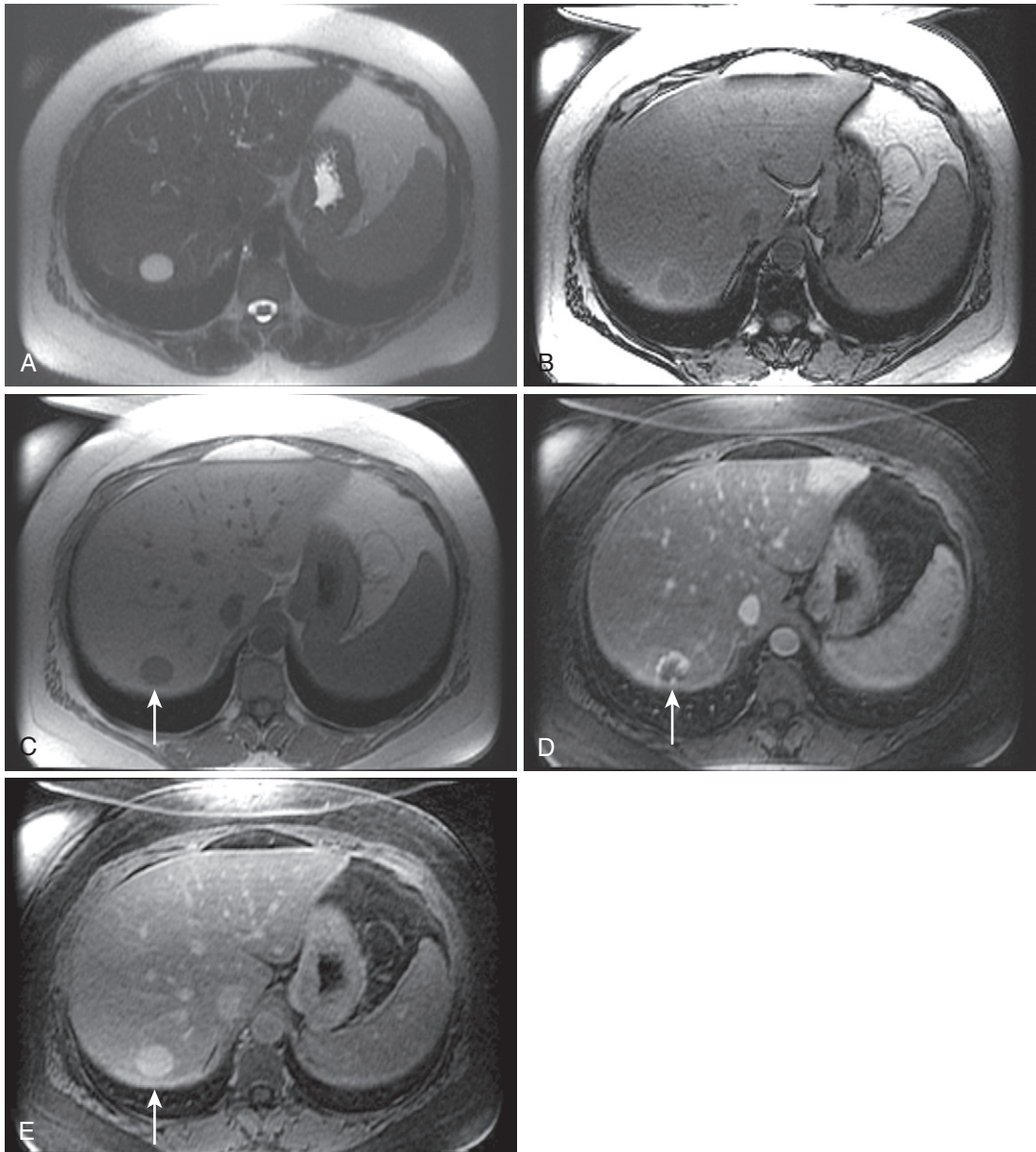


FIGURE 2-2. Liver MRI obtained on a 1.5-Tesla system. In-phase (A) and out-of-phase (B) images demonstrate steatosis reflected by relative signal loss on the out-of-phase image. Axial T2-weighted single-shot fast spin-echo (SSFSE) image (C) reveals a small hyperintense lesion (*arrow*) in the posterior segment of the liver. The axial arterial (D) and delayed (E) images show initial clumped, peripheral, discontinuous enhancement with uniform, persistent enhancement (*arrow*). Note the higher signal-to-noise (SNR) and improved image quality compared with [Figure 2-1A–D](#).

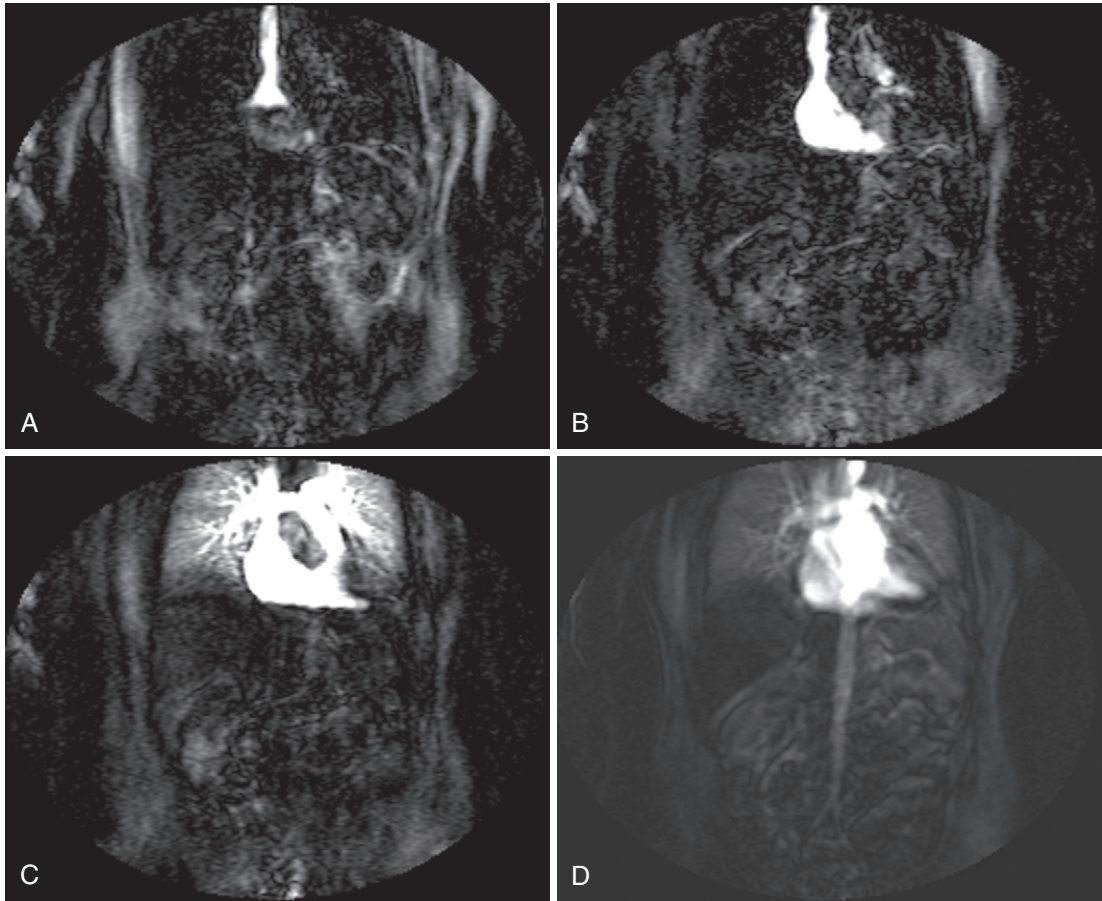


FIGURE 2-3. Example of BolusTrack timing sequence to initiate the dynamic acquisition. Selected serial coronal large field-of-view gradient-echo images obtained immediately after the intravenous administration of gadolinium (A–D) reveal the inflow of gadolinium into the superior vena cava (SVC; **A**), the right ventricle (**B**), through the pulmonary outflow tract and into the pulmonary arterial system (**C**), and into the thoracic aorta, down the abdominal aorta (**D**).

TABLE 2-2. Gadolinium Formulations

Brand Name	Generic Name	Chemical Structure	Charge	Elimination	Cases of NSF
Omniscan	Gadodiamide	Linear	Nonionic	Kidney	Yes
OptiMARK	Gadoversetamid	Linear	Nonionic	Kidney	Yes
Magnevist	Gadopentetic acid	Linear	Ionic	Kidney	Yes
MultiHance	Gadobenic acid	Linear	Ionic	97% kidney/3% bile	Yes
Primovist	Gadoxetic acid	Linear	Ionic	50% kidney/50% bile	No
Vasovist	Gadofosveset	Linear	Ionic	91% kidney/9% bile	No
Eovist	Gadoxetic acid disodium	Linear	Ionic	50% kidney/50% bile	No
ProHance	Gadoteridol	Cyclic	Nonionic	Kidney	No
Gadovist	Gadobutrol	Cyclic	Nonionic	Kidney	No
Dotarem	Gadoteric acid	Cyclic	Ionic	Kidney	No

NSF, nephrogenic systemic fibrosis.

TABLE 2-3. Protocol with Sequence Parameters

Sequence	Planes	TR/TE	Slice Thickness	Details
Steady-state	Three-plane, axial or coronal	min/min	6 × 0	
Heavily T2-weighted	Coronal and/or axial	NA/180	5 × 0	
In-/out-of-phase	Axial	min/2.2, 4.4	7 × 1	
Dynamic 3D	Axial	min/min	4-5 (interpolated ⇒ 2-2.5)	
Moderately T2-weighted	Axial	3000/80	7 × 0.5	
Delayed (3D)	Axial	min/min	4-5 (interpolated ⇒ 2-2.5)	
Delayed (2D)	Axial	20/min	5 × 0	
MRCP (2D)	Radial	NA~850	40	
MRCP (3D)	Coronal	1300/680	2 (interpolated ⇒ 1)	Respiration triggered
Diffusion (B = 20)	Axial	min/min	8 × 1	Breathhold
Diffusion (B = 500)	Axial	min/min	8 × 1	Respiration triggered

MRCP, magnetic resonance cholangiopancreatography; NA, not applicable; 3D, three-dimensional; TE, time to excitation; TR, time to repetition; 2D, two-dimensional.

Real-time viewing of contrast transit (Bolus-Track, Philips; CARE Bolus, Siemens; SmartPrep, GE; VisualPrep, Toshiba) involves careful monitoring by the technologist of serial large field-of-view (FOV) GE images after administration of the entire bolus of contrast (see Fig. 2-3). Transit of gadolinium through the superior vena cava (SVC) into the right heart through the pulmonary circulation and from the left heart into the aorta is portrayed on the monitor cinematically. With impending arrival of contrast into the abdominal aorta, the technologist instructs the patient to suspend respiration in preparation to acquire the arterial phase images. Portal phase images are subsequently obtained after allowing the patient to breathe after the arterial phase acquisition.

Practical demands prioritize throughput, necessitating economy of pulse sequences and mandating a rational approach to designing the MR protocol (Table 2-3). Begin the examination with a large FOV (~34 cm) T2-weighted (single-shot fast spin-echo [SSFSE], GE; HASTE, Siemens; SSH-TSE, Philips; FASE, Toshiba; SSFSE, Hitachi) or balanced GE sequence (balanced FFE, Philips; true-FISP, Siemens; True SSFP, Toshiba; FIESTA, GE). Each is a rapid sequence serving as an anatomic overview. Assess proper coil placement—maximal signal should originate from the ROI—the center of the abdomen. Needless to say, the entire ROI should be visible with adequate SNR (Fig. 2-4).

Thereafter, spatial resolution needs and acquisition time constraints determine FOV. Keeping the matrix constant (between 256 and 320 in the frequency axis), adapt the FOV to the patient's size in order to maximize spatial resolution. Sacrifice visualization of the abdominal

wall in order to boost spatial resolution, as long as wraparound artifact does not obscure the ROI. Assign phase encoding to the anteroposterior (AP) axis and customize the phase FOV to the AP dimension of the patient because most patients are narrower in the AP dimension. Phase encoding costs time, according to the equation: acquisition time = TR × number of phase encoding steps × number of signal averages. Therefore, decreasing phase-encoding FOV commensurate with patient size in the AP dimension saves time by eliminating phase-encoding steps (Fig. 2-5) (see Chapter 1).

The standard protocol includes moderately and heavily T2-weighted, in- and out-of-phase GE, dynamic gadolinium-enhanced, and delayed postcontrast T1-weighted images (see Table 2-3). Add MRCP (magnetic resonance cholangiopancreatography) sequences if indicated. The SSFSE conventionally serves as the heavily T2-weighted sequence. Heavy T2-weighting means designing the sequence to favor signal from substances with long T2 values (e.g., free unbound water—bile, urine). Sequence parameters include prolonged TE (time to excitation; 180–200 msec) and TR (time to repetition) values. SSFSE sequences are obtained with a single excitation pulse followed by a rapid series of 180° pulses, each refocusing an echo until all of the k space data for a single slice are acquired. So, technically, TR is nonexistent or infinite, because the excitation pulse is not repeated. Although relatively signal-starved (because of the single excitation pulse), the SSFSE sequence resists motion and susceptibility artifact (Fig. 2-6). The rapid acquisition protects against motion artifact and the multiple refocusing pulses repeatedly undo or correct for

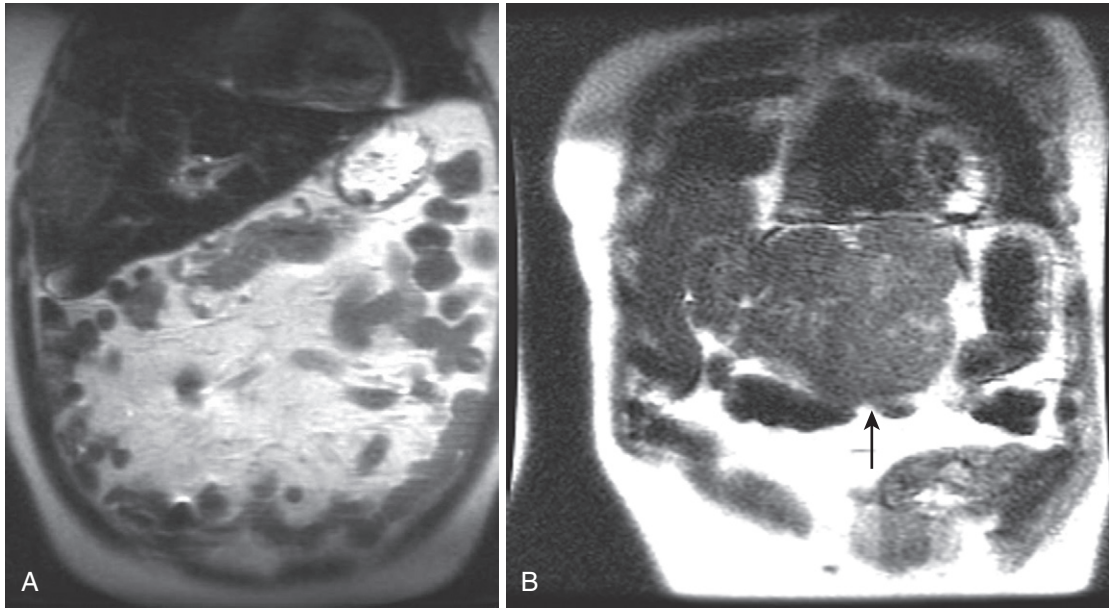


FIGURE 2-4. Assessing coil placement. **A**, Coronal localizing SSFSE T2-weighted image reveals maximal signal emanating from the lower abdomen, instead of the upper abdomen. **B**, Coronal localizing SSFSE T2-weighted image of a different patient reveals a mildly hyperintense exophytic lesion (*arrow*) arising from the lateral segment of the liver, which is well visualized because of optimal coil placement yielding superior signal over the region of interest.

susceptibility artifact. Heavy T2-weighting optimizes tissue contrast for visualizing fluid-filled structures, such as the gallbladder and biliary tree—sort of a “poor man’s MRCP.”

In- and out-of-phase images are T1-weighted GE images with TE values timed to coincide with fat and water molecules precessing in-phase and out-of-phase, respectively. On most scanners, these images are obtained simultaneously as a double-echo sequence in a single breath-hold; at each slice, one image with an in-phase TE and one image with an out-of-phase TE are obtained concurrently. TE values are fixed by magnetic field strength according to the Larmor equation (Table 2-4). These images provide T1-weighting and the ability to detect fat deposition (among other things, which are discussed in the forthcoming section).

The examination revolves around the dynamic gadolinium-enhanced sequence. *Dynamic* refers to the temporal sense of the word—obtaining views at the same location repetitively after contrast. Since gadolinium is a T1-shortening agent, detection of gadolinium enhancement necessitates a T1-weighted sequence. Improved dynamic range afforded by fat suppression further improves enhancement conspicuity. High spatial resolution requirements recommend the use of a three-dimensional (3-D) pulse

TABLE 2-4. In- and Out-of-Phase Times to Excitation by Magnetic Field Strength

Magnetic Field Strength (T)	Out-of-Phase (msec)	In-Phase (msec)
0.3	11.3	22.6
0.7	4.8	9.2
1.0	3.4	6.8
1.5	2.2	4.4
3.0	1.1	2.2

sequence, which boosts SNR compared with two-dimensional (2-D) counterparts (allowing for smaller voxels). The increased SNR also permits the use of parallel imaging (which costs SNR), reducing acquisition time and breath-hold duration. A set of images preceding the injection functions as the unenhanced images. The next set of images with identical parameters synchronized with the arrival of gadolinium in the arterial system (as previously discussed) constitutes the arterial phase images. Following a short delay to allow the patient to breathe, a third set of images with the same parameters is acquired—the portal phase images.

At this point, only moderately T2-weighted and delayed enhanced images remain to complete the examination. Deferral of the delayed enhanced images until after acquiring

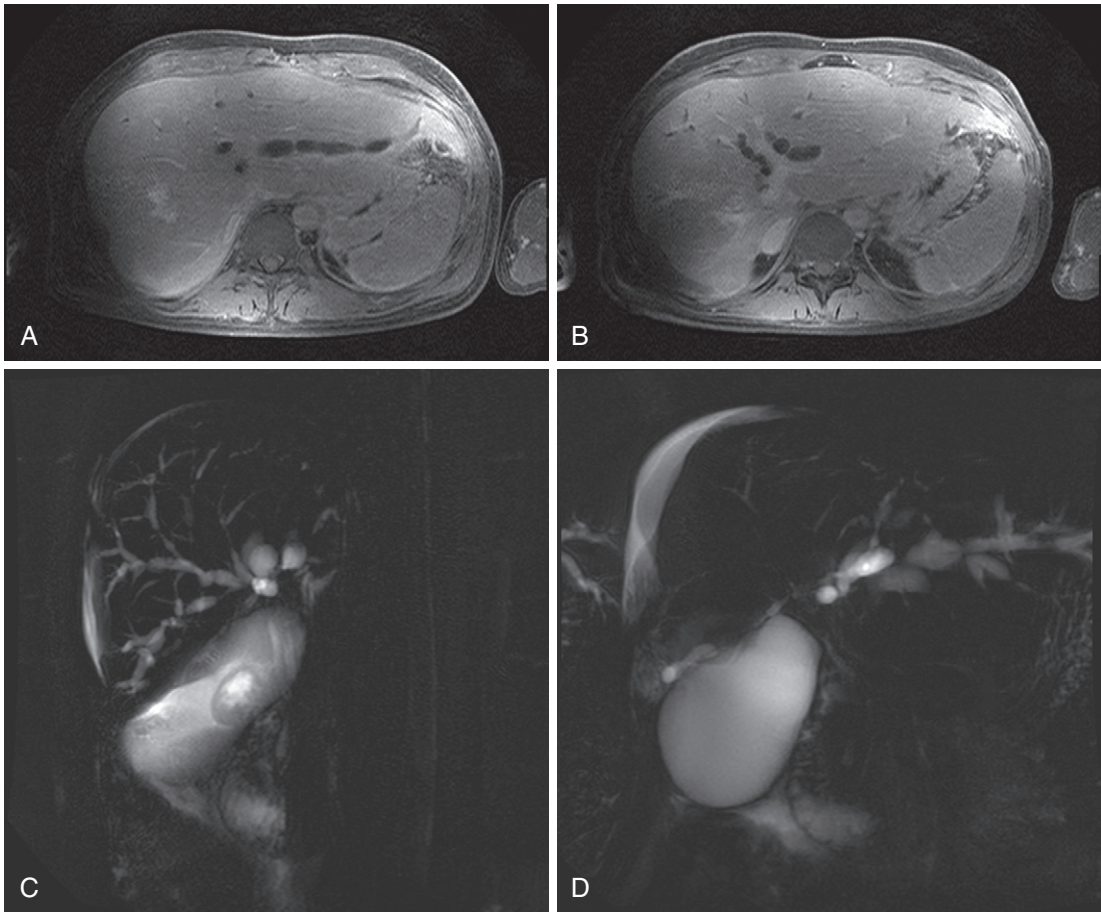


FIGURE 2-5. Rectangular field of view. Axial T1-weighted enhanced images (A and B) performed on a 3-Tesla system with a relatively large square field of view—adding time-consuming phase-encoding steps to cover air over the patient—in a patient with primary sclerosing cholangitis reveal irregular beaded biliary ductal dilatation and structuring as corroborated on the corresponding magnetic resonance cholangiopancreatography (MRCP) images (C and D).

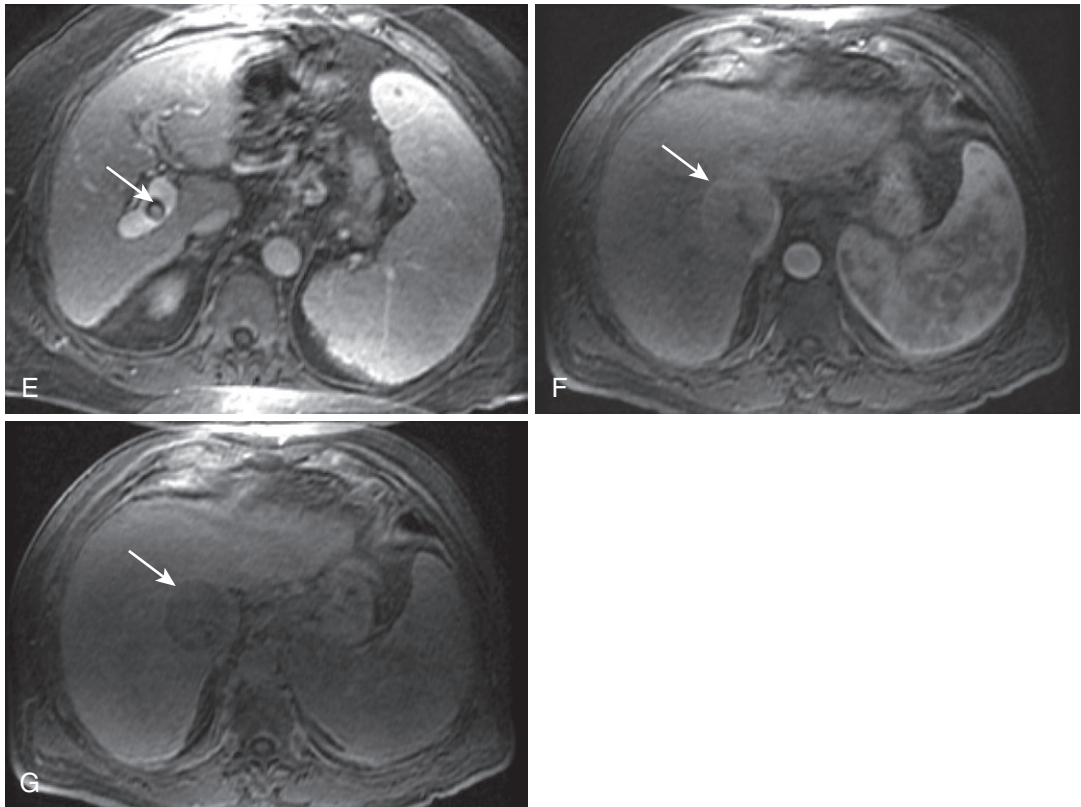


FIGURE 2-5, cont'd The axial postcontrast image in a patient with a patent transjugular intrahepatic portosystemic shunt (TIPS) (*arrow* in E) exemplifies the use of rectangular field of view, which results in prominent wraparound of the anterior and posterior abdominal wall without obscuring the relevant visceral structures. Arterial phase (F) and delayed postcontrast (G) images in a different patient show a lesser degree of wraparound of the posterior abdominal wall also not interfering with the assessment of the liver and hypervascular lesion (*arrow*) with delayed washout—typical features of hepatocellular carcinoma.

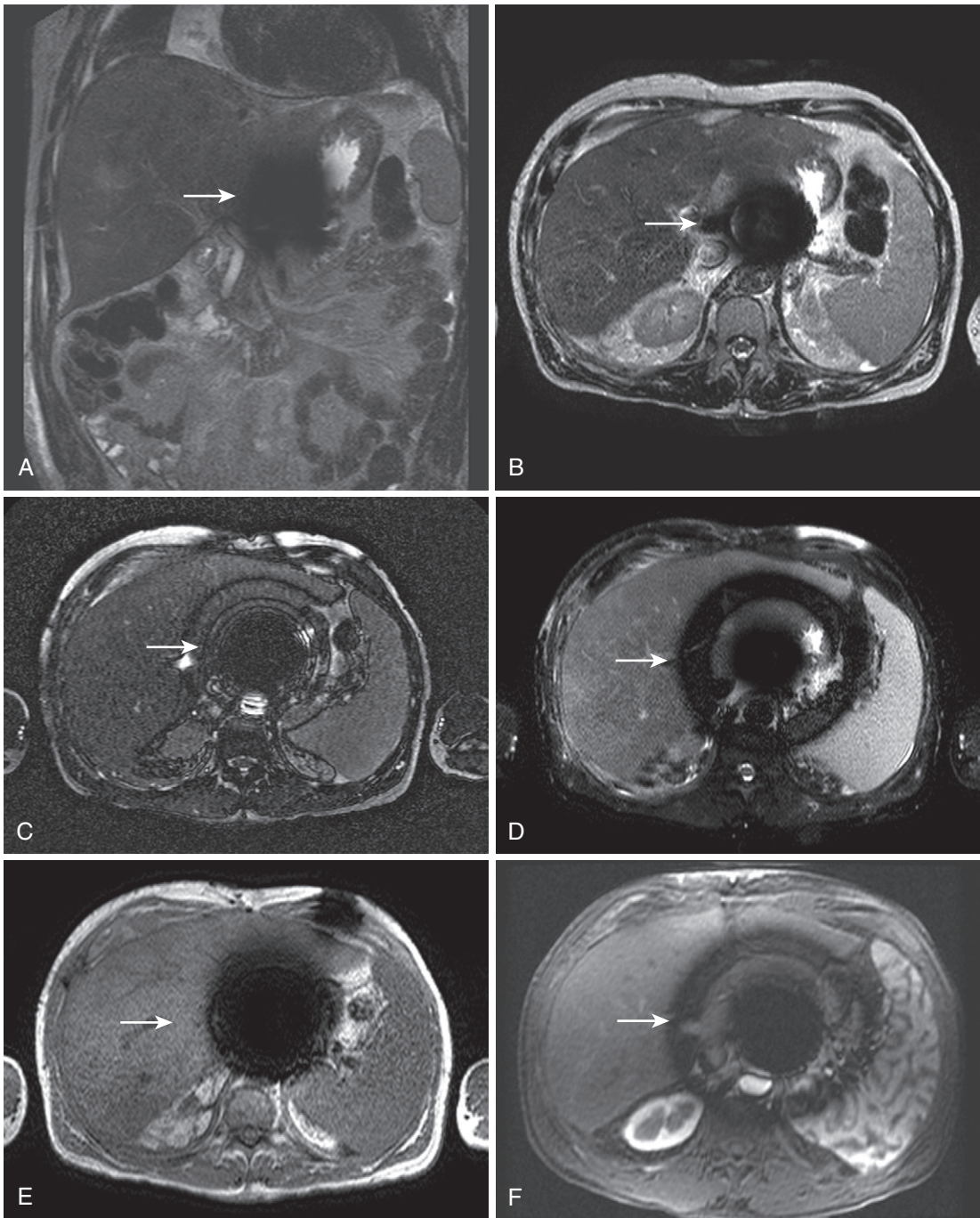


FIGURE 2-6. SSFSE images minimizing susceptibility artifact. Coronal (A) and axial (B) T2-weighted SSFSE images in a patient with embolization coils in gastrohepatic collaterals corresponding to susceptibility artifact (*arrow* in A-F) in the epigastric region, which is minimized compared with the axial steady-state image (C)—an alternative localizer—the fat-suppressed T2-weighted fast spin-echo (FSE; D), the in-phase (E) and the fat-suppressed arterial phase (F) gradient-echo images. Note the clear depiction of loops of small and large bowel on the coronal SSFSE image.

the moderately T2-weighted images achieves a reasonable delay. Moderately T2-weighted images possess better tissue contrast compared with their heavily T2-weighted counterpart and the presence of intravenous gadolinium confers even higher conspicuity for solid liver lesions compared with normal parenchyma.¹ Normal tissue retains more gadolinium and the associated magnetization transfer effects diminish parenchymal signal, resulting in greater lesion-to-liver contrast-to-noise ratio (CNR). Fat suppression conveys greater tissue contrast by improving dynamic range. Moderate T2-weighting requires TE values on the order of 80 msec and the fast spin-echo (FSE)—or turbo spin-echo (TSE)—sequence adapts best to this parameter requirement within the constraints of a breath-hold. Whereas the FSE sequence rapidly fills k space enabling breath-hold imaging, the relatively longer acquisition time compared with other sequences (such as the SSFSE), especially on older systems, challenges breath-holding. Respiratory triggering circumvents this problem.

The delayed (or interstitial or equilibrium) phase images depict the eventual passage of contrast into the extravascular space, perfusing the interstitial tissues. Either 3-D or 2-D T1-weighted fat-suppressed GE sequences suffice. Three-dimensional pulse sequences potentially suffer more from breathing motion artifact—obviated on the 2-D sequence, when fragmented into multiple breathholds. A delay of up to 7 minutes has been proposed, defined by the time enhancement occurs in cholangiocarcinoma. Practically, this is rarely achieved in order to maximize throughput.

INTERPRETATION

An effective search pattern acknowledges the specific utility of each pulse sequence (Tables 2-5 and 2-6). The multiplicity of arcanelly named pulse sequences is simplified according to a basic T1-weighting versus T2-weighting scheme. T1-weighted images include the in- and out-of-phase, dynamic, and delayed T1-weighted GE pulse sequences. In addition to the inherent T1 contrast inherent to all of these pulse sequences, each possesses unique properties. The out-of-phase sequence is T1-weighted with sensitivity to microscopic fat. The in-phase sequence is T1-weighted with sensitivity to susceptibility artifact or iron (practically speaking). The

TABLE 2-5. Magnetic Resonance Imaging Liver Checklist

Technical

- Magnetic field strength
- Coil position
 - Signal ⇒ maximal signal arising from liver
- Enhancement ⇒ note amount and type of contrast administered
 - Arterial phase adequacy
- Artifacts
 - Susceptibility ⇒ surgical hardware, embolization coils, TIPS, bowel gas, etc.
 - Motion ⇒ bulk motion, respiratory motion, vascular flow artifacts
 - Conductivity/dielectric effects ⇒ focal signal loss (↑ at 3 T)

Signal

- Fat ⇒ loss of signal on out-of-phase
 - Diffuse versus segmental versus focal
 - Fatty sparing
- Iron ⇒ loss of signal on in-phase
 - Pancreatic signal loss
 - Splenic signal loss
 - Bone marrow signal loss
- Fibrosis ⇒ reticular versus confluent

Morphology

- Atrophy/hypertrophy
- Nodularity
- Capsular retraction

Vascular

- Portal system
 - Portal vein and branches
 - Superior mesenteric vein
 - Splenic vein
- Hepatic veins
- Arterial system
 - Celiac axis
 - Stenosis
 - Variant anatomy
 - Left hepatic artery from left gastric artery
 - Common hepatic artery from SMA
 - Replaced or accessory right hepatic artery from SMA
 - Hepatic artery
 - Occlusion or stenosis after liver transplantation

Focal Lesions

- Cystic versus solid
- Solitary versus multiple

SMA, superior mesenteric artery; TIPS, transjugular intrahepatic portosystemic shunt.

precontrast fat-saturated sequence is T1-weighted with sensitivity to blood, protein, and melanin (paramagnetic substances). The post-contrast dynamic T1-weighted sequences are T1-weighted with sensitivity to solid tissue (enhancement) and vascular structures. Enhancement on the delayed T1-weighted sequence represents a map of extracellular spaces, because conventional gadolinium agents are extracellular agents. With time, gadolinium eventually travels throughout the extracellular space (including the vascular space and interstitium). Substances with large extracellular

TABLE 2-6. Pulse Sequence Scheme

T2-Weighted Sequences

- Moderately T2-weighted sequence = water-sensitive sequence = bound water sequence
TE \approx 80 msec, usually fat-suppressed
Superior tissue contrast \Rightarrow subtle differences in bound water
Sensitive for solid lesions
Depicts lymph nodes
- Heavily T2-weighted sequence = water-specific sequence = free water sequence
TE \approx 180 msec, usually performed with single-shot technique
Depicts free water with benefit of anatomic detail
Lacks tissue contrast
Rapid \Rightarrow motion insensitive
Resistant to susceptibility artifact ($\uparrow\uparrow$ 180° refocusing pulses)
- MRCP sequence = water-only sequence
TE > 500–750 msec, 2D and 3D techniques
Renders only free water protons due to $\uparrow\uparrow$ TE
Perform after intravenous gadolinium to eliminate signal from collecting systems
- Steady-state sequence = fluid-solid tissue sequence
T2/T1-weighted sequence but functionally T2-weighted
Dephasing of moving spins refocused \Rightarrow vessels yield signal
Accessory vascular sequence

T1-Weighted Sequences

- Out-of-phase sequence = microscopic fat sequence
TE = 2.2 msec (at 1.5T), usually performed with in-phase as one pulse sequence
Shows microscopic fat as hypointensity compared with in-phase
Phase cancellation artifact \Rightarrow signal void at fat/water interfaces (“India ink” artifact)
- In-phase sequence = susceptibility sequence
TE = 4.4 msec (at 1.5T), usually performed with out-of-phase as one pulse sequence
Shows ferromagnetic substances (iron, surgical clips, metallic objects) as susceptibility artifact (or signal void more prominent compared with out-of-phase)
- Precontrast fat-suppressed sequence = paramagnetic sequence
Precontrast phase of dynamic sequence, usually performed with 3D technique
Only paramagnetic sequences yield signal \Rightarrow hemorrhage, protein, melanin, etc.
- Dynamic postcontrast sequences = solid tissue (and vascular) sequences
Each phase after contrast offers specificity for different solid lesions and vascular structures
3D sequences \Rightarrow better SNR, thinner contiguous slices, prone to saturation
2D sequences \Rightarrow lower SNR, thicker noncontiguous slices, avoid saturation
Time-of-flight effect \Rightarrow inflow of fresh protons in vessels yields signal
- Delayed postcontrast sequence = interstitial phase sequence
Same parameters as dynamic sequence
Substances with large extracellular spaces gradually enhance most avidly on delayed images

MRCP, magnetic resonance cholangiopancreatography; SNR, signal-to-noise ratio; 2D, two-dimensional; 3D, three-dimensional; TE, time to excitation.

spaces, such as fibrosis and inflammation, often enhance most avidly on the delayed sequence—the interstitial phase sequence.

T2-weighted images include the moderately and heavily T2-weighted (and steady-state) and MRCP images. The heavily T2-weighted sequence is specific for free water molecules,

showcasing fluid and cystic lesions—the water-specific (or free water) sequence. The moderately T2-weighted sequence depicts subtle differences in bound water (found in solid tissue), sensitive to the increased bound water in malignant lesions—the water-sensitive (or bound water) sequence. The MRCP sequence receives signal only from free water protons—the (free) water-only sequence.

The individual properties of each sequence dictate the approach to that particular set of images. For example, heavily T2-weighted SSFSE images are grant conspicuity to fluid-filled objects and are resistant to motion and susceptibility artifact—optimally adapting them to evaluate the gallbladder, hepatobiliary tree, pancreatic duct, and gastrointestinal tract (minimizing peristaltic motion artifact and gas-related susceptibility artifact) (Fig. 2-7). Cystic lesions (such as simple cysts and hemangiomas)—as opposed to solid lesions—and other fluid-filled structures (such as the renal collecting system) are clearly depicted on these images.

Steady-state images exploit T2/T1 contrast and portray superior fluid-to-solid tissue contrast. Practically, the chief diagnostic utility of these sequences is the evaluation of fluid-filled structures and blood vessels (and heart) (Fig. 2-8). Susceptibility artifact plagues these sequences, limiting utility for evaluating bowel.

In- and out-of-phase sequences yield multifaceted diagnostic information (Fig. 2-9). Use the T1-weighted microscopic fat sequence (out-of-phase) by comparing signal intensity of the opposed-phase images with the in-phase images. Signal loss on opposed-phase images indicates microscopic fat. Use the T1-weighted susceptibility sequence (in-phase) to detect susceptibility artifact and iron by comparing signal intensity between in-phase and opposed phase images; loss of signal on the in-phase image suggests susceptibility artifact (e.g., cholecystectomy clips, iron deposition in the liver and/or spleen or pancreas). In addition to the unique attributes of these images, their T1 contrast lends conspicuity to blood, melanin, and (macroscopic) fat. Search the kidneys for hemorrhagic cysts; the liver for dysplastic nodules (in the appropriate clinical setting of cirrhosis); the liver, spleen, and kidneys for subcapsular hematomas (in the appropriate clinical setting); and the liver for melanotic melanoma or hemorrhagic metastases (in the setting of a known primary malignancy).

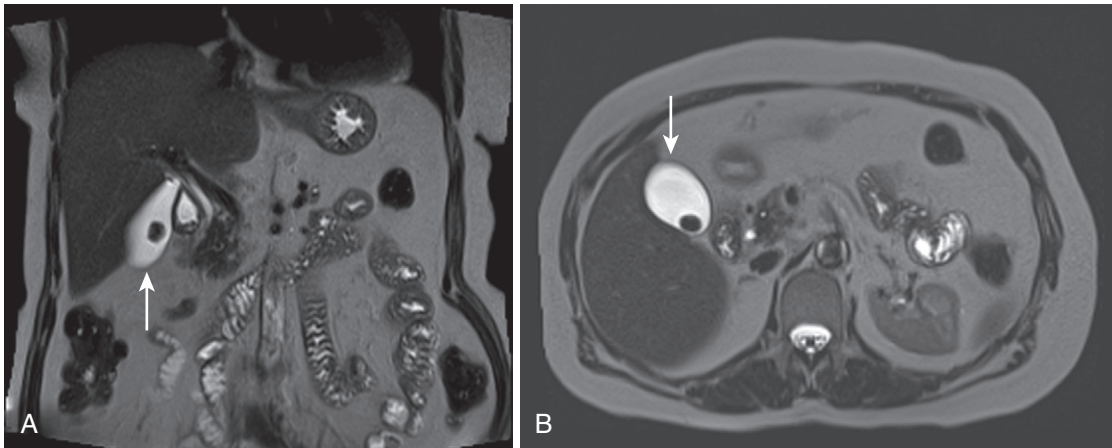


FIGURE 2-7. SSFSE image resistance to motion and susceptibility artifact and utility for fluid-filled structures. Coronal (A) and axial (B) heavily T2-weighted SSFSE images depict fluid-filled structures, such as the stone-containing gallbladder (*arrow*) and loops of bowel, with great detail and clarity and absence of susceptibility and motion artifact.

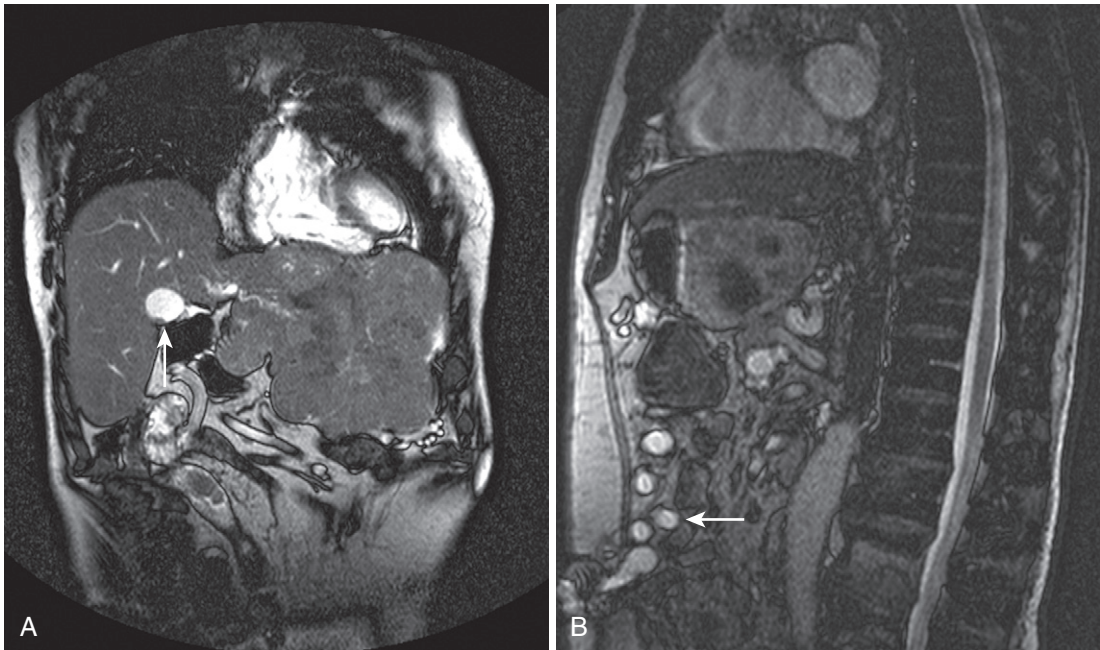


FIGURE 2-8. Steady-state images. A, Coronal steady-state image in the same patient depicted in [Figure 2-4B](#) demonstrates robust fluid-to-solid tissue contrast, with exquisite depiction of the imaged cardiac chambers, gallbladder (*arrow*), and intrahepatic vessels and bile ducts. B, A sagittal steady-state image in a different patient with cirrhosis shows hyperintensity of the cerebrospinal fluid and cardiac chambers and a tortuous hyperintense structure (*arrow*) extending to the umbilicus—a paraumbilical portosystemic collateral.

However, the fat-suppressed precontrast T1-weighted sequence is the paramount T1-weighted blood (paramagnetic) sequence ([Fig. 2-10](#)). By spectrally eliminating macroscopic fat signal and dramatically improving dynamic range, methemoglobin in hematomas, hemorrhagic cysts, hemorrhagic metastases, melanoma in melanotic metastases, copper in dysplastic nodules and protein in normal

pancreatic parenchyma become far more conspicuous.

Change in signal on the postcontrast images compared with the precontrast images equals enhancement, which occurs in solid lesions and vascular structures—hence, the designation T1-weighted images for solid and vascular lesions. The multiphasic nature of the dynamic sequence furnishes layered, multifaceted

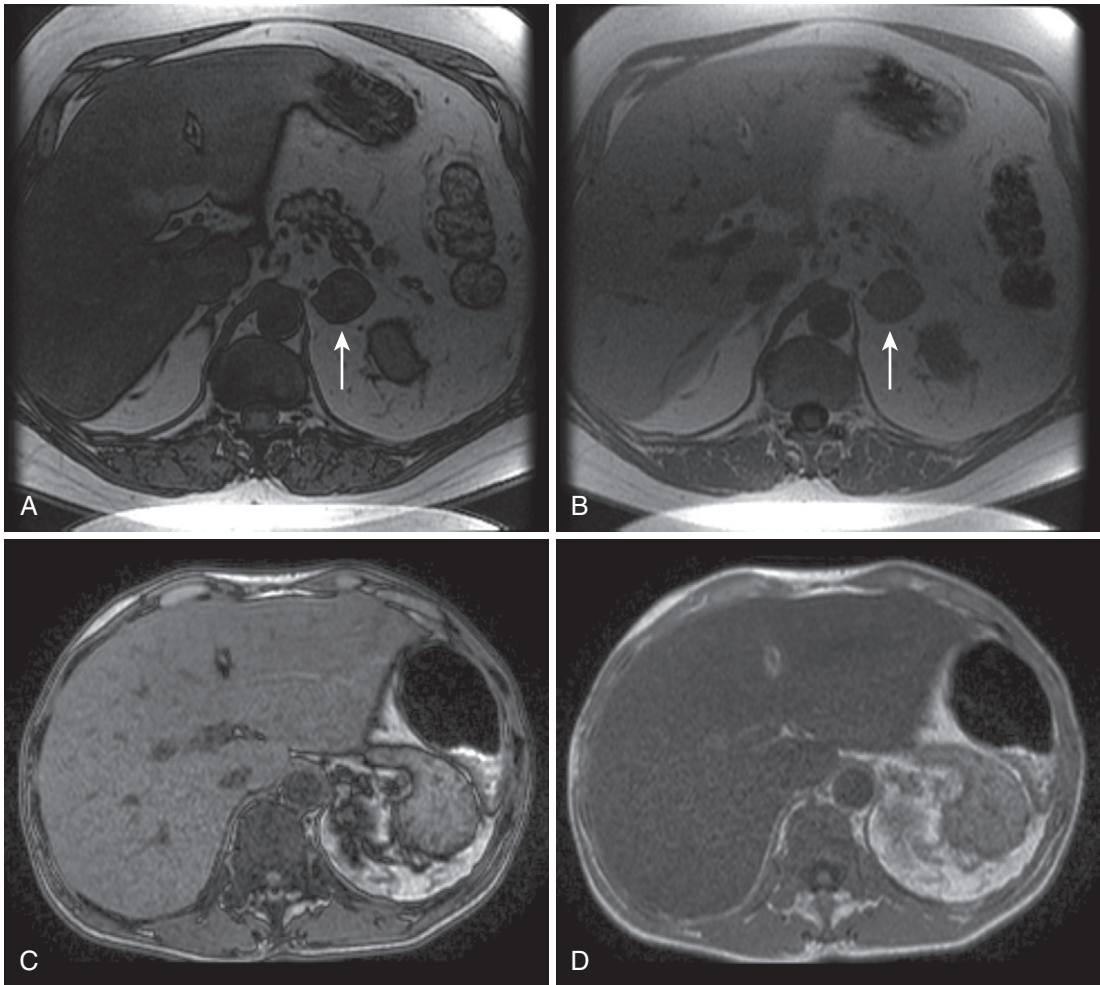


FIGURE 2-9. In- and out-of-phase images. Axial out-of-phase (A) and in-phase (B) images in a patient with severe steatosis show marked reduction in signal on the out-of-phase image and similar signal drop in a left adrenal adenoma (*arrow*). Axial out-of-phase (C) and in-phase (D) images in a different patient with hemosiderosis portray the opposite pattern with relative signal loss on the in-phase image as a consequence of susceptibility artifact.

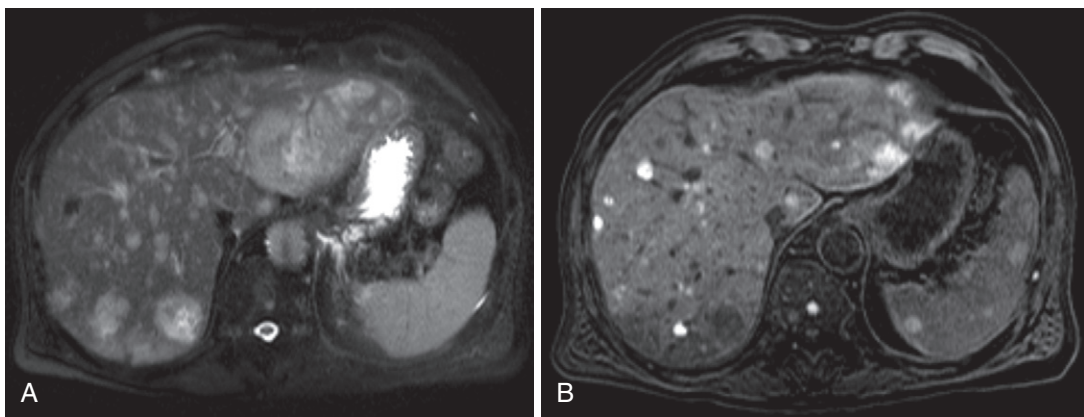


FIGURE 2-10. T1-weighted fat-suppressed image. The T2-weighted fat-suppressed image (A) reveals multiple nonspecific hyperintense lesions, many of which appear hyperintense on the T1-weighted fat-suppressed image (B) due to their melanotic content in a patient with metastatic uveal melanoma.

information that requires careful attention to technique. Compare the arterial phase images for technical adequacy—the signal intensity of the hepatic parenchyma on the arterial phase images should approximate the signal on the unenhanced images (because the liver is largely perfused by the portal vein under normal circumstances) (Fig. 2-11). Arterially enhancing lesions (such as focal nodular hyperplasia [FNH], adenoma, vascular shunts, hypervascular metastases, and HCC) brightly contrast with the relatively dark, unenhanced background liver parenchyma. On portal phase images, hypovascular liver lesions gain conspicuity as the background parenchyma enhances—cysts and hypovascular metastases are relatively dark. Identify arterial stenoses and aberrant arterial anatomy on the arterial phase images and venous occlusion and anatomic anomalies on the portal venous images.

Moderately T2-weighted images (the T2 solid lesion images) supplement the dynamic sequence in identifying and characterizing liver lesions and, generically speaking, serve as a “pathology sequence.” Whereas heavily

T2-weighted images discriminate fluid-filled lesions, such as cysts and hemangiomas, from liver parenchyma, solid masses and lesions approximate normal parenchymal signal. Conceptually, most pathologic conditions, although not cystic, generally harbor more water protons compared with normal tissue. Whereas long TE values—in heavily T2-weighted images—target substances with very long T2 values and fail to discriminate subtle differences in tissue water content, moderately T2-weighted images retain sensitivity to slight differences in tissue water content (Fig. 2-12). Moderately T2-weighted image contrast is designed to detect solid lesions with slightly greater water content from normal liver parenchyma (Fig. 2-13). Malignant lesions generally contain slightly greater water content and appear mildly hyperintense compared with liver parenchyma. Outside the liver, lymph nodes, pancreatic parenchymal lesions and peripancreatic inflammation, pericholecystic inflammation, and other pathology are conspicuous as a consequence of increased water resulting in hyperintensity (especially with fat saturation).

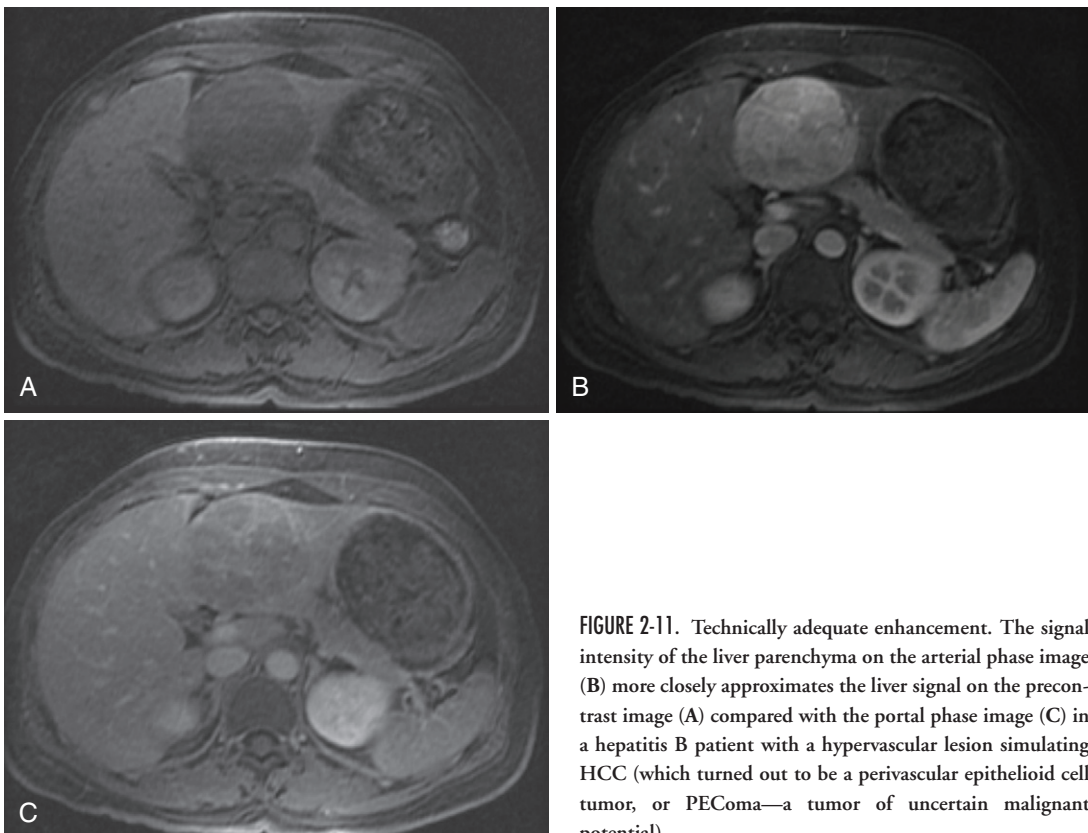


FIGURE 2-11. Technically adequate enhancement. The signal intensity of the liver parenchyma on the arterial phase image (B) more closely approximates the liver signal on the precontrast image (A) compared with the portal phase image (C) in a hepatitis B patient with a hypervascular lesion simulating HCC (which turned out to be a perivascular epithelioid cell tumor, or PEComa—a tumor of uncertain malignant potential).

Delayed images confirm absence of enhancement in cystic lesions and delayed enhancement in specific lesions, such as hemangiomas, cholangiocarcinoma, and fibrous lesions (scarring). Inspect venous structures again for potential anatomic anomalies and/or occlusion. Use delayed enhancement as a potential indication of inflammation, which becomes more conspicuous as gadolinium accumulates in the expanded interstitial space associated with inflammation and edema.

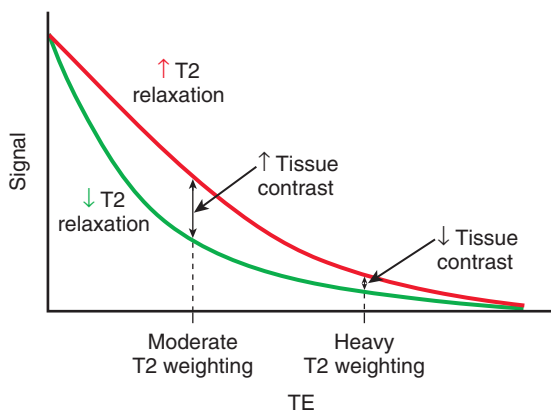


FIGURE 2-12. T2 relaxation curves show heavily versus moderately T2-weighted contrast. TE, time to excitation.

In summary, simplify the myriad potentially confusing pulse sequences into a few basic categories (see Table 2-6). The three T2-weighted pulse sequences include (1) water-sensitive T2-weighted images—the heavily T2-weighted SSFSE sequence; (2) pathology-sensitive images, or moderately T2-weighted images; and (3) water-only images—MRCP images. The T1-weighted images also enjoy uniquely different properties. Out-of-phase images are T1-weighted images with sensitivity to microscopic fat. In-phase images are T1-weighted images with sensitivity to susceptibility artifact, such as iron deposition and artifact arising from surgical clips or clumps of calcium. Precontrast fat-suppressed images are T1-weighted images with sensitivity to hemorrhage, melanin, and protein. Postcontrast dynamic images are T1-weighted images with sensitivity to viable tumor and vascular anatomy.

NORMAL FEATURES

Morphology, signal, and texture are the currency used to describe the MRI appearance of the liver. The normal liver is usually described from a negative reference point—“lack of

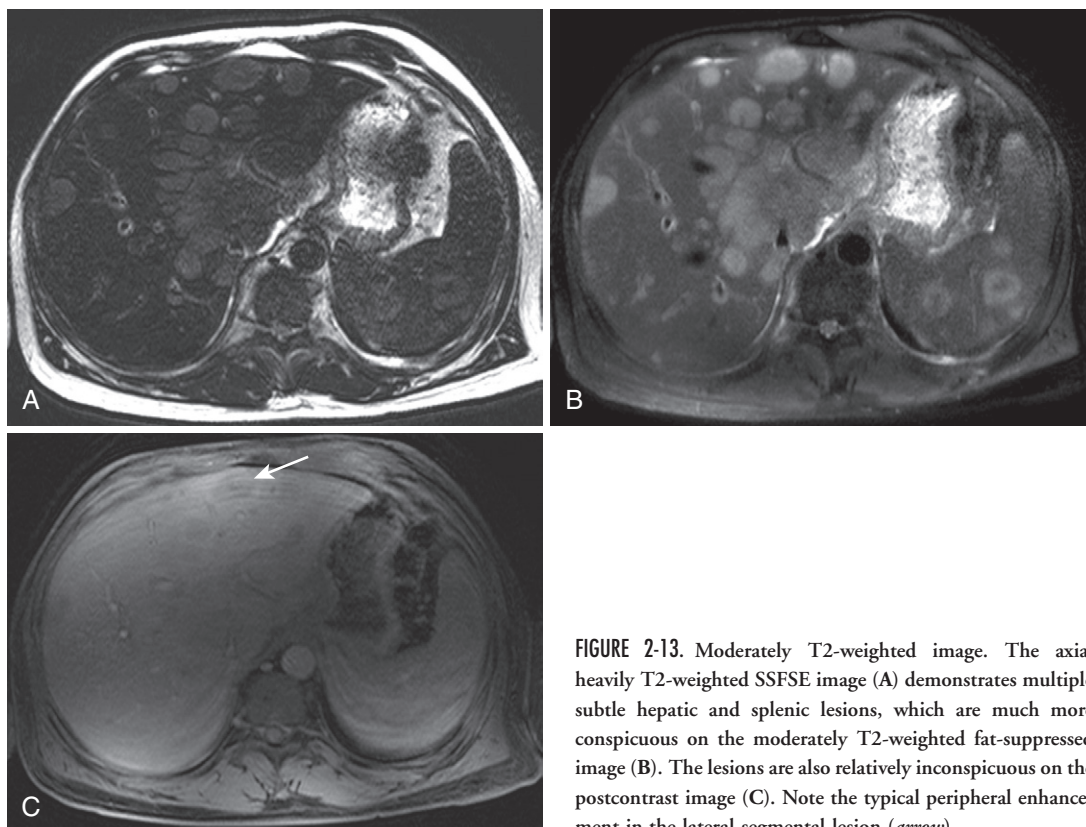


FIGURE 2-13. Moderately T2-weighted image. The axial heavily T2-weighted SSFSE image (A) demonstrates multiple subtle hepatic and splenic lesions, which are much more conspicuous on the moderately T2-weighted fat-suppressed image (B). The lesions are also relatively inconspicuous on the postcontrast image (C). Note the typical peripheral enhancement in the lateral segmental lesion (*arrow*).

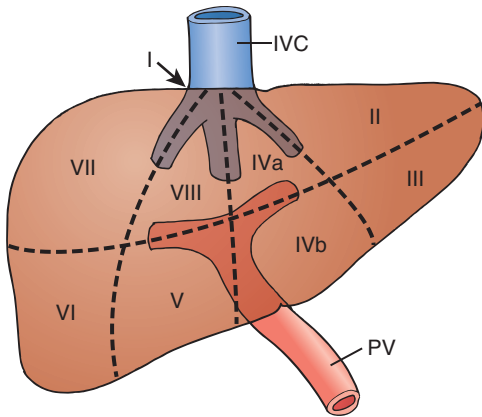


FIGURE 2-14. Liver segments. IVC, inferior vena cava; PV, portal vein.

nodularity” or “no atrophy/hypertrophy pattern.” Normal liver texture is smooth, reflected by an absence of both surface nodularity and an underlying reticular appearance. The liver occupies most of the right upper quadrant and global morphology varies. Mentally deconstruct the liver into segments—right lobe, medial segment, lateral segment, and caudate lobe—to establish the basis for normal and morphologic derangements associated with cirrhosis (the former two atrophy and the latter two hypertrophy) (Fig. 2-14).

Further deconstruct the liver spatially into segments according to the Couinaud system in order to facilitate communication with referring physicians and specifically locate lesions and pathology. Each Couinaud segment functions independently with unique vascular inflow, outflow, and biliary drainage; the central portal vein, hepatic artery, and bile duct define the segment. Consequently, each segment is independently resectable without affecting neighboring liver tissue. The horizontal plane of the portal vein bifurcation transects the vertical planes of the hepatic veins to delineate the Couinaud segments.

Relatively low water content accounts for hepatic parenchymal signal characteristics—relative T1 hyper- and T2 hypointensity. Hepatic T1 signal nearly matches pancreatic T1 hyperintensity, and most tumors contain more water and appear relatively T1 hypointense and T2 hyperintense to normal liver. Isointensity between in- and out-of-phase images reflects an absence of fat and iron deposition under normal circumstances.

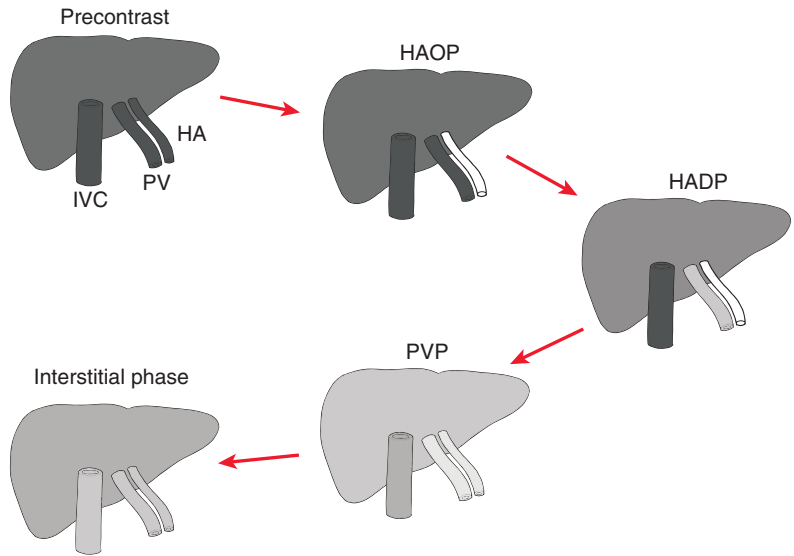
Signal characteristics generally supplement enhancement data in assessing liver lesions. Gadolinium enhancement is a biphasic phenomenon in the liver as a consequence of dual blood supply. The portal vein delivers 75% of blood flow to the liver, with the hepatic artery accounting for the rest. Four discrete phases describe the transit of intravenous contrast through the liver: the *hepatic artery-only phase* (HAOP), the *hepatic artery-dominant phase* (HADP; also known as the *capillary phase*), the *portal venous phase* (PVP; also known as the *early hepatic venous phase*), and the *hepatic venous phase* (HVP; otherwise known as the *interstitial phase*) (Fig. 2-15).

Liver imaging relies heavily on the HADP. HADP image acquisition begins approximately 15 seconds after contrast administration. Modest enhancement, or relative T1 hyperintensity compared with unenhanced images, and contrast within the hepatic arteries and portal veins characterize the HADP in which the parenchyma has been perfused by the hepatic arterial circulation (Fig. 2-16). Arterial contrast preceding parenchymal and portal venous enhancement corresponds to the HAOP, preceding the HADP. Successful acquisition of an HADP phase permits lesion enhancement stratification into four categories relative to liver parenchyma: hypervascular (more arterial perfusion), isovascular, hypovascular, and avascular (Fig. 2-17). Correlating this information with data from subsequent timepoints often yields specific diagnostic information. Before making this assessment, corroborate adequate timing of the intended HADP; early or delayed timing potentially obscures hypervascular lesions.

PVP acquisition time begins approximately 45 to 60 seconds after contrast administration and corresponds to peak parenchymal enhancement. All vessels, including hepatic veins, are enhanced. Liver features during the HVP resemble the PVP and underlying lesion enhancement changes, such as washout, may be more conspicuous with time. PVP timing constraints are less rigorous and may be obtained between 90 seconds and 5 minutes after contrast administration.

FOCAL LESIONS

Exquisite tissue contrast and enhancement conspicuity distinguish MRI as the definitive noninvasive diagnostic authority on liver lesions.



HA = Hepatic artery	HAOP = HA only phase
PV = Portal vein	HADP = HA dominant phase
IVC = Inferior vena cava	PVP = PV phase

FIGURE 2-15. Dynamic enhancement phases with schematic representations.

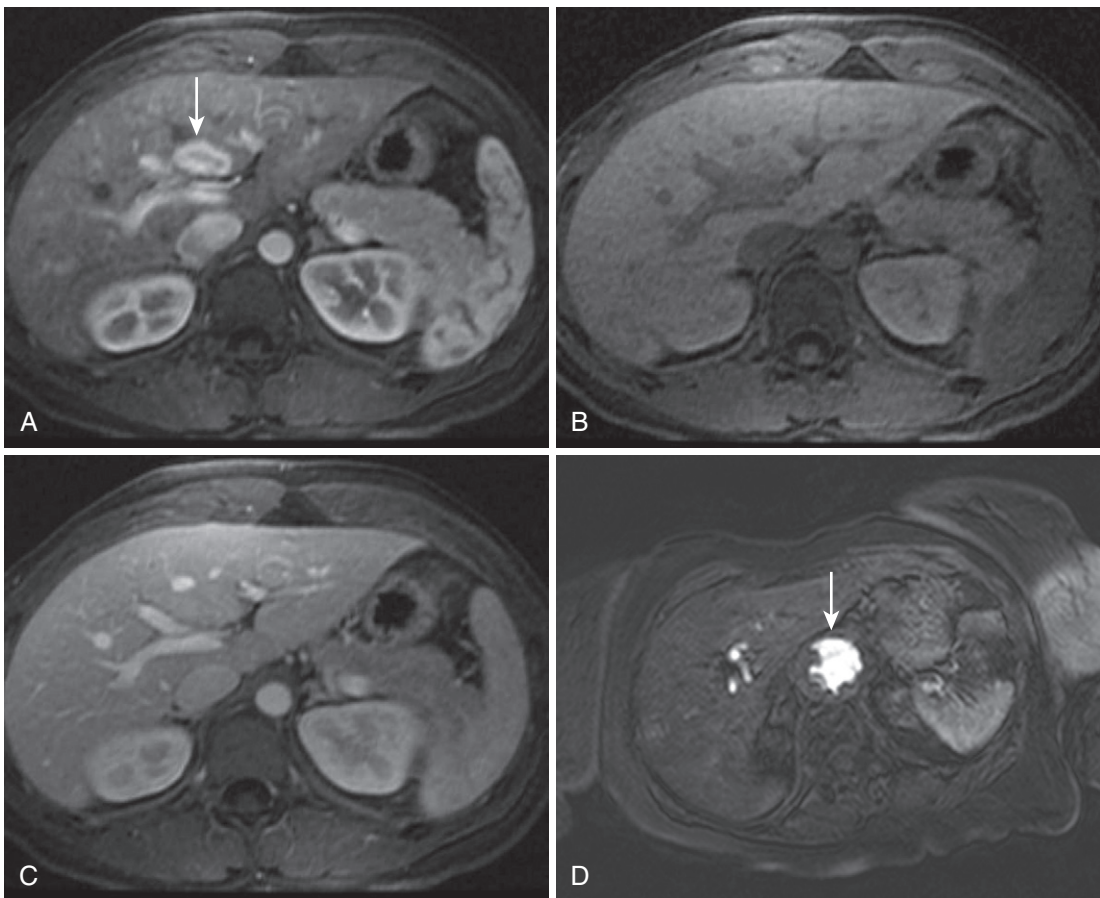


FIGURE 2-16. Hepatic artery–dominant phase (HADP). Notice the relatively similar intensity of the liver parenchyma on the (hepatic artery–dominant) arterial phase image (A) compared with the unenhanced image (B) and hypointensity compared with the portal phase image (C), indicating a lack of portal perfusion despite gadolinium in the main portal vein. Note the focal nodular hyperplasia (FNH) in the medial segment (*arrow* in A) enhancing avidly in the arterial phase. Compare the HADP image (A) with a prematurely obtained hepatic artery–only phase image (D), which shows lack of parenchymal enhancement with isolated enhancement of arterial structures without portal venous enhancement in a different patient with an aortic aneurysm (*arrow* in D) responsible for slow flow.

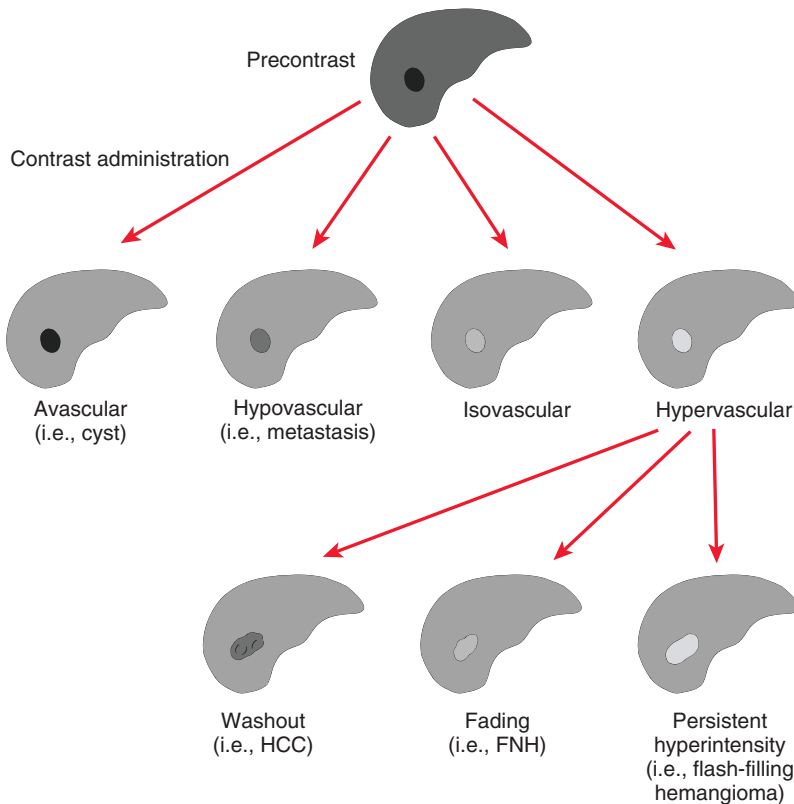


FIGURE 2-17. Liver lesion enhancement scheme based on hepatic artery-dominant phase (HADP) findings. FNH, focal nodular hyperplasia; HCC, hepatocellular carcinoma.

Like ultrasound, MRI unequivocally discriminates solid from cystic lesions and, like CT, incorporates enhancement characteristics into the diagnostic analysis. T2 values differentiate cystic (almost always benign) from solid (benign or malignant) lesions with virtually no overlap. Review the heavily T2-weighted images to identify cystic lesions; visibility on these images connotes predominantly fluid content and excludes solid masses. Cysts, biliary hamartomas, and hemangiomas—all benign lesions—dominate this category, referred to as *cystic lesions*, for the purposes of this discussion. Inflammatory lesions, such as echinococcal cysts and abscesses, enter the differential only in the appropriate clinical setting. In the neoplastic category, only the exceedingly rare biliary cystadenoma (and cystadenocarcinoma) breaches the cystic liver lesion differential and only when characteristic features coexist. Whereas cystic or necrotic metastases feature cystic components, peripheral solid tissue excludes true cystic etiology. Enhancement indicates solid tissue excluding cystic etiologies and serves as the basis for solid versus cystic lesion classification and diagnosis (supplemented by T2 characteristics).

Cystic Lesions

Establish cystic lesion character using heavily T2-weighted images and pre- and postcontrast images. As T2-weighting increases, signal decays from everything but unbound water protons and free fluid. Consequently, on heavily T2-weighted images, all hyperintense lesions are effectively cystic. Cystic designation effectively connotes benign etiology. Simple cysts and biliary hamartomas define the highest end of the T2 signal intensity spectrum as purely fluid-filled structures (Fig. 2-18). Hemangiomas are slightly less intense and frame the lower limit of signal intensity for fluid-intensive liver lesions. Echinococcal cysts are generally similar in intensity to simple cysts, but might be complicated with wall thickening, septation (pericyst), (daughter cyst), and/or internal debris (matrix, hydatid sand). Fungal and pyogenic abscesses are usually not technically cystic and are more accurately described as “liquefying,” but for the purposes of our discussion, they are included in the cystic category. The only neoplastic lesion—biliary cystadenoma/cystadenocarcinoma—is predominantly cystic with variable septation and scant solid tissue (unless rarely flagrantly malignant).

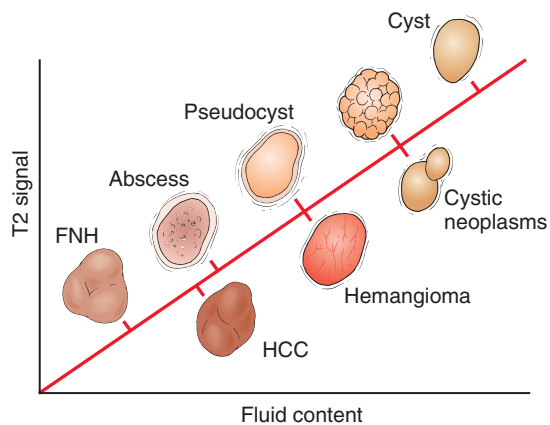


FIGURE 2-18. T2 signal lesion graph. Normal liver tissue plots to the same point as FNH on the graph. FNH, focal nodular hyperplasia; HCC, hepatocellular carcinoma.

Developmental Lesions

SIMPLE HEPATIC CYST

Simple hepatic (bile duct) cysts are benign incidental lesions not communicating with the biliary tree,² although lined with biliary endothelium. They arise from a defect in bile duct formation. Hepatic cyst prevalence has been reported in the 2.5% range,³ although anecdotal experience suggests a higher prevalence. These lesions are almost always incidental, unless associated with an inherited polycystic syndrome.

The water content of cysts dictates the imaging appearance—uniform T2 hyperintensity and T1 hypointensity equivalent to cerebrospinal fluid (Fig. 2-19). No solid tissue complicates the appearance and the wall is imperceptible. Size ranges from a few millimeters to (usually) less than 10 cm. Occasional thin (essentially unmeasurable) septa are present. Simple cysts maintain maximum signal intensity even on heavily T2-weighted images, whereas other relatively high fluid content substances (such as hemangiomas) lose signal compared with moderately T2-weighted images. The absence of solid tissue is confirmed when contrast enhances the background liver parenchyma and the water-filled cyst remains a T1 signal void. Complications explain aberrancy in the monotonous appearance of simple cysts and include infection, rupture, and hemorrhage. Infected cysts may contain septa and debris, which changes the internal signal profile. Hemorrhagic cysts usually exhibit T1 hyperintense internal contents with possible fluid-fluid levels. Although minimal reactive rim enhancement may accompany

these complications, lack of enhancement is otherwise maintained.

Of course, the probability of complications increases with an increased number of cysts. With more than 10 cysts, the possibility of polycystic liver disease (PCLD) should be considered (see Fig. 2-19). PCLD is in the family of fibropolycystic liver diseases that include bile duct hamartoma, Caroli's disease, congenital hepatic fibrosis, and choledochal cysts. Imaging features do not distinguish these cysts from simple hepatic cysts and histology is identical. Although commonly associated with polycystic kidney disease, PCLD also occurs in isolation.

BILE DUCT HAMARTOMA

The bile duct hamartoma (von Meyenburg complex) is another liver lesion that is usually cystic. It is a focal cluster of disorganized bile ducts and ductules surrounded by fibrous stroma. Bile duct hamartomas are incidental developmental lesions of uncertain pathogenesis—possibly ischemia, inflammation, or genetic anomalies. Although present in 3% of autopsy specimens,^{4,5} more than half evade detection on imaging studies. Lesion size ranges from 2 to 15 mm, and they tend to be peripherally distributed. The MRI appearance is defined by a spectrum extending from simple fluid with no enhancement on one end to solid, enhancing tissue (fibrous stroma) on the other. The simple fluid appearance dominates, simulating a hepatic cyst, although a thin, peripheral rim of enhancement occasionally coexists (Fig. 2-20). When solid, these lesions exhibit intermediate signal intensity on T2-weighted images and generally gradually solidly enhance. Progressive enhancement of the fibrous tissue simulates metastases and follow-up imaging to confirm stability or biopsy ensues.

CAROLI'S DISEASE

Caroli's disease (or "congenital communicating cavernous ectasia of the biliary tract," if you prefer—less mellifluous but descriptive) simulates other polycystic liver diseases—PCLD, multiple simple (biliary) hepatic cysts, and biliary hamartomas. Many of these cystic diseases (except the biliary cyst) derive from primordial ductal plate disorders.^{6,7} Caroli's disease represents one of the family of fibrocystic ductal plate diseases to which the following diseases also belong: autosomal recessive polycystic kidney disease, congenital hepatic fibrosis, autosomal

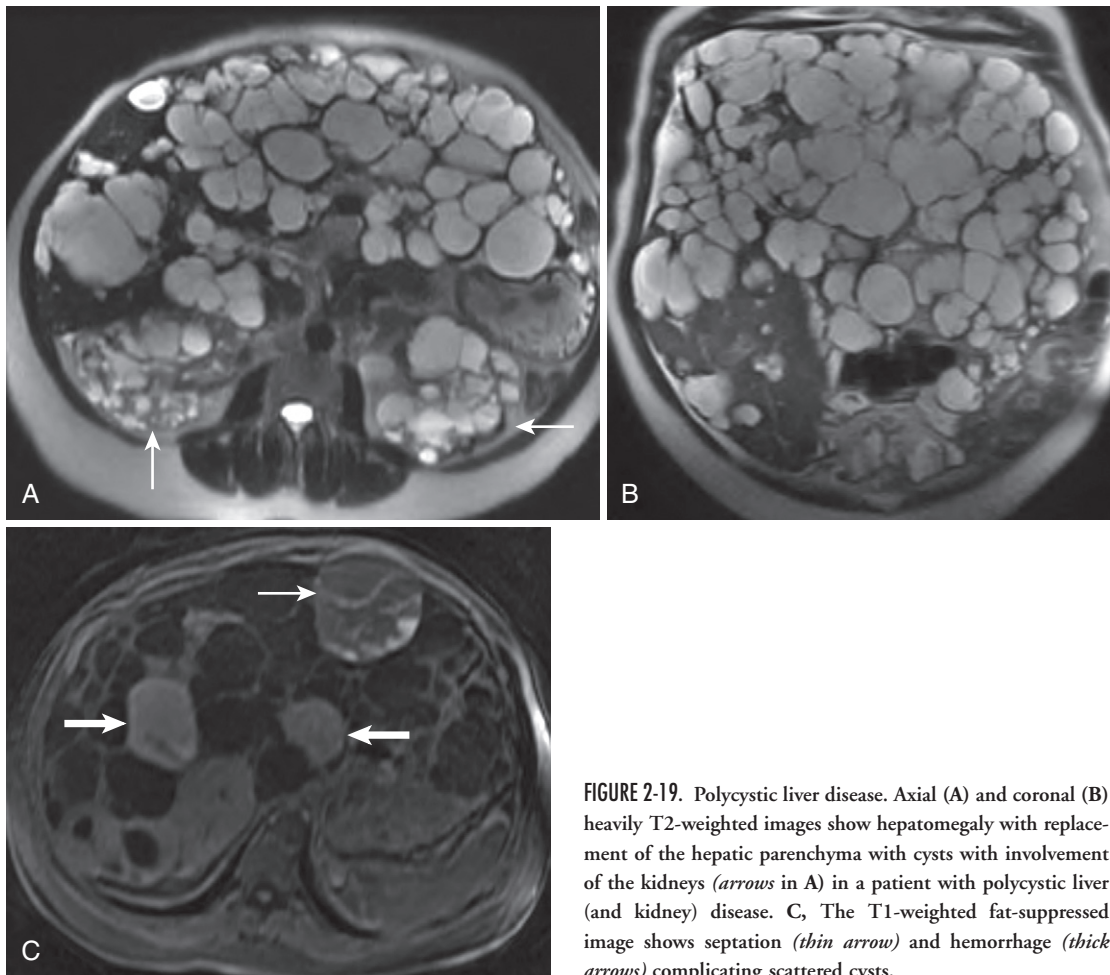


FIGURE 2-19. Polycystic liver disease. Axial (A) and coronal (B) heavily T2-weighted images show hepatomegaly with replacement of the hepatic parenchyma with cysts with involvement of the kidneys (*arrows in A*) in a patient with polycystic liver (and kidney) disease. C, The T1-weighted fat-suppressed image shows septation (*thin arrow*) and hemorrhage (*thick arrows*) complicating scattered cysts.

TABLE 2-7. Fibrocystic Ductal Plate Diseases

Congenital hepatic fibrosis
Autosomal recessive polycystic kidney disease
Autosomal dominant polycystic kidney disease
Autosomal dominant polycystic liver disease
Caroli's disease
Choledochal cysts
Biliary hamartomas

dominant polycystic kidney disease, biliary hamartomas, and mesenchymal hamartomas (Table 2-7). The ductal plate represents the anlage of the intrahepatic biliary system. Ductal plate remodeling into the mature intrahepatic biliary dilatation follows a complex series of precisely timed events. In the case of Caroli's disease, arrest in ductal plate remodeling involves the larger bile ducts (interlobular and more central); Caroli's syndrome affects the smaller, peripheral intrahepatic ducts, which undergo remodeling later in embryonic life and manifest with co-existent hepatic fibrosis. A pattern of segmental

inflammation and stricturing alternating with saccular and fusiform dilatation of the involved ducts results.

MRI reveals innumerable round and/or tubular fluid collections within the liver measuring up to 5 cm in Caroli's disease. Although the presence of multiple cystic intrahepatic foci simulates PCLD or biliary hamartomas, communication with the biliary tree discriminates Caroli's disease from these entities. An additional discriminating feature—the central dot sign⁸—seen on enhanced images, reflects the portal vein branch within the dilated biliary radicle. Intraductal/intracystic filling defects (usually bilirubin stones) may also differentiate Caroli's disease from the other cystic liver disorders and are best visualized on fluid-sensitive sequences—either heavily T2-weighted or MRCP images.

Other diseases to consider in the differential diagnosis include primary sclerosing cholangitis (PSC) and recurrent pyogenic cholangitis (RPC). Ductal dilatation is less severe and more

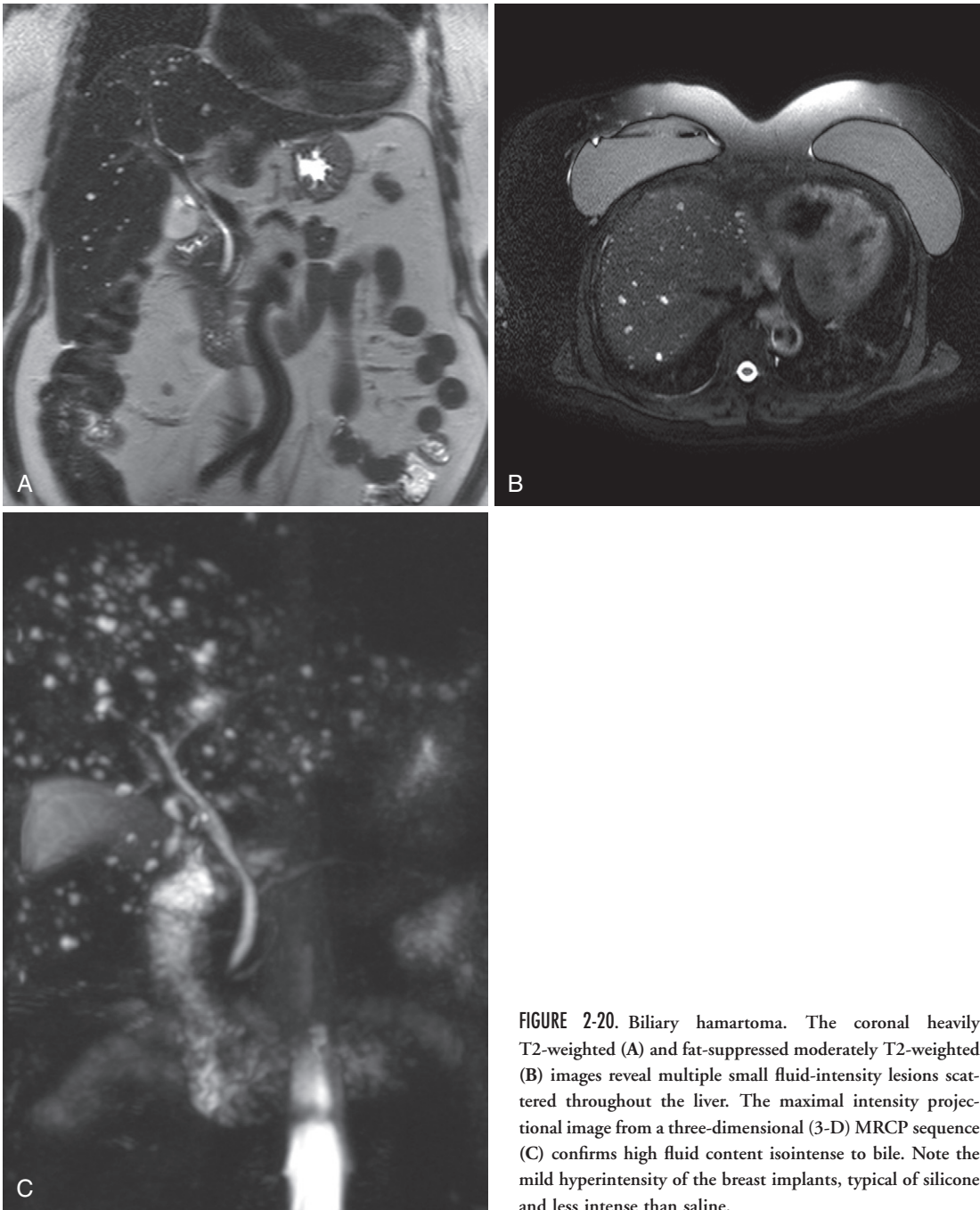


FIGURE 2-20. Biliary hamartoma. The coronal heavily T2-weighted (A) and fat-suppressed moderately T2-weighted (B) images reveal multiple small fluid-intensity lesions scattered throughout the liver. The maximal intensity projectional image from a three-dimensional (3-D) MRCP sequence (C) confirms high fluid content isointense to bile. Note the mild hyperintensity of the breast implants, typical of silicone and less intense than saline.

cylindrical (as opposed to saccular) in PSC and RPC compared with Caroli's disease. Involvement of the extrahepatic duct often characterizes PSC and RPC and excludes Caroli's disease. Complications in Caroli's disease occur as a consequence of bile stagnation and include stones, cholangitis, hepatic abscesses, postinflammatory strictures, and secondary biliary cirrhosis. Cholangiocarcinoma develops in 7% of patients.

CAVERNOUS HEMANGIOMA

Hemangiomas (cavernous hemangiomas) are classified as cystic for the purposes of this discussion because of the high fluid content and MR signal characteristics similar to fluid—even though the internal contents are blood, instead of water, or serous fluid. Blood flowing slowly enough to avoid flow artifacts and/or flow voids accounts for the signal characteristics; a single

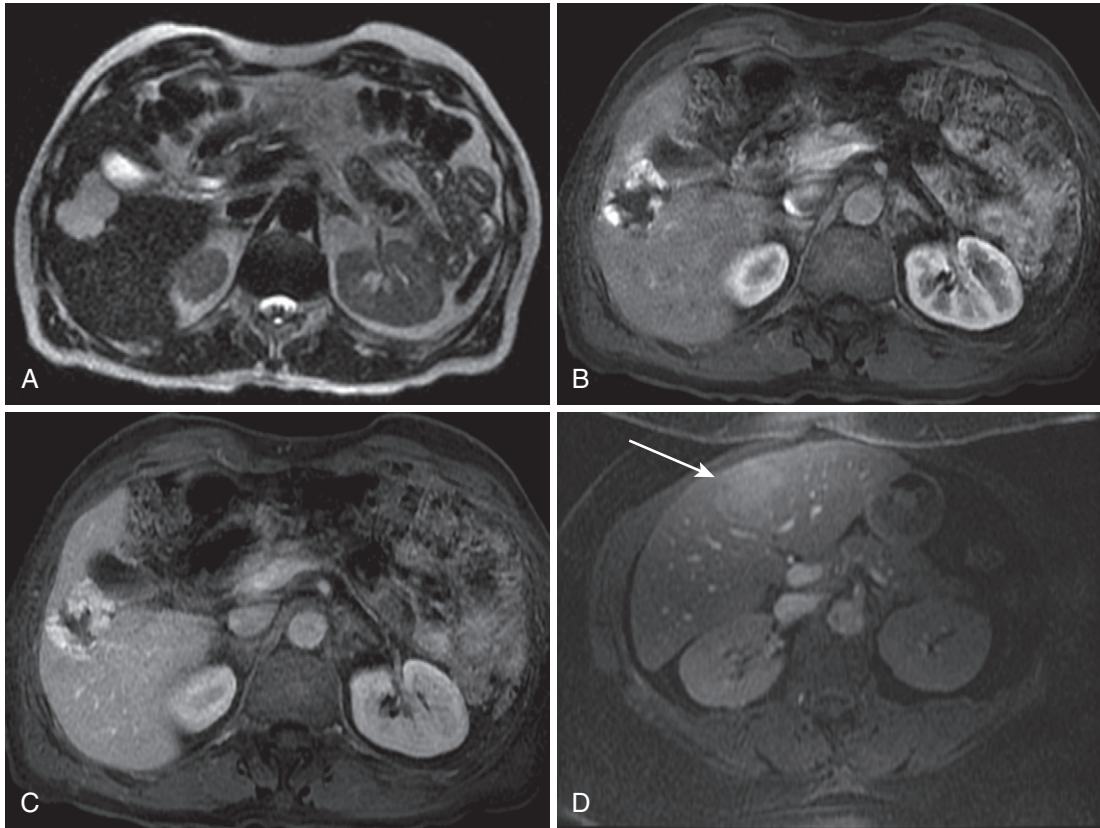


FIGURE 2-21. Hemangioma. A, The hemangioma with a characteristic lobulated border demonstrates moderately high hyperintensity on the heavily T2-weighted image (A), but less than the adjacent fluid-filled gallbladder. The arterial phase image (B) demonstrates the typical clumped, discontinuous peripheral enhancement, which gradually progresses centripetally to complete uniform hyperintensity, as seen (*arrow* in D) on the portal phase (C) and delayed (D) images in a different patient.

layer of endothelial lining suspended by fibrous stroma constitutes the only solid component. Hemangiomas are almost invariably incidental lesions representing a collection of dilated vascular channels replacing hepatic parenchyma. Hemangiomas are found in 7% of patients with a slight female predominance (1.5:1). Multiple hemangiomas are present in up to 50% of patients.

Hemangiomas range in size from a few millimeters to well over 10 cm and complexity is generally proportional to size. The prototypic hemangioma exhibits homogeneous near-isointensity to simple fluid (cyst) on heavily T2-weighted images with well-defined, lobulated borders and exhibits a unique enhancement pattern. Early peripheral, nodular, discontinuous enhancement centripetally progressively fills in on successive delayed images until uniform hyperattenuation (relative to hepatic parenchyma) is achieved (Fig. 2-21).

The aforementioned imaging features define the standard appearance of hemangiomas (type

2; Fig. 2-22). Relatively smaller and larger hemangiomas have a predilection for variant enhancement patterns. Small hemangiomas (<2 cm) more often demonstrate uniform early and persistent hyperenhancement (type 1; Fig. 2-23). Early hyperenhancement also characterizes other benign and malignant lesions, such as FNH, adenoma, HCC, and hypervascular metastases. Marked T2 hyperintensity and persistent hyperenhancement single out the so-called flash-filling hemangioma from the other hypervascular lesions (none of which exhibit marked T2 hyperintensity and all of which either washout or fade on delayed images). Perilesional perfusional alterations most commonly accompany the smaller flash-filling hemangiomas (see Fig. 2-23). Segmental or nodular hyperattenuation (usually peripheral to the lesion) on HADP images fades to isointensity on delayed images and reflects either increased arterial inflow or arteriportal shunting resulting in contrast overflow into perilesional sinusoids.⁹⁻¹¹

Giant hemangiomas often display complex imaging features. The definition of *giant hemangioma* varies from 4 to 10 or 12 cm, depending on the source (4 cm is the conventional size cutoff).¹²⁻¹⁶ The enhancement pattern of the giant hemangioma often reiterates the typical pattern with peripheral, nodular, discontinuous centripetal propagation, except for the presence of a central nonenhancing “scar.” The

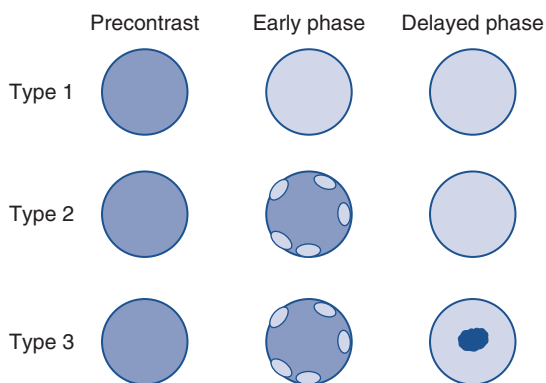


FIGURE 2-22. Hemangioma enhancement types.

central variably shaped “scar” (linear, round, oval, cleftlike, or irregular) conforms to cystic degeneration, liquefaction, or myxoid change and usually appears relatively T1 hypo- and T2 hyperintense to the surrounding lesion (Fig. 2-24). Although other liver lesions possess central scars, such as FNH, fibrolamellar HCC, and cholangiocarcinoma, these scars usually enhance late and overall lesion enhancement features are distinctly different (FNH and fibrolamellar HCC hyperenhance then washout, whereas rim enhancement with patchy, irregular progression typifies cholangiocarcinoma).

Less common features complicate the MR appearance of hemangiomas, such as pedunculation, calcification, capsular retraction, and hyalinization or thrombosis (Fig. 2-25). Whereas torsion and/or ischemia may complicate the appearance of an exophytic or pedunculated hemangioma, the appearance is otherwise typical—just be aware that pedunculation rarely occurs. Reported prevalence of calcification varies from 1% to 20%, and anecdotally, the

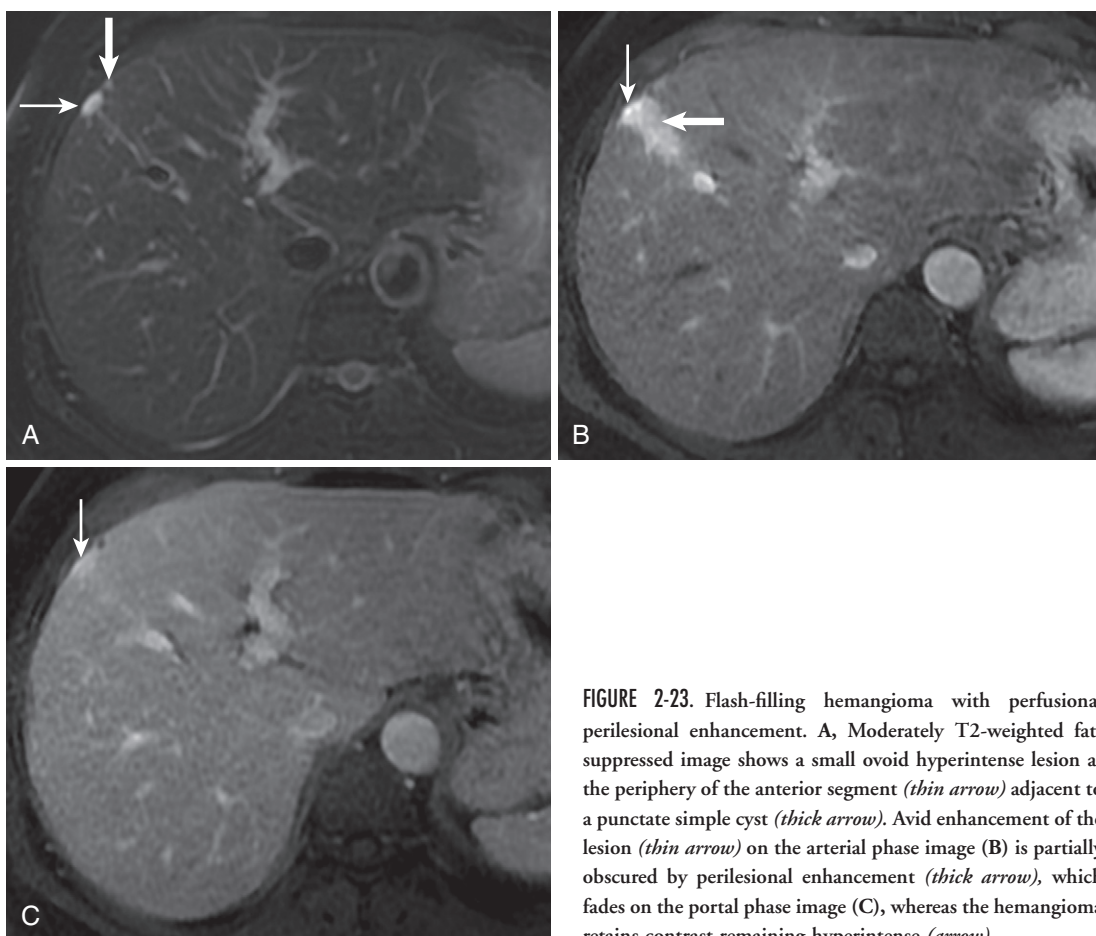


FIGURE 2-23. Flash-filling hemangioma with perfusional perilesional enhancement. A, Moderately T2-weighted fat-suppressed image shows a small ovoid hyperintense lesion at the periphery of the anterior segment (*thin arrow*) adjacent to a punctate simple cyst (*thick arrow*). Avid enhancement of the lesion (*thin arrow*) on the arterial phase image (B) is partially obscured by perilesional enhancement (*thick arrow*), which fades on the portal phase image (C), whereas the hemangioma retains contrast remaining hyperintense (*arrow*).

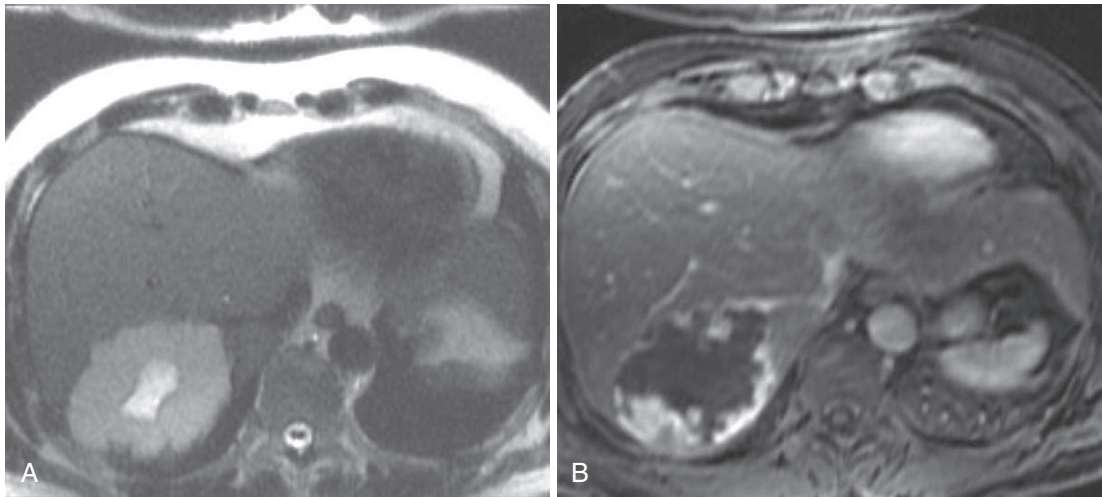


FIGURE 2-24. Giant hemangioma with cystic degeneration. **A**, The axial heavily T2-weighted image reveals a large hemangioma in the posterior segment with central hyperintensity. Whereas the periphery of the hemangioma exhibits the typical early nodular peripheral enhancement (**B**) with complete fill-in on the delayed image (**C**), the central cystic focus fails to enhance.

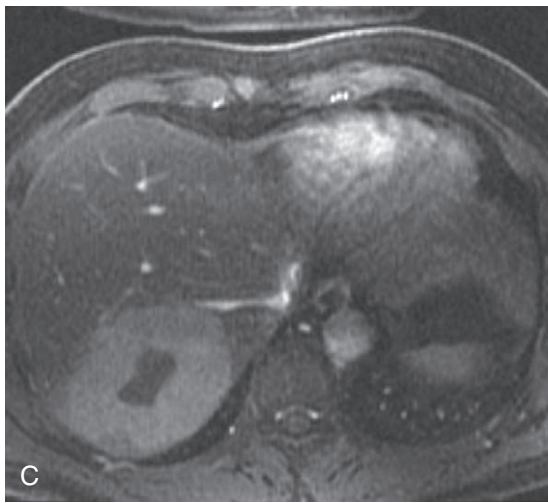


FIGURE 2-25. Complex hemangioma. The stellate central hypointensity (*arrow* in **A**) within the hyperintense hemangioma on the moderately T2-weighted image (**A**) fails to enhance on the delayed image (**B**).

actual prevalence seems to be closer to the lower end of the range, or even lower.^{17,18} Calcification in a hemangioma corresponds to phleboliths and/or dystrophic changes in areas of fibrosis and thrombosis. Practically speaking, calcification rarely, if ever, confounds the MR appearance of hemangiomas, and if present, most likely manifests as a signal void. When

peripheral, fibrosis associated with a hemangioma potentially results in capsular retraction. The other focal hepatic lesion known to induce capsular retraction is cholangiocarcinoma, which should not present diagnostic difficulty. Hyalinization indicates hemangioma involution and histologically corresponds to thrombosis of vascular channels.^{12,19} T2 signal decreases

remaining relatively hyperintense to liver and enhancement is variably absent with as little as minimal peripheral delayed enhancement.

A few parting thoughts about hemangiomas are worth mentioning. Although usually static, hemangiomas have been shown to grow on occasion (sometimes with exogenous estrogens), and conversely, they are usually eradicated in the setting of cirrhosis. Malignant transformation has never been described and spontaneous rupture is exceedingly rare (~30 cases have been reported).²⁰ There is no known association with other tumors or other diseases, except Kasabach-Merritt syndrome (KMS). KMS involves a vascular tumor—such as a hemangioma or hemangioendothelioma—sequestering

platelets causing thrombocytopenia. Consumption of clotting factors ensues, leading to disseminated intravascular coagulation (DIC). Unless associated with KMS or DIC, for which surgical resection may be warranted, no treatment or follow-up is necessary.

Hemangiomatosis refers to diffuse replacement of hepatic parenchyma by multiple, often innumerable, ill-defined hemangiomas. Diffuse enlargement of the liver with multiple lesions with signal and enhancement characteristics typical of hemangiomas—albeit frequently with ill-defined margins—often profoundly disfigures the liver, rendering it virtually unrecognizable (Fig. 2-26). Although commonly resulting in high-output cardiac failure and mortality in

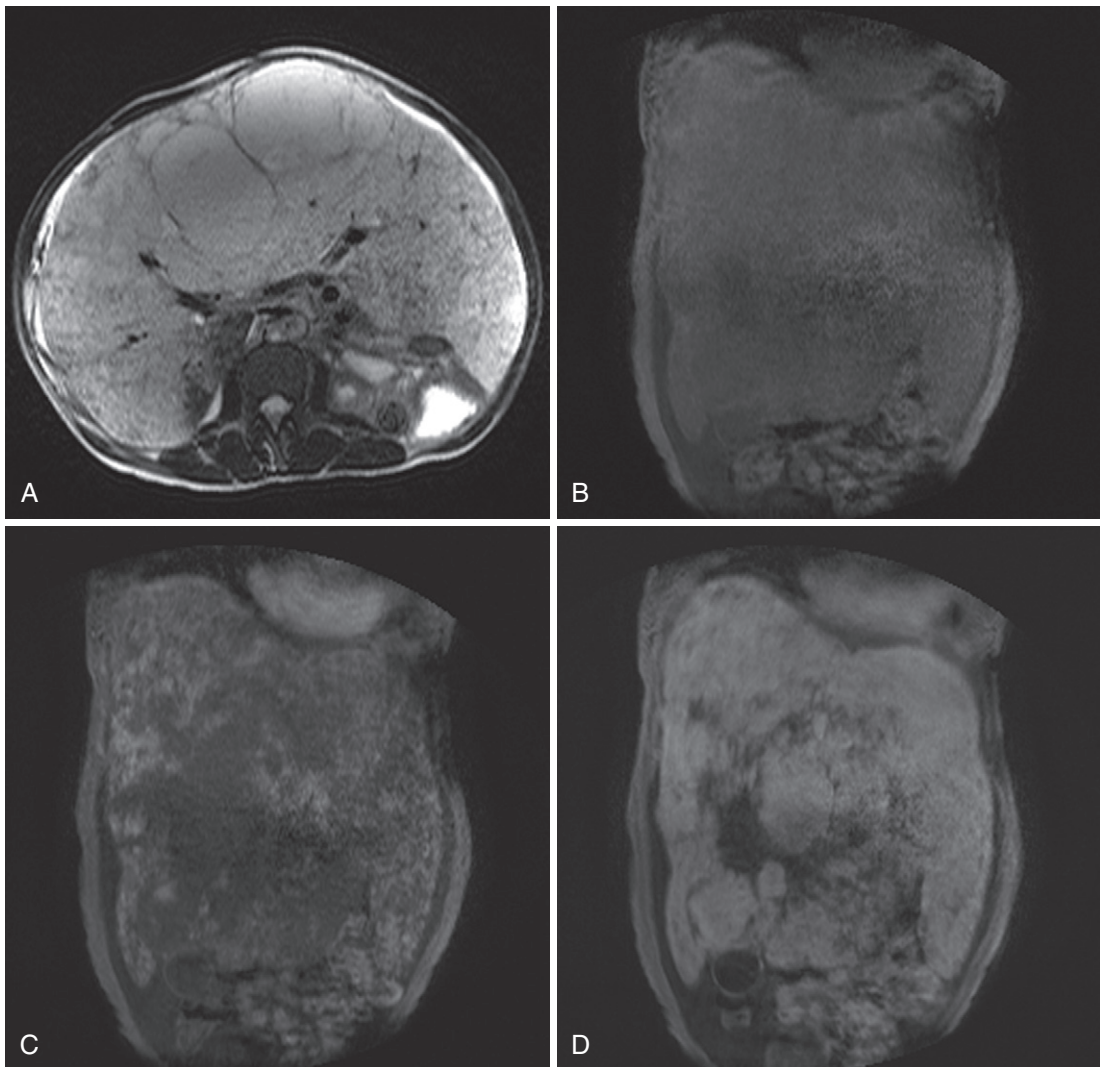


FIGURE 2-26. Hemangiomatosis. Replacement of the normal hepatic parenchyma by ill-defined, near-fluid hyperintensity on the axial T2-weighted image (A) with gross hepatomegaly evident on the precontrast T1-weighted image (B). Following the administration of intravenous gadolinium, multifocal nodular enhancement on the arterial phase image (C) progresses to near-complete enhancement on the delayed image (D), reminiscent of a hemangioma.

infants, hemangiomas usually symptomatically spares adults—only potentially generating diagnostic uncertainty on imaging studies.

Unlike the previously discussed lesions, the remaining cystic liver lesions—biliary cystadenoma/cystadenocarcinoma and infectious lesions—exhibit more complexity and variability. Multilocularity and wall thickening are common features, and these lesions rarely simulate the other simple cystic lesions already discussed. Clinical factors assume a greater role in diagnosis, which is important because all of these lesions require further treatment.

Neoplastic Lesions

BILIARY CYSTADENOMA (-ADENOCARCINOMA)

Biliary cystadenomas and cystadenocarcinomas require surgical resection for treatment and potential cure. These lesions arise from bile duct epithelium—constituted from mucin-secreting epithelial cells. Approximately 85% arise from intrahepatic bile ducts (as opposed to extrahepatic bile ducts and gallbladder).²¹ Most commonly affecting middle-aged females, two histologic subtypes—with or without ovarian stroma (accounting for the female preponderance)—confer different prognostic outcomes. Lesions with ovarian stroma exhibit a more indolent course compared with lesions with absent ovarian stroma.²² Differentiating benign (cystadenoma) from malignant (cystadenocarcinoma) is less relevant than discriminating neoplasm from nonneoplastic etiologies, because of the treatment implications—biopsy and ultimately resection. In any event, no imaging features reliably discriminate benign from malignant.

To put things in perspective, these lesions reportedly constitute less than 5% of cystic liver lesions²³ and empirically far less than that. Size ranges from a few centimeters to up to 40 cm and, when detected on imaging studies, these lesions are usually fairly large (Fig. 2-27). Although occasionally unilocular, multilocularity, septation, and nodularity distinguish these lesions from other cystic liver lesions. Variable signal intensity of internal contents depends on mucin content and occasional hemorrhage. Whereas mild wall thickening is common and nonspecific, associated T2 hypointensity from hemorrhage excludes many other potential

confounders. Septal and mural calcification best visualized on CT usually evades detection on MRI. Communication with the biliary tree—albeit rare and more likely noted on endoscopic retrograde cholangiopancreatography (ERCP) than MRCP—does not exclude biliary cystadenoma/cystadenocarcinoma.²⁴

Nonneoplastic cystic lesions dominate the differential diagnostic possibilities. Echinococcal cyst, pyogenic abscess, and complicated (hemorrhagic) bile duct cyst most frequently approximate the MR appearance of biliary cystadenoma. Rare cystic HCC and cystic metastases are worth considering in the differential, but usually manifest a greater solid component, irregular margins, and suggestive clinical features.

Infectious Lesions

ECHINOCOCCAL CYST

Inflammatory cystic lesions rarely afflict the liver and definitive diagnosis usually relies on clinical information, such as concurrent infection in the gastrointestinal tract or demographic data in the case of echinococcal cyst—endemic in certain parts of the world (Table 2-8). Echinococcal cysts are a manifestation of hydatid disease, which encompasses infestation by either of two different species of parasites—*Echinococcus granulosus* and *Echinococcus multilocularis*. Dogs, sheep, and cattle serve as (definitive and intermediate) host organisms for these parasites. Ingestion of food contaminated with embryonated eggs (in feces) leads to human infestation. Ingested organisms penetrate the intestinal wall and migrate hematogenously (usually) to the

TABLE 2-8. Inflammatory Cystic Liver Lesions

Lesion	Pathogen	Imaging
Pyogenic abscess	<i>Clostridium</i> Gram-negative organisms	Variable liquefaction Cluster sign Reactive enhancement
Nonpyogenic abscess Amoebic abscess	<i>Entamoeba histolytica</i>	Well-defined Peripheral right lobe Extrahepatic findings
Fungal abscess	<i>Candida albicans</i>	<1 cm Peripheral Prominent T2 hyperintensity Splenic, renal involvement
Mycobacterial abscess	<i>Mycobacterium tuberculosis</i>	Possibly T2 hypointense Calcification Lymphadenopathy
Echinococcal cyst	<i>Echinococcus granulosus</i>	Daughter cysts Hypointense pericyst Internal debris, membranes

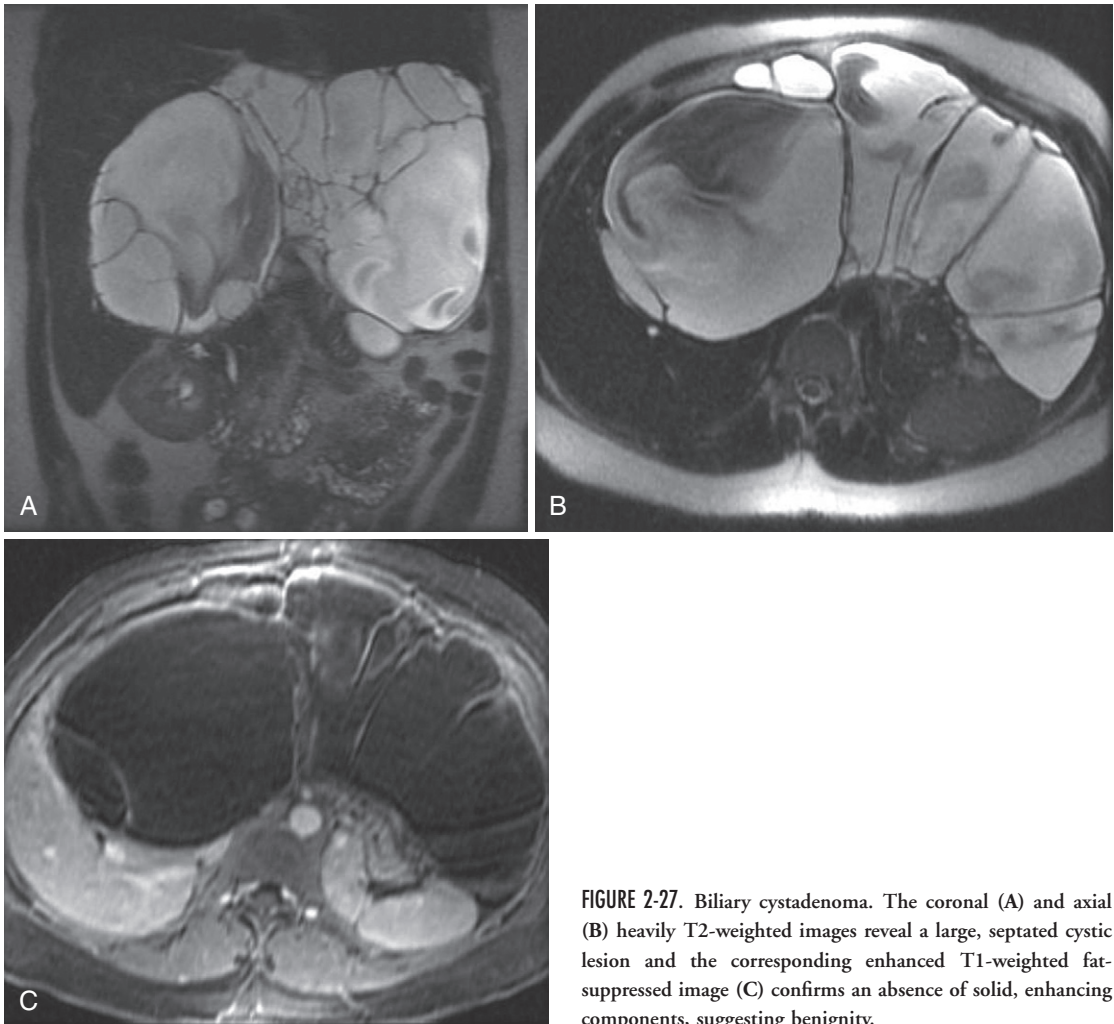


FIGURE 2-27. Biliary cystadenoma. The coronal (A) and axial (B) heavily T2-weighted images reveal a large, septated cystic lesion and the corresponding enhanced T1-weighted fat-suppressed image (C) confirms an absence of solid, enhancing components, suggesting benignity.

liver and lungs (but not exclusively)—liver 63%, lungs 25%, muscles (5%), bones (3%), kidneys (2%), brain (1%), and spleen (1%). In the target organ, the parasite develops into a cyst. Internal daughter cysts and protoscolices proliferate.

Notwithstanding the respective names, *E. granulosus* exhibits a multiloculated imaging appearance contrasted with the infiltrative pattern typified by *E. multilocularis*. Although neither is endemic in the United States, *E. granulosus* cases outnumber *E. multilocularis* in the United States, with approximately 1 per 1 million inhabitants. Endemic areas include the Middle East, southern South America, southern Africa, the Mediterranean region, Australia, and New Zealand. Increasing size and pressure effects lead to symptoms such as abdominal pain, jaundice, cough, pleuritic chest pain, and dyspnea.

Understanding the mature hydatid cyst structure and life cycle facilitates appreciation of the imaging appearance. Mature hydatid cystic trilaminar cyst wall structure encompasses the outer pericyst (the fibrous host response layer), the middle laminated membrane (i.e., ectocyst, transmitting the passage of nutrients), and the inner germinal layer (endocyst), from which the laminated membrane and larvae (scolices) are produced. Scolices spawned from the endocyst are contained within daughter cysts (“brood capsules”) within the cyst. Over time, the hydatid cyst degenerates and progressively calcifies (Fig. 2-28).

The imaging appearance corresponds to the phase of the life cycle and the presence/absence of complications. In fact, a radiologic classification system expresses this fact visually (see Fig. 2-28).²⁵ The hydatid cyst generally progresses

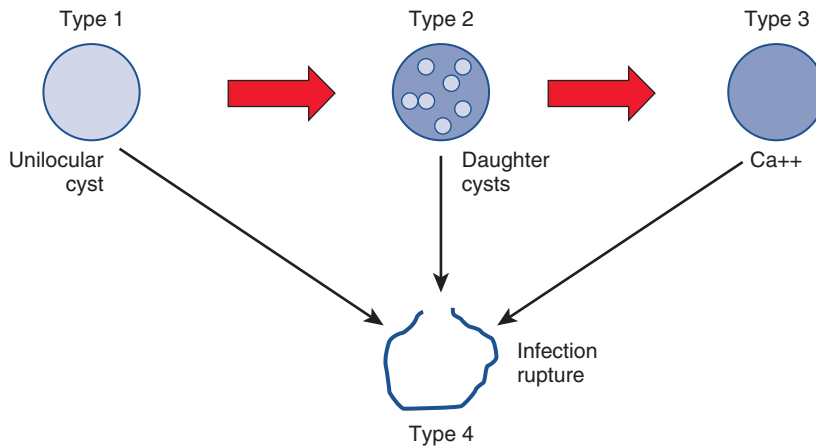


FIGURE 2-28. Hydatid cyst evolution and structure.

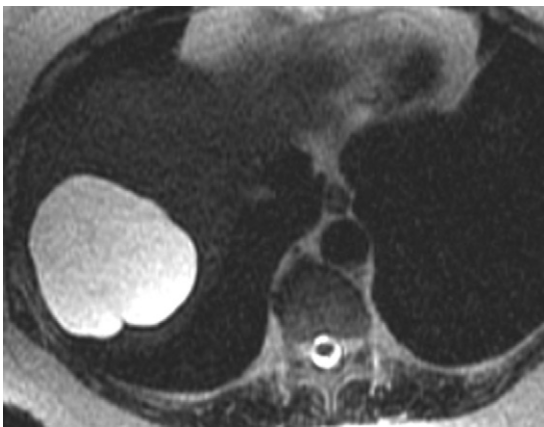


FIGURE 2-29. Echinococcal cyst. Except for a mildly irregular contour, the thin hypointense rim is the only finding complicating the large echinococcal cyst in the right lobe—daughter cysts would seal the diagnosis.

from a simple unilocular cyst (type I) (Fig. 2-29) to a multilocular cyst with internal, peripherally arrayed daughter cysts (type II), to wall calcification to complete calcification at the end of the cycle (type III). Cyst complication with rupture and/or infection is the type IV hydatid cyst. The fibrous pericyst accounts for the commonly observed T2 hypointense rim, a characteristic finding in hydatid disease.²⁶ Developing daughter cysts contain fluid with simple features compared with surrounding endocystic fluid, which is generally more T1 hyperintense and T2 hypointense. Endocystic internal contents are further complicated by collapsed parasitic membranes—twisted curvilinear hypointensities representing detached, involuted daughter cysts.

Imaging occasionally discloses cyst rupture or infection—the primary complications of hepatic hydatid disease. The cyst rupture classification

scheme describes three categories: contained, communicating, and direct.²⁷ *Contained rupture* connotes endocyst rupture with pericyst integrity with the detached endocyst reflected by “floating membranes,” a contracted serpiginous intraluminal hypointensity. *Communicating rupture* happens when cyst contents pass into biliary radicles incorporated into the pericyst. *Direct rupture* involves both the endocyst and the pericyst with spillage into the peritoneal cavity. Communicating and direct ruptures result in cyst deflation and focal loss of integrity of the hypointense pericyst, although interruption of the hypointense rim is often difficult to visualize. Communicating and direct ruptures permit intracystic passage of bacteria and superinfection. Poorly defined margins, increasing complexity, a solid appearance, and intraluminal gas suggest infection.

The differential diagnosis of uncomplicated hydatid cysts includes simple hepatic (bile duct) cysts and biliary cystadenoma—biliary hamartomas are generally smaller although similar in appearance. Pyogenic abscess, biliary cystadenoma/cystadenocarcinoma, and cystic metastases share common imaging features with complicated echinococcal cysts. Inclusion of hydatid cyst in the differential hopefully precludes inadvertent spillage of cyst contents during attempted biopsy or aspiration, which potentially incites an anaphylactic response. Recognition of the typical features of echinococcus eliminates this risk and directs the clinician to the appropriate workup—serology. Medical therapy (antihelminthics, e.g., albendazole) is the first-line treatment; surgical resection generally follows failure of medical therapy.

PYOGENIC ABSCESS

Clinical history and demographic factors usually distinguish other infectious lesions from hydatid cysts. Pyogenic, amebic, and fungal types constitute the different varieties of liver abscesses encountered in clinical practice. An identifiable source is established in 40% to 50% of cases of pyogenic, or bacterial, abscesses. Ascending biliary infection and hematogenous spread via the portal system account for most cases of pyogenic abscesses; with the advent of antibiotics, biliary transmission has surpassed portal venous hematogenous spread. Other etiologies include hematogenous spread via the hepatic arterial circulation (in the setting of septicemia), direct extension from intraperitoneal infection, and posttraumatic or postprocedural causes. In contradistinction to echinococcal cysts, aspiration—for the purposes of diagnosis and treatment/drainage—is routine in the case of pyogenic abscess. Mixed pathogens are cultured 50% of the time and common organisms include *Escherichia coli* (associated with biliary infection and pylephlebitis from hematogenous portal venous transmission), gram-positive cocci (in the setting of sepsis), and others, such as clostridium, proteus, klebsiella, and bacteroides.

The temporal evolution of pyogenic abscess explains the protean appearance. In the first of three phases—the acute phase—spanning the first 10 days, parenchymal necrosis and liquefaction begin to develop. The subacute phase—days 10 to 15—entails ongoing liquefaction and resorption of debris. The chronic phase—beyond day 15—is heralded by the development of a thick fibrous wall enveloping the central necrotic material (Fig. 2-30). Consequently, the MRI appearance depends on the phase of evolution along this time course—the degree of liquefaction and encapsulation increases with chronicity. Although occasionally unilocular and solitary, pyogenic abscesses are usually multilocular and multiple. The “cluster” sign

describes the characteristic coalescence of small abscess cavities thought to represent an early step in the development of a large multiseptated abscess cavity (Fig. 2-31; see also Fig. 2-30).²⁸ Solid components, including the abscess wall and septa, enhance dramatically on arterial phase images and remain hyperintense on delayed images. Circumferential or triangular edema extending peripherally from the lesion arising from sinusoidal congestion appears hyperintense on T2-weighted images and usually enhances avidly, although less than solid components of the abscess.

Without suggestive clinical and laboratory findings, pyogenic abscess is not a straightforward diagnosis. Hydatid cyst, amebic abscess, cystic metastases, and biliary cystadenoma/cystadenocarcinoma share common features. The presence of (usually curvilinear) calcification occasionally seen in echinococcal cysts (predominantly on CT) excludes the possibility of pyogenic abscess; internal, peripherally arrayed daughter cysts conceivably simulate the cluster sign—but encapsulation within, rather than coalescence to contrive a dominant cyst, distinguishes daughter cysts from the cluster sign, respectively. Whereas the enhancement pattern of the amebic abscess mimics the pyogenic abscess enhancement pattern,²⁹ the amebic abscess is usually solitary (85%) and well defined. Cystic, or necrotic, metastases closely simulate the appearance of pyogenic abscesses, lacking only the cluster sign. The biliary cystadenoma fails to exhibit surrounding inflammatory changes and multiplicity. Intralesional gas—perhaps the most specific sign—reflected by uniform punctate hypointensities with susceptibility artifact excludes other etiologies, although present only 20% of the time.

AMEBIC ABSCESS

Although *Entamoeba histolytica*—the causative parasite in amebic liver abscess—colonizes

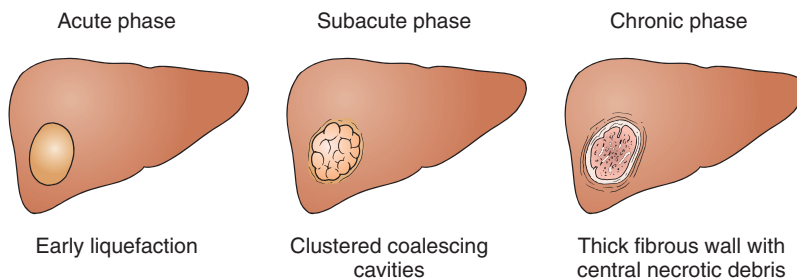


FIGURE 2-30. Pyogenic liver abscess evolution.

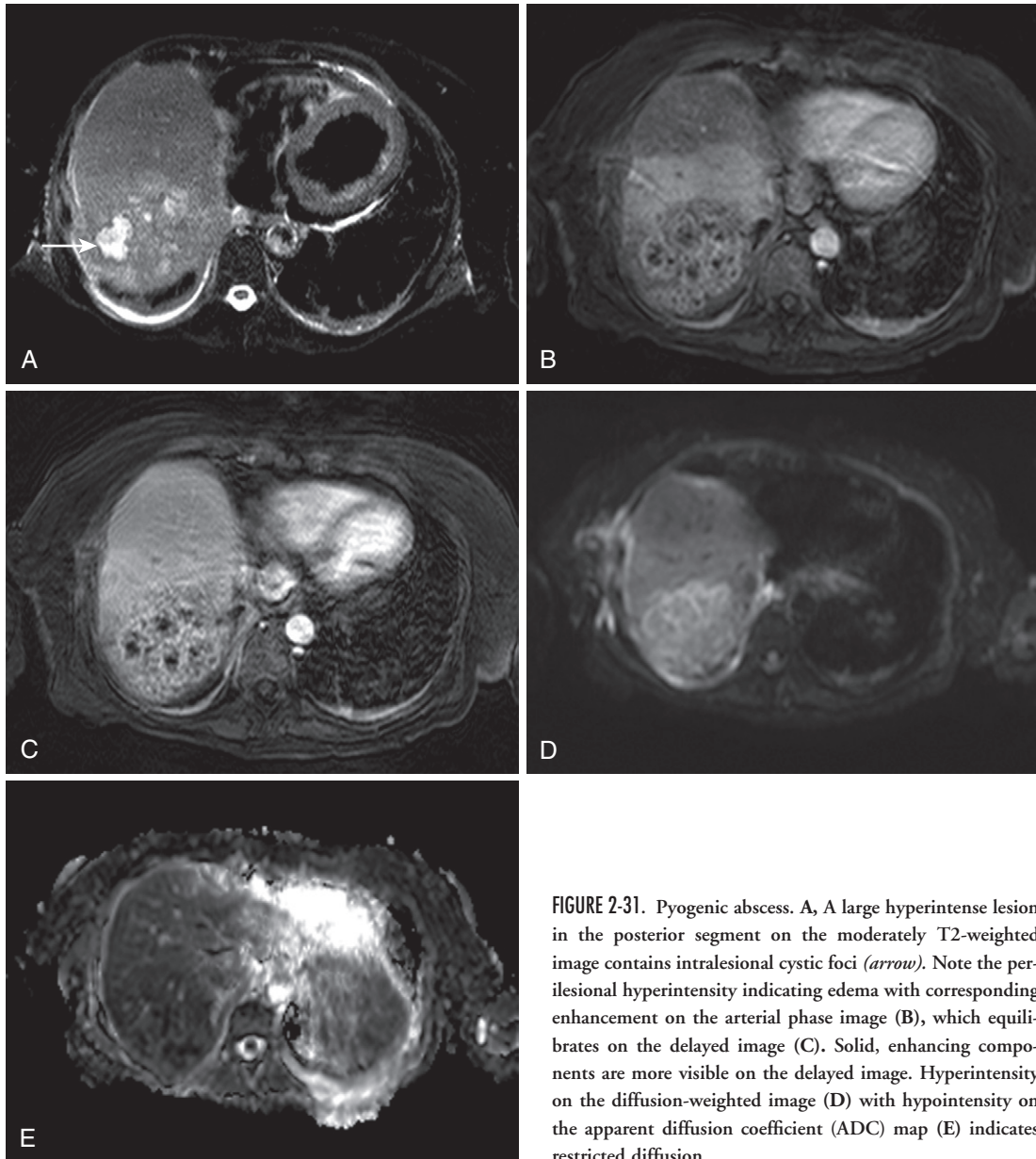


FIGURE 2-31. Pyogenic abscess. **A**, A large hyperintense lesion in the posterior segment on the moderately T2-weighted image contains intralesional cystic foci (*arrow*). Note the perilesional hyperintensity indicating edema with corresponding enhancement on the arterial phase image (**B**), which equilibrates on the delayed image (**C**). Solid, enhancing components are more visible on the delayed image. Hyperintensity on the diffusion-weighted image (**D**) with hypointensity on the apparent diffusion coefficient (ADC) map (**E**) indicates restricted diffusion.

the large bowel in 12% of the world population, the amebic hepatic abscess is a rare entity in the United States (<3000 reported to the Centers for Disease Control and Prevention [CDC] in 1994). The highest rates of infestation are observed in Mexico, Central and South America, India, and tropical areas of Asia and Africa. Ingesting the larval, cystic form of the organism in feces leads to colonization of the cecum, where trophozoites penetrate the mucosa, initiating symptomatic infection and potentially mesenteric venous dissemination to the liver (the right lobe in ~75% of cases).

Amebic abscess MRI features are not highly specific. Right lobe predominance most likely reflects mesenteric laminar flow—the superior mesenteric vein (SMV), which drains the colonized colon flows toward the right hepatic lobe. Peripheral location presumably also reflects hematogenous origin. Whereas sharper margins distinguish the amebic abscess from the pyogenic abscess, enhancement and signal characteristics overlap.³⁰ A high prevalence of extrahepatic manifestations—right pleural effusion, perihepatic fluid collections, and gastric and/or colonic involvement—potentially

discriminates the amebic abscess from other etiologies.

Serologic testing identifying antibodies specific for *E. histolytica* clinches the diagnosis. Amebicidal medical therapy (metronidazole) eradicates liver infestation. Aspiration is avoided unless (1) medical therapy fails in 5 to 7 days, (2) impending rupture is imminent, (3) pyogenic abscess is not definitively excluded, and (4) the left lobe is involved (associated with greater mortality and potential peritoneal and pericardial spread).

FUNGAL ABSCESS

Fungal abscesses are distinguished by the clinical scenario—neutropenia—and the characteristic imaging appearance. Usually caused by the fungus *Candida albicans* and otherwise known as hepatic candidiasis, fungal abscesses spread in immunocompromised patients with hematopoietic malignancies, intensive chemotherapy, and acquired immunodeficiency syndrome (AIDS). Bowel wall trauma in the immunosuppressed state permits transmural migration of the organism and hematogenous dissemination. Subsequent clinical symptoms and abscess formation often signify the onset of recovery from neutropenia with a mounting immune response.

Small size (<1 cm) and diffuse, random distribution throughout the liver (and spleen—rarely involving the kidneys) characterize candidiasis. Slight T1 hypointensity, prominent T2 hyperintensity, and hypointensity on enhanced images typify these microabscesses before treatment.³¹ In the subacute phase after antimycotic treatment, signal characteristics convert to mild hyperintensity on T1-weighted, T2-weighted, and enhanced images; a peripheral hypointense rim corresponds to hemosiderin-laden macrophages surrounding the granulomas.³²

Whereas the clinical features strongly suggest the diagnosis in the appropriate setting, MRI plays a role in the diagnosis.³³ MRI sensitivity and specificity exceed other diagnostic imaging studies, and harvesting organisms from either blood cultures or biopsy samples is difficult. Despite its diagnostic utility, MRI features of candidiasis may raise the specter of alternative diagnoses, such as pyogenic abscesses, metastases, lymphomatous infiltration, and biliary hamartomas. Clustering, larger size, more extensive cystic/necrotic features, and lack of splenic involvement favor pyogenic abscesses. Larger size and smaller number, along with clinical

parameters and absence of splenic involvement, generally separate metastases from hepatic candidiasis. Although hepatic lymphomatous infiltration often involves the spleen, larger, less numerous lesions with more infiltrative margins differentiate the imaging appearance from candidiasis. The solid variant of biliary hamartomas closely simulates the appearance of hepatic candidiasis; absence of clinical findings, stability confirmed on prior imaging studies, and peripheral distribution hopefully suggest the diagnosis and exclude candidiasis. Other infectious/inflammatory lesions beyond the scope of this text potentially simulate the imaging appearance of hepatic candidiasis, including hepatic tuberculosis and hepatic sarcoidosis.

Traumatic Lesions

Traumatic lesions of the liver—hematoma and biloma—rarely warrant MRI. Nonetheless, misdiagnosis because of lack of familiarity with imaging features and failure to suggest the appropriate diagnosis potentially leads to morbidity and a brief discussion of these lesions will hopefully help prevent that.

HEMATOMA

Liver hemorrhage most commonly follows either blunt trauma or surgery. Bleeding complicating a solid liver mass—most notably adenoma—accounts for another mechanism.³⁴ The most specific imaging features are associated with the underlying etiology: rib fractures, liver laceration, hemoperitoneum (e.g., in the case of blunt trauma); spatial and temporal relationships to the surgical plane and procedure in the case of postoperative bleeding; and the presence of an underlying lesion in the case of neoplastic etiology. The T1 hyperintensity of methemoglobin in the acute-subacute phase implicates hemorrhage (Fig. 2-32); after 10 days or so, signal intensity approximates simple fluid.

BILOMA

Rupture of the biliary system leading to the formation of a biloma is usually either traumatic or iatrogenic in etiology. Location near the procedural site and often abutting the porta hepatis or gallbladder fossa is characteristic. Other features, such as relatively sharply defined margins, relative absence of complexity, and bland signal characteristics, are otherwise nonspecific (Fig. 2-33). Further analysis needs to substantiate

whether hepatocyte-specific agents with biliary excretion confirming biliary origin contribute to the diagnosis (i.e., mangofodipir trisodium [Teslascan]—now unavailable—and cholescintigraphy).

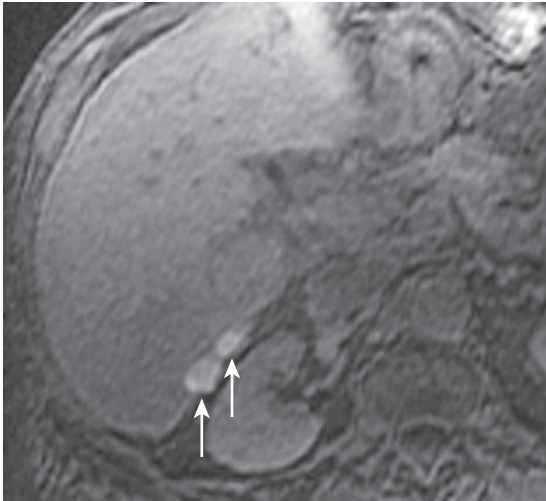


FIGURE 2-32. Hematoma. Axial T1-weighted fat-suppressed image after a liver biopsy reveals tandem small hyperintense hematomas in the posterior segment (*arrows*).

Solid (and Pseudosolid) Lesions

Enhancement connotes solid (and pseudosolid) tissue in MRI and indicates viability (in ablated lesions), with one exception—lesions of lipid content (i.e., angiomyolipoma and lipoma). Whereas a precise cut-off between cystic or necrotic solid lesions and complex cystic lesions eludes imaging capabilities, differentiation is usually possible. Solid lesions with secondary cystic or necrotic degeneration usually exhibit a cavitated appearance—the central cystic component appears excavated, a defect in an otherwise solid lesion—whereas primary cystic lesions generally exhibit more outwardly expansile cystic components.

Solid lesions fall into two main groups defined by their enhancement pattern compared with normal liver parenchyma—hypervascular and hypovascular (avascular ablated lesions are relegated to the hypovascular category, and discussion of rare isovascular lesions is deferred in the interest of brevity) (see Fig. 2-17). On arterial phase images, hypervascular lesions enhance more, and hypovascular lesions less, than hepatic parenchyma, respectively. Attenuation

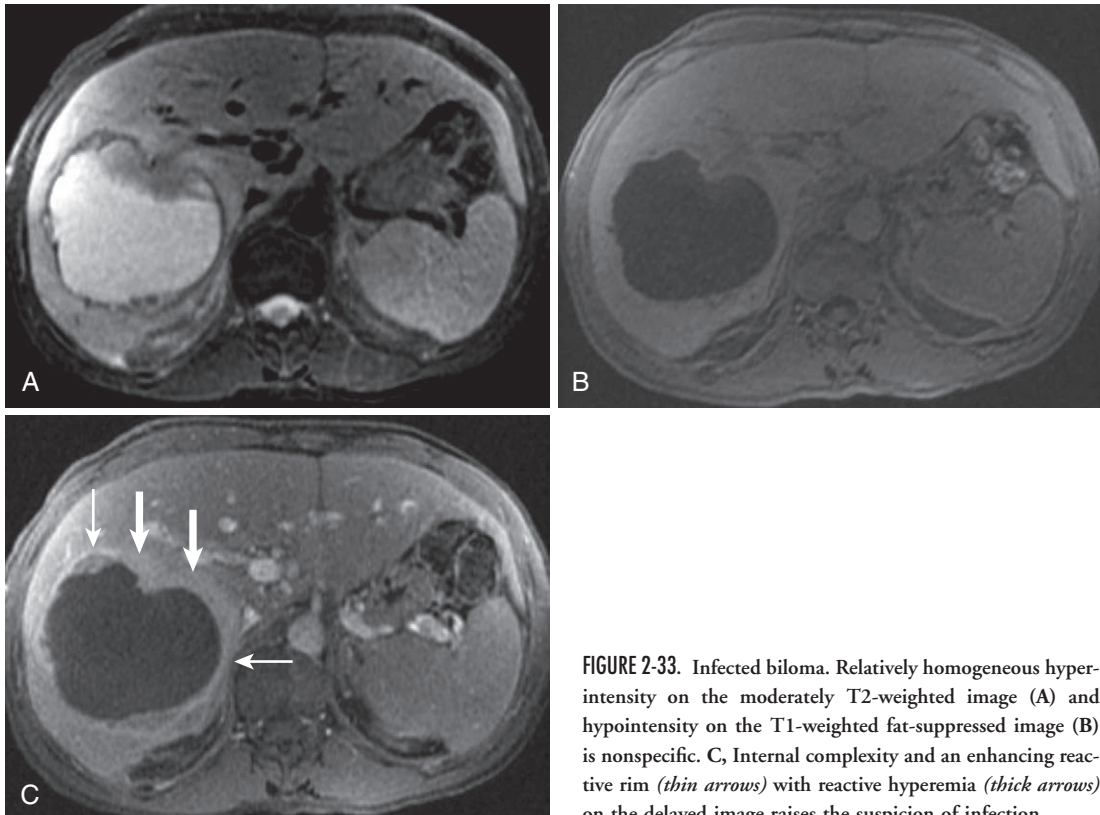


FIGURE 2-33. Infected biloma. Relatively homogeneous hyperintensity on the moderately T2-weighted image (A) and hypointensity on the T1-weighted fat-suppressed image (B) is nonspecific. C, Internal complexity and an enhancing reactive rim (*thin arrows*) with reactive hyperemia (*thick arrows*) on the delayed image raises the suspicion of infection.

pattern on subsequent timepoints further subclassifies lesions within each category (see Fig. 2-17). Signal and morphologic features add ancillary information; clinical information and underlying liver pathology and clinical conditions (e.g., chronic hepatitis, cirrhosis) help predict the likelihood of malignancy.

HYPERVASCULAR LESIONS

Hypervascular liver lesions include a wide range of lesions ranging from benign, incidental developmental lesions (such as FNH) to aggressive malignant lesions (such as HCC and hypervascular metastases). Accurate characterization demands stepwise analysis of intensity on successive timepoints (see Fig. 2-17). Hypervascularity on the arterial phase connotes hypervascularity. Signal intensity on delayed images discriminates benign from malignant with diagnostic confidence. Hypervascularity followed by delayed hyperintensity or fading (isointensity to liver parenchyma) connotes benign etiology—flash-filling hemangioma or FNH, vascular shunt and adenoma, respectively. Hypervascularity followed by delayed hypointensity (to liver parenchyma) equals washout—a malignant feature. Malignant hypervascular lesions with washout include HCC and hypervascular metastases. To be clear, a critical semantic distinction deserves reiteration. In the setting of hypervascularity, *washout* means delayed signal intensity less than liver, whereas *fading* refers to delayed signal intensity equal to liver. Washout equals malignancy and fading equals benignity (Fig. 2-34).

HEPATIC ADENOMA

Hepatocellular adenoma (or, simply, adenoma) represents a cluster of hepatocytes lacking the normal hepatic architecture, biliary ductal system, and functional Kupffer cells. Dilated sinusoids perfused by arterial feeding vessels separate sheets of hepatocytes. The absence of a coexistent portal venous system accounts for the arterial enhancement. Adenoma cells often contain large amounts of glycogen and lipid.³⁵ A pseudocapsule of compressed parenchyma and/or fibrosis often incompletely encircles the lesion.

Adenomas afflict two major population groups: (1) patients using estrogen- or androgen-containing steroids and (2) patients with type I glycogen storage disease. Whereas 70% to 80% of adenoma cases are solitary, extreme multiplicity defines a third recently described category, adenomatosis, characterized by the presence of multiple (usually > 10) adenomas. These patients lack the conventional risk factors (e.g., steroids, glycogen storage disease) and suffer from progressive symptomatic disease, impaired liver function, hemorrhage, and occasionally malignant degeneration.³⁶ In all cases, malignant degeneration is a concern, although the risk estimates are variable. Thin-walled sinusoids subjected to the high pressures of the feeding arteries explain the propensity of adenomas to bleed. Frequent discontinuity of the pseudocapsule permits transgression of hemorrhage, and proximity to the capsule predicts extrahepatic rupture and hemoperitoneum.

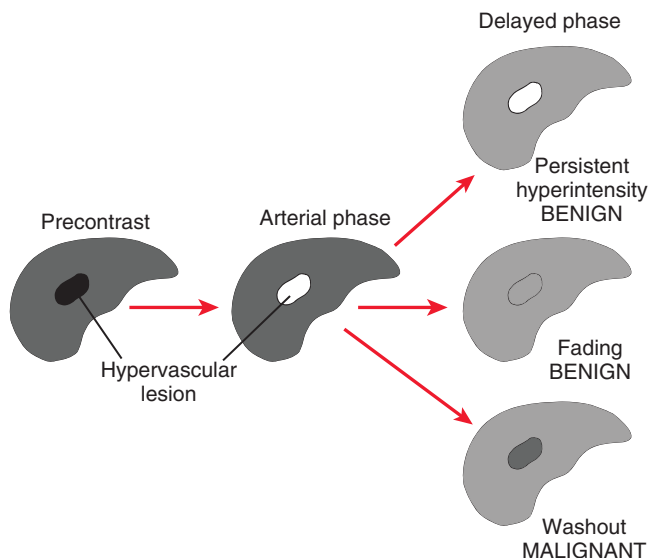


FIGURE 2-34. Hypervascular lesion scheme.

Adenomas usually exhibit iso- to hyperintensity on (in-phase) T1-weighted images due to either hemorrhage (52%–93%) and/or lipid (36%–77%) (Fig. 2-35).^{35,37,38} Because intralesional lipid usually manifests microscopically, as opposed to macroscopically, T1 hyperintensity drops on out-of-phase more frequently than on fat-saturated images. T1 hyperintensity arising from hemorrhage does not suppress on these pulse sequences. Intralesional hemorrhage and necrosis interrupt mild baseline T2 hyperintensity. The pseudocapsule exhibits T1 hypointensity and variable T2 hyperintensity with roughly equal proportions of iso-, hypo-, and hyperintense rims. Except where complicated by hemorrhage and/or necrosis, adenomas enhance avidly in the arterial phase and fade on delayed images. The pseudocapsule demonstrates the

reverse pattern—hypovascularity with possible delayed enhancement.

Without intralesional hemorrhage or fat, adenomas simulate other hypervascular lesions. Imaging features often fail to discriminate hepatic adenoma from HCC, except for the absence of vascular invasion in adenomas and washout versus fading in HCC and adenoma, respectively. Variable signal, hypervascularity, intralesional lipid and hemorrhage, and surrounding pseudocapsule characterize both lesions. Discrepant clinical features suggest the underlying diagnosis. Adenomas occur in young, otherwise healthy patients on oral contraceptives or steroids with normal α -fetoprotein (AFP) levels; HCC prevails in cirrhotic livers and often elicits AFP. Imaging features also overlap with FNH. The presence of hemorrhage and/or fat

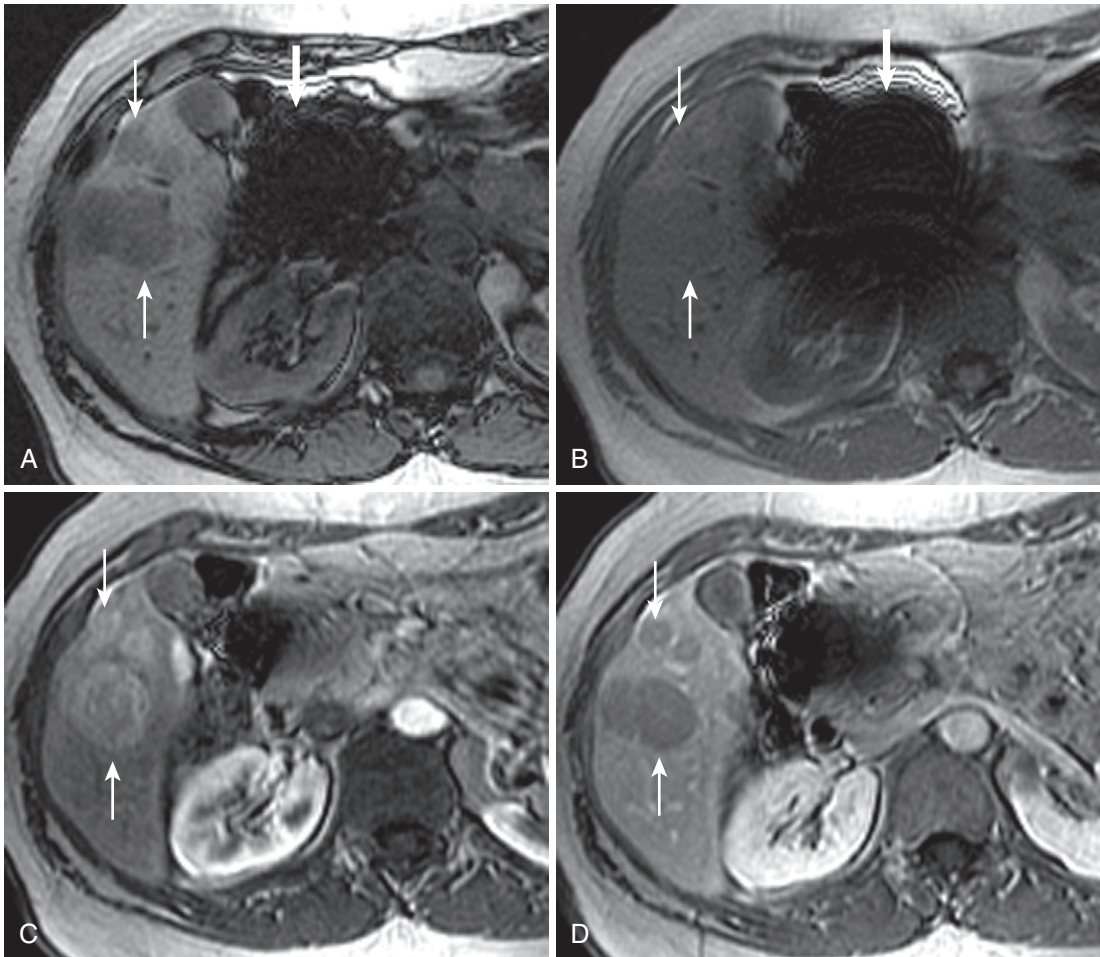


FIGURE 2-35. Hepatic adenomas. Multiple liver lesions (*thin arrows* in A-D) demonstrate relative signal loss on the out-of-phase image (A) compared with the in-phase image (B), indicating microscopic fat with corresponding hypervascularity on the arterial phase image (C). D, On the portal phase image, the lesions become uncharacteristically hypointense. Note the exaggeration of the susceptibility artifact from embolization coils (*thick arrow* in A and B) on the in-phase image compared with the out-of-phase image owing to the longer time to excitation (TE).

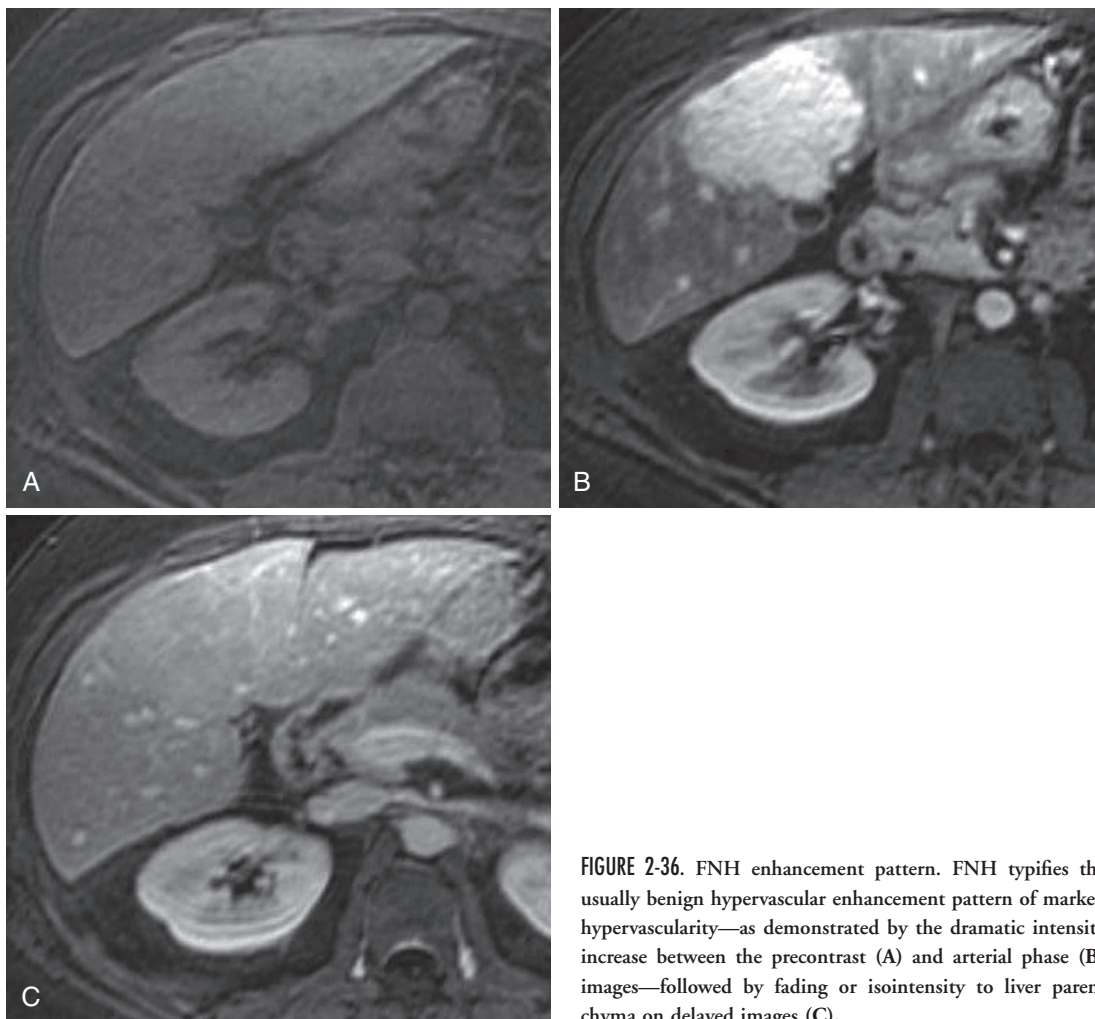


FIGURE 2-36. FNH enhancement pattern. FNH typifies the usually benign hypervascular enhancement pattern of marked hypervascularity—as demonstrated by the dramatic intensity increase between the precontrast (A) and arterial phase (B) images—followed by fading or isointensity to liver parenchyma on delayed images (C).

excludes FNH and a central scar suggests FNH, not being a characteristic of adenoma.

FOCAL NODULAR HYPERPLASIA

FNH deserves the designation “pseudosolid” because it is composed of elements of normal liver tissue—hepatocytes, bile ducts, and arteries embedded in fibrous septa. FNH is the second most common benign liver tumor (after hemangioma), representing a hyperplastic response to a localized vascular malformation—in other words, a hamartoma. Consequently, FNH is an incidental lesion with virtually no risk of complications (except exceedingly rare rupture and hemorrhage³⁹) requiring no treatment or follow-up, assuming adequate characterization.

FNH enhances avidly during the arterial phase and fades on portal venous and delayed images (Fig. 2-36). Approximately one half of lesions

demonstrate the classic “central scar.” The central scar enhances gradually—exhibiting delayed hyperenhancement (Fig. 2-37). Whereas the lesion itself is nearly isointense on T1-weighted and T2-weighted images—minimally hypo- and hyperintense, respectively—the central scar exaggerates this pattern, conferring greater conspicuity on unenhanced images. Ancillary findings include relatively small size (85% < 5 cm), frequent subcapsular right lobe distribution, and solitary and rare pedunculation and multiplicity.

Other etiologies in the differential diagnosis are eliminated with multiparametric analysis including temporal enhancement pattern, clinical features, and ancillary signal characteristics. Although hypervascular, HCC washes out and usually arises in the setting of cirrhosis and/or chronic hepatitis. Fibrolamellar HCC more closely simulates the imaging appearance of

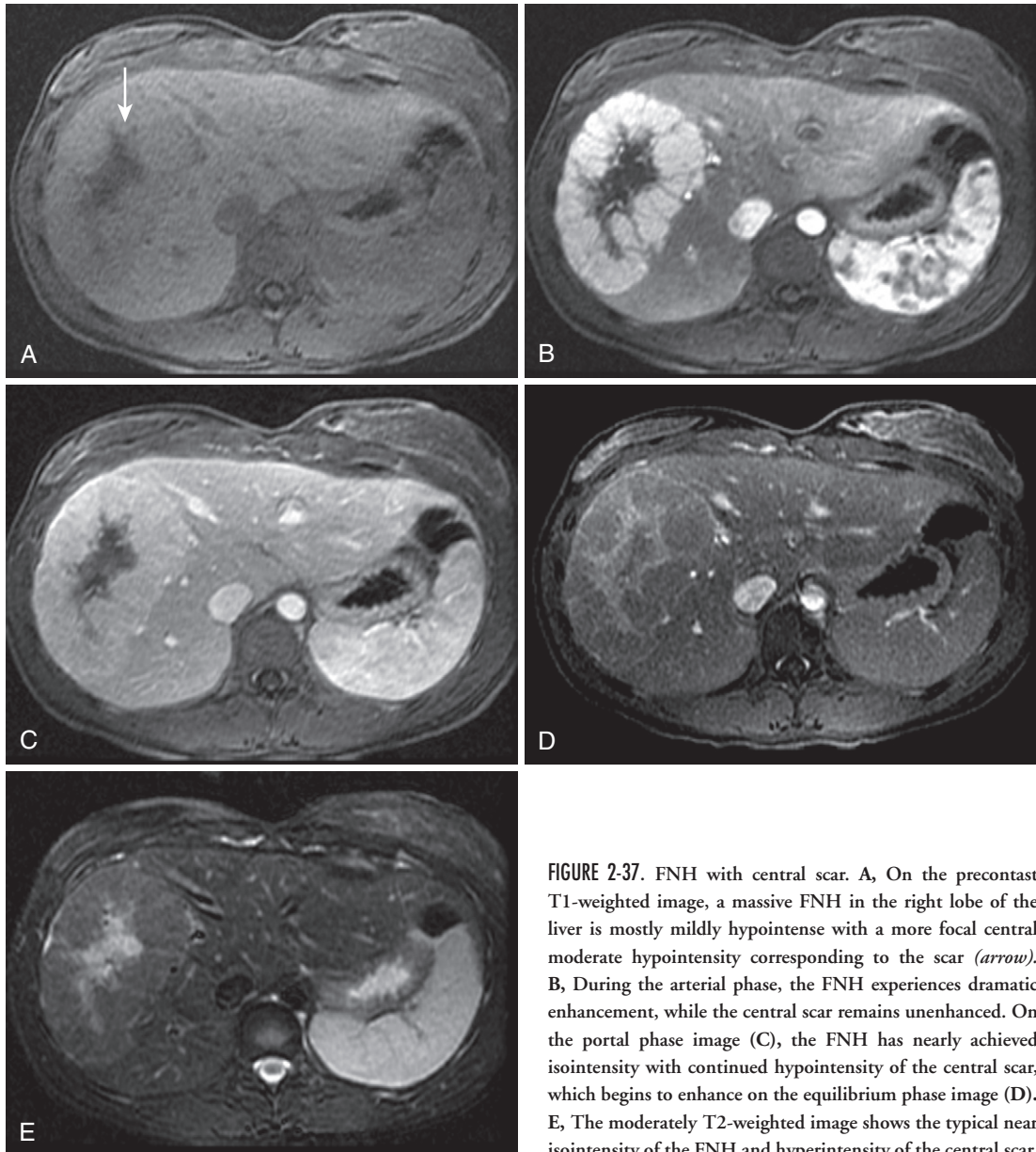


FIGURE 2-37. FNH with central scar. **A**, On the precontrast T1-weighted image, a massive FNH in the right lobe of the liver is mostly mildly hypointense with a more focal central moderate hypointensity corresponding to the scar (*arrow*). **B**, During the arterial phase, the FNH experiences dramatic enhancement, while the central scar remains unenhanced. On the portal phase image (**C**), the FNH has nearly achieved isointensity with continued hypointensity of the central scar, which begins to enhance on the equilibrium phase image (**D**). **E**, The moderately T2-weighted image shows the typical near isointensity of the FNH and hyperintensity of the central scar.

FNH, but usually achieves much larger size and heterogeneity and the central scar is usually T2 hypointense. Hypervascular metastases washout and exhibit multiplicity. Hypervascular hemangiomas demonstrating arterial hypervascularity remain hyperintense (without fading) and exhibit near-water attenuation on unenhanced images. When not complicated by hemorrhage, lipid, or necrosis, hepatic adenoma closely mimics FNH. Adenomas are usually less hypervascular, lack a central scar, and may be associated with oral contraceptive use, anabolic steroids, and glycogen storage disease.

Occasionally, atypical features or diagnostic uncertainty demands additional testing to establish the diagnosis in cases of possible FNH. In an effort to avoid an invasive diagnostic procedure, repeat MR examination with a hepatocyte-specific agent confirms the presence of hepatocytes on delayed enhanced images with lesion hyperintensity (Fig. 2-38).⁴⁰ While the agent has been channeled through the biliary system, clearing the normal parenchyma, hepatocytes within the lesion imbibe the contrast agent, but lack the organized biliary system for excretion.

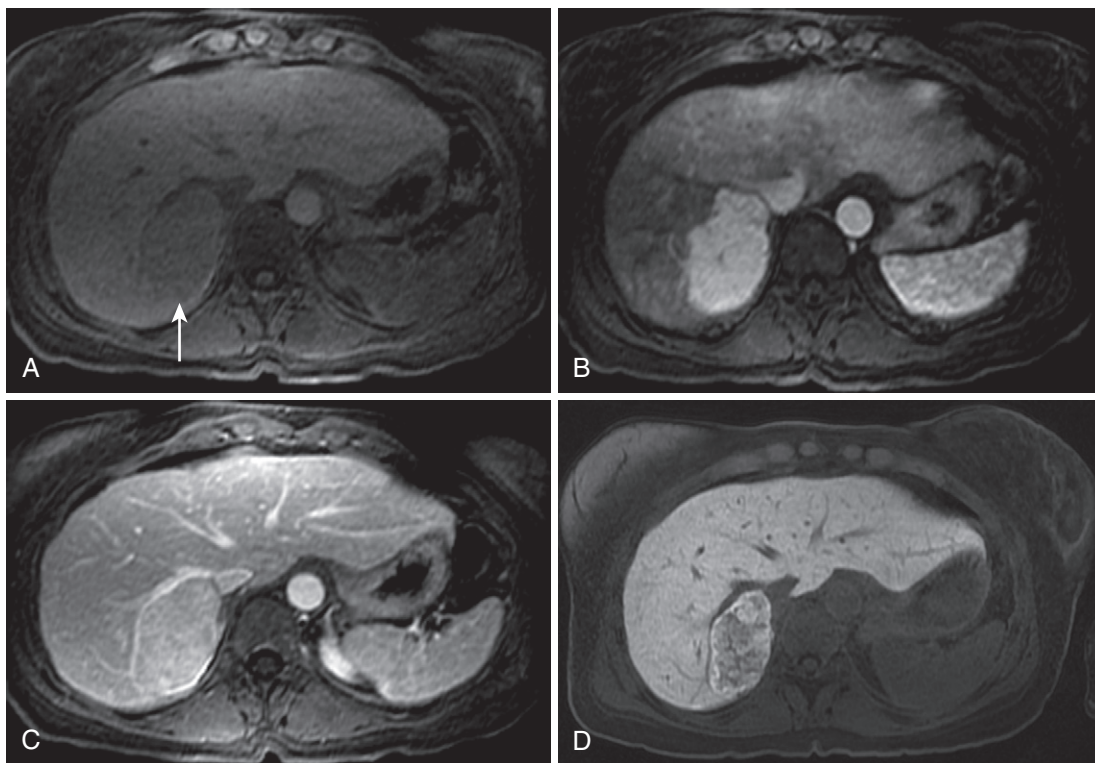


FIGURE 2-38. FNH imaging with hepatocyte-specific agent. **A**, The precontrast image from the dynamic sequence reveals a subtly hypointense lesion (*arrow*) in the posterior segment abutting the right hepatic vein. Following the administration of Eovist (gadoxetate), avid enhancement is observed during the arterial phase (**B**), followed by near isointensity during the portal phase (**C**), characteristic of FNH. **D**, On the delayed T1-weighted fat-suppressed image obtained 20 minutes later, intralesional hyperintensity confirms the diagnosis of FNH.

FOCAL TRANSIENT HEPATIC INTENSITY DIFFERENCE

Without the benefit of hepatocyte-specific imaging, transient hepatic intensity differences (THIDs) mimic FNH.^{41,42} The duality of liver blood supply explains the basis of this phenomenon. Increased arterial flow compensates for compromised portal flow reflected by hyperintensity on the HADP with corresponding isointensity on delayed phases. THIDs exist with or without underlying lesions and manifest variable appearances, depending on the etiology. Geographic distribution, triangular shape, and sharp, linear borders commonly observed in these lesions reflect vascular anatomy—hepatic tissue subtended by the affected vascular tree enhances arterially (**Fig. 2-39**).

The diagnostic dilemma arises in the case of “pseudoglobular” THIDs. Blind vessels not reaching Glisson’s capsule defy the geographic pattern and appear more nodular or round (**Fig. 2-40**). Larger lesions (>1.5 cm) present no diagnostic difficulty because the absence of signal changes and washout excludes HCC of this size

(although small HCCs sometimes lack these imaging features). These lesions raise concern in cirrhotic livers because of the higher prevalence of HCC—also hypervascular. When small hypervascular lesions such as these so-called THIDs populate cirrhotic livers, follow-up imaging urgency increases in order to exclude a small HCC.

CIRRHOTIC NODULES (PREHYPERVASCULAR)

Other small nodular lesions inhabit cirrhotic livers, including regenerative nodules, siderotic nodules, dysplastic nodules, and HCC. Whereas not all hypervascular, they deserve a collective discussion because of their strong etiologic connection (**Fig. 2-41**). For the purposes of our discussion, the nonhypervascular lesions in this group can be thought of as “prehypervascular.” Conceptually, these nodules represent an evolutionary spectrum from regenerative nodule to dysplastic nodule to HCC. The term *siderotic* applies to iron deposition in regenerative and dysplastic nodules, which are indistinguishable. With chronic inflammation, liver parenchyma is

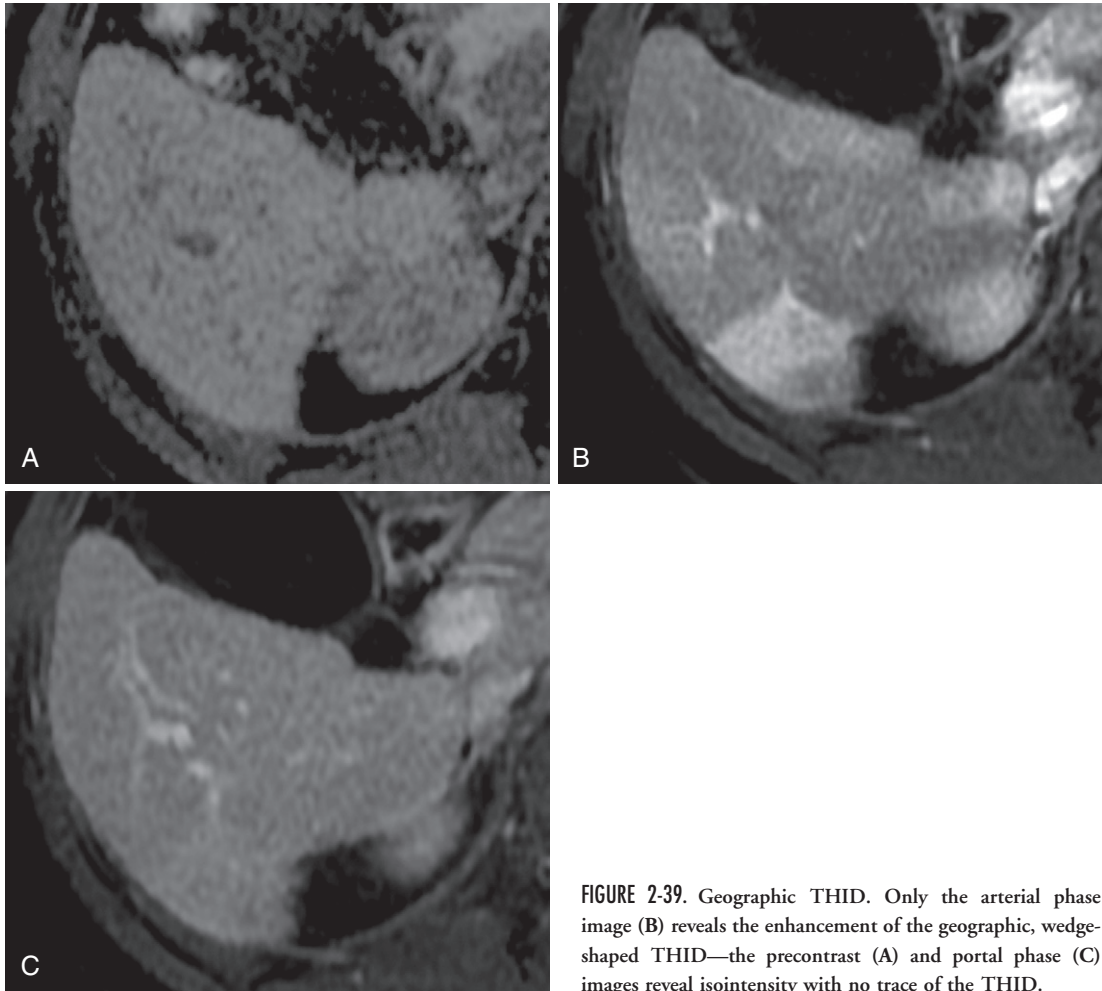


FIGURE 2-39. Geographic THID. Only the arterial phase image (B) reveals the enhancement of the geographic, wedge-shaped THID—the precontrast (A) and portal phase (C) images reveal isointensity with no trace of the THID.

destroyed and the liver's natural ability to regenerate yields regenerative nodules, which are composed of normal liver cells. Dysplastic nodules harbor histologically abnormal cells (e.g., nuclear crowding, increased nuclear:cytoplasmic ratio) with variable neoplastic angiogenesis—pathologic arteries—replacing the normal portal triads.^{43,44} HCC represents the final endpoint along the malignant degeneration pathway—most cases are associated with chronic liver disease. Whereas many histologic subtypes exist, for our purposes, HCC simply connotes malignant hepatocytes with arterial blood supply.

Regenerative nodules reiterate normal liver parenchymal signal and enhancement characteristics and differ only in their morphology and surroundings (assuming the absence of iron deposition). By definition, regenerative nodules inhabit a damaged hepatic environment, usually cirrhosis, and are spatially and visually defined

by the effects of that damage—surrounding fibrous septa. Regenerative nodule proliferation due to cirrhosis falls into two gross pathologic categories: micronodular (i.e., Laennec's cirrhosis, often synonymous with alcoholic cirrhosis) and macronodular (usually viral), depending on the size of the regenerative nodules. Micronodular nodules measure up to 3 mm and macronodular nodules measure more than 3 mm and up to 5 cm. Whatever the pathologic descriptor, nodules are delineated by bands of T2 hyperintense, gradually enhancing fibrosis (Fig. 2-42).

Under normal circumstances, regenerative nodules have no differential diagnosis. Rarely, regenerative nodules enhance arterially, imperceptibly HCC (at least on the arterial phase).⁴⁵ Delayed enhancement of peripheral fibrosis conceivably mimics the late-enhancing capsule of an HCC. Corroboration with unenhanced and dynamic images confirms absence of signal

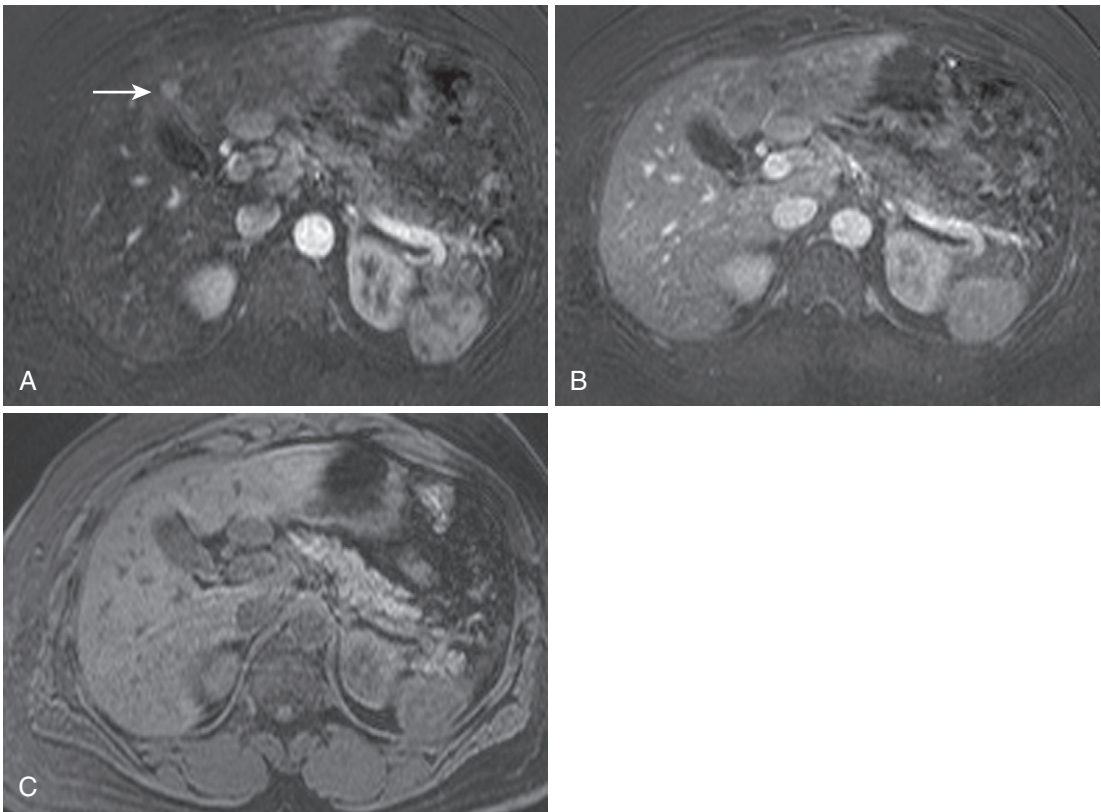


FIGURE 2-40. Pseudoglobular transient hepatic intensity difference (THID). The arterial phase image (A) shows a round focus of arterial enhancement (*arrow* in A) adjacent to the gallbladder, which fades on the portal phase image (B) and demonstrates no signal changes on the precontrast image (C).

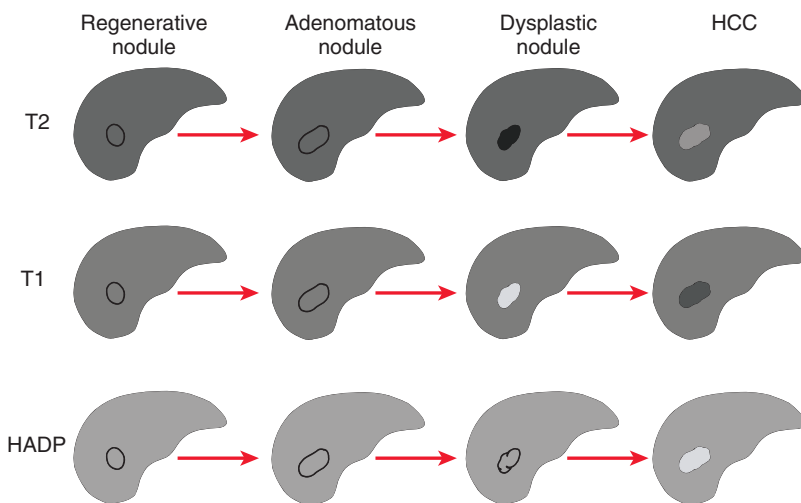


FIGURE 2-41. Pathogenesis of hepatocellular carcinoma (HCC). HADP, hepatic artery–dominant phase.

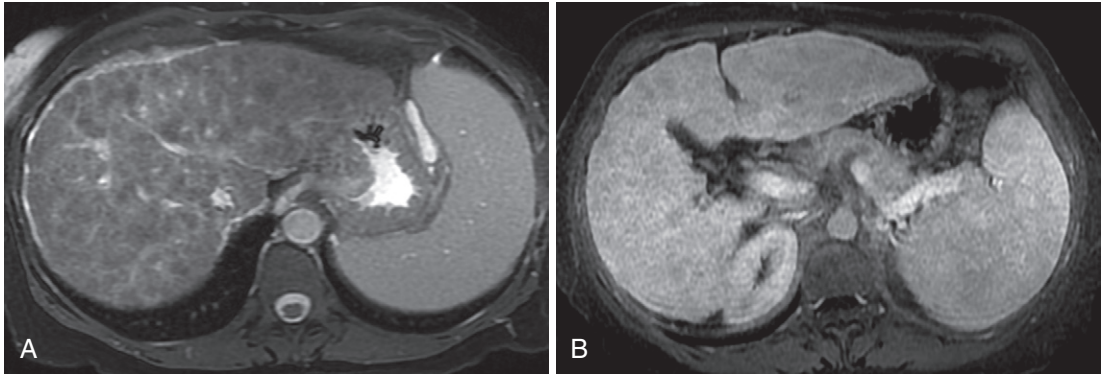


FIGURE 2-42. Regenerative nodules surrounded by fibrosis. **A**, Innumerable nodular islands of hepatic parenchyma are margined by bridging bands of hyperintensity on the moderately T2-weighted image in a very cirrhotic liver—the typical appearance of regenerative nodules with intervening reticular fibrosis. **B**, Delayed enhancement of the fibrotic bands surrounding the relatively hypointense nodules conjures a honeycomb appearance.

derangements—T1 hypo- and T2 hyperintensity—and usually arterial enhancement, which would otherwise suggest HCC. Rarely, diagnostic imaging uncertainty provokes follow-up imaging or biopsy.

A *dysplastic nodule* is defined as a cluster of histologically atypical hepatocytes measuring at least 1 cm not meeting histologic criteria for malignancy.⁴⁶ Dysplastic nodules afflict 15% to 25% of cirrhotic livers. Dysplastic nodules display greater variability and less commonality with normal liver parenchymal MR characteristics. Although the signal profile varies, prototypically, dysplastic nodules are hyperintense on T1-weighted images and hypointense on T2-weighted images (compared with liver) (Fig. 2-43). The paramagnetic effects of glycogen and/or copper explains the T1 hyperintensity. T2 hypointensity, at least occasionally attributable to iron content, is virtually always present. Although sporting unpaired arteries (not part of a portal triad), dysplastic nodules typically enhance commensurate with normal liver tissue and fail to enhance during the arterial phase (prehypervascular). With precontrast T1 hyperintensity, enhancement is difficult to perceive; subtraction images remove the intrinsic hyperintensity and display the change from baseline (i.e., enhancement).

With further evolution or dedifferentiation—depending on your perspective—the term *prehypervascular* becomes prophetic and the dysplastic nodule enhances arterially and usually fades (isointense to liver on delayed images). Conceptually, this enhancement pattern distinguishes the high-grade dysplastic nodule from the prehypervascular low-grade dysplastic

nodule (although actually 34% of high-grade and 4% of low-grade dysplastic nodules have been shown to enhance arterially⁴⁷). High-grade dysplastic nodules also differ in signal characteristics with isointensity on T2-weighted images and iso- to hypointensity on T1-weighted images.

The T1 hyperintensity of low-grade dysplastic nodules should not be confused with (microscopic or macroscopic) fat. The T1 hyperintensity in dysplastic nodules (which is not attributable to fat) does not suppress on out-of-phase or fat-suppressed images. Hemorrhage or protein complicating an underlying cyst or solid lesion lacks the enhancement seen in dysplastic nodules (check subtracted images). Whereas the signal characteristics of melanotic and hemorrhagic metastases overlap with T1 hyperintense dysplastic nodules, metastases washout on delayed images and rarely invade the cirrhotic liver (the obligate home of the dysplastic nodule).

High-grade dysplastic nodules show considerable overlap in imaging features with HCC. A few features compel consideration of HCC over dysplastic nodule. T2 hyperintensity is not a feature of dysplastic nodules and at least two thirds of HCCs exhibit T2 hyperintensity.⁴⁸ Washout after arterial enhancement also favors HCC over dysplastic nodule. Finally, the presence of a late-enhancing capsule also preempts the diagnosis of dysplastic nodule in favor of HCC. Size considerations also weigh in on the management of these lesions, because over 95% of dysplastic nodules are less than 2 cm. Lesion diameter of 2 cm or more or growth in a lesion over 1 cm prompts consideration of ablation and the presumptive diagnosis of HCC.

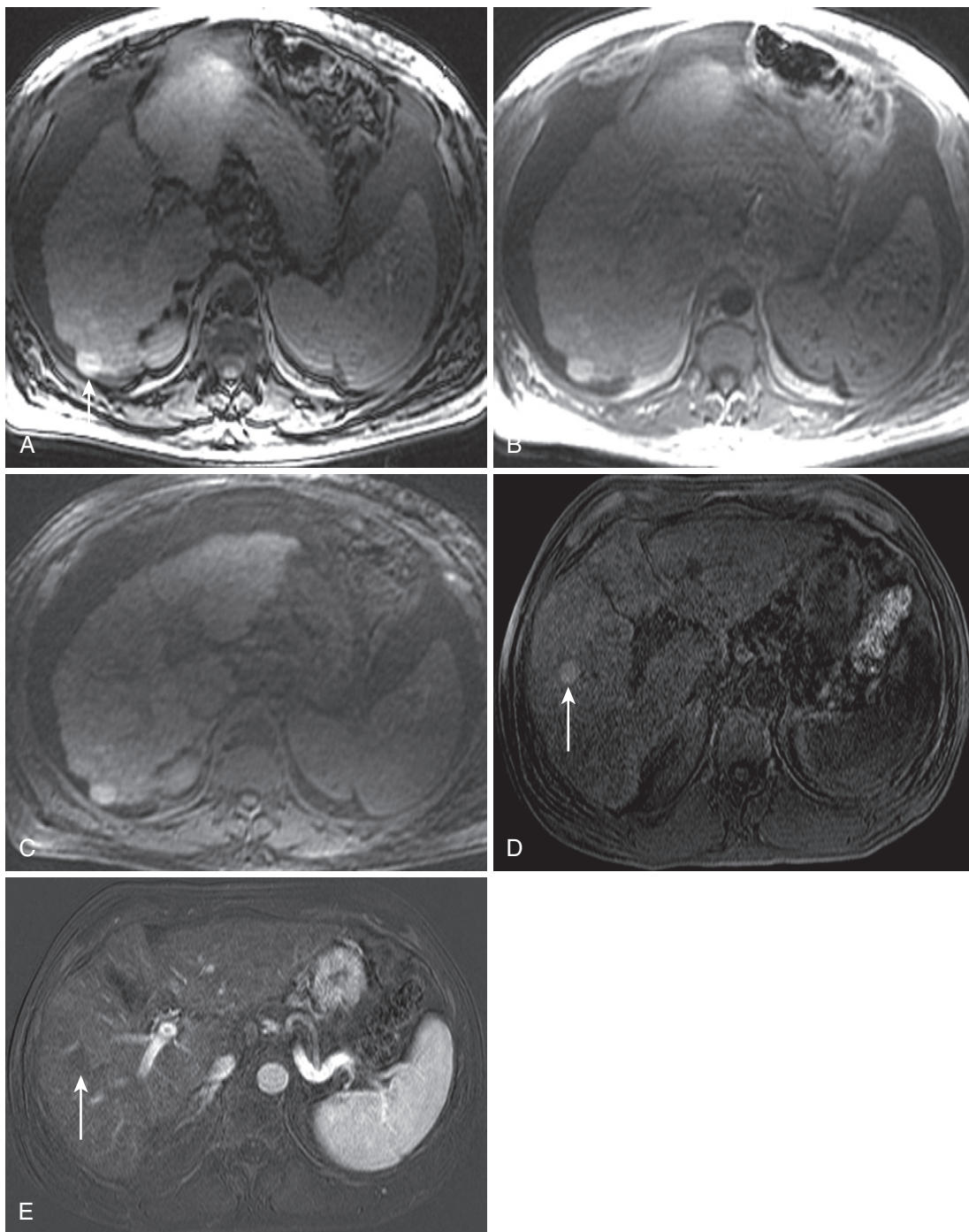


FIGURE 2-43. Dysplastic nodule. The opposed phase (A) and in-phase (B) images reveal a hyperintense nodular lesion (*arrow* in A) at the periphery of the posterior segment in a diffusely nodular, cirrhotic liver. C, The fat-saturated T1-weighted unenhanced image excludes T1 hyperintense fat. The T1-weighted fat-saturated image (D) in a different patient shows a similar hyperintense lesion (*arrow* in D and E) with lack of enhancement confirmed on the subtracted arterial phase image (E).

The earliest definitive sign of dysplastic nodule dedifferentiation is the “nodule within a nodule” phenomenon, which also prompts (usually invasive) action. The nodule within a nodule appearance describes a

focus of T2 hyperintensity—corresponding to HCC—within a T2 hypointense dysplastic nodule (Fig. 2-44). Associated HCC enhancement characteristics increase diagnostic confidence.

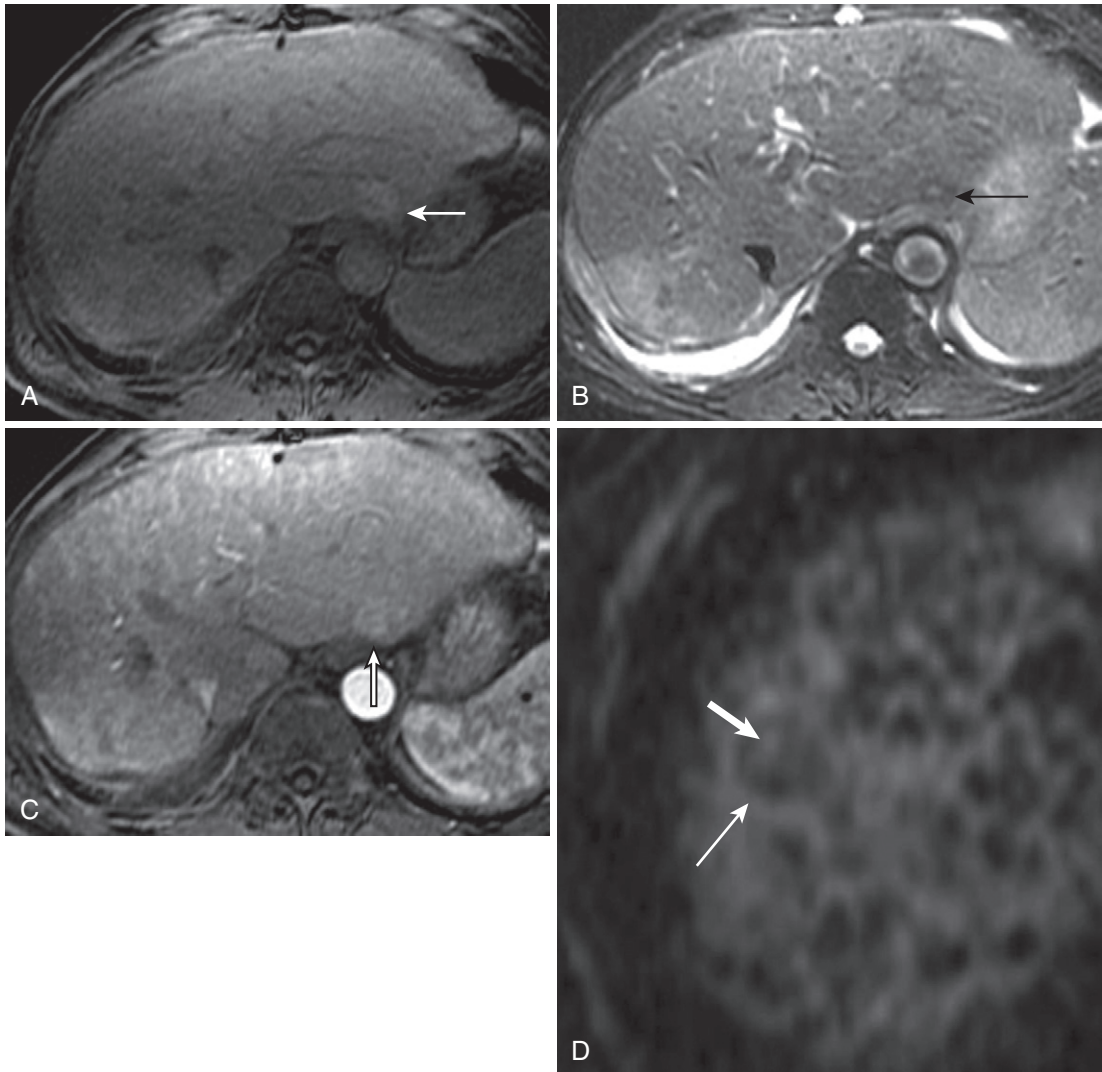


FIGURE 2-44. Nodule within a nodule. The axial fat-suppressed unenhanced T1-weighted image (A) reveals a hyperintense lesion (*arrow* in A) in the lateral segment of a cirrhotic liver characteristic of a dysplastic nodule, which is hypointense on the moderately T2-weighted image (*arrow* in B) with a punctate intralesional hyperintensity. C, The arterial phase image demonstrates corresponding ill-defined central enhancement (*arrow*) suspicious for HCC. D, A magnified axial moderately T2-weighted image in a different patient with severe cirrhosis reveals a dominant hypointense nodule (*thin arrow*) with intralesional hyperintensity (*thick arrow*) exemplifying the nodule-within-a-nodule appearance of early HCC.

HEPATOCELLULAR CARCINOMA

The discussion so far has been a preamble for the topic of HCC. HCC (or “hepatoma”) is the most common primary hepatic malignancy, although secondary malignancies (metastases) outnumber HCCs. Most cases evolve along the aforementioned dedifferentiation pathway in the cirrhotic liver in the setting of chronic hepatitis B (HBV) or C virus (HCV) or alcoholism. Because of the dismal long-term survival of untreated HCC (<5% 5-year survival rate⁴⁹), surveillance in the appropriate high-risk population, prompt diagnosis, and treatment planning

are vital. Annual screening (with MRI or other modalities, depending on the institution) in corroboration with AFP helps detect these lesions at an early phase and preserves the hopes of liver transplantation (LT), if planned. Considering HCC doubling time of approximately 2 to 3 months⁵⁰ and high MR detection rate⁵¹ virtually reaching 100% with increasing lesion size (>1.5 cm), an annual screening scheme generally guarantees early HCC detection before violation of transplantation size rules.

Screening high-risk patients with chronic liver disease for the purpose of early HCC detection

TABLE 2-9. The Milan Criteria

One tumor < 5 cm **or**
Up to three tumors ≤ 3 cm

TABLE 2-10. Tumor-Node-Metastasis Staging of Hepatocellular Carcinoma

Stage	Tumor (T)	Node (N)	Metastasis (M)
I	T1	N0	M0
II	T2	N0	M0
IIIA	T3	N0	M0
IIIB	T1	N1	M0
	T2	N1	M0
	T3	N1	M0
IVA	T4	Any N	M0
IVB	Any T	Any N	M1

Primary Tumor (T)

T1 = Solitary tumor ≤ 2 cm without vascular invasion

T2 = Solitary tumor ≤ 2 cm with vascular invasion

Multiple tumors limited to one lobe all ≤ 2 cm without vascular invasion

Solitary tumor > 2 cm without vascular invasion

T3 = Solitary tumor > 2 cm with vascular invasion

Multiple tumors limited to one lobe all ≤ 2 cm with vascular invasion

Multiple tumors limited to one lobe any > 2 cm with or without vascular invasion

T4 = Multiple tumors in more than one lobe

Tumor involvement of major portal or hepatic venous branch(es)

Regional Lymph Nodes (N)

N0 = No regional lymph node metastases

N1 = Regional lymph node metastases

Distant Metastases (M)

M0 = No distant metastases

M1 = Distant metastases

and treatment is driven by the Milan Criteria (Table 2-9)—the universally adopted rules governing LT. The Milan Criteria is based on research showing improved survival rates when restricting LT to patients with early HCC—defined as T1 and T2 tumors, according to the TNM (tumor-node-metastasis) staging system (Table 2-10).

Three dominant patterns describe HCC growth: solitary, multifocal or nodular, and diffuse (“cirrhotomimetic”; Fig. 2-45). The *solitary form* predominates at least 50% of the time. The *nodular form* follows in prevalence, and the *diffuse form* accounts for approximately 10%.⁵² Soft, fleshy HCCs have a propensity for hemorrhage and necrosis and increased levels of fat and glycogen observed in the cytoplasm also occasionally affects the MR appearance of these lesions (Fig. 2-46). The host reaction to the

presence of HCC manifests as a pseudocapsule of inflammatory and stromal cells and bile ducts, thought to reflect an attempt to contain the lesion and/or passive centrifugal compression of liver parenchyma (Fig. 2-47).⁵³ Although malignant angiogenesis recruits unpaired arteries—the dominant HCC blood supply—hepatic and portal veins proliferate around the lesion and provide a portal for metastatic spread.

Although imperfect, the classic dogma of HCC MRI features—T2 hyperintensity, (heterogeneous) hypervascularity, and washout—applies to most lesions (see Figs. 2-46 and 2-47). Although not unanimously present (more often in larger lesions), the late-enhancing pseudocapsule further clinches the diagnosis (Fig. 2-48). Portal or hepatic venous invasion—rarely observed in other tumors—also confirms the diagnosis of HCC. Ancillary factors further elevating the diagnostic confidence level include elevated AFP, cirrhosis, and HBV infection (even without cirrhosis).

The classic HCC imaging features become more vividly depicted with increasing size. HCCs less than 2 cm often enhance more homogeneously in the arterial phase and 10% to 15% simulate arteriportal shunts with relative inconspicuity on unenhanced and delayed images (Fig. 2-49).⁵⁴ (Most HCCs generally exhibit hypointensity on T1-weighted images and hyperintensity on T2-weighted images, as previously discussed.) In fact, although arterial enhancement is virtually the sine qua non of HCC, before the onset of increased arterial flow, portal venous flow begins to wane and relative hypointensity on arterial and portal phase images results.⁵⁵ With larger lesion size and dedifferentiation, variegated arterial enhancement develops as a consequence of larger sinusoidal spaces exaggerating arterial enhancement punctuated by hypo- or avascular foci representing necrosis, hemorrhage, and/or fat (Fig. 2-50). Perilesional edema and enhancement derangements (THIDs or hypovascular regions) reflect vascular invasion and usually correspond to the vascular territory subtended by the vessel invaded by the mass (i.e., the HCC defines the apex of the vascular derangement induced by the vascular invasion).

HCC more frequently invades the portal veins than the hepatic veins.⁵⁶ Vascular invasion connotes a poorer prognosis and higher likelihood of metastatic spread. The lack of vascular invasion also helps predict the success of surgical

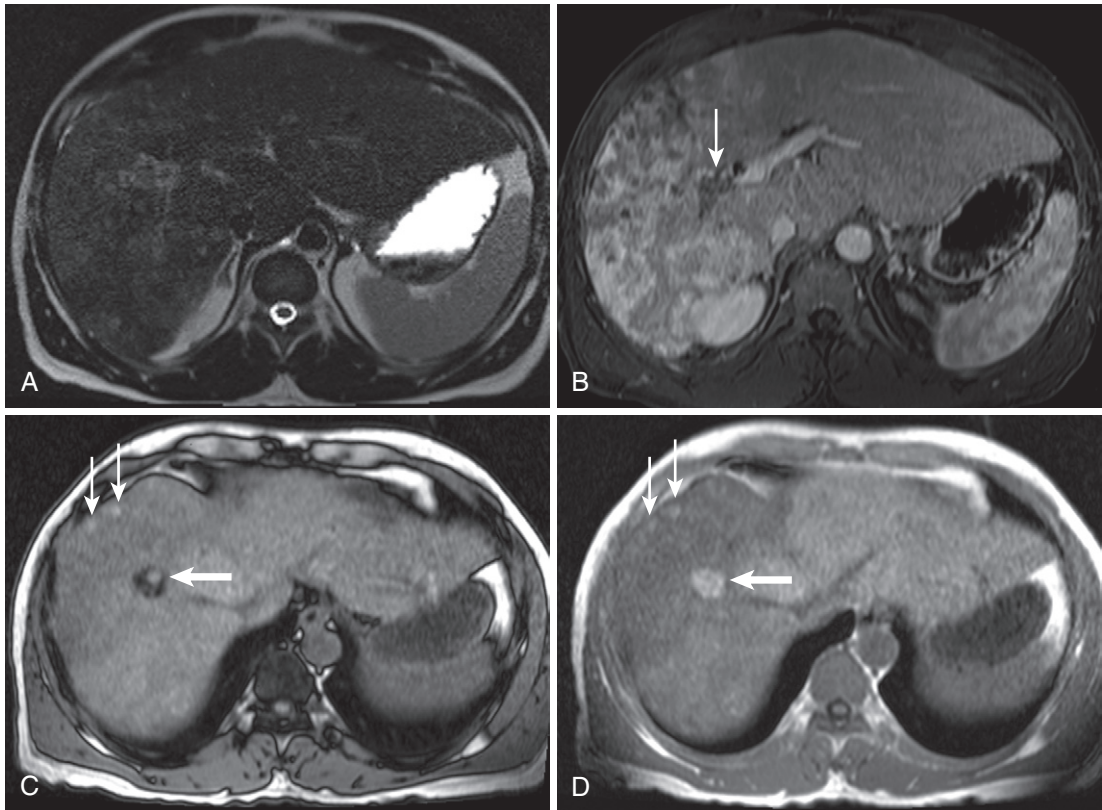


FIGURE 2-45. Infiltrative HCC with portal venous thrombosis. The heavily T2-weighted (A) and arterial phase (B) images show nodular infiltrative hyperintensity and enhancement throughout the posterior segment with thrombus in the right portal vein (*arrow* in B). The out-of-phase (C) and in-phase (D) images demonstrate punctate hyperintense foci of hemorrhage (*thin arrows*) and a large focus of microscopic fat (*thick arrow*).

excision, along with the absence of extrahepatic metastases, baseline liver function, and size of the residual liver. Occasionally, vascular invasion heralds an underlying occult HCC. Detecting tumor thrombus (as opposed to bland thrombus) requires establishing thrombus enhancement—most easily appreciated on subtracted images (Fig. 2-51).

Extrahepatic sites of spread include lymph nodes, lungs, bones, adrenal glands, and peritoneum/omentum.⁵⁷ In addition to vascular invasion, extrahepatic involvement (>stage II) precludes surgical treatment and the hopes of transplantation. Regional lymphadenopathy is ambiguous; hepatic inflammation—ubiquitous in this population—and metastatic spread incite regional lymphadenopathy. Most commonly observed metastatic lymph node distributions include periceliac, porta hepatis, para-aortic, portocaval, peripancreatic, aortocaval, and retrocaval (Fig. 2-52).

Hypervascular metastases and other cirrhosis-related lesions dominate the list of differential

diagnoses. Although in isolation, imaging features overlap very closely, extraneous factors differentiate hypervascular metastases from HCCs using a commonsense approach. Cirrhosis predicts HCC over hypervascular metastases for two reasons: (1) cirrhosis predisposes to HCC and (2) metastases rarely spread to the cirrhotic liver. Elevated AFP and an absence of known primary malignancy further boost diagnostic confidence. Metastatic lesion enhancement patterns simulate HCC patterns with uniform homogeneous enhancement, ring enhancement, and heterogeneous enhancement patterns. Frequent hypervascular shunts and rare hypervascular dysplastic nodules account for most of the rest of the hypervascular lesions encountered in the cirrhotic liver. FNH and flash-filling hemangioma declare themselves on delayed images as discussed (with fading and persistent hyperintensity, respectively), differentiating themselves from HCC.

Despite high diagnostic accuracy, equivocal cases require a consistent approach to

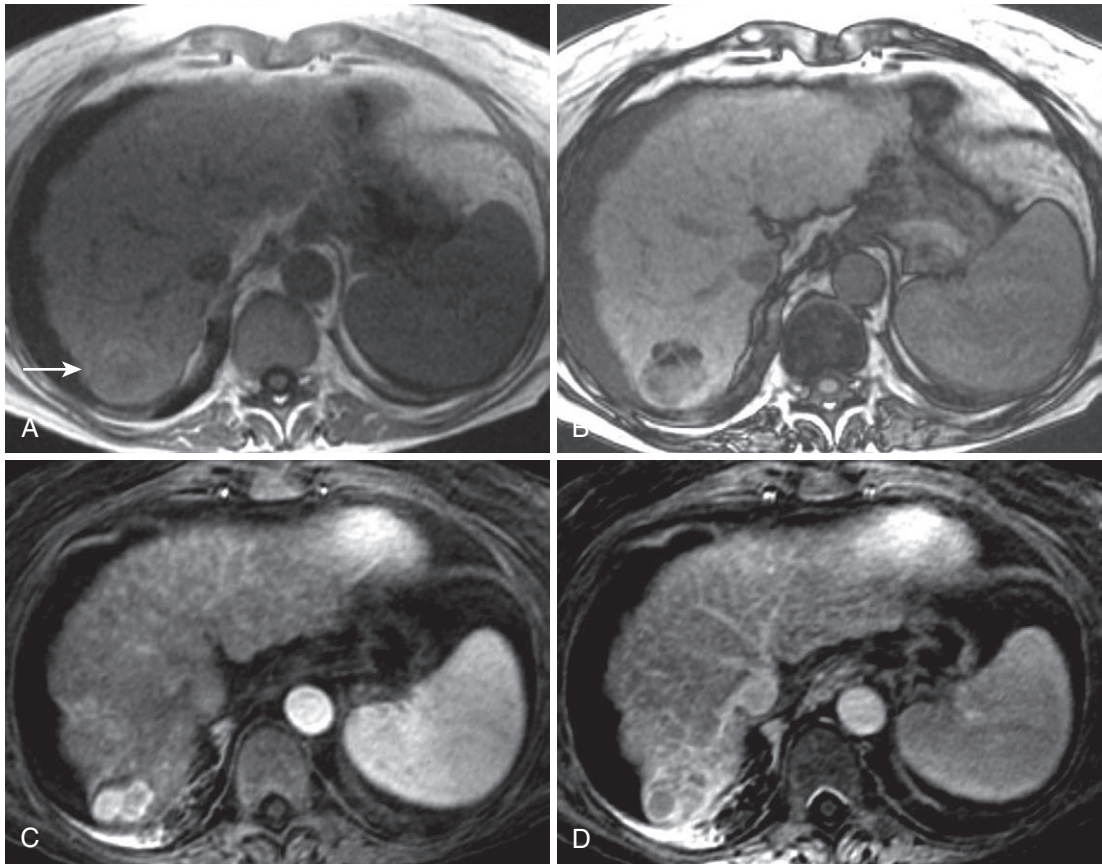


FIGURE 2-46. HCC with microscopic fat. The in-phase image (A) of a nodular, cirrhotic liver shows a heterogeneous lesion at the bulging posterior contour (*arrow* in A) with faint hyperintensity, which drops in signal on the out-of-phase image (B). Avid arterial enhancement (C) followed by washout on delayed images (D) and a late-enhancing capsule typify HCC.

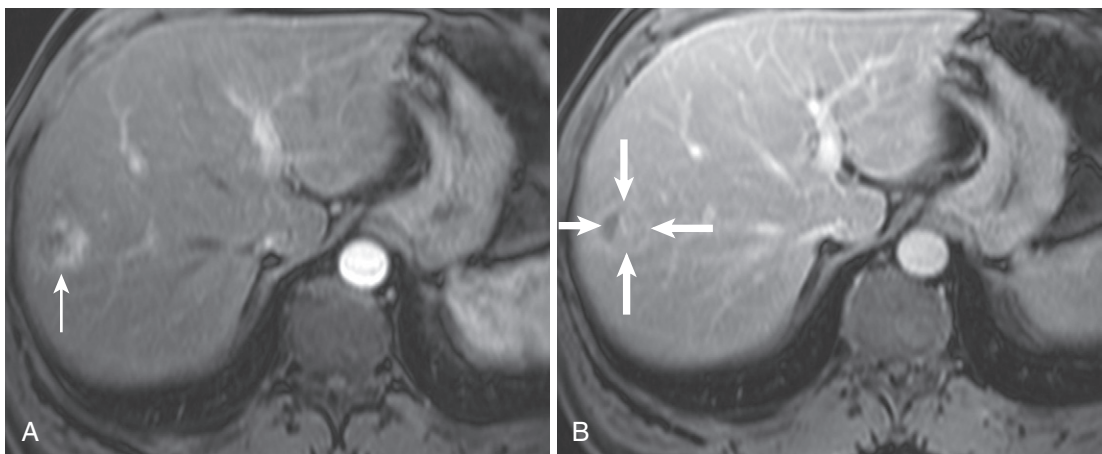


FIGURE 2-47. HCC pseudocapsule. A, Hypervascularity is evident in the lesion in the right lobe of the liver (*arrow*) on the arterial phase image. B, Enhancement of the pseudocapsule (*arrows*) develops on the delayed image.

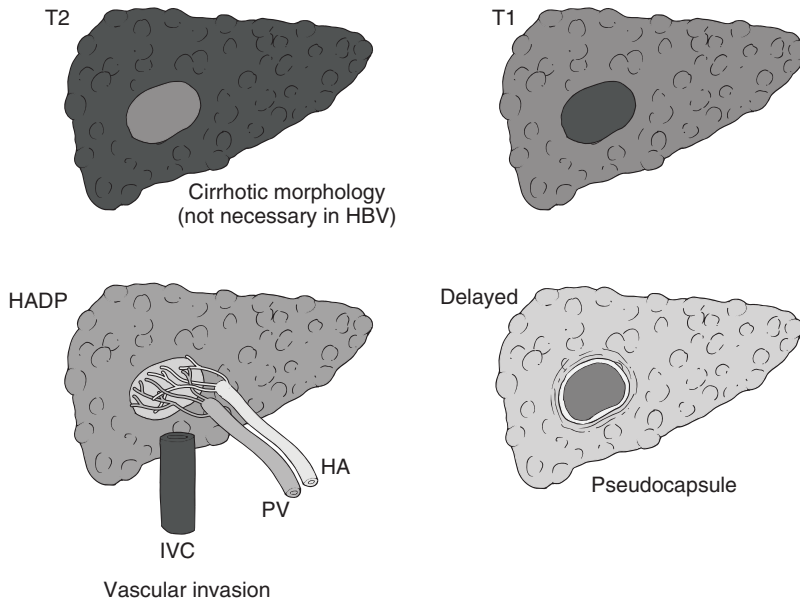


FIGURE 2-48. Hepatocellular carcinoma (HCC) schematic diagram. HA, hepatic artery; HADP, hepatic artery–dominant phase; HBV, hepatitis B virus; IVC, inferior vena cava; PV, portal vein.

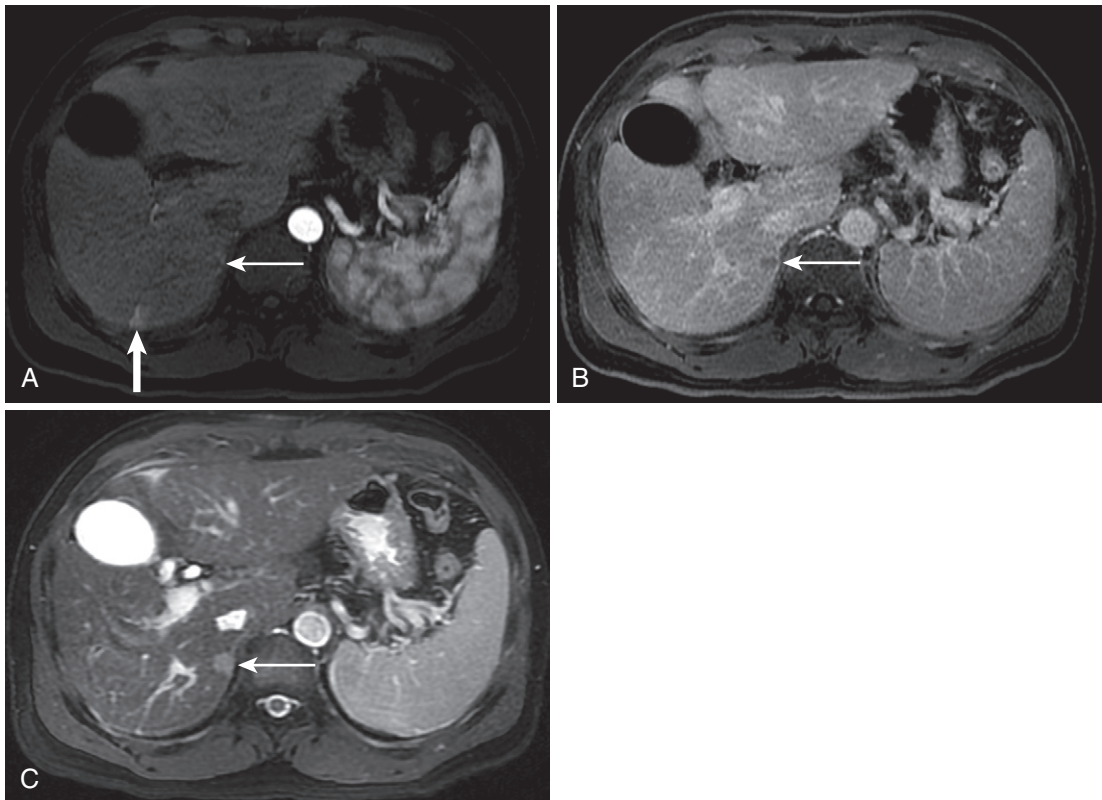


FIGURE 2-49. Small HCC. A, The arterial phase image shows a heterogeneously enhancing lesion in the medial aspect of the posterior segment (*thin arrow*) and a homogeneously enhancing lesion in the posterior aspect to the posterior segment (*thick arrow*). B, On the delayed image, the medial lesion washes out (*arrow*) betraying its malignant etiology—HCC—whereas the posterior lesion has faded, characteristic of a THID or benign vascular shunt. C, Note the HCC hyperintensity (*arrow*) on the T2-weighted steady-state image.

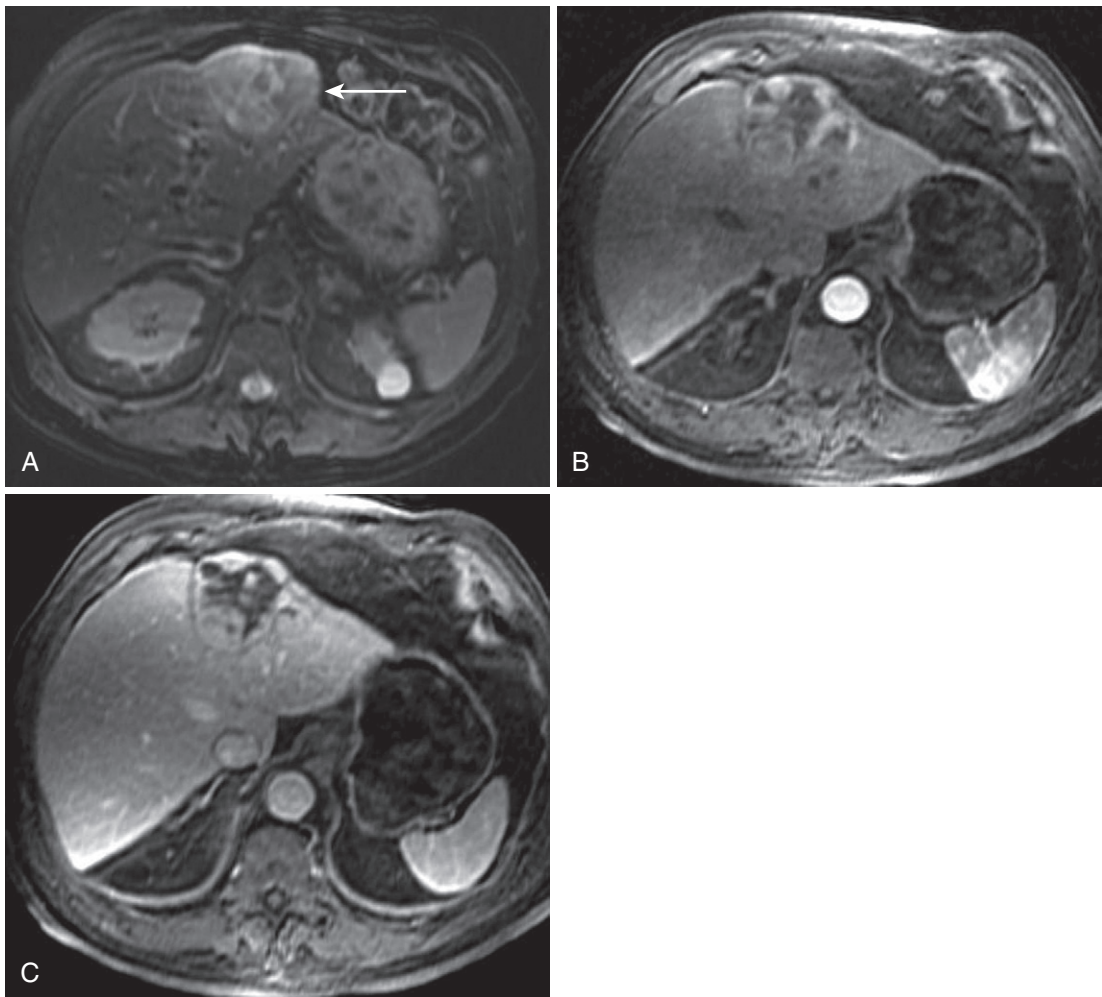


FIGURE 2-50. Large complex HCC. A, The moderately T2-weighted image shows a large heterogeneously hyperintense lesion (*arrow*) bulging the liver capsule. The arterial phase (B) and delayed (C) images show variegated enhancement, often seen in large lesions.

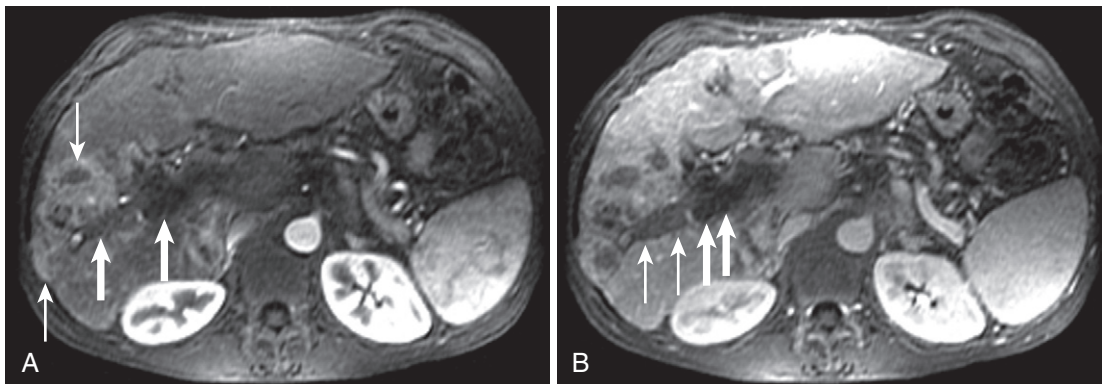


FIGURE 2-51. HCC with tumor thrombus. A, The arterial phase image reveals an infiltrative hypervascular lesion (*thin arrows*) with portal venous thrombus (*thick arrows*). B, The portal venous phase image shows lesion washout and exemplifies the difference between tumor thrombus (*thin arrows*)—which is relatively more intense and enhancing—compared with bland thrombus (*thick arrows*).

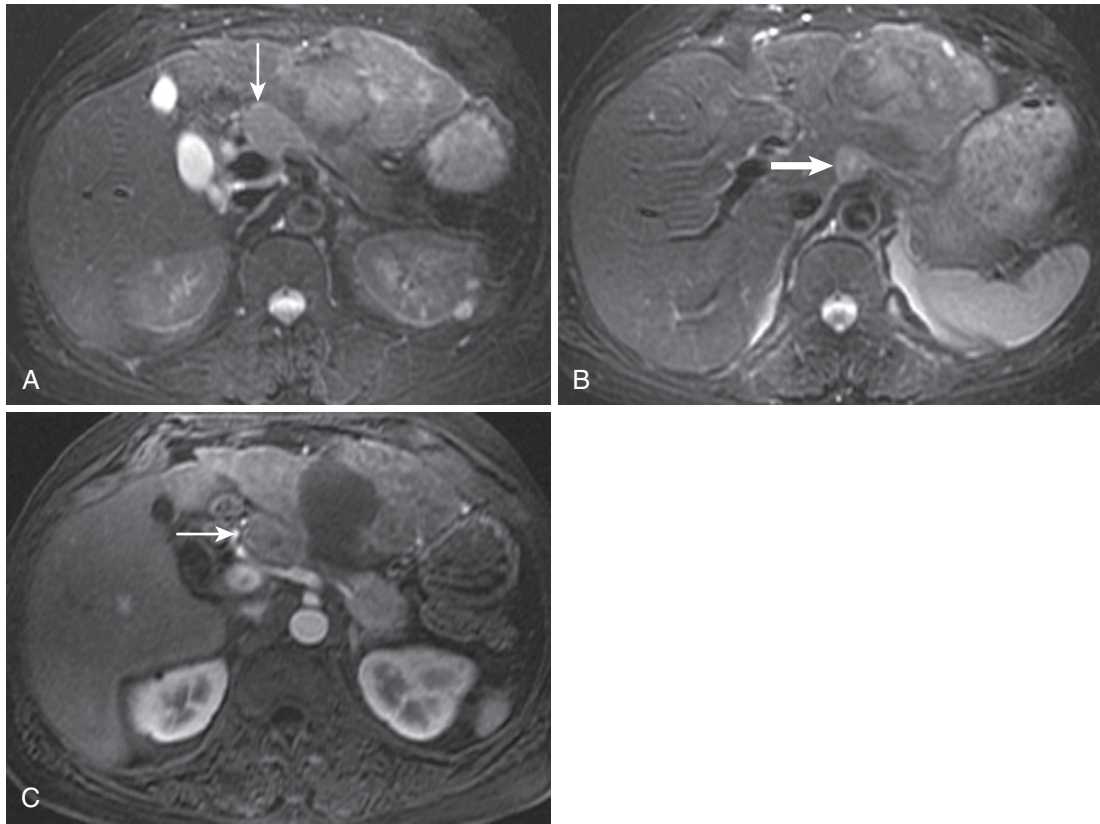


FIGURE 2-52. HCC with metastatic lymphadenopathy. **A** and **B**, The moderately T2-weighted images show enlarged lymph nodes in periportal (*arrow* in **A**) and celiac distributions (*arrow* in **B**) and heterogeneous hyperintensity throughout the lateral segment corresponding to a large HCC. **C**, The large, mildly hypervascular, necrotic HCC (*arrow*) replacing the lateral segment is evident on the arterial phase image.

TABLE 2-11. Liver Imaging and Reporting Data System

LIRADS 0 = Insufficient data
LIRADS 1 = No evidence of HCC
LIRADS 2 = Focal unequivocally benign lesions (e.g., cyst, hemangioma)
LIRADS 3 = Indeterminate nodule
LIRADS 4 = Intermediate suspicion for HCC
LIRADS 5 = High suspicion for HCC
LIRADS 6 = Histologically confirmed HCC

HCC, hepatocellular carcinoma; LIRADS, Liver Imaging and Reporting Data System.

management. In an effort to manage equivocation consistently, classification schemes are being devised to stratify liver lesions into categories based on the likelihood of HCC. The Liver Cancer Group collaborates on the LIRADS system (Liver Imaging and Reporting Data System) (Table 2-11). An initiative in our own department, termed the Lesion Characterization in Diffuse Liver Disease System, stratifies lesions into five categories based on the risk estimate of HCC (Table 2-12). These schemes promote

consistency in diagnosis and management and eliminate the potential for perceived lack of departmental cohesiveness and consensus by referring clinicians.

FIBROLAMELLAR CARCINOMA

A variant of HCC inhabits the normal liver in younger, healthy patients—fibrolamellar carcinoma (FLC)—and accounts for less than 10% and potentially as little as 1% of HCCs overall. The lesion is named for its microscopic appearance of malignant cells arranged in sheets separated by fibrous bands, or lamellae. The typical demographic, biochemical, and serologic features are the exact opposite of HCC: (1) no history of underlying cirrhosis or chronic hepatitis, (2) younger age (median age 33 compared with 66 for HCC), and (3) normal AFP (at least 85% of the time).

A large (mean size ≤ 13 cm), lobulated mildly T1 hypointense, mildly T2 hyperintense heterogeneously hypervascular mass with a uniformly hypointense, nonenhancing central scar

TABLE 2-12. TJU Lesion Characterization in Chronic Liver Disease

Category 1: No Focal Lesion Suspicious for HCC (Risk Estimate < 5%)

(*Note:* Because these features are not clinically significant, they do not necessarily have to be mentioned in the report.)

Imaging Features

No lesion demonstrated.

<1 cm, transient arterial enhancing, and seen on the arterial phase images only.

<1 cm, T1 hyperintense, and enhances similar to background liver.

<1 cm nodular area of focal fatty or iron sparing without arterial enhancement in the setting of diffuse fatty liver.

Suggested Management

Continue routine surveillance.

Category 2: Probably Benign Lesion (Risk Estimate 5–20%)
Imaging Features

Round transient arterial enhancing, 1–2 cm, and not visible on other sequences.

Round, 1–2 cm, hypointense on delayed images, and isointense on other images.

New, <1 cm T1 hyperintense, and enhances similar to background liver.

Suggested Management

Short-term (3-mo) follow-up, possibly with Eovist.

Category 3: Indeterminate Lesion (Risk Estimate 21–70%)
Imaging Features

>2 cm, T1 hyperintense, and enhances similar to background liver.

Suggested Management

Short-term follow-up, biopsy or alternative imaging (e.g., angiography, US, Eovist-MRI).

Indeterminate lesion should not be considered a diagnosis of HCC.

Category 4: Probable HCC (Risk Estimate 71–95%)
Imaging Features

As in category 5. Suboptimal image quality or other factors, at radiologist's discretion, may decrease confidence.

Suggested Management

Treat, biopsy, or transplant. Consider alternative imaging (e.g., angiography, US, Eovist-MRI).

Category 5: HCC (Risk Estimate >95%)
Imaging Features

Hyperenhancement with either washout, T2 brightness, or a delayed enhancing capsule.

A solid round mass that is T2 bright. The presence of any additional feature (e.g., enhancing capsule, washout, or enhancement) increases confidence that this is not confluent fibrosis.

Note that many HCCs have washout and other HCC features, but not T2 brightness. T2 brightness is specific but not extremely sensitive.

Multinodular texture (nodules-in-nodule) is an important confirmatory finding of HCC.

Management

Treat or transplant. Biopsy is not needed.

HCC, hepatocellular carcinoma; MRI, magnetic resonance imaging; TJU, Thomas Jefferson University; US, ultrasound.

TABLE 2-13. Hypervascular Metastases

RCC
 Neuroendocrine tumors
 Carcinoid tumors
 Thyroid carcinoma
 Uveal melanoma
 Choriocarcinoma
 Leiomyosarcoma
 Breast (occasionally)
 Ovary (occasionally)
 Pancreas (occasionally)

RCC, renal cell carcinoma.

describes the typical MR appearance of FLC (Fig. 2-53). Intensity becomes more homogeneous and equilibrates with or slightly drops compared with normal parenchyma. Chief differential considerations include HCC, FNH, and adenoma. The absence of cirrhosis and chronic liver disease and presence of a central scar favor FLC, but HCC still figures prominently in the differential because of the much higher incidence. Although the central scar and hypervascularity are reminiscent of FNH, the heterogeneous enhancement, signal alterations on unenhanced images, and specific features of the central scar point away from FNH. The central scar of an FLC demonstrates hypointensity on both T1-weighted and T2-weighted images and usually fails to enhance even on delayed images. FLC and adenoma share the common features of hypervascularity and heterogeneous enhancement. Adenoma visibility on unenhanced images derives from the presence of fat and/or hemorrhage, both of which uncommonly affect FLC—in fact, intratumoral fat has never been reported.⁵⁸

METASTASES

Metastases are the most common malignant lesion in the liver, and the liver follows lymph nodes as the most common sites of metastatic spread in the human body. Multiple routes of spread provide tumor emboli access to the liver: the hepatic artery, portal vein, lymphatics, and peritoneal ascitic flow. Established metastases recruit arterial blood supply, whether hyper- or hypovascular. Hypervascular metastases arise from hypervascular primary tumors, such as renal cell carcinoma, islet cell/neuroendocrine tumor, thyroid carcinoma, carcinoid, breast carcinoma, and melanoma (predominantly ocular, as opposed to dermal) (Table 2-13).

Detecting metastases dictates potential treatment course, prognosis, and response to treatment. Ten percent of metastases are solitary and

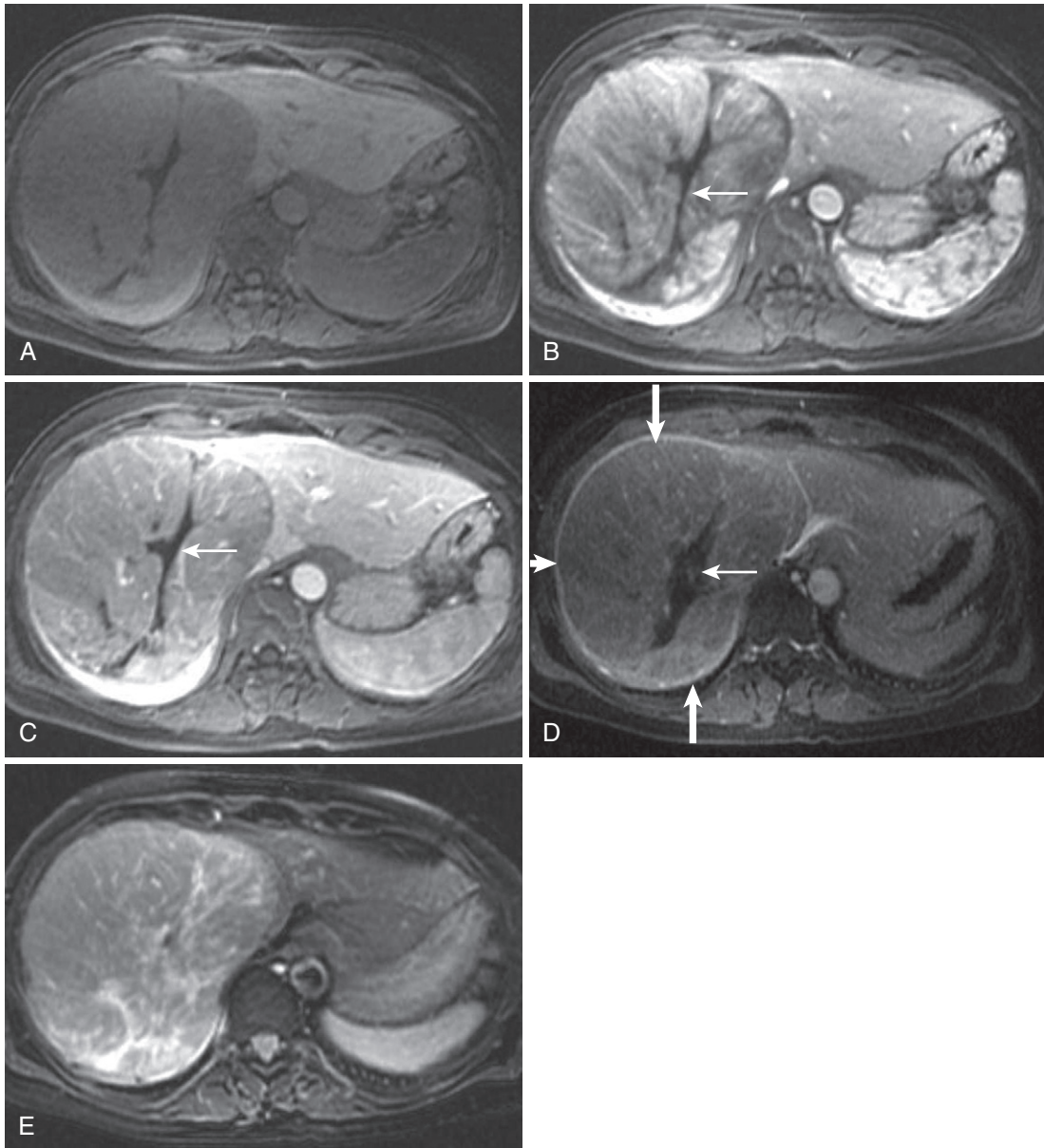


FIGURE 2-53. Fibrolamellar HCC. The large hypervascular mass has a central hypointense scar on the precontrast image (A), enhances on the arterial phase image (B) with the exception of the central scar (*thin arrow* in B-D). Washout is progressively evident on the portal phase image (C) compared with the delayed image (D), as is the late-enhancing capsule (*thick arrows* in D). E, Hyperintensity is evident on the moderately T2-weighted image. Note the lack of cirrhotic features.

77% inhabit both lobes; variable size reflects different lesion age and ongoing embolic delivery. Hypervascular metastases typically enhance as avidly as the pancreas and enhancement pattern varies (Fig. 2-54). Smaller lesions tend to be more homogeneous in enhancement with heterogeneity increasing with lesion size. Whether hyper- or hypovascular, metastases commonly exhibit a continuous rim of enhancement.^{59,60} The peripheral washout sign describes a delayed inversion of the arterial phase enhancement

with hypointensity of the peripheral rim and relative central hyperintensity as the interstitium gradually perfuses with contrast.⁶¹ These enhancement characteristics reflect the tumor's ability to induce angiogenesis peripherally with relative central hypovascularity ultimately trending to central fibrosis and/or necrosis as it outgrows its blood supply.

Signal intensity patterns on unenhanced images vary but hover around the basic template of T1 hypointensity and T2 hyperintensity,

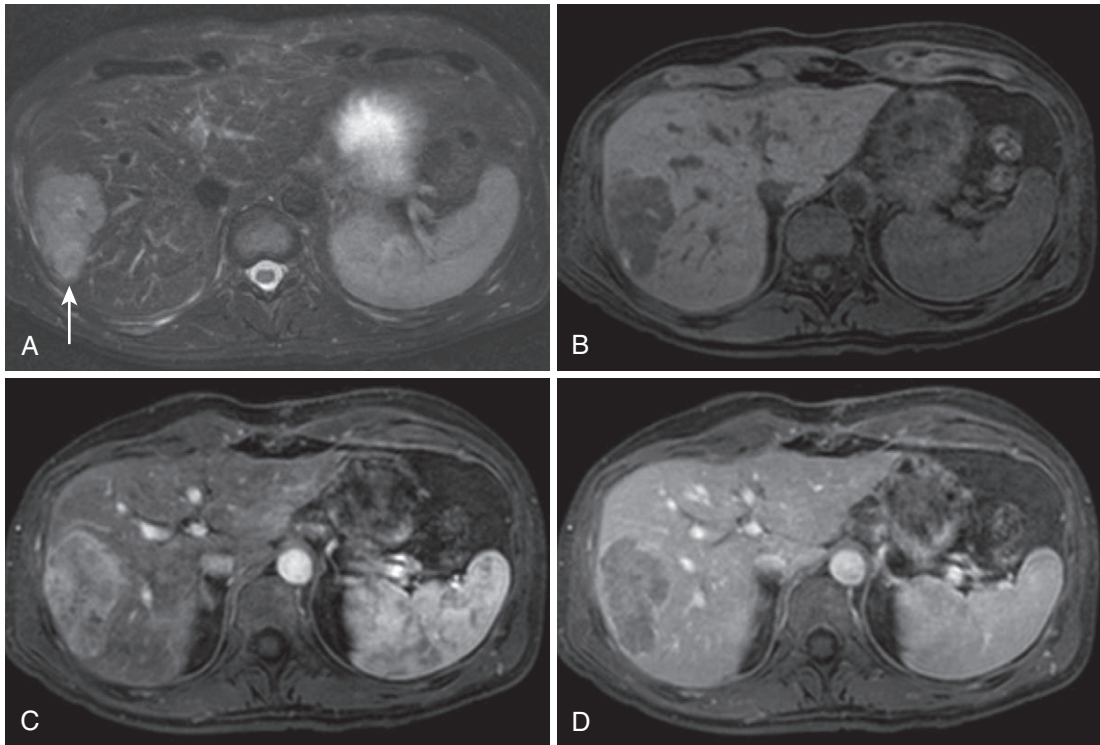


FIGURE 2-54. Hypervascular metastasis. The moderately T2-weighted image (A) shows a hyperintense uveal melanoma metastasis in the right lobe of the liver (*arrow* in A), which is hypointense on the corresponding precontrast T1-weighted image (B), enhancing avidly on the arterial phase image (C) and washing out on the delayed image (D).

reflecting increased intralesional water content compared with liver parenchyma. Concentric variations of this pattern on both T1-weighted and T2-weighted images have earned the descriptors “doughnut” sign and “lightbulb” sign, respectively.⁶² These signs are essentially the pulse sequence counterpart of each other: doughnut sign = mildly T1 hypointense rim surrounding markedly hypointense center; lightbulb sign = mildly T2 hyperintense rim surrounding markedly hyperintense center (Fig. 2-55). These signs conjure the notion of viable tumor surrounding a nonviable central necrotic core.

Aberrations in metastatic signal intensity template emerge for a variety of reasons. Whereas T2 values between benign lesions (i.e., cysts and hemangiomas) and malignant lesions (i.e., metastases and HCCs) do not overlap, for all intents and purposes, some hypervascular metastases demonstrate marked T2 hyperintensity. Hypervascularity, increased interstitial water content, vascular lakes, and dilated vascular spaces (and mucin as in the case of colorectal metastases—typically *hypovascular*) confer higher signal on T2-weighted images, although

still usually relatively hypointense to cystic lesions, including hemangioma.⁶³ Heavily T2-weighted images confirm a relative signal drop in metastatic lesions compared with hemangiomas and cysts.

T2 hypointensity is uncommon and usually accompanies T1 hyperintensity, indicating hemorrhage or melanin. Preservation of T1 hyperintensity on fat-suppressed images excludes fat and confirms a paramagnetic substance—either blood or melanin. Without a known history of ocular melanoma, T1 hyperintensity most likely represents hemorrhage, most commonly arising from renal, melanoma, breast, and choriocarcinoma metastases in the hypervascular realm (and lung, pancreatic, gastric, prostatic, and gallbladder carcinoma in the hypovascular category).³⁴ Melanoma metastases contain variable quantities of melanin, which facilitates T1 relaxation, enhances T2 relaxation, and promotes T1 hyperintensity and T2 hypointensity, respectively. Increasing melanin content equates with increasing T1 and decreasing T2 signal.⁶⁴

Imaging features of hypervascular metastases most closely overlap with (multifocal) HCCs, multiple hepatic adenomas, and/or FNHs.

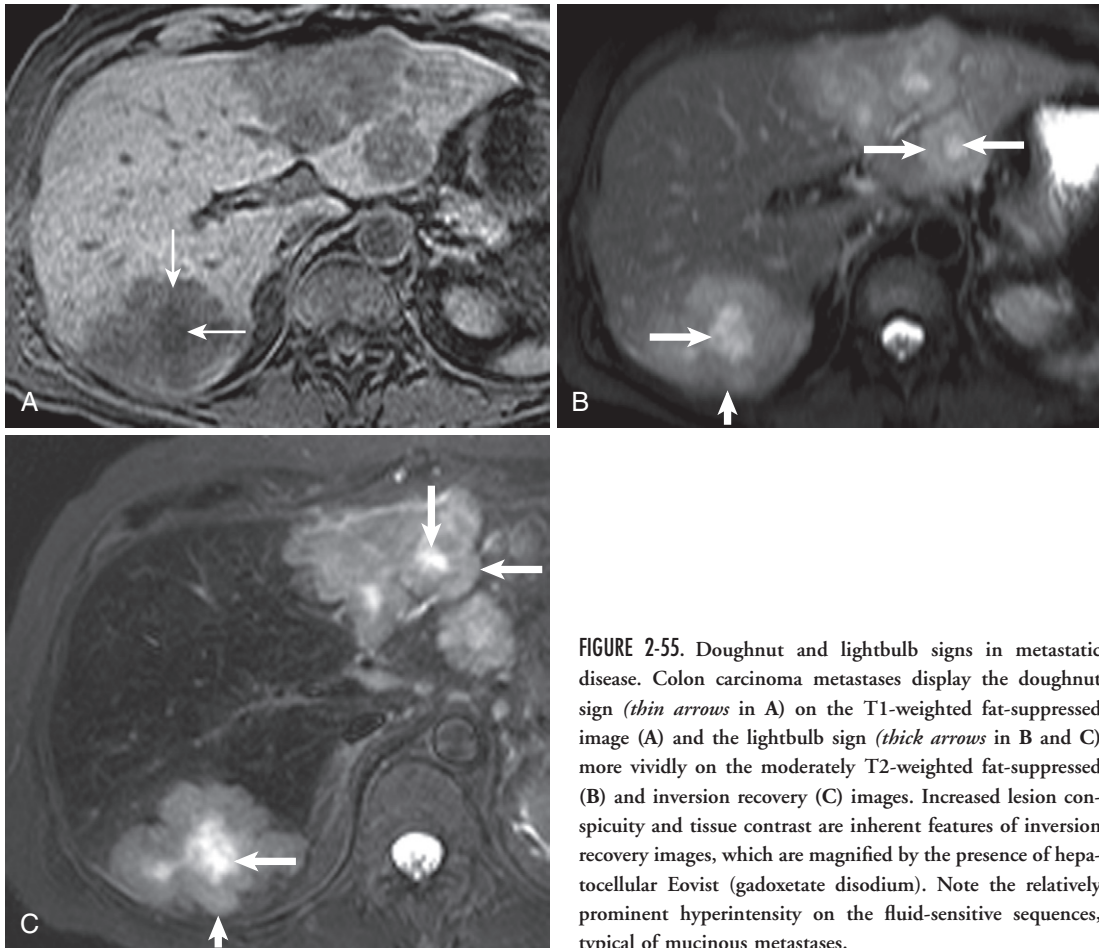


FIGURE 2-55. Doughnut and lightbulb signs in metastatic disease. Colon carcinoma metastases display the doughnut sign (*thin arrows* in A) on the T1-weighted fat-suppressed image (A) and the lightbulb sign (*thick arrows* in B and C) more vividly on the moderately T2-weighted fat-suppressed (B) and inversion recovery (C) images. Increased lesion conspicuity and tissue contrast are inherent features of inversion recovery images, which are magnified by the presence of hepatocellular Eovist (gadoxetate disodium). Note the relatively prominent hyperintensity on the fluid-sensitive sequences, typical of mucinous metastases.

Lesion for lesion, HCCs and hypervascular metastases are often indistinguishable—multiplicity, absence of chronic liver disease, normal AFP, and history of primary extrahepatic malignancy argue in favor of metastatic disease. T1 hyperintensity not attributable to lipid is noncontributory; blood complicates HCCs and metastases and is not distinguishable from melanin. T1 hyperintensity attributable to fat favors HCC—lipid-containing metastases (i.e., metastatic liposarcoma) are exceedingly rare. Vascular invasion is diagnostic of HCC and excludes extrahepatic malignancy. The presence of multiple adenomas theoretically echoes the appearance of hypervascular metastases—albeit not entirely faithfully—lacking washout and often containing lipid and/or hemorrhage with suggestive demographic data. FNHs even less closely simulate hypervascular metastases owing to their relatively homogeneous enhancement and invisibility on unenhanced images.

Infection appropriately factors in the differential diagnosis in the absence of known primary malignancy in a suggestive clinical scenario. During the liquefactive stage of pyogenic abscess evolution, the hypervascular wall encapsulating central necrosis and debris mirrors the appearance of necrotic and cystic metastases. However, primary cystic metastases are often hypovascular, such as mucinous cystadenocarcinoma (i.e., colon, gastric, pancreatic, ovarian). The clustering sign and relatively prominent perilesional reactive change favor pyogenic abscess, along with suggestive signs of underlying infection—including adjacent findings of right pleural effusion and basal atelectasis/consolidation.

HYPOVASCULAR LESIONS

Hypointensity relative to liver on dynamic images translates to hypovascularity; hypovascular lesion conspicuity peaks on portal phase images when the liver maximally enhances. Metastases dominate this category of solid

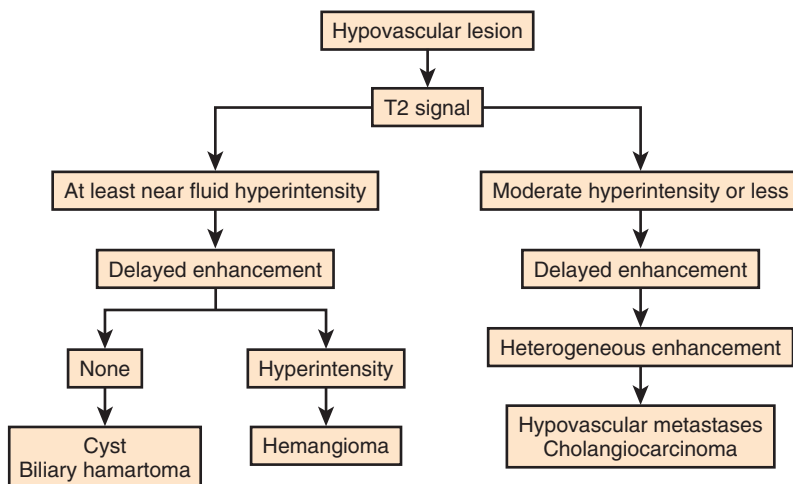


FIGURE 2-56. Hypovascular liver lesion diagnostic algorithm.

TABLE 2-14. Hypovascular Liver Lesions

Developmental Bile duct cyst Biliary hamartoma	Potentially Malignant Ablated lesions
Inflammatory Pyogenic abscess Echinococcal cyst Fungal abscess	Malignant Peripheral cholangiocarcinoma Metastases Colon adenocarcinoma Lung carcinoma Gastric adenocarcinoma Breast carcinoma Pancreatic adenocarcinoma Lymphoma
Neoplasms Benign Hemangioma (usually) Angiomyolipoma Lipoma	

lesions, distantly followed by treated (i.e., embolized, ablated) malignancies, peripheral cholangiocarcinoma, and miscellaneous assorted lesions (Table 2-14). The presence of solid tissue exhibiting at least gradual enhancement usually excludes consideration of simple cysts or cysts complicated by hemorrhage or protein. Successfully ablated lesions lack enhancement and carry an underlying diagnosis, disclosing their true identity (Fig. 2-56).

Metastases

Hypovascular hepatic metastases most commonly originate from the colon and remainder of the gastrointestinal tract (see Table 2-14). The portal venous system transports these tumor emboli to the liver, where they are either obstructed by macrophages or filtered into the space of Disse, gaining a foothold for sustenance and growth (peritoneal seeding accounts for a

small fraction of hypovascular liver metastases). Metastatic lesions restricted to the liver present the opportunity for successful treatment, such as chemotherapy, chemoembolization, radioembolization, and immunoembolization. Metastatic disease frequently beyond the liver—pancreas, breast, lung, and melanoma—is less amenable to these treatments. So, while cataloguing metastases on MRI studies of the liver seems academic and rote, the potential impact on treatment course is real. Many of these schemes depend on RECIST (Response Evaluation Criteria in Solid Tumors) criteria (recommended by the National Cancer Institute), which offers a standardized analytic method to stratify metastatic disease into four categories: (1) complete response (CR), (2) partial response (PR), (3) stable disease (SD), and (4) progressive disease (PD). These assessments are based on the sum of the index lesions—referred to as *target lesions*—compared with baseline. An increase of 20% or more connotes PD, a decrease of 30% or more indicates PR, SD encompasses the middle ground, and CR denotes complete regression of all lesions. Although clinical radiology reporting demands more layered nuancing and comprehensiveness, familiarity with this stratification scheme helps understand the imaging impact on treatment decisions, especially in clinical trials (Table 2-15).

Whereas the arterial phase identifies hypervascular lesions, because of their marked conspicuity compared with adjacent tissue, the portal phase generally most clearly depicts hypovascular metastases. Prominent parenchymal enhancement contrasts with the hypointensity

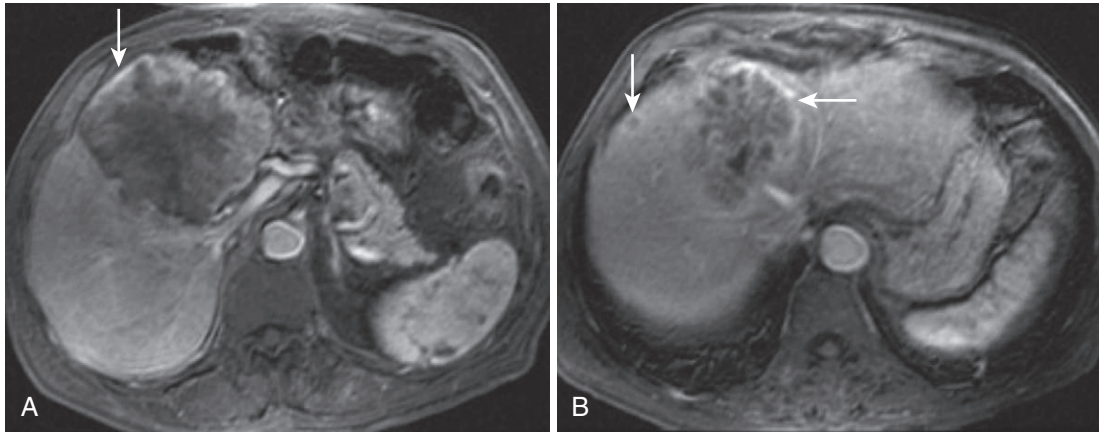


FIGURE 2-57. Hypovascular metastases. **A and B,** Urothelial metastases are characteristically hypovascular with an occasional rim (*arrows*) on arterial phase images.

TABLE 2-15. Response Evaluation Criteria in Solid Tumors Criteria

Target Lesions

Amenable to reproducible repeated measurements

Up to 5 target lesions

Up to 2 per organ

Response = sum of long axis of non-nodal lesions and short axis of nodal lesions

Nontarget Lesions

All other pathologic lesions

Nonmeasurable lesions

Not measured: present, unequivocally progressed or resolved

Response Criteria

Target Lesions

Complete response (CR) = disappearance of all target lesions (all nodes <10 mm)

Partial response (PR) = $\geq 30\%$ decrease in the sum of diameters of target lesions compared with baseline

Progressive disease (PD) = $>20\%$ increase in the sum of diameters of target lesions above smallest size

Stable disease (SD) = insufficient change to qualify for PR or PD

Nontarget Lesions

Complete response (CR) = disappearance of all nontarget lesions (all nodes <10 mm)

Non-CR/non-PD = persistence of ≥ 1 nontarget lesion(s)

Progressive disease (PD) = unequivocal progression of nontarget lesions or appearance of new lesion

of the hypovascular metastases, which often gradually enhance over time and move toward equilibration with liver parenchyma (Fig. 2-57). Arterial phase images occasionally reveal a thin hypervascular rim. Hypovascular metastases resemble their hypervascular counterparts on unenhanced images with mild T2 hyper- and T1 hypointensity. Mucin from mucinous metastases (i.e., rectal, gastric, ovarian mucinous adenocarcinoma) magnifies T2 hyperintensity, approaching the signal of benign fluid-filled

structures, such as hemangiomas (see Fig. 2-55). Conversely, colorectal carcinoma frequently undergoes central coagulative necrosis and desmoplasia accounting for central hypointensity in 50% of cases.⁶⁵

Nonneoplastic cystic lesions, such as incidental hepatic cysts, biliary hamartomas, hemangiomas, and pyogenic abscesses, share some imaging features (see Fig. 2-56). The complete absence of enhancement and uniform fluid content of simple hepatic cysts (and usually biliary hamartomas) attest to the lack of solid, metastatic tissue and endorse the benign etiology. The uniformly peripheral distribution, consistently small size of biliary hamartomas and (usual) absence of solid components, excludes the diagnosis of metastases. The unique enhancement characteristics, including persistent hyperattenuation of hemangiomas, differentiates them from T2 hyperintense metastases. The liquefactive stage of pyogenic abscesses resembles hypovascular metastases; clustering and secondary signs of infection, including right pleural effusion and basal parenchymal changes, imply an infectious etiology.

Lymphoma

Lymphoma rarely involves the liver, and hepatic involvement is almost invariably secondary. Primary hepatic lymphoma prompts consideration of underlying diseases, such as AIDS, other immune disorders, chronic HCV infection, and other liver diseases. Secondary hepatic involvement occurs with both Hodgkin's disease (HD) and non-Hodgkin's lymphoma (NHL). Histopathologically, secondary hepatic lymphoma entails

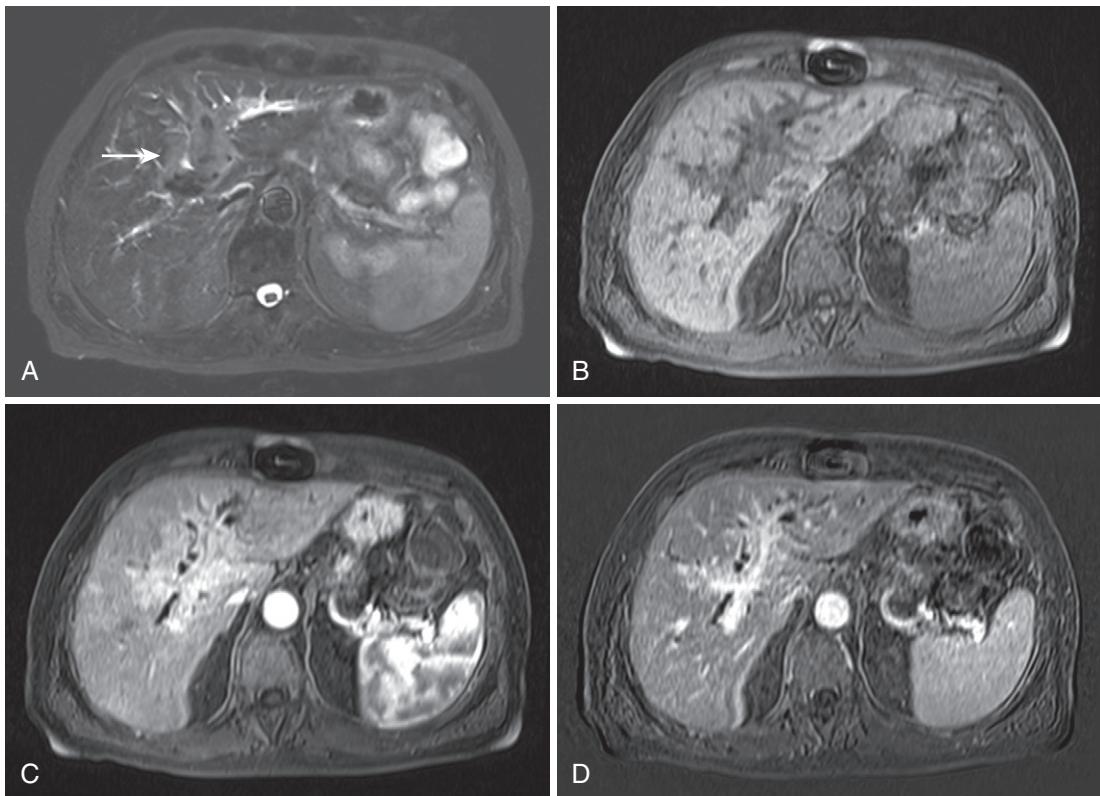


FIGURE 2-58. Hepatic lymphoma. A, Axial moderately T2-weighted image shows uniformly hyperintense material extending along the central portal tracts (*arrow*). Precontrast (B) and postcontrast (C) images depict associated enhancement, which is more conspicuous with the advantage of subtraction (D).

tumor deposits within the portal tracts, potentially leading to visible periportal infiltration reflected by T2 hyperintense infiltration along the portal tracts. Whereas this pattern is fairly specific for lymphoma and is associated with both secondary forms of lymphoma, HD more consistently exhibits this pattern. Secondary hepatic NHL more frequently displays a multifocal nodular pattern. Lymphomatous deposits are usually monotonously T2 hyperintense and hypovascular with relative peripheral enhancement (Fig. 2-58).

The diagnosis generally relies on the underlying history of lymphoma and multifocality. Multifocal HCC usually invades a diseased liver with a history of chronic liver disease and demonstrates arterial enhancement. Multifocal cholangiocarcinoma exhibits hypovascularity, but often displays specific characteristic features, such as capsular retraction, biliary involvement, and segmental or lobar atrophy. Hypovascular metastases from another primary malignancy more closely mirror the appearance of hepatic lymphoma, and clinical history and/or tissue sampling ultimately establishes the etiology.

Ablated Tumors

Ablated hepatic malignancies encompass a wide range of primary and secondary tumors treated with a variety of methods. A comprehensive review of this topic exceeds the scope of this text, but a targeted discussion facilitates understanding MR findings in these patients. Therapeutic agent delivery options to liver lesions include systemic, organ-specific, and lesion-specific. Systemic therapy is synonymous with chemotherapy, for the purposes of this discussion. Organ-specific therapy regimens include chemoembolization, immunoembolization, and radioembolization. Chemical (ethanol), thermal, and cryoablation account for most of the (percutaneous) lesion-specific ablation techniques (Table 2-16).

Whatever the technique, the common objective of destruction of solid tissue equates with absence of enhancement on MR images.⁶⁶ Thin, peripheral, reactive enhancement often surrounds percutaneously treated lesions and measures a few millimeters in thickness (usually ≤ 3 mm) and persists up to 3 to 6 months (Fig. 2-59).⁶⁷ Focal nodularity or thickening is

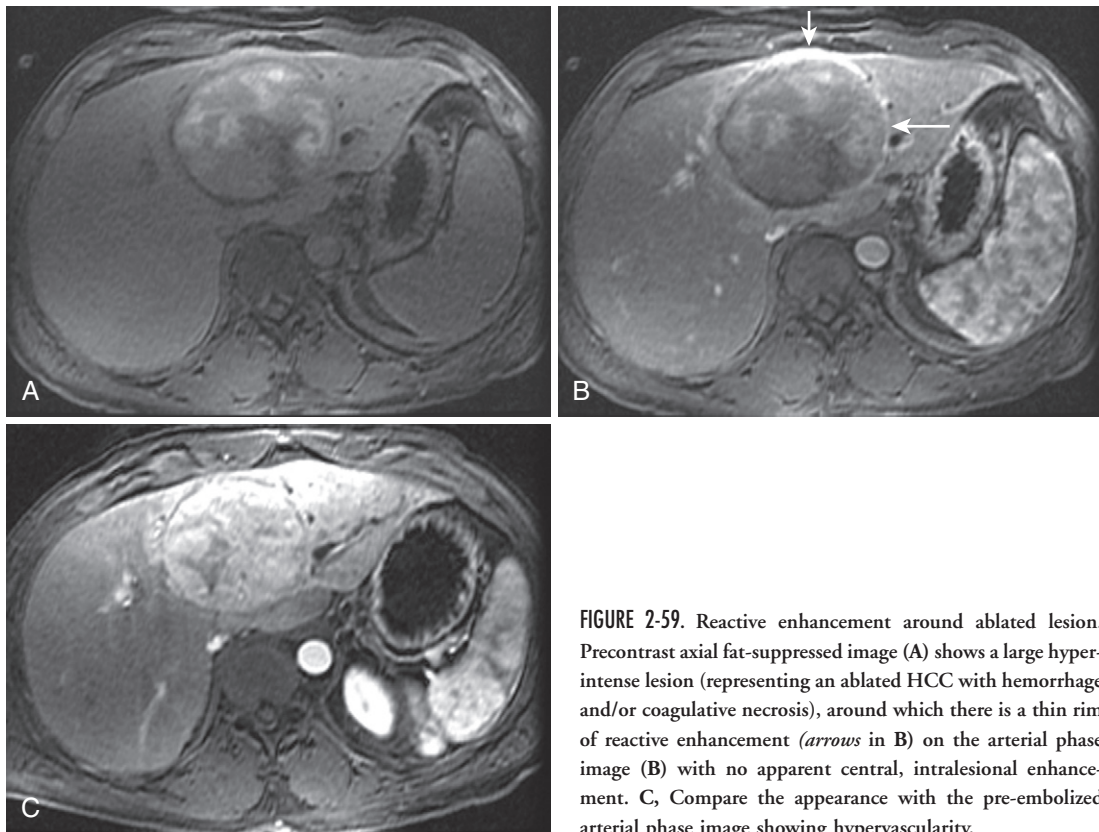


FIGURE 2-59. Reactive enhancement around ablated lesion. Precontrast axial fat-suppressed image (A) shows a large hyperintense lesion (representing an ablated HCC with hemorrhage and/or coagulative necrosis), around which there is a thin rim of reactive enhancement (arrows in B) on the arterial phase image (B) with no apparent central, intralesional enhancement. C, Compare the appearance with the pre-embolized arterial phase image showing hypervascularity.

TABLE 2-16. Liver Lesion Ablation/Treatment Methods

Chemical Ablation	Cold Deposition
Ethanol injection	Cryoablation
Acetic acid injection	
Thermal Ablation	Arterial Delivery of
Heat Deposition	Ablative Substances
Radiofrequency ablation	Chemoembolization
Laser ablation	Immunoembolization
Microwave ablation	
High-intensity focused ultrasound	

a potential sign of residual or recurrent tumor, and short-term follow-up imaging or retreatment is pursued (Fig. 2-60). Because many ablative techniques result in coagulation, often manifesting with T1 shortening and hyperintensity, subtracted images more accurately impart the presence, nature, and degree of enhancement. Size changes are less meaningful; in fact, a desired ablative margin of 5 to 10 mm increases the measureable size of an image-guided ablated lesion.

The most realistic differential diagnosis is persistent tumor, and a brief discussion of potential

complications is more practical. Systemic chemotherapy potentially induces hepatic steatosis and pseudocirrhosis (hepatotoxic effects of the chemotherapy agent), in addition to the extrahepatic side effects. Non-target organ delivery of embolization material is the main source of complications and most commonly affects the lungs and celiac artery branches (to the pancreas, duodenum, stomach, gallbladder, and spleen). Liver infarction rarely occurs—probably more likely with coexistent portal venous occlusion—providing fertile ground for superimposed infection (Fig. 2-61). Subcapsular hematoma rarely complicates both percutaneous treatments and chemoembolization, especially after prior intervention (Fig. 2-62). Other complications have been reported, most of which result from the direct effects of image-guided percutaneous intervention (e.g., perihepatic abscess, biloma, hemorrhage).⁶⁸

Peripheral Cholangiocarcinoma

Anatomic location classifies cholangiocarcinoma into three groups: peripheral cholangiocarcinoma (PCC—arising from intrahepatic

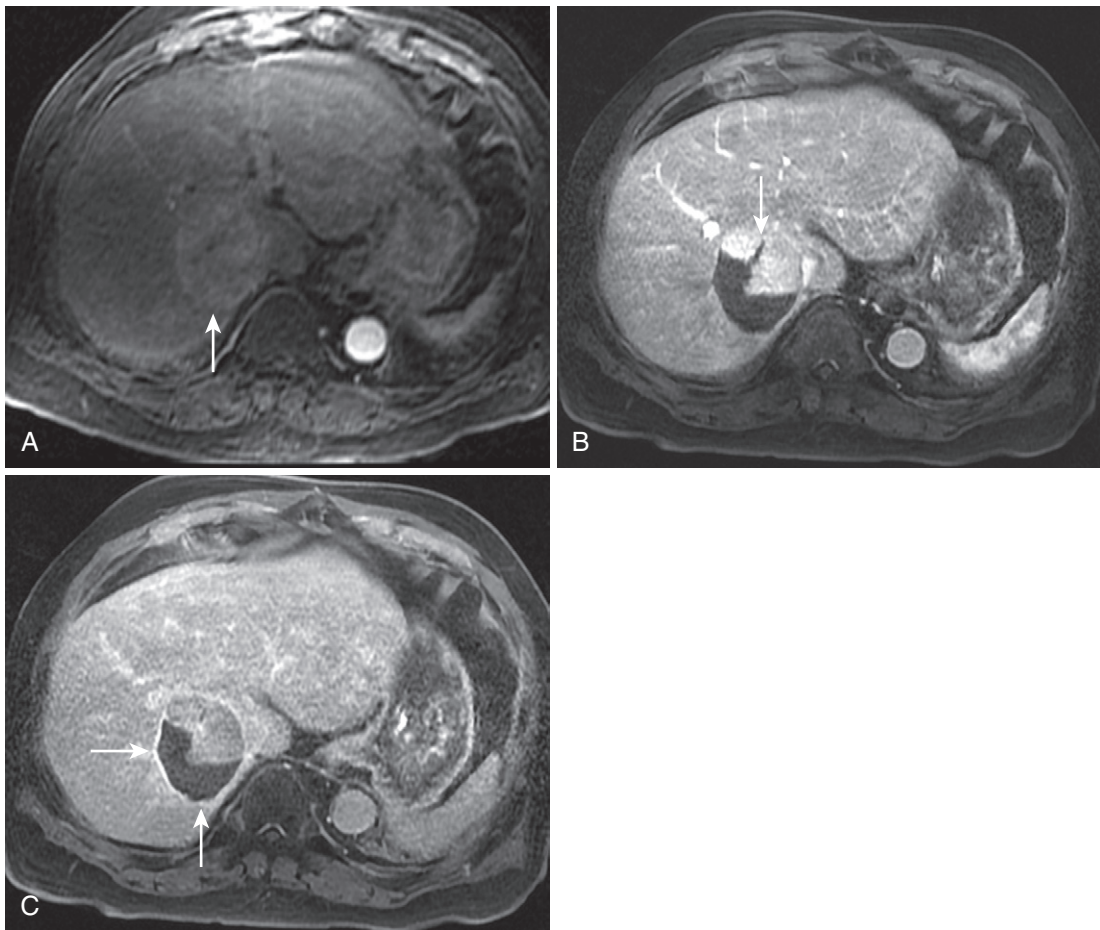


FIGURE 2-60. Nodular enhancement of ablated lesion. Following ablation of the large hypervascular hepatocellular carcinoma in the right lobe of the liver (*arrow* in A), gross nodular enhancement (*arrow* in B) on the arterial phase image (B) of a subsequent examination indicates residual tumor, which contrasts with the thin, reactive rim surrounding the successfully ablated component of the tumor (*arrows* in C) seen on the delayed image (C).

TABLE 2-17. Cholangiocarcinoma Classification

Intrahepatic (peripheral) cholangiocarcinoma (10%)
Hilar cholangiocarcinoma (Klatskin's tumor) (65%)
Extrahepatic cholangiocarcinoma (25%)

ducts distal to the second-order branches, 10%); hilar cholangiocarcinoma, or Klatskin's tumor (involving the first-order bile ducts or confluence, 60%); and extrahepatic cholangiocarcinoma (originating from the common hepatic or common bile duct, 30%) (Table 2-17). Because PCC imaging features more closely simulate primary hepatic lesions, inclusion in the discussion of liver lesions is more relevant; distal types of cholangiocarcinoma are deferred to Chapter 3.

PCC is an adenocarcinoma originating from bile duct epithelium accounting for 5% to 30% of primary malignant hepatic tumors, and a distant second to HCC.⁶⁹⁻⁷¹ Cholangiocarcinoma predominates in the 6th and 7th decades with predisposing factors promoting earlier onset, such as PSC, choledochal cyst, Caroli's disease, hepatolithiasis, *Clonorchis sinensis* infection, and Thorotrast exposure.

PCC exhibits three growth patterns, codified into a classification scheme by the Liver Cancer Study Group of Japan^{72,73}: mass-forming, periductal infiltrating, and intraductal papillary types (Fig. 2-63). PCC most commonly subscribes to the mass-forming variety and presents as a large (usually > 5 cm) lobulated mass. Large size is attributable to the relative lack of symptoms because of the peripheral location and relative lack of biliary obstruction. Nonspecific

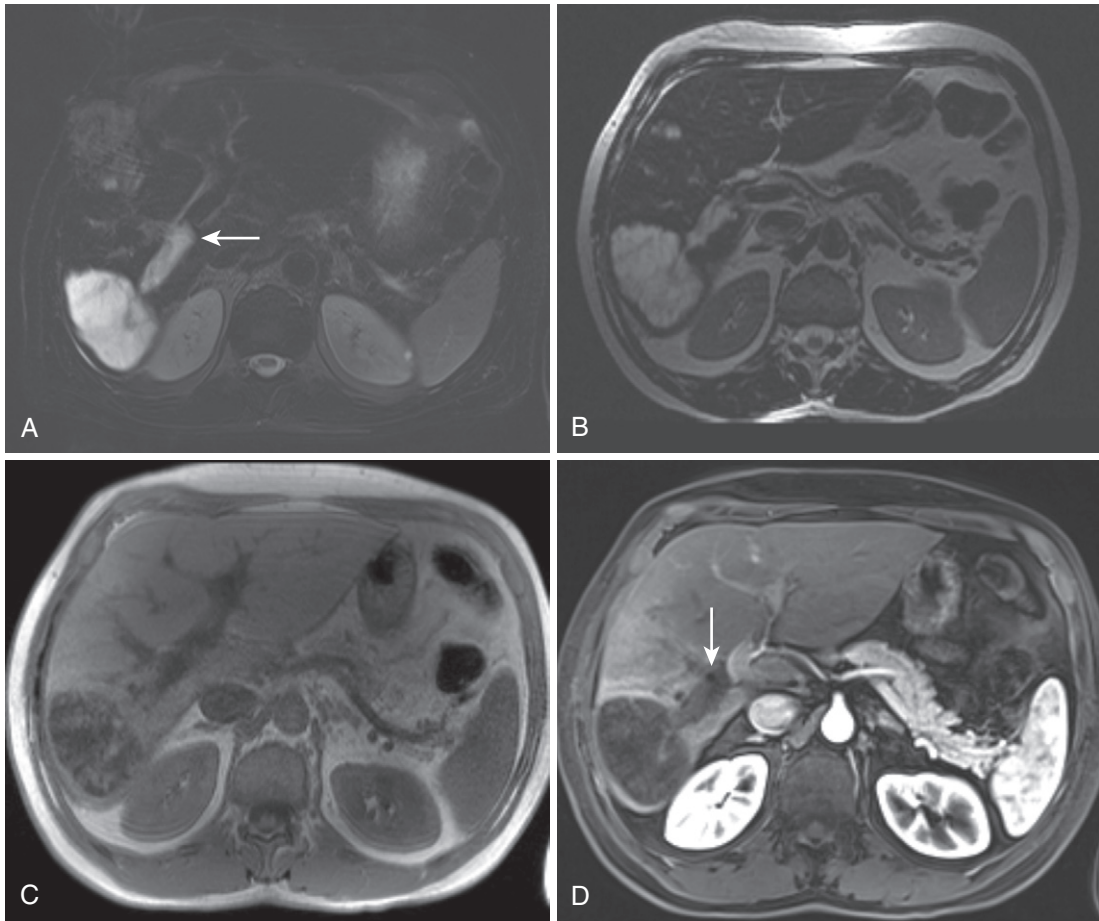


FIGURE 2-61. Liver infarction/infection due to chemoembolization. **A**, The moderately T2-weighted image demonstrates a markedly hyperintense, segmental roughly wedge-shaped lesion in the posterior segment of the liver with an adjacent tubular hyperintensity (*arrow*) at its apex—the thrombosed portal venous branch. Hyperintensity persists on the heavily T2-weighted image (**B**) with corresponding hypointensity on the T1-weighted in-phase image (**C**). **D**, Lack of enhancement of both the liver infarct and the thrombosed portal venous branch (*arrow*) is depicted on the contrast-enhanced image.

hypointensity on T1-weighted images accompanied by peripheral T2 hyperintensity and central T2 hypointensity typifies the classic appearance of mass-forming PCCs (Fig. 2-64).⁷⁴ Peripheral cellularity and central fibrosis explains the T2 signal characteristics. Enhancement characteristics reiterate this centripetal architecture with hypovascular enhancement of the peripheral cellular zone followed by progressive enhancement of the central fibrotic/desmoplastic zone (see Fig. 2-64). Foci of coagulative necrosis, also hypointense on T2-weighted images, do not enhance. The relatively delayed enhancement of PCC differentiates it from the other most common primary hepatic malignancy, HCC,^{75,76} and justifies the acquisition of delayed enhanced images. Slowly, gradually increasing, progressively centripetal enhancement evolves over minutes. Relative hypovascularity with progressive filling

clearly distinguishes PCC from HCC, but potentially overlaps with the appearance of a hypovascular metastasis. Capsular retraction, presumably induced by desmoplasia associated with PCC, stands in contradistinction to capsular bulging exerted by other space-occupying masses in the liver (Fig. 2-65 and Table 2-18). Although not commonly observed, biliary invasion excludes other etiologies. Lobar or segmental atrophy due to (usually portal) venous encasement uniquely characterizes PCC.

The presence of vascular invasion is an important consideration in staging PCC and predicting resectability (Table 2-19).⁷⁷ Other prognostic factors include: size (>2–3 cm confers poor prognosis), metastatic lymphadenopathy, and multifocality.^{78,79} Unfortunately, PCC usually surpasses these parameters at the time of diagnosis, precluding surgical resection. In summary, PCC

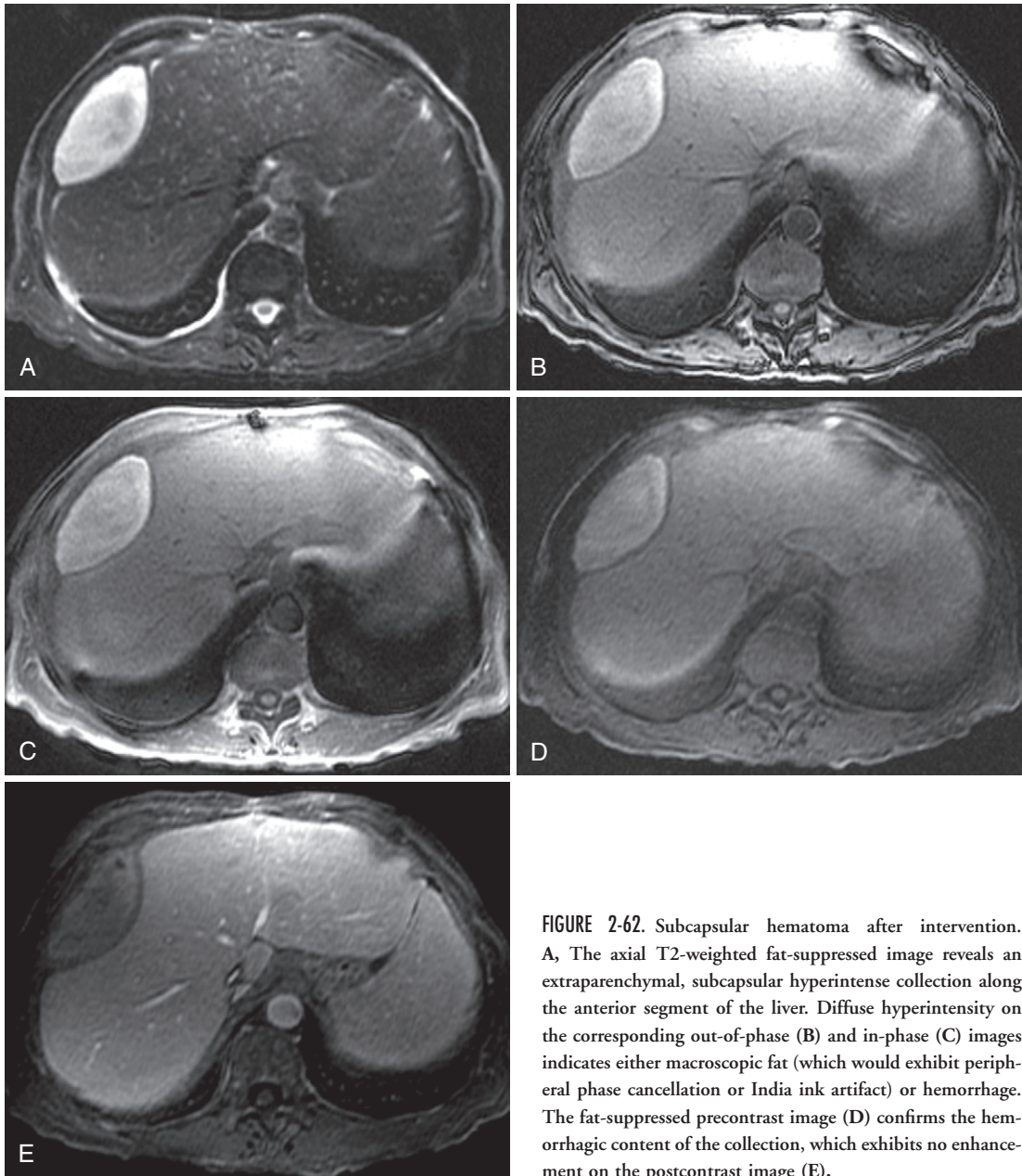


FIGURE 2-62. Subcapsular hematoma after intervention. A, The axial T2-weighted fat-suppressed image reveals an extraparenchymal, subcapsular hyperintense collection along the anterior segment of the liver. Diffuse hyperintensity on the corresponding out-of-phase (B) and in-phase (C) images indicates either macroscopic fat (which would exhibit peripheral phase cancellation or India ink artifact) or hemorrhage. The fat-suppressed precontrast image (D) confirms the hemorrhagic content of the collection, which exhibits no enhancement on the postcontrast image (E).

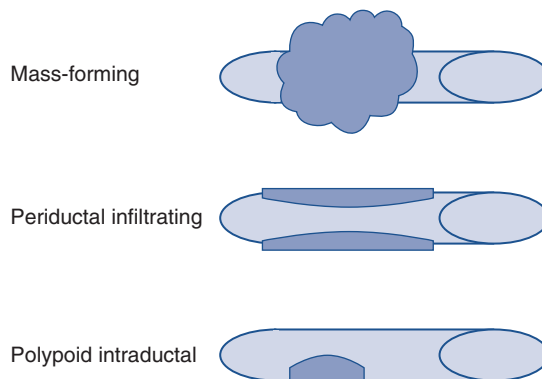


FIGURE 2-63. Cholangiocarcinoma growth patterns. (From Han JK, Choi BI, Kim AY, et al. Cholangiocarcinoma: Pictorial essay of CT and cholangiographic findings. *Radiographics* 22:173–187, 2002.)

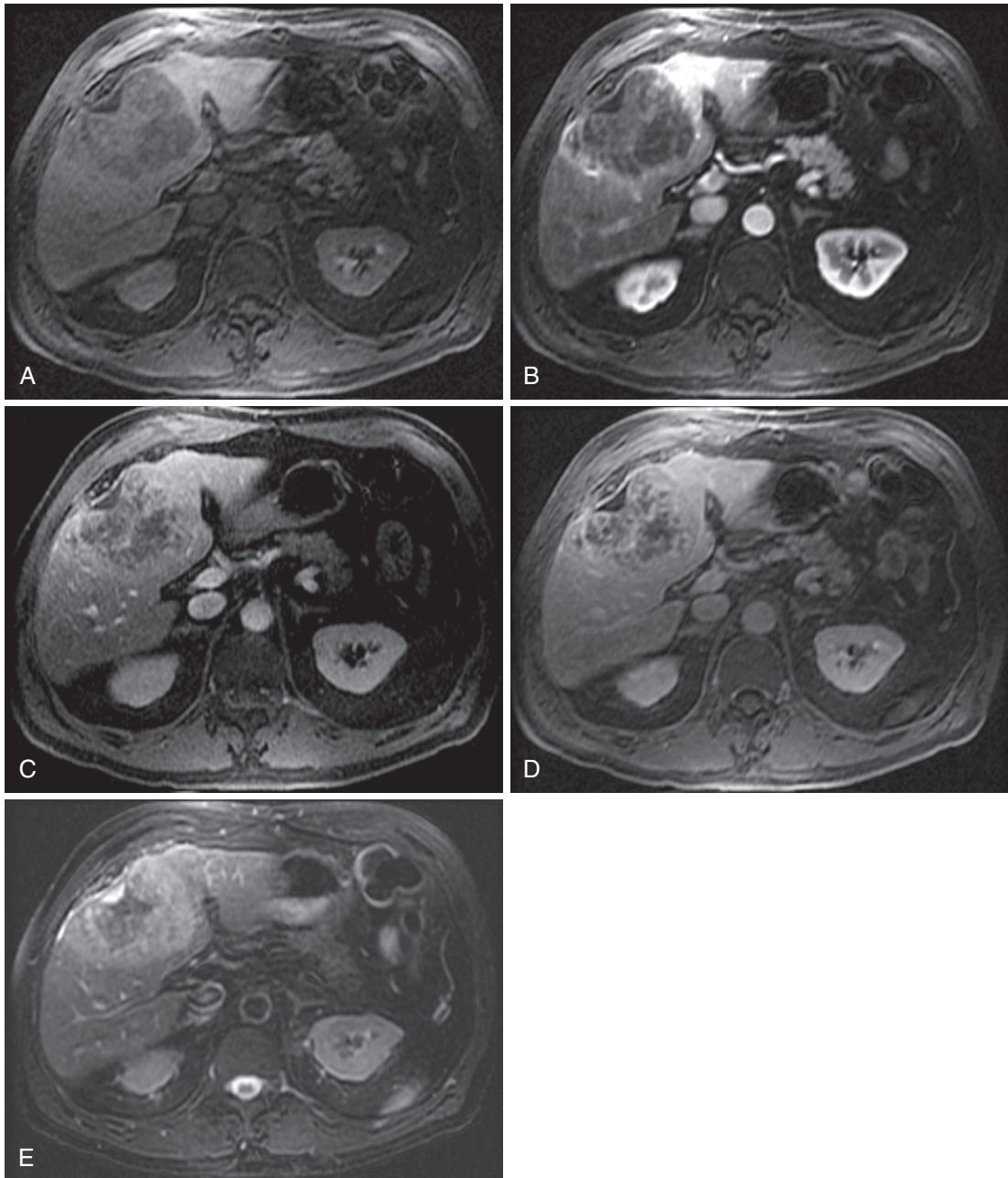


FIGURE 2-64. Cholangiocarcinoma signal and enhancement patterns. Mild patchy enhancement of the central aspect of the large peripheral cholangiocarcinoma on the arterial phase image (B) compared with the precontrast image (A) progresses on the serial delayed images (C and D). E, Patchy central enhancement likely reflects a combination of coagulative necrosis and desmoplasia—both hypointense on the moderately T2-weighted image. Note the classic peripheral hyperintensity, central hypointensity, and capsular retraction.

modes of spread explain some of its features and propensity for metastatic spread: lymphatic spread = lymphadenopathy; vascular invasion = (usually portal) venous obliteration and associated segmental or lobar atrophy; and biliary

spread = proximal biliary dilatation and/or abnormal wall thickening and enhancement. Parenthetically, cholangiocarcinoma also undergoes perineural spread, which eludes MRI capabilities.

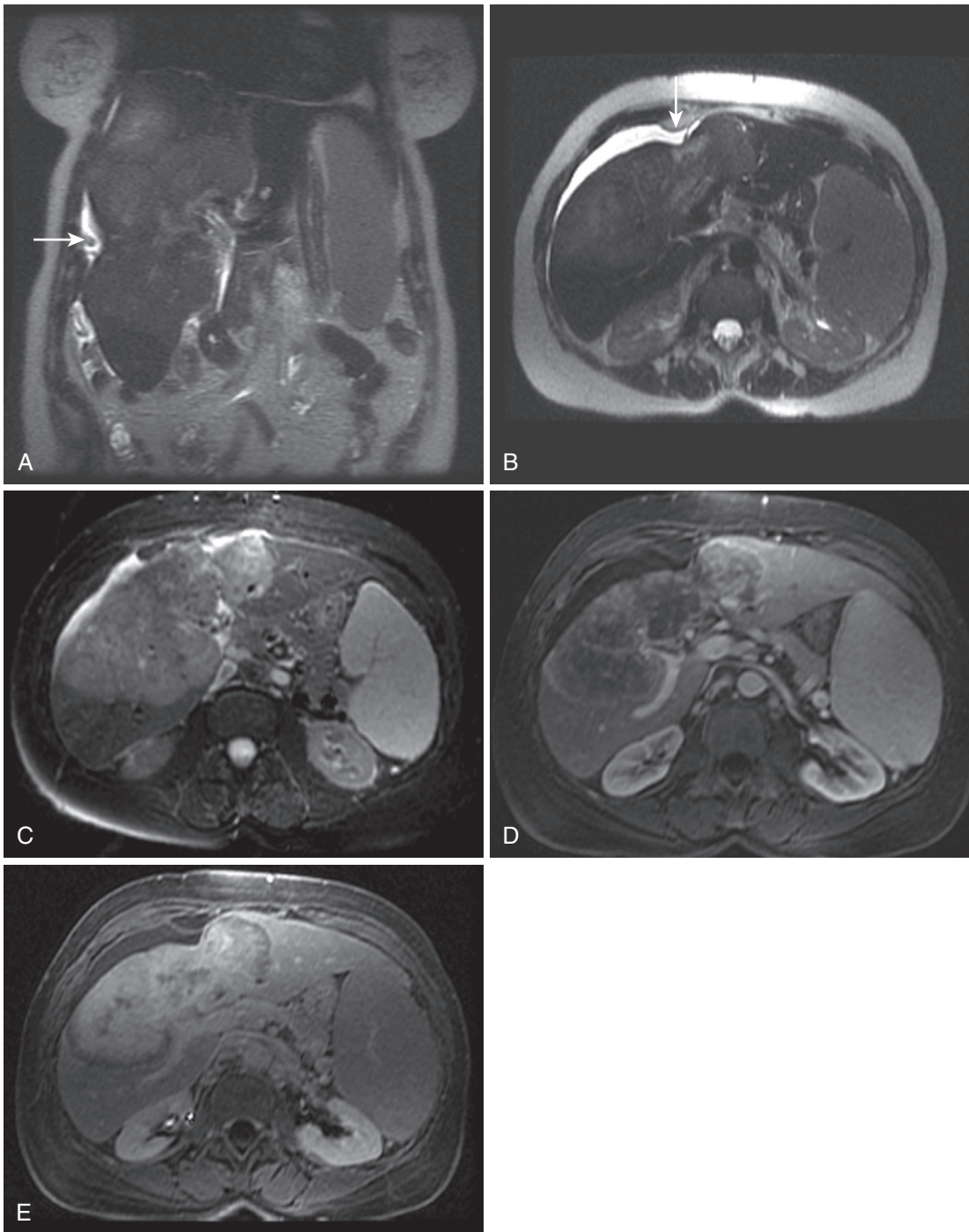


FIGURE 2-65. Cholangiocarcinoma with capsular retraction. Coronal (A) and axial (B) heavily T2-weighted and fat-suppressed moderately T2-weighted (C) images show a large mildly hyperintense lesion bridging the right and left hepatic lobes with convexity of the outer liver margin, indicating capsular retraction (*arrow* in A and B). Arterial phase (D) and delayed (E) images after contrast portray the typical hypovascular enhancement pattern with delayed, centripetal progression.

TABLE 2-18. Causes of Capsular Retraction

Tumors
HCC
FLC
PCC
Adenocarcinoma (colon, stomach, breast, lung, pancreas, GB)
HCC postembolization
Malignant tumor postchemotherapy
Hemangioma
Absent Tumor
Confluent hepatic fibrosis
Oriental cholangiohepatitis
Bile duct necrosis
Pseudoretraction
Accessory fissure
Normal liver between protruding lesions

FLC, fibrolamellar carcinoma; GB, gallbladder; HCC, hepatocellular carcinoma; PCC, peripheral cholangiocarcinoma.

From Yang DM, Kim HS, Cho SW, et al. Pictorial review, various causes of hepatic capsular retraction: CT and MR findings. *Br J Radiol* 75:994-1002, 2002.

TABLE 2-19. Peripheral Cholangiocarcinoma Staging

T Groups
TX: Primary tumor cannot be assessed
T0: No evidence of primary tumor
T1: Single tumor (any size) with no vascular involvement
T2: Either single tumor (any size) with vascular involvement, or > 1 tumor with none > 5 cm
T3: Multiple tumors > 5 cm, or tumor involvement of major portal or hepatic venous branch
T4: Direct invasion into adjacent organ (not including gallbladder), or visceral peritoneal involvement
N Groups
NX: Regional lymph node cannot be assessed
N0: No regional lymph node involvement
N1: Regional lymph node involvement
M Groups
MX: Distant metastatic spread cannot be assessed
M0: No distant metastatic spread
M1: Spread to distant lymph nodes or organs
Stage I: T1, N0, M0
Stage II: T2, M0, M0
Stage IIIA: T3, N0, M0
Stage IIIB: T4, N0, M0
Stage IIIC: Any T, N1, M0
Stage IV: Any T, Any N, M1

M, metastasis; N, node; T, tumor.

From American Joint Committee on Cancer (AJCC) Liver Cancer Staging (histologically insensitive; also applies to hepatocellular carcinoma [HCC]).

Lipid-Based Lesions

The dominant remaining hypovascular solid lesions share a common feature—intralesional lipid—and include angiomyolipoma, lipoma, and nodular steatosis. In a literal sense, these lesions are not actually hypovascular and form

a separate category that is more appropriately entitled *lipid-rich lesions* or *lipid-dominant lesions* (so as not to confuse the issue by including adenoma and HCC, which may harbor small quantities of fat). These lesions plot along a scale from solely microscopic fat (steatosis) to some macroscopic fat (angiomyolipoma) to gross macroscopic fat (lipoma). The common thread unifying these lesions is the presence of fat—usually the diagnostic endpoint of these lesions.

HEPATIC ANGIOMYOLIPOMA

Hepatic angiomyolipoma (AML) is a benign hamartomatous lesion and the liver follows the kidney in incidence. AMLs are associated with tuberous sclerosis, but also arise in isolation. The name belies the histologic constituents of the angiomyolipoma: blood vessels (angio-), smooth muscle (-myo-) and fat (-lipoma). The only variable is the relative quantity of each component. The presence of fat generally establishes the diagnosis and lipid content varies from less than 10% to more than 90% of tumor volume.

A mixed signal pattern including macroscopic fat with T1 hyperintensity and suppression on fat-saturated images describes the typical MR appearance (Fig. 2-66). Voxels containing lipid and nonlipoid elements experience loss of signal on out-of-phase images. Angioid components or tumoral vessels enhance avidly (and lend a hypervascular quality to these lesions) and connect to a draining (hepatic) vein. Monotonous smooth muscle elements enhance blandly and contribute no specific imaging features, tending to exaggerate heterogeneity and increase nonspecificity.

AML fat content raises the suspicion of HCC and adenoma (in addition to the other usually incidental lesions—lipoma and nodular steatosis). The absence of a capsule and the presence of tumoral vessels connecting to a draining vein discriminate AML from HCC and adenoma.⁸⁰ These features should be sought, because gross, macroscopic fat alone suggests an alternative to HCC and adenoma (either AML or lipoma), but does not necessarily forestall biopsy. Other rare fat-containing lesions to consider (on the boards or in conference) include metastatic teratoma and liposarcoma; teratomas often calcify and liposarcomas often contain significant solid, hypervascular tissue—both not features of AML. Whereas otherwise incidental, large size confers

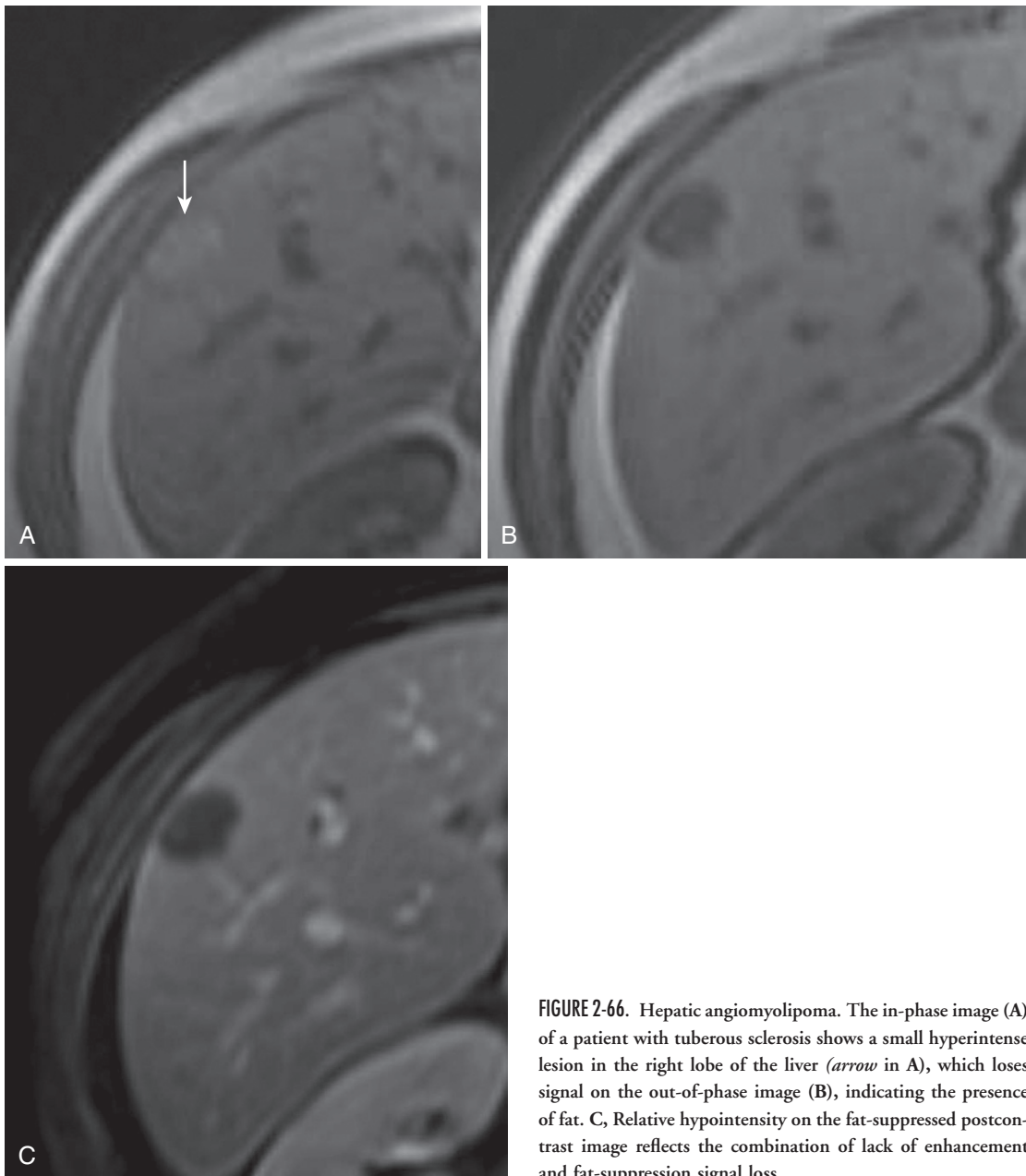


FIGURE 2-66. Hepatic angiomyolipoma. The in-phase image (A) of a patient with tuberous sclerosis shows a small hyperintense lesion in the right lobe of the liver (*arrow* in A), which loses signal on the out-of-phase image (B), indicating the presence of fat. C, Relative hypointensity on the fat-suppressed postcontrast image reflects the combination of lack of enhancement and fat-suppression signal loss.

risk of hemorrhage and/or rupture—the only reported complication, which may prompt surgical resection or embolization. AMLs have no malignant potential.

HEPATIC LIPOMA

Lipomas rarely affect the liver and present little diagnostic difficulty when they do. Uniform macroscopic fat signal suppressed on fat-saturated images with no appreciable enhancement or complexity pathognomonically

characterizes hepatic lipoma (and all simple lipomas). The absence of vascular enhancement excludes AML, and lack of solid, enhancing components excludes other lipid-containing lesions, such as HCC and adenoma. Nodular steatosis exemplifies microscopic fat signal with little to no signal loss on out-of-phase images with no perceptible signal loss on fat-suppressed images, in contradistinction to lipomas. Lipomas incur no risk of complications or need for further evaluation.⁸¹

FOCAL STEATOSIS (FATTY INFILTRATION)

Hepatic steatosis manifests in various patterns: diffuse, patchy, segmental or geographic, and focal or nodular.⁸² Steatosis signifies abnormal accumulation of fat (i.e., triglycerides) in hepatocytes and develops in underlying conditions such as alcoholism, medication effects or toxin exposure, obesity, insulin resistance, and hypertriglyceridemia. Micro- and macrovesicular histopathologic types portend different disease processes, and this classification scheme reflects the size of the fat droplets within the hepatocytes. Microvesicular steatosis involves deficient hepatic β -oxidation of fatty acids and more frequently accompanies severe hepatic dysfunction. Multifactorial causes lead to macrovesicular steatosis, including enhanced lipolysis of triglycerides (associated with insulin resistance), lipogenesis promotion, and increased delivery and secretion of lipids. Although these histopathologic designations confer different prognostic and disease specific information, the MR appearance is identical, with relative loss of signal on out-of-phase images. When focal or geographic, steatosis often indicates underlying portal or systemic venous anomalous supply.

The juxtaposition of intracellular fat vesicles with cytoplasm, interstitial fluid, and any other free water protons in the same imaging voxel results in destructive interference on out-of-phase images. The TE of out-of-phase images (2.2–2.3 msec at 1.5 Tesla) is timed to occur when fat and water have precessed 180° apart from one another, which means that the signal contributions of each respective proton—fat and water—are subtractive. With increasing hepatocytic lipid, parenchymal signal progressively darkens. Visual appreciation of this phenomenon suffices; comparison with a reference that is unlikely to harbor fat—such as the spleen—confirms a relative drop in signal on out-of-phase images. More detailed analysis and quantification techniques are deferred to the forthcoming discussion of diffuse steatosis.

Common characteristic locations for focal steatosis include the medial segment, periligamentous regions (i.e., adjacent to the falciform ligament), around the gallbladder fossa and porta hepatic, and in subcapsular distributions (Fig. 2-67).^{82–84} Generalized, multifocal steatosis potentially generates diagnostic ambiguity, especially when nodular or round, simulating solid masses. In addition to the chemical shift

artifact reflected by signal loss on out-of-phase images, lack of mass effect (note normal vessels coursing through the lesions), enhancement equivalent to liver parenchyma, stability over time, and relative inconspicuity on all other images characterize focal fat.⁸⁵ These features discriminate multifocal steatosis from other lesions in the differential diagnosis containing microscopic fat. Although HCC occasionally contains microscopic lipid, focal intralesional inclusions are the norm and the heterogeneous visibility on unenhanced and arterial phase images, clear mass effect, and vascular invasion differentiate HCC from steatosis. Adenomas also demonstrate mass effect and usually manifest focal intralesional fat. Macroscopic fat indicates an alternative diagnosis, as previously discussed.

FOCAL FATTY SPARING

Focal fatty sparing simulates a T1 hyperintense pseudolesion (not to be confused with an adenoma, hemorrhagic or melanotic metastasis, or dysplastic nodule in the cirrhotic liver) compared with the out-of-phase hypointensity of the background fatty liver. Actually, spared tissue is the only normal part of hepatic parenchyma in steatosis. Anomalous venous circulation spares the affected parenchyma from fatty infiltration, resulting in focal sparing.⁸⁶ Periligamentous (around the falciform ligament and ligamentum venosum), periportal, and pericholecystic regions most often exhibit fatty sparing. Isointensity between in- and out-of-phase images against the backdrop of generalized signal loss on out-of-phase images points to spared liver parenchyma (Fig. 2-68). The key is to appreciate that the diffuse steatosis is the abnormality and not falsely identify relatively hyperintense zones on out-of-phase images as potential lesions.

GEOGRAPHIC OR SEGMENTAL LESIONS

Most liver pathology manifests either focally or diffusely. Occasionally, abnormalities involving only a segment or territory of the liver defy focal or diffuse spatial pattern classification. Mentally segregate these lesions into primary versus secondary (to an occult lesion) abnormalities. Geographic changes—especially enhancement—often belie the presence of an underlying liver mass and the presence of a segmental abnormality demands further investigation to detect a

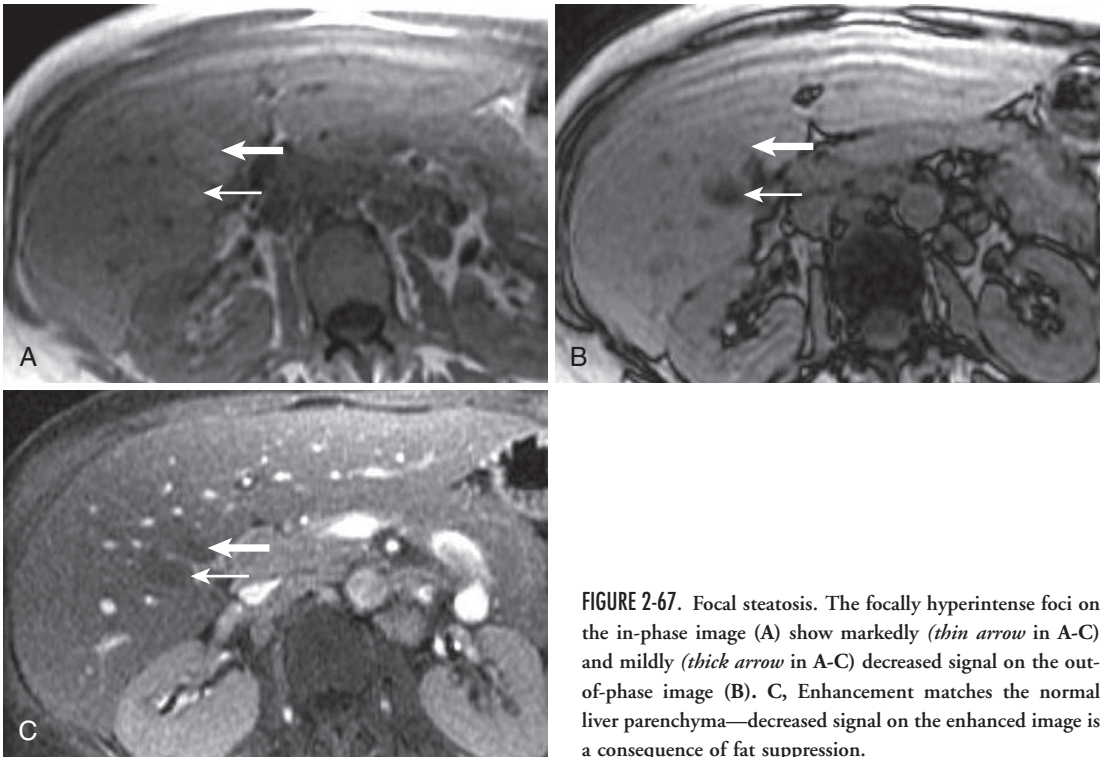


FIGURE 2-67. Focal steatosis. The focally hyperintense foci on the in-phase image (A) show markedly (*thin arrow* in A-C) and mildly (*thick arrow* in A-C) decreased signal on the out-of-phase image (B). C, Enhancement matches the normal liver parenchyma—decreased signal on the enhanced image is a consequence of fat suppression.

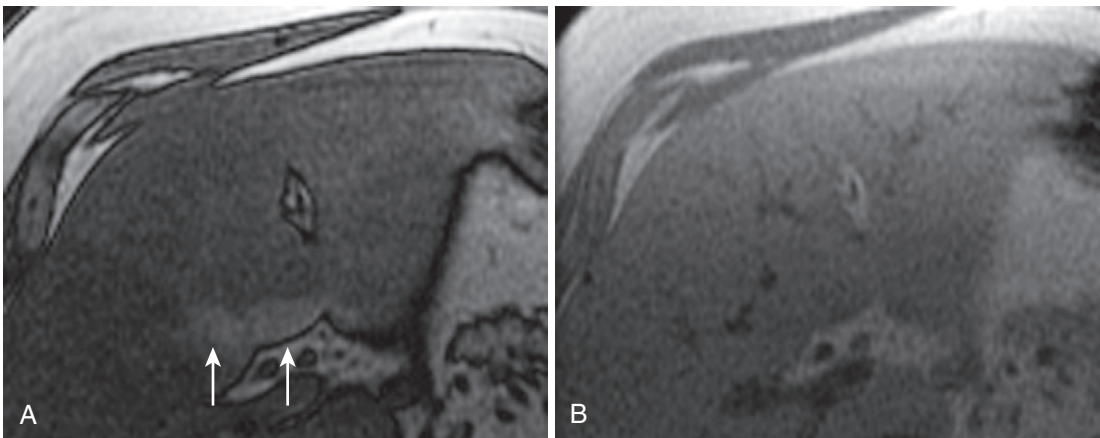


FIGURE 2-68. Focal fatty sparing. The out-of-phase image (A) shows a residual rim of hyperintensity in the periportal region (*arrows* in A) against the backdrop of hypointense fatty infiltration, which becomes isointense on the in-phase image (B) where the surrounding liver regains normal signal.

subtle underlying mass. Whereas geographic signal changes often accompany an underlying focal mass, signal abnormalities more frequently signify a primary disorder, such as steatosis or fibrosis. Enhancement tends to predominate over signal changes in secondary lesions, whereas signal predominates in primary lesions (although abnormal enhancement characterizes some lesions such as confluent fibrosis). Based on these general principles, consider a binary approach to segmental lesions according to

primarily signal changes versus primarily enhancement changes (Fig. 2-69).

Primarily Enhancement Lesions

Primarily enhancement lesions encompass THIDs, macrovascular occlusion (usually portal venous), and hepatic infarct—rarely seen as a consequence of dual hepatic blood supply. These lesions share the common theme of normal underlying hepatic parenchyma usually

GEOGRAPHIC LESIONS

Enhancement Lesions	Signal Lesions
THID	Geographic steatosis
Portal venous occlusion	Confluent fibrosis
Hepatic infarct	

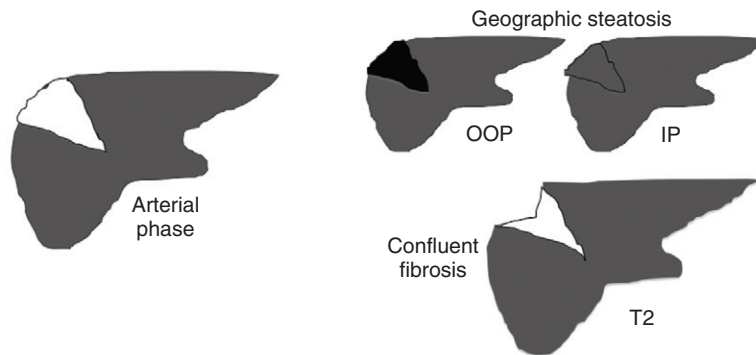


FIGURE 2-69. Geographic lesions including diagram of secondary perfusion changes. IP, in phase; OOP, out of phase; THID, transient hepatic intensity difference.

exhibiting fading (or isointensity) on delayed images.

GEOGRAPHIC THID

THIDs originate for a variety of reasons, depending on the presence or absence of an underlying lesion. The dual portal venous–hepatic arterial blood supply allows increased arterial flow to compensate for a decrease in portal venous flow—the basic premise of a THID. Pathogenetic mechanisms of primary lesions include portal venous compression (due to portal branch compression or thrombosis), flow diversion (due to arteriportal shunt or anomalous blood supply), and effects of adjacent inflammation. Secondary causes include siphoning (increase in arterial flow), portal hypoperfusion (due to compression or infiltration), portal venous thrombosis (PVT), and flow diversion (due to an arteriportal shunt associated with an underlying lesion).^{41,42}

Sharp margins, arterial enhancement, and an absence of signal changes on unenhanced images usually characterize these lesions (see Fig. 2-39). Occlusion or truncation of vessels proximal to the capsule and distal to the lesion potentially results in a rounded appearance. Nonsectorial or amorphous morphology results from extrinsic compression (i.e., subcapsular collections), anomalous vascular supply, hyperemia due to adjacent inflammation (i.e.,

cholecystitis), and postprocedural changes (i.e., transcutaneous biopsy or ablation).

OTHER GEOGRAPHIC VASCULAR LESIONS

Other vascular etiologies resemble THIDs, such as hepatic infarct and portal venous occlusion. Hepatic infarcts are not incidental lesions and usually accompany LT, laparoscopic cholecystectomy, vasculitis, and profound hypovolemia.⁸⁷ Temporal stability excludes infarct, which atrophies, degenerates, and may undergo necrosis. PVT also rarely manifests spontaneously and usually accompanies inflammation (i.e., pancreatitis, peritonitis, diverticulitis) or malignancy. Wedge-shaped morphology and hypervascularity often associated with portal venous occlusion reiterate the appearance of a THID and only direct visualization of a filling defect in a portal venous branch excludes THID.

Because of its rare occurrence and protective dual hepatic perfusion, infarct should be realistically entertained only in appropriate clinical settings (e.g., LT, laparoscopic cholecystectomy, vascular intervention; see Figs. 2-61 and 2-70). Signal changes develop gradually along with atrophy and volume loss of the affected segment. In the acute phase, only the clinical scenario and direct signs of arterial occlusion (lack of enhancement of the hepatic artery or one of its branches) positively identify arterial infarction as the correct diagnosis.

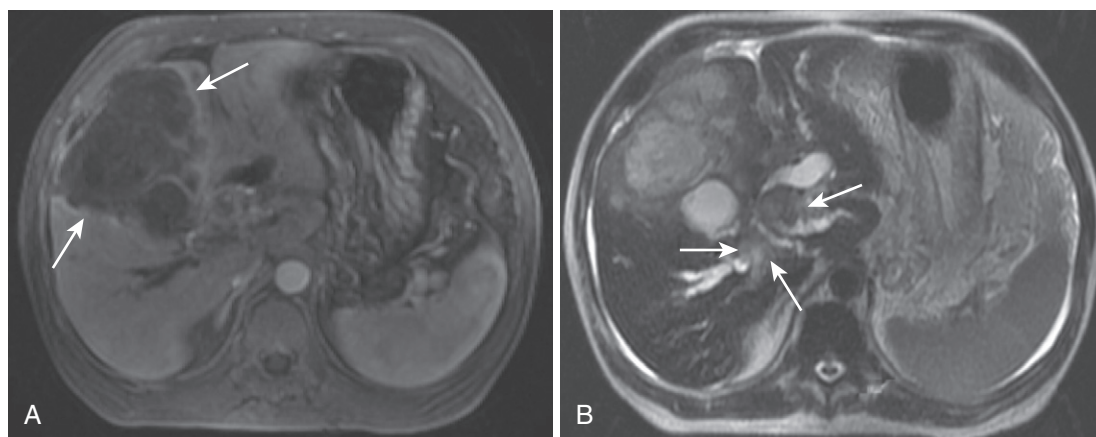


FIGURE 2-70. Liver infarct associated with malignant vascular invasion. The postcontrast image (A) shows a roughly wedge-shaped geographic nonenhancing lesion in the anterior and medial hepatic segments (*arrows*), thought to represent a liver infarct in a patient with hilar cholangiocarcinoma, which is better seen on the T2-weighted image (*arrows* in B) at the confluence of the dilated intrahepatic ducts.

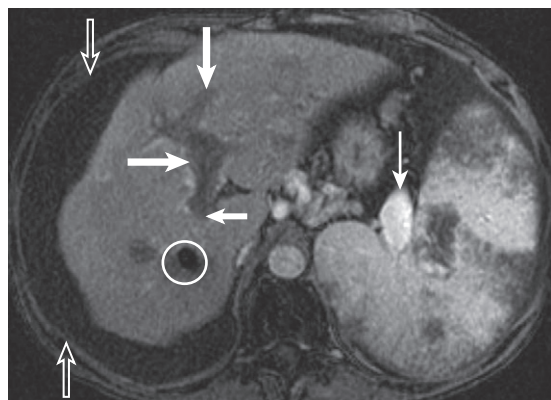


FIGURE 2-71. Portal venous thrombosis with filling defect. Portal venous phase contrast-enhanced image shows an avidly enhancing splenic vein (*thin arrow*) with an occlusive filling defect in the main and right and left portal veins (*thick arrows*). Note the ascites (*open arrows*) and susceptibility artifact arising from the TIPS shunt in the posterior segment (*circle*).

Portal venous occlusion also rarely arises spontaneously. Identification of segmental arterial enhancement prompts inspection of the regional portal venous branches in pursuit of a filling defect (Fig. 2-71). A history of visceral inflammation or malignancy (particularly HCC) increases the likelihood of portal venous occlusion. In the absence of an underlying culprit lesion—such as HCC—signal or morphologic changes are usually absent. When associated with malignancy, check for enhancement of the filling defect, which indicates tumor thrombus, as opposed to bland thrombus (which does not enhance).

Signal ± Enhancement Lesions

Many geographic liver lesions manifest primarily with signal changes, with or without abnormal enhancement. Geographic steatosis and iron deposition constitute the segmental lesions solely manifesting signal changes. Signal changes arising from confluent fibrosis and segmental biliary obstruction often experience abnormal enhancement and a greater potential for diagnostic uncertainty.

GEOGRAPHIC STEATOSIS/IRON DEPOSITION

Geographic steatosis (or fatty infiltration) exhibits the same signal characteristics as its nodular counterpart (Fig. 2-72). Isolated loss of signal on out-of-phase images with no mass effect on normal hepatic structures characterizes steatosis. Whereas iron deposition also lacks mass effect, the opposite signal loss pattern is observed—loss of signal on in-phase images—reflecting increasing susceptibility effects of iron as a consequence of the longer echo time (and iron deposition is usually diffuse). Enhancement equivalent to hepatic parenchyma characterizes both entities. Neither demonstrates profound signal changes on spin-echo (or FSE) images, however, because the 180° pulse(s) correct for phase changes (in the case of steatosis) and susceptibility artifact (in the case of iron deposition). Spin-echo images generally brandish mild relative hyperintensity due to fat and hypointensity due to iron, respectively.

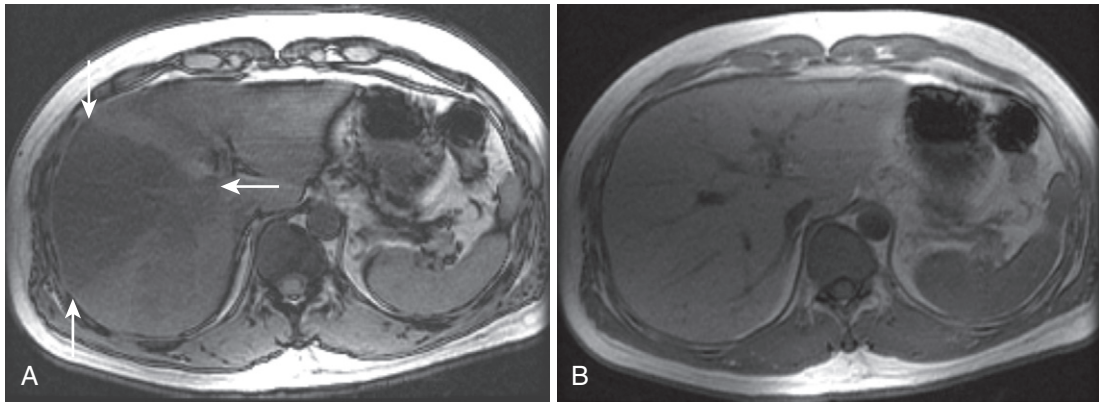


FIGURE 2-72. Geographic steatosis. A segmental wedge-shaped region of hypointensity (*arrows* in A) on the out-of-phase image (A) is isointense to surrounding liver parenchyma on the in-phase image (B).

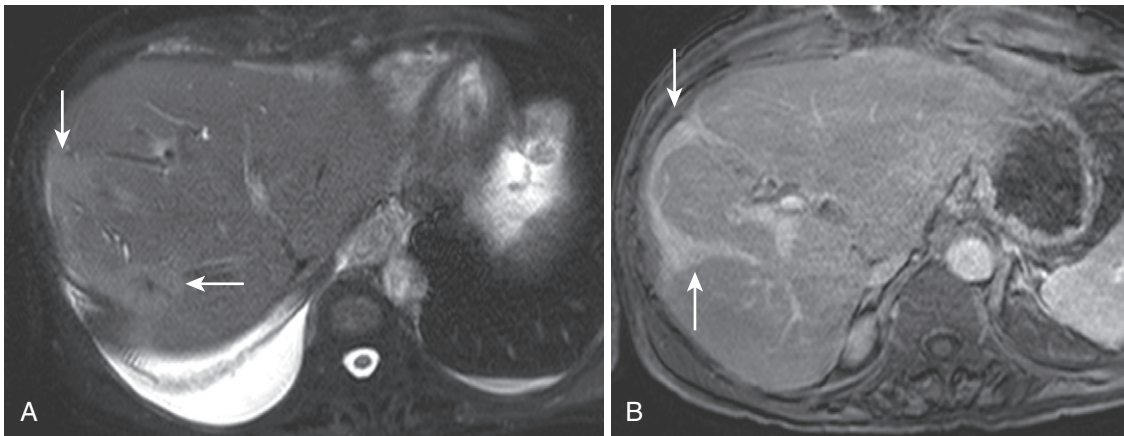


FIGURE 2-73. Confluent fibrosis. Two adjacent, peripheral, wedge-shaped lesions (*arrows*) with capsular retraction exhibit hyperintensity on the T2-weighted, fat-suppressed image (A) and delayed enhancement on the corresponding interstitial phase T1-weighted image (B).

CONFLUENT FIBROSIS

Confluent fibrosis connotes a segmental area of scarring or collagenous tissue forming in response to a hepatic insult, most commonly cirrhosis (although reticular fibrosis predominates in cirrhosis). Confluent fibrosis affects approximately 14% of cirrhotic livers and usually involves the medial and/or anterior segments.⁸⁸ Confluent fibrosis occasions hepatic parenchymal atrophy, and volume loss—reflected by capsular retraction—is a hallmark (Fig. 2-73). Lesion margins are sharp and morphology is usually triangular or pyramidal with the vertex centrally positioned. Signal characteristics differ from fibrosis arising in other body parts, which is globally hypointense. Although dark on T1-weighted images, confluent fibrosis demonstrates moderate hyperintensity on T2-weighted images, probably reflecting a combination of edema and residual vascular spaces.⁸⁹ Gradual, delayed enhancement reflects the presence of

vascular structures and the extracellular dead space of fibrosis. Negative mass effect generally differentiates confluent fibrosis from most other T2 hyperintense lesions, including neoplasms. The enhancement pattern discriminates confluent fibrosis from the hypervascularity of HCCs and other hypervascular masses. Cholangiocarcinoma most closely approximates the appearance of confluent fibrosis, exhibiting similar signal characteristics and enhancement pattern. Lack of upstream ductal dilatation and other signs of mass effect and association with cirrhosis favor confluent fibrosis.

INTRAHEPATIC CHOLESTASIS

Intrahepatic cholestasis is included in the category of parenchymal geographic lesions because of the propensity to manifest signal changes—specifically T1 hyperintensity.⁹⁰ Still, T1 hyperintensity affects a minority of cases of cholestasis and its absence clearly does not exclude it.

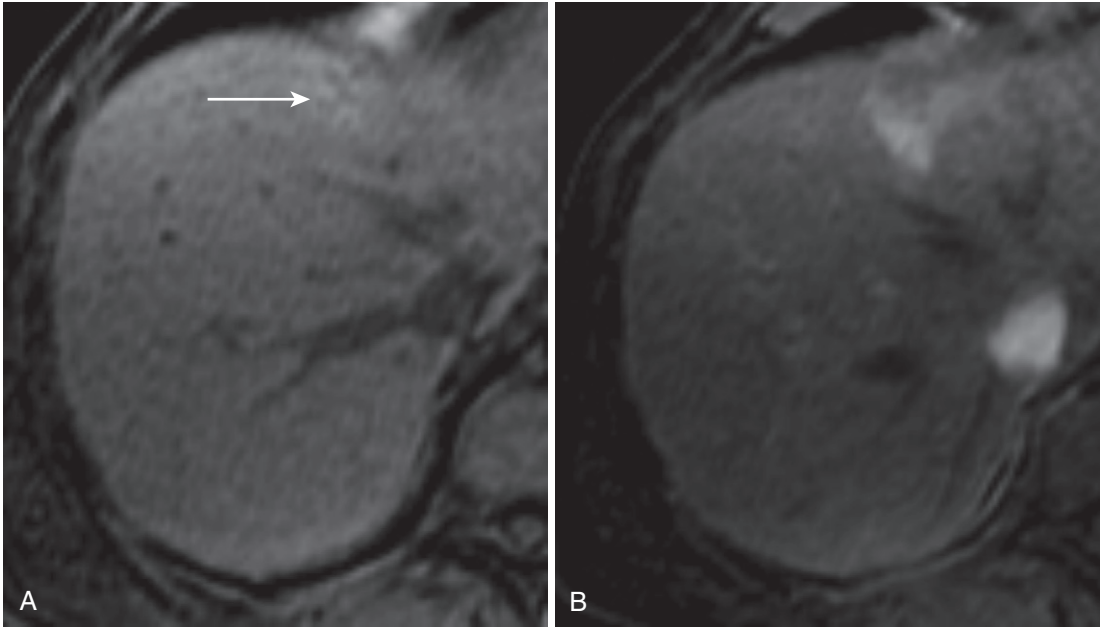


FIGURE 2-74. Intrahepatic cholestasis. **A** and **B**, Note the central tubular hypointensities within the peripheral triangular hyperintensity (*arrow* in **A**) in the T1-weighted fat-suppressed image in the medial segment correspond to dilated biliary radicles.

Absent T2 signal changes and possibly arterial enhancement (possibly due to increased pressures) are additional imaging features. Associated dilatation of the biliary radicles and characteristic T1 hyperintensity increase diagnostic confidence (Fig. 2-74).

DIFFUSE ABNORMALITIES

Diffuse liver abnormalities fall loosely into two broad imaging categories: morphology and signal derangements (Table 2-20). Morphologic conditions include cirrhosis, Budd-Chiari syndrome (BCS), and other lesions, such as biliary cirrhosis and sclerosing cholangitis, which etiologically belong to the biliary classification. Signal abnormalities encompass some lesions already covered and include steatosis, iron deposition (hemochromatosis and hemosiderosis), and rare conditions (beyond the scope of this text) such as glycogen storage disease. A third phantom, or occult, category includes diseases with significant clinical findings often revealing no (obvious or specific) imaging abnormality: acute hepatitis/fulminant liver failure, chronic hepatitis, and autoimmune hepatitis (AIH). Conceptually, the occult disorders present acutely and the disorders involving morphologic and signal derangements represent the effects of longstanding disease and depositional

TABLE 2-20. Diffuse Liver Diseases

<p>Morphology Diseases Cirrhosis (Primary) sclerosing cholangitis (Primary) biliary cirrhosis Budd-Chiari syndrome</p>	<p>Occult Diseases Acute hepatitis Fulminant liver failure Autoimmune hepatitis Liver transplantation</p>
<p>Signal Diseases Steatosis Hemochromatosis Hemosiderosis</p>	

processes, respectively, and lack acute symptomatology.

Occult (General Lack of Signal and Morphologic Changes) Processes

The occult category serves as an auspicious starting point for the discussion of diffuse liver disease because the normal liver appearance is reiterated and the feared endpoint is cirrhosis—the preeminent diffuse liver disease. Most cases of acute hepatitis are attributable to viral hepatitis and the most frequent culprits are hepatitis A through E viruses. Although acute hepatitis manifests histologically with hepatocytic damage and scattered necrosis, the imaging features are nonspecific and often absent. Imaging accomplishes the objective of excluding other potential etiologies that simulate the clinical and

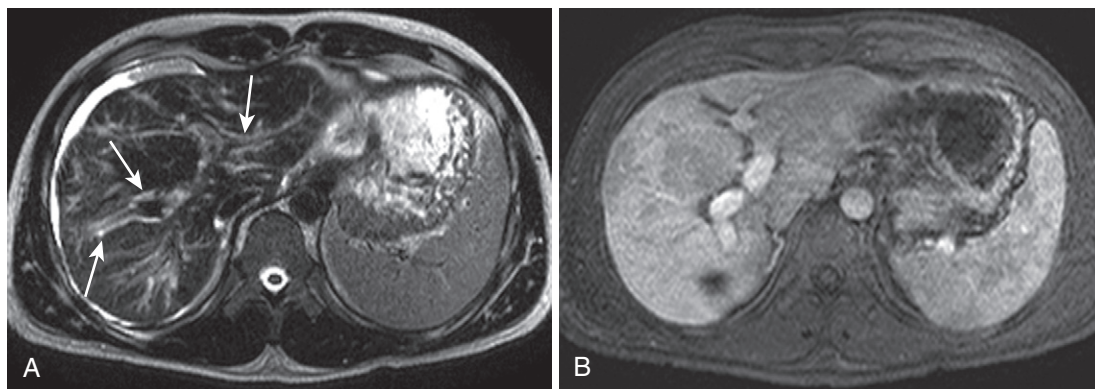


FIGURE 2-75. Hepatic inflammation. Periportal edema (arrows in A) and patchy, multifocal parenchymal hyperintensity on the heavily T2-weighted image (A) corresponding to inflammation and edema in a patient with acute fulminant liver failure demonstrate enhancement on the delayed image (B).

biochemical derangements, such as cholestasis, metastatic disease, and chronic liver disease.⁵¹ Imaging studies generally lack positive findings, and when present, they are usually nonspecific—hepatomegaly, periportal lymphadenopathy, and periportal edema indicate hepatic inflammation. Periportal T2 hyperintensity and delayed, gradual enhancement correspond to edema and inflammatory infiltrate (Fig. 2-75). Extrahepatic secondary inflammatory changes, such as edematous gallbladder wall thickening and ascites, are also nonspecific.

Persistence of hepatic inflammation continuing for at least 6 months qualifies as chronic hepatitis. HBV and HCV are the usual suspects. Periportal lymphadenopathy may or may not persist with ongoing inflammation, which progresses temporally unpredictably to cirrhosis (to be discussed in the section on “Primarily Morphology Diseases,” later).

Many other pathogens and idiopathic phenomena afflict the liver, triggering the acute hepatitis pattern. In addition to viruses, nonviral pathogens (such as toxoplasma and leptospirosis), alcohol and other toxins, medications, metabolic diseases (such as Wilson’s disease), and autoimmune conditions cause acute hepatitis (Table 2-21).

AIH accounts for a small fraction of acute hepatitis cases, but deserves recognition because of the frequent progression to chronic liver disease and cirrhosis and the unique treatment scheme. Although up to 80% of patients initially respond to corticosteroid and immunosuppressive treatment, most relapse and AIH accounts for nearly 20% of cases of chronic liver disease overall. The same nonspecific imaging findings

TABLE 2-21. Etiologies of Acute Hepatic Inflammation

Viral Etiologies	Toxins
Hepatitis A	Amanita toxin (mushrooms)
Hepatitis B	Carbon tetrachloride
Hepatitis C	
Hepatitis D	Drugs
Hepatitis E	Amoxicillin
Ebstein-Barr virus	Minocycline
Cytomegalovirus	Antituberculous agents
Adenovirus	
Bacterial Etiologies	Autoimmune Etiologies
	Systemic lupus erythematosus
Parasitic Etiologies	Metabolic Diseases
Toxoplasma	Wilson’s disease
Q fever	
Leptospira	Other
Rocky Mountain spotted fever	Alcohol
	Pregnancy

apply to AIH, and lymphadenopathy is relatively uncommon. Diagnosis relies on a scoring system based on clinical, serologic, and histologic findings (and not on imaging findings) devised by the International Autoimmune Hepatitis Group.^{91,92} Autoantibodies, an association with other autoimmune diseases (such as thyroiditis, ulcerative colitis, rheumatoid arthritis, and celiac disease), and overlap syndromic pathology (i.e., coexistence with primary biliary cirrhosis [PBC] and PSC) provide the only potential specific or suggestive diagnostic data.

Primarily Signal Processes

FATTY LIVER DISEASE

Fatty liver disease subdivides into two basic categories: steatosis alone and steatosis with necro-inflammatory activity (steatohepatitis), which

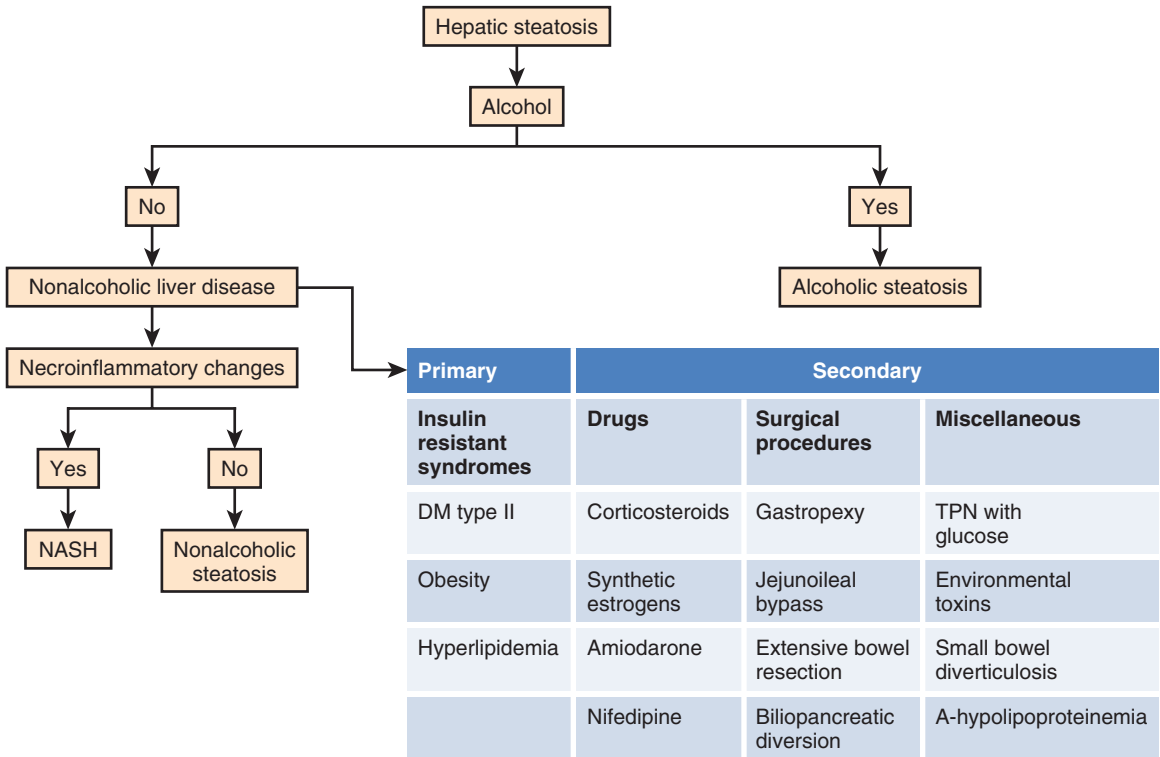


FIGURE 2-76. Classification of steatosis syndromes. DM, diabetes mellitus; NASH, nonalcoholic steatohepatitis; TPN, total parenteral nutrition.

encompasses alcoholic and nonalcoholic steatohepatitis (NASH) (Fig. 2-76). When not associated with alcoholism, steatosis is termed *nonalcoholic fatty liver disease (NAFLD)*, which is an evolving concept afflicting a large segment of the population ($\leq 15\%$), and up to 10% have steatohepatitis.⁹³ NAFLD is the hepatic component of the systemic metabolic syndrome of obesity, type II diabetes mellitus, insulin resistance, dyslipidemia, and hypertension. Predicting the onset and progression of steatohepatitis eludes current diagnostic modalities. Obesity and insulin resistance reportedly promote hepatic inflammation, and fibrogenesis and genetic factors likely play a role. Treatment focuses on minimizing risk factors, such as obesity, and pharmacologic therapy attempting to improve insulin sensitivity, treat dyslipidemia, and protect hepatocytes. Monitoring treatment effects requires accurate assessment of lipid content. Liver biopsy had been considered the gold standard for lipid quantification, but recent work in MR and specifically MR spectroscopy, challenges that assumption.⁹⁴ Calculations based on in- and out-of-phase imaging also yields accurate quantification of intrahepatocellular lipid content. Fat quantification is calculated

with or without using the spleen as a reference standard:

$$\begin{aligned}
 &(\text{liver IP} - \text{liver OP}) / (\text{liver} \times 100) : \text{uncorrected} \\
 &[(\text{liver IP} / \text{spleen IP}) - (\text{liver OP} / \text{spleen OP})] \\
 &\quad / (\text{liver IP} / \text{spleen IP} \times 100) : \text{spleen-corrected}
 \end{aligned}$$

where IP = in-phase and OP = out-of-phase.

Ultimately, the diagnosis of NAFLD/NASH depends on histologic findings and an absence of alcohol intake. MR findings of pronounced signal loss on out-of-phase images—reflecting microscopic fat—corroborates the diagnosis. Development of MR features of cirrhosis confirms chronic inflammation after it is already too late. NASH and alcoholic steatohepatitis present no unique imaging findings, until fibrosis and morphologic hallmarks of cirrhosis set in. Despite the presence of inflammation, reactive lymphadenopathy is typically absent.

IRON DEPOSITIONAL DISEASE

Iron depositional diseases account for the other major category of diffuse hepatic signal abnormalities and consist of two disease entities: (primary) hemochromatosis and hemosiderosis (secondary hemochromatosis) (Fig. 2-77).

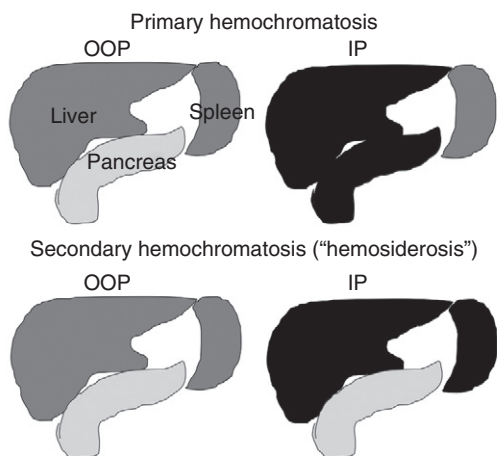


FIGURE 2-77. Hemochromatosis and hemosiderosis. IP, in phase; OOP, out of phase.

Primary hemochromatosis is an autosomally recessive inherited disease of gastrointestinal iron absorption resulting in parenchymal deposition of iron. Hemosiderosis connotes iron overload of the reticuloendothelial system (RES), usually from repeated blood transfusions or ineffective erythropoiesis (i.e., thalassemia major, sideroblastic anemia). **P**arenchymal—or **p**rietary—hemochromatosis involves the **p**ancreas and liver (and myocardium), and **R**ES—or **s**econdary—hemochromatosis involves the **s**pleen and liver (and bone marrow). Toxic parenchymal iron incites fibrosis in primary hemochromatosis whereas RES cells accumulate iron in secondary hemochromatosis, sparing hepatocytes and avoiding fibrogenesis. Consequently, primary hemochromatosis leads to cirrhosis and secondary hemochromatosis usually does not (see Fig. 2-77).

Despite the different histology and cellular deposition of iron in primary and secondary hemochromatosis, the MR appearance of iron deposition in the two diseases is the same. Visualization of iron is a reflection of its strong susceptibility relative to surrounding tissues, which locally distorts the magnetic field resulting in signal loss. Because the 180° refocusing pulses in spin-echo pulse sequences correct for susceptibility, GE sequences are much more sensitive to this phenomenon. Increasing the TE increases the duration of the distortion with proportionally greater signal loss. Therefore, GE sequences with longer TE are more sensitive to the presence of iron. Using the out-of-phase as a baseline, compare the liver signal on the in-phase image, which has twice the TE. If the in-phase

liver signal intensity is significantly less than the out-of-phase liver signal intensity, susceptibility artifact is at work, which is almost always attributable to iron (Figs. 2-78 and 2-79).

Using the same approach, assess the spleen and pancreas for the same signal loss phenomenon. Pancreatic signal loss signifies parenchymal, or primary, hemochromatosis and splenic signal loss indicates RES, or secondary, hemochromatosis (see Figs. 2-78 and 2-79). This diagnostic approach is useful not because iron can be detected only on the in- and out-of-phase images, but because this sequence is obtained whether or not iron is suspected and because the out-of-phase serves as a baseline or reference standard. Difficulty arises when coexistent steatosis decreases hepatic signal on the out-of-phase images. In that case, obtaining a longer series of in- and out-of-phase images reveals oscillating signal between in- and out-of-phase images with a pronounced downward trend due to the susceptibility of iron. Exaggerated signal loss on the standard SSFSE or FSE T2-weighted images is a more subjective means of detecting iron, which is not subject to the presence of lipid.

Because of the deleterious effects of parenchymal iron, chelation therapy is administered to hopefully stave off the onset of cirrhosis. Assessment of response to therapy involves T2 (spin-echo) and T2*(GE) mapping, which involves ROI measurement on multiple sets of T2-weighted and T2*-weighted images. In fact, an on-line calculation algorithm generated by the University of Rennes provides a useful, accessible calculation method (<http://www.radio.univ-rennes1.fr/Sources/EN/Hemo.html>). ROI measurements and adherence to specific protocol parameters are required (Table 2-22).

No realistic differential diagnosis is worth considering in the case of diffuse hepatic susceptibility or signal loss. Punctate or focal signal loss signifies calcified granulomas, siderotic nodules in the liver, or Gamna-Gandy bodies in the spleen. Segmental signal loss on T1-weighted images without a TE-dependent increase characterizes confluent fibrosis, which also demonstrates T2 hyperintensity (as opposed to relative T2 hypointensity in iron deposition).

Primarily Morphology Diseases

Broadly speaking, morphologic derangements of the liver parenchyma signify chronic or advanced disease and define the endpoint of

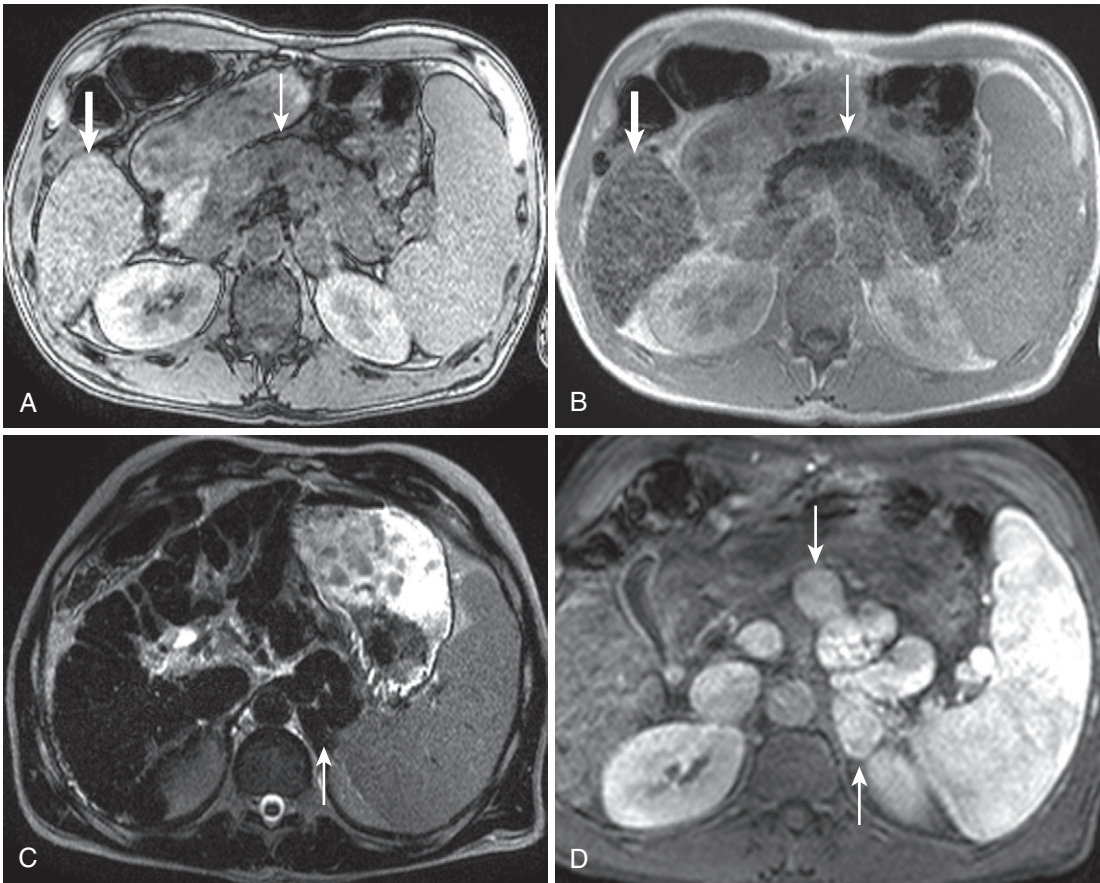


FIGURE 2-78. Primary hemochromatosis. The pancreas (*thin arrow* in A and B) and liver (*thick arrow* in A and B) drop in signal between the out-of-phase (A) and the in-phase (B) images, reflecting susceptibility artifact. C, The heavily T2-weighted image shows the characteristic nodular atrophy-hypertrophy pattern of cirrhosis (*arrow*). D, Note the tubular signal voids (*arrows*), which enhance on the delayed postcontrast image and correspond to massively enlarged portosystemic splenorenal collaterals (due to portal hypertension).

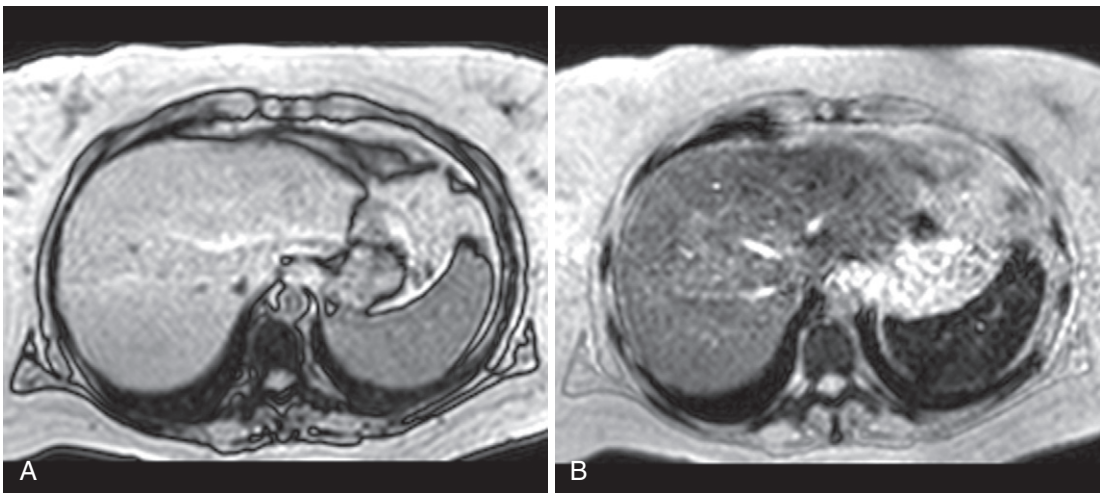


FIGURE 2-79. Secondary hemochromatosis (hemosiderosis). Gradient-echo images with short TE (A, -1 msec) and long TE (B, -7 msec) exemplify iron deposited in the liver and spleen with susceptibility artifact more severely affecting the spleen.

TABLE 2-22. Liver Iron Quantification Instructions

T2 Mapping ⇒ GRASE

T2* Mapping ⇒ multi-echo GRE

Use dual GRE (in-/out-of-phase) to assess for superimposed steatosis

Sample Template Dictation

Exam Type: «Order Procedure Description»

Exam Date and Time: «Order Observation End Time»

Indication: «Clinical information» [Additional available history...]

Comparison: [None].

Impression:

- [No evidence of] [mild] [moderate] [severe] [secondary] iron overload in the [heart] [with an estimated cardiac iron concentration] [of [] mg/g]. [Normal left ventricular wall motion].
- [No evidence of] [mild] [moderate] [severe] [secondary] iron overload in the [liver], [spleen] & [bone marrow]. The estimated liver iron concentration is [] mg/g. [Findings likely represent iron overload consistent with the patient's history of] [transfusional siderosis] [thalassemia] [primary hemochromatosis].
- [No evidence of iron overload] [iron overload] involving the pancreas.

Procedure:

Non contrast MRI of the abdomen was performed on a [1.0/1.5/3.0] Tesla [open-bore] scanner. Image quality is [good] [satisfactory] [degraded by motion].

Liver Iron Quantification:

- A total of 16 breathhold multiecho gradient echo images were obtained at multiple TE time points to calculate the T2* value in the liver. From this value, an iron concentration was generated based on data in an article from the European Heart Journal, December 2001, pages 2171–2179. An ROI was placed in the liver on 2 separate series. The calculated liver T2* on 2 separate measurements is [] and []. This corresponds to a liver iron concentration of [] and [] mg/g respectively.
- A total of 5 GRASE images were obtained to calculate the T2 value in the liver. From this value, an iron concentration was generated based on data in an article from Blood Journal, January 2005, pages 855–861. An ROI was placed in the liver on two separate series. The calculated liver T2 on 2 separate measurements is [] and []. This corresponds to a liver iron concentration of [] and [] mg/g respectively.
- The liver iron concentration was estimated at [] (± 50) $\mu\text{mol/g}$ (normal < 36 $\mu\text{mol/g}$) using a calculator (<http://www.radio.univ-rennes1.fr/Sources/EN/HemoCalc15.html>). This calculation takes into account the MRI signal intensity in three separate regions of interest in the liver measuring [], [], and [] and two separate regions of interest in the paraspinal muscles measuring [] and []. These values were obtained with GRE images (TE 4.6 msec/Flip angle 20 degrees), using the built-in body coil to ensure a homogeneous signal profile.

Cardiac Iron Quantification:

- Cardiac gated, short axis multiecho gradient echo images were obtained for cardiac iron mapping. From this, an ROI was placed in the interventricular septum and a T2* value of the myocardium was obtained to calculate a cardiac iron concentration based on data in an article from the European Heart Journal, December 2001, pages 2171–2179.

Findings:

Liver: There is [no] fatty infiltration. No liver mass is demonstrated.

Spleen: [Within normal limits]. [No evidence of] [mild] [moderate] [severe] [secondary] iron overload.

Heart: Cine cardiac imaging demonstrates normal heart size and cardiac function. [No pericardial effusion]. The calculated T2* in the interventricular septum is [].

Pancreas: [The pancreas and pancreatic duct are normal]. [The pancreatic parenchyma has normal signal intensity]. [No evidence of iron overload]. [The main pancreatic duct is normal].

There is [no] ascites. Abdominal Vessels: [The superior mesenteric vein, portal vein, splenic vein, and hepatic veins are grossly patent. There is standard hepatic arterial anatomy. The proximal celiac artery, superior mesenteric artery, and inferior mesenteric artery are patent.]

Biliary system: [No biliary ductal dilatation]. Gallbladder is [within normal limits].

Adrenal glands: [Within normal limits].

Kidneys: [Within normal limits].

Lymph nodes: [No lymphadenopathy].

Bones: [Within normal limits]. [No evidence of iron overload].

Lung bases: [Within normal limits].

GRASE, gradient and spin echo; GRE, gradient-recalled echo; MRI, magnetic resonance imaging; ROI, region of interest; TE, time to excitation.

many of the previously discussed disorders. Whereas cirrhosis dominates this category, different patterns of cirrhosis typify different disease processes. For example, sclerosing cholangitis characteristically exhibits a macronodular cirrhotic pattern, whereas many other etiologies demonstrate a micronodular pattern.

BCS exhibits a protean appearance depending on the temporal phase, ultimately demonstrating morphologic abnormalities in the chronic phase. LT represents a morphologic derangement with reference to the patient's native liver and is relegated to this category by default (see Table 2-20).

CIRRHOSIS

Cirrhosis is the common endpoint of chronic liver diseases undergoing parenchymal necrosis and fibrosis with ongoing regeneration. Whereas parenchymal injury induces scarring or fibrosis, the unique ability of the liver to regenerate manifests in the form of intervening islands—or nodules—of hepatocytes. The macroscopic result is a patchwork quilt of bridging bands of fibrosis surrounding regenerative nodules. In addition to nodularity, global morphologic features usually develop as a function of differences in portal venous circulation. A sectorial atrophy-hypertrophy pattern reflects relative portal venous supply. Compromised portal venous flow starves the affected parenchyma resulting in atrophy, with hypertrophy of the tissue enjoying more robust portal flow (Fig. 2-80). Consequently, the right lobe atrophies owing to the long, tenuous intrahepatic course of the right portal vein through a scarred, cirrhotic liver compromising portal blood flow. Although the protective course of the left portal vein in the falciform ligament explains the lateral segmental hypertrophy, factors uniquely affecting the medial segment counteract this protective phenomenon, resulting in medial segmental atrophy. The helical portal venous flow pattern directs flow away from the medial segment and concurrent blood flow from the gastric, cystic, peribiliary, and capsular veins throttle portal venous inflow. The short intrahepatic course of the portal venous supply to the caudate ensures

adequate portal flow, typically reflected by caudate hypertrophy.

Multiple imaging signs announcing these morphologic derangements have been described (Fig. 2-81). Enlargement of the hilar periportal space (between the anterior wall of the right portal vein and the posterior edge of the medial segment of the liver) beyond 10 mm is observed with atrophy of the medial segment (see Fig. 2-80).^{95,96} The “expanded gallbladder fossa” sign reflects a combination of trophic phenomena: (1) medial segment atrophy, (2) caudate

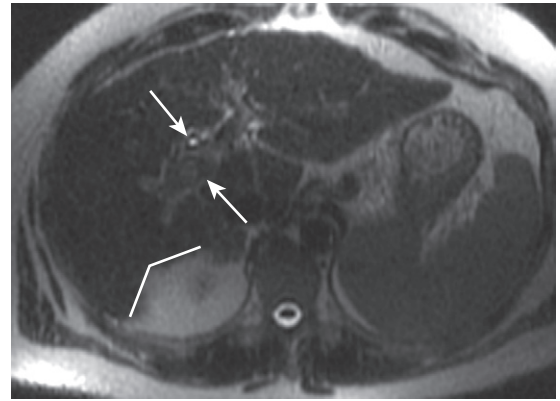


FIGURE 2-80. Atrophy-hypertrophy pattern in cirrhosis. The axial heavily T2-weighted image of a cirrhotic liver shows the typical atrophy-hypertrophy pattern resulting in the hepatic notch sign (*angled lines*) due to right lobe atrophy and caudate hypertrophy and prominence of the periportal space (*arrows*) due to medial segment atrophy. Note the nodularity and lateral segmental hypertrophy.

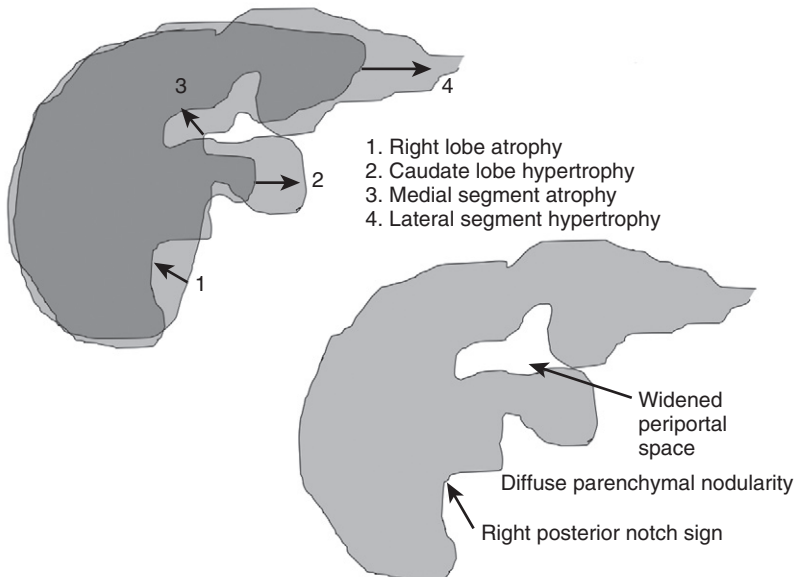


FIGURE 2-81. Imaging signs of cirrhosis.

hypertrophy, (3) right lobe atrophy, and (4) lateral segment hypertrophy.⁹⁷ The “right posterior notch” sign describes the appearance of the posterior margin of the liver on axial images.^{98,99} Concurrent right lobe atrophy and caudate hypertrophy invert the normal smoothly convex posterior liver margin, eventually forming an angular concave margin—the “right posterior notch sign.”

A measurement scheme has been devised to detect early cirrhosis before these signs develop. The (modified) caudate–right lobe ratio reflects the hypertrophy–atrophy pattern by comparing the size of the caudate lobe—defined laterally by the lateral wall of the right portal vein and medially by the medial extent of the caudate—with the size of the right lobe—defined medially by the right portal vein and laterally by the capsular surface (Fig. 2-82). A ratio of greater than 0.90 predicts cirrhosis with a sensitivity, specificity, and accuracy of 72%, 77% and 74%, respectively.¹⁰⁰

Along with the global morphologic changes, textural changes develop. Parenchymal

regeneration manifests with nodules of regenerating parenchyma with surrounding fibrosis representing the byproduct of hepatotoxic effects. MR images portray this as parenchymal nodularity with interdigitating fibrotic bands (Fig. 2-83).

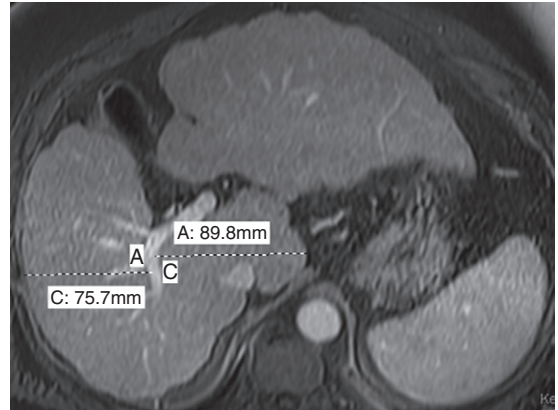


FIGURE 2-82. Modified caudate–to–right lobe ratio. The axial enhanced image of a nodular, cirrhotic liver with the characteristic atrophy–hypertrophy pattern exemplifies the elevated modified caudate–to–right lobe ratio.

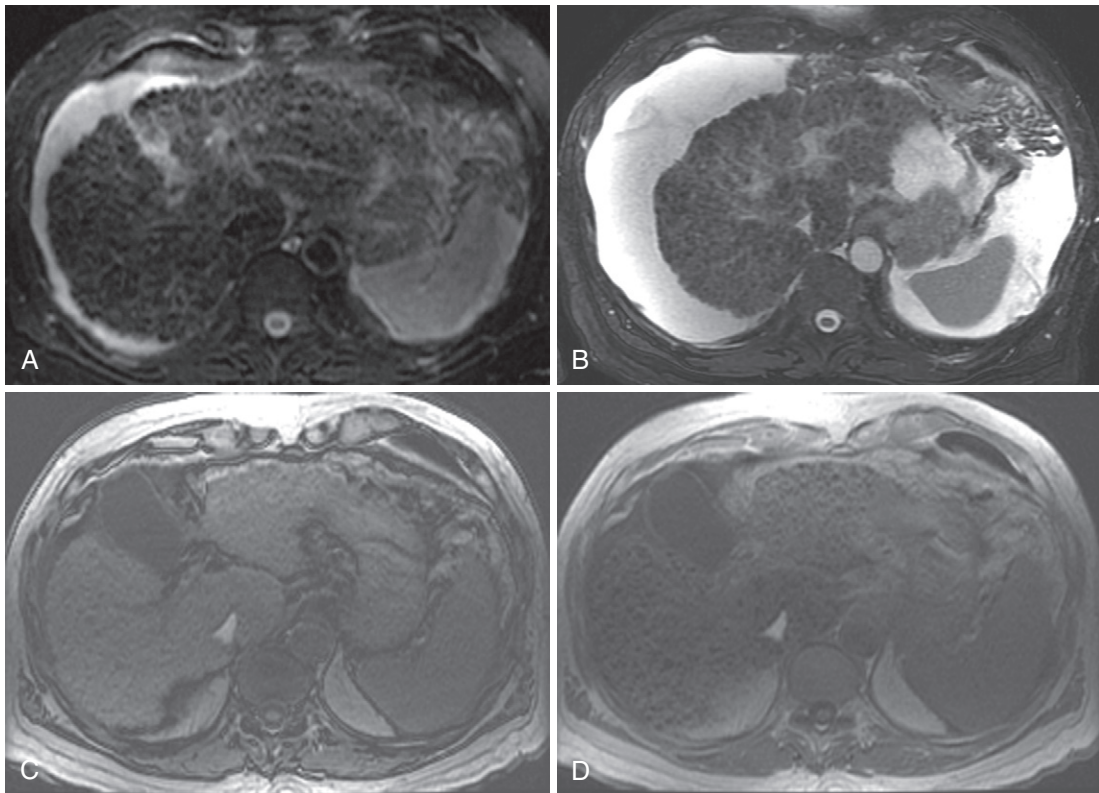


FIGURE 2-83. Parenchymal nodularity with bridging bands of fibrosis. The axial moderately T2-weighted fat-suppressed images at baseline (A) and follow-up (B) portray advanced cirrhosis reflected by diffuse nodularity with intervening reticular hyperintensity corresponding to fibrosis with worsening ascites. Comparing the out-of-phase (C) with the in-phase (D) images reveals susceptibility artifact arising from the parenchymal (siderotic) nodules due to their iron content.

Nodular parenchymal signal intensity and enhancement do not differ from noncirrhotic parenchyma. Reticular fibrosis appearing as bridging bands of fibrosis between islands of nodular parenchyma is the more common manifestation of fibrosis; confluent fibrosis occurs less frequently and often coexists with reticular fibrosis (see Fig. 2-73). As previously discussed in reference to confluent fibrosis, signal characteristics typically reflect edema and vascular spaces with T2 hyperintensity (and T1 hypointensity). Delayed enhancement is also characteristic. Therefore, moderately T2-weighted and delayed images most clearly depict fibrosis. Novel methods are being tested to increase the sensitivity of MR for fibrosis, including diffusion-weighted imaging. Increased connective tissue (fibrosis), distorted sinusoids, decreased blood flow, and possibly other factors restrict diffusion in the cirrhotic liver, reflected by diminished apparent diffusion coefficient (ADC) values compared with normal liver.¹⁰¹ Quantifying fibrosis as a marker for disease severity, traditionally achieved with liver biopsy, influences treatment (i.e., antiviral therapy for HBV and HCV). Although potentially useful, diffusion-weighted imaging has not been established for

routine use in this capacity and morphologic descriptors are the mainstay.

Assessing the degree of cirrhosis with attention to the risk of developing HCC and other complications—such as portal venous occlusion and portal hypertension with collaterals—assumes prime importance in cirrhosis surveillance. As an aside, remember that cirrhosis is not a prerequisite for the development of HCC in chronic HBV infection (unlike HCV). In addition to assessing the degree of cirrhosis, evaluate the portal circulation to ensure patency for transplant technical considerations. Whereas occlusion of the portal vein and/or SMV historically precluded transplantation, innovative technical methods—such as thrombectomy or interposition grafting—must be employed to circumvent the compromised circulation. Note the presence of portosystemic collaterals signifying portal hypertension with attendant risks, such as upper gastrointestinal bleeding. The common portosystemic collateral pathways include (1) paraumbilical vein (contributing to the caput medusa), (2) left gastric vein feeding submucosal esophageal and paraesophageal varices, (3) splenorenal shunting, (4) retroperitoneal varices, and (5) mesorectal collaterals (Figs. 2-84

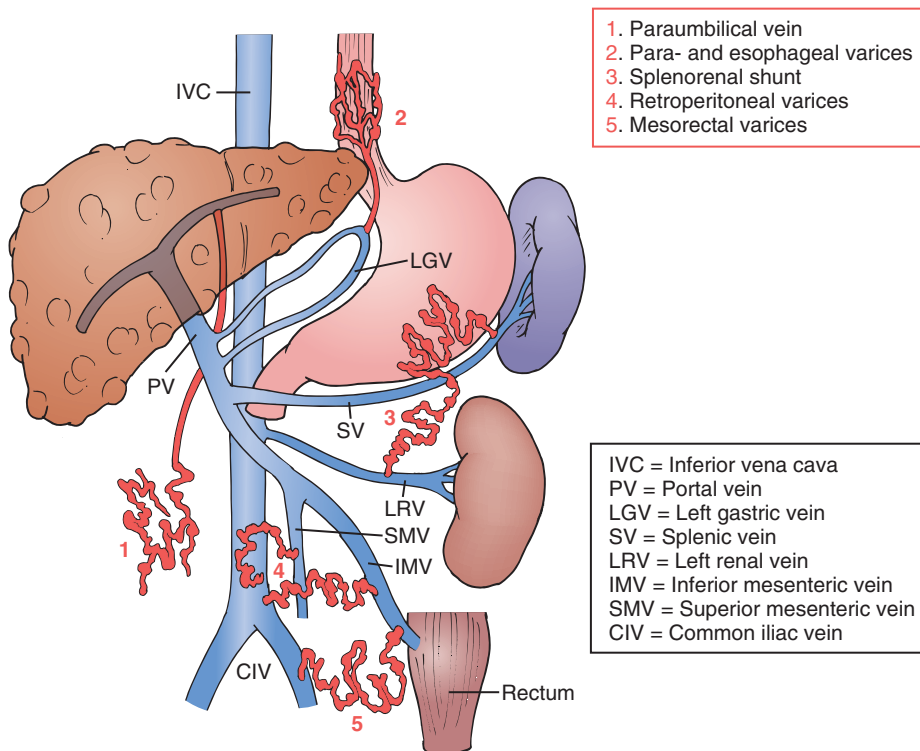


FIGURE 2-84. Portosystemic collateral pathways.

and 2-85).¹⁰² Other signs of portal hypertension include splenomegaly, ascites, and enlargement of the cisterna chyli (>6 mm) (Fig. 2-86).¹⁰³ Ascites grading ranges from mesenteric edema, constituting the *forme fruste* of ascites, to severe when fluid volume exceeds visceral volume. The cisterna chyli courses cephalad along the right side of the aorta appearing as a mildly tortuous, fluid-filled structure exhibiting delayed enhancement (usually enhancing a few minutes after gadolinium administration). Recent work suggests that a diameter greater than 6 mm predicts uncompensated cirrhosis.

Few cirrhotic etiologies demonstrate specific findings. Most cases of cirrhosis develop from chronic hepatitis (HBV and HCV) and alcoholic liver disease. Among the myriad other etiologies of cirrhosis, the most commonly encountered include PSC, primary and secondary biliary cirrhosis, hemochromatosis, AIH, and vascular etiologies, such as BCS (Table 2-23). Few specific

TABLE 2-23. Etiologies of Cirrhosis

Most Common Causes of Cirrhosis (in the United States)

Hepatitis C (26%)
 Alcoholic liver disease (21%)
 Hepatitis C plus alcoholic liver disease (15%)
 Cryptogenic causes (18%)
 Hepatitis B, which may be coincident with hepatitis D (15%)
 Miscellaneous (5%)

Miscellaneous Causes of Chronic Liver Disease and Cirrhosis

Autoimmune hepatitis
 Primary biliary cirrhosis
 Secondary biliary cirrhosis (associated with chronic extrahepatic bile duct obstruction)
 Primary sclerosing cholangitis
 Hemochromatosis
 Wilson's disease
 Alpha₁-antitrypsin deficiency
 Granulomatous disease (e.g., sarcoidosis)
 Type IV glycogen storage disease
 Drug-induced liver disease (e.g., methotrexate, alpha methyl-dopa, amiodarone)
 Venous outflow obstruction (e.g., Budd-Chiari syndrome, veno-occlusive disease)
 Chronic right-sided heart failure
 Tricuspid regurgitation

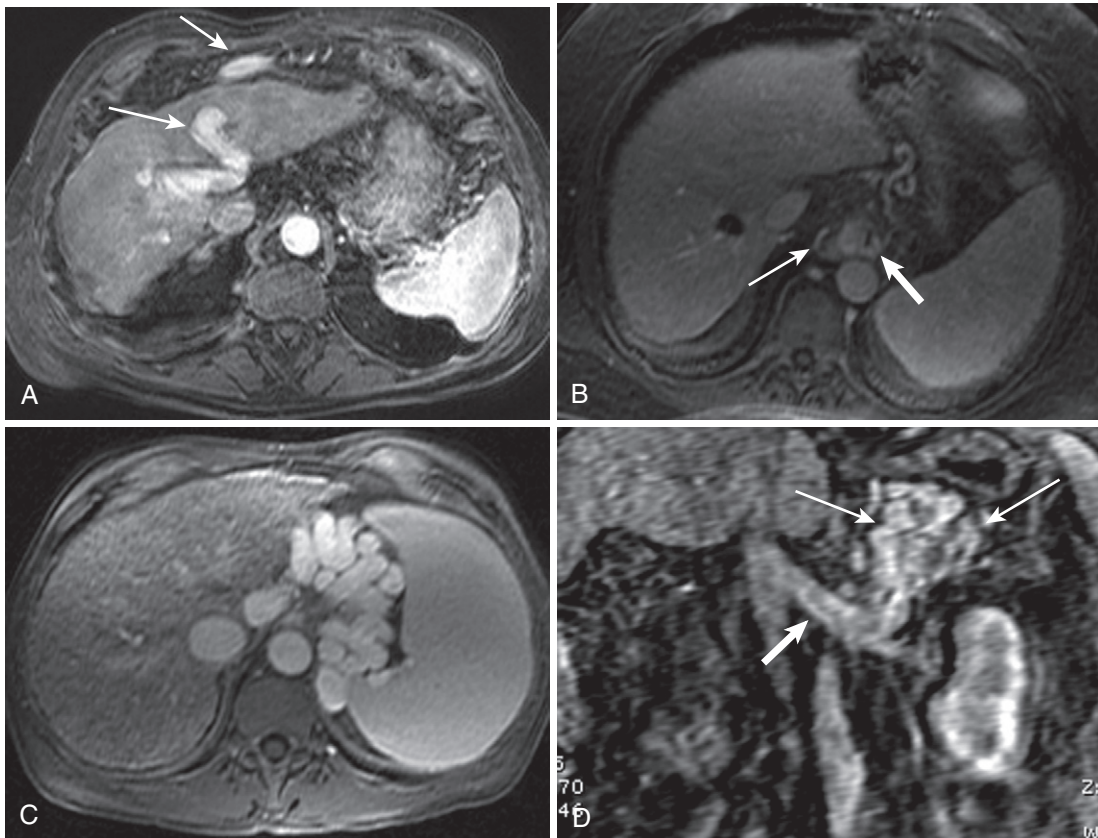


FIGURE 2-85. Portosystemic collateral vessels. A, A large paraumbilical collateral vessel (arrows) courses through the left lobe in the region of the falciform ligament. B, Parasophageal varices (thin arrow) and submucosal esophageal varices (thick arrow) in a different patient. C, Markedly enlarged splenorenal varices in the periportal region eventually channel caudally and drain into the left renal vein (not shown). D, A coronal image in a different patient shows clustered splenorenal varices (thin arrows) draining into the left renal vein (thick arrow).

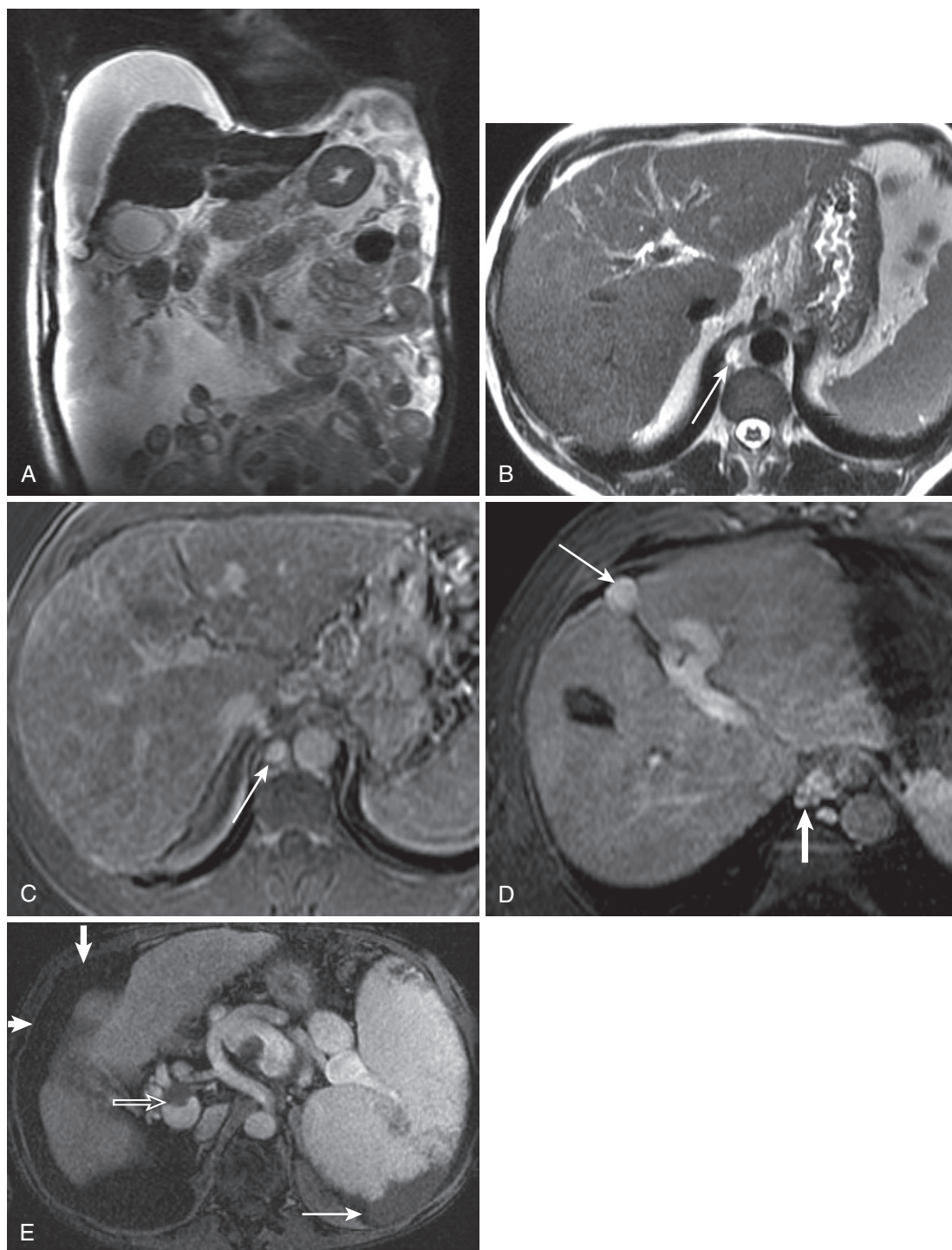


FIGURE 2-86. Signs of portal hypertension. **A**, Coronal heavily T2-weighted image shows the extent of marked generalized ascites and a cirrhotic liver. The axial T2-weighted image (**B**) at the level of the aortic hiatus shows a hyperintense fluid-filled structure (*arrow* in **B** and **C**), which enhances on the delayed image (**C**), characteristic of a lymphatic structure and in the expected location of the cisterna chyli—in this case, enlarged due to portal hypertension. **D**, Delayed postcontrast image in a different patient with portal hypertension reveals portosystemic collateral channels, including a large paraumbilical portosystemic collateral vessel (*thin arrow*) and paraesophageal varices (*thick arrow*). **E**, A different patient with cirrhosis exemplifies features of portal hypertension—splenomegaly with a splenic infarct (*thin arrow*), ascites (*thick arrows*), and nonocclusive portal venous thrombus (*open arrow*).

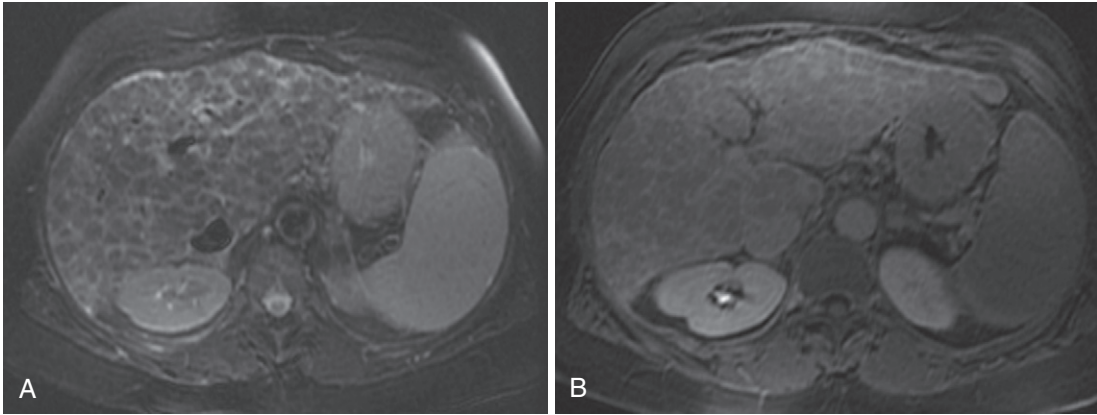


FIGURE 2-87. Cirrhosis in primary biliary cirrhosis (PBC). Parenchymal macronodularity with interdigitating reticular fibrosis characterizes PBC.

features distinguish these disorders, with some exceptions. Chronic viral hepatitis and alcoholic liver disease present no specific features and are indistinguishable, accounting for the vast majority of cases. Many other etiologies also lack specific features, but a few characteristic findings potentially identify some etiologies.

AUTOIMMUNE HEPATITIS

AIH is often a diagnosis of exclusion characterized by chronic hepatocellular inflammation and necrosis. AIH classically afflicts young women and frequently follows the typical cirrhotic pattern—distinguished by a frequent coexistence with other autoimmune disease, such as inflammatory bowel disease, PBC and PSC among others. A composite score incorporating clinical, serologic, and histologic findings predicts the probability of the diagnosis.⁹¹ Note the lack of imaging findings included in the diagnostic algorithm.

PRIMARY BILIARY CIRRHOSIS

Although PBC is a chronic cholestatic liver disease targeting the small and medium-sized bile ducts, the primary imaging manifestations are parenchymal. Demographic features are similar to AIH and other autoimmune diseases—such as autoimmune thyroiditis, CREST (calcinosis cutis, Raynaud's phenomenon, esophageal dysfunction, sclerodactyly, and telangiectasia) syndrome, and sicca syndrome—frequently coexist. The diagnosis relies on combination of clinical, biochemical, histologic, and serologic features—antimitochondrial antibodies are considered the hallmark of the disease. PBC often progresses to chronic disease frequently

resulting in nonspecific cirrhosis. Occasionally, relative macronodularity with reticulated fibrosis develops (Fig. 2-87). Despite the biliary nature of the disease, biliary findings are absent. During the course of inflammation, two imaging features occasionally suggest the diagnosis—prominent periportal lymph nodes¹⁰⁴ and peripheral, periportal hypointensities (“the periportal halo sign,” referring to 5- to 10-mm hypointensities encircling portal triads) (Fig. 2-88).¹⁰⁵

PRIMARY SCLEROSING CHOLANGITIS

PSC is another inflammatory chronic cholestatic disease that affects large and extrahepatic ducts. Unlike its inflammatory counterparts, specific imaging features confirm the diagnosis. The diagnostic criteria include (1) typical (MR or endoscopic) cholangiographic abnormalities; (2) suggestive clinical, biochemical, and histologic findings; and (3) the absence of secondary causes of sclerosing cholangitis.¹⁰⁶ Although also associated with other inflammatory diseases—most notably inflammatory bowel disease—the demographics differ in that young males are most commonly affected and 71% are associated with inflammatory bowel disease.

The imaging appearance evolves over time. In the early phase, relatively circumferential short segmental strictures usually located at biliary ductal bifurcations alternate with mildly dilated segments yielding the “beaded” appearance characteristic of PSC (Fig. 2-89). Progressive biliary ductal inflammation leads to the characteristic imaging appearance with multifocal strictures, segmental ectasia, ductal wall thickening and enhancement, and irregular ductal

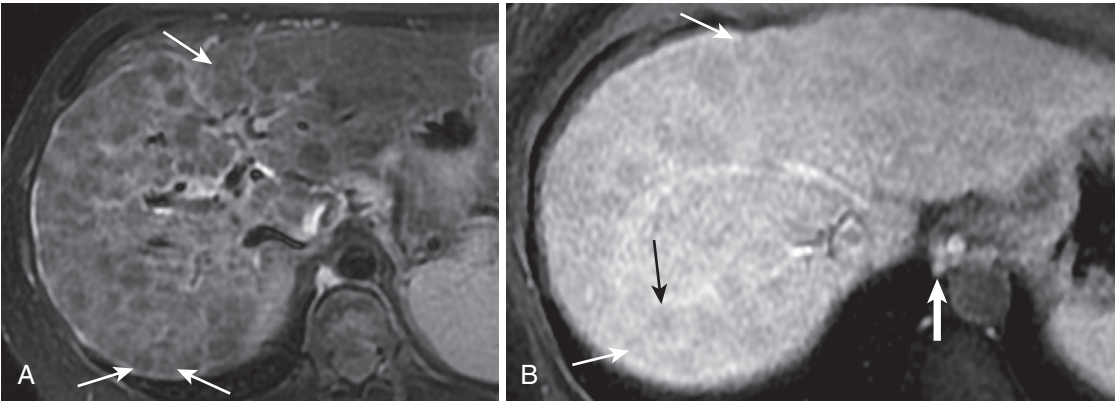


FIGURE 2-88. Periportal halo sign in PBC. Numerous hypointensities (*thin arrows* in A and B) surround central portal hyperintensities on the axial moderately T2-weighted fat-suppressed image (A) and enhanced image (B). Note the paraesophageal varices (*thick arrow* in B).

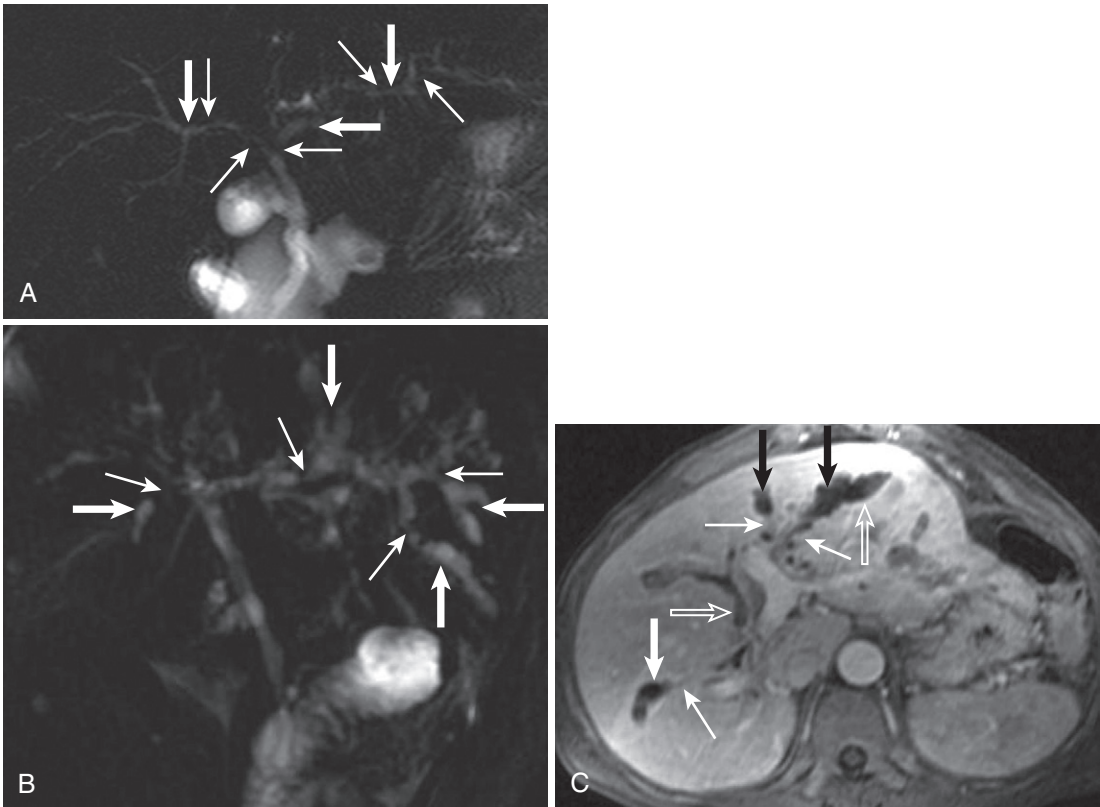


FIGURE 2-89. Beaded ductal appearance in primary sclerosing cholangitis (PSC). A, Mild changes are apparent on the 2D MRCP radial slab image with mild stricturing (*thin arrows*) and upstream ectasia (*thick arrows*). Another 2D MRCP image (B) showcases more advanced biliary stricturing (*thin arrows* in B and C) and ectasia (*thick arrows* in B and C), also shown on the corresponding enhanced image (C), revealing direct signs of inflammation in the form of periductal enhancement (*open arrows* in C).

beading.¹⁰⁷ Peripheral ducts are eventually obliterated, resulting in the “pruned tree” appearance, and biliary branching becomes more obtusely angulated. Inflammation and fibrosis presumably restricts upstream dilatation,

accounting for relative underdistention proximal to PSC strictures.

Idiosyncratic parenchymal changes also typify PSC. Relatively early peripheral ductal involvement ultimately generates a peripheral

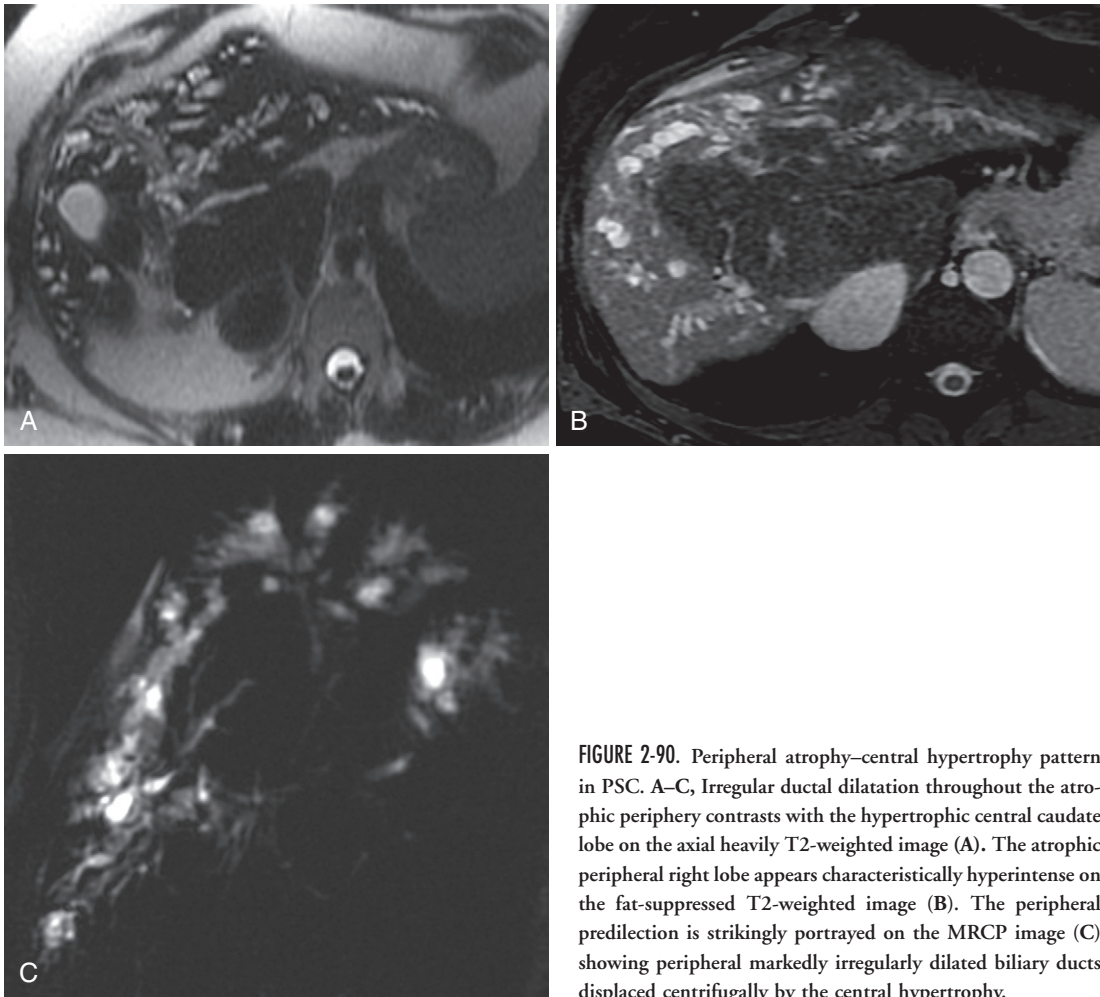


FIGURE 2-90. Peripheral atrophy–central hypertrophy pattern in PSC. A–C, Irregular ductal dilatation throughout the atrophic periphery contrasts with the hypertrophic central caudate lobe on the axial heavily T2-weighted image (A). The atrophic peripheral right lobe appears characteristically hyperintense on the fat-suppressed T2-weighted image (B). The peripheral predilection is strikingly portrayed on the MRCP image (C) showing peripheral markedly irregularly dilated biliary ducts displaced centrifugally by the central hypertrophy.

atrophy–central hypertrophy pattern (Fig. 2-90). Macronodular cirrhosis (nodules measuring at least 3 cm)—with central nodular predominance—commonly ensues, in contradistinction to most other etiologies, which more typically develop micronodular cirrhosis.¹⁰⁸

Although PSC findings are described as classic and diagnostic, a differential diagnosis exists. Secondary causes of sclerosing cholangitis include drug side effects, recurrent pyogenic cholangitis, AIDS, cholangiopathy, ischemic cholangiopathy, and posttraumatic/postsurgical bile duct injury. Clinical history differentiates these etiologies from PSC. Cirrhosis due to other etiologies deforms the biliary ducts, simulating the appearance of PSC on MRCP and ERCP images, but generally lacks the suggestive clinical findings, macronodularity and the classic peripheral atrophy–central hypertrophy pattern of PSC. Tumors invading the biliary tree, particularly cholangiocarcinoma, occasionally mimic

PSC, although rarely present with the diffuse involvement seen in PSC. However, the rare segmental form of PSC simulates the periductal infiltrating form of cholangiocarcinoma. Signs of an underlying mass (e.g., enhancing tissue, mass effect), bile wall thickening greater than 4 mm, and relatively greater progressive upstream dilatation predict cholangiocarcinoma. Remember that cholangiocarcinoma complicates PSC with a frequency of 13%. The other feared complication of PSC is HCC, with an incidence rate of 1.5%/yr.¹⁰⁹

BUDD-CHIARI SYNDROME

BCS is the final disease in the diffuse morphologic category. The morphologic derangement develops as a consequence of hepatic venous occlusion. Occlusion at any point from the small hepatic veins through the suprahepatic IVC leads to centrilobular congestion, sinusoidal dilatation, and ultimately, hepatocellular

necrosis and fibrosis. Not surprisingly, underlying thrombotic diatheses are usually blamed for the development of this disease, although no etiology is discovered in one third of patients. Common causative etiologies include hematologic disorders (e.g., polycythemia vera, myeloproliferative disorders, essential thrombocytosis, antiphospholipid antibody syndrome), inherited thrombotic diseases (e.g., protein C deficiency, protein S deficiency, Factor V Leiden deficiency, antithrombin III deficiency), pregnancy, oral contraceptives, chronic infections and inflammatory conditions, malignancies (especially HCC and renal cell carcinoma), and intravascular webs (Table 2-24).¹¹⁰

Untreated BCS usually progresses and medical therapy (anticoagulation, antithrombotic therapy, and management of ascites), intravascular intervention (angioplasty or TIPS), and surgical treatments (vascular decompression and transplant) become necessary to preserve life; medical therapy alone incurs an 80% to 85% 2-year mortality rate. Four clinical syndromes are observed: (1) acute liver disease, (2) subacute liver disease, (3) fulminant liver disease, and (4) liver failure. Portal hypertension frequently complicates the disease process.

MRI features depend on the temporal phase of the process. The direct finding of hepatic venous thrombosis becomes less prevalent with chronicity and is more likely visualized in the acute or subacute setting, whereas intrahepatic and extrahepatic collaterals are more conspicuous in the chronic phase (Fig. 2-91). Because dense contrast enhancement of (hepatic) veins cannot be directly timed and contrast is invariably diluted at the time of venous enhancement, consider using double-dose gadolinium to evaluate the hepatic veins and IVC in potential cases of BCS. Also incorporate steady-state images, which possess intrinsic fluid-to-solid tissue contrast and do not rely on time-of-flight or T1 shortening from gadolinium to display vascular anatomy. “Comma-shaped” intrahepatic collateral veins are reportedly specific for BCS. Sonographically demonstrated large caudate veins (>3 mm) in the appropriate clinical setting strongly suggest the diagnosis of BCS.¹¹¹ Narrowing or obliteration of the hepatic veins and/or IVC develops over time. Acute parenchymal changes reflect the differential venous drainage between the peripheral and the central (caudate lobe, primarily) portions of the liver. Peripheral T2 hyperintensity and diminished enhancement

TABLE 2-24. Etiologies of Budd-Chiari Syndrome

Hematologic Disorders
Polycythemia rubra vera
Paroxysmal nocturnal hemoglobinuria
Unspecified myeloproliferative disorder
Antiphospholipid antibody syndrome
Essential thrombocytosis
Inherited Thrombotic Diathesis
Protein C deficiency
Protein S deficiency
Antithrombin III deficiency
Factor V Leiden deficiency
Pregnancy and Postpartum
Membranous Webs
Oral Contraceptives
Chronic Infections
Hydatid cysts
Aspergillosis
Amebic abscess
Syphilis
Tuberculosis
Chronic Inflammatory Diseases
Behçet's disease
Inflammatory bowel disease
Sarcoidosis
Systemic lupus erythematosus
Sjögren's syndrome
Mixed connective-tissue disease
Tumors
Hepatocellular carcinoma
Renal cell carcinoma
Leiomyosarcoma
Adrenal carcinoma
Wilms' tumor
Right atrial myxoma
Miscellaneous
Alpha ₁ -antitrypsin deficiency
Trauma
Dacarbazine
Urethane
Idiopathic

reflect the edema and increased tissue pressure, respectively (see Figs. 2-91 and 2-92). The protected caudate lobe enlarges and demonstrates relatively increased enhancement. Centripetal signal changes fade with time, and regenerative nodules begin to proliferate.

Regenerative nodules in BCS represent regions of the liver with relatively preserved blood flow. BCS nodules range in size from 0.5 to 4 cm and are hyperintense on T1-weighted images because of the hypointensity of the edematous surrounding tissue and/or increased

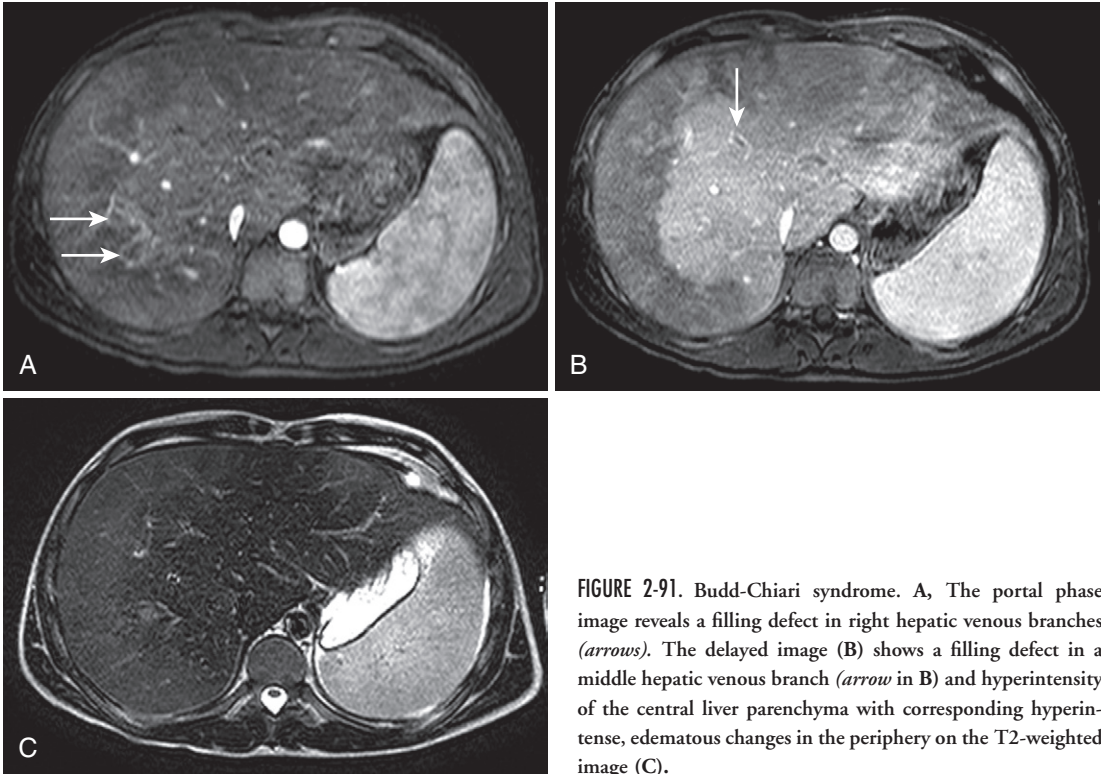


FIGURE 2-91. Budd-Chiari syndrome. **A**, The portal phase image reveals a filling defect in right hepatic venous branches (*arrows*). The delayed image (**B**) shows a filling defect in a middle hepatic venous branch (*arrow* in **B**) and hyperintensity of the central liver parenchyma with corresponding hyperintense, edematous changes in the periphery on the T2-weighted image (**C**).

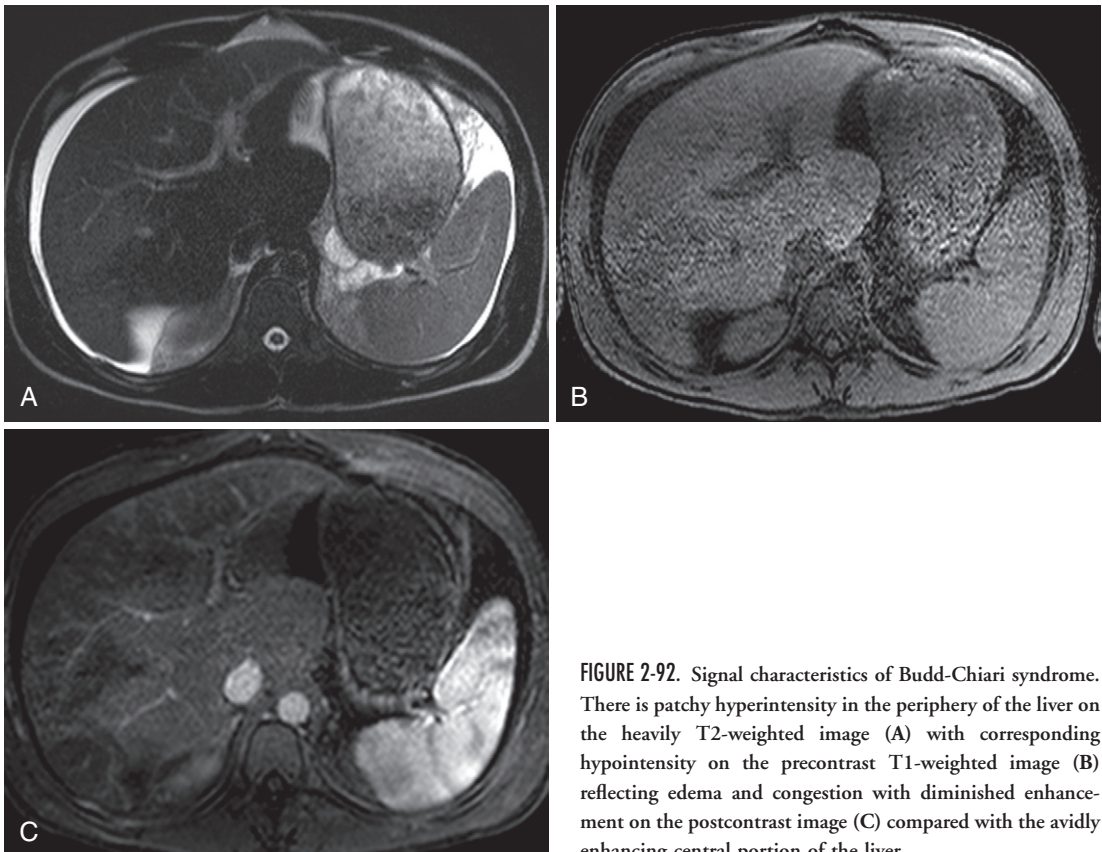


FIGURE 2-92. Signal characteristics of Budd-Chiari syndrome. There is patchy hyperintensity in the periphery of the liver on the heavily T2-weighted image (**A**) with corresponding hypointensity on the precontrast T1-weighted image (**B**) reflecting edema and congestion with diminished enhancement on the postcontrast image (**C**) compared with the avidly enhancing central portion of the liver.

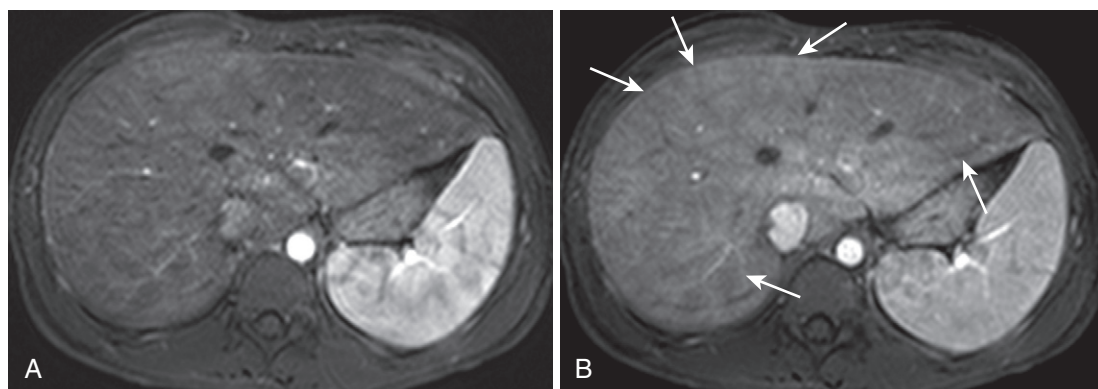


FIGURE 2-93. Passive hepatic congestion. In a patient with congestive failure, the arterial phase image (A) reveals heterogeneous enhancement reiterated on the portal phase image (B), highlighted by a reticulated network of curvilinear hypointensities (*arrows* in B).

copper content. T2 isointensity to mild hypointensity is the norm in BCS regenerative nodules. Hyperintensity on T2-weighted images probably reflects infarction, which is a risk given the precarious hepatic venous drainage. Regenerative nodule hypervascularity reflects arterial supply with persistent hyperintensity on portal phase images. Unfortunately, this appearance overlaps significantly with the appearance of HCC in BCS (which has an annual occurrence rate reported at 4%,¹¹² similar to other chronic liver diseases). In addition, the typical HCC washout pattern on delayed images yields low sensitivity in BCS—most HCCs (in BCS) remain hyperintense. Because specific HCC imaging features are forfeited in BCS, greater reliance on AFP is necessary. A central scar reminiscent of FNH is an occasional feature of benign, regenerative BCS nodules and not characteristic of HCC.

Differentiating the chronic form of BCS from cirrhosis is often problematic. Nodularity and diffuse derangement of the hepatic morphology with intervening fibrosis characterize both clinical entities. Coexistent portal hypertension complicates both diseases. Definitive identification of hepatic venous and/or caval thrombosis or occlusion establishes the diagnosis of BCS. Passive hepatic congestion produces a heterogeneous, reticulated enhancement pattern with curvilinear hypovascular regions corresponding to relative hepatic venous hypertension (Fig. 2-93) and potentially confused with BCS.¹¹³ In contradistinction to BCS, the hepatic veins and IVC are abnormally distended and evidence of either right heart failure or constrictive pericarditis is usually forthcoming.

LIVER TRANSPLANTATION

LT involves replacement of a failed recipient liver with a healthy cadaveric (orthotopic liver transplantation [OLT]) or part of a living donor's liver (living donor liver transplantation [LDLT]). LT treats end-stage hepatic parenchymal disease, such as cirrhosis, portal hypertension, and unresectable localized tumors (i.e., HCC). Serial MR examinations in patients with chronic liver disease and HBV and HCV are ordered to screen the liver and exclude HCC that would violate transplant criteria. Most transplant centers adhere to the Milan Criteria—solitary HCC less than 5 cm or up to three lesions less than 3 cm—shown to guarantee over 70% 5-year survival.¹¹⁴ Pretransplant imaging guides treatment of small, early HCC lesions with ablation to obviate transplant contraindication. Posttransplant imaging focuses on tumor surveillance (in the case of chronic HBV or HCV infection) and posttransplant complications, such as post-fluid collections, biliary strictures, and vascular complications. Biliary and vascular complications arise from the multiple anastomoses involved in transplantation: (1) common bile duct, (2) hepatic artery, (3) portal vein, (4) suprahepatic IVC, and (5) infrahepatic IVC (Fig. 2-94).

Expected perihepatic findings usually outnumber parenchymal findings after LT. A small amount of (usually not encapsulated or localized) perihepatic, interlobar fissural and right pleural fluid resolves within weeks (Fig. 2-95).¹¹⁵ Expect susceptibility at the IVC anastomotic site (particularly the suprahepatic anastomosis). Mild portal venous narrowing at the porta hepatic (probably due to extrinsic compression by edematous liver) and anastomotic site (due

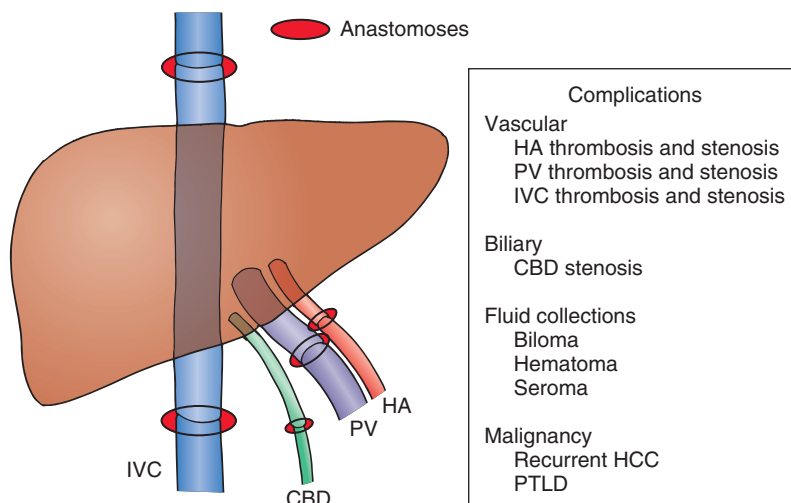


FIGURE 2-94. Diagram of liver transplantation and complications. CBD, common bile duct; HA, hepatic artery; HCC, hepatocellular carcinoma; IVC, inferior vena cava; PTLD, posttransplant lymphoproliferative disorder; PV, portal vein.

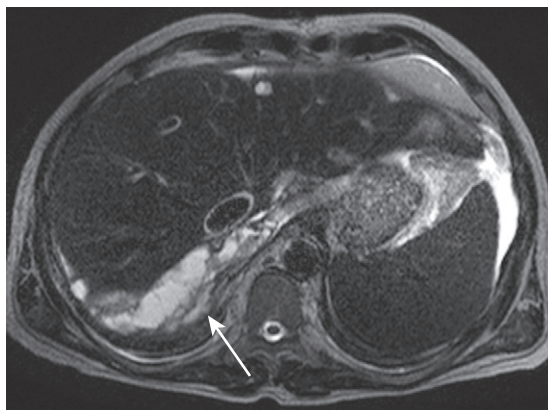


FIGURE 2-95. Perihepatic fluid after liver transplant. The heavily T2-weighted sequence in a patient with a recently placed orthotopic liver transplant shows a perihepatic fluid collection along the posterior margin of the liver dome (arrow).

to discrepancy in size between recipient and donor portal vein) is frequently observed. Periportal edema peaks in the postoperative period as a consequence of lack of lymphatic drainage (Fig. 2-96). Reactive periportal and portocaval nodes are only worrisome when enlarged and detected in the posttransplant lymphoproliferative disorder (PTLD) window—4 to 12 months after transplantation.

The most obvious transplant complication—rejection—has no reliable MRI correlate.¹¹⁶ Vascular insufficiency, biliary abnormalities, fluid collections, and malignancy constitute the main complications confronted by imaging. Hepatic artery thrombosis (HAT), the most common vascular complication, occurs in up to 9% of patients and has declined in incidence. HAT

often presents within 4 weeks with graft failure, biliary stricturing or leak (due to ischemia), or liver abscess or sepsis (arising from infarcted parenchyma). HAT demands urgent surgical intervention with revascularization techniques or retransplantation.¹¹⁷ MR angiography images provide the most detailed assessment of the hepatic arterial anatomy and require little modification of the standard abdominal protocol. Consider increasing the gadolinium dose (for increased vascular conspicuity, including venous structures, which are also at risk), increasing the flip angle to increase T1-weighting enhancing vascular structures, and increasing the spatial resolution (at the expense of coverage, which is probably expendable in this setting). If substantial susceptibility artifact arises from surgical clips around the hepatic artery, consider invoking metal minimization strategies (minimal TE with fractional echo sampling afforded by using 1 NEX [number of excitations] instead of partial k-space filling, increasing the bandwidth to drive down the TE, and eliminating fat suppression). Look for occlusion at the anastomotic site, where it usually occurs. Stenosis, the second most common vascular complication (~5% incidence) also develops at the anastomotic site and leads to similar complications—biliary ischemia and stricturing and infection—evolving over a longer timecourse. Other arterial complications—pseudoaneurysm and arteriovenous fistula—occur in less than 5% of cases. Pseudoaneurysms potentially form at the anastomotic site or at the ligated gastroduodenal artery site. Intraparenchymal arteriovenous fistulae

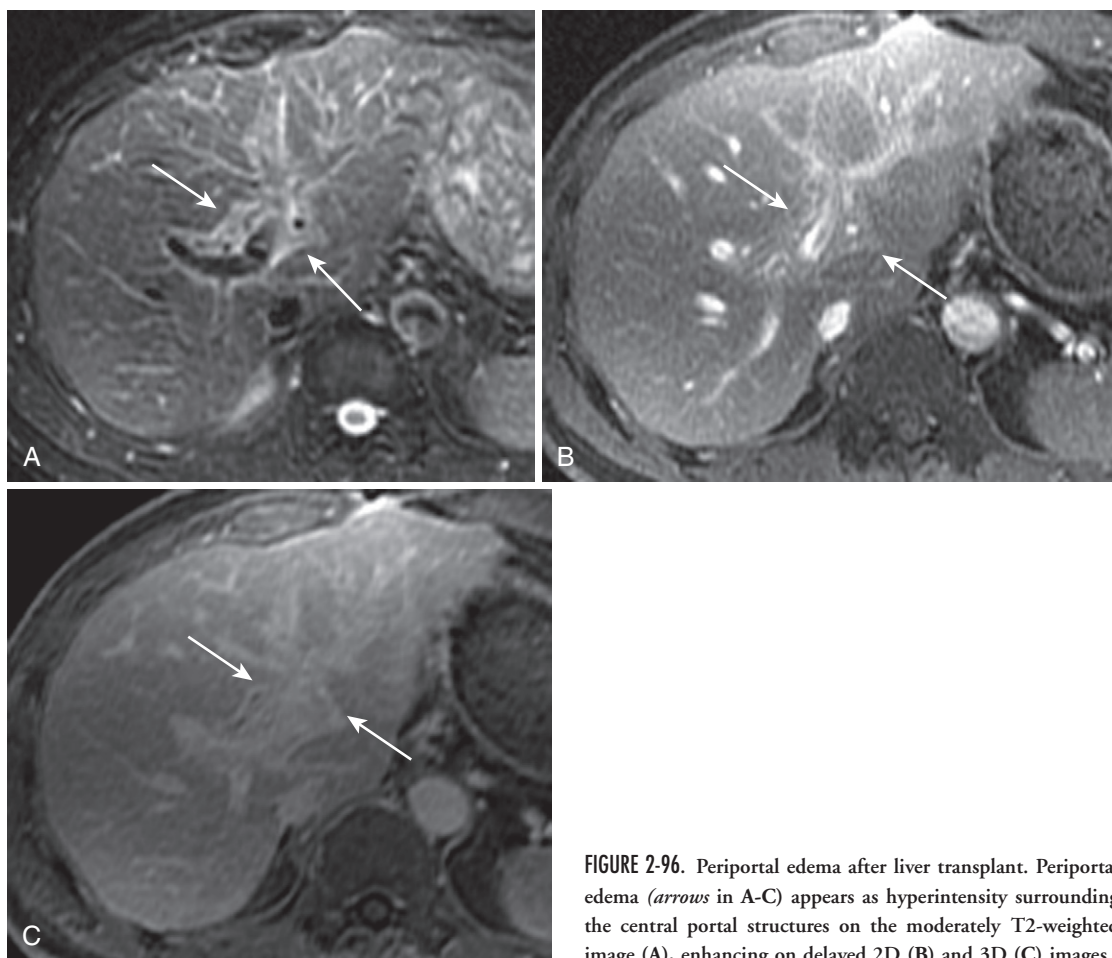


FIGURE 2-96. Periportal edema after liver transplant. Periportal edema (*arrows in A-C*) appears as hyperintensity surrounding the central portal structures on the moderately T2-weighted image (A), enhancing on delayed 2D (B) and 3D (C) images.

and pseudoaneurysms complicate biopsy, biliary interventions, and other procedures.

Portal venous complications occur less commonly. Portal venous stenosis (PVS) threatens the onset of portal hypertension, graft failure, and progression to PVT, which further elevates the risk of these complications. Surgical technical factors and hypercoagulable states are the major risk factors for portal venous complications. PVS usually occurs at the anastomotic site and PVT usually involves the extrahepatic main portal vein (Fig. 2-97). When portal venous complications are suspected, consider using a higher dose of gadolinium (up to twice the standard dose) and rely mostly on portal phase and delayed images, using either direct coronal acquisition or coronally reformatted images to assess the portal vein for stenosis or thrombosis. If available, use steady-state images to supplement the gadolinium-enhanced images, with the caveat that adjacent fluid-filled structures (common bile duct and hepatic artery)

potentially confound or obscure the portal vein. Parenchymal changes have not been extensively reported, but probably manifest predominantly on dynamic imaging with compensatory arterial enhancement. IVC stenosis and/or thrombosis occurs in less than 2% of patients (Fig. 2-98). IVC complications predispose to BCS, lower extremity edema, ascites, and diminished hepatic venous outflow with hepatomegaly. Employ the same imaging strategy as in the case of portal venous complications.

Parenchymal infarcts resulting from vascular insufficiency—usually arterial—must be differentiated from other parenchymal complications, such as abscess and biloma. Although occasionally peripheral, geographic, and wedge-shaped and respecting vascular anatomy (see Fig. 2-61), hepatic infarcts also demonstrate ill-defined and round morphology (Fig. 2-99). Absent enhancement with relative fluid signal potentially overlaps with the appearance of abscess and biloma, but relative preservation

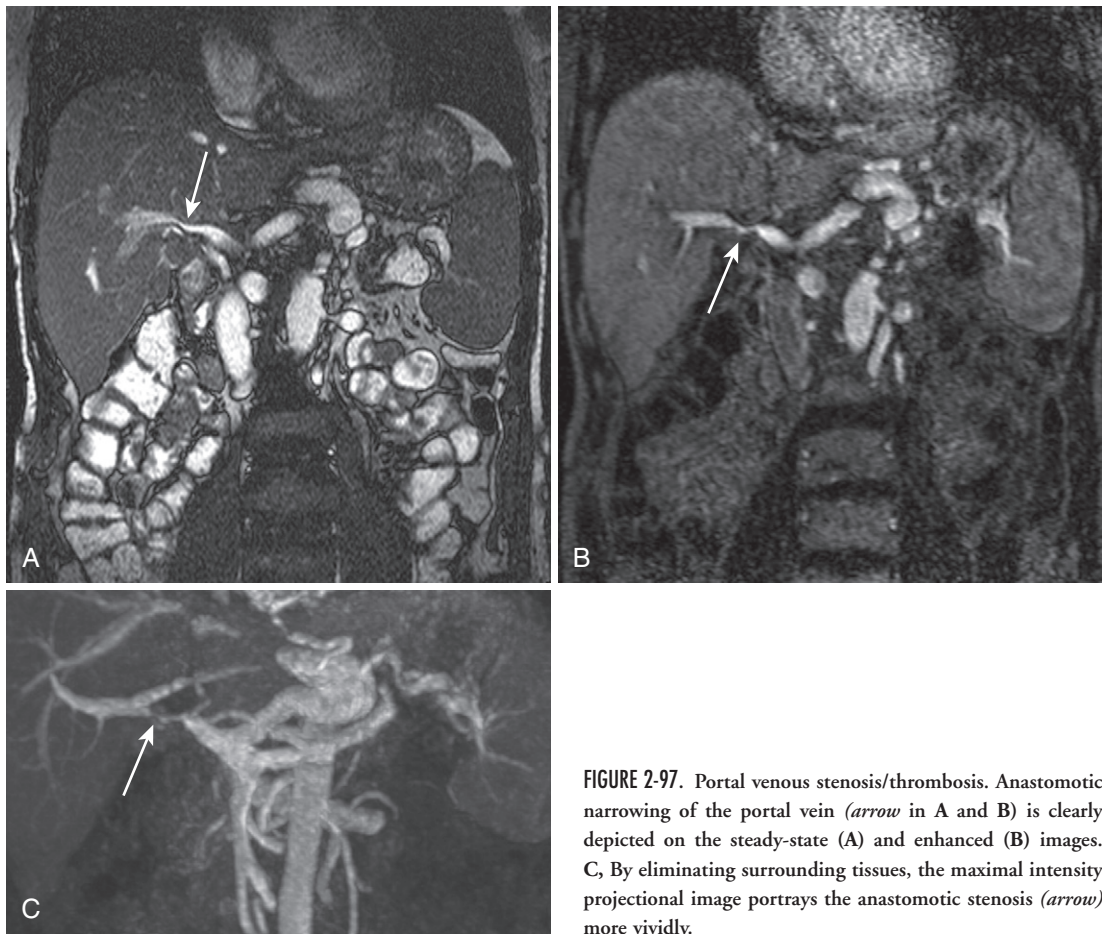


FIGURE 2-97. Portal venous stenosis/thrombosis. Anastomotic narrowing of the portal vein (*arrow* in A and B) is clearly depicted on the steady-state (A) and enhanced (B) images. C, By eliminating surrounding tissues, the maximal intensity projectional image portrays the anastomotic stenosis (*arrow*) more vividly.

of hepatic architecture and portal triads excludes other diagnoses.

Postoperative fluid collections are either expected and incidental or potentially problematic and requiring treatment or intervention. Incidental fluid collections include right pleural effusion and small perihepatic hematomas/seromas. Typical locations include the gallbladder fossa and hepatorenal space, and most incidental perihepatic fluid collections measure a few centimeters. These collections usually demonstrate simple fluid characteristics with T2 hyperintensity—T1 hyperintensity indicating methemoglobin may be present, depending on the timecourse. Remember that right adrenal hemorrhage occasionally follows LT due to either ligation complicating caval resection or coagulopathy associated with underlying liver disease. Small intraparenchymal collections are also incidental and include contusions, hematomas, and small, incidental bilomas.

However, be circumspect regarding fluid collections because they may belie serious complications. Biloma and abscess are the fluid collections prompting serious concern. Although occasionally intraparenchymal, bilomas usually inhabit the porta hepatis or gallbladder fossa and exhibit uniform T2 hyperintensity with variable, but homogeneous T1 signal.¹¹⁸ Consider substituting a hepatocyte-specific gadolinium agent with delayed imaging if biloma is suspected; continuity with the biliary system associated with progressive accumulation of contrast indicates biliary origin. Although bile incites an inflammatory reaction reflected pathologically by a pseudocapsule, no rim is usually perceived on MRI. Identification of an enhancing rim raises the suspicion of an abscess (see Fig. 2-33). Identification of internal complexity and septation elevates the suspicion (see the section on “Cystic Lesions,” earlier).

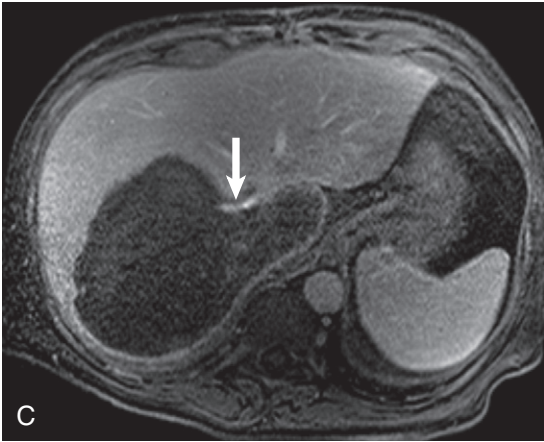
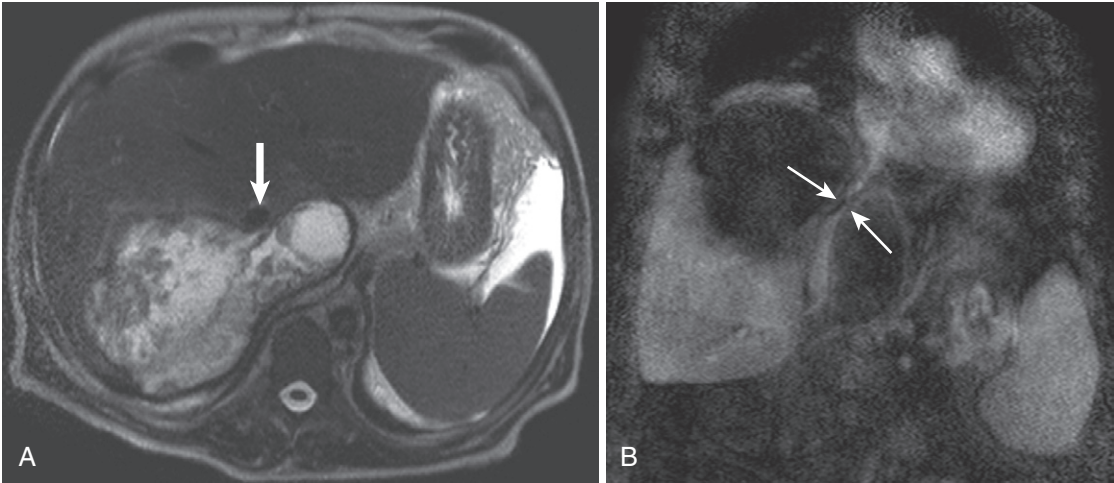


FIGURE 2-98. Inferior vena cava (IVC) stenosis. A large complex posttransplant fluid collection abuts the IVC (*arrow* in A) on the T2-weighted image (A) and encircles and narrows the IVC (*arrows* in B) on the coronal enhanced image (B). C, The axial enhanced image corroborates the IVC stenosis (*arrow*).

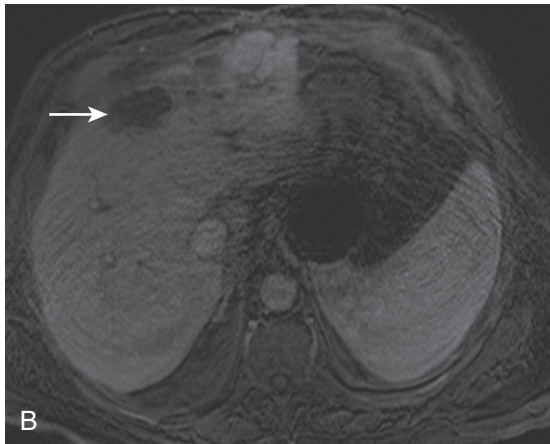
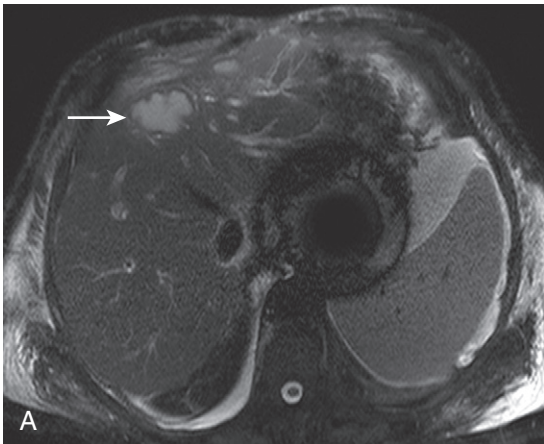


FIGURE 2-99. Hepatic infarct. The T2-weighted fat-saturated image (A) shows a round, subcapsular hyperintensity (*arrow*), which lacks enhancement on the postcontrast image (*arrow* in B), corresponding to an infarct in a transplanted liver. The susceptibility artifact arises from embolization coils in esophageal varices.

Biliary complications arise from technical difficulties or ischemia (the native biliary tree is collateralized by the gastroduodenal artery, unlike the transplanted biliary system, which is solely reliant on the hepatic artery).

Anastomotic technique depends on the type of surgery. OLT involves primary, end-to-end choledochocholedochostomy, and LDLT cases often involve hepatojejunostomy. Anastomotic strictures are technical or ischemic in etiology.

Nonanastomotic strictures represent arterial insufficiency and most severely affect the hilum and progress peripherally. MRCP images supplemented by heavily T2-weighted images provide the best overview of the biliary system to identify biliary stenoses. Waistings with relative narrowing often characterizes the anastomotic site; in the absence of a physiologically significant stenosis, no proximal, upstream biliary dilatation is present. Three-dimensional gadolinium-enhanced images supplement fluid-sensitive sequences in evaluating the biliary system with the advantage of high spatial resolution and negative contrast effect (the bile ducts appear dark against enhanced parenchyma). Hepatocyte-specific gadolinium agents provide an additional means of evaluating the biliary tree.

Posttransplant malignancy includes recurrent HCC, de novo HCC (patients with chronic HBV and HCV infection), and PTLD. Recurrent HCC complicates 7% to 40% of transplanted livers,¹¹⁶ demonstrating the same hepatic features observed in native livers. Along with the liver, the other most common sites of HCC recurrence after LT are the lungs and local and distant lymph nodes.¹¹⁹

PTLD spans a spectrum from hyperplastic lymphoid hyperplasia to a lymphoma-type disease process (Table 2-25). Epstein-Barr viral infection predating or during transplantation generally characterizes these patients, who usually experience B-cell proliferations. Disease onset typically occurs 4 to 12 months after transplant. Lymph nodes, the gastrointestinal tract, the central nervous system, the lungs, and the transplanted liver are target organs. Extranodal

involvement is the hallmark of PTLD, and the liver is the most frequent site of abdominal involvement. Multifocal parenchymal lesions or periportal infiltration constitutes the dominant forms of hepatic PTLD. PTLD is problematic because treatment involves counterproductive measures—reduction or cessation of immunosuppressive therapy instituted for the sake of the allograft. Anti-B-cell therapy regimens follow inadequate response to discontinuation of immunosuppressive therapy.¹²⁰

Figures 2-100 to 2-103 are available online on Expert Consult at www.expertconsult.com



References

- Jeong YY, Mitchell DG, Holland GA. Liver lesion conspicuity: T2-Weighted breath-hold fast spin echo MR imaging before and after gadolinium enhancement—Initial experience. *Radiology* 219:455–460, 2001.
- VanSonnenberg E, Wroblecka JT, D'Agostino HB, et al. Symptomatic hepatic cysts: Percutaneous drainage and sclerosis. *Radiology* 190:387–392, 1994.
- Mathieu D, Vilgrain V, Mahfourz A, et al. Benign liver tumors. *Magn Reson Imaging Clin North Am* 5:255–288, 1997.
- Semelka RC, Hussain SM, Marcos HB, et al. Biliary hamartomas: Solitary and multiple lesions shown on current MR techniques including gadolinium enhancement. *J Magn Reson Imaging* 10:196–201, 1999.
- Maher MM, Dervan P, Keogh B, et al. Bile duct hamartomas (Von Meyenburg complexes): Value of MR imaging in diagnosis. *Abdom Imaging* 24:171–173, 1999.
- Desmet VJ. Pathogenesis of ductal plate abnormalities. *Ludwig Symposium on Biliary Disorders—Part 1. Mayo Clin Proc* 73:80–89, 1999.
- Brancatelli G, Federle MP, Vilgrain V, et al. Fibropolycystic liver disease: CT and MR imaging findings. *Radiographics* 25:659–670, 2005.
- Choi BI, Yeon KM, Kim SH, et al. Caroli disease: Central dot sign in CT. *Radiology* 174:161–163, 1990.
- Jeong MG, Yu JS, Kim KW. Hepatic cavernous hemangioma: Temporal peritumoral enhancement during multiphase dynamic MR imaging. *Radiology* 216:692–697, 2000.
- Li CS, Chen RC, Chen WT, et al. Temporal peritumoral enhancement of hepatic cavernous hemangioma: Findings at multiphase dynamic magnetic resonance imaging. *J Comput Assist Tomogr* 27:854–859, 2003.
- Kato H, Kanematsu M, Matsuo M, et al. Atypically enhancing hepatic cavernous hemangiomas: High spatial-resolution gadolinium-enhanced triphasic dynamic gradient-recalled-echo imaging findings. *Eur Radiol* 11:2510–2515, 2001.
- Vilgrain V, Boulos L, Vullierme MP, et al. Imaging of atypical hemangiomas of the liver with pathologic correlation. *Radiographics* 20:379–397, 2000.
- Nelson RC, Chezmar JL. Diagnostic approach to hepatic hemangiomas. *Radiology* 176:11–13, 1990.
- Yamashita Y, Hatanaka Y, Yamamoto H, et al. Differential diagnosis of focal liver lesions: Role of spin-echo and contrast-enhanced dynamic MR imaging. *Radiology* 193:59–65, 1994.

TABLE 2-25. Posttransplant Lymphoproliferative Disorder Syndromes

Hyperplastic PTLD
 Infectious mononucleosis–like PTLD
 Plasmacytic hyperplasia

Polymorphic PTLD
 Polymorphic diffuse B-cell hyperplasia
 Polymorphic diffuse B-cell lymphoma

Monomorphic PTLD
 Diffuse large B-cell lymphoma
 Burkitt's-like PTLD
 Plasma cell myeloma
 Plasmacytoma-like PTLD
 T-cell neoplasms

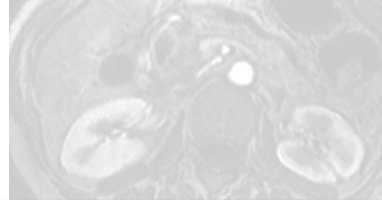
Hodgkin's-like PTLD

PTLD, posttransplant lymphoproliferative disorder.

15. Valls C, Rene M, Gil M, et al. Giant cavernous hemangioma of the liver: Atypical CT and MR findings. *Eur Radiol* 6:448-450, 1996.
16. Choi BI, Han MC, Park JH, et al. Giant cavernous hemangioma of the liver: CT and MR imaging in 10 cases. *AJR Am J Roentgenol* 152:1221-1226, 1989.
17. D'Ippolito G, Appezzato LF, Caivano A, et al. Unusual presentations of hepatic hemangioma: An iconographic essay. *Radiol Bras* 39(3):219-225, 2006.
18. Stoupis C, Taylor HM, Paley MR, et al. The rocky liver: Radiologic-pathologic correlation of calcified hepatic masses. *Radiographics* 18:675-685, 1998.
19. Siegelman ES, editor. *Body MR techniques and MR of the liver*. In *Body MRI*. Philadelphia: Elsevier Saunders, 2005, pp. 1-62.
20. Jenkins RL, Johnson LB, Lewis WD. Surgical approach to benign liver tumors. *Semin Liver Dis* 14:178-189, 1994.
21. Devaney K, Goodman ZD, Ishak KG. Hepatobiliary cystadenoma and cystadenocarcinoma: A light microscopic and immunohistochemical study of 70 patients. *Am J Surg Pathol* 18:1078-1091, 1994.
22. Buetow PC, Buck JL, Pantongrag-Brown L, et al. Biliary cystadenoma and cystadenocarcinoma: Clinical-imaging-pathologic correlation with emphasis on the importance of ovarian stroma. *Radiology* 196:805-810, 1995.
23. Seidel R, Weinrich M, Pistorious G, et al. Biliary cystadenoma of the left intrahepatic duct. *Eur Radiol* 17:1380-1383, 2007.
24. Levy AD, Murakata LA, Abbott RM, et al. Benign tumors and tumorlike lesions of the gallbladder and extrahepatic bile ducts: Radiologic-pathologic correlation. *Radiographics* 22:387-413, 2002.
25. Polat P, Kantarci M, Alper F, et al. Hydatid disease from head to toe. *Radiographics* 23:475-494, 2003.
26. Pedrosa I, Saiz A, Arrazola J, et al. Hydatid disease: Radiologic and pathologic complications. *Radiographics* 20:795-817, 2000.
27. Lewall DB. Hydatid disease: Biology, pathology, imaging and classification. *Clin Radiol* 52:863-874, 1998.
28. Jeffrey RB, Tolentino CS, Chang FC, et al. CT of small pyogenic hepatic abscesses: The cluster sign. *AJR Am J Roentgenol* 151:487-489, 1988.
29. Balci NC, Sirvanci M. MR imaging of infective liver lesions. *Magn Reson Imaging Clin North Am* 10:121-135, 2002.
30. Ralls PW, Henley DS, Colletti PM, et al. Amebic liver abscess: MR imaging. *Radiology* 165:801-804, 1987.
31. Morteale KJ, Segatto E, Ros PR. The infected liver: Radiologic-pathologic correlation. *Radiographics* 24:937-955, 2004.
32. Semelka RC, Shoenuit JP, Greenberg HM, et al. Detection of acute and treated lesions of hepatosplenic candidiasis: Comparison of dynamic contrast-enhanced CT and MR imaging. *J Magn Reson Imaging* 2:341-345, 1992.
33. Semelka RC, Kelekis NL, Sallah S, et al. Hepatosplenic fungal disease: Diagnostic accuracy and spectrum of appearances on MR imaging. *AJR Am J Roentgenol* 169:1311-1316, 1997.
34. Casillas VJ, Amendola MA, Gascue A, et al. Imaging of nontraumatic hemorrhagic hepatic lesions. *Radiographics* 20:367-378, 2000.
35. Grazioli L, Federle MP, Brancatelli G, et al. Hepatic adenomas: Imaging and pathologic findings. *Radiographics* 21:877-892, 2001.
36. Grazioli L, Federle MP, Ichikawa T, et al. Liver adenomatosis: Clinical, pathologic, and imaging findings in 15 patients. *Radiology* 216:395-402, 2000.
37. Paulson EK, McClellan JS, Washington K, et al. Hepatic adenoma: MR characteristics and correlation with pathologic findings. *AJR Am J Roentgenol* 163:113-116, 1994.
38. Arrive L, Flejou JF, Vilgrain F, et al. Hepatic adenoma: MR findings in 51 pathologically proved lesions. *Radiology* 193:507-512, 1994.
39. Buetow PC, Pantongrag-Brown L, Buck JL, et al. Focal nodular hyperplasia of the liver: Radiologic-pathologic correlation. *Radiographics* 16:369-388, 1996.
40. Grazioli L, Morana G, Federle MP, et al. Focal nodular hyperplasia: Morphologic and functional information from MR imaging with gadobenate dimeglumine. *Radiology* 221:731-739, 2001.
41. Colagrande S, Centi N, Galdiero R, et al. Transient hepatic intensity differences: Part 1, Those associated with lesions. *AJR Am J Roentgenol* 188:154-159, 2007.
42. Colagrande S, Centi N, Galdiero R, et al. Transient hepatic intensity differences: Part 2, Those not associated with lesions. *AJR Am J Roentgenol* 188:160-166, 2007.
43. Ueda K, Terada T, Nakanuma Y, et al. Vascular supply in adenomatous hyperplasia of the liver and hepatocellular carcinoma: A morphometric study. *Hum Pathol* 23:619-626, 1992.
44. Lim JH, Cho JM, Kim EY, et al. Dysplastic nodules in liver cirrhosis: Evaluation of hemodynamics with CT during arterial portography and CT hepatic arteriography. *Radiology* 214:869-874, 2000.
45. Baron RL, Peterson MS. Screening the cirrhotic liver for hepatocellular carcinoma with CT and MR imaging: Opportunities and pitfalls. *Radiographics* 21:S117-S132, 2001.
46. International Working Party. Terminology of nodular hepatocellular lesions. *Hepatology* 22:983-993, 1995.
47. Hayashi M, Matsui O, Ueda K, et al. Correlation between the blood supply and grade of malignancy of hepatocellular nodules associated with liver cirrhosis: Evaluation by CT during intraarterial injection of contrast medium. *AJR Am J Roentgenol* 172:969-976, 1999.
48. Kelekis LK, Semelka RC, Worawattanakul S, et al. Hepatocellular carcinoma in North America: A multi-institutional study of appearance on T1-weighted, T2-weighted, and serial gadolinium-enhanced gradient-echo images. *AJR Am J Roentgenol* 170:1005-1103, 1998.
49. El-Serag HB, Mason AC. Rising incidence of hepatocellular carcinoma in the United States. *N Engl J Med* 340:745-750, 1999.
50. Yoshino M. Growth kinetics of hepatocellular carcinoma. *Jpn J Clin Oncol* 13:45-52, 1983.
51. Karadeniz-Bilgili MY, Braga L, Birchard KR, et al. Hepatocellular carcinoma missed on gadolinium enhanced MR imaging, discovered in liver explants: Retrospective evaluation. *J Magn Reson Imaging* 23:210-215, 2006.
52. Semelka RC, Braga L, Armao D, et al. Liver. In Semelka RC, editor, *Liver in Abdominal-Pelvic MRI*. Hoboken, NJ: John Wiley & Sons, 2006, pp. 47-445.
53. Grazioli L, Olivetti L, Fugazzola C, et al. The pseudocapsule in hepatocellular carcinoma: Correlation between dynamic MR imaging and pathology. *Eur Radiol* 9:62-67, 1999.
54. Fisher A, Siegelman ES, editors. *Body MR Techniques and MR of the Liver from Body MRI*. Philadelphia: Elsevier Saunders, 2005, pp. 1-62.
55. Efreimidis SC, Hytioglou P. The multistep process of hepatocarcinogenesis in cirrhosis with imaging correlation. *Eur Radiol* 12:753-764, 2002.

56. Low RN. MR imaging of the liver using gadolinium chelates. *Magn Reson Imaging Clin North Am* 9:717-743, 2001.
57. Katyal S, Oliver JH, Peterson MS, et al. Extrahepatic metastases of hepatocellular carcinoma. *Radiology* 216:698-703, 2000.
58. McLarney JK, Rucker PT, Bender GN, et al. Fibrolamellar carcinoma of the liver: Radiologic-pathologic correlation. *Radiographics* 19:453-471, 1999.
59. Manoharan P, Ward J. MRI in the assessment of focal liver lesions in the non-cirrhotic patient. *Imaging* 16:338-350, 2004.
60. Danet IM, Semelka RC, Leonardou P, et al. Spectrum of MRI appearances of untreated metastases of the liver. *AJR Am J Roentgenol* 181:809-817, 2003.
61. Mahfouz AE, Hamm B, Wolf KJ. Peripheral washout: A sign of malignancy on dynamic gadolinium-enhanced MR images of focal lesions. *Radiology* 190:49-52, 1994.
62. Wittenberg J, Stark DD, Forman DH, et al. Differentiation of hepatic metastases from hepatic hemangiomas and cysts by using MR imaging. *AJR Am J Roentgenol* 151:79-84, 1988.
63. McNicholas MM, Saini S, Echeverri J, et al. T2 relaxation times of hypervascular and non-hypervascular liver lesions: Do hypervascular lesions mimic haemangiomas on heavily T2-weighted MR images? *Clin Radiol* 51:401-405, 1996.
64. Premkumar A, Marincola F, Taubenberg J, et al. Metastatic melanoma: Correlation of MRI characteristics and histopathology. *J Magn Reson Imaging* 6:190-194, 1996.
65. Outwater E, Tomaszewski JE, Daly JM, et al. Hepatic colorectal metastases: Correlation of MR imaging and pathologic appearance. *Radiology* 180:327-332, 1991.
66. Braga L, Semelka RC, Pedro MS, et al. Post-treatment malignant liver lesions, MR imaging. *MRI Clin North Am* 10:53-73, 2002.
67. Goldberg SN, Charboneau JW, Dodd GD, et al. Image-guided tumor ablation: Proposal for standardization of terms and reporting criteria. *Radiology* 228:335-345, 2003.
68. Curley SA, Marra P, Beatty K, et al. Early and late complications after radiofrequency ablation of malignant liver tumors in 608 patients. *Ann Surg* 239:450-458, 2004.
69. Vanderveen KA, Hussain HK. Magnetic resonance imaging of cholangiocarcinoma. *Cancer Imaging* 4:104-115, 2004.
70. Craig JR, Peters RL, Edmonson HA, editors. Tumors of the liver and intrahepatic ducts. In *Atlas of Tumor Pathology*. 2nd series, fasc. 26. Washington, DC: Armed Forces Institute of Pathology, 1988, pp. 16B-43B.
71. Ros PR, Buck JL, Goodman ZD, et al. Intrahepatic cholangiocarcinoma: Radiologic-pathologic correlation. *Radiology* 167:689-693, 1988.
72. Liver Cancer Study Group of Japan. Classification of Primary Liver Cancer. Tokyo: Kanehara, 1997, pp. 6-8.
73. Han JK, Choi BI, Kim AY, et al. Cholangiocarcinoma: Pictorial essay of CT and cholangiographic findings. *Radiographics* 22:173-187, 2002.
74. Maetani Y, Itoh K, Watanabe C, et al. MR imaging of intrahepatic cholangiocarcinoma with pathologic correlation. *AJR Am J Roentgenol* 176:1499-1507, 2001.
75. Loyer EM, Chin H, DuBrow RA, et al. Hepatocellular carcinoma and intrahepatic peripheral cholangiocarcinoma: Enhancement patterns with quadruple phase helical CT—A comparative study. *Radiology* 212:866-875, 1999.
76. Lacomis JM, Baron RL, Oliver JH, III, et al. Cholangiocarcinoma: Delayed CT contrast enhancement patterns. *Radiology* 203:98-104, 1997.
77. Vilgrain V. Staging cholangiocarcinoma by imaging studies. *HPB (Oxford)* 10:106-109, 2008.
78. Yamasaki S. Intrahepatic cholangiocarcinoma: Macroscopic type and stage classification. *J Hepatobiliary Pancreat Surg* 10:288-291, 2003.
79. Okabayashi T, Yamamoto J, Kosuge T, et al. A new staging system for mass-forming intrahepatic cholangiocarcinoma. *Cancer* 92:2374-2383, 2001.
80. Jeon TY, Kim SH, Lim HK, et al. Assessment of triple-phase CT findings for the differentiation of fat-deficient hepatic angiomyolipoma from hepatocellular carcinoma in non-cirrhotic liver. *Eur J Radiol* 73:601-606, 2010.
81. Horton KM, Bluemke DA, Hruban RH, et al. CT and MR imaging of benign hepatic and biliary tumors. *Radiographics* 19:431-451, 1999.
82. Basaran C, Karcaaltincaba M, Akata D, et al. Fat-containing lesions of the liver: Cross-sectional imaging findings with emphasis on MRI. *AJR Am J Roentgenol* 184:1103-1110, 2005.
83. Anderson SW, Kruskal JB, Kane RA. Benign hepatic tumors and pseudotumors. *Radiographics* 29:211-229, 2009.
84. Prasad SR, Wang H, Rosas H, et al. Fat-containing lesions of the liver: Radiologic-pathologic correlation. *Radiographics* 25:321-331, 2005.
85. Hamer OW, Aguirre DA, Casola G, et al. Fatty liver: Imaging patterns and pitfalls. *Radiographics* 26:1637-1653, 2006.
86. Karcaaltincaba M, Okan A. Imaging of hepatic steatosis and fatty sparing. *Eur J Radiol* 61:33-43, 2007.
87. Lipson JA, Qayyum A, Avrin DE, et al. CT and MRI of hepatic contour abnormalities. *AJR Am J Roentgenol* 184:75-81, 2005.
88. Yang DM, Kim HS, Cho SW, et al. Pictorial review, various causes of hepatic capsular retraction: CT and MR findings. *Br J Radiol* 75:994-1002, 2002.
89. Lipson JA, Qayyum A, Arvin DE, et al. Pictorial Essay: CT and MRI of hepatic contour abnormalities. *AJR Am J Roentgenol* 184:75-81, 2005.
90. Gabata T, Matsui O, Kadoya M, et al. Segmental hyperintensity on T1-weighted MRI of the liver: Indication of segmental cholestasis. *J Magn Reson Imaging* 7:855-857, 2005.
91. Alvarez F, Berg PA, Bianchi FB, et al. International Autoimmune Hepatitis Group Report: Review of criteria for diagnosis of autoimmune hepatitis. *J Hepatol* 31:928-938, 1999.
92. Krawitt EL. Autoimmune hepatitis. *N Engl J Med* 354:54-66, 2006.
93. Lali CG, Aisen AM, Bansal N, et al. Nonalcoholic fatty liver disease. *AJR Am J Roentgenol* 190:993-1002, 2008.
94. Cowin GJ, Jonsson JR, Bauer JE, et al. Magnetic resonance imaging and spectroscopy for monitoring liver steatosis. *J Magn Reson Imaging* 28:937-945, 2008.
95. Ito K, Mitchell DG, Gabata T. Enlargement of the hilar periportal space: A sign of early cirrhosis at MR imaging. *J Magn Reson Imaging* 11:136-140, 2000.
96. Tan KC. Signs in imaging: Enlargement of the hilar periportal space. *Radiology* 248:699-700, 2008.
97. Ito K, Mitchell DG, Gabata T, et al. Expanded gallbladder fossa: Simple MR imaging sign of cirrhosis. *Radiology* 211:723-726, 1999.
98. Ito K, Mitchell DG. Right posterior hepatic notch sign: A simple diagnostic MR finding of cirrhosis. *J Magn Reson Imaging* 18:561-566, 2003.
99. Tan KC. Signs in imaging: The right posterior hepatic notch sign. *Radiology* 248:317-318, 2008.

100. Awaya H, Mitchell DG, Kamishima T, et al. Cirrhosis: Modified caudate-right lobe ratio. *Radiology* 224:769-774, 2002.
101. Taouli B, Tolia AJ, Losada M, et al. Diffusion-weighted MRI for quantification of liver fibrosis: Preliminary experience. *AJR Am J Roentgenol* 189:799-806, 2007.
102. Brancatelli G, Federle MP, Pealar K, et al. Portal venous thrombosis or sclerosis in liver transplantation candidates: Preoperative CT findings and correlation with surgical procedure. *Radiology* 220:321-328, 2001.
103. Verma SK, Mitchell DG, Bergin D, et al. Dilated cisternae chyli: A sign of uncompensated cirrhosis at MR imaging. *Abdom Imaging* 34:211-216, 2009.
104. Blachar A, Federle MP, Brancatelli G. Primary biliary cirrhosis: Clinical, pathologic and helical CT findings in 53 patients. *Radiology* 220:329-336, 2001.
105. Wenzel JS, Donohoe A, Ford KL, et al. MR imaging findings and description of MR imaging periportal halo sign. *AJR Am J Roentgenol* 176:885-889, 2001.
106. Vitellas KM, Keogan KT, Freed KS, et al. Radiologic manifestations of sclerosing cholangitis with emphasis on MR cholangiopancreatography. *Radiographics* 20:959-975, 2000.
107. Menias CO, Surabhi VR, Prasad SR, et al. Mimics of cholangiocarcinoma: Spectrum of disease. *Radiographics* 28:1115-1129, 2008.
108. Bader TR, Beavers KL, Semelka RC. MR imaging features of primary sclerosing cholangitis: Patterns of cirrhosis in relationship to clinical severity of disease. *Radiology* 226:675-685, 2003.
109. Bergquist A, Ekblom A, Olsson R, et al. Hepatic and extrahepatic malignancies in primary sclerosing cholangitis. *J Hepatol* 36:321-327, 2002.
110. Menon KV, Shah V, Kamath PS. The Budd-Chiari syndrome. *N Engl J Med* 350:578-585, 2004.
111. Bargallo X, Gilibert R, Nicolau C, et al. Sonography of the caudate vein: Value in diagnosing Budd-Chiari syndrome. *AJR Am J Roentgenol* 181:1641-1645, 2003.
112. Moucari R, Rautou P-E, Cazals-Hatem D, et al. Hepatocellular carcinoma in Budd-Chiari syndrome: Characteristics and risk factors. *Gut* 57:828-835, 2008.
113. Gore RM, Mathieu DG, Whie EM, et al. Passive hepatic congestion: Cross-sectional imaging features. *AJR Am J Roentgenol* 162:71-75, 1994.
114. Mazzaferro V, Regalia E, Doci R, et al. Liver transplantation for the treatment of small hepatocellular carcinomas in patients with cirrhosis. *N Engl J Med* 334:693-699, 1996.
115. Ito K, Siegelman ES, Mitchell DG. MR imaging of complications after liver transplantation. *AJR Am J Roentgenol* 175:1145-1149, 2000.
116. Pandharipande PV, Lee VS, Morgan GR, et al. Vascular and extravascular complications of liver transplantation: Comprehensive evaluation with three-dimensional contrast-enhanced volumetric MR imaging and MR cholangiopancreatography. *AJR Am J Roentgenol* 177:1101-1107, 2001.
117. Silva MA, Jambulingam PS, Gunson BK, et al. Hepatic artery thrombosis following orthotopic liver transplantation: A 10-year experience from a single centre in the United Kingdom. *Liver Transpl* 12:146-151, 2006.
118. Shigemura T, Yamamoto F, Shilpakar SK, et al. MRI differential diagnosis of intrahepatic biloma from subacute hematoma. *Abdom Imaging* 20:211-213, 1995.
119. Ferris JV, Baron RL, Marsh JW Jr, et al. Recurrent hepatocellular carcinoma after liver transplantation: Spectrum of CT findings and recurrence patterns. *Radiology* 198:233-238, 1996.
120. Jain A, Nalesnik M, Reyes J, et al. Posttransplant lymphoproliferative disorders in liver transplantation: A 20-year experience. *Ann Surg* 236:429-437, 2002.



MRI of the Pancreaticobiliary System

Sandeep Deshmukh and Christopher G. Roth

PANCREAS

Anatomy and Function

The pancreas is a nonencapsulated organ of the digestive system located within the retroperitoneum, posterior to the stomach and anterior to the spine. The pancreas is approximately 2 inches wide and 6 to 8 inches in length. The pancreas can be subdivided into the head, uncinate process, neck, body, and tail (Fig. 3-1). The head and uncinate process are cradled by the duodenum. The body sits posterior to the body of the stomach. The tail of the pancreas tickles the hilum of the spleen.

The pancreas possesses exocrine and endocrine function. The exocrine tissues of the pancreas (acinar cells) constitute approximately 95% of the pancreatic tissue and are made up of acinar cells. The acinar cells produce pancreatic enzymes, which flow through the pancreatic duct and enter the duodenum via the ampulla of Vater (at the major papilla) to aid in digestion. (In a minority of patients, the minor papilla, situated slightly cephalad to the major papilla, also transmits digestive fluids into the duodenal lumen.) The remaining 5% of the pancreatic tissue is responsible for the endocrine function of the gland and is made up of small clusters of cells throughout the gland, called *islets of Langerhans*. The endocrine tissues produce hormones that are released into the bloodstream.

Normal Appearance

The normal pancreas has the highest signal intensity of the abdominal organs on in-phase T1-weighted gradient recalled-echo images (except in the presence of hepatic steatosis) owing to the aqueous proteins in the glandular elements, intracellular paramagnetic substances (like manganese), and abundant endoplasmic reticulum in the pancreatic exocrine cells (Fig. 3-2A).^{1,2} The relative signal intensity of the

pancreas increases on fat-suppressed T1-weighted images owing to the increased dynamic range (see Fig. 3-2B). Normal pancreas is slightly hyperintense to muscle on T2-weighted imaging (Fig. 3-3A). With the addition of fat-suppression, there is minimal contrast between normal pancreatic parenchyma and the surrounding suppressed fat (see Fig. 3-3B).^{1,2}

Owing to the highly vascular nature of the pancreas, the normal pancreatic parenchyma demonstrates a homogeneous blush shortly after the arrival of gadolinium in the abdominal aorta. Because the liver receives the majority of its blood flow via the portal system, the pancreas is hyperintense to liver and fat during the arterial phase (Fig. 3-4).^{3,4}

Imaging Techniques

Optimal imaging of the pancreas demands high-field-strength systems with an adequate fat-water frequency shift for chemically selective fat suppression (≥ 1 Tesla) and high-performance gradients that enable the use of fast magnetic resonance (MR) sequences.¹ Protocols should include axial T1-weighted imaging with and without fat suppression (either breathhold gradient recalled-echo or breathing signal-averaged spin-echo sequences). T1-weighted images with fat suppression are ideal for depicting the extent of extrapancreatic involvement of inflammatory and neoplastic processes (i.e., vascular encasement).^{1,5} As discussed previously, fat suppression increases the dynamic range and improves the detection of small pancreatic lesions by providing the greatest contrast between normal and abnormal pancreatic tissues. Fat-suppressed T2-weighted imaging is useful for depicting ductal anatomy, cystic pancreatic lesions, islet cell tumors, peripancreatic fluid collections, and hepatic metastases.⁵

Two-dimensional (2-D) or three-dimensional (3-D) dynamic postgadolinium fat-suppressed

T1-weighted gradient recalled-echo sequences aid in the characterization of pancreatic masses, diffuse inflammatory pancreatic processes, and vascular involvement. Postcontrast imaging involves imaging of both the pancreatic

parenchymal and the peripancreatic vascular phases. In general, this can be accomplished by imaging at 15 seconds and 35 to 45 seconds after the arrival of gadolinium in the abdominal aorta.⁶

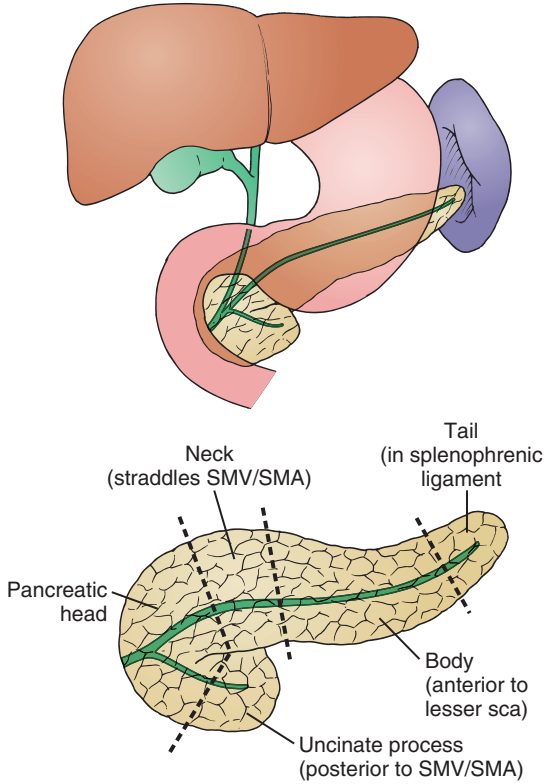


FIGURE 3-1. Anatomy of the pancreas.

Congenital/Developmental Anomalies of the Pancreas

During normal development, the ventral and dorsal pancreatic buds rotate about the duodenum and fuse. The ventral pancreatic bud constitutes the posteroinferior pancreatic head as well as the uncinate process. The dorsal pancreatic bud constitutes the anterior head, body, and tail. Following rotation and fusion of the ventral and dorsal pancreatic buds, there is fusion of the main pancreatic duct (Wirsung) and the accessory pancreatic duct (Santorini) (Fig. 3-5). Migrational disturbances result in a variety of congenital lesions marked by different structural deformities in pancreatic anatomy.

ANNULAR PANCREAS

Annular pancreas is a rare congenital anomaly that results when there is abnormal migration and rotation of the ventral bud of the pancreas resulting in a ring of pancreatic tissue that completely or partially encircles the duodenum (Fig. 3-6). The majority of patients with annular pancreas present with gastric outlet obstruction

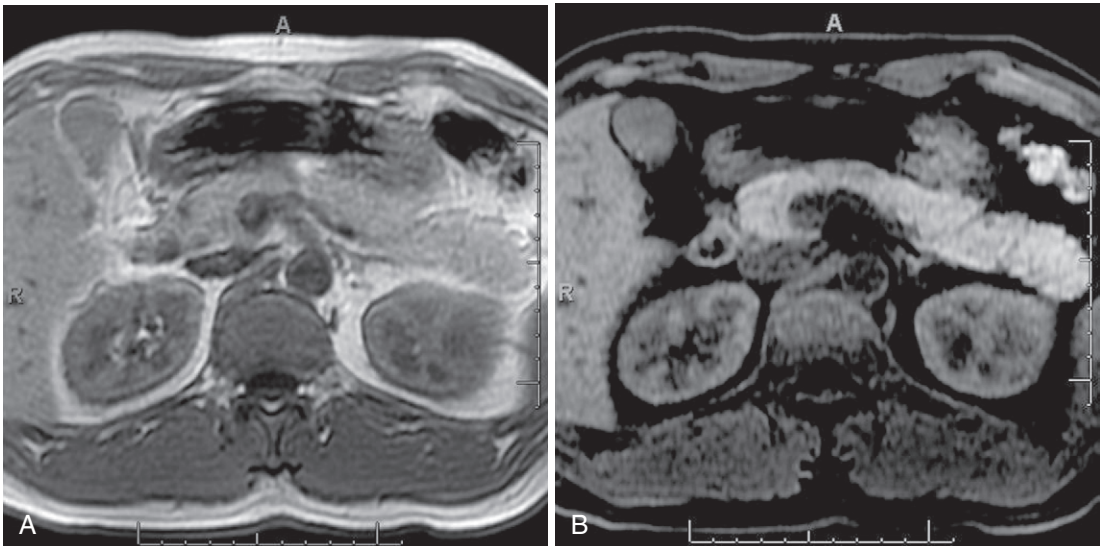


FIGURE 3-2. Normal appearance of the pancreas on T1-weighted images. A, In-phase T1-weighted image of the pancreas demonstrates the highest signal intensity of the abdominal organs secondary to aqueous proteins, paramagnetic substances, and endoplasmic reticulum. B, Relative increased signal intensity of the pancreas after fat suppression due to increased dynamic range.

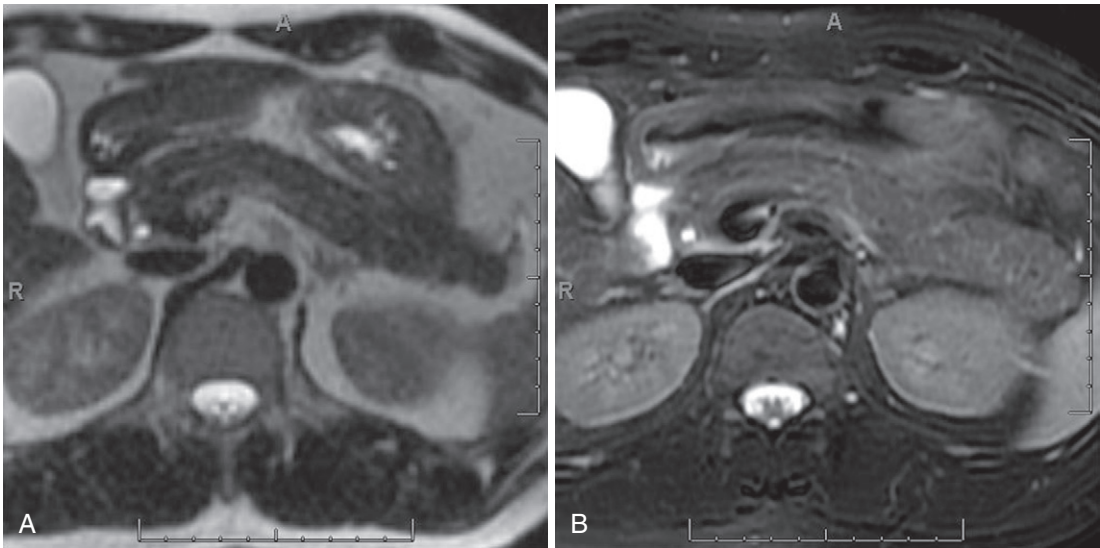


FIGURE 3-3. Normal appearance of the pancreas on T2-weighted images. Slightly increased T2-weighted signal intensity of the pancreas when compared with muscle (A), which is brought out after the addition of fat-suppression (B).

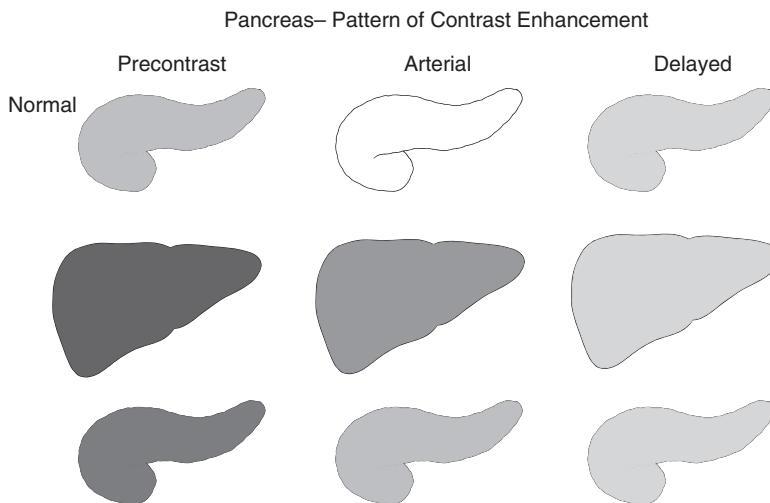


FIGURE 3-4. Pancreatic enhancement patterns. The normal pancreas (top row) is T1 hyperintense to the liver (middle row) with greater arterial enhancement (middle column). The bottom row represents the pancreas in the setting of (acute or chronic) pancreatitis.

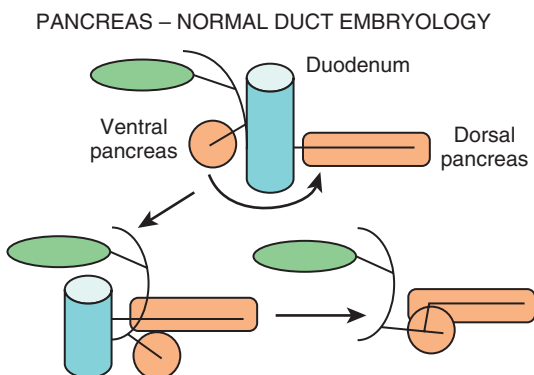


FIGURE 3-5. Pancreatic duct embryology.

during infancy. Infants with symptomatic annular pancreas also tend to have associated anomalies, such as trisomy 21, duodenal atresia, and tracheoesophageal fistula. Adults with annular pancreas present with peptic ulcer disease and pancreatitis.

At imaging, annular pancreas demonstrates a ring of normal pancreatic parenchyma (high T1-weighted signal intensity) about the duodenum and an aberrant pancreatic duct encircling the duodenum and joining the main pancreatic duct (best seen on magnetic resonance cholangiopancreatography [MRCP]).⁷

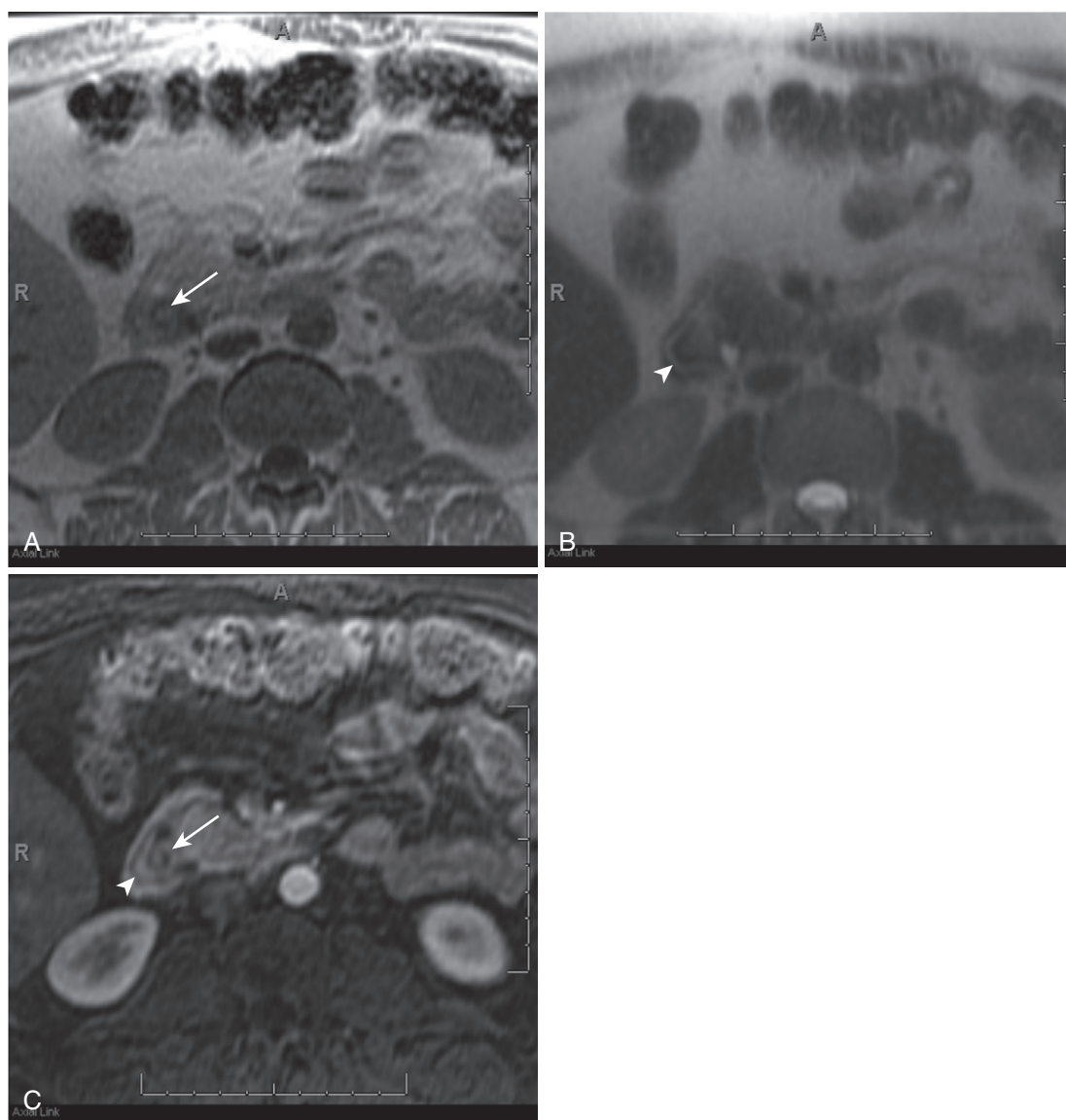


FIGURE 3-6. Annular pancreas. T1-weighted in-phase (A), T2-weighted (B), and fat-suppressed T1-weighted postcontrast (C) images demonstrate pancreas and aberrant duct of Santorini (*arrowhead*) encircling the duodenum (*arrow*) in this patient with annular pancreas.

PANCREAS DIVISUM

Pancreas divisum is the most common congenital variant of the pancreatic duct, representing the failure of fusion of the ducts of the ventral and dorsal pancreatic buds (Fig. 3-7). The clinical significance of this congenital variant is controversial because most patients are asymptomatic. However, in a subset of these patients with recurrent pancreatitis or abdominal pain, functional stenosis of the minor papilla with resultant obstruction of the exocrine juices causing increased intraductal pressure, ductal distention, and recurrent pancreatitis is believed to be the pathogenesis. These patients often

benefit from endoscopic or surgical drainage of the minor papilla.⁷

Variation in pancreatic ductal anatomy potentially simulates pancreas divisum (Fig. 3-8). Aberrations in embryologic fusion of the pancreatic anlage result in different pancreatic ductal configurations and potential persistent patency of the duct of Santorini through the minor papilla.

AGENESIS

Complete agenesis of the pancreas is a very rare condition and incompatible with life. Partial

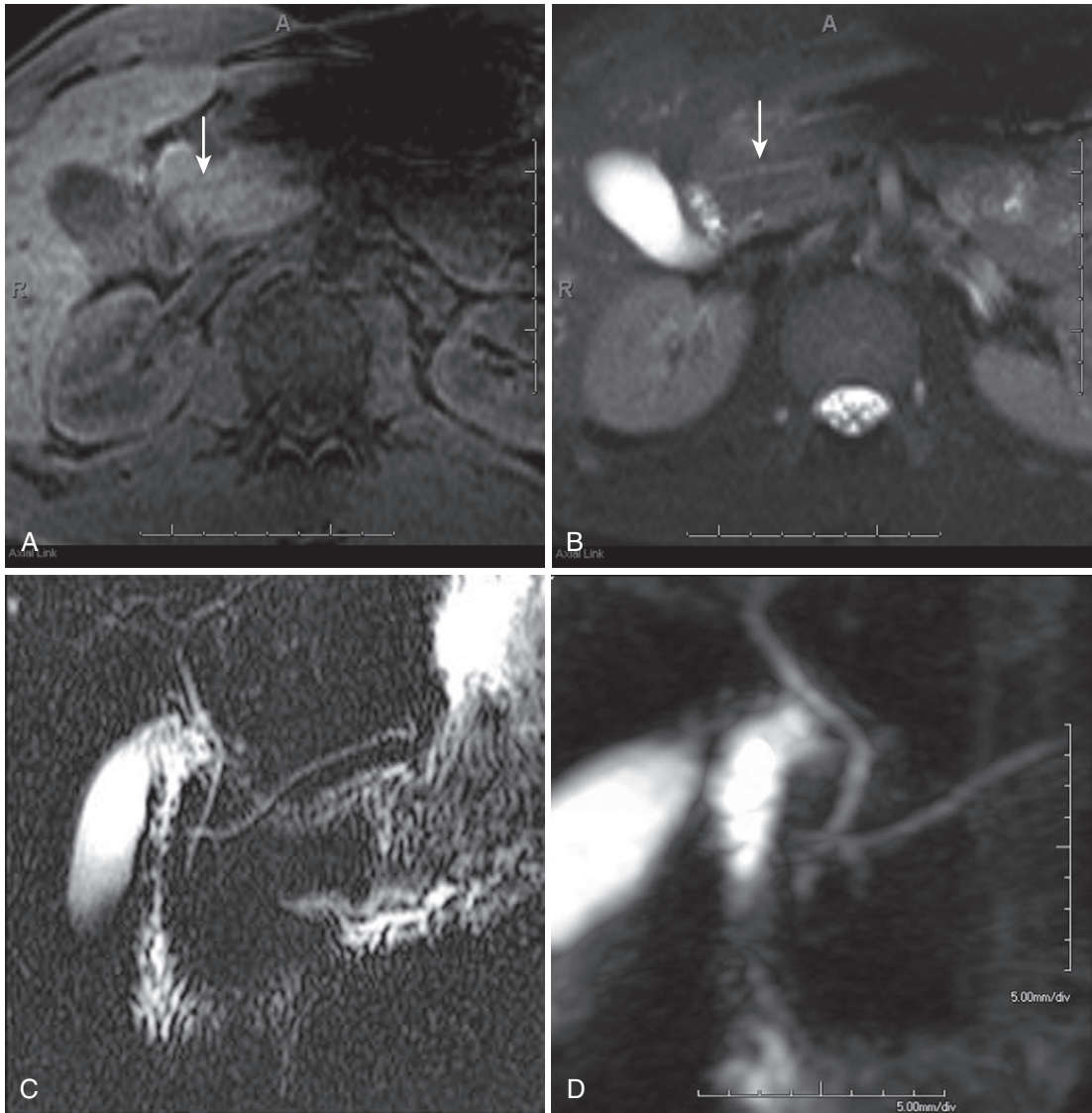


FIGURE 3-7. Pancreas divisum. Fat-suppressed T1-weighted gradient recalled-echo (A) and T2-weighted (B) images depict the drainage of the accessory duct of Santorini into the second portion of the duodenum (*arrows*). Thick-slab three-dimensional (3-D) magnetic resonance cholangiopancreatography (MRCP) and coned down views (C and D, respectively) show the classic crossed-duct appearance of the pancreatic accessory duct of Santorini and the common bile duct (CBD).

agenesis is rare, with either the ventral or the dorsal segment of the pancreas failing to develop. Partial agenesis of the pancreas is associated with polysplenia and intrathoracic abnormalities. Patients with agenesis of the dorsal bud or hypoplasia are more common, but also rare. Agenesis of the dorsal bud is related to a mutation in the gene for insulin promoter factor-1 (IPF-1). Patients with pancreatic hypoplasia generally have a normal development of the pancreas, but later in life, they have replacement of the normal glandular elements with fatty tissue

and present with exocrine insufficiency and normal endocrine function.

Diffuse Pancreatic Disorders

LIPOMATOSIS

Severe pancreatic lipomatous depositions can occur in adult patients with severe obesity, senile atrophy, or cystic fibrosis. The pancreatic parenchyma demonstrates some degree of atrophy with preservation of the pancreatic margins and normal lobulations.

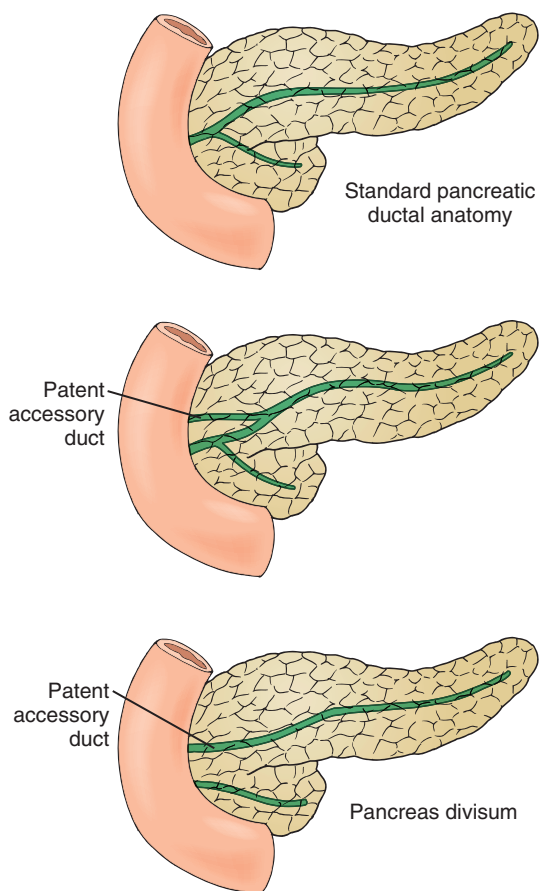


FIGURE 3-8. Variations in pancreatic ductal anatomy.

PANCREATITIS

Pancreatitis is the most common benign disease of the pancreas. The majority of cases are caused by cholelithiasis or alcohol abuse (~80% of cases), but a wide variety of uncommon etiologic factors have been identified (Fig. 3-9).⁸ The diagnosis of pancreatitis is clinical, based on laboratory abnormalities and clinical presentation. The role of magnetic resonance imaging (MRI) is to identify possible etiologies (e.g., choledocholithiasis) or complications (necrosis, peripancreatic inflammation and fluid collections, pseudocysts, hemorrhage, abscess, pseudoaneurysm, and/or venous thrombosis). However, when the cause of abdominal pain is unclear, imaging findings help establish the diagnosis of pancreatitis.

Acute Pancreatitis. Acute pancreatitis encompasses a wide spectrum from mild inflammation of the pancreatic parenchyma to severe disease possibly including hemorrhage, necrosis, and/or superimposed infection (Fig. 3-10).

As such, the imaging appearance is varied ranging from normal homogeneous T1 hyperintensity to heterogeneous T1 hypointensity with glandular enlargement, heterogeneous enhancement, and loss of the normal pancreatic contours with thickening of the left anterior pararenal fascia (see Fig. 3-10).⁹⁻¹¹

With pancreatic inflammation, the gland focally or diffusely enlarges. Associated peripancreatic fluid is best detected on fat-suppressed T2-weighted images with even trace T2-hyperintense peripancreatic fluid standing out from the intermediate to low T2-weighted signal intensity of the pancreatic parenchyma and the signal suppressed peripancreatic fat. As the severity of pancreatitis increases, there is decreased T1-weighted parenchymal signal intensity with blunted heterogeneous early phase contrast enhancement (Fig. 3-11).⁹⁻¹¹

In the majority of severe cases of pancreatitis, there is a reaction to the pancreatic inflammatory process resulting in the development of fluid collections within the pancreatic parenchyma, peripancreatic tissues, lesser sac, and paracolic gutters. The majority of these fluid collections are resorbed in 4 to 6 weeks; however, approximately 10% of these collections develop a capsule and eventually become pseudocysts (Fig. 3-12).¹²

Pancreatic necrosis is a complication of severe pancreatitis in which there is either focal or diffuse nonviable pancreatic parenchyma (Fig. 3-13). Absent enhancement, superimposed on findings of acute pancreatitis, indicates necrosis. Pancreatic necrosis tends to involve the body and tail of the pancreas and spare the head owing to its abundant vascular supply.¹³ The potential for abscess development and the high morbidity of pancreatic necrosis usually necessitate percutaneous drainage or surgical débridement.^{10,13} When 75% or more of the gland is necrotic or there is progression of pancreatic necrosis on serial examinations, necrosectomy is generally performed owing to the high morbidity.¹³

Leakage of pancreatic enzymes from the inflamed pancreas can result in autodigestion of the arterial wall with subsequent pseudoaneurysm formation (Fig. 3-14). The most commonly involved artery is the splenic artery followed by the pancreaticoduodenal and gastroduodenal arteries.¹⁴

The most common vascular complication of pancreatitis is venous thrombosis. The close

Drugs	Infectious	Inherited	Mechanical	Metabolic	Toxins	Other
Furosemide	Coxsackie B	Autosomal dominant PRSS1 mutation	Gallstones	Hypertriglyceridemia	Alcohol	Pregnancy
Azathioprine	CMV	Cystic fibrosis	ERCP	Hypercalcemia	Methanol	Post renal transplant
Asparaginase	Mumps		Pancreatic or ampullary carcinoma			Tropical pancreatitis
Pentamidine	Salmonella		Pancreas divisum			Ischemia (i.e., hypotension)
Valproate			Sphincter of Oddi stenosis			Groove pancreatitis
Sulfa drugs			Choledochal cyst			Pancreatic cancer
ACE inhibitors						

FIGURE 3-9. Etiologies of pancreatitis. ACE = angiotensin-converting enzyme; CMV = cytomegalovirus; ERCP = endoscopic retrograde cholangiopancreatography.

proximity of the splenic vein to the body and tail of the pancreas renders it the most susceptible to thrombosis. However, the superior mesenteric vein and portal confluence can also be involved.¹⁵

Chronic Pancreatitis. Chronic pancreatitis is a progressive inflammatory disease of the pancreas with irreversible morphologic changes of the pancreatic parenchyma eventually resulting in loss of endocrine and exocrine function of the gland.¹⁶

Imaging stigmata of this disease process include decreased T1-weighted signal intensity of the gland owing to decreased protein content due to glandular atrophy and fibrosis (also contributing to T1 hypointensity). Furthermore, the fibrotic changes of the parenchyma result in attenuation of the vascular supply reflected by decreased enhancement on immediate postgadolinium images.¹⁷ The spectrum of changes in the pancreatic duct are broad including dilatation, stricture, stenosis, intraductal calculi, occasionally side branch duct dilatation (“chain of lakes” or “string of pearls” appearance) (Fig. 3-15).¹⁸ The most pathognomonic imaging

feature of chronic pancreatitis is parenchymal calcification; however, this occurs late in the disease process and is best seen on computed tomography (CT) (Fig. 3-16).

Autoimmune Pancreatitis. Autoimmune pancreatitis (AIP, also known as lymphoplasmacytic sclerosing pancreatitis) is a rare form of chronic pancreatitis. The autoimmune inflammatory process is marked by a lack of classic acute attacks of pancreatitis with a predilection for older males (over 50 years of age). Because of the uniquely dramatic response to steroids, consider AIP in the appropriate clinical setting.

Imaging findings also differ from other forms of pancreatitis. AIP tends to be mass-forming with either focal or diffuse pancreatic enlargement with minimal peripancreatic inflammation and an absence of vascular encasement or calcification. Diffuse irregular narrowing of the main pancreatic duct and a peripancreatic hypointense hypovascular rind are characteristic features. These imaging features occasionally simulate the appearance of pancreatic carcinoma (Fig. 3-17).^{19,20} An abrupt ductal caliber

Text continued p. 144

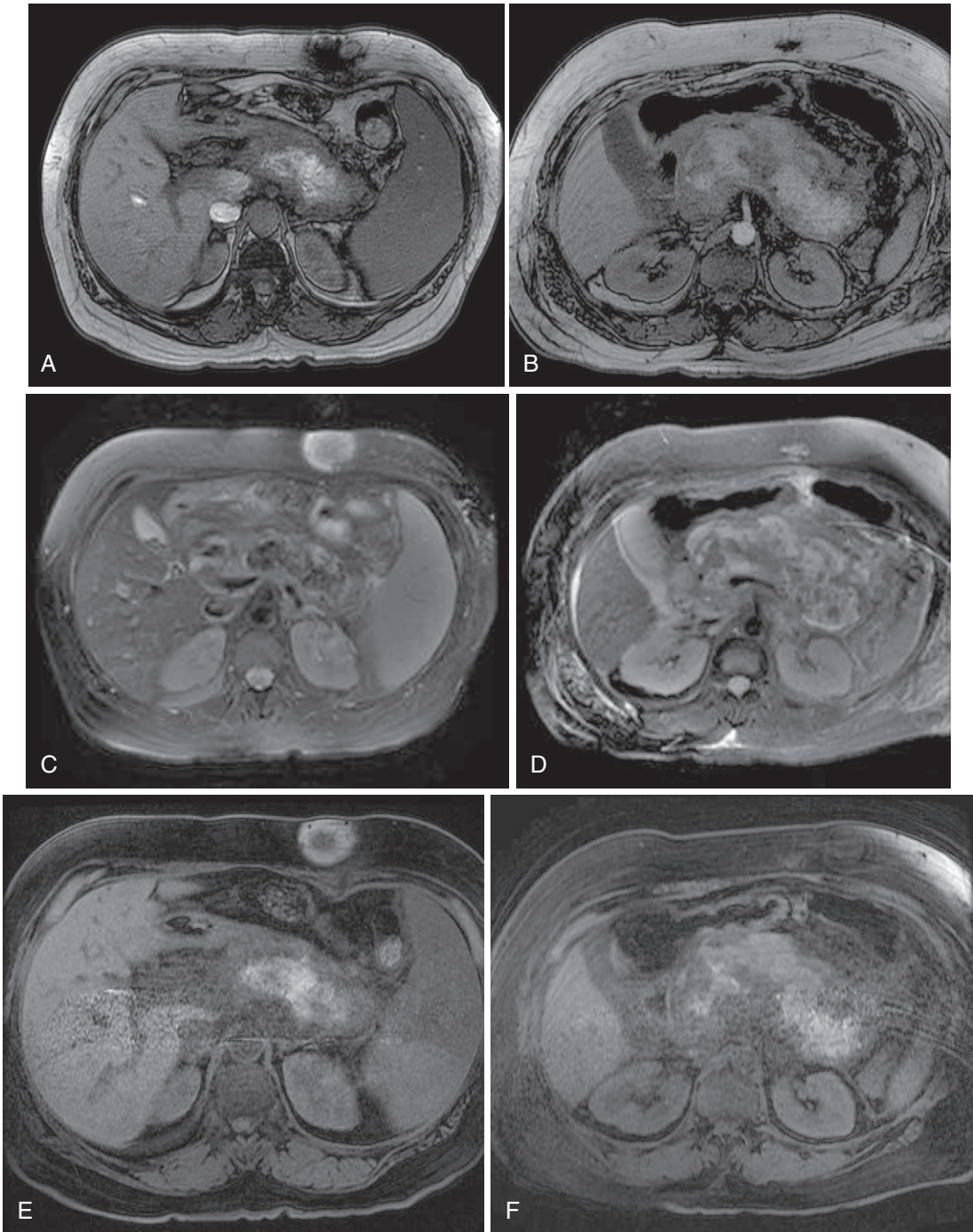


FIGURE 3-10. Acute hemorrhagic pancreatitis. Out-of-phase T1-weighted gradient recalled-echo (A and B), fat-suppressed T2-weighted (C and D), and fat-suppressed T1-weighted gradient recalled-echo (E and F) images demonstrate marked acute pancreatitis with increased T1-weighted signal intensity and corresponding decreased T2-weighted signal intensity related to hemorrhage, as well as marked peripancreatic inflammation.

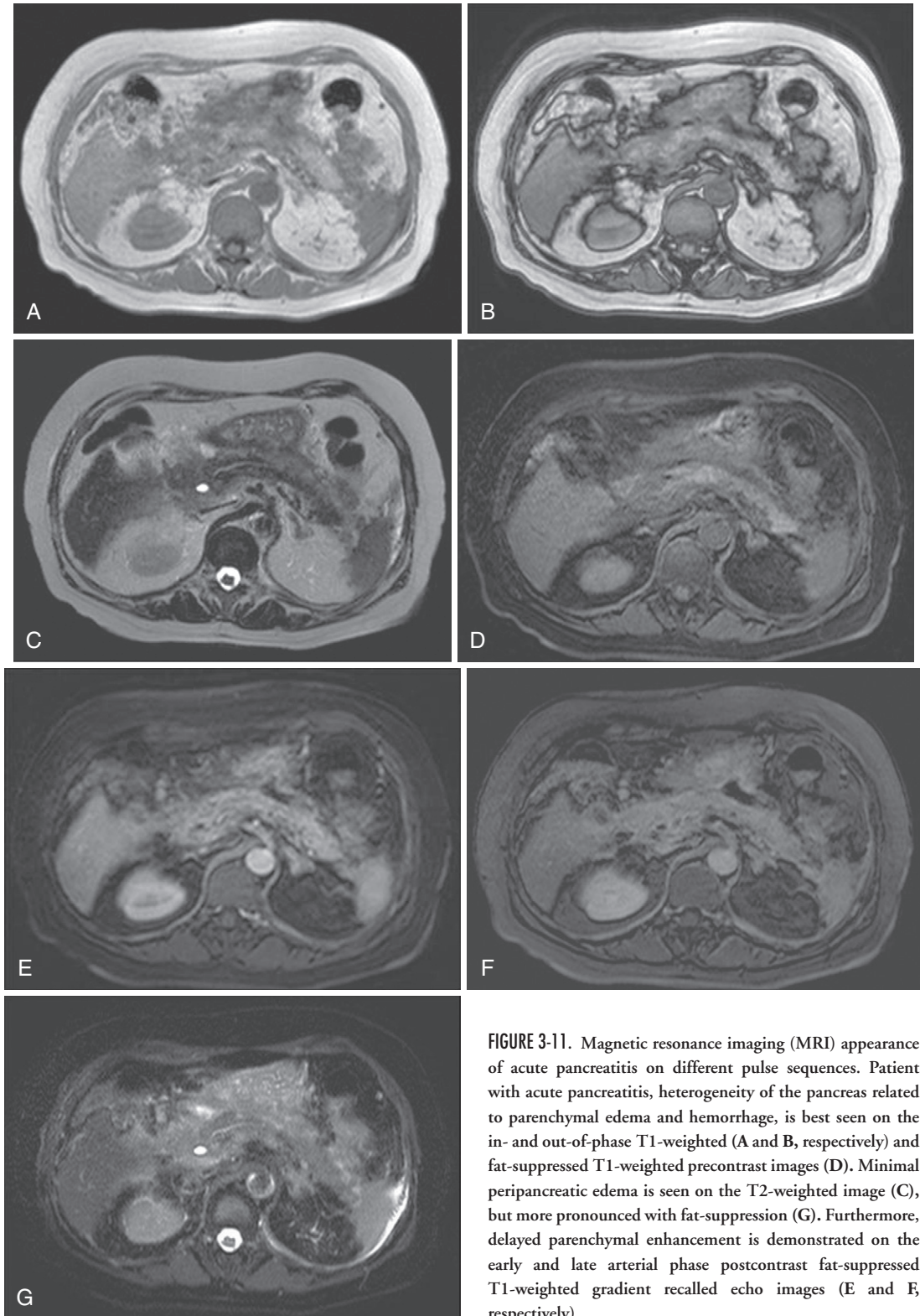


FIGURE 3-11. Magnetic resonance imaging (MRI) appearance of acute pancreatitis on different pulse sequences. Patient with acute pancreatitis, heterogeneity of the pancreas related to parenchymal edema and hemorrhage, is best seen on the in- and out-of-phase T1-weighted (A and B, respectively) and fat-suppressed T1-weighted precontrast images (D). Minimal peripancreatic edema is seen on the T2-weighted image (C), but more pronounced with fat-suppression (G). Furthermore, delayed parenchymal enhancement is demonstrated on the early and late arterial phase postcontrast fat-suppressed T1-weighted gradient recalled echo images (E and F, respectively).

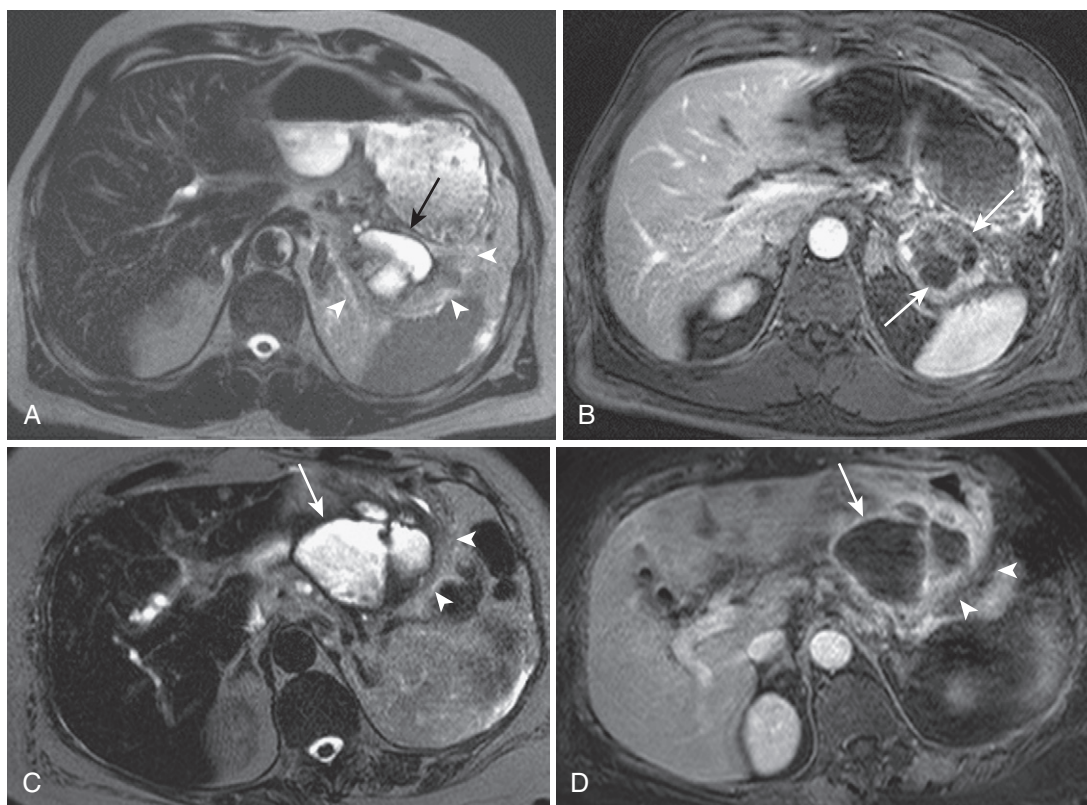


FIGURE 3-12. Pancreatic pseudocysts. **A**, Heavily T2-weighted image shows an irregularly shaped, septated pseudocyst in the pancreatic tail (*arrow*), which is surrounded by edema (*arrowheads*). **B**, The postcontrast image demonstrates absent enhancement in the locules (*arrows*). In a different patient with pancreatitis, the heavily T2-weighted (**C**) and postcontrast (**D**) images reveal a large, complex, multiloculated pseudocyst (*arrow*) abutting the lesser curvature of the stomach. Mild surrounding edema and inflammation (*arrowheads*) and a history of pancreatitis help confirm the etiology and exclude neoplastic lesions.

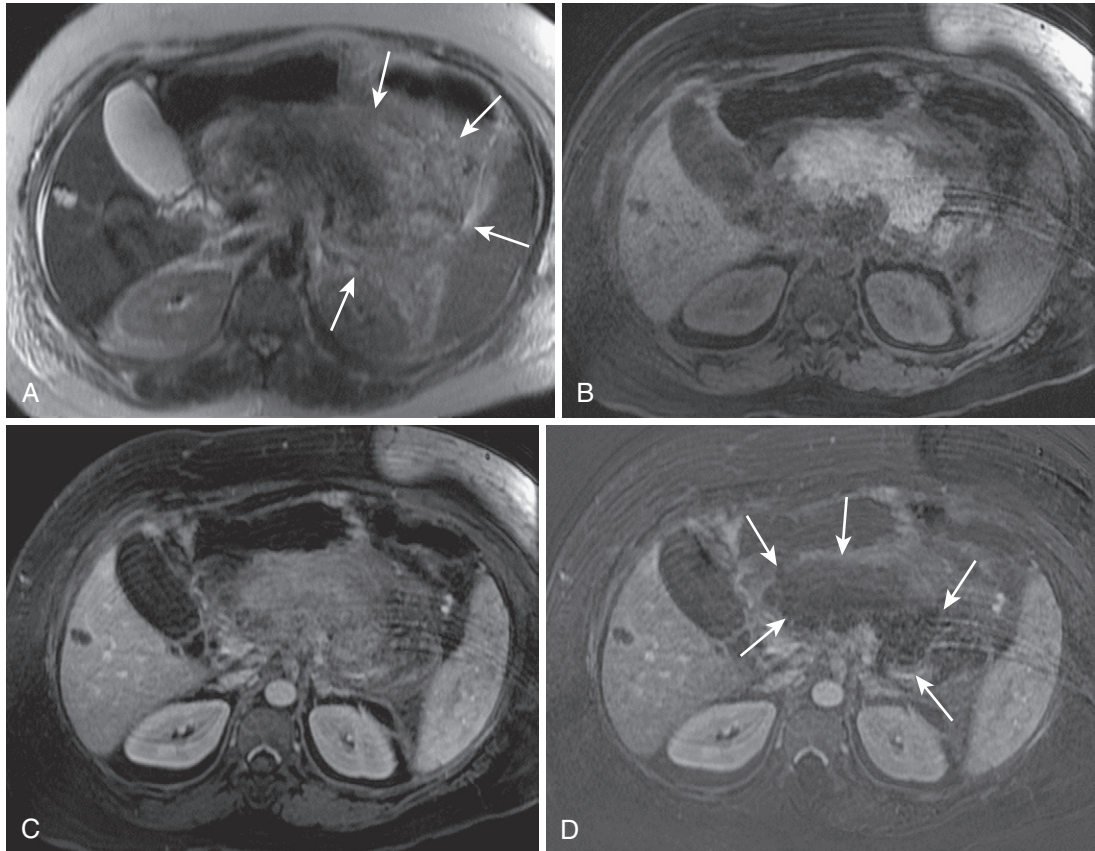


FIGURE 3-13. Pancreatic necrosis. **A**, The heavily T2-weighted image shows extensive peripancreatic inflammation (*arrows*) surrounding an ill-defined pancreatic body and neck with relative hypointensity in the setting of acute inflammation. **B**, Marked parenchymal hyperintensity on the fat-suppressed T1-weighted image signifies hemorrhage. The relative hypointensity on the postcontrast image (**C**) reflects the preferential enhancement of surrounding structures, and the pancreatic signal void (*arrows*) on the subtracted image (**D**) confirms necrosis.

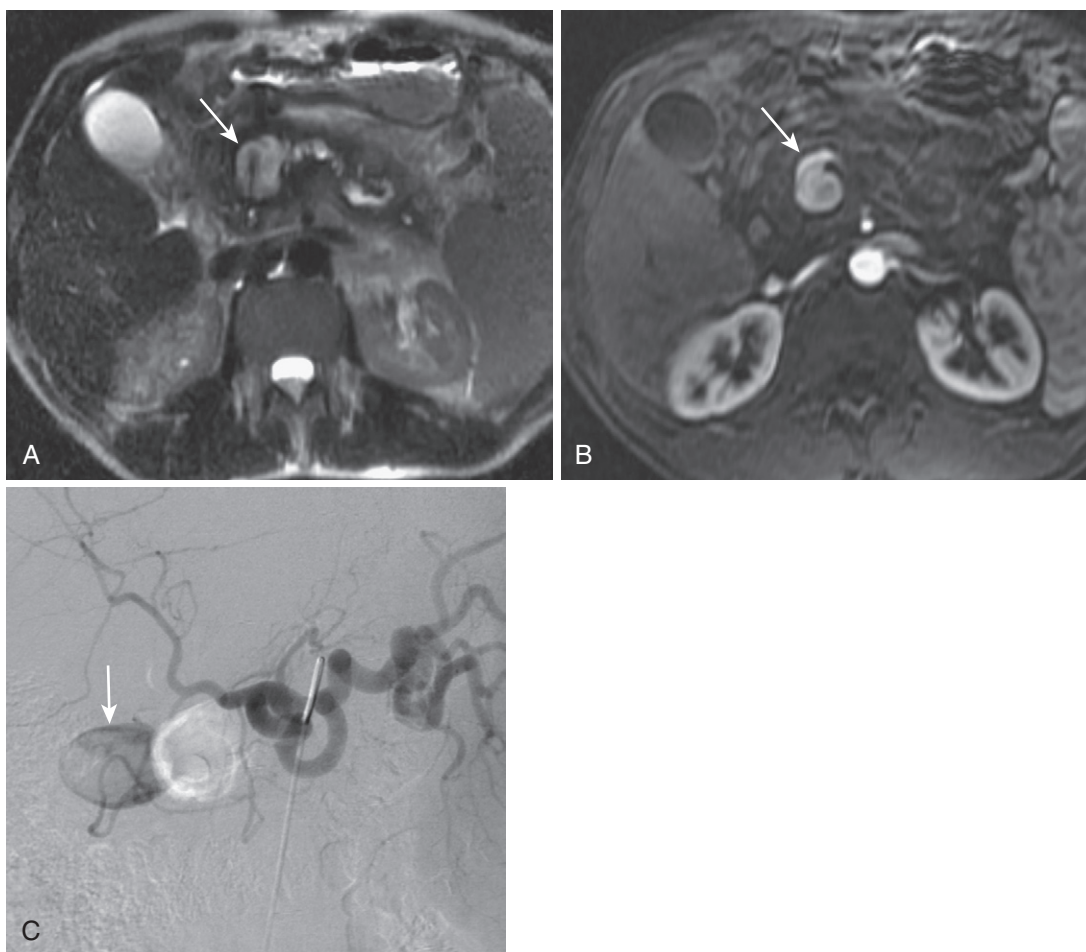


FIGURE 3-14. Arterial pseudoaneurysm complicating pancreatitis. **A,** Heavily T2-weighted image in a patient with acute or chronic pancreatitis reflected by peripancreatic inflammation and irregular ductal dilatation, respectively, shows a near–fluid-intensity lesion in the pancreatic head (*arrow*). **B,** Following intravenous contrast, the lesional enhancement (*arrow*) is equivalent to arterial enhancement, indicating arterial etiology and, specifically, a pseudoaneurysm arising from the gastroduodenal artery. **C,** The image from the celiac axis injection showed prompt enhancement (*arrow*) and confirmed direct continuity with the gastroduodenal artery.

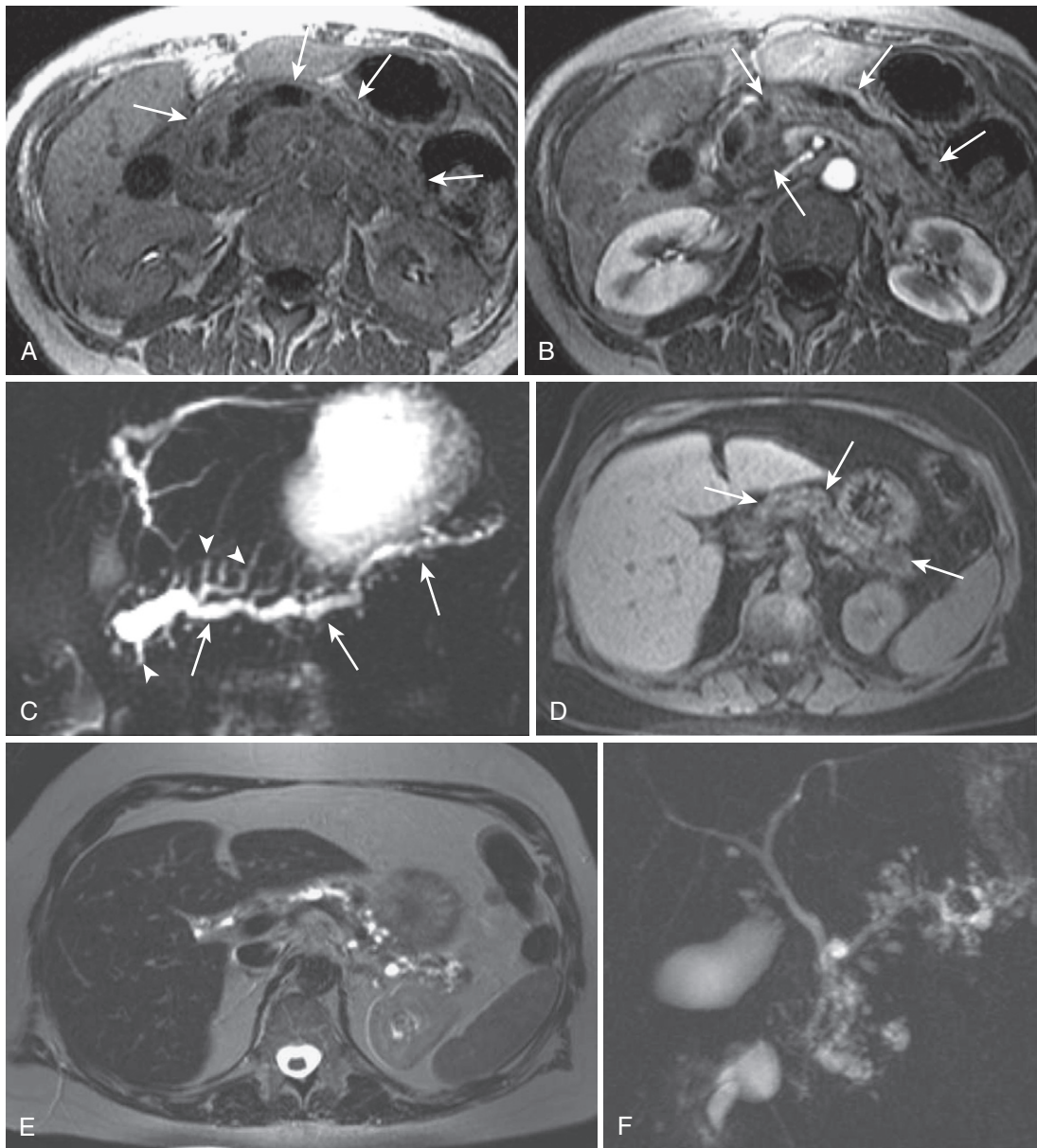


FIGURE 3-15. Chronic pancreatitis. **A**, The in-phase (T1-weighted) image through a chronically inflamed pancreas (*arrows*) reveals relative parenchymal hypointensity and irregular beaded ductal dilatation. **B**, The early phase postcontrast image shows the extent of ductal dilatation (*arrows*) in the pancreatic body and heterogeneously decreased enhancement. **C**, The MRCP image isolates the pancreatic duct (*arrows*) from the parenchyma and surrounding tissues, depicting the irregular pancreatic ductal and side branch dilatation (*arrowheads*). **D**, The T1-weighted fat-suppressed image in a different patient with chronic pancreatitis exemplifies the typical heterogeneous decrease in parenchymal signal intensity (*arrows*). The heavily T2-weighted (**E**) and MRCP (**F**) images show the associated ductal changes, typifying the “chain of lakes” or “string of pearls” appearance.

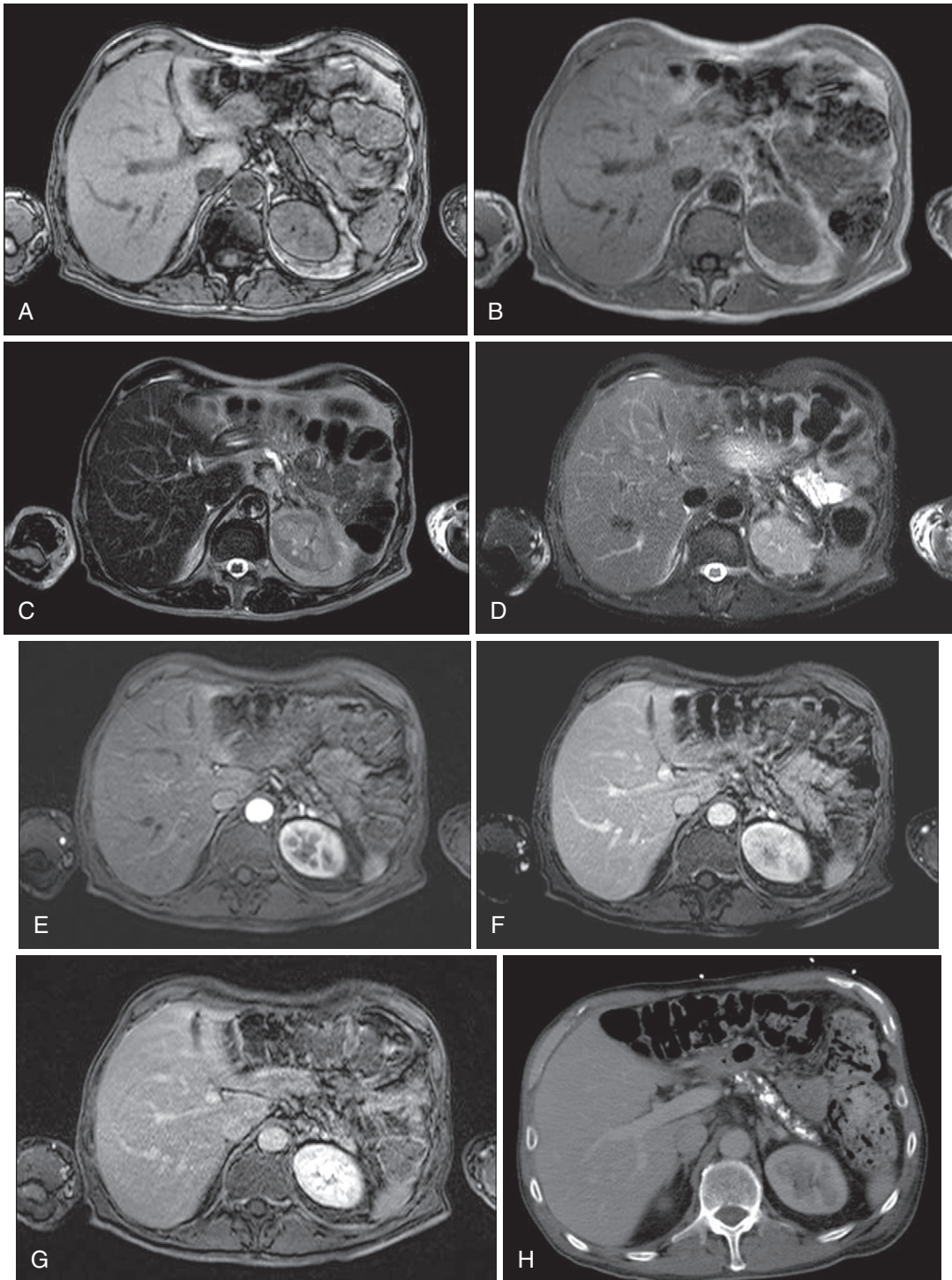


FIGURE 3-16. Chronic calcific pancreatitis. Out-of-phase (A) and in-phase (B) T1-weighted gradient recalled-echo images demonstrate atrophy of the glandular pancreatic parenchyma with blooming on the in-phase (B) image related to pancreatic calcifications. T2-weighted (C) and fat-suppressed T2-weighted (D) images of the pancreas reveal multiple areas of pancreatic duct stricturing and dilatation. Pre-contrast (E), arterial (F), and delayed (G) fat-suppressed T1-weighted gradient recalled-echo images depict the decreased T1-weighted pancreatic signal intensity with mottled early enhancement and homogeneous delayed enhancement. Enhanced computed tomography (CT; H) image better depicts the extent of pancreatic parenchymal calcification.

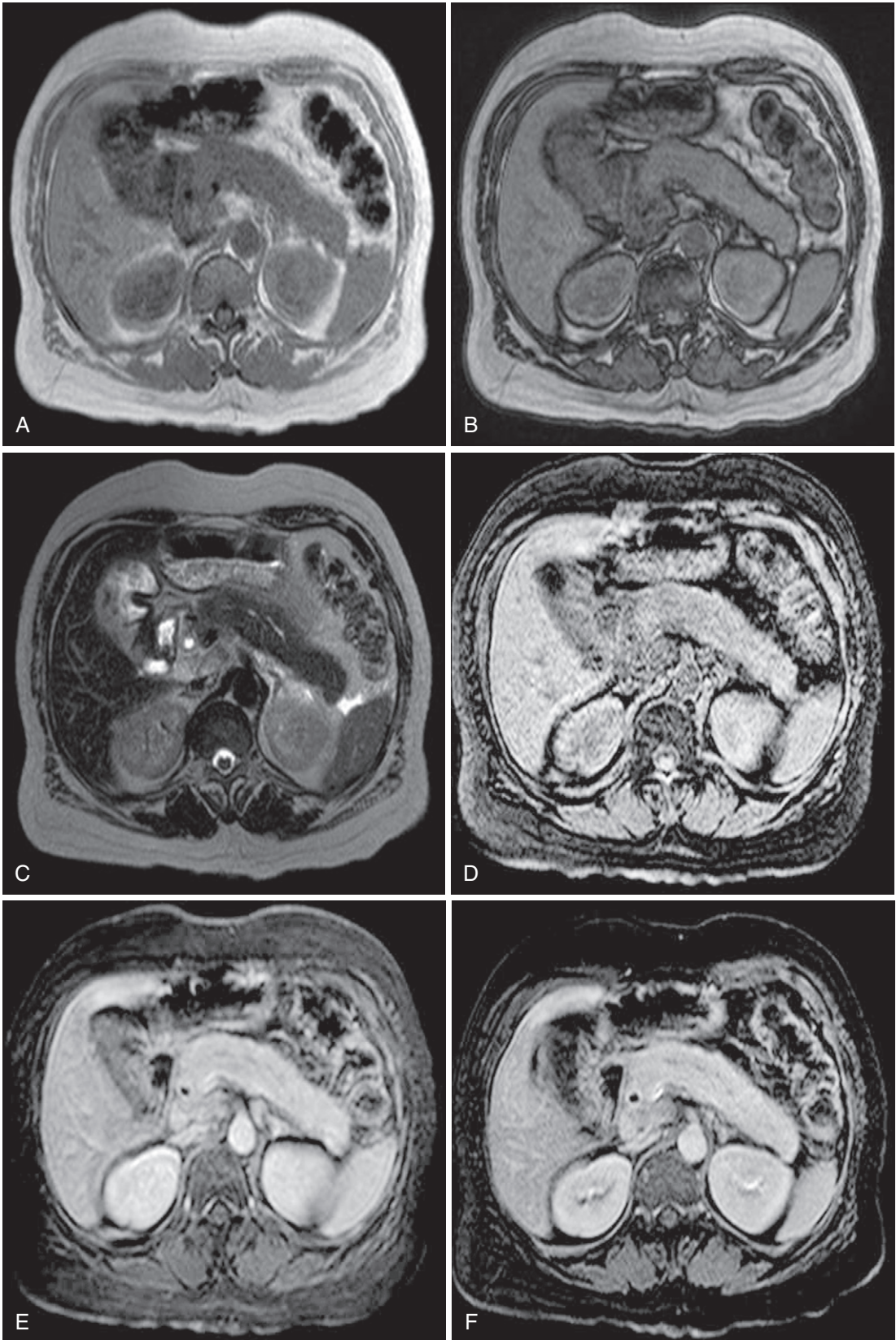


FIGURE 3-17. Autoimmune pancreatitis. In-phase (A) and out-of-phase (B) T1-weighted and T2-weighted (C) images of the pancreas demonstrate decreased T1-weighted signal intensity, a smooth contour, and focal duct dilatation in a patient with autoimmune pancreatitis. Precontrast (D), arterial (E), and delayed (F) fat-suppressed T1-weighted gradient recalled-echo images of the same patient demonstrate delayed pancreatic parenchymal enhancement.

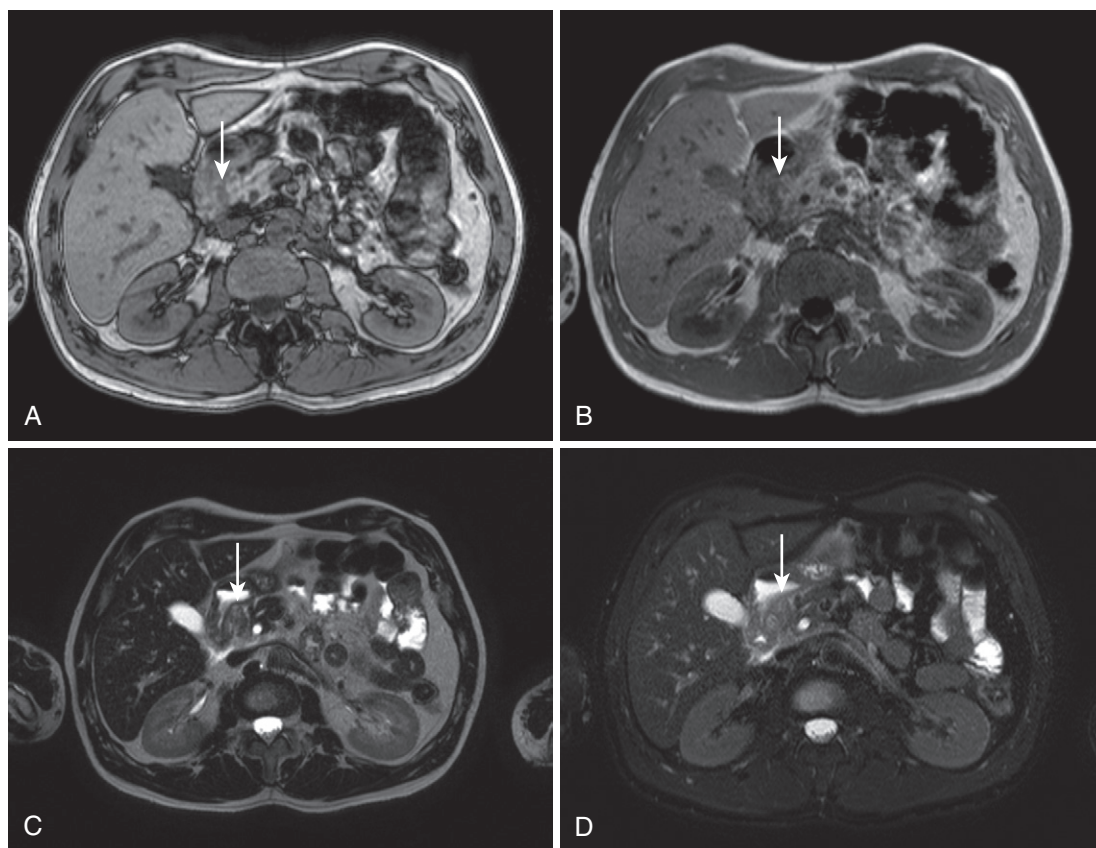


FIGURE 3-18. Groove pancreatitis. Out-of-phase (A) and in-phase (B) T1-weighted gradient recalled-echo images demonstrate decreased T1-weighted signal intensity in the pancreaticoduodenal groove with corresponding increased signal intensity on T2-weighted (C) and fat-suppressed T2-weighted (D) images (arrows) as well as retroperitoneal edema in a patient with groove pancreatitis.

change with upstream dilatation and glandular atrophy and vascular encasement favor pancreatic carcinoma. Elevated IgG and autoantibody levels and clinical response to corticosteroids favor AIP.

Groove Pancreatitis. Groove pancreatitis is a form of segmental pancreatitis occurring between the pancreatic head, the common bile duct, and the duodenum. Although usually occurring in young men with a history of alcohol abuse, the etiology and pathogenesis of groove pancreatitis remain unknown. The imaging is similar to that of acute pancreatitis; however, the focal nature of this process makes differentiation from a peripancreatic tumor difficult (Figs. 3-18 and 3-19).²¹ The characteristic MRI findings include a sheetlike mass between the second segment of the duodenum and the pancreatic head often with superimposed cysts (frequently in the duodenal wall), duodenal stenosis,

and widening of the space between the distal common bile/pancreatic ducts and the duodenal lumen (best seen on MRCP) (Fig. 3-19).²¹

Hereditary Pancreatitis. Hereditary pancreatitis is a rare autosomal dominant disease with variable penetrance leading to exocrine dysfunction. This disease arises from mutations in the trypsinogen gene. The natural history is very similar to that of chronic alcoholic pancreatitis; however, symptom onset occurs at an earlier age and there is a higher prevalence of pseudocyst formation. There is an elevated risk for the development of pancreatic adenocarcinoma (~50–60 times) with smoking increasing the risk and lowering the age of onset. Prominent pancreatic duct calcifications are a hallmark of this disease and are similar to those seen in chronic alcoholic pancreatitis; however, affliction of a much younger age group distinguishes hereditary pancreatitis (Fig. 3-20).²²

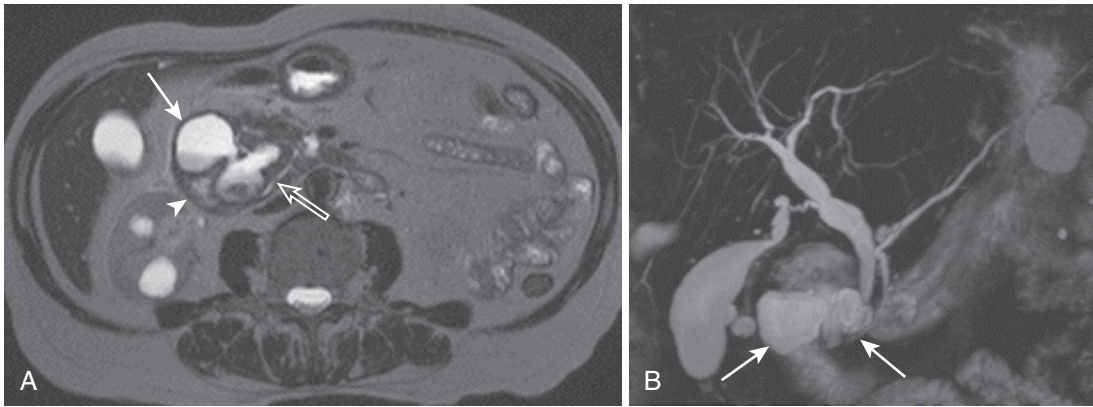


FIGURE 3-19. Cystic groove pancreatitis. A, The heavily T2-weighted image portrays a large, complex cystic lesion (*closed arrow*) in the pancreaticoduodenal groove between the duodenum (*arrowhead*) and the pancreatic head, displacing the main pancreatic duct (*open arrow*). B, The maximal intensity projection reconstructed from a 3-D MRCP shows the cystic lesion (*arrows*) between the distal CBD and the pancreatic duct and duodenum.

Genetic Disorders

CYSTIC FIBROSIS

Cystic fibrosis is an autosomal recessive disease characterized by secretory dysfunction of the exocrine pancreas. Impaired mucociliary transport results in mucous plugging of the exocrine glands. MRI findings encompass a spectrum of imaging appearances including pancreatic enlargement with complete fatty replacement with or without loss of the normal lobulated contour, pancreatic atrophy with partial fatty replacement, and diffuse atrophy of the pancreas without fatty replacement.^{23,24} Superimposed pancreatic cysts secondary to duct obstruction are another manifestation of cystic fibrosis.²⁴ Enlargement of the pancreas with complete fatty replacement is the most common imaging appearance (Fig. 3-21).²³ Fatty replacement imitates the appearance of retroperitoneal (macroscopic) fat with uniform T1 hyperintensity and signal loss on fat-suppressed images.

PRIMARY (IDIOPATHIC) HEMOCHROMATOSIS

Primary (idiopathic or genetic) hemochromatosis is an autosomal recessive disease caused by a mutation that results in excessive iron absorption from the gastrointestinal tract with deposition of iron in the liver, heart, anterior pituitary, pancreas, joints, and skin (see Chapter 2). Cardiac and pancreatic deposition progresses over time. The presence of iron deposition in the pancreas correlates with irreversible changes of cirrhosis in the liver.

MR images demonstrate decreased T1-weighted and T2-weighted pancreatic

parenchymal signal intensity (lower than skeletal muscle) due to the paramagnetic effects of iron. These paramagnetic effects are exaggerated on gradient recalled-echo images with increasing echo times; therefore, on the in-phase T1-weighted images, the pancreas will lose signal when compared with the out-of-phase images (Fig. 3-22).^{25,26}

VON HIPPEL-LINDAU DISEASE

Von Hippel-Lindau disease is an autosomal dominant condition with variable penetration (see Chapter 4). This condition is characterized by cerebellar, spinal cord, renal, and retinal hemangioblastomas and is associated with renal angioma, renal cell carcinoma, and pheochromocytoma.

Pancreatic lesions include single or multiple cysts, cystic replacement of the pancreas, microcystic adenomas, and islet cell tumors. Cysts are the most common pancreatic manifestation (Fig. 3-23).²⁷

SCHWACHMAN-DIAMOND SYNDROME

Schwachman-Diamond syndrome is a rare congenital disorder of pancreatic insufficiency, growth retardation, and other congenital abnormalities. Imaging demonstrates extensive replacement of the pancreatic tissue with fat.

JOHANSON-BLIZZARD SYNDROME

Johanson-Blizzard syndrome is an autosomal recessive disorder of ectodermal dysplasia with both endocrine and exocrine insufficiency. The primary defect is in the acinar cells with fatty replacement occurring over time.

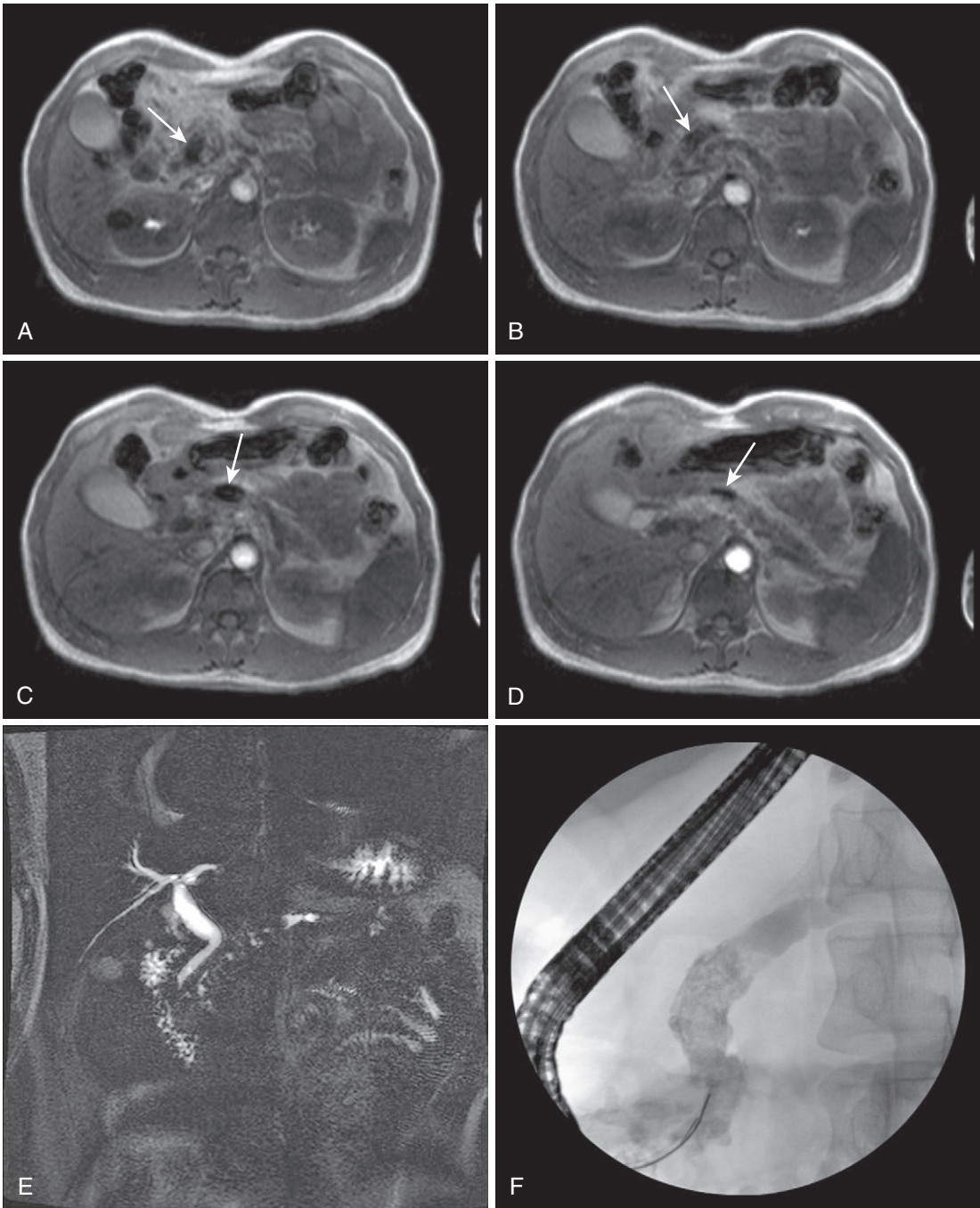


FIGURE 3-20. Hereditary pancreatitis. Four in-phase T1-weighted gradient recalled echo (A–D) and coronal thick-slab maximal intensity projectional MRCP (E) images through the pancreas demonstrate blooming within the head and proximal body of an atrophic pancreas with decreased T1-weighted signal intensity related to ductal calcification (*arrows*), better seen on the fluoroscopic spot radiograph (F), in a patient with hereditary pancreatitis.

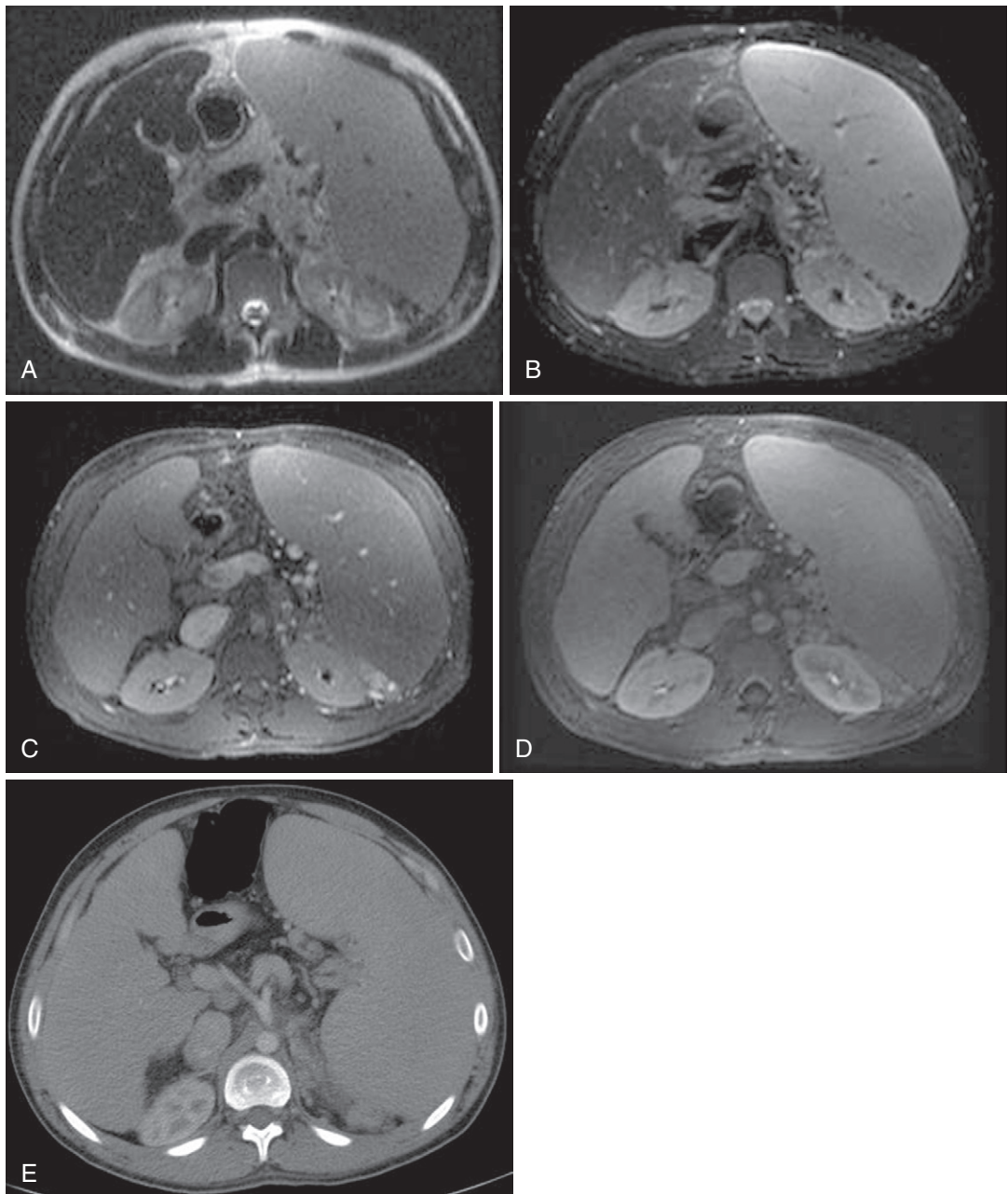


FIGURE 3-21. Cystic fibrosis. T2-weighted (A), fat-suppressed T2-weighted (B), venous phase (C), and delayed phase (D) postcontrast fat-suppressed T1-weighted gradient recalled-echo images and unenhanced CT image (E) demonstrate complete fatty replacement of the pancreas in a patient with cystic fibrosis.

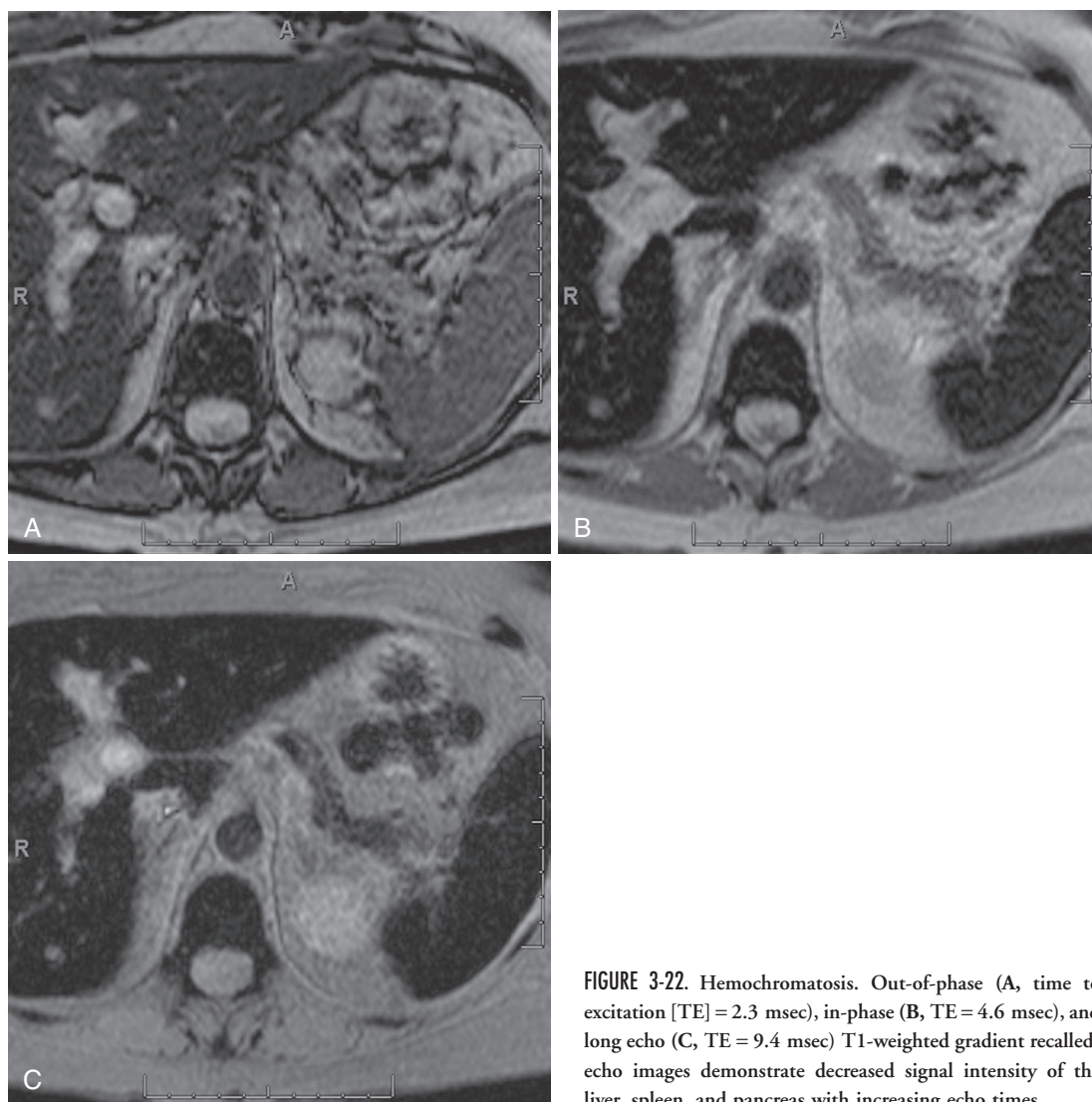


FIGURE 3-22. Hemochromatosis. Out-of-phase (A, time to excitation [TE] = 2.3 msec), in-phase (B, TE = 4.6 msec), and long echo (C, TE = 9.4 msec) T1-weighted gradient recalled-echo images demonstrate decreased signal intensity of the liver, spleen, and pancreas with increasing echo times.

Both Schwachman-Diamond and Johanson-Blizzard syndromes have preserved ductal output of fluid and electrolytes.

Focal Pancreatic Lesions

Focal pancreatic lesions stratify into two basic categories: cystic and solid (Fig. 3-24). The distinction helps lower the suspicion of malignancy—solidity usually implies malignancy. Solid tissue raises the specter of pancreatic adenocarcinoma—the diagnosis of exclusion. Cystic etiology incurs a better prognosis but still threatens malignancy in the form of intraductal papillary mucinous neoplasm (IPMN), cystic metastases, and other conditions. T2-weighted sequences and postcontrast imaging collude to establish cystic versus solid

tissue. Marked hyperintensity on T2-weighted sequences, indicating free water protons, characterizes cystic lesions. Postcontrast images bear binary information: enhancement = solid (enhancement) versus cystic (absent enhancement). The discrimination between lesions within cystic and solid categories becomes more difficult. Specific features within each category (discussed later) narrow the differential diagnosis.

SOLID PANCREATIC LESIONS

The two most common solid pancreatic neoplasms are adenocarcinoma and neuroendocrine tumors. These lesions have drastically different enhancement patterns and establish the archetypal enhancement categories—hypovascular and hypervascular, respectively.

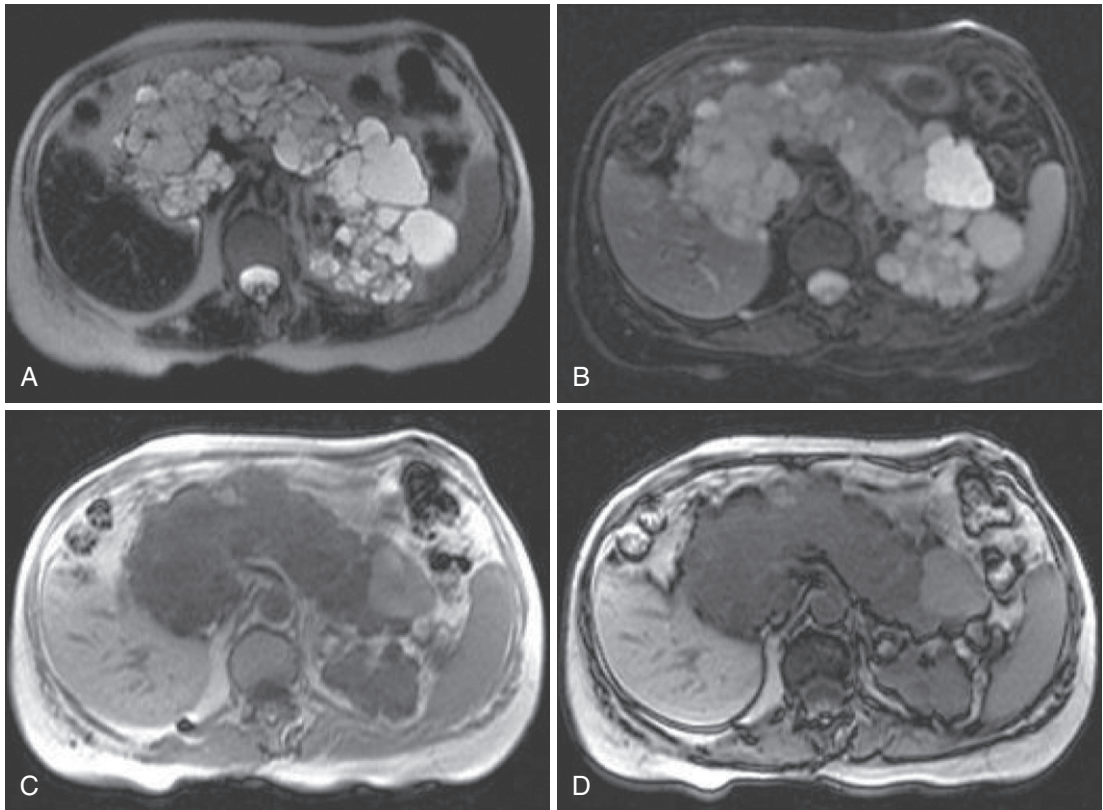


FIGURE 3-23. von Hippel-Lindau disease. T2-weighted (A), fat-suppressed T2-weighted (B), in-phase T1-weighted (C), and out-of-phase T1-weighted (D) images of cystic pancreatic replacement in a patient with von Hippel-Lindau disease.

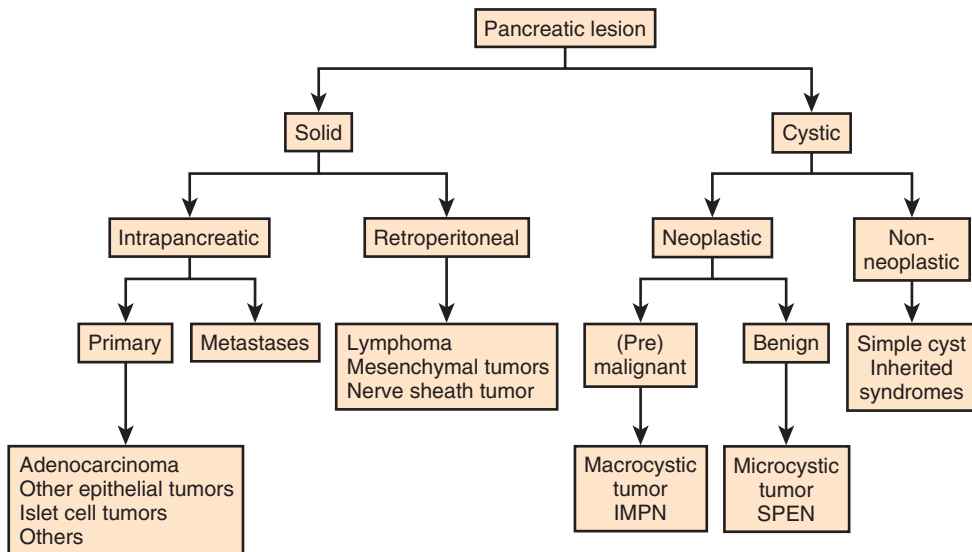
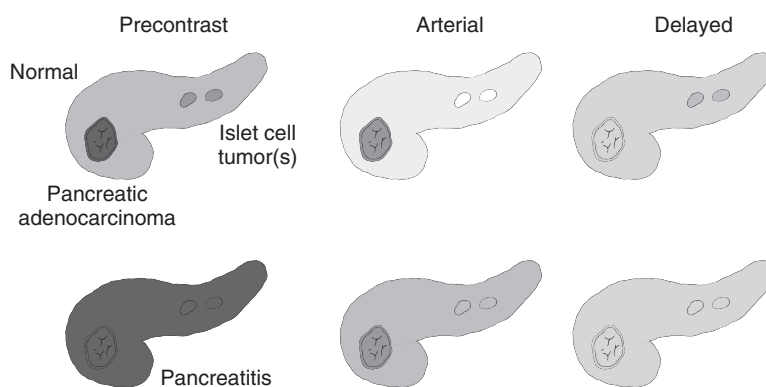


FIGURE 3-24. Focal pancreatic lesion scheme. IMPEN = intraductal mucinous papillary neoplasm; SPEN = solid-cystic papillary epithelial neoplasm.

Pancreas – T1 Appearance of Solid Lesions

FIGURE 3-25. Pancreatic lesion enhancement patterns. **Top,** In the normal pancreas, most solid lesions appear relatively hypointense on T1-weighted images. **Middle,** Because of the normal avid pancreatic arterial enhancement, most solid lesions are relatively hypovascular, with the notable exception of islet cell tumors. **Bottom,** The T1 hypointensity associated with pancreatitis often renders lesions less conspicuous.



These designations depend on comparison with the background pancreatic parenchyma (Fig. 3-25). Under normal circumstances, the pancreatic parenchyma avidly enhances, approximating the hypervascularity of islet cell tumors and significantly out-enhancing hypovascular pancreatic adenocarcinoma. However, with coexistent pancreatitis, pancreatic parenchymal enhancement (and precontrast signal intensity) drops, closely simulating adenocarcinoma. For this reason, the pancreatic lesion assessment depends on the status of the background pancreatic parenchyma.

Pancreatic Adenocarcinoma. Pancreatic adenocarcinoma is the most common pancreatic malignancy, accounting for approximately 95% of all pancreatic malignant tumors. Based on incidence rates from 2004 to 2006, approximately 1.4% of all men and women born today will be diagnosed with pancreatic adenocarcinoma at some time during their lifetime. Pancreatic adenocarcinoma is the fifth leading cause of cancer death in the United States, mainly attributable to the extremely poor survival: less than 20% of newly diagnosed patients survive the first year. There is an overall dismal prognosis with 5-year survival rates between 4.5% and 6%. Patients with localized disease at diagnosis have improved survival rates relative to those with advanced disease at diagnosis (22% 5-year survival for those with localized disease vs. 2% for those with distant metastases). Pancreatic adenocarcinoma predominantly affects the elderly population, with 80% of patients diagnosed older than 60 years, with the median age at diagnosis being 72 years. The majority of cases of pancreatic adenocarcinoma occurs within

the head of the pancreas and presents with either jaundice, weight loss, pain, or nausea. Carbohydrate antigen 19-9 (CA 19-9) has been shown to be an effective diagnostic serum tumor marker with good sensitivity and specificity.^{28,29}

Pancreatic adenocarcinoma is typically hypointense compared with the normal pancreatic parenchyma on T1-weighted imaging (Fig. 3-26; see also Fig. 3-25). Fat suppression increases lesion conspicuity by increasing the dynamic range between the low signal intensity tumor and the higher signal intensity of the normal parenchyma. Tumors have variable signal intensity on T2-weighted imaging depending on the degree of hemorrhage, necrosis, and inflammatory changes. In general, T2-weighted imaging is less helpful than T1-weighted imaging because of the poor contrast between the mass and the normal pancreas. Pancreatic adenocarcinoma is usually hypovascular to the normal glandular tissue on arterial phase imaging followed by gradual enhancement on delayed imaging, related to its desmoplastic content (see Fig. 3-25). Immediate contrast-enhanced imaging is the most sensitive for detecting pancreatic adenocarcinoma, especially in lesions that are small or do not deform the contour of the normal pancreas (Fig. 3-27). Obstruction of the main pancreatic duct is one of the most common findings in pancreatic adenocarcinoma (Fig. 3-28). Contiguous obstruction of the pancreatic and common bile ducts due to the presence of a pancreatic head mass is known as the “double duct” sign and is highly suggestive of malignancy (Fig. 3-29).³⁰⁻³² Because pancreatic adenocarcinomas frequently progress undetected until inciting symptoms, distal gland

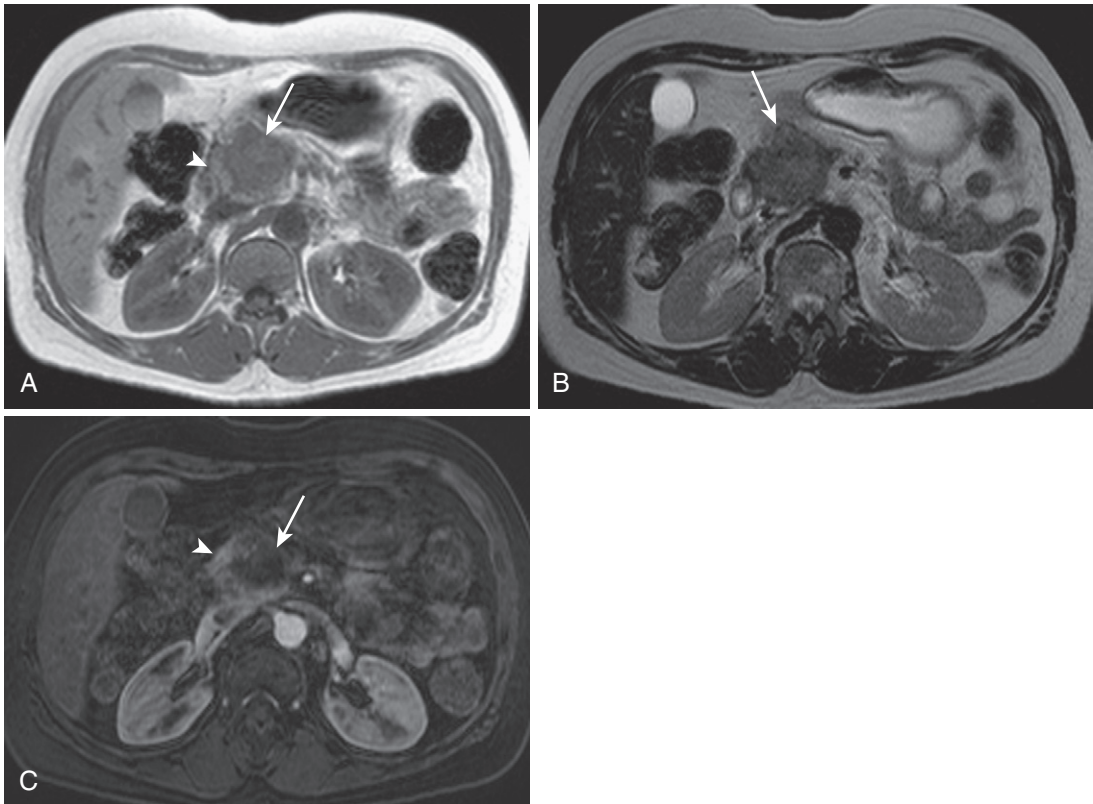


FIGURE 3-26. Pancreatic adenocarcinoma. **A**, The in-phase (T1-weighted) image in a patient with pancreatic adenocarcinoma in the pancreatic head (*arrow*) shows relative hypointensity compared with normal parenchyma (*arrowhead*). **B**, The T2-weighted image exemplifies the usual hypointensity (*arrow*) with little contrast between normal tissue and neoplasm. **C**, The enhanced image bears the highest tissue contrast between the lesion (*arrow*) and normal pancreatic tissue (*arrowhead*).

atrophy is often associated with the aforementioned duct dilatation.³³

In the setting of underlying pancreatitis, detecting underlying adenocarcinoma is problematic because both the tumor and the surrounding pancreas demonstrate similar T1 hypointensity. However, immediate contrast-enhanced images better delineate the size and extent of pancreatic adenocarcinomas, which tend to enhance less than adjacent inflamed pancreatic parenchyma (see Fig. 3-25).³³ However, focal pancreatitis presents diagnostic difficulty because focal pancreatic enlargement, distortion of the normal glandular contour, ductal dilatation, and abnormal enhancement simulate pancreatic adenocarcinoma. Short-term follow-up imaging after resolution of the acute illness hopefully eliminates equivocation.

For the majority of cases, the diagnosis of pancreatic adenocarcinoma is straightforward and the role of imaging is to determine resectability (Fig. 3-30).³⁴ Among the factors preempting respectability and surgical cure, distant

metastases and local spread account for most cases (40% each). Because the pancreas lacks a capsule to obstruct neoplastic spread and because most lesions arise in the pancreatic head densely surrounded by adjacent structures, regional spread proceeds rapidly (Fig. 3-31). Pancreatic continuity with the superior mesenteric vessels promotes vascular encasement of these vessels, which also precludes curative surgical resection. Vessel enhancement of 180° constitutes vascular encasement (see Fig. 3-31). Metastatic spread progresses from regional lymph nodes to the liver and, uncommonly, to the lungs. In addition to direct invasion of adjacent structures, such as the duodenum and stomach, spread to any peritoneal surface is at risk from peritoneal dissemination.

Pancreatic Neuroendocrine (Islet Cell) Tumors. Neuroendocrine (islet cell) tumors are uncommon, slow-growing pancreatic or peripancreatic masses that may result in symptomatic hormonal overproduction (and,

Text continued p. 156

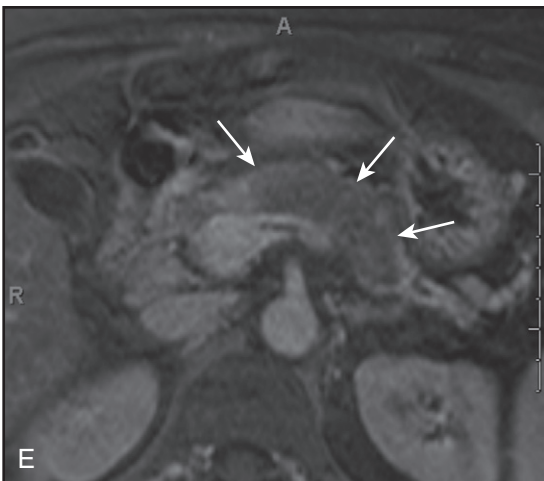
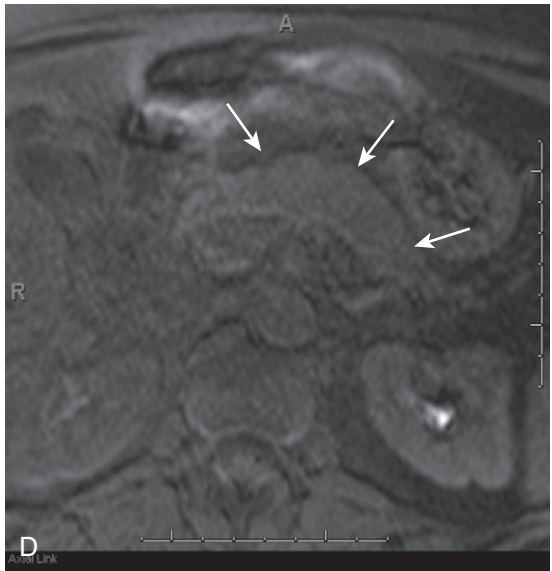
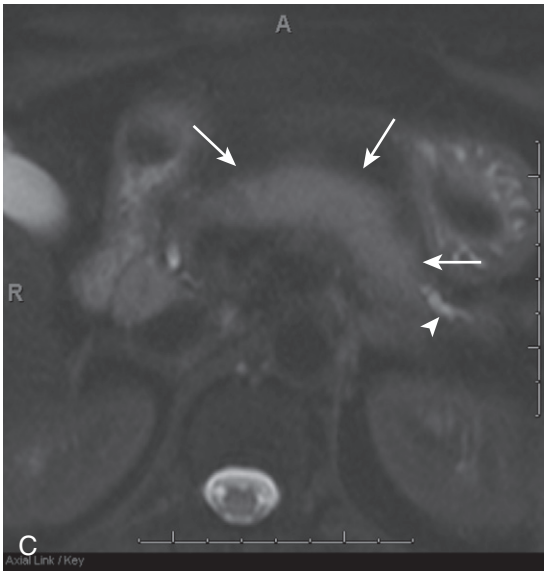
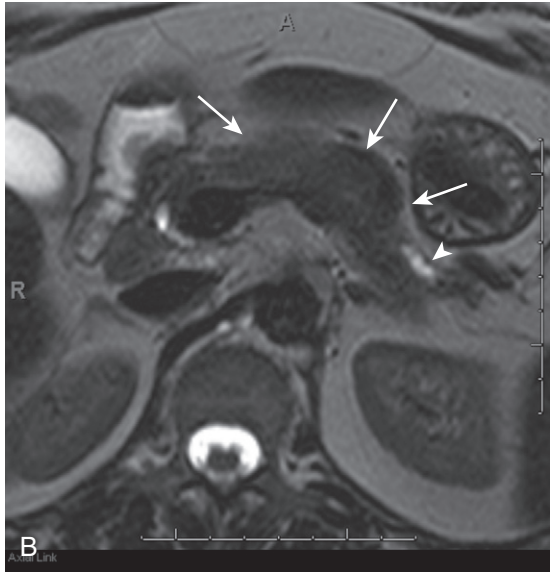


FIGURE 3-27. Pancreatic adenocarcinoma—arterial phase imaging. Infiltrative mass enlarges the body of the pancreas (*arrows*), which can be seen on the in-phase T1-weighted (A) and the precontrast fat-suppressed T1-weighted gradient recalled-echo (D) images in contrast to the normal pancreatic parenchyma in the head of the pancreas. This mass demonstrates mildly increased signal intensity on T2-weighted imaging (B), which is pronounced on fat-suppressed T2-weighted imaging (C). In addition, distal gland atrophy and duct dilatation (*arrowheads*) can be seen on the T2-weighted (B) and fat-suppressed T2-weighted (C) images. Furthermore, this mass demonstrates decreased enhancement when compared with the normal pancreas, most pronounced on early arterial phase fat-suppressed T1-weighted gradient recalled-echo imaging (E), with gradual enhancement on delayed phase fat-suppressed T1-weighted gradient recalled-echo imaging (F) related to desmoplastic content.

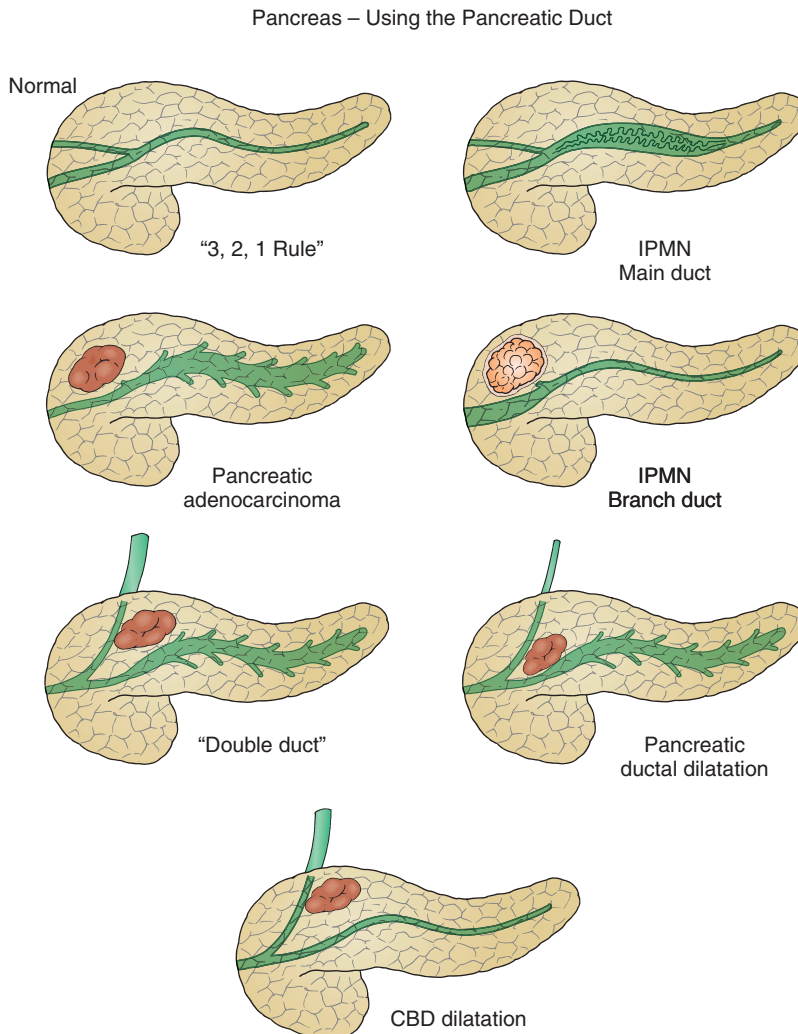


FIGURE 3-28. The pancreatic duct differential. The normal pancreatic duct measures 3 mm in the head of the pancreas, tapering to 2 mm in the body. The normal accessory duct of Santorini measures 1 mm. In the setting of pancreatic adenocarcinoma, there is dilatation of the duct and possibly its side branches, upstream from the lesion. Intraductal papillary mucinous neoplasms (IPMNs) secrete mucin and, therefore, have downstream duct dilatation. Main duct IPMN harbors a higher malignant potential; concern for development of adenocarcinoma within these lesions should increase when there are papillary projections/internal architecture and/or enhancement. In contradistinction to IPMN, dilatation occurs proximal to the lesion in pancreatic adenocarcinoma. The pattern of pancreatic and/or common bile duct (CBD) dilatation in pancreatic adenocarcinoma depends on the location of the lesion. Three basic patterns include (1) the “double duct sign,” referring to dilatation of both the CBD and the pancreatic duct, (2) pancreatic ductal dilatation, and (3) isolated CBD dilatation.

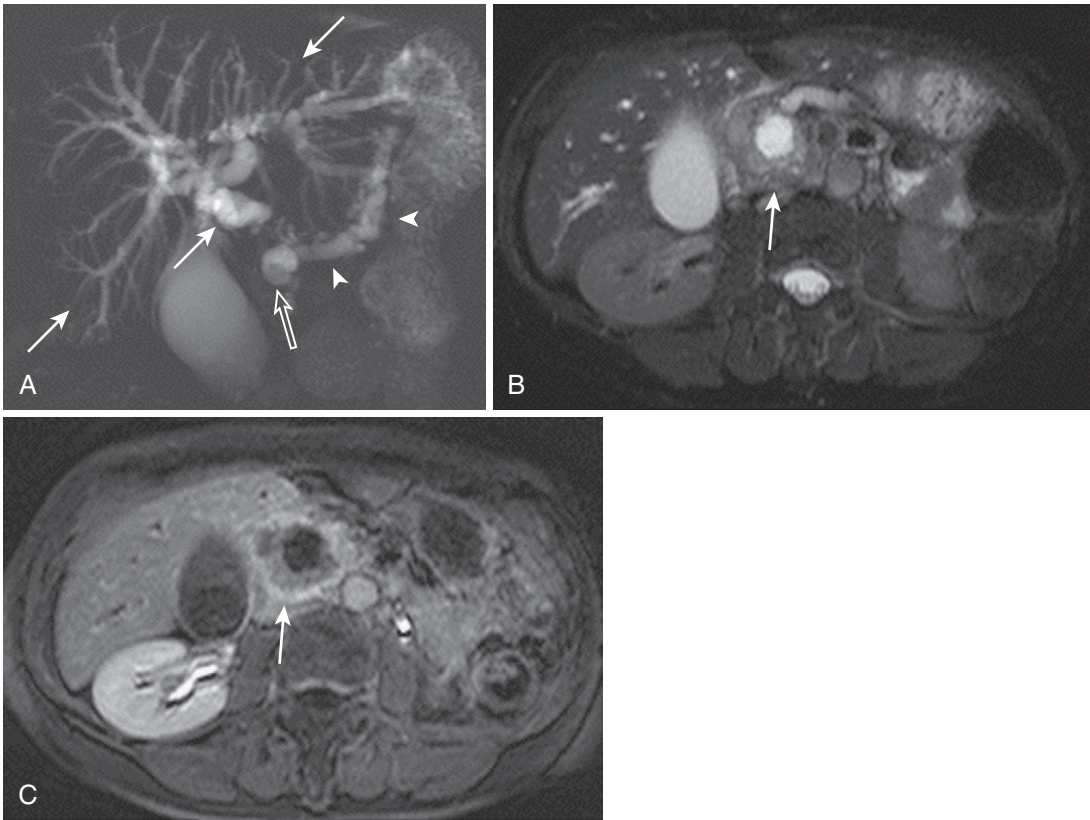
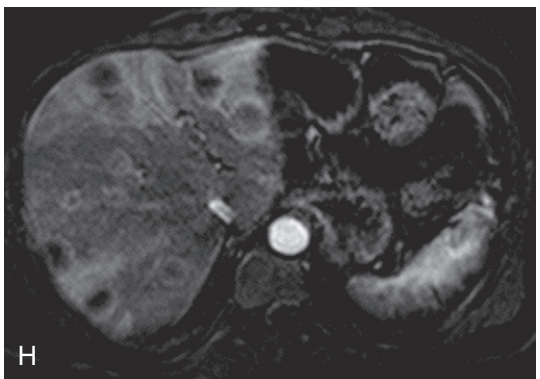
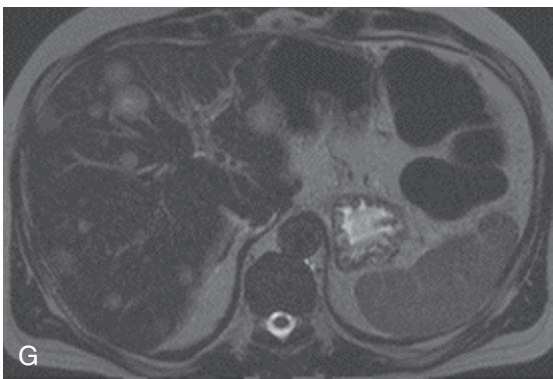
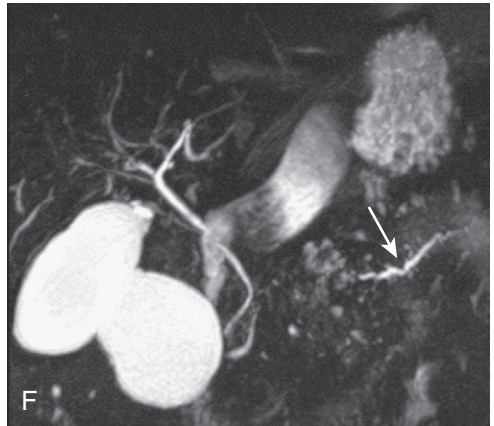
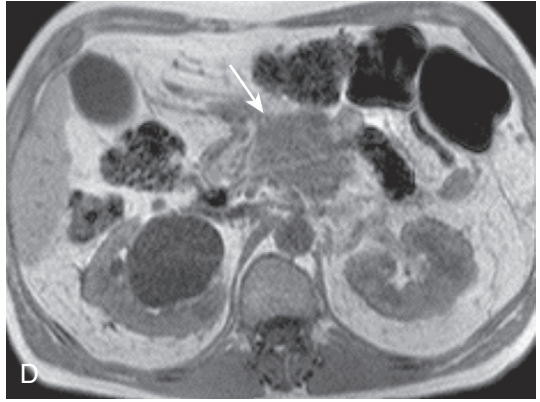
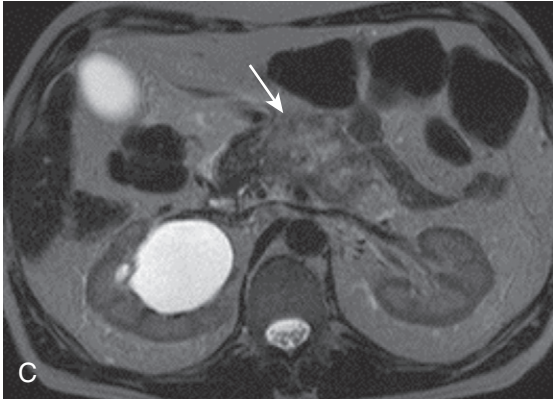


FIGURE 3-29. Pancreatic adenocarcinoma—the double duct sign. **A**, The MRCP image shows marked biliary (*closed arrows*) and pancreatic (*arrowheads*) dilatation, abruptly terminating at the level of the pancreatic head, where there is a cystic lesion (*open arrow*). The fat-suppressed T2-weighted (**B**) and postcontrast (**C**) images reveal the obstructing pancreatic head mass (*arrow*) with central necrosis, accounting for the cystic lesion on the MRCP image.

- Liver metastases
- Vascular encasement (180°)
- Peritoneal implants
- Peripancreatic spread
- Size >3 cm
- Adenopathy
 - Retroperitoneal
 - Mesenteric

FIGURE 3-30. Factors predisposing to unresectability in pancreatic cancer.

FIGURE 3-31. Pancreatic adenocarcinoma—regional and metastatic spread. **A**, The T2-weighted image shows an ill-defined hypointense lesion (*closed arrow*) inducing upstream pancreatic ductal dilatation (*arrowhead*) and confluent peripancreatic tissue indicating local spread (*open arrow*). **B**, The early phase postcontrast image depicts the hypovascularity of the pancreatic mass (*arrow*) with encasement of the superior mesenteric artery (*arrowheads*). T2-weighted (**C**), in-phase T1-weighted (**D**), and arterial phase postcontrast (**E**) images show a large, mildly hyperintense mass (*arrow*) in a different patient with pancreatic adenocarcinoma, which causes upstream pancreatic ductal dilatation (*arrow*), demonstrated on the MIP image (**F**) from a 3-D MRCP. Multiple T2-hyperintense, hypovascular metastases are visible on the T2-weighted (**G**) and postcontrast (**H**) images.



ISLET CELL TUMORS

Tumor	Cell	Malignancy rate	Clinical	Imaging
Insulinoma	Beta	10%	Hypoglycemia	Small, solitary
Gastrinoma	Alpha-1	60%	Zollinger-Ellison syndrome	Small, may be multiple, ectopic
Glucagonoma	Alpha-2	80%	Diabetes mellitus	Larger, usually body and tail
VIPoma	Delta-1	50%	Watery diarrhea, hypokalemia, achlorhydria (WDHA) syndrome	Large, usually body and tail
Somatostatinoma	Delta	67%	Diarrhea, weight loss	Large, usually head
Non-functioning		Usually	Abdominal pain, jaundice	Very large

FIGURE 3-32. Islet cell tumor types.

therefore, are called functional) or elicit no clinical findings of hormone production (and, therefore, called nonfunctional). Incidence of pancreatic neuroendocrine tumors is 1 to 1.5 per 100,000 in the general population. Functioning neuroendocrine tumors manifest earlier owing to symptoms of hormone overproduction and are named according to the hormone they produce (Fig. 3-32).

Neuroendocrine tumors are well depicted on MRI because of the high contrast between the high T1-weighted signal intensity of the normal pancreatic parenchyma and the low T1-weighted signal intensity of the tumor, and potentially because of their typical hypervascular enhancement.³⁵ Fat-suppressed T2-weighted images often demonstrate high signal intensity components within the tumor compared with the adjacent pancreatic parenchyma.³⁶ Less frequently, tumors may demonstrate hypointense or isointense T2-weighted signal intensity to the adjacent pancreas secondary to increased fibrous tissue content (Fig. 3-33).³⁵

Insulinomas. Insulinomas are the most common functional neuroendocrine tumors and often present with symptomatic hypoglycemia secondary to insulin oversecretion. These tumors are frequently benign, are usually solitary, are less than 2 cm in size, and occur equally throughout all parts of the pancreas.

At imaging, insulinomas demonstrate decreased T1-weighted signal intensity on T1-weighted images with homogeneously increased T2-weighted signal intensity and marked contrast

enhancement with dynamic imaging (Fig. 3-34).³⁶

Gastrinomas. Gastrinomas are the second most common functional neuroendocrine tumor. Increased gastrin secretion results in a fulminant peptic ulcer disease known as *Zollinger-Ellison syndrome*. Approximately 75% of gastrinomas are sporadic, with the remaining 25% occurring as part of the multiple endocrine neoplasia (MEN)-I syndrome. Tumors are generally less than 4 cm in size. Most gastrinomas are located within the “gastrinoma triangle,” which is bounded by the cystic duct, second and third portion of the duodenum, and the pancreatic neck. Approximately 60% to 80% of gastrinomas are malignant but follow a protracted or indolent course.

Gastrinomas typically demonstrate decreased T1-weighted signal intensity on T1-weighted images, increased signal intensity on T2-weighted images, and smooth rim enhancement after contrast administration.³⁶

Glucagonomas, VIPomas, and Somatostatinomas. Glucagonomas, VIPomas, and somatostatinomas are functional neuroendocrine tumors that are not frequently detected until later in the disease course because the clinical findings related to hormonal overproduction are nonspecific. As such, they are frequently larger (3–5 cm) at the time of diagnosis. The majority of these less common functional neuroendocrine tumors are malignant.

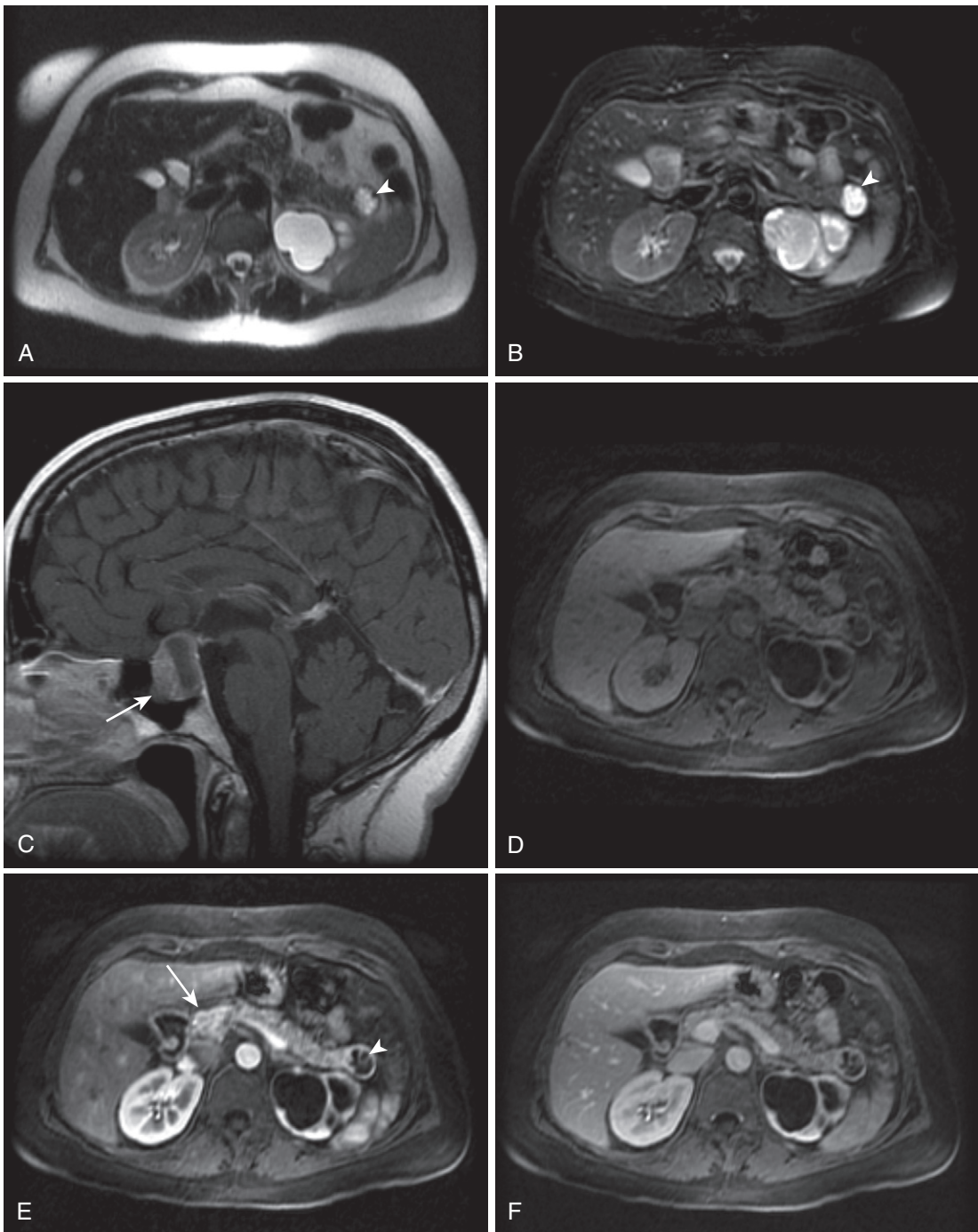


FIGURE 3-33. Islet cell tumor. T2-weighted (A), fat-suppressed T2-weighted (B), and dynamic precontrast (D), early arterial phase (E), and late arterial phase (F) 3-D fat-suppressed T1-weighted gradient recalled-echo images demonstrate two arterial enhancing lesions in the pancreas. The solid lesion (*arrow*) is best appreciated on the early arterial phase image (E), and the cystic lesion (*arrowhead*) is best identified on the fat-suppressed T2-weighted image (B). These lesions in a patient with a pituitary adenoma (identified on the sagittal T1-weighted image [C] of the brain [*arrow*]) and a known parathyroid adenoma are solid and cystic islet cell tumors in the setting of multiple endocrine neoplasia (MEN)-I or Wermer's syndrome.

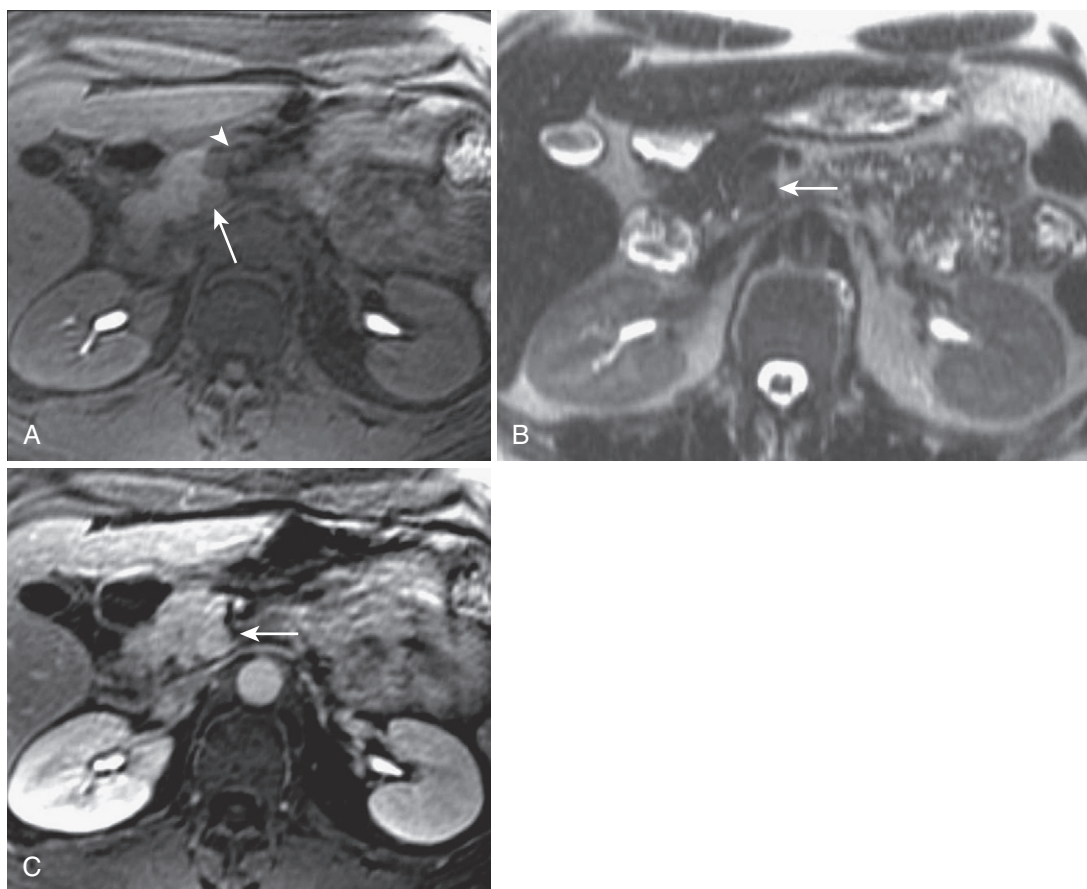


FIGURE 3-34. Insulinoma. A, The precontrast T1-weighted fat-suppressed image in a patient with hyperinsulinemia reveals a small hypointense lesion (*arrow*) in the uncinate process behind the superior mesenteric vessels (*arrowhead*). The T2-weighted image (B) shows mild lesional hyperintensity (*arrow*) and the postcontrast image (C) demonstrates the hypervascularity typical of an insulinoma (*arrow*).

At imaging, all three of these less common functional neuroendocrine tumors demonstrate decreased T1-weighted signal intensity, increased T2-weighted signal intensity, and heterogeneous solid enhancement after contrast administration.³⁶

Nonfunctioning Islet Cell Tumors. Nonfunctioning islet cell tumors may be discovered incidentally or when abdominal pain is induced by mass effect or metastatic disease (Fig. 3-35). Nonfunctioning tumors are typically large and have foci of cystic degeneration and necrosis on T2-weighted imaging with associated heterogeneous enhancement (see Fig. 3-35).³⁷ More than 50% of nonfunctioning tumors are malignant, demonstrating local invasion and distant metastatic disease; therefore, they have poor prognosis compared with functioning tumors.

Pancreatic Metastases. Metastatic disease to the pancreas is uncommon, occasionally arising from tumors with hematogenous spread, such as renal cell carcinoma, lung carcinoma, breast carcinoma, colon carcinoma, and melanoma.

Differentiation of metastatic disease to the pancreas from pancreatic adenocarcinoma is important because metastases portend a better prognosis. Metastases in general are hypointense in signal intensity on T1-weighted images relative to the normal pancreatic parenchyma; however, unlike pancreatic adenocarcinoma, metastases tend to demonstrate homogeneous or heterogeneous enhancement compared with the hypovascularity of pancreatic adenocarcinoma.³⁸ Furthermore, certain metastases may be diagnosed based on their imaging characteristics, which are similar to the primary tumor. For example, melanomas metastases may

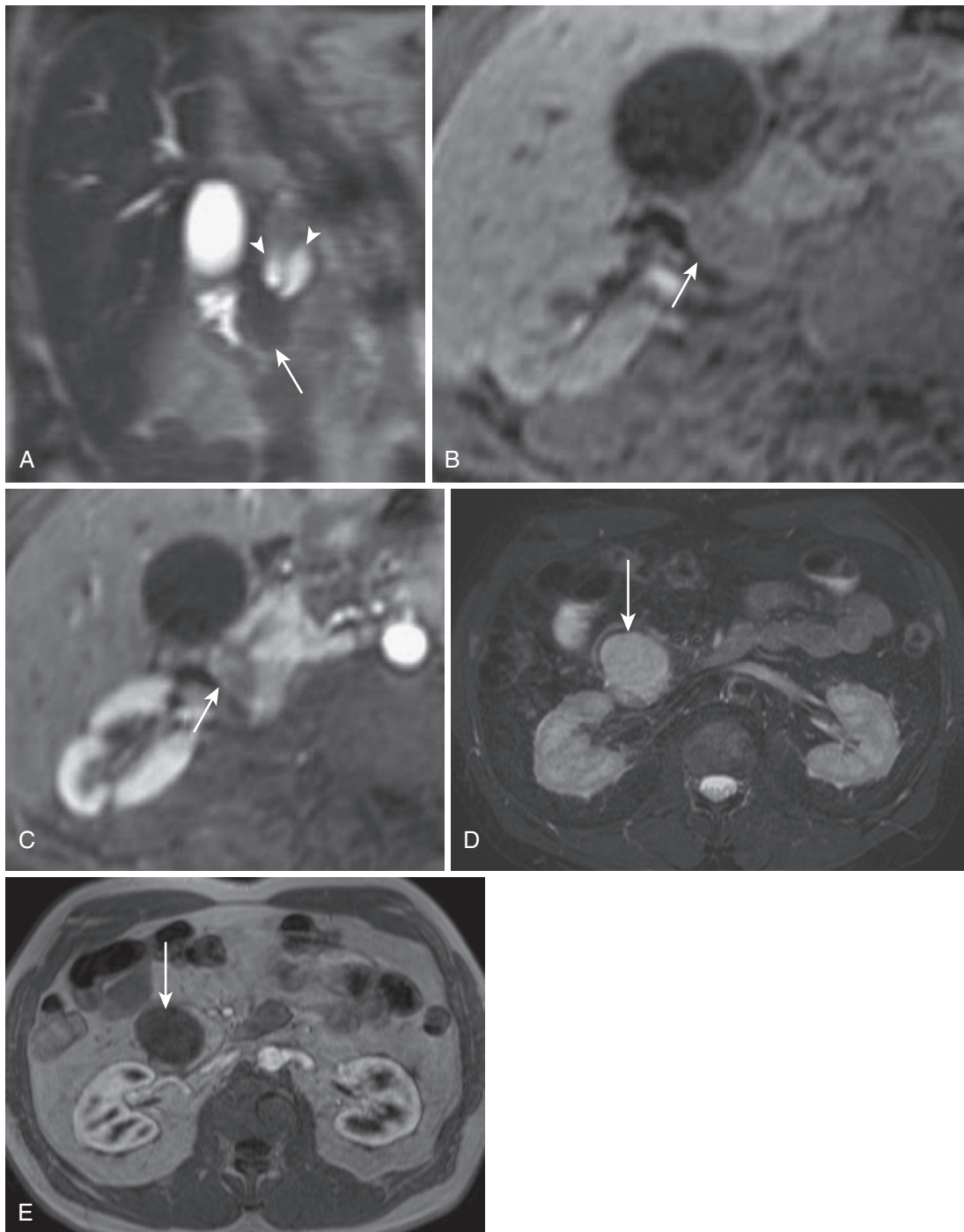


FIGURE 3-35. Nonfunctioning islet cell tumors. **A**, The T2-weighted image shows a small polypoid lesion in the ampullary region (*arrow*) obstructing the CBD and pancreatic duct (*arrowheads*). Precontrast (**B**) and postcontrast (**C**) images demonstrate corresponding lesional T1 hypointensity and hypovascularity (*arrow*) in this small nonfunctional islet cell tumor presenting with biliary obstruction. A large nonfunctional islet cell tumor in the pancreatic head (*arrow*) in a different patient demonstrates marked hyperintensity on the T2-weighted image (**D**) and absent enhancement on the postcontrast image (**E**).

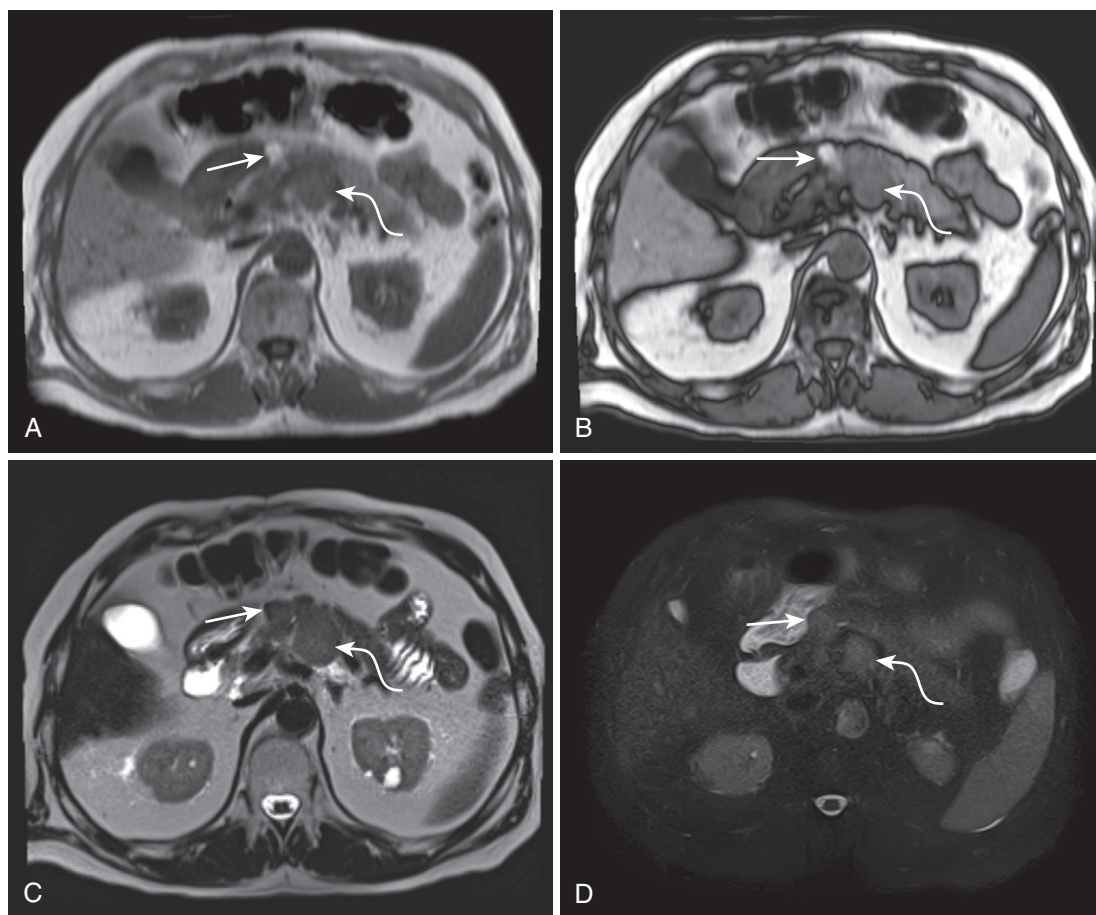


FIGURE 3-36. Pancreatic melanotic melanoma metastases. In-phase (A) and out-of-phase (B) T1-weighted gradient recalled-echo, T2-weighted (C) and fat-suppressed T2-weighted (D), and precontrast (E), arterial (F), and delayed (G) fat-suppressed T1-weighted gradient recalled-echo images of two pancreatic melanoma metastases. One of these metastases contains more melanin (*straight arrow*), increasing its T1-weighted signal intensity compared with the other lesion (*curved arrow*). Both metastases are slightly hyperintense to the pancreas on the T2-weighted images (more pronounced with fat suppression owing to increased dynamic range). The metastases demonstrate varied enhancement on postcontrast imaging.

demonstrate elevated T1-weighted signal intensity secondary to intratumoral hemorrhage or the paramagnetic properties of melanin (Fig. 3-36). Clear cell type renal cell carcinoma metastases potentially harbor microscopic lipid, mirroring the primary lesion (Fig. 3-37).

Other Solid Pancreatic Lesions

Acinar Cell Carcinoma. Although acinar cells constitute approximately 80% of the pancreatic parenchyma, acinar cell carcinoma of the pancreas is a rare malignancy, accounting for 1% of pancreatic exocrine tumors and occurs primarily in men. This neoplasm is occasionally associated with a syndrome of subcutaneous and intraosseous fat necrosis and polyarthralgia due to the release of lipase.

Imaging findings are nonspecific and vary from a large mass with an enhancing capsule and areas of necrosis to a hyperenhancing mass similar to a neuroendocrine tumor.³⁸

Lymphoma. Primary pancreatic lymphoma is very rare. However, secondary involvement of the pancreas occurs in approximately 30% of non-Hodgkin's lymphoma involving peripancreatic and para-aortic lymph nodes.

Imaging findings typically include lymphadenopathy with direct extension and infiltration of the pancreas. The pancreatic infiltration and lymph nodes have similar imaging characteristics, including low T1-weighted signal intensity, variable T2-weighted signal intensity, and decreased enhancement in comparison with the

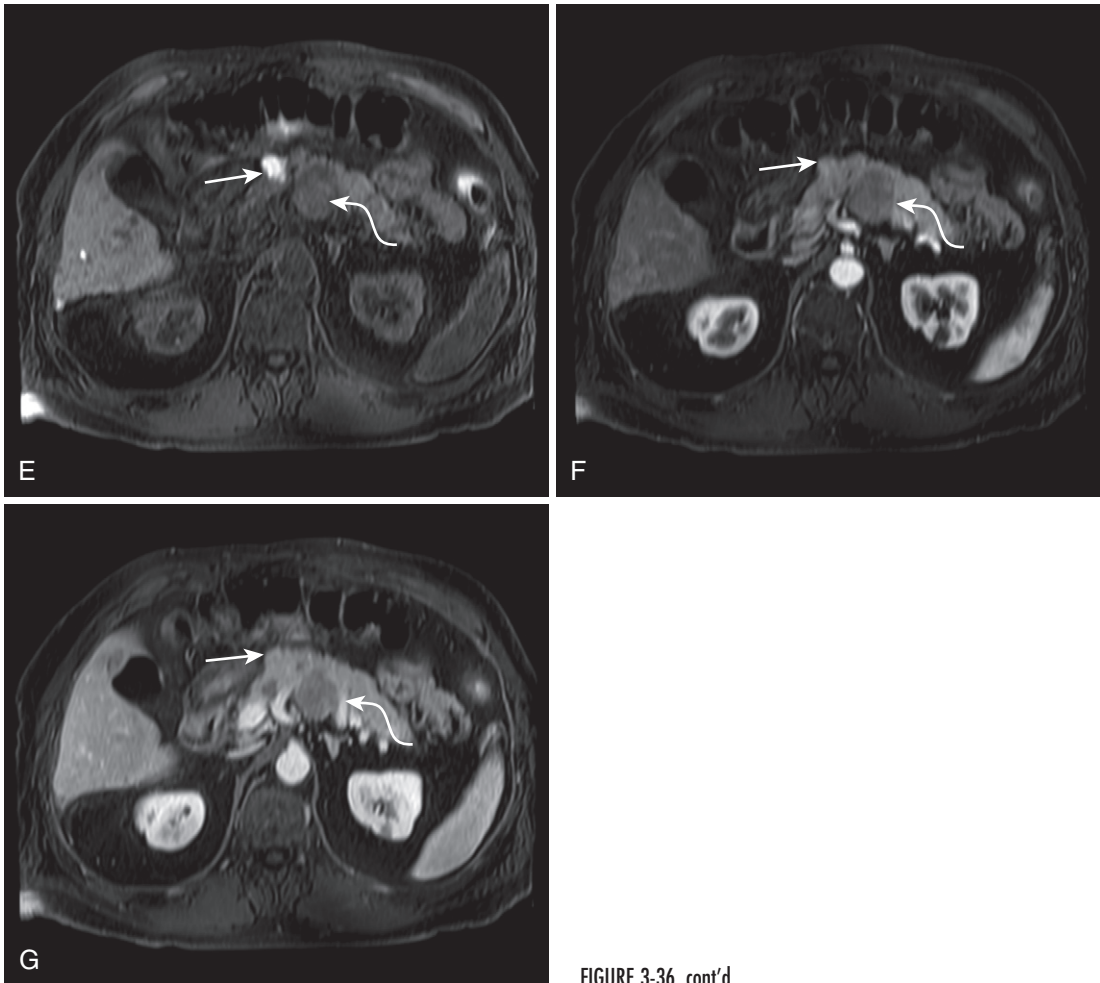


FIGURE 3-36, cont'd

normal pancreatic parenchyma (Fig. 3-38). Whereas pancreatic lymphoma potentially causes duct dilatation, the degree of duct dilatation is generally less than expected for a pancreatic mass of similar size.³⁹

CYSTIC PANCREATIC LESIONS

Cystic pancreatic lesions have a broad differential diagnosis; however, morphology of the cystic component and connectivity with the pancreatic duct are the main factors in narrowing the differential (Fig. 3-39). Fluid hyperintensity on T2-weighted images and absent enhancement (optimally confirmed with subtracted images) establish cystic etiology.

Cysts

True Cysts. True cysts of the pancreas are very rare and thought to be congenital in origin. These cysts are lined by epithelial cells, generally multiple, and seen with adult polycystic

kidney disease, von Hippel-Lindau disease, and cystic fibrosis.⁴⁰

Pseudocysts. Pseudocysts evolve during the course of pancreatitis within areas of necrosis or exudate developing a surrounding wall of granulation tissue without an epithelial lining. The contents of pseudocysts include pancreatic debris, pancreatic excretion, or blood products. As such, the imaging appearance varies considerably (see Fig. 3-12). The center typically shows low T1-weighted signal intensity and high T2-weighted signal intensity. Sludge and hemorrhagic components cause lower T2-weighted signal intensity.⁴⁰⁻⁴²

Von Hippel-Lindau Disease. As discussed previously, multiple true pancreatic cysts are the most common manifestation of von Hippel-Lindau disease (see Fig. 3-23) (see Chapter 4).

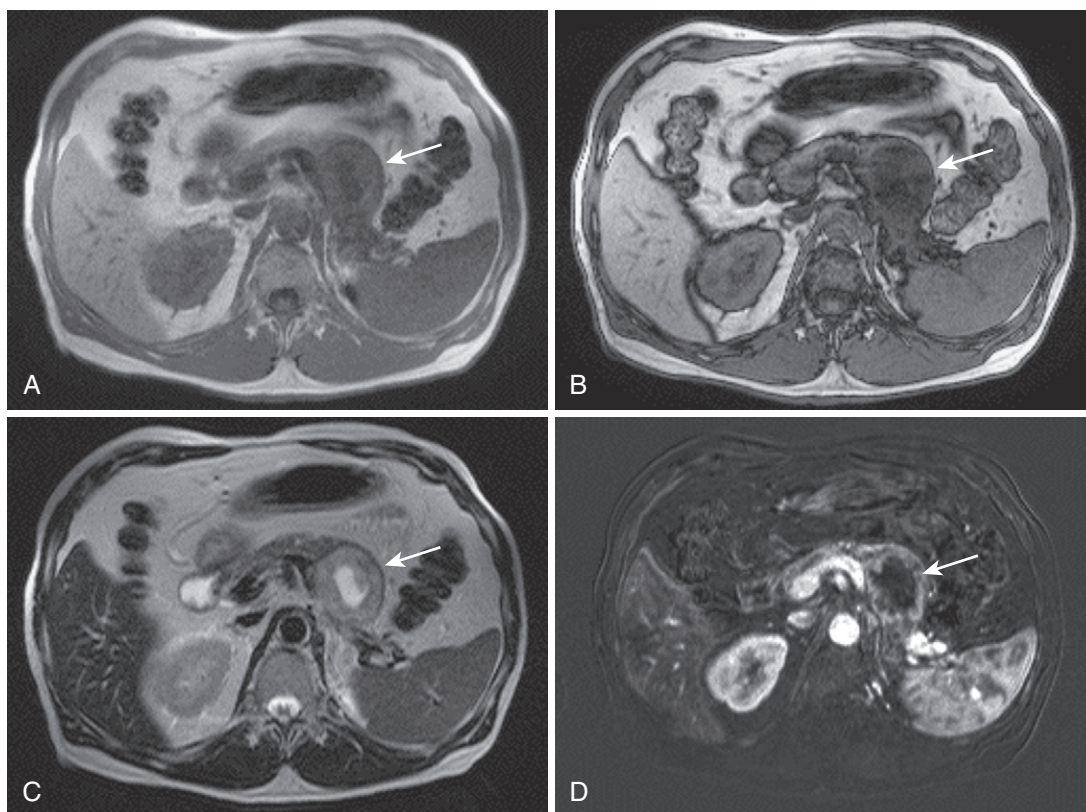


FIGURE 3-37. Pancreatic renal cell carcinoma metastases. The in-phase image (A) in a patient with metastatic clear cell renal cell carcinoma shows a large lesion in the pancreatic body (*arrow*), which loses signal on the out-of-phase image (B). Central cystic necrosis and peripheral hypervascularity on the T2-weighted (C) and subtracted arterial phase (D) images reiterate the typical appearance of this type of tumor (*arrow*).

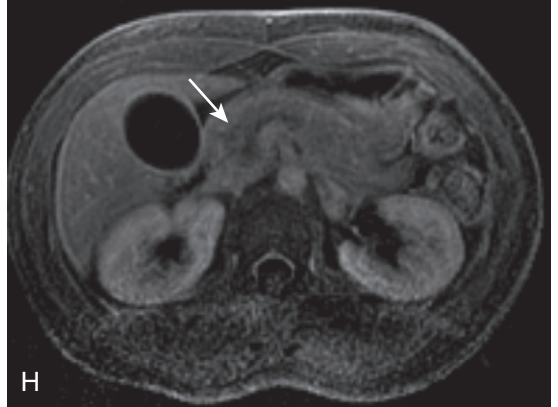
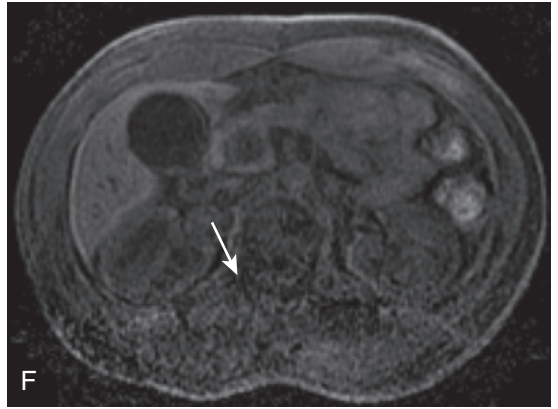
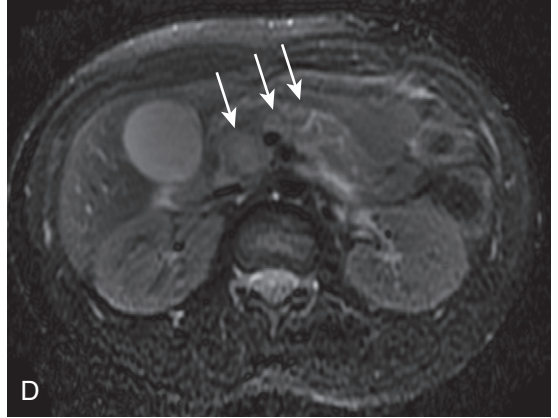
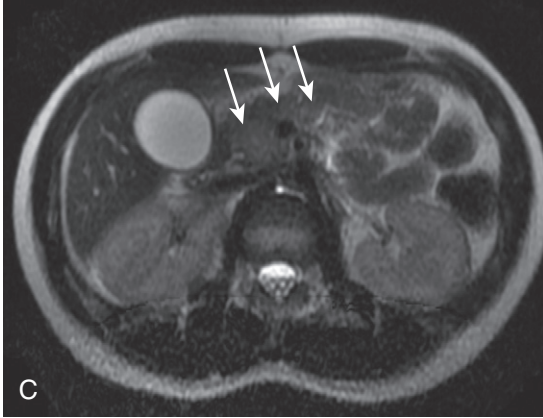
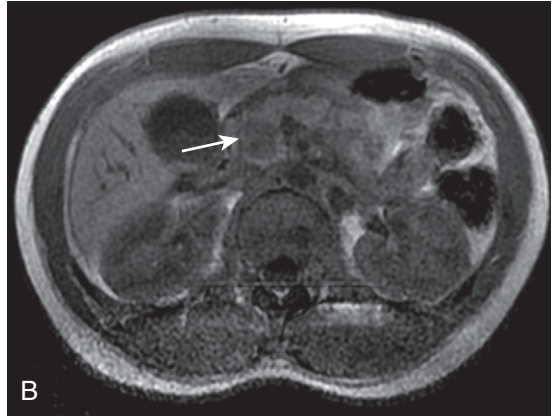
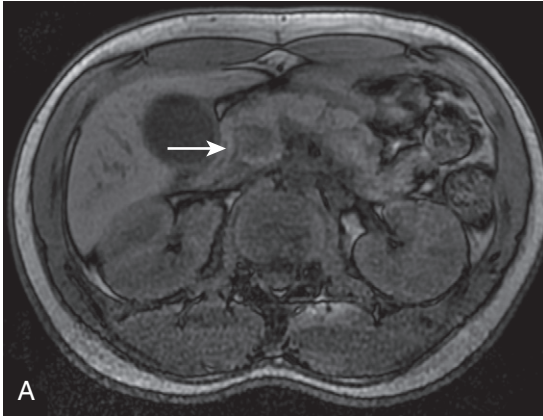
Neoplasms

Intraductal Papillary Mucinous Neoplasms. IPMNs are a spectrum of neoplasms composed of proliferation of pancreatic ductal epithelium lining the main pancreatic duct or side branch ducts (see Fig. 3-28). The mucin-filled dilated ducts demonstrate high T2-weighted signal intensity and variable T1-weighted signal intensity depending on the hydration of the mucin (Fig. 3-40). Low signal intensity filling defects represent papillary projections or mural nodules. The presence of these lesions can be more accurately assessed after contrast administration because the papillary projections or mural nodules demonstrate enhancement whereas mucin does not.⁴³⁻⁴⁵ IPMNs are

typically more common in males and occur during the sixth to eighth decades of life.

Main pancreatic duct IPMNs can be difficult to distinguish from chronic pancreatitis. The main duct is either diffusely or segmentally involved with progressive duct dilatation and parenchymal atrophy. At the time of diagnosis, 30% to 40% of patients with main duct IPMNs have invasive malignancy and the remainder have cellular atypia, dysplasia, or carcinoma in situ; therefore, these lesions should be resected.⁴⁶ Features that suggest malignancy include: papillary projections, mural nodules, size greater than 3 cm, interval growth, or main pancreatic duct dilatation greater than 7 mm is suspicious for malignancy (Fig. 3-41).⁴⁷

FIGURE 3-38. Pancreatic lymphoma. Hypointense T1-weighted (axial in-phase [A], out-of-phase [B], and precontrast [F]) and slightly hyperintense T2-weighted (axial single-shot fast spin-echo [SSFSE]; C), axial fat-suppressed T2-weighted [D], and coronal SSFSE [E]) pancreatic lesions (*arrows*) with mild enhancement on early (G) and delayed (H) postcontrast images in a 19-year-old female with pathologically proven primary pancreatic lymphoma.



Pancreas – Cystic Lesions

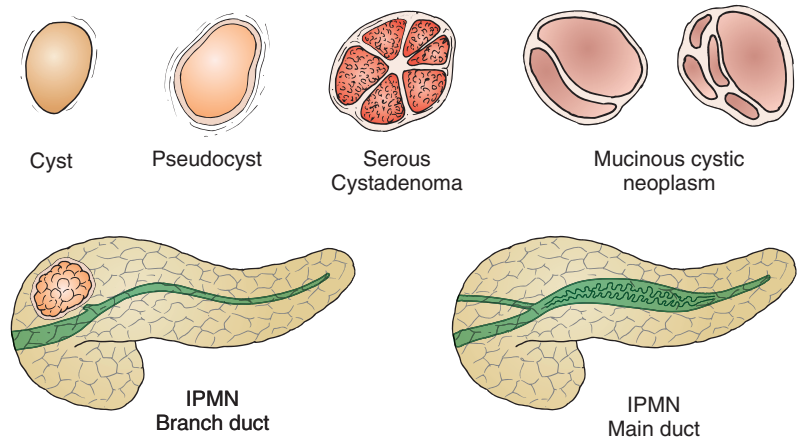


FIGURE 3-39. Pancreatic cystic lesions. IPMN = intraductal papillary mucinous neoplasm.

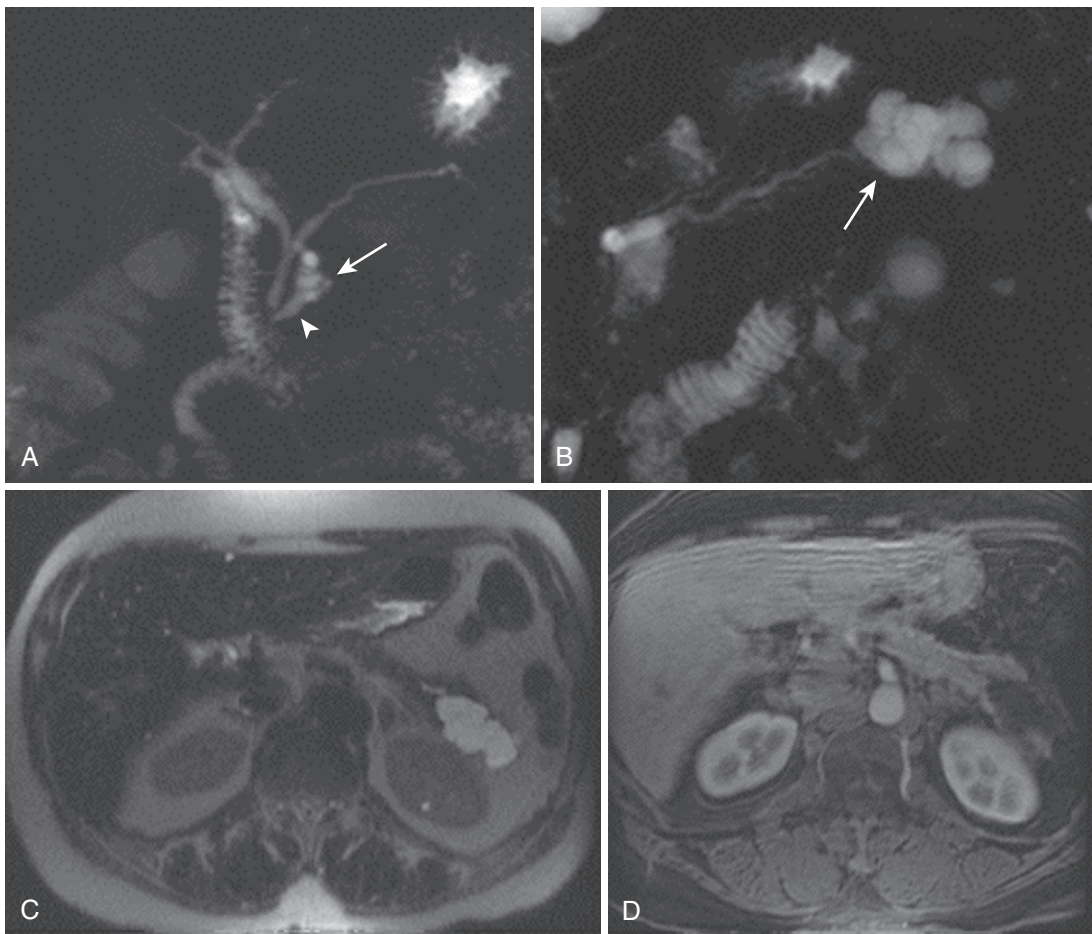
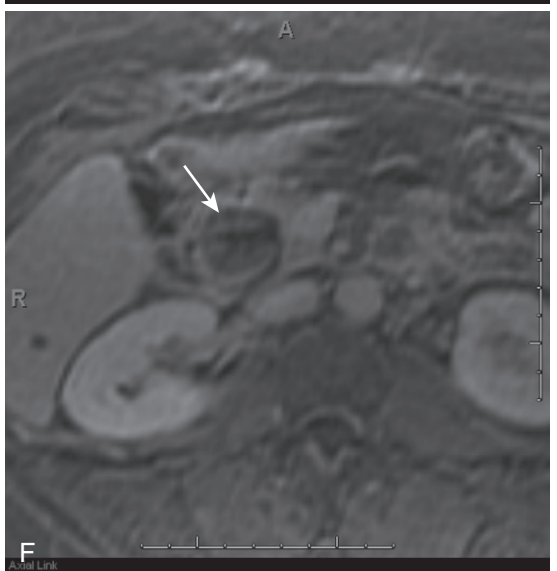
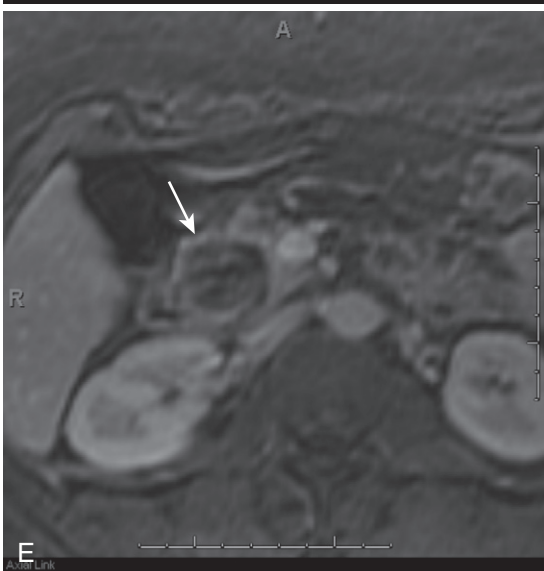
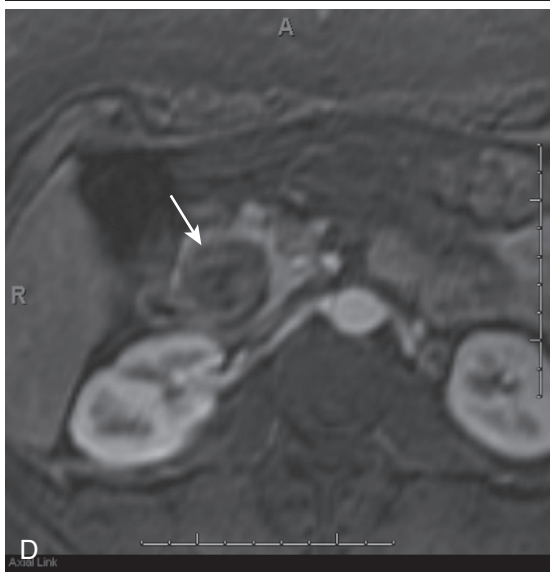
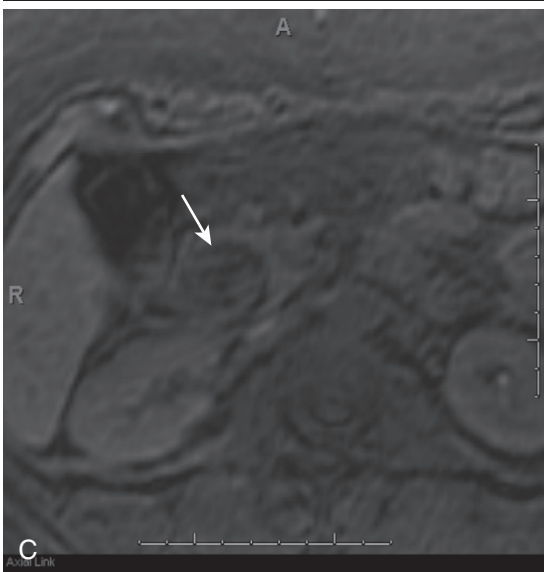
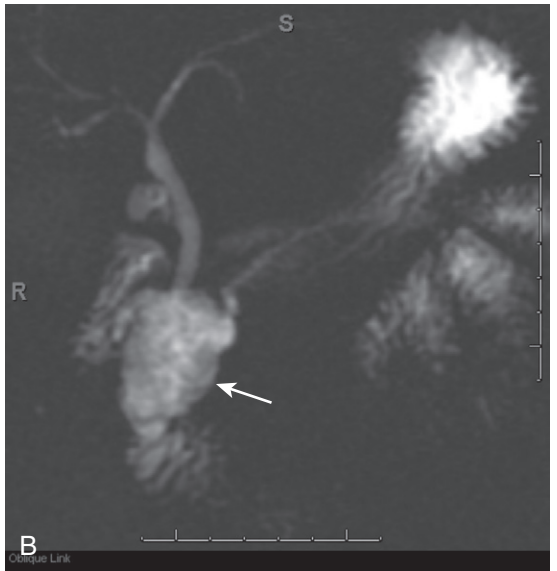
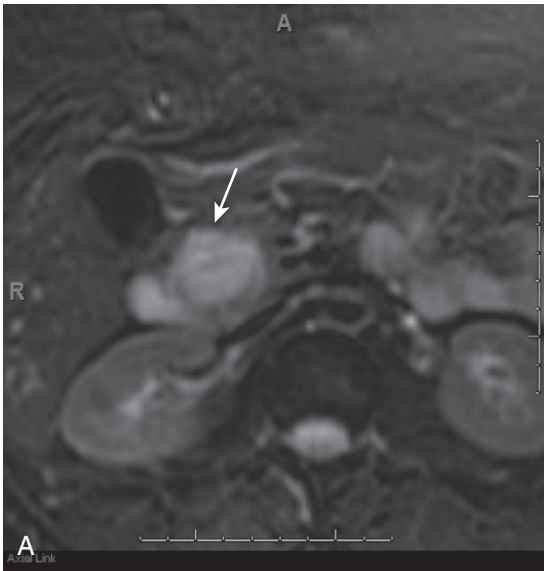


FIGURE 3-40. IPMN, main duct type. A, An MRCP image in a patient with a small main duct IPMN at the level of the pancreatic head/neck (*arrow*) is associated with mild downstream dilatation (*arrowhead*). B, An MRCP image in a different patient with main duct IPMN in the tail (*arrow*) shows continuity with the adjacent duct, which is not dilated. The T2-weighted (C) and postcontrast (D) images exclude malignant features.

FIGURE 3-41. IPMN with malignant features. Fat-suppressed T2-weighted (A) and coronal thick slab maximal intensity projectional MRCP (B) images demonstrating a large cystic lesion in the pancreatic head (*arrows*). Precontrast (C), early arterial phase (D), late arterial phase (E), and delayed phase (F) fat-suppressed T1-weighted gradient recalled-echo images demonstrate enhancement of internal papillary projections and proximity to the main pancreatic duct, in keeping with a side branch intraductal papillary mucinous neoplasm which has undergone malignant degeneration.



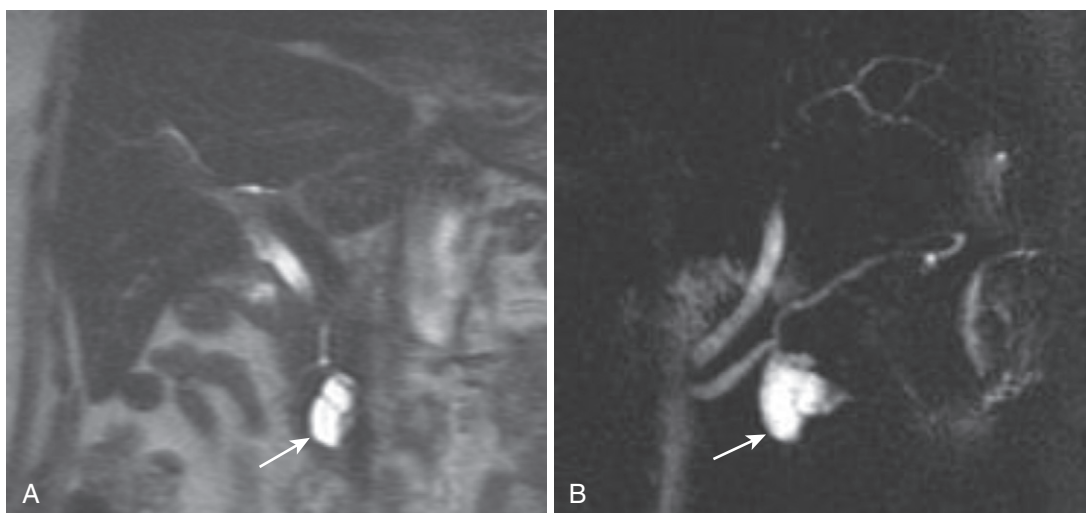


FIGURE 3-42. IPMN side branch type. The coronal T2-weighted image (A) shows a simple-appearing cystic lesion in the pancreatic head (*arrow*). The corresponding MRCP image (B) depicts the connection with the main pancreatic duct and characteristic downstream dilatation (*arrow*).

Side branch IPMNs appear as oval-shaped cystic masses in proximity to the main duct. These lesions may have a cluster of grapes appearance, and identifying a communication to the main pancreatic duct allows differentiation from serous cystadenoma.⁴⁸ Branch duct IPMNs most commonly occur in the uncinata process or pancreatic head but can also involve the body and tail (Fig. 3-42).

Serous Cystadenoma. Serous cystadenoma is a benign tumor occurring in older, predominantly female, patients characterized by a cluster of greater than six cysts—all less than 20 mm in diameter. Parenthetically, serous cystadenoma is seen with increased frequency in patients with von Hippel-Lindau disease. These tumors have a slight predilection for the pancreatic head. The tumor septations and cyst walls demonstrate minimal enhancement (Fig. 3-43). The tumor may contain a central scar that demonstrates low T1-weighted signal intensity with variable contrast enhancement. The central scar occasionally calcifies (better depicted on CT).⁴⁰⁻⁴² Although similar in appearance to branch duct IPMN, lack of connection with the main pancreatic duct excludes this diagnosis.

Mucinous Cystic Neoplasm. Mucinous cystic neoplasm is an uncommon neoplasm with malignant potential, prompting surgical resection. They are characterized by the formation of unilocular or multilocular cysts filled

with abundant, thick gelatinous mucin and have a predilection for the pancreatic tail. The individual cysts are generally larger than 20 mm and may have papillary projections. These lesions do not communicate with the main pancreatic duct and may have peripheral calcification (Fig. 3-44). These lesions occur primarily in women (6:1) in the fourth to sixth decades of life. Seventy to 90% of mucinous cystic neoplasms occur in the distal pancreatic body or tail. The mucin may have high T1-weighted and high T2-weighted signal intensity. When these lesions are multilocular, they tend to have thick septations (Fig. 3-45).⁴⁹⁻⁵¹

Cystic Neuroendocrine (Islet Cell) Tumor. As neuroendocrine tumors (see discussion under “Solid Lesions”) grow, they may develop a cystic appearance secondary to degeneration and necrosis (see Figs. 3-33 and 3-35). Therefore, it is important to consider islet cell tumors in the differential of cystic lesions. The central cystic component typically demonstrates moderately T1-weighted and T2-weighted signal intensity. The T1-weighted increased signal is a nonspecific finding as can be seen in pseudocysts and solid and papillary epithelial neoplasms (SPENs) with hemorrhage and mucinous neoplasms. Cystic islet cell tumors have an irregular thick wall that demonstrates avid enhancement after the administration of gadolinium, helping to differentiate them from other cystic lesions.⁴²

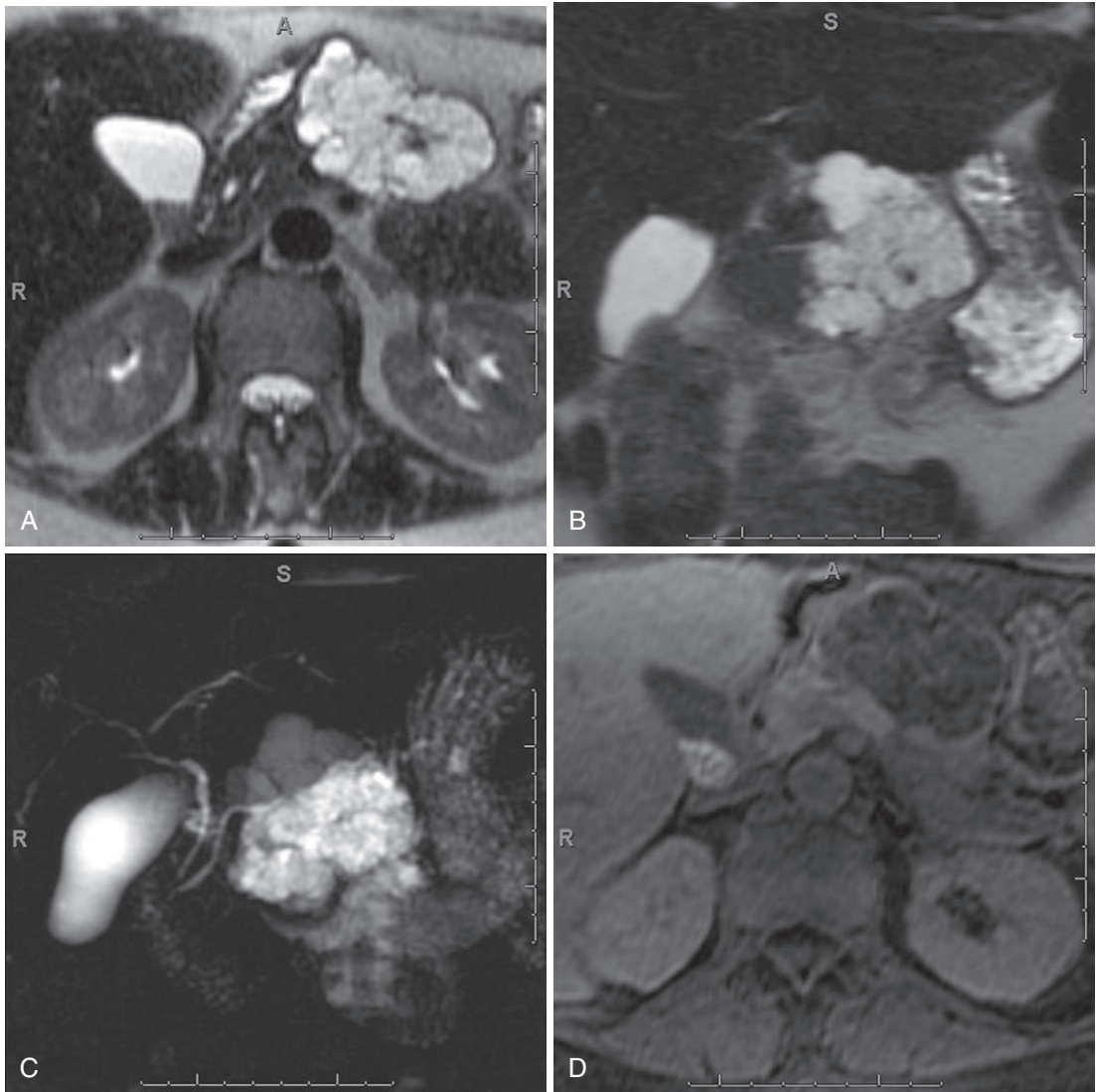


FIGURE 3-43. Pancreatic serous cystadenoma. Axial (A) and coronal (B) T2-weighted, coronal thick-slab MRCP (C), and dynamic pre-contrast (D), early arterial (E), late arterial (F), and delayed (G) 3-D fat-suppressed T1-weighted gradient recalled-echo images depict a large multiloculated cystic lesion in the distal body of the pancreas with minimal enhancement of the septations, in keeping with a pancreatic serous cystadenoma.

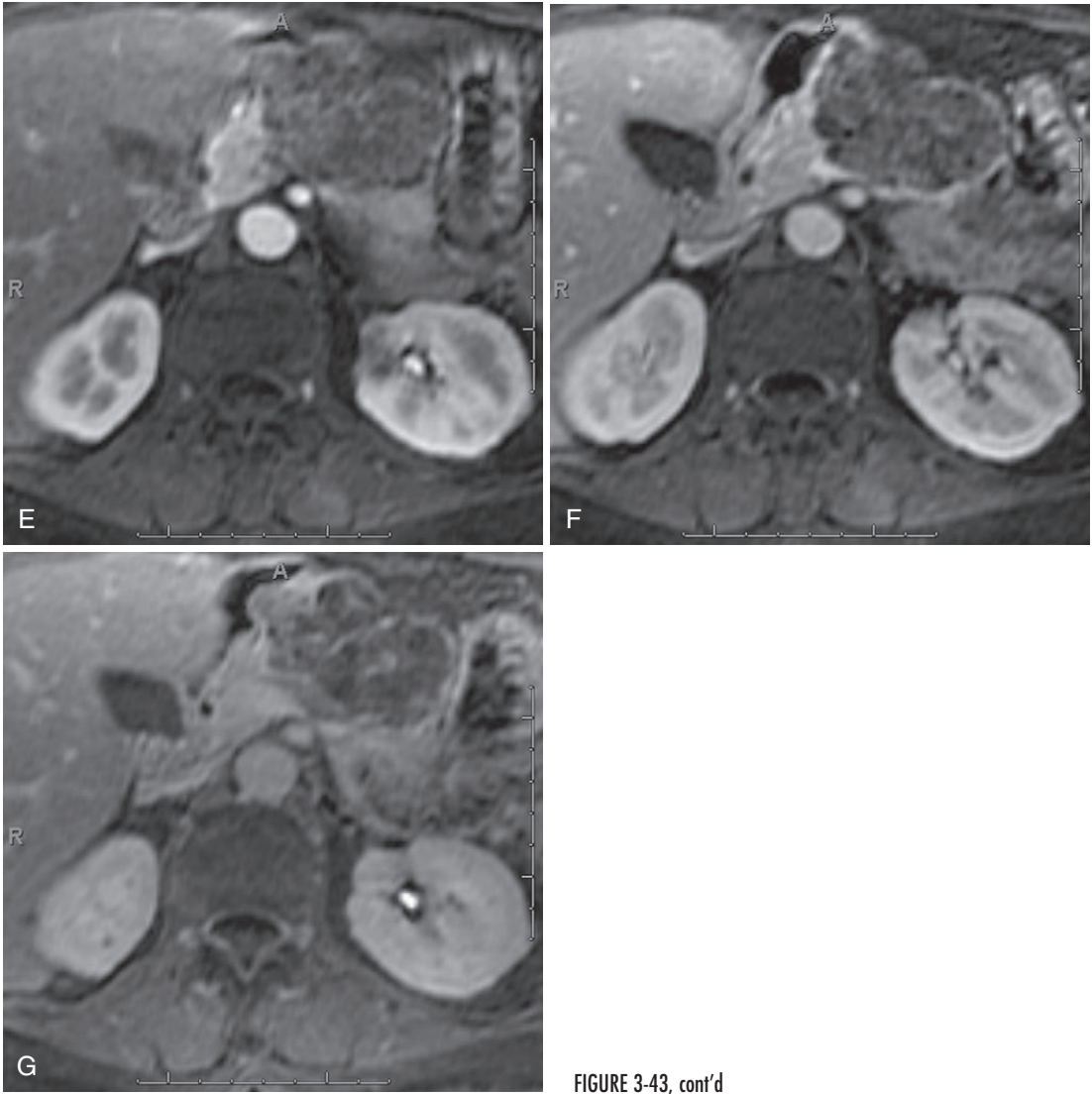


FIGURE 3-43, cont'd

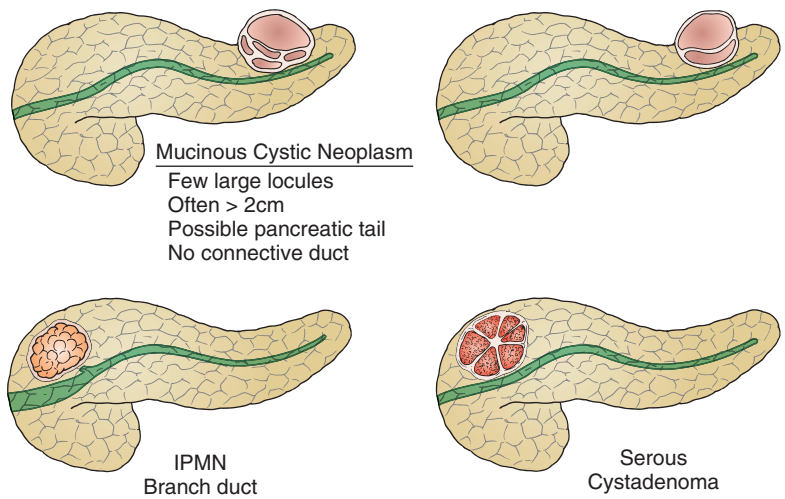


FIGURE 3-44. Pancreatic cystic neoplasms. IPMN = intraductal papillary mucinous neoplasm.

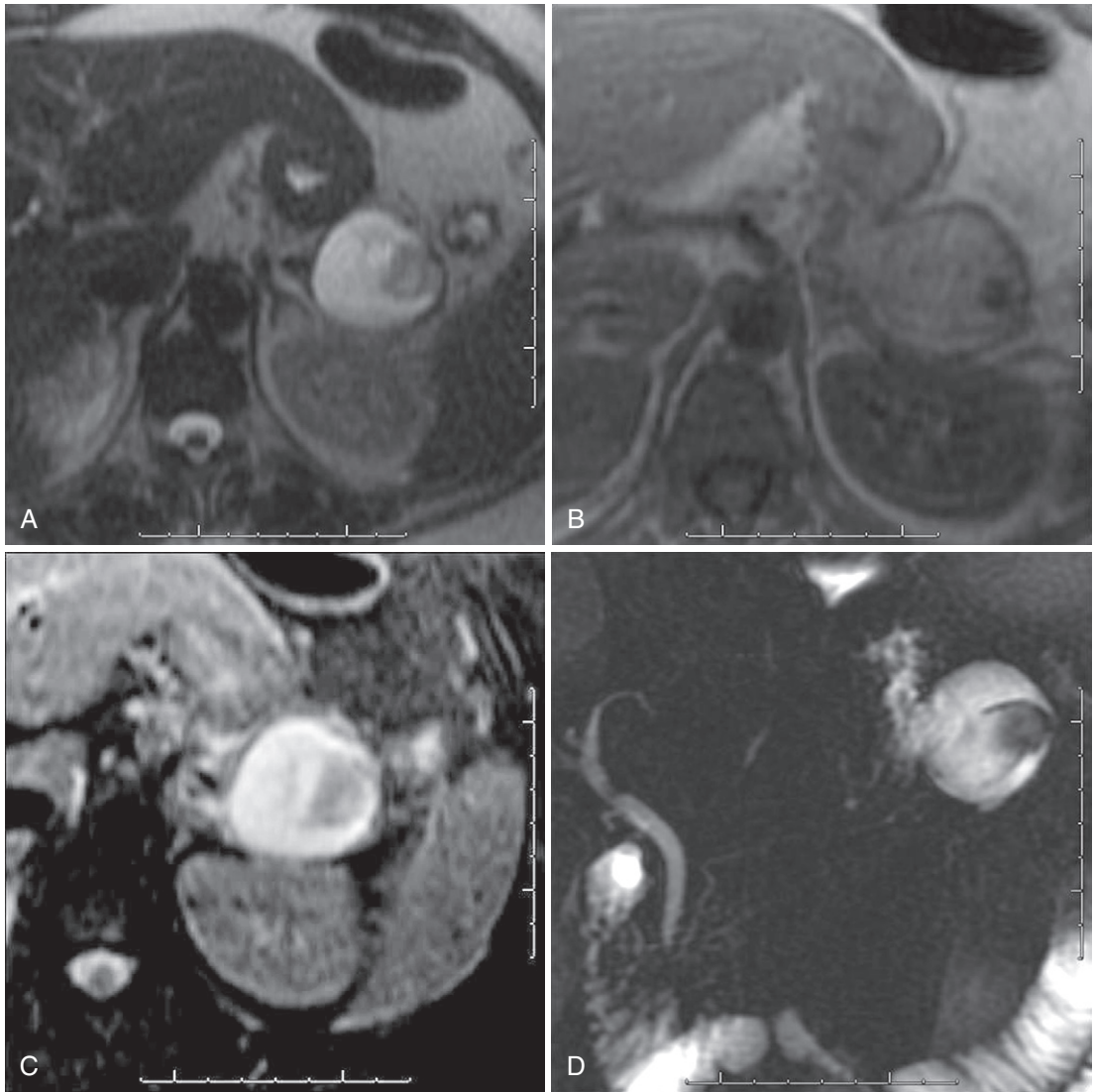


FIGURE 3-45. Mucinous cystic neoplasm. Mucinous cystic neoplasm of the pancreatic tail in a 47-year-old woman. T2-weighted (A), T1-weighted gradient recalled-echo (B), fat-suppressed T2-weighted (C), coronal thick-slab MIP MRCP (D), dynamic precontrast, early arterial phase (E), and late phase 3-D fat-suppressed T1-weighted gradient recalled echo (F and G), and coronal T2-weighted (H) images demonstrate a large cystic mass in the tail of the pancreas separate from the main pancreatic duct, with increased T1-weighted signal intensity (related to the mucin content) and minimal internal enhancement.

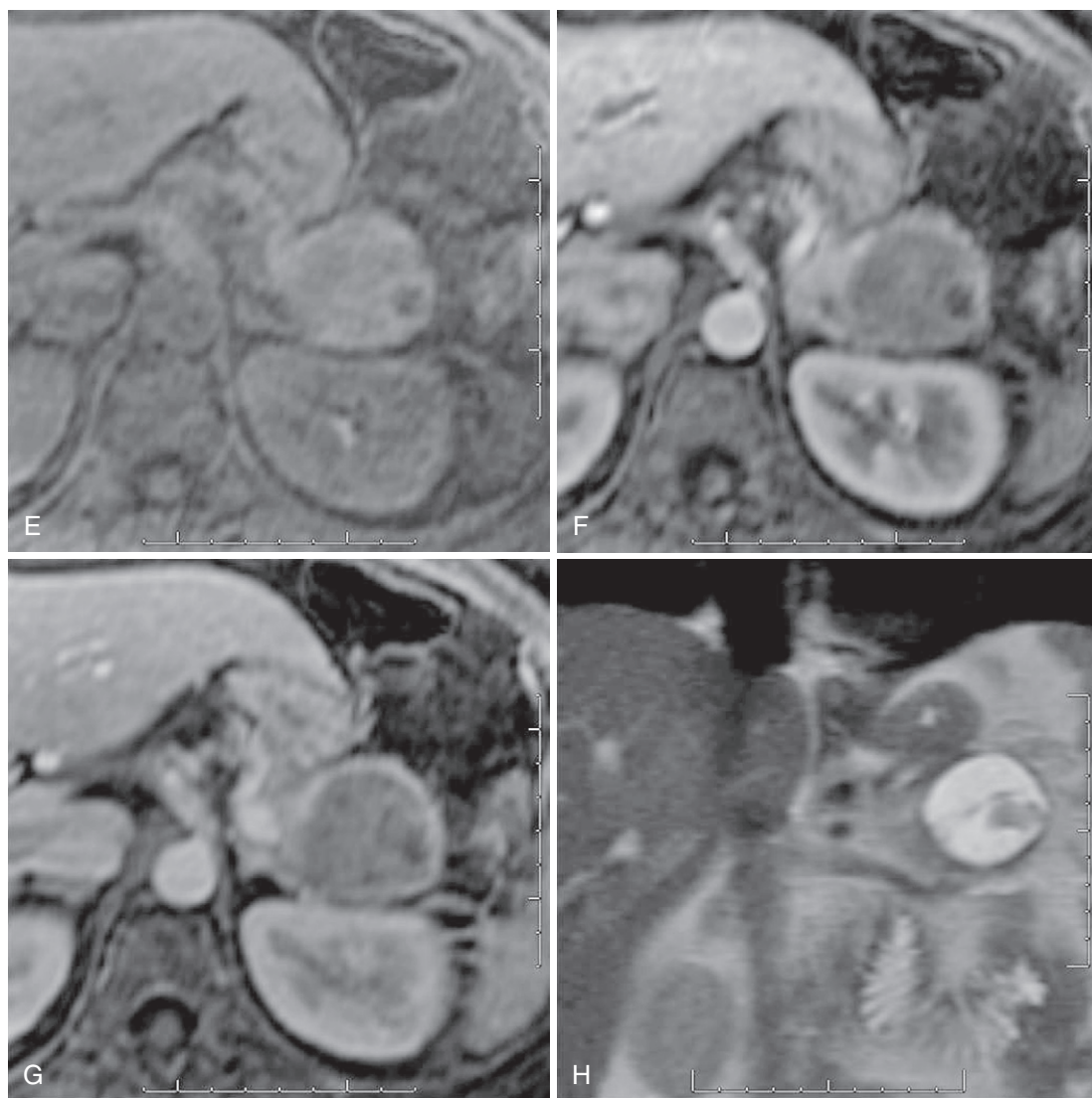


FIGURE 3-45, cont'd

Solid-Cystic Papillary Epithelial Neoplasm. SPENs are lesions with low-grade malignant potential. SPENs occur frequently in females between 20 and 30 years of age, typically of African American or Asian descent (Fig. 3-46). The imaging appearance is a large, well-encapsulated mass with variable internal architecture (from solid to solid and cystic to a thick-walled cyst), with focal signal voids (due to calcification) and regions of hemorrhagic degeneration. Although these lesions occur throughout the pancreas, the most common location is the pancreatic tail. The hemorrhagic portion of the tumor may demonstrate high T1-weighted signal intensity and variable T2-weighted signal intensity with or without a fluid-debris level. The fibrous capsule

demonstrates low T1-weighted and T2-weighted signal intensity. The most common imaging appearance is mixed solid and cystic lesion with areas of hemorrhagic necrosis.^{52,53}

GALLBLADDER

Anatomy

The gallbladder is an ovoid cystic organ along the undersurface of the liver at the interlobar fissure between the right and the left lobes of the liver. Although the size and shape of the gallbladder vary with fasting state, it is approximately 10 cm long and 3 to 5 cm in diameter. The normal capacity of the gallbladder is approximately 50 mL. The normal gallbladder wall is 2 to 3 mm in thickness and composed of

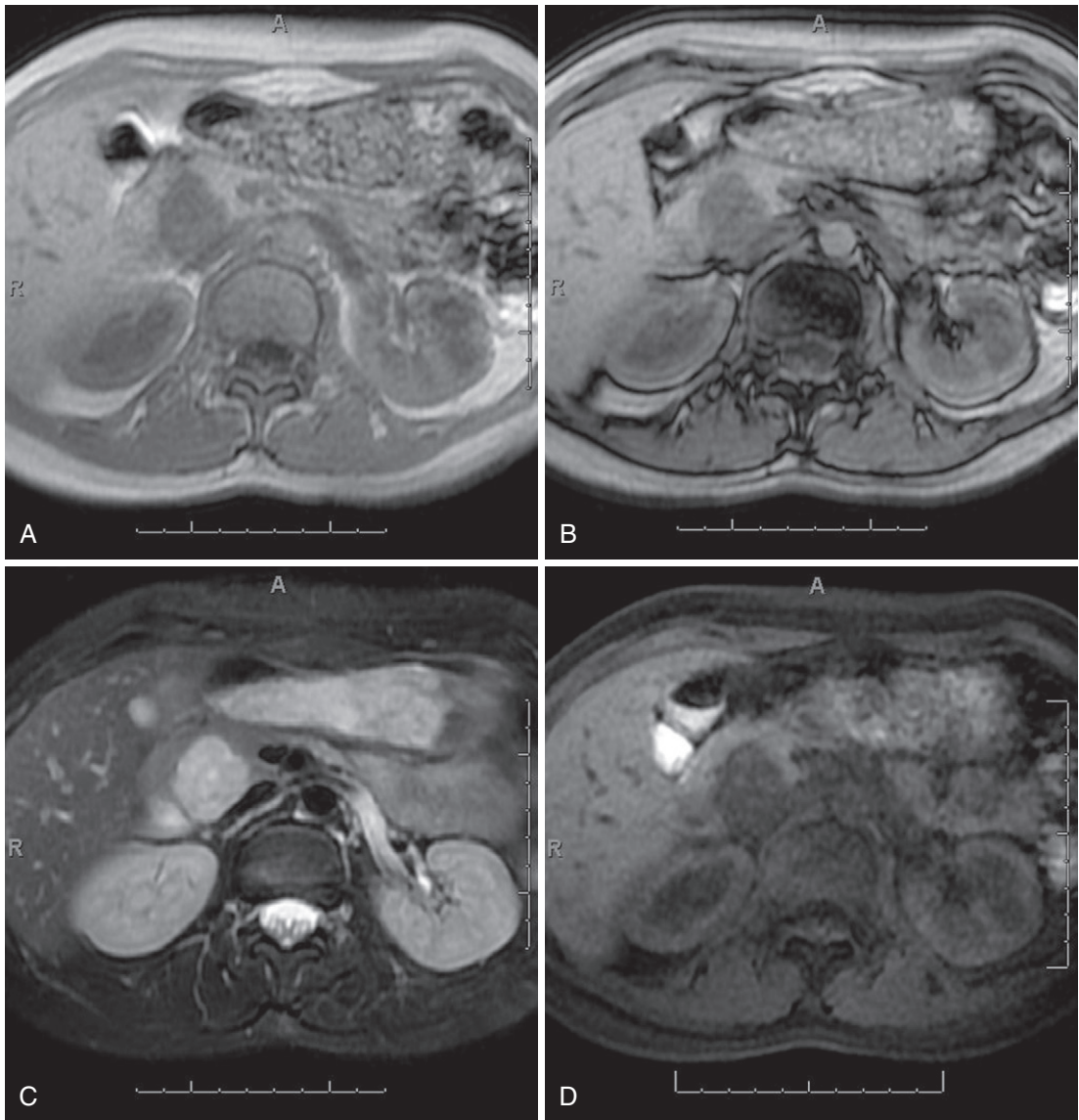


FIGURE 3-46. Solid-cystic papillary epithelial neoplasm (SPEN). In-phase (A) and out-of-phase (B) T1-weighted gradient recalled-echo, fat-suppressed T2-weighted (C), and fat-suppressed T1-weighted gradient recalled-echo (D) images demonstrate a decreased T1-weighted signal intensity, increased T2-weighted signal intensity mass, without upstream pancreatic duct dilatation, within the head of the pancreas in this young female African American patient. Noncontrast (E), early arterial (F), late arterial (G), and delayed (H) CT images demonstrate calcification and mild delayed enhancement of the same mass. These findings are characteristic of SPEN of the pancreas, which was confirmed at surgery.

columnar epithelium. The gallbladder connects with the biliary tree via the cystic duct, measuring 2 to 4 cm in length and 1 to 5 mm in caliber, characterized by prominent concentric folds, known as the *spiral valves of Heister*. The cystic duct usually joins the extrahepatic bile duct halfway between the porta hepatis and the ampulla of Vater. Variant anatomy, such as low medial cystic duct insertion, occurs approximately 20% of the time.

Normal Appearance

The function of the gallbladder is to store and concentrate bile. As such, the T1-weighted appearance of the gallbladder lumen varies with the concentration of the bile. In general, bile salts are of increased signal intensity on T1-weighted imaging in the fasting state; however, the bile salt and protein concentration affects the degree of the T1-weighted signal intensity. The gallbladder contents demonstrate

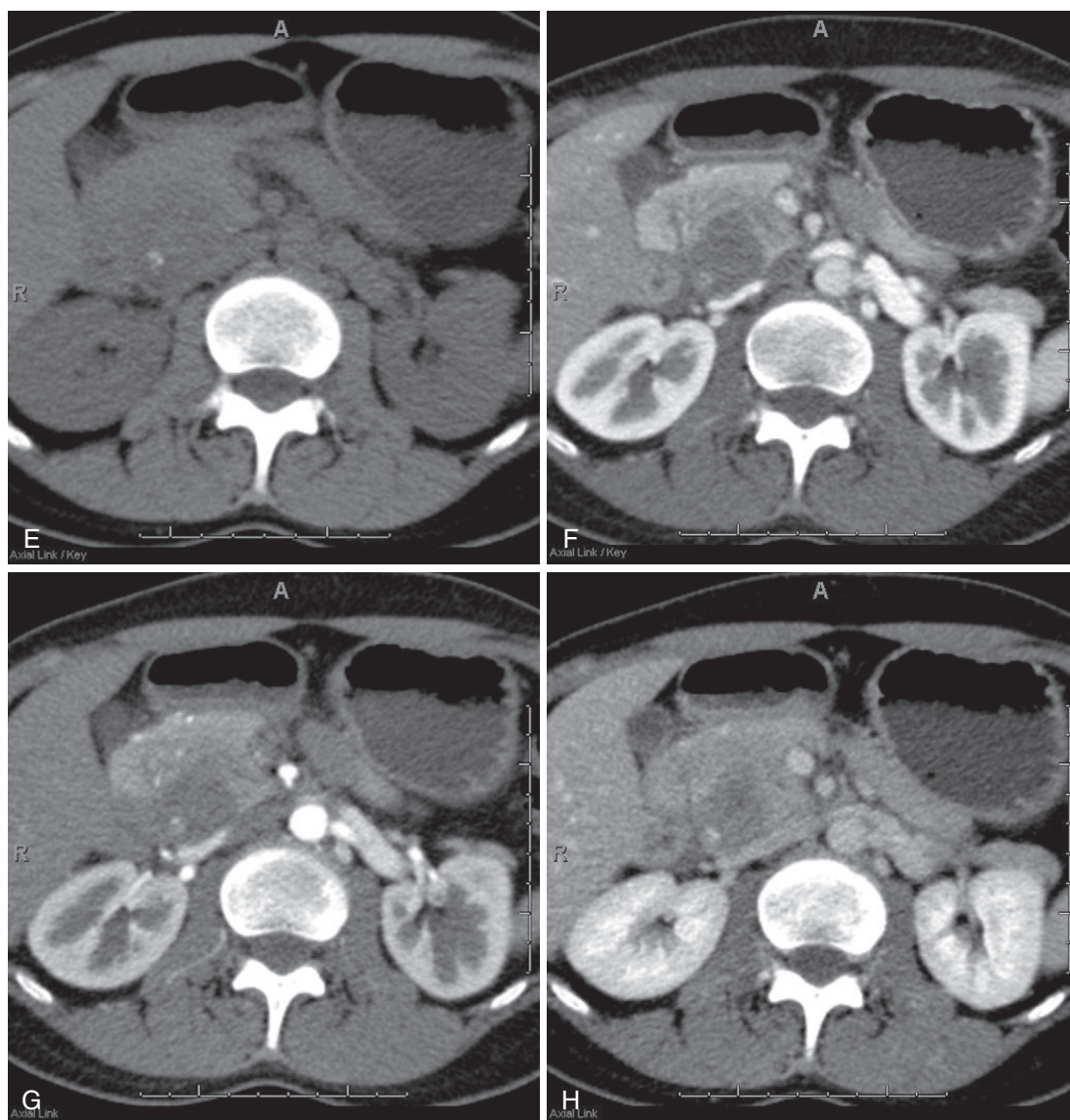


FIGURE 3-46, cont'd

increased signal on T2-weighted imaging as a result of the static fluid content of bile.⁵⁴

Imaging Technique

MRI of the gallbladder should be performed in a manner similar to other abdominal imaging protocols. When possible, the patient should fast for at least 4 hours to promote adequate gallbladder distention. In addition, the use of newer contrast agents with increased hepatobiliary excretion can provide limited information regarding gallbladder and biliary function.

Congenital/Developmental Abnormalities of the Gallbladder

ACCESSORY GALLBLADDERS, ECTOPIA, AND AGENESIS

When there is aberrant branching of the foregut during development, gallbladder anomalies potentially arise. Frequently, these anomalies are part of a larger picture of heterotaxy syndrome with more significant anomalies (i.e., cardiac and pulmonary). Congenital and developmental anomalies of the gallbladder are often incidentally noted at autopsy; their only clinical relevance is for presurgical planning (Fig. 3-47).

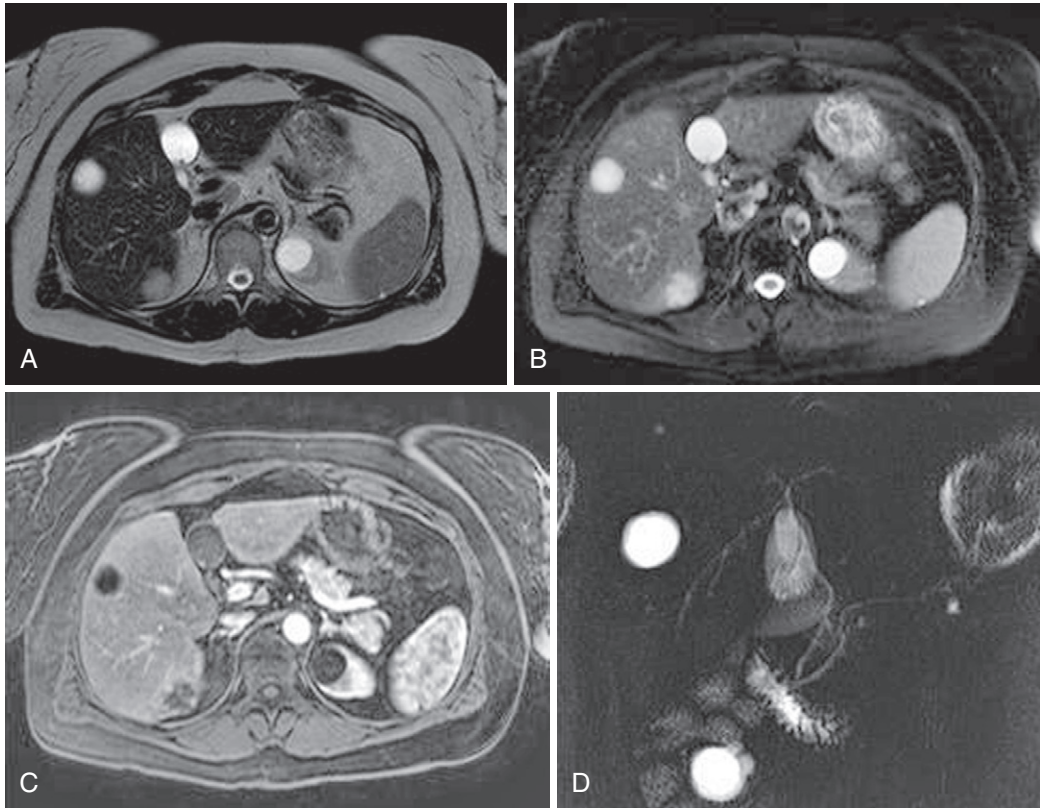


FIGURE 3-47. Ectopic gallbladder. T2-weighted (A), fat-suppressed T2-weighted (B), postcontrast fat-suppressed T1-weighted gradient recalled-echo (C), and coronal thick-slab MIP MRCP (D) images demonstrate an ectopic gallbladder in the fissure for the ligamentum teres.

CHOLELITHIASIS

Cholelithiasis (or gallstones) is the most common gallbladder disorder by a wide margin, afflicting 10% of the population. Risk factors include obesity, pregnancy, rapid weight loss and estrogens and women are affected twice as often as men. While most often asymptomatic, pain (or biliary colic) occasionally ensues. Cholelithiasis is also the usual culprit in acute and chronic cholecystitis.

Gallstones appear as filling defects within the gallbladder lumen. The rigid internal structure of gallstones facilitates relaxation resulting in signal voids—best visualized against the bright background of fluid on T2-weighted images (Fig. 3-48). The two dominant forms of gallstones feature slightly different imaging findings. Cholesterol stones—the more common variety (80%)—are hypointense signal voids on all pulse sequences. Pigmented stones are hypointense on T2-weighted images, but exhibit variable T1 signal depending on the degree of hydration. Regardless of the composition, the sensitivity of MRI for detecting gallstones approaches 100%.

Diffuse Processes of the Gallbladder

CHOLECYSTITIS

Acute. Acute inflammation of the gallbladder is caused by cystic duct obstruction in the majority of cases. At imaging, gallstones are identified in the gallbladder and/or cystic duct as signal voids best visualized on T2-weighted images. Associated findings include mural thickening (>3 mm), mural hyperemia (as evidenced by hyperenhancement on postgadolinium images), and occasionally, transient adjacent hepatic hyperemia on immediate postgadolinium images (Fig. 3-49). Pericholecystic inflammatory changes and fluid are best appreciated on T2-weighted and postcontrast images (Fig. 3-50).⁵⁴⁻⁵⁷ Occasionally, abscesses form within or outside the gallbladder wall (Fig. 3-51). Acute acalculous cholecystitis accounts for the remainder of the cases of acute cholecystitis and is often related to decreased gallbladder motility, decreased blood flow, or bacterial infection.^{54,55}

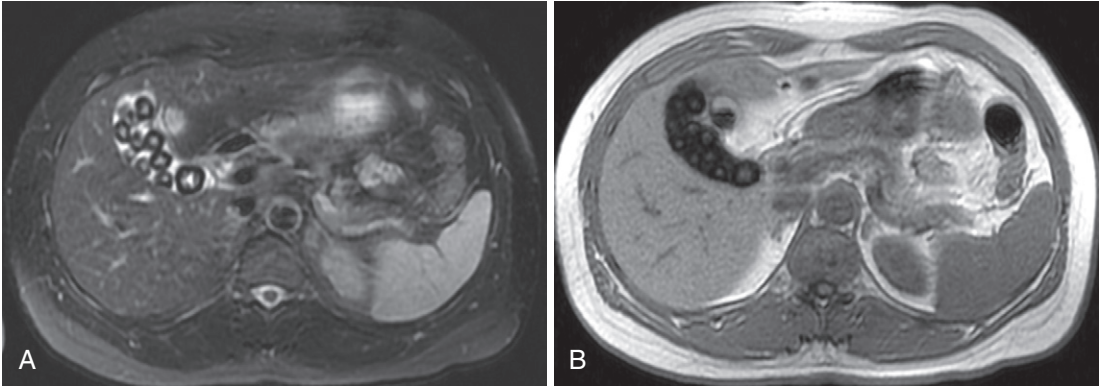


FIGURE 3-48. Cholelithiasis. The axial T2-weighted fat-suppressed image (A) through the gallbladder shows multiple intraluminal filling defects corresponding to gallstones. In the in-phase image (B), the gallstones are conspicuous only because of the hyperintensity, suggesting pigmented composition.

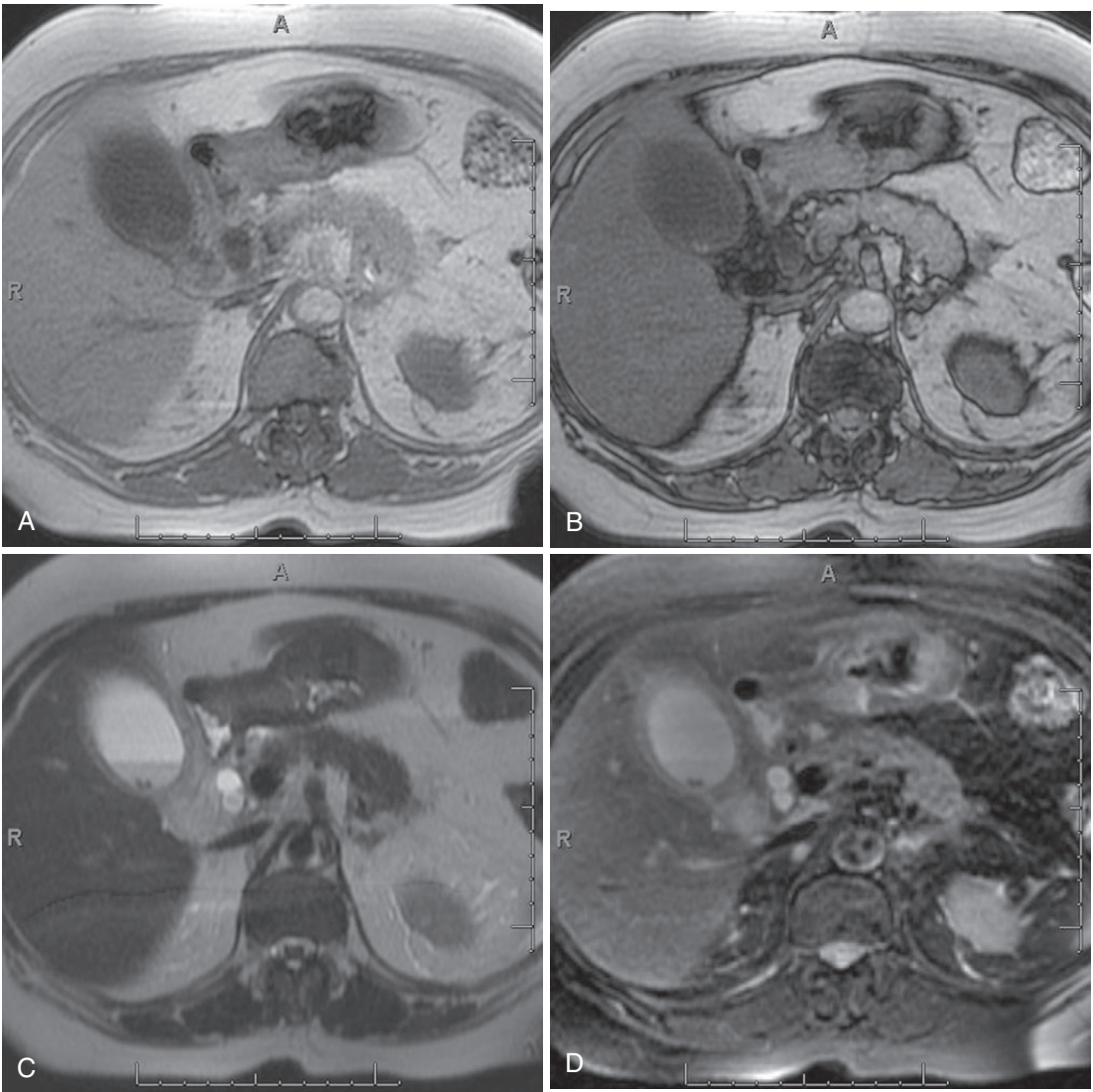


FIGURE 3-49. Acute cholecystitis. In-phase (A) and out-of-phase (B) T1-weighted, T2-weighted (C), fat-suppressed T2-weighted (D), and precontrast (E) and postcontrast (F) fat-suppressed T1-weighted gradient recalled-echo images demonstrate gallstones, mural thickening, mural hyperemia, and adjacent hepatic hyperemia of acute cholecystitis caused by an obstructing T1 hyperintense gallstone within the cystic duct (*arrow* in E).

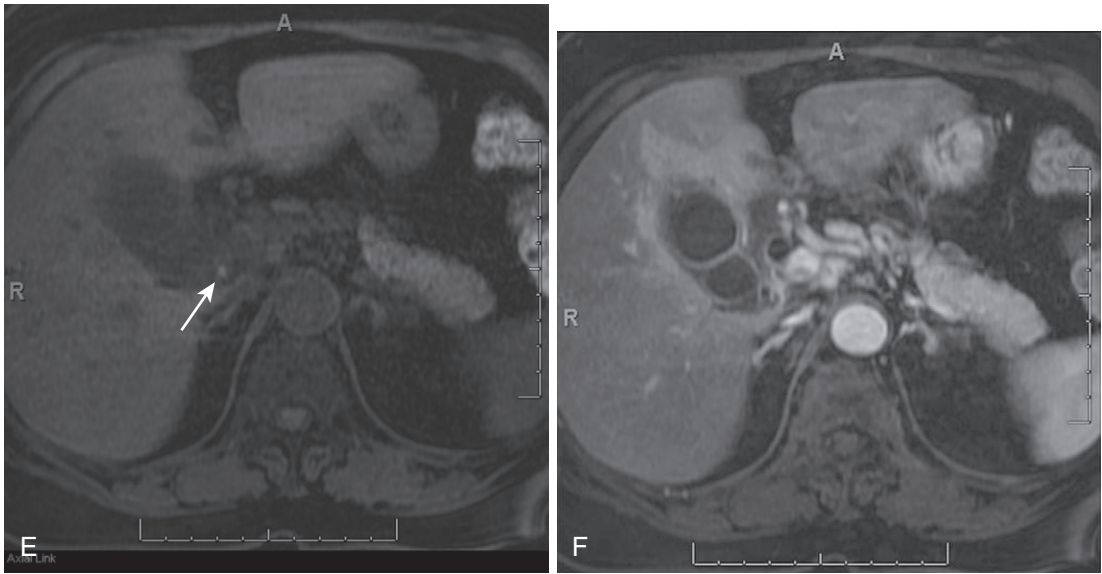


FIGURE 3-49, cont'd

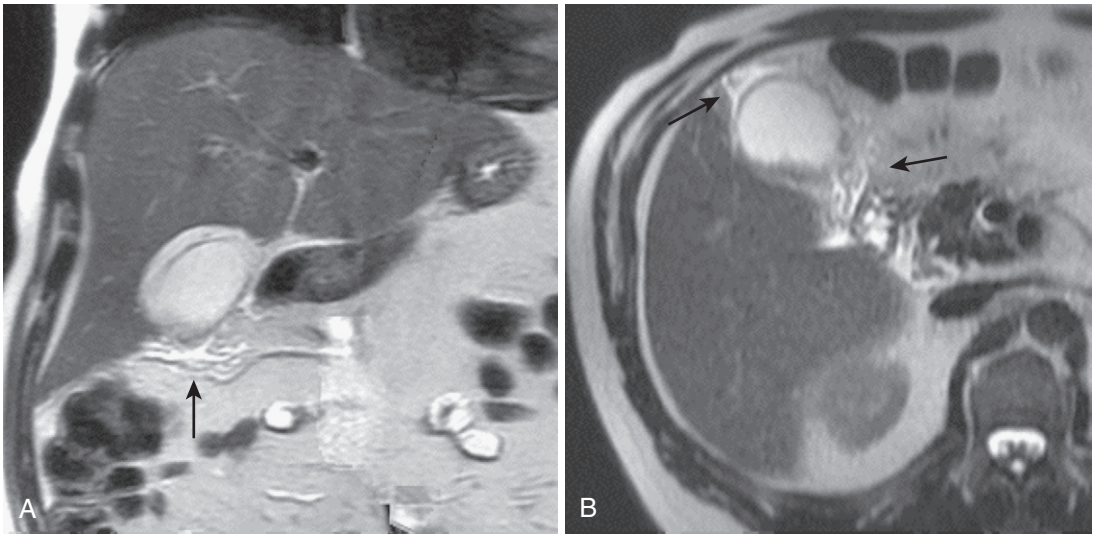


FIGURE 3-50. Acute cholecystitis with pericholecystic inflammatory changes. Coronal (A) and axial (B) T2-weighted images in a patient with acute cholecystitis reveal wall thickening, gallstones, and pericholecystic inflammation and fluid (*arrow*).

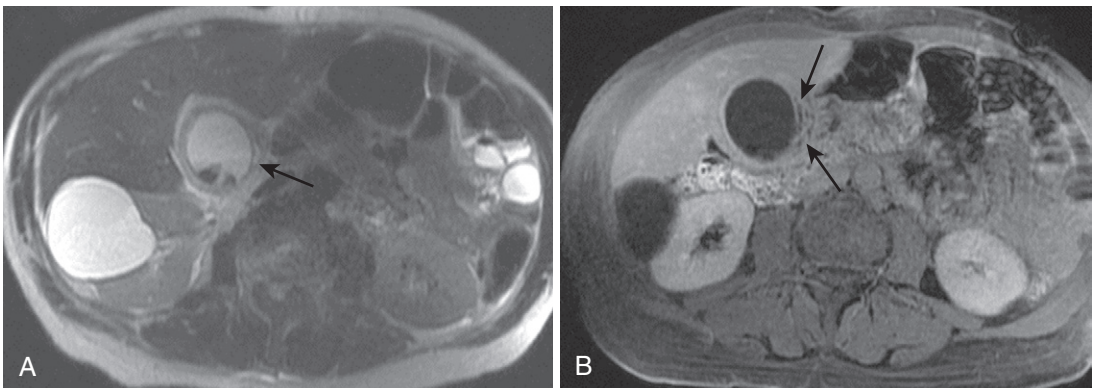


FIGURE 3-51. Acute cholecystitis with intramural abscesses. Axial T2-weighted (A) and postcontrast (B) images in a patient with severe acute cholecystitis show gallstones and mural thickening with intramural abscesses (*arrows*).

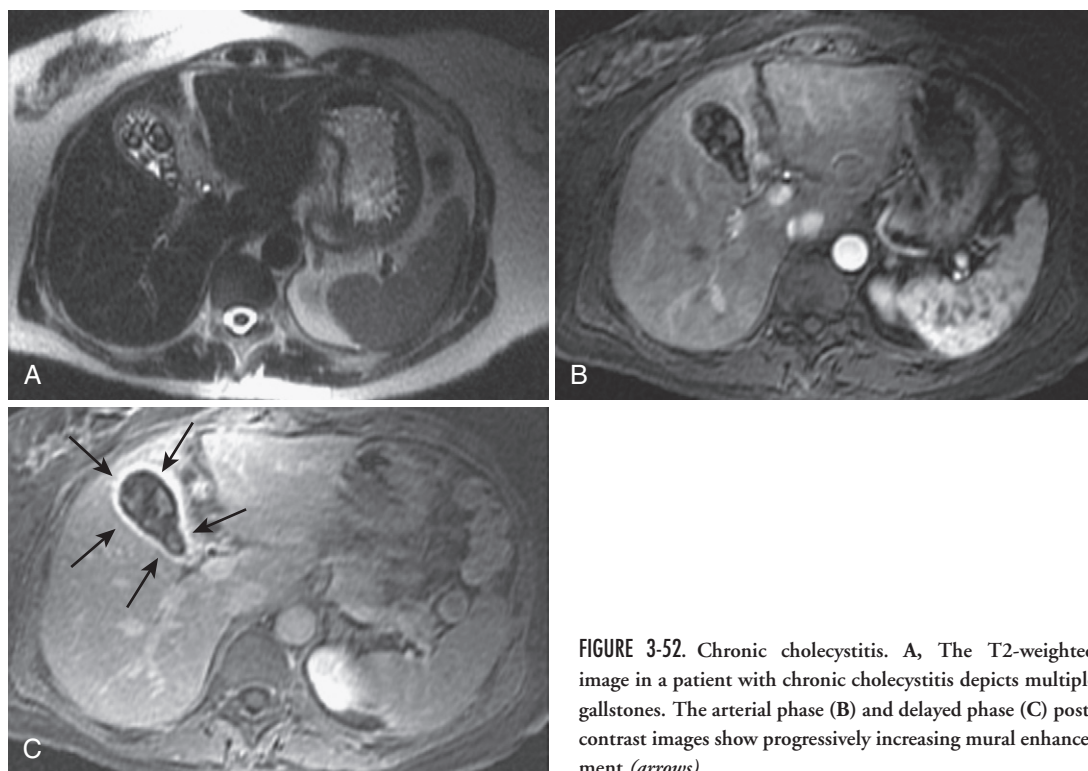


FIGURE 3-52. Chronic cholecystitis. **A**, The T2-weighted image in a patient with chronic cholecystitis depicts multiple gallstones. The arterial phase (**B**) and delayed phase (**C**) post-contrast images show progressively increasing mural enhancement (*arrows*).

Chronic. In chronic cholecystitis, mural enhancement is mild and most prominent on delayed postgadolinium images, related to fibrosis within the gallbladder wall (Fig. 3-52). In addition, the gallbladder is often small and/or contracted with no adjacent hepatic hyperemia. The gallbladder wall may calcify, resulting in a porcelain gallbladder.^{54,55}

Gangrenous. Gangrenous or necrotizing cholecystitis is a severe form of acute cholecystitis with increased morbidity and mortality. Older men with cardiovascular disease and diabetic patients are at increased risk for developing gangrenous cholecystitis and are, therefore, more likely to require an open cholecystectomy. Segmental absence of mucosal enhancement on postgadolinium images is suggestive of gangrenous cholecystitis.^{54,55,58}

NONSPECIFIC EDEMA

Nonspecific edema manifests as diffuse gallbladder wall thickening, in the setting of any of a number of hepatic, pancreatic, and biliary diseases. Common etiologies include cirrhosis (Fig. 3-53)—which is the most common—

hypoproteinemia, hypertension (both systemic and portal), and renal failure. The gallbladder wall demonstrates normal enhancement with no hyperemia of the adjacent hepatic parenchyma.^{54,55}

ADENOMYOMATOSIS

Gallbladder adenomyomatosis is a benign condition occurring either focally (most commonly at the fundus), diffusely, or segmentally. There is hyperplasia of epithelial and muscular elements resulting in mucosal outpouchings into a thickened wall, forming intramural diverticula (also known as Rokitansky-Aschoff sinuses) (Fig. 3-54). Although there is no malignant potential, adenomyomatosis and gallbladder carcinoma may have similar presentations (gallbladder wall thickening, intraluminal mass, and gallstones). Therefore, if diagnosis is equivocal, close follow-up or cholecystectomy is recommended.^{59,60}

Focal Processes of the Gallbladder

POLYP

The generic term, “gallbladder polyp” encompasses a few distinctly different lesions that are

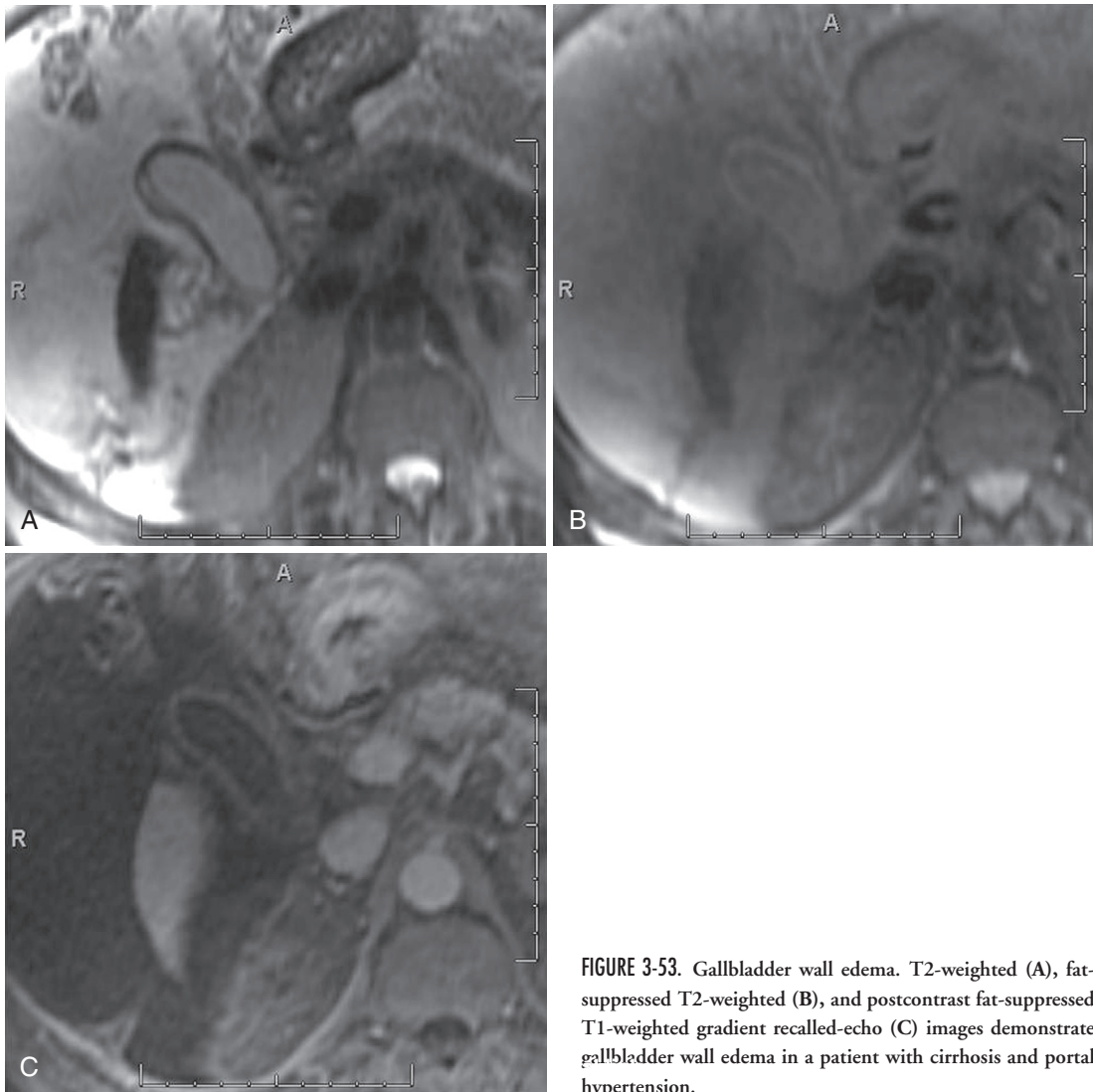


FIGURE 3-53. Gallbladder wall edema. T2-weighted (A), fat-suppressed T2-weighted (B), and postcontrast fat-suppressed T1-weighted gradient recalled-echo (C) images demonstrate gallbladder wall edema in a patient with cirrhosis and portal hypertension.

categorized according to their etiology and malignant potential. Polypoid mural-based lesions develop in the setting of the hyperplastic cholecystoses (a term used to include a spectrum of proliferative and degenerative changes involving the gallbladder wall and including cholesterosis and adenomyomatosis). These lesions, exemplified by the cholesterol polyp and adenomyoma, represent polypoid ingrowths of the hyperplastic epithelium, lack enhancement and harbor no malignant potential. In the case of the cholesterol polyp, signal loss on out-of-phase images reflects intracytoplasmic lipid. Polypoid lesions measuring less than 5 mm in size are almost always cholesterol polyps.

The adenoma is another benign, usually incidental polypoid lesion. More frequently

polypoid than sessile in morphology, the gallbladder adenoma is usually composed of glandular tissue with epithelial lining and an inner fibrovascular core. Most lesions enhance and measure less than 2 cm in diameter (Fig. 3-55). Because adenomas are not reliably differentiated from the third category of polypoid lesions—gallbladder carcinoma (except after aggressive features such as metastatic invasion or growth are evident)—follow-up (ultrasound) is warranted in lesions over 5 mm.⁶¹

CARCINOMA

Gallbladder carcinoma occurs primarily in the sixth to seventh decade of life with a female predominance (3:1). Early stage tumors are asymptomatic and often detected incidentally at

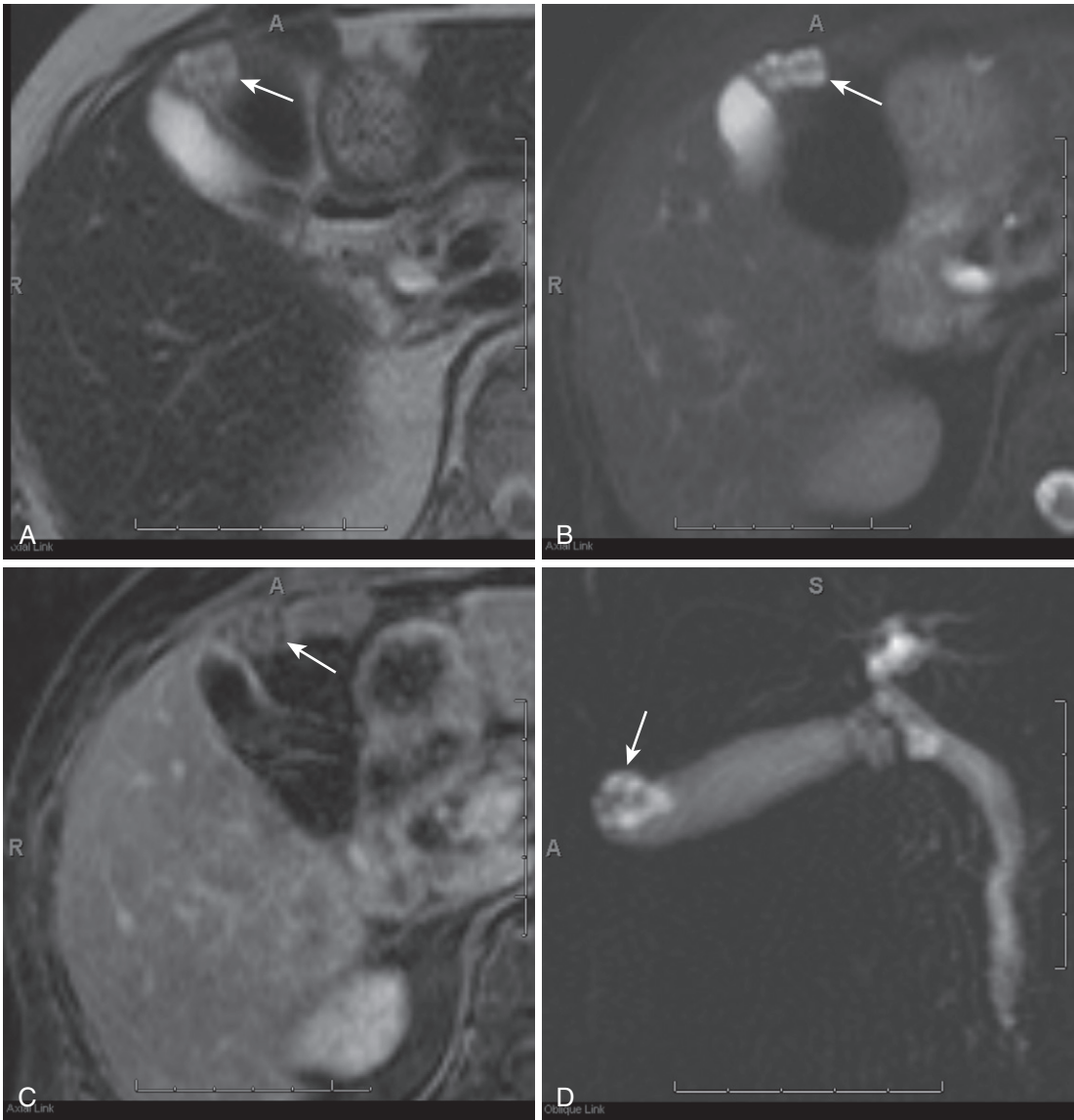


FIGURE 3-54. Adenyomyomatosis. T2-weighted (A), fat-suppressed T2-weighted (B), postcontrast fat-suppressed T1-weighted gradient recalled-echo (C), and coronal thick-slab MIP MRCP (D) images demonstrate a cluster of cystic structures at the fundus of the gallbladder (*arrow*), corresponding to multiple intramural diverticula (Rokitansky-Aschoff sinuses) of adenyomyomatosis.

surgery for benign disease. Advanced stage disease often presents with anorexia, weight loss, abdominal pain, and jaundice. MRI findings suggestive of gallbladder carcinoma include a mass protruding into the gallbladder lumen or replacing the lumen entirely, focal or diffuse gallbladder wall thickening (Fig. 3-56), and soft tissue invasion of local organs (especially the liver) (Fig. 3-57).⁶² Signal characteristics include T1 hypointensity and T2 hyperintensity relative to liver and heterogeneously hypovascular enhancement.⁶³

METASTASES

The gallbladder is infrequently involved by malignancies other than primary gallbladder carcinoma. However, melanoma and breast cancer metastasize to the gallbladder on rare occasions (Fig. 3-58).⁶⁴

BILIARY TREE

Anatomy and Normal Appearance

Intrahepatic biliary ducts follow the internal hepatic segmental anatomy; however, variations

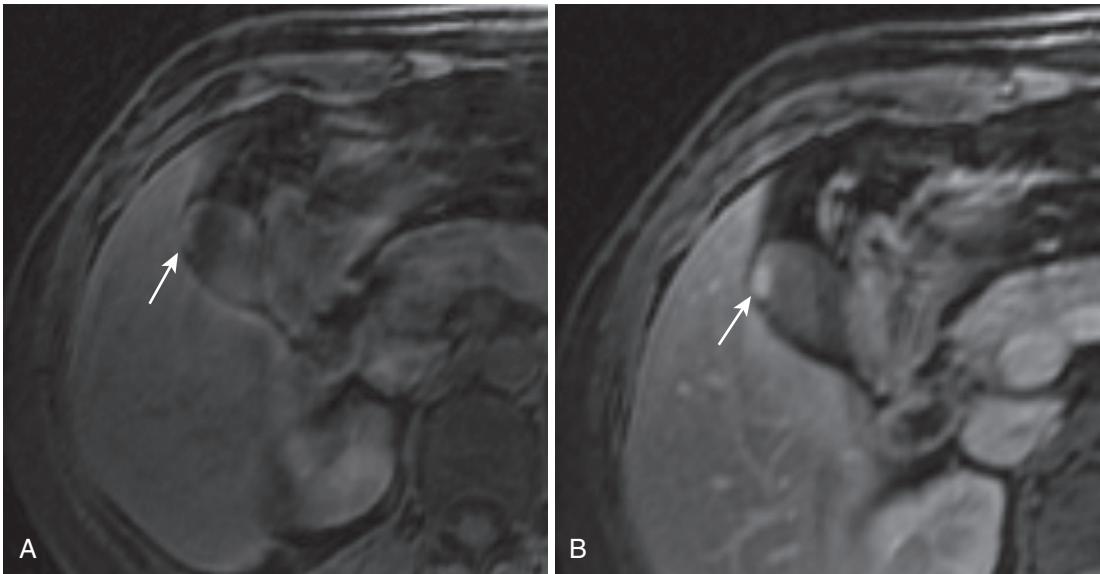


FIGURE 3-55. Gallbladder adenoma. A sessile mural-based lesion (*arrow*) exhibits moderate enhancement comparing the precontrast image (A) with the postcontrast image (B).

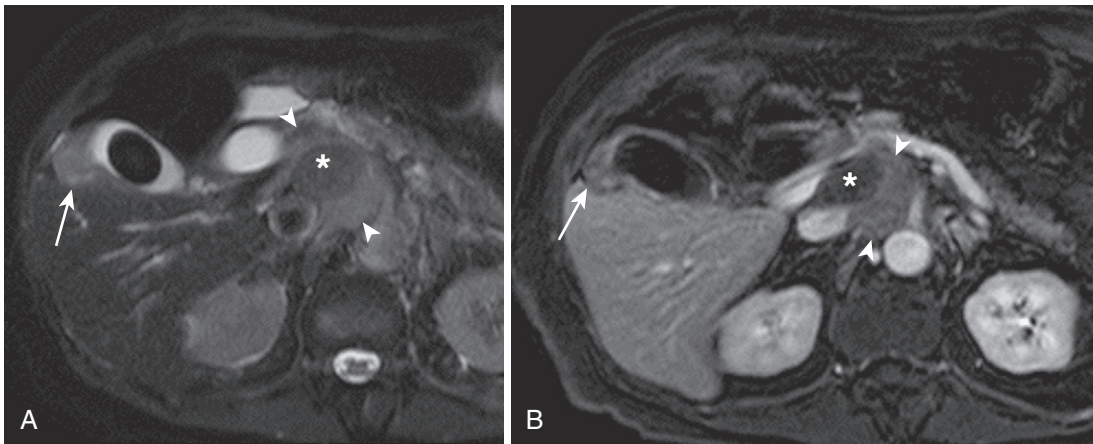


FIGURE 3-56. Gallbladder carcinoma. A, Focal gallbladder fundal mural thickening focally obliterating the lumen (*arrow*) on the T2-weighted fat-suppressed image corresponds to the primary tumor in a patient with gallbladder carcinoma (and a gallstone) with metastatic lymphadenopathy (*arrowheads*). B, The postcontrast image shows heterogeneous hypovascular enhancement of both the primary tumor (*arrow*) and the metastatic lymph nodes (*arrowheads*). Note the associated portal venous thrombosis (*asterisk*).

in the branching pattern commonly exist. Delineation of peripheral branches is variable based on patient factors, but the branches are visible when dilated. Segmental intrahepatic ducts commonly measure 3 to 4 mm in diameter. The extrahepatic bile duct (common hepatic duct and common bile duct) commonly measures up to 7 mm (10 mm in postcholecystectomy patients).^{65,66}

Pain, obstruction, and inflammatory conditions involving the biliary tree may be related to

congenital anomalies of the biliary tree, most commonly anomalies of the pancreaticobiliary junction and congenital cystic biliary disease.⁶⁶

Biliary tree variants have become of increasing importance as the role of laparoscopic surgery has increased in hepaticobiliary disease.⁶⁶

As stated in the gallbladder section, bile salts are hyperintense on T1-weighted imaging; however, this can be variable based on the concentration of the bile. The fluid content of the bile also contributes to its T2-weighted increased signal.

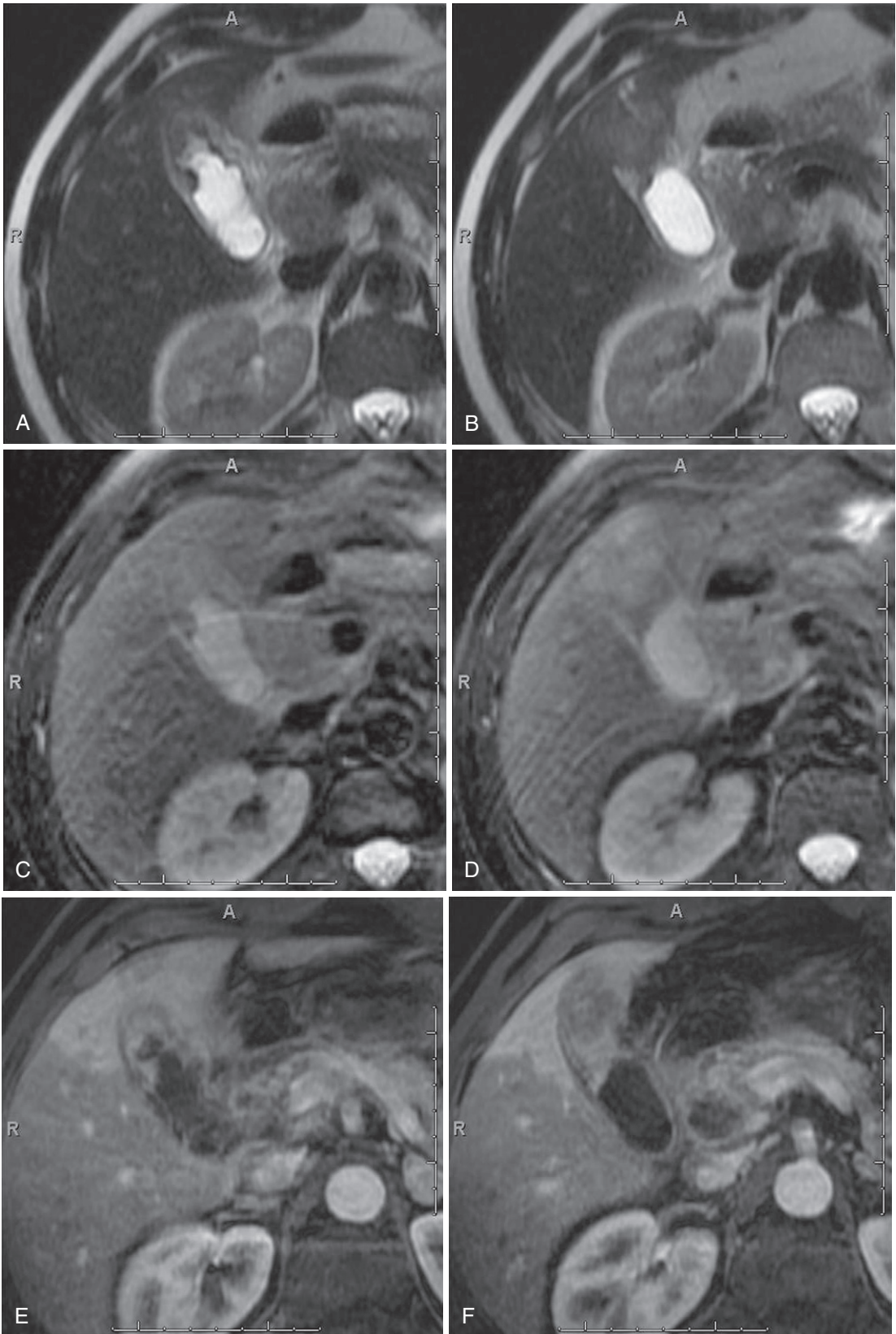


FIGURE 3-57. Gallbladder carcinoma with local invasion. Superior and inferior T2-weighted (A and B), fat-suppressed T2-weighted (C and D), and postcontrast fat-suppressed T1-weighted gradient recalled-echo (E and F) images demonstrate an enhancing soft tissue mass at the fundus of the gallbladder with direct invasion into the adjacent hepatic parenchyma, in keeping with gallbladder adenocarcinoma.

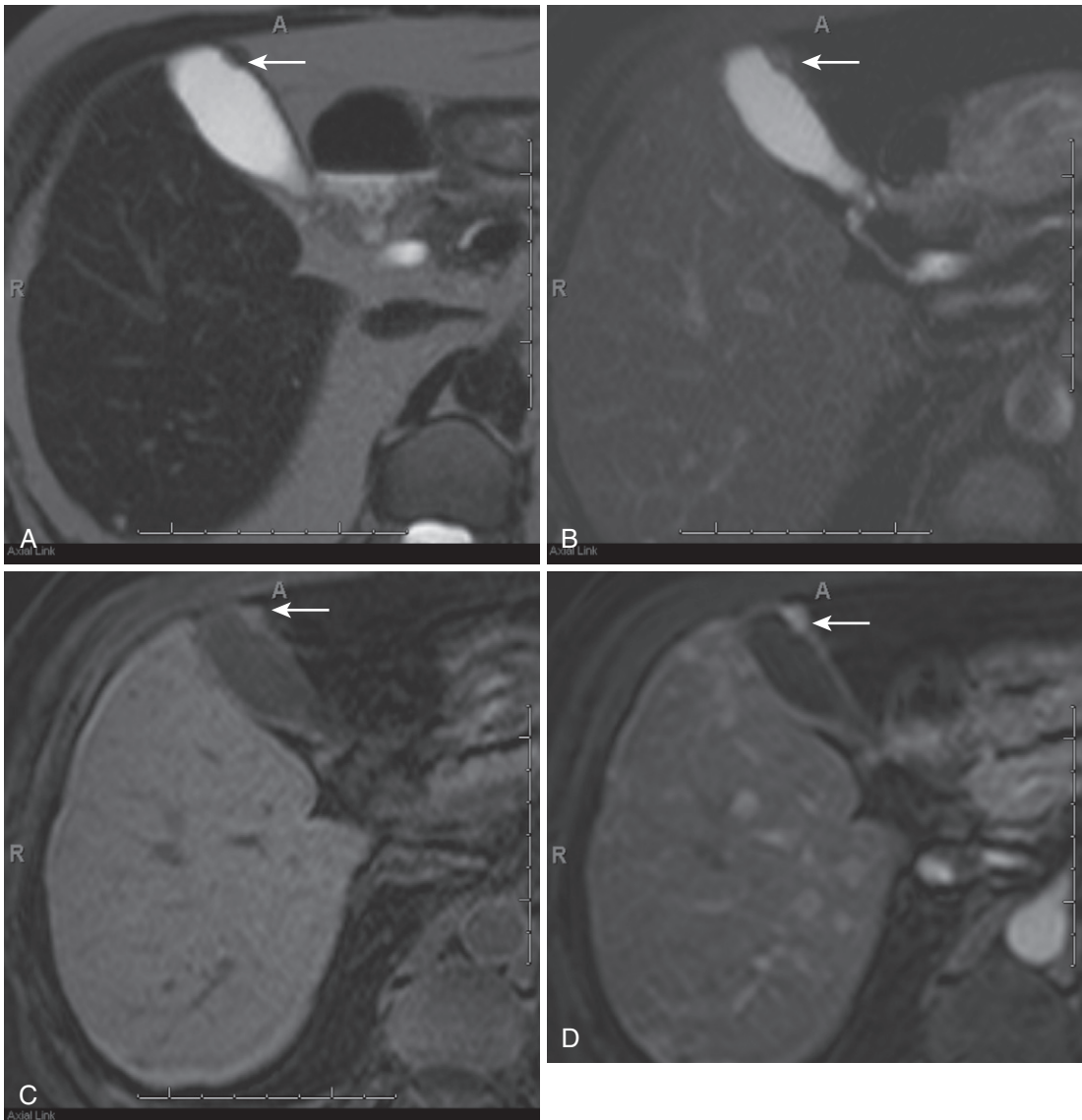


FIGURE 3-58. Gallbladder metastasis. T2-weighted (A), fat-suppressed T2-weighted (B), precontrast fat-suppressed T1-weighted (C), and postcontrast fat-suppressed T1-weighted gradient recalled-echo (D) images demonstrate an enhancing mural nodule (*arrow*), in keeping with a metastasis to the gallbladder wall.

Imaging Techniques

MRCP is a noninvasive imaging method for imaging the biliary tree that complements invasive endoscopic retrograde cholangiopancreatography (ERCP) while avoiding its complications. Furthermore, MRI has nearly replaced ERCP in situations in which the anatomy has been surgically altered, rendering ERCP difficult or impossible to perform.⁶⁵

MRCP capitalizes on the T2-weighted contrast difference between the fluid-filled structures of the biliary tree and the surrounding soft tissues. Imaging is frequently performed in the axial

and coronal planes, allowing separation from the adjacent fluid-filled bowel. Radial oblique coronal images can provide additional information in the evaluation of anatomic variants.

Subsecond breathhold techniques are critical in the acquisition of these images, eliminating respiratory motion and bowel peristalsis. Two-dimensional slab acquisition can provide an overview of the entire pancreaticobiliary tree; however, these images also need to be complemented by 3-D thin-section acquisition, which may require postprocessing to delineate subtle biliary pathology and intraductal pathology.

For evaluation of the extraductal pathology, T1-weighted pre- and postgadolinium images are crucial for evaluation of fibrosis and infiltrating masses.

Choledochal Cyst

The term choledochal cyst comprises a spectrum of congenital biliary dilatation patterns including the intrahepatic and extrahepatic ducts. The Todani classification system nicely

Type	Appearance
I	Solitary fusiform extrahepatic
II	Saccular extrahepatic
III	Choledochocele
IVa	Fusiform intra- and extrahepatic
IVb	Multiple extrahepatic
V	Caroli disease (multiple intrahepatic)

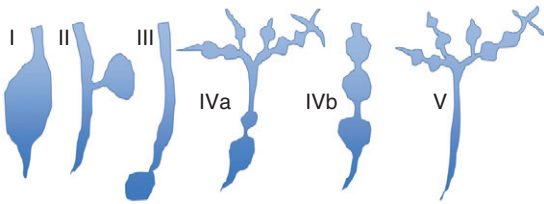


FIGURE 3-59. Todani classification of choledochal cysts.

groups this protean entity into categories according to anatomic involvement (Fig. 3-59) with type I choledochal cysts constituting 80-90% of all choledochal cysts. Postulated etiologies include an anomalous junction between the common bile and pancreatic ducts and congenital defects in bile duct wall formation. Proximal emptying of the pancreatic duct into the common bile duct exposes the common bile duct to the damaging effects of the pancreatic enzymes.

The majority of choledochal cysts are detected in childhood. While not uniformly present, the classic clinical triad includes right upper quadrant pain, jaundice and a palpable mass. Biliary stasis predisposes to gallstones, cholangitis and pancreatitis. The feared long-term complication is cholangiocarcinoma.

The imaging appearance depends on the anatomic involvement. Type I choledochal cysts appear as fusiform dilatation of the common bile duct of variable degree, simulating the appearance of mechanical biliary dilatation (i.e., by pancreatic adenocarcinoma or gallstones) (Fig. 3-60). The smooth, tapering distal margins of a choledochal cyst differ from either the irregular or polypoid margins of a dilated duct in the setting of malignant obstruction or the meniscoid margin of a dilated duct proximal to an obstructing stone (Fig. 3-61). Benign biliary strictures most closely simulate the appearance of type I choledochal cysts (see Fig. 3-61); a

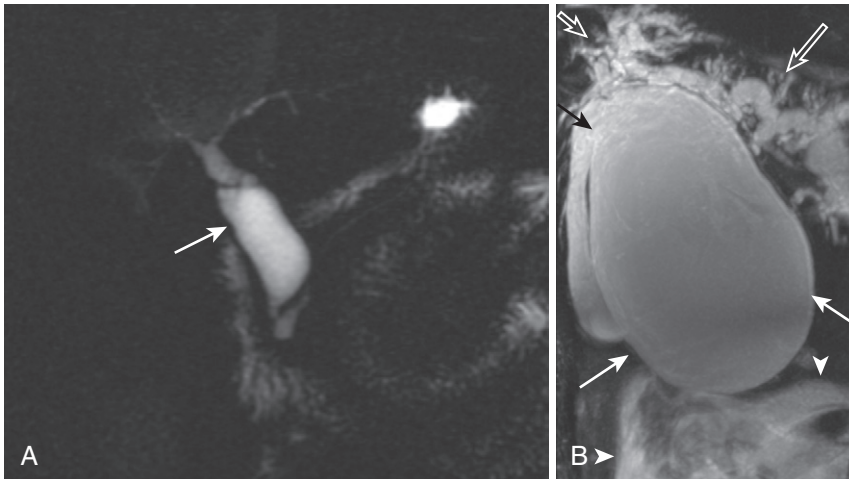


FIGURE 3-60. Type I choledochal cyst. The MRCP image (A) shows moderate fusiform dilatation of the common bile duct (arrow) without intrahepatic biliary dilatation tapering smoothly distally without evidence of an intraluminal filling defect or distal obstructing mass. The maximal intensity projectional image from a 3D MRCP image (B) in a different patient with a type I choledochal cyst (arrows) massively dilated—likely exacerbated by the gravid uterus (arrowheads) also inducing intrahepatic biliary dilatation (open arrows).

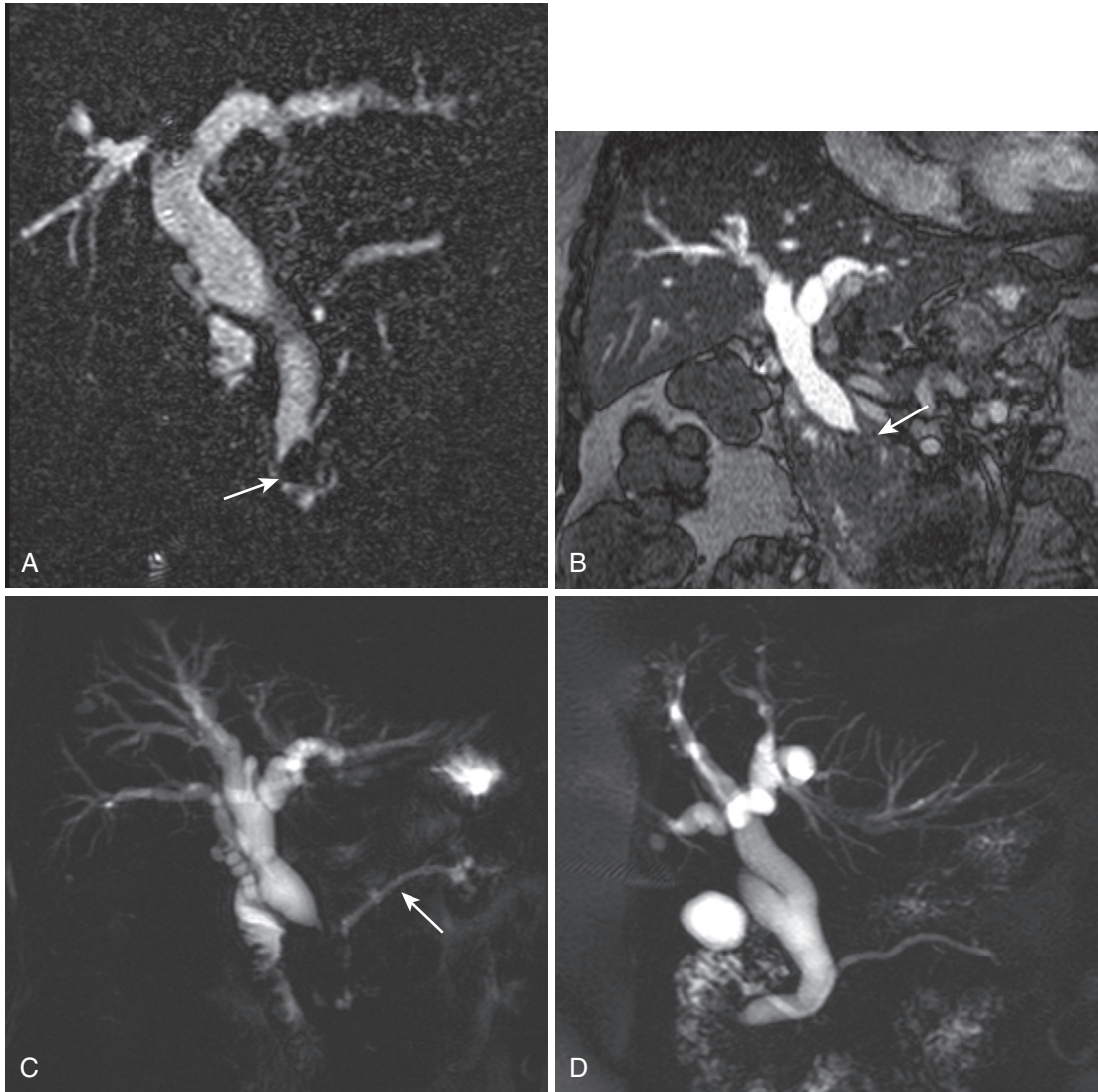


FIGURE 3-61. Differential diagnosis of type I choledochal cyst. The 3D MRCP image (A) reveals a dilated common bile duct with a distal meniscoid configuration proximal to an obstructing stone (*arrow*). In a different patient, the coronal steady state (B) and MRCP (C) images also show dilatation of the common bile duct with irregular distal margins at the level of a pancreatic head mass (*arrow* in B). Note the mildly dilated pancreatic duct (*arrow* in C). The MRCP image in a patient with a benign biliary stricture (D) depicts common bile duct dilatation with smooth distal tapering.

different clinical scenario—older patients with cholelithiasis, for example—and presence of intrahepatic biliary dilatation favor a benign biliary stricture.

Type II choledochal cysts present diagnostic uncertainty either because of the difficulty in establishing an anatomic origin from the common bile duct or because of the rarity of the entity. A narrow channel connects the saccular type II choledochal cyst with the common bile duct (Fig. 3-62). Careful attention to this feature (facilitated by using high-resolution MRCP images including 3D technique and potentially

delayed images following injection of a hepatocellular agent) differentiates the type II choledochal cyst from a duodenal diverticulum or a pancreatic pseudocyst.

The type III choledochal cyst is synonymous with choledochoceles, or intraduodenal diverticulum. The type III choledochal cyst arises from the intraduodenal segment of the common bile duct and prolapses into the duodenal lumen (Fig. 3-63). An intraduodenal cystic lesion at the level of the ampulla of Vater with continuity with the common bile duct establishes the diagnosis.

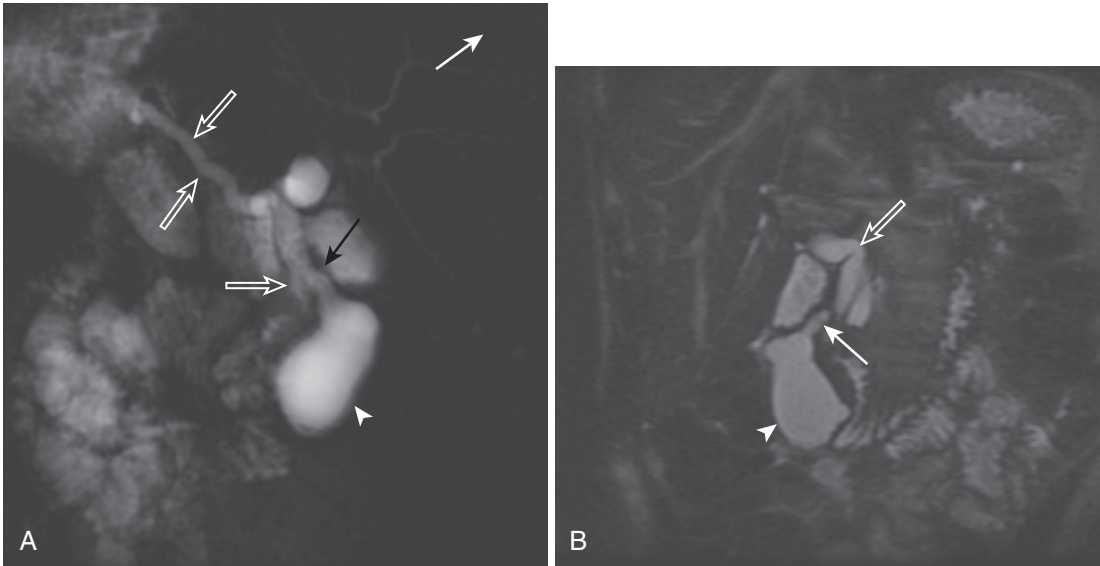


FIGURE 3-62. Type II choledochal cyst. A narrow channel (*arrow*) connecting the saccular type II choledochal cyst (*arrowhead*) with the common bile duct (*open arrows*) is better depicted on the thick-slab 2D MRCP image (A) compared with the coronal T2-weighted SSFSE image (B) due to the relatively thinner slices and lack of orientation along the plane of the connecting channel.

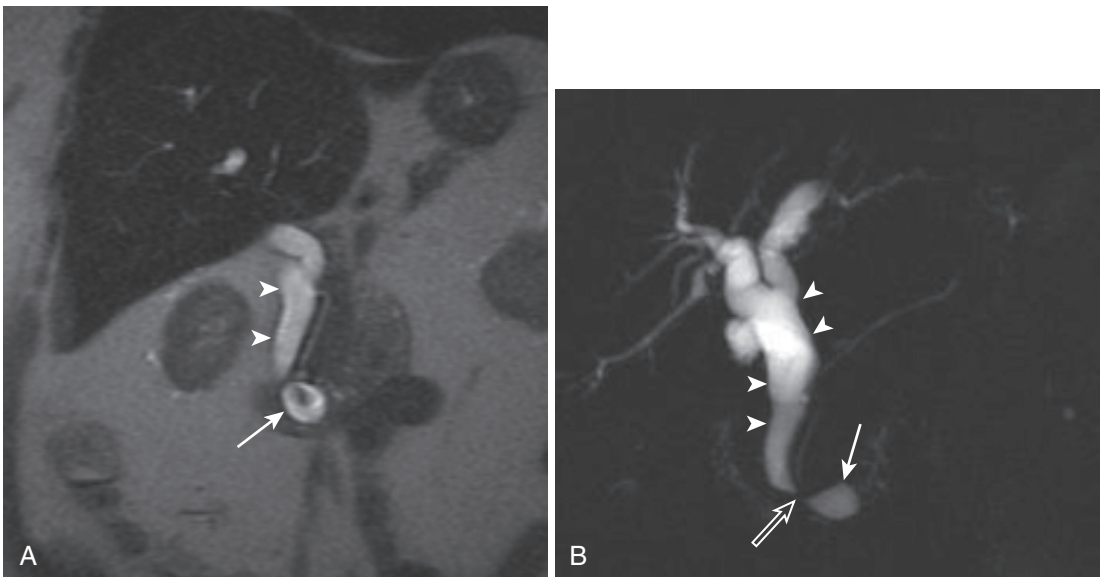


FIGURE 3-63. Type III choledochal cyst. An intraduodenal cystic lesion (*arrow*) is apparent on the MRCP (A) and coronal T2-weighted image (B), which is seen to be continuous with the common bile duct (*arrowheads*) consistent with a choledochoceles. Note the waisting at the level of the intraduodenal segment (*open arrow*).

The type IV (and V) designation connotes multiplicity. Type IVa involves the intra- and extrahepatic biliary tree, while the type IVb only involves the extrahepatic biliary tree. Chief differential considerations include biliary dilatation from mechanical causes and Caroli disease (in the case of type IVa choledochal cysts). Alternating segmental caliber changes and lack of an obstructing lesion

differentiate the type IV choledochal cysts from mechanical biliary obstruction and dilatation (Fig. 3-64). Extrahepatic involvement and lack of the “central dot sign” excludes Caroli disease.

Caroli disease is a congenital autosomal recessive disorder characterized by “(congenital) communicating cavernous ectasia of the intrahepatic biliary tract” (see Chapter 2).

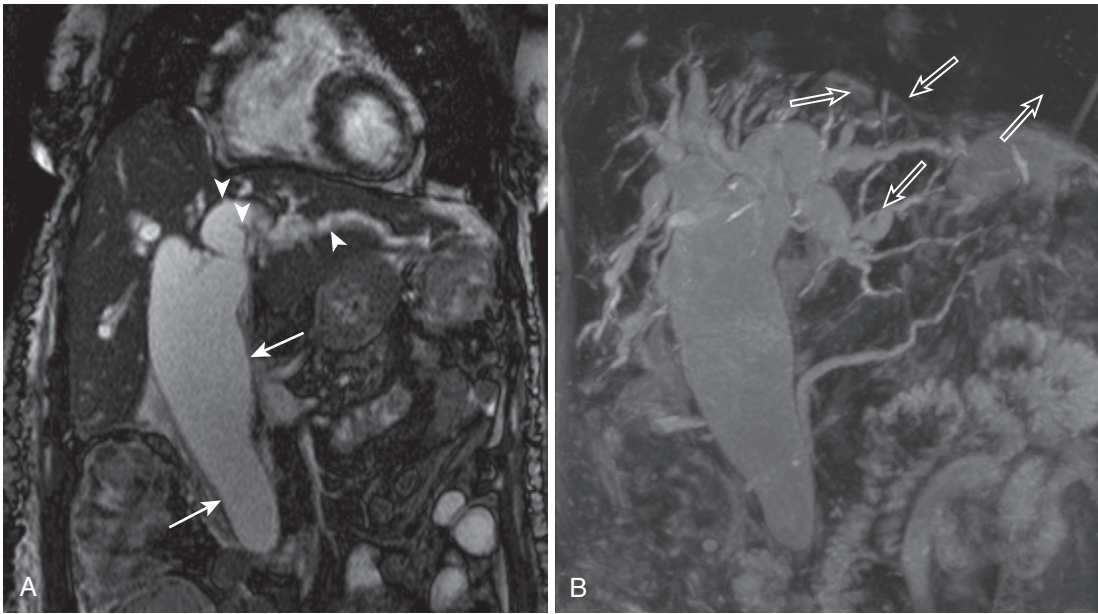


FIGURE 3-64. Type IVa choledochal cyst. The coronal steady-state image (A) shows marked fusiform dilatation of the common bile duct (*arrows*) with abnormally dilated intrahepatic ducts (*arrowheads*). The extent of multifocal intrahepatic cystic dilatation is better appreciated on the MIP image (B) from a 3D MRCP sequence.

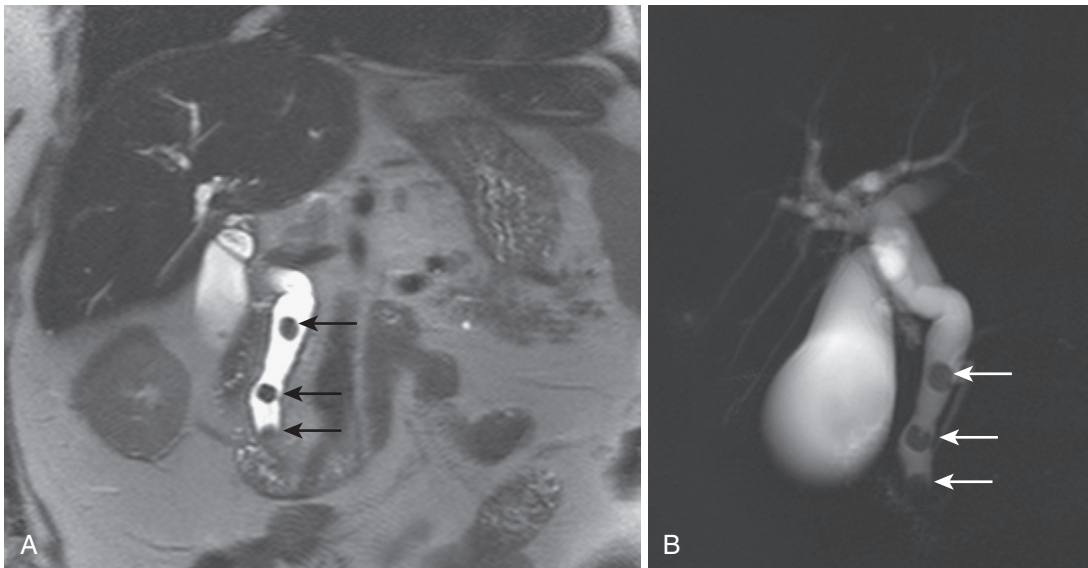


FIGURE 3-65. Choledocholithiasis. A, The coronal heavily T2-weighted image shows three filling defects (*arrows*) in the dilated CBD. B, The thick-slab MRCP image yields a more comprehensive appraisal of the biliary tree, showing choledocholithiasis (*arrows*) and the full extent of intra- and extrahepatic biliary dilatation.

Choledocholithiasis

Choledocholithiasis is the most common cause of biliary obstruction. Patients with cholelithiasis who undergo laparoscopic cholecystectomy are at higher risk for choledocholithiasis. MRCP then becomes the best noninvasive tool for determining which patients require endoscopic stone extraction (Fig. 3-65).

MIRIZZI'S SYNDROME

Mirizzi's syndrome is the obstruction of the common hepatic duct secondary to impaction of a stone within the cystic duct near its confluence with the common hepatic duct (Fig. 3-66). The role of imaging is to differentiate from other causes of obstructive jaundice. MRCP allows for noninvasive assessment of the level of

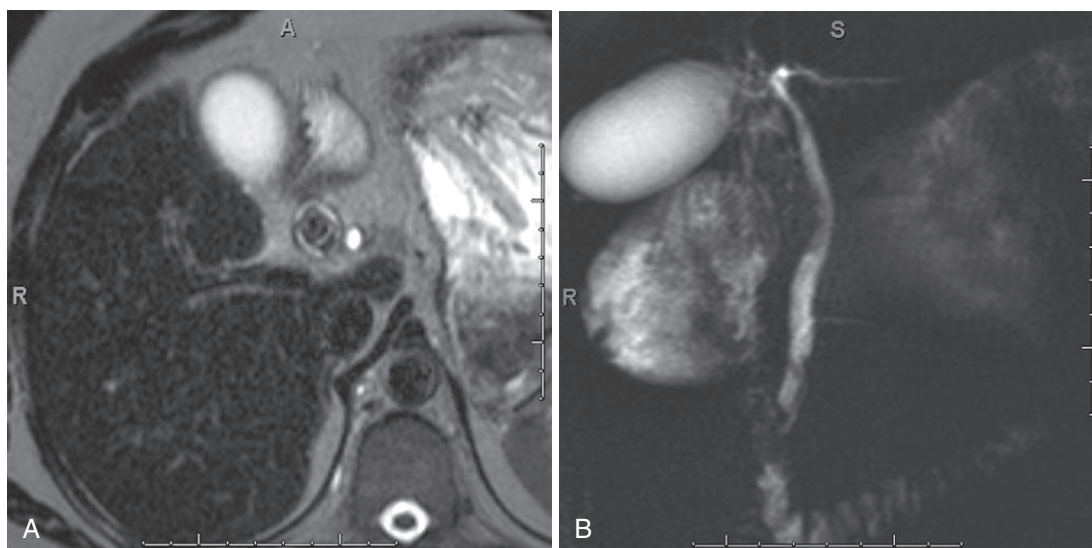


FIGURE 3-66. Mirizzi's syndrome. T2-weighted (A) and coronal thick-slab MIP MRCP (B) images demonstrate multiple stones in the cystic duct causing extrinsic compression of the adjacent common hepatic duct in this patient with Mirizzi's syndrome.

obstruction and the presence of associated gallbladder inflammatory changes.^{67,68}

BILIARY OBSTRUCTION

While measurement guidelines exist to help discriminate between unobstructed and obstructed biliary systems (intrahepatic ducts <3mm and extrahepatic ducts <7-8 mm or <10 mm post-cholecystectomy), biliary obstruction is truly a physiologic state defined by a luminal caliber reduction impeding biliary flow reflected by abnormal blood chemistry. Benign and malignant etiologies include stone disease and iatrogenic, infectious/inflammatory and neoplastic strictures (cholangiocarcinoma, pancreatic carcinoma and periampullary tumors). The goal of imaging is to identify the etiology and anatomy of the obstruction.

Benign Etiologies

Strictureing of the biliary tree occurs in both intra- and extrahepatic locations and is most commonly related to recurrent inflammatory change related to biliary stone disease. MRCP allows for assessment of length and location of these strictures. The imaging findings of benign strictures generally differ from malignant strictures in several ways: (1) mild, smooth concentric wall biliary wall thickening with mild enhancement, (2) relative short segment of involvement ($\leq 1-2$ cm) and (3) absence of an

obvious solid or mass-like component (Fig. 3-67). In addition, in the initial evaluation of these lesions, the adjacent parenchyma can be evaluated.⁵²

POSTOPERATIVE BILIARY STRICTURES

Postoperative biliary complications include a range of problems often coexisting and frequently involving biliary dilatation and/or obstruction. These include retained stones, hemorrhage, hemobilia, biliary leak, bile duct ligation and stricturing. Postsurgical strictures usually develop over months to years postoperatively and account for the majority of benign biliary strictures. The rise of laparoscopic cholecystectomy has increased the incidence of bile duct injury and stricturing (approximately 1% of laparoscopic cholecystectomies). Regardless of the procedure, the imaging appearance is the same—short segmental smooth narrowing with or without mild concentric wall thickening and enhancement. The surgical approach to treatment depends on the length and location of injury and various classification systems have been proposed to convey this information—most famously the Bismuth classification.

MRI/MRCP affords the ability to investigate surgically altered anatomy not amenable to ERCP (i.e., hepaticojejunostomy). MRI/MRCP also proffers a wealth of information in liver transplant patients in whom a host of potential complications arise, including anastomotic and nonanastomotic stenoses (see Chapter 2).

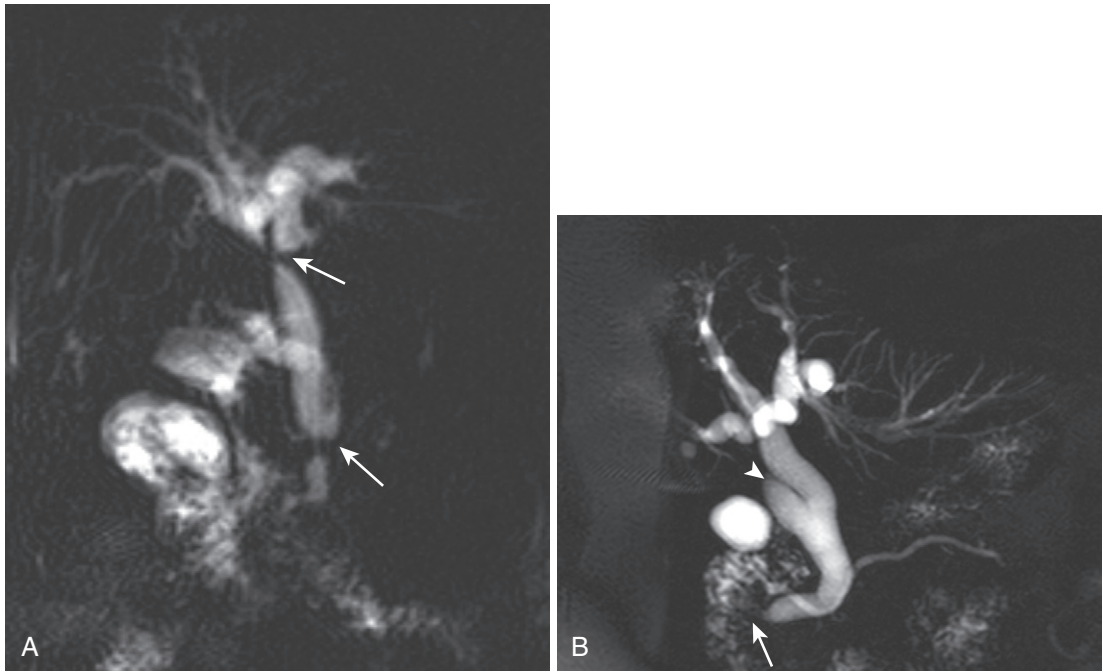


FIGURE 3-67. Benign strictures. The MRCP image in a patient with intra- and extrahepatic biliary dilatation and proximal and distal CBD strictures (arrows in A) exemplifies the smooth, short segmental involvement typical of benign biliary strictures. In a different patient with a distal CBD stricture (arrow in B) postcholecystectomy, the same features are evident, including dilatation of the cystic duct remnant (arrowhead).

INFLAMMATORY ETIOLOGIES

Cholangitis

PRIMARY SCLEROSING CHOLANGITIS

Primary sclerosing cholangitis (PSC) is a chronic idiopathic disease of the intra- and extrahepatic biliary ducts with progressive fibrosis ultimately resulting in biliary ductal obliteration and biliary cirrhosis. PSC is frequently associated with inflammatory bowel disease (70%) and incurs an increased risk for development of cholangiocarcinoma. PSC more frequently afflicts males with peak incidence in the third and fourth decades of life.

The PSC imaging features evolve over time. Early in the disease process, imaging frequently reveals randomly distributed short annular structures (1-2 mm) of the intrahepatic ducts alternating with normal or mildly dilated segments, creating the classic beaded appearance (Fig. 3-68). With continued progression of disease and destruction of peripheral ducts related to chronic inflammation, destruction, and fibrosis, the peripheral ducts will not be visible, causing a pruned appearance of the biliary tree. Relative lack of upstream biliary dilatation reflects decreased compliance of the inflamed bile duct

wall. With disease progression, the normally acute angles at bile duct intersections become gradually more obtuse approaching right angular configuration. T1-weighted, T2-weighted and postcontrast images complement MRCP images by depicting the biliary/peribiliary wall thickening and enhancement, periportal edema, as well as the reactive periportal lymphadenopathy commonly observed in PSC, as well as the reactive periportal lymphadenopathy (commonly observed in PSC).^{69,70} Cirrhosis generally ensues approximately a decade after decade onset and because of preferential involvement peripherally, end-stage PSC exhibits a characteristic peripheral atrophy-central hypertrophy pattern (see Fig. 3-68).⁷¹

INFECTIOUS CHOLANGITIS

Infectious cholangitis (also known as ascending or bacterial cholangitis) is a clinical syndrome of biliary obstruction seeded with infection arising from the gastrointestinal tract. Central intrahepatic biliary dilatation is the rule—the opposite of PSC. Smooth, circumferential ductal wall thickening and enhancement reflects underlying inflammation. Superimposed

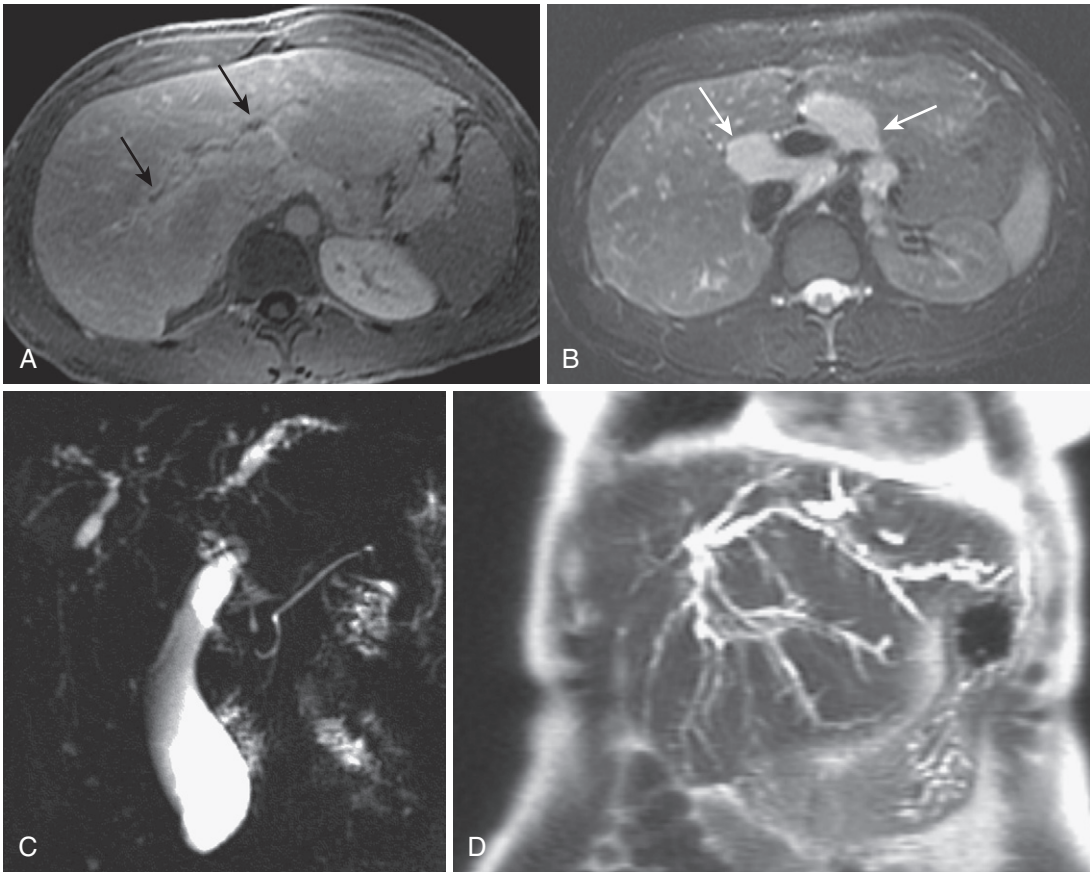


FIGURE 3-68. Primary sclerosing cholangitis (PSC). A, Delayed postcontrast image in a patient with mild, early PSC reveals periportal enhancement with irregular biliary ductal dilatation (*arrows*). B, The corresponding fat-suppressed T2-weighted image shows markedly enlarged reactive periportal lymph nodes (*arrows*). More extensive irregular, beaded ductal dilatation and stricturing is exemplified in patients with more advanced PSC on the MRCP (C) and coronal T2-weighted (D) images. Marked irregular ductal dilatation and stricturing peripherally with a characteristic central hypertrophy–peripheral atrophy pattern typifies end-stage PSC, as seen in this case on the heavily T2-weighted (E), fat-suppressed steady-state (F), and MRCP (G) images.

parenchymal inflammatory changes include avidly enhancing, geographic, wedge-shaped T2-hyperintense segments of inflamed tissue and potentially parenchymal abscesses (see Chapter 2).⁷²

MALIGNANT ETIOLOGIES

Cholangiocarcinoma

Cholangiocarcinoma is a tumor arising from intra- or extrahepatic biliary epithelium (90% adenocarcinoma and 10% squamous cell carcinoma) affecting men and women in equal proportions. Increased risk exists in patients with PSC, recurrent pyogenic cholangitis, and congenital cystic biliary disease.

Cholangiocarcinoma stratifies into three anatomic categories: (1) peripheral tumors (see

Chapter 2), (2) hilar (Klatskin) tumors involving the right and/or left first order bile ducts and/or their confluence and (3) extrahepatic tumors. While generally exhibiting infiltrative growth dissecting along tissue planes, on a macroscopic/imaging level, three distinct growth patterns are observed: (1) mass-forming, (2) periductal-infiltrating and (3) intraductal-growing or polypoid (Fig. 3-69).

Central/hilar lesions classically follow the periductal-infiltrative growth pattern and the subtle periductal signal alteration and enhancement is often perceived only after the upstream biliary dilatation is noted and traced to the point of obstruction (Figs. 3-70 and 3-71).

Occasionally, extrahepatic cholangiocarcinoma follows an intraductal masslike growth pattern, which simulates choledocholithiasis on MRCP images (Fig. 3-72). There may be

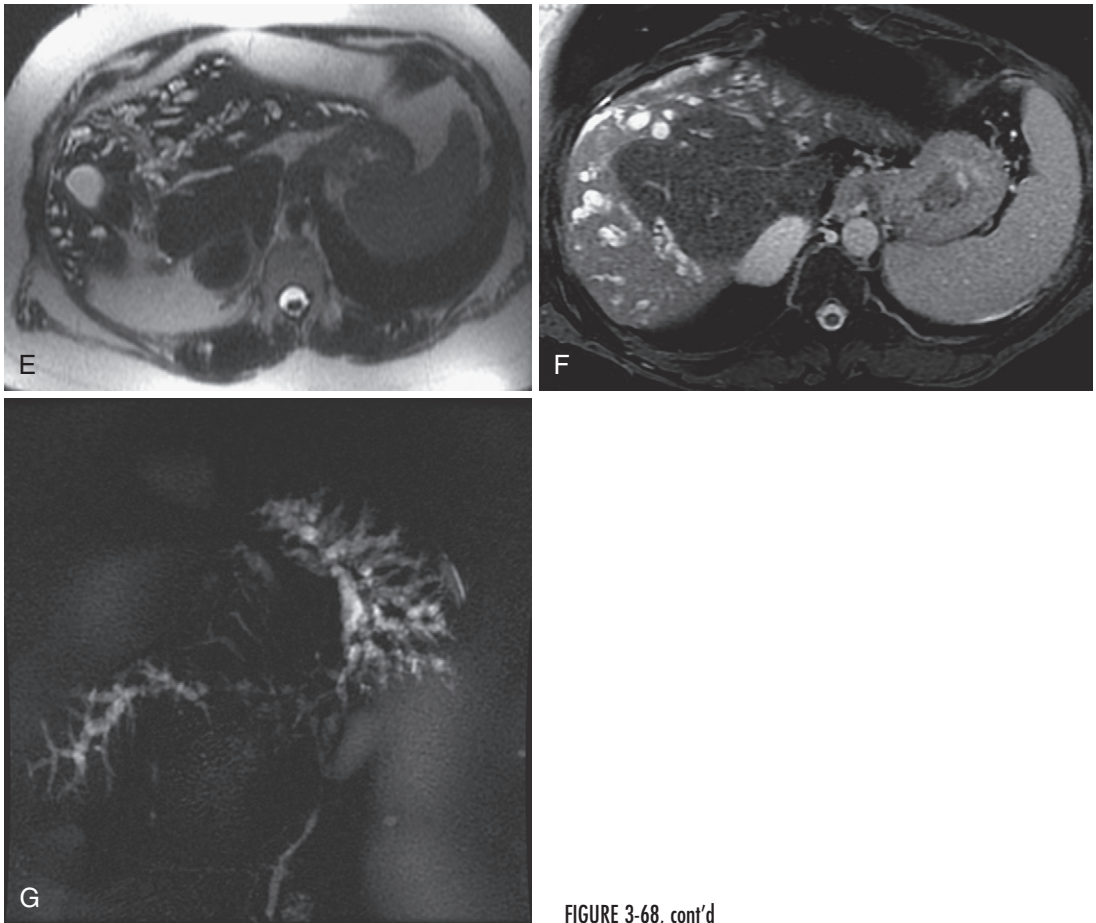


FIGURE 3-68, cont'd

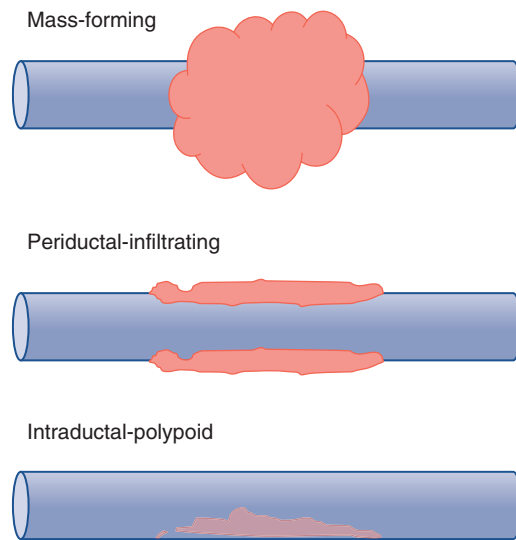


FIGURE 3-69. Cholangiocarcinoma growth patterns.

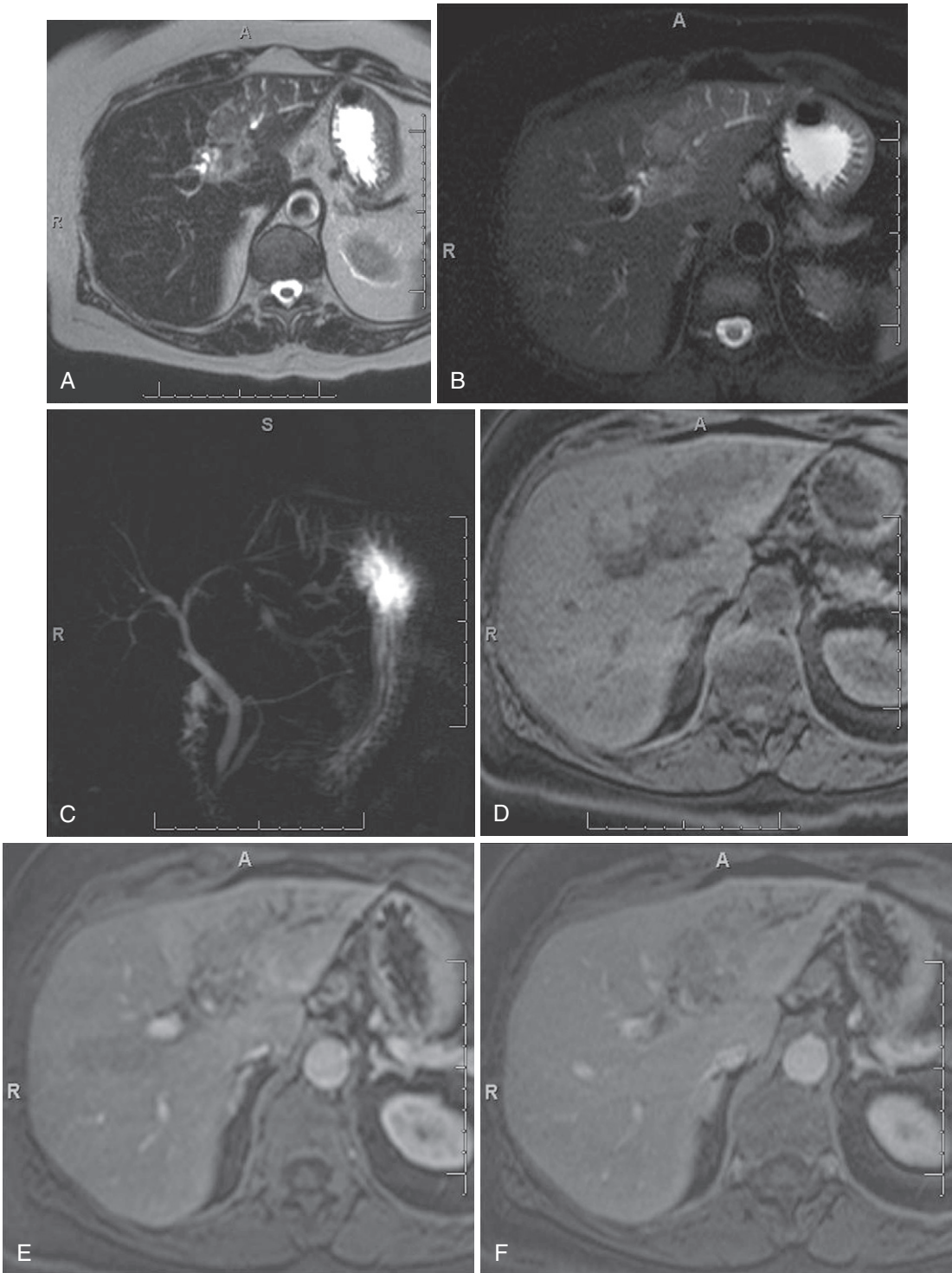


FIGURE 3-70. Hilar cholangiocarcinoma. T2-weighted (A), fat-suppressed T2-weighted (B), coronal thick-slab MIP MRCP (C), and precontrast (D), early arterial phase (E), and delayed phase (F) fat-suppressed T1-weighted gradient recalled-echo images demonstrate a mildly T2 hyperintense, gradually enhancing, intrahepatic, infiltrative mass with peripheral biliary radical dilatation.

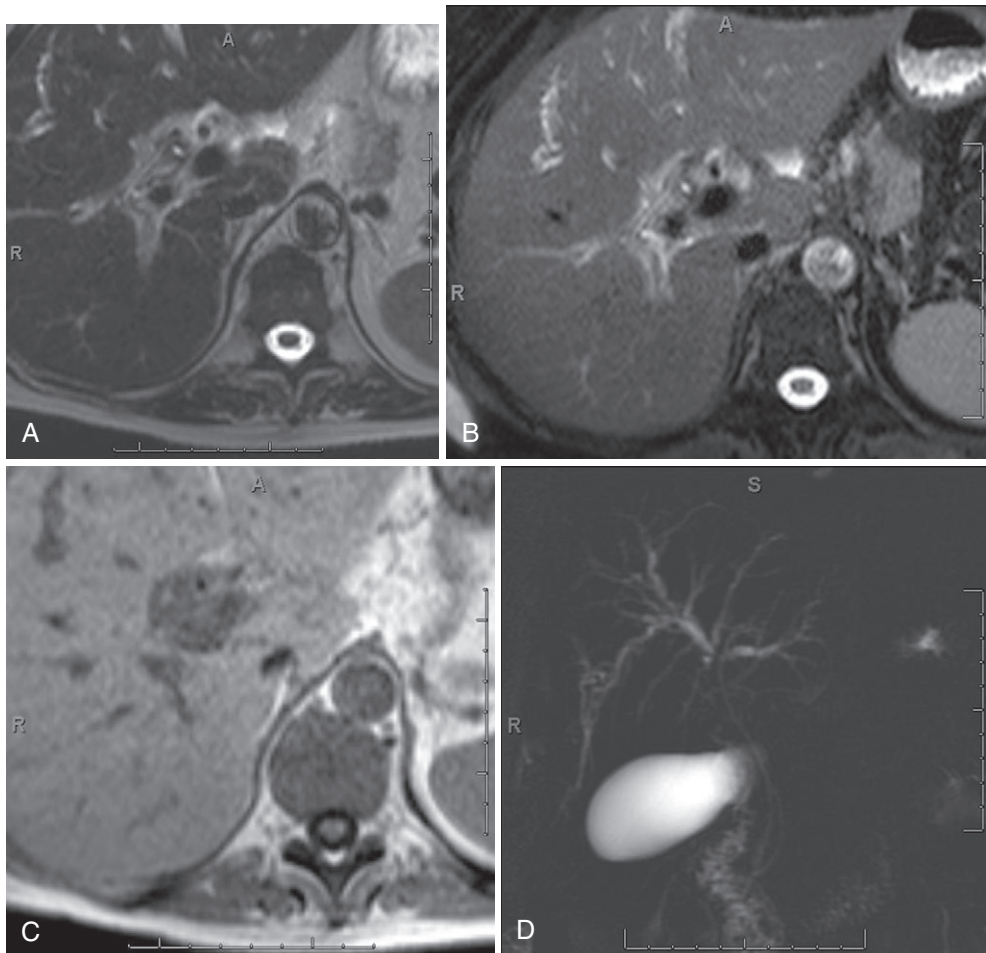


FIGURE 3-71. Cholangiocarcinoma with periductal-infiltrating growth pattern. T2-weighted (A), fat-suppressed T2-weighted (B), in-phase T1-weighted (C), coronal thick-slab MIP MRCP (D), and precontrast (E), early arterial phase (F), and delayed phase (G) fat-suppressed T1-weighted gradient recalled-echo images demonstrate gradually enhancing soft tissue about the extrahepatic bile duct causing intrahepatic biliary ductal dilatation in keeping with cholangiocarcinoma.

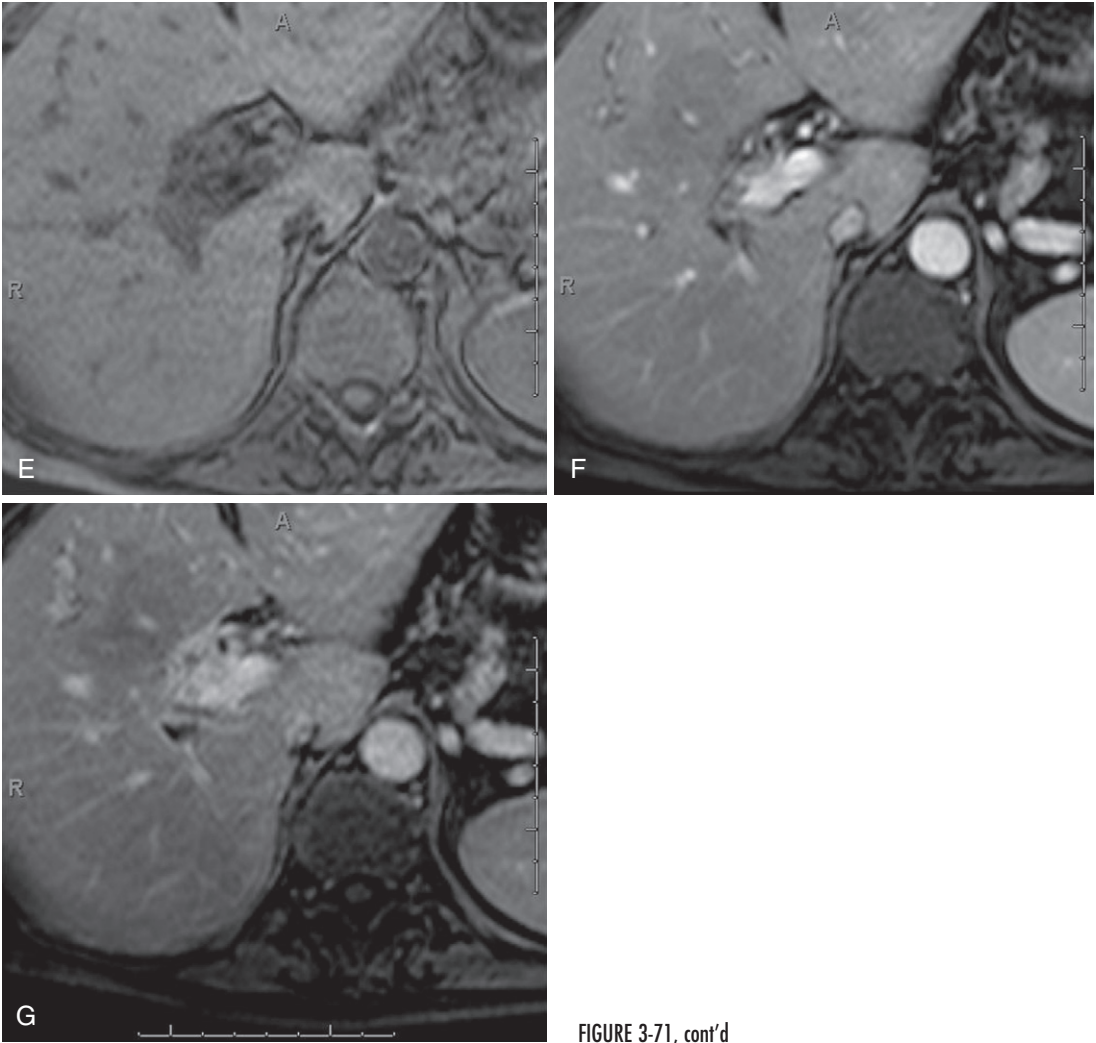


FIGURE 3-71, cont'd

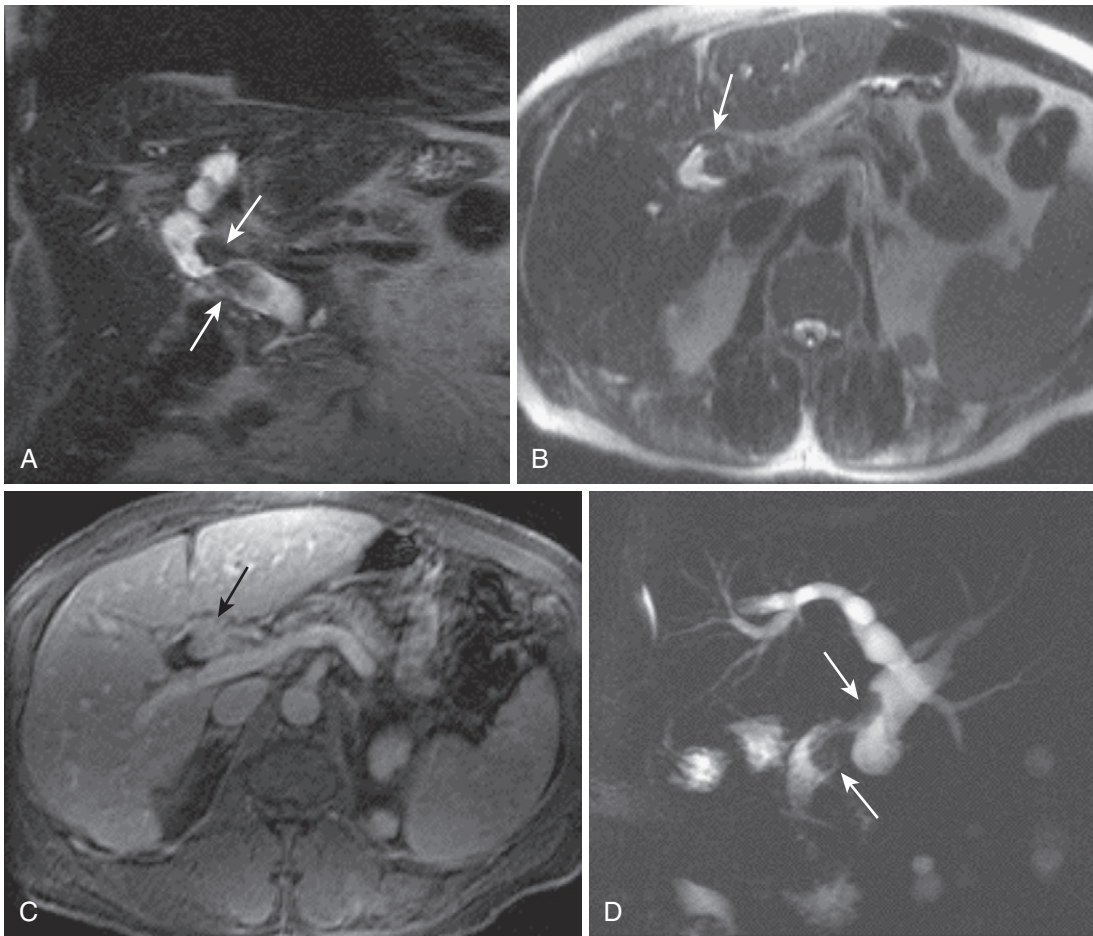


FIGURE 3-72. Cholangiocarcinoma with intraductal growth pattern. The coronal (A) and axial (B) heavily T2-weighted images depict hypointense irregular filling defects in the CBD (*arrows*) with enhancement revealed on the postcontrast image (C), indicating solid tissue in this uncommon case of extrahepatic, intraductal, mass-forming cholangiocarcinoma (*arrow*). D, MRCP shows stricturing of the CBD with upstream biliary dilatation (*arrows*).

intrahepatic duct crowding in the setting of ipsilateral hepatic lobar atrophy related to central duct obstruction or portal vein occlusion.^{73,74}

AMPULLARY CARCINOMA

Ampullary carcinoma is a neoplasm developing from either ductal epithelium within the ampulla (i.e., ampullary CBD, ampullary pancreatic duct or the common ampullary channel) or the duodenal papillary epithelium. Ampullary carcinoma generally portends a favorable prognosis because of the early presentation provoked by either biliary obstruction or gastrointestinal bleeding.

More commonly seen in males, an association with familial adenomatous polyposis has been documented. Most patients present secondary to biliary obstruction or gastrointestinal bleeding.

At imaging, these patients have biliary and pancreatic duct dilatation (with or without side branch dilatation), and the ampullary lesion is frequently not visualized. Under these circumstances, it is impossible to distinguish between ampullary carcinoma and a benign ampullary stricture. When the ampullary lesion is visualized, imaging features include a nodular or infiltrative mass, low signal intensity on T1-weighted and T2-weighted images with homogeneous early enhancement and variable rim

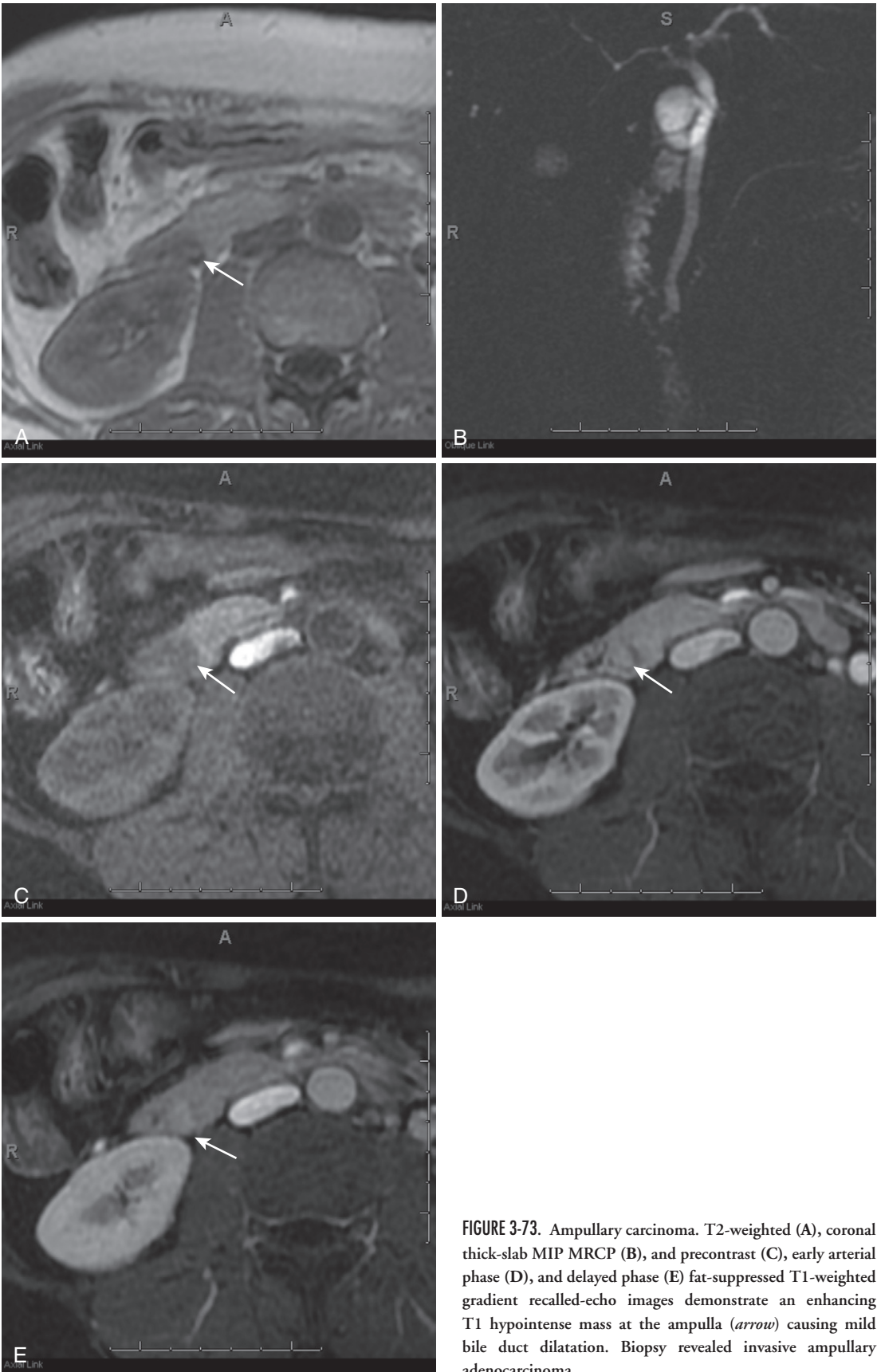


FIGURE 3-73. Ampullary carcinoma. T2-weighted (A), coronal thick-slab MIP MRCP (B), and precontrast (C), early arterial phase (D), and delayed phase (E) fat-suppressed T1-weighted gradient recalled-echo images demonstrate an enhancing T1 hypointense mass at the ampulla (*arrow*) causing mild bile duct dilatation. Biopsy revealed invasive ampullary adenocarcinoma.

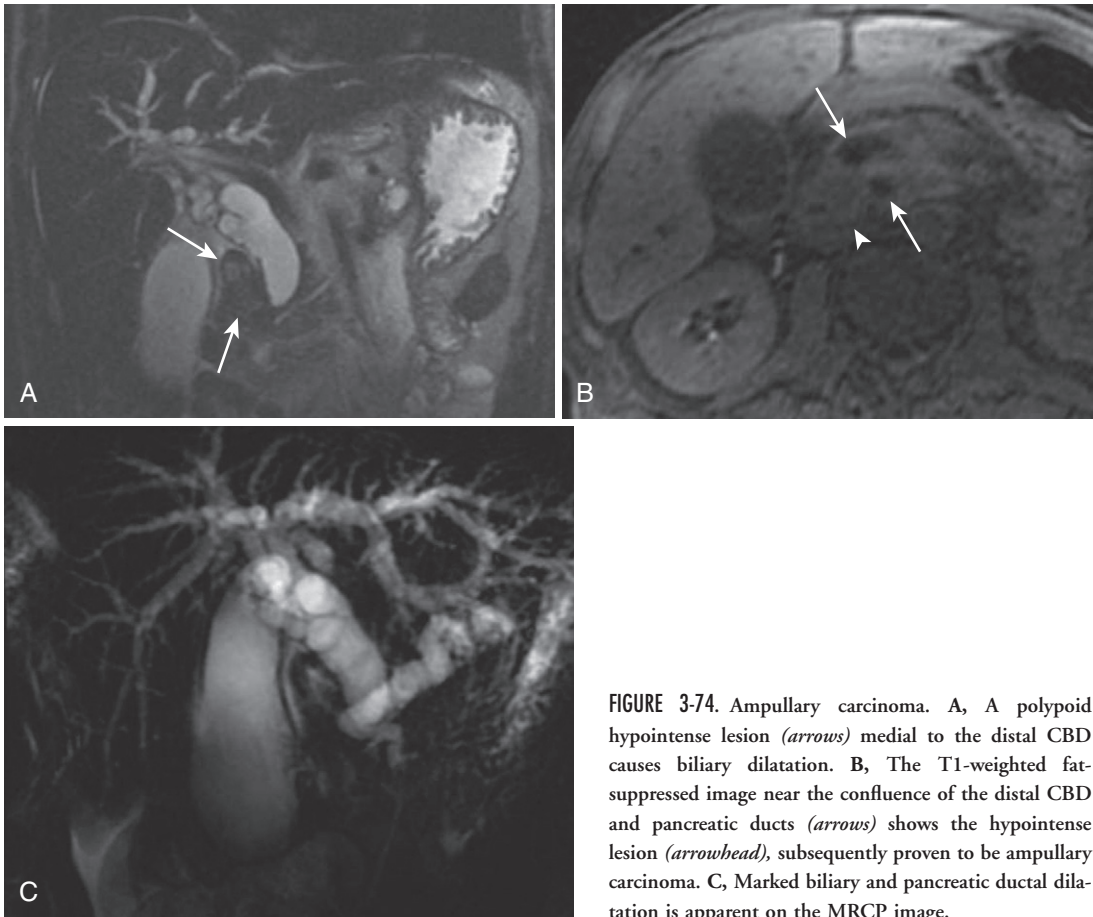
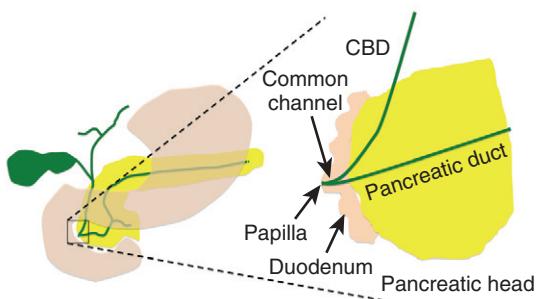


FIGURE 3-74. Ampullary carcinoma. **A**, A polypoid hypointense lesion (*arrows*) medial to the distal CBD causes biliary dilatation. **B**, The T1-weighted fat-suppressed image near the confluence of the distal CBD and pancreatic ducts (*arrows*) shows the hypointense lesion (*arrowhead*), subsequently proven to be ampullary carcinoma. **C**, Marked biliary and pancreatic ductal dilatation is apparent on the MRCP image.



Periampullary carcinomas

Common channel	Duodenum	Pancreatic head	CBD
Ampullary carcinoma	Duodenal adenocarcinoma	Pancreatic adenocarcinoma	Cholangiocarcinoma

FIGURE 3-75. The periampullary region.

enhancement on delayed images with papillary bulging (Figs. 3-73 and 3-74). The ductal dilatation pattern depends on the anatomy of the intersection of the pancreatic and common bile ducts—which is variable—either demonstrating isolated biliary dilatation or dilatation of both the biliary and pancreatic ducts (double duct sign).^{75,76} However, establishing a specific histologic diagnosis in the setting of a suspected “periampullary mass” is problematic because of the multiplicity of lesions originating from the ampullary region and overlap in imaging findings (Fig. 3-75). The term “periampullary mass” serves to convey the fact that an obstructing mass requiring further investigation (ERCP) is warranted without potentially erroneously assigning a tissue diagnosis.

Additional images for this chapter are available online on Expert Consult at www.expertconsult.com.



References

- Semelka RC, Ascher SM. MR imaging of the pancreas. *Radiology* 188:593-602, 1993.
- Winston CB, Mitchell DG, Outwater EK, Ehrlich SM. Pancreatic signal intensity on T1-weighted fat saturation MR images: Clinical correlation. *J Magn Reson Imaging* 5:267-271, 1995.
- Hamed MM, Hamm B, Ibrahim ME, et al. Dynamic MR imaging of the abdomen with gadopentetate dimeglumine: Normal enhancement of the liver, spleen, stomach, and pancreas. *AJR Am J Roentgenol* 158:303-307, 1992.
- Brailsford J, Ward J, Chalmers A, et al. Dynamic MRI of the pancreas-gadolinium enhancement in normal tissue. *Clin Radiol* 49:104-108, 1994.
- Mitchell DG, Winston CB, Outwater EK, Ehrlich SM. Delineation of pancreas with MR imaging: Multiobserver comparison of five pulse sequences. *J Magn Reson Imaging* 5:193-199, 1995.
- Kanematsu M, Shiratori Y, Hoshi H, et al. Pancreas and peripancreatic vessels: Effect of imaging delay on gadolinium enhancement at dynamic gradient-recalled echo MR imaging. *Radiology* 215:95-102, 2000.
- Yu J, Turner MA, Fulcher AS, et al. Congenital anomalies and normal variants of the pancreaticobiliary tract and the pancreas in adults: Part 2: Pancreatic duct and pancreas. *AJR Am J Roentgenol* 187:1544-1553, 2006.
- Wang G-J, Gao C-F, Wei D, et al. Acute pancreatitis: Etiology and common pathogenesis. *World J Gastroenterol* 15:1427-1430, 2009.
- Piironen A. Severe acute pancreatitis: Contrast-enhanced CT and MRI features. *Abdom Imaging* 26:225-233, 2001.
- Ward J, Chalmers A, Guthrie A, et al. T2-weighted and dynamic enhanced MRI in acute pancreatitis: Comparison with contrast enhanced CT. *Clin Radiol* 52:109-114, 1997.
- Amano Y, Oishi T, Takahashi M, Kumazaki T. Nonenhanced magnetic resonance imaging of mild acute pancreatitis. *Abdom Imaging* 26:59-63, 2001.
- Pitchumoni C, Agarwal N. Pancreatic pseudocysts: When and how should drainage be performed? *Gastroenterol Clin North Am* 28:615-639, 1999.
- Paulson EK, Vitellas KM, Keogan MT, et al. Acute pancreatitis complicated by gland necrosis: Spectrum of findings on contrast-enhanced CT. *AJR Am J Roentgenol* 172:609-613, 1999.
- Stabile B, Wilson S, Debas HT. Reduced mortality from bleeding pseudocysts and pseudoaneurysms caused by pancreatitis. *Arch Surg* 118:45-51, 1983.
- Crowe P, Sagar G. Reversible superior mesenteric vein thrombosis in acute pancreatitis: The CT appearance. *Clin Radiol* 50:628-633, 1995.
- Etemad B, Whitcomb DC. Chronic pancreatitis: Diagnosis, classification, and new genetic developments. *Gastroenterology* 120:682-707, 2001.
- Johnson PT, Outwater EK. Pancreatic carcinoma versus chronic pancreatitis: Dynamic MR imaging. *Radiology* 212:213-218, 1999.
- Miller FH, Keppke AL, Wadhwa A, et al. MRI of pancreatitis and its complications: Part 2, Chronic pancreatitis. *AJR Am J Roentgenol* 183:1645-1652, 2004.
- Sahani DV, Kalva SP, Farrell J, et al. Autoimmune pancreatitis: Imaging features. *Radiology* 233:345-352, 2004.
- Kawamoto S, Siegelman SS, Hruban RH, Fishman EK. Lymphoplasmacytic sclerosing pancreatitis (autoimmune pancreatitis): Evaluation with multidetector CT. *Radiographics* 28:157-170, 2008.
- Blasbalg R, Baroni RH, Costa DN, et al. MRI features of groove pancreatitis. *AJR Am J Roentgenol* 189:73-80, 2007.
- Rothstein FC, Wyllie R, Gauderer MW. Hereditary pancreatitis and recurrent abdominal pain of childhood. *J Pediatr Surg* 20:535-537, 1985.
- Ferrozzi F, Bova D, Campodonico F, et al. Cystic fibrosis: MR assessment of pancreatic damage. *Radiology* 198:875-879, 1996.
- King U, Scurr ED, Murugan N, et al. Hepatobiliary and pancreatic manifestations of cystic fibrosis: MR imaging appearances. *Radiographics* 20:767-777, 2000.
- Siegelman ES, Mitchell DG, Outwater E, et al. Idiopathic hemochromatosis: MR imaging findings in cirrhotic and precirrhotic patients. *Radiology* 188:637-641, 1993.
- Siegelman ES, Mitchell DG, Semelka RC. Abdominal iron deposition: Metabolism, MR findings, and clinical importance. *Radiology* 199:13-22, 1996.
- Hammel PR, Vilgrain V, Terris B, et al. Pancreatic involvement in von Hippel-Lindau disease. *Gastroenterology* 119:1087-1095, 2000.
- Tamm E, Silverman P, Charnsangavej C, Evans DB. Diagnosis, staging, and surveillance of pancreatic cancer. *AJR Am J Roentgenol* 180:1311-1323, 2003.
- Horner MJ, Ries LAG, Krapcho M, et al, editors. SEER Cancer Statistics Review, 1975-2006. Bethesda, MD: National Cancer Institute. Available at http://seer.cancer.gov/csr/1975_2006/ Based on November 2008 SEER data submission, posted to the SEER website, 2009.
- Soto JA, Alvarez O, Lopera JE, et al. Biliary obstruction: Findings at MR cholangiography and cross-sectional MR imaging. *Radiographics* 20:353-366, 2000.
- Lopez HE, Amthauer H, Hosten N, et al. Prospective evaluation of pancreatic tumors: Accuracy of MR imaging with MR cholangiopancreatography and MR angiography. *Radiology* 224:34-41, 2002.
- Ahualli J. The double duct sign. *Radiology* 244:314-315, 2007.
- Martin DR, Semelka RC. MR imaging of pancreatic masses. *Magn Reson Imaging Clin North Am* 8:787-812, 2000.
- Kozuch P, Petryk M, Evans A, Bruckner HW. Treatment of metastatic pancreatic adenocarcinoma. *Surg Clin North Am* 81:683-690, 2001.
- Owen N, Sahib S, Peppercorn P, et al. MRI of pancreatic neuroendocrine tumours. *Br J Radiol* 74:968-973, 2001.
- Semelka RC, Custodio CM, Balci NC, Wooslev JT. Neuroendocrine tumors of the pancreas: Spectrum of appearances on MRI. *J Magn Reson Imaging* 11:141-148, 2000.
- Lewis RB, Lattin GE, Paal E. Pancreatic endocrine tumors: Radiologic-clinicopathologic correlation. *Radiographics* 30:1445-1464, 2010.
- Klein KA, Stephen DH, Welch TJ. CT characteristics of metastatic disease of the pancreas. *Radiographics* 18:369-378, 1998.
- Merkle EM, Bender GN, Brams HJ. Imaging findings in pancreatic lymphoma: Differential aspects. *AJR Am J Roentgenol* 174:671-675, 2000.
- Ros PR, Hamrick-Turner JE, Chiechi MV, et al. Cystic masses of the pancreas. *Radiographics* 12:673-686, 1992.
- Box JC, Douglass HO. Management of cystic neoplasms of the pancreas. *Am Surg* 66:435-501, 2000.
- Demos TC, Posniak HV, Harmath C, et al. Cystic lesions of the pancreas. *AJR Am J Roentgenol* 179:1375-1388, 2002.
- Taouli B, Vilgrain V, O'Toole D, et al. Intraductal papillary mucinous tumors of the pancreas: Features with multimodality imaging. *J Comput Assist Tomogr* 26:223-231, 2002.

44. Fukukura Y, Fujiyoshi F, Hamada H, et al. Intraductal papillary mucinous tumors of the pancreas: Comparison of helical CT and MR imaging. *Acta Radiol* 44:464-471, 2003.
45. Irie H, Yoshimitsu K, Aibe H, et al. Natural history of pancreatic intraductal papillary mucinous tumor of branch duct type. *J Comput Assist Tomogr* 28:117-122, 2004.
46. Sarr MG, Kendrick ML, Nagorney DM, et al. Cystic neoplasms of the pancreas: Benign to malignant epithelial neoplasms. *Surg Clin North Am* 81:497-509, 2001.
47. Sugiyama M, Izumisato Y, Abe N, et al. Predictive factor for malignancy in intraductal papillary-mucinous tumours of the pancreas. *Br J Surg* 90:1244-1249, 2003.
48. Sugiyama M, Atomi Y, Hachiya J. Intraductal papillary tumors of the pancreas: Evaluation with magnetic resonance cholangiopancreatography. *Am J Gastroenterol* 93:156-159, 1998.
49. Iselin C, Meyer P, Hauser H, et al. Computed tomography and fine needle aspiration cytology for preoperative evaluation of cystic tumours of the pancreas. *Br J Surg* 80:1166-1169, 1993.
50. Mergo PJ, Helmberger TK, Buetow PC, et al. Pancreatic neoplasms: MR imaging and pathologic correlation. *Radiographics* 17:281-301, 1997.
51. Buetow PC, Rao P, Thompson LD. Mucinous cystic neoplasms of the pancreas: Radiologic-pathologic correlation. *Radiographics* 18:433-449, 1998.
52. Buetow PC, Buck JL, Pantongrag-Brown L, et al. Solid and papillary epithelial neoplasm of the pancreas: Imaging-pathologic correlation in 56 cases. *Radiology* 199:707-711, 1996.
53. Coleman KM, Doherty MC, Bigler SA. Solid-pseudopapillary tumor of the pancreas. *Radiographics* 23:1644-1648, 2003.
54. Kelekis N, Semelka R. MR imaging of the gallbladder. *Top Magn Reson Imaging* 8:312-320, 1996.
55. Loud P, Semelka R, Kettritz U, et al. MRI of acute cholecystitis: Comparison with the normal gallbladder and other entities. *Magn Reson Imaging* 14:349-355, 1996.
56. Abou-Saif A, Al-Kawas F. Complications of gallstone disease: Mirizzi syndrome, cholecystocholedochal fistula, and gallstone ileus. *AJR Am J Roentgenol* 97:249-254, 2002.
57. Yamashita K, Jin M, Hirose Y, et al. CT finding of transient focal increased attenuation of the liver adjacent to the gallbladder in acute cholecystitis. *AJR Am J Roentgenol* 164:343-346, 1995.
58. Pedrosa I, Guarise A, Goldsmith J, et al. The interrupted rim sign in acute cholecystitis: A method to identify the gangrenous form with MRI. *J Magn Reson Imaging* 18:360-363, 2003.
59. Kim M, Oh Y, Park Y, et al. Gallbladder adenomyomatosis: findings on MRI. *Abdom Imaging* 24:410-413, 1999.
60. Haradome H, Ichikawa T, Sou H, et al. The pearl necklace sign: an imaging sign of adenomyomatosis of the gallbladder at MR cholangiopancreatography. *Radiology* 227:80-88, 2003.
61. Collett J, Allan R, Chisholm R, et al. Gallbladder polyps: prospective study. *J Ultrasound Med* 17:207-211, 1998.
62. Furlan A, Ferris JV, Hosseinzadeh K, et al. Gallbladder carcinoma update: Multimodality imaging evaluation staging, and treatment options. *AJR Am J Roentgenol* 191:1440-1447, 2008.
63. Schwartz L, Black J, Fong Y, et al. Gallbladder carcinoma: Findings at MR imaging with MR cholangiopancreatography. *J Comput Assist Tomogr* 26:405-410, 2002.
64. Holloway B, King D. Ultrasound diagnosis of metastatic melanoma of the gallbladder. *Br J Radiol* 70:1122-1125, 1997.
65. Kim M-J, Mitchell DG, Ito K, Outwater EK. Biliary dilatation: Differentiation of benign from malignant causes: Value of adding conventional MR imaging to MR cholangiopancreatography. *Radiology* 214:173-181, 2000.
66. Mortelet K, Ros PR. Anatomic variants of the biliary tree: MR cholangiographic findings and clinical applications. *AJR Am J Roentgenol* 177:389-394, 2001.
67. Matthews BD, Sing RF, Heniford BT. Magnetic resonance cholangiopancreatographic diagnosis of Mirizzi's syndrome. *J Am Coll Surg* 190:630, 2000.
68. Kim PN, Outwater EK, Mitchell DG. Mirizzi syndrome: Evaluation by MR imaging. *Am J Gastroenterol* 94:2546-2550, 1999.
69. Ernst O, Asselah T, Sergent G, et al. MR cholangiography in primary sclerosing cholangitis. *AJR Am J Roentgenol* 171:1027-1030, 1998.
70. Ito K, Mitchell D, Outwater E, Blasbalg R. Primary sclerosing cholangitis: MR imaging features. *AJR Am J Roentgenol* 172:1527-1533, 1999.
71. Bader TR, Beavers KL, Semelka RC. MR imaging features of primary sclerosing cholangitis: Patterns of cirrhosis in relationship to clinical severity of disease. *Radiology* 226:675-685, 2003.
72. Bader TR, Braga L, Beavers KL, Semelka RC. MR imaging findings of infectious cholangitis. *Magn Reson Imaging* 19:781-788, 2001.
73. Lee WF, Kim HK, Fang KM, et al. Radiologic spectrum of cholangiocarcinoma: Emphasis on unusual manifestations and differential diagnosis. *Radiographics* 21:S97-S116, 2001.
74. Worawattanakul S, Semelka RC, Noone TC, et al. Cholangiocarcinoma: Spectrum of appearances on MR images using current techniques. *Magn Reson Imaging* 16:993-1003, 1998.
75. Semelka RC, Kelekis NL, Gesine J, et al. Ampullary carcinoma: Demonstration by current MR techniques. *J Magn Reson Imaging* 7:153-156, 1997.
76. Kim JH, Kim MJ, Chung JJ, et al. Differential diagnosis of periampullary carcinomas at MR imaging. *Radiographics* 22:1335-1352, 2002.



MRI of the Kidneys and Adrenal Glands

INTRODUCTION

The tissue contrast and spectroscopic properties of magnetic resonance imaging (MRI) recommend its use as a problem solver for renal and adrenal imaging. The unsurpassed ability to discriminate cystic from solid lesions and higher sensitivity to solid, neoplastic elements explains the superiority of MRI compared with other imaging modalities in renal imaging. Extreme sensitivity to the microscopic lipid—present in the form of cholesterol compounds in adenomas—explains the utility in adrenal imaging. Typical indications for MRI in renal and adrenal imaging include indeterminate adrenal lesion evaluation, endocrinologic workup for potential adrenal adenoma or pheochromocytoma, indeterminate renal lesion, and posttreatment follow-up of renal neoplasms (Table 4-1).

TECHNIQUE

Technical considerations in renal and adrenal MRI are essentially the same as for other abdominal indications (see Chapter 2, “Technique”), with a few occasional modifications.

Hardware considerations—for example, high-field imaging, dedicated torso coil, power injection—deserve equal priority in renal and adrenal imaging. Although a standard liver protocol may suffice for most renal and adrenal indications, certain considerations recommend protocol deviations and/or modifications (Fig. 4-1). Steady-state localizer images are useful for the same reason in renal and adrenal imaging—for example, identification of cystic lesions, vascular patency. Heavily T2-weighted images (or single-shot images), usually obtained in coronal and axial planes, provide an anatomic roadmap and serve to discriminate cystic from solid lesions and to detect potential solid components of cystic lesions. The ability to detect and quantify microscopic fat through in- and out-of-phase images is indispensable in renal and

adrenal imaging. Adrenal adenomas and clear cell type renal cell carcinomas (RCCs) distinguish themselves from other lesions (such as adrenal metastases and renal angiomyolipomas—AMLs) by the presence of intralesional microscopic fat. In adrenal imaging, supplemental three-dimensional (3-D) in- and out-of-phase sequences with thinner slices (and potentially smaller field of view [FOV] and voxel size) better assess small adrenal lesions—often inadequately evaluated with standard two-dimensional (2-D) sequences (see Fig. 4-1).

Rigorous dynamic contrast-enhanced imaging is less vital in renal and adrenal imaging, compared with liver and pancreatic imaging, because the issue of enhancement generally reduces to a binary question of presence versus absence of enhancement. The temporal nature of lesion enhancement matters less (although adrenal lesion characterization supplementally depends on early versus delayed enhancement). Nonetheless, the information gleaned by dynamic imaging, including solid lesion enhancement characteristics (used to differentiate between different malignant lesions), adequacy of renal parenchymal enhancement/perfusion, and arterial anatomic depiction, validates the effort. The choice of imaging planes depends on lesion location relative to organ of origin. For example, in the case of a renal lesion arising from the posterior aspect of the kidney, the axial plane displays the lesion-kidney interface better than the coronal plane, which shows it en face tangentially. Conversely, in the case of an exophytic lesion arising from the upper or lower pole of the kidney, the coronal plane better depicts the lesion-kidney interface.

Subtracted images (precontrast from post-contrast images) serve a central role in differentiating benign from malignant in renal lesions. Certain common features—such as modest enhancement and precontrast T1 hyperintensity—challenge the human eye to detect or exclude enhancement. Subtractions eliminate precontrast hyperintensity and

Sequence	Planes	TR/TE	Slice thickness	Details
Steady-state	3-plane	min/min	6 × 0	
Heavily T2-weighted	Coronal, axial	NA/180	5 × 0	
In/out-of-phase (2-D)	Axial	min/2.2, 4.4	7 × 1	Obtained as 1 sequence
In/out-of-phase*	Axial	min/2.2, 4.4	3 (interpolated to 1.5)	No fat saturation
Dynamic 3-D	Axial or coronal	min/min	4 (interpolated to 2)	Fat saturation
Moderately T2-weighted	Axial	3000/80	7 × 0.5	
Delayed 3-D	Axial or coronal	min/min	4 (interpolated to 2)	Fat saturation
<i>2-D T2-weighted MRU</i>	<i>Radial below each kidney</i>	<i>NA/≈850</i>	<i>40</i>	<i>Same as MRCP sequence before IV gadolinium</i>
<i>3-D T2 weighted MRU</i>	<i>Coronal</i>	<i>1300/680</i>	<i>2 (interpolated to 1)</i>	<i>Same as MRCP sequence respiratory triggered before IV gadolinium</i>
<i>3-D T1 weighted MRU</i>	<i>Coronal</i>	<i>min/min</i>	<i>≤4 (interpolated)</i>	<i>Flip angle 15° and 40°</i>

* Optional: use for characterization of small adrenal lesions (<1.5 cm)
MRU sequences are in italics

FIGURE 4-1. Renal and adrenal MRI protocols. MRCP, magnetic resonance cholangiopancreatography; MRU, magnetic resonance urography; NA, not applicable; TR, time to repetition; TE, time to excitation; 2-D, two-dimensional; 3-D, three-dimensional.

TABLE 4-1. Common Indications for Renal and Adrenal Magnetic Resonance Imaging

Adrenal
Indeterminate adrenal lesion (adenoma vs. other)
Endocrinologic workup (adrenal adenoma or pheochromocytoma)
Kidney
Indeterminate renal lesions
Follow-up likely benign renal lesions
Characterization of renal lesions in renal insufficiency
Surveillance posttreatment RCC
Collecting System/Ureter
Surveillance posttreatment TCC
Collecting system and/or ureteral abnormality

RCC, renal cell carcinoma; TCC, transitional cell carcinoma.

improve dynamic range to detect subtle enhancement.

Another protocol consideration includes the decision whether to include urographic sequences—usually performed in the setting of transitional cell carcinoma or potential collecting system or ureteral abnormality (see Table 4-1). Lasix administration before imaging augments the excretion of gadolinium and collecting system distention. Magnetic resonance urography (MRU) sequences include T1-weighted and T2-weighted varieties. T1-weighted sequences are obtained after contrast during the excretory phase, usually in the

coronal plane as a modification of the dynamic sequence (see Fig. 4-1). 2-D and 3-D T2-weighted sequences are performed before contrast administration; otherwise, excreted gadolinium in the collecting systems shortens the T2 of urine, precluding signal on heavily T2-weighted images. The 2-D and 3-D MRU sequences are the magnetic resonance cholangiopancreatography (MRCP) sequences targeted to the collecting systems and ureters; instead of centering on the common bile duct, the slices are oriented to the renal collecting systems and ureters.

INTERPRETATION

Each MRI pulse sequence uniquely possesses specificity for certain tissues, and search patterns must acknowledge this fact to be useful. Steady-state images highlight fluid—whether moving or static—against solid tissue. Use them both as a vascular sequence and to assess cystic lesions. Heavily T2-weighted images are specific for only static fluid and eliminate many of the artifacts observed in steady-state imaging. These images permit more detailed evaluation of cystic lesions and mural nodules, septations, and other solid components.

Moderately T2-weighted images also depict cystic lesions and underlying complexity. The

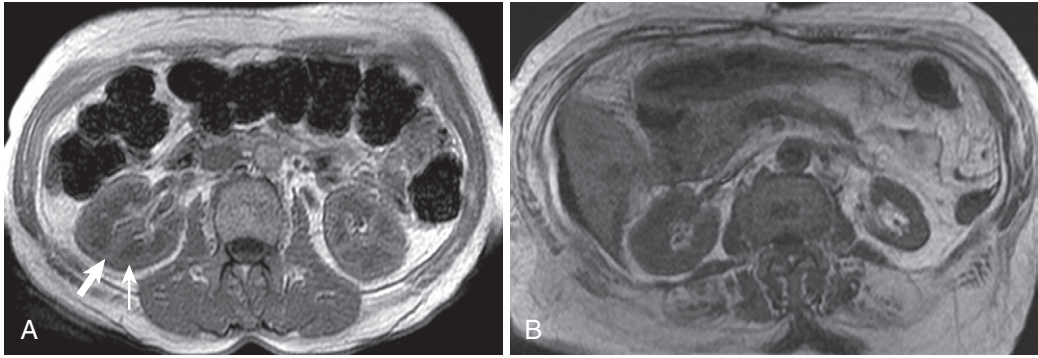


FIGURE 4-2. T1-weighted image of the kidneys shows corticomedullary differentiation. The axial in-phase image (A) in a patient with normal renal function shows greater contrast between the hypointense renal medulla (*thin arrow* in A) and relatively hyperintense renal cortex (*thick arrow* in A) compared with the axial in-phase image (B) in a patient with severely depressed renal function (glomerular filtration rate 14).

improved tissue contrast supplemented by elimination of signal from fat confers a high sensitivity to lymphadenopathy, which appears bright against the dark background of retroperitoneal fat. Macroscopic fat in AMLs and myelolipomas loses signal, generally clinching the diagnosis.

In- and out-of-phase images serve many purposes. Inspect the parenchyma for corticomedullary differentiation (relatively hypointense medulla), which connotes functional tissue (Fig. 4-2). T1-weighting confers sensitivity to protein and hemorrhage, which appear bright on these images. Of course, macroscopic fat appears equally bright on in- and out-of-phase images, and microscopic fat (occasionally present in clear cell type RCC) appears dark on out-of-phase images relative to in-phase images. Macroscopic fat (present in renal AMLs and adrenal myelolipomas), hyperintense on in- and out-of-phase images, loses signal on the T1-weighted fat suppressed sequence—the paramagnetic sequence (the precontrast phase of the dynamic sequence).

In addition to establishing the presence of macroscopic fat through signal suppression, the paramagnetic sequence (precontrast T1-weighted fat-suppressed) showcases hemorrhage and other paramagnetic substances, such as protein, and other molecules, such as melanin. This sequence is optimized to receive signal solely from (nonfat) substances with very short T1 values—usually hemorrhage in the realm of renal and adrenal imaging.

The postcontrast dynamic phases share the same attributes as the precontrast phase, supplemented by the addition of intravenous gadolinium. Signal augmentation (i.e., enhancement) compared with the precontrast images indicates

the presence of gadolinium, which is confined to the extracellular space (intravascular space and interstitial space). This means that blood vessels (assuming patency) and solid tissues (except for fat) will enhance. Because of the extreme sensitivity to enhancement, MRI is the ultimate arbiter of indeterminate renal lesions to differentiate solid masses (treated surgically) from nonneoplastic cystic lesions (treated expectantly).

Difficulty in assessing enhancement arises in the case of the T1 hyperintense lesion (such as hemorrhagic cysts). Precontrast hyperintensity plus even more signal (from enhancement) is difficult for the human eye to detect. Subtracted images negate precontrast hyperintensity, showing only changes in signal intensity between the precontrast and the postcontrast image by literally subtracting the signal from each pixel on the precontrast image from each pixel on the postcontrast image. All that remains is a map of contrast enhancement (assuming no intervening patient motion causing misregistration).

If subtractions are not available, comparing the region of interest (ROI) with a reference standard establishes or excludes enhancement. As a rule of thumb, normal muscle enhances 15%, which serves as a lower limit threshold for renal mass enhancement; most renal tumors enhance avidly, but relatively hypovascular papillary renal cell carcinomas tend to enhance approximately 15%. Compare the ROI signal intensity values of the pre- and postcontrast renal lesion with ROI values of normal muscle (e.g., psoas, longissimus). An equal or greater increase compared with muscle indicates enhancement and solid tissue (Fig. 4-3).

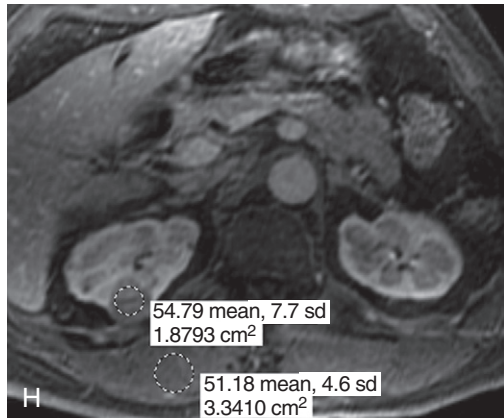
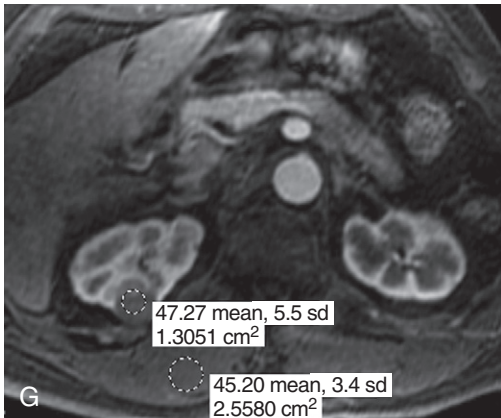
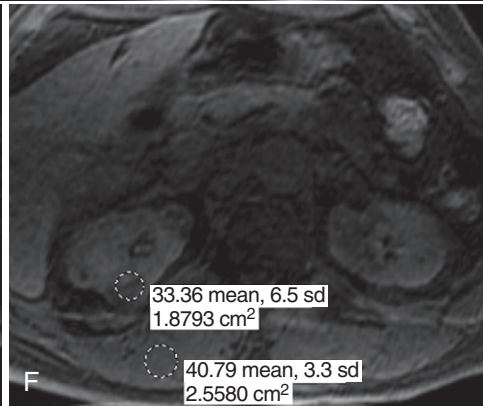
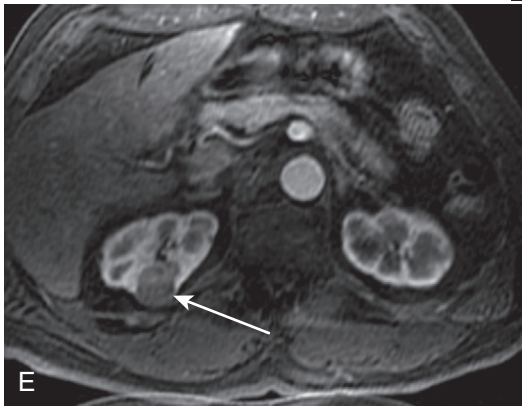
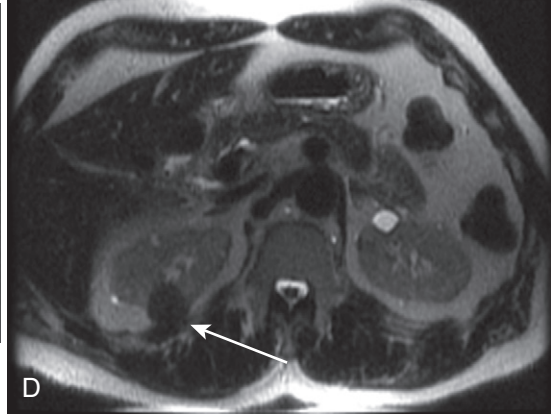
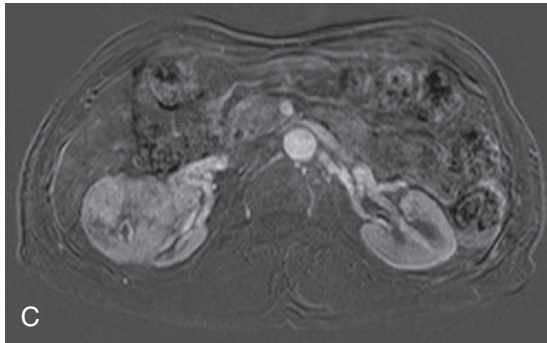
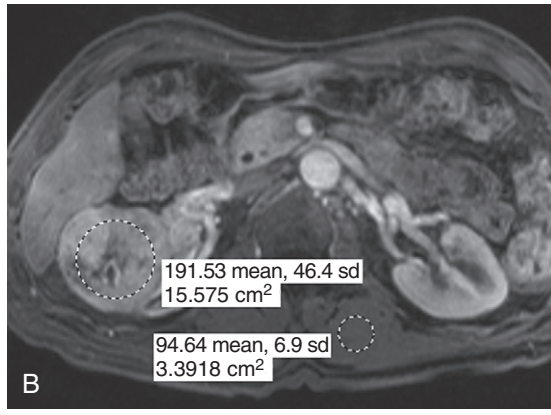
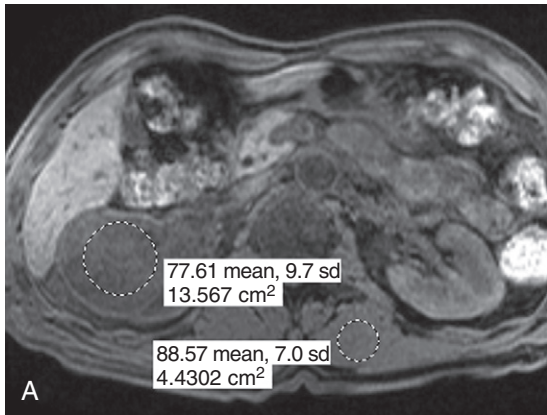


FIGURE 4-3. Solid renal enhancement demonstrated using region of interest (ROI) measurements. ROIs placed over a large right renal lesion and left erector spinae muscles on the precontrast (A) and postcontrast (B) images reveal a much greater lesional increase in signal intensity (from 77.61 to 191.53 = 113.92) compared with muscle (from 88.57 to 94.64 = 6.07). C, The corresponding subtracted image confirms avid enhancement. In a different patient with a small T2 hypointense right renal lesion (*arrow* in D), enhancement is questionable (*arrow* in E). Serial ROIs placed over the lesion and erector spinae muscles document relatively greater lesional signal change (from 33.36 to 47.27 to 54.79 = 21.43) compared with muscle (from 40.79 to 45.20 to 51.18 = 10.39), signaling mild enhancement—typical of papillary-type RCC (subsequently confirmed at nephrectomy).

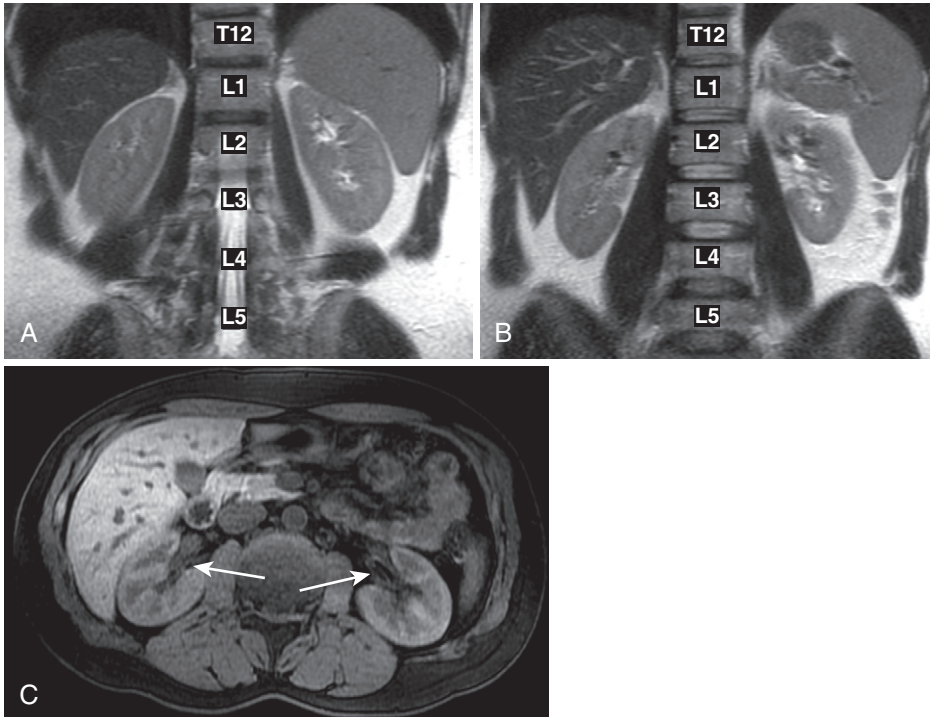


FIGURE 4-4. Normal kidneys and adrenal glands. Coronal T2-weighted images positioned through the posterior aspects (A) and midportions (B) of the kidneys show typical craniocaudal positioning and medial tilting. C, The axial fat-suppressed T1-weighted image illustrates normal corticomedullary differentiation and orientation of the renal hila (*arrows*).

KIDNEYS

Normal Features

Normal kidneys measure approximately 10 to 14 cm in length.¹ Renal axes tilt medially at the upper poles with anteromedial rotation (according to the position of the hilum) and the kidneys extend from the T12–L1 to the L3 levels (Fig. 4-4). The kidneys are cloaked in a sheath of retroperitoneal fat with interdigitating fibrous septa capped by the adrenal glands. A barely perceptible linear hypointensity encircles the retroperitoneal fat—Gerota’s fascia—an important landmark in staging RCC (Fig. 4-5).

Normal kidneys exhibit corticomedullary differentiation characterized by relatively greater

fluid content in the medulla relatively to the cortex (see Fig. 4-2).² The kidneys enhance avidly with earlier enhancement of the renal cortex during the arterial phase, reiterating the corticomedullary pattern—renal cortical phase for our purposes. Within 60 to 90 seconds, contrast perfuses the medullary renal parenchyma, resulting in global renal parenchymal enhancement—the parenchymal phase.

The renal collecting system is generally biconcave or flat and excreted urine demonstrates water signal. Occasional flow voids on T2-weighted images sometimes simulate renal calculi. The collecting system urothelial lining appears as inconspicuous linear hypointensity exhibiting no discernible enhancement.

Primary tumor (T)	Regional lymph nodes	Distant metastasis (M)
T0: no evidence of first-degree tumor	N0: no regional lymph node metastasis	M0: no distant metastasis
T1: tumor ≤ 7 cm limited to kidney	N1: metastasis in a single regional lymph node	M1: distant metastasis
T2: tumor > 7 cm limited to kidney	N2: metastasis in > 1 regional lymph node	
T3: tumor extends into major veins, invades adrenal gland or perinephric tissues not beyond Gerota's fascia		
T3a: tumor invades adrenal gland or perinephric tissues not beyond Gerota's fascia		
T3b: tumor extends into major renal veins or IVC below diaphragm		
T3c: tumor extends into major renal veins/IVC above diaphragm		
T4: tumor invading beyond Gerota's fascia		

Robson staging system

Stage I (T1 or 2, N0, M0): tumor confined to kidney

Stage II (T3a, N0, M0): tumor spread to perinephric fat confined with renal fascia; possible ipsilateral adrenal involvement

Stage IIIA (T3b-3c, N0, M0): tumor spread to renal vein, IVC or both

Stage IIIB (T1-3a, N1-3, M0): tumor spread to local lymph nodes

Stage IIIC (T3b-3c, N1-3, M0): tumor spread to local vessels and lymph nodes

Stage IVA (T4, any N, M0): tumor spread to adjacent organs (except ipsilateral adrenal gland)

Stage IVB (any T & N, M1): distant metastases

American joint committee on cancer system

Stage I: T1, N0, M0

Stage II: T2, N0, M0

Stage III: T1-2, N1, M0 or T3a-c, N0-1, M0

Stage IV: T4 or any T, N2, M0 or any T, any N, M1

FIGURE 4-5. RCC staging. IVC, inferior vena cava.

TABLE 4-2. Common Renal Developmental Anomalies and Pseudolesions

Inductional	Fusion
Renal agenesis	Horseshoe kidney
Renal hypoplasia	Crossed fused renal ectopia
Supernumerary kidney	Pancake kidney
Positional	Structural
Renal ectopia	Fetal lobulation
Malrotation	Prominent column of Bertin
	Hilar lip

Anomalies and Pseudolesions

A few common developmental anomalies and pseudolesions (Table 4-2) are worth mentioning before discussing pathologic renal lesions. Renal and collecting system embryogenesis is a

complex process following a series of steps necessary for the execution of subsequent developmental steps. Incomplete or absent interfacing of the ureteric bud (primordial collecting system and ureter) and metanephric blastema (primordial renal parenchyma) results in renal agenesis and/or a number of other potential parenchymal and ureteral/collecting system anomalies.

Positional anomalies include ectopia and malrotation. Embryonic growth results in a relative ascent of the kidneys during the fourth through eighth week of gestation, ultimately positioned between the first and the third lumbar vertebrae. Underascent occurs far more commonly than overascent, and the ptotic kidney ranges in position from the true pelvis to the iliac fossa and anywhere below the expected location centered at the L2 level (Fig. 4-6). Contralateral

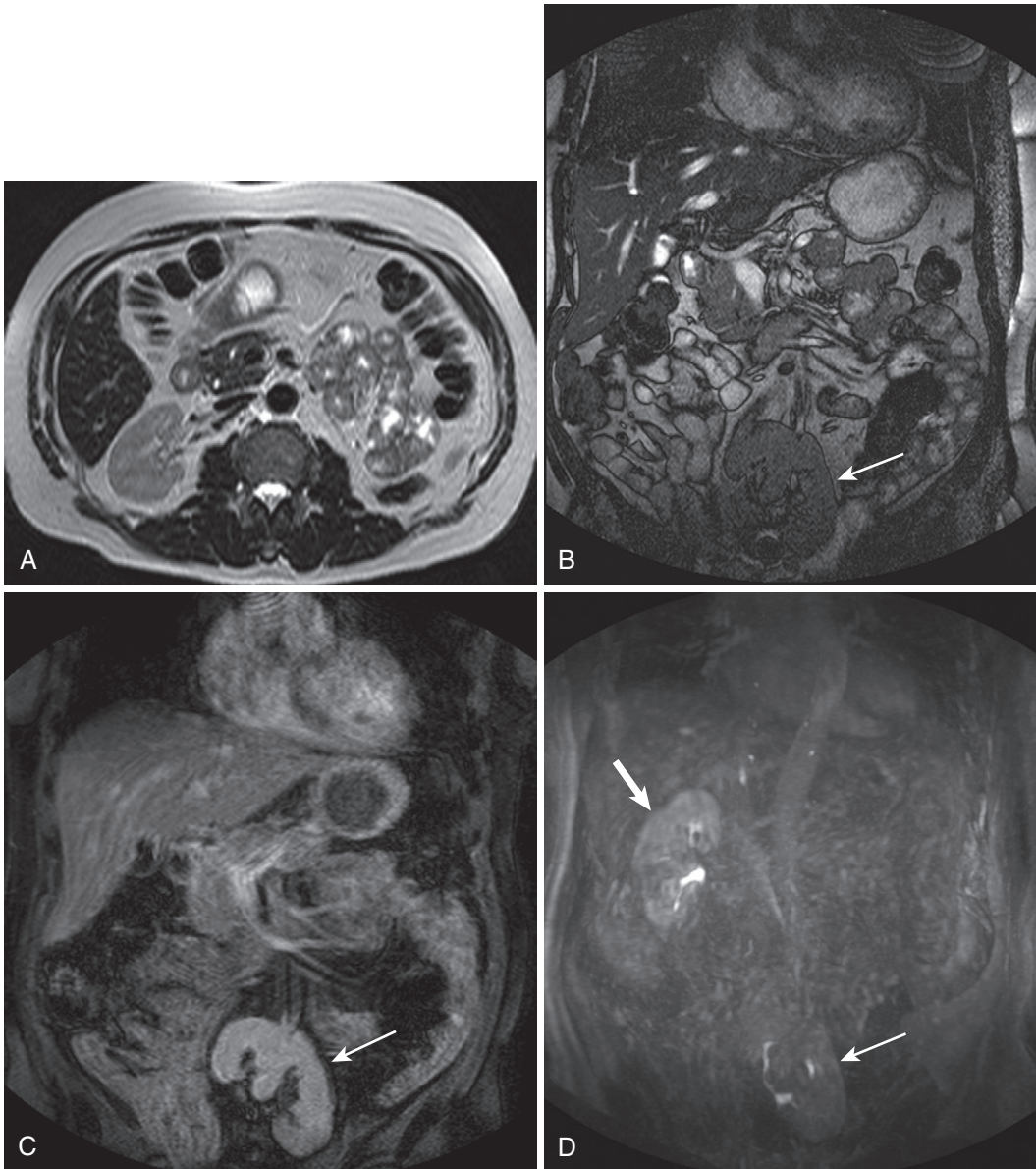


FIGURE 4-6. Ptotic kidney. **A**, The axial T2-weighted image through the upper abdomen shows a normal right kidney with no visible left kidney. **B**, The steady-state coronal localizing image with a large field of view (FOV) shows a reniform structure in the pelvis (*arrow*). The post-contrast coronal image (**C**) corroborates the presence of a pelvic kidney (*arrow*) and the coronal maximal intensity projection image (**D**) illustrates the relative positioning and orientation of the left (*thin arrow* in **D**) and right (*thick arrow* in **D**) kidneys.

renal anomalies, such as renal agenesis or ptosis, frequently coexist.

Concomitant medial rotation along the longitudinal renal axis during ascent orients the ureteropelvic junction (UPJ) medially. Nonrotation or incomplete rotation leaves the UPJ facing anteriorly, and renal calyces in the medial segment of the kidney lie medial to the renal pelvis (Fig. 4-7). Overrotation results in a posteriorly facing UPJ.

Renal fusion anomalies generally incur positional and rotational derangements. Medial renal fusion results in a solitary discoid lump of renal tissue in the pelvis, referred to as “pancake kidney.” Crossed fused renal ectopia represents the sequela of embryologic renal fusion with the relatively normally positioned kidney dragging its fused counterpart across the midline, resulting in a single ipsilateral S-shaped renal mass with two separate moieties and normal bilateral

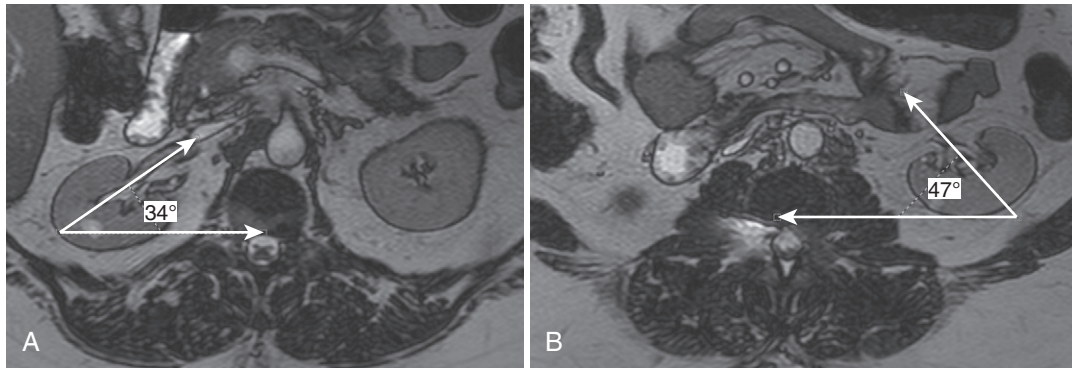


FIGURE 4-7. Renal malrotation. Compare the orientation of the right renal hilum on the steady-state images through the right renal hilum (A) and the left renal hilum (B)—note the underrotation of the left kidney reflected by the incomplete medial rotation. Normal renal rotation is approximately 30°.

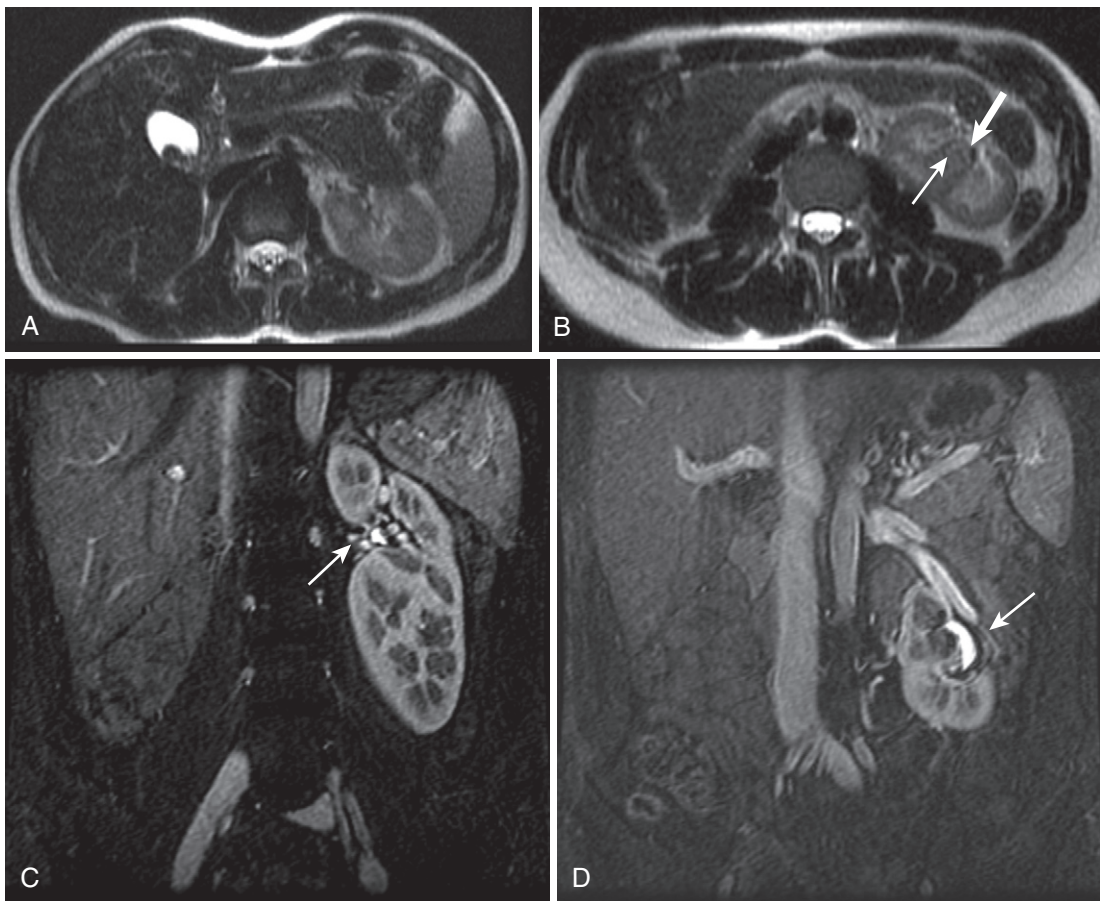


FIGURE 4-8. Crossed fused renal ectopia. A, Axial T2-weighted image through the upper abdomen reveals absence of the right kidney. B, More caudally positioned axial T2-weighted image shows orientation of the left lower renal moiety (*thin arrow*) following the expected rotation of the right kidney with the hilum facing laterally (*thick arrow*). C and D, Coronal postcontrast images show the fused conglomerate renal mass with separate hilar structures (*arrow*) and disparate orientation.

ureterovesical junctional positioning (Fig. 4-8). Horseshoe kidney is the most common renal anomaly reflecting midline fusion of the metanephric blastema. Ascent is arrested at the level of the inferior mesenteric artery (Fig. 4-9).

Coexistent anomalies, such as UPJ obstruction and duplication anomalies, conspire with the geometric and rotational distortion and urinary stasis to lead to complications, including stone formation and infection.

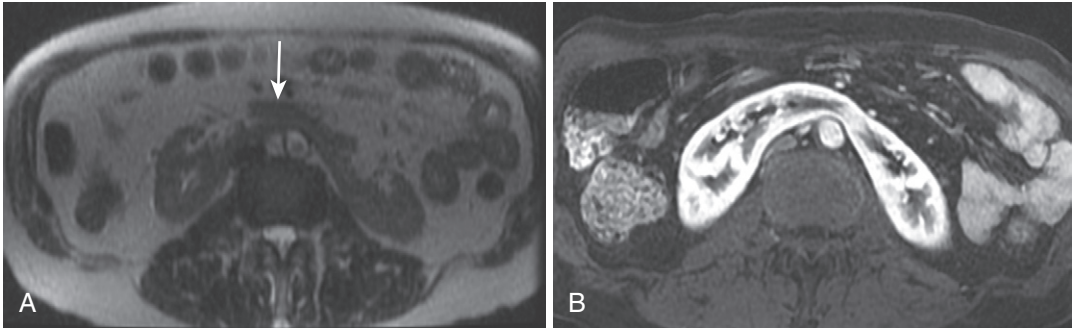


FIGURE 4-9. Horseshoe kidney. **A**, The axial T2-weighted image shows midline fusion of the lower renal poles (*arrow*) ventrally across the midline, anterior to the aorta. **B**, The corresponding arterial phase postcontrast image depicts characteristic corticomedullary enhancement of the fused renal mass.

Structural anomalies incur no risk of complications and deserve mention only to prevent misdiagnosis. Fetal lobulation persists in 5% of adults with a smooth undulating outer renal contour conforming to the position of the renal pyramids. Smoothly margined indentations conform to the edges of renal pyramids with normal appearance and thickness of underlying parenchyma (≥ 14 mm), excluding the possibility of an underlying mass or scarring. The column of Bertin potentially simulates a renal mass, but represents invagination of normal renal cortical tissue into the renal sinus, usually occurring at the upper polar/interpolar junction and averaging 3.5 cm in size (Fig. 4-10). The hilar lip represents fusion of medial renal lobes, usually occurring in the upper pole and potentially protruding and distorting the renal sinus. Signal characteristics and enhancement identical to adjacent renal parenchyma occurring in the expected location confirm the presence of normal functional renal tissue in cases of renal anomalies.

Focal Lesions

Focal renal lesions are encountered everyday in clinical practice on cross-sectional imaging studies—the vast majority of which are incidental, and many indeterminate. Thirteen percent to 27% of abdominal imaging studies incidentally detect a renal lesion.³ Whereas many of these lesions are incompletely characterized, the overwhelming majority of these lesions are simple or minimally complex cysts with no malignant potential. Establishing true cystic etiology eliminates the need for further work-up and/or follow-up.⁴ The presence of solid

components implies malignancy, which usually mandates surgical resection (Fig. 4-11).

Most renal cysts are simple in appearance with fluid signal characteristics (T2 hyperintensity and T1 hypointensity), no enhancement, septation, wall-thickening, or nodularity. Signal alterations alone pose no risk of malignancy, although they often challenge interpretation. The most common signal alteration is due to hemorrhage, resulting in T1 hyperintensity and T2 hypointensity. Proteinaceous contents induce a similar appearance.

Complex cystic lesions pose greater diagnostic difficulty. Superimposed infection and trauma induce reactive wall thickening, which overlaps with the appearance of cystic neoplasms (especially RCC, clear cell type). These neoplasms often harbor more complex features with mural nodularity and solid components. In an effort to stratify renal lesions based on likelihood of malignancy, Bosniak^{5,6} developed a predictive classification system (for computed tomography [CT]) to guide management (Table 4-3). Although not specifically adapted for MRI, this scheme illustrates the range of imaging complexity of renal lesions and offers management guidance.⁷ Although calcification escapes detection, the classification scheme applies to magnetic resonance (MR) findings, replacing intensity changes for density changes.⁸

Solid lesions include benign and malignant neoplasms. Macroscopic fat is the only finding that connotes a benign etiology—AML. Although renal infection and infarction and benign lesions (such as oncocytoma) account for enhancing lesions, for the most part, solid tissue (enhancement) equals malignancy. Unless clinical findings raise the suspicion of inflammatory or

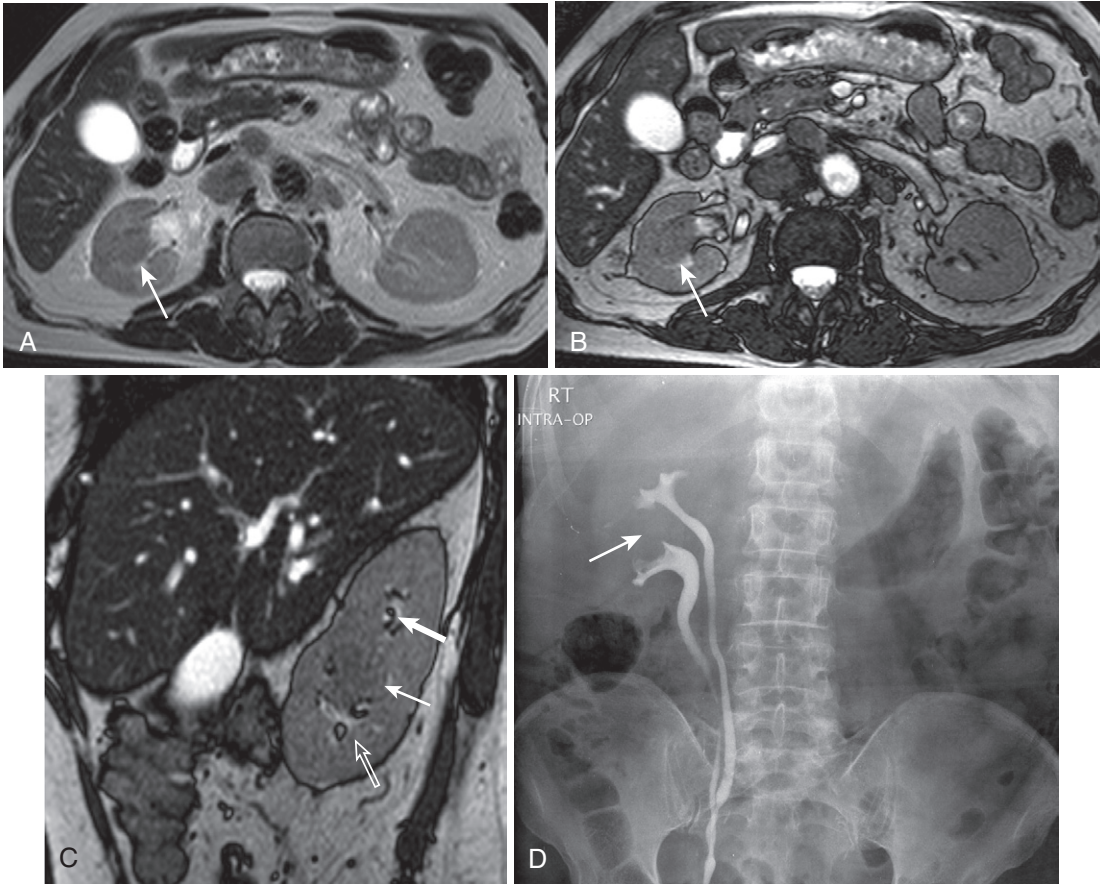


FIGURE 4-10. Column of Bertin. A, The axial T2-weighted image illustrates protrusion of solid tissue isointense to surrounding normal renal parenchyma (*arrow*) and indenting the renal pelvis. B, The finding (*arrow*) is more pronounced on the axial steady-state image. C, The sagittal steady-state image portrays this finding as an isointensity (*thin arrow*) dividing the upper polar calyces (*thick arrow*) from the lower polar calyces (*open arrow*). D, The corresponding film from a retrograde pyelogram shows duplication of the renal collecting system, which is separated by the column of Bertin (*arrow*).

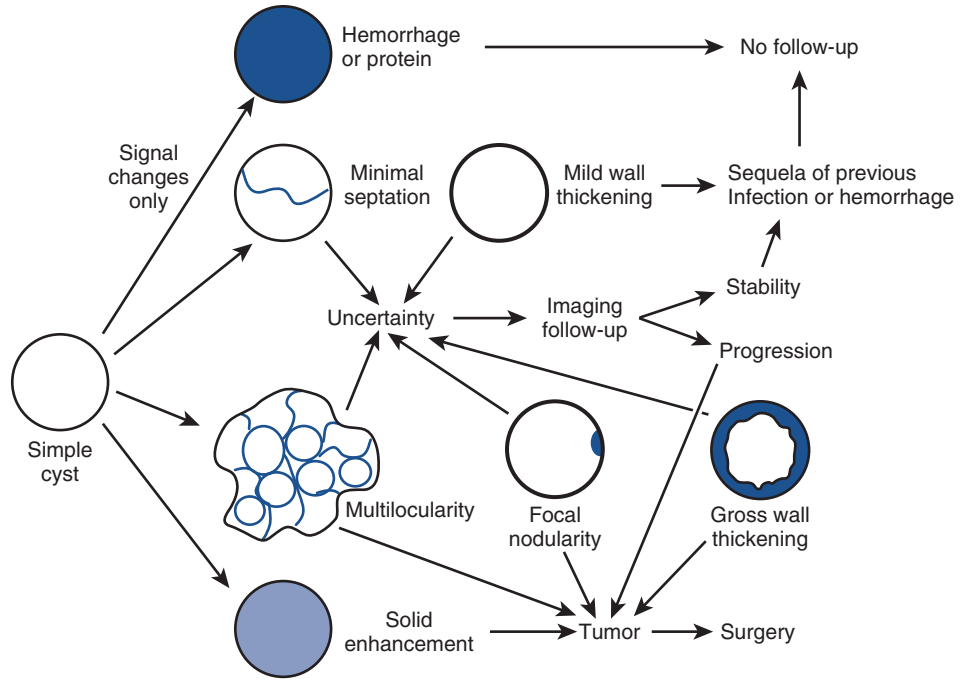


FIGURE 4-11. Focal renal lesion algorithm.

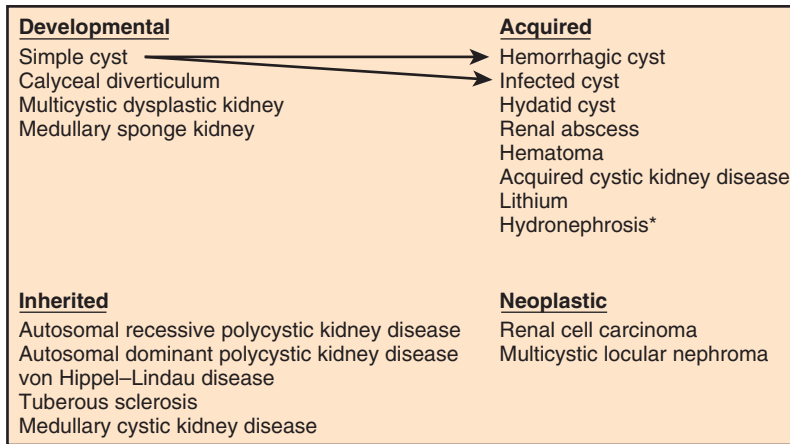


FIGURE 4-12. Differential diagnosis of renal cystic lesions.

TABLE 4-3. Bosniak Classification Scheme for Cystic Renal Lesions

Bosniak Category	Imaging Features	Management
I	Thin wall; no septa, calcifications, or solid components, water features; no enhancement	No follow-up
II	Few thin septa with less than or minimal enhancement; fine calcification or focal thick calcification; homogeneous high-density sharply marginated lesion (<3 cm) with no enhancement	No follow-up
IIIF	Multiple thin septa with less than or minimal enhancement; thick or nodular calcification; no enhancing soft tissue components; high-density lesions (>3 cm) with no enhancement	Observe
III	Thickened irregular or smooth walls or septa with enhancement	Surgery
IV	Same features as III also with enhancing soft tissue components	Surgery

TABLE 4-4. Management Scheme for Solid Renal Lesions

Size	Presumptive Diagnosis	Management
Large (>3 cm)	RCC	Surgery
Small (1–3 cm)	RCC	Surgery
Minimal (<1 cm)	RCC, AML, oncocytoma	Observe up to 1 cm

AML, angiomyolipoma; RCC, renal cell carcinoma.

vascular etiology, the presumptive diagnosis is malignancy until proved otherwise. Because biopsy results are notoriously confusing, solid renal lesion management involves surgical pathologic diagnosis and treatment. Because very small lesions (<1 cm) challenge the resolution of imaging methods, limiting diagnostic confidence, imaging surveillance preempts potentially unnecessary surgery (Table 4-4).

CYSTIC LESIONS

Using the combination of heavily T2-weighted images to detect fluid hyperintensity with post-contrast images to exclude enhancement confirms cystic etiology. T1-weighted sequences

depict hemorrhagic cysts with variable hyperintensity, and postcontrast images exclude enhancement. Ninety percent of all renal cystic lesions are simple cysts (Fig. 4-12). Hemorrhage, debris, and infection complicate renal cysts. With an increasing number of cystic lesions (and renal enlargement), consider the possibility of polycystic disease. Cystic lesions prevail in other inherited diseases, such as von Hippel–Lindau (VHL) disease and tuberous sclerosis (TS) (with assorted solid lesions, to be discussed later). Developmental etiologies include multicystic dysplastic kidney and calyceal diverticulum. Acquired conditions, such as renal cystic disease of dialysis and lithium therapy, present with renal cystic lesions. RCC (clear cell types) dominates the cystic neoplastic category; consider multilocular cystic nephroma (MLCN) in the appropriate demographic categories (young males and middle-aged females) with herniation into the renal pelvis.

SIMPLE RENAL CYST

The simple renal cyst is ubiquitous, with a prevalence of up to two thirds of the population, and increasingly prevalent with age.⁹ Renal cysts

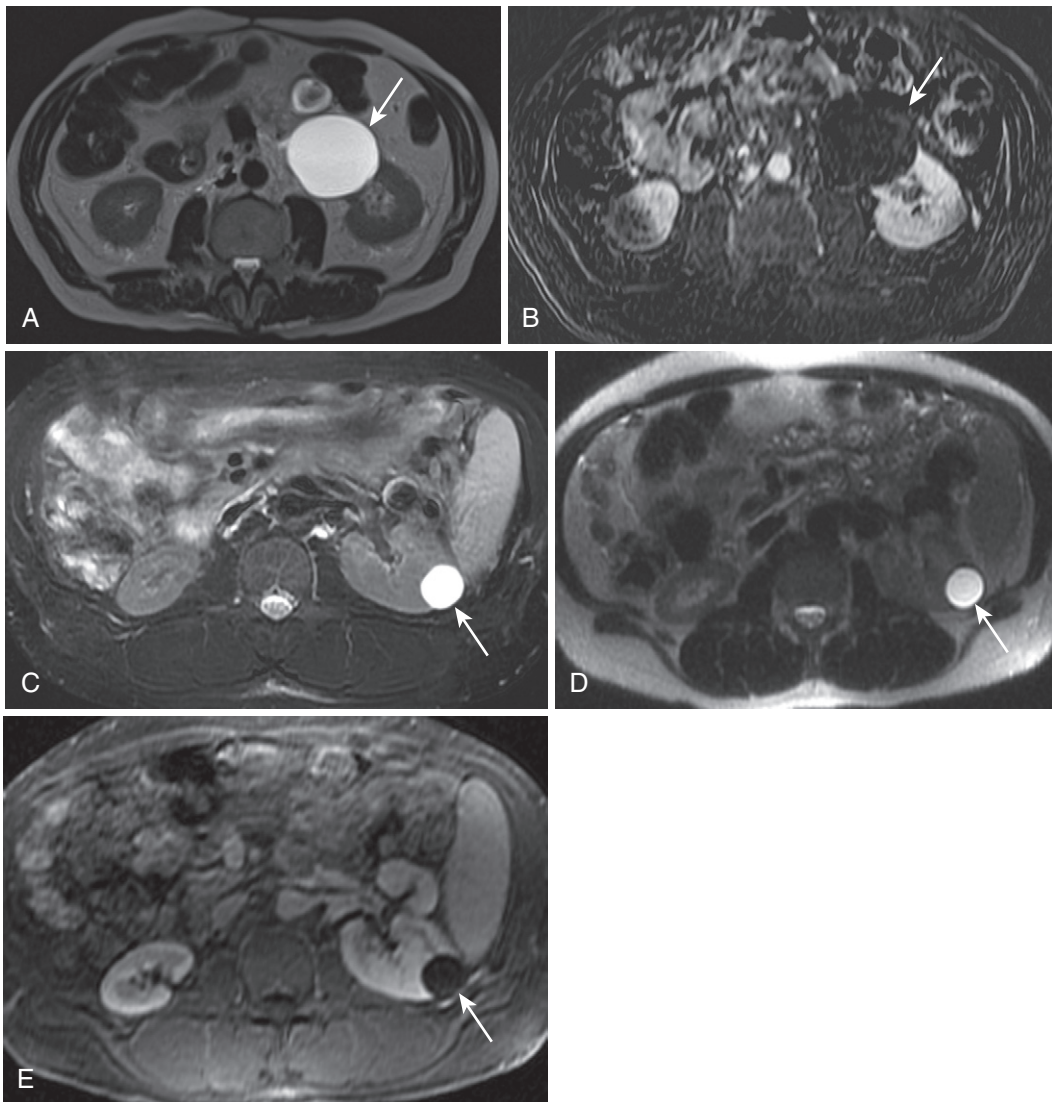


FIGURE 4-13. Simple renal cyst. A large, exophytic simple cyst (*arrow*) arising from the left kidney exhibits typical features—simple fluid T2-hyperintensity (A) and lack of enhancement (B)—based on the heavily T2-weighted (A) and the subtracted postcontrast (B) images. A comparison of the moderately T2-weighted fat-saturated (C) with the heavily T2-weighted (D) images in a different patient with a simple left renal cortical cyst (*arrow*) illustrates the effects of TE on free water (cyst) versus bound water (solid organs); free water maintains signal with increasing TE whereas bound water loses signal. E, The postcontrast image confirms absent enhancement (*arrow*).

detach from the parent renal tubule and become self-enclosed; continued fluid secretion distends the cavity, resulting in an isolated cystic structure. Ongoing fluid secretion accounts for continued growth of simple renal cysts ($\leq 5\%/yr$), despite the lack of neoplastic or autonomously regenerating cells.¹⁰ Therefore, careful attention to imaging features is paramount in excluding neoplasm.

The contents of the simple renal cyst—free water protons—account for its appearance: extreme T2 hyperintensity and T1 hypointensity with no enhancement. If even visible, the cyst

wall is uniformly smooth with no perceptible enhancement on postcontrast images (Fig. 4-13). Size varies from millimeters to over 10 cm. Cysts are stratified into different categories based on location: exophytic, parenchymal, and parapelvic (Figs. 4-14 and 4-15). Because most renal cysts arise from the cortex (although some develop from the medulla), most renal cysts are exophytic and/or intraparenchymal (see Figs. 4-13 and 4-14).

Renal cyst complexity assumes many forms, which fall into two major categories—morphologic and signal-related. *Morphologic*

derangements include deviation from simple sphericity and/or septation; *signal derangements* deviate from simple fluid characteristics with evidence of hemorrhage or debris (Fig. 4-16). Occasional fluid-fluid levels depict

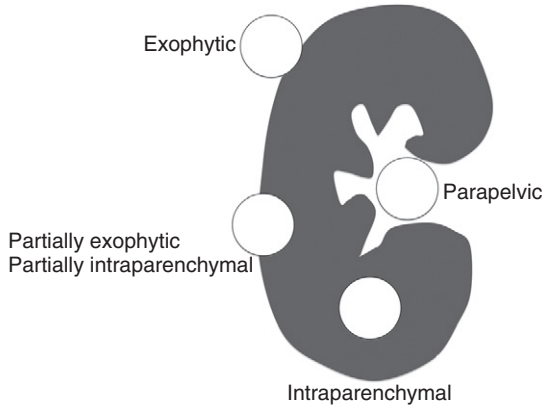


FIGURE 4-14. Renal cyst classification by location.

layering hematocrit (Fig. 4-17)—a relatively infrequent manifestation of a hemorrhagic cyst. Signal alterations from hemorrhage present the greatest challenge to interpretation; precontrast hyperintensity limits the ability to detect augmented T1 signal from enhancement (see Fig. 4-16). Fibrinous septations from previous infection generally measure less than 2 mm in thickness with no other evidence of complexity to suggest neoplasm (Fig. 4-18).¹¹ As long as no enhancement beyond minimal linear septal or wall enhancement is present, simple cystic etiology is confirmed.

Careful scrutiny of these features is critical, because a minority of clear cell RCC (~5%) is mostly cystic. In Bosniak's terms, the discrimination of type II and IIF lesions from understated type III lesions bears close inspection. Usually, a solid enhancing component differentiates RCC from a nonneoplastic cyst—especially with the benefit of subtractions. When subtractions

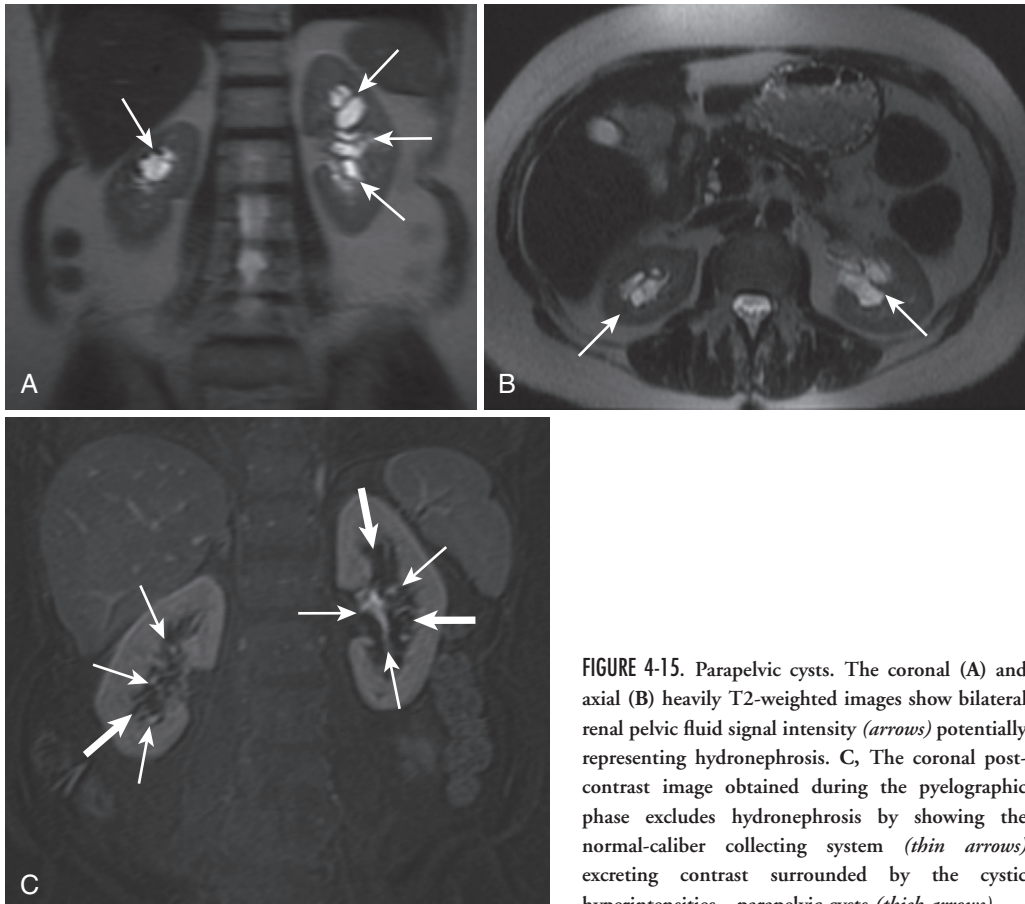


FIGURE 4-15. Parapelvic cysts. The coronal (A) and axial (B) heavily T2-weighted images show bilateral renal pelvic fluid signal intensity (arrows) potentially representing hydronephrosis. C, The coronal post-contrast image obtained during the pyelographic phase excludes hydronephrosis by showing the normal-caliber collecting system (thin arrows) excreting contrast surrounded by the cystic hyperintensities—parapelvic cysts (thick arrows).

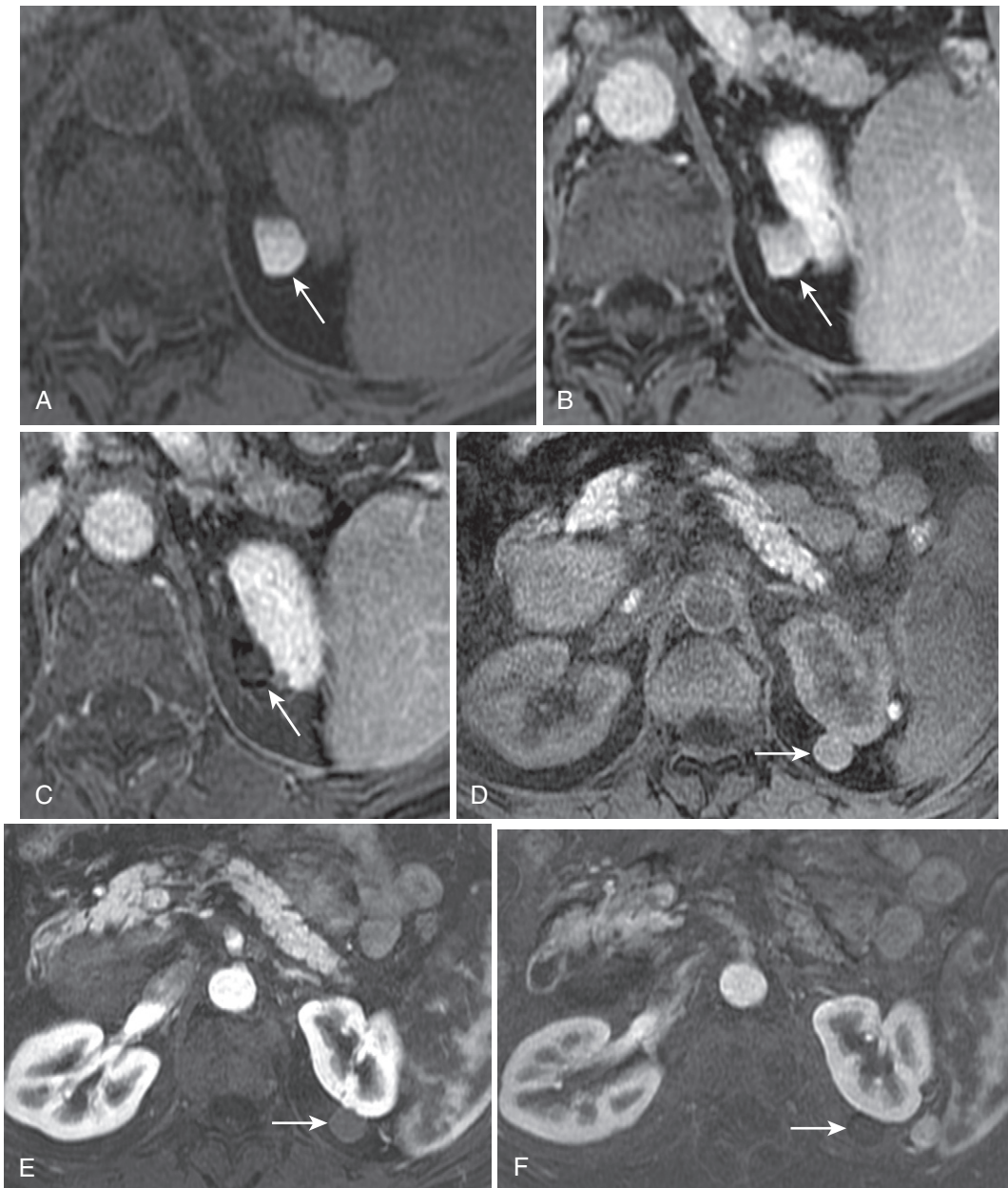


FIGURE 4-16. Hemorrhagic cyst with subtractions. Precontrast fat-suppressed image (A) shows an exophytic hyperintensity (*arrow* in A) protruding from the upper pole of the left kidney. No apparent change in signal intensity is evident after intravenous contrast (*arrow* in B), but subtle enhancement seems difficult to exclude. Subtracting the precontrast (A) from the postcontrast (B) image yields an enhancement map image—subtraction (C)—that depicts a signal void corresponding to the lesion (*arrow*) in question, excluding enhancement and confirming the diagnosis of a hemorrhagic cyst. D, Another lesion (*arrow*) in the same patient exhibits modest T1 hyperintensity, which is more equivocal. The postcontrast image (E) suggests absent enhancement (*arrow*), which is confirmed on the subtracted image (F).

are not available and signal alterations limit assessment of enhancement, rely on ROI measurements compared with a reference standard (see Figs. 4-3 and 4-16). Other etiologies are not realistic considerations, except under specific circumstances. For instance, with

multilocularity and when herniating into the renal pelvis, consider MLCN in the appropriate demographic settings (young males and middle-aged females). Infectious cysts—renal abscess and echinococcal cyst—require a suggestive history.

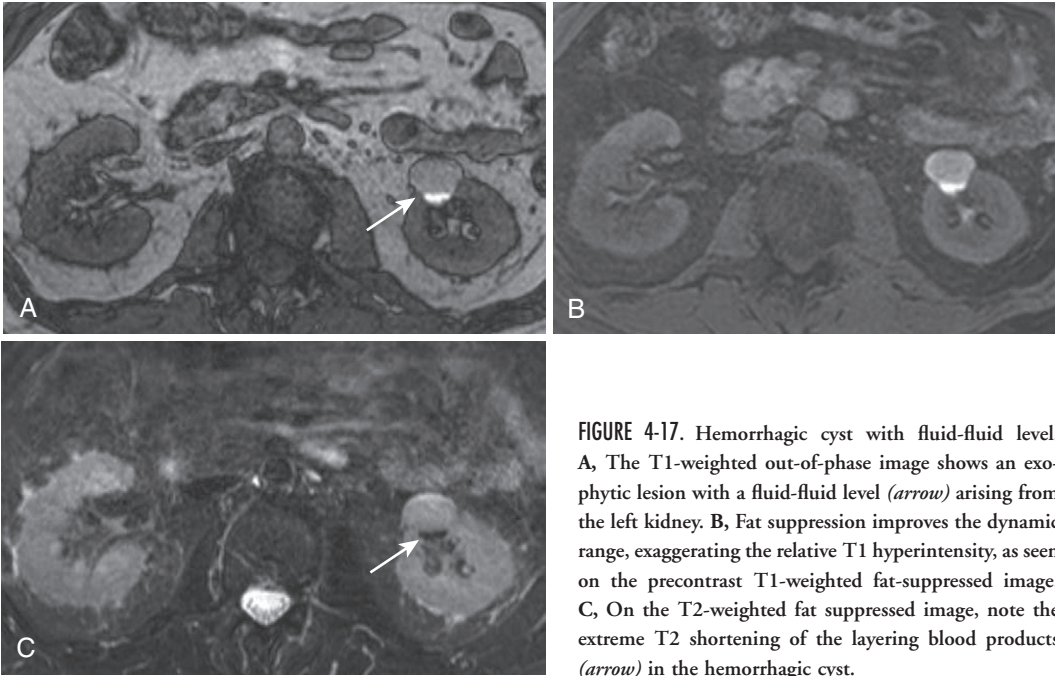


FIGURE 4-17. Hemorrhagic cyst with fluid-fluid level. **A**, The T1-weighted out-of-phase image shows an exophytic lesion with a fluid-fluid level (*arrow*) arising from the left kidney. **B**, Fat suppression improves the dynamic range, exaggerating the relative T1 hyperintensity, as seen on the precontrast T1-weighted fat-suppressed image. **C**, On the T2-weighted fat suppressed image, note the extreme T2 shortening of the layering blood products (*arrow*) in the hemorrhagic cyst.

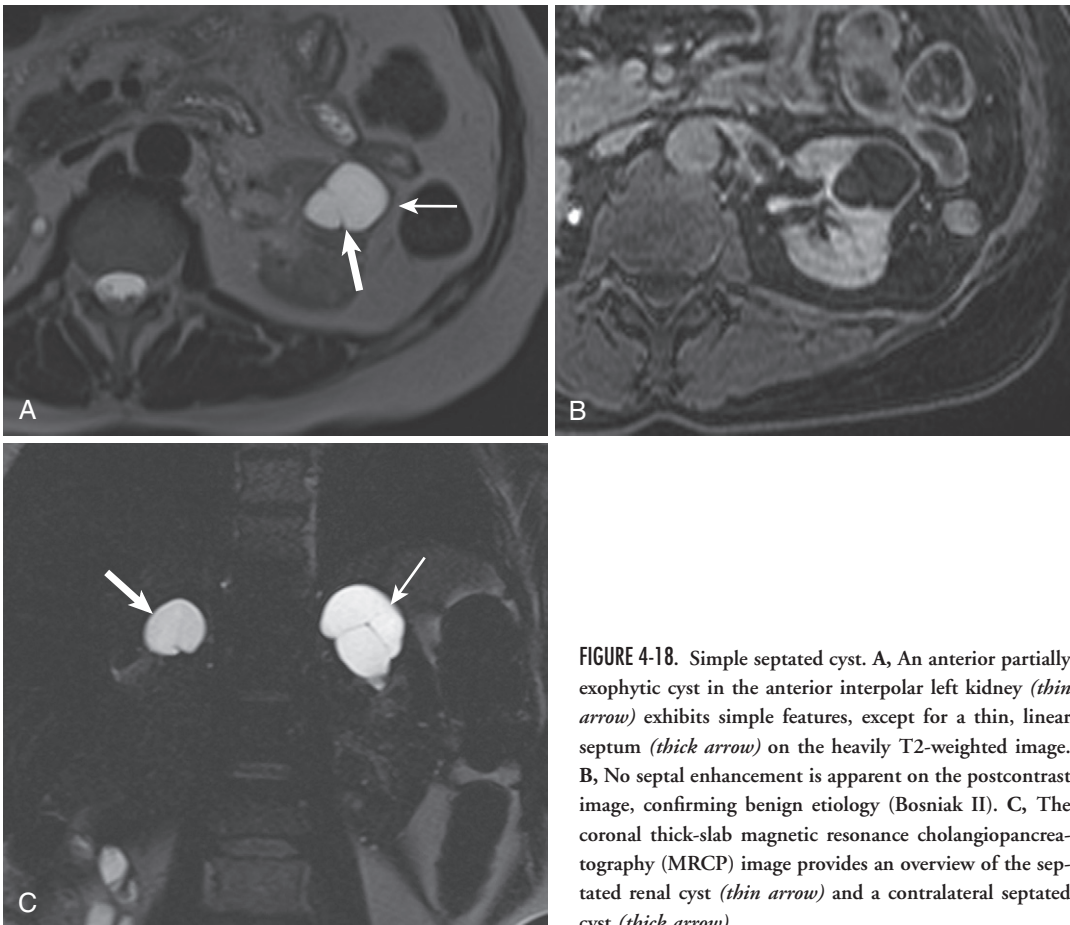


FIGURE 4-18. Simple septated cyst. **A**, An anterior partially exophytic cyst in the anterior interpolar left kidney (*thin arrow*) exhibits simple features, except for a thin, linear septum (*thick arrow*) on the heavily T2-weighted image. **B**, No septal enhancement is apparent on the postcontrast image, confirming benign etiology (Bosniak II). **C**, The coronal thick-slab magnetic resonance cholangiopancreatography (MRCP) image provides an overview of the septated renal cyst (*thin arrow*) and a contralateral septated cyst (*thick arrow*).

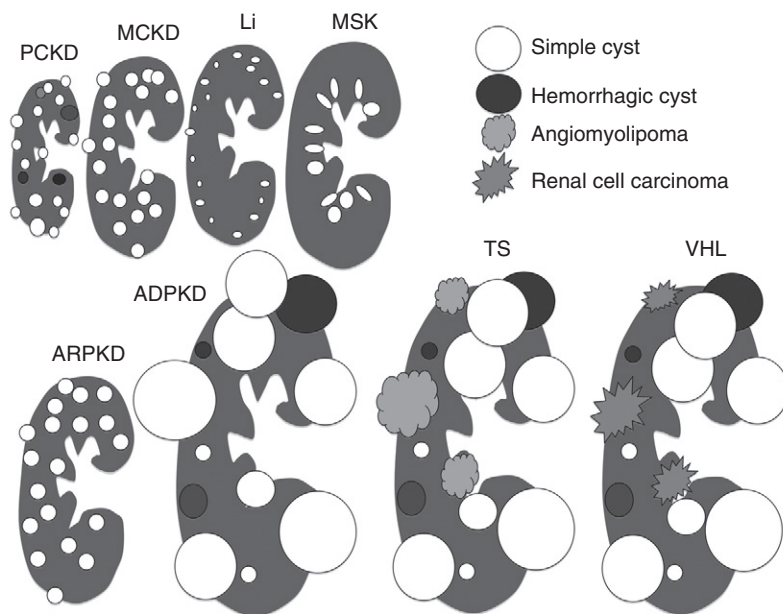


FIGURE 4-19. Schematic representation of the renal polycystic diseases showing the distribution of cystic and solid lesions and relative kidney size (with Li and MCKD representing normal-sized kidneys). ADPKD, autosomal dominant polycystic kidney disease; ARPKD, autosomal recessive polycystic kidney disease; Li, lithium; MCKD, multicystic kidney disease; MSK, medullary sponge kidney; PCKD, polycystic kidney disease; TS, tuberous sclerosis; VHL, von Hippel–Lindau.

POLYCYSTIC DISEASES

Renal cystic bilaterality and multiplicity characterize polycystic diseases (Fig. 4-19).¹¹ Polycystic kidney diseases fall into three categories: inherited, developmental, and acquired. *Inherited diseases* include autosomal recessive polycystic kidney disease (ARPKD), autosomal dominant polycystic kidney disease (ADPKD), medullary cystic kidney disease (MCKD), and the phakomatoses—TS and VHL. ARPKD and ADPKD induce renal failure, but incur no risk of malignancy (Fig. 4-20). Solid renal lesions complicate TS and VHL in addition to renal cysts. Clinical and demographic features separate ARPKD and ADPKD, whereas ARPKD presents early in childhood with renal and/or liver failure. ADPKD develops gradually over time, resulting in end-stage renal disease in middle age. Without the benefit of the genetic profile, the early phase of ADPKD is indistinguishable from incidental, noninherited simple renal cysts. Because renal cysts occur sporadically, age-based numeric criteria have been generated to distinguish incidental sporadic cysts from ADPKD (Table 4-5).¹² In the adult general population (45- to 59-year-old age group), an average of two cysts are detectable at MRI (1.2 in women and 2.9 in men).¹³

TABLE 4-5. Diagnostic Criteria for Autosomal Dominant Polycystic Kidney Disease

Age (yr)	Criteria
15–39	≥3 unilateral or bilateral cysts
40–59	≥2 cysts in each kidney
≥60	>4 cysts in each kidney or >6 cysts in women/>9 cysts in men (specifically based on MRI)

MRI, magnetic resonance imaging.

Phakomatoses—such as TS and VHL—are diseases characterized by dysplasia and/or neoplasia of organs arising from embryonic ectoderm (and often mesoderm and endoderm). TS and VHL feature a unique profile of extrarenal lesions (Fig. 4-21 and Table 4-6). The presence of solid and/or noncystic lesions eliminates the possibility of ADPKD from consideration. Macroscopic fat arising from an AML suggests TS, and solid, enhancing lesion(s) favors VHL. MCKD is an inherited tubulointerstitial nephropathy characterized by progressive renal failure and small cysts—usually less than 3 cm—predominating at the corticomedullary junction in relatively normal-sized kidneys.¹⁴

Although recognized as a *developmental disorder*, the etiology of medullary sponge kidney (MSK) is not fully understood. The burden of

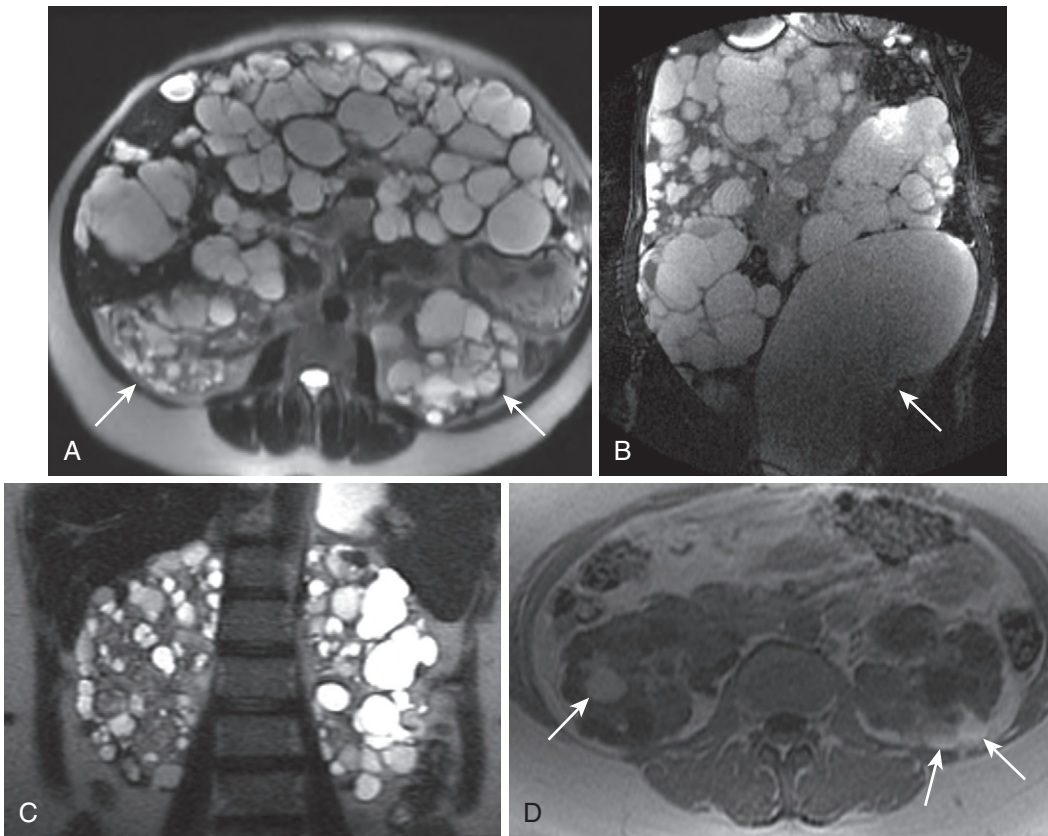


FIGURE 4-20. ADPKD. **A**, The axial T2-weighted image reveals innumerable, mostly simple hyperintense renal cysts (*arrows*) replacing renal parenchyma bilaterally in a patient with ADPKD in whom the liver is also involved. **B**, The coronal steady-state image shows the polycystic liver and kidneys with upward displacement of the left kidney by a large pelvic lymphocele (*arrow*) complicating left iliac fossa renal transplantation. **C**, The coronal T2-weighted image in a different patient shows multiple renal cysts bilaterally without liver involvement. **D**, Hyperintensity complicating scattered cysts (*arrows*) on the in-phase image indicates hemorrhage.

evidence supports a disruption of the ureteral bud–metanephric blastema interface. Cysts predominate in the medullary pyramids and usually measure less than 1 cm in size. The kidneys are generally normal to mildly enlarged.

Acquired renal cystic diseases include renal cystic disease of chronic renal insufficiency (or acquired cystic kidney disease [ACKD]) and lithium-induced renal cystic disease (see Fig. 4-19). Dilated renal tubules ultimately form cysts in failing kidneys, leading to ACKD. Hemorrhage complicates cysts in 50% of patients with ACKD,¹⁵ resulting in a combination of simple cystic and hemorrhagic cysts (see Fig. 4-19). The appearance potentially simulates ADPKD and incidental sporadic cysts, but the history of underlying renal failure and visible renal atrophy generally exclude these etiologies. Patients with ACKD incur an annual risk of 0.2% of developing RCC—the feared complication—compared with 0.005% in the general population. Papillary type

RCC constitutes a greater share of RCC in ACKD compared with the general population (50% compared with 5%–7%), and is discussed further in the upcoming section on “Solid Lesions.”

Lithium nephropathy stratifies into three temporal categories: acute nephropathy, nephrogenic diabetes insipidus, and chronic nephropathy. Chronic lithium nephropathy is the cystic variety. Punctate cysts (a few millimeters) inhabit the cortex and medulla (Fig. 4-22; see also Fig. 4-19).

Unilateral renal cystic lesions include a variety of additional rare developmental, infectious, and neoplastic lesions; hydronephrosis is added to the category of renal cystic lesions because of the potential to simulate parapelvic cysts. Collecting system lesions—hydronephrosis and calyceal diverticulum—are usually more easily differentiated from parapelvic cysts because of (1) the ability to selectively image free water

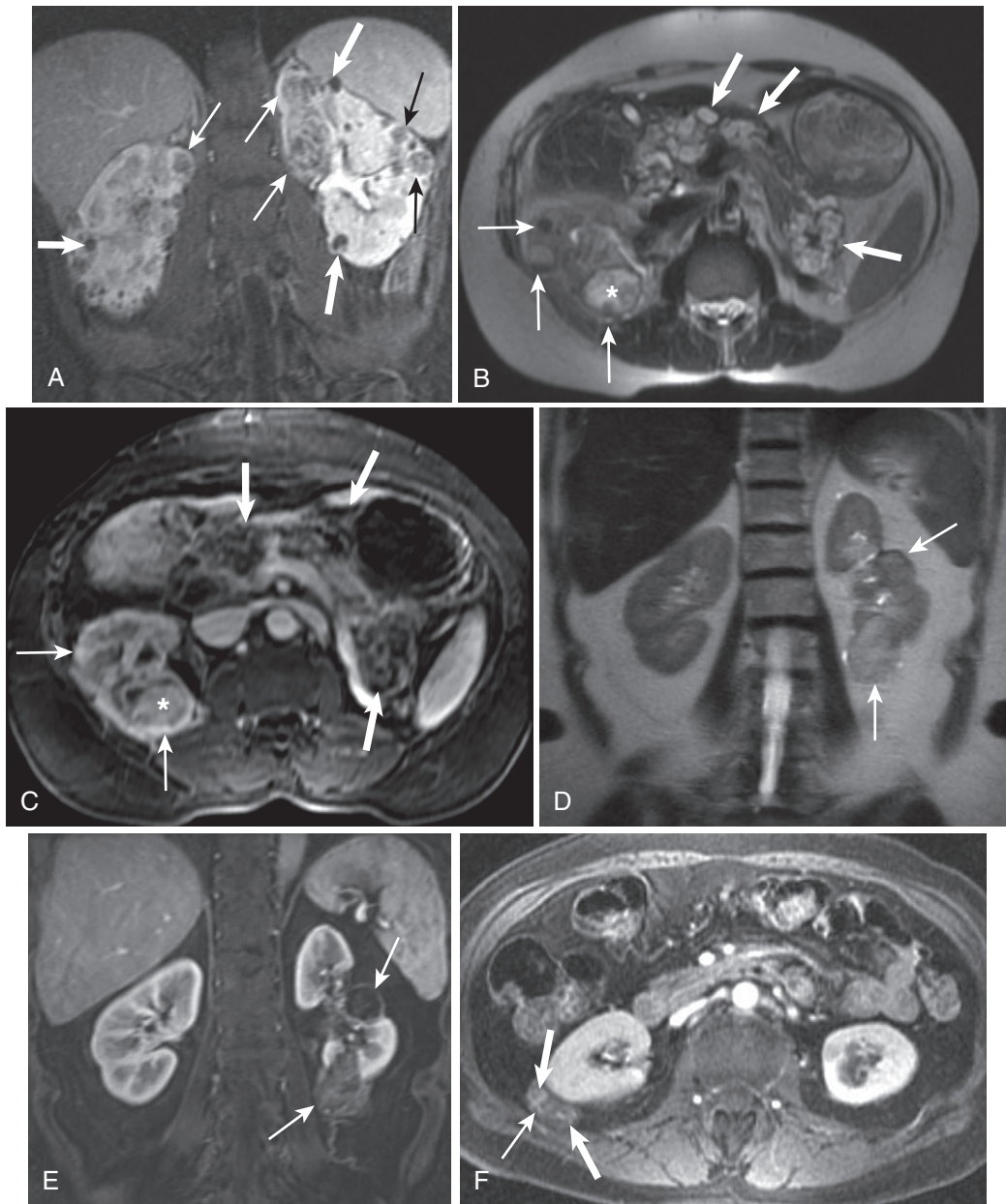


FIGURE 4-21. VHL and TS. **A**, The coronal postcontrast image in a patient with VHL disease shows multiple bilateral enhancing (*thin arrows*) and nonenhancing cystic lesions (*thick arrows*). Axial T2-weighted (**B**) and enhanced (**C**) images in a different patient with VHL reveal complex cystic lesions (*thin arrows*) in the right kidney (post left nephrectomy), including a cystic RCC (*asterisk*), and multiple complex cystic pancreatic lesions (*thick arrows*). Two heterogeneous noncystic left renal lesions (*arrows*) on the coronal T2-weighted image (**D**) in a different patient with TS fail to yield signal on the fat-suppressed image (**E**), and the corresponding fat-suppressed axial image (**F**) shows a similar lesion in the right kidney (*arrows* in **E** and **F**) with eccentric vascular enhancement (*thick arrows* in **F**)—all consistent with AMLs.

TABLE 4-6. Polycystic Kidney Diseases

Disease	Renal Lesions	Extrarenal Lesions
Polycystic Kidney Disease		
ADPKD	Cysts	Liver, pancreatic, splenic, epididymal, seminal vesicular, uterine, ovarian and thyroid cysts; circle of Willis berry aneurysms; aortic dissection; cardiac valvular disease
ARPKD	Cysts	Portal hepatic fibrosis
Hereditary Malformation Syndromes		
TS	Cysts, AMLs RCC very rare	Subependymal and cortical tubers, giant cell astrocytoma
VHL	Cysts, RCC, adenoma	Cerebellar hemangioblastoma; lung cyst; cardiac rhabdomyoma; pancreatic islet cell tumor, cyst, adenoma, microcystic adenoma; liver cyst and adenoma
Acquired Renal Cystic Disease		
Dialysis	Cysts, RCC	N/A
Chronic renal insufficiency (without dialysis)		

ADPKD, autosomal dominant polycystic disease; ARPKD, autosomal recessive polycystic disease; AML, angiomyolipoma; N/A, not applicable; RCC, renal cell carcinoma; TS, tuberous sclerosis; VHL, von Hippel-Lindau.

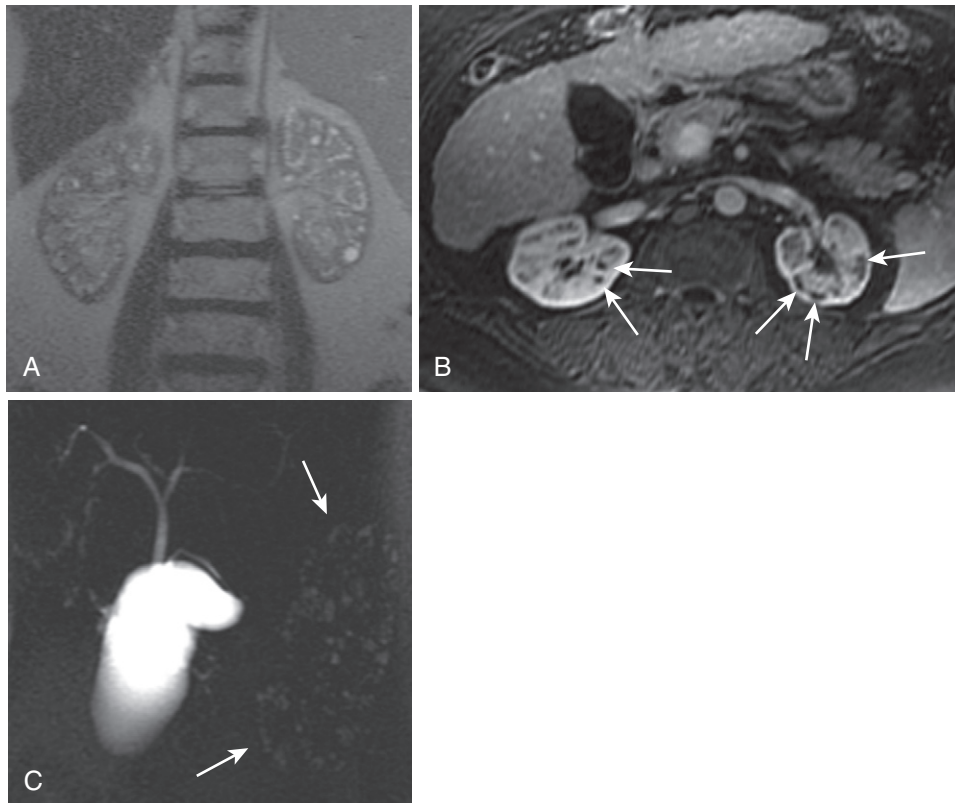


FIGURE 4-22. Lithium cystic nephropathy. **A**, The coronal heavily T2-weighted image shows innumerable punctate simple cysts in the cortex and medulla, most of which measure no more than a few millimeters. **B**, The postcontrast image confirms cystic etiology through absent enhancement (*arrows*). **C**, The MRCP image portrays the multiplicity of punctate simple cysts in the left kidney (*arrows*) to better advantage.

TABLE 4-7. Etiologies of Hydronephrosis

Ureter	Functional
Intrinsic	<ul style="list-style-type: none"> • Gram-negative infection • Neurogenic bladder
<ul style="list-style-type: none"> • Ureteropelvic junction stricture • Ureterovesical junction obstruction • Papillary necrosis • Ureteral folds • Ureteral valves • Ureteral stricture (iatrogenic) • Blood clot • Benign fibroepithelial polyps • Ureteral tumor • Fungus ball • Ureteral calculus • Ureterocele • Endometriosis • Tuberculosis • Retrocaval ureter 	Bladder
	Intrinsic
	<ul style="list-style-type: none"> • Bladder carcinoma • Bladder calculi • Bladder neck contracture • Cystocele • Primary bladder neck hypertrophy • Bladder diverticula
	Extrinsic
	<ul style="list-style-type: none"> • Pelvic lipomatosis
Extrinsic	Functional
<ul style="list-style-type: none"> • Retroperitoneal lymphoma • Retroperitoneal sarcoma • Cervical cancer • Prostate cancer • Retroperitoneal fibrosis • Aortic aneurysm • Inflammatory bowel disease • Ovarian vein syndrome • Retrocaval ureter • Uterine prolapse • Pregnancy • Iatrogenic ureteral ligation • Ovarian cysts • Diverticulitis • Tubo-ovarian abscess • Retroperitoneal hemorrhage • Lymphocele 	<ul style="list-style-type: none"> • Neurogenic bladder • Vesicoureteral reflux
	Urethra
	Intrinsic
	<ul style="list-style-type: none"> • Urethral stricture • Urethral valves • Urethral diverticula • Urethral atresia • Labial fusion
	Extrinsic
	<ul style="list-style-type: none"> • Benign prostatic hyperplasia and prostate cancer

(urine) and appreciate continuity with the collecting system and (2) exquisite sensitivity to enhancement by excreted gadolinium.

HYDRONEPHROSIS

Hydronephrosis refers to the distention of the collecting system with urine—obstructive (more common) versus nonobstructive (Table 4-7). The imaging agenda is twofold: detecting hydronephrosis and identifying the etiology and point of obstruction (if present). Heavily T2-weighted sequences depict hydronephrosis most clearly—demonstrating collecting system and ureteral continuity (Fig. 4-23). T2-weighted images help establish obstruction by demonstrating perinephric hyperintensity (shown to be present in cases of acute obstructive uropathy).^{16,17} Delayed postcontrast images with urine enhancement by excreted gadolinium also depict collecting system and ureteral anatomy and continuity. Enhancement on delayed postcontrast images

confirms collecting system etiology, although increased pressure associated with high-grade obstruction delays urinary excretion and an insufficient delay preempts enhancement. Delayed collecting system enhancement excludes the only differential diagnosis—parapelvic cysts (see Fig. 4-15).

Although a full discussion of hydronephrotic obstructing lesions is beyond the scope of this text, the most common obstructing lesion—renal calculus—deserves attention. The MR appearance of renal calculi is basically the photographic negative of the CT appearance. On all pulse sequences, renal calculi induce a signal void owing to magnetic susceptibility (Fig. 4-24). Hypointense renal calculi are most conspicuous when surrounded by hyperintense urine on fluid-sensitive sequences. Although quoted as up to 97% sensitive for renal calculi, anecdotally, MR sensitivity to renal stones is far lower.

COMPLEX CYSTIC LESIONS

For the purposes of our discussion, *cystic complexity* means wall thickening, peripheral nodularity, septation, and/or enhancement—IIF or higher on the Bosniak scale. Using these features to identify a category distinct from simple cystic (and solid) lesions defines our differential diagnostic scheme (Fig. 4-25). Complex cystic lesions include infectious, posttraumatic, and neoplastic etiologies.

PYOGENIC RENAL ABSCESS

One of the chief complex cystic infectious lesions is the pyogenic renal abscess, which accounts for approximately 2% of all renal masses. Renal abscesses present 1 to 2 weeks after the onset of infection and most commonly complicate ascending urinary tract infection; the minority arises hematogenously. Although the clinical features skew the differential diagnosis toward an inflammatory etiology, circum-spection is warranted because of the shared imaging features with cystic neoplasms.

Internal contents are mildly relatively T1 hyperintense and T2 hypointense compared with simple fluid with no enhancement (Fig. 4-26).¹⁸ Rim enhancement with perilesional enhancement and edema imply an inflammatory etiology. Obliteration of the adjacent renal sinus or perinephric fat, urothelial thickening and enhancement, thickening of Gerota's fascia, and perinephric septa also advocate inflammation.¹⁹

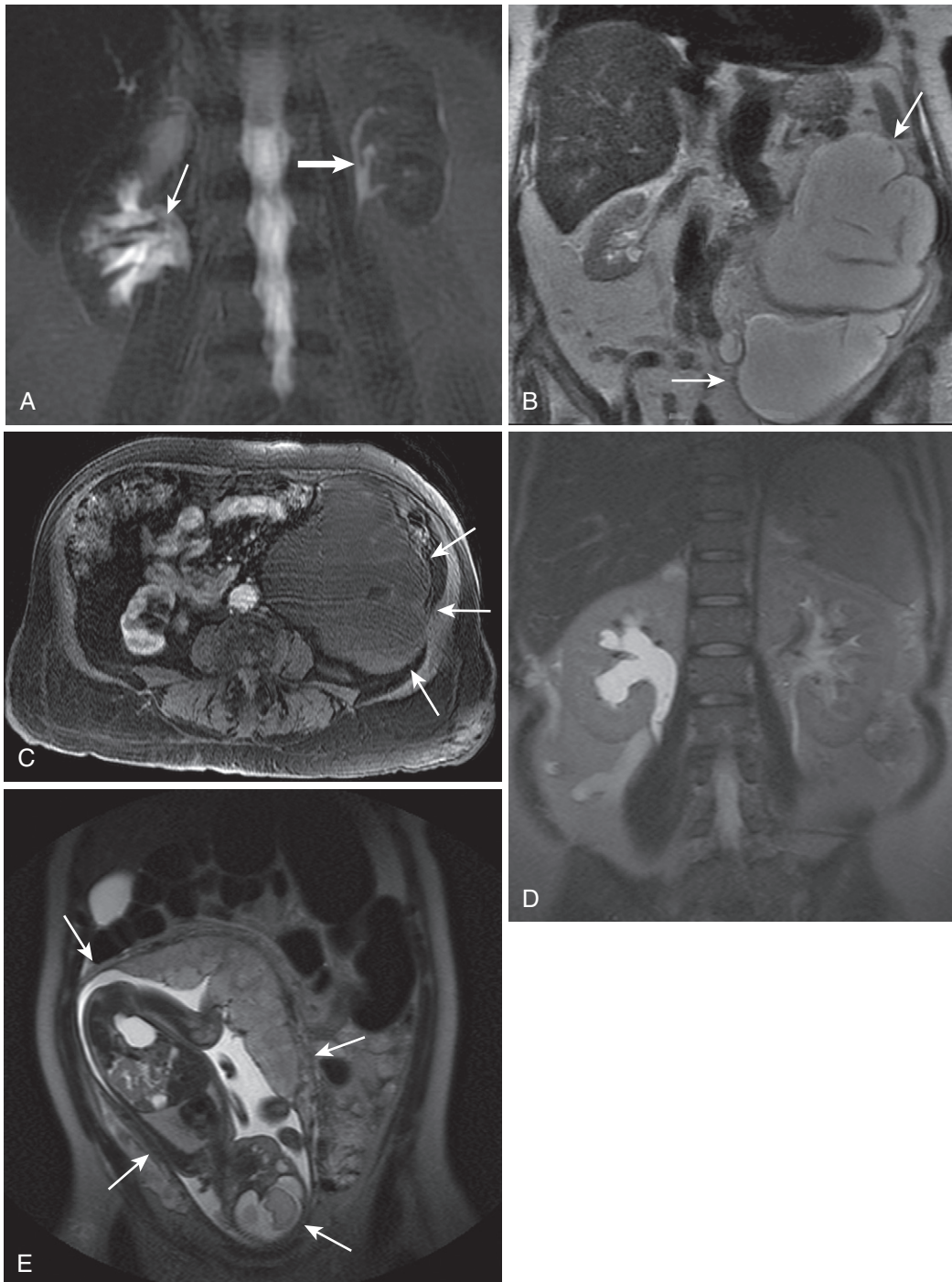


FIGURE 4-23. Hydronephrosis. A, The heavily T2-weighted magnetic resonance urography (MRU) image shows asymmetrical right-sided collecting system (*thin arrow*) compared with the normal left-sided collecting system (*thick arrow*) in a patient with mild hydronephrosis. The coronal heavily T2-weighted single-shot fast spin-echo (SSFSE) image (B) portrays an example of severe, longstanding left-sided hydronephrosis (*arrows*), and the axial postcontrast image (C) shows the thinned, virtually obliterated, nonenhancing rim of nonfunctioning enhancement (*arrows*). Mild to moderate right-sided hydronephrosis is apparent on the coronal T2-weighted image in a different patient (D) due to the mass effect of the gravid uterus, as seen on a more caudally positioned T2-weighted image (*arrows* in E).

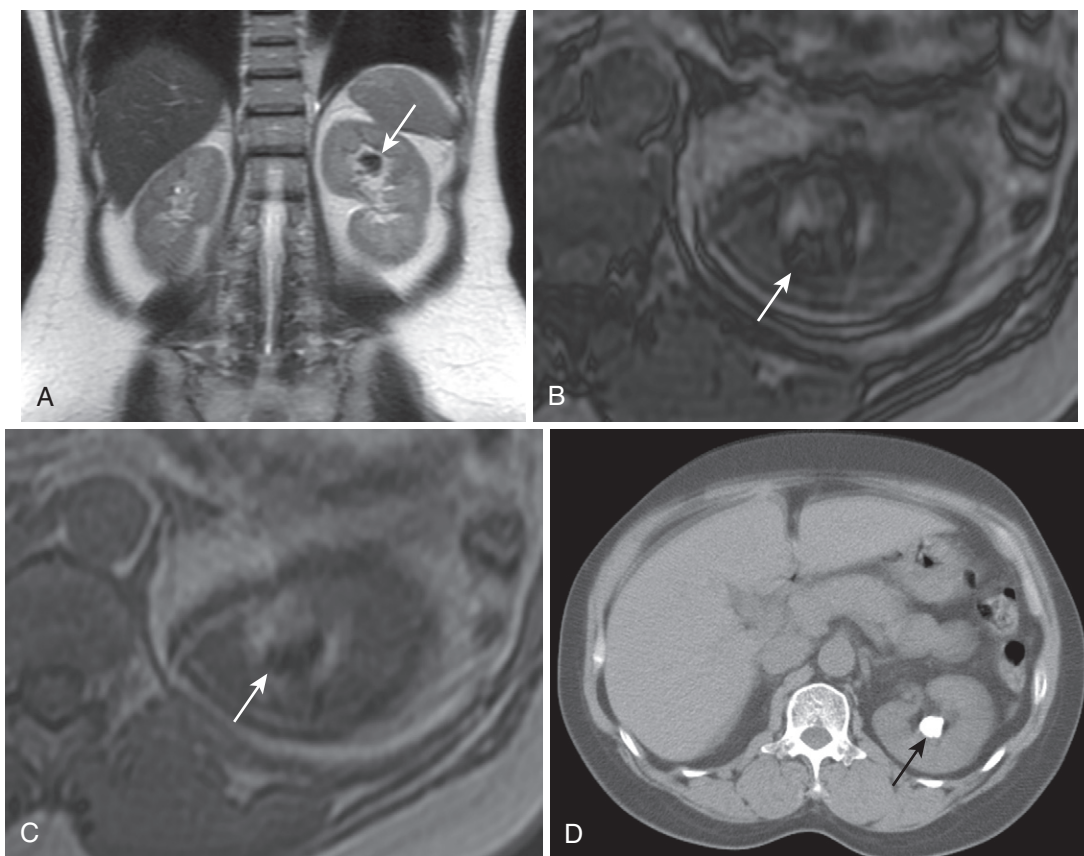


FIGURE 4-24. Renal calculi. **A**, The coronal heavily T2-weighted image demonstrates a signal void in the collecting system of the upper pole of the left kidney (arrow). Vague hypointensity (arrow in **B**) on the corresponding out-of-phase image (**B**), degraded by motion, blooms on the in-phase image (arrow in **C**) due to susceptibility artifact, induced by the presence of calcium, as seen on the corresponding computed tomography (CT) image (arrow in **D**).

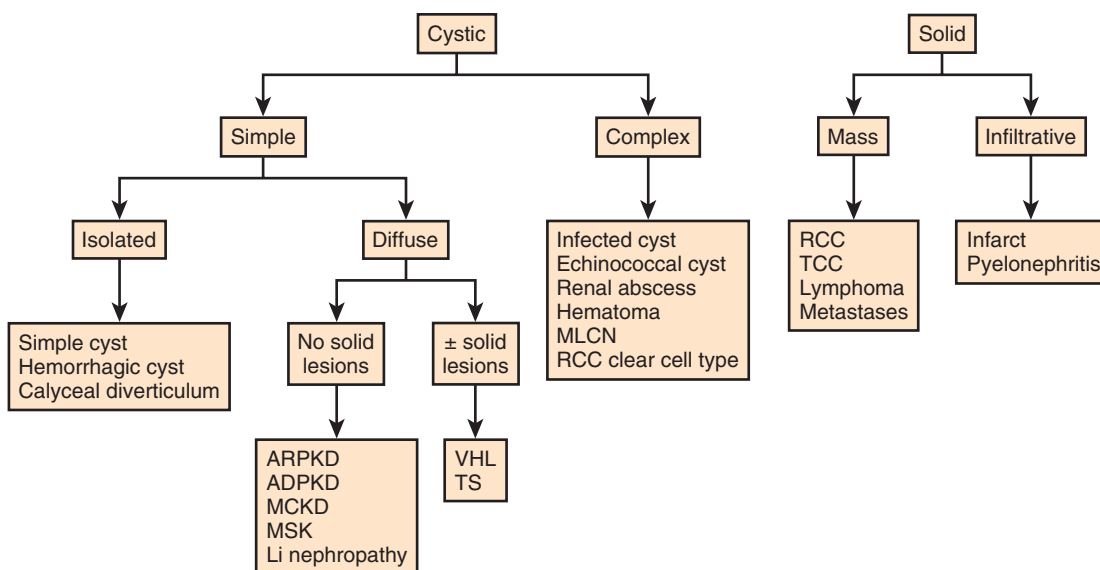


FIGURE 4-25. Kidney lesion diagnostic scheme. ADPKD, autosomal dominant polycystic kidney disease; ARPKD, autosomal recessive polycystic kidney disease; Li, lithium; MCKD, multicystic kidney disease; MLCN, multilocular cystic nephroma; MSK, medullary sponge kidney; RCC, renal cell carcinoma; TCC, transitional cell carcinoma; TS, tuberous sclerosis; VHL, von Hippel-Lindau.

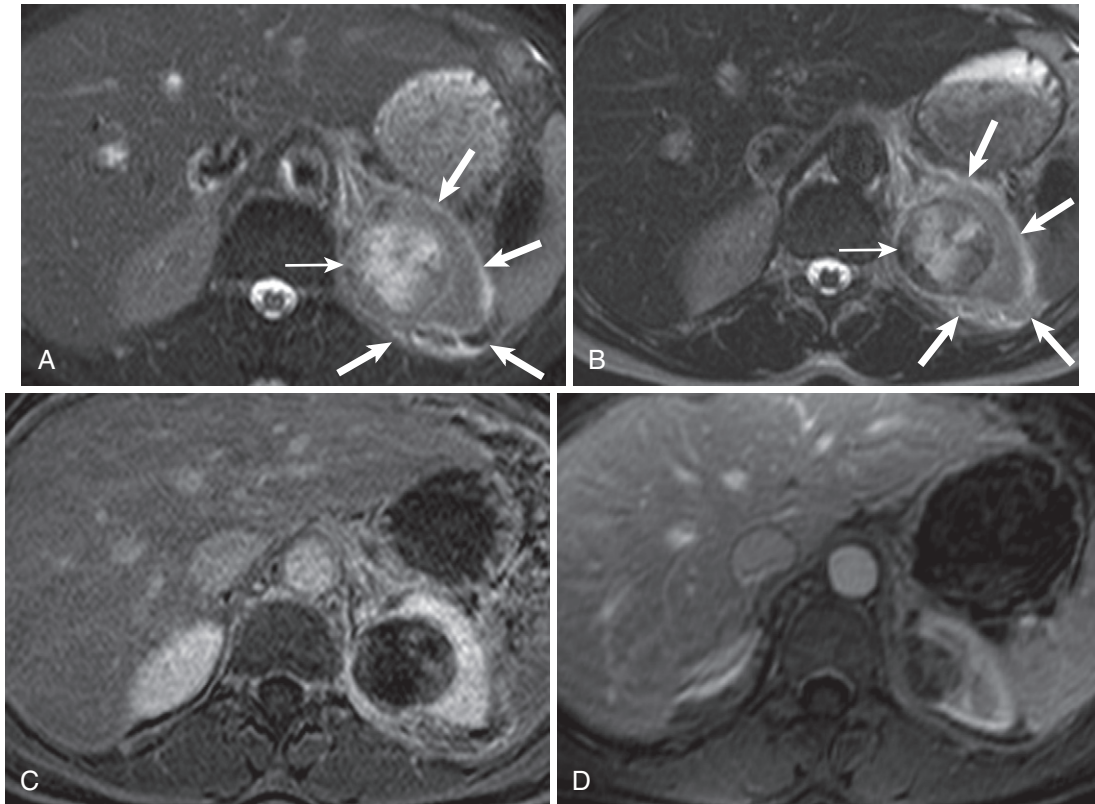


FIGURE 4-26. Renal abscess. **A**, The axial fat-suppressed T2-weighted image shows a heterogeneously hyperintense lesion in the upper pole of the left kidney (*thin arrow* in **A** and **B**) associated with perinephric edema (*thick arrows* in **A** and **B**). **B**, The corresponding T2-weighted image without fat suppression exaggerates the internal complex hypointensity not typical of a simple or hemorrhagic cyst. **C**, The postcontrast image reveals virtual absence of internal signal (minimal internal signal represents debris—also hyperintense on the corresponding unenhanced image [not shown]). **D**, An axial T2-weighted image from a follow-up examination 1 month later establishes involution and improvement after antibiotic treatment, confirming infectious (and non-neoplastic) etiology.

Although RCC is the main differential consideration, clinical and imaging signs of inflammation and lack of enhancing solid tissue favor non-neoplastic etiology. In addition to the clinical features and surrounding inflammatory changes, the main discriminating feature is the presence of hypervascular solid components. The markedly restricted diffusion of renal abscess contents also proposes the correct diagnosis.²⁰

Differentiating renal abscess from an infected renal cyst may seem academic because both are manifestations of infection, but treatment regimens differ. Whereas both are treated with a trial course of antibiotics, a lower success rate with renal abscess prompts a lower threshold for percutaneous drainage.²¹ Imaging features overlap, but a greater degree of inflammatory changes, relatively poorer definition, and a shaggy inner wall favor abscess.

TABLE 4-8. Renal Cell Carcinoma
Histologic Subtypes

Clear cell (65–70%)
Papillary (15–20%)
Chromophobe (6–11%)
Multilocular cystic (<1%)
Collecting duct (<1%)
Medullary (<1%)
Mucinous tubular and spindle cell (<1%)

Based on Eble JN, Sauter G, Epstein JI, Sesterhenn IA, eds. Pathology and Genetics of Tumours of the Urinary and Genital Organs. World Health Organization Classification of Tumours. International Agency for Research on Cancer. 2004;12–43.

CYSTIC RENAL CELL CARCINOMA

RCC accounts for 90% of renal tumors with protean clinical and imaging manifestations depending on the subtype (**Table 4-8**).^{22,23} The

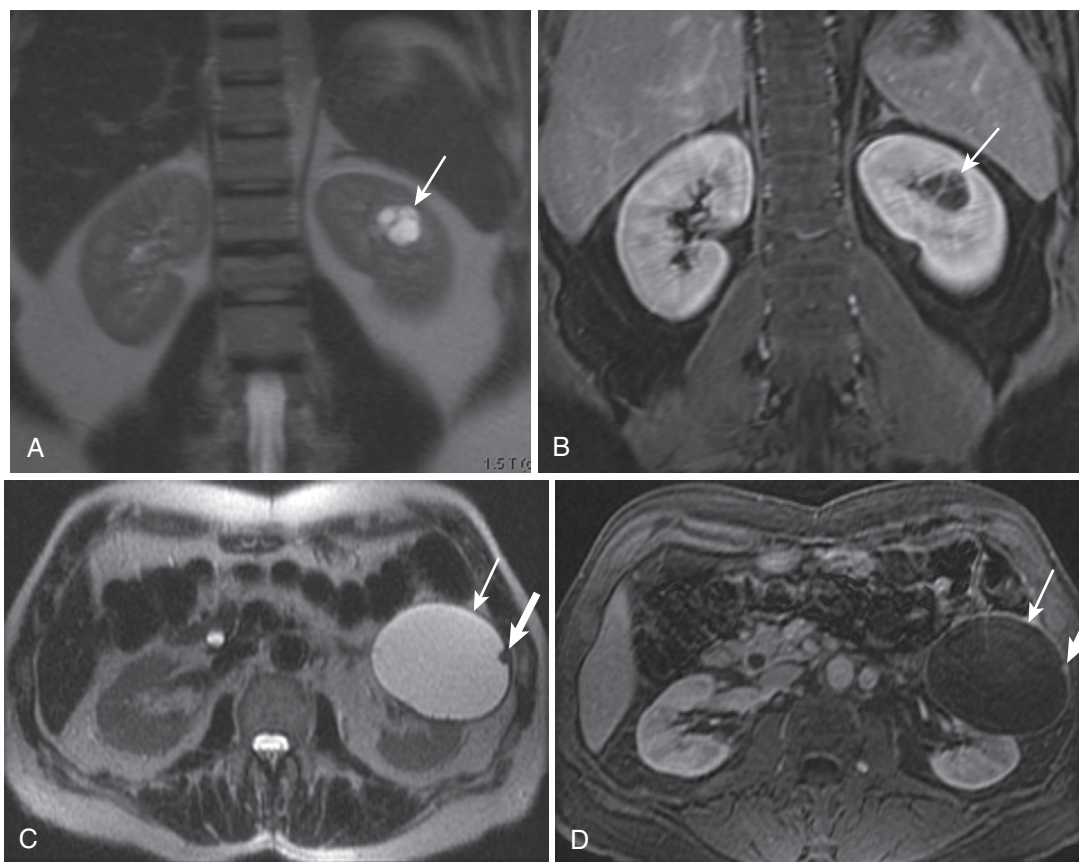


FIGURE 4-27. Cystic RCC. The coronal T2-weighted (A) and enhanced (B) images show a cystic lesion (*arrow*) with mildly thickened enhancing septa in a cystic clear cell RCC. Axial T2-weighted (C) and enhanced (D) images in a different patient reveal a clear cell RCC (*thin arrow*) with even less complexity—mild wall thickening and a punctate mural nodule (*thick arrow*).

clear cell subtype accounts for most cystic RCCs and 10% to 15% of clear cell RCCs are cystic. Even when predominantly cystic, careful inspection usually discloses a solid, enhancing component. Solid components (of clear cell RCCs) are usually hyperintense to renal parenchyma on T2-weighted images and enhance avidly, although usually less than renal parenchyma (Fig. 4-27). Motion artifact and lack of subtracted images hamper the ability to detect solid components, which are invariably present. Because most RCCs are predominantly solid, a more comprehensive review of RCC is deferred to the section on “Solid Lesions.”

Multilocular cystic RCC is the only consistently cystic subtype (see Table 4-8). Multilocularity with thin septal enhancement and occasional septal asymmetry characterize the typical appearance, which closely approximates MLCN.

MULTILOCULAR CYSTIC NEPHROMA

MLCN constitutes a potential confounder of cystic RCC in the appropriate demographic categories. MLCN is a benign nonhereditary neoplasm arising from metanephric blastema with a bimodal predilection for young males (3 mo–2 yr) and older females (fifth and sixth decades). Classically, MLCN is a multiloculated cystic lesion with thin, septal enhancement, an absence of solid tissue, and herniation into the renal pelvis (putatively pathognomonic) (Fig. 4-28). Because most fall into the Bosniak III category, excision is advocated. Also, imaging feature overlap with cystic and multilocular RCC force circumspection and (at least) consideration of excision.

RENAL HEMATOMA

Hematomas occur within the renal parenchyma, within the renal capsule (subcapsular), and outside the capsule (perinephric). Blunt and

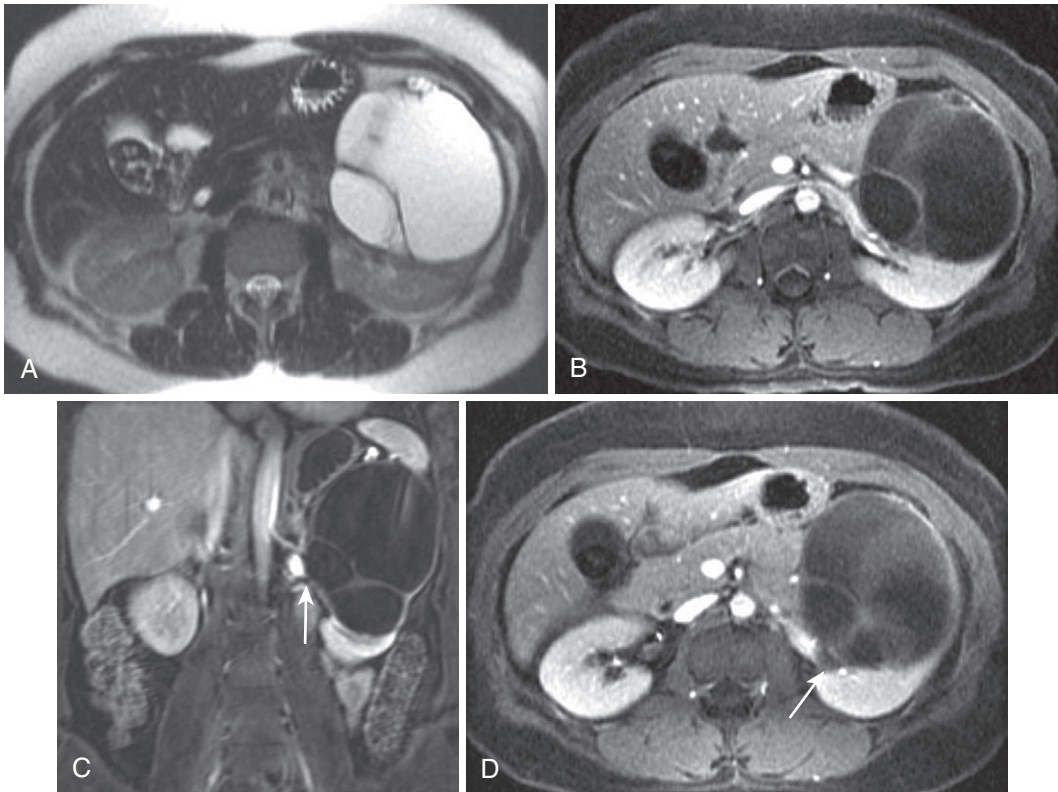


FIGURE 4-28. Multilocular cystic nephroma. The axial heavily T2-weighted (A) and postcontrast (B) images reveal a large multiloculated cystic lesion in a 45-year-old woman. The coronal postcontrast image (C) portrays the size of the lesion and subtle medial protrusion (arrows in C and D), corroborated on the coronal enhanced image (D), conforming to herniation into the renal pelvis at surgical resection.

penetrating trauma and surgical and percutaneous procedures account for the majority of renal hematomas. Occasionally, underlying vascular disease, such as arteriovenous malformation (AVM) and vasculitis, induces hemorrhage. Hemorrhage originating from an underlying renal mass is the diagnosis of exclusion and the usual culprits are AML and RCC. The T1 hyperintensity of hemorrhage uniquely proclaims itself (Fig. 4-29), although underlying etiologies must be entertained. Without an explanative etiology, RCC must be excluded with follow-up imaging.

SOLID LESIONS

Solid renal lesions essentially equal malignancy. The rare exceptions are renal adenoma and oncocytoma, which cannot be differentiated from malignant solid renal lesions. Pseudolesions—nonneoplastic lesions simulating neoplasms—confound the assessment of solidity. These lesions include renal infarct, pyelonephritis, renal vein thrombosis (RVT), and renal trauma. Because these lesions reflect

derangements of underlying renal parenchyma, morphology is preserved at the expense of signal and enhancement. These lesions tend to manifest with either geographic or diffuse (signal and/or enhancement) findings, rather than focal, masslike features—or the “bean” versus “ball” renal lesion scheme (Fig. 4-30).

Neoplastic masses expand more or less centrifugally, conforming roughly to spheres, or “balls.” In the process, the “bean” shape of the kidney is deformed. Meanwhile, other lesions preserve the bean shape of the kidney by either infiltrative neoplastic growth or nonneoplastic affliction of a segment or entirety of the kidney (e.g., infection, infarction). This useful diagnostic scheme serves to frame differential diagnoses, not separate benign from malignant, because benign and malignant lesions fall into both categories.

RENAL CELL CARCINOMA

The quintessential (solid) ball lesion is RCC. RCC represents over 90% of renal neoplasms. For this reason, solidity generally equals RCC

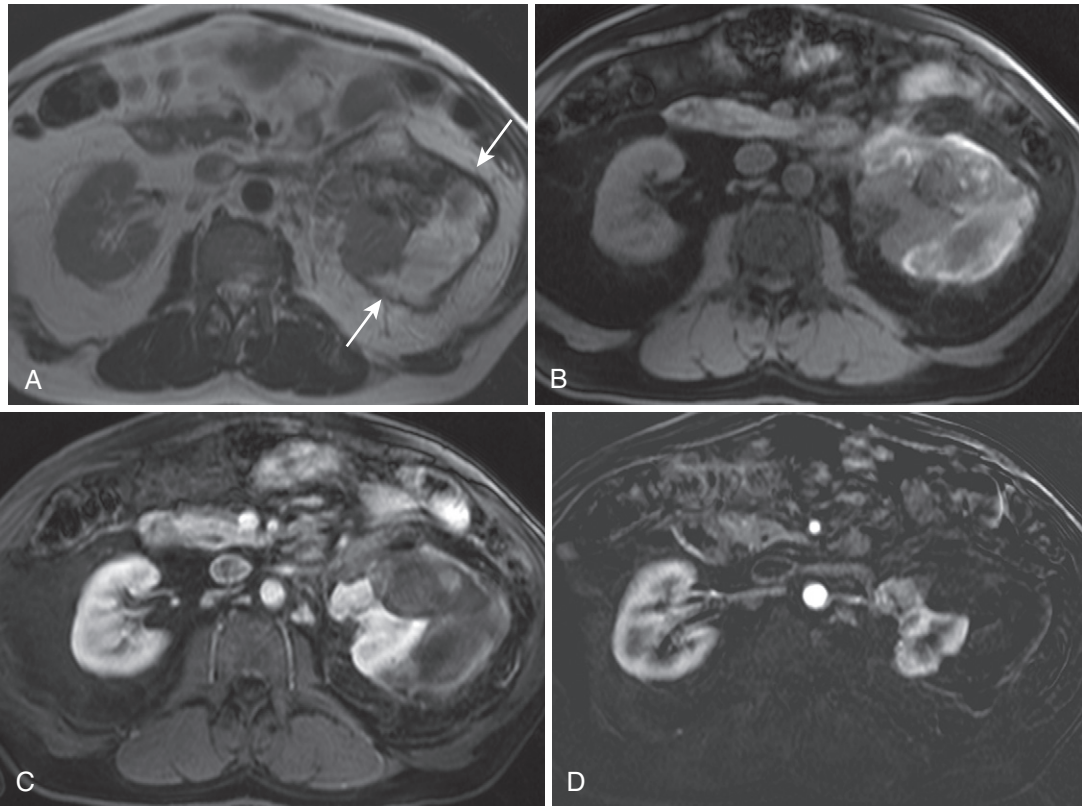


FIGURE 4-29. Renal hematoma. A large left perinephric collection (*arrows* in A) demonstrates heterogeneous hyperintensity on the T2-weighted image (A) with corresponding hyperintensity on the T1-weighted fat-suppressed image (B). The postcontrast image (C) shows mild intralésional hyperintensity not corresponding to enhancement, proven by the lack of signal on the subtracted image (D).

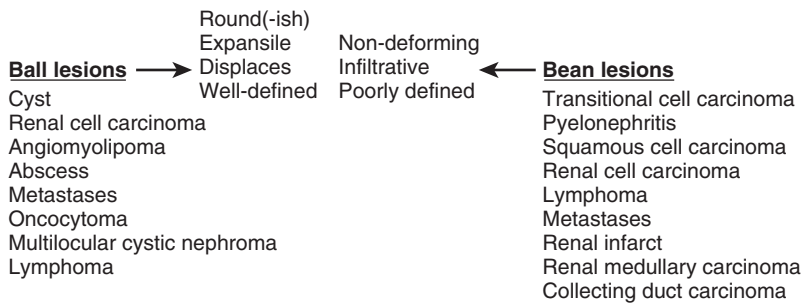


FIGURE 4-30. Ball versus bean diagnostic approach.

Syndrome	Chromosomal abnormality	RCC	Other tumors
VHL	VHL gene (3p), autosomal dominant	Clear cell, bilateral and multifocal	Pheochromocytoma, pancreatic cysts, islet cell tumors, epididymal cystadenomas, others
Familial clear cell carcinoma with translocation	Chromosome 3	Clear cell, unilateral, bilateral solitary or multifocal	Thyroid carcinoma
Familial clear cell carcinoma	? (absence of established genetic source), ≥ 2 first-degree relatives with RCC	Clear cell, solitary and unilateral	None
Hereditary papillary renal cell carcinoma	7q, autosomal dominant	Papillary, multiple, bilateral	Breast, lung, pancreatic, skin, gastric
Hereditary leiomyomatosis and RCC	1q, autosomal dominant	Papillary, solitary and unilateral (aggressive and metastasize early)	Uterine fibroids, cutaneous leiomyomas
Birt-Hogg-Dube syndrome	17p, autosomal dominant	Oncocytomas, oncocytoma-chromophobe hybrids, chromophobe RCC, clear cell RCC, papillary RCC	Skin tumors, medullary thyroid carcinoma, pulmonary cysts (spontaneous pneumothorax)
Familial renal oncocytoma	?	Oncocytomas, multiple and bilateral	Renal cysts
Tuberous sclerosis	TSC gene 1 or 2 (9q), autosomal dominant	Clear cell, bilateral and multifocal (rarely reported)	Angiomyolipomas, adenoma sebaceum, periungual fibromas, cardiac rhabdomyomas, retinal hamatomas, pulmonary lymphangioliomyomatosis, giant cell astrocytomas, others

FIGURE 4-31. Inherited renal cell carcinoma (RCC) syndromes. TSC, tuberous sclerosis complex; VHL, von Hippel–Lindau.

(until proved otherwise). RCC is a malignant neoplasm arising from renal tubular epithelium with protean clinical and imaging manifestations, according to the histologic subtype (see Table 4-8). Although all subtypes arise from the tubular epithelial cell, cytogenetic factors induce wide variations in cell type and tumor growth patterns, reflected in the variable appearance of RCC on MR images. RCC cytogenetic analyses have elucidated a number of inherited RCC syndromes (Fig. 4-31), which account for 4% of RCCs.²⁴ The imaging approach to RCC most rationally focuses on histologic subtypes, which usually dictates imaging appearance. The most common subtypes—clear cell and papillary—tend to differ dramatically. Clear cell tumors tend to be heterogeneously hypervascular and fluid-rich with hyperintensity on fluid-sensitive sequences. Papillary tumors tend to be hypovascular and homogeneously hypointense on fluid-sensitive sequences.

Clear cell RCC tumors, like other subtypes, arise from renal tubular epithelium in the

cortex of the kidney. Hemorrhage, necrosis, and cyst formation frequently accompany tumor growth. The *clear cell* designation derives from the microscopic appearance, attributable to intracytoplasmic glycogen and lipid. Tumor hypervascularity—thought to be related to inactivation of tumor suppressor genes—is relative to other renal tumors; parenchymal enhancement usually exceeds tumoral enhancement (Fig. 4-32). Intracytoplasmic lipid often induces loss of signal on out-of-phase images (Fig. 4-33).^{25,26} Whereas measurable loss of signal on opposed-phase images is substantiated in up to 60% of clear cell tumors, visibly detectable signal loss prevails far less commonly.

After establishing probable etiology, staging issues deserve attention (see Fig. 4-5). The multiplanar capabilities of MRI render size assessment simple and accurate. The sensitivity of perinephric space extension is limited—approximately 60% to 70%. The most specific CT finding—likely shared with MRI—is the presence of a discrete mass measuring at least 1 cm

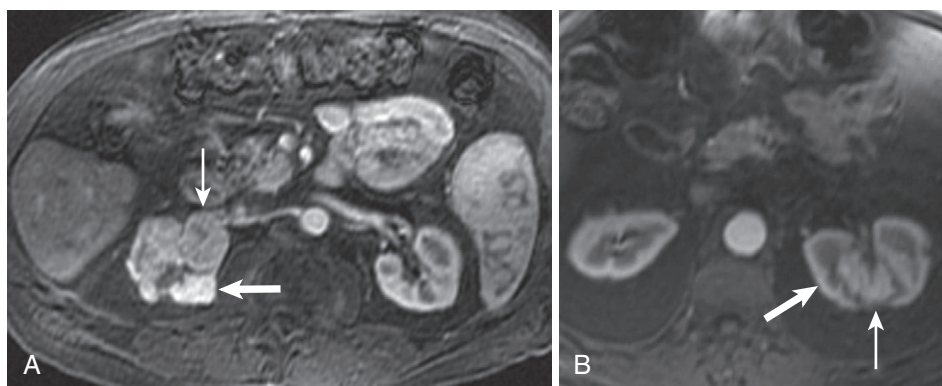


FIGURE 4-32. Clear cell RCC enhancement. A and B, Arterial (corticomedullary) phase postcontrast images in different patients with right-sided (*thin arrow* in A) and left-sided (*thin arrow* in B) clear cell RCCs, respectively, show lesion enhancement less than adjacent parenchyma (*thick arrow* in A) and approximating renal cortex (*thick arrow* in B).

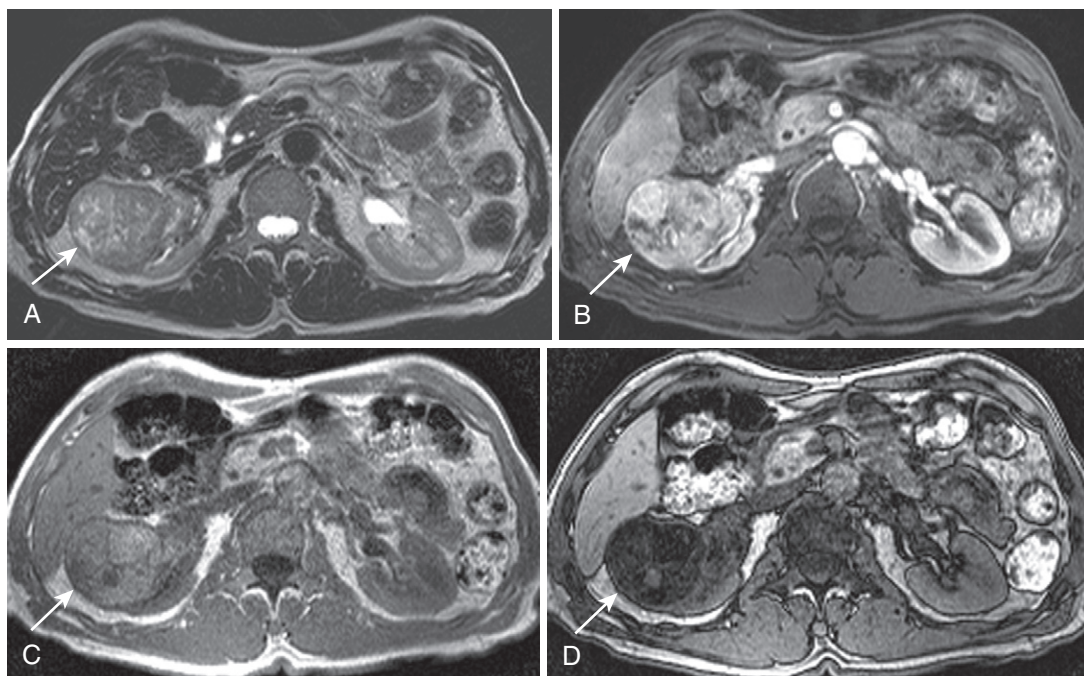


FIGURE 4-33. Clear cell RCC with intracytoplasmic lipid. An exophytic T2 hyperintense (A), heterogeneously enhancing (B) right renal lesion (*arrow*), relatively hyperintense on the in-phase image (C), dramatically loses signal on the out-of-phase image (D), indicating microscopic fat.

in the perinephric space.²⁷ Linear strands infiltrating the perinephric space raise the suspicion of perinephric invasion with low specificity (Fig. 4-34).

The sensitivity to enhancement and venous patency versus occlusion and ability to detect tumor thrombus recommend MRI in the staging of RCC.²⁸ Whereas routine contrast-enhanced images often suffice to detect intraluminal venous thrombus, dedicated magnetic resonance venography (MRV) images (with a higher dose of gadolinium; a high flip angle

and slice thickness, and FOV and coronal plane orientation modifications) anecdotally increase sensitivity (Figs. 4-35 and 4-36). Unenhanced images supplement enhanced images by showing vessel expansion and signal alterations, including loss of the normal signal void (especially on T2-weighted images) and hypointense filling defects on steady-state images. To optimally differentiate tumor thrombus from bland thrombus by detecting enhancement, include and review subtracted images.

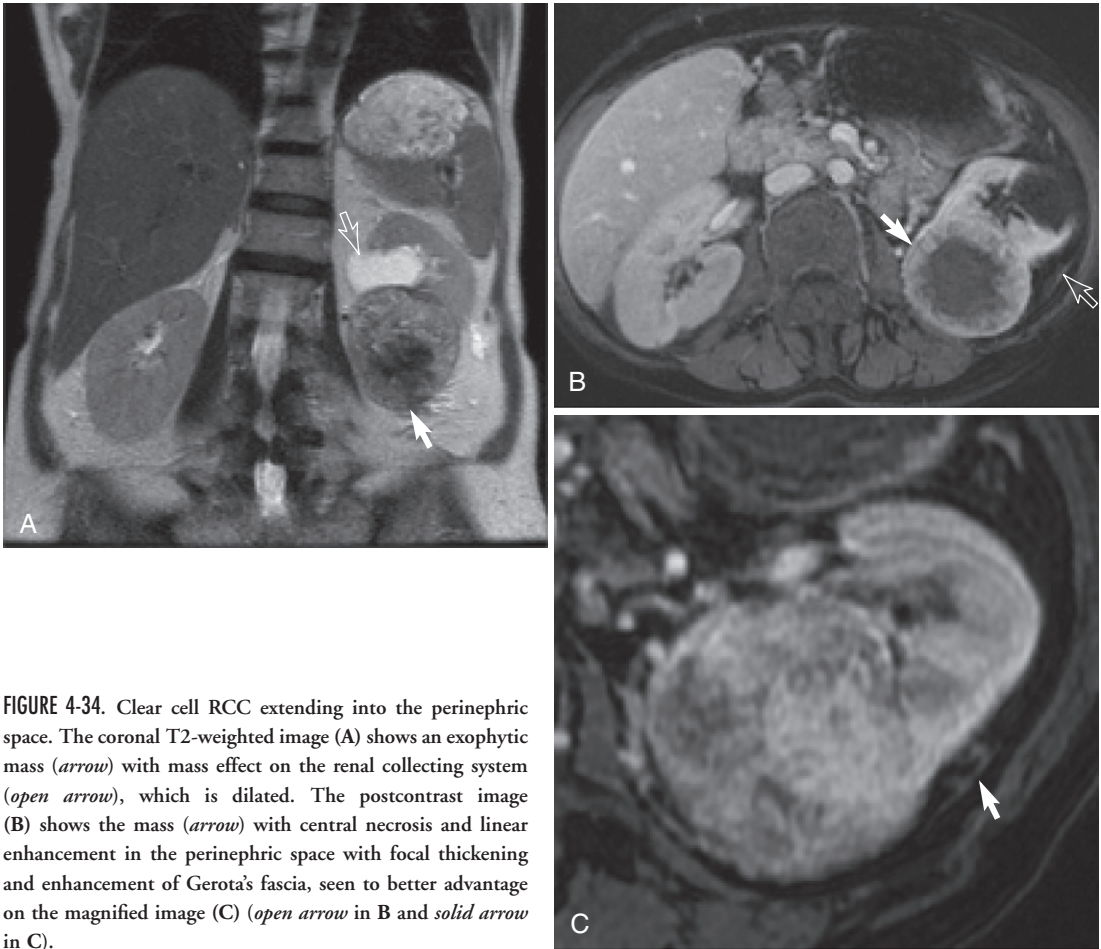


FIGURE 4-34. Clear cell RCC extending into the perinephric space. The coronal T2-weighted image (A) shows an exophytic mass (*arrow*) with mass effect on the renal collecting system (*open arrow*), which is dilated. The postcontrast image (B) shows the mass (*arrow*) with central necrosis and linear enhancement in the perinephric space with focal thickening and enhancement of Gerota's fascia, seen to better advantage on the magnified image (C) (*open arrow* in B and *solid arrow* in C).

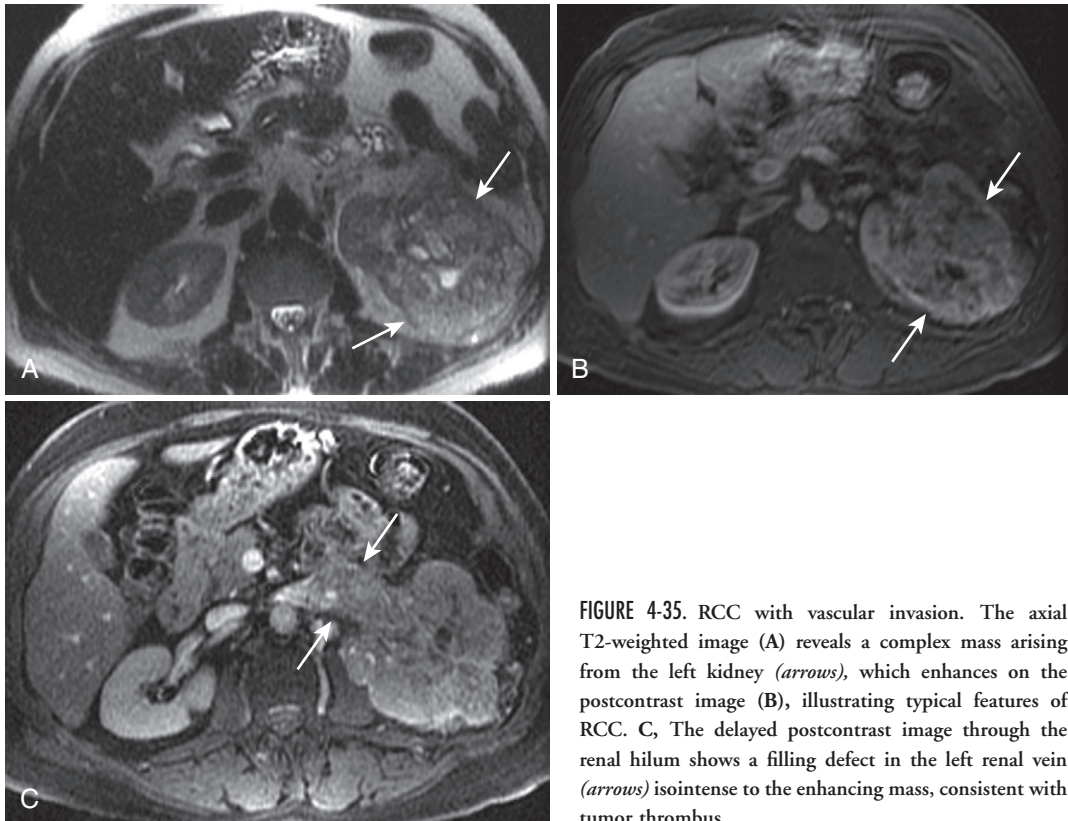


FIGURE 4-35. RCC with vascular invasion. The axial T2-weighted image (A) reveals a complex mass arising from the left kidney (*arrows*), which enhances on the postcontrast image (B), illustrating typical features of RCC. C, The delayed postcontrast image through the renal hilum shows a filling defect in the left renal vein (*arrows*) isointense to the enhancing mass, consistent with tumor thrombus.

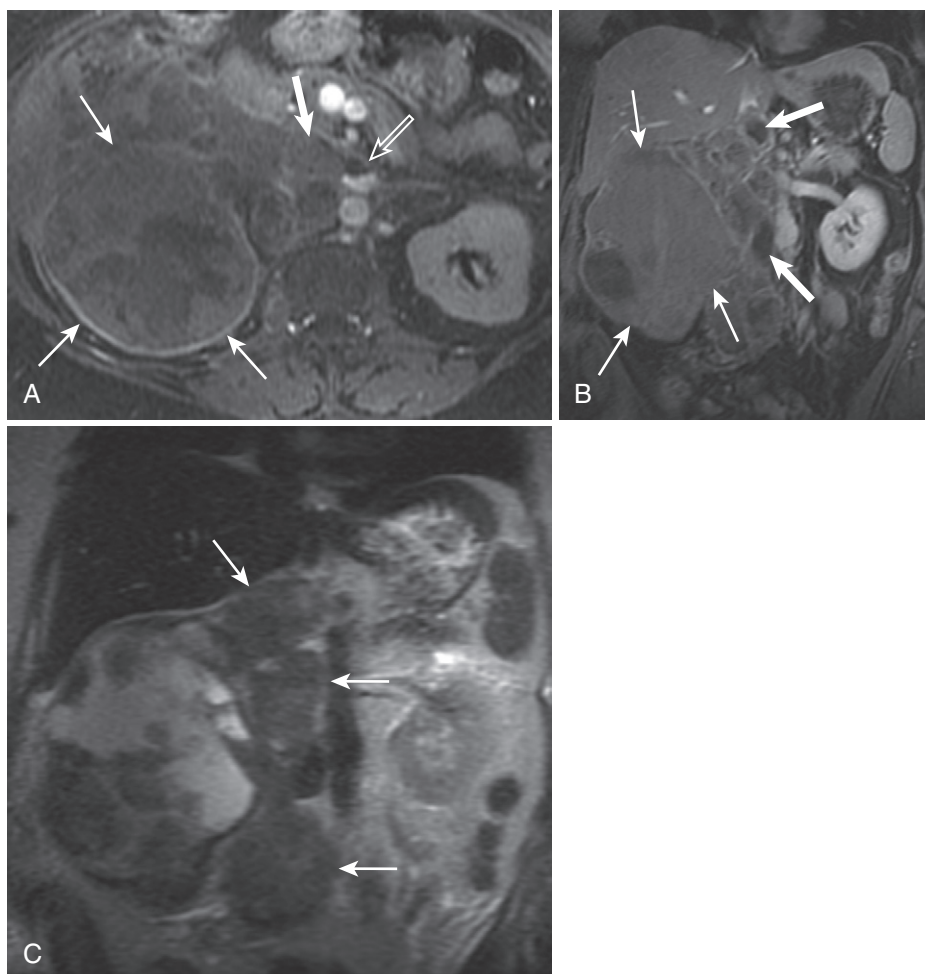


FIGURE 4-36. RCC with tumor and bland thrombus. A, A large complex mass replacing the right kidney (*thin arrows*) on the postcontrast image is associated with enhancing tumor thrombus in the IVC (*thick arrow*) and bland thrombus extending into the left renal vein (*open arrow*). B, The coronal enhanced image shows the large right renal mass (*thin arrows*) with bland thrombus superior and inferior to the renal vein (*thick arrows*). C, The coronal T2-weighted image catalogs the extent of retroperitoneal lymphadenopathy in the right paracaval region (*arrows*).

Lymph node assessment is straightforward, although relatively nonspecific. Although renal lymphatic drainage is variable, most detectable lymphatic metastases are (ipsilateral) para-aortic nodes (see [Fig. 4-36](#)). Heavy reliance on size criteria results in low specificity. Although the generally accepted threshold for normal retroperitoneal nodes is 1.0 cm in short-axis diameter, reactive nodes often exceed this size. Direct invasion and distant spread to adjacent muscles, the adrenal glands, the liver, the contralateral kidney, the pancreas, and osseous structures must be addressed by your search pattern ([Fig. 4-37](#)).

Other subtypes follow different clinical and imaging patterns. The papillary subtype accounts for most of the remainder of RCC cases (see

[Table 4-8](#)). The papillary subtype owes its name to the microscopic papillary growth pattern and not to any macroscopically definable imaging feature. The salient imaging features are the relative hypovascularity and signal characteristics occasionally simulating incidental benign (hemorrhagic or proteinaceous) cystic lesions. Papillary tumoral enhancement is modest; tumoral-to-aortic and/or tumoral-to-parenchymal enhancement of more than 0.25 nearly effectively excludes papillary RCC.²⁹ As previously discussed, precontrast T1 hyperintensity confounds detection of enhancement, which relies on perceiving an increase in signal. An increase in signal from a signal void is much easier to visually appreciate, justifying the use of subtracted images. Relative T2 hypointensity

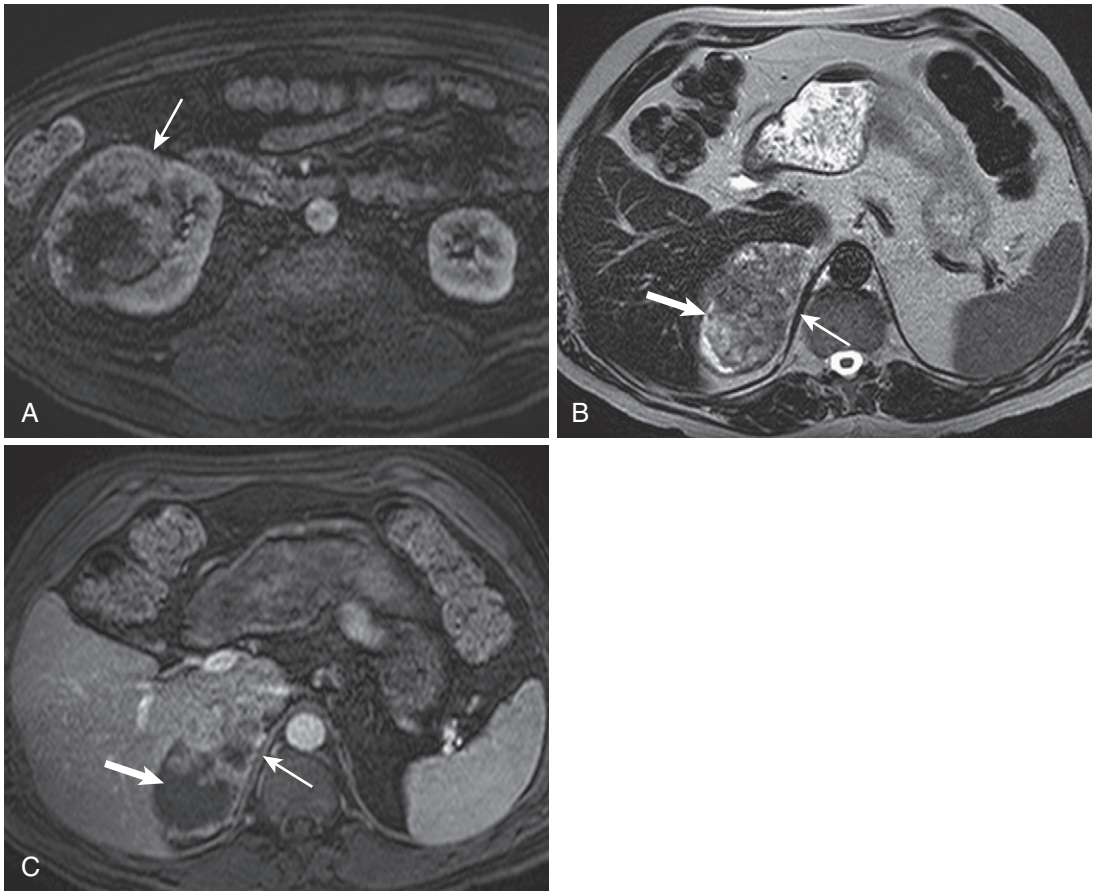


FIGURE 4-37. RCC with spread to other organs. **A**, The postcontrast image reveals a large heterogeneously enhancing mass in the right kidney (*arrow*), typical of a clear cell RCC. T2-weighted (**B**) and postcontrast (**C**) images at the superior extent of the mass (*thin arrow*) show extrarenal extension with neoplastic replacement of the right adrenal gland (*thick arrow*).

likely reflects the byproducts of hemorrhage and/or necrosis (Fig. 4-38). Papillary tumors are generally homogeneous and usually lack microscopic lipid. Although usually sporadic, papillary RCC multifocality and bilaterality suggest an underlying inherited syndrome (see Fig. 4-31), prompting chromosomal analysis. Papillary RCC usually presents at a low stage—70% are intrarenal at diagnosis.

Chromophobe RCC also exhibits fairly nonaggressive biologic behavior and 86% present in stage 1 or 2. The name refers to the fact that the cells fail to stain on histologic analysis. The intercalated cell of the collecting tubule is the postulated cell of origin (also for oncocytoma). Shared ontogeny with oncocytoma is recapitulated in some of the imaging features. The occasional “spoke-wheel” enhancement pattern in chromophobe RCC is the classic oncocytoma enhancement pattern. Chromophobe RCC also shares imaging features with papillary

RCC—relative hypovascularity and T2 hypointensity (Fig. 4-39).

Multilocular cystic RCC technically belongs in the complex cystic section and bears consideration only because it simulates a benign lesion—MLCN. Although the multilocular cystic appearance is generally indistinguishable from MLCN, unlike MLCN, multilocular cystic RCC spares children. Like MLCN, resection confers an excellent prognosis.

Whereas malignant neoplasms of renal cell origin dominate the solid renal lesion category, a number of benign renal neoplasms exist, including lesions of renal cell origin (Fig. 4-40).³⁰ Benign renal cell, or epithelial, neoplasms outnumber other benign renal neoplasms by a wide margin. Although the renal papillary adenoma is exceedingly common—40% of adults over 70 according to autopsy series—very few are recognized on imaging studies. According to the

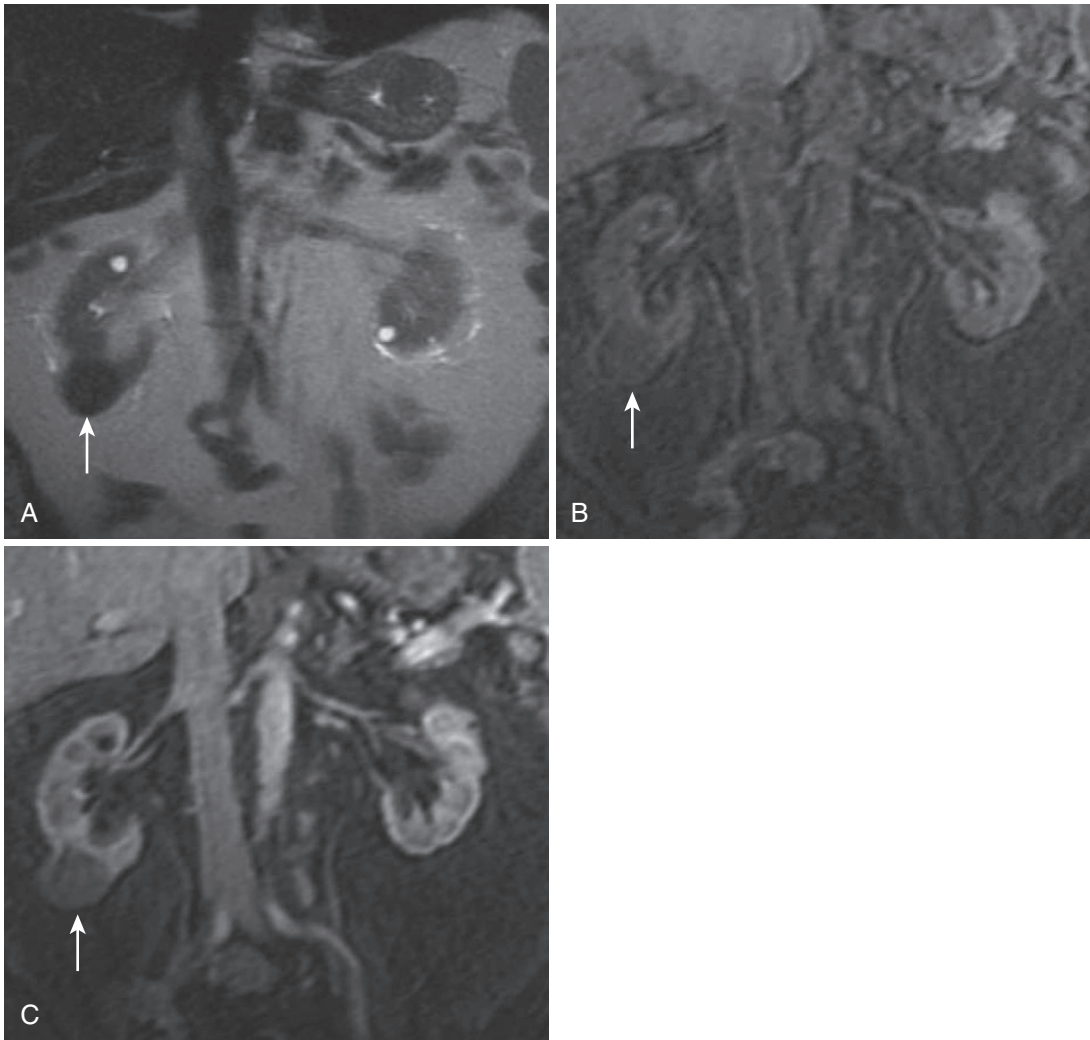


FIGURE 4-38. Papillary RCC with T2 hypointensity. A markedly hypointense lesion (*arrow*) arises from the lower pole of the right kidney on the coronal T2-weighted image (A), which appears to mildly enhance based on mild relative hyperintensity after gadolinium administration from the precontrast (B) to the postcontrast (C) images—typical of papillary RCC.

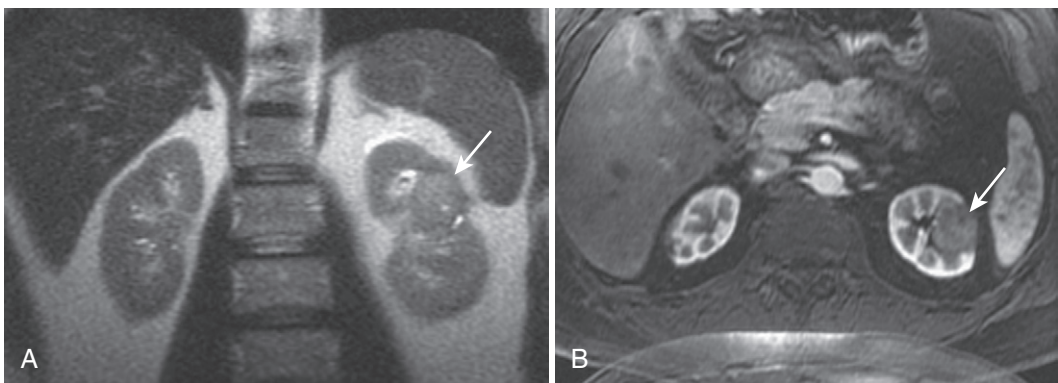


FIGURE 4-39. Chromophobe RCC. A near-isointense lesion in the upper pole of the left kidney (*arrow*) on the T2-weighted image (A) mildly enhances on the postcontrast image (B), simulating a papillary RCC.

Renal Cell tumors	Metanephric tumors	Mesenchymal tumors	Mixed mesenchymal and epithelial tumors
Oncocytoma	Metanephric adenoma	Angiomyolipoma	Cystic nephroma
Papillary adenoma	Metanephric adenofibroma	Leiomyoma	Mixed epithelial and stromal tumor
	Metanephric stromal tumor	Hemangioma	
		Lymphangioma	
		Reninoma	
		Fibroma	
		Schwannoma	

FIGURE 4-40. Benign renal neoplasms. (Based on Eble JN, Sauter G, Epstein JI, Sesterhenn IA, eds. Pathology and Genetics of Tumours of the Urinary and Genital Organs. World Health Organization Classification of Tumours. International Agency for Research on Cancer. 2004;12–43.)

World Health Organization (WHO) classification system, the renal papillary adenoma measures no more than 5 mm, which means that imaging detection and characterization is essentially impossible. Interestingly, malignant transformation pathogenesis theories promote the papillary adenoma as a precursor to RCC.

ONCOCYTOMA

The oncocytoma is a benign neoplasm accounting for 5% of adult primary renal epithelial neoplasms. Occasionally present distinctive imaging features potentially suggest the diagnosis and argue in favor of a partial nephrectomy instead of a radical nephrectomy. A stellate central scar (one third of cases) and “spoke-wheel” enhancement (Fig. 4-41), although not pathognomonic, are specific enough to suggest partial instead of total nephrectomy. Otherwise, the imaging appearance is nonspecific in the form of a relatively homogeneously enhancing, well-demarcated solid cortical mass.

ANGIOMYOLIPOMA

The AML is a benign hamartomatous lesion named for its histologic components—blood vessels (angio-), smooth muscle (-myo-), and adipose tissue (-lipoma). Eighty percent of AMLs occur sporadically and are usually solitary; the remainder arise in the setting of inherited syndromes, such as TS, and are often multiple. (AMLs are present in 80% of patients with TS.) Although AMLs equate with benignity in clinical practice, the rare epithelioid subtype is potentially malignant.

The MRI appearance depends on the relative composition of the three tissue elements. Macroscopic fat diagnosed by signal suppression on spectrally selective sequences (fat-saturated or short tau inversion recovery [STIR]) definitively confirms the diagnosis and precludes further investigation (Fig. 4-42). Solid, usually monotonously enhancing smooth muscle elements cloud diagnostic certainty, especially when present in large quantities at the expense of fat. Avid enhancement of dysplastic vessels reflects the third tissue component—blood vessels. These dysmorphic vessels predispose to aneurysmal dilatation and hemorrhage; large tumor size (>4 cm) and tumoral aneurysms (>5 mm) positively correlate with hemorrhage.³¹ Because of this risk, partial nephrectomy is advocated for lesions over 4 cm in size. Lesions with spontaneous bleeding are treated initially with embolization.

The problem of spontaneous hemorrhage, otherwise known as *Wunderlich's syndrome* (defined as spontaneous extracapsular hemorrhage contained within the perinephric fascia), is diagnostically and therapeutically difficult.³² Management depends to some extent on the underlying etiology, which includes neoplasms (AML and RCC), vascular disease (renal artery aneurysm and vasculitis), and hematologic disorders. Whereas the hemorrhage presents little diagnostic difficulty (see Fig. 4-29)—relying on T1 hyperintensity and absent enhancement—its presence obscures the underlying etiology. Management options range from conservative measures to embolization to emergent

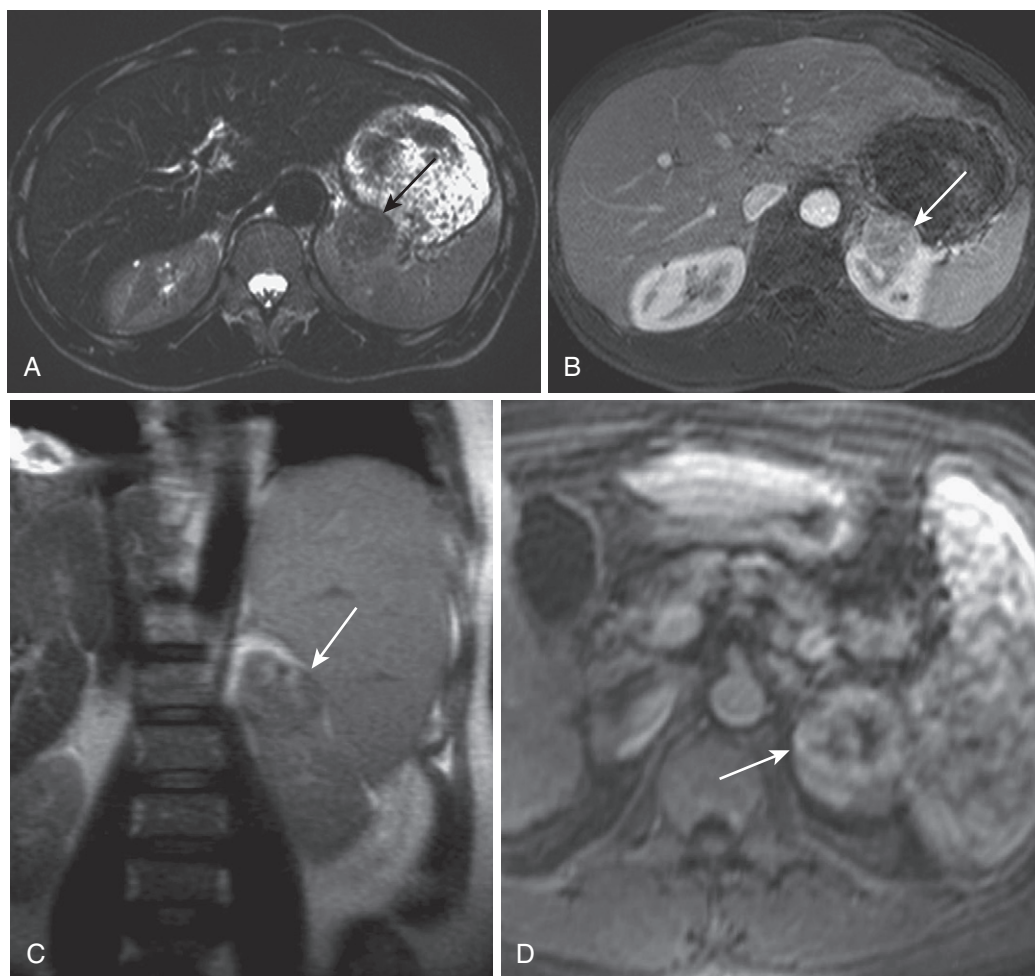


FIGURE 4-41. Oncocytoma. **A**, The axial image shows a lesion arising from the upper pole of the left kidney (*arrow*), which is hypointense relative to the typical T2 appearance of oncocytoma. **B**, The corresponding arterial phase image shows a radiating enhancement pattern (*arrow*), faintly reminiscent of the classic “spoke-wheel” pattern. The coronal T2-weighted image (**C**) in a different patient shows an exophytic lesion (*arrow*), intensely enhancing in a loose “spoke-wheel” fashion on the arterial phase image (**D**).

nephrectomy depending on hemodynamic considerations.

The remaining focal solid renal lesions constitute an array of uncommon primary and malignant lesions—transitional cell carcinoma (TCC), squamous cell carcinoma (SCC), metastases, and lymphoma. Although lacking pathognomonic imaging features, distinctive findings usually prompt diagnostic consideration. These lesions more frequently exhibit the “bean” morphologic growth pattern. Although exhibiting papillary, expansile growth within the collecting system, when involving the renal parenchyma, TCC and SCC always conform to an infiltrative growth pattern. Protean manifestations of lymphoma include three parenchymal patterns: (1)

multiple bilateral renal masses, (2) diffuse infiltration, and (3) solitary mass. Predilection for perinephric and renal sinus involvement results from spread along the lymphatics. Metastases to the kidneys usually simulate metastases in other more commonly affected organs—multiple small randomly scattered bilateral lesions—infiltrative spread is rare.

UROTHELIAL NEOPLASMS

Urothelial neoplasms—TCC and SCC among others—arise from urothelial epithelium extending from the renal collecting system through the bladder. TCC accounts for most (90%), followed by SCC. When arising from the intrarenal collecting system, TCC and SCC infiltrate the renal parenchyma in 25% of cases. Imaging findings

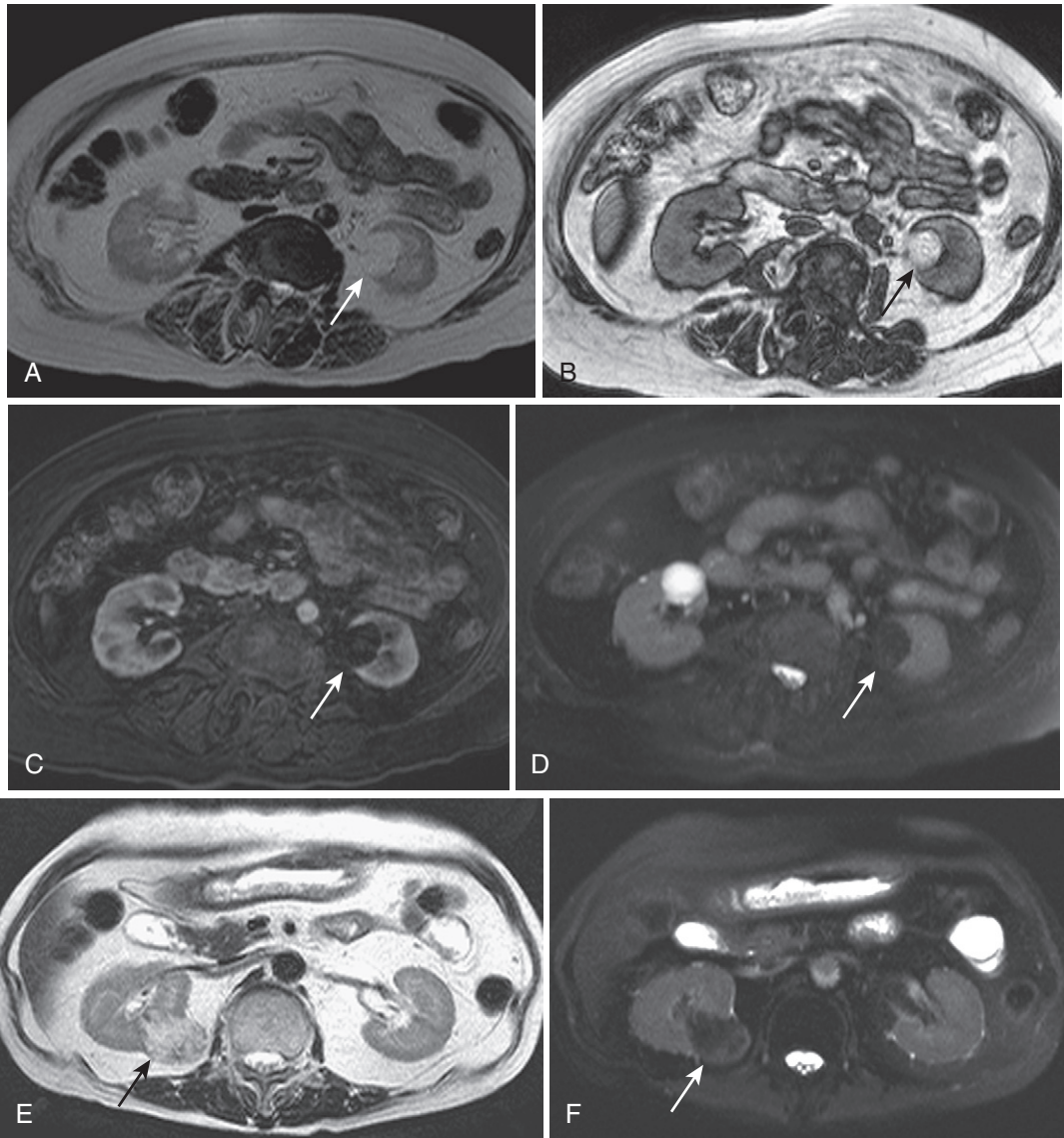


FIGURE 4-42. Macroscopic fat in AML. A partially exophytic lesion in the lower pole of the left kidney (*arrow* in A-D) blends imperceptibly with the retroperitoneal fat on the T2-weighted image (A) and on the out-of-phase image (B)—note the phase cancellation artifact at the interface with the water-rich kidney. Complete loss of signal on the fat-suppressed postcontrast (C) and T2-weighted (D) images confirms macroscopic fat. In a different patient, near isointense T2 signal compared with retroperitoneal fat in an exophytic lesion (*arrow*) extending from the lower pole of the right kidney (E) is suppressed on the corresponding T2-weighted fat-saturated image (F).

when involving the intrarenal collecting system and kidney split into two major categories: primary mass-related findings and secondary collecting system changes (Fig. 4-43). The primary collecting system mass typically grows in a papillary, expansile fashion; invasion of the renal parenchyma follows an infiltrative pattern (Figs. 4-44 and 4-45). Heavily T2-weighted and MRU images identify the primary urothelial mass by depicting the lesion as a filling defect within the

hyperintense lumen of the renal collecting system and/or the associated findings, such as the curvilinear rim of fluid along the proximal margin of the mass, the oncocalyx (abnormally dilated, tumor-distended calyx), phantom or amputated calyx (isolation of a calyx from the collecting system by the invading tumor), and calyceal obliteration (see Fig. 4-45).

Contrast-enhanced images are supplemented by T2-weighted images in detecting the primary

Primary findings	Secondary findings
Sessile, flat or polypoid mass	Phantom calyx
Hypovascular infiltrative mass	Oncocalyx
Intraluminal pelvic mass	Nonfunctioning parenchymal segments
Compression or invasion of renal sinus fat	Curvilinear collecting system rim at tumor margin
	IVC invasion
	Lymphadenopathy
	Stippled contrast within interstices of tumor

FIGURE 4-43. Urothelial neoplastic findings. IVC, inferior vena cava.

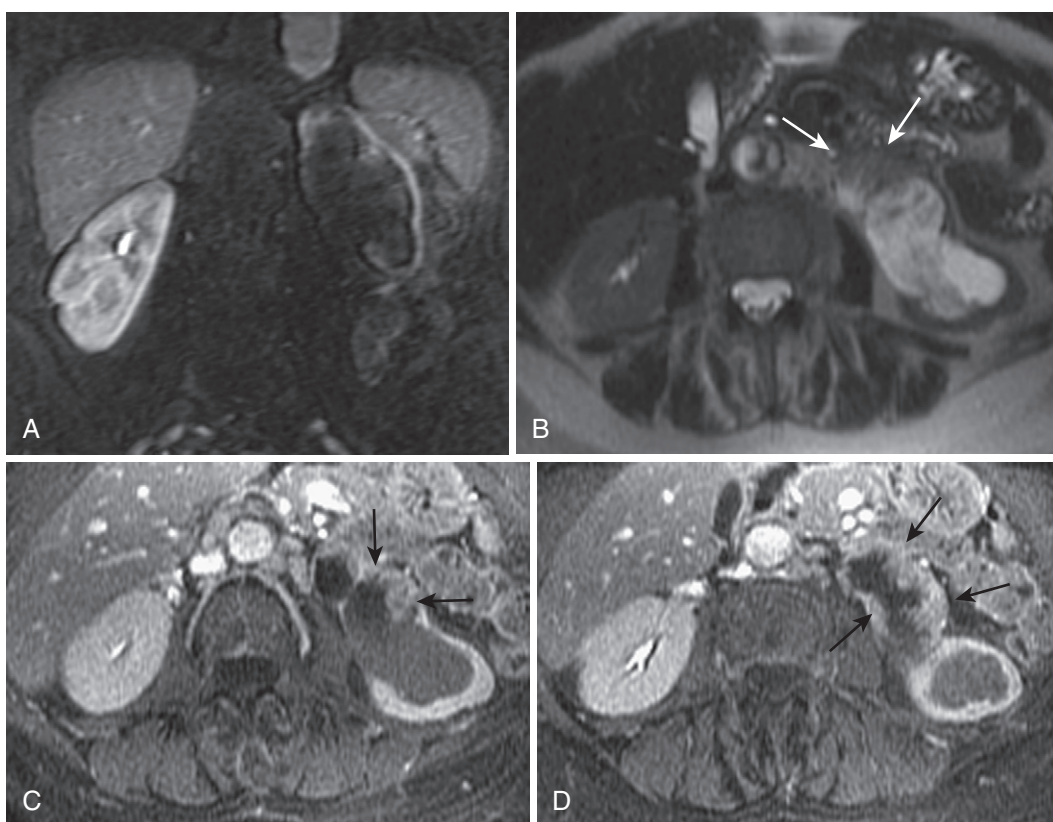


FIGURE 4-44. TCC. A, Severe left-sided hydronephrosis is apparent on the delayed, pyelographic phase postcontrast image due to dilatation of the collecting system with absent enhancement and thinning of the overlying renal parenchyma. B, The axial T2-weighted image suggests the presence of a sessile, mildly hyperintense lesion (*arrows*) arising from the anterior aspect of the renal pelvis, possibly simulated by urinary flow artifact. C and D, Adjacent axial postcontrast images confirm the presence of an enhancing, papillary mass involving the renal pelvis (*arrows*).

tumor and parenchymal invasion. Nonspecific T2 hyperintensity and hypovascularity relative to renal parenchyma are the common denominator urothelial tumor imaging features. Eccentric urothelial thickening and enhancement conform to either sessile, polypoid, or plaque-like morphology. Associated invasion and/or

displacement of renal sinus fat and/or parenchymal invasion ensues. Infiltrative parenchymal infiltration preserves the “bean” shape of the kidney and blends subtly with the surrounding renal parenchyma. Eventual loss of the normal renal parenchymal architecture has been dubbed the “faceless kidney,” with obliteration of the

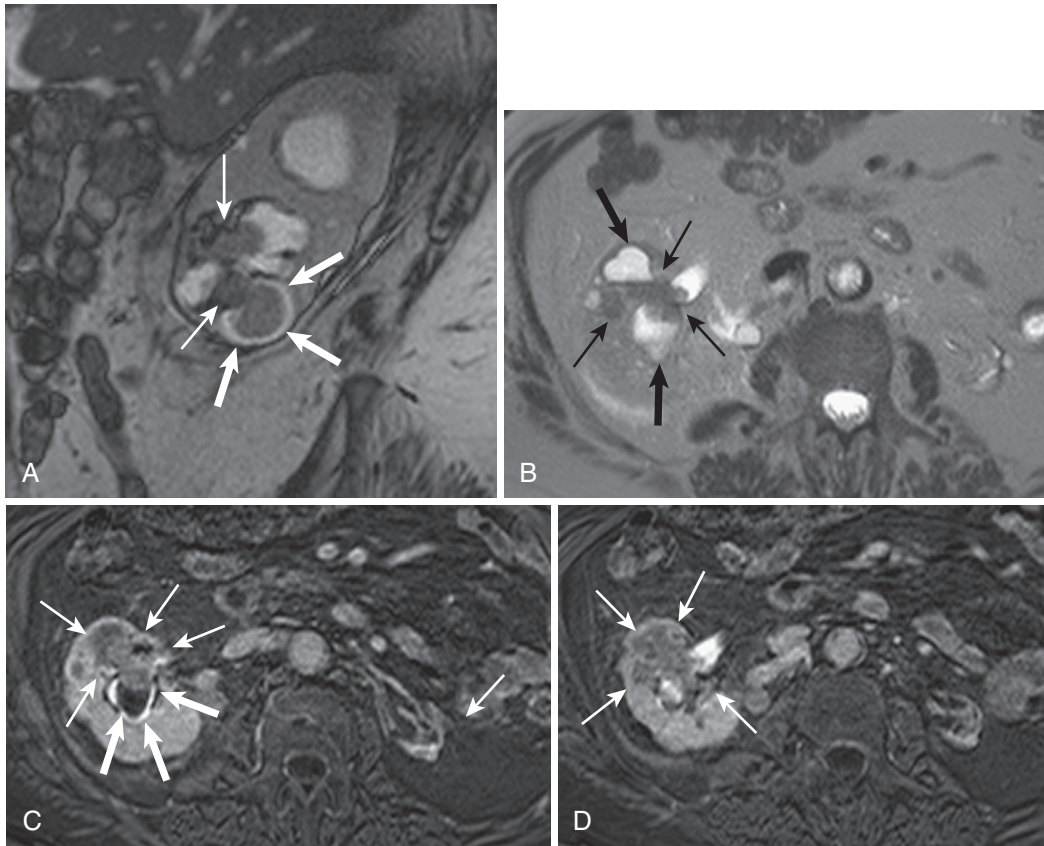


FIGURE 4-45. Calyceal findings of TCC. **A**, The sagittal steady-state image reveals an ill-defined mass (*thin arrows*) surrounded by dilated calyces; a thin rim of fluid hyperintensity (*thick arrows*) encircles tumor protruding into a lower polar calyx. **B**, The axial T2-weighted image portrays the infiltrative intrarenal mass (*thin arrows*) inducing oncocalyces (*thick arrows*). **C** and **D**, The postcontrast pyelographic phase images better depict the infiltrative nature of the hypovascular mass (*thin arrows*), encircled by a thin rim of excreted contrast (*thick arrows* in **C**) in a dilated calyx, which also contains hypointense debris or hemorrhage.

Stage	Findings
Stage 1	Limited to urothelial mucosa and lamina propria
Stage 2	Invasion of pelvic or ureteral muscularis
Stage 3	Invasion beyond muscularis into adventitial fat or renal parenchyma
Stage 4	Distant metastasis

FIGURE 4-46. TCC staging. (Based on Greene FL, Page DL, Fleming ID, eds. Renal pelvis and ureter. In: American Joint Committee on Cancer: AJCC Cancer Staging Manual. 6th ed. New York: Springer, 2002;329–334.)

corticomedullary pattern. TCC spreads locally, invading within or along the inferior vena cava (IVC) and/or along the lymphatics reflected by lymphadenopathy. Because of the high incidence of multifocality (30%–50%) and bilaterality (15%–25%), imaging the entire urothelial axis (collecting system through bladder) is warranted.

Limited data on MRI staging TCC of the upper urinary tract suggests at least moderate success (Fig. 4-46).³³ Staging deficiencies hinge on the potential to miss renal parenchymal invasion. Surgical management entails total nephroureterectomy and bladder cuff excision. Metastatic disease is treated with chemotherapy and/or radiation therapy.

Although TCC is the paradigm infiltrative, or “bean,” mass, other less common lesions generate similar imaging features. Other urothelial tumors, such as SCC, mimic the appearance of TCC and are generally indistinguishable (although TCC accounts for 90% of urothelial tumors). RCC rarely manifests infiltrative growth pattern. Rare subtypes, including collecting duct and medullary RCCs, exhibit infiltrative growth. Both of these lesions arise from the renal parenchyma centrally and grow into the renal sinus and collecting system (the opposite progression of TCC). Both of these lesions follow an aggressive clinical course; renal medullary carcinoma is distinguished by its unique association with sickle cell trait and usually afflicts patients younger than 40 years old. Secondary tumors also mimic the infiltrative appearance of TCC, including lymphoma and metastases. Relative homogeneity of the primary mass(es) and disproportionately enlarged lymph nodes characterize lymphoma. Extrarenal tumors that metastasize to the kidneys include lung, breast, and gastrointestinal malignancies

and melanoma. The propensity for multifocality and bilaterality and the association with a primary tumor usually seal the diagnosis. The imaging appearance of nonneoplastic etiologies, such as pyelonephritis, infarction, and papillary necrosis, also overlaps with the infiltrative pattern of TCC. The clinical scenario hopefully suggests these lesions, which fail to progress on follow-up imaging (and are discussed in greater detail).

RENAL LYMPHOMA

Although detected commonly postmortem (approximately half of lymphoma patients), renal lymphoma is rarely seen on imaging studies (<10% of patients). Renal involvement more frequently occurs in (B-cell) non-Hodgkin’s lymphoma and usually indicates widely disseminated disease and a poor prognosis. As previously mentioned, renal lymphoma presents three growth patterns: (1) multiple bilateral renal masses, (2) diffuse infiltration, and (3) solitary mass (Fig. 4-47). The renal parenchyma lacks lymphoid tissue, and the pathogenesis of

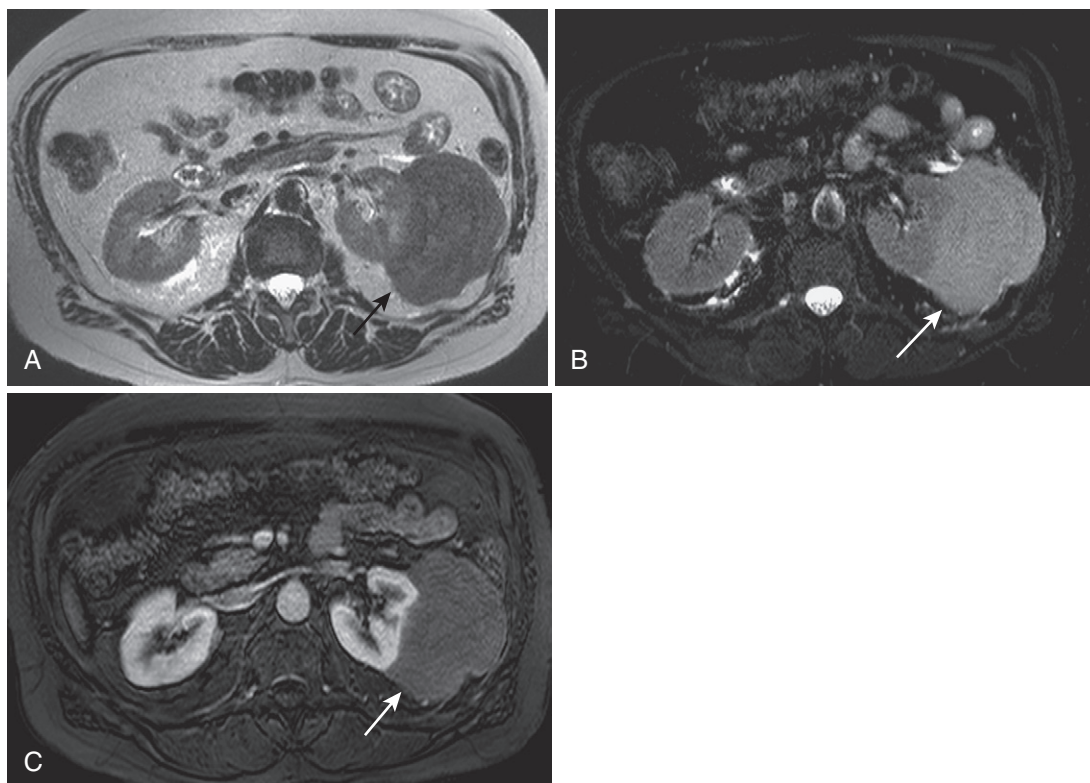


FIGURE 4-47. Renal lymphoma. A, The axial T2-weighted image reveals a large left-sided lesion (*arrow*) that exhibits multiple features typical of lymphoma: (1) T2 hypointensity, (2) involvement of the perinephric space, and (3) lack of necrosis despite large size. B, Note the relative hyperintensity (*arrow*) on the fat-suppressed T2-weighted image, benefiting from increased dynamic range. C, The early postcontrast image shows characteristic minimal enhancement (*arrow*).

development of renal lymphoma has not been elucidated. The frequent bilateral involvement (50%) and multifocality of parenchymal masses conjure hematogenous spread. The lymphatic origin is illustrated by the propensity to involve the renal sinus and perinephric space where the lymphatics reside.

Lymphomatous masses tend to be monotonously homogeneously nearly isointense on T1-weighted and T2-weighted images with modest homogeneous enhancement, even when large (in contradistinction to RCC, which typically undergoes necrosis with increasing size). Another characteristically unique feature is the relative lack of mass effect on adjacent structures. To summarize, a number of unique features distinguish lymphoma from RCC and other solid lesions, such as homogeneity, lack of necrosis, lack of mass effect, central/medullary involvement and/or centering outside the renal contour, lack of vascular invasion, massive lymphadenopathy, and bilaterality/multifocality.

RENAL METASTASES

Renal metastases usually occur in the setting of widespread, end-stage disease from primary melanoma or breast, lung, or gastrointestinal malignancies. Unlike lymphoma, metastases arise within the renal parenchyma, rarely deforming the renal contour. Most metastatic lesions enhance minimally—hypervascular melanoma is the notable exception.

Segmental/Diffuse Lesions

Segmental and diffuse lesions include mostly nonneoplastic etiologies—some previously discussed neoplastic lesions straddle the line between solid/focal and segmental or diffuse, such as TCC and lymphoma (Fig. 4-48).

Segmental and diffuse lesions generally respect the “bean” pattern, altering the renal signal intensity and/or enhancement pattern rather than the renal morphology. Whether segmental or diffuse, detection relies on comparison with normal renal tissue. Segmental lesions deviate in signal and/or enhancement from adjacent parenchyma; diffuse lesions (unless bilateral) deviate in signal and/or enhancement from the contralateral kidney. The degree of renal involvement, ranging from segmental to diffuse to bilateral, hints at the diagnosis. Segmental lesions include mainly neoplasms, infarcts (i.e., embolic and vasculitic etiologies), pyelonephritis, and traumatic injury. Diffuse lesions include vascular lesions—such as RVT and renal artery stenosis (RAS)—and xanthogranulomatous pyelonephritis (XGP). Bilateral lesions include intravascular hemolysis, human immunodeficiency virus (HIV) nephropathy, and medical renal disease.

Whereas previously discussed neoplasms—such as TCC, SCC, RCC medullary type, and lymphoma—occasionally manifest with segmental imaging features, ill-defined margins, some degree of mass effect, and/or a superimposed discrete mass distinguish these lesions from nonneoplastic segmental lesions. The other segmental lesions—pyelonephritis, renal infarct, and renal trauma—often include sharply marginated triangular lesions pointing to the renal hilum. Associated imaging and clinical features help suggest the diagnosis.

PYELONEPHRITIS

Pyelonephritis—ascending infection of the renal pelvis, tubules, and surrounding interstitium—reiterates the pyramidal morphology of the collecting system unit (Fig. 4-49). Actually, although pyelonephritis spreads segmentally along the collecting system scaffolding accounting for

Infectious	Vascular	Neoplastic
Pyelonephritis	Renal vein thrombosis	Transitional cell
Xanthogranulomatous pyelonephritis	Renal artery stenosis	Lymphoma
HIV nephropathy	Renal infarction	Renal medullary
	Intravascular hemolysis	

Usually segmental
Usually diffuse (unilateral)
Usually bilateral

FIGURE 4-48. Segmental and diffuse lesions. HIV, human immunodeficiency virus.

segmental features, diffuse involvement often eventually ensues. Three basic patterns typify acute pyelonephritis: (1) hypoperfused, edematous segment(s), (2) diffusely edematous, hypoperfused enlargement, and (3) the striated nephrogram appearance. Wedge-shaped T2 hyperintense segments with decreased

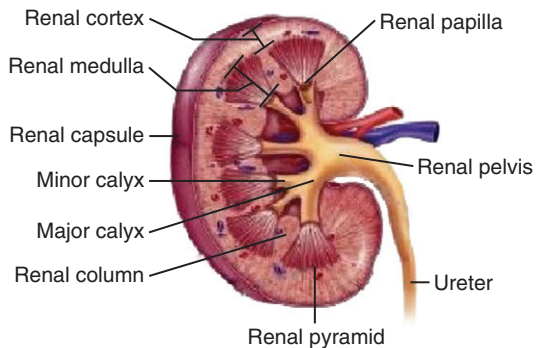


FIGURE 4-49. Anatomy of the renal collecting system.

enhancement radiating from the papillary tip to the peripheral cortex reflect poorly functioning tissue with interstitial edema, vasospasm, and tubular obstruction (Fig. 4-50).³⁵ The striated nephrogram appearance of alternating parallel enhancing and nonenhancing bands of renal parenchyma arranged centripetally toward the renal hilum represent intermingled normal and obstructed tubules, respectively. Diffuse involvement results in renal enlargement, hyperintensity, and decreased perfusion. Secondary findings include infiltration of the perinephric fat, perinephric fluid, and thickening and enhancement of the ipsilateral urothelial collecting system wall (see Fig. 4-50).

In the setting of renal infection, pyonephrosis and pyogenic abscess are the feared complications. Ongoing liquefaction without adequate treatment leads to pyogenic abscess, potentially necessitating percutaneous drainage (in addition to antibiotic treatment). Pyonephrosis

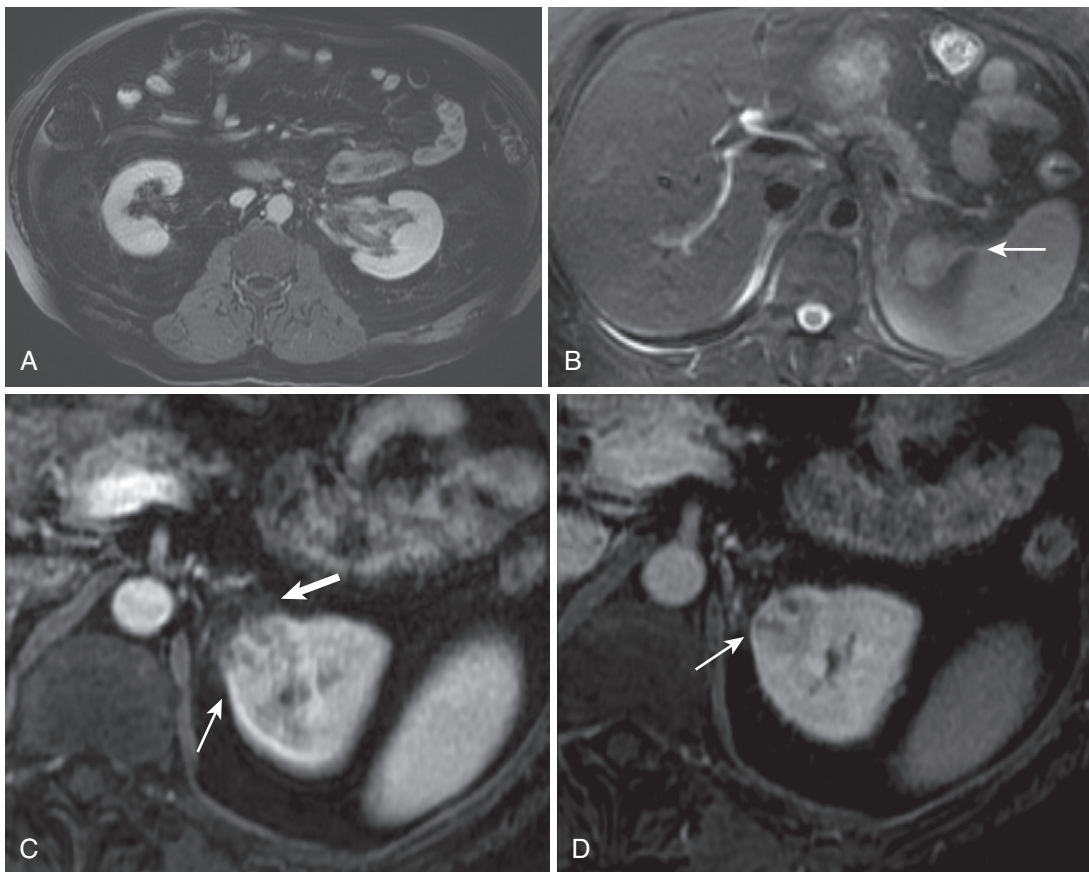


FIGURE 4-50. Acute pyelonephritis. The axial postcontrast image (A) shows infiltration of the left renal sinus fat and urothelial thickening and enhancement. The fat-suppressed T2-weighted image through the upper pole of the left kidney (B) shows perinephric edema (*arrow*). The early (C) and delayed (D) postcontrast images show an evolving pyogenic abscess (*thin arrow*) with perinephric inflammation (*thick arrow* in C) and dilated tubules with the striated nephrogram appearance.

signifies obstruction plus infection and necessitates prompt intervention because of the potential for rapid clinical deterioration, shock, and irreversible kidney damage. Pyonephrosis develops from either infection of an obstructed kidney or suppurative impaction inducing obstruction and hydronephrosis. In addition to findings of pyelonephritis, findings suggesting pyonephrosis include obstruction, collecting system fluid complexity with debris and fluid-fluid levels, and urothelial thickening and enhancement.

RENAL INFARCT

Renal infarcts are usually embolic and rigidly observe segmental morphology as a function of renal arterial anatomy (Fig. 4-51). The wedge-shaped region(s) of decreased enhancement, representing the renal tissue deprived of blood flow subtending the occluded renal artery branch, mimics hypoperfused segments in pyelonephritis with sharper linear margins (Fig. 4-52). Findings that favor infarction over infection include (1) absence of the striated nephrogram, (2) secondary findings (perinephric

infiltration and fluid and urothelial thickening and enhancement), and (3) clinical signs of infection. The “cortical rim” sign of preserved capsular/subcapsular enhancement overlying hypoperfused parenchyma reliably indicates

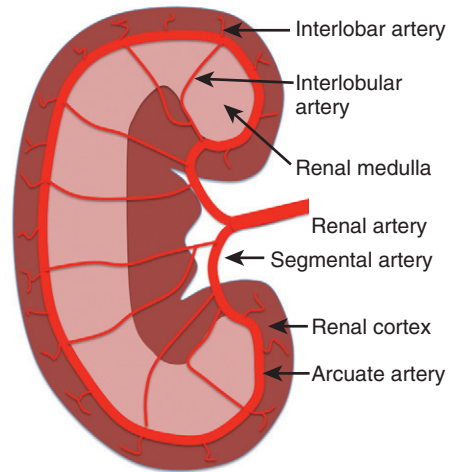


FIGURE 4-51. Renal arterial anatomy. (From Fox SI. Human Physiology, 6th ed. New York: William C. Brown, 1998:529.)

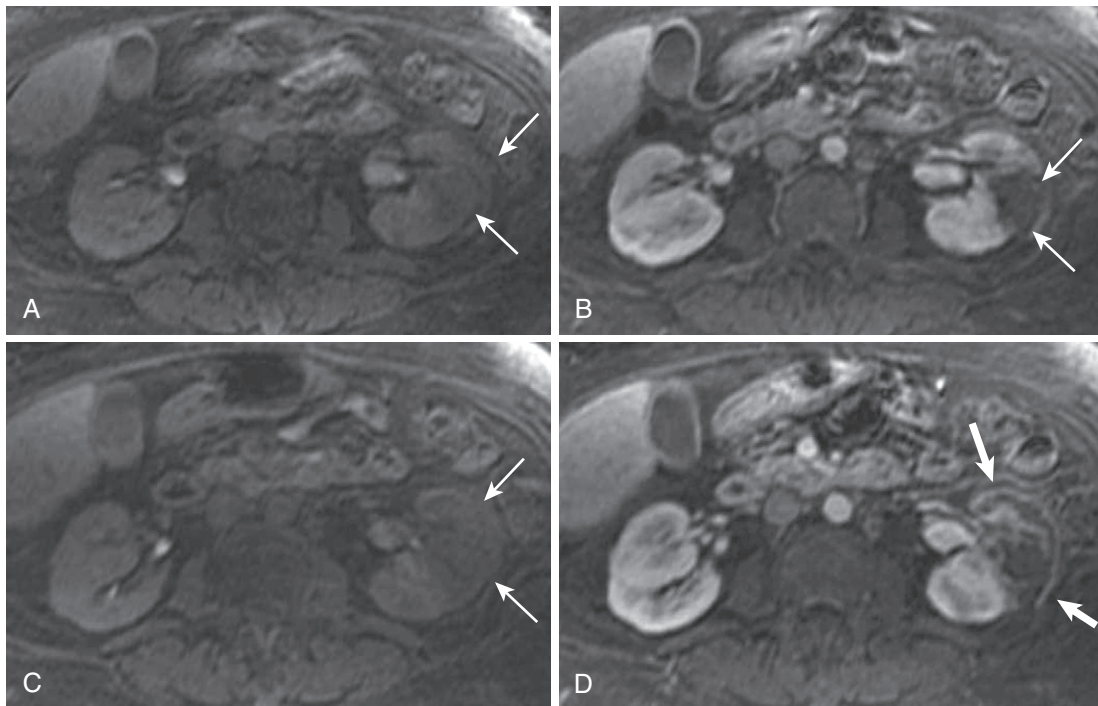


FIGURE 4-52. Renal infarct. The precontrast T1-weighted image (A) shows a sharply demarcated wedge-shaped lesion in the anterior interpoler aspect of the left kidney (arrows), clearly delineated by adjacent enhancing renal tissue on the postcontrast image (B) due to the lack of enhancement. Similar features (thin arrows in C) on adjacent sections (precontrast [C] and postcontrast [D]) with the cortical rim sign on the enhanced image (thick arrows in D).

TABLE 4-9. Diffuse Unilateral Renal Disorders

Unilaterally Small
Chronic renal artery stenosis
Chronic renal venous thrombosis
Renal hypoplasia
Longstanding subcapsular collection
Longstanding obstructive uropathy
Unilaterally Enlarged
Acute renal vein thrombosis
Acute renal artery occlusion
Acute obstructive uropathy
Pyelonephritis
Infiltrative neoplasms
Xanthogranulomatous pyelonephritis

ischemia over infarction and other etiologies (see Fig. 4-52). The cortical rim sign reflects patent collateral circulation and develops 6 to 8 hours after onset.

In addition to embolism, etiologies of ischemia include vasculitis and renal trauma. Bilateral diffuse involvement and arterial microaneurysms characterize vasculitis (i.e., systemic lupus erythematosus and polyarteritis nodosa) and effectively exclude isolated embolic infarcts. Blunt trauma usually fails to respect anatomic boundaries, resulting in irregular linear or segmental devitalized renal tissue with or without parenchymal disruption or subcapsular or perinephric hematoma.

Diffuse unilateral renal disorders separate into two major categories: unilaterally small kidney and unilaterally enlarged kidney (Table 4-9). In routine clinical practice, chronic RAS accounts for most cases of unilaterally small kidney.

CHRONIC RENAL ARTERY STENOSIS

Chronic RAS results in a unilaterally globally atrophic kidney (as opposed to segmental infarction—previously discussed—resulting in focal atrophy). Other causes of a unilateral small kidney include chronic RVT, renal hypoplasia, longstanding subcapsular hematoma (Page's kidney), and postobstructive uropathy. Delayed nephrographic and urographic phases in chronic RAS are nonspecific—seen in other etiologies of unilaterally small kidney, such as obstruction and RVT (Fig. 4-53), except for renal hypoplasia. Although best visualized on a dedicated angiographic study, direct visualization of the arterial stenosis excludes other etiologies of unilateral

small kidney. Except for RVT, other etiologies distinguish themselves through other easily discernible primary imaging features: hydronephrosis (postobstructive uropathy), normal signal and enhancement characteristics (renal hypoplasia), and subcapsular collection (Page's kidney). Except for the primary renal versus arterial lesion, no imaging features distinguish chronic RVT from RAS.

RENAL VEIN THROMBOSIS

Acutely, both RVT (more common) and renal artery occlusion enlarge the kidney as a consequence of diffuse parenchymal edema (and the appearance potentially simulates diffuse pyelonephritis). Other etiologies of unilateral renal enlargement result from acute obstructive uropathy and infiltrative processes, such as pyelonephritis, infiltrating neoplasm, and XGP. The renal venous filling defect is best visualized on delayed contrast-enhanced images and steady-state images (Fig. 4-54), usually accompanying edematous renal enlargement and other nonspecific findings, including delayed nephrographic and pyelographic phases. When suspected, RVT benefits from targeted MRV technique, sharing parameters with renal magnetic resonance angiography (MRA)—higher dose of gadolinium, higher flip angle, and thinner slices—and including focused steady-state images targeted to the renal veins.

Nonvascular etiologies of unilaterally enlarged kidney show their colors by directly altering the renal parenchymal and/or collecting system appearance. Hydronephrosis indicates obstructive uropathy; signal and enhancement derangement attend infiltrative neoplasms and inflammatory etiologies, such as pyelonephritis and XGP. XGP represents chronic renal parenchymal inflammation usually by *Proteus* or *Escherichia coli* in patients with renal calculi. Lipid-laden macrophages replace normal renal parenchyma, leading to grossly reniform non-functioning renal enlargement.³⁶ The classic XGP triad includes (1) nephrolithiasis, (2) renal enlargement, and (3) diminished or absent function. Visible fat accumulation increases diagnostic confidence, although other lesions, such as RCC and AML, also contain fat.³⁷ “The fractured stone” sign is another unique XGP finding historically described as a CT finding, not practically transferable to MRI, given the relative insensitivity of renal calculi.

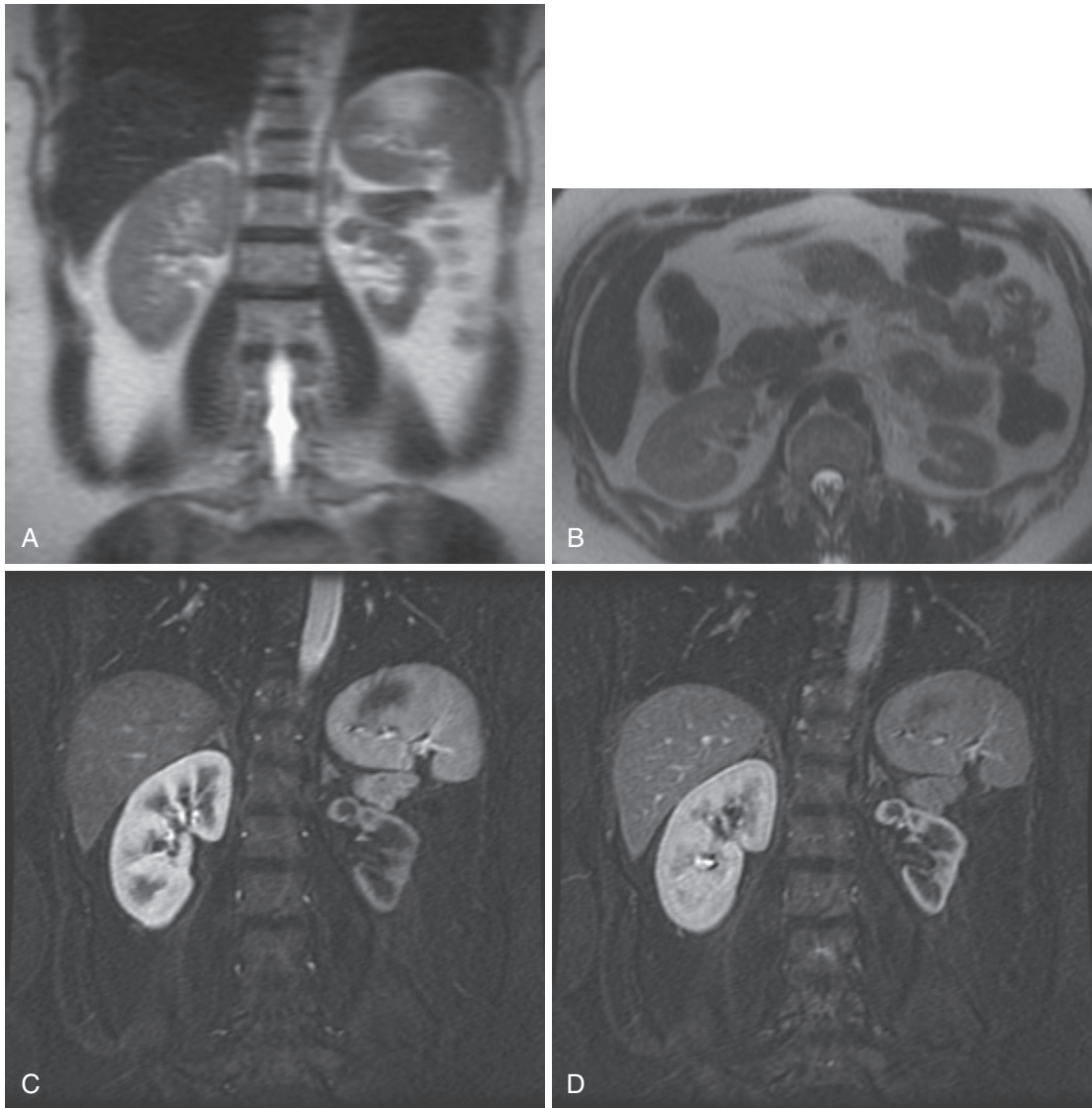


FIGURE 4-53. Renal artery stenosis. The coronal (A) and axial (B) T2-weighted images reveal marked asymmetrical left-sided renal atrophy and lack of corticomedullary differentiation. Early (C) and delayed (D) postcontrast coronal images show a corresponding delayed left-sided nephrographic phase compared with the normal right kidney.

Diffuse bilateral renal disorders include a long list of diseases rarely seen on MR images (Table 4-10). These lesions divide into generic “medical renal disease,” diffuse infiltrative neoplastic etiologies, and signal-based diseases. Bilateral renal disorders under the medical renal disease umbrella are associated with renal insufficiency by definition with variably sized kidneys. The etiology is rarely forthcoming at MRI and usually evades diagnosis in routine clinical practice.

Diffuse bilateral diseases inducing signal derangement feature exclusive, distinctive MRI findings. Although rare, these lesions are worth discussing because of the ability to render

TABLE 4-10. Diffuse Bilateral Renal Disorders

Diabetic nephropathy
Acute glomerulonephritis
Collagen vascular diseases
AIDS nephropathy
Lymphoma/leukemia
Acute interstitial nephritis
Hemoglobinopathy
Acromegaly
Acute urate nephropathy
Amyloidosis
Fabry's disease
Von Gierke's disease
Intravascular hemolysis

AIDS, acquired immunodeficiency syndrome.

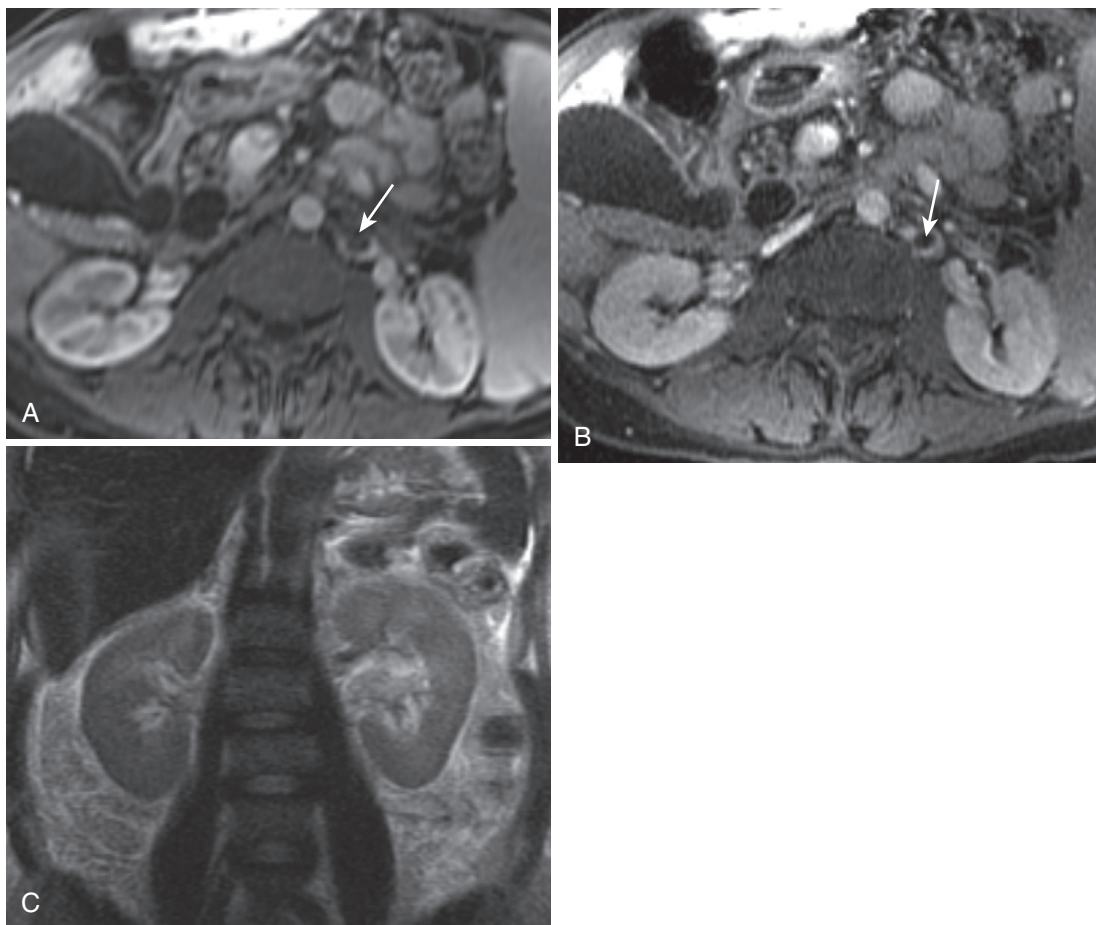


FIGURE 4-54. Renal vein thrombosis. The early (A) and delayed (B) postcontrast images demonstrate an at least nearly complete occlusive filling defect in the left renal vein (*arrow*). The coronal T2-weighted image (C) shows subtle left renal enlargement.

specific diagnoses. Parenchymal signal disorders are synonymous with parenchymal T2 hypointensity, for the most part, and the vast majority arises from hemorrhagic etiologies.³⁸ Hemolytic etiologies—paroxysmal nocturnal hemoglobinuria (PNH), mechanical hemolysis, and sickle cell disease (SCD)—dominate this category. Other rare etiologies include hemorrhagic fever with renal syndrome (HFRS) and vascular etiologies (often not bilateral), such as acute cortical necrosis, acute RVT, and arterial ischemia and infarction. PNH results from an acquired sensitivity to complement, ultimately inducing intravascular hemolysis. Mechanical hemolysis—exemplified by malfunctioning prosthetic cardiac valves—generates an identical imaging appearance with marked hypointensity restricted to the cortex (Fig. 4-55). Hypointensity is most dramatically apparent on T2-weighted images and gradient-echo sequences (see Fig. 4-55), owing to the sensitivity to susceptibility artifact.

Although the renal findings in etiologies of intravascular hemolysis are identical, splenic hypointensity implicates SCD. Few, if any, disorders simulate this appearance. Whereas other disorders, such as acute hemorrhage from trauma, amyloidosis, or acute cortical necrosis, potentially mimic the MR appearance of intravascular hemolysis, the pattern of involvement and clinical features differ.

ADRENAL GLANDS

Normal Features

The adrenal glands are Y-shaped structures inhabiting the superior extent of the retroperitoneum. The adrenal body measures approximately 10 to 12 mm in length and the medial and lateral limb measures 5 to 6 mm.^{39,40} As a general rule of thumb, adrenal limbs measure 5 mm or less in thickness.⁴¹ The right adrenal

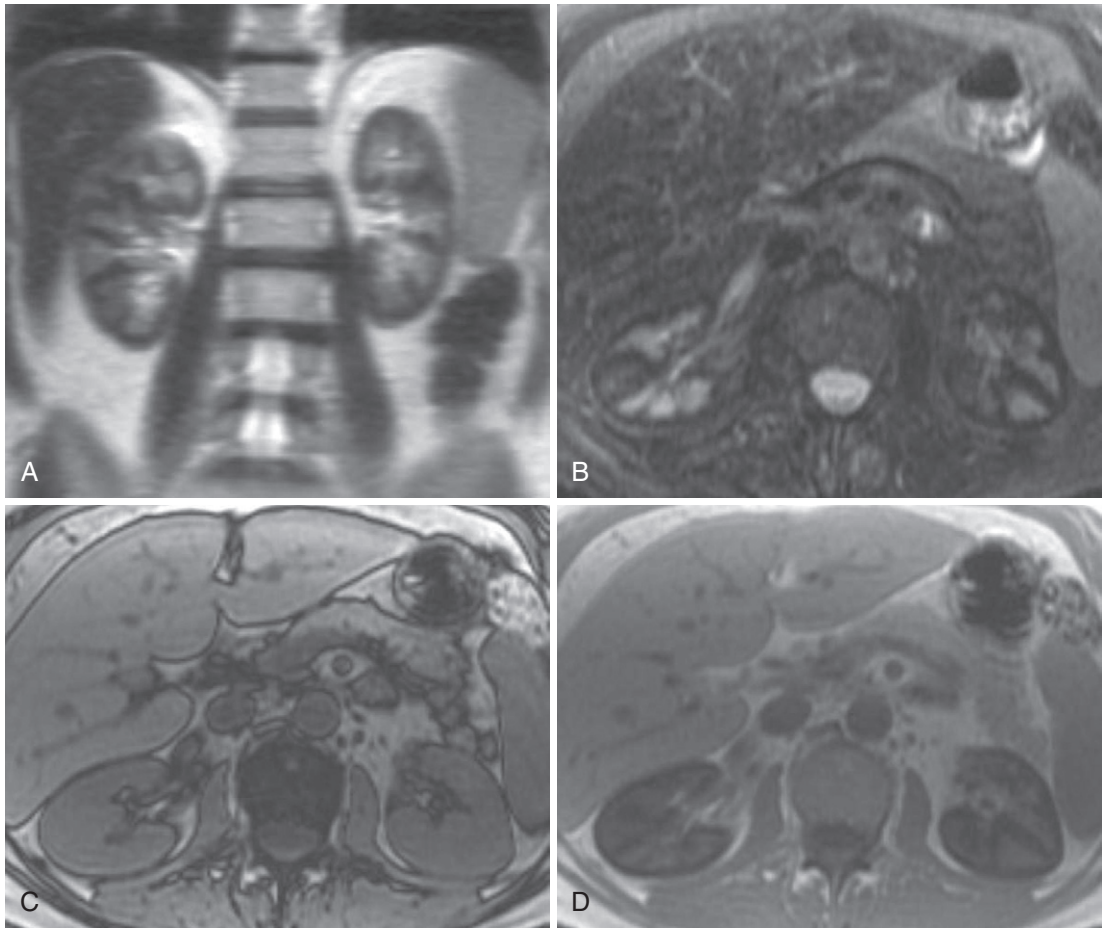


FIGURE 4-55. Mechanical hemolysis. Coronal T2-weighted (A) and axial T2-weighted fat-suppressed (B) images reveal marked hypointensity restricted to the renal cortex, not apparent on the out-of-phase image (C). D, Pronounced cortical signal loss on the in-phase image connotes susceptibility artifact due to hemosiderin deposition.

gland sits 1 to 2 cm above the upper pole of the right kidney, and the left adrenal gland rests ventral to the upper pole of the left kidney). Adrenal gland dimensions vary, precluding the use of specific normal size criteria. Dual parallel adrenal embryology explains adrenal microanatomy and physiology, imaging appearance, and the spectrum of adrenal lesions. The outer cortex develops from coelomic mesoderm and accounts for most of the bulk of adrenal tissue, responsible for synthesizing cholesterol-derived hormones—glucocorticoids and mineralocorticoids. The cholesterol compounds constituting the building blocks of the adrenal hormones account for the loss of signal on out-of-phase images. The inner adrenal medulla derives from neural crest cells and produces catecholamines—mostly epinephrine.

Adrenal lesion differential diagnosis hinges on cystic (or nonsolid because hemorrhage is included in this category) versus solid tissue composition (Fig. 4-56). Lack of enhancement versus enhancement classifies adrenal lesions into the respective categories. With the exception of hemorrhage, nonsolid etiologies exhibit nonspecific free water imaging features. Solid lesion tissue composition often demonstrates specific imaging features suggesting the underlying diagnosis. Microscopic fat connotes adenoma, and macroscopic fat equals myelolipoma. High fluid content and hypervascularity explain the T2 hyperintensity and avid enhancement of pheochromocytoma, respectively. Other solid lesions, such as lipid-poor adenoma, metastasis, and adrenal cortical carcinoma are less specific.

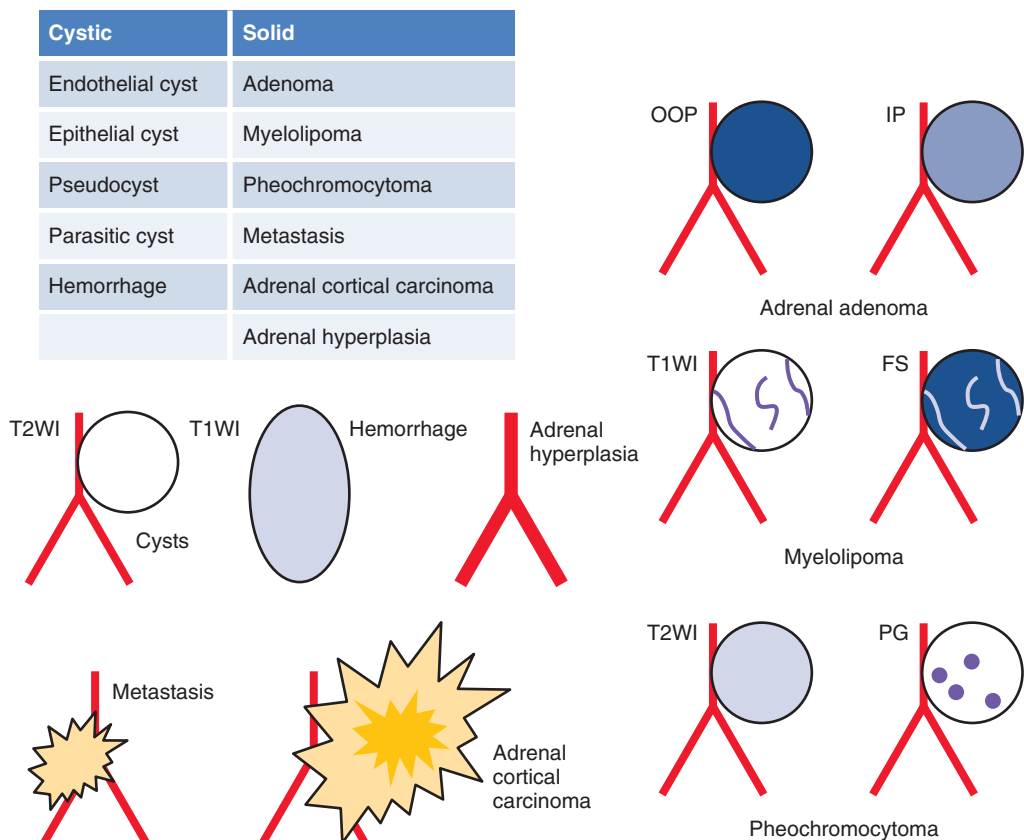


FIGURE 4-56. Adrenal differential diagnosis. FS, fast spin-echo; IP, in-phase; OOP, out-of-phase; PG, postgadolinium.

Unilateral	Bilaterals
Blunt trauma	Stress
Liver transplant (right-sided)	Hemorrhagic diatheses
Primary or metastatic tumors	Thromboembolic disease
Uncomplicated pregnancy	Complicated pregnancy
Spontaneous/idiopathic	Meningococcal septicemia

FIGURE 4-57. Differential diagnosis of adrenal hemorrhage.

Cystic (Nonsolid) Lesions

Adrenal cystic lesions are rare, with an incidence of less than 1%.⁴² Adrenal cystic lesions divide into two main categories: (1) true endothelial (lymphatic—lymphangiomatous and vascular—hemangiomas) and epithelial cysts (40%–45%) and (2) pseudocysts (40%)—usually represents the sequela of previous hemorrhage but also includes infectious (parasitic) cysts and other rare cystic lesions. Hemorrhage constitutes a third nonsolid category (although metastases are included in the differential diagnosis of adrenal hemorrhage, technically belying the term *nonsolid*) (Fig. 4-57).

ADRENAL CYSTS

Adrenal cystic lesions are almost always asymptomatic and virtually always detected incidentally on imaging studies. Symptoms manifest only with large size through mass effect on adjacent organs. Nonspecific imaging features usually fail to discriminate among the different cystic types.⁴³ Most lesions share features of typical cysts, with internal free water signal with absent central enhancement and a thin or imperceptible wall (Fig. 4-58). Internal contents in pseudocysts from previous hemorrhage exhibit a greater degree of heterogeneity (see Fig. 4-58).

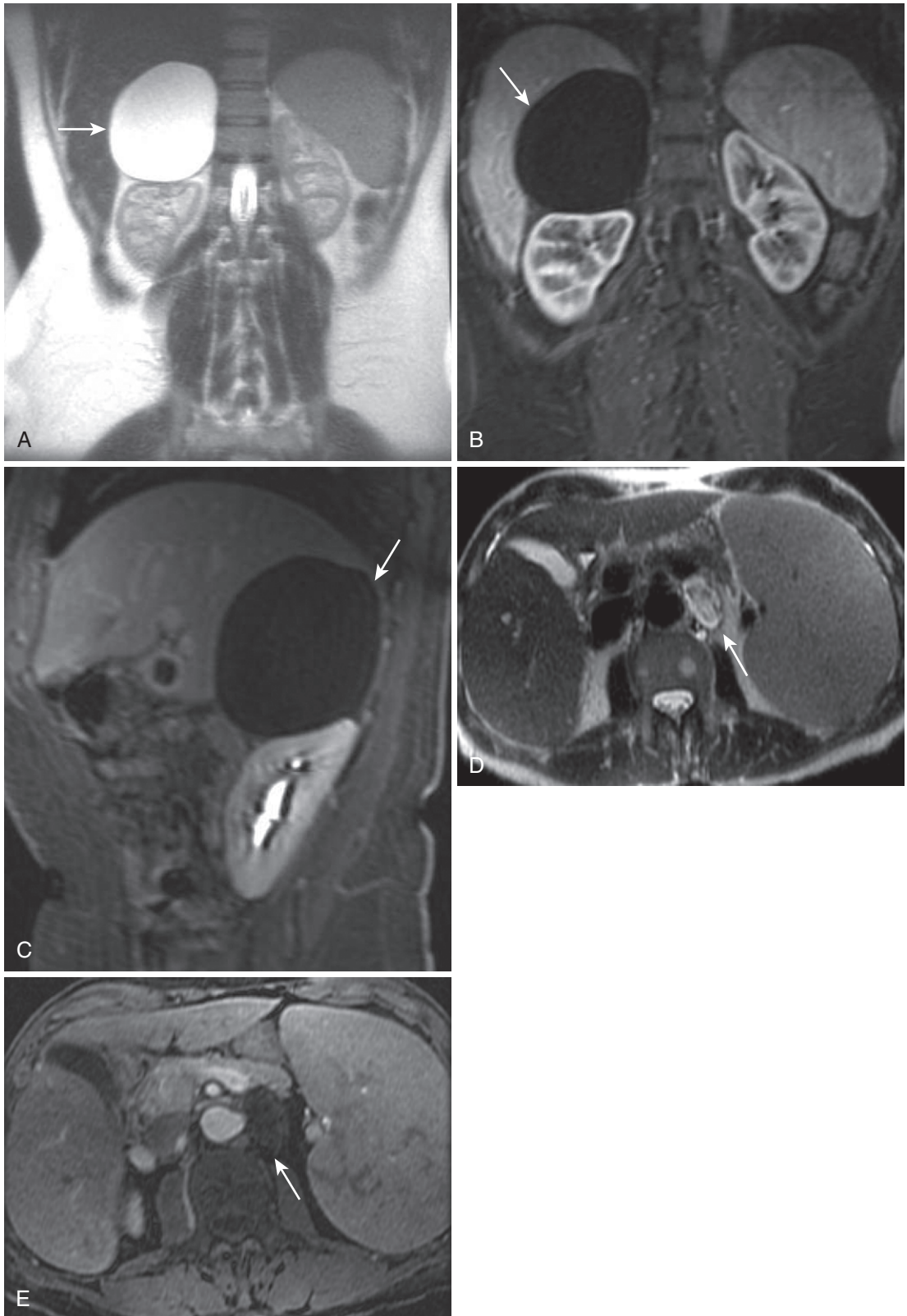


FIGURE 4-58. Adrenal cyst. Coronal T2-weighted (A) and enhanced (B) images show a right-sided true adrenal cyst (*arrow*) with simple cystic features. C, The sagittal postcontrast image confirms the extrarenal origin with reciprocally convex margins (*arrow*). A more complex left-sided adrenal pseudocyst (*arrow* in D and E) in a different patient demonstrates internal complexity on the T2-weighted image (D), but no enhancement on the postcontrast image (E).

Mimickers of adrenal cysts and pseudocysts, which are not incidental, include parasitic (echinococcal) cysts, pheochromocytoma, and cystic neoplasms. Adrenal echinococcal cysts share imaging features with echinococcal cysts infesting other body parts, such as the liver (see Chapter 2).⁴⁴ At the early stages of development, the hydatid cyst simulates adrenal pseudocysts and true cysts. With continued development, characteristic features corroborate the diagnosis (e.g., daughter cysts, floating membrane). The extreme T2 hyperintensity of the pheochromocytoma conjures cystic etiology on T2-weighted images, but avid enhancement confirms solid tissue, excluding fluid contents. Solid tumors—such as metastases and adrenal cortical carcinoma—with cystic degeneration and necrosis harbor solid neoplastic, occasionally subtle, components. Subtracted images improve solid tissue conspicuity.

ADRENAL HEMORRHAGE

Although not exactly cystic, adrenal hemorrhage—except when induced by underlying adrenal metastases—is nonsolid. Lack of enhancement best establishes the absence of solid tissue, which benefits from the incorporation of subtracted images, given the precontrast T1 hyperintensity of hemorrhage. Rich adrenal arterial supply—hormonally enhanced under certain conditions—with limited venous drainage through a single adrenal vein (prone to spasm induced by catecholamines) predisposes to hemorrhage.

Distortion of the adreniform shape depends on the degree of hemorrhage. Methemoglobin T1 hyperintensity in acute/subacute hemorrhage signals the diagnosis (Fig. 4-59). Follow-up imaging shows involution and confirms the diagnosis, while potentially identifying or excluding underlying lesions.

Solid Lesions

Solid lesions much more commonly affect the adrenal gland than do cystic lesions. In fact, adrenal lesion evaluation is the most common adrenal indication for MRI—dubbed the adrenal “incidentaloma.”⁴⁵ Adrenal adenomas account for the vast majority of these lesions—approximately 90%. In the setting of the adrenal incidentaloma, the clinical mandate is to exclude nonadenoma etiologies (especially metastasis). Adrenal incidentalomas potentially harbor one

of two clinically important features: (1) hormonal activity (as a functional adenoma) and (2) malignant histology (usually metastatic from nonadrenal primary). Luckily, 70% of adrenal adenomas are “lipid-rich,” facilitating diagnosis through signal loss on out-of-phase images (if not detected on unenhanced CT). Endocrinologically functional lesions manifest characteristic clinical findings (e.g., Conn’s syndrome, Cushing’s syndrome). Among the remaining lesions—lipid-poor adenomas, myelolipoma, pheochromocytomas, metastases, and adrenal cortical carcinomas—some specific imaging features help establish the correct diagnosis (Fig. 4-60).

ADRENAL ADENOMA

Adrenal adenomas are benign tumors of the adrenal cortex with no malignant potential. The vast majority is nonhyperfunctioning; a small minority induces Cushing’s syndrome, Conn’s syndrome, or virilization, depending on the hormone synthesized—cortisol, aldosterone, and androgens, respectively. Nonhyperfunctioning adenomas usually measure less than 2 cm and almost always less than 3 or 4 cm, whereas hyperfunctioning adenomas more likely measure greater than 2 cm. Other than size differences, no difference in imaging features is observed. High intracellular lipid content accounts for loss of signal on out-of-phase imaging in most adenomas (Fig. 4-61). If small lesions are anticipated, a 3-D sequence (without fat suppression) supplements routine 2-D in- and out-of-phase images in potentially detecting intracytoplasmic lipid. The lower slice thickness and potentially higher matrix improve conspicuity to microscopic fat in small lesions.

Identifying microscopic fat is paramount—unique to adenomas and excluding all potentially sinister lesions, especially metastases. Subjective signal loss on out-of-phase images usually suffices. In equivocal cases, objective measurement relies on comparison with a reference standard—the spleen.⁴⁶ A relative drop in lesion signal on out-of-phase images compared with the spleen establishes the presence of microscopic fat, according to the following equation:

$$\frac{\text{Adrenal lesion IP}}{\text{Spleen IP}} \div \frac{\text{Adrenal lesion OOP}}{\text{Spleen OOP}}$$

when the ratio is less than 0.7 (IP = in-phase; OOP = out-of-phase).^{47,48} In the setting of iron

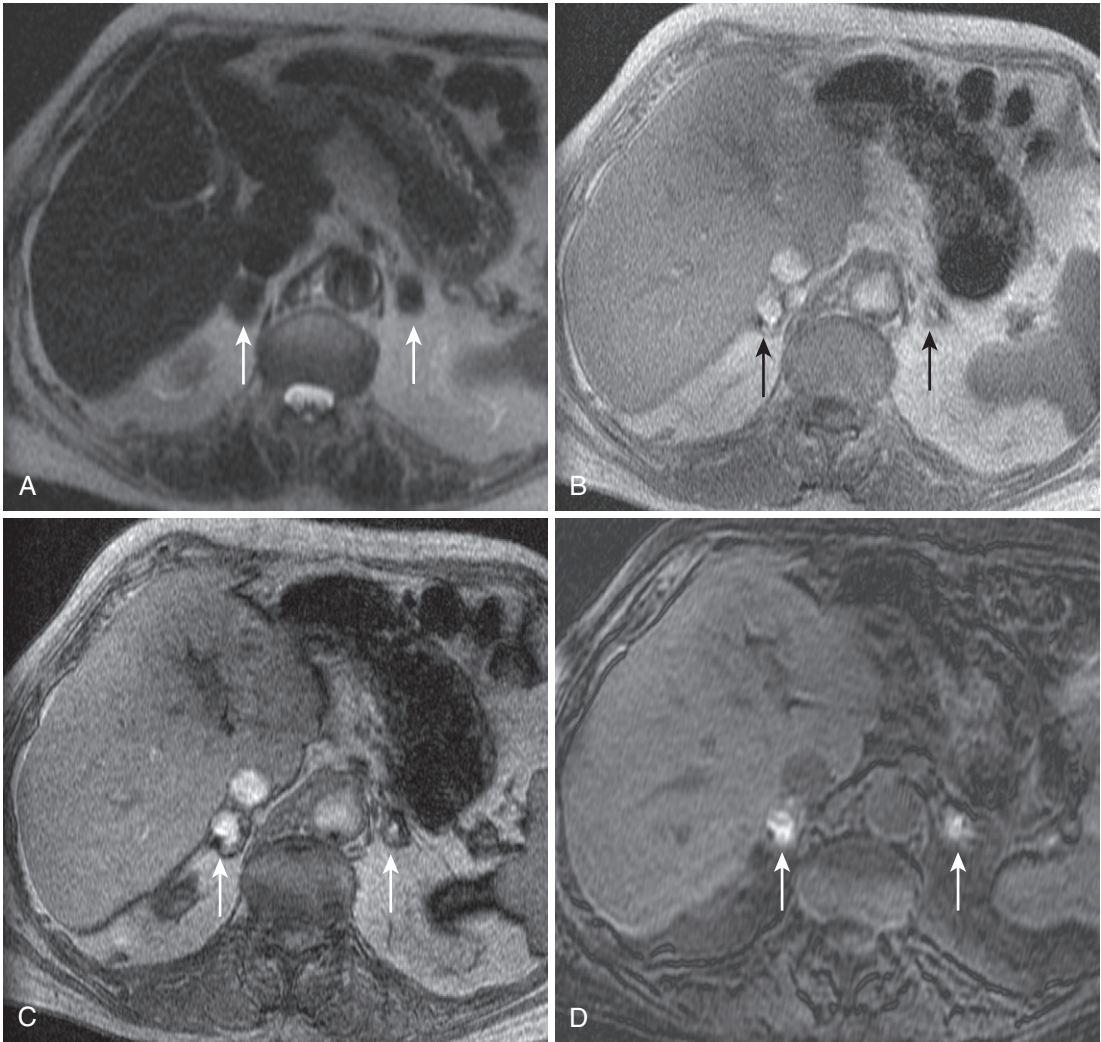


FIGURE 4-59. Adrenal hemorrhage. The T2-weighted image (A) shows bilateral adrenal lesions (arrows), which are hypointense relative to adenomas or other adrenal lesions with marked hyperintensity on the in-phase image (B). C, Preservation of signal and peripheral phase cancellation artifact (arrows) on the out-of-phase image excludes microscopic fat. D, Preservation of signal on the T1-weighted fat-suppressed image excludes macroscopic fat and the signal characteristics typify hemorrhage (arrows).

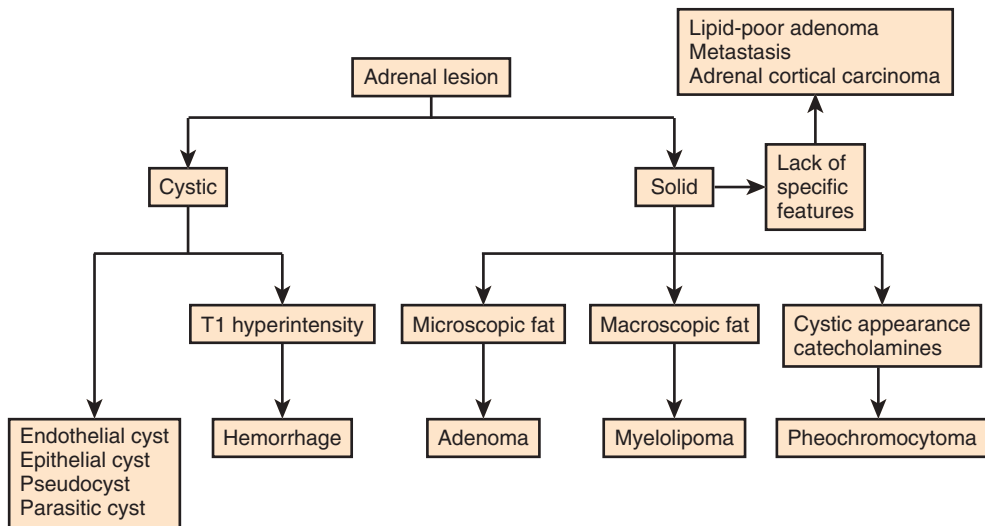


FIGURE 4-60. Solid adrenal lesions.

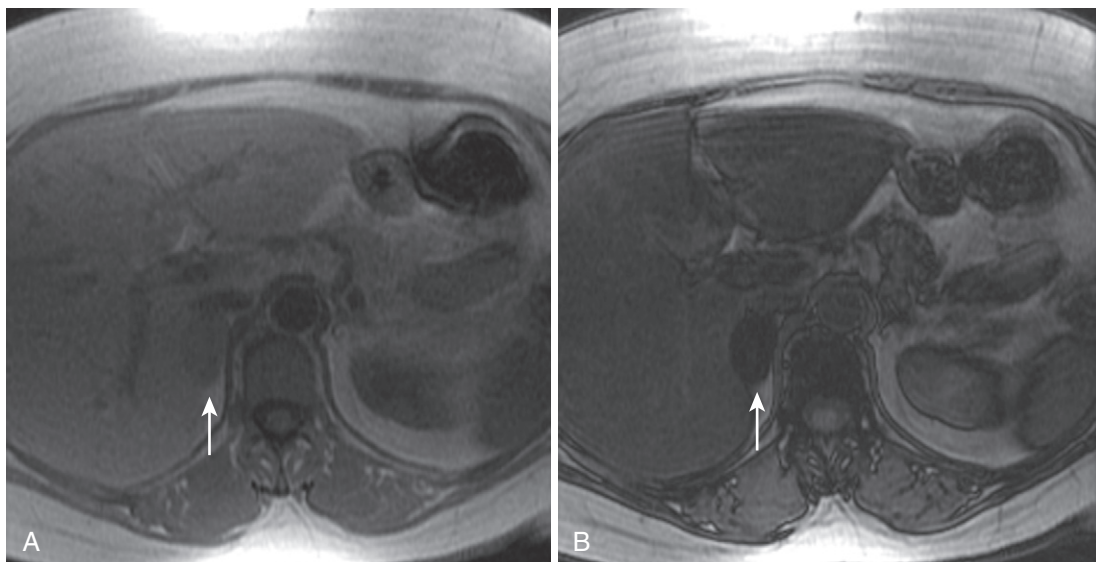


FIGURE 4-61. Adrenal adenoma. The mildly hyperintense lesion (*arrow*) on the in-phase image (A) loses signal on the out-of-phase image (B), indicating microscopic fat, diagnostic of an adenoma. Note the parallel loss of signal in the liver consistent with steatosis.

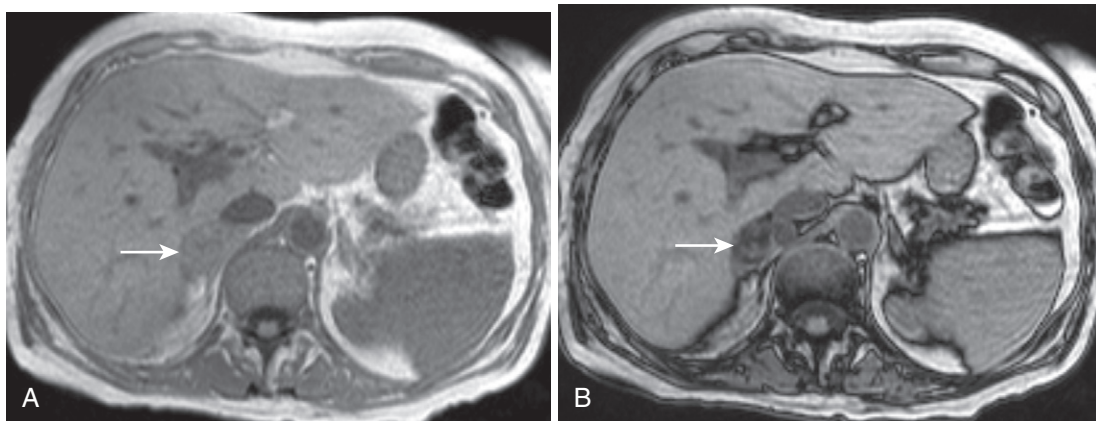


FIGURE 4-62. Lipid-poor adenoma with enhancement. There is modest signal drop in the right adrenal lesion (*arrow*) from the in-phase (A) to the out-of-phase (B) image illustrating the potential diagnostic uncertainty in the case of a lipid-poor adenoma.

deposition (with signal loss on in-phase images), the renal cortex or muscle serves as a reference standard alternative.

Homogenous signal characteristics and enhancement typify adenomas. Adenomas are usually iso- to hypointense on T2-weighted images. Prompt adenoma enhancement and washout on CT has been observed and substantiated on multiple studies. Adenoma CT enhancement parameters range from a drop of 40% at 15 minutes to 50% at 10 minutes. The MR enhancement pattern typically parallels the CT enhancement pattern, and a relatively early peak to enhancement—within 52 seconds—has been proposed as a discriminating feature between

adenoma and probably malignant lesions.⁴⁹ These features—homogenous T2 iso- or hypointensity and homogeneous enhancement—help to suggest the diagnosis of lipid-poor adenoma over alternative lesions, such as metastases (Fig. 4-62). However, ultimately follow-up imaging excludes metastasis by establishing size stability (correlative studies, such as positron-emission tomography, are another option).

ADRENAL HYPERPLASIA

Signal characteristics of adrenal hyperplasia (AH) mirror adrenal adenoma. AH respects adreniform morphology, either diffusely or asymmetrically enlarging the adrenal glands.

Adrenal gland limb width over 10 mm suggests AH and limb thickening may be smooth or nodular. AH signal intensity follows the signal intensity of normal adrenal glands—mild subjective signal loss on out-of-phase images. Adreniform shape and signal characteristics generally exclude other bilateral lesions from consideration, such as metastases, lymphoma, and hemorrhage.

MYELOLIPOMA

Myelolipoma shares one common feature with adenoma—the presence of fat. Unlike adrenal adenoma fat, myelolipoma fat is macroscopic. The myelolipoma is a “metaplasia-choristoma,” which means that it is composed of a mass of histologically normal tissue—in this case, bone marrow—in an abnormal location. Intralesional fat signal follows normal macroscopic fat signal—loss of signal on fat suppressed and STIR sequences. Hematopoietic elements demonstrate nonspecific imaging features with relative T2 hyperintensity and enhancement. The typical appearance of a well-circumscribed suprarenal lesion with a relatively higher proportion of mature adipose tissue mixed with strands and/or swirls of hematopoietic is pathognomonic (Fig. 4-63). Rarely, relative preponderance of hematopoietic tissue and paucity of adipose tissue precludes signal loss on fat-suppressed sequences and out-of-phase images potentially show signal loss, reflecting lipid content.

PHEOCHROMOCYTOMA

The pheochromocytoma is a paraganglioma arising from the adrenal medulla, composed of chromaffin cells synthesizing, storing, and releasing catecholamines. As an aside, the paraganglioma follows the “rule of 10s”: 10% bilateral adrenal, 10% malignant, 10% extra-adrenal. Most are sporadic, but 5% are inherited: in the form of multiple endocrine neoplasia type IIa and type IIb, VHL, or neurofibromatosis type 1.

Although the classic “lightbulb bright” T2 appearance of pheochromocytoma occurs in fewer than half of patients, T2 signal intensity always exceeds the T2 signal of adrenal adenomas (Fig. 4-64). Avid enhancement occurs either immediately or progressively and may demonstrate a “salt-and-pepper” texture reflecting enhancing tissue with intervening signal voids corresponding to vessels. Lack of intralesional lipid precludes signal loss on out-of-phase images and fat-suppressed images, avoiding confusion

with adenoma or myelolipoma. Potential confounders include cystic lesions and cystic neoplasms. The presence of solid, enhancing tissue excludes cystic lesions, and clinical features (paroxysmal hypertension, headaches and tremors) suggest the correct diagnosis.

METASTASES

Adrenal metastases constitute the greatest malignant threat to the adrenal glands. The adrenal glands are the fourth most common site of metastatic involvement (following lungs, liver, and bone). Primary malignancies usually responsible for adrenal metastases include lung, breast, skin (melanoma), kidney, thyroid, and colon cancers. When discovered in the setting of known malignancy, adrenal incidentalomas incur a risk of metastasis ranging from 33% to 75%. Because of the high prevalence, the adrenal adenoma is the chief differential consideration. Without microscopic lipid, diagnostic ambiguity ensues. Growth based on size increase between successive studies effectively eliminates benign etiologies. Other imaging features favoring metastasis include T2 hyperintensity compared with adenoma, irregular margins, heterogeneity, and the presence of widespread (metastatic) lesions (Fig. 4-65).

OTHER ADRENAL MALIGNANCIES

Other adrenal malignancies are exceedingly rare, such as adrenal lymphoma and adrenal cortical carcinoma. Adrenal lymphoma usually represents spread of ipsilateral renal or retroperitoneal lymphoma—usually non-Hodgkin’s lymphoma. Adrenal lymphoma manifests either as diffuse adrenal enlargement or as a discrete mass(es)—frequently bilateral (50%). Adrenal cortical carcinoma usually raises the prospect of malignancy based on its large size and pronounced heterogeneity (despite occasional intralesional lipid) (Fig. 4-66). These lesions usually measure at least 5 cm in diameter, and often much more. Cystic and necrotic degeneration figures prominently in the imaging appearance.

RETROPERITONEUM

Although this entire chapter is devoted to the retroperitoneum, inhabited by the kidneys and adrenal glands, this particular section specifically focuses on extraparenchymal lesions of the retroperitoneum. Because the retroperitoneum

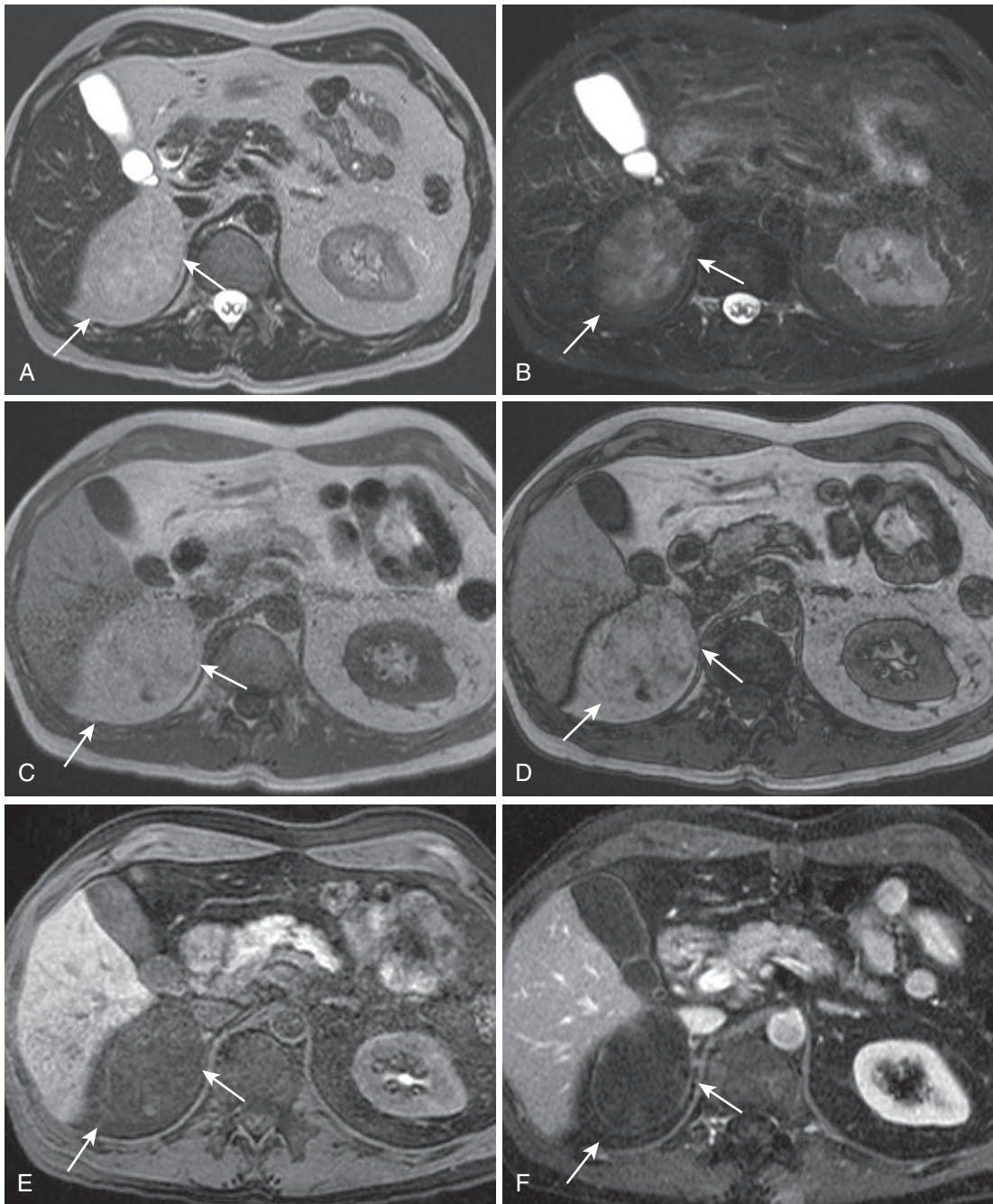
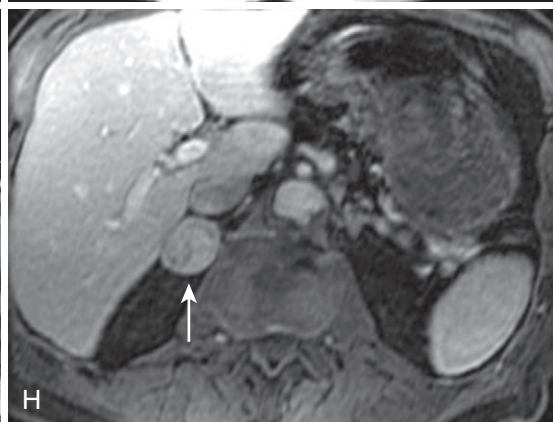
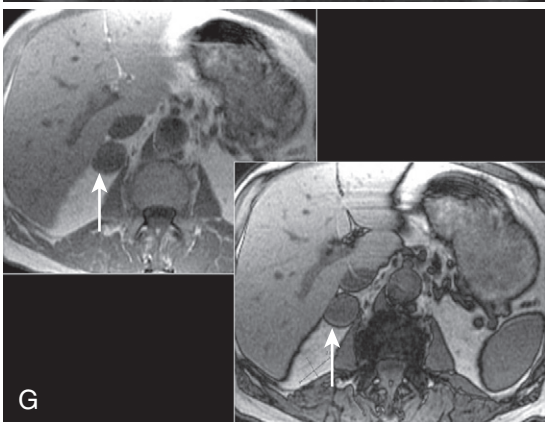
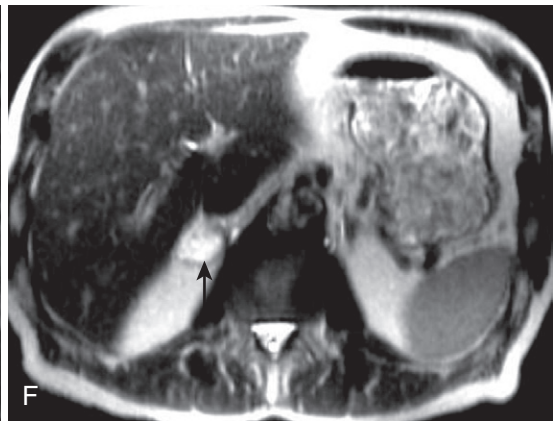
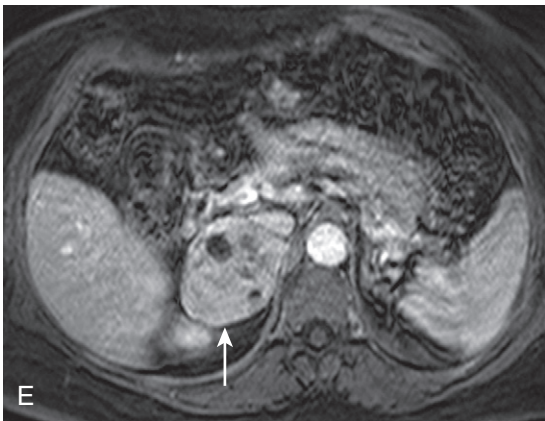
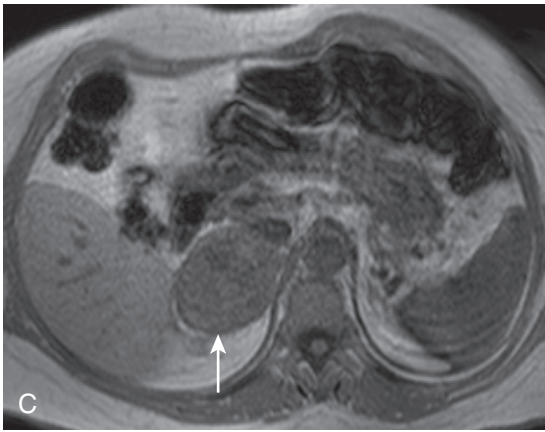
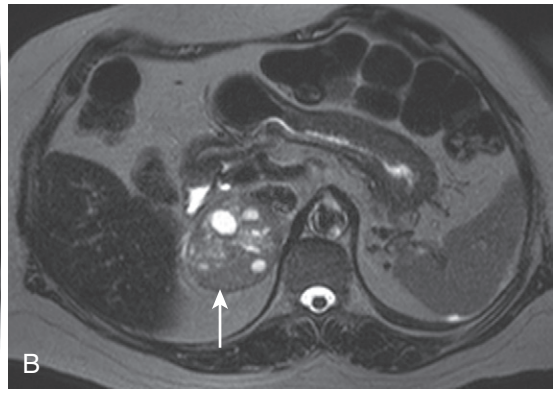
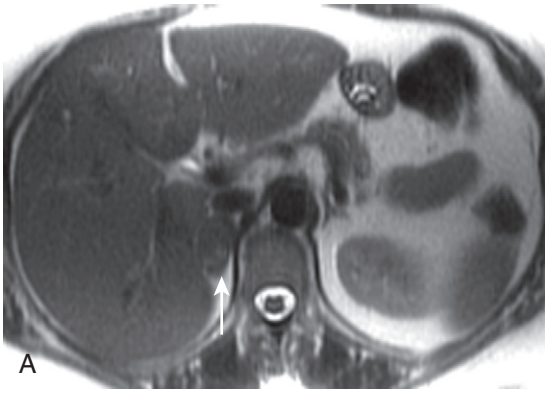


FIGURE 4-63. Adrenal myelipoma. **A**, On the T2-weighted image, a lesion occupying the right suprarenal space (*arrows*) blends with retroperitoneal fat—inconspicuous, despite its large size. Signal loss on the T2-weighted fat-suppressed (**B**) image and hyperintense signal on the in-phase image (**C**), maintained on the out-of-phase image (**D**), characterize macroscopic fat (*arrows*). Expected signal loss on the T1-weighted fat-suppressed image (**E**) and lack of enhancement on the postcontrast image (**F**) is observed in an AML (*arrows*) mostly composed of fat.

FIGURE 4-64. Pheochromocytoma. Compared with relative T2 hypointensity of the adrenal adenoma (*arrow* in **A**), a large, partially cystic pheochromocytoma exhibits relative T2 hyperintensity (*arrow* in **B**). Note the lack of signal loss (*arrow* in **C** and **D**) when comparing the in-phase (**C**) with the out-of-phase (**D**) image. **E**, Avid enhancement (*arrow*) is clear on the postcontrast image. **F**, The “lightbulb bright” appearance is apparent on the heavily T2-weighted image in a different patient with a right-sided pheochromocytoma (*arrow*). Absent microscopic fat results in lack of signal change (*arrow* in **G**) between the in-phase (left in **G**) and the out-of phase (right in **G**) images, and the solid nature of the mass (*arrow* in **H**) is reflected by avid enhancement on the postcontrast image (**H**).



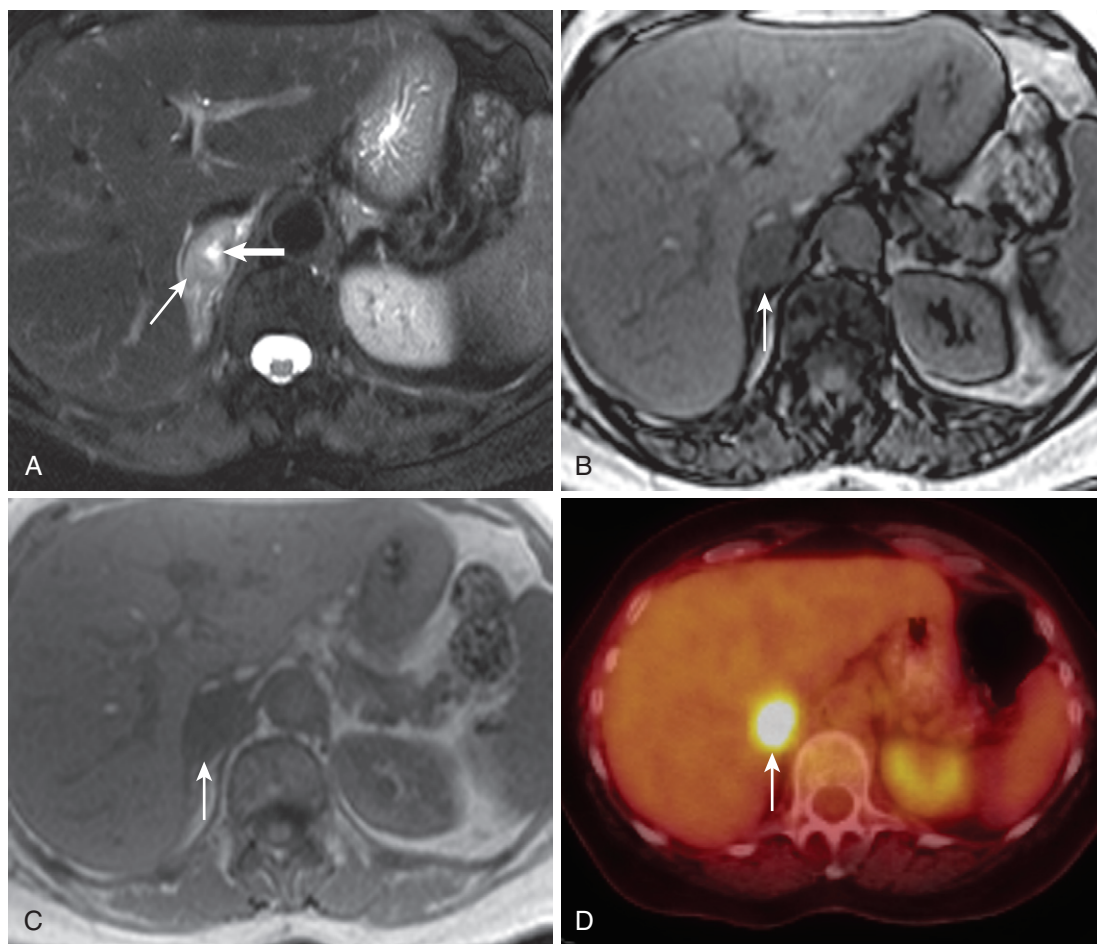


FIGURE 4-65. Adrenal metastasis. A, Note the heterogeneously hyperintense right adrenal lesion (*thin arrow*) on the T2-weighted fat-suppressed image harboring a central cystic necrotic focus (*thick arrow*) in a patient with metastatic lung cancer. No perceptible signal loss (*arrow* in B and C) on the out-of-phase image (B) compared with the in-phase image (C) indicates a lack of microscopic lipid. D, A corresponding image from a positron-emission tomography–computed tomography (PET-CT) scan reveals the hypermetabolic activity typical of a metastasis (*arrow*).

is a space, by definition, in which organs happen to reside,⁵⁰ primary lesions of the retroperitoneum are few and far between (Fig. 4-67). Fascial planes divide the retroperitoneum into three compartments: (1) the anterior pararenal space, (2) the perinephric space, and (3) the posterior pararenal space (Fig. 4-68). Although lesions arise in all three compartments, our objective is to focus on those relegated to the space between the perinephric spaces around the great vessels (discussion of lesions in the anterior pararenal space related to the pancreas appears in Chapter 3).

IVC Anomalies

Anomalies of the IVC (Table 4-11) speak for themselves and harbor no direct complications.

TABLE 4-11. Inferior Vena Cava Anomalies

IVC duplication
Left-sided IVC
Azygous continuation of the IVC
Absent (infrarenal) IVC

IVC, inferior vena cava.

Avoiding procedural complications arising from failure to acknowledge these anomalies is the main objective. For example, unilateral right-sided IVC filter placement in IVC duplication leaves the left-sided IVC untreated. Planning abdominal surgical procedures, liver or kidney transplant, and interventional procedures benefits from preprocedural recognition of these anomalies.

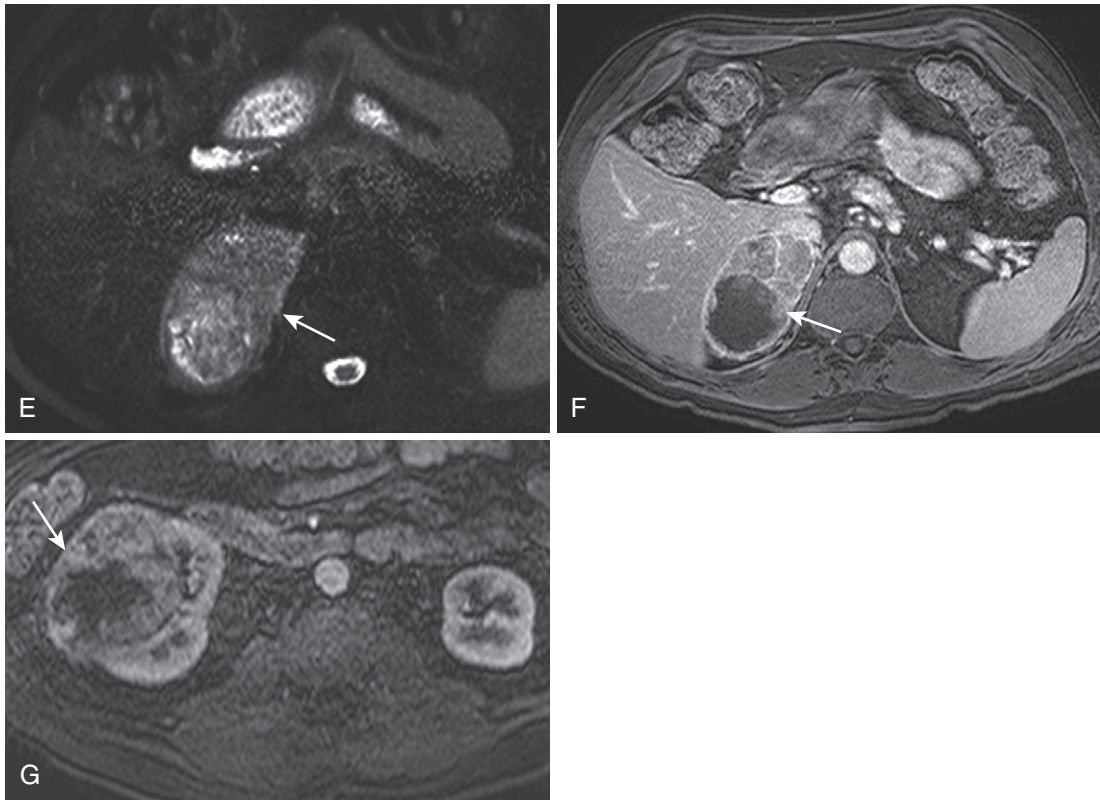


FIGURE 4-65, cont'd A large right adrenal mass (arrow in E and F) demonstrates even more heterogeneous signal and enhancement with cystic necrosis on the T2-weighted fat-suppressed (E) and postcontrast (F) images in a different patient with metastatic RCC. G, The primary mass is shown on the postcontrast image through the kidneys (arrow).

Retroperitoneal Fibrosis

Inflammatory retroperitoneal etiologies—retroperitoneal fibrosis (RF) and inflammatory abdominal aortic aneurysm (IAAA) share common imaging features. In fact, etiologic and histologic features also overlap. Although precise mechanisms are incompletely understood, both conditions involve autoimmune-mediated fibrosis. Imaging features diverge significantly, however.

RF represents a common inflammatory pathway induced by a number of potential pathogens, such as drugs (methysergide, beta blockers, hydralazine, ergotamine, and lysergic acid diethylamide [LSD]), irradiation, autoimmune diseases, retroperitoneal hemorrhage, and malignancies (gastrointestinal, breast, prostate, lung, cervical, and renal malignancies). However, two thirds of cases are idiopathic and referred to as *Ormond's disease*. A rind of soft tissue envelops the aorta, IVC, and ureters in RF (Fig. 4-69), without “lifting the aorta away from the

spine,” which is a feature of retroperitoneal lymphoma (RL). The MR appearance evolves with chronicity, initially appearing hyperintense on fluid-sensitive sequences with avid enhancement and ill-defined margins. Over time, T2 signal and enhancement wane and margins sharpen (see Fig. 4-69). Ureteral encasement occurs frequently, leading to functional obstruction due to suppression of peristalsis. RF is typically centered in the retroperitoneum (L3–5), but potentially extends caudally into the pelvis or cephalad into the mediastinum. Suggesting the diagnosis facilitates treatment, which is relatively specific to RF—withdrawal of the inciting agent, corticosteroids, and relief of ureteral obstruction.

Potential confounders include RL, IAAA, and retroperitoneal hemorrhage. As previously mentioned, RL more commonly extends along the posterior margin of the aorta, lifting it off the spine, whereas RF relatively spares the posterior aortic perimeter. Lymphoma—a relatively soft, pliable neoplasm—rarely obstructs the ureters

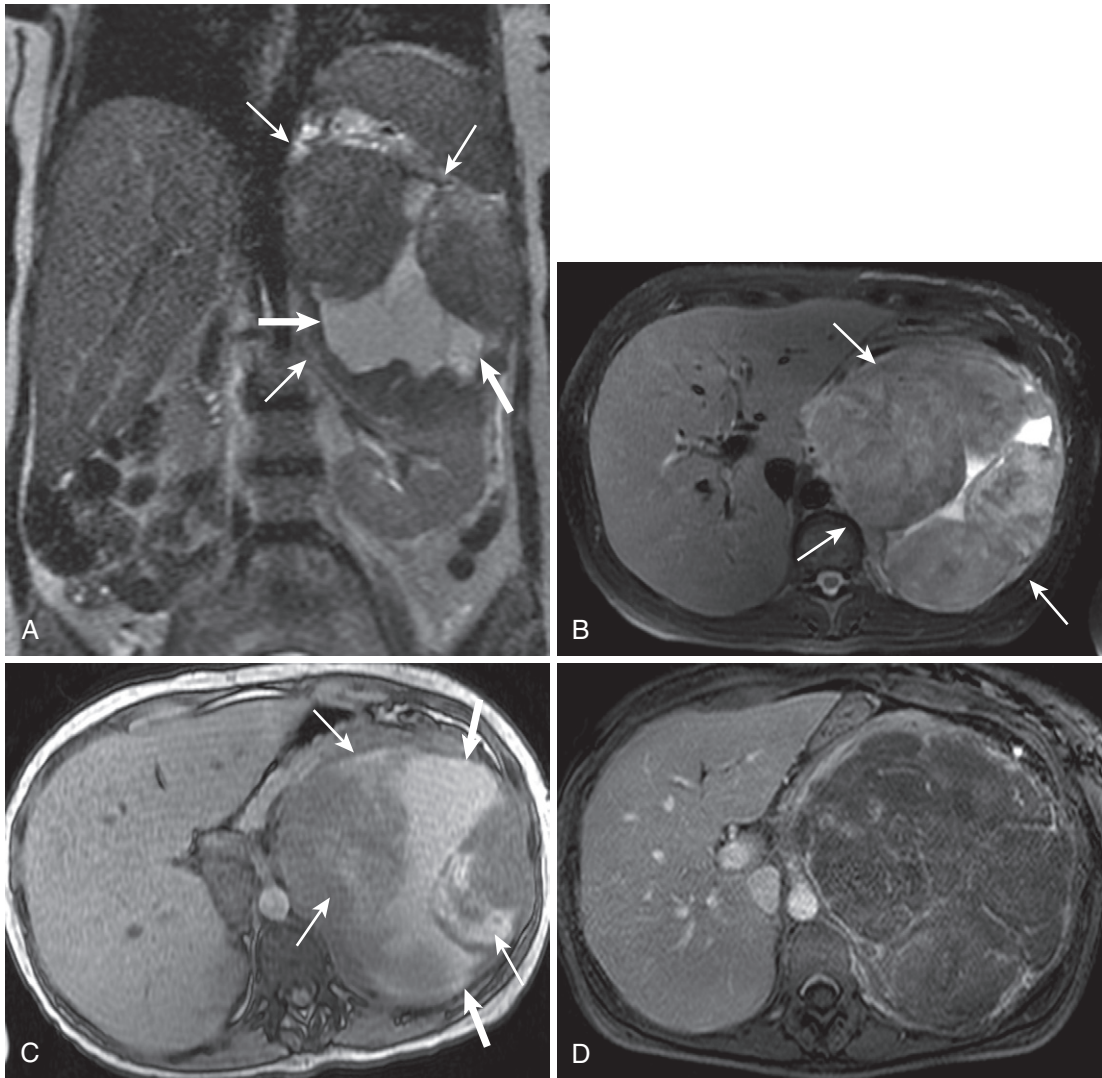


FIGURE 4-66. Adrenal cortical carcinoma. A, The coronal T2-weighted image reveals a large, complex mass (*thin arrows*) with central necrosis (*thick arrows*) flattening the upper pole of the right kidney. B, The corresponding axial T2-weighted fat-suppressed image shows the large size of the lesion (*arrows*). C, Signal preservation on the out-of-phase image excludes microscopic lipid and hyperintensity suggests hemorrhage (*thin arrows*) and hemorrhagic necrosis (*thick arrows*). D, The postcontrast image discloses the hypovascularity of the large, necrotic mass.

Normal variant	Inflammation	Trauma	Neoplasm
IVC anomalies	Retroperitoneal fibrosis	Retroperitoneal hemorrhage	Lymphoma
	Inflammatory aneurysm		Metastases
			Sarcoma

FIGURE 4-67. Retroperitoneal lesions. IVC, inferior vena cava.

ARF = Anterior renal fascia
 PRF = Posterior renal fascia

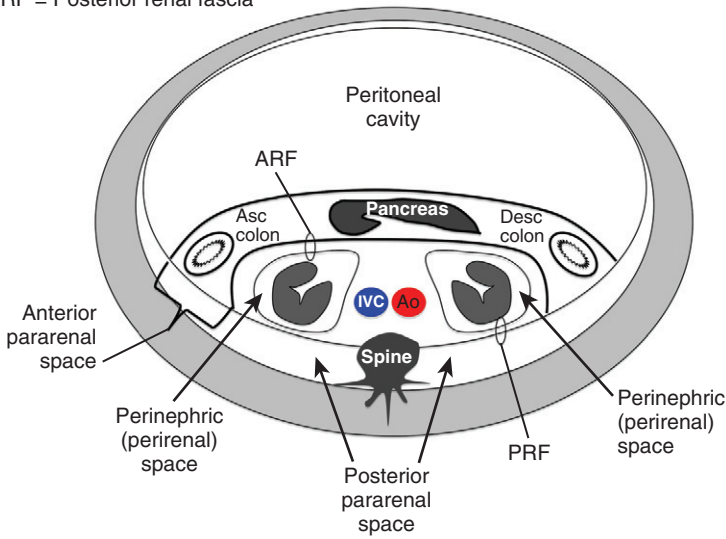


FIGURE 4-68. Retroperitoneal anatomy. Ao, aorta; asc, ascending; desc, descending.

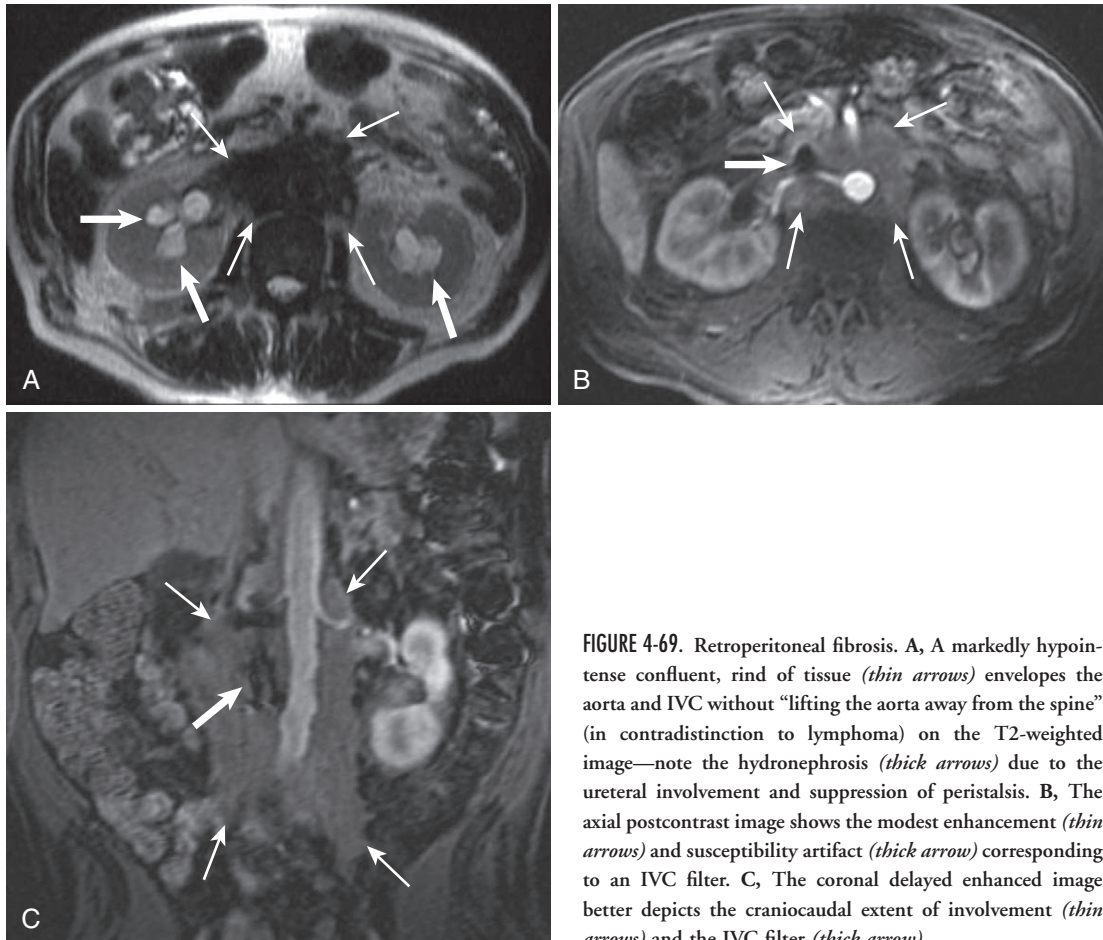


FIGURE 4-69. Retroperitoneal fibrosis. A, A markedly hypointense confluent, rind of tissue (*thin arrows*) envelops the aorta and IVC without “lifting the aorta away from the spine” (in contradistinction to lymphoma) on the T2-weighted image—note the hydronephrosis (*thick arrows*) due to the ureteral involvement and suppression of peristalsis. B, The axial postcontrast image shows the modest enhancement (*thin arrows*) and susceptibility artifact (*thick arrow*) corresponding to an IVC filter. C, The coronal delayed enhanced image better depicts the craniocaudal extent of involvement (*thin arrows*) and the IVC filter (*thick arrow*).

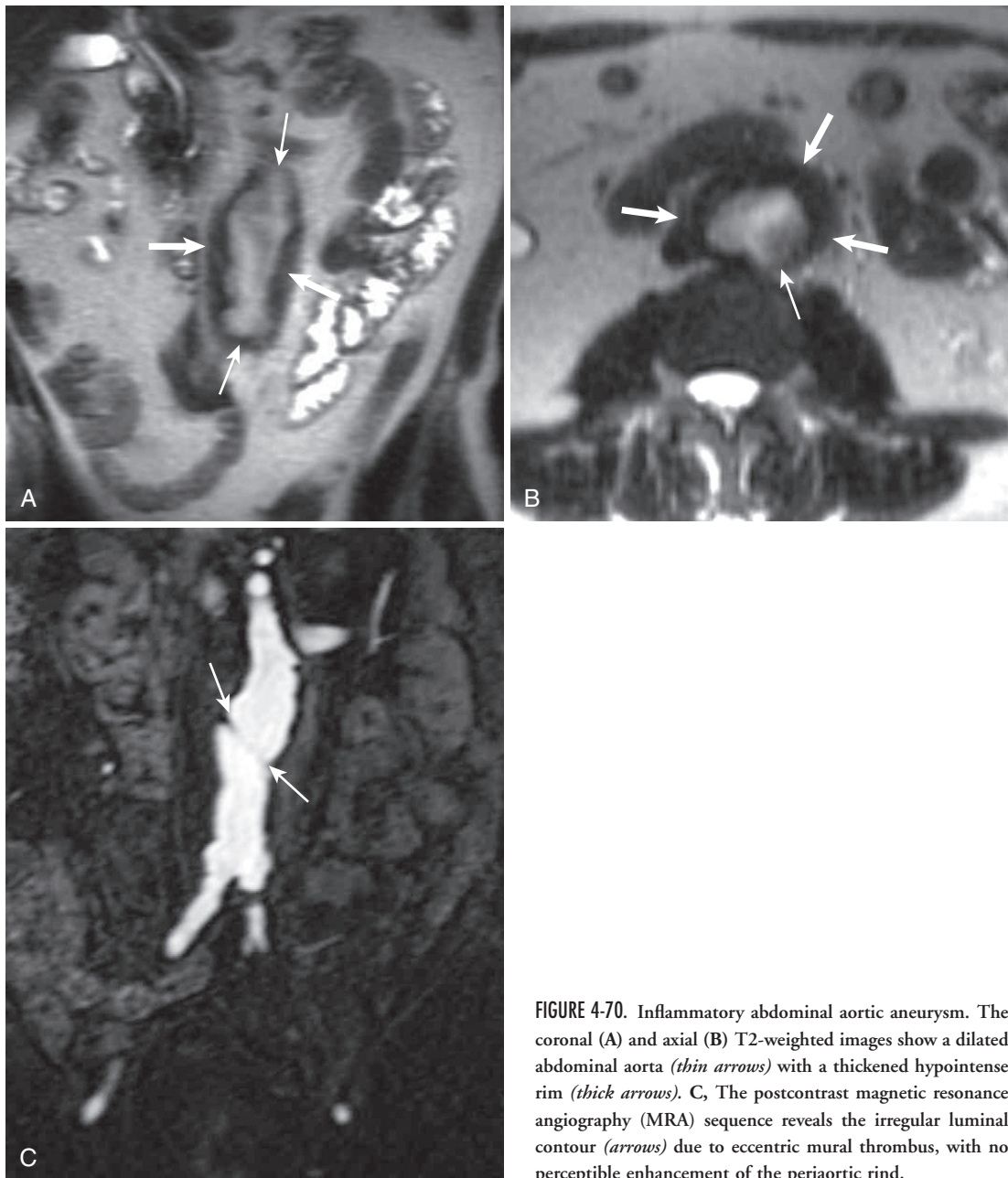


FIGURE 4-70. Inflammatory abdominal aortic aneurysm. The coronal (A) and axial (B) T2-weighted images show a dilated abdominal aorta (*thin arrows*) with a thickened hypointense rim (*thick arrows*). C, The postcontrast magnetic resonance angiography (MRA) sequence reveals the irregular luminal contour (*arrows*) due to eccentric mural thrombus, with no perceptible enhancement of the periaortic rind.

and discrete nodes are usually discernible. IAAA is essentially the same process as RF owing to inciting antigen in the wall of the aorta, thought to reside in atheromatous plaque. The extent of involvement is generally restricted focally to the aortic aneurysm. Retroperitoneal hemorrhage fails to enhance and exhibits signal characteristics expected of hemorrhage rather than fibrosis.

Inflammatory Aortic Aneurysm

In IAAA, dense connective tissue infiltrated by inflammatory cells extends beyond the normal confines of the aneurysmal aortic adventitia, resulting in a periaortic enhancing rind of tissue (Fig. 4-70). The periaortic tissue mantle measures up to 2 cm in thickness, and signal characteristics seem to be less predictable than the

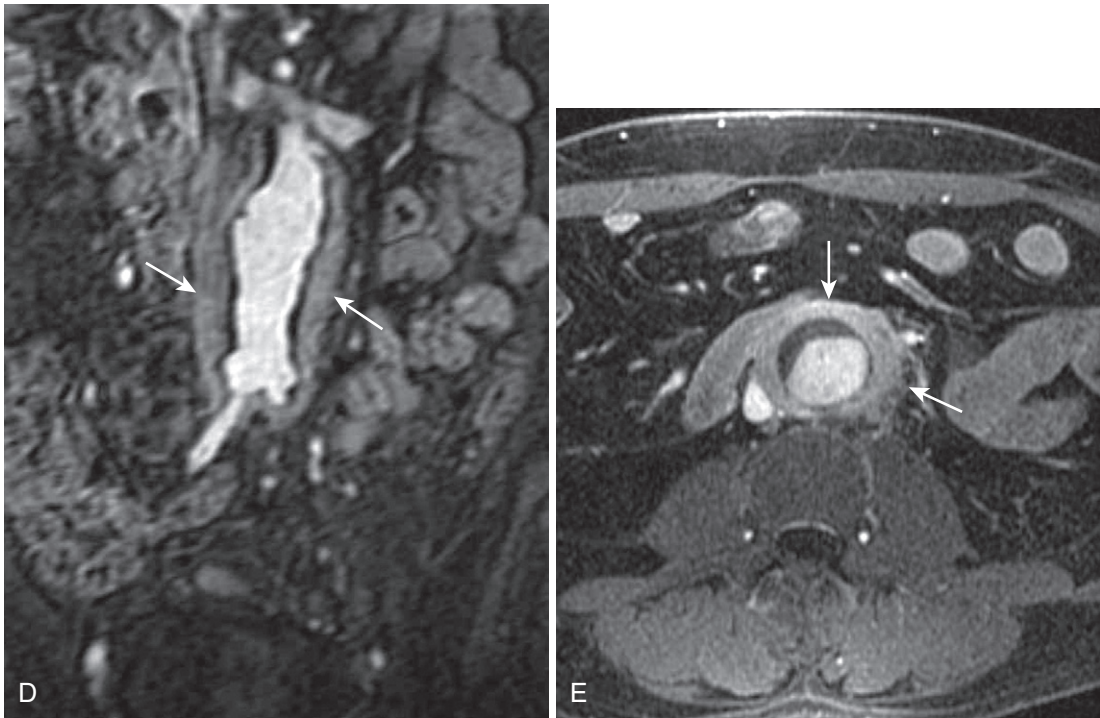


FIGURE 4-70, cont'd Delayed coronal (D) and axial (E) postcontrast images show prominent enhancement of the periaortic mantle (arrows).

predictably prominent enhancement.⁵¹ Prompt diagnosis and discrimination from uncomplicated abdominal aortic aneurysm ensure appropriate treatment. The presence of perianeurysmal inflammation prompts consideration of presurgical treatment with corticosteroids to minimize inflammation and operative technical modifications to minimize duodenal and ureteral dissection and improve surgical outcomes.

Retroperitoneal Lymphoma

Retroperitoneal neoplasms encompass a wide range of lesions (including a variety of sarcomas), many of which are beyond the scope of this text. RL is the most common retroperitoneal malignancy, with either Hodgkin's or non-Hodgkin's lymphoma invading the retroperitoneal lymph nodes. Hodgkin's lymphoma tends to involve the spleen and retroperitoneum with a contiguous spread pattern. Non-Hodgkin's lymphoma more often involves a variety of nodal groups, with a predilection for mesenteric nodes and extranodal sites. Overall, RL most commonly involves para-aortic, aortocaval, and retrocaval nodal groups. Nodes tend to measure greater than 1.5 cm in short-axis diameter with bilateral involvement. Often,

a confluent nodal mass encircles the aorta and IVC, displacing the aorta from the spine (Fig. 4-71). Monotonous features with mild homogeneous hyperintensity on fluid-sensitive sequences, mild enhancement with relative lack of mass effect (even despite large size), and extensive retroperitoneal involvement typify lymphoma.

RF and metastases from primary malignancies, such as testicular and prostate carcinoma, figure most prominently in the differential diagnosis. RF and metastatic disease fail to lift the aorta from the spine and RF frequently obstructs the ureters, unlike RL. Extension along lymphatic drainage pathways from the pelvis points to genitourinary metastasis, such as testicular or prostate carcinoma.

Retroperitoneal Metastases

Retroperitoneal metastases originate from hematogenous or lymphatic spread or from direct extension (Fig. 4-72). Metastatic lymphadenopathy is best appreciated as either (1) a conglomerate hyperintense mass on fat-suppressed enhanced or T2-weighted sequences against the signal void of signal-suppressed retroperitoneal fat or (2) on T1-weighted sequences without fat

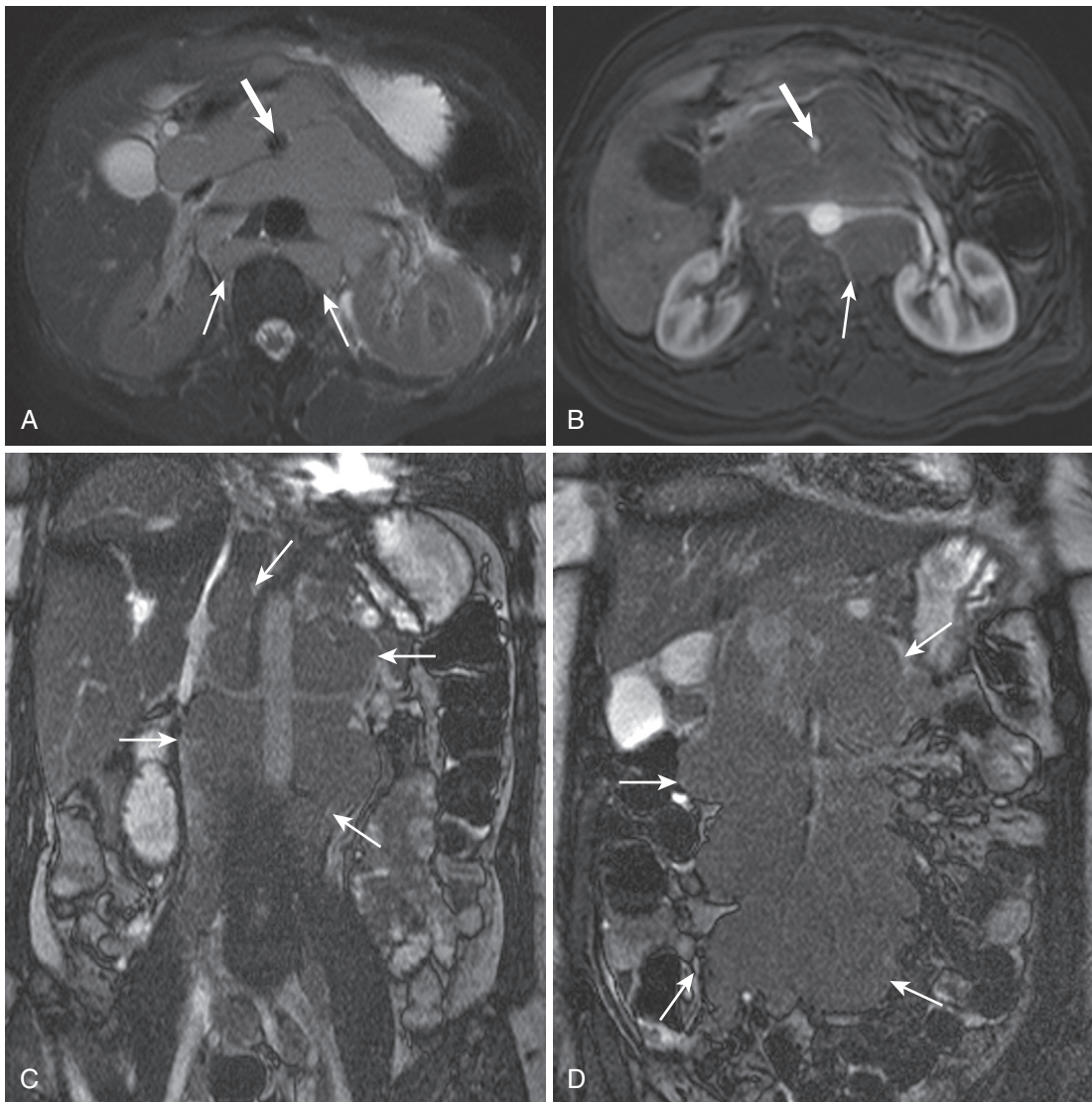


FIGURE 4-71. Retroperitoneal lymphoma. The T2-weighted fat-suppressed (A) and postcontrast (B) images depict nearly coalescent lymph nodes throughout the retroperitoneum, including retroaortic extension (*thin arrows*), with monotonous features—homogeneous T2 hyperintensity and modest homogeneous enhancement. Encirclement of the superior mesenteric artery (SMA; *thick arrow*) denotes concurrent mesenteric involvement. C and D, The coronal steady-state images show the extent of craniocaudal involvement (*arrows*).

Lymphatic spread	Hematogenous spread	Direct Invasion
Testicular carcinoma	Lung carcinoma	Pancreatic carcinoma
Prostate carcinoma	Breast carcinoma	Gastrointestinal carcinoma
Bladder carcinoma	Melanoma	
Ovarian carcinoma		
Endometrial carcinoma		
Colorectal carcinoma		

FIGURE 4-72. Primary malignancies in retroperitoneal metastasis.

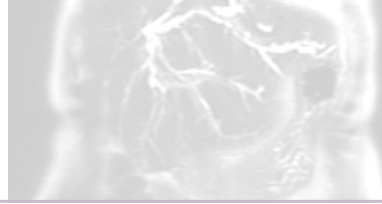
saturation as a conglomerate mass against the background of hyperintense retroperitoneal fat. Lymph nodes appear moderately hyperintense on T2-weighted sequences, hypointense on T1-weighted sequences, and usually approximate primary tumor enhancement. Generally speaking, enlarged retroperitoneal lymph nodes are nonspecific and the diagnosis is inferred by the known history of primary malignancy.

Differential diagnostic considerations include RL, RF, and retroperitoneal sarcomas (RSs). RS split into four basic histologic categories: (1) liposarcoma (most common), (2) leiomyosarcoma, (3) fibrosarcoma, and (4) rhabdomyosarcoma. Angiosarcoma and lymphangiosarcoma are exceedingly rare additional subtypes. RS classically manifests as a large heterogenous mass, often with intralesional fat (liposarcoma), frequently in the vicinity of the kidney. Whereas precise histologic diagnosis usually eludes MRI capabilities (except with liposarcoma with intralesional fat), malignant nature is reflected in the large size, heterogeneity, and lack of benign confounders (except for, potentially, a large renal AML).

References

- Cheong B, Muthupillai R, Rubin MF, Flamm SD. Normal values for renal length and volume as measured by magnetic resonance imaging. *Clin J Am Soc Nephrol* 2:38-45, 2007. Epub 2006;Dec 6.
- Lee VS, Kaur M, Bokacheva L, et al. What causes diminished corticomedullary differentiation in renal insufficiency? *J Magn Reson Imaging* 25:790-795, 2007.
- Gill IS, Aron M, Gervais DA, et al. Small renal mass. *N Engl J Med* 362:624-634, 2010.
- Israel GM, Bosniak MA. How I do it: Evaluating renal masses. *Radiology* 236:441-450, 2005.
- Bosniak MA. Difficulties in classifying cystic lesions of the kidney. *Urol Radiol* 13:91-93, 1991.
- Bosniak MA. The current radiological approach to renal cysts. *Radiology* 158:1-10, 1986.
- Silverman SG, Israel GM, Herts BR, et al. Management of the incidental renal mass. *Radiology* 249:16-31, 2008.
- Israel GM, Bosniak MA. MR imaging of cystic renal masses. *Magn Reson Imaging Clin* 12:403-412, 2004.
- Carrim ZI, Murchison JT. The prevalence of simple renal and hepatic cysts detected by spiral computed tomography. *Clin Radiol* 58:626-629, 2003.
- Marumo K, Horiguchi Y, Nakagawa K, et al. Incidence and growth pattern of simple cysts of the kidney in patients with asymptomatic microscopic hematuria. *Int J Urol* 10:63-67, 2003.
- El-Merhi FM, Bae KT. Cystic renal disease. *Magn Reson Imaging Clin North Am* 12:449-467, 2004.
- Pei Y, Obaji J, Dupuis A, et al. Unified criteria for ultrasonographic diagnosis of ADPKD. *J Am Soc Nephrol* 20:1-8, 2008.
- Nascimento AB, Mitchell DG, Zhang X, et al. Rapid MR imaging detection of renal cysts: Age-based standards. *Radiology* 221:628-632, 2001.
- Meier P, Farres MT, Mougnot B, et al. Imaging medullary cystic kidney disease with magnetic resonance. *Am J Kidney Dis* 42:E5-E10, 2003.
- Choyke PL. Acquired cystic kidney disease. *Eur Radiol* 10:1716-1721, 2000.
- Regan F, Petronis J, Bohlman M, et al. Perirenal MR high signal—A new and sensitive indicator of acute ureteric obstruction. *Clin Radiol* 52:445-450, 1997.
- Sudah M, Vanninen R, Partanen K, et al. MR urography in evaluation of acute flank pain. *AJR Am J Roentgenol* 176:105-112, 2001.
- Cyran KM, Kenney PJ. Asymptomatic renal abscess: Evaluation with gadolinium DTPA-enhanced MRI. *Abdom Imaging* 19:267-269, 1994.
- Brown ED, Brown JJ, Ketriz U, et al. Renal abscesses: Appearance on gadolinium-enhanced magnetic resonance images. *Abdom Imaging* 21:172-176, 1996.
- Verswijvel G, Vandecaveye V, Gelin G, et al. Diffusion-weighted MR imaging in the evaluation of renal infection: Preliminary results. *JBR-BTR* 85:100-103, 2002.
- Dembry L-M, Andriole VT. Renal and perirenal abscesses. *Infect Dis Clin North Am* 11:663-680, 1997.
- Sun MRM, Ngo L, Genega EM, et al. Renal cell carcinoma: Dynamic contrast-enhanced MR imaging for differentiation of tumor subtypes—Correlation with pathologic findings. *Radiology* 253:793-802, 2009.
- Prasad SR, Humphrey PA, Catena JR, et al. Common and uncommon histologic subtypes of renal cell carcinoma: Imaging spectrum with pathologic correlation. *Radiographics* 26:1795-1806, 2006.
- Cohen D, Zhou M. Molecular genetics of familial renal cell carcinoma syndromes. *Clin Lab Med* 25:259-277, 2005.
- Outwater EK, Bhatia M, Siegelman ES, et al. Lipid in renal clear cell carcinoma: Detection on opposed-phase gradient-echo MR images. *Radiology* 205:103-107, 1997.
- Pedrosa I, Sun MR, Spencer M, et al. MR imaging of renal masses: Correlation with findings at surgery and pathologic analysis. *Radiographics* 28:985-1003, 2008.
- Reznek RH. CT/MRI in staging renal cell carcinoma. *Cancer Imaging* 4:S25-S32, 2004.
- Laissy JP, Menegazzo D, Debray M-P, et al. Renal carcinoma: Diagnosis of venous invasion with Gd-enhanced MR venography. *Eur Radiol* 10:1138-1143, 2000.
- Herts BR, Coll DM, Novick AC, et al. Enhancement characteristics of papillary renal neoplasms revealed on triphasic helical CT of the kidneys. *AJR Am J Roentgenol* 178:367-372, 2002.
- Prasad SR, Surabhi VR, Menias CO, et al. Benign renal neoplasms in adults: Cross-sectional imaging findings. *AJR Am J Roentgenol* 190:158-164, 2008.
- Yamakado K, Tanaka N, Nakagawa T, et al. Renal angiolipoma: Relationships between tumor size, aneurysm formation and rupture. *Radiology* 225:78-82, 2002.
- Casey RG, Murphy CG, Hickey DP, et al. Wunderlich's syndrome, an unusual cause of the acute abdomen. *Eur J Radiol Extra* 57:91-93, 2006.
- Weeks SM, Brown ED, Adamis MK, et al. Transitional cell carcinoma of the upper urinary tract: Staging by MRI. *Abdom Imaging* 20:365-367, 1995.
- Greene FL, Page DL, Fleming ID, eds. Renal pelvis and ureter. In: *American Joint Committee on Cancer: AJCC Cancer Staging Manual*. 6th ed. New York: Springer, 2002:329-334.
- Stunell H, Buckley O, Feeney J, et al. Imaging of acute pyelonephritis in the adult. *Eur Radiol* 17:1820-1828, 2007.
- Verswijvel G, Oyen R, Van Poppel H, et al. Xanthogranulomatous pyelonephritis: MRI findings in the diffuse and the focal type. *Eur Radiol* 10:586-598, 2000.

37. Loffroy R, Guiu B, Watfa J, et al. Xanthogranulomatous pyelonephritis in adults: Clinical and radiological findings in diffuse and focal forms. *Clin Radiol* 62:884-890, 2007.
38. Jeong JY, Kim SH, Lee HJ, et al. Atypical low-signal-intensity renal parenchyma: Causes and patterns. *Radiographics* 22:833-846, 2002.
39. Vincent JM, Morrison ID, Armstrong P, et al. Computed tomography of diffuse, non-metastatic enlargement of the adrenal glands in patients with malignant disease. *Clin Radiol* 49:456-460, 1994.
40. Lockhart ME, Smith JK, Kenney PJ. Imaging of adrenal masses. *Eur J Radiol* 41:95-112, 2002.
41. Peppercorn PD, Reznick RH. State-of-the-art CT and MRI of the adrenal gland. *Eur Radiol* 7:822-836, 1997.
42. Rozenblit A, Morehouse HT, Amis ES Jr. Cystic adrenal lesions: CT features. *Radiology* 201:541-548, 1996.
43. Elsayes KM, Mukundan G, Narra VR, et al. Adrenal masses: MR imaging features with pathologic correlation. *Radiographics* 24:S73-S86, 2004.
44. Otal P, Escourrou G, Mazerolles C, et al. Imaging features of uncommon adrenal masses with histopathologic correlation. *Radiographics* 19:569-581, 1999.
45. Dunnick NR, Korobkin M. Imaging of adrenal incidentalomas: Current status. *AJR Am J Roentgenol* 179:559-568, 2002.
46. Bilbey JH, McLoughlin RE, Kurkjian PS, et al. MR imaging of adrenal masses: Value of chemical-shift imaging for distinguishing adenomas from other tumors. *AJR Am J Roentgenol* 164:637-642, 1995.
47. Outwater EK, Siegelman ES, Huang AB, et al. Adrenal masses: Correlation between CT attenuation value and chemical shift ratio at MR imaging with in-phase and opposed-phase sequence. *Radiology* 200:749-752, 1996.
48. Israel GM, Korobkin M, Wang C, et al. Comparison of unenhanced CT and chemical shift MRI in evaluation of lipid-rich adrenal adenomas. *AJR Am J Roentgenol* 183:215-219, 2004.
49. Inan N, Arslan A, Akansel G, et al. Dynamic contrast enhanced MRI in the differential diagnosis of adrenal adenomas and malignant adrenal masses. *Eur J Radiol* 65:154-162, 2008.
50. Lim JH, Kim B, Auh YH. Anatomical communications of the perirenal space. *Br J Radiol* 71:450-456, 1998.
51. Wallis F, Roditi GH, Redpath TW, et al. Inflammatory abdominal aortic aneurysms: Diagnosis with gadolinium enhanced T1-weighted imaging. *Clin Radiol* 55:136-139, 2000.



Magnetic Resonance Imaging of the Female Pelvis

INTRODUCTION

Magnetic resonance imaging (MRI) serves as the most comprehensive and conclusive modality available to image the female pelvis. The inherent zonal anatomy of the uterus is exquisitely depicted as a function of the different water content and histology of each mural layer. The predictable MRI appearance of the uterus renders identification of abnormalities straightforward (Fig. 5-1).

The evaluation of the adnexa hinges on the unique spectroscopic capability of MRI to differentiate between lesions of different tissue composition, such as lipid (dermoid cyst), water (functional ovarian cyst), and hemorrhage (endometrioma). Improved tissue contrast elevates the sensitivity for neoplastic and malignant features compared with other modalities. The most common indications for MRI of the female pelvis include characterization of adnexal lesions, identification and characterization of fibroids, assessment of fibroid treatment response, problem solving inconclusive ultrasound or computed tomography (CT) findings, and adjunctive staging of malignancies (Table 5-1).

TECHNIQUE

Given the potentially small size of ovarian, cervical, and uterine lesions and the need for high-resolution imaging, the examination justifies the use of a high-field-strength system (≥ 1.0 T). Nonetheless, diagnostic images can be obtained on systems of lower field strength (Fig. 5-2). A dedicated phased array coil guarantees optimal signal to noise. An antiperistaltic agent to eliminate motion artifacts from bowel activity (such as glucagons or hyoscyamine) ensures minimization of motion artifact. Consider the application of vaginal gel to facilitate evaluating vaginal and cervical lesions.¹

Start off viewing a localizer sequence with a large field of view to assess coil placement (ensuring maximal signal emanating from the

region of interest and not the upper thighs or lower abdomen). Single-shot fast spin-echo T2-weighted images or balanced gradient echo sequences yield the most diagnostic information. Configure the localizer sequence to include the kidneys because of the association of renal anomalies with müllerian duct (fallopian tubes, uterus, and proximal vagina) anomalies. The remainder of the examination demands a focused approach with a higher spatial resolution and a field of view in the range of 24 cm.

A combination of T1-weighted, T2-weighted, and fat-saturated sequences suffices to solve most problems encountered in the pelvis (Table 5-2). T2-weighted images are the mainstay of pelvic imaging. T2-weighted images display the trilaminar anatomy of the uterus—the inner endometrium, the central inner myometrium (junctional zone), and the outer myometrium (see Fig. 5-1)—and confer conspicuity to the ovaries and most adnexal lesions, especially cystic lesions. Oblique coronal and axial images orthogonal to the axis of the uterus supplement the examination to characterize potential müllerian duct anomalies, if suspected (Figs. 5-3 and 5-4). T2-weighted images highlight cystic adnexal lesions and any potential septa, mural nodules, or other complex features. T1-weighted images depict hemorrhage and lipid, and the addition of fat-saturated sequences allows for differentiating between blood and fat (which both appear hyperintense on T1-weighted images without fat suppression). In-phase and out-of-phase images serve as a time-saving alternative to spin-echo T1-weighted images (~20 sec compared with 3–5 min) with sensitivity to both intracellular fat and susceptibility artifact, although potentially degraded by low signal-to-noise on low-field-strength systems.

Gadolinium-enhanced images provide additional information regarding the complexity and/or blood supply of a lesion and its tissue content and often increase lesion conspicuity. Enhancement of an ovarian lesion confirms its neoplastic etiology. Enhancement patterns

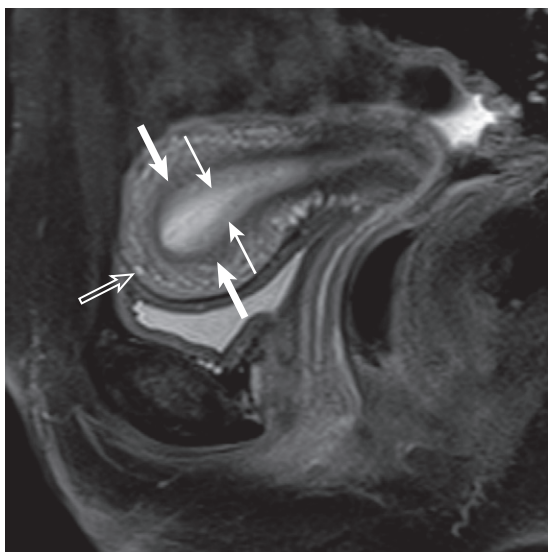


FIGURE 5-1. Normal uterine mural stratification. Fat-suppressed sagittal T2-weighted image through the uterus shows the normal trilaminar appearance with the central hyperintense zone (the endometrium—*thin arrows*), the middle hypointense zone (the junctional zone—*thick arrows*), and the outer isointense zone (outer myometrium—*open arrow*).

provide diagnostic information.² For example, arterial enhancement characterizes an arteriovenous fistula and delayed enhancement characterizes fibrous lesions (Table 5-3), such as an ovarian fibroma. Dynamic imaging provides a reliable timeframe to assess enhancement patterns, whereas static pregadolinium and postgadolinium images yield only binary information (enhancement vs. no enhancement). Quantitative evaluation of fibroid vascularity demands dynamic images.

Three-dimensional fat-saturated gradient echo images offer the best spatial resolution and tissue contrast. Approximately 20 mL of gadolinium (0.1 mmol/kg) is administered intravenously at approximately 1 to 2 mL/sec. A timing bolus or timing sequence triggers the arterial phase of the acquisition and one or two additional phases obtained in succession suffice. A delayed T1-weighted (preferably fat-saturated) sequence detects delayed enhancement, if present.

TABLE 5-1. Female Pelvis Magnetic Resonance Imaging Indications

Clinical Presentation	Imaging Objective	Details
Pelvic pain Dysmenorrhea (painful menstruation)	Nonspecific Exclude endometrial and/or cervical lesions (polyp, fibroid, neoplasm) Exclude adenomyosis and endometriosis	Standard protocol
Menorrhagia (>80 mL/cycle) Metrorrhagia (light bleed, irregular intervals) Menometrorrhagia (heavy bleed > 80 mL, irregular intervals)	Same as above Same as above Same as above	
Abnormal pelvic examination Delayed menses or precocious puberty Postmenopausal bleeding Evaluation of pelvic pain or mass Pain or fever after pelvic surgery or delivery	Exclude endometrial or cervical cancer or polyp Exclude endometritis, hematoma	Standard protocol Review gradient echo images for susceptibility
Localization of intrauterine device	Nonanatomic susceptibility artifact (usually linear or curvilinear)	Review gradient echo images for susceptibility
Evaluation infertility Congenital anomalies Uterine fibroid evaluation	Müllerian duct anomalies Müllerian duct anomalies Location (submucosal vs. intramural vs. subserosal), vascularity degeneration (cystic, hemorrhagic)	± Dedicated imaging planes ± Dedicated imaging planes ± Dedicated imaging planes
Assessment for pelvic floor defects Clarification of indeterminate imaging findings	Cystocele, enterocele, vagocele, rectocele abnormal pelvic floor descent Follow-up previously detected abnormality (i.e., hemorrhagic cyst) Further characterization abnormality detected on another imaging study	± Dynamic maneuvers
Known or risk of malignancy	Screening for malignancy in patients with increased risk Detection and staging of gynecologic malignancies Tumor recurrence assessment Presurgical/laparoscopic evaluation Cervical and endometrial carcinoma staging <i>Cervical:</i> Violation of fibrous stroma (intact 1A-B, disrupted 2B), parametrial invasion (2B), vaginal invasion (upper vagina 2A, lower one third 3A), spread to adjacent structures, spread to pelvic sidewall (3B), spread to bladder/rectum (4A), pelvic lymphadenopathy <i>Endometrial:</i> Depth of myometrial invasion (1A-C), cervical extension (2A-B), spread to ovary/adnexa (3A), evidence of peritoneal spread (3A), vaginal extension (3B), pelvic lymphadenopathy (3C), bladder/bowel invasion (4A)	Consider vaginal gel if cervical or vaginal involvement

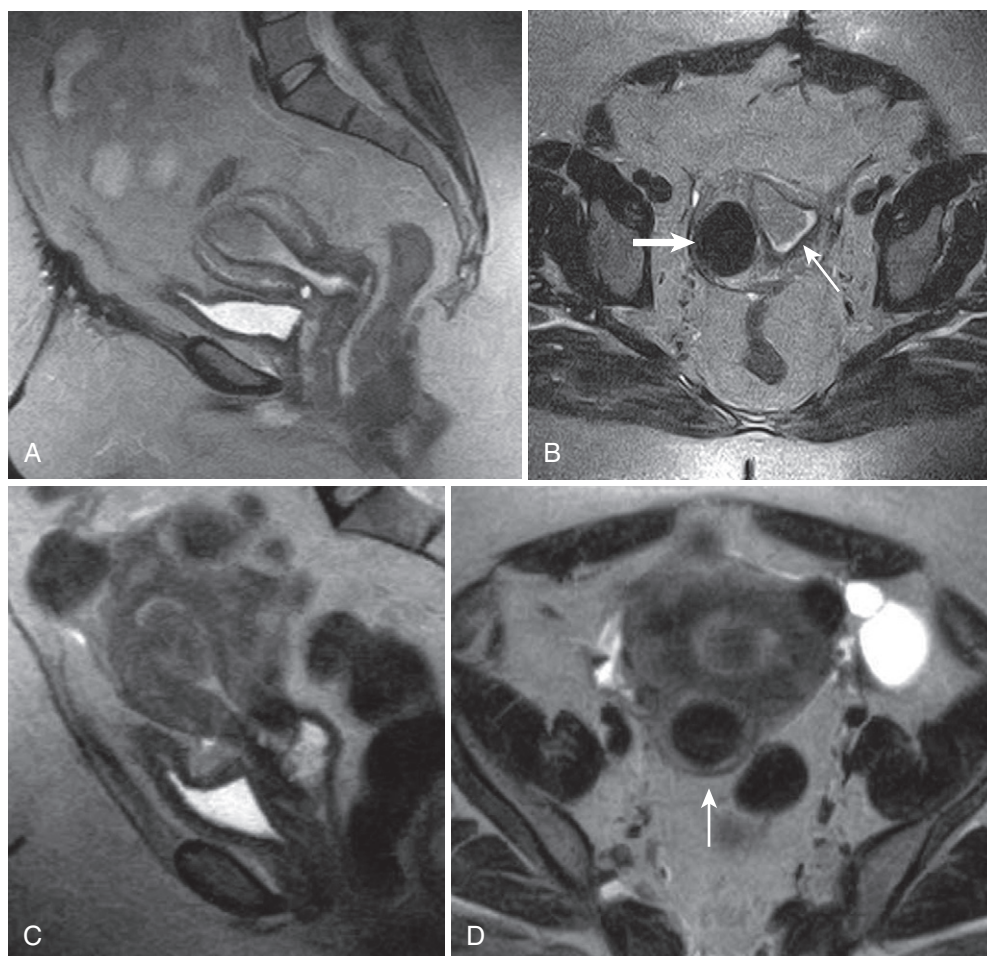


FIGURE 5-2. 0.3-Tesla images. **A**, Sagittal T2-weighted image through the uterus obtained on a 0.3-Tesla system reveals an isointense endometrial mass with no deep myometrial invasion corresponding to endometrial carcinoma. **B**, The corresponding axial T2-weighted image shows normal endometrium (*thin arrow*) abutting the distal aspect of the mass and an intramural fibroid (*thick arrow*). Sagittal (**C**) and axial (**D**) T2-weighted images through the uterus obtained on a 0.3-Tesla system in a different patient show a tubular mildly hyperintense lesion with a hypointense core within the endometrial cavity found to be an endometrial polyp. Also note the partially subserosal fibroid arising from the posterior uterine body (*arrow* in **D**).

TABLE 5-2. Female Pelvis Magnetic Resonance Imaging Protocol

Pulse Sequence	Details	Field of View	Slice Thickness
Localizing sequence (coronal)	SSFSE (5000/180)	32 cm	5 mm
	b-FFE (min/min)	32 cm	5 mm
Axial T2	± Fat saturated (4000/100)	24 cm	4 mm
Axial T1	FSE (5/200)	24 cm	4 mm
	In-/out-of-phase (2.3, 4.6/200)	24 cm	7 mm
Sagittal T2	± Fat saturated (80/2500)*	24 cm	6 mm
Dynamic	Sagittal or axial (min/min) with fat suppression*	24 cm	4 mm (interpolated ⇒ 2 mm)
Delayed postgadolinium	Three-dimensional GRE (min/min)	24 cm	4 mm (interpolated ⇒ 2 mm)
	Two-dimensional SPGR (min/22)	24 cm	5 mm

*At least one fat-suppressed sequence is necessary to identify dermoid cyst and discriminate between hemorrhage and lipid.

FFE = fecal fat extraction; FSE = fast spin echo; GRE = gradient-recalled echo; SPGR = spoiled gradient echo; SSFSE = single-shot fast spin-echo.

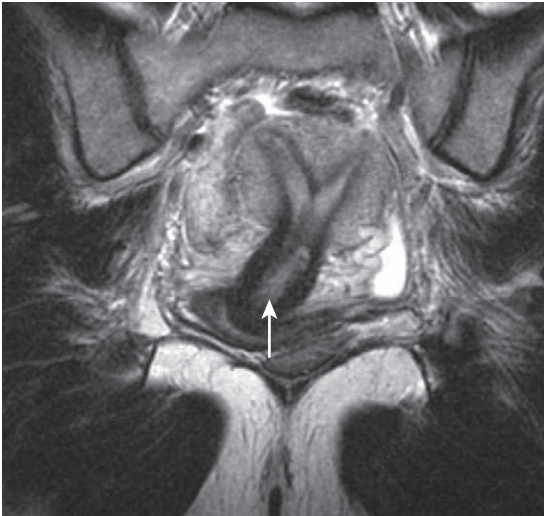


FIGURE 5-3. Oblique coronal imaging of the uterus. The full extent of a fibrous septum (*arrow*) of a septate uterus (and other congenital anomalies) is well delineated by orienting the imaging plane along the long axis of the uterus to obtain an oblique coronal image.

TABLE 5-3. Adnexal Lesion Enhancement Patterns

Lack of enhancement	Simple/functional ovarian cyst Parovarian cyst Ovarian torsion
Mild rim enhancement	Corpus luteal cyst Endometrioma Some cystadenomas ± Ovarian torsion
Marked rim enhancement	Some cystadenomas/ cystadenocarcinomas Tubo-ovarian abscess
Solid enhancement	
Arterial	Arteriovenous malformation
Early	Malignant > benign epithelial ovarian neoplasms
Delayed	Fibroma Benign > malignant epithelial ovarian neoplasms

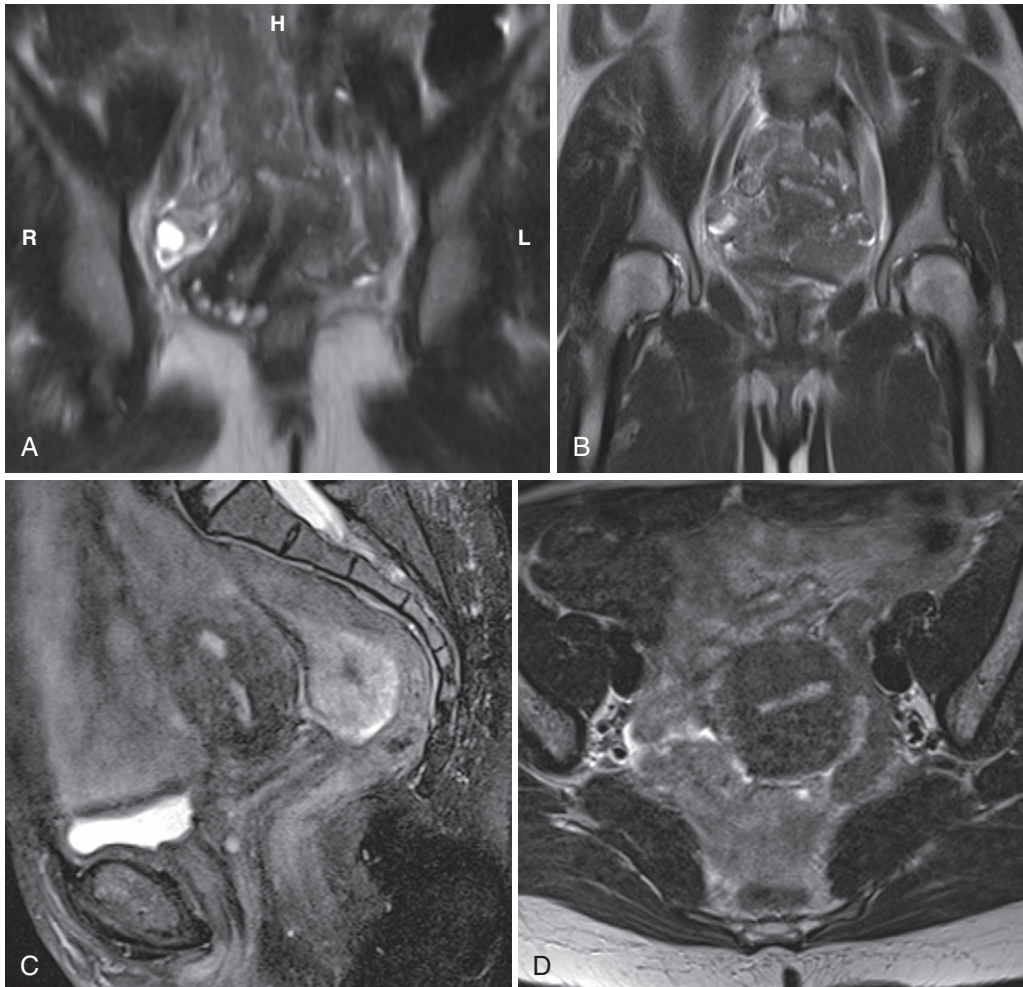


FIGURE 5-4. T-shaped uterus. A, Obliquely coronally reformatted T2-weighted image in a 47-year-old woman with a history of fetal diethylstilbestrol exposure elegantly portrays the aberrant anatomy that is less clearly rendered with coronal (B), sagittal (C), and axial (D) planes prescribed orthogonally to the axes of the body.

INTERPRETATION

If pictures are worth a thousand words, imagine how much the hundreds of images in the multi-image sets in a female pelvis MRI study are worth. This much information compels the use of a directed search pattern (Table 5-4). First of all, assess the technical adequacy of the examination. Review the localizer sequence, which usually includes large field-of-view coronal images, and ensure that coil placement is adequately reflected by the highest signal emanating from the region of interest (and not the abdomen or subpelvic region) (Fig. 5-5). Note whether gadolinium was administered and whether enhancement is perceptible. Assess the degree of motion artifact and any other artifact that degrades image quality (Fig. 5-6).

Look at the uterus, keeping in mind the age and menstrual status of the patient and any relevant history, such as endometrial or cervical carcinoma, cesarean section, or treated or untreated fibroids. Measuring the uterus in three orthogonal planes is standard and helps objectively assess overall uterine size. Observe uterine zonal anatomy (central endometrium, middle junctional zone, and outer myometrium) and measure the thickness of each. Identify any fibroids or other uterine lesions and record sizes. Comment on whether the uterus is anteverted or retroverted or retroflexed. In the setting of hysterectomy, record the presence and status of the vaginal cuff and residual cervical or uterine tissue. Look for susceptibility artifact on gradient echo images corresponding to surgical clips, if present.

TABLE 5-4. Female Pelvis Checklist

<p>Technical</p> <p>Magnetic field strength</p> <p>Coil position</p> <p>Signal \Rightarrow optimal signal corresponding to pelvis</p> <p>Kidneys \Rightarrow at least one large field-of-view coronal should include kidneys</p> <p>Enhancement \Rightarrow note amount and type of contrast agent</p> <p>Inspect vessels for adequate enhancement</p> <p>Artifacts</p> <p>Bowel peristalsis (see Fig. 5-6D-F)</p> <p>Susceptibility \Rightarrow surgical hardware, gas (e.g., bowel)</p> <p>Motion \Rightarrow bulk motion, respiratory motion, vascular flow artifacts</p> <p>Conductivity/dielectric effects \Rightarrow focal signal loss (fl at 3T)</p> <p>Uterus</p> <p>Size (height \times width \times length)</p> <p>Position</p> <p>Anteverted vs. retroverted</p> <p>Anteverted vs. retroflexed</p> <p>Endometrium</p> <p>Thickness</p> <p>Homogeneity</p> <p>Focal lesions</p> <p>Presence of intraluminal fluid or susceptibility (e.g., gas, IUD)</p> <p>Inner myometrium (junctional zone)</p> <p>Thickness</p> <p>Sharpness of border</p> <p>Intramyoetrial hyperintensities</p> <p>Cesarean section defect</p> <p>Fibroids</p> <p>Size(s)</p> <p>Submucosal vs. intramural vs. subserosal</p> <p>Degeneration: cystic vs. hemorrhagic vs. other</p> <p>Vascularity: necrotic vs. hypovascular vs. hypervascular</p> <p>Cervix</p> <p>Mucosa</p> <p>Naboth's cysts</p> <p>Thickness</p> <p>Luminal fluid</p> <p>Stroma</p> <p>Integrity</p> <p>Parametrial infiltration</p>	<p>Vagina</p> <p>Cystic lesions (upper vs. lower)</p> <p>Vaginal wall</p> <p>Focal vs. diffuse thickening</p> <p>Invasion from adjacent structures</p> <p>Tampon</p> <p>Adnexa</p> <p>Ovaries</p> <p>Dimensions</p> <p>Cystic lesions</p> <p>Size</p> <p>Hemorrhage</p> <p>Shading</p> <p>Lipid</p> <p>Rim enhancement</p> <p>Solid component/complexity</p> <p>Solid lesions</p> <p>T2 signal</p> <p>Unilateral vs. bilateral involvement</p> <p>Parovarian region</p> <p>Cystic lesions</p> <p>Vascular lesions</p> <p>Lymphadenopathy</p> <p>Other Anatomy</p> <p>Bladder</p> <p>Bowel</p> <p>Musculoskeletal structures</p> <p>Bony pelvis</p> <p>Lower lumbar spine</p> <p>Muscles</p> <p>Gluteal</p> <p>Adductor</p> <p>Hip flexor</p> <p>Piriformis</p> <p>Tendons</p> <p>Iliopsoas</p> <p>Rectus femoris</p> <p>Hamstring</p>
--	--

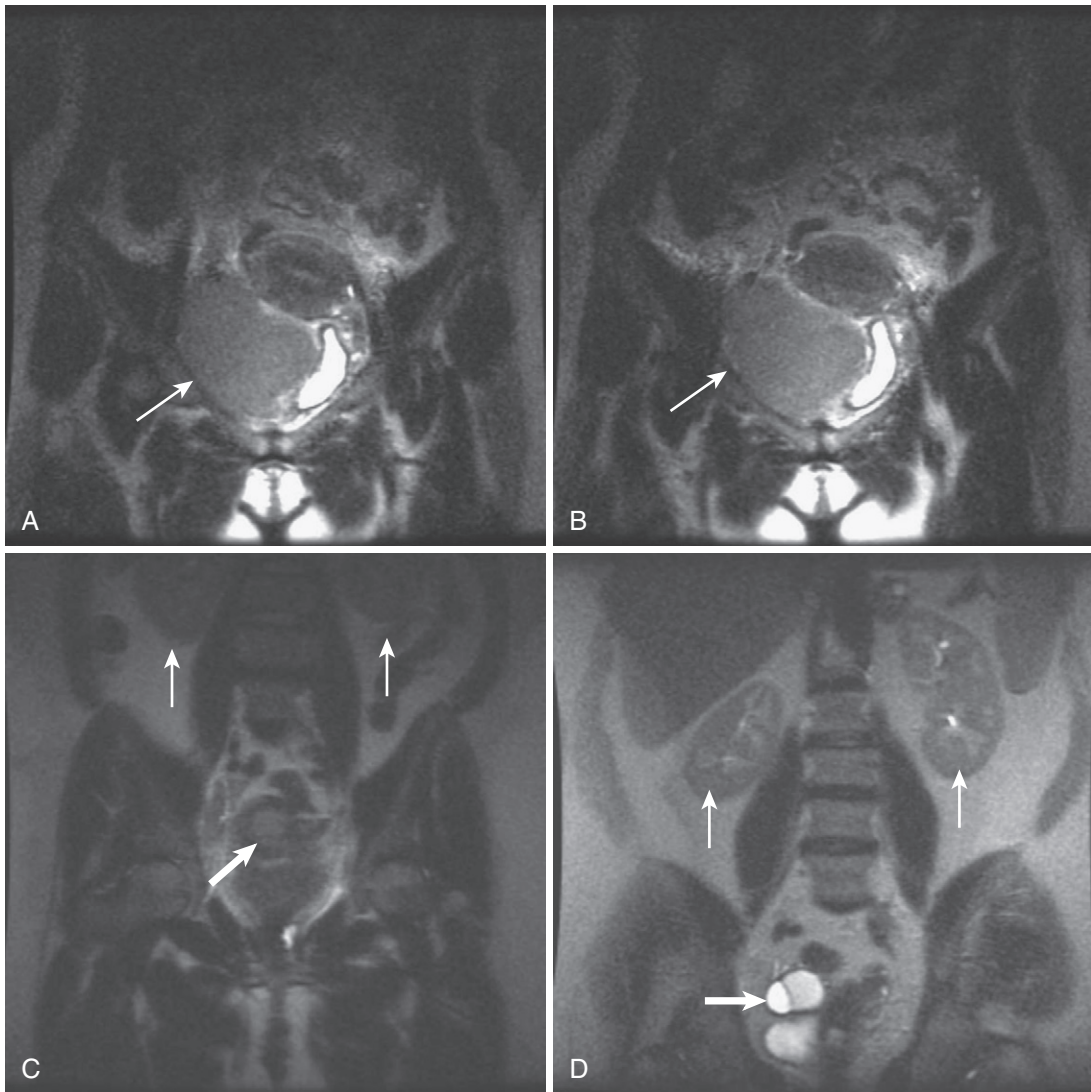


FIGURE 5-5. Poor coil placement. A and B, Coronal T2-weighted images of the pelvis show maximal signal centered at the level of the pubic symphysis rather than the region of interest—the uterus and adnexa—and remember that the kidneys should be visualized in all cases. Note the homogeneously hyperintense mass in the right hemipelvis in this patient with pelvic lymphoma (*arrow*). C, Coronal T2-weighted image in a different patient demonstrates maximal signal arising from the region of the uterus with visualization of the kidneys (*thin arrows*) in a patient with cervical carcinoma (*thick arrow*). D, The kidneys (*thin arrows*) are conspicuously well visualized on this coronal T2-weighted image with maximal signal emanating from the abdominopelvic junction in this patient with a right-sided cystadenofibroma (*thick arrow*).

Confirm the integrity of the fibrous stroma of the cervix and exclude the presence of any cystic or solid cervical lesions. Inspect the vagina and vulva and keep in mind the prevalence of benign developmental and acquired cystic lesions. Exclude vaginal focal or diffuse vaginal wall thickening and note intraluminal fluid if present.

Look for the ovaries, often a difficult task owing to their small size in prepubertal and

older women and to their variable location. The presence of ovarian cysts often attracts the examiner's attention to their location. In the absence of an easily identifiable ovariform structure, remember the relevant anatomy tethering the ovaries in the pelvis (Fig. 5-7). The suspensory ligament contains the vascular structures and originates from the pelvic sidewall in the region of the iliac bifurcation connecting to the ovary. The round "ligament" (actually composed

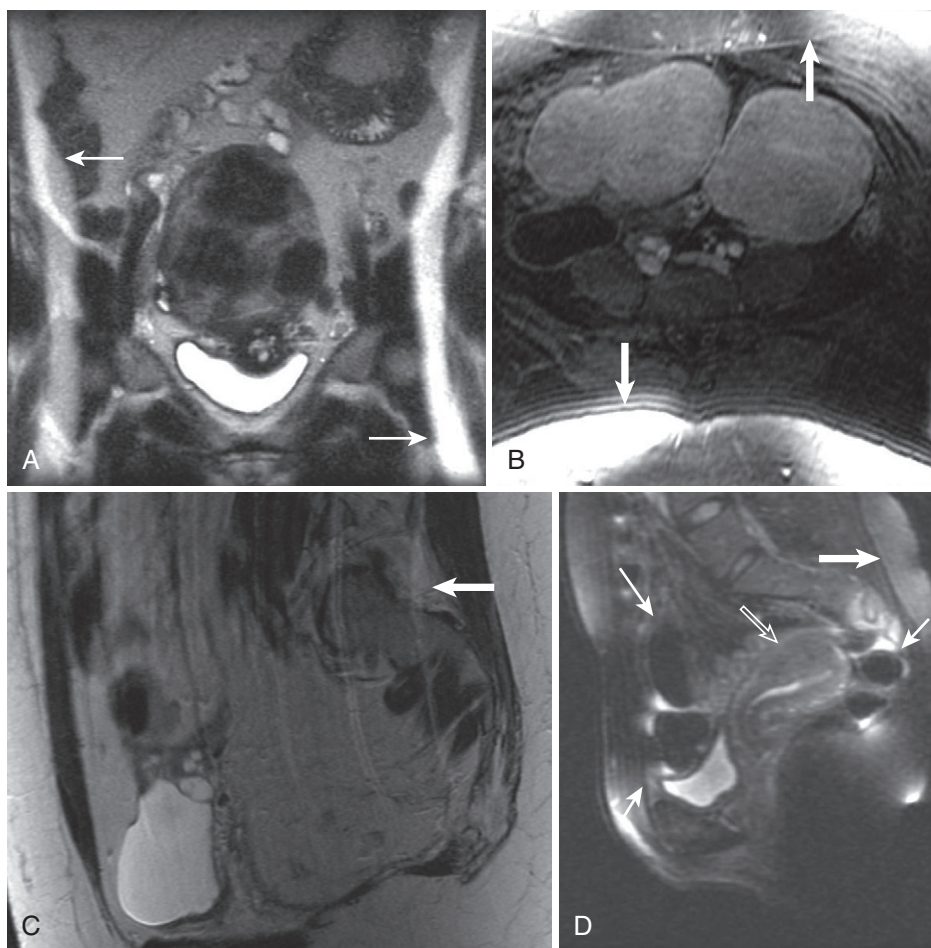


FIGURE 5-6. Image degradation due to artifacts. A and B, Coronal T2-weighted (A) and axial T1-weighted fat-saturated gradient echo (B) images depict wraparound artifact along the phase encoding axis (arrows in A and B), which do not obscure underlying anatomy and reflect selection of a small field of view resulting in aliasing of subcutaneous fat. C, Sagittal T2-weighted image mildly degraded by breathing motion artifact along the phase encoding axis (arrow). D, A combination of susceptibility artifact (thin arrows) and failure of fat suppression (thick arrows) degrades this sagittal T2-weighted fat saturated image in a patient with a focal fundal adenomyoma (open arrow).

largely of smooth muscle) is the female equivalent of the spermatic cord and courses from the uterine cornua into the inguinal canal through the deep inguinal ring in an effort to maintain anteversion. The proper ovarian ligament originates adjacent to the round ligament but, unfortunately, usually averts detection as a discrete structure. Measure the ovaries in three planes and record measurements of any associated ovarian lesions.

Parenthetically, MRI occasionally supplements ultrasound in detecting acute ovarian/adnexal pathology. Under acute circumstances, consider the possibility of (ectopic) pregnancy, tubo-ovarian abscess (TOA), torsion, and rupture of a preexisting ovarian lesion (such as dermoid)

TABLE 5-5. Acute Adnexal Pathology

Ectopic pregnancy
Ovarian torsion
Tubo-ovarian abscess
Ruptured cystic lesion (e.g., ruptured dermoid cyst)
Fibroid degeneration

(Table 5-5). Pay particular attention to fluid-sensitive sequences (such as T2-weighted fat-saturated and inversion recovery sequences), which most vividly portray the edema, inflammation, and/or fluid almost always associated with acute pathology.

Assess the quantity of free fluid in the pelvis and remember that a small quantity is

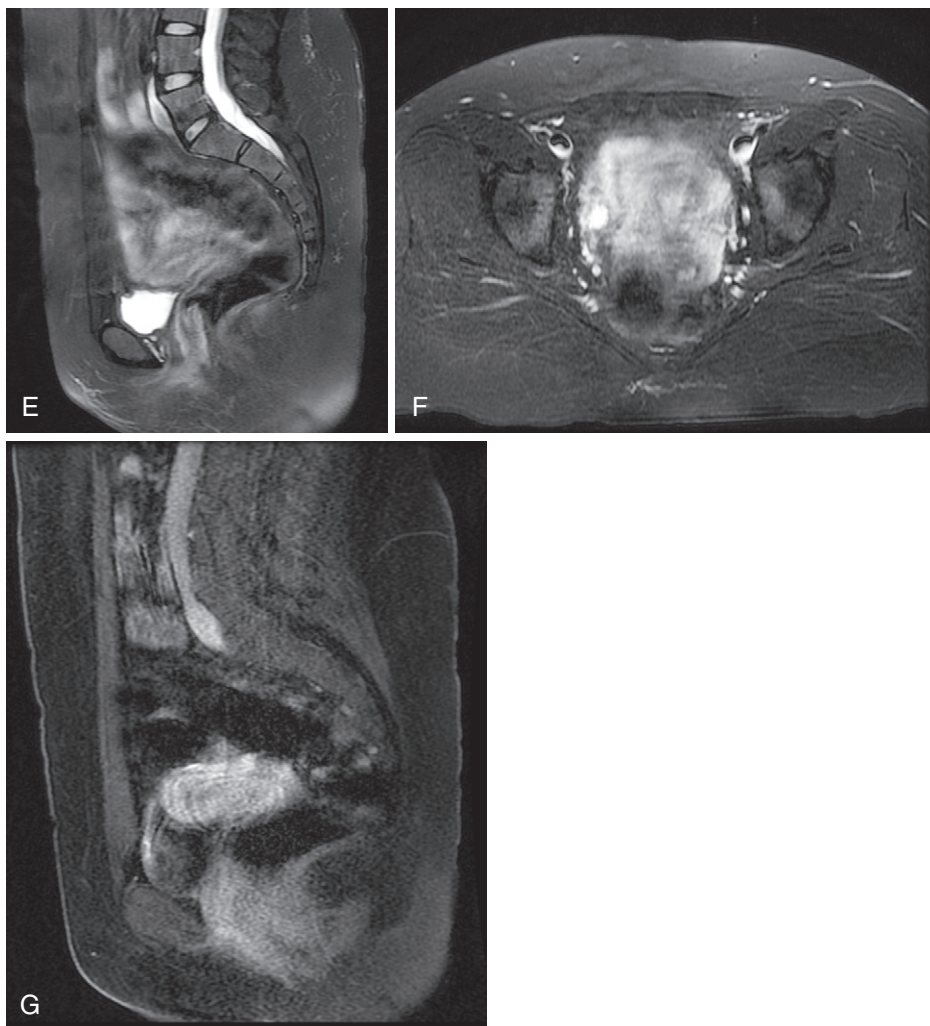


FIGURE 5-6, cont'd E-G, Artifact arising from bowel peristalsis blurs and obscures normal pelvic anatomy with no evidence of gross patient motion.

physiologic in reproductive-age females. Especially if there is a history of (ovarian) carcinoma, exclude the presence of peritoneal thickening, enhancement, or nodularity/implants. Look for pelvic lymph nodes and record any enlarged nodes.

Although the bladder is often not optimally evaluated because of incomplete distention (usually patients are instructed to void in order to promote comfort and obviate motion for the duration of examination), do not ignore it. Observe any focal lesions, filling defects/stones, wall thickening, or diverticula. Check the urethra for diverticula.

Trace the bowel from the anus proximally as far as possible. Look at the coronal images, which are often performed with the largest field of view to visualize as much of the bowel and

peritoneal cavity as possible. View sagittal and coronal images to assess for pelvic floor laxity.

Finally, use T1-weighted and fluid-sensitive sequences to exclude osseous lesions. Sagittal images are useful to detect disk pathology in the lower lumbar spine. Evaluate muscles and tendons (such as the gluteal, adductor, and hip flexor muscles and iliopsoas, rectus femoris, and hamstring tendons) on T2-weighted axial and coronal sequences.

UTERUS

Normal Features

In medical parlance, “uterus” signifies the uterus body or corpus and “cervix” refers to the uterine cervix. Before you can intelligently comment on

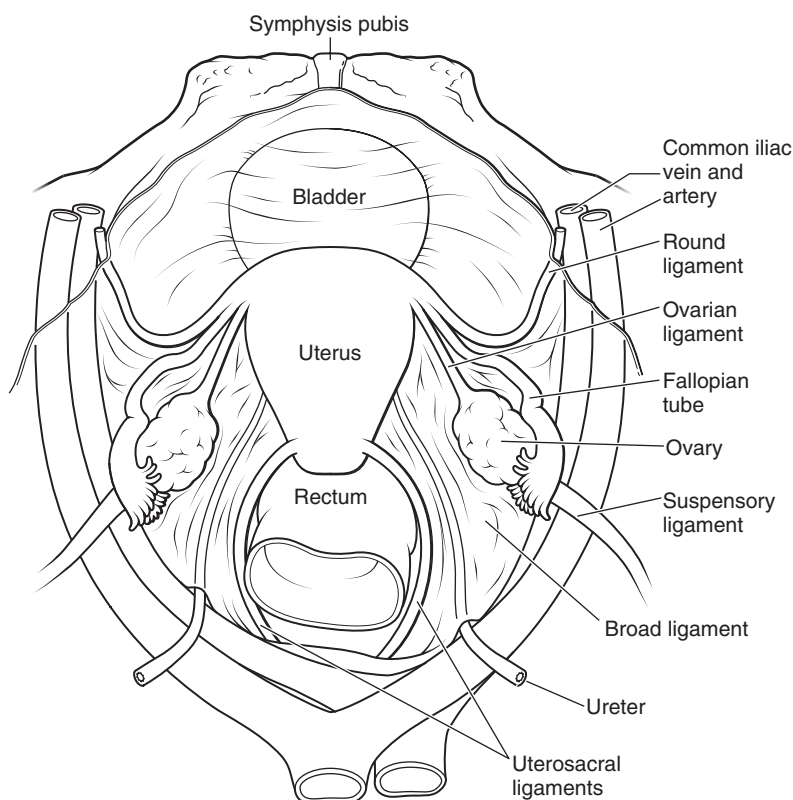


FIGURE 5-7. Adnexal ligamentous anatomy.

TABLE 5-6. Normal Dimensions of the Ovaries and Uterus

Uterus reproductive age: 8 × 5 cm
Uterus premenarchal and postmenopausal: 5 × 2 cm
Endometrium
Proliferative: 3–8 mm
Secretory: 5–16 mm
Postmenopausal (no bleeding): ≤8 mm
Postmenopausal (bleeding): ≤5 mm
Ovaries (volume = 0.523 × length × width × thickness)
Premenstrual: 3.0 mL
Reproductive age: 9.8 mL
2.5–5.0 × 1.5–3.0 × 1.0–2.0 cm
Postmenopausal: 5.8 mL

the status of the (body of the) uterus you need to know the age and menstrual status of the patient and any relevant surgical history. The size of the uterus is a function of age and reproductive/menstrual history (Table 5-6).³⁻⁵ Without the stimulating effects of female hormones before puberty, cervical stature exceeds uterine size. Measure the uterus in three orthogonal dimensions along its axis and comment on uterine positioning or flexion (anteversion, retroversion, anteflexure, or retroflexure) (Fig. 5-8).

Try to appreciate the zonal anatomy or mural stratification of the uterus, which is most developed in reproductive-age females (Fig. 5-9; see also Fig. 5-1) and fades during menopause. Endometrial cyclical changes occur only in menstruating females; in premenopausal and postmenopausal females, the endometrial changes are only incurred by pathologic or iatrogenic phenomena and normally measure up to 4 to 5 mm in maximal thickness. In menstruating females, endometrial thickness is variable.⁶ From the proliferative phase, the endometrium thickens from a minimum of 3 to 8 mm to 5 to 16 mm during the secretory phase. Notwithstanding age and menstrual status, normal endometrium demonstrates uniformly homogeneously near-fluid hyperintensity on T2-weighted images.

If the appearance and/or thickness falls outside the normal range, try to characterize the abnormality as intracavitary fluid or gas versus a focal or diffuse process. Fluid is a frequent and generally nonpathologic finding in menstruating females. Prepubertal endometrial fluid generally indicates an obstructing lesion (hydrometrocolpos or hydrocolpos). Postmenopausal patients with endometrial fluid often harbor an underlying endometrial or

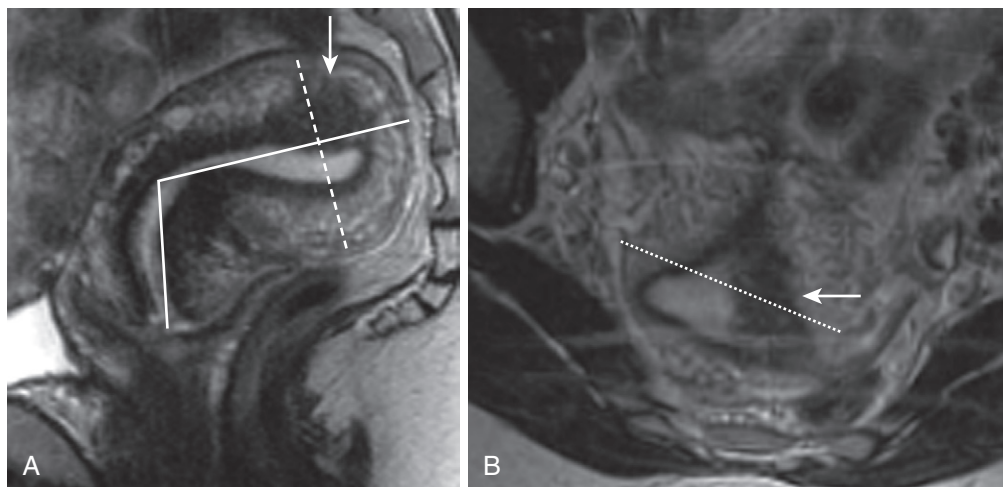


FIGURE 5-8. Uterine measurement technique and assessment of anteversion/retroversion/anteflexure/retroflexure. Sagittal (A) and axial (B) T2-weighted images of a retroverted uterus illustrate the measurement technique for obtaining the longitudinal (*solid line*), height (*dashed line*) and width (*dotted line*) measurements. Note the focal adenomyoma (*arrow*).

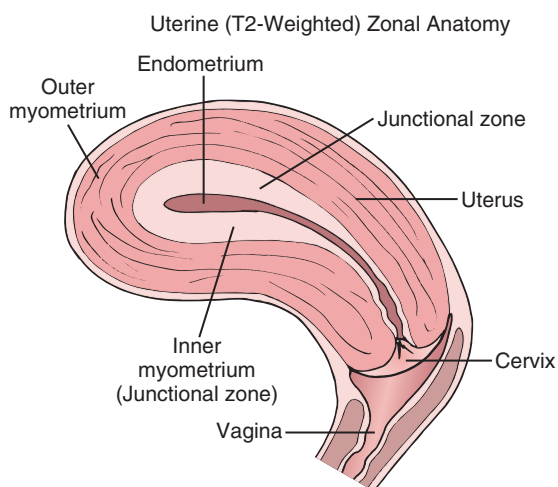


FIGURE 5-9. Zonal anatomy/mural stratification of the uterus.

cervical lesion (such as endometrial atrophy, hyperplasia, polyp or carcinoma, and cervical stenosis), but fluid has not been conclusively proved to be pathologic.⁷ Gas may be present postprocedurally, postpartum, or in the context of infection (endometritis). Gas induces susceptibility artifact and is most conspicuous on gradient echo sequences.

Endometrial Pathology

DIFFUSE ABNORMALITIES

Diffuse endometrial abnormalities include predominantly endocrinologic/proliferative, infectious, iatrogenic, and neoplastic etiologies (Fig. 5-10). Global alteration in thickness or

homogeneity of the T2 hyperintense endometrial layer is the common denominator.

ENDOMETRITIS

Endometritis falls into two main categories—postpartum and non-postpartum. Endometritis most commonly follows vaginal delivery, especially with prolonged rupture of membranes, chorioamnionitis, prolonged labor, and retained products of conception. Risk factors for non-postpartum endometritis include uterine artery embolization (UAE), venereal disease, and presence of an intrauterine device (IUD). Whereas endometritis usually relies on clinical findings for diagnosis, imaging studies exclude additional abnormalities in patients with refractory symptoms. Typical findings include diffuse uterine enlargement, intracavitary gas and (often complex) fluid, and a thickened, heterogeneous endometrium.⁸ Look for edematous, relatively hypovascular foci subjacent to the abnormal endometrium.

HORMONAL FACTORS

Hormonal (endogenous and iatrogenic) etiologies account for another major cause of diffuse endometrial abnormality. Endometrial hyperplasia generally arises from unopposed estrogen, a potential etiology of diffuse endometrial thickening and heterogeneity without associated gas (and less likely) intracavitary fluid. Remember that hormonal stimulation due to pregnancy (including ectopic pregnancy) results in endometrial thickening.

DIFFUSE ENDOMETRIAL ABNORMALITIES

Endocrinologic/ proliferative	Infectious	Iatrogenic	Neoplastic
Polycystic ovarian syndrome	Postpartum endometritis	Exogenous estrogen	Endometrial carcinoma
Pregnancy	Non-postpartum endometritis	Tamoxifen	Cervical carcinoma
Obesity			

FIGURE 5-10. Diffuse endometrial abnormalities.

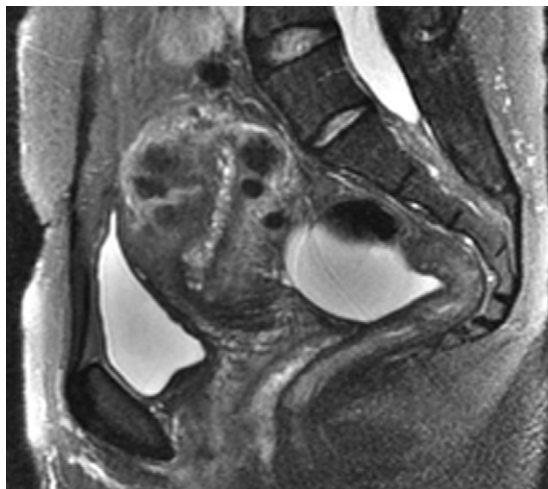


FIGURE 5-11. Endometrial tamoxifen changes. The sagittal T2-weighted fat-suppressed image in a patient on tamoxifen shows the typical cystic endometrial thickening.

TAMOXIFEN

Tamoxifen (adjunctive treatment for metastatic breast cancer) possesses estrogenic activity, stimulating the endometrium. In addition to endometrial hyperplasia, tamoxifen engenders a number of endometrial abnormalities, including polyps, cystic atrophy, and endometrial carcinoma. The presence of multiple cystic foci associated with diffuse heterogeneous endometrial thickening typifies tamoxifen change (Fig. 5-11). The definition of endometrial thickening in the setting of tamoxifen defies precise limits. The general consensus suggests an upper limit of 8 to 9 mm.⁹ If vaginal bleeding coexists, hysteroscopy and biopsy are pursued. Remember the increased risk of nonendometrial abnormalities, such as endometriosis and adenomyosis, with tamoxifen use.¹⁰

FOCAL ABNORMALITIES

Focal endometrial abnormalities include a wide range of pathology most of which manifests specific MRI features. Most of these lesions are

either iatrogenic, neoplastic (benign and malignant), or pregnancy-related (Fig. 5-12). Focal iatrogenic lesions—intrauterine adhesions (Asherman's syndrome) and intrauterine devices (IUDs)—do not pose a diagnostic dilemma. Pregnancy-related lesions, such as retained products of conception, GTD, and the gestational sac itself, rarely provoke MRI and fall outside the scope of this text. Neoplastic lesions encompass primary endometrial lesions, such as endometrial polyps and endometrial carcinoma, and myometrial-derived lesions with endometrial extension, such as submucosal fibroids.

INTRAUTERINE ADHESIONS

Intrauterine adhesions, also known as Asherman's syndrome, manifests as multiple linear intracavitary enhancing hypointensities, bridging the normal hyperintense endometrium (Fig. 5-13). These endometrial adhesions reflect the sequela of endometrial trauma from curettage, cesarean section, myomectomy, irradiation, IUD, or endometritis. Patients may be asymptomatic or present with menstrual disorders, such as secondary amenorrhea, or infertility. Few lesions simulate the appearance of intrauterine adhesions and their common denominator is T2 hypointensity—submucosal fibroids, endometrial polyps, IUDs, and occasionally blood clots. The central fibrous core of a polyp and the susceptibility artifact-inducing linear/tubular shape of IUDs simulate the linear hypointensity of intrauterine synechiae but lack the perpendicular orientation spanning the endometrial cavity. Fibroids and blood clots lack the linear morphology and the predictable orientation.

INTRAUTERINE DEVICE

IUDs do not present diagnostic difficulty. Endocavitary linear hypointensity on all pulse sequences signals the presence of an IUD (Fig.

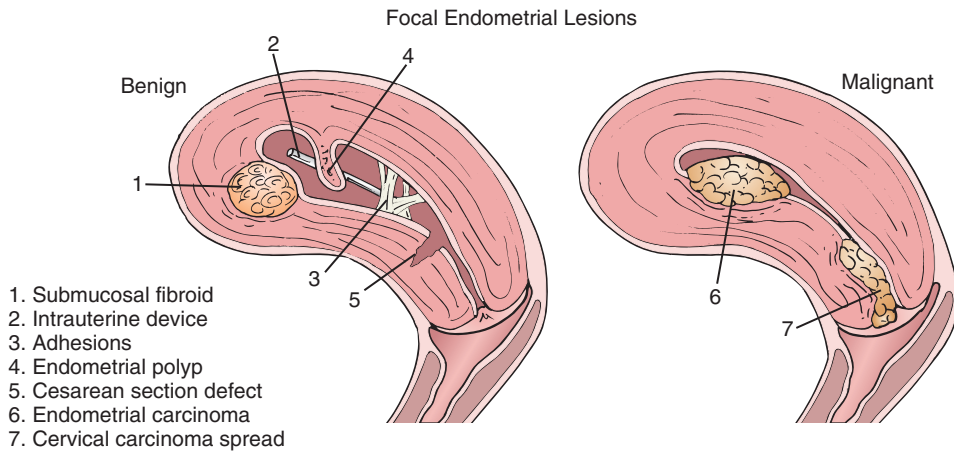


FIGURE 5-12. Differential diagnosis of focal endometrial abnormalities.

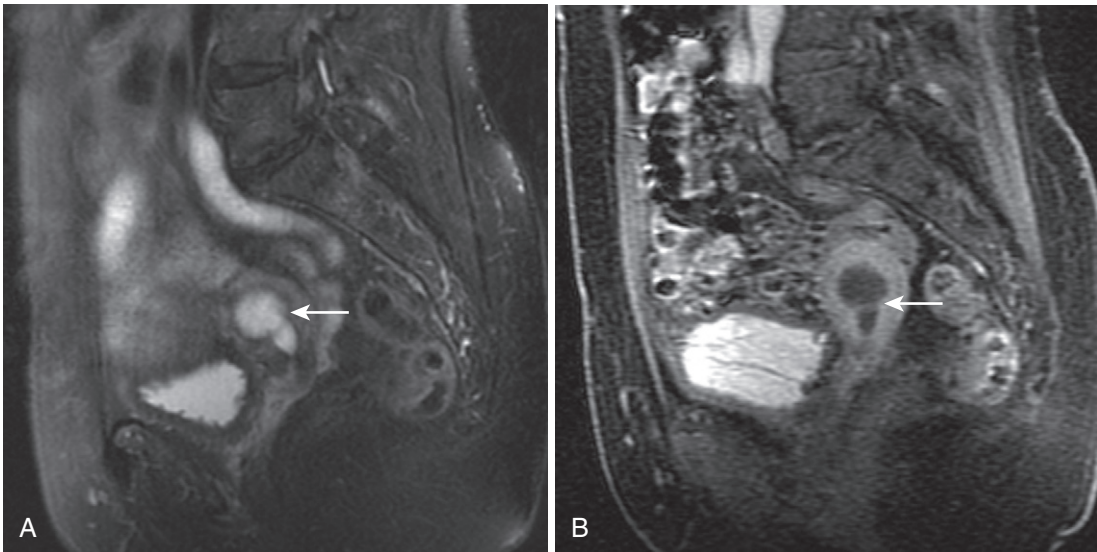


FIGURE 5-13. Intrauterine adhesions. Sagittal T2-weighted fat-saturated (A) and T1-weighted fat-saturated postgadolinium gradient echo (B) images show fluid distention of the endometrial canal proximal to an adhesion at the level of the internal cervical os (arrow).

5-14). The perfect linearity virtually excludes organic etiologies.

CESAREAN SECTION DEFECT

The most common lesion in the category of iatrogenic lesions is the cesarean section defect. Because of its ubiquity, an awareness of the typical appearance of the cesarean section scar is essential. The changes are best appreciated on sagittal T2-weighted images as focal thinning of the anterior myometrium in the lower uterine segment just above the internal cervical os with or without a fluid triangular hyperintensity projecting into the defect continuous with adjacent endometrium (Fig. 5-15). Alternative etiologies are easily excluded, such as

adenomyosis—which might exhibit intralesional hyperintensities, but not myometrial thinning—and myometrial cysts, which also do not exhibit myometrial thinning and are generally spherical in morphology. Extreme uterine anteversion simulates the defect at the point of flexion with maintenance of the integrity of the myometrial layer (Fig. 5-16).

ENDOMETRIAL POLYP

The endometrial polyp is among the most common focal endometrial abnormalities. Endometrial polyps conceptually represent focal glandular and stromal hyperplasia covered by endometrium and come in different varieties (hyperplastic, atrophic, functional, and

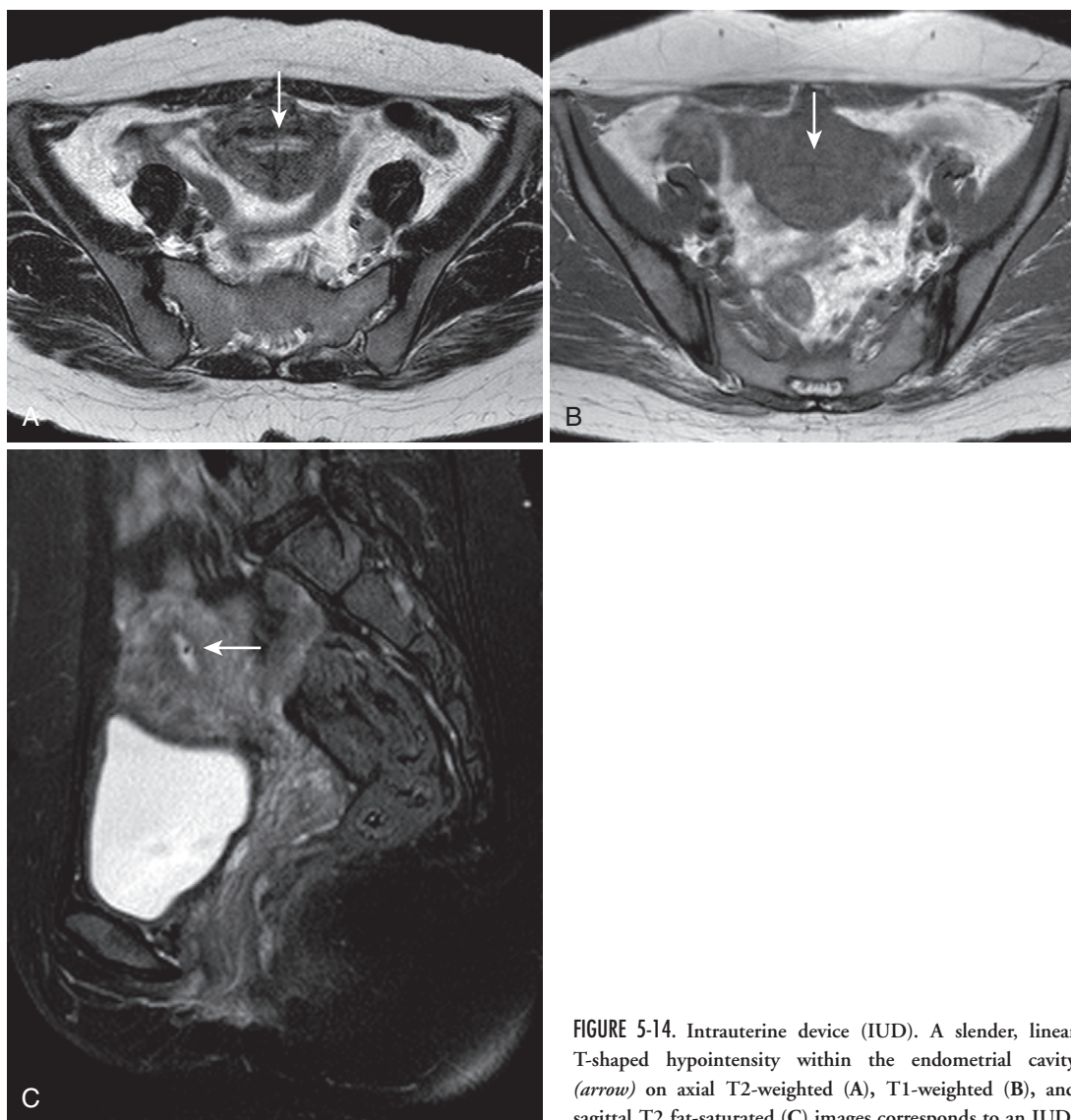


FIGURE 5-14. Intrauterine device (IUD). A slender, linear T-shaped hypointensity within the endometrial cavity (*arrow*) on axial T2-weighted (A), T1-weighted (B), and sagittal T2 fat-saturated (C) images corresponds to an IUD.

adenomyomatous). Discrimination from endometrial carcinoma, let alone between the different types of polyps, is academic. Despite the accuracy of MRI, definitive exclusion of endometrial carcinoma defies imaging capabilities and excision is always recommended. Nonetheless, certain features suggest the diagnosis, including pedunculated (occasionally sessile) morphology, a cornual or fundal point of endometrial attachment, intralesional cystic foci, a T2 hypointense central fibrovascular core, and lacy enhancement (Fig. 5-17; see also Fig. 5-2C and D). These features render the endometrial polyp conspicuous against the hyperintense, hypovascular endometrium and, when present, suggest the diagnosis, but not at the expense of biopsy—

ultimately, discrimination from endometrial carcinoma requires tissue sampling.

ENDOMETRIAL CARCINOMA

Unfortunately, research has not substantiated the ability of MRI (or other imaging modalities) to differentiate endometrial carcinoma from endometrial polyps (or other benign endometrial pathology) with enough confidence to obviate biopsy. Nonetheless, practically speaking, endometrial carcinoma is unlikely to simulate the pedunculated morphology of a polyp and is usually infiltrative and does not contain a central hypovascular core or intralesional cystic foci. Endometrial carcinoma more closely approximates the appearance of diffuse

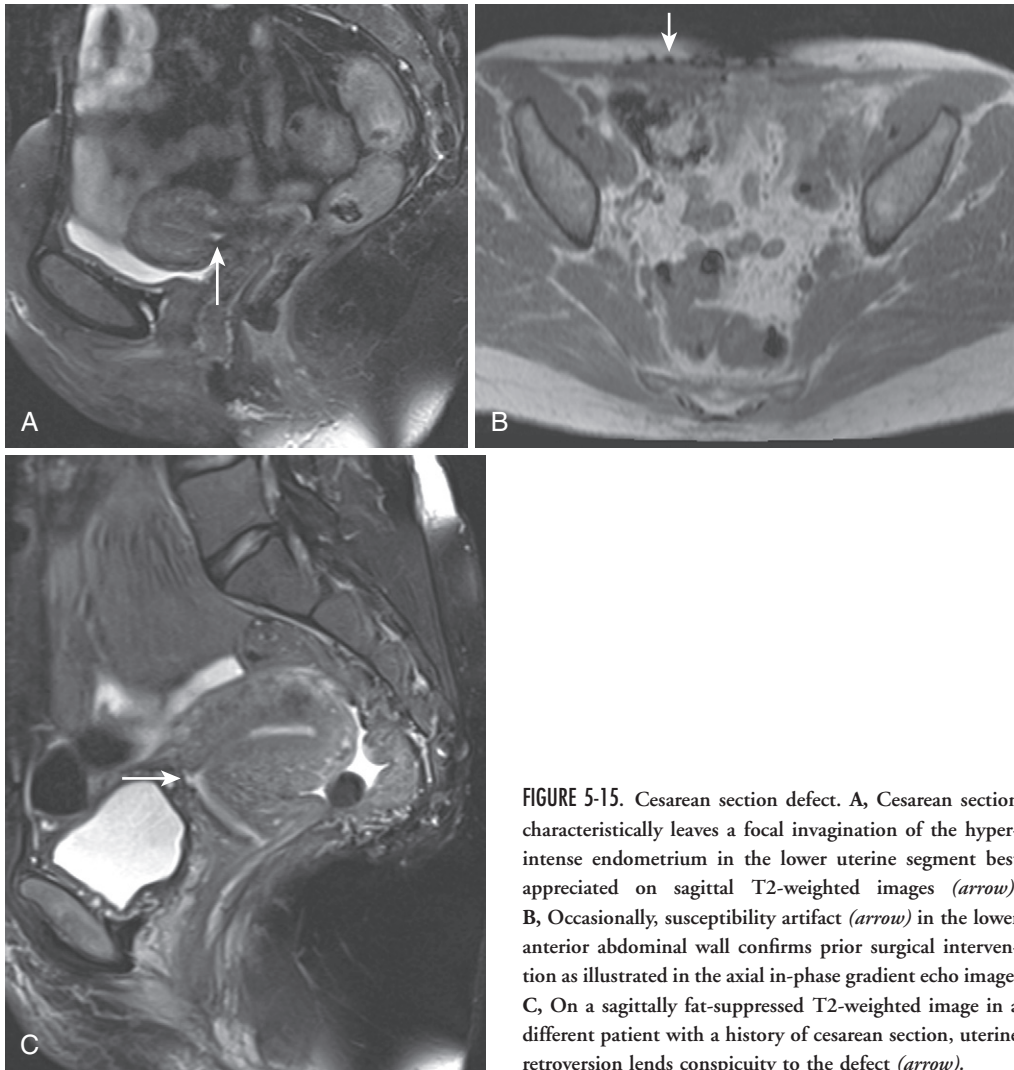


FIGURE 5-15. Cesarean section defect. A, Cesarean section characteristically leaves a focal invagination of the hyperintense endometrium in the lower uterine segment best appreciated on sagittal T2-weighted images (*arrow*). B, Occasionally, susceptibility artifact (*arrow*) in the lower anterior abdominal wall confirms prior surgical intervention as illustrated in the axial in-phase gradient echo image. C, On a sagittally fat-suppressed T2-weighted image in a different patient with a history of cesarean section, uterine retroversion lends conspicuity to the defect (*arrow*).

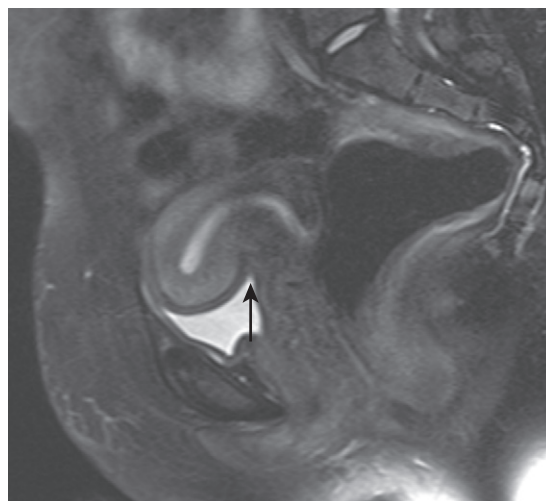


FIGURE 5-16. Extreme uterine anteversion and anteversion simulate cesarean section. The apparent defect in the lower anterior myometrium (*arrow*) on the sagittal T2-weighted fat-suppressed image is a consequence of anteversion superimposed on anteversion. The lack of associated endometrial protrusion confirms the artifactual nature of this finding.

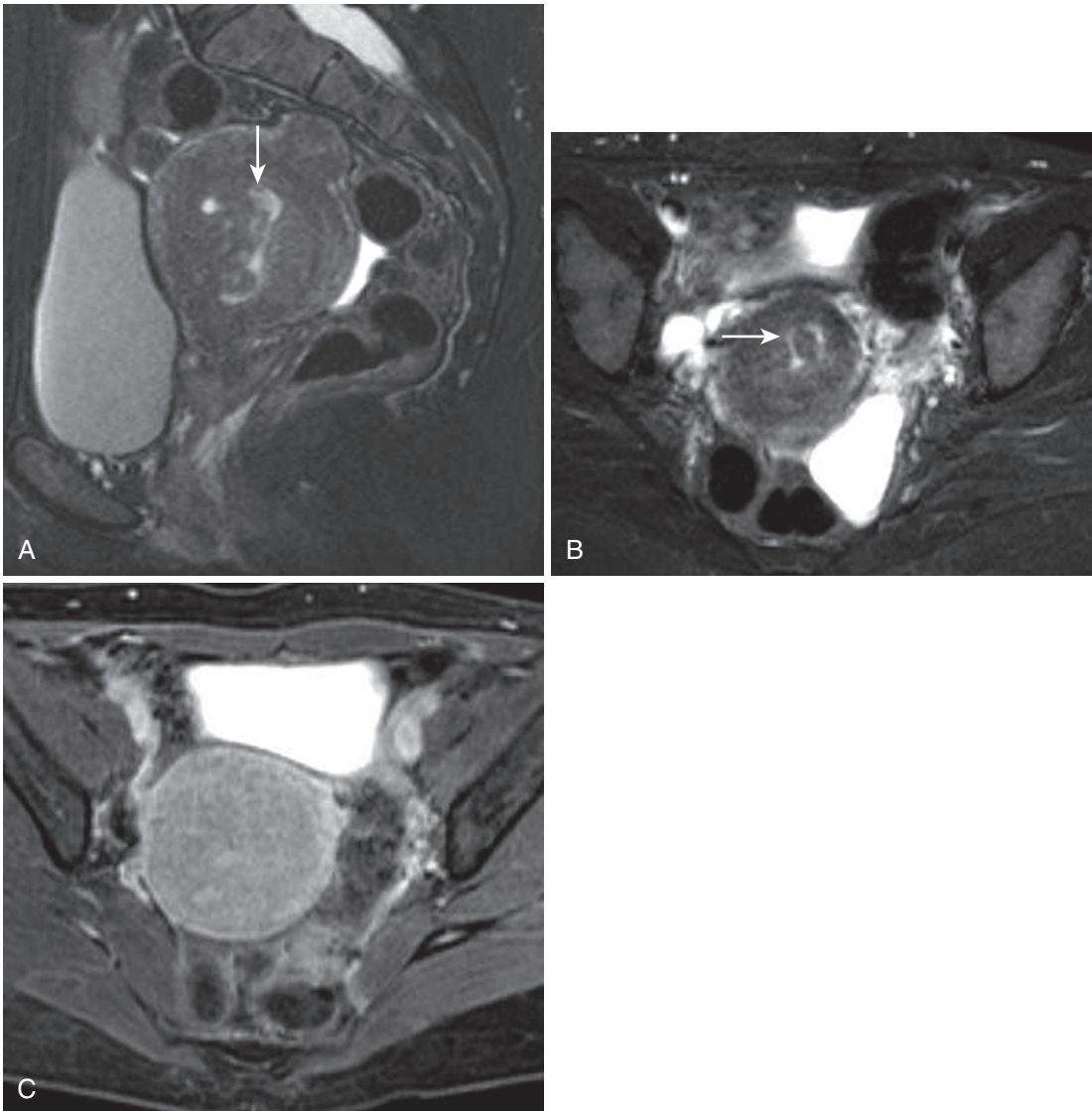


FIGURE 5-17. Endometrial polyp. Sagittal (A) and axial (B) T2-weighted images reveal a tubular isointense structure with cystic foci within the endometrial canal (*arrow*). C, On the axial T1-weighted fat saturated postgadolinium image, the lesion is not clearly discriminated from the adjacent myometrium, indicating moderate enhancement.

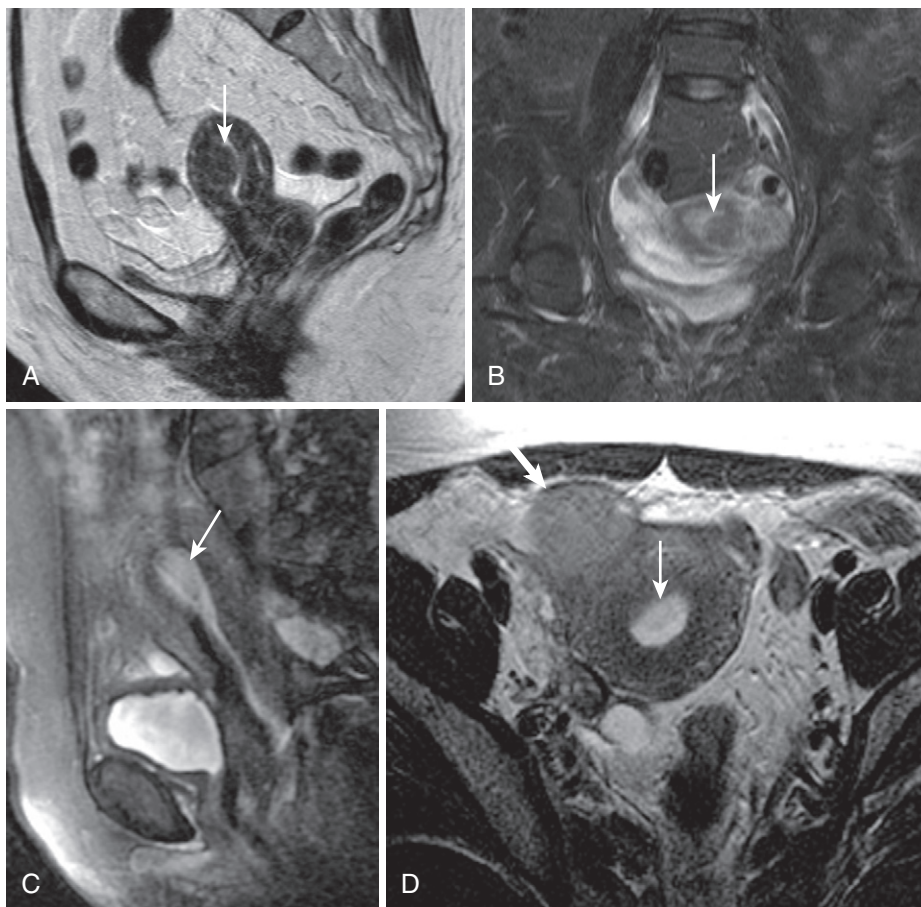


FIGURE 5-18. Endometrial carcinoma (pedunculated type). **A**, Sagittal T2-weighted image reveals an isointense lesion indenting the anterior endometrial contour (*arrow*). **B**, Coronal T2-weighted fat-saturated image corroborates distortion of the endometrium (*arrow*). The appearance simulates an endometrial polyp (see Fig. 5-17). **C-G**, Compare the appearance with the endometrial polyp in a different patient.

thickening due to hyperplasia (or tamoxifen use), and even then, clinical factors may suggest the diagnosis. Notwithstanding, whenever a focal lesion or diffuse thickening is noted and unless the abnormality conforms to a short list of obvious benign and/or incidental lesions, such as submucosal fibroid, IUD, or simple fluid, tissue sampling follows.

The variable MRI features of endometrial carcinoma reflect its protean growth patterns, degree of myometrial invasion, and stage. Whereas many subtypes of endometrial carcinoma exist, adenocarcinoma prevails, accounting for 90% of cases and histologic subtype has not been shown to correspond to specific imaging features (Table 5-7).

A few generalities typify the MRI appearance of endometrial carcinoma. Endometrial

TABLE 5-7. Clinical and Histologic Features of Endometrial Carcinoma

Endometrioid adenocarcinoma (75–80%)
Vary from well-differentiated to undifferentiated (grade 1–3)
Low-grade ⇒ estrogen-related endometrial hyperplasia (younger perimenopausal)
Serous papillary carcinoma (5–10%)
Older women
Atrophic endometrium
Aggressive
Predislection for myometrial and vascular invasion
Clear cell carcinoma (3–5%)
Older patients
Dismal prognosis
Mucinous adenocarcinoma
Squamous cell carcinoma
Miscellaneous rare
Mixed cell type carcinoma
Choriocarcinoma
Endodermal sinus tumor
Small cell carcinoma
Metastatic carcinoma

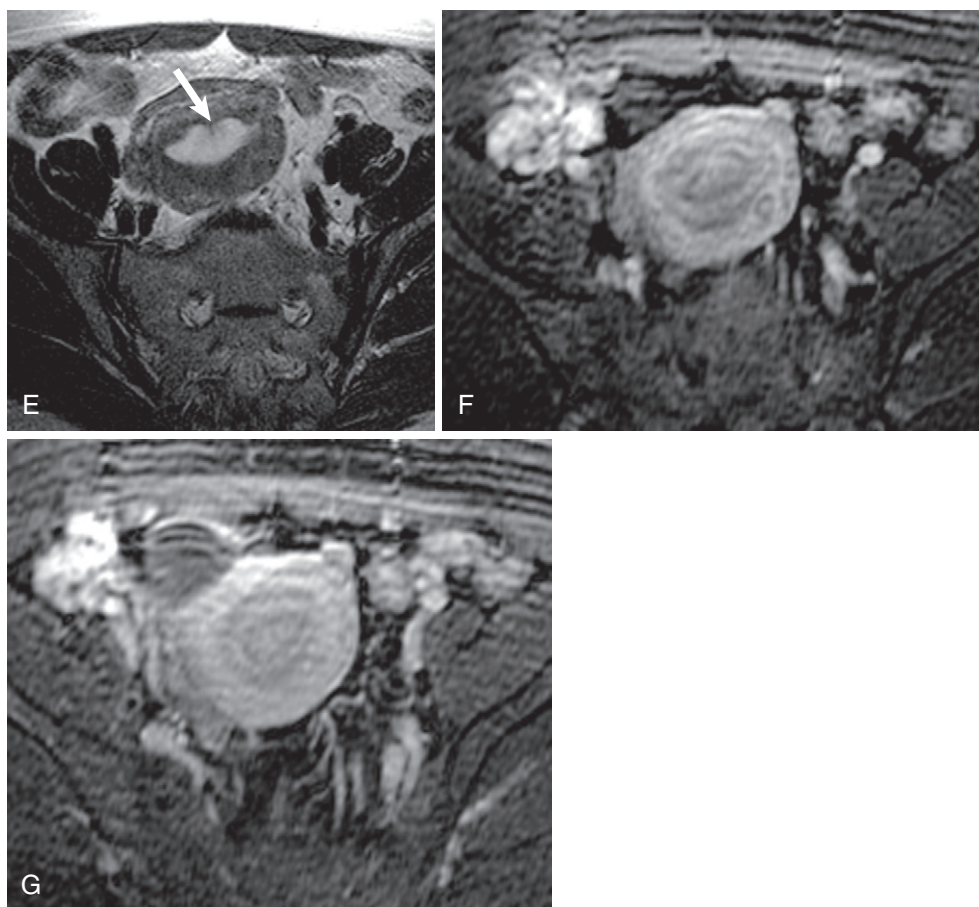


FIGURE 5-18, cont'd The sagittal fat-suppressed (C) and axial (D and E) T2-weighted images reveal a more hyperintense tubular lesion (*thin arrow* in C and D) with a well-defined stalk with a hypointense core (*thick arrow* in E). Early (F) and delayed (G) enhanced images show clear delineation of the mass and lacy or textured and more avid enhancement compared with endometrial carcinoma. Note the T2 hypointense (shading) right adnexal lesion—an endometrioma—abutting the anterior uterine fundus (*thick arrow* in D).

carcinoma begins as a mass arising from the endometrium ultimately expanding the endometrial cavity. Growth patterns generally conform to either infiltrative or sessile polypoid (Figs. 5-18 and 5-19; see also Fig. 5-2A and B) types, which is why biopsy ensues whenever endometrial thickening or focal pedunculated lesion is identified. The lesion evades detection on (unenhanced) T1-weighted images and is more conspicuous on T2-weighted images. Endometrial carcinoma is usually heterogeneously isointense to mildly hyperintense on T2-weighted images, rendering it visible compared with hypointense inner myometrium (junctional zone). Endometrial carcinoma is a

relatively hypovascular lesion with gradual enhancement. Hypovascularity is best depicted on the early/arterial phase of the dynamic sequence; the avidly enhancing normal myometrium highlights the relatively hypointense lesion and the discrepancy in intensity generally fades over time (Fig. 5-20). Margins are generally indistinct and the lesion expands the endometrial cavity with continued growth (Table 5-8). Whereas the location strongly suggests endometrial origin, keep in mind the overlap in imaging features with cervical carcinoma, which occasionally extends into the endometrial cavity, simulating endometrial carcinoma.

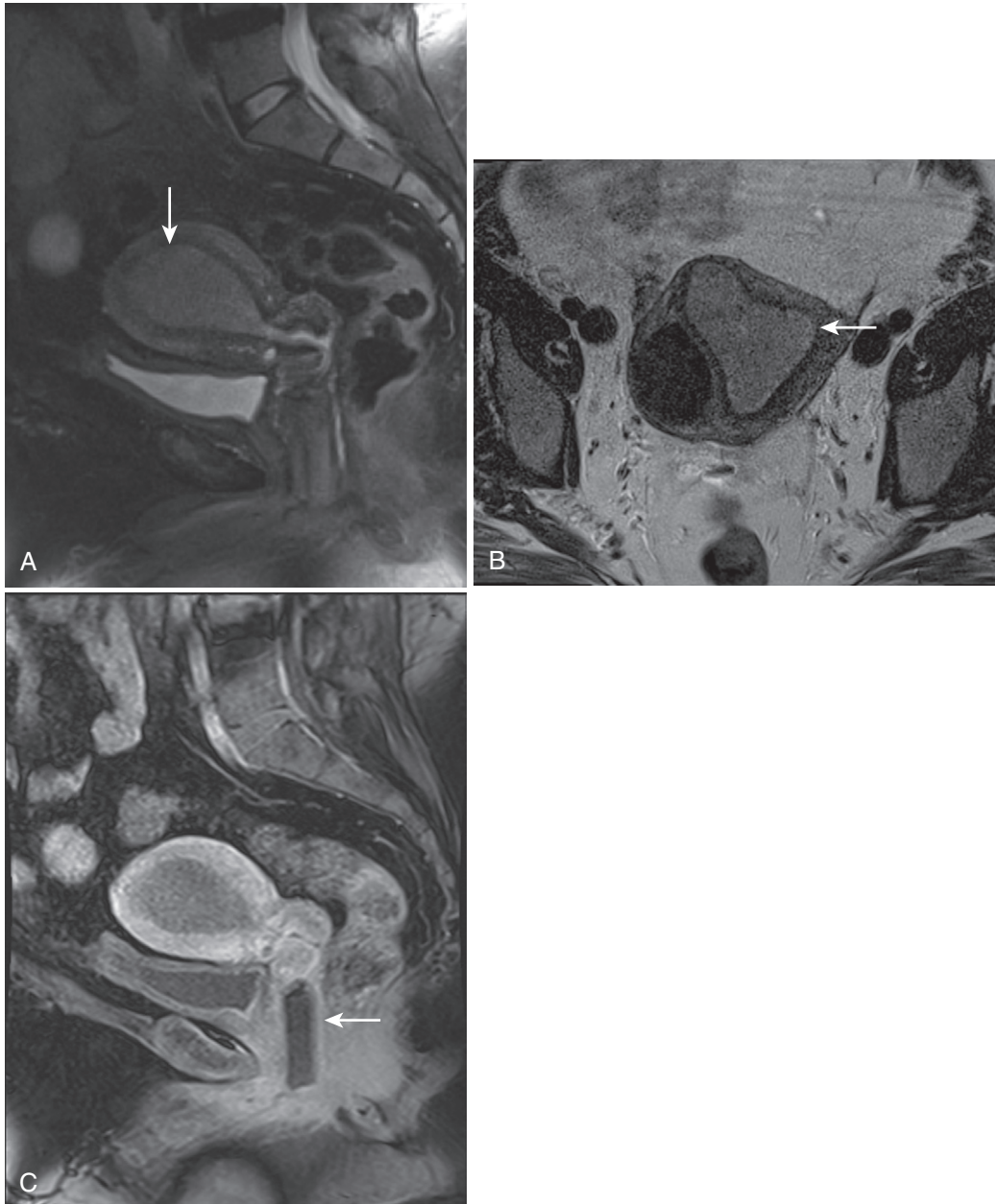


FIGURE 5-19. Endometrial carcinoma (sessile type). Sagittal T2-weighted fat-suppressed (A) and axial T2-weighted (B) images depict a mildly hyperintense endometrial mass (*arrow*) within the hypointense junctional zone, indicating lack of deep myometrial invasion. C, Relative hypointensity of the mass after gadolinium administration indicates hypovascularity. Note susceptibility artifact arising from a tampon (*arrow*).

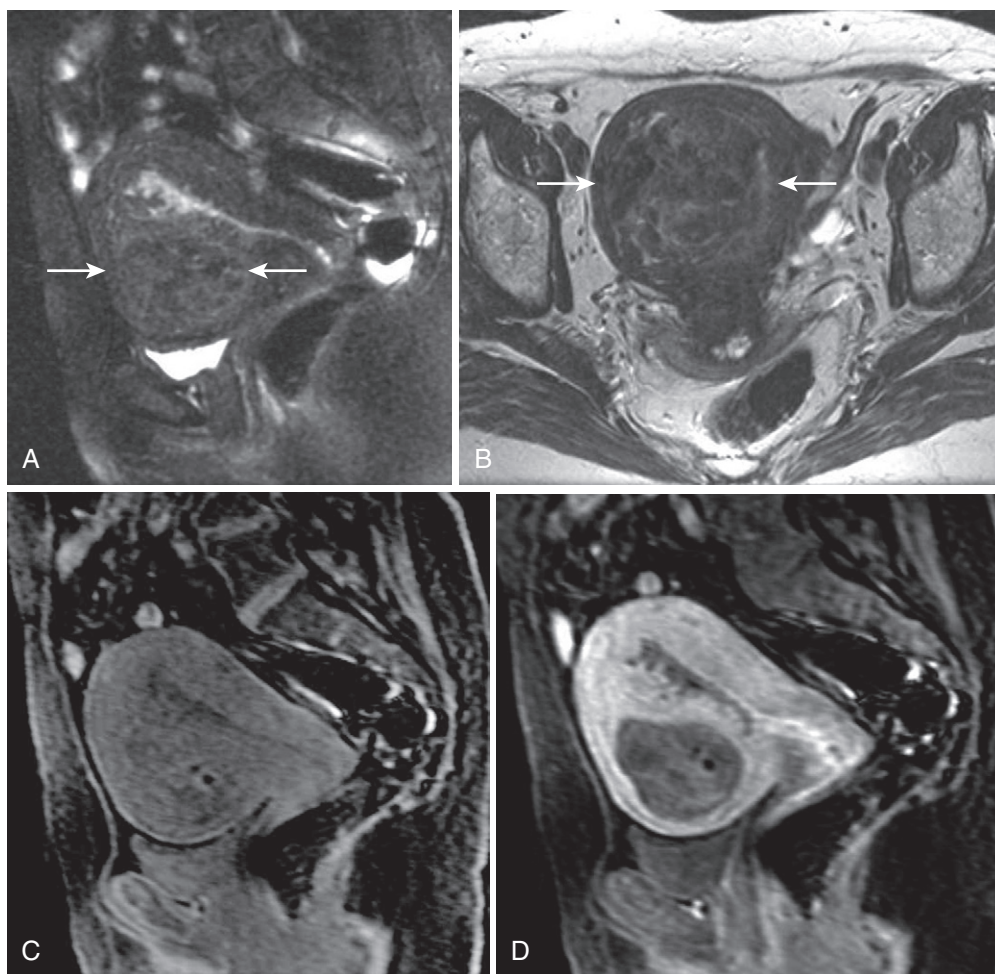


FIGURE 5-20. Endometrial carcinoma with myometrial invasion. Sagittal (A) and axial (B) T2-weighted images show a heterogeneous mass (*arrows*) centered in the anterior myometrium nearly reaching the serosal surface indicating deep myometrial invasion. Sagittal pregadolinium (C) and postgadolinium (D) T1-weighted fat saturated gradient echo images show marked lesion hypovascularity compared with enhancing myometrium (which exceeds the more commonly observed milder hypovascularity). The enhanced image vividly portrays the deep myometrial invasion (predicting distant metastatic spread).

TABLE 5-8. Imaging Features of Endometrial Carcinoma

Early ⇒ exophytic, spreading pattern
Later ⇒ myometrial invasion, cervical extension
Distant spread ⇒ direct (majority of local extraterine spread)
lymphatic (pelvic, para-aortic nodes)
hematologic (lungs, liver, bones, brain)
peritoneal/transubal (intraperitoneal implants)

However, staging rather than diagnosis of endometrial carcinoma is often the objective of MRI (Table 5-9). FIGO (International Federation of Gynecology and Obstetrics) recommends surgical staging (total abdominal hysterectomy

and bilateral salpingo-oophorectomy, peritoneal washings and/or pelvic lymphadenectomy). The depth of myometrial invasion and cervical extension predicts the likelihood of pelvic and para-aortic lymph node metastases. Presurgical knowledge of these factors potentially influences surgical technique, encouraging lymphadenectomy and adjuvant radiation and chemotherapy. Remember that endometrial cancer spreads by various pathways—direct invasion of the cervix, vagina, and myometrium; lymphatic dissemination to pelvic and para-aortic nodes; transluminal spread through the fallopian tubes into the peritoneal cavity; and hematogenous spread predominantly to the lungs, liver, and bone.

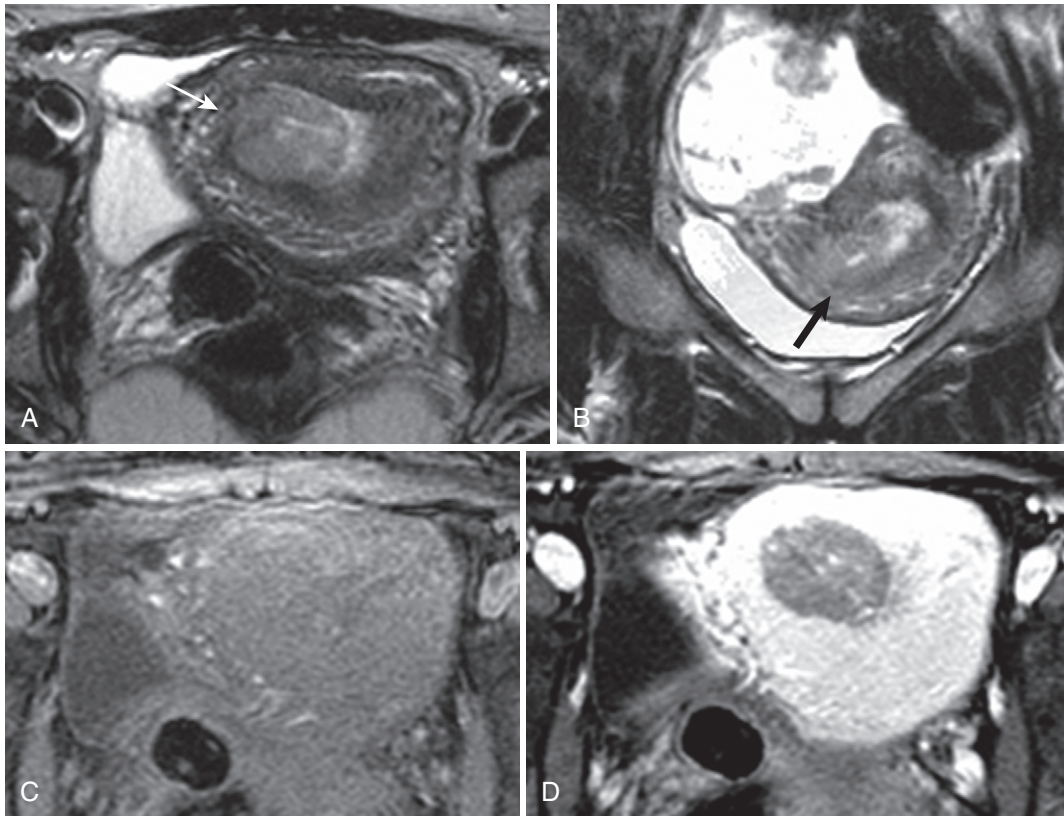


FIGURE 5-21. Endometrial carcinoma without and with myometrial invasion. Axial (A) and coronal (B) T2-weighted images show a mostly well-defined endometrial mass (*thin arrow* in A) focally invading the inner myometrium (junctional zone; *thick arrow* in B). Precontrast (C) and postcontrast (D) images reflect lesion hypovascularity and render exquisite tissue contrast, confirming absence of deep myometrial invasion.

TABLE 5-9. Staging of Endometrial Carcinoma

Stage IA: Tumor is limited to the endometrium.
Stage IB: Invasion of less than half the myometrium.
Stage IC: Invasion of more than half the myometrium.
Stage IIA: Endocervical glandular involvement only.
Stage IIB: Cervical stromal invasion.
Stage IIIA: Tumor invades serosa or adnexa, or malignant peritoneal cytology.
Stage IIIB: Vaginal metastasis.
Stage IIIC: Metastasis to pelvic or para-aortic lymph nodes.
Stage IVA: Invasion of bladder or bowel.
Stage IVB: Distant metastasis, including intra-abdominal or inguinal lymph nodes.

As a predictor of metastatic probability, the depth of myometrial invasion is of paramount importance (Fig. 5-21; see also Fig. 5-20). T2-weighted images and (early phase) postgadolinium images exceed all others in assessing

myometrial extension.^{11,12} Scrutinize the junctional zone; preservation of the junctional zone precludes deep myometrial invasion (>50%, or IC disease) and the concomitant likelihood of metastasis. Inspect the outer contour of the uterus to detect blurring of the normal sharp serosal margin. Wherever growth of tumor abuts an adjacent organ, such as the bladder or rectum, ensure that the tissue planes are preserved—the margins of each organ should be clearly identifiable. Do not forget to look for lymph nodes—nodes as small as 4 mm in short-axis diameter in the pelvis may potentially be pathologic.¹³

Other malignant endometrial lesions are extremely rare and beyond the scope of this text. Among these neoplasms are lesions such as metastases from direct extension of cervical (or vaginal) carcinoma (Fig. 5-22), endometrial stromal sarcomas, and mixed müllerian tumors.¹⁴ Gestational trophoblastic disease (GTD) is

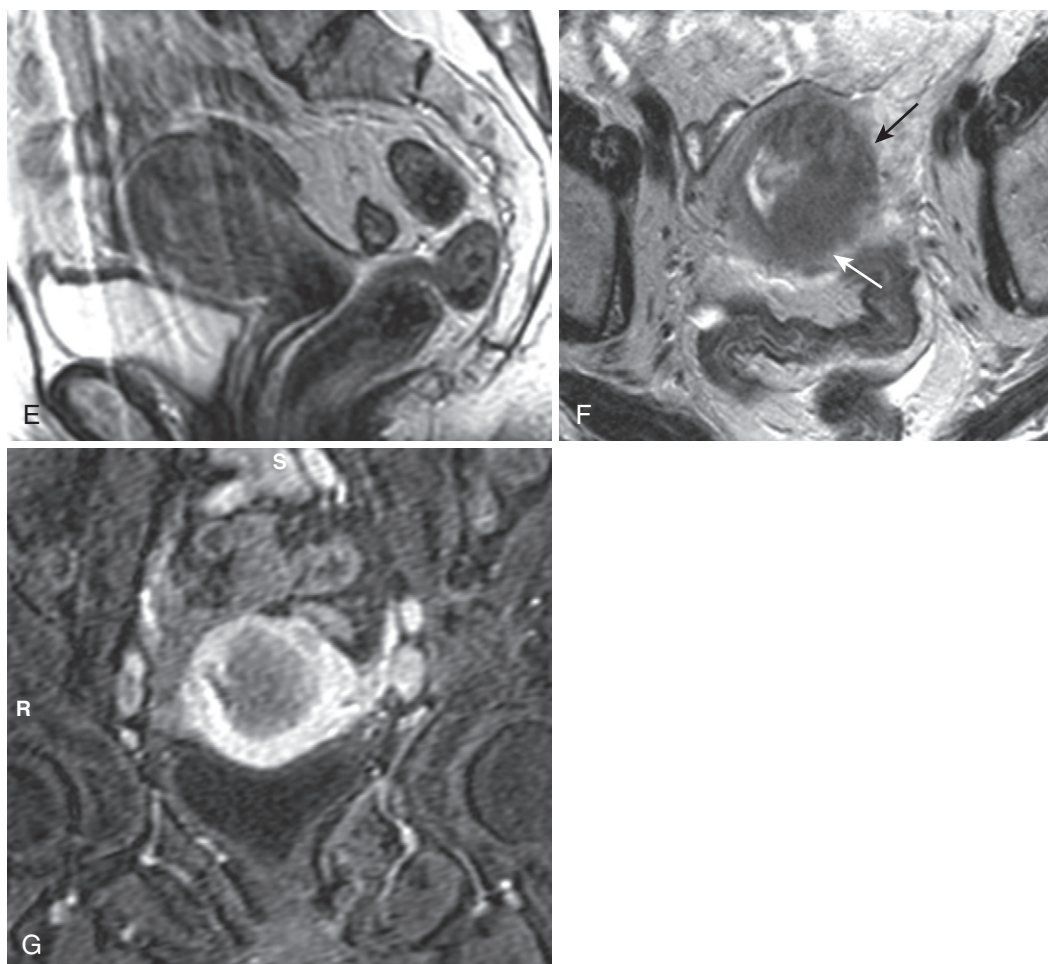


FIGURE 5-21, cont'd Sagittal T2-weighted image (E) in a different patient degraded by motion artifact poorly depicts uterine zonal anatomy, which is seen to be due to an infiltrative mass on the axial image (arrows in F). G, Coronal enhanced image demonstrates deep invasion of the enhanced myometrium by the hypovascular mass.

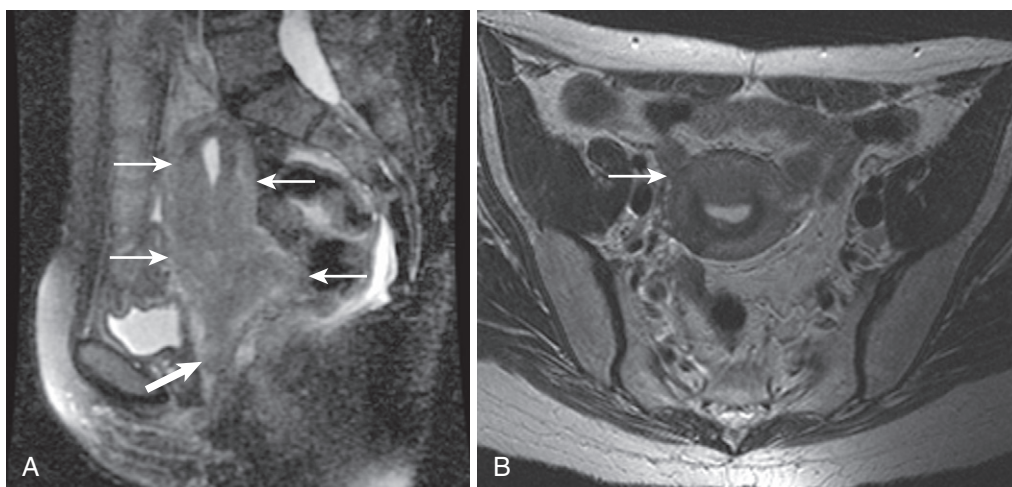


FIGURE 5-22. Cervical carcinoma extending cephalad to endometrium/uterus. A, Sagittal midline T2-weighted image depicts loss of the normal cervical and lower uterine mural stratification pattern as a consequence of an infiltrative mass (thin arrows) obscuring both the cervical fibrous stroma and the inner myometrium. The mass also extends into the upper vagina (thick arrow in A). B, Axial T2-weighted image through the level of the uterine body shows the infiltrative mass (arrow) obliterating the junctional zone and invading the myometrium.

hardly more common (0.5–2 per 1000 pregnancies) and rarely proceeds to MRI, given the characteristic sonographic appearance, suggestive clinical scenario, and unpredictable behavior and less clearly defined staging methods.

PREGNANCY

Pregnancy is a rare unanticipated finding. Parenthetically, known pregnancy merits informed consent, not because of any known complications, but rather to acknowledge our limits. The patient deserves to understand that, although no known fetal complications of static and time-varying magnetic fields exist or have been observed, absolute certainty has not been established and the risk to the patient (and/or fetus) justifies the (infinitesimal) risk. The same holds true for gadolinium, but current recommendations discourage the use of gadolinium in pregnancy.^{15,16}

By approximately 7 weeks, an embryo is usually visible and the diagnosis is clear; however, obstetric imaging is beyond the scope of this text. Aberrations in pregnancy constitute a category of lesions known collectively as *gestational trophoblastic disease (GTD)*. Hydatidiform mole (partial, complete, and invasive), choriocarcinoma, and placental site trophoblastic tumor compose this neoplastic disease of pregnancy. The common denominator is pregnancy and clinical course generally mirrors postevacuation serum human chorionic gonadotropin (hCG) levels. hCG levels fall in 80% of postevacuation (partial and complete) hydatidiform moles, indicating benign disease. All other lesions are malignant.

Myometrial Disease

FOCAL AND DIFFUSE LESIONS

Myometrial disorders are headlined by benign, but frequently symptomatic conditions—fibroids and adenomyosis. To detect these lesions, remember the normal appearance of the myometrium. The myometrium is a bilaminar structure with an inner myometrium, referred to as the *junctional zone*, and an outer myometrial layer. The inner myometrium is hypointense relative to the hyperintense endometrium and mildly hyperintense outer myometrium (see Figs. 5-1 and 5-9). An increased density of smooth muscle with a commensurate increase in nuclear-to-cytoplasmic ratio and decreased extracellular matrix accounts for the relatively

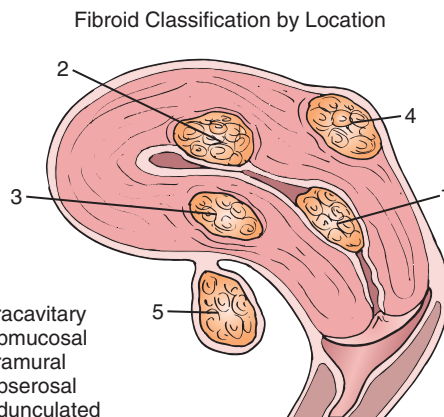


FIGURE 5-23. Fibroid classification by location.

decreased signal on T2-weighted images. The inner myometrium normally measures no more than 8 mm in thickness.

FIBROIDS

Fibroids (otherwise known as *leiomyomas*) represent benign proliferations of smooth muscle cells interspersed with collagen, explaining the uniform hypointensity to myometrium on all pulse sequences—especially T2-weighted sequences. Although occasionally solitary, they are often multiple and are present in approximately 20% of reproductive-age females. Symptoms depend on the size and location of the fibroid(s) and manifest approximately 50% of the time.¹⁷ Submucosal fibroids abut and displace the adjacent endometrial mucosal surface, projecting into the endometrial cavity and predisposing to menorrhagia, infertility, miscarriage, menstrual dysfunction, dyspareunia, and/or pelvic discomfort. Submucosal fibroids mostly within the endometrial canal with a relatively smaller myometrial point of attachment are subclassified as intracavitary and potentially decrease fertility rates. Intramural fibroids are confined to the myometrium and rarely provoke symptoms. Subserosal fibroids protrude outwardly from the external surface of the uterus under the serosal surface (Figs. 5-23 to 5-28) infrequently inciting symptoms (pressure effects and pain). Subserosal fibroids are substratified as pedunculated when predominantly extramural with a (sometimes imperceptible) stalk or point of myometrial attachment. Pedunculation predisposes to torsion and diagnostic confusion by simulating adnexal masses.

The main indications for imaging fibroids include (1) explaining pelvic/menstrual symptoms

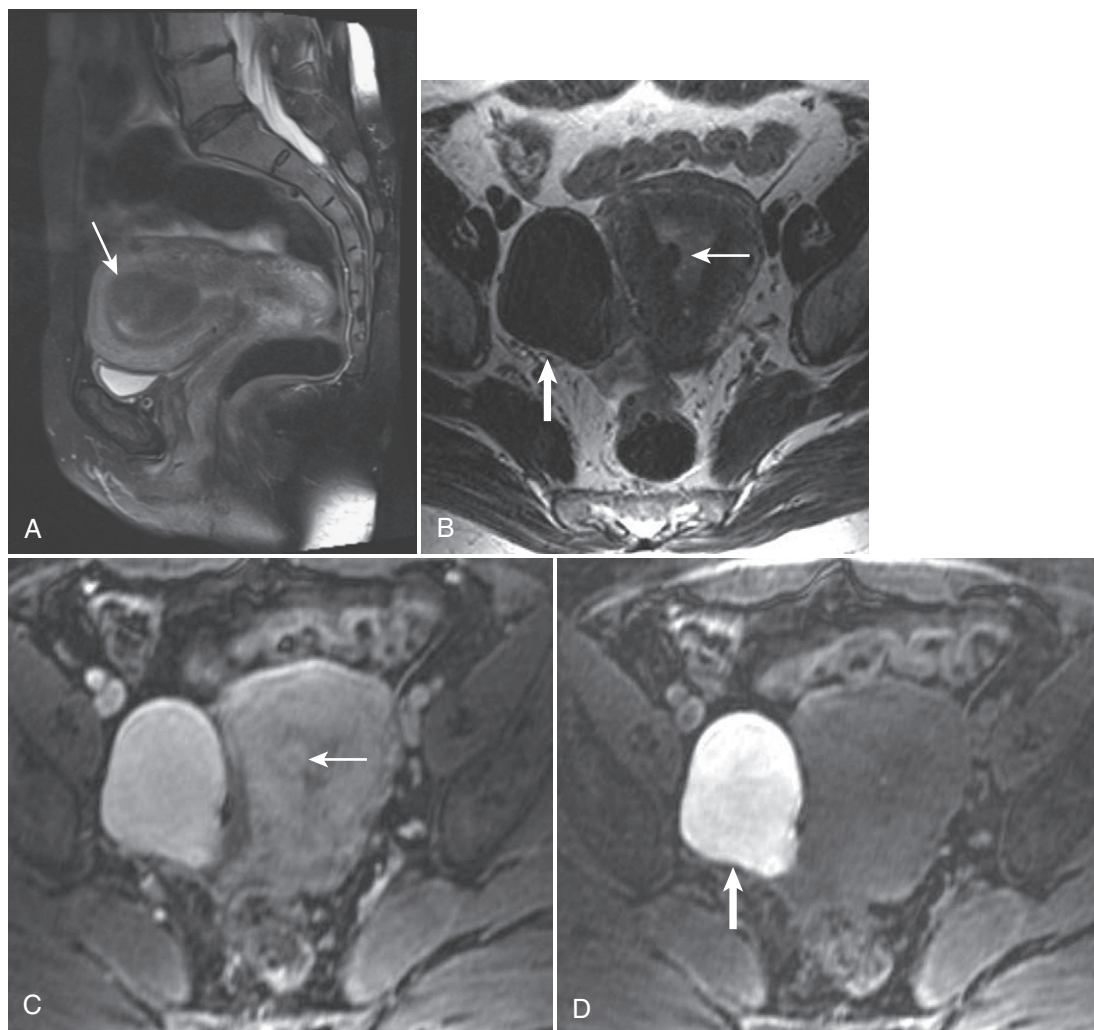


FIGURE 5-24. Submucosal fibroid. **A**, T2-weighted fat-saturated image reveals an ovoid hypointense lesion arising from the anterior fundal myometrium protruding into the endometrial cavity consistent with a submucosal fibroid (*arrow*). The axial T2-weighted (**B**) and enhanced T1-weighted fat-suppressed (**C**) images show a second small submucosal fibroid arising from the right lateral myometrium (*thin arrow* in **B** and **C**). **D**, A large hypointense right adnexal lesion mimics the appearance of a fibroid on the T2-weighted image (*thick arrow*)—in combination with the marked T1 hyperintensity on the T1-weighted unenhanced image (*thick arrow*)—the constellation of signal characteristics is most typical of chronic or concentrated blood products and diagnostic of an endometrioma.

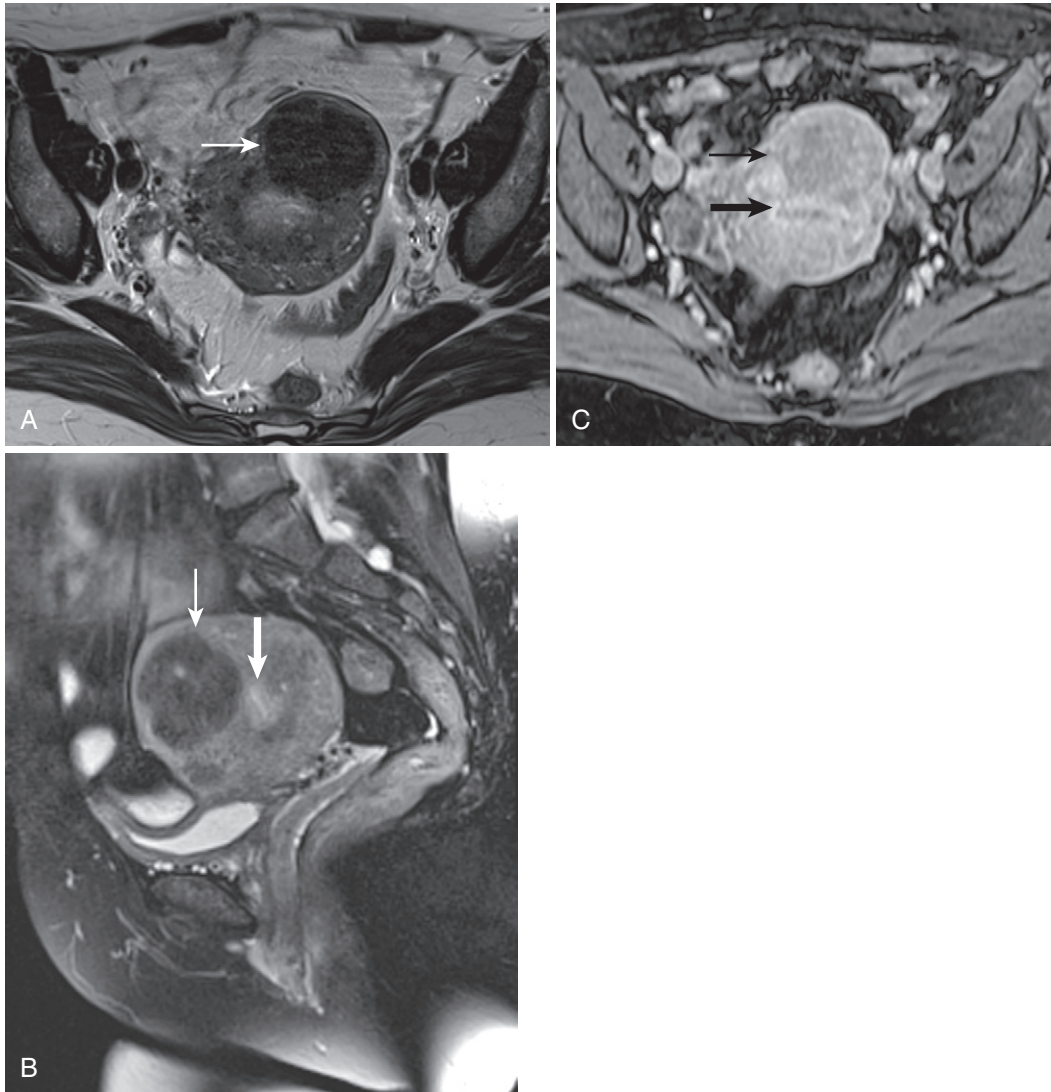


FIGURE 5-25. Intramural fibroid. The myometrium completely contains the hypointense, hypovascular fibroid (*thin arrow* in A-C) seen to be distinct from the endometrium (*thick arrow* in B and C) on axial T2-weighted (A), sagittal T2-weighted fat-saturated (B), and axial enhanced T1-weighted fat-saturated gradient echo (C) images.

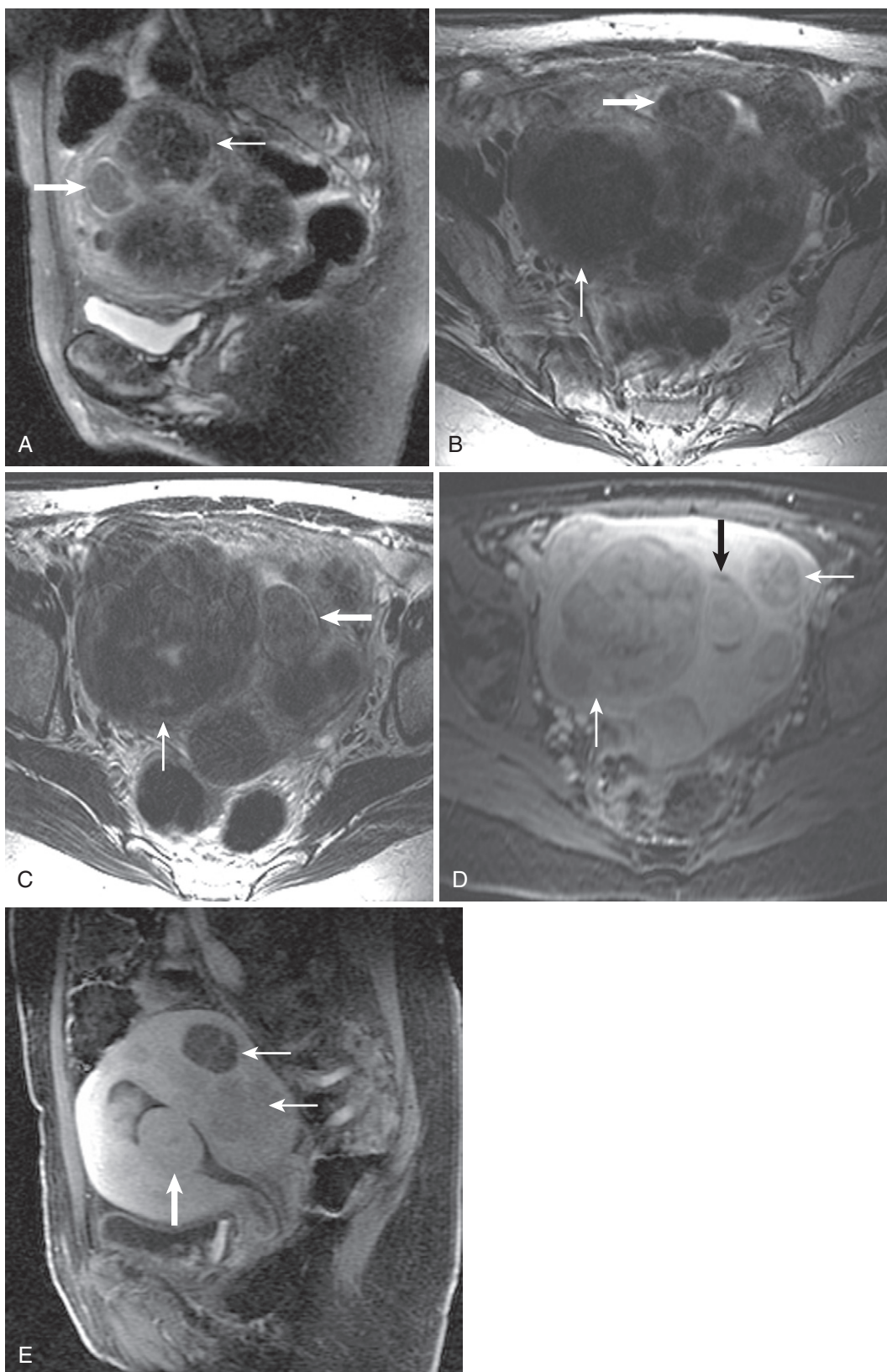


FIGURE 5-26. Intramural and subserosal fibroids. A-E, Multiple fibroids—some completely contained within the myometrium (*thin arrows*) and some protruding into the endometrial canal (*thick arrow*)—indicate a combination of intramural and submucosal fibroids, respectively.

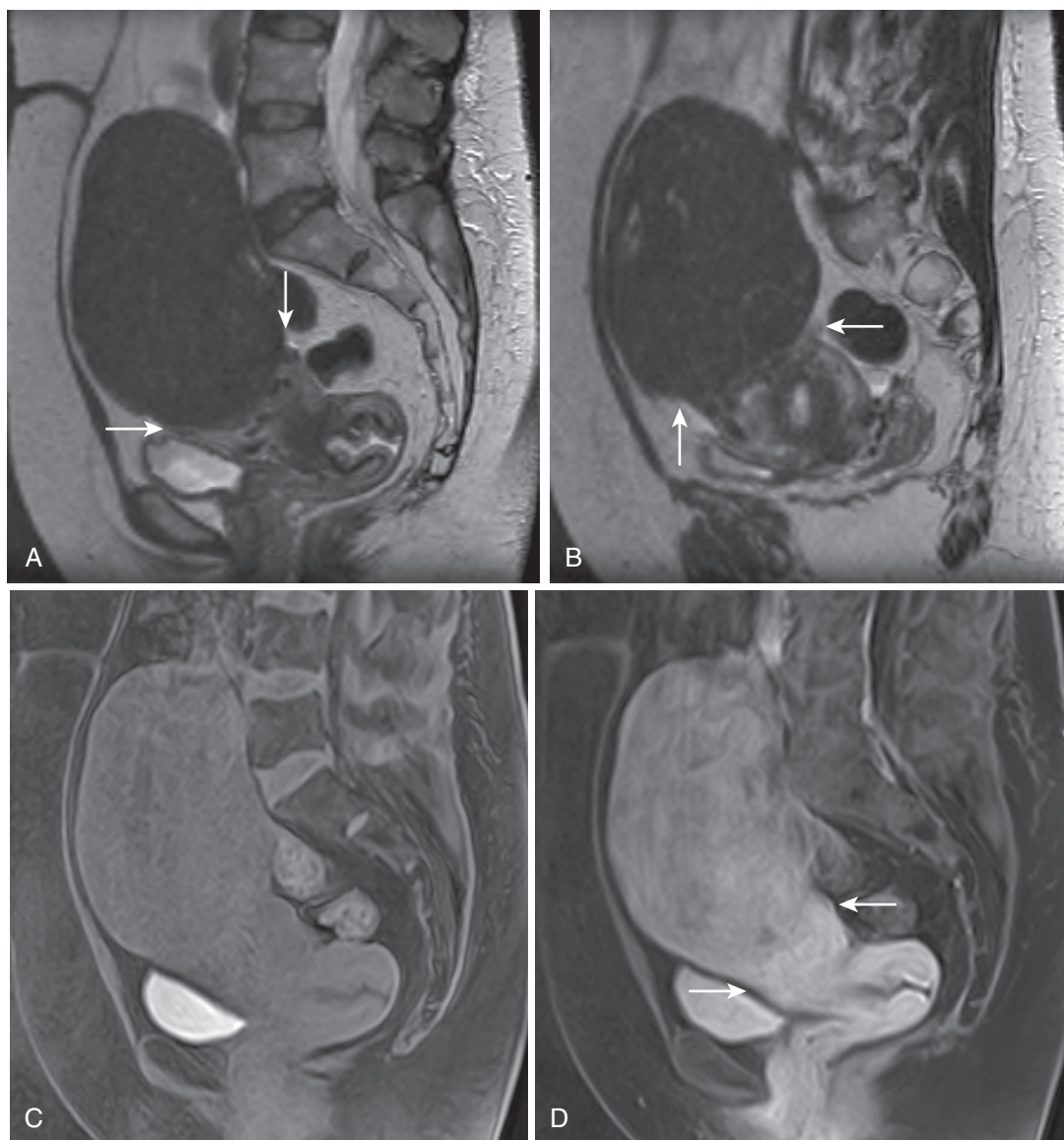


FIGURE 5-27. Subserosal fibroid. Sagittal T2-weighted (A and B) and T1-weighted fat-saturated gradient echo unenhanced (C) and enhanced (D) images depict myometrium encircling the caudal aspect of a large subserosal pedunculated fibroid (arrows in A, B, and D).

and detecting (if not known) and/or classifying fibroids, (2) establishing uterine origin in the case of subserosal pedunculated fibroids, which are often difficult to characterize with other modalities (vs. primary ovarian lesion), (3) pre-treatment planning, and (4) assessing the response to treatment (UAE).¹⁸ The imaging objectives include (1) identification of fibroid(s), (2) spatial localization of fibroid(s) (submucosal, intramural, subserosal), and (3) characterization of fibroid(s) (i.e., degeneration, degree of vascularity).

Individual fibroids are generally round to oval well-circumscribed hypointense lesions, ranging in size from a few millimeters to over 10 cm. Growth is mediated by sex steroids—especially estrogen—generally growing during pregnancy and shrinking in menopause. Vascularity varies and enhancement ranges from virtually absent (avascular) to marked enhancement (hypervascular) (compared with adjacent myometrium) (Figs. 5-29 and 5-30). Despite the degree of early enhancement (which defines fibroid vascularity), hypointensity on delayed images compared

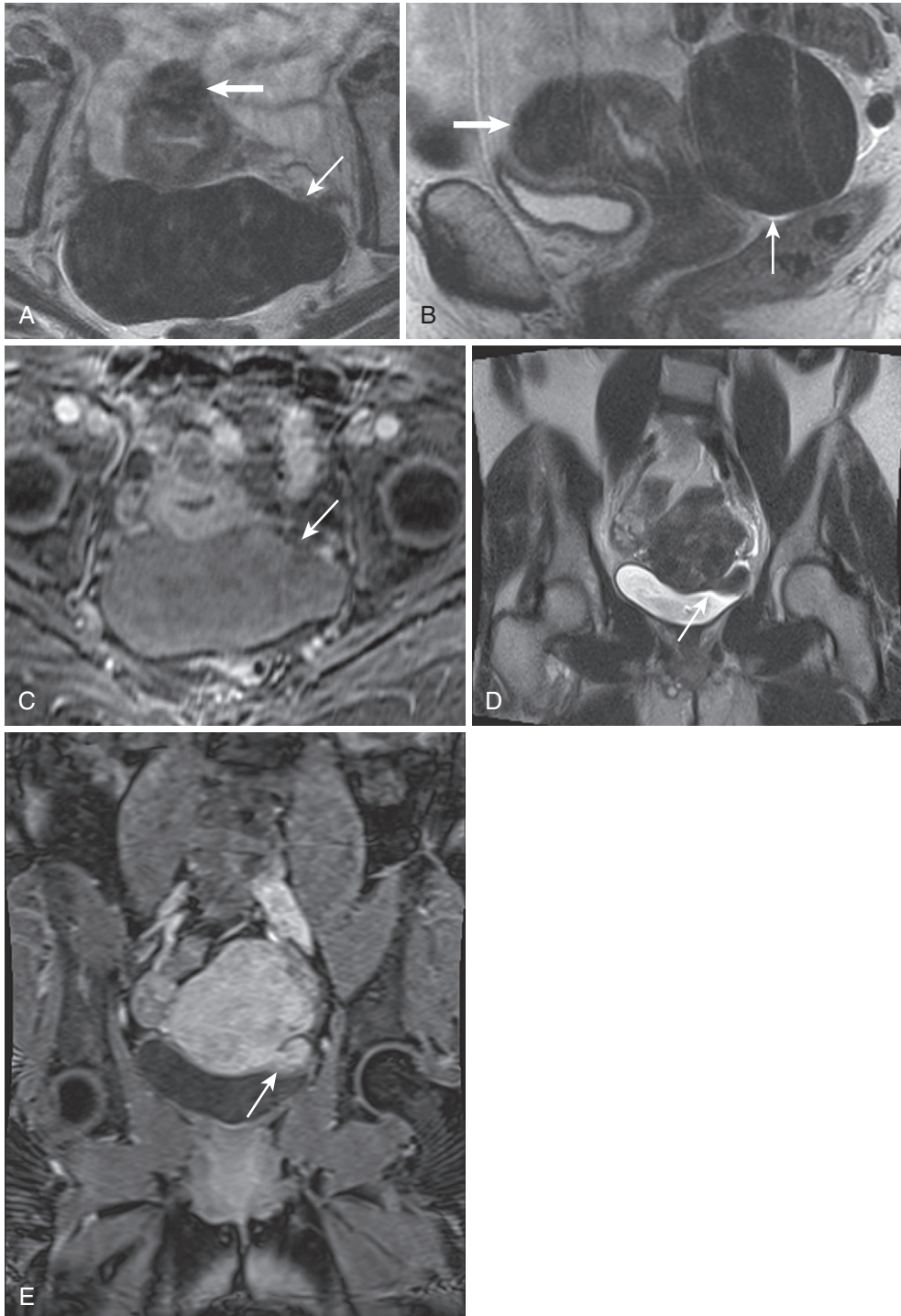


FIGURE 5-28. Subserosal fibroids simulating adnexal masses. Axial (A) and sagittal (B) T2-weighted images reveal a large hypointense lesion in the cul-de-sac (*thin arrow* in A-C) of uncertain origin with hypovascularity depicted on the enhanced axial image (C); an anterior intramural fibroid is incidentally noted (*thick arrow* in A and B). D and E, A stalk (*arrow*) connecting the lesion to the uterus confirms uterine origin and the diagnosis of a fibroid in a different patient.

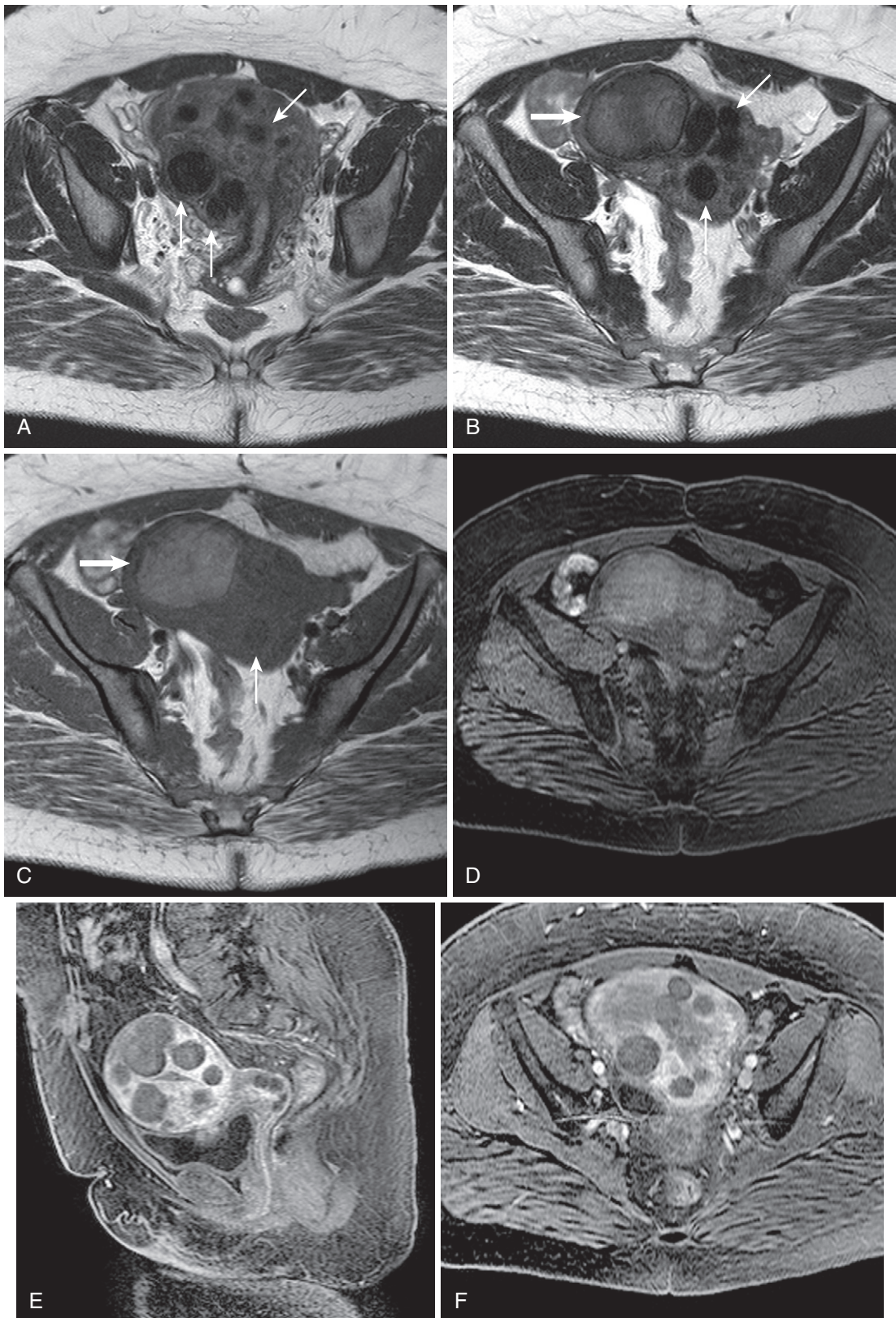


FIGURE 5-29. Hypovascular fibroids. Axial T2-weighted (A and B) and T1-weighted (C) images reveal multiple hypointense intramural fibroids (*thin arrows* in A-C) and a large hyperintense (hemorrhagic) fibroid arising from the right lateral myometrium (*thick arrow* in B and C). Comparing the precontrast (D) with the enhanced images (E and F) indicates a relative lack of enhancement.

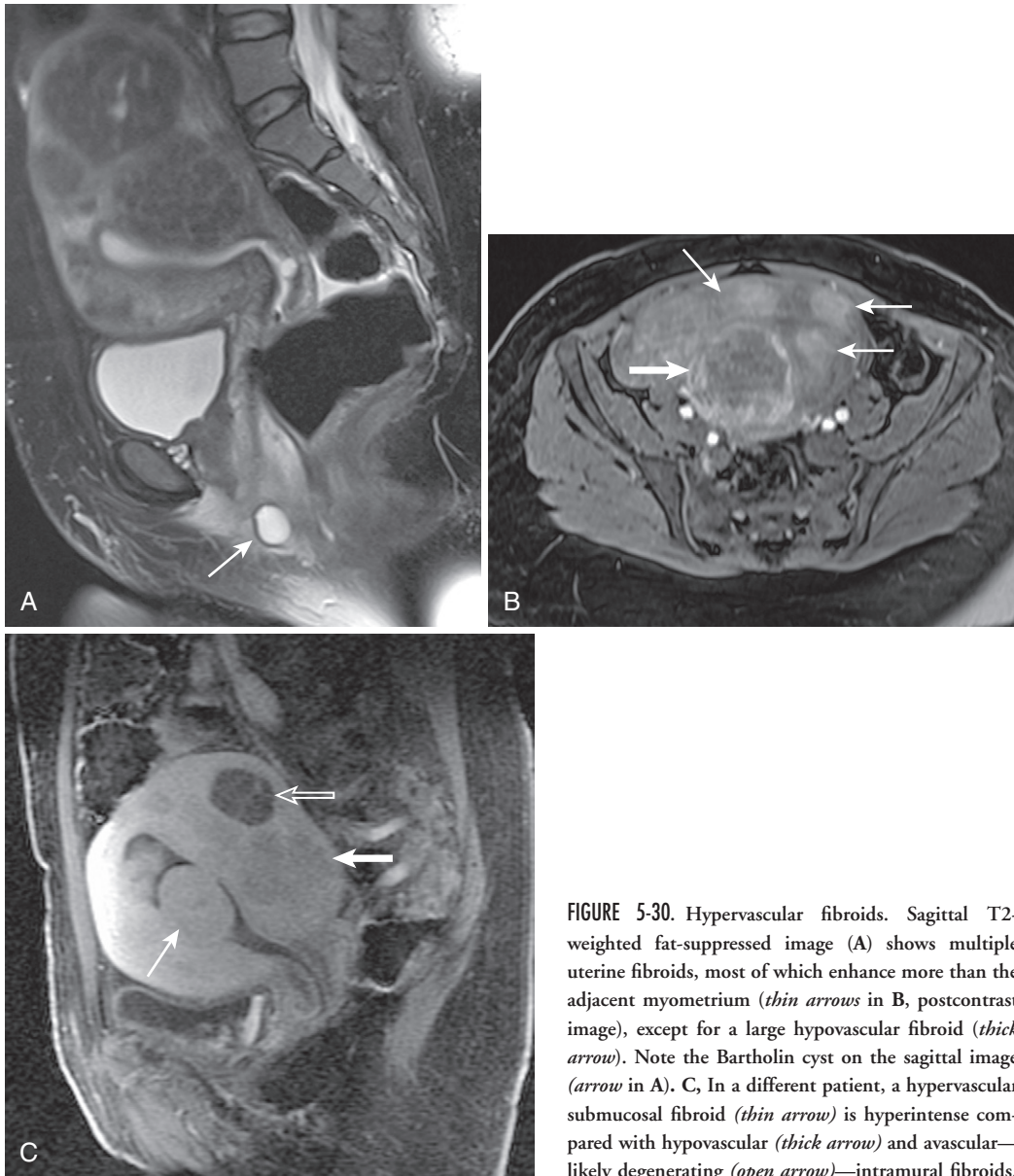


FIGURE 5-30. Hypervascular fibroids. Sagittal T2-weighted fat-suppressed image (A) shows multiple uterine fibroids, most of which enhance more than the adjacent myometrium (*thin arrows* in B, postcontrast image), except for a large hypovascular fibroid (*thick arrow*). Note the Bartholin cyst on the sagittal image (*arrow* in A). C, In a different patient, a hypervascular submucosal fibroid (*thin arrow*) is hyperintense compared with hypovascular (*thick arrow*) and avascular—likely degenerating (*open arrow*)—intramural fibroids.

with myometrium is essentially unanimous. With relatively increased smooth muscle (and less collagen) content, fibroids appear relatively T2 hyperintense with greater enhancement. Diagnostic uncertainty arises in the case of pedunculated subserosal fibroids, which simulate adnexal lesions (see Fig. 5-28), and occasionally in the case of an intracavitary submucosal fibroid, which must be discriminated from an endometrial polyp and endometrial carcinoma. The presence of enhancement differentiates a subserosal fibroid from a dark (shading) endometrioma, and a stalk connecting the fibroid with the parent uterus differentiates a

subserosal fibroid from a primary adnexal mass (such as a fibroma). Marked hypointensity, sharp margins, spherical to ovoid morphology, and enhancement patterns usually differentiate an intracavitary submucosal fibroid from chiefly differential considerations (Table 5-10). Adenomyosis, when focal, often mimics an intramural fibroid, and differential features are deferred to the upcoming discussion of adenomyosis.

Aberration in the otherwise monotonous appearance of fibroids is usually explained by degeneration. Fibroids often exhibit different manifestations of involution, which is usually asymptomatic. Types of degeneration are

TABLE 5-10. Intracavitary Fibroid Differential Diagnosis Scheme

Lesion	T2 Signal	Morphology	Margins	Enhancement
Intracavitary fibroid	↓↓↓	Ovoid-round	Sharp	Often hypovascular, homogeneous unless degenerating
Endometrial polyp	Isointense ↑↑, cystic foci	Tubular	Sharp	Moderate, lacy
Endometrial carcinoma	↓↓	Sessile-pedunculated	Ill-defined	Hypovascular

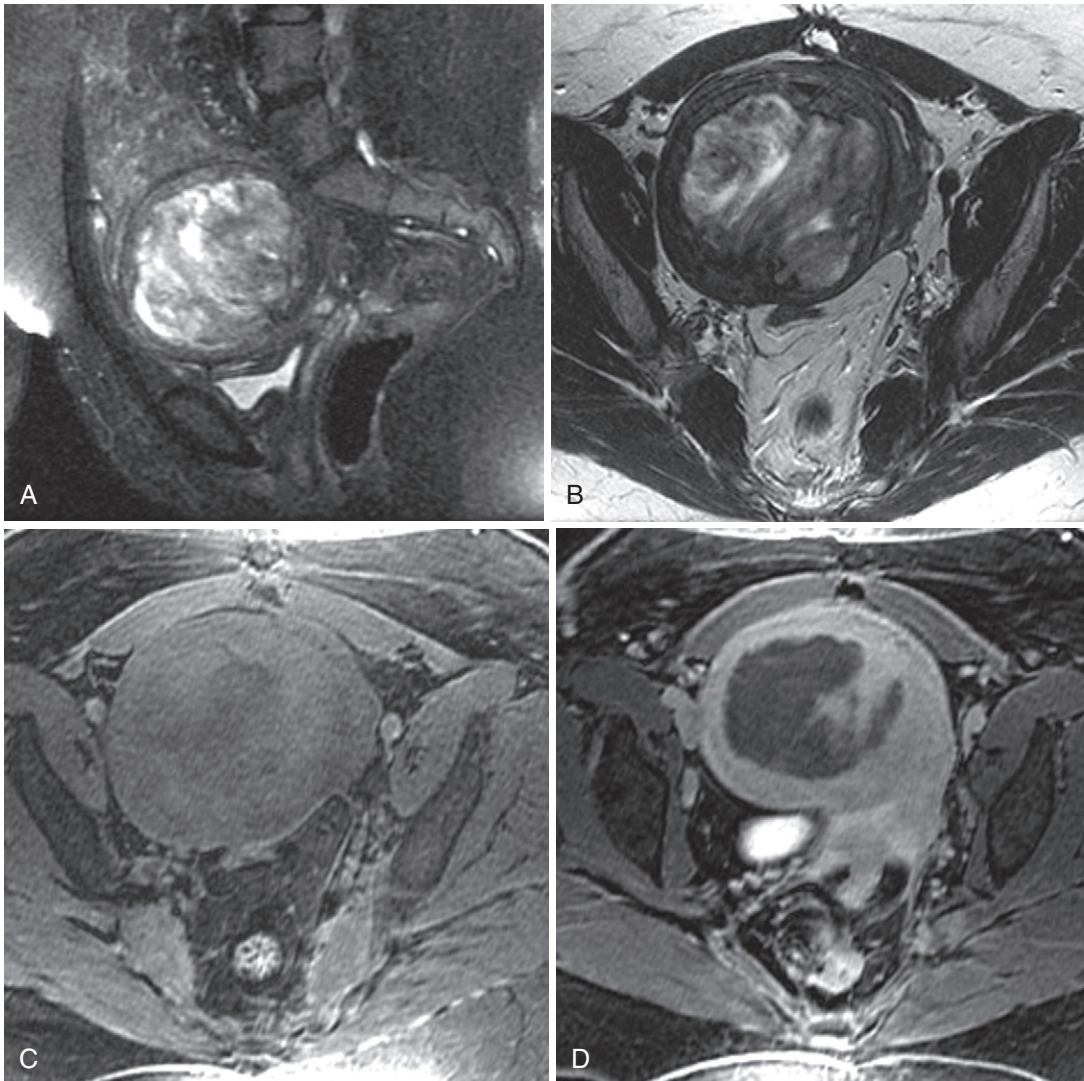


FIGURE 5-31. Fibroid with myxoid degeneration. Sagittal fat-saturated (A) and axial (B) T2-weighted images show heterogeneous hyperintensity throughout the large fibroid undergoing myxoid degeneration. Pre-gadolinium (C) and post-gadolinium enhanced (D) T1-weighted fat-saturated gradient echo images document an absence of enhancement indicating absent perfusion and degeneration.

TABLE 5-11. Fibroid Degeneration Table

Type	Magnetic Resonance Signal Characteristics		
	T1	T2	Gadolinium
Cystic	↓↓↓	↑↑↑	—
Hyaline	↑/↓	↓	—
Myxoid	↓	↑↑	±
Hemorrhagic	↑↑	↑/↓, ± ↓ rim	—

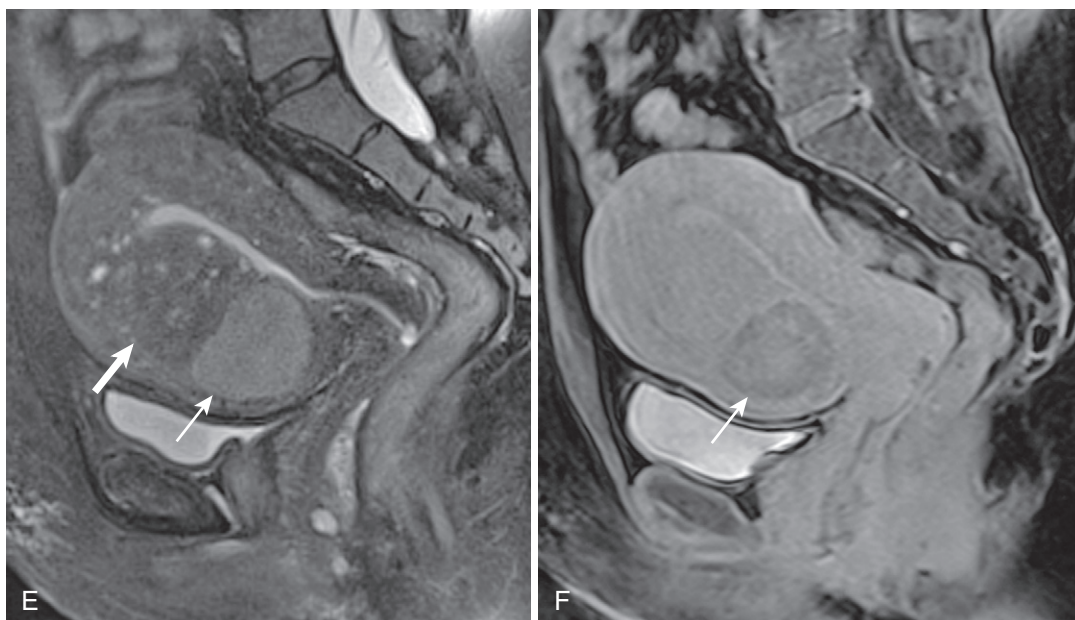


FIGURE 5-31, cont'd E and F, In a different patient, an intramural fibroid undergoing myxoid degeneration in the anterior lower uterine segment (*thin arrow* in E) demonstrates much greater T2 hyperintensity than the adjacent adenomyoma (*thick arrow* in E) on the sagittal T2-weighted fat-suppressed image (E) and minimal enhancement (*arrow* in F).

described: hyaline, myxoid, cystic, and hemorrhagic (Table 5-11).¹⁹ Fibroids undergoing hyaline degeneration exhibit T2 hypointensity similar to nondegenerating fibroids. Associated calcification occasionally induces susceptibility artifact. Myxoid degeneration appears T2 hyperintense with minimal enhancement (Fig. 5-31); cystic degeneration corresponds to T2 hyperintensity and absence of enhancement (Fig. 5-32). Hemorrhagic transformation corresponds to T1 hyperintensity, which is often peripheral or diffuse (Fig. 5-33; see also Fig. 5-29B and C).

MRI postembolization often reveals hemorrhagic transformation and decreased or absent enhancement, which indicates successful treatment. Look for these features and an overall decrease in uterine size postembolization (Fig. 5-34). Hypervascularity, submucosal location, and smaller size predict higher likelihood of embolization treatment success. Expected MRI features of successfully embolized fibroids include T1 hyperintensity with corresponding T2 hypointensity and an absence of enhancement.

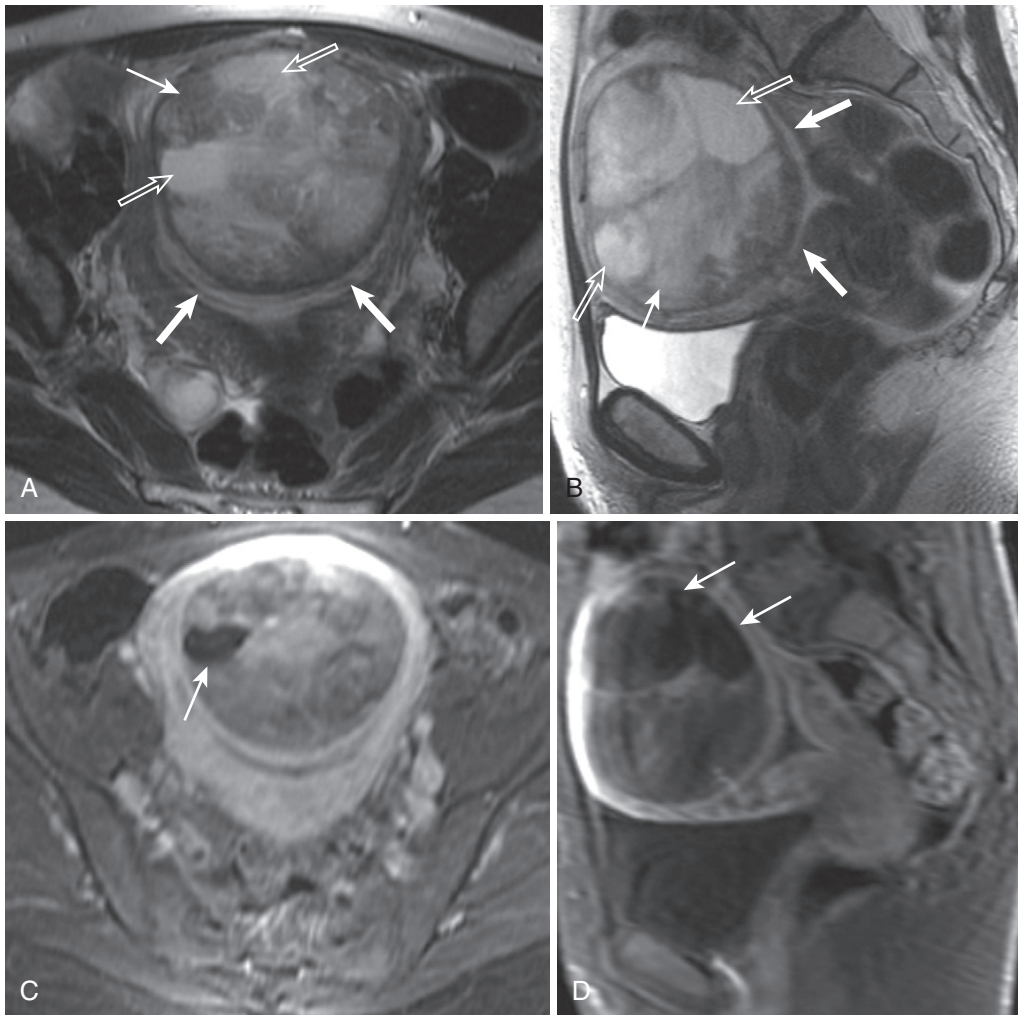


FIGURE 5-32. Fibroid with cystic degeneration. Axial (A) and sagittal (B) T2-weighted images of a uterus with a large heterogeneously hyperintense fibroid (*thin arrow* in A and B) with submucosal extension (*thick arrows* in A and B) reveal multiple fluid intensity foci (*open arrows*), which do not enhance (*arrows* in C and D), as seen on the axial (C) and sagittal (D) fat-suppressed T1-weighted images after gadolinium administration.

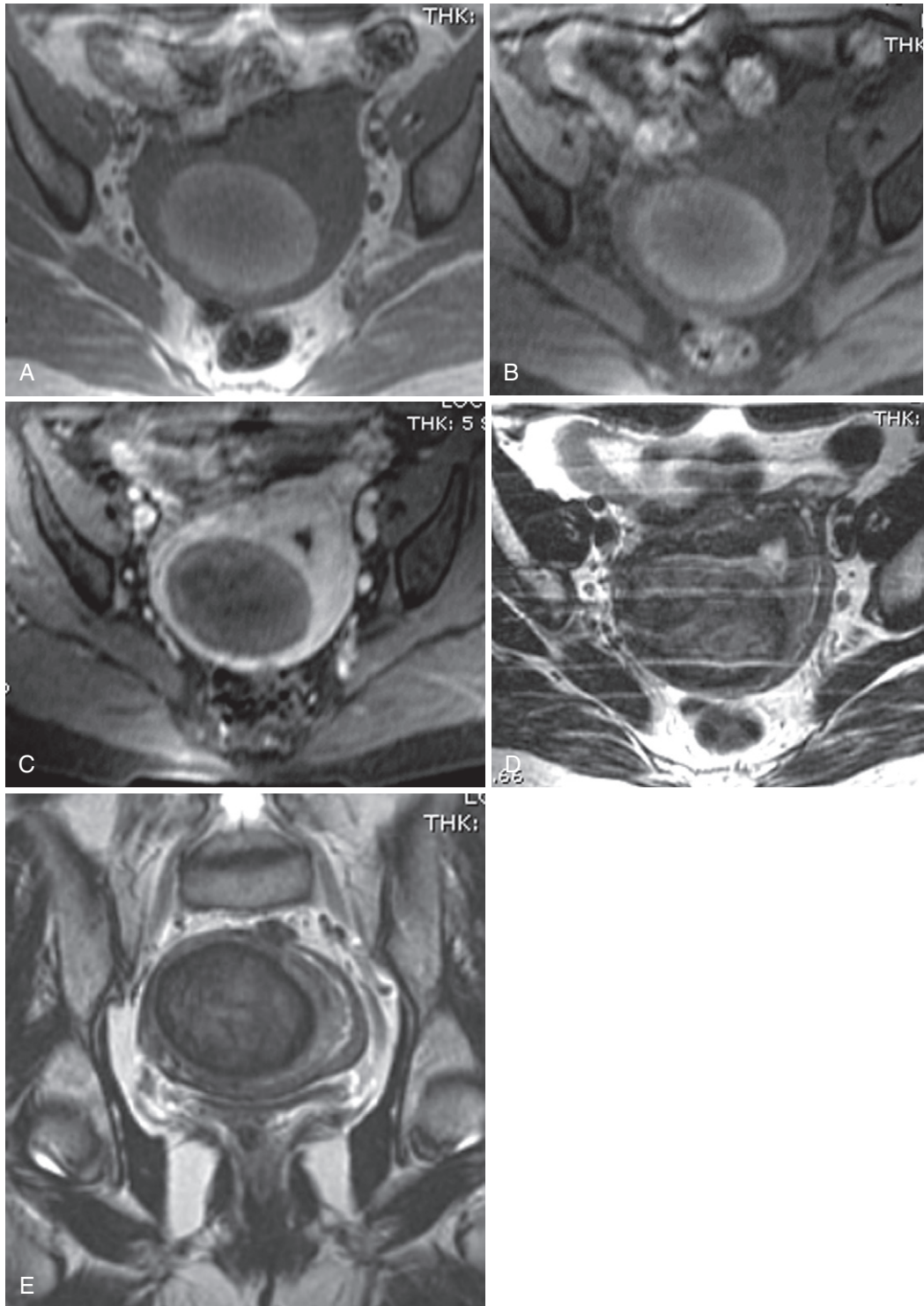


FIGURE 5-33. Fibroid with hemorrhagic degeneration. A mostly intramural fibroid with focal submucosal extension hyperintense on a T1-weighted (in-phase) image without fat suppression (A) maintains hyperintensity on the corresponding T1-weighted fat saturated image (B), confirming hemorrhage. C, The absence of enhancement on the postcontrast image confirms degeneration. Axial (D) and coronal (E) T2-weighted images reveal mild relative hyperintensity compared with uncomplicated fibroids.

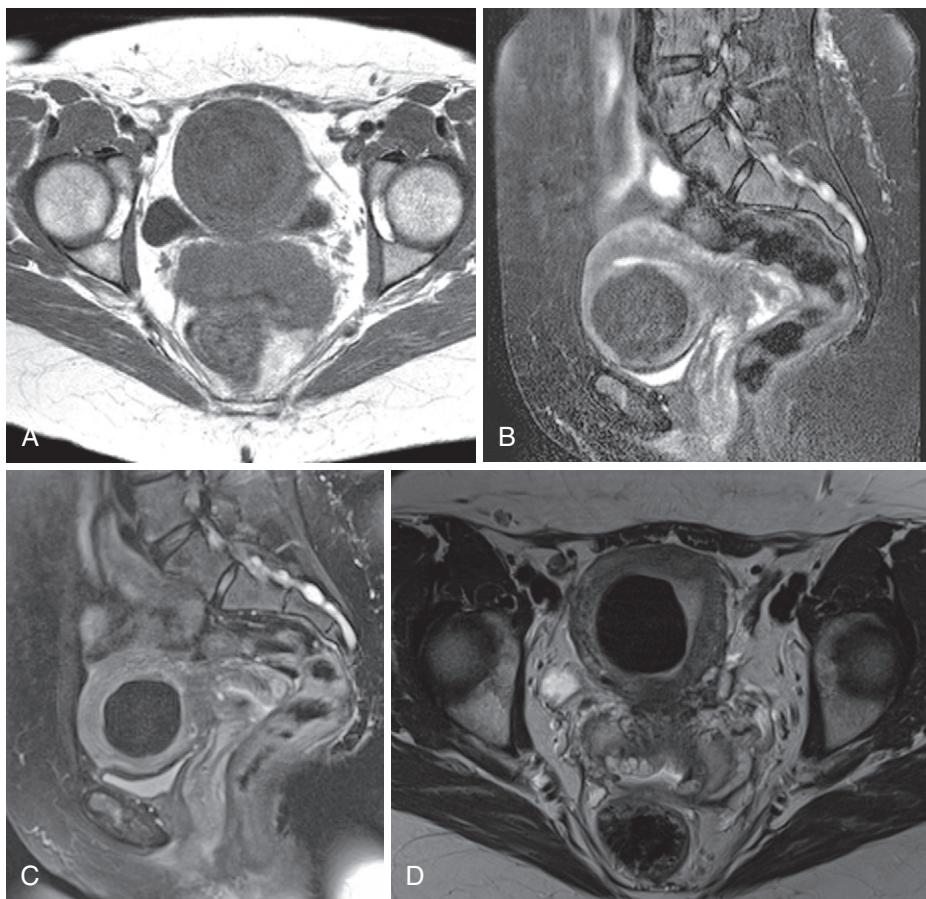


FIGURE 5-34. Fibroid hypovascularity postembolization. Axial T1-weighted (A) and sagittal T2-weighted (B) images of a large intramural fibroid with the typical homogeneous hypointensity before embolization contrast with signal characteristics indicating hemorrhagic degeneration after embolization—marked T2 hypointensity as seen on sagittal T2-weighted fat-suppressed (C) and axial T2-weighted (D) images and T1 hyperintensity on axial gradient echo T1-weighted (E) and fat-suppressed gradient echo T1-weighted (F) images and absence of enhancement—compare pregadolinium (E) with postgadolinium (G) images.

Despite the rising popularity, UAE involves the risk of complications (Table 5-12).⁸ If treated with embolization, pedunculated subserosal fibroids tethered to the uterus with a thin pedicle risk detachment and expulsion into the peritoneal cavity with infarction. Expulsion of submucosal fibroids also leads to potential complications. Detachment connotes infarction with the attendant MRI findings; additional findings may coexist, such as migration and an absence of a point of attachment. Poor collateral circulation, among other factors, predisposes to uterine necrosis—a life-threatening complication of UAE. Relative T2 hyperintensity, isointensity to hyperintensity on T1-weighted images, and an absence of enhancement with or without signal voids indicating gas signify uterine necrosis. Other uterine complications include fibroid

regrowth and inadvertent treatment of a degenerated fibroid (leiomyosarcoma).

Malignant degeneration of fibroids (leiomyosarcoma) is very rare—approximately 0.1%. Features of malignant degeneration include a marked increase in size (compared with prior examinations), indistinct margins, and invasion of adjacent structures (Fig. 5-35). Although relatively little established criteria exist for discriminating these lesions from fibroids, suggestive features based on more recent work include greater than 50% T2 hyperintensity, small T1 hyperintense foci, and pockets of avascularity.²⁰

ADENOMYOSIS

Other benign myometrial lesions include adenomyosis (or focal adenomyoma) and focal myometrial contraction—both of which occasionally

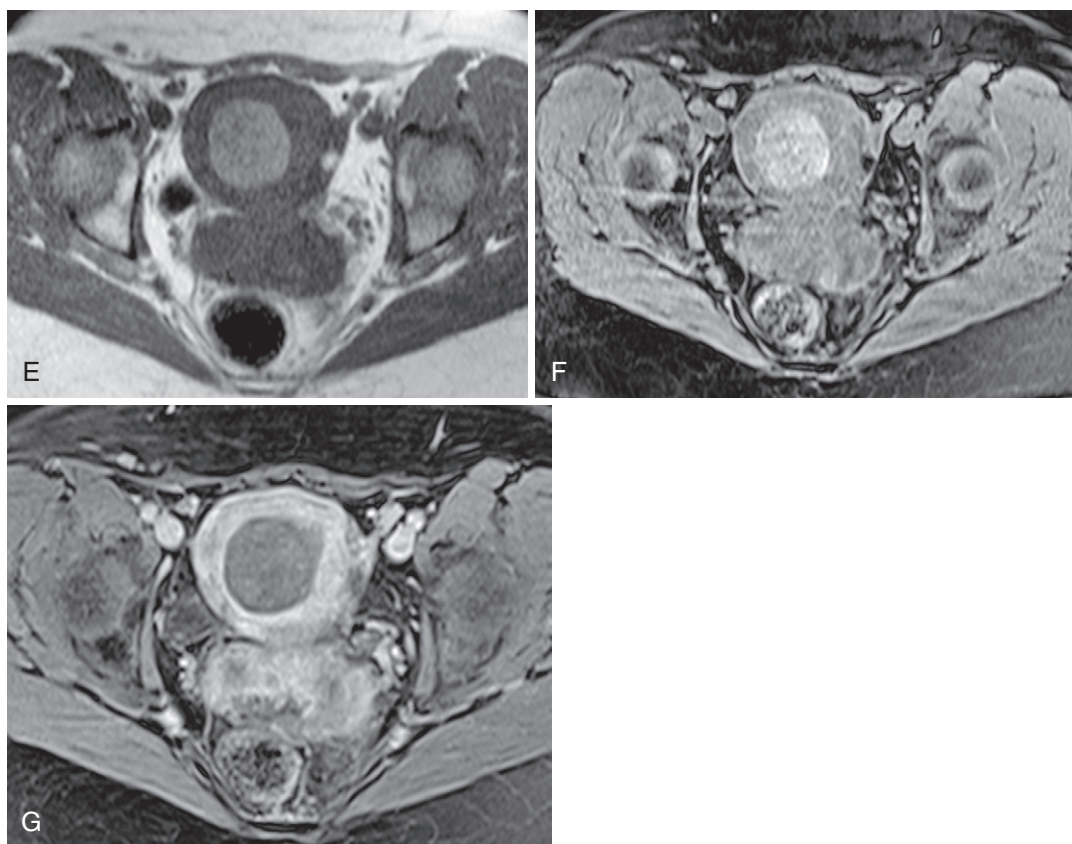


FIGURE 5-34, cont'd

TABLE 5-12. Uterine Artery Embolization Complications

Major Complications

Fibroid passage
 Infectious complications
 Endometritis
 PID-TOA
 Pyomyoma
 DVT
 PE
 Malignant leiomyosarcoma (inadvertently embolized)
 Ovarian dysfunction
 Fibroid regrowth
 Uterine necrosis
 Death

Minor Complications

Hematoma
 UTI
 Urinary retention
 Transient pain
 Nerve/vessel injury

DVT = deep venous thrombosis; PE = pulmonary embolism;
 PID = pelvic inflammatory disease; TOA = tubo-ovarian abscess;
 UTI = urinary tract infection.

From Kitamura Y, Ascher SM, Cooper C, et al. Imaging manifestations of complications associated with uterine artery embolization. *Radiographics* 25:S119-S132, 2005.

simulate fibroids. Adenomyosis is the intrauterine counterpart to endometriosis—abnormal implantation of endometrial cells into the myometrium. Adenomyosis is either diffuse or focal (adenomyoma)—either type manifests the same features (Figs. 5-36 and 5-37). Unlike fibroids, adenomyosis generally lacks distinct margins and exerts no mass effect. Instead of displacing or distorting the adjacent endometrium, adenomyosis abuts the endometrium without displacement. Whereas fibroids maintain acute margins with the endometrium, the interface between adenomyosis and endometrium is usually convex. Adenomyosis signal intensity approximates junctional zone hypointensity with possible intralesional T1 and/or T2 hyperintensities. A junctional zone measurement of 12 mm or greater confirms the diagnosis of adenomyosis; between 8 and 12 mm is indeterminate (Table 5-13). Cyclical menstrual uterine changes suppress the zonal anatomy during the late secretory phase extending into the menstrual phase as the outer myometrium fades

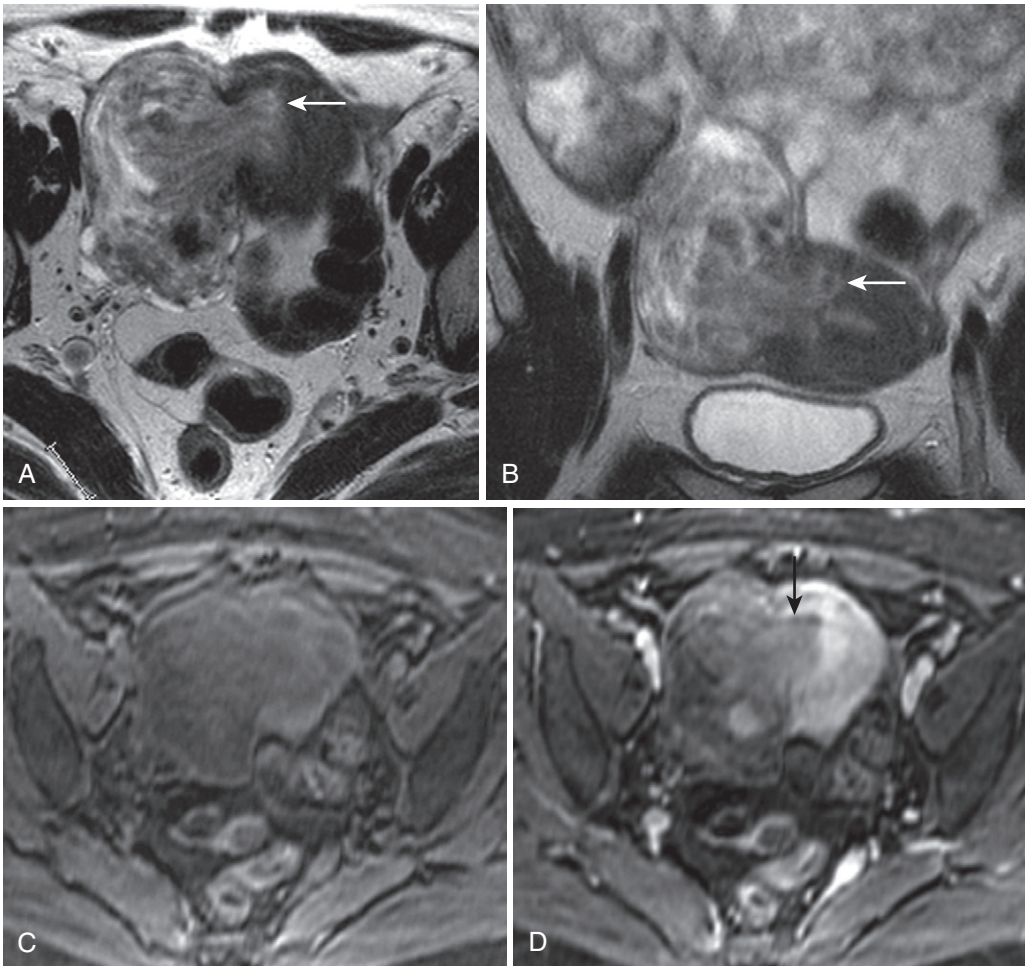


FIGURE 5-35. Malignant degeneration of a fibroid. Axial (A) and coronal (B) T2-weighted images show a moderately heterogeneously hyperintense ovoid lesion adjacent to the uterine fundus attached to the uterus with ill-defined margins in contradistinction to the normally sharply defined stalk seen with a benign leiomyoma, indicating invasion of the adjacent myometrium (*arrow*). Differential enhancement between the enhancing myometrium (*thick arrow* in D) and hypovascular mass (*thin arrow* in D) is evident when comparing the precontrast image (C) with the postcontrast image (D).

TABLE 5-13. Adenomyosis Features

Inner Myometrial Features	Thickness	Diagnosis
Sharply defined Uniformly hypointense	<8 mm	Normal junctional zone
Indistinct margins	8–12 mm	Indeterminate adenomyosis
Indistinct margins Intralesional T1/T2 hyperintensities	≥12 mm	Adenomyosis

from its peak hyperintensity from the midsecretory phase to near isointensity with the dark inner myometrium.²¹

MYOMETRIAL CONTRACTIONS

Myometrial contractions manifest as regional myometrial low signal, which may be confused with adenomyosis or fibroids.²² Focal buckling or folding or thickening of the junctional zone and/or myometrium is an occasional associated finding. The key to this diagnosis is changeability—a contraction is an ephemeral phenomenon and most examinations span 30 minutes or more. Check each sequence for interval change or resolution to confirm a myometrial contraction.

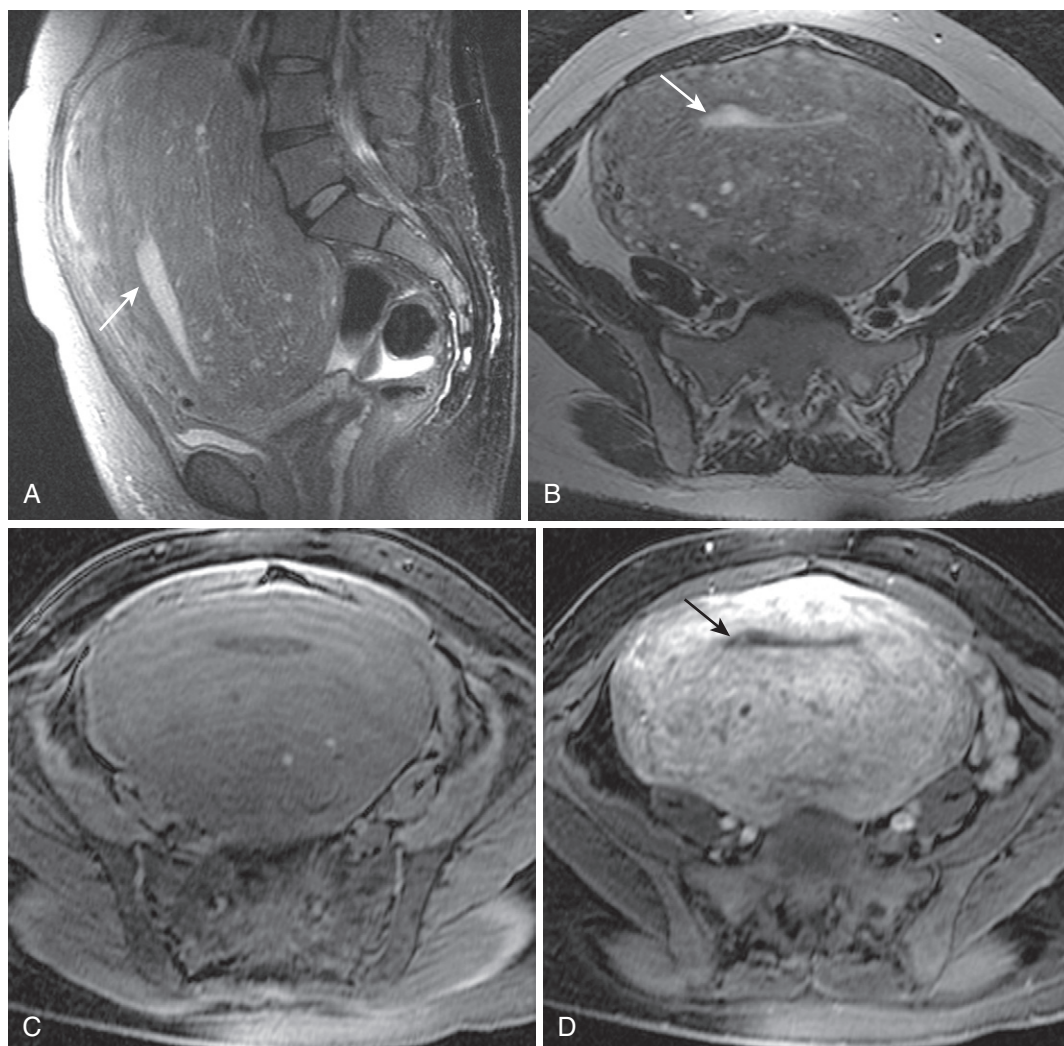


FIGURE 5-36. Diffuse adenomyosis. Sagittal (A) and axial (B) T2-weighted images of a grossly enlarged uterus fail to demonstrate the normal discrimination between the inner and the outer myometrium with multiple myometrial hyperintensities in a patient with severe diffuse adenomyosis (*arrow*, endometrium). C, T1-weighted fat-saturated image shows scattered T1 hyperintensities reflecting hemorrhagic foci. D, The corresponding enhanced T1-weighted fat-saturated gradient echo image shows diffuse heterogeneous enhancement throughout the myometrium without evidence of an underlying focal lesion (*arrow*, endometrium).

MALIGNANT LESIONS

I have virtually excluded malignant myometrial lesions from this discussion because they are exceedingly rare. This category includes uterine sarcomas—leiomyosarcoma, stromal sarcoma, and carcinosarcoma (formerly mixed mesodermal/müllerian tumor)—and lymphoma. Whenever you see a large, heterogenous mass with necrosis and evidence of rapid growth, think about the possibility of a sarcoma (Fig. 5-38). Differentiating these lesions from benign disease—fibroids—and adenomyosis is critical. Signal characteristics (T2 hypointensity), margins (sharply defined), and lack of

invasiveness discriminate fibroids from sarcomas. Lack of mass effect, thickening of the junctional zone, and the characteristic appearance of heterotopic endometrial tissue differentiates adenomyosis from these lesions. Differentiating sarcomas from endometrial cancer is less important because both will eventually require tissue sampling for treatment. Confinement to the endometrium or primary involvement of the endometrium with myometrial invasion favors endometrial carcinoma. The final lesion in this category, lymphoma, more characteristically manifests with multiple lesions—although solitary lesions do occur—a monotonous

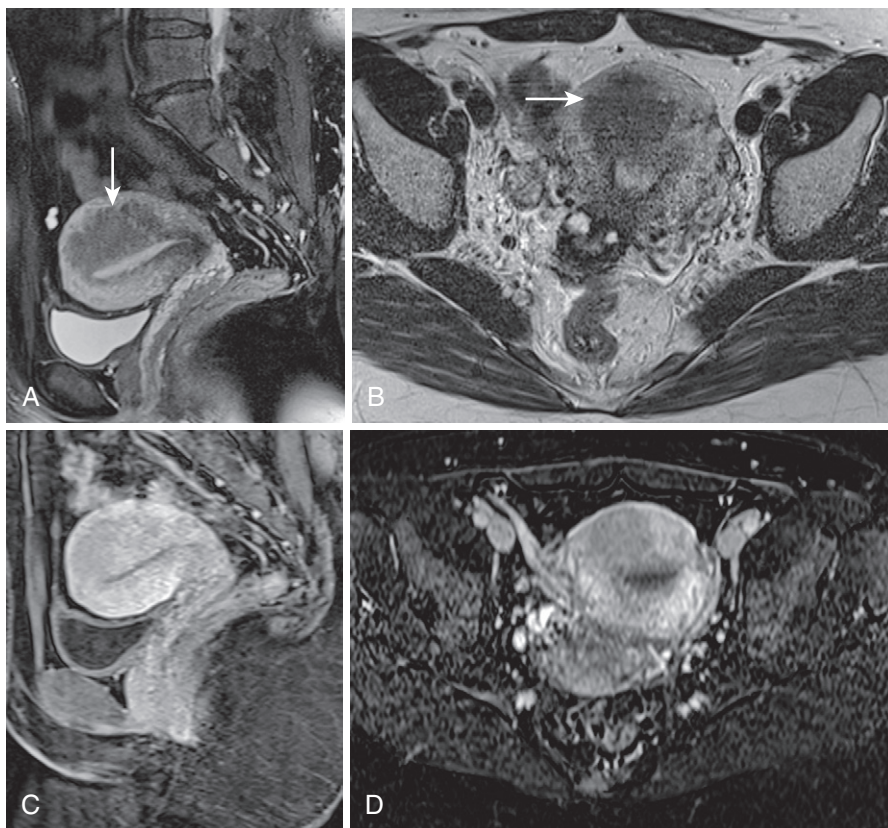


FIGURE 5-37. Focal adenomyoma. Sagittal (A) and axial (B) T2-weighted images reveal a lesion isointense to and blending with adjacent junctional zone with indistinct margins and exerting no significant mass effect on the underlying endometrium (*arrow*). Sagittal (C) and axial (D) enhanced T1-weighted gradient echo images with fat saturation confirm the inner myometrial origin.

appearance with relative isointensity to muscle on T1-weighted images and possibly generalized lymphadenopathy.

GLOBAL UTERINE ABNORMALITIES

This category of global uterine abnormality is essentially restricted to congenital or embryologic disorders, otherwise known as müllerian duct anomalies. The incidence of müllerian duct anomalies is approximately 1%, and they account for approximately 3% of reproductive failures.²³ A detailed discussion of the embryology of the genitourinary system is beyond the scope of this book, but a general understanding facilitates remembering the spectrum of anomalies.

The primordial paramesonephric (müllerian) ducts develop to constitute the upper vagina, uterus, and fallopian tubes. The distal ends of the ducts grow caudally and medially and eventually fuse to become the uterine body, cervix, and upper two thirds of the vagina. After fusion, a residual septum regresses, yielding a common

channel. The unfused proximal segments constitute the fallopian tubes.

Although differentiating between the different types of müllerian duct anomalies is important and can be challenging, they usually do not pose a diagnostic dilemma. The degree of absence or fusion of the ducts accounts for the deficiency or abnormal configuration. Think about these lesions along a spectrum from global deficiency—agenesis/hypoplasia to unilateral deficiency—unicornuate—to a range in incomplete fusion from didelphys to arcuate (*Fig. 5-39*).

There is even a subclassification scheme for type 1 müllerian anomalies, depending on the degree of vagina/cervical/uterine/tubal involvement. Type 2 (unicornuate) müllerian duct anomalies are also subdivided depending on the presence and patency of the aplastic/hypoplastic horn. The type 3 (didelphys) anomaly represents a greater degree of müllerian duct fusion. Global duplication of structures from the

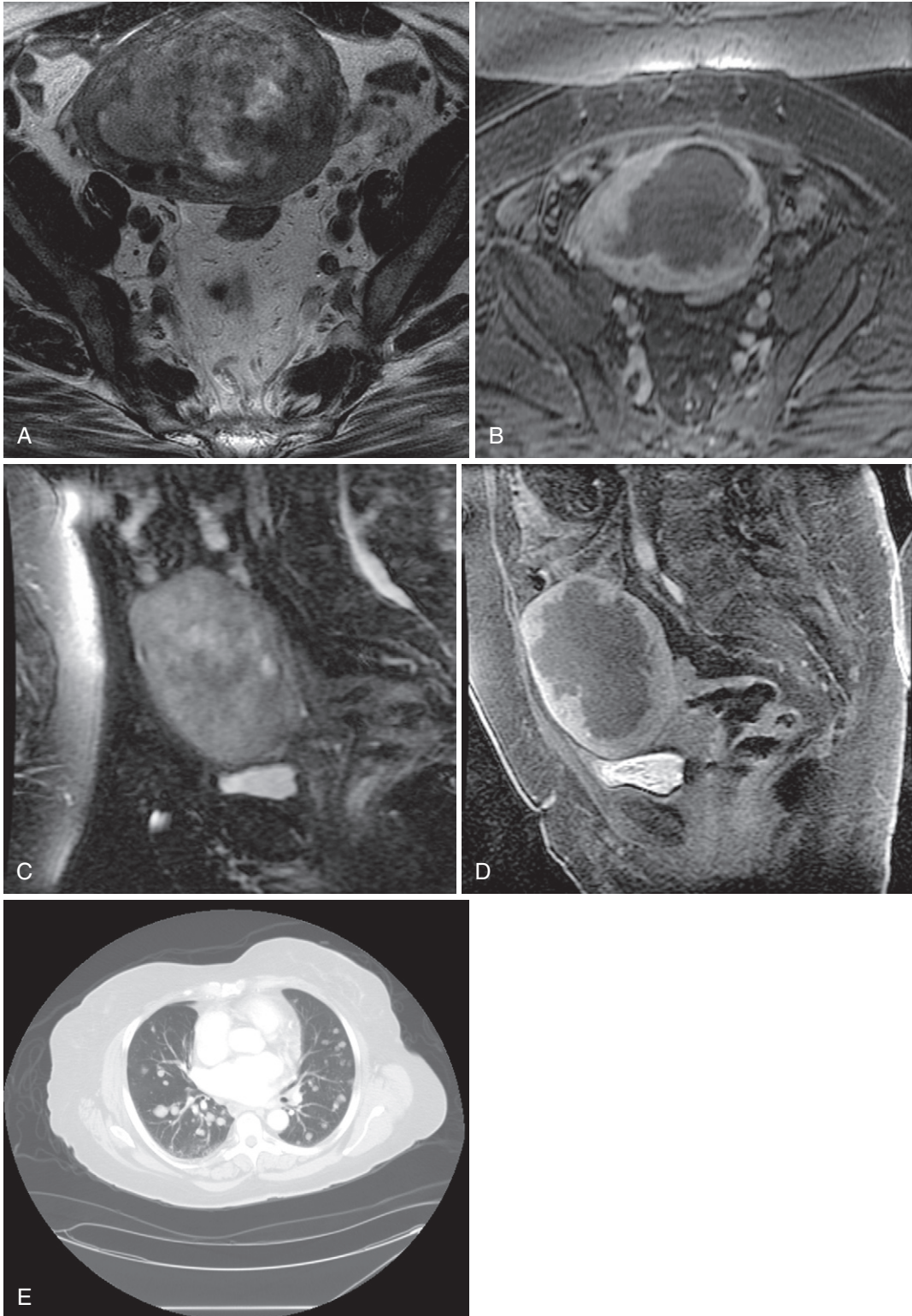


FIGURE 5-38. Leiomyosarcoma. Axial T2-weighted (A) and enhanced (B) and sagittal T2-weighted fat-suppressed (C) and enhanced (D) images show a large, necrotic, poorly defined mass essentially replacing the entire uterine corpus and associated with lung metastases on the corresponding computed tomography (CT) scan (E).

MÜLLERIAN DUCT ANOMALIES

Class I (hypoplasia/agenesis): uterovaginal hypoplasia/agenesis

Class II (unicornuate uterus): partial or complete unilateral hypoplasia

Class III (didelphys uterus): complete müllerian duct nonfusion

Class IV (bicornuate uterus): partial müllerian duct nonfusion

Class V (septate uterus): incomplete resorption of septum between müllerian ducts

Class VI (arcuate uterus): anatomic variation with flat or mildly convex outer uterine fundus with shallow endometrial cleft

Class VII (diethylstilbestrol-related anomaly): dysmorphic abnormalities of the uterus, cervix; and/or vagina, including T-shaped uterus, hypoplastic uterus and/or cervix; and a variety of other derangements

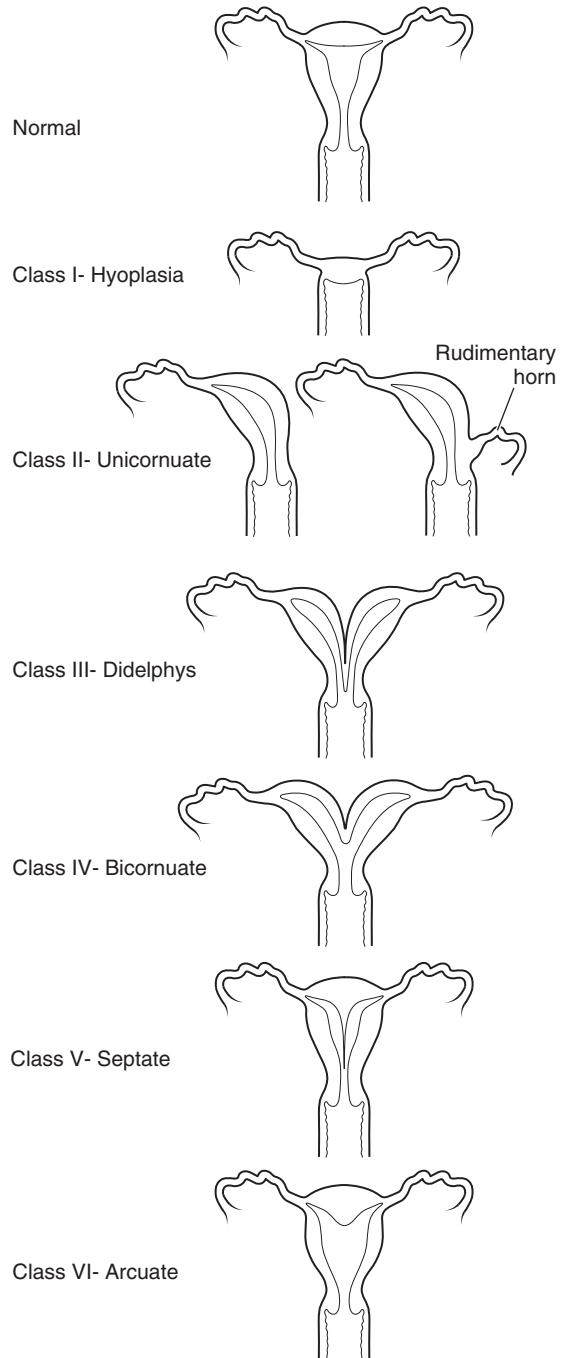


FIGURE 5-39. Classification of müllerian duct anomalies.

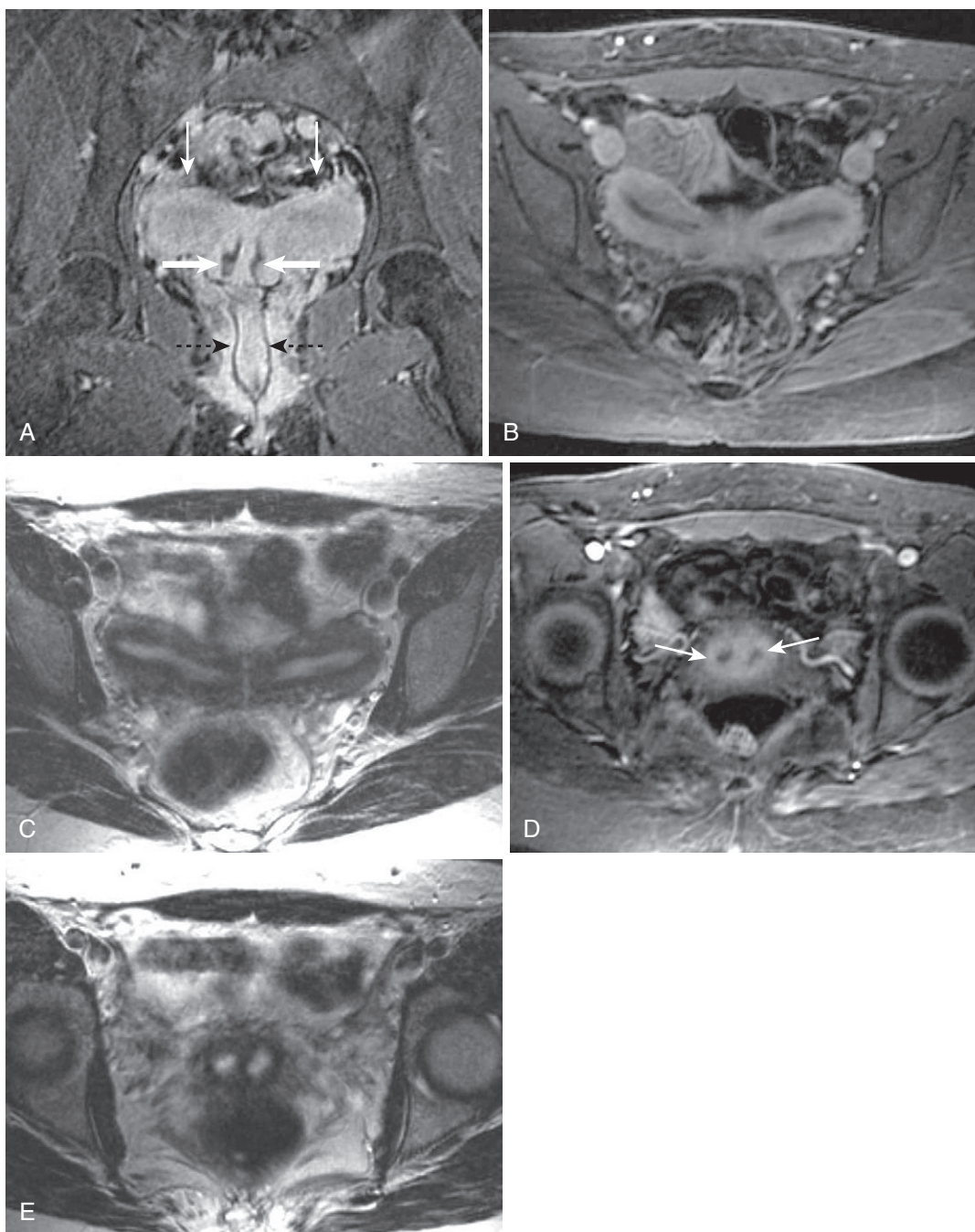


FIGURE 5-40. Uterus didelphys. **A**, Coronal enhanced T1-weighted gradient echo image shows widely splayed uterine cornua (*thin white arrows*) and separate endocervical (*thick arrows*) and vaginal canals (*black arrows*). Widely splayed uterine horns characterize uterus didelphys (and bicornuate uterus), as illustrated on axial enhanced (**B**) and T2-weighted (**C**) images. Separate cervical canals (*arrows* in **D**) are confirmed on axial enhanced (**D**) and T2-weighted (**E**) images.

cervices through the uterine cornua characterizes this anomaly with a variable longitudinal vaginal septum (Fig. 5-40).

The chief differential is between the bicornuate (type 4) and the septate (type 5) uterus because of the difference in surgical approach—

a septate uterus is approached hysteroscopically for septoplasty, and a bicornuate uterus is approached transabdominally. Hysteroscopic metroplasty of a bicornuate uterus may result in myometrial perforation (Figs. 5-41 and 5-42).

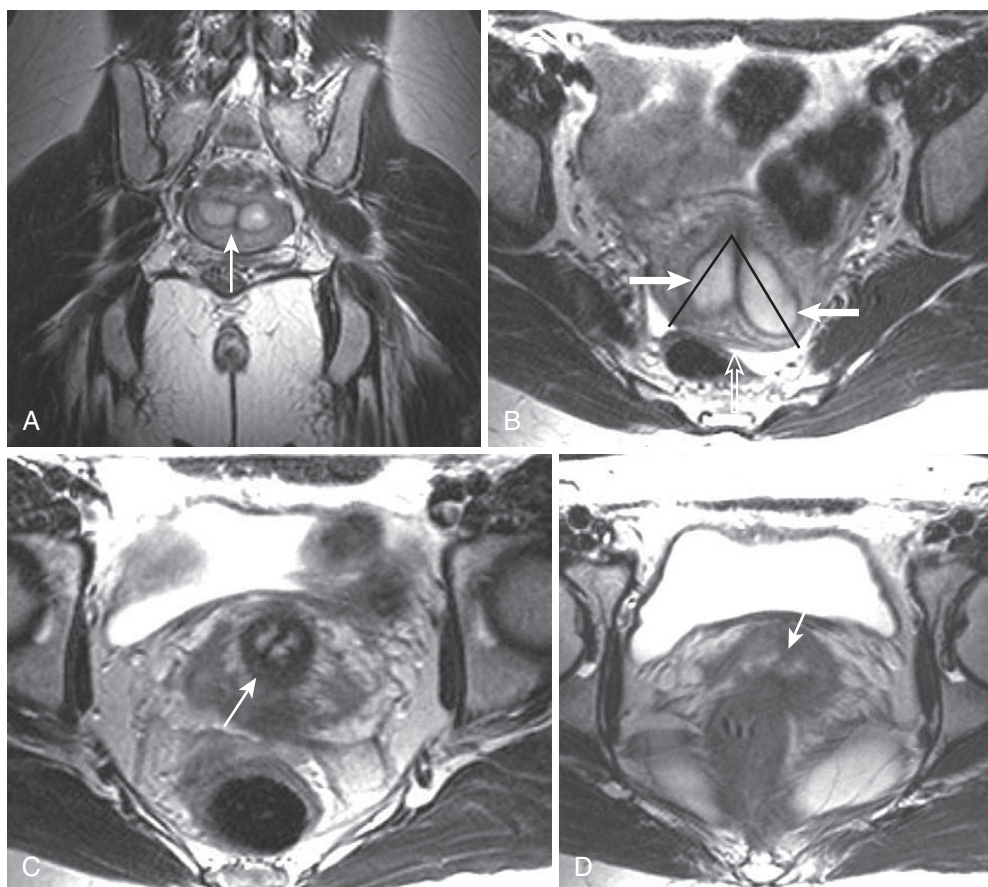


FIGURE 5-41. Septate uterus. A, Coronal T2-weighted image shows a hypointense fibrous septum (*arrow*) dividing the endometrial hemicavities. Axial T2-weighted images show the fibrous septum extending from the uterine fundus (B) through the cervix (C) and into the upper vagina (D) and confirming features consistent with septate uterus—convex outer fundal contour (*open arrow* in B), closely apposed uterine horns (*thick arrows* in B), and relatively low intercornual angle (*black lines* in B).



FIGURE 5-42. Bicornuate uterus. Note the wider displacement and more obtuse angulation between uterine horns compared with [Figure 5-41](#).

The outer fundal contour is a major discriminating factor between the two entities. The septate uterine fundal contour ranges from normal (convex) to flat to minimally concave (<1 cm), whereas the bicornuate features a deeper fundal cleft (≥ 1 cm). Try to measure the intercornual angle by approximating the medial margins of the endometrial hemicavities— 105° or greater suggests bicornuate, 75° or less suggests septate.²⁴ Wider splaying between the apices of the cornua—or intercornual distance—of 4 cm or more is a finding that potentially discriminates between the two entities, suggesting bicornuate uterus.²⁵ Comparing the relative positioning of the apices of the cornua with the apex of the external fundal contour informs the (sonographic) differentiation between the two ([Fig. 5-43](#))—greater than 5 mm cephalad positioning of the intercornual line above the fundal indentation purportedly separates the septate

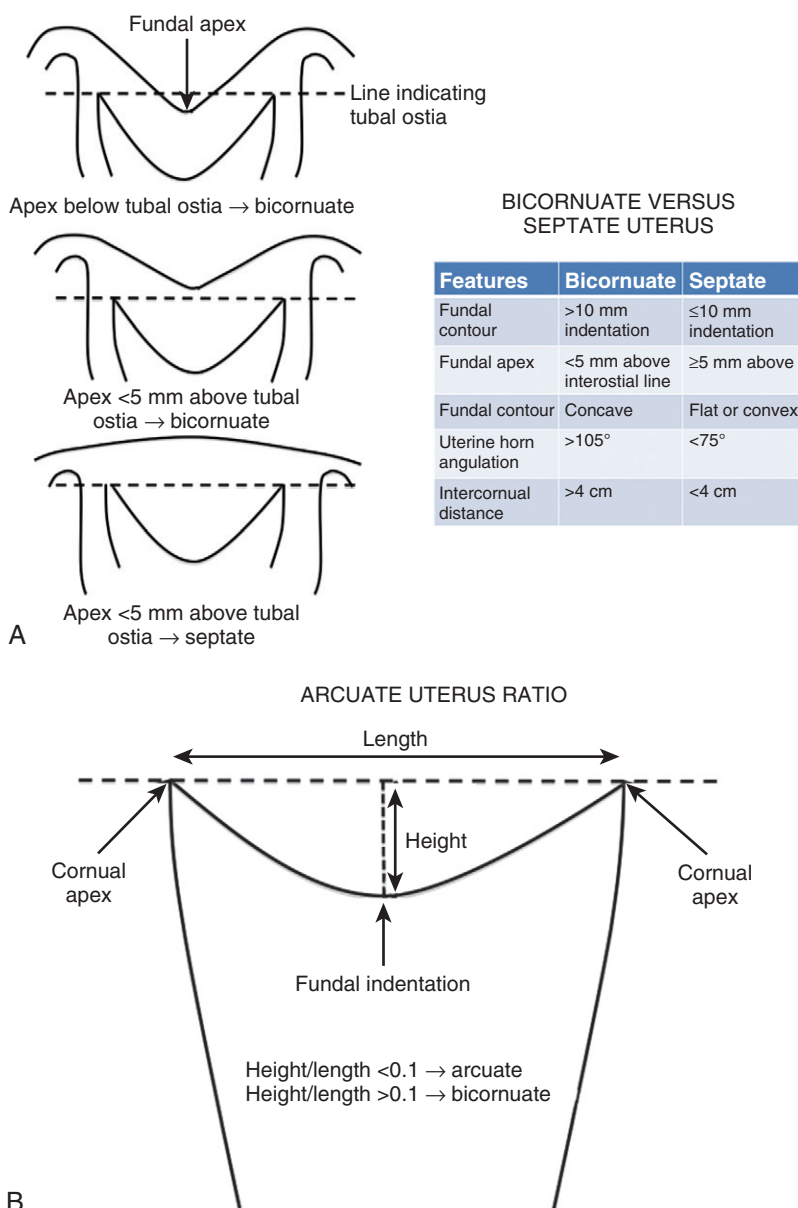


FIGURE 5-43. Bicornuate versus septate uterus and arcuate uterus ratio. Bicornuate versus septate uterus. Modified from references 24-28.

from the bicornuate (and didelphys) uterus (according to ultrasound-generated data, which have not been substantiated with MRI).^{26,27} Of course, do not forget to assess the intercornual tissue; intervening myometrial tissue indicates bicornuate uterus; a thin linear uniform hypointensity (typical of fibrous tissue) suggests septate uterus.

Arcuate uterus (type 6 müllerian duct anomaly) is the forme fruste of this disorder—essentially an anatomic variant, representing near-complete resorption of the uterovaginal septum (Fig.

5-44). “Arcuate” refers to the minimal indentation of the external fundal contour and fertility rates approximate normal. The arcuate uterus also approximates the bicornuate uterus, and a measurement scheme has been proposed to differentiate the two based on hysterosalpingography findings—the arcuate uterus ratio (see Fig. 5-43).^{28,29} A ratio of fundal indentation height to intercornual length of less than 10% favors arcuate uterus.

Remember that urinary tract anomalies such as renal agenesis, horseshoe kidney, pelvic

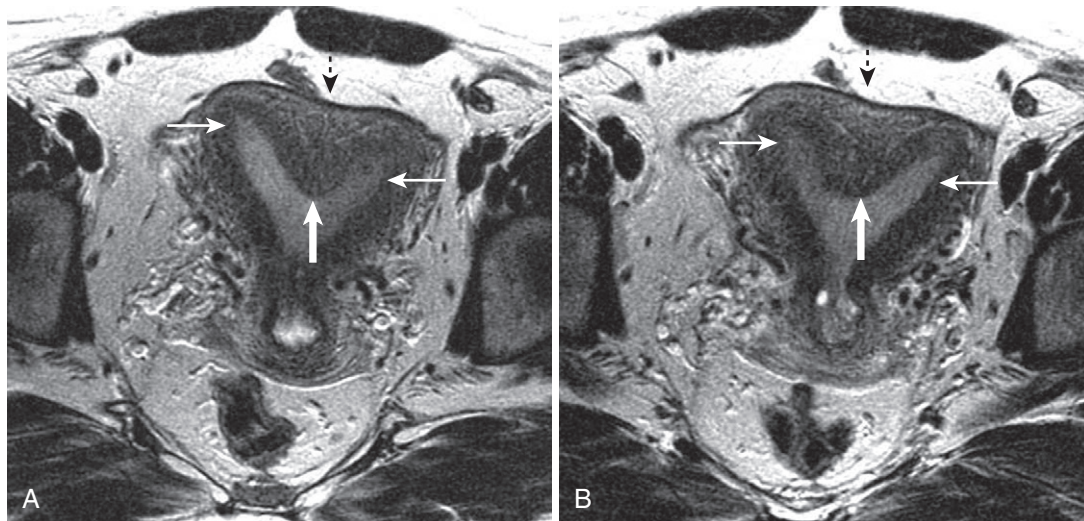


FIGURE 5-44. Arcuate uterus. A and B, Myometrial tissue (*thick arrow*) separating relatively closely apposed uterine cornua (*thin arrows*) associated with a convex fundal contour (*broken arrow*) defines the arcuate uterus, as seen on these axial T2-weighted images.

kidney, and collecting system duplication often coexist with müllerian duct anomalies. For this reason, large field-of-view coronal localizing images including the kidneys are recommended. Finally, a separate subtype addresses a teratogenic anomaly rather than a congenital one—diethylstilbesterol-induced anomalies. The T-shaped uterus (see Fig. 5-4) is the most widely recognized form, and most reflect some degree of hypoplasia.

CERVIX AND VAGINA

Normal Features

The cervix is the cylindrically shaped lowest segment of the uterus—sort of a trunk or pedestal supporting the uterine corpus. The lower half of the cervix protrudes into the upper segment of the vagina and is known as the *portio*. The overall dimensions of the cervix average 3.5 cm in length and 2 cm in diameter. Prolapse, postmenopausal status, or cerclage elongates the cervix. The uterine trilaminar mural stratification pattern is (less graphically) recapitulated in the cervix dominated by a thick central hypointense fibromuscular stromal layer, an inner epithelial layer that generally measures less than 10 mm in thickness, and an outer thin fibromuscular layer. The same T2 signal intensity pattern is demonstrated by the cervix: inner hyperintensity, central hypointensity, and outer intermediate intensity.

Cystic Lesions

NABOTHIAN CYST

The pivotal question in evaluating a cervical lesion is “cystic or solid?” The answer is usually straightforward. Courtesy of the ubiquitous Nabothian cyst, cystic lesions are far more common. A Nabothian cyst is a benign retention cyst reflecting an obstructed mucin-secreting endocervical gland. They are often multiple, usually measure less than 2 cm, and exhibit simple fluid signal (T1 hypointensity and T2 hyperintensity)—but may be mildly hyperintense on T1-weighted images—and do not enhance (Fig. 5-45).

OTHER BENIGN CYSTIC LESIONS

Less common cervical cystic lesions include predominantly benign lesions, such as endocervical or glandular hyperplasia, chronic cervicitis, cervical adenomyosis, and Gartner’s duct cysts (Table 5-14).³⁰ Glandular hyperplasia usually accompanies oral (progestational) contraceptive agents, pregnancy, and postpartum status. MRI features of glandular hyperplasia include well-circumscribed, nonenhancing lesions in the endocervical mucosal layer exhibiting T1 and T2 hyperintensity (Fig. 5-46).

Features of adenomyosis of the cervix simulate uterine adenomyosis and are difficult to perceive in the cervix. Aberrant cervical signal changes, such as T1 hyperintensity or T2 hypointensity, are the only clues, suggesting the presence of hemorrhage.

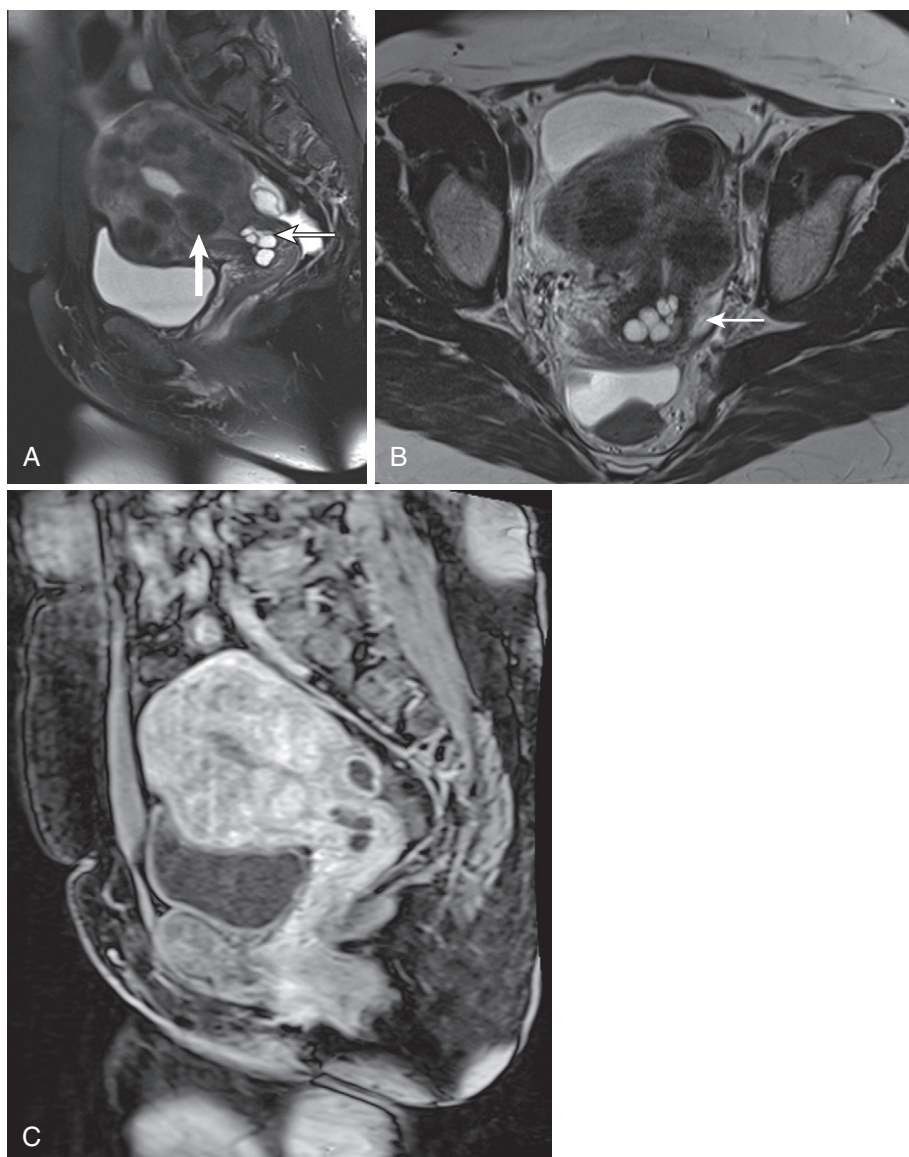


FIGURE 5-45. Nabothian cysts. Sagittal T2-weighted fat-saturated (A) and axial T2-weighted (B) images show a cluster of simple Nabothian cysts (*thin arrow* in A and B) apposed to the endocervical canal in a patient with multiple fibroids, including a submucosal fibroid (*thick arrow* in A). C, Sagittal enhanced T1-weighted fat-saturated image confirms an absence of enhancement.

TABLE 5-14. Differential Diagnosis of Cystic Cervical Lesions

Lesion	Etiology	Magnetic Resonance Features
Cystic Lesions		
Nabothian cyst	Obstructed duct/retention cyst	Usually simple cyst
Endocervical hyperplasia	Hormonal stimulation	Multiple small simple cysts
Chronic cervicitis	Inflammation	Thickened mucosal layer
		Possible cysts
Adenomyosis	Ectopic islands of endometrial tissue	Hemorrhage
Complex Cystic Lesions		
Adenoma malignum	Mucinous adenocarcinoma subtype	Complex cystic mass
Extravaginal Lesions		
Gartner's duct cyst	Congenital—mesonephric duct	Simple cyst
		Anterolateral upper vagina

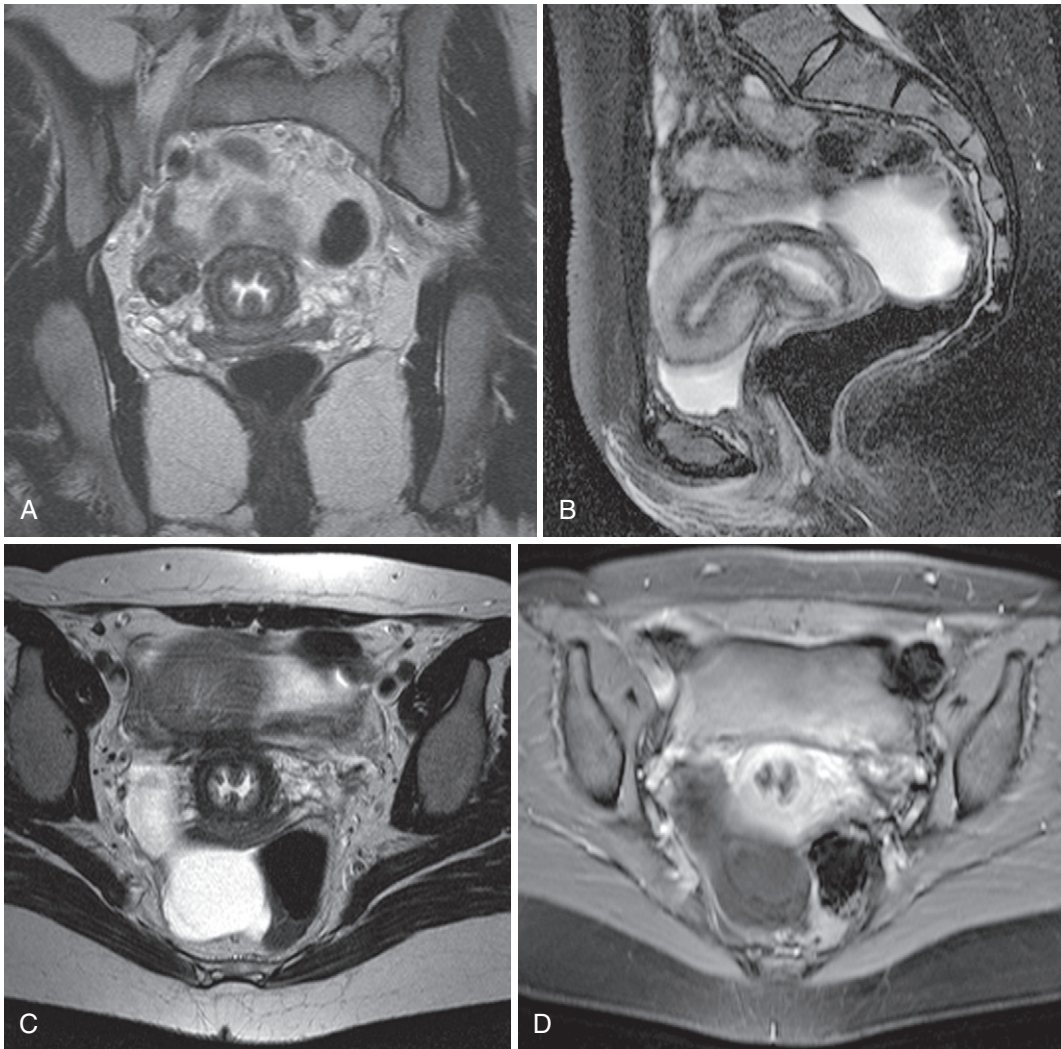


FIGURE 5-46. Cervical glandular hyperplasia. A-D, The cervical endothelium appears uniformly thickened and redundant with preservation of the hypointense fibrous stroma.

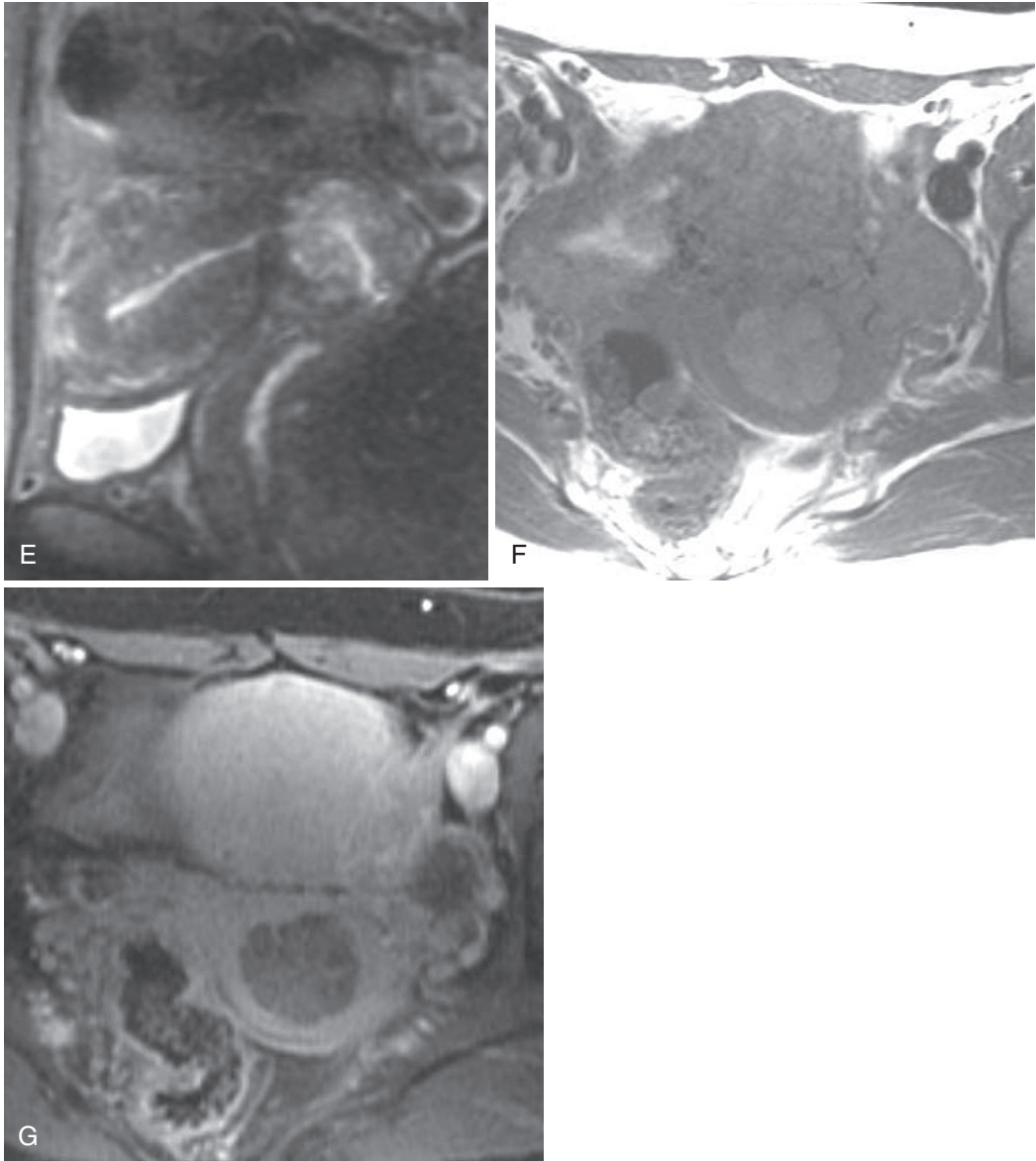


FIGURE 5-46, cont'd E-G, A more florid example of endocervical hyperplasia simulates Nabothian cysts on the sagittal T2-weighted fat-suppressed image (E). Note the mild hyperintensity on the axial T1-weighted image (F) and the lack of enhancement on the fat-suppressed T1-weighted postcontrast image (G)—only thin septal enhancement of intervening tissue is noted.

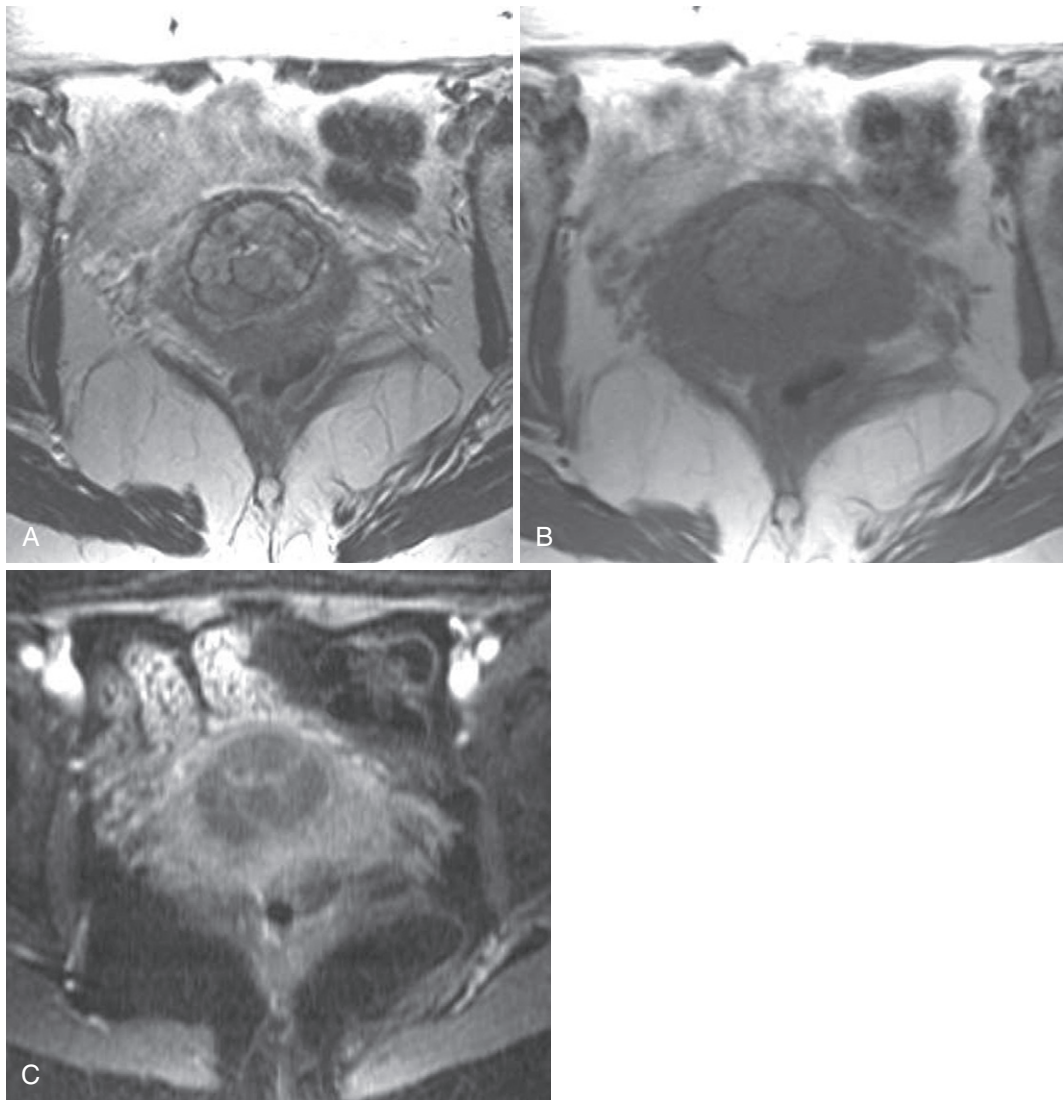


FIGURE 5-47. Chronic cervicitis. Axial T2-weighted (A), T1-weighted (B), and enhanced fat-suppressed T1-weighted (C) images reveal mildly hyperintense cystic cervical lesions with an absence of masslike enhancement.

Cervicitis is a very common gynecologic disease and is probably most commonly not detectable on imaging studies. The disease involves the inner mucosal layer, which may thicken and contain small (often T1-hyperintense) cystic lesions (Fig. 5-47). In the absence of cystic lesions, the only clue may be an absence of zonal anatomy with diffuse intermediate signal throughout the cervix.

Gartner's duct cysts represent remnants of the mesonephric (or wolffian) duct that involutes in the absence of a Y chromosome. Gartner's duct cysts rarely present a diagnostic dilemma because of their simple features and characteristic location. Gartner's duct cysts arise from the anterolateral wall of the vagina above the level

of the pubic symphysis and usually contain simple fluid (Fig. 5-48). Occasionally, higher protein content results in mildly decreased T2 and increased T1 signal compared with simple fluid. Cystic lesions of the female genital tract are easily differentiated based on their characteristic locations but frequently provoke confusion because of their multiplicity.

Various cystic lesions inhabit the female genital tract (Table 5-15). Unless large lesion size induces symptoms, diagnosis is academic. For the most part, location dictates diagnosis. Müllerian and Gartner's duct cysts are embryologic remnants of the müllerian or paramesonephric or wolffian or mesonephric ducts, respectively, arising from the anterolateral wall of the upper

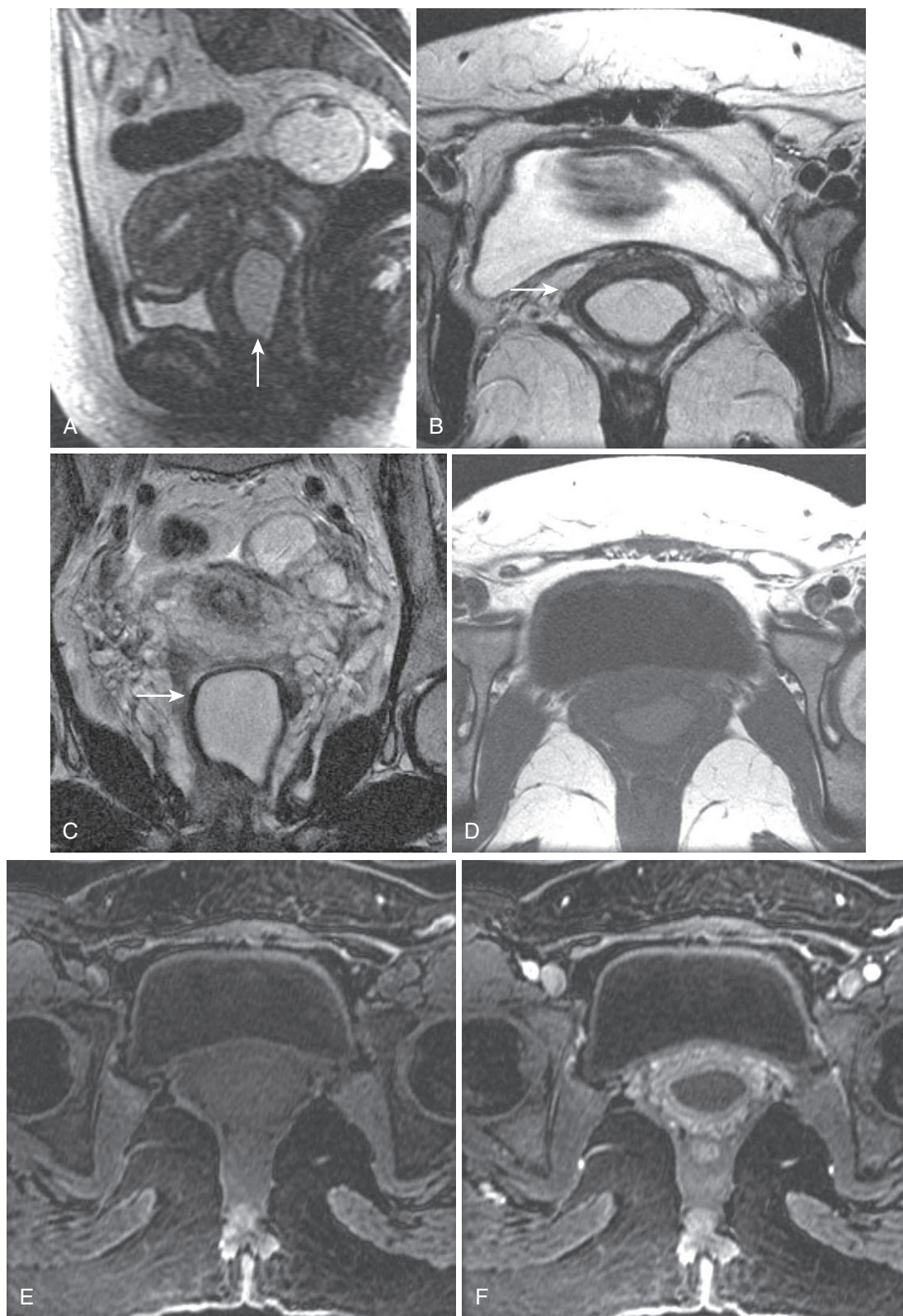


FIGURE 5-48. Gartner's duct cyst. Sagittal (A), axial (B), and coronal (C) T2-weighted images reveal a uniformly hyperintense lesion in the upper vagina seen to be anteriorly located on the sagittal image (*arrow*). Mild hyperintensity indicates proteinaceous content on the T1-weighted image (D), and lack of enhancement is reflected on the precontrast (E) and postcontrast (F) images.

TABLE 5-15. Cystic Lesions of the Female Genital Tract

Lesion	Etiology	Magnetic Resonance Features
Gartner's duct cyst	Congenital—mesonephric duct	Simple cyst Anterolateral upper vagina
Müllerian duct cyst	Congenital—Müllerian duct	Anywhere in vagina, usually large simple cyst
Vaginal inclusion cyst	Postsurgical or traumatic	Simple cyst Lower posterior or lateral vagina
Bartholin's gland cyst	Dilated Bartholin's gland	Posterolateral vaginal introitus
Skene's gland cyst	Dilated periurethral gland	Adjacent to distal urethra
Urethral diverticulum	Infection/inflammation	Arise from posterior urethra Often encircle urethra

vagina above the level of the pubic symphysis (Fig. 5-49). Bartholin's gland cysts are abnormally dilated Bartholin's glands in the posterolateral vaginal introitus seen medial to the labia minora (Figs. 5-50 and 5-51). Skene's gland cysts represent abnormal dilatation of the periurethral glands adjacent to the distal urethra (Fig. 5-52). Vaginal inclusion cysts are the most common acquired vaginal cysts, usually located within the lower posterior or lateral vaginal wall, often postsurgical or traumatic in etiology.

ADENOMA MALIGNUM

Cervical neoplasms—dominated by cervical cancer—are rarely cystic. An infamous subtype of mucinous adenocarcinoma of the cervix, known as *adenoma malignum* (or “minimal deviation adenocarcinoma”) has a deceptively benign, cystic appearance. Despite its deceptive well-differentiated histopathologic features, adenoma malignum disseminates promptly into the peritoneal cavity and to distant sites.³¹ The classic morphologic description of adenoma malignum is a botryoidal (grapelike) cluster of cysts within background stroma. Whereas cysts dominate, relatively understated complex features—thick septae, irregular margins, and enhancing solid components—at least suggest the possibility of malignancy (Fig. 5-53). The characteristic presentation of vaginal discharge occasionally correlates with fluid within the uterine/cervical or vaginal canal on MRI.

Solid Lesions

CERVICAL CARCINOMA

The vast majority (85%) of cervical carcinomas are of the squamous cell histopathologic type and exhibit solid morphology. Cervical carcinoma originates from the mucosal layer at the squamocolumnar junction—the boundary between the squamous mucosa of the vagina and the columnar mucosa of the uterus. The tumor is intermediate in signal on T2-weighted images—darker than normal cervical mucosa and brighter than inner fibromuscular stroma (Fig. 5-54). Enhancement is variable but present and should be confirmed with careful comparison between pregadolinium and postgadolinium images and/or subtracted images. A bimodal growth pattern is explained by age-related changes; more caudal growth in younger patients and cephalad extension toward the uterus in older patients are a function of cephalad migration of the squamocolumnar junction with aging.

Although staging is usually the primary objective because the diagnosis is often already established, always consider alternative etiologies. If the diagnosis is still in doubt, other potential etiologies include endometrial carcinoma, lymphoma/metastasis, benign cervical polyp, and cervical fibroid (Table 5-16). The features of endometrial and cervical carcinoma overlap, and the chief distinguishing characteristic is endometrial versus endocervical origin (if this can be ascertained). In the end, establishing an etiology with precision is moot. Unless a fibroid is confidently diagnosed, biopsy or excision is the next step.

Start with identifying the endocervical canal—if still identifiable. Assess the location of the tumor with respect to the canal and assess the integrity of the hypointense fibrous cervical stroma (Fig. 5-55)—the key issue in MRI of cervical carcinoma. Violation of the hypointense fibrous cervical stroma separates stage IB from stage IIB disease and surgical disease from non-surgical disease treated with radiation therapy (Table 5-17). Look for tumor extending into the vagina (best assessed on axial and sagittal T2-weighted and T1-weighted postgadolinium images)—IIA and IIIA disease. Next, inspect the parametrial tissues for extracervical extension of tumor. T1-weighted images without fat saturation and T2-weighted and T1-weighted

Text continued on p. 317

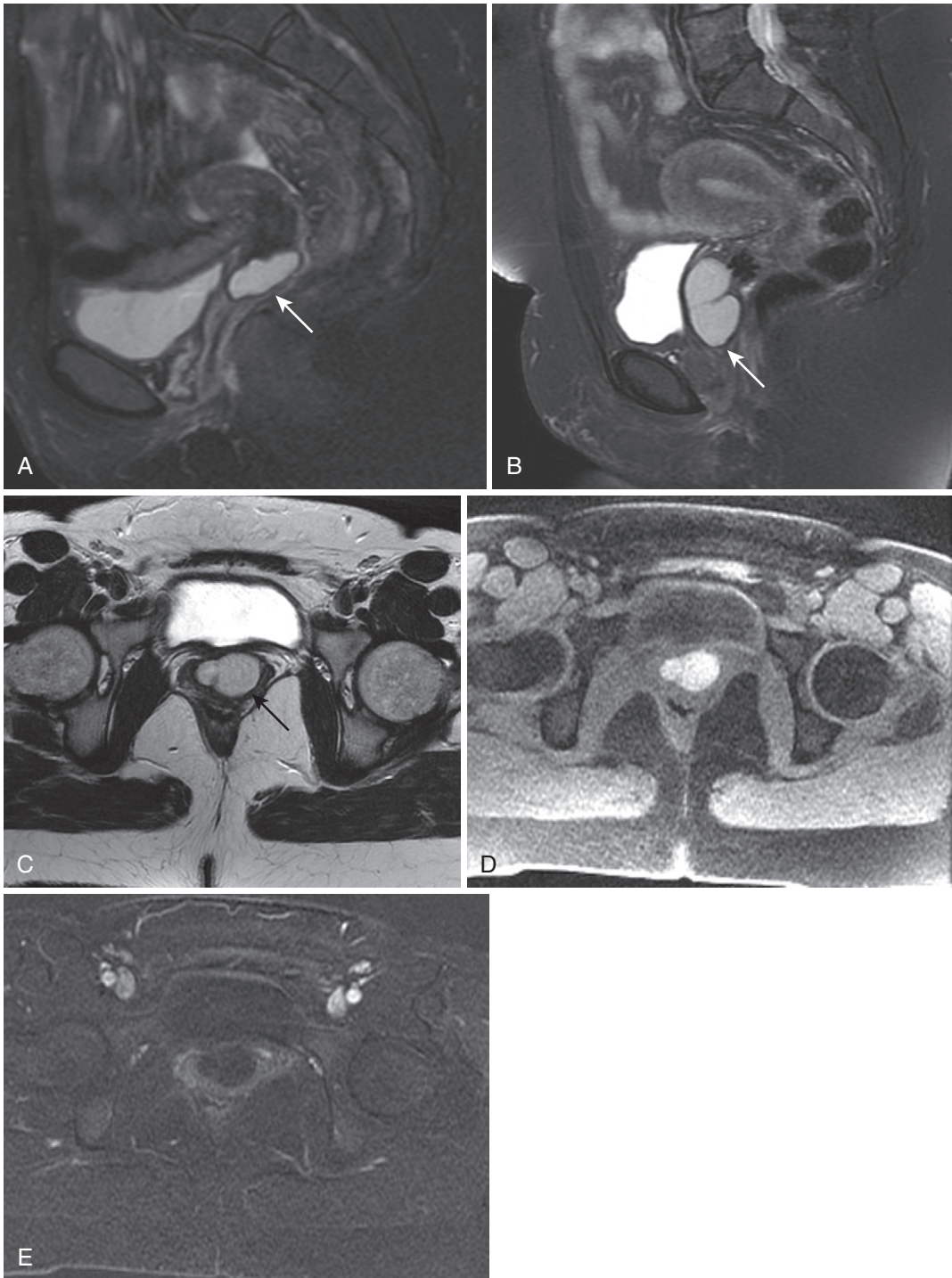


FIGURE 5-49. Müllerian duct cyst. The sagittal T2-weighted fat-suppressed image (A) demonstrates a large cystic lesion in the upper vagina (*arrow*). In a different patient (B), the sagittal fat-suppressed (B) and axial (C) images shows a large septated cystic lesion (*arrow*) also in the upper vagina. The fat-saturated T1-weighted image (D) demonstrates hyperintensity due to mucinous/proteinaceous content and the subtracted postcontrast image (E) confirms cystic nature with lack of enhancement.

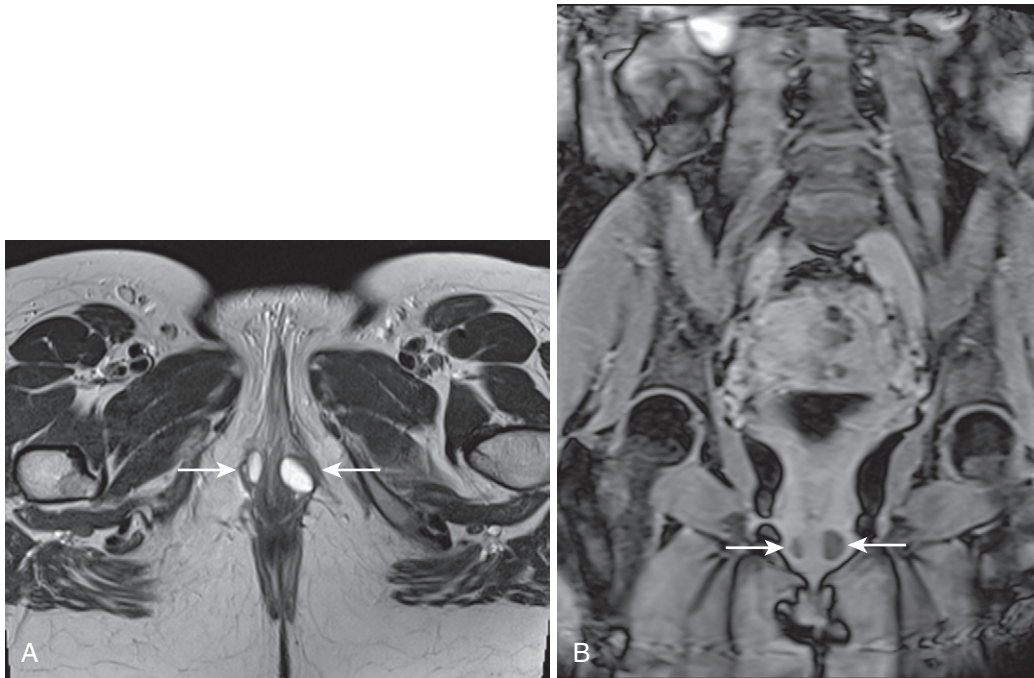


FIGURE 5-50. Bartholin's gland cysts. **A**, Axial T2-weighted image reveals two small cystic lesions inhabiting the vaginal introitus, located posteriorly and caudally, as illustrated on the coronal enhanced T1-weighted image (**B**), revealing the cystic nature of the lesions (*arrows*).

TABLE 5-16. Differential Diagnosis of Cervical Carcinoma

Solid Lesions	
<i>Benign</i>	
Cervical fibroid	Usually small (5–10 mm) Well-circumscribed
Cervical Polyp	
<i>Malignant</i>	
Endometrial carcinoma with cervical spread	Endometrial origin Myometrial invasion
Vaginal carcinoma with cervical spread	Vaginal origin Far less common No mucosal involvement
Lymphoma	Disseminated lymphadenopathy Larger size Far less common
Uterine sarcoma (leiomyosarcoma, endometrial sarcoma, hemorrhage, cystic necrosis, malignant mixed müllerian tumor)	
Complex Cystic Lesions	
Cervicitis	Absence of solid component No enhancement Preservation of mural stratification
Glandular hyperplasia	Absence of solid component No enhancement Preservation of mural stratification

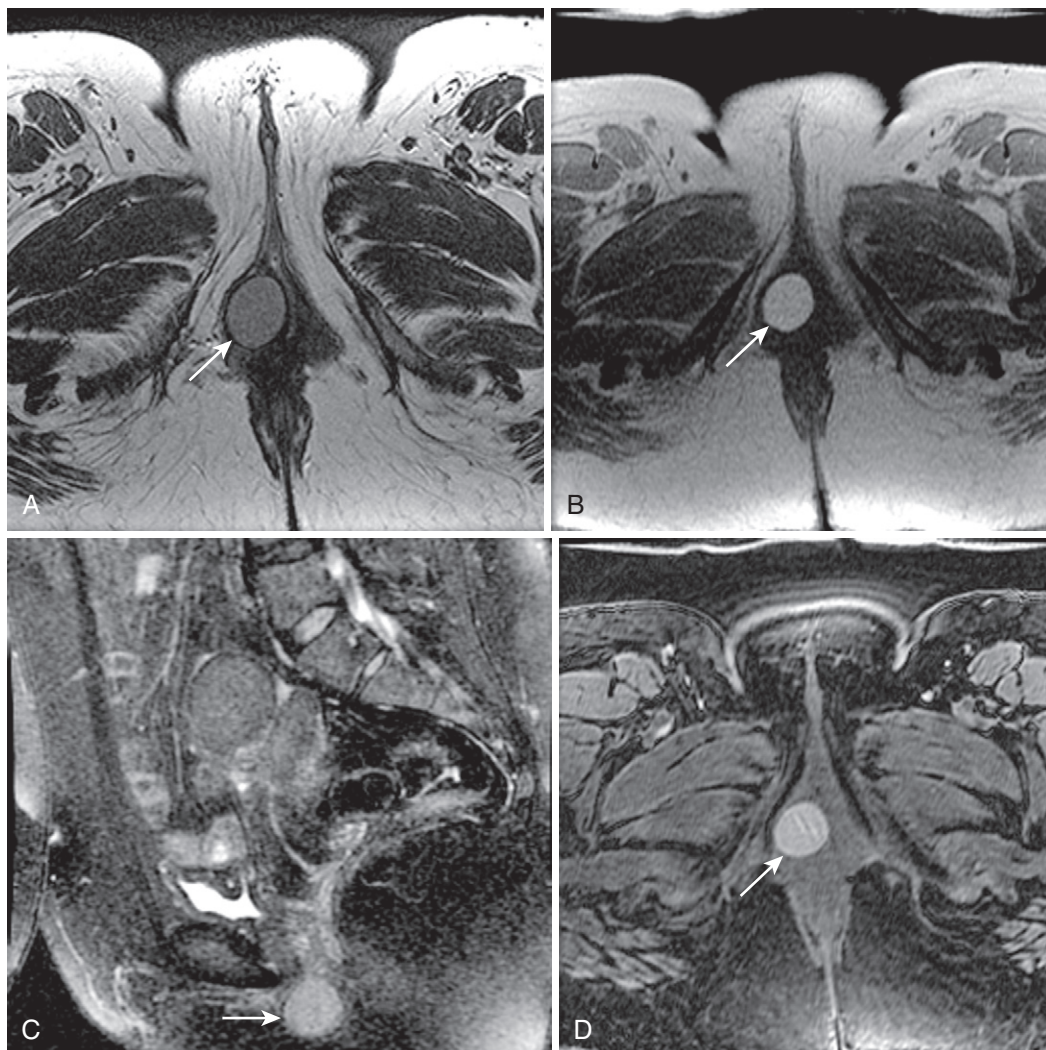


FIGURE 5-51. Large complex Bartholin's gland cyst. A large T2 hypointense and T1 hyperintense lesion (*arrow*) on axial T2- (A) and T1-weighted in-phase gradient echo (B) images in the lateral aspect of the vagina with preserved hyperintensity on the corresponding fat-suppressed image (C) is localized to the lower vaginal introitus below the level of the symphysis pubis as seen on the sagittal T2-weighted fat-suppressed image (D).

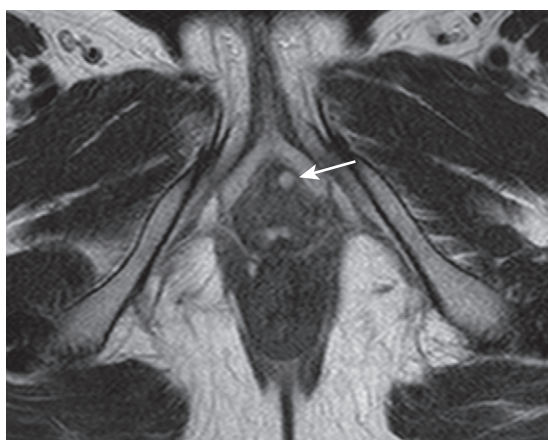


FIGURE 5-52. Skene's gland cyst. A small cystic structure abutting the distal urethra represents a dilated periurethral (or Skene's) gland cyst (*arrow*).

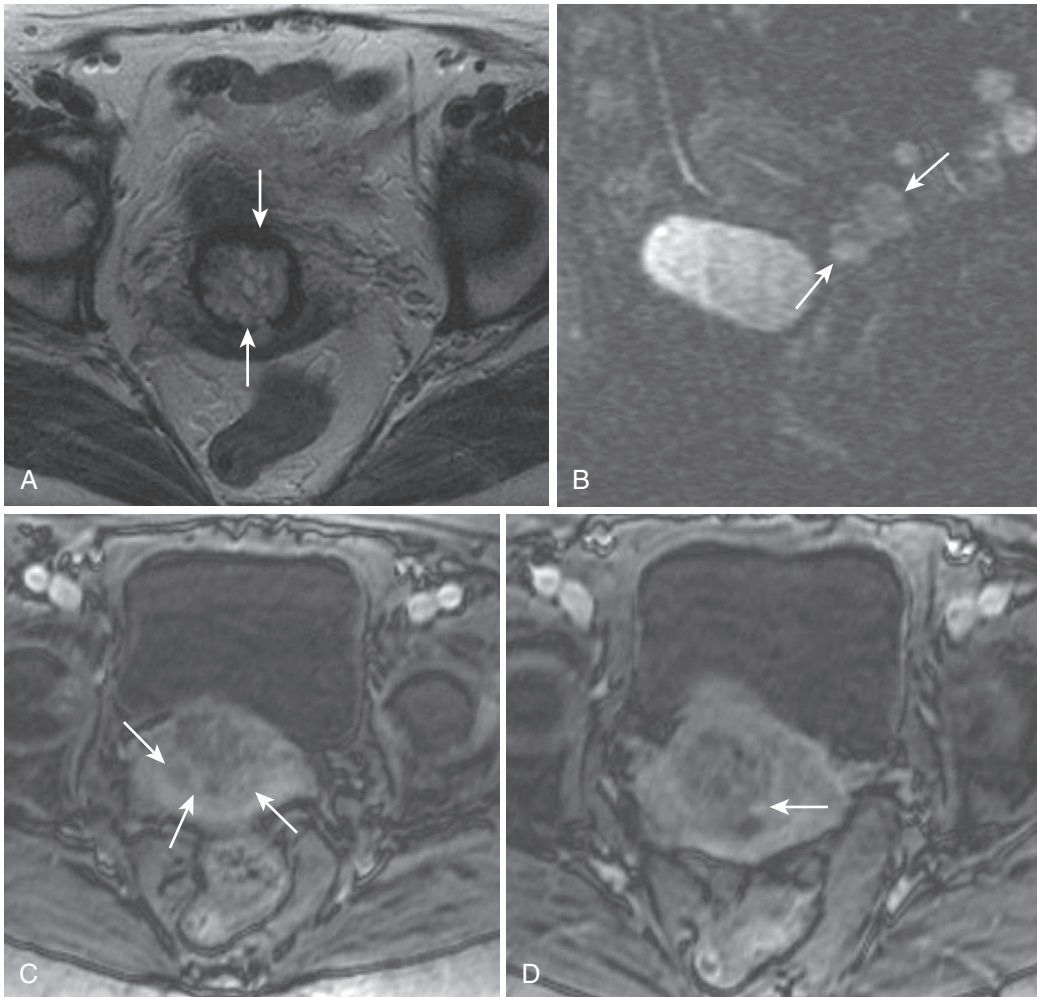


FIGURE 5-53. Adenoma malignum. **A**, Axial T2-weighted image depicts a hyperintense cervical lesion (*arrows*) within the fibrous stroma with a botrioidal, or grapelike, morphology. **B**, The signal-starved T2-weighted fat-saturated image shows the lesion expanding the cervix (*arrows*) and the appearance simulates Nabothian cysts. **C** and **D**, T1-weighted images after intravenous gadolinium administration reveal multifocal solid linear and nodular enhancing foci (*arrows*) not present in benign cervical lesions, such as Nabothian cysts or cervicitis (compare with [Figs. 5-45 to 5-47](#)).

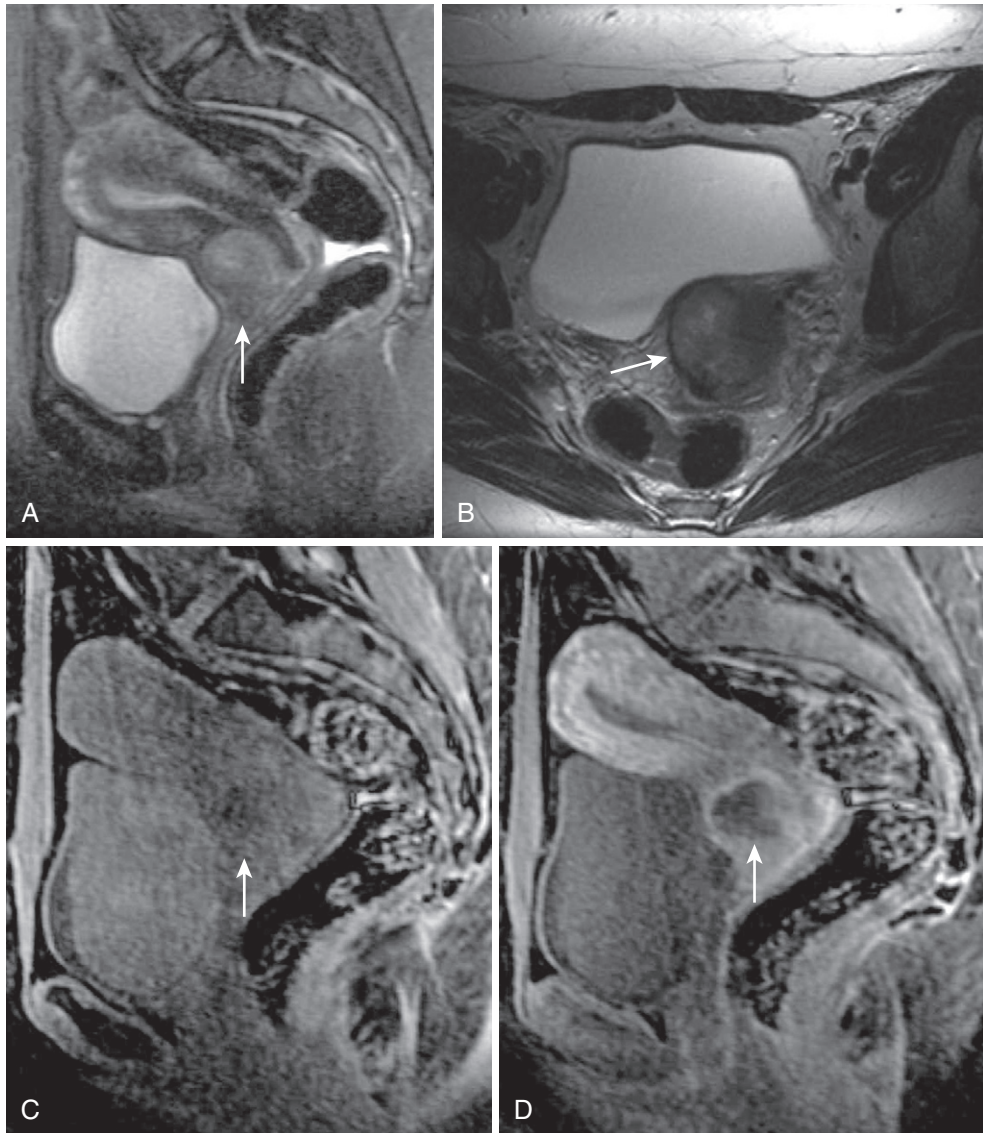


FIGURE 5-54. Cervical carcinoma. An ill-defined mildly hyperintense lesion (*arrow*; hypointense to endometrium and hyperintense compared with fibrous stroma) invades anteriorly on sagittal (A) and axial (B) T2-weighted images. Comparing precontrast (C) with post-contrast (D) images confirms enhancement and relative hypovascularity.

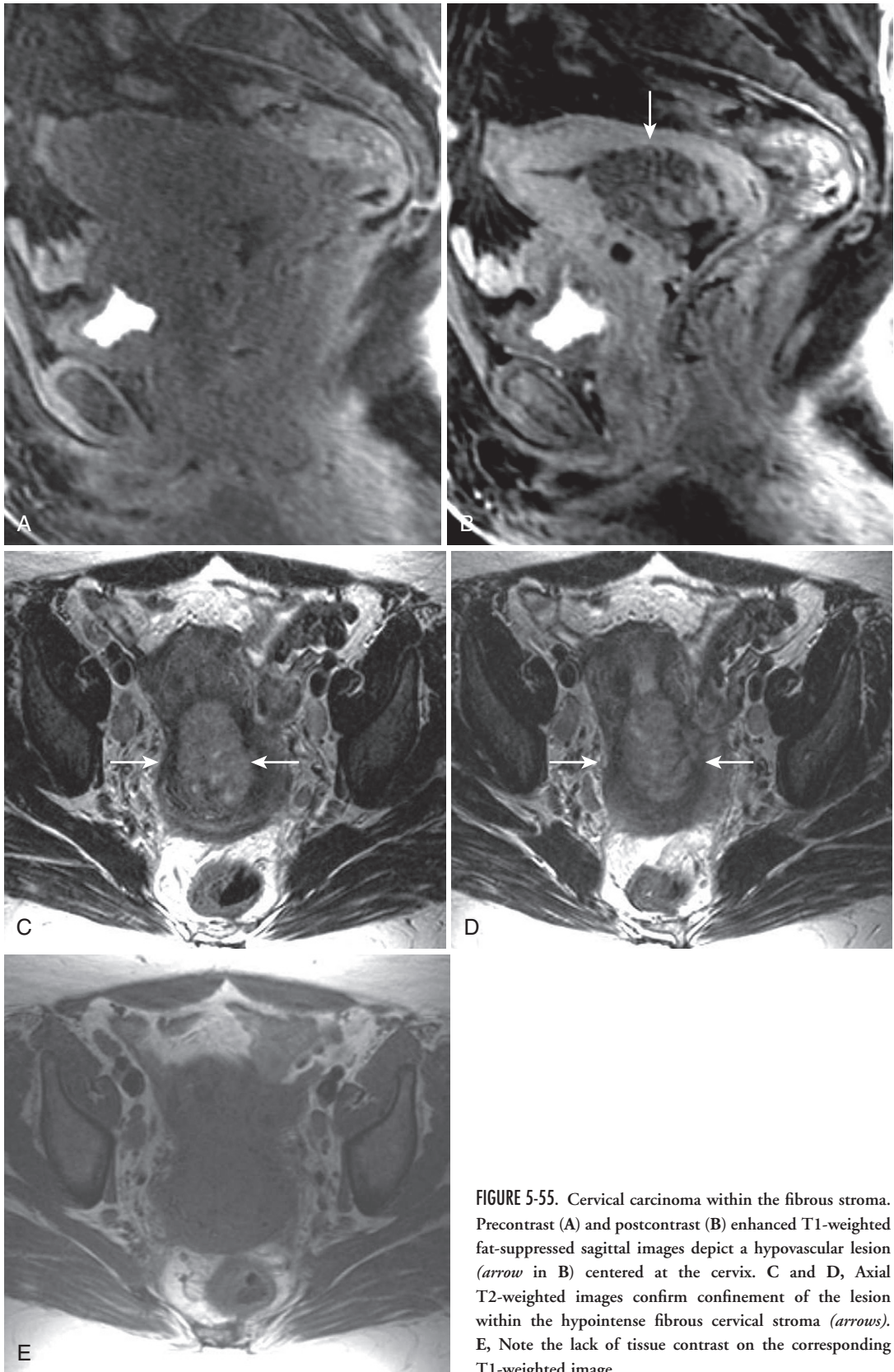


FIGURE 5-55. Cervical carcinoma within the fibrous stroma. Precontrast (A) and postcontrast (B) enhanced T1-weighted fat-suppressed sagittal images depict a hypovascular lesion (arrow in B) centered at the cervix. C and D, Axial T2-weighted images confirm confinement of the lesion within the hypointense fibrous cervical stroma (arrows). E, Note the lack of tissue contrast on the corresponding T1-weighted image.

TABLE 5-17. Staging of Cervical Carcinoma

International Federation of Gynecology and Obstetrics Staging	Magnetic Resonance Imaging Findings	Treatments
0. Carcinoma in situ	Not visible	
I. Confined to cervix		
• IA. Microscopic		
◦ IA-1. Stromal invasion <3 mm	Not visible	Surgery
◦ IA-2. >3-mm, <5-mm invasion	Small enhancing tumor	Surgery
• IB. Clinically visible (>5 mm)	Tumor visible (intact stroma)	Surgery
◦ IB-1. <4 cm		Surgery
◦ IB-2. >4 cm		X-ray therapy
II. Extends beyond uterus but not to pelvic wall or lower third of vagina		
• IIA. Vaginal extension, no parametrial invasion	Vaginal wall disruption	Surgery (<4 cm), x-ray therapy (>4 cm)
• IIB. Parametrial invasion	Stromal, parametrial invasion	X-ray therapy
III. Extension to lower third of vagina or pelvic wall invasion with hydronephrosis		
• IIIA. Extension to lower third of vagina	Invasion lower vagina	X-ray therapy
• IIIB. Pelvic wall invasion with hydronephrosis	Pelvic muscle or dilated ureter	X-ray therapy
IV. Located outside true pelvis		
• IVA. Bladder or rectal mucosa	Loss low signal bladder/rectal wall	X-ray therapy
• IVB. Distant metastasis		X-ray therapy

From Nicolet V, Carignan L, Bourdon F, Prosmann O. MR imaging of cervical carcinoma: A practical staging approach. *Radiographics* 20:1539-1549, 2000.

postgadolinium images with fat saturation are most sensitive for parametrial spread—IIB disease. Look for ill-defined hypointensity infiltrating the hyperintense parametrial fat or hyperintensity infiltrating the saturated parametrial fat, respectively (Fig. 5-56). Assess the status of the ureters on axial and/or coronal T2-weighted images for abnormal dilatation conceivably due to neoplastic involvement—IIIB. Check the axial and sagittal T2-weighted and T1-weighted postgadolinium images for obliteration of tissue planes separating the cervix and bladder and/or rectum (Fig. 5-57)—IVA. Do not forget to inspect the pelvic sidewall—not only for direct extension of tumor but also for lymphadenopathy. The pivotal findings are parametrial invasion and violation of the fibrous stroma, which generally preclude surgical treatment. Keep in mind that the accuracy of MRI staging ranges between 76% and 92%.^{33,34}

Occasionally, vaginal carcinoma simulates cervical carcinoma depending on its location and extent. The MRI appearance is basically indistinguishable—the tumor usually appears as a relatively T2 hyperintense, infiltrative, indistinct mass. Only when clearly confined to the vagina should vaginal carcinoma be considered because of its low incidence compared with cervical carcinoma. Combined vaginal and cervical involvement implicates cervical carcinoma over vaginal carcinoma proportional to the relatively higher prevalence.

OVARIES AND ADNEXA

Normal Anatomy

The adnexa includes the ovaries and everything else—paired fallopian tubes, broad and other parametrial ligaments, and the associated vascular structures. Only the ovaries are consistently well visualized and of clinical relevance—disorders of the supporting structures are beyond the scope of this text. The size and appearance of the normal ovary depend on menstrual status (Fig. 5-58). Female hormones induce growth, and functional cyst development in the ovary and normal ovarian features are listed in Figure 5-59.

The first task is to find the ovaries, usually located in proximity to the iliac vessels near the bifurcation. However, the ovaries are not rigidly tethered. Medially, they are adherent to the fallopian tubes, caudally to the broad ligament, medially to the proper ovarian ligament, and superolaterally to the suspensory ligament, which contains the ovarian vessels (Fig. 5-60). Usually, T2-weighted images provide the best anatomic roadmap and chance of finding the ovaries. First, scan the adnexa for an ovariform structure with or without cysts. Next, trace the ovarian vein caudally over the iliac vessels into the suspensory ligament, hopefully into a recognizable ovary. If that fails, try to find the round ligament entering the internal inguinal os and follow it posteromedially—proximally,

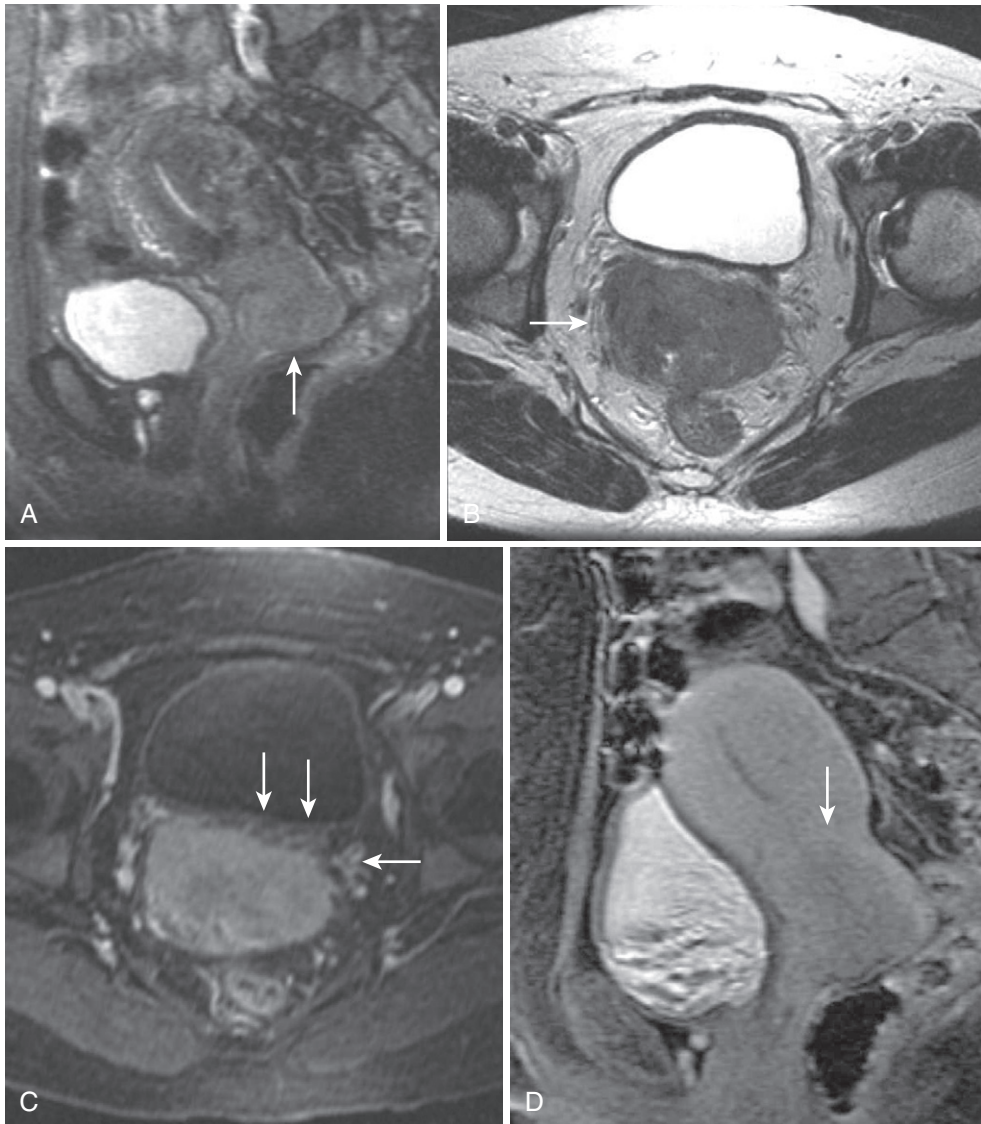


FIGURE 5-56. Cervical carcinoma with parametrial invasion. Sagittal fat-suppressed (A) and axial (B) T2-weighted images reveal a mildly hyperintense mass arising from the uterine cervix replacing normal anatomy (*arrow*) and obliterating the fibrous stroma, extending into the parametrium. C, Parametrial spread is better depicted on the axial enhanced image (*arrows*). D, The corresponding sagittal delayed postcontrast image illustrates the hypovascular, gradual enhancement of the mass (*arrow*).

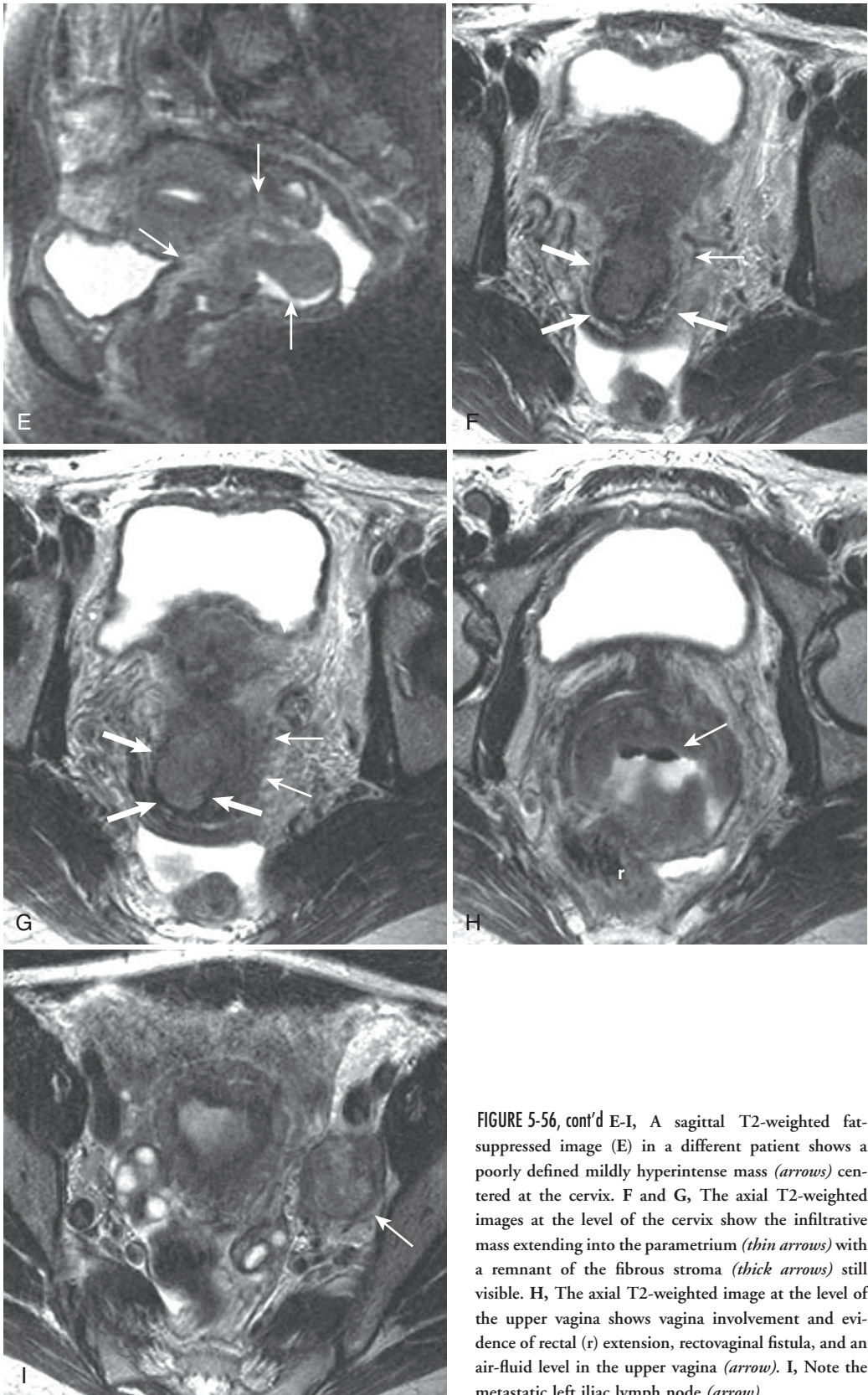


FIGURE 5-56, cont'd E-I, A sagittal T2-weighted fat-suppressed image (E) in a different patient shows a poorly defined mildly hyperintense mass (*arrows*) centered at the cervix. F and G, The axial T2-weighted images at the level of the cervix show the infiltrative mass extending into the parametrium (*thin arrows*) with a remnant of the fibrous stroma (*thick arrows*) still visible. H, The axial T2-weighted image at the level of the upper vagina shows vagina involvement and evidence of rectal (r) extension, rectovaginal fistula, and an air-fluid level in the upper vagina (*arrow*). I, Note the metastatic left iliac lymph node (*arrow*).

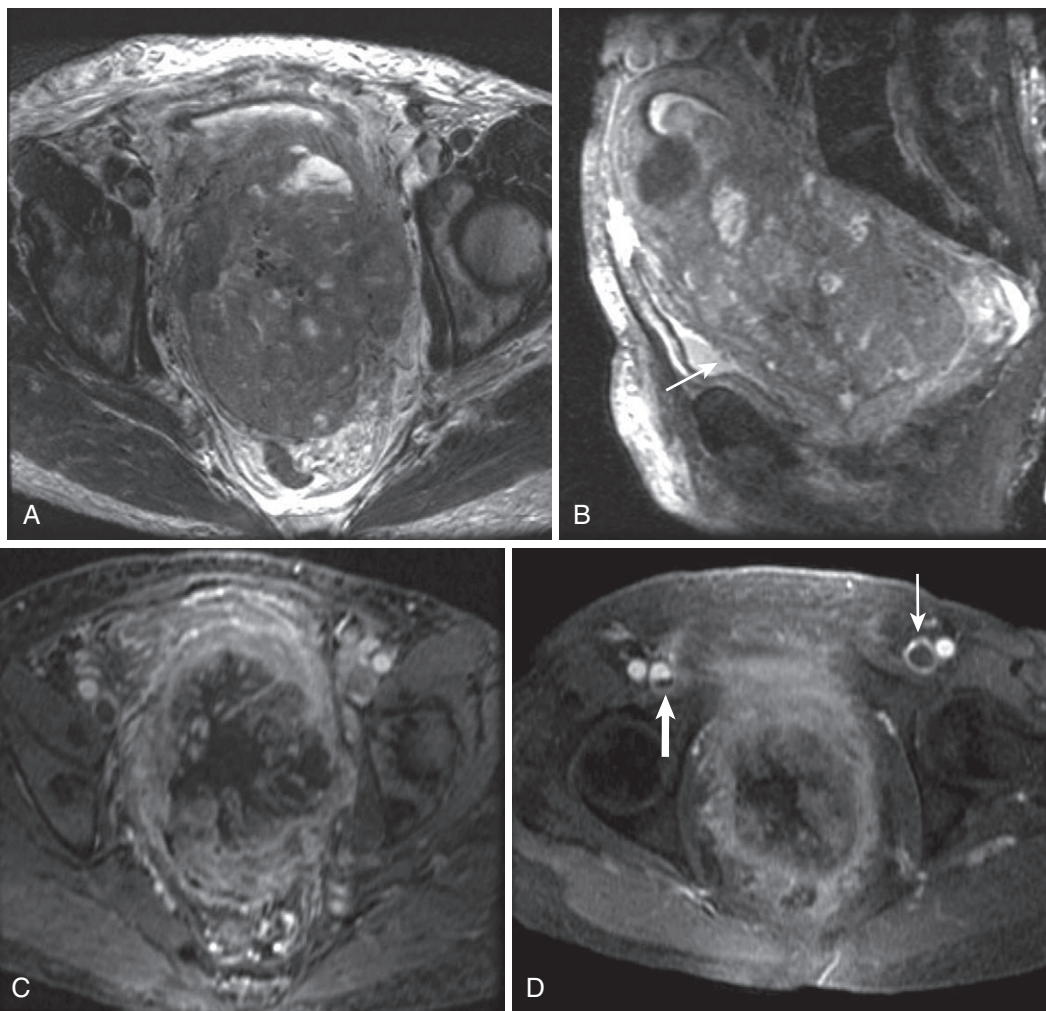


FIGURE 5-57. Cervical carcinoma with local invasion of rectum and/or bladder. A large, heterogeneous mass displaces the bladder anteriorly on the axial T2-weighted image (A), virtually replaces the entire uterus on the sagittal T2-weighted image (B), and invades the bladder, which features endoluminal irregularity indicating transmural extension (arrow in B). C, Gadolinium enhancement shows central necrosis. D, The delayed image shows near-occlusive (*thin arrow*) and nonocclusive (*thick arrow*) thrombus in the common femoral veins.

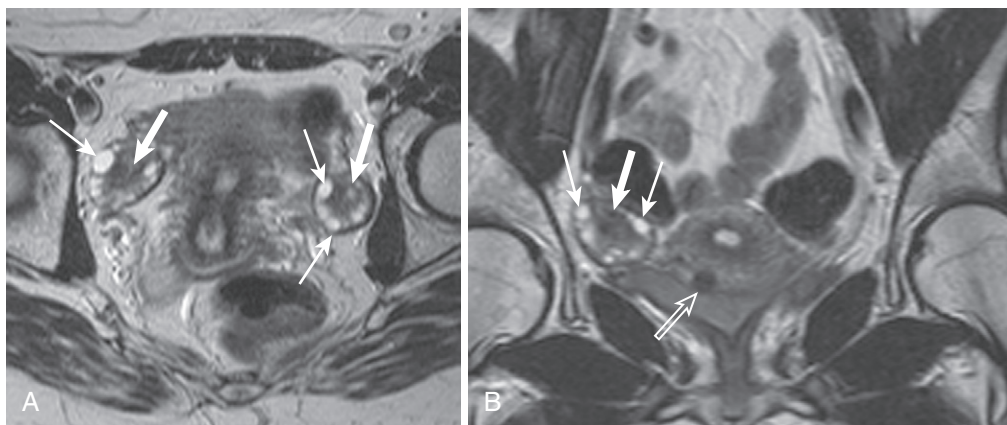


FIGURE 5-58. Normal ovaries. Normal ovaries averaging 10 cc in size with subcentimeter ovoid, peripheral subcentimeter follicle cysts (*thin arrows*), and central stroma (*thick arrows*) are easily identified when noting these typical characteristics, as exemplified on the axial (A) and coronal (B) T2-weighted images. A small, partially subserosal fibroid protrudes from the anterior uterine body (*open arrow* in B).

NORMAL OVARIAN FEATURES

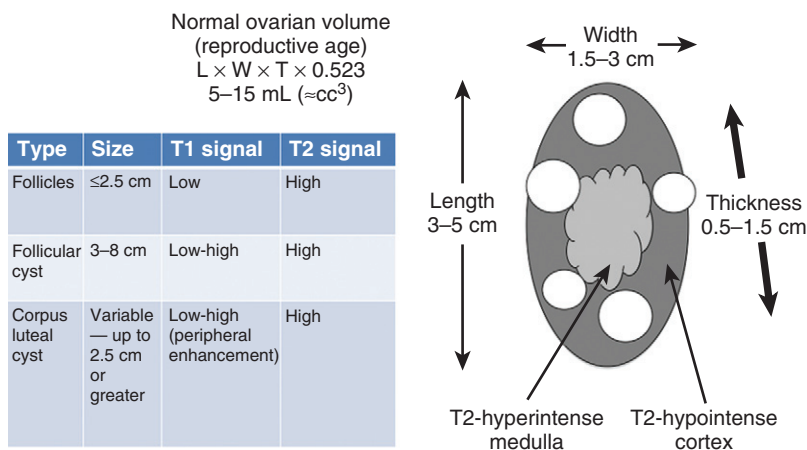


FIGURE 5-59. Normal ovarian features.

it courses along the anterior edge of the broad ligament in the vicinity of the ovary and abutting the proper ovarian ligament (see Figs. 5-7 and 5-60). Inevitably, loops of (usually small) bowel occupy the adnexal regions and complicate the process. As long as you exclude the presence of an underlying adnexal mass, you have accomplished your mission.

Ovarian lesion characterization and diagnosis figure prominently among the major indications for pelvic MRI and boast a high probability of success. A major discriminator is solid (or at least partially solid) versus cystic. Cystic lesions are far more common and the approach should focus on two things—cyst content and complexity (differentiating neoplastic from non-neoplastic cysts) (Tables 5-18 and 5-19).

Cystic Lesions

First of all, to call a lesion “cystic,” you must exclude a change in intensity between T1-weighted pregadolinium and postgadolinium images (which is an analog to perfusion, implying solid tissue). Catalog the signal intensity on the various pulse sequences. Using these data, almost all cysts fall into one of three broad categories based on their content: (1) water, (2) lipid, and (3) hemorrhage.

Cystic ovarian lesions cannot be assessed on one pulse sequence alone. Accurate classification requires binary information from various pulse sequence. The T2-weighted axial sequence portrays cystic lesions consistently as round hyperintense foci—albeit mildly variable

TABLE 5-18. Differential Diagnosis of Cystic Ovarian Lesions

Lesion	Tissue Content
T2-Hypointense Adnexal Lesions	
Subserosal pedunculated fibroids	Collagen
Endometrioma (shading)	Concentrated blood products
Ovarian torsion	Hemorrhage
Ectopic pregnancy	Hemorrhage
Vascular lesions	Signal voids
Cystadenofibroma (cystic components dominate)	Fibrous tissue
Fibroma/fibrothecoma	Fibrous stroma
Brenner tumor	Fibrous stroma
T1-Hyperintense Adnexal Lesions	
Hemorrhagic cyst	Hemorrhage
Endometrioma	Hemorrhage
Subserosal pedunculated fibroid with hemorrhagic degeneration	Hemorrhage
Ovarian torsion (peripheral hyperintensity)	Hemorrhage
Dermoid cyst (hypointense with fat saturation)	Fat
Bilateral Adnexal Lesions	
Functional ovarian cysts	
Ovarian epithelial neoplasms	
Metastatic lesions (Krukenberg's tumors)	
Endometriomas	
Estrogenic Adnexal Masses	
Granulosa cell tumor (most common)	
Thecoma/fibrothecoma	
Virilizing Adnexal Masses	
Sertoli-Leydig tumor	
Cystic teratoma	
Metastatic tumors	

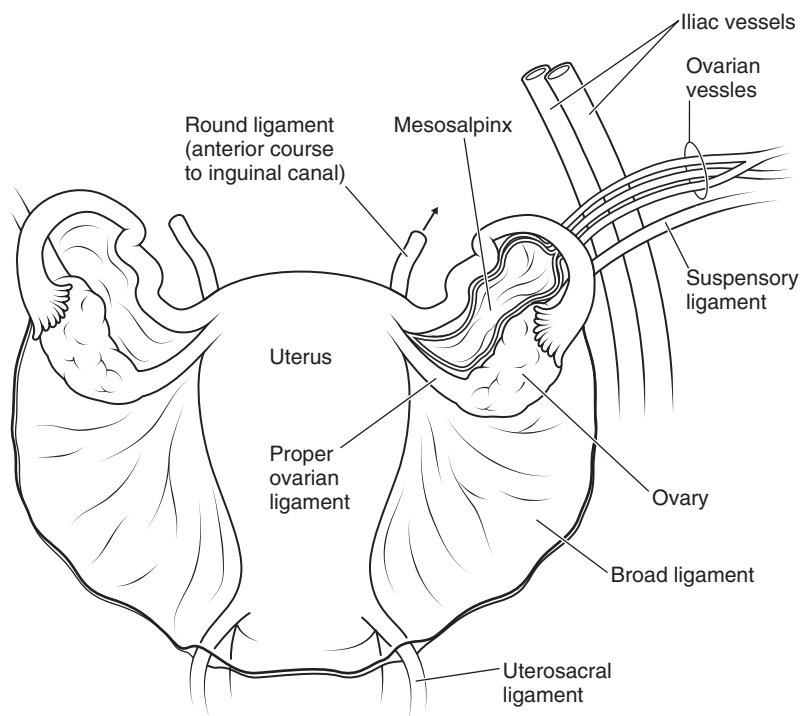


FIGURE 5-60. Ovarian attachments.

TABLE 5-19. Age-Predictive Probability Scheme for Cystic Ovarian Lesions

Prepubertal	Reproductive	Menopausal
Germ cell 80%	Functional 70%	Malignant 50%
Malignant 10%	Endometrioma 10%	
	Neoplastic 20%	
	Benign 85%	
	Malignant 15%	

From Gant NF, Cunningham FG. *Basic Gynecology and Obstetrics*. Norwalk, CT: Appleton and Lange, 1993.

depending on cyst content (water > blood and fat). Next, note the signal intensity on a T1-weighted sequence without fat saturation—hypointensity connotes water and hyperintensity indicates lipid or blood. Finally, review T1-weighted fat-saturated images to distinguish between fat and blood; signal cancellation indicates fat. Although this seems redundant, following this scheme avoids errors in characterization. Some common errors include designating a T1-hyperintense lesion as a hemorrhagic cyst or endometrioma without noting signal suppression on fat-saturated images, or misclassifying a T2-hyperintense lesion with no signal on T1-weighted fat saturated images as a dermoid without considering the possibility of a simple cyst with no signal on T1-weighted images without fat saturation.

WATER CONTENT

Of course, to equate “water” with ovarian cyst content of any etiology is an oversimplification. Nonetheless, this construct serves its purpose to identify a population of ovarian cysts that are further subclassified. “Water” defines the upper limit of hyperintensity on T2-weighted images with commensurate hypointensity on T1-weighted images. Enhancement is absent (Fig. 5-61). Under these circumstances, as long as the size of the lesion does not violate physiologic limits and there is no evidence of wall thickening, septation, or mural nodularity to suggest underlying neoplasm, no further analysis is necessary.

FUNCTIONAL OVARIAN CYSTS

The normal menstrual cycle involves the recruitment of a cohort of functional (or follicular) cysts that are generally smaller than 1 cm. A single dominant cyst enlarges up to 2.5 cm and usually undergoes ovulation, evolving into the corpus luteal cyst. Hemorrhagic cysts join the other two categories of functional cysts (follicular and corpus luteal) and reflect blood from a ruptured vessel in the wall of a follicular cyst (see “Blood Content” under “Cystic Lesions”). Even the postmenopausal ovary often continues to produce cysts that are usually spherical, simple, and unilocular. Therefore, regardless of

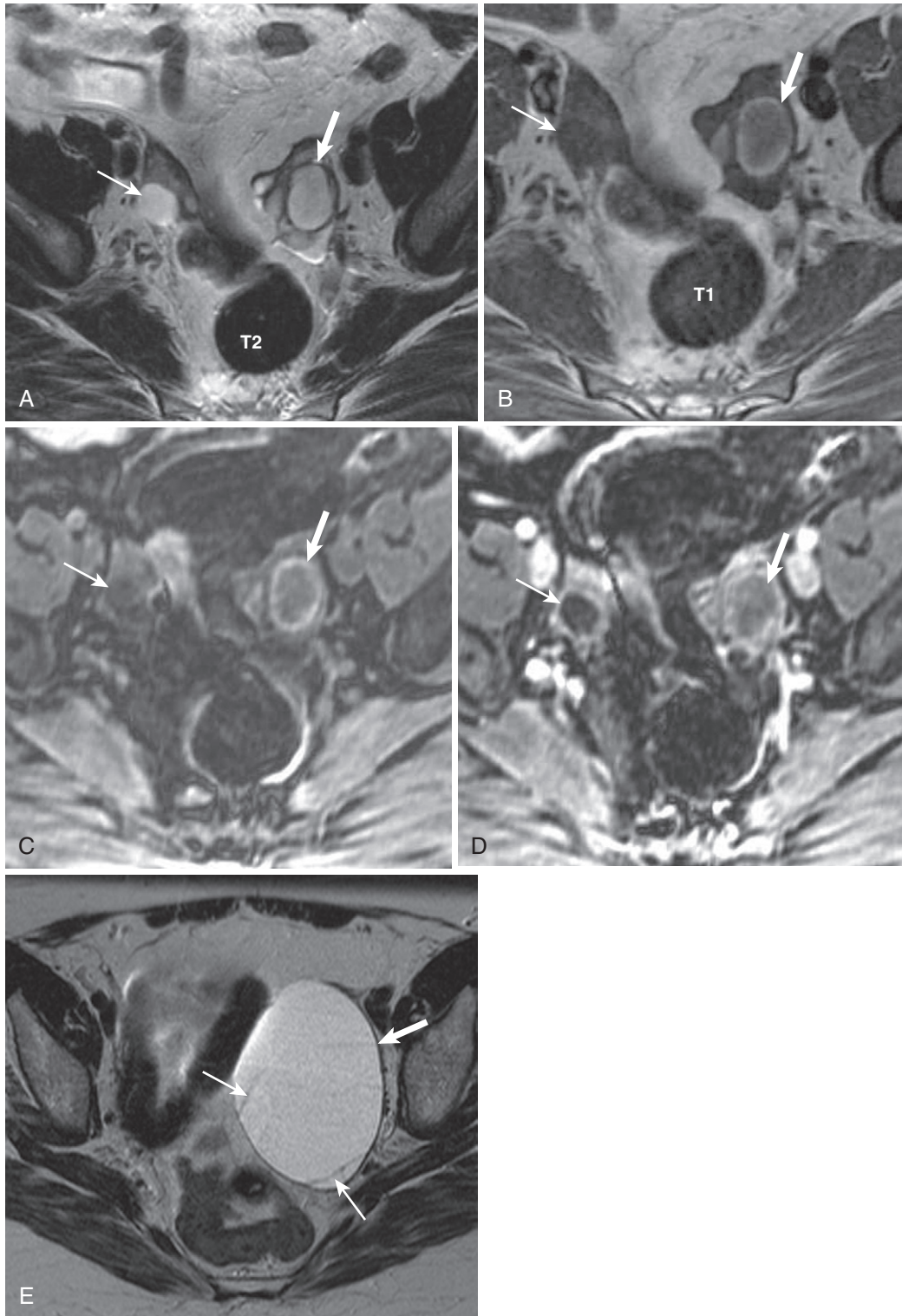


FIGURE 5-61. Simple ovarian cyst. Axial T2-weighted (A), T1-weighted (B), precontrast (C), and postcontrast (D) T1-weighted fat-saturated images show a small, simple right-sided ovarian cyst (*thin arrow* in A-D) exhibiting simple fluid characteristics with no complexity or enhancement coexisting with a probable left ovarian corpus luteal cyst (*thick arrow* in A-C) with a thin rim of T1 hyperintensity (blood) and otherwise simple cystic features. With increased size (especially > 5 cm) and complexity, the probability of neoplasm escalates, as illustrated in the axial T2-weighted image of a different patient (E) with a benign ovarian cystic epithelial neoplasm with septation (*thin arrows*) and mild eccentric wall thickening (*thick arrow*).

TABLE 5-20. Ovarian Cyst Management

<2.5 cm ⇒ no follow-up necessary (regardless of age)
2.5–5 cm ⇒ imaging (ultrasound) follow-up different phase of menstrual cycle (6 wk)
>5 cm ⇒ suggest surgical management (risk of torsion)

age, simple ovarian cysts up to 2.5 cm in diameter require no follow-up (Table 5-20). This includes corpus luteal cysts, which characteristically exhibit a rim of enhancement and a nonspherical shape (Fig. 5-62). Whereas the internal contents often approximate simple fluid, hemorrhage occasionally may coexist resulting in T1 hyperintensity (without T2 hypointensity—or shading—which indicates concentrated, or long-standing blood products characteristic of endometriomas, to be considered later).

OVARIAN INCLUSION CYST

An ovarian inclusion cyst is an equally benign, incidental lesion common in menopause and during the reproductive years. Imagine the ovarian surface epithelium invaginating, forming a self-enclosed cavity and losing its connection with the surface from which it arose (which likely occurs during ovulation)—that is the etiology of an ovarian inclusion cyst. Whereas ovarian inclusion cysts may be a precursor to ovarian epithelial neoplasms, they exhibit simple features indistinguishable from a follicle cyst, usually measuring no more than 1.5 cm. Because of the absence of physiologic ovarian cysts and the relative prevalence of postmenopausal cystic ovarian neoplasms, surveillance of postmenopausal ovarian cysts has been observed historically, according to different, often institutionally driven, guidelines. Follow-up algorithms informed by the features of inclusion cysts and the risk of torsion with increasingly large lesion size generally conformed to the following guideline: (1) less than 16 mm, no follow-up; (2) 16 mm to 5 cm, 4-month follow-up, and (3) 5 cm or larger, surgical resection. However, the burden of evidence indicates an exceedingly low likelihood of neoplasm associated with cystic lesions regardless of age. Consequently, cystic ovarian lesions up to 2.5 cm generally require no surveillance.

PERITONEAL INCLUSION CYST

Another variety of inclusion cysts developing in the appropriate clinical setting is actually extraovarian. The peritoneal inclusion cyst should be

considered only when a history of pelvic surgery or trauma (or possibly endometriosis) is confirmed. The necessary precursors to a peritoneal inclusion cyst are adhesions and active ovarian tissue. Ovarian secretions gradually accumulate as traumatized, reactive mesothelial tissue absorbs fluid less freely, forming locules between leaves of peritoneum and/or adhesions. As a consequence of this pathogenesis and growth pattern, peritoneal inclusion cyst margins are at least partially spatially defined by anatomic structures; they fill (potential) spaces rather than creating their own space like tumors or endothelially derived cystic lesions. Obtusely angulated margins with adjacent structures are observed, because they insinuate around instead of displacing structures. They are usually located around (occasionally surrounding) or in proximity to the ovary. The contents usually approximate simple fluid (T1 hypointense and T2 hyperintense) with no enhancement (Fig. 5-63).

The problem with this diagnosis is the protean appearance of peritoneal inclusion cysts, which overlaps with the appearance of multiple other lesions, including ovarian neoplasms, hydrosalpinx or pyosalpinx, and parovarian cysts.³⁶ First of all, this diagnosis should not be considered without the appropriate preexisting condition—history of peritoneal injury/manipulation. Second, an extraovarian location must be established. With septation or other evidence of complexity (which is usually relatively sparse and often attributable to envelopment of adjacent structures), stability on prior or follow-up examinations is confirmatory. Finally, margins that conform to extralesional structures, such as the pelvic sidewall, loops of bowel, or uterus, are characteristic of peritoneal inclusion cysts.

PAROVARIAN CYSTS

True parovarian cysts are uncommon, usually simple, water-containing cysts and occasionally simulate simple ovarian cysts. They arise in the mesosalpinx between the ovary and the fallopian tube. Parovarian cysts are usually mesothelial or embryologic remnants (usually paramesonephric vs. mesonephric). Their clinical importance lies in their frequent symptomatic nature and diagnostic confusion with primary ovarian pathology.

LIPID CONTENT

In addition to simple fluid—or water—ovarian cysts may contain hemorrhage or lipid (in

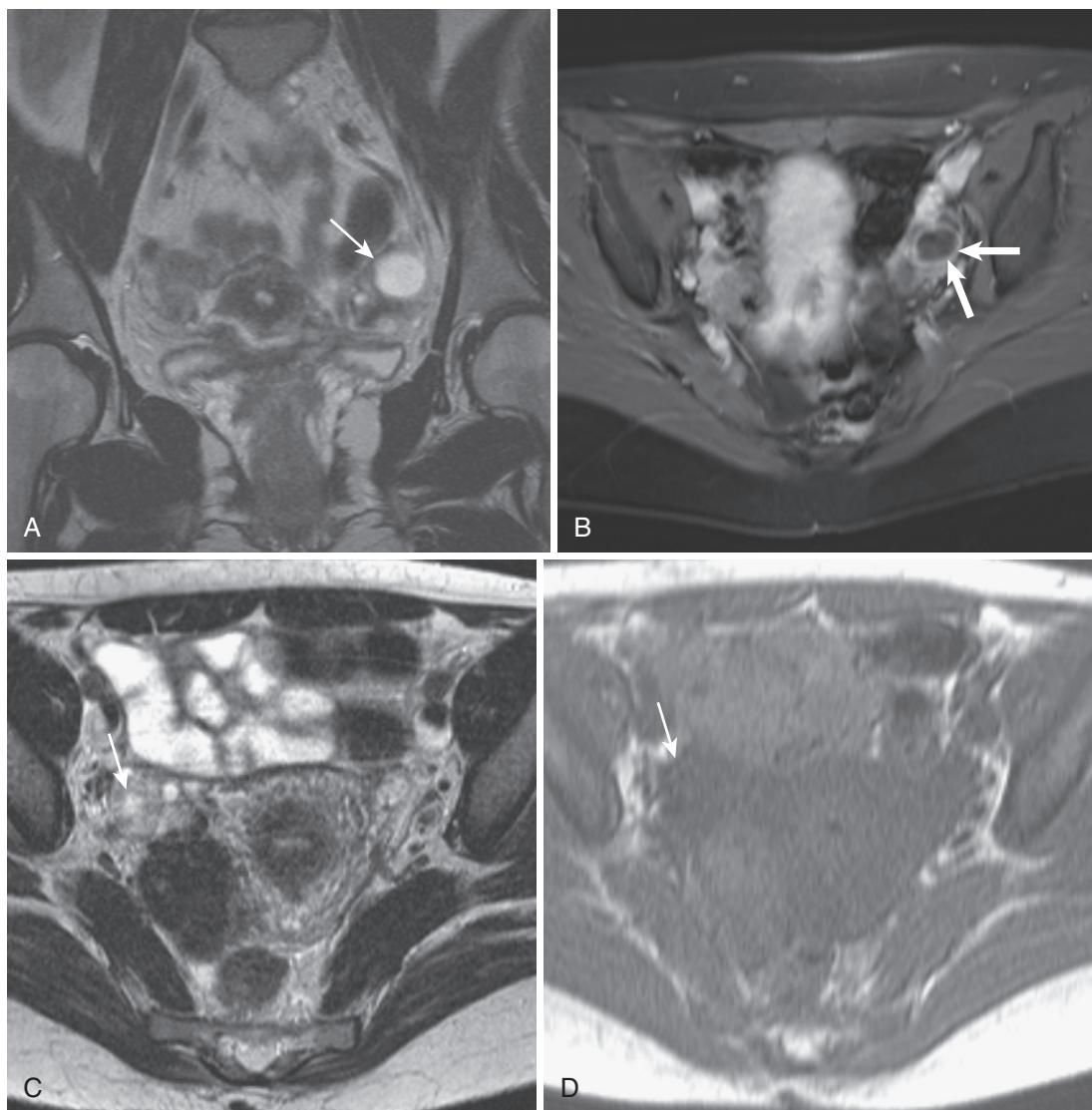


FIGURE 5-62. Corpus luteal cyst. Coronal T2-weighted (A) and axial fat-saturated enhanced T1-weighted (B) images show a small cystic lesion (*thin arrow* in A) with a thin peripheral rim of enhancement (*thick arrows* in B) and no other evidence of complexity. C-F, In a different patient, a thicker rim of enhancement delineates a right-sided corpus luteal cyst (*arrow*) on T2-weighted (C), T1-weighted (D), enhanced T1-weighted unsuppressed (E), and fat-suppressed (F) images. G, An irregular—collapsed or deflated—morphology often characterizes corpus luteal cysts, as seen in a different patient (*arrow*).

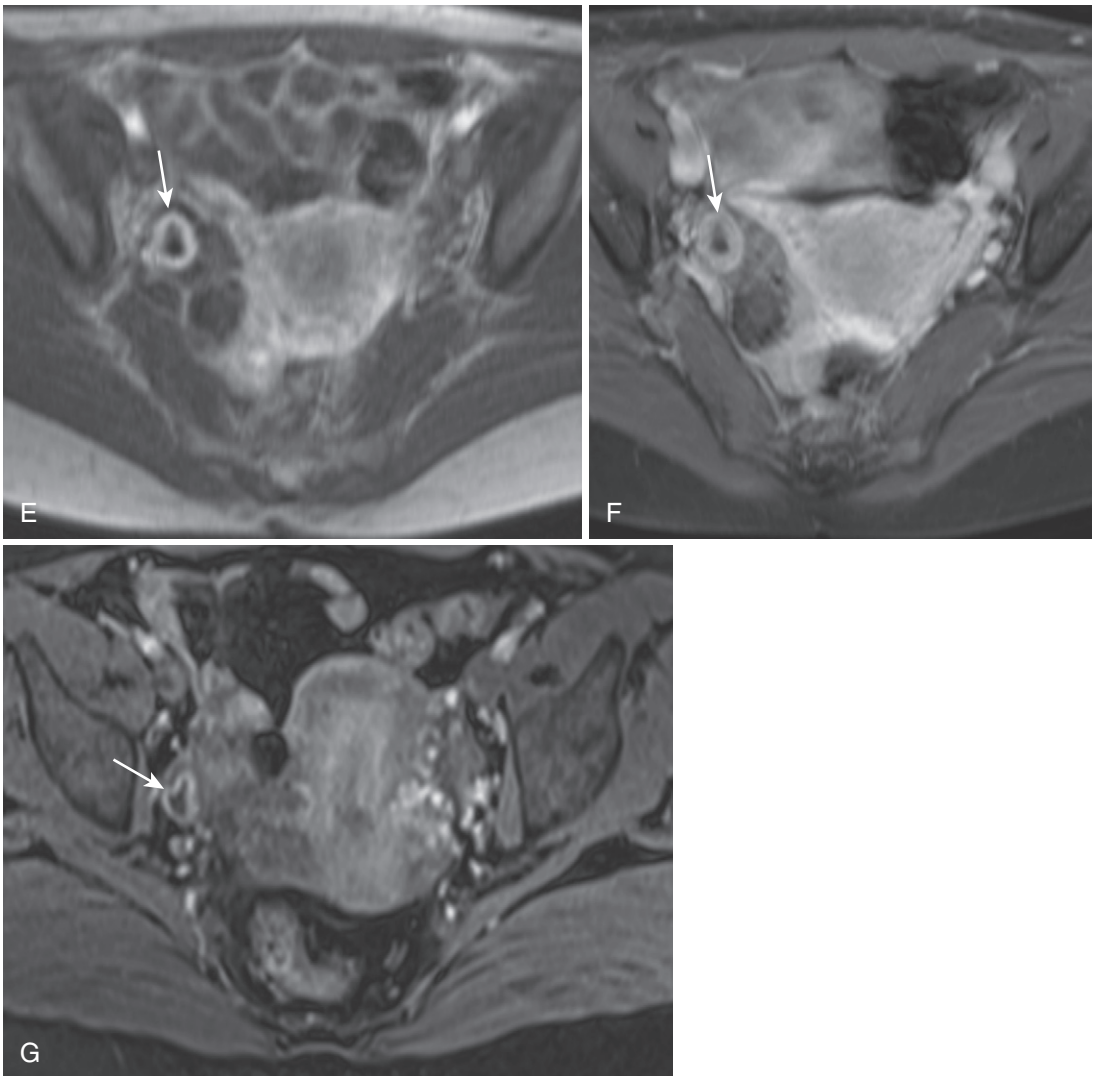


FIGURE 5-62, cont'd

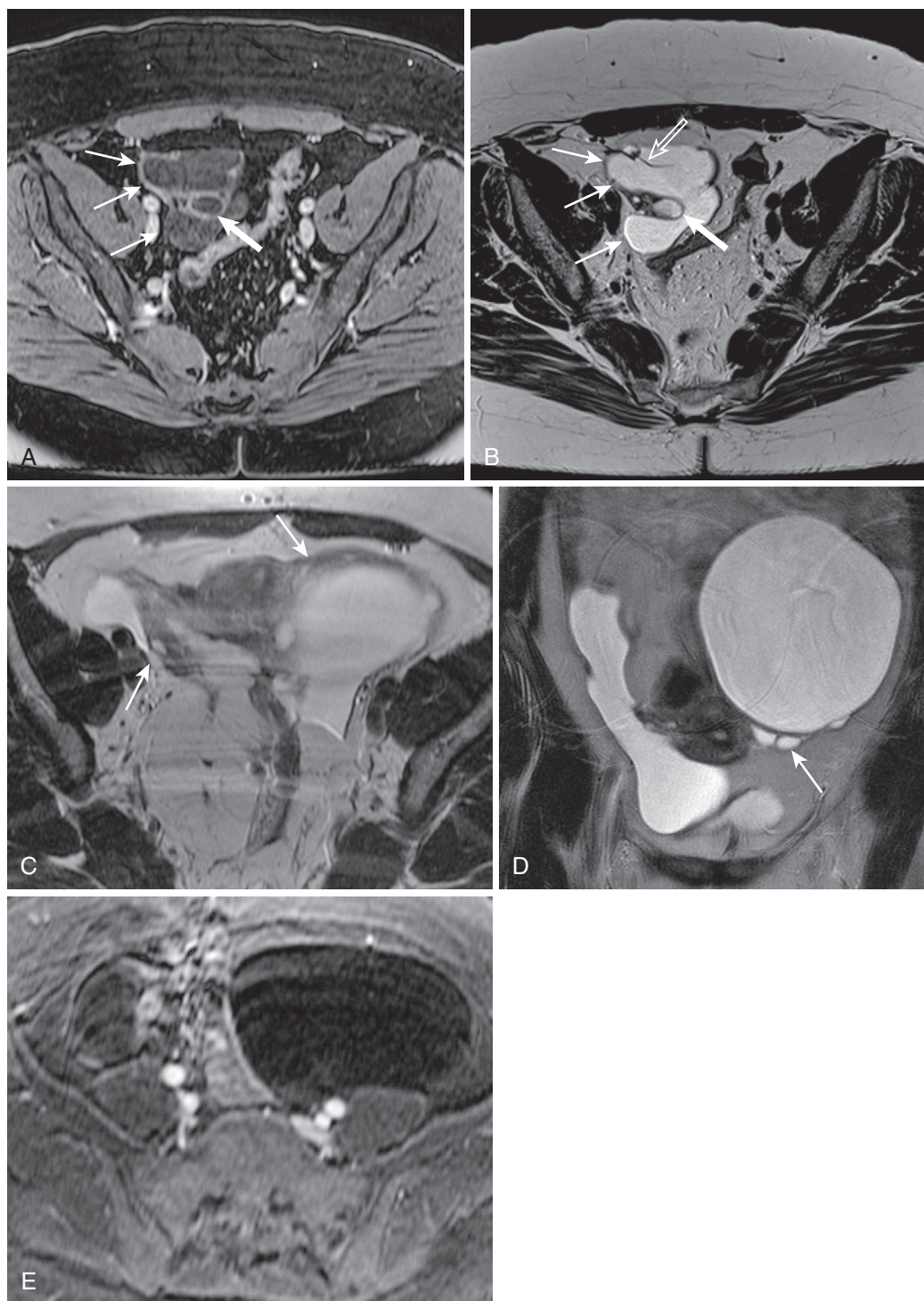


FIGURE 5-63. Peritoneal inclusion cyst. **A** and **B**, The lateral margin (*thin arrows* in **A**) of a fluid collection encircling the right ovary (*thick arrow* in **A** and **B**) is bounded by the pelvic sidewall. Minimal wall thickening (*thin arrows* in **B**) and internal septation (*open arrow* in **B**) are observed—seen to better advantage on the enhanced image (**A**) compared with the T2-weighted image (**B**)—and the features are characteristic of a peritoneal inclusion cyst. Axial (**C**) and coronal (**D**) T2-weighted and axial enhanced T1-weighted (**E**) images in a different patient reveal bilateral cystic lesions abutting the ovaries (*arrows* in **C** and **D**) and at least partially spatially defined by anatomic borders—namely, the pelvic sidewalls. The left-sided lesion appears more masslike and an appropriate clinical history (i.e., surgery), stability, and an absence of neoplastic features should be confirmed.

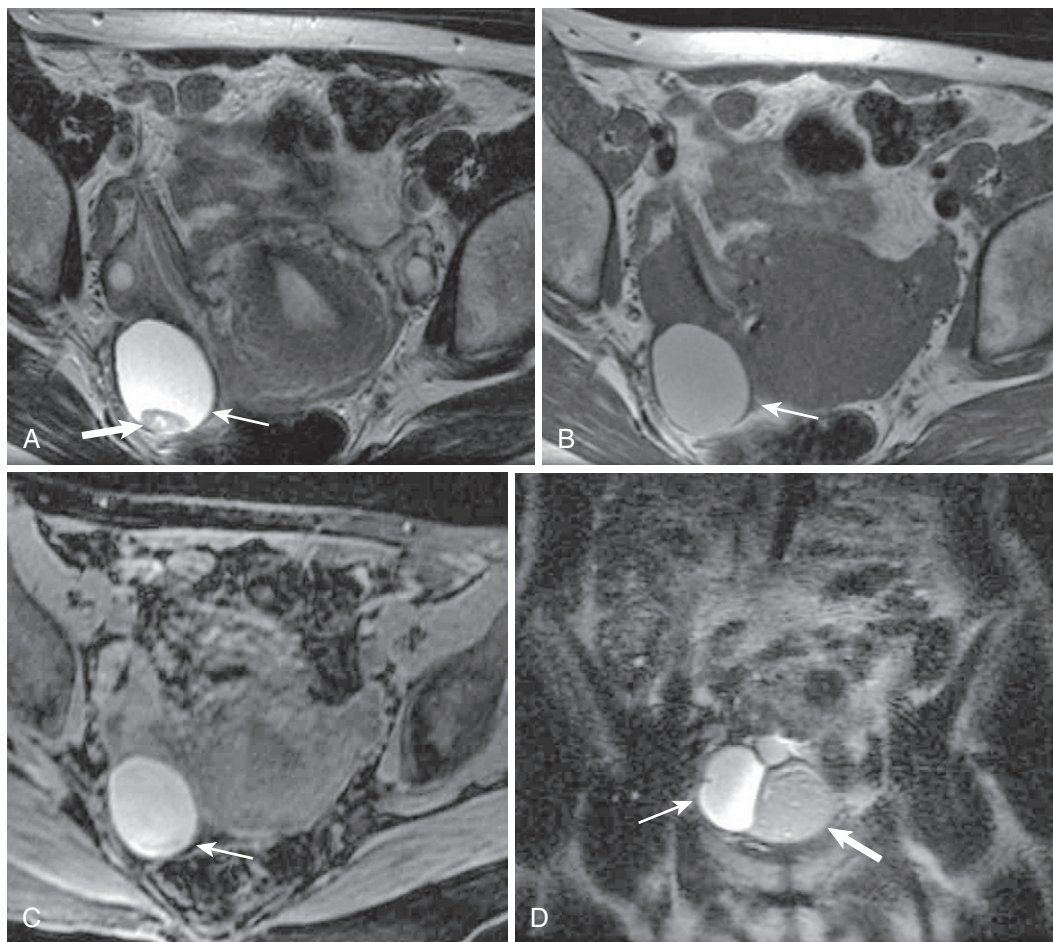


FIGURE 5-64. T1 hyperintense ovarian cysts—hemorrhagic cyst and dermoid cyst. The hemorrhagic cyst (*thin arrow* in A-C) exhibits hyperintense signal on all pulse sequences—T2-weighted (A), T1-weighted (B), and T1-weighted fat-suppressed (C) images. Dependent clot (*thick arrow* in A) and/or wall thickening occasionally complicate the appearance of hemorrhagic cysts. D-H, A biloculated dermoid cyst in a different patient contains water (*thin arrow*) and sebaceous or fatty (*thick arrow*) components. Although the sebaceous locule maintains signal on T2-weighted (D), T1-weighted out-of-phase (E), and in-phase (F) images, in contradistinction to the hemorrhagic cyst, signal is nullified with fat suppression (G). H, After gadolinium administration, no enhancement is observed in either lesion.

the case of a dermoid cyst). Both of these types of cysts are differentiated from water-containing cysts by their hyperintensity on (non-fat-saturated) T1-weighted images. The key to differentiating between the hemorrhagic and the lipid-containing cyst is the loss of signal on fat-suppressed images in the case of a dermoid (fat-containing) cyst (Fig. 5-64). Avoid the mistake of assuming that hypointensity on T1-weighted fat saturated images alone connotes lipid—this appearance indicates either a long T1 value (i.e., water) or a suppressed signal from fat. T1 hyperintensity plus evidence of fat suppression equals fat—confirming this requires inspecting unsuppressed T1-weighted images (look for isointensity to subcutaneous fat) and

short tau inversion recovery (STIR) or spectrally fat-saturated images (documenting signal suppression from the inversion pulse or frequency-specific pulse targeted to fat).

DERMOID CYST (MATURE CYSTIC TERATOMA)
Once fat signal is identified, the diagnosis is sealed—dermoid cyst. Additional findings, such as multilocularity or internal complexity, such as linear strands, septa, and debris, are common findings and do not suggest alternative diagnoses (Figs. 5-65 to 5-68). Dermoid cysts are protean, but the common thread and the (practically speaking) MRI sine qua non diagnostic feature is intralésional lipid signal. Rarely, fat signal is subtle to absent and the dermoid

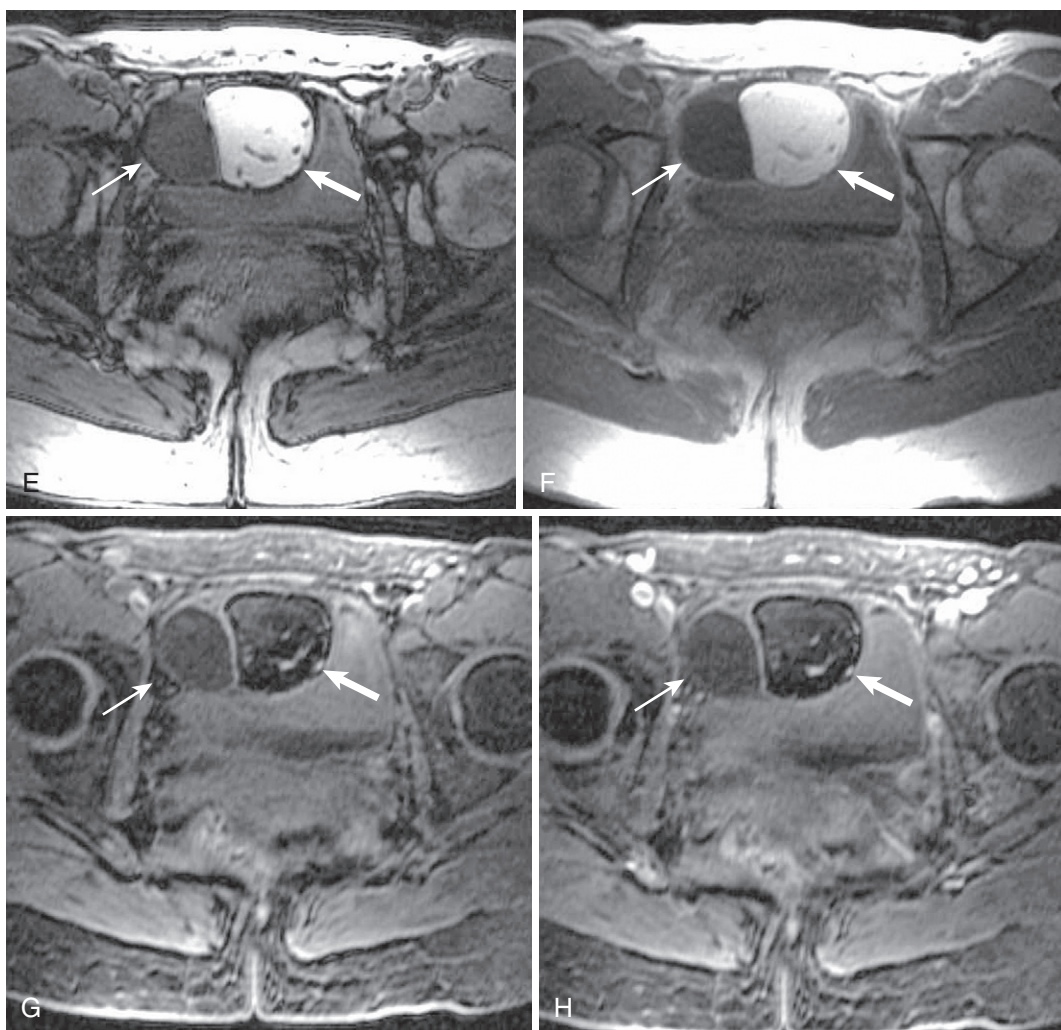


FIGURE 5-64, cont'd

simulates a neoplastic lesion (although careful inspection should exclude enhancement and evidence of a solid component).

Even though we call it a “dermoid *cyst*,” this lesion is actually a benign *neoplasm*. The dermoid cyst is more appropriately termed “mature cystic teratoma,” and is the benign counterpart to its malignant cousin, the immature teratoma (to be discussed in the Complex Cystic and Solid Lesions section). The mature cystic teratoma arises from a single pluripotential germ cell and is composed of tissues from at least two of the three germ cell layers (ectoderm, mesoderm and endoderm). In the case of the mature cystic teratoma, these tissues are mature and not aggressive in contradistinction to the immature teratoma.

BLOOD CONTENT

Endometrioma. If hemorrhage is confirmed by T1 hyperintensity and no loss of signal on fat-suppressed images, the next step is to assess signal intensity on T2-weighted images. Hemorrhage exhibiting relatively low signal on T2-weighted images (called “shading”) harbors concentrated iron products, which is a sign of chronicity implying endometriosis (Fig. 5-69). This is in contradistinction to other hemorrhagic lesions, the functional lesions—the hemorrhagic and corpus luteal cysts, which are ephemeral lesions. Additional supporting findings include a nonspherical shape and multiplicity (Figs. 5-70 to 5-72).

Text continued on p. 338

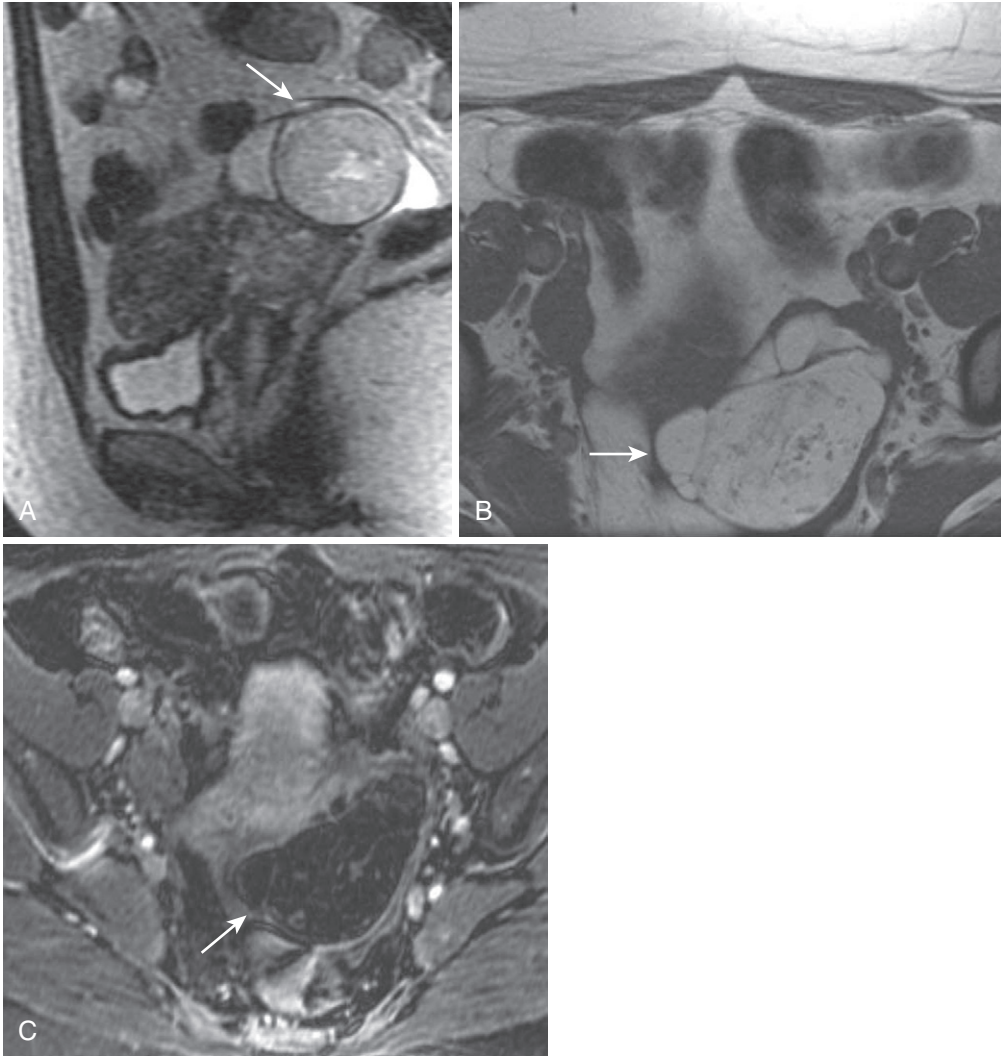


FIGURE 5-65. Dermoid cyst. **A**, The sagittal T2-weighted image reveals a relatively nonspecific moderately hyperintense lesion (*arrow*). **B**, Axial T1-weighted image reiterates isointensity to fat (*arrow*) and reveals mild complexity—wall thickening and septation. **C**, The addition of fat saturation (and intravenous gadolinium) confirms predominantly lipid content (*arrow*), an absence of enhancement and the diagnosis of a dermoid cyst.

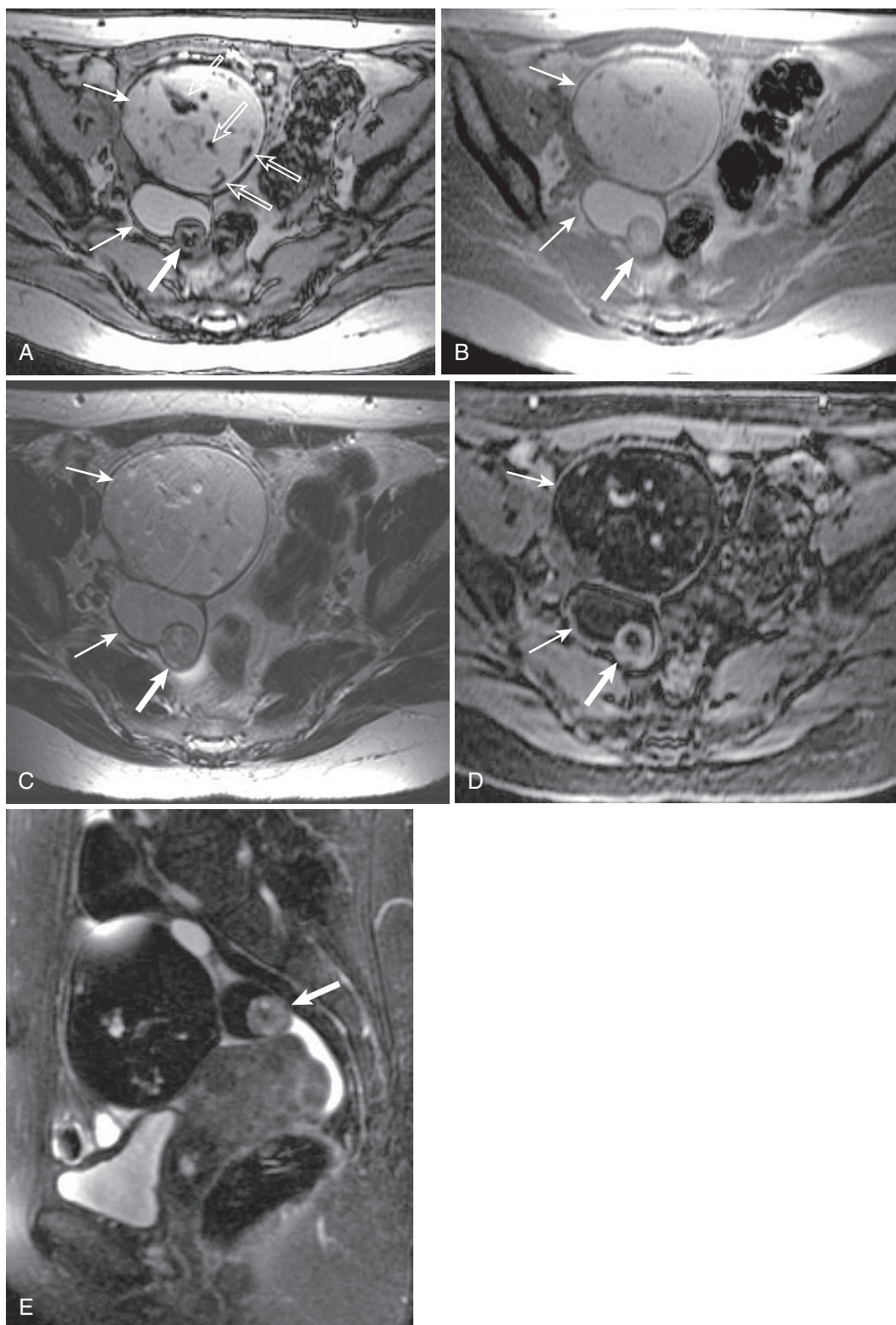


FIGURE 5-66. Dermoid cyst, Rokitansky's nodule. T1-weighted out-of-phase (A) and in-phase (B) images demonstrate a bilobed hyperintense lesion (*thin arrows* in A-D) with a peripheral nodule—the Rokitansky nodule (*thick arrow* in A-E). Exaggerated hypointensity surrounding internal debris within the locules on the out-of-phase image (*open arrows* in A) shows the effects of phase cancellation when the water-rich debris and surrounding fat exist in the same voxel. C, Axial T2-weighted image reveals signal isointense to subcutaneous fat and relatively hypointense to simple fluid. The application of fat saturation to T1-weighted (D) and T2-weighted (E) images results in complete signal suppression, indicating gross fat content.

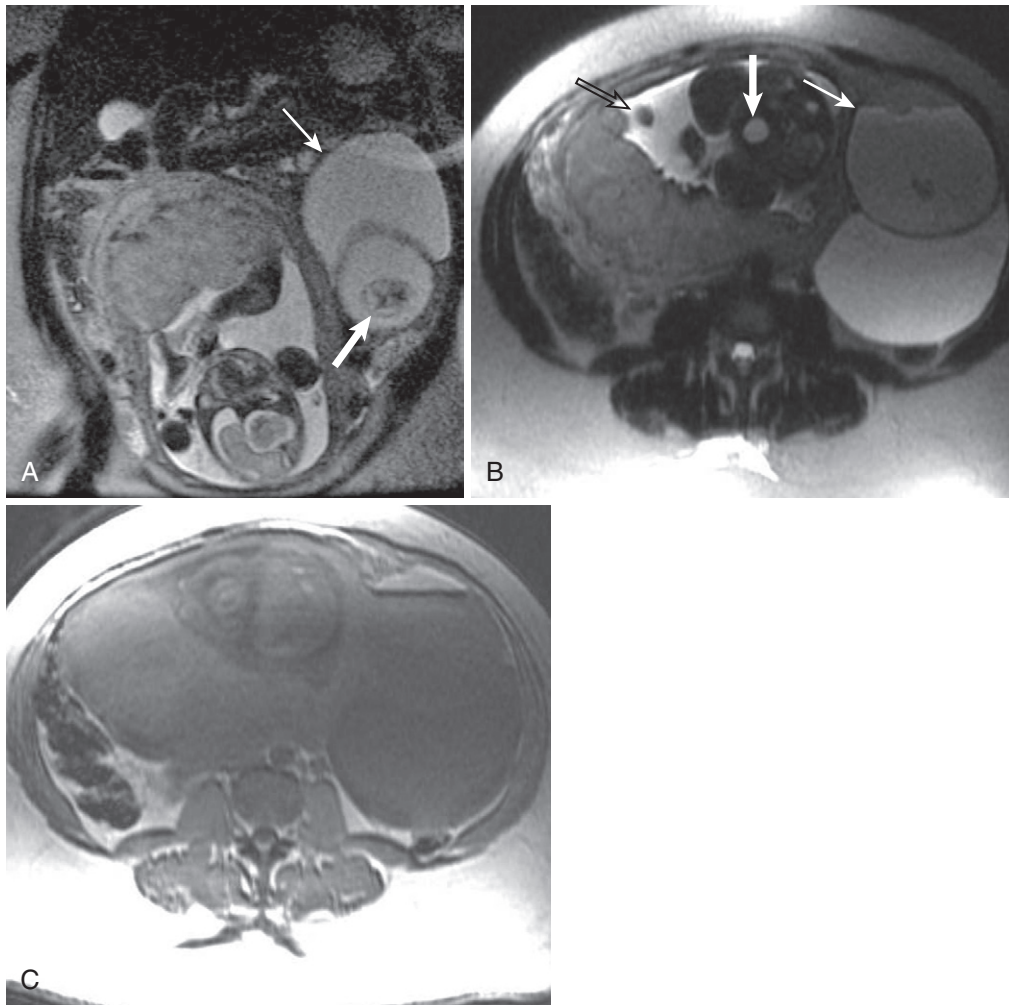


FIGURE 5-67. Dermoid cyst, fluid-fluid level. **A**, T2-weighted coronal localizing image in a pregnant patient (note the vertex presentation and fundal placentation) also show a large left adnexal, at least biloculated cystic lesion (*thin arrow*) with internal debris and/or nodularity (*thick arrow*). **B**, The axial T2-weighted image through the level of the fetal bladder (*thick arrow*) shows a fluid-fluid level (*thin arrow*) with dependent fluid isointense to amniotic fluid (*open arrow*). **C**, The fluid-fluid level signal intensities are reversed on the out-of-phase T1-weighted image with the nondependent fluid isointense to subcutaneous fat. The signal void at the fluid-fluid level suggests destructive interference between the water (dependent) and the lipid (nondependent) protons—phase cancellation artifact—additional evidence of fat composition and the diagnosis of a dermoid cyst.

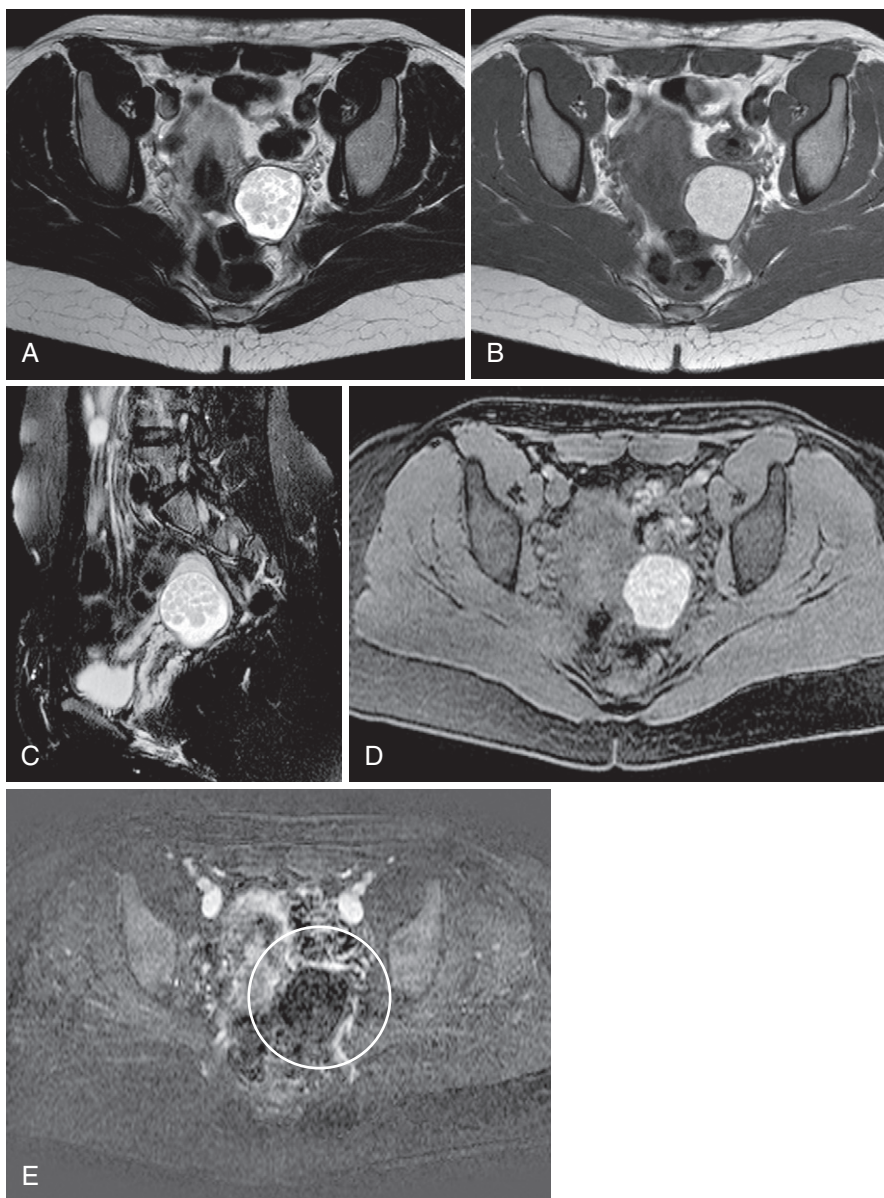
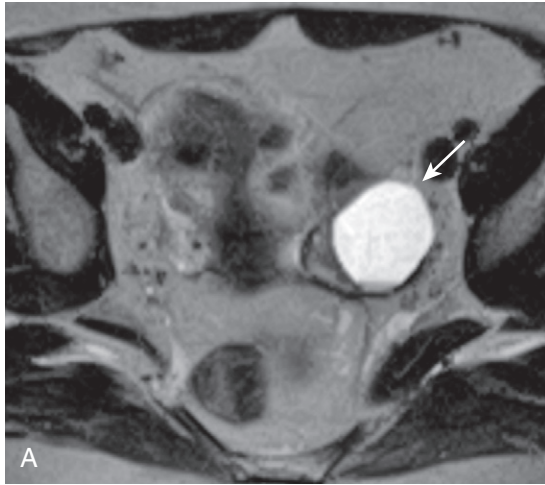


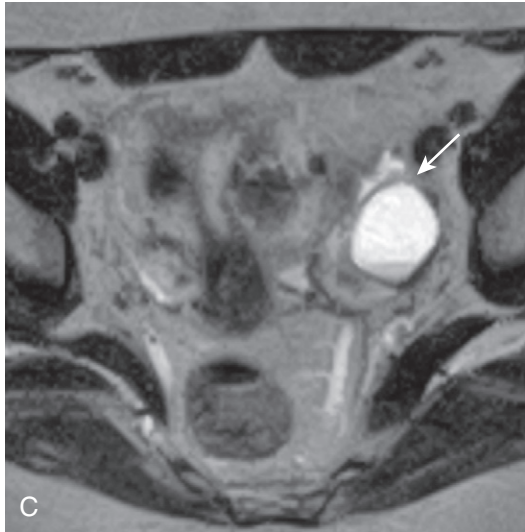
FIGURE 5-68. Dermoid cyst, minimal to no lipid. Axial T2-weighted (A) and T1-weighted (B) images show a hyperintense lesion with internal debris. The addition of fat suppression to the sagittal T2-weighted (C) and T1-weighted (D) images confers slightly greater conspicuity to the internal globules without convincing fat saturation. E, Subtracted image after gadolinium administration shows a corresponding signal void (*circle*), excluding enhancement. Although this strongly suggests a benign cystic etiology and minimal fat content may be suggested by the slight loss of signal in the relatively nondependent internal globules, the signal characteristics do not allow for a definitive diagnosis of any of the dominant cystic lesions and surgery should be considered (as in this case—the final diagnosis was “mature cystic teratoma”).



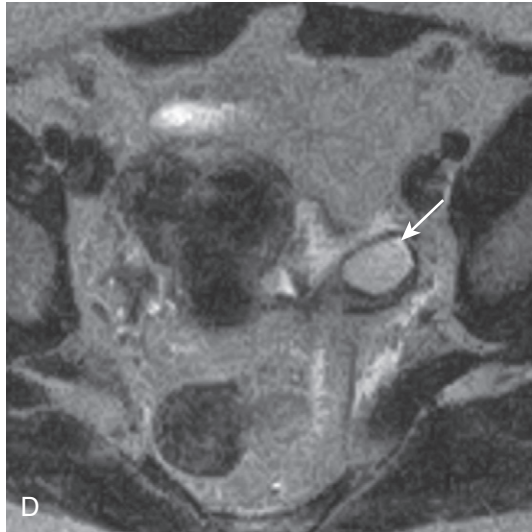
2002



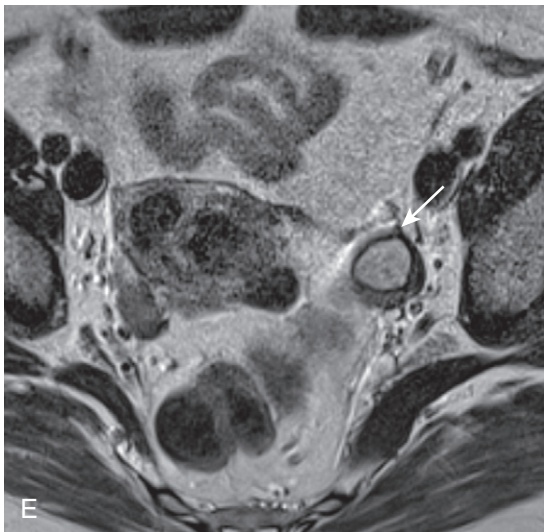
2003



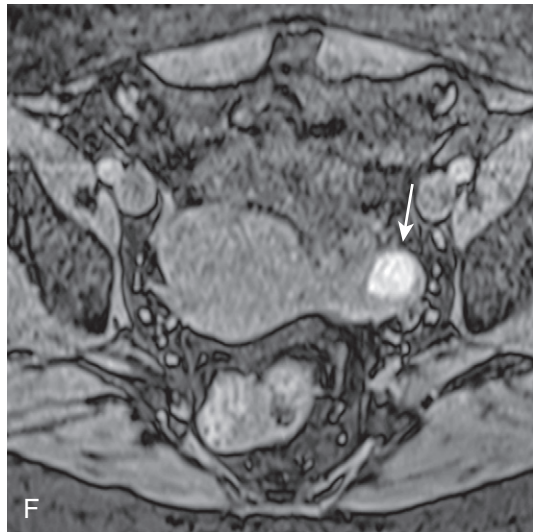
2004



2006



2008



2008

FIGURE 5-69. Shading in an endometrioma. A-E, Sequential T2-weighted images of an evolving endometrioma (*arrow*) over a 6-year time course showcase the phenomenon of shading—progressive T2 shortening due to ongoing concentration of blood products over time, which results in gradually decreasing T2 signal over time. F, Axial T1-weighted fat-suppressed image obtained at the last timepoint confirms the presence of hemorrhage (*arrow*).

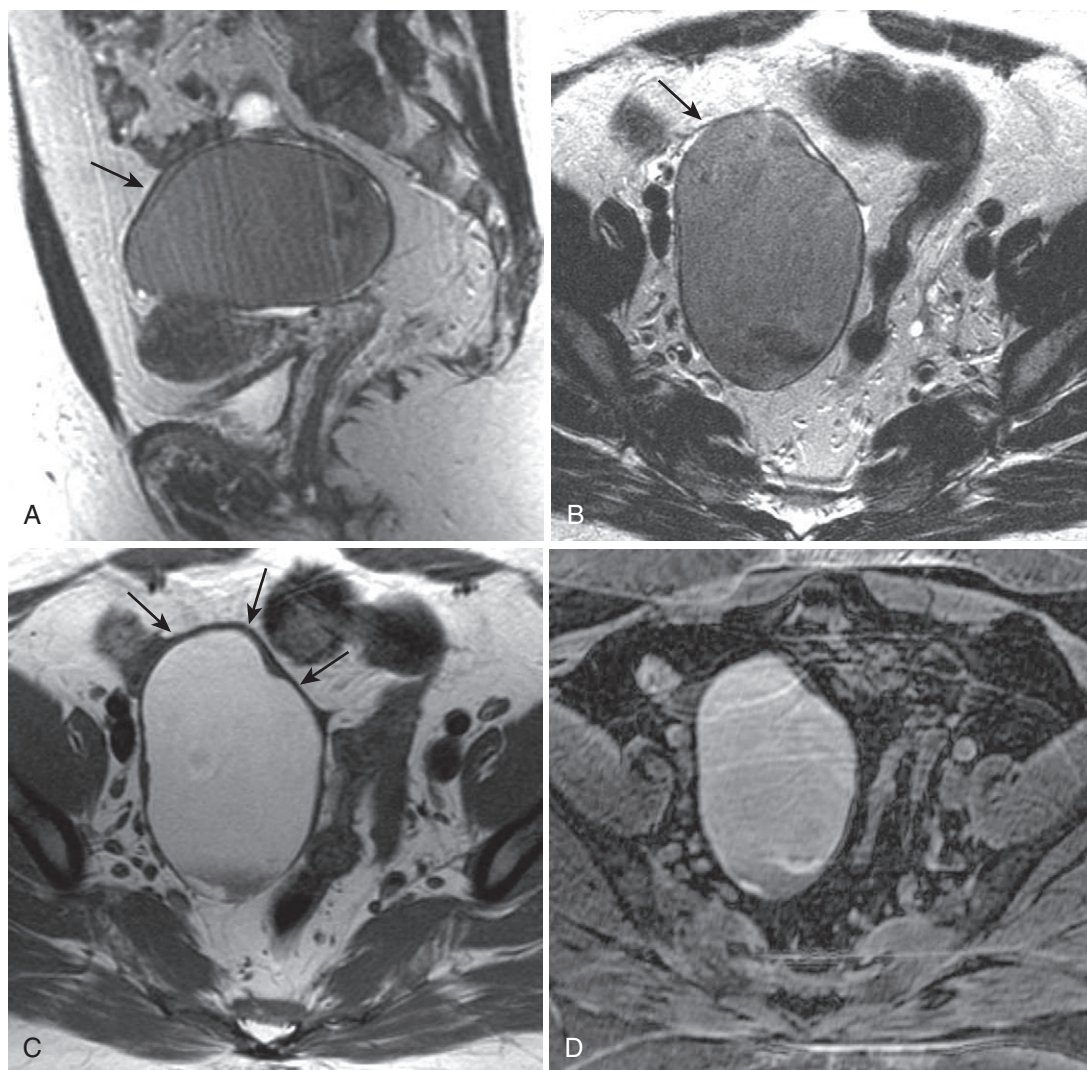


FIGURE 5-70. Endometrioma. Sagittal scout (A) and axial (B) T2-weighted images display a large moderately hypointense right adnexal lesion (*arrow*) dwarfing the adjacent uterus. C, The corresponding T1-weighted image confers hyperintensity and discloses mild wall thickening (*arrows*), an occasional feature seen in endometriomas. D, Preservation of hyperintensity on the T1-weighted fat-saturated image excludes the possibility of lipid and confirms the presence of blood.

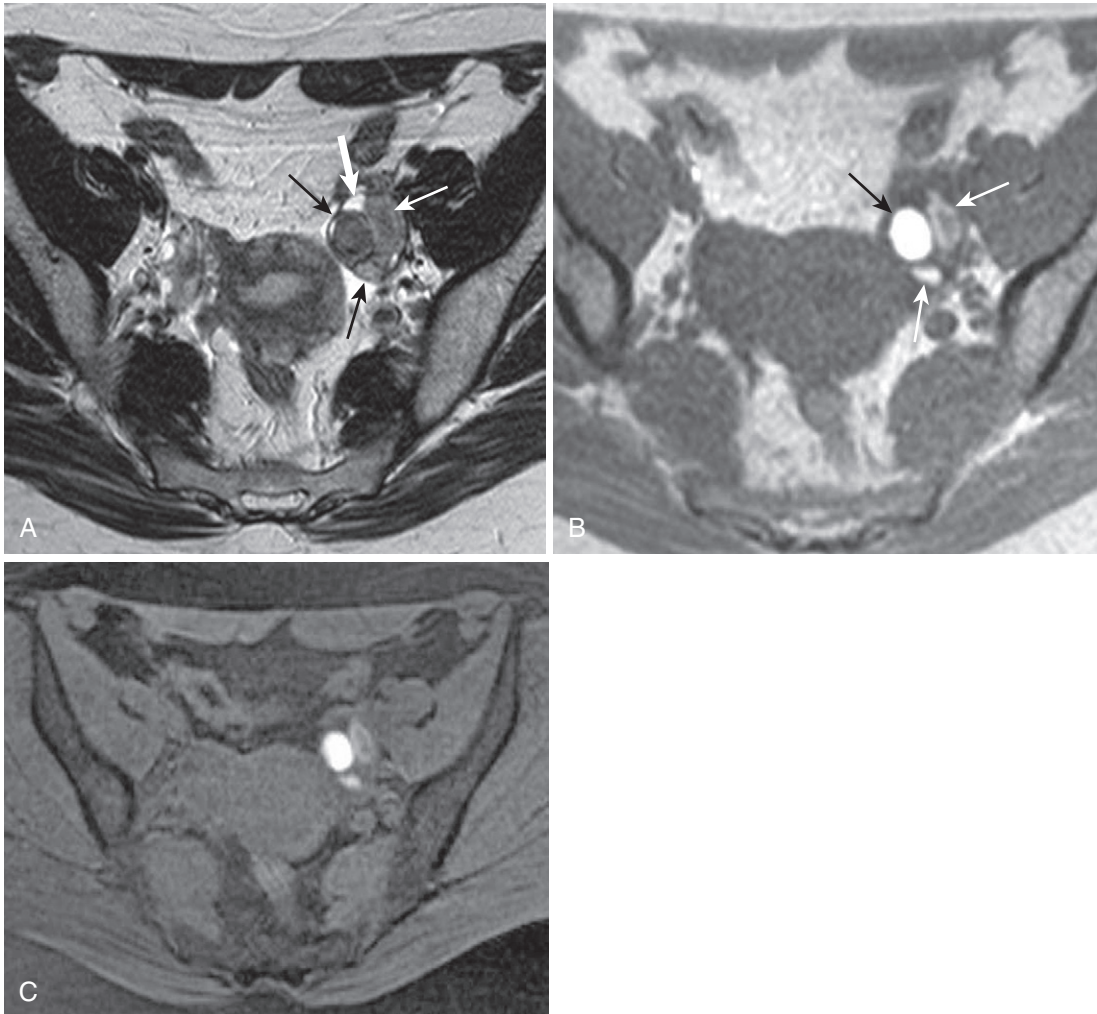


FIGURE 5-71. Endometriosis. **A**, Axial T2-weighted image. The left ovary appears mildly heterogeneously enlarged with distortion of the normal ovarian architecture with a few hypointense lesions (*thin arrows*) and a paucity of functional cysts (*thick arrow*). **B**, In-phase T1-weighted image. Corresponding hyperintensity (*arrows*) in the T2 hypointense irregularly shaped left ovarian lesions indicates either blood or lipid. **C**, Failure of signal suppression on the T1-weighted fat saturated image excludes fat and confirms hemorrhage. The combination of nonsuppressing T1-hyperintensity, T2-shortening, multiplicity, ovarian location, and irregular morphology typifies endometriosis.

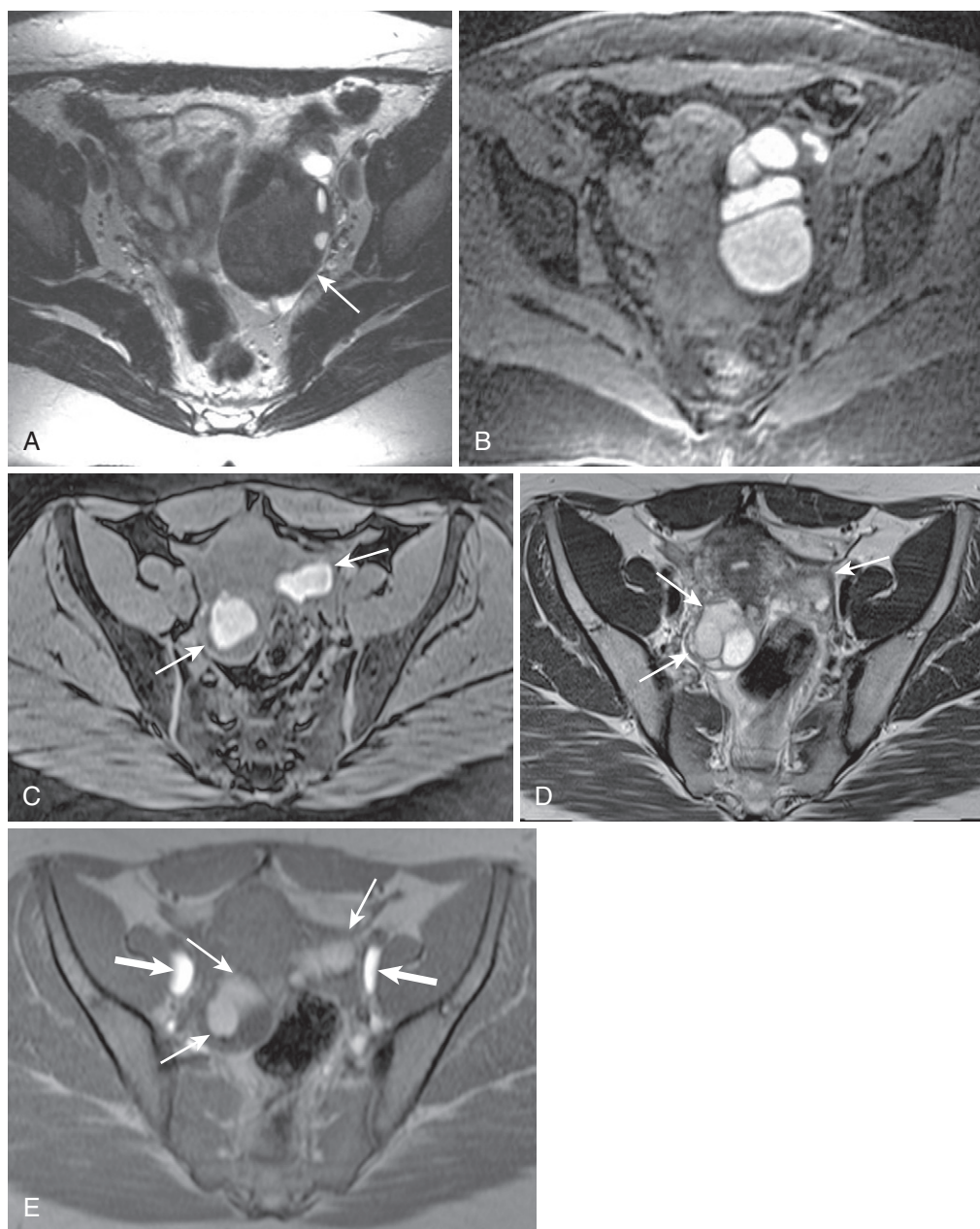


FIGURE 5-72. Endometriomas. Another typical case of endometriosis reveals an ill-defined left adnexal lesion with marked T2-shortening (*arrow* in A) combined with corresponding hyperintensity on T1-weighted fat-saturated image (B)—signifying concentrated hemorrhage—lesion multiplicity, and nonspherical morphology. C-E, In a different patient, multiple irregular lesions (*arrows* in C and E) with similar signal characteristics on the T1-weighted fat-suppressed image (C) with shading—albeit less profound—on the T2-weighted image (*arrows* in D) typify endometriosis. E, The T1-weighted in-phase gradient echo image reveals additional bilateral hyperintense lesions in the iliac fossa (*thick arrows*) not to be confused with endometriomas (or other hemorrhagic or fatty lesions). Flow-related enhancement accounts for hyperintensity in the iliac veins, in this case. Remember that gradient echo images are time-of-flight images (without the parameter modifications of dedicated vascular sequences) and prone to the in-flow effect (especially in two-dimensional sequences in the case of the entry slice with respect to the vessel).

TABLE 5-21. Hemorrhagic Adnexal Lesion Features

Lesion	T1 Signal	T2 Signal	Number	Morphology
Corpus luteal cyst	Usually ↓↓ (usually no hemorrhage)	↑↑	1	Flattened, “deflated”
Hemorrhagic cyst	↑↑↑	↑↑	Usually 1	Usually round-oval
Endometrioma	↑↑	↑-↓↓	1-many	Ovoid-irregular

FUNCTIONAL HEMORRHAGIC CYST

The chief differential diagnostic hemorrhagic cystic lesions to distinguish from an endometrioma are functional hemorrhagic and corpus luteal cysts (Table 5-21)—assuming acute pathology is excluded (i.e., ectopic pregnancy and torsion). The hemorrhagic cyst reveals none of the complex features of the endometrioma; except for the T1 hyperintensity indicating hemorrhage, it approximates a simple cyst in all other respects. When complicated by hemorrhage—which is infrequent—the corpus luteal cyst may simulate an endometrioma. The corpus luteal cyst’s inner lining of luteinized cells corresponds to a mildly thickened wall exhibiting mild enhancement (Fig. 5-73). The nonspherical shape, deflated shape, communicates recent rupture.

HEMATOSALPINX

The fallopian tube is essentially the innocent bystander of the adnexa and contributes an item to the list of hemorrhagic adnexal lesions—hematosalpinx. Blood in the fallopian tube usually reflects secondary accumulation of hemorrhage from pathology arising elsewhere: endometriosis, infection, müllerian duct anomalies, ectopic pregnancy, cervical stenosis, and even tubal ligation and IUDs. Consider hematosalpinx to be a clue to potential associated pathology, such as endometriosis or ectopic pregnancy. Tubular morphology and T1 hyperintensity go without saying. Relatively central (periuterine) location, tubular/tortuous morphology, and consideration of presence or exclusion of primary etiologies summarize the imaging approach to hematosalpinx (Fig. 5-74).

Other hemorrhagic lesions distinguish themselves with an acute clinical presentation and evidence of localizing inflammation—ectopic pregnancy and ovarian torsion. Along with TOA, these lesions deserve special mention and a topic of their own—acute adnexal lesions.

ACUTE LESIONS

Acute adnexal pathology, such as tuboovarian abscess (TOA), ovarian torsion, and ectopic pregnancy (Table 5-22),³⁷ may mimic endometriomas, functional cysts, or cystic neoplasms, but these usually distinguish themselves by their abrupt clinical presentation (and/or pregnant status). The equalizing factor is rupture, resulting in pelvic fluid, which is present (especially) in TOA/pelvic inflammatory disease (PID) and ectopic pregnancy and torsion (to a lesser extent). Edema is the sentinel finding of acute adnexal pathology and is really the hallmark of TOA/PID (Fig. 5-75).

TUBOVARIAN ABSCESS

PID spans the spectrum from endometritis/myometritis (which we have already discussed) to pyosalpinx to a TOA. Pyosalpinx and TOA manifest as complex cystic masses with thickened walls. Generally, the contents are nearly identical to simple fluid. Compared with urine, the contents are mildly T1 hyperintense and mildly T2 hypointense owing to the presence of debris and/or hemorrhage. Morphologically, pyosalpinx is characteristically a tortuous, tubular structure, and confirmation of this feature usually requires reviewing images in all planes (Fig. 5-76). TOA is most often multiloculated and both lesions are occasionally difficult to differentiate from adjacent bowel loops (Fig. 5-77).

Before such a diagnosis of pyosalpinx or TOA (or any other diagnosis of extraintestinal origin) is confirmed, exclusion from bowel loops is essential. Follow the bowel retrograde from the anus and rectum and antegrade from the cecum, ileocecal valve, and terminal ileum if possible. Changeable appearance over time favors bowel loops undergoing peristalsis. Internal foci of gas have been promoted as specific for an abscess, which is self-evident when discriminating between different adnexal lesions, but not

TABLE 5-22. Acute Adnexal Pathology

Ectopic pregnancy	β -hCG	Evidence of blood
Ovarian torsion	Nonspecific	Evidence of blood
		Ovarian enlargement
		Enlarged follicles
		Traction adjacent structures
Tubo-ovarian abscess	Signs of infection	Edema/inflammatory changes
		\uparrow Fluid
Ruptured dermoid cyst	Nonspecific	Signs of lipid (extracystic)
		Evidence of peritonitis
Hemorrhagic ovarian cyst	Midcycle	Hemorrhage without shading

β -hCG = β -human chorionic gonadotropin.

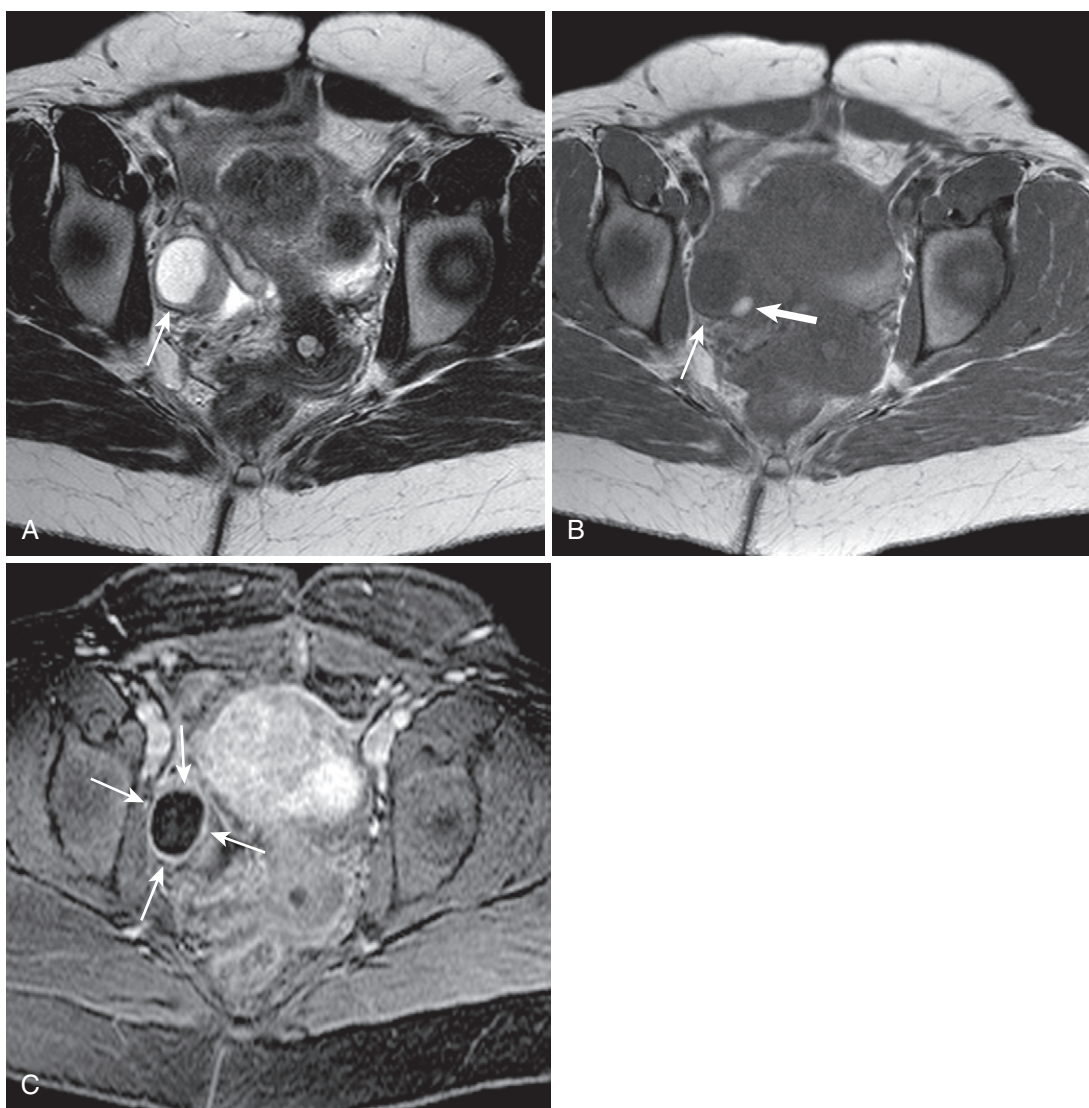


FIGURE 5-73. Corpus luteal cyst. Axial T2-weighted (A) and T1-weighted (B) images show a simple-appearing right ovarian cystic lesion (*thin arrow*) adjacent to a punctate lesion with inverted signal characteristics most typical of an endometrioma (*thick arrow*). C, Thin rim enhancement (*arrows*) clinches the diagnosis of corpus luteal cyst, assuming the appropriate attendant features (menstrual status, size ≤ 2.5 cm, and lack of obvious complexity).

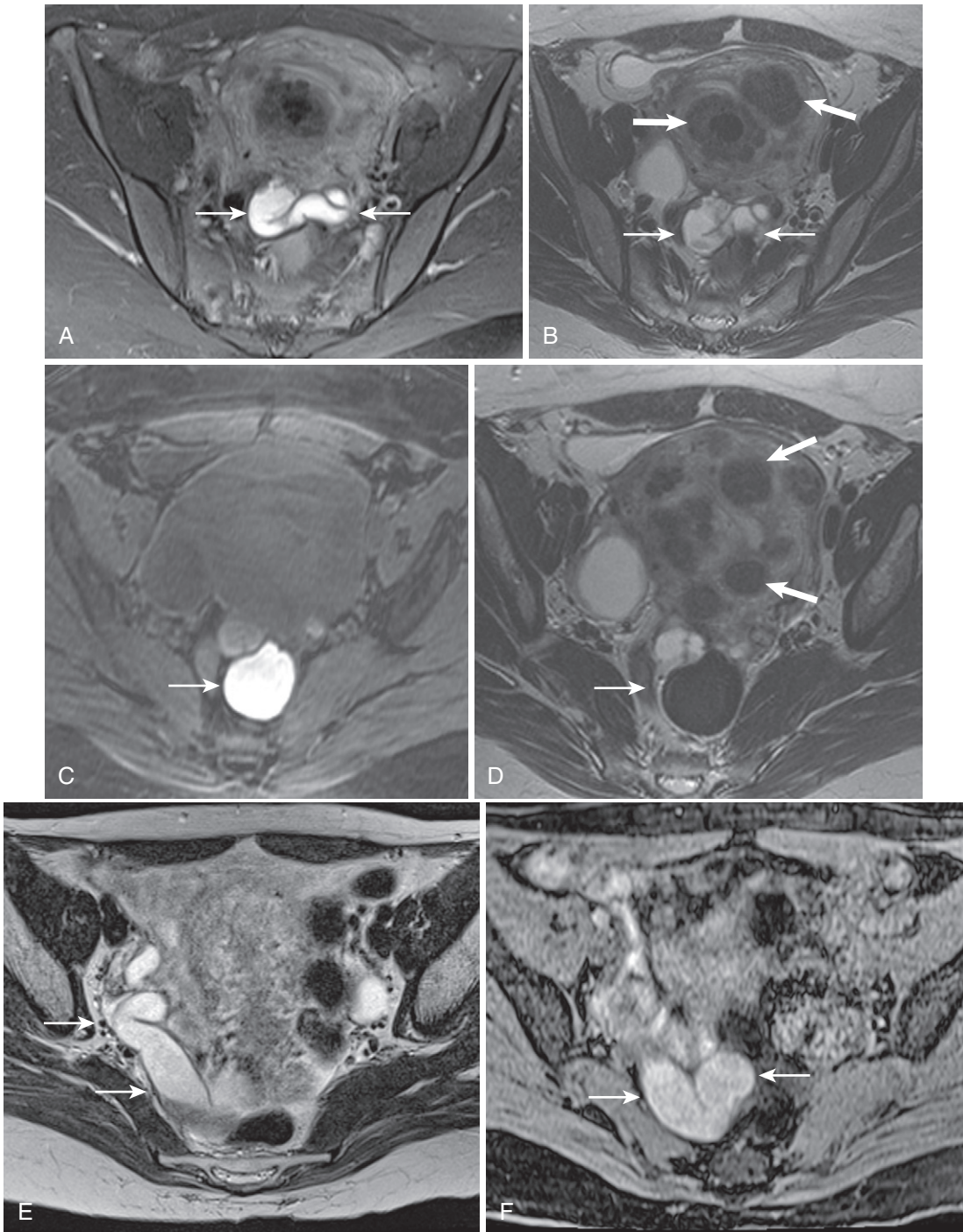


FIGURE 5-74. Hematosalpinx. Tubular morphology, T1 hyperintensity, and periuterine location are all easily appreciated in this case of hematosalpinx (*thin arrows* in A and B) showcased on axial T1-weighted fat-suppressed (A) and T2-weighted (B) images. C and D, An adjacent endometrioma in the cul-de-sac (*arrow*) demonstrates the typical signal characteristics—T1 hyperintensity (C) and shading, or T2 hypointensity (D). Note the multiple incidental intramural fibroids (*thick arrows* in B and D). E and F, Tubular morphology is even better demonstrated in a different patient with dependent-lying concentrated blood products (*arrows*) exhibiting shading on the T2-weighted image (E) and hyperintensity on the T1-weighted fat-suppressed image (F).

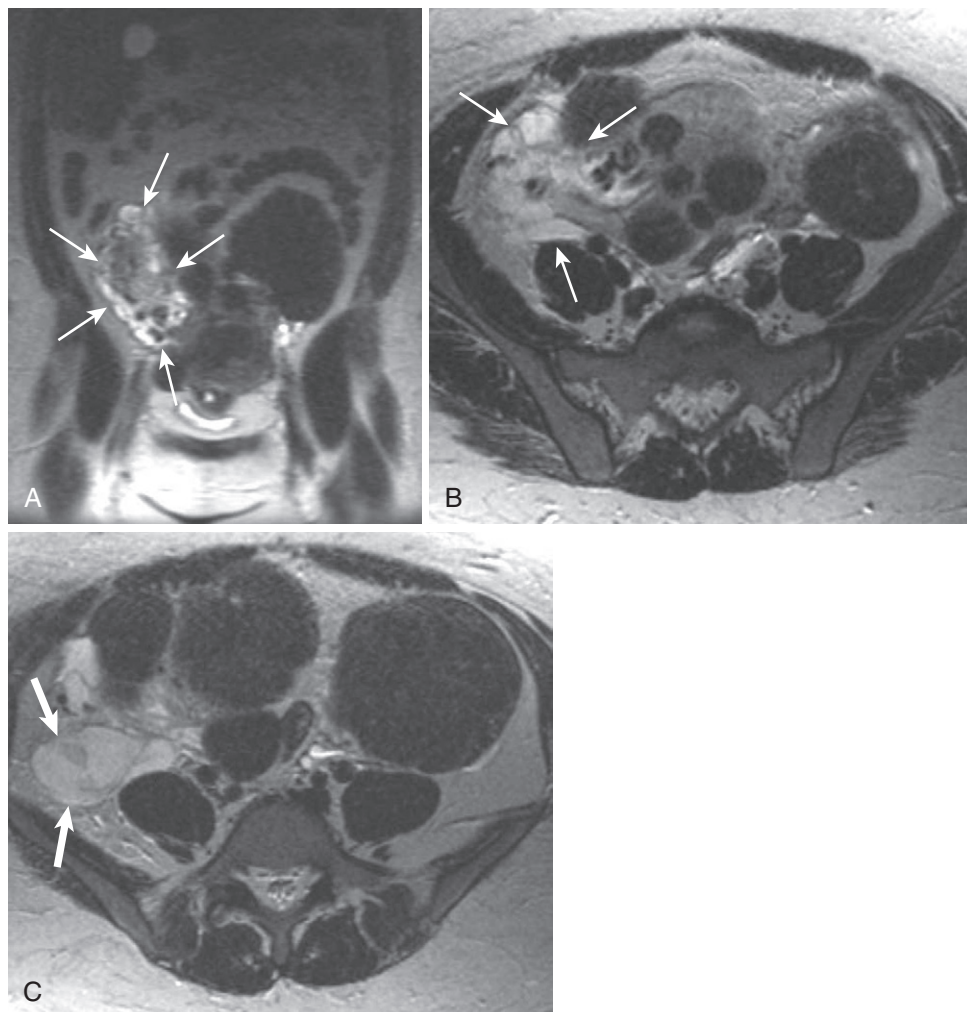


FIGURE 5-75. Edema associated with tubo-ovarian abscess (TOA) or acute adnexal pathology. **A**, Coronal T2-weighted image. Unilateral edema (*arrows*) in a young female with acute symptomatology practically limits diagnostic consideration to acute inflammatory pathology, including appendicitis and other gastrointestinal conditions and acute adnexal conditions. **B** and **C**, Axial T2-weighted images showing asymmetrical edema (*thin arrows* in **B**) emanating from a complex cystic fluid collection in the right adnexa (*thick arrows* in **C**), in the absence of bowel pathology (and the appropriate clinical findings), which indicates pelvic inflammatory disease.

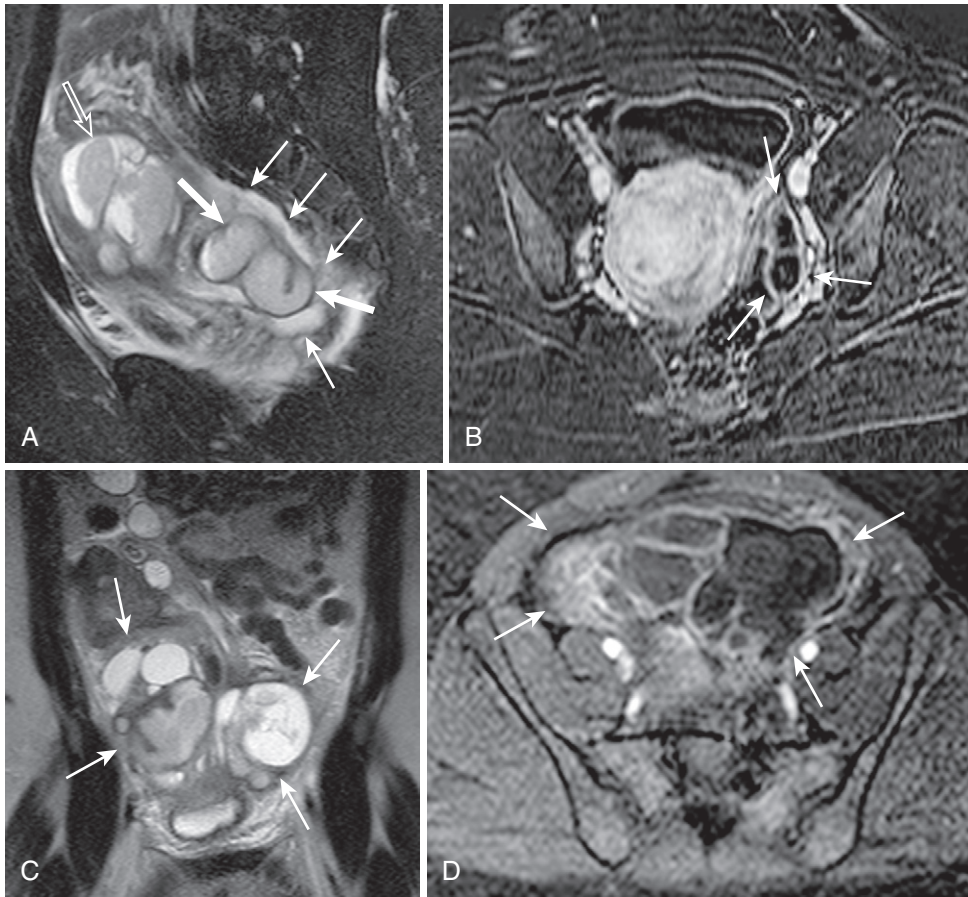


FIGURE 5-76. Pyosalpinx. **A**, Sagittal T2-weighted fat-suppressed image shows edema (*thin arrows*) surrounding a dilated fallopian tube (*thick arrows*), which indicates inflammation, further supported by the complex, heterogeneous fluid collection (*open arrow*). **B**, The subtracted image after gadolinium administration reveals a greater degree of wall thickening and enhancement (*arrows*) than would be expected in the absence of inflammation. Coronal T2-weighted (**C**) and axial enhanced T1-weighted fat-suppressed (**D**) images disclose the full extent of the TOA (*arrows*).

necessarily helpful when trying to differentiate from bowel. In any event, gas bubbles are signal voids that are the least confluent on multiecho sequences, progressively blooming with single-echo technique to T1-weighted gradient echo images to T2*-weighted images.

OVARIAN TORSION

Ovarian torsion has a protean imaging appearance, exhibiting a few common themes. First of all, there is often an underlying adnexal lesion leading to torsion. Dermoid cysts and ovarian cysts are common offenders. Second, the symptom generator is the vascular occlusion that theoretically manifests as an absence of enhancement. At least near-complete absence of enhancement is the rule and subtraction images

are often helpful. Third, interstitial hemorrhage (reflecting vascular congestion) is common and virtually diagnostic, especially in a suggestive clinical setting (**Figs. 5-78 and 5-79**). Trace the vascular pedicle, if possible, to identify abnormal twisting. Occasionally, none of these features is evident and the only clue is an abnormally enlarged ovary with proliferation of the central stoma and peripheral displacement of enlarged follicles (**Fig. 5-80**). This appearance reflects relatively mild and gradual and/or intermittent development of torsion with relative compensation. This phenomenon is referred to as “massive ovarian edema.” A curious feature of this disorder is the predilection for the right ovary, which is explained by the higher pressure in the left ovarian vein, conferring a higher tolerance to torsion.

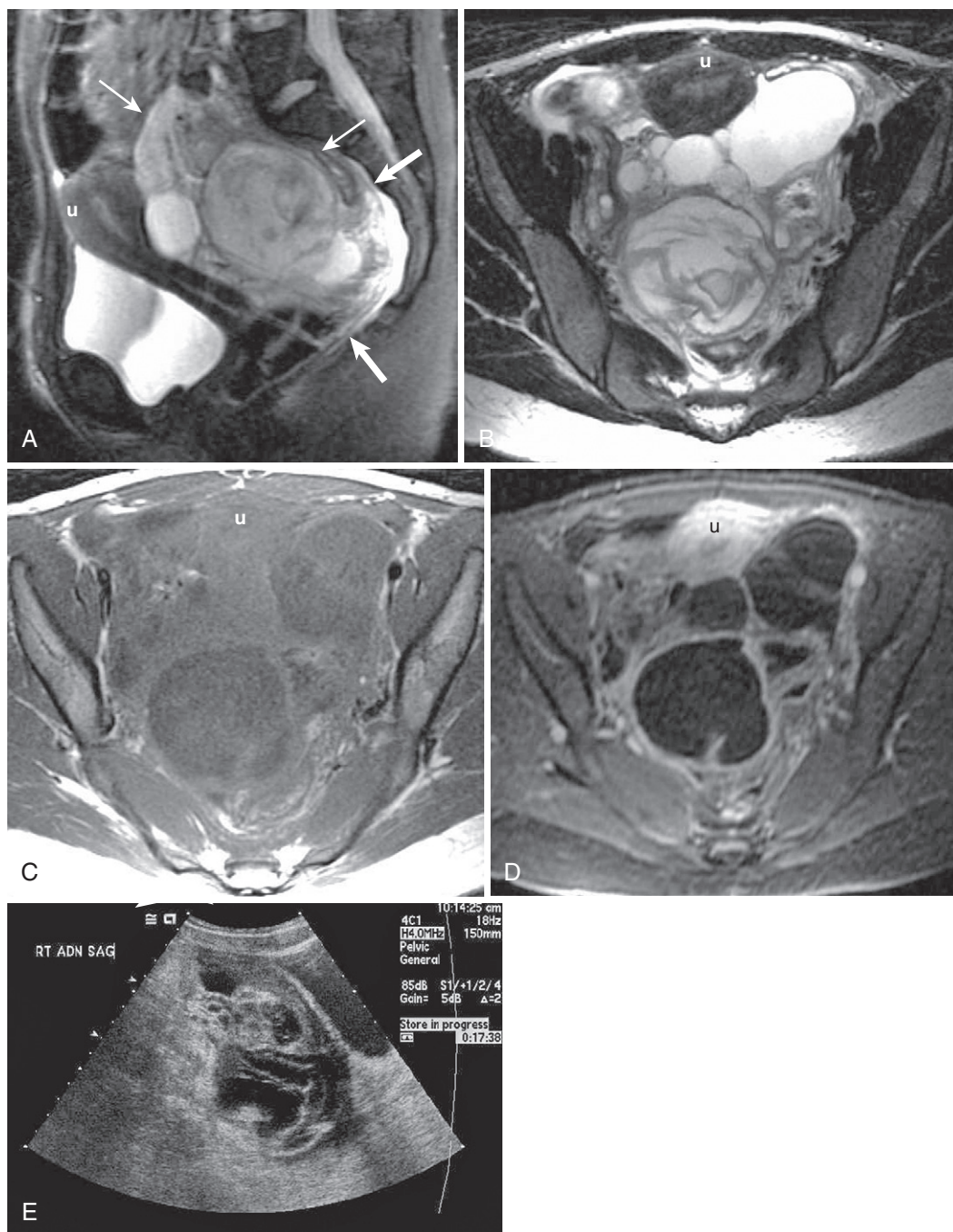


FIGURE 5-77. TOA. **A**, The sagittal T2-weighted fat-suppressed image demonstrates a complex cystic lesion (*thin arrows*) with surrounding edema (*thick arrows*) in the cul-de-sac displacing and compressing the uterus (u). The axial T2-weighted image (**B**) reveals the extent of the multiloculated inflammatory process, and the corresponding T1-weighted image (**C**) excludes hemorrhage. **D**, After gadolinium administration, the T1-weighted fat-suppressed image shows the degree of wall thickening and enhancement. **E**, An ultrasound performed immediately before the magnetic resonance imaging (MRI) corroborates the complexity of the collection.

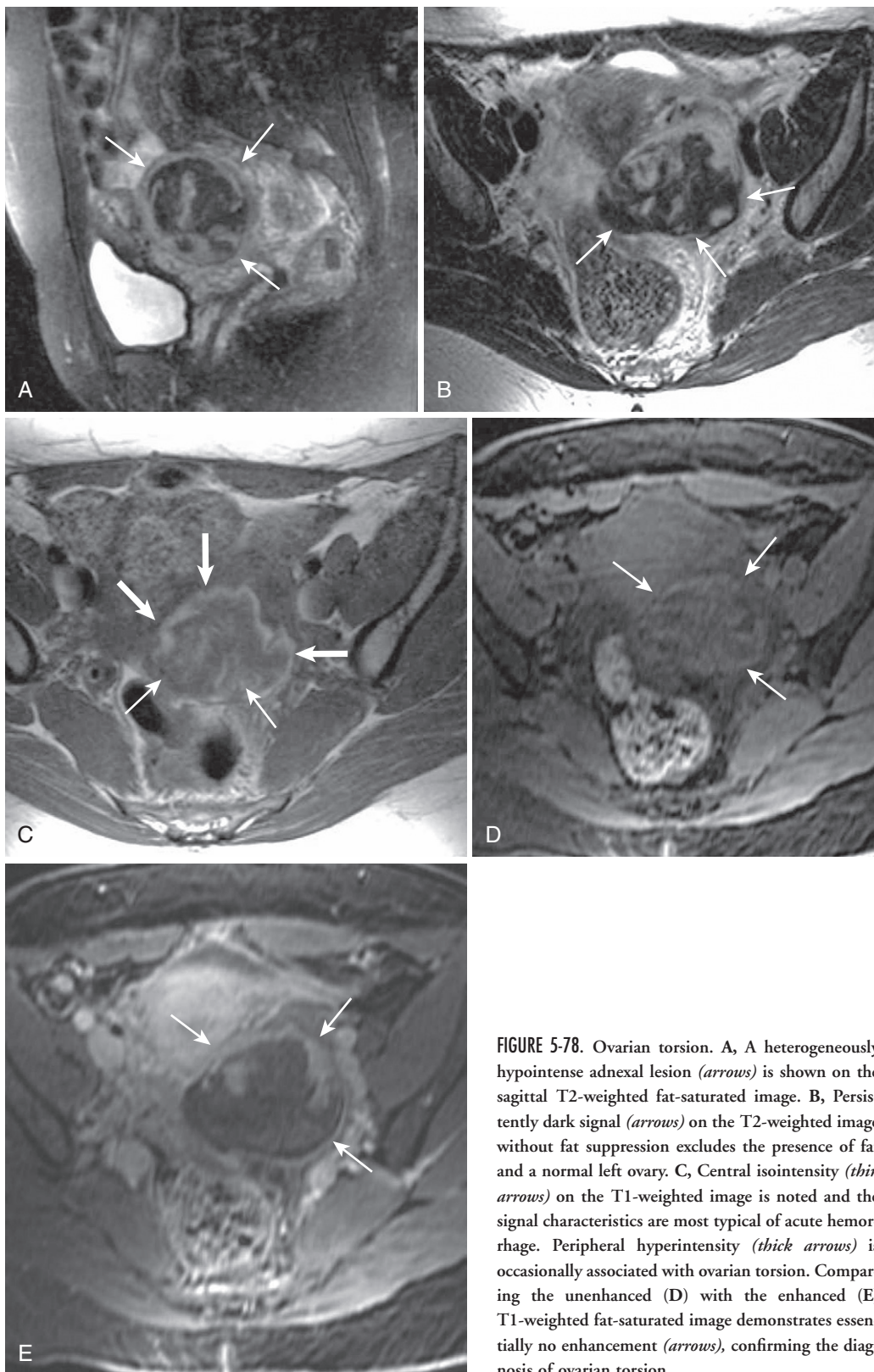


FIGURE 5-78. Ovarian torsion. **A**, A heterogeneously hypointense adnexal lesion (*arrows*) is shown on the sagittal T2-weighted fat-saturated image. **B**, Persistently dark signal (*arrows*) on the T2-weighted image without fat suppression excludes the presence of fat and a normal left ovary. **C**, Central isointensity (*thin arrows*) on the T1-weighted image is noted and the signal characteristics are most typical of acute hemorrhage. Peripheral hyperintensity (*thick arrows*) is occasionally associated with ovarian torsion. Comparing the unenhanced (**D**) with the enhanced (**E**) T1-weighted fat-saturated image demonstrates essentially no enhancement (*arrows*), confirming the diagnosis of ovarian torsion.

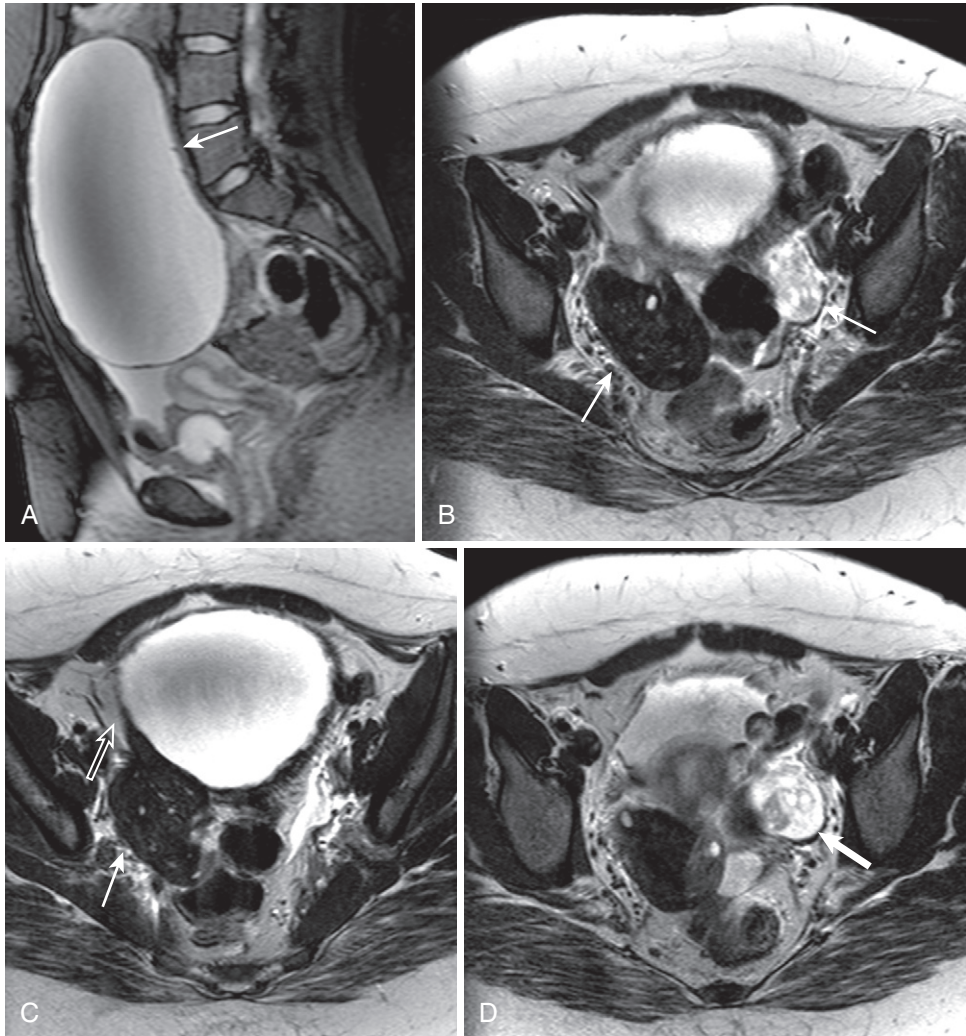


FIGURE 5-79. Bilateral ovarian torsion. **A**, Sagittal T2-weighted fat-suppressed image reveals a large unilocular cystic lesion with a mildly irregular wall thickening (*arrow*) shown to be a serous cystadenoma after surgical resection. **B**, Axial T2-weighted image shows diffusely abnormal right ovarian hypointensity (*thick arrow*) and diffusely abnormal left ovarian hyperintensity (*thin arrow*). **C–E**, Axial T2-weighted images through the caudal aspect of the lesion demonstrate the spatial relationship to bilaterally heterogeneously abnormal ovaries (right ovary, *thin arrow* in **C** and **E**; left ovary, *thick arrow* in **D** and **E**). The diffusely hypointense enlarged right ovary appears directly adherent with a tapering rind of tissue extending along the lateral aspect of the mass (*open arrow* in **C**), indicating right ovarian origin. The markedly hyperintense left ovary is enlarged to a lesser degree. T1-weighted images without (**E**) and with (**F**) fat suppression reveal ovarian hypointensity, particularly on the left (right ovary, *thin arrow* in **E** and **F**; left ovary, *thick arrow* in **E** and **F**), with a minimal peripheral rim of hyperintensity seen to better advantage on the fat-suppressed image (*open arrow* in **F**). **G**, Lack of enhancement is more definitively identified (*arrow*). **H**, Mild relative ovarian enhancement (*thick arrow*) and a focal serpiginous lesion (*open arrow*) likely representing the sequela of an involuted corpus luteal cyst are discernible. Surgical resection confirmed right ovarian hemorrhagic ischemia; the left ovary was described as edematous, but not ischemic—probably the effects of intermittent low-grade ischemia/partial torsion.

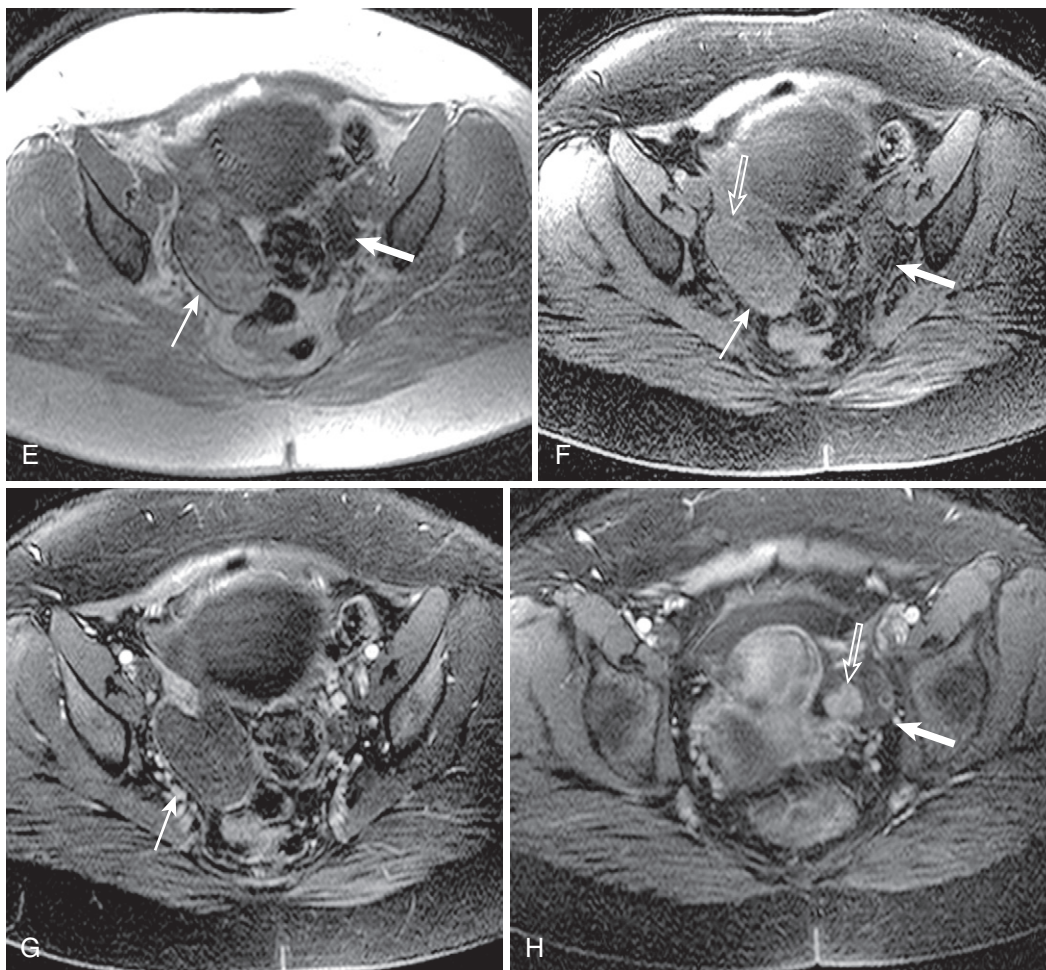


FIGURE 5-79, cont'd

ECTOPIC PREGNANCY

In the presence of blood (and pregnancy), keep ectopic pregnancy in mind, because of its life-threatening potential. The only potentially specific, pathognomonic finding is a gestational sac. Other findings overlap with other acute gynecologic diseases—especially torsion—and include hematosalpinx/adnexal hematoma, hemorrhagic ascites, and a complex hemorrhagic adnexal mass (Fig. 5-81).¹⁵ Always consider ectopic pregnancy in a reproductive-age female presenting acutely with a complex adnexal mass and edema and/or hemorrhage and encourage correlation with pregnancy status and β -hCG.

Complex Cystic and Solid Lesions

PRIMARY

Outside the acute adnexal lesions, complexity confers solid tissue or neoplasm. Ovarian neoplasms range from nearly entirely cystic (usually

epithelial type) to solid. Management of cystic lesions pivots on the identification of complex features. Simple cysts can be ignored or followed, whereas cysts with evidence of solid tissue demand surgical resection. Acknowledgment of this fact and accurate discrimination from simple cysts is more important than specific diagnosis of complex cystic or solid lesions.

EPITHELIAL NEOPLASMS

Almost invariably, cystic ovarian neoplasms derive from the ovarian epithelial cell line with two major subtypes dominating: serous cystadenoma (or cystadenocarcinoma) or mucinous cystadenoma (or cystadenocarcinoma)—among the five total subtypes. For the sake of maintaining perspective on the issue of ovarian neoplasms, there are four major categories: epithelial, germ cell, sex cord-stromal, and metastatic (Table 5-23). Epithelial tumors account for 60% of all ovarian neoplasms and the vast

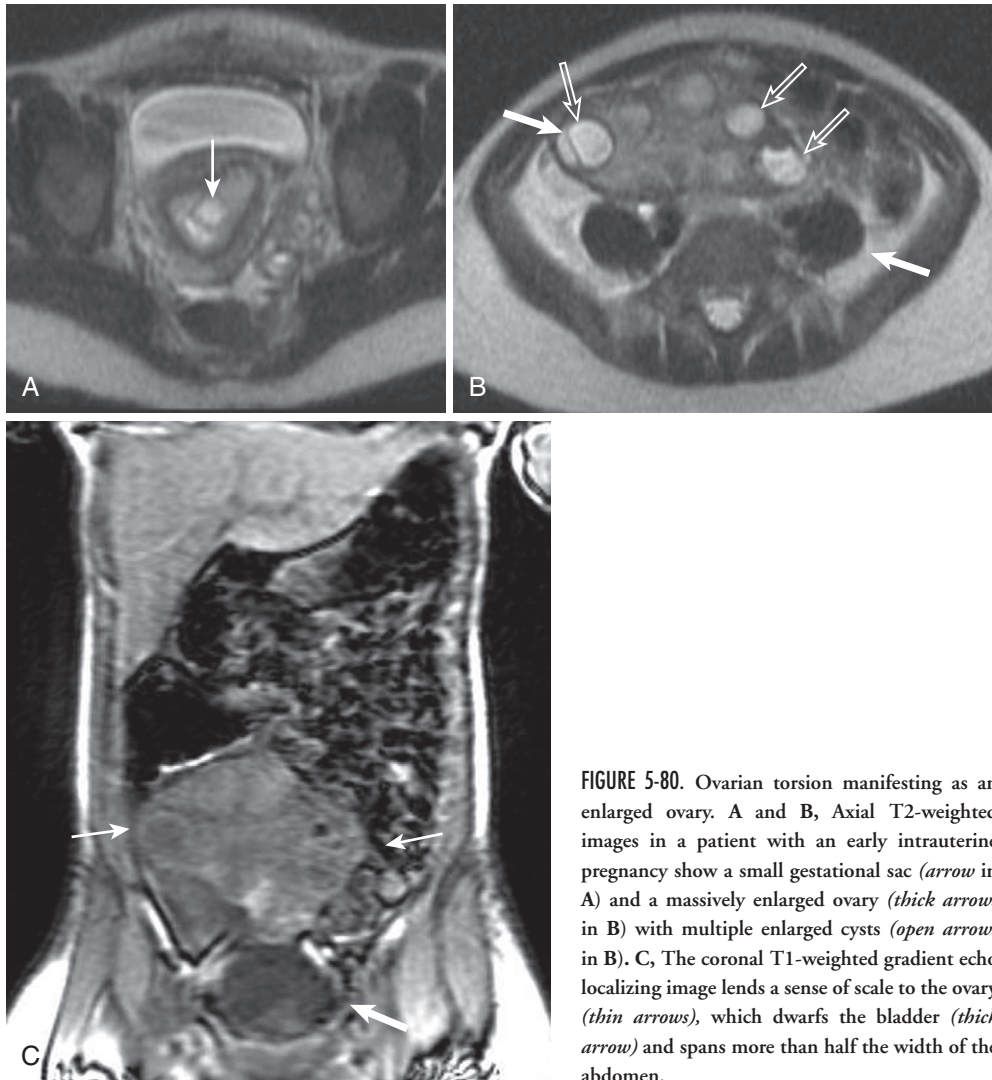


FIGURE 5-80. Ovarian torsion manifesting as an enlarged ovary. A and B, Axial T2-weighted images in a patient with an early intrauterine pregnancy show a small gestational sac (*arrow* in A) and a massively enlarged ovary (*thick arrows* in B) with multiple enlarged cysts (*open arrows* in B). C, The coronal T1-weighted gradient echo localizing image lends a sense of scale to the ovary (*thin arrows*), which dwarfs the bladder (*thick arrow*) and spans more than half the width of the abdomen.

TABLE 5-23. Classification Scheme for Ovarian Neoplasms

Epithelial	Sex Cord–Stromal Tumor
Serous	Granulosa–stromal cell tumor
Mucinous	Granulosa cell tumor
Endometrioid	Fibrothecoma
Clear cell	Sclerosing stromal tumor
Brenner	Sertoli–Leydig cell tumor
Undifferentiated	Steroid cell tumors
Germ Cell Tumors	Metastatic Tumors
Teratoma	
Mature	
Immature	
Dysgerminoma	
Endodermal sinus tumor	
Embryonal cell carcinoma	
Choriocarcinoma	

From Jung SE, Lee JM, Rha SE, et al. CT and MR imaging of ovarian tumors with emphasis on differential diagnosis. *Radiographics* 22;1305–1325, 2002.

majority of malignant ovarian neoplasms (~85%).³⁹

Epithelial ovarian neoplasms are a disease of older women, peaking in the sixth and seventh decades of life. They are classified as benign (60%), borderline or low-grade (5%), or malignant (35%), depending on the histologic and clinical behavior. Our job is to detect features that suggest malignancy—such as an obvious solid component, large size (>4 cm), wall thickening, papillary projections—or metastatic spread—ascites, adenopathy or peritoneal implants, and pelvic sidewall invasion (Tables 5-24 and 5-25 and Fig. 5-82). Clinical management depends less on local spread compared with cervical (and endometrial) carcinoma. Discriminating benign from malignant and identifying metastatic spread constitute the chief

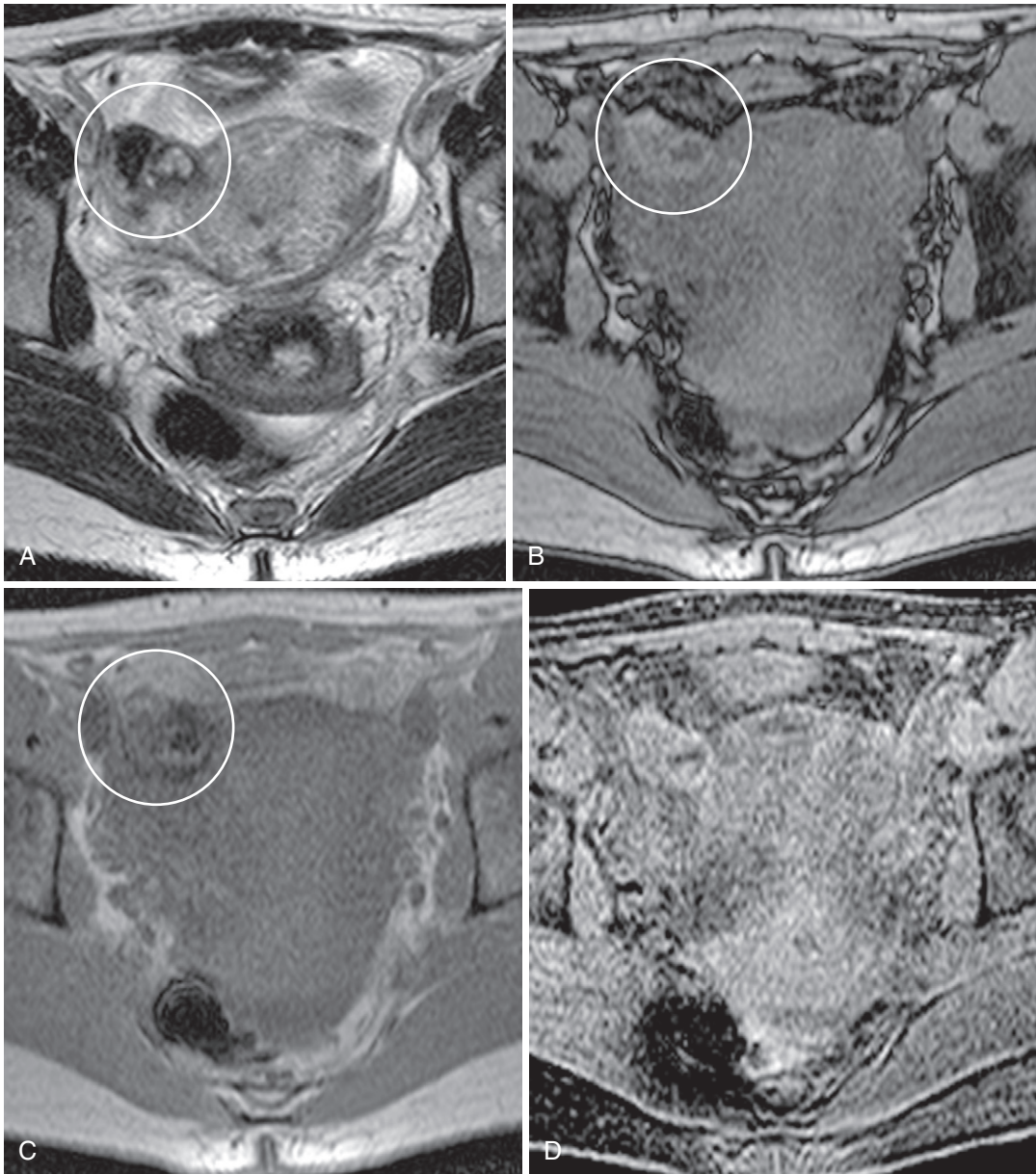


FIGURE 5-81. Ectopic pregnancy. Axial T2-weighted (A), T1-weighted out-of-phase (B) and T1-weighted in-phase (C) images. The right cornual region has a small complex cystic lesion (*circle*) with central fluid signal, a thin peripheral rim of hemorrhage, and an adjacent, lateral hypointense focus (presumably blood). Precontrast (D) and postcontrast (E and F) T1-weighted fat-suppressed images reveal enhancement around the lesion indicating inflammation (*arrow* in E and F). G, Corresponding CT image shows the right lower quadrant inflammation (*arrows*) adjacent to the lesion (*circle*). The α -fetoprotein measured approximately 35, and no intrauterine pregnancy was identified.

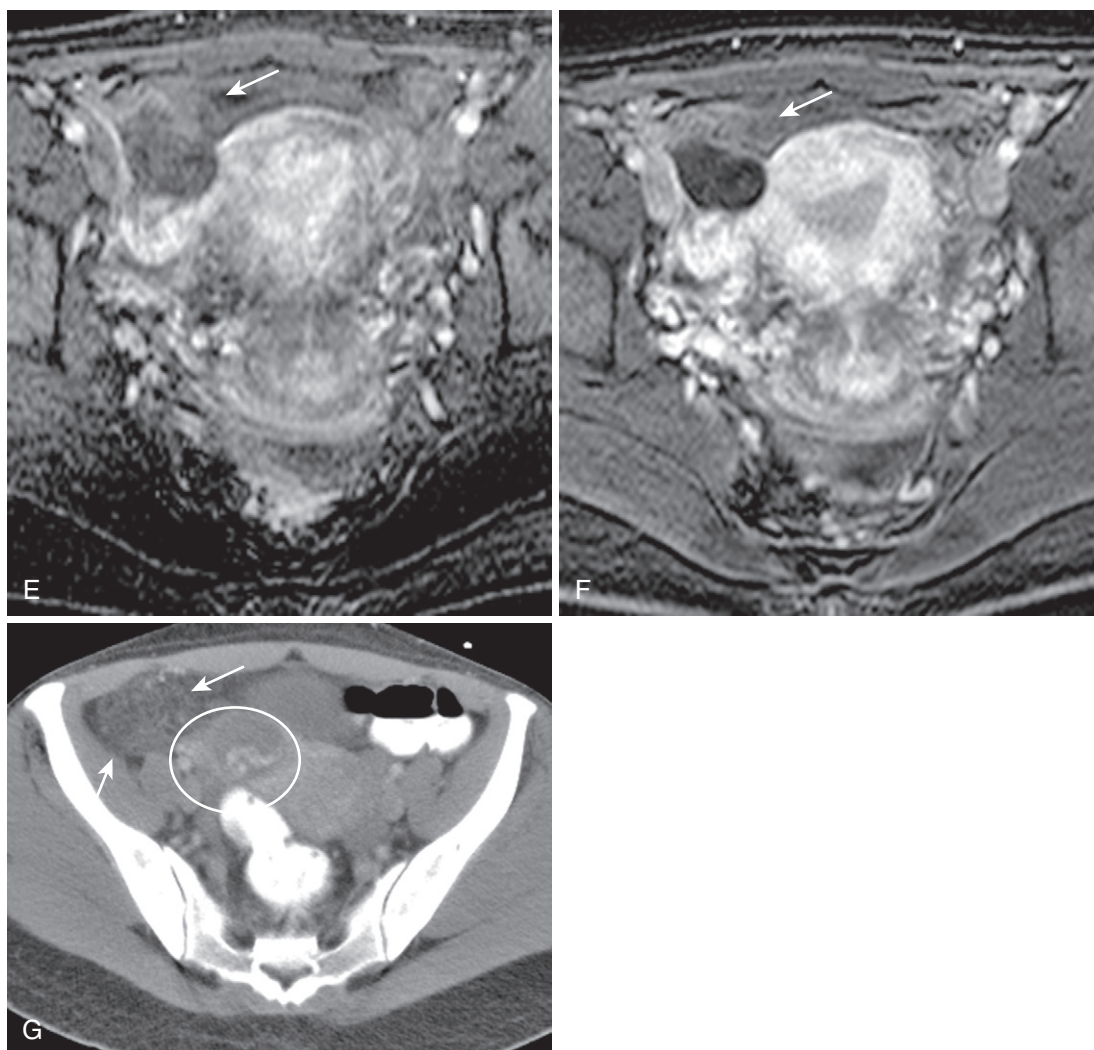


FIGURE 5-81, cont'd

TABLE 5-24. Ovarian Carcinoma Staging

Stage	Description
I	Grossly confined to one or both ovaries IA: Intracapsular and unilateral IB: Intracapsular and bilateral IC: Actual or potential peritoneal contamination*
II	Local extension; grossly confined to the true pelvis IIA: Involvement of Fallopian tubes or uterus IIB: Involvement of other pelvic tissues, e.g. sigmoid, pelvic implants IIC: Actual or potential peritoneal contamination*
III	Nodal metastases, or peritoneal implants outside the pelvis IIIA: Microscopic abdominal implants IIIB: <2 cm abdominal implants IIIC: >2 cm abdominal implants or positive nodes
IV	Distant spread (e.g., malignant pleural effusion, intrahepatic metastases)

*Based on the presence of surface tumor, tumor rupture, ascites containing malignant cells, or positive washings.

TABLE 5-25. Features Suggesting Malignancy in Ovarian Epithelial Neoplasms

Feature	Benign	Malignant
Size		
Component	Entirely cystic	Solid tissue Papillary projections
Wall	Thin (<3 mm)	Thick
Ascites	None	With possible implants
Other		Adenopathy Invasion

From Jung SE, Lee JM, Rha SE, et al. CT and MR imaging of ovarian tumors with emphasis on differential diagnosis. *Radiographics* 22:1305-1325, 2002.

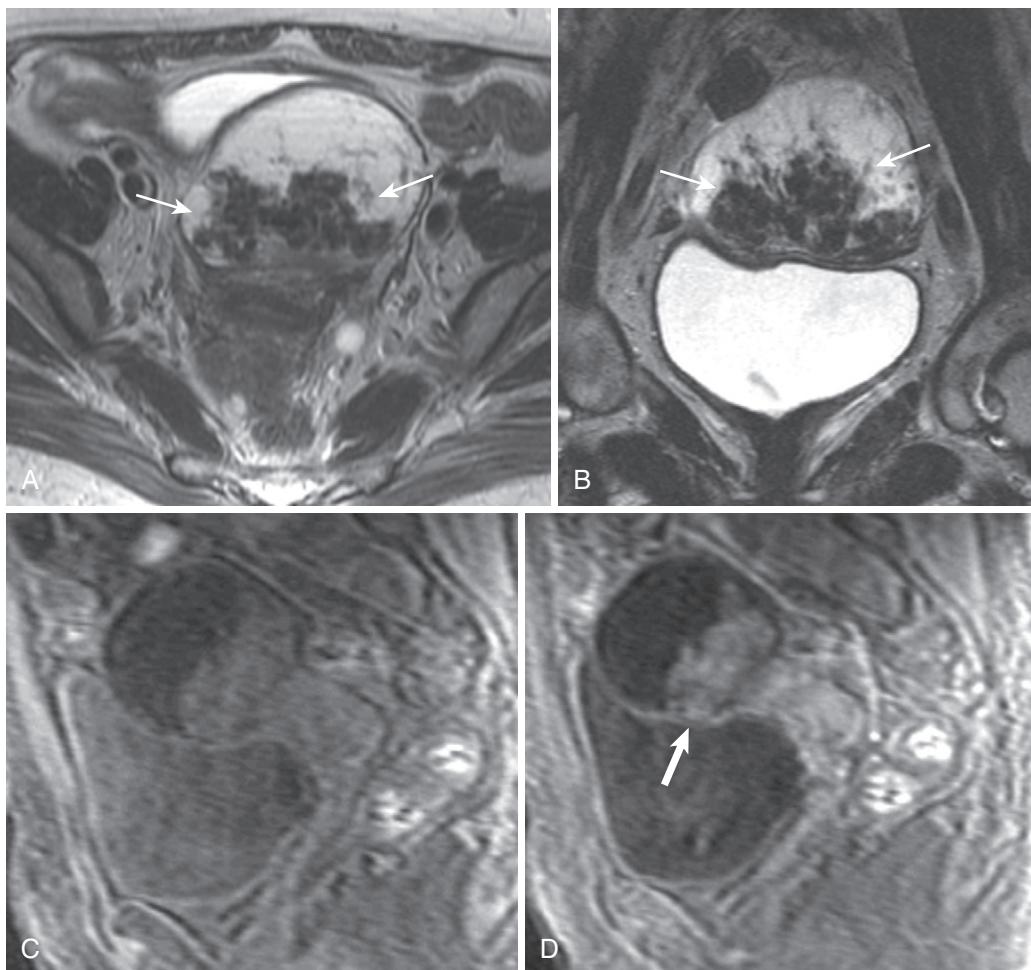


FIGURE 5-82. Malignant features of ovarian epithelial neoplasm. Axial (A) and coronal (B) T2-weighted images show gross mural papillary excrescences (*arrows*) virtually filling the contents of the mildly thick-walled unilocular cystic adnexal mass. Precontrast (C) and post-contrast (D) fat-suppressed T1-weighted sagittal images show enhancement of the mural excrescences (*thick arrow* in D) signifying solid, viable tissue in a serous cystadenocarcinoma. A low-grade seromucinous adenocarcinoma in a different patient (axial T2-weighted [E], axial T1-weighted [F], sagittal T2-weighted fat-suppressed [G], and sagittal T2-weighted enhanced [H] images) manifests similar—albeit less complex—features with a smaller, more confined papillary excrescence (*thin arrow* in E-G) exhibiting mild enhancement (*thick arrow* in H).

imaging objectives. Ultimately, staging is accomplished surgically.

Whereas differentiating between the different epithelial subtypes is largely academic, prognosis and malignant potential differ. Approximately 40% of serous tumors are low-grade or malignant compared with only 20% of mucinous neoplasms. MRI features of the two main histologic subtypes largely overlap, but there are some important discriminating characteristics (Table 5-26 and Figs. 5-83 and 5-84). Keep in mind that serous tumors are more likely to be malignant and that mucinous tumors have a propensity for low-grade mucinous intraperitoneal spread (pseudomyxoma peritonei). The most

important objective is to identify or exclude malignant features.⁴⁰ Even relatively indolent lesions may harbor malignancy and your threshold should be low in suggesting the possibility (Fig. 5-85).

The other subtypes of ovarian epithelial neoplasms are far less common. Endometrioid and clear cell types are usually malignant and are the most common malignant neoplasms arising from endometriosis (endometrioid is first). There are few suggestive, although not entirely reliable, features of the less common epithelial neoplasms. Endometrioid carcinoma appears as a large complex cystic mass with solid components with frequent bilaterality

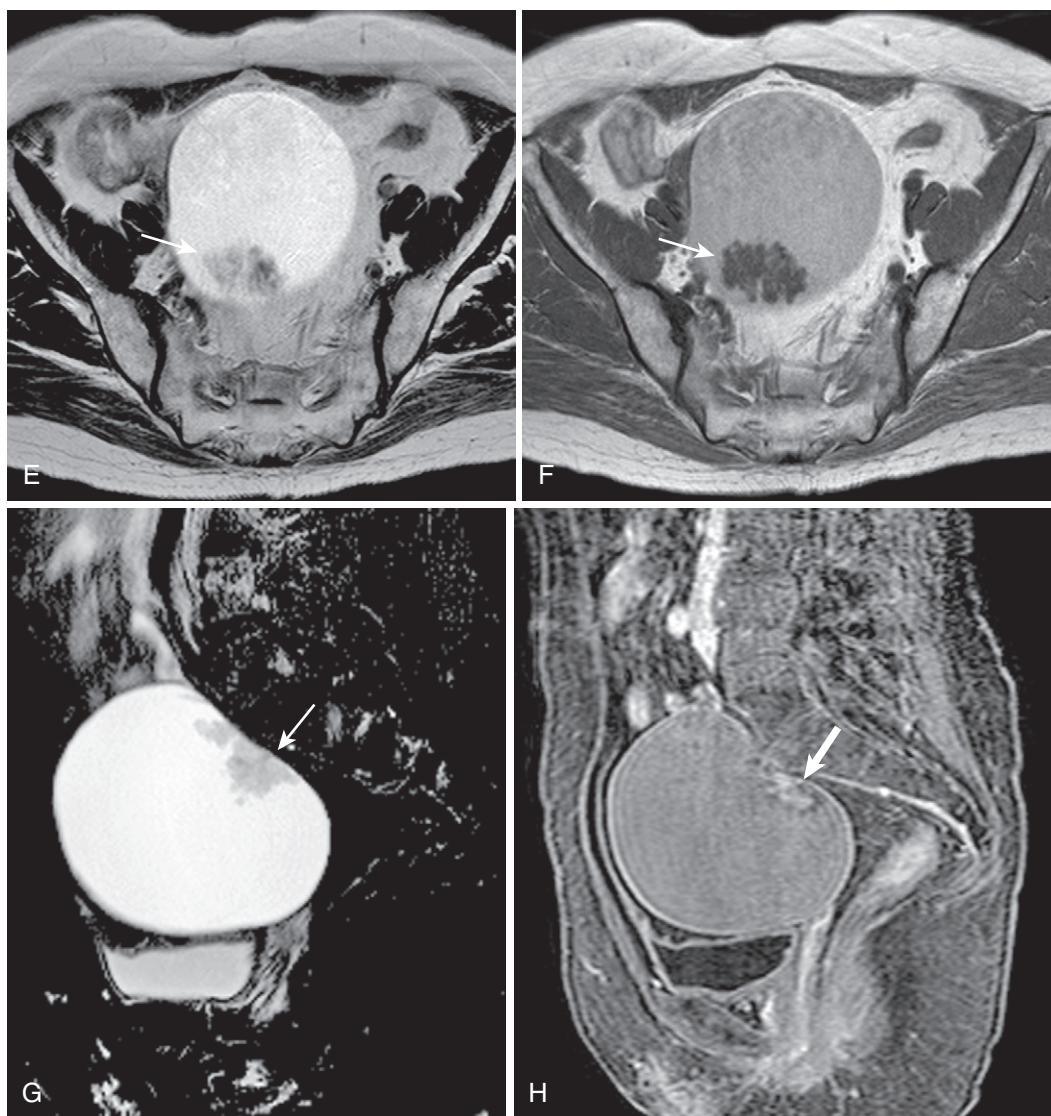


FIGURE 5-82, cont'd

(30–50%). Clear cell carcinoma commonly manifests as a unilocular cyst with solid protrusions. Brenner's tumors, which are rarely malignant, are usually small (T2) hypointense solid or multiloculated cystic lesions with solid components (which may exhibit exuberant calcifications); the uniform hypointensity reflects the fibrous stroma and generally limits the scope of diagnostic possibilities (Table 5-27). An association with endometriosis suggests endometrioid or clear cell carcinoma.

Cystadenofibroma is another subtype of ovarian epithelial neoplasm. Usually benign, these tumors often express a multiloculated morphology and contain intralesional fibrous

tissue in the form of nodules, plaques, or septa (Fig. 5-86).

OTHER PRIMARY OVARIAN NEOPLASMS

Other ovarian neoplastic varieties are fairly uncommon, constituting between 8% (sex cord-stromal) and 15% to 20% (germ cell) of ovarian neoplasms. Germ cell tumors include the (mature and immature) teratoma, dysgerminoma, endodermal sinus tumor, embryonal cell carcinoma, and choriocarcinoma; a comprehensive discussion of these mostly rare tumors is beyond the scope of this text. As previously discussed, the mature teratoma—or dermoid cyst—is the most common benign ovarian

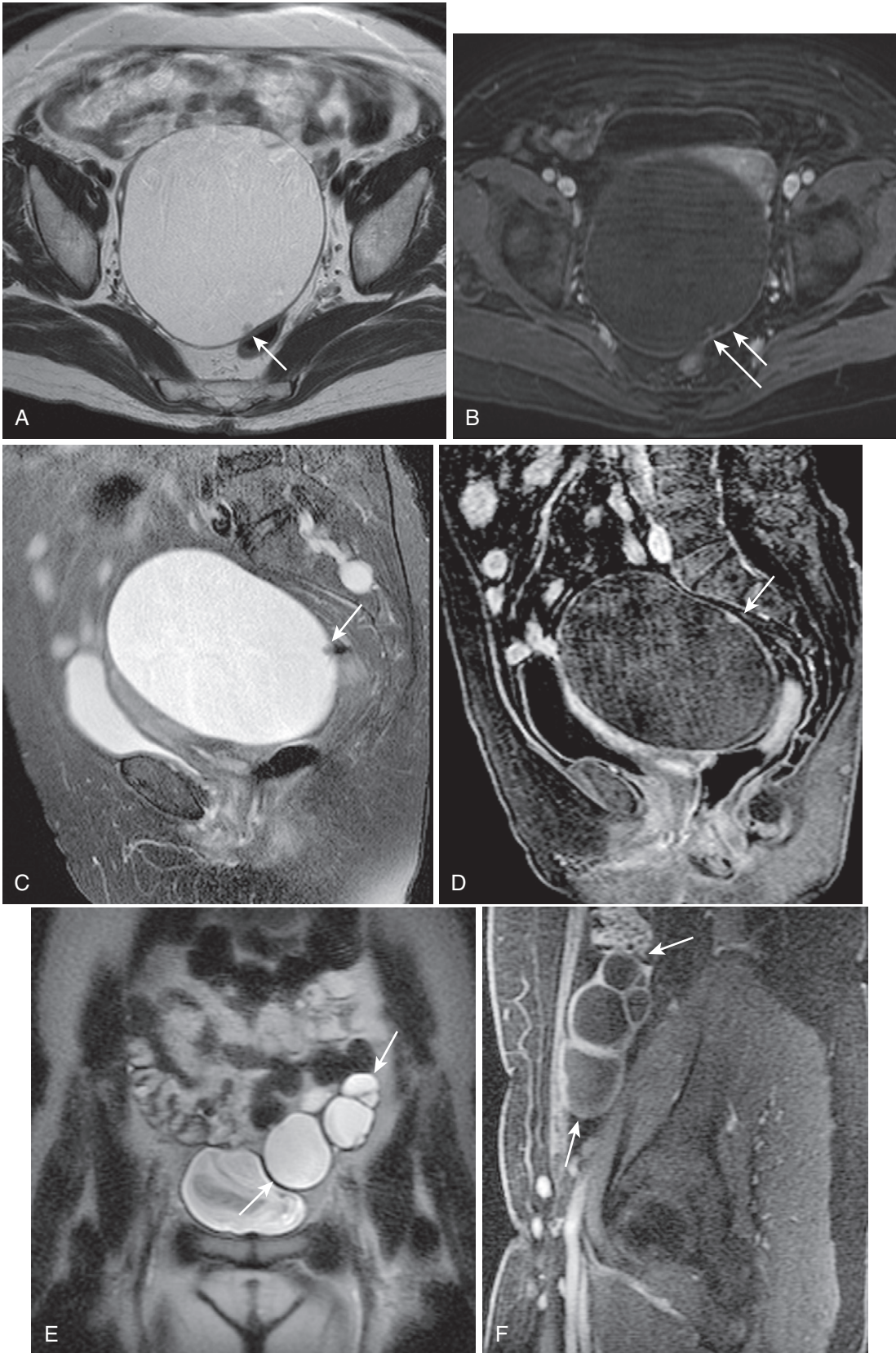


FIGURE 5-83. Serous cystadenoma. Axial T2-weighted (A) and enhanced (B) and sagittal T2-weighted (C) and enhanced (D) images. A large unilocular cystic lesion is virtually indistinguishable from a simple (functional) cyst except for the relatively large size and few inconspicuous mural nodules (*arrows* in A, B, C, and D) underscoring the importance of closely scrutinizing these lesions, especially when large. Although more often unilocular than its mucinous counterpart, the serous cystadenoma also expresses multilocular morphology (*arrows* in E and F), as seen in a different patient (coronal T2-weighted [E] and sagittal [F] enhanced images).

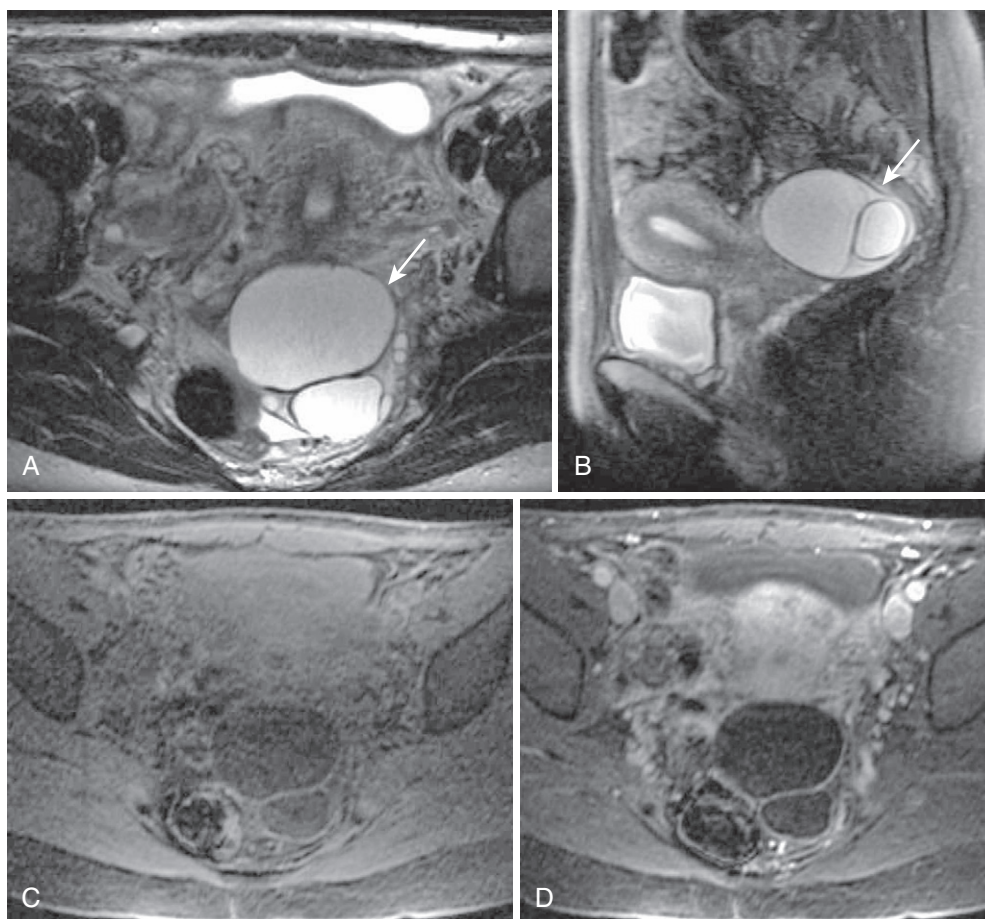


FIGURE 5-84. Mucinous cystadenoma. Axial T2-weighted (A) and sagittal fat-suppressed T2-weighted (B) images of a left ovarian mucinous cystadenoma (*arrow*) show multilocularity with thin septation and no other evidence of complexity. Precontrast (C) and postcontrast (D) images confirm the lack of malignant features.

TABLE 5-26. Features of Serous versus Mucinous Epithelial Ovarian Neoplasms

Feature	Serous	Mucinous
Clinical		
Benign	25%	20%
Malignant	50%	10%
Ratio	60% benign 15% low-grade 25% malignant	80% benign 10–15% low-grade 5–10% malignant
Imaging		
Size	Smaller	Larger
Morphology	Unilocular Thin-walled	Multilocular Small locules
Signal intensity	Uniform	Variable
Papillary projections	Common	Rare
Calcification	Psammomatous	Linear
Bilaterality	Frequent	Rare
Carcinomatosis	More common	Pseudomyxoma peritonei

TABLE 5-27. Differential Diagnosis of T2 Hypointense Ovarian Lesions

Lesion	Tissue Composition
Non-neoplastic	
Endometrioma	Concentrated blood products
Ovarian torsion	Acute blood
Neoplastic	
Cystadenofibroma	Dense collagenous stromal proliferations
Fibroma	Fibrous stromal tissue
Brenner's tumor	Abundant fibrous stroma
Krukenberg's tumor	Reactive stromal proliferation
Extra-ovarian	
Subserosal pedunculated fibroid	Dense collagen

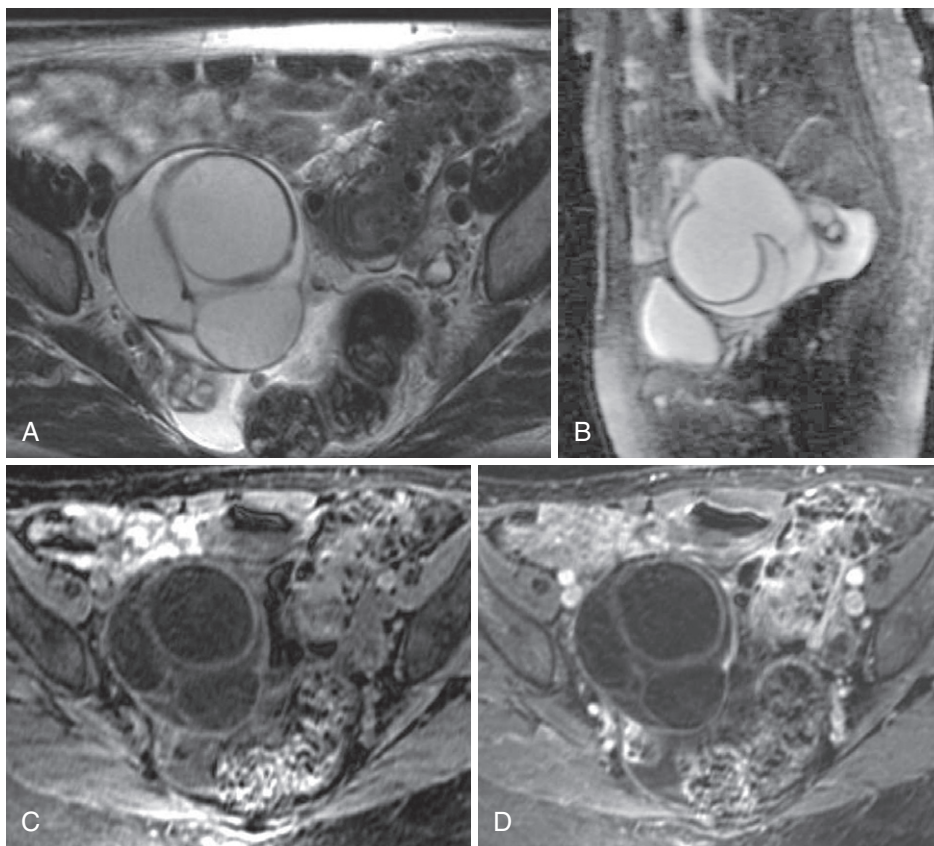


FIGURE 5-85. Mucinous cystadenocarcinoma. Axial T2-weighted (A) and sagittal T2-weighted fat-suppressed (B) images demonstrate a moderate-sized multiloculated cystic lesion with mildly thickened septa. T1-weighted precontrast (C) and postcontrast (D) images fail to detect any additional potential malignant features. Based on imaging findings, the likelihood of neoplasm is definite and the likelihood of malignancy is indeterminate. Surgery was recommended and a mucinous cystadenocarcinoma without evidence of invasion was resected.

tumor in young women. The imaging appearance of a mature teratoma ranges from entirely cystic to a largely fat-containing mass, corresponding to T1 hyperintensity that is suppressed on fat-saturated sequences (see Figs. 5-65 to 5-68). Mural nodules are common and may exhibit hypointensity or susceptibility artifact due to calcium or hair (see Figs. 5-65 and 5-66). Although the immature teratoma may also harbor small foci of fat, its complexity, poor definition, internal necrosis and/or hemorrhage, and solid components belie its malignant nature.

The endodermal sinus tumor (yolk sac tumor) and dysgerminoma are probably most characteristic for the associated hormonal secretions and their predilection for young women. Endodermal sinus tumors often elicit α -fetoprotein, and dysgerminomas occasionally produce hCG. Both have a variable appearance and exhibit complexity and solid components. Both of these

tumors (and the other even rarer germ cell tumors) are in the differential diagnosis of a complex solid adnexal mass in a young woman (Fig. 5-87).

Sex cord-stromal tumors derive from the mesenchyme of the embryonic gonads, which means that they arise from the ovarian cells surrounding the oocytes.^{41,42} Among these nongerm cell and nonepithelial cell types are granulosa cells, thecal cells, Sertoli cells, Leydig cells, and fibroblasts. Granulosa and theca cells participate in the production of estrogen, and Leydig cells secrete androgens and tumors of these cell types—granulosa cell tumors, thecomas, and Leydig cell tumors, respectively—are often associated with elevations in these hormone levels. These lesions may be benign or malignant.

Fibroblasts and thecal cells often collaborate to form a spectrum of benign tumors named according to the relative contribution of fibrous

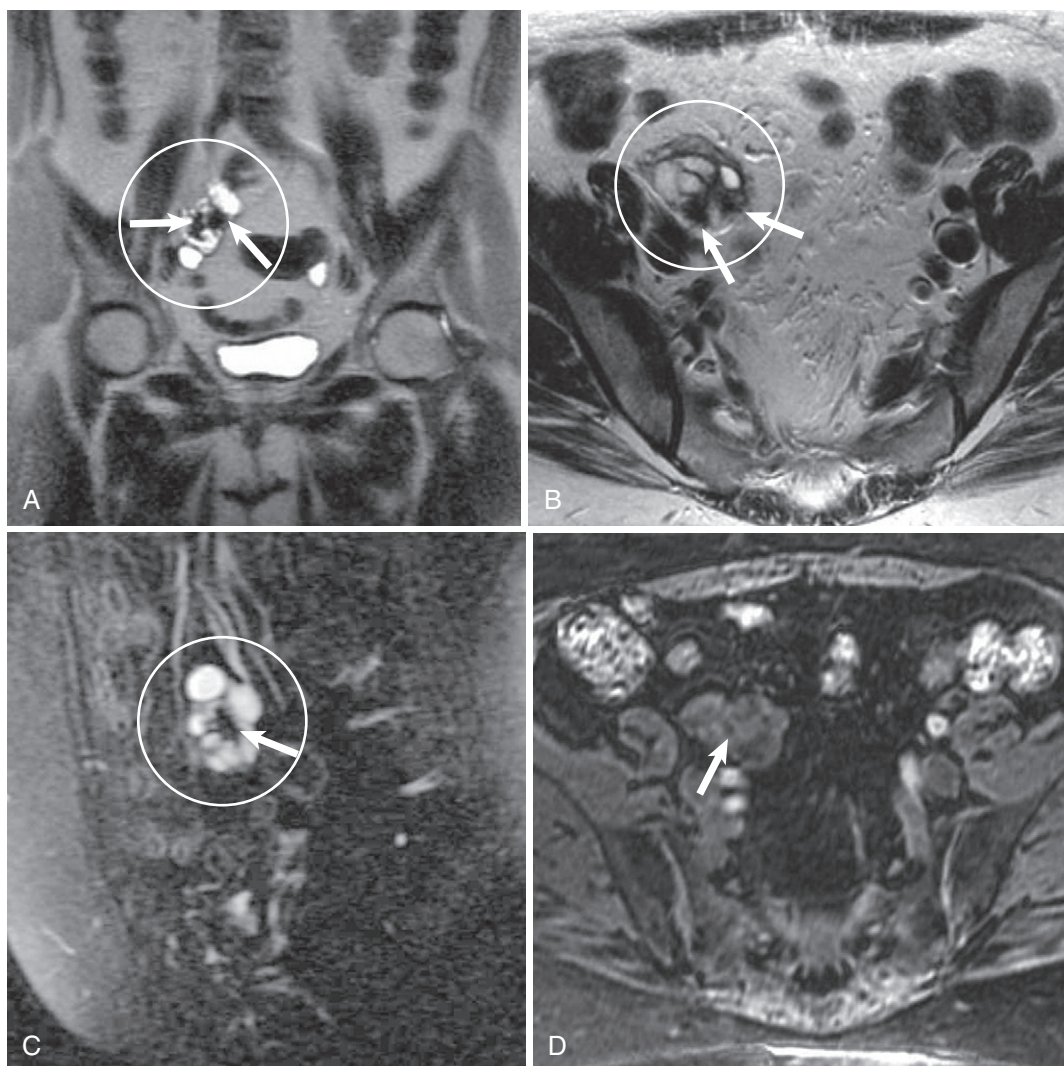


FIGURE 5-86. Cystadenofibroma. Coronal (A) and axial (B) T2-weighted and sagittal fat-suppressed (C) images of a right ovarian cystadenofibroma (*circle*) show at least two dark clumps of fibrous tissue (*arrows*). D, There is mild enhancement of the septa and fibrous plaque (*arrow*).

tissue and hormonally active thecal cells. Fibromas are the most common stromal tumors and usually occur in postmenopausal females. They are usually unilateral and are not hormonally active. Fibromas are usually monotonous uniformly hypointense lesions on all pulse sequences and exhibit mild enhancement, which may be difficult to visually perceive (Figs. 5-88 and 5-89). Review subtracted images or measure intensity values compared with a control, such as muscle, which enhances approximately 15%. Check for the presence of ascites (and pleural effusion) constituting the triad of Meigs' syndrome (benign ovarian tumor, pleural effusion, and ascites). This is an odd

condition that resolves after resection of the tumor that is postulated to arise from the frictional effects of a hard mass stimulating peritoneal fluid production.

Thecomas and fibrothecomas, although lipid-containing and hormonally active, generally do not contain enough lipid to be detected on MRI (or microscopically, for that matter). Only in postmenopausal women in whom no uterine estrogenic stimulation is expected is a thecoma/fibrothecoma distinguished from a fibroma.

Granulosa cell tumors are the most common malignant sex cord-stromal ovarian tumor, constituting less than 5% of all malignant ovarian neoplasms. Granulosa cell tumors are also the

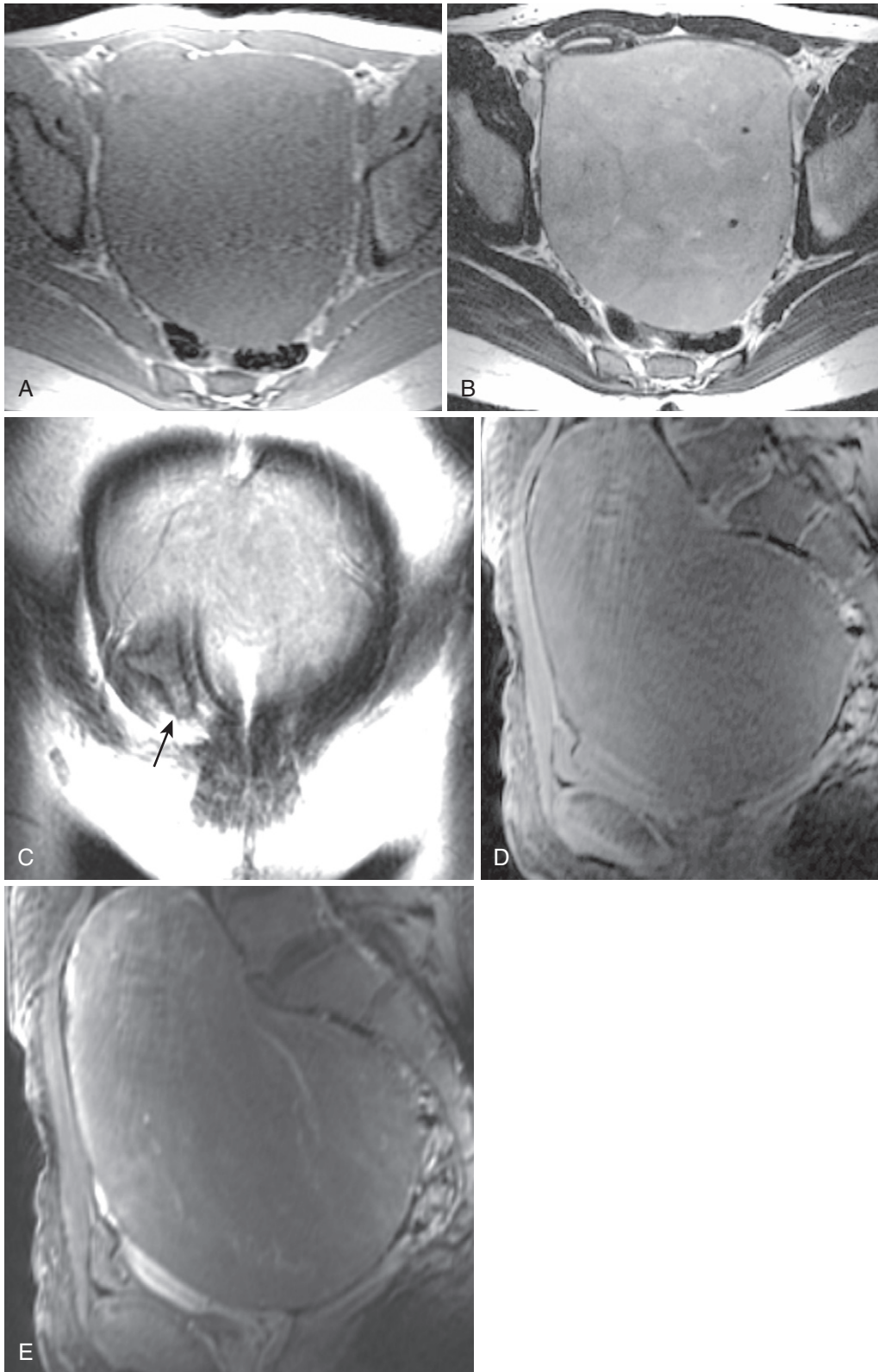


FIGURE 5-87. Dysgerminoma. Axial gradient echo T1-weighted in-phase (A) and axial (B) and coronal (C) T2-weighted images. A non-specific monotonous solid mass exerts marked mass effect on surrounding structures of the pelvis (note the uterus ventrally flattened against the abdominal wall—*arrow* in C). Precontrast (D) and postcontrast (E) images show diffuse enhancement.

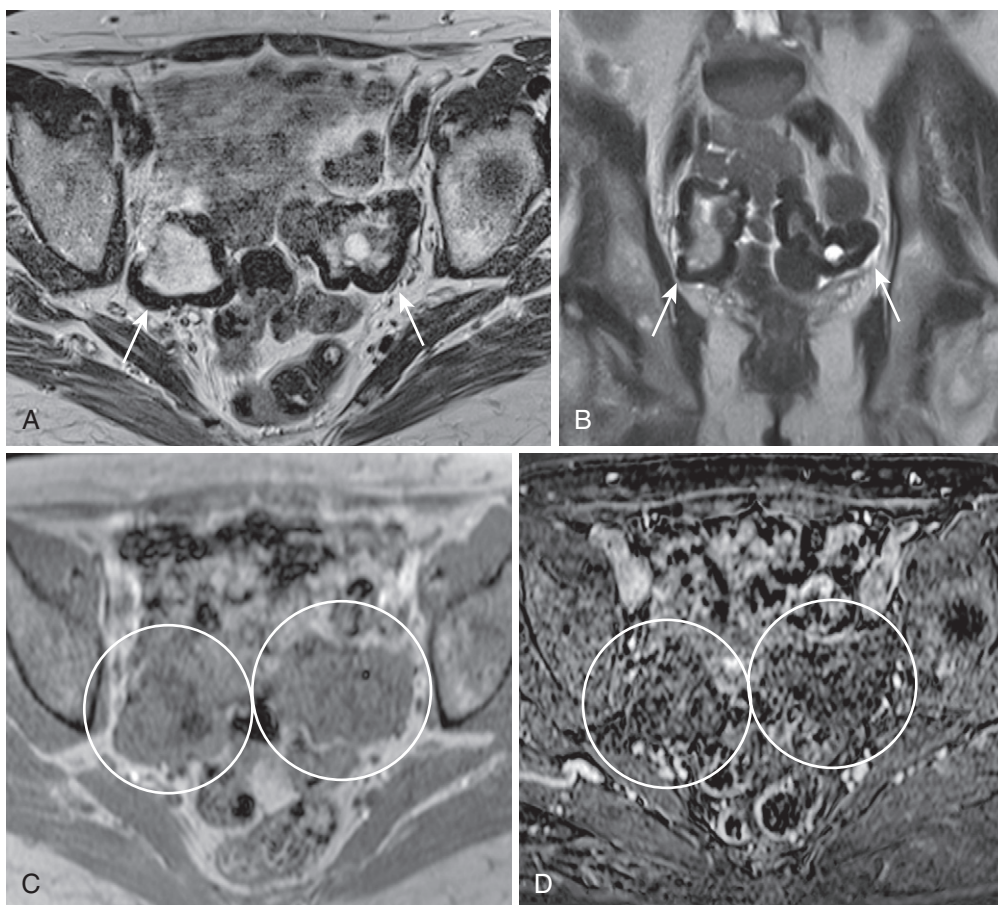


FIGURE 5-88. Bilateral fibromas. Serpiginous hypointensity (*arrows*) distorts the appearance of the ovaries bilaterally on axial (A) and coronal (B) T2-weighted images. C, Axial T1-weighted in-phase gradient echo image shows monotonous mild hypointensity to isointensity (*circles*), and signal characteristics most strongly suggest fibrous tissue. D, Mild bilateral enhancement (*circles*) is noted on the subtracted postcontrast image.

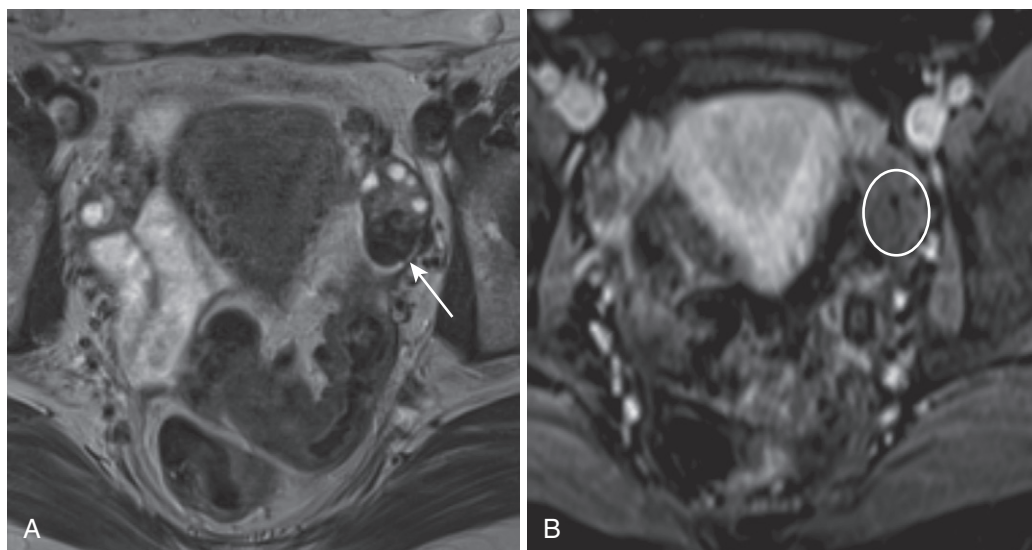


FIGURE 5-89. Ovarian fibroma. Axial T2-weighted image (A) shows a small left ovarian fibroma (*arrow* in A) with very low signal and mild enhancement (*circle* in B) on the T1-weighted fat-suppressed enhanced image (B).

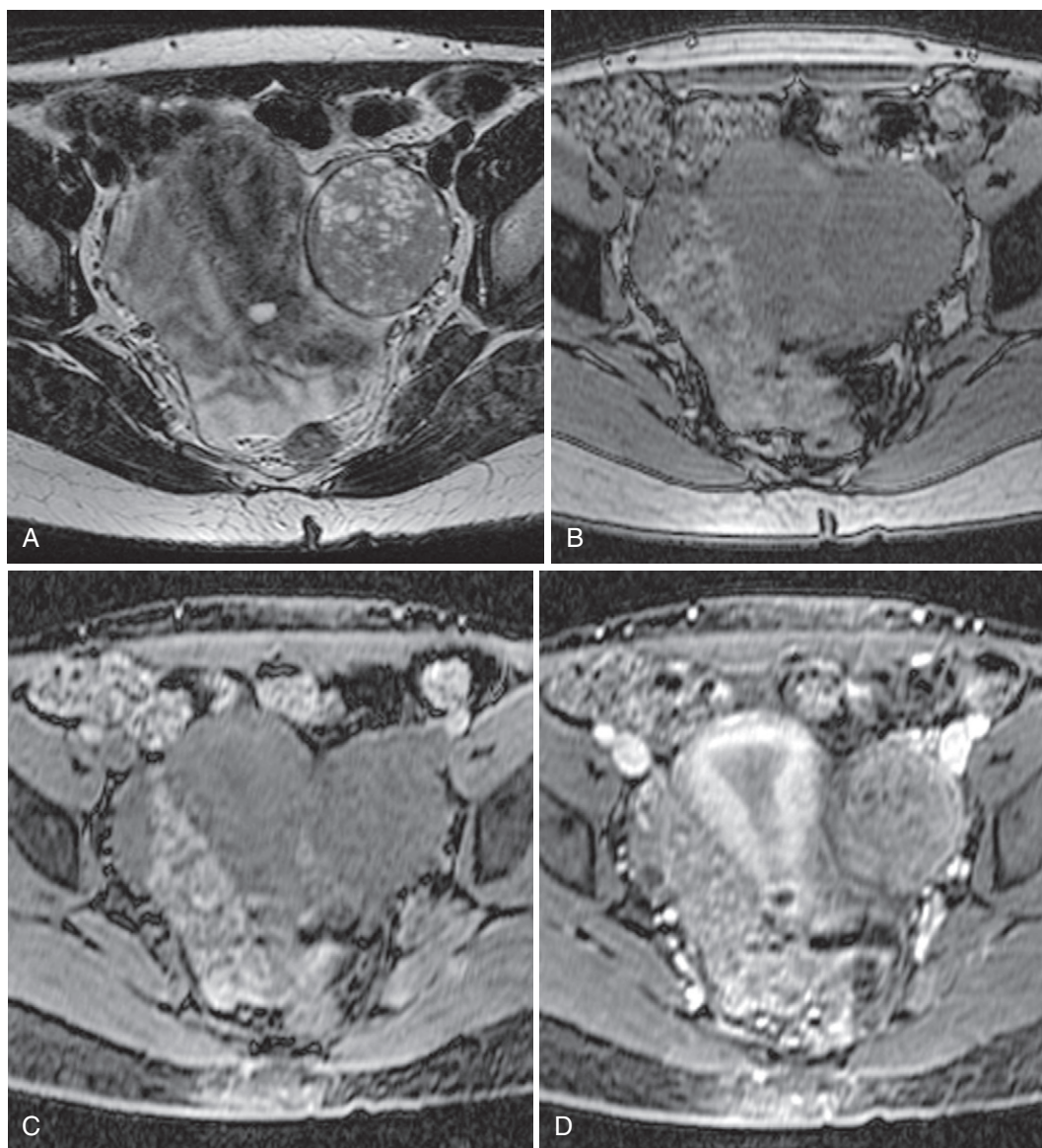


FIGURE 5-90. Granulosa cell tumor. A, In this case, the tumor is mostly solid with punctate hyperintense cystic foci on the axial T2-weighted image. The monotonous isointensity on the out-of-phase (B) and fat suppressed T1-weighted (C) images excludes hemorrhage. D, After intravenous gadolinium, moderate enhancement is noted.

most common estrogenic ovarian tumor, and a small subset occurs in prepubescent girls (unlike the thecoma/fibrothecoma). Following a macro-follicular growth pattern with multilocular cystic spaces, the imaging appearance is often complicated by hemorrhage, fibrous degeneration, irregular growth, or necrosis. Consequently, the granulosa cell tumor appearance ranges from largely solid to largely cystic possibly with hemorrhagic foci (Fig. 5-90).

Sertoli-Leydig cell tumors represent a spectrum of lesions composed of Sertoli and Leydig cells that secrete androgenic hormones. As the

most common virilizing ovarian tumor, the Sertoli-Leydig cell tumor is very rare, representing less than 0.5% of ovarian tumors. The appearance is nonspecific, ranging from solid to cystic, and variable T2 hypointensity reflects fibrous stroma; the most characteristic feature is the androgenic hormone secretion.

Sclerosing stromal tumors are rare sex cord-stromal tumors usually occurring in the second or third decade of life. The imaging appearance has been described as a “pseudobubular pattern” with hypointense, mildly enhancing nodules surrounded by T2 hyperintense stroma. A

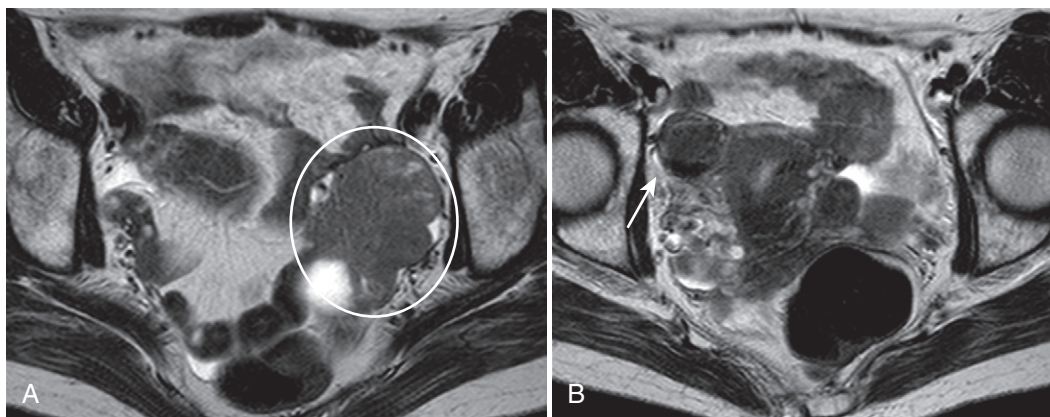


FIGURE 5-91. Metastatic ovarian lesions. A and B, Axial T2-weighted images. An amorphous solid mass replaces the left ovary (circle in A) and a smaller, more hypointense lesion mildly expands and distorts the right ovary (arrow in B).

combination of rapidly enhancing cellular and gradually enhancing collagenous hypocellular components exhibiting peripheral enhancement with centripetal progression characterizes the imaging appearance.

SECONDARY

Secondary ovarian tumors are predominantly composed of metastatic gastric, breast, and colon carcinoma. When arising from a primary gastrointestinal malignancy, the eponym “Krukenberg’s tumor” is applied. Although the appearance is nonspecific, the process is usually bilateral and ovarian tissue has a tendency to form desmoplastic tissue in response to the metastases resulting in T2 hypointense solid components. Bilateral (hypointense) solid ovarian lesions in elderly patients—especially with a known primary (gastric, breast, or colonic) malignancy—strongly suggest metastatic disease (Fig. 5-91).

MISCELLANEOUS

The final category is composed of miscellaneous lesions not belonging to any of the other categories. These are entities to keep in the back of your mind to use whenever another, more likely diagnosis is not forthcoming. Among these lesions are pelvic lymphoma, aggressive angio-myxoma, peritoneal carcinomatosis, fallopian tube carcinoma, and other rare primary lesions of the peritoneum, such as multicystic mesothelioma (Table 5-28).⁴³

PELVIC LYMPHOMA

Primary lymphoma of the pelvis is a rare entity and the most common site of origin in the

TABLE 5-28. Miscellaneous Pelvic Lesions

Uterus	Gastrointestinal Neoplasms
Endometrial stromal sarcoma	Rectal carcinoma
Adenosarcoma	GIST
Carcinosarcoma	
Fallopian Tube	Soft Tissue Tumors
Fallopian tube adenocarcinoma	Hemangiopericytoma
	Liposarcoma
	Aggressive angio-myxoma
Ovary	
Clear cell adenocarcinoma	
Metastatic disease	
Peritoneal Neoplasms	
Multicystic mesothelioma	
Pseudomyxoma peritonei	
Desmoid tumor	

GIST = gastrointestinal stromal tumor.

From Szklaruk J, Tamm EP, Choi H, Varavithya V. MR imaging of common and uncommon large pelvic masses. *Radiographics* 23:403-434, 2003.

female genital tract is the cervix. To keep it in perspective, cervical lymphoma constitutes less than 1% of cervical malignancies. Compared with cervical carcinoma, lymphoma is more homogeneous and undergoes less necrosis. Perhaps the only definitive findings are the lack of mucosal involvement and sparing of the cervical stroma and uterine junctional zone.⁴⁴ The imaging features are otherwise nonspecific with mild T2 hyperintensity and mild enhancement. The term “monotonous” is often applied to describe the imaging appearance of lymphomatous masses, referring to the relatively homogeneous uniformly solid, mildly enhancing mass with no unique identifiers.

AGGRESSIVE ANGIOMYXOMA

Aggressive angiomyxoma is an unusual uncommon tumor almost exclusively arising from the female perineum. They are composed of mesenchymal stellate or spindle cells with a loose myxoid background of collagen with small thick-walled vessels. Despite the name, these tumors are deceptively aggressive in appearance; actually these tumors displace and/or grow around adjacent structures, rather than invading (Fig. 5-92). These uniformly solid lesions exhibit an enhancement pattern that has been described as “whorled.”

Globally Abnormal Ovaries

Bilaterally globally abnormal ovaries usually derive from hormonal imbalances (unless involved with an extrinsic process, such as metastatic disease). Consider this category to extend from nearly normal ovaries to massively enlarged, cystic ovaries, or from multifollicular ovaries (which is a forme fruste of polycystic ovary syndrome [PCOS] seen in puberty associated with mildly reduced follicle-stimulating hormone [FSH] levels) at the nearly normal end of the spectrum to ovarian hyperstimulation syndrome.

POLYCYSTIC OVARY SYNDROME

Multifollicular ovaries and polycystic ovaries differ mainly in their clinical context. PCOS (or Stein-Leventhal syndrome) is a clinical entity defined as hyperandrogenism with chronic anovulation without underlying adrenal or pituitary etiology. The ovaries in these patients enlarge (usually bilaterally) and classically contain multiple, mildly enlarged, peripherally distributed follicles (Fig. 5-93). Imaging criteria have been generated to assist in the diagnostic process and include (1) ovarian volume greater than 10 cm³, (2) 12 or more follicles per ovary, (3) no dominant follicle of 10 mm or larger, and (4) peripheral follicular distribution; at least two or three of these items should be present to entertain the diagnosis.⁴⁵ Be advised that these criteria were designed as a sonographic diagnostic tool, and consider them as a general guideline for MRI. Polycystic ovaries differ from PCOS ovaries only in the absence of the clinical syndrome, not in the imaging appearance.

Multifollicular ovaries are essentially polycystic ovaries in mid to late puberty. Incomplete pulsatile gonadotropin with relatively low levels

of FSH induces mild global changes in the ovaries. Ovarian size ranges from normal to slightly enlarged and numerous small follicles (≤ 10 mm) are observed. The findings are generally less dramatic than in polycystic ovaries.

OVARIAN HYPERSTIMULATION SYNDROME

Ovarian hyperstimulation syndrome (OHSS) is a rare iatrogenic phenomenon induced by fertility drugs, particularly gonadotropin therapy. The clinical manifestations run the gamut from mild discomfort to life-threatening multiorgan derangements (including hemoconcentration, decreased blood volume, clotting disorders, abnormal renal function, and respiratory distress). The main clinical categories—mild, moderate, and severe—stratify patients based on clinical and imaging data. Patients with mild OHSS experience mild abdominal discomfort and the ovaries usually measure less than 5 cm in diameter. In moderate OHSS, the ovaries measure between 5 and 10 cm and weight gain, vomiting, ascites develop. The ovaries enlarge to over 10 cm in severe OHSS with worsening clinical manifestations including gross intraperitoneal fluid, pleural effusions, hypotension, and electrolyte imbalances. Multiple enlarged ovarian cysts are also typically observed and the MRI appearance overlaps with massive ovarian edema and PCOS (Fig. 5-94). Whereas the imaging features may be indistinguishable in some cases, the clinical presentations diverge significantly, allowing for a precise diagnosis (although with ovarian enlargement in OHSS, the possibility of torsion increases).

Vascular Lesions

Although vascular lesions bear little conceptual resemblance to other adnexal lesions, some imaging features overlap. Whereas flowing blood often induces signal voids on spin-echo images, dilated pelvic veins occasionally appear hyperintense on T2-weighted images, mimicking other tubular structures, such as hydrosalpinx (Fig. 5-95). Intraluminal enhancement matching venous enhancement obviates potential misdiagnosis.

The three dominant vascular disorders are pelvic arteriovenous malformation (AVM), pelvic congestion syndrome or pelvic varices, and ovarian vein thrombosis (Table 5-29). Reviewing the normal anatomy of the pelvis is a good starting point for a discussion of these

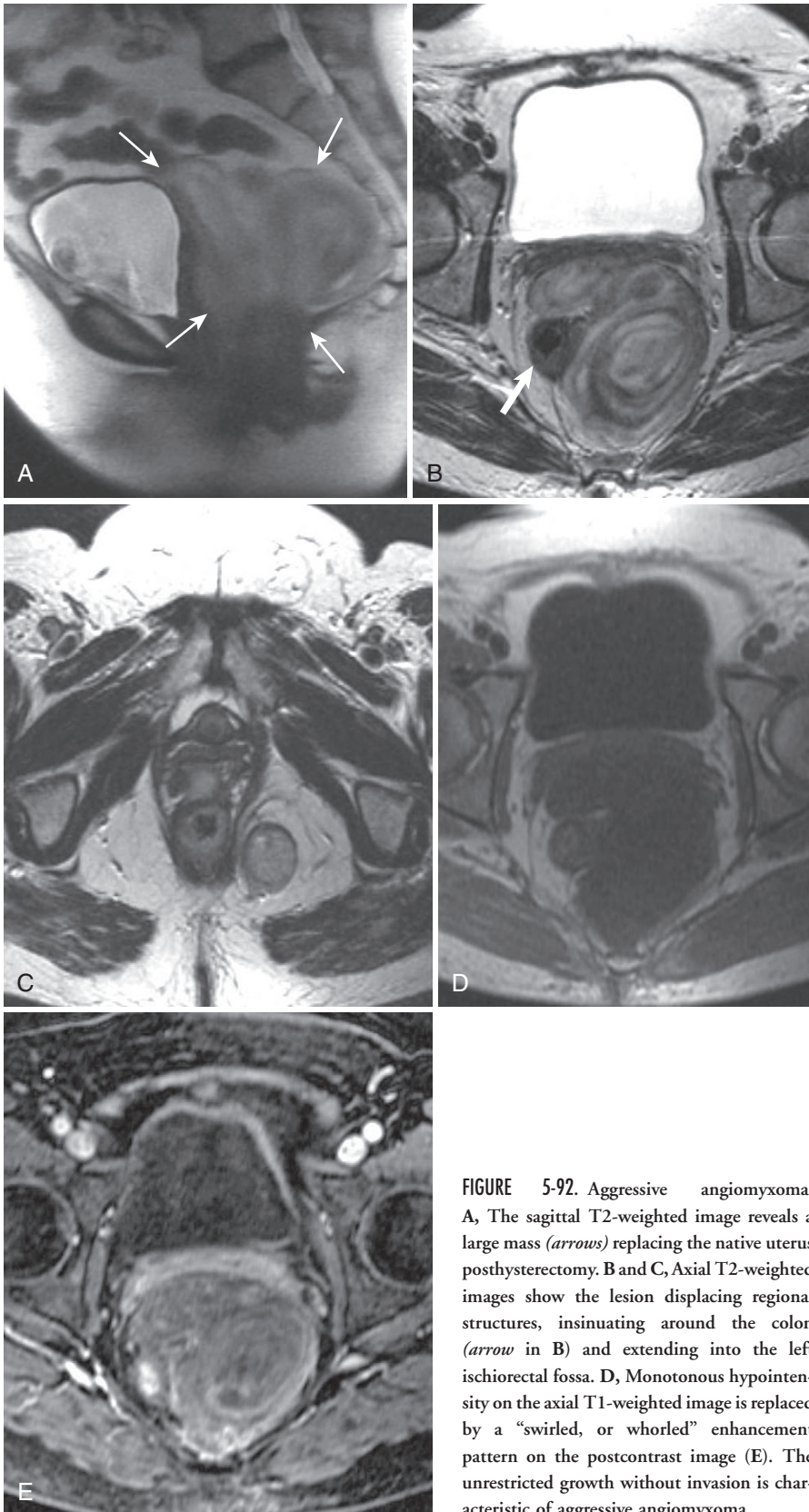


FIGURE 5-92. Aggressive angiomyxoma. A, The sagittal T2-weighted image reveals a large mass (*arrows*) replacing the native uterus posthysterectomy. B and C, Axial T2-weighted images show the lesion displacing regional structures, insinuating around the colon (*arrow* in B) and extending into the left ischio-rectal fossa. D, Monotonous hypointensity on the axial T1-weighted image is replaced by a “swirled, or whorled” enhancement pattern on the postcontrast image (E). The unrestricted growth without invasion is characteristic of aggressive angiomyxoma.

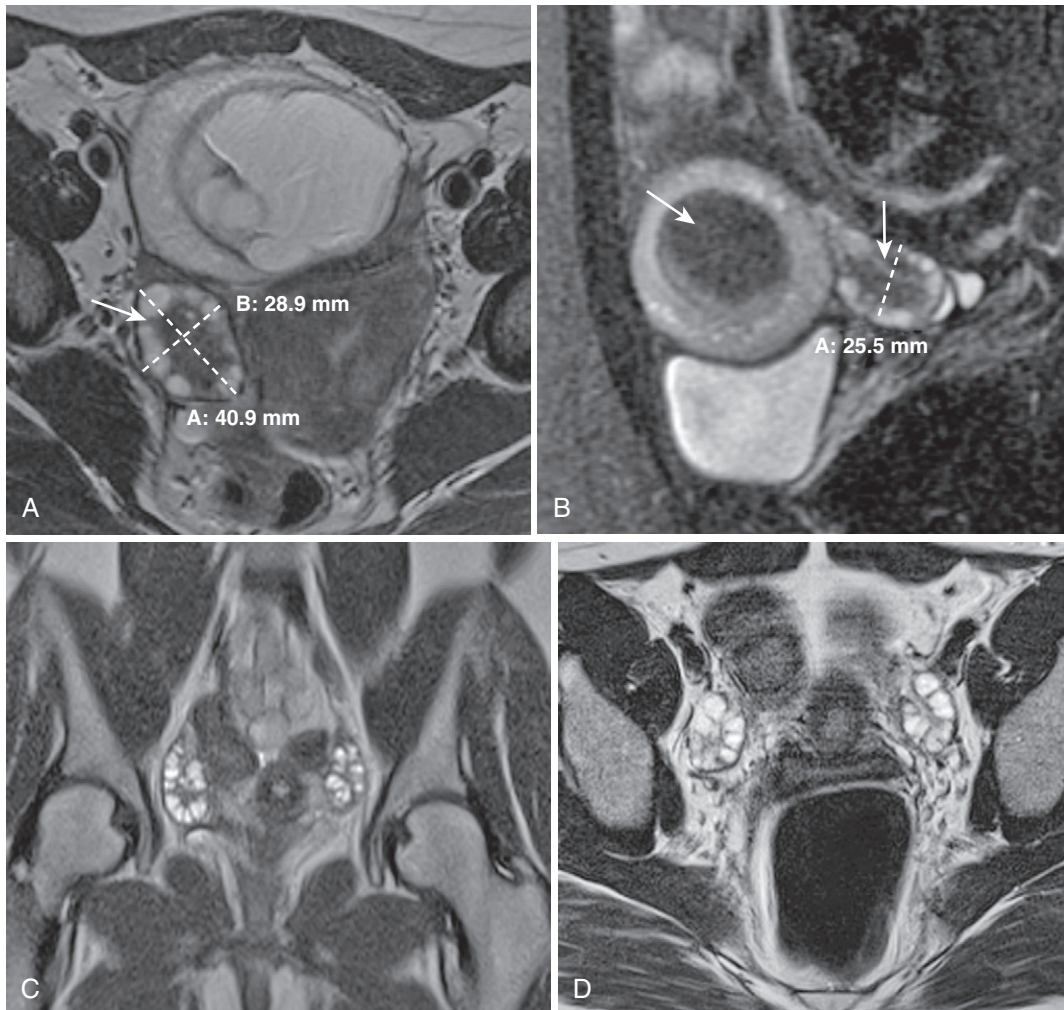


FIGURE 5-93. Polycystic ovaries. The axial (A) and sagittal fat-suppressed (B) T2-weighted images in a patient clinically presenting with polycystic ovary syndrome (PCOS) show an enlarged right ovary with multiple subcentimeter peripheral follicles and hypertrophic central stromal tissue (*arrow* in A), supporting the clinical diagnosis. The left ovary (not shown) exhibited similar features. The complex cystic mass anteriorly demonstrates central signal cancellation (*arrows* in B) on the fat-suppressed image, indicating fat in a dermoid cyst. In a second patient without the clinical stigmata of PCOS (coronal [C] and axial [D] T2-weighted images), bilaterally mildly enlarged ovaries contain multiple peripherally distributed follicles with no dominant cyst.

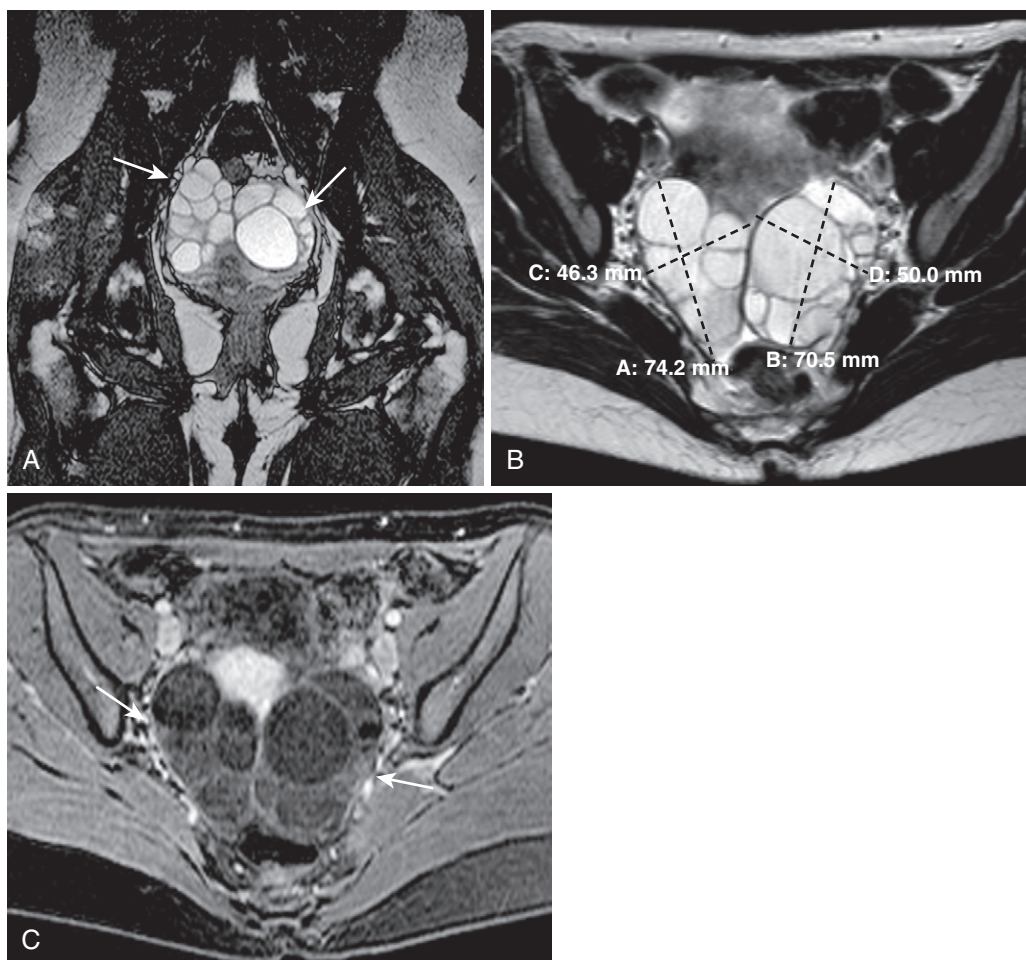


FIGURE 5-94. Ovarian hyperstimulation syndrome. **A**, The coronal localizer steady-state image in a patient undergoing fertility treatment shows bilaterally enlarged cystic ovaries (*arrows*). **B**, Measurements obtained on the axial T2-weighted image far exceed normal parameters and the increased size and number of ovarian cysts obliterates ovarian architecture and stromal tissue. **C**, Axial enhanced fat-suppressed T1-weighted image reveals enhancing tissue centrifugally compressed around the peripheral margins of the enlarged cysts (*arrows*).

TABLE 5-29. Vascular Lesions

Lesion	Clinical Features	Imaging Findings
Pelvic arteriovenous malformation	Preexisting trauma	Early enhancement Dilated vessels Tangled, tortuous vessels
Pelvic congestion syndrome	Physiologic factors	Dilated veins ↑ Prominent veins
Ovarian vein thrombosis	Nonspecific triad	Lack of enhancement Lack of signal void

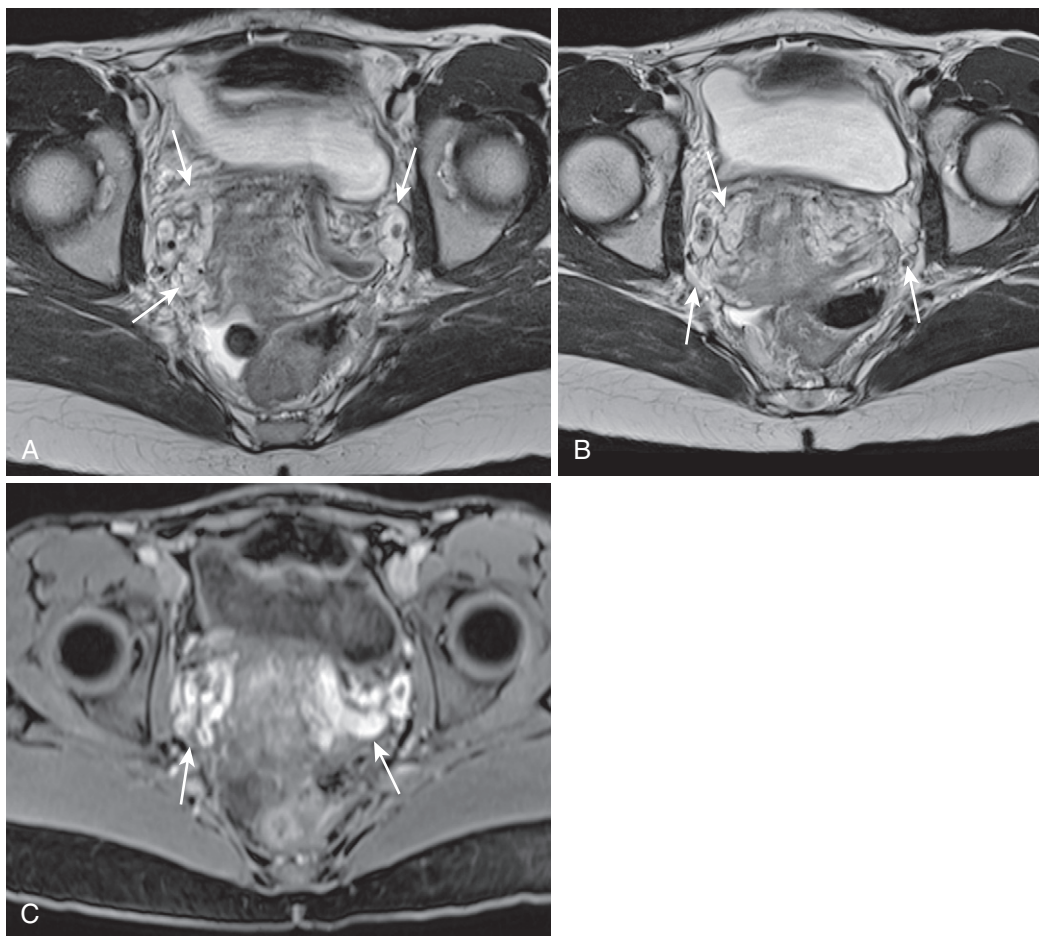


FIGURE 5-95. Normal pelvic veins simulating hydrosalpinx/fluid-filled tubular structures. Axial T2-weighted (A and B) and T1-weighted postcontrast fat-suppressed (C) images through the lower pelvis at the level of the cul-de-sac. Multiple tubular hyperintense lesions (less intense than the bladder) enhance avidly (*arrows*), more than the iliac veins, probably as a consequence of arteriovenous shunting.

lesions (Fig. 5-96). The arterial supply of the pelvic viscera is derived from the paired ovarian arteries (arising from the aorta caudal to the renal arteries) and paired branches of the internal iliac arteries—primarily the uterine and vaginal arteries. These vessels form paired arcades anastomosing with one another along the lateral aspects of the pelvic viscera. Venous drainage essentially mirrors the arterial supply, except that the left ovarian vein drains into the left renal vein instead of the inferior vena cava.

PELVIC ARTERIOVENOUS MALFORMATION

The main categories of AVMs are uterine, vaginal, and pelvic. The underlying abnormality is an abnormal connection between arteries and veins. The result is a nest of dilated vascular channels promoting increased arterial flow and

venous drainage. The common features of all AVMs are serpiginous, tubular structures exhibiting flow and enhancement with early enhancement of the draining vein (Fig. 5-97). On spin-echo sequences, the AVM appears as a signal void. Blood protons are a moving target and flow out of the region of interest too rapidly to be exposed to the 90° excitation and 180° refocusing pulses necessary to generate signal. As a vascular structure, the AVM enhances avidly—equivalent to an artery—maintaining hyperintensity on T1-weighted postgadolinium images matching vascular structures. In the case of uterine AVMs, the lesion is centered in the myometrium with consequential disruption of the normal uterine zonal anatomy.

Acquired AVMs are more common than congenital AVMs and commonly arise from

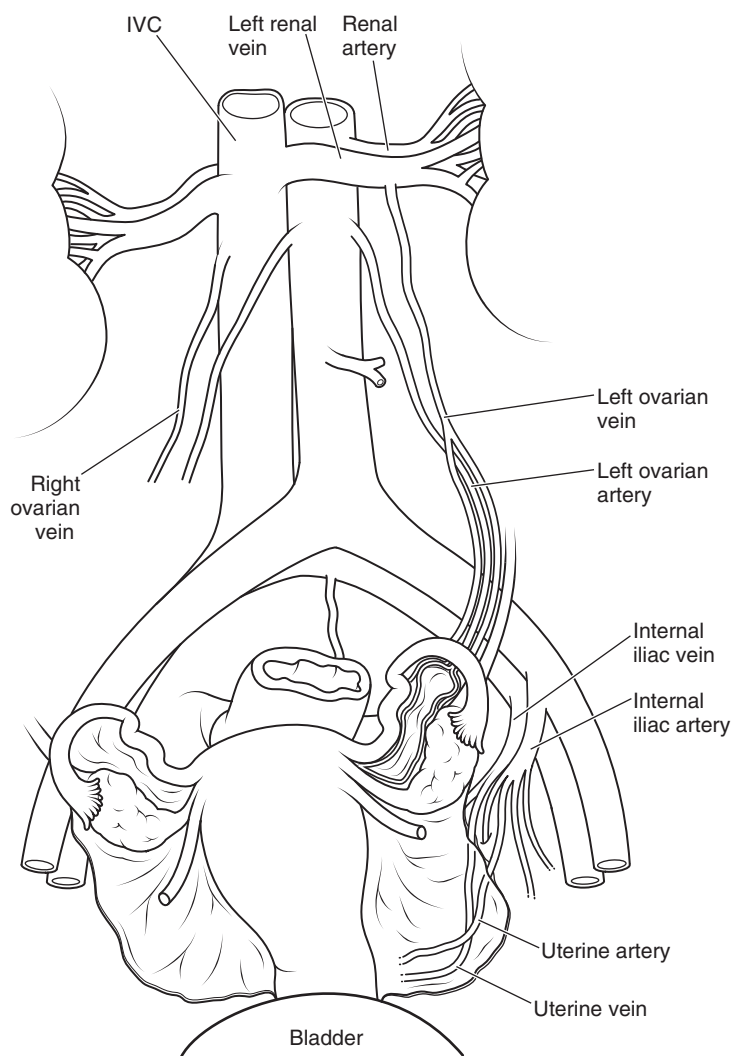


FIGURE 5-96. Pelvic vascular anatomy.

traumatic and infectious etiologies, such as dilatation and curettage, IUDs, pelvic surgery, infection, GTD, endometrial or cervical carcinoma, and diethylstilbestrol exposure. Differential diagnostic considerations include GTD (which may coexist with uterine AVMs), retained products of conception (associated with recent pregnancy and elevated β -hCG), and pelvic congestion syndrome.

PELVIC CONGESTION SYNDROME

Synonyms for pelvic congestion syndrome are pelvic varices, pelvic venous incompetence, and pelvic vein syndrome. This disorder is not well understood and multiple etiologic factors have been proposed. Among these factors are physiologic increase in pelvic blood flow during

puberty and pregnancy, hormonal vasodilatation, mechanical obstruction (left renal vein between the aorta and the superior mesenteric vein, the right common iliac vein under the right common iliac artery, and the retroaortic left renal vein behind the aorta), and primary valvular insufficiency. Although the disorder is defined as noncyclical chronic pelvic pain caused by dilated pelvic veins, there is probably overlap in the imaging appearance between afflicted and unafflicted women. In the appropriate clinical setting, the imaging criteria of pelvic congestion syndrome include four ipsilateral tortuous parauterine veins, at least one which measures at least 4 mm in diameter or an ovarian vein diameter of greater than 8 mm.⁴⁶

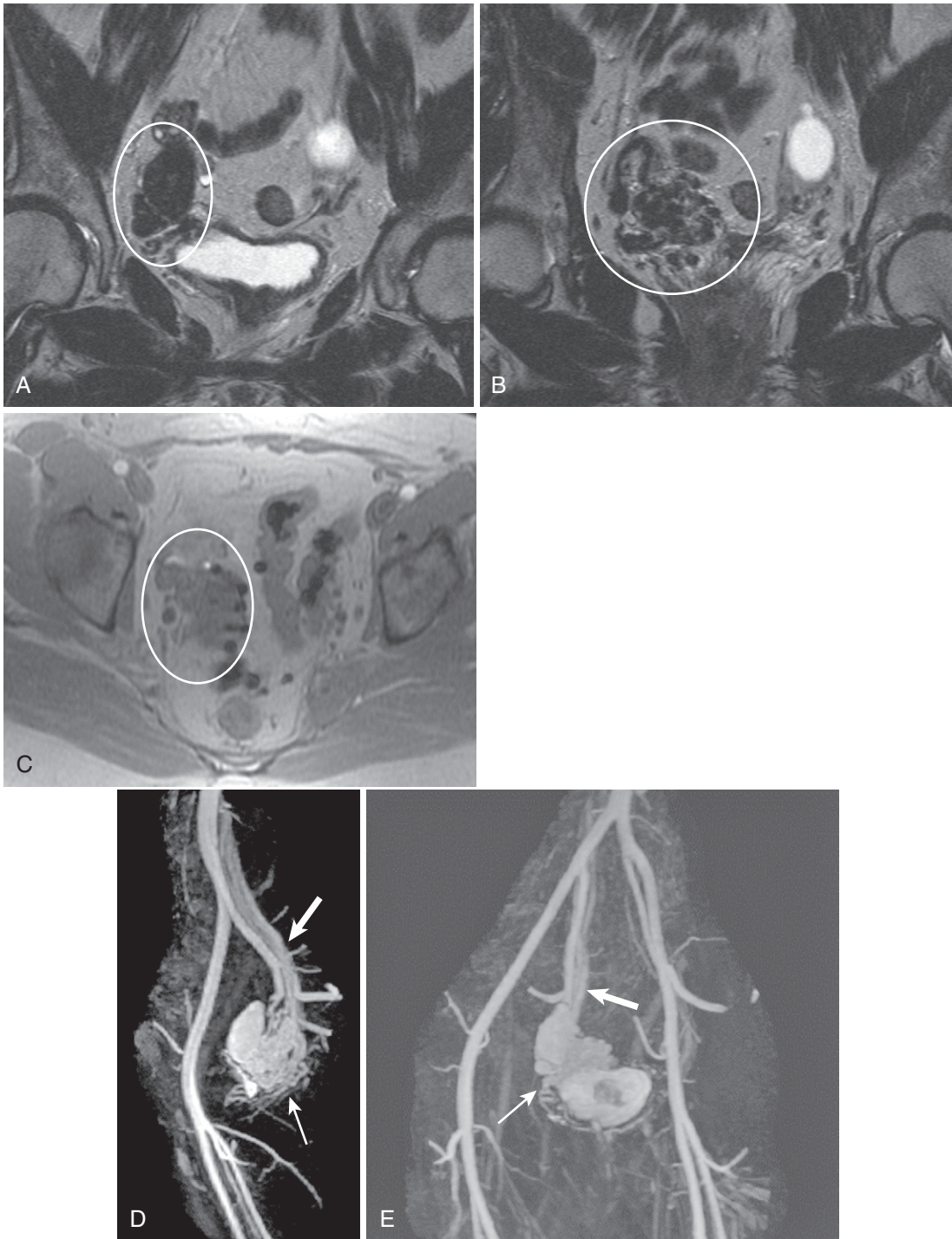


FIGURE 5-97. Pelvic arteriovenous malformation (AVM). A hypointense pelvic AVM with ovoid and serpiginous morphology (*circle* in A and B) coexisting on adjacent slices of a coronal T2-weighted sequence (A and B) lacks signal voids on the companion T1-weighted in-phase gradient echo image (*circle* in C). (Adjacent blooming hypointensities arise from gas in sigmoid diverticula.) D and E, The reformatted maximal intensity projection images (D) from the arterial phase of the pelvic magnetic resonance angiography (MRA) demonstrates pronounced enhancement (*thin arrow*) with early draining into the internal iliac vein (*thick arrow*)—compare with the contralateral side (E).

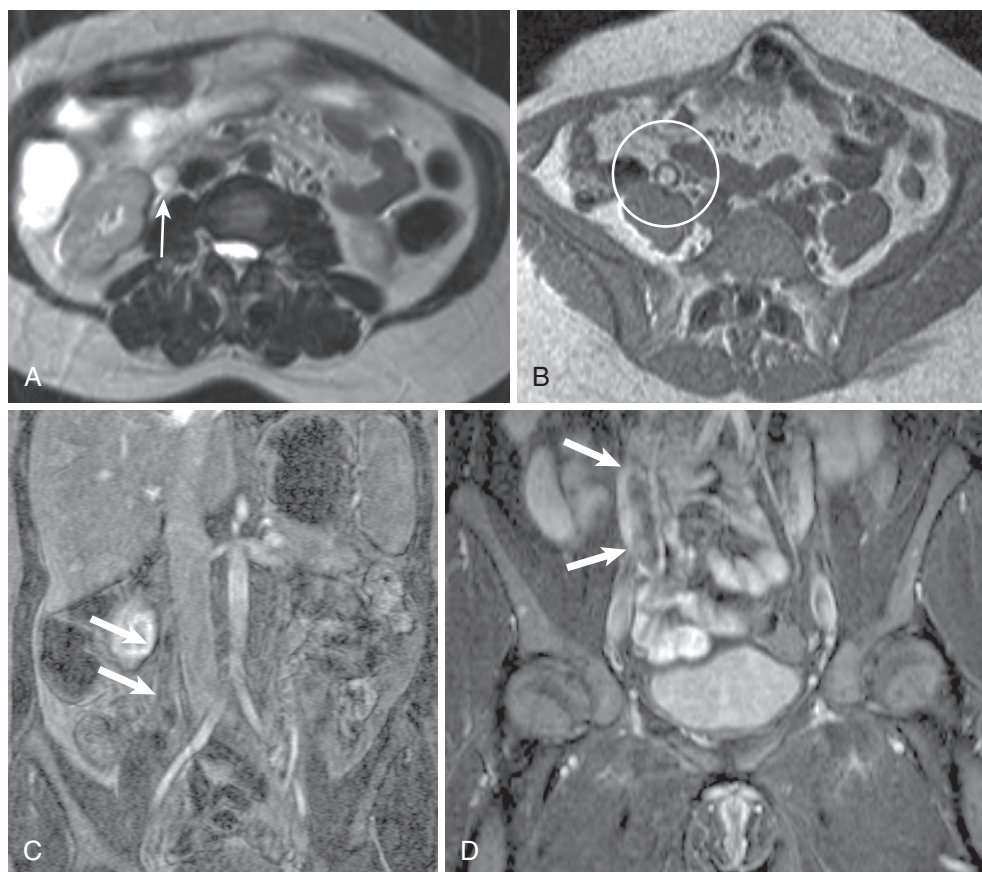


FIGURE 5-98. Ovarian vein thrombosis. **A**, A circular hyperintensity (*arrow*) corresponding to the distal ovarian vein abuts the inferior vena cava near the right kidney on the T2-weighted image. **B**, Corresponding hyperintensity on the in-phase T1-weighted gradient echo image indicates acute clot (*circle*). **C** and **D**, Coronal images from a gadolinium-enhanced three-dimensional magnetic resonance venography (MRV) display filling defect (*arrows*) within the upper (**C**) and lower (**D**) ovarian vein.

OVARIAN VEIN THROMBOSIS

Ovarian vein thrombosis does not present diagnostic difficulty because it simulates other (vascular) diagnoses, but rather because it usually flies below the clinician and radiologist's radar. The classic clinical triad includes right lower quadrant pain, fever, and ropelike palpable abdominal mass, and clinical and radiologic energy is focused on other, more potentially ominous entities, such as torsion and TOA. Just remember to include the vascular structures in your search pattern. Look for the normal signal void on spin-echo images; hyperintensity on T1-weighted images suggests the possibility of a clot. Confirm a filling defect on the postgadolinium images (or time-of-flight or steady-state images, if available) (Fig. 5-98).

References

1. Brown MA, Mattrey RF, Stamato S, Sirlin CB. MRI of the female pelvis using vaginal gel. *AJR Am J Roentgenol* 185:1221-1227, 2005.
2. Thomassin-Naggara I, Bazot M, Daraï E, et al. Epithelial ovarian tumors: Value of dynamic contrast-enhanced MR imaging and correlation with tumor angiogenesis. *Radiology* 248:148-159, 2008.
3. Merz E, Miric-Tesanic D, Bahlmann F, et al. Sonographic size of uterus and ovaries in pre- and postmenopausal women. *Ultrasound Obstet Gynecol* 7:38-42, 1996.
4. Nalaboff KM, Pellerito JS, Ben-Levi E. Imaging the endometrium: Disease and normal variants. *Radiographics* 21:1409-1424, 2001.
5. Hauth EAM, Jaeger HJ, Libera H, et al. MR imaging of the uterus and cervix in healthy women: Determination of normal values. *Eur Radiol* 17:734-742, 2007.
6. Hoad CL, Raine-Fenning NJ, Fulford J, et al. Uterine tissue development in healthy women during the normal menstrual cycle and investigations with magnetic resonance imaging. *Am J Obstet Gynecol* 192:648-654, 2005.
7. Schmidt T, Nawroth F, Breidenbach M, et al. Differential indication for histological evaluation of endometrial fluid in postmenopause. *Maturitas* 50:177-181, 2005.



8. Kitamura Y, Ascher SM, Cooper C, et al. Imaging manifestations of complications associated with uterine artery embolization. *Radiographics* 25:S119-S132, 2005.
9. Franchi M, Ghezzi F, Donadello N, et al. Endometrial thickness in tamoxifen-treated patients: An independent predictor of endometrial disease. *Obstet Gynecol* 93:1004-1008, 1999.
10. Ascher SM, Imaoka I, Lage JM. Tamoxifen-induced uterine abnormalities: The role of imaging. *Radiology* 214:29-38, 2000.
11. Utsunomiya D, Notsute S, Hayashida Y, et al. Endometrial carcinoma in adenomyosis: Assessment of myometrial invasion on T2-weighted spin-echo and gadolinium-enhanced T1-weighted images. *AJR Am J Roentgenol* 182:399-404, 2004.
12. Saez F, Urresola A, Larena JA, et al. Endometrial carcinoma: Assessment of myometrial invasion with plain and gadolinium-enhanced MR imaging. *J Magn Reson Imaging* 12:460-466, 2000.
13. Grubnic S, Vinnicombe SJ, Norman AR, Husband JE. MR evaluation of normal retroperitoneal and pelvic lymph nodes. *Clin Radiol* 57:193-200, 2002.
14. Rha SE, Byun JY, Jung SE, et al. CT and MRI of uterine sarcomas and their mimickers. *AJR Am J Roentgenol* 181:1369-1374, 2003.
15. Nagayama M, Watanabe Y, Okumura A, et al. Fast MR imaging in obstetrics. *Radiographics* 22:563-580, 2002.
16. Levine D, Barnes PD, Edelman RR. Obstetric MR imaging. *Radiology* 211:609-617, 1999.
17. Buttram VC Jr, Reiter RC. Uterine leiomyomata: Etiology, symptomatology, and management. *Fertil Steril* 36:433-445, 1981.
18. Pelage J-P, Cazejust J, Pluot E, et al. Uterine fibroid vascularization and clinical relevance to uterine fibroid embolization. *Radiographics* 25:S99-S117, 2005.
19. Murase E, Siegelman ES, Outwater EK, et al. Uterine leiomyomas: Histopathologic features, MR imaging findings, differential diagnosis, and treatment. *Radiographics* 19:1179-1197, 1999.
20. Tanaka YO, Nishida M, Tsunoda H, et al. Smooth muscle tumors of uncertain malignant potential and leiomyosarcomas of the uterus: MR findings. *J Magn Reson Imaging* 20:998-1007, 2004.
21. Togashi K, Nakai A, Sugimura K. Anatomy and physiology of the female pelvis: MR imaging revisited. *J Magn Reson Imaging* 13:842-849, 2001.
22. Ozsarlak O, Schepens E, de Schepper AM, et al. Transient uterine contraction mimicking adenomyosis on MRI. *Eur Radiol* 8:54-56, 1998.
23. Troiano RN. Magnetic resonance imaging of müllerian duct anomalies of the uterus. *Top Magn Reson Imaging* 14:269-280, 2003.
24. Reuter KL, Daly DC, Cohen SM. Septate versus bicornuate uteri: errors in imaging diagnosis. *Radiology* 172:749-752, 1989.
25. Carrington BM, Hricak H, Nuruddin RN, et al. Müllerian duct anomalies: MR imaging evaluation. *Radiology* 176:715-720, 1990.
26. Homer HA, Li TC, Cooke ID. The septate uterus: A review of management and reproductive outcome. *Fertil Steril* 73:1-14, 2000.
27. Fedele L, Ferrazzi E, Dorta M, et al. Ultrasonography in the differential diagnosis of "double" uteri. *Fertil Steril* 47:89-93, 1988.
28. Troiano RN, McCarthy SM. Müllerian duct anomalies: Imaging and clinical issues. *Radiology* 233:19-34, 2004.
29. Ott DJ, Fayed JA, Zagorian RJ. Congenital anomalies. In *Hysterosalpingography: A Text and Atlas*. 2nd ed. Baltimore: Williams & Wilkins, 1998, pp. 59-69.
30. De Graef M, Karam R, Juhan V, et al. High signals in the uterine cervix on T2-weighted MRI sequences. *Eur Radiol* 13:118-126, 2003.
31. Sugiyama K, Takehara Y. MR findings of pseudoneoplastic lesions in the uterine cervix mimicking adenoma malignum. *Br J Radiol* 80:878-883, 2007.
32. Nicolet V, Carignan L, Bourdon F, Prossmanne O. MR imaging of cervical carcinoma: A practical staging approach. *Radiographics* 20:1539-1549, 2000.
33. Hricak H, Yu KK. Radiology in invasive cervical cancer. *AJR Am J Roentgenol* 167:1101-1108, 1996.
34. Hricak H, Powell CB, Yu KK, et al. Invasive cervical carcinoma: role of MR imaging in pretreatment work-up—cost minimization and diagnostic efficacy analysis. *Radiology* 198:403-409, 1996.
35. Gant NF, Cunningham FG. *Basic Gynecology and Obstetrics*. Norwalk, CT: Appleton and Lange, 1993.
36. Jain KA. Imaging of peritoneal inclusion cysts—Pictorial essay. *AJR Am J Roentgenol* 174:1559-1563, 2000.
37. Dohke M, Watanabe Y, Okumura A, et al. Comprehensive MR imaging of acute gynecologic diseases. *Radiographics* 20:1551-1566, 2000.
38. Jung SE, Lee JM, Rha SE, et al. CT and MR imaging of ovarian tumors with emphasis on differential diagnosis. *Radiographics* 22:1305-1325, 2002.
39. Jung SE, Lee JM, Rha SE, et al. CT and MR imaging of ovarian tumors with emphasis on differential diagnosis. *Radiographics* 22:1305-1325, 2002.
40. Saini A, Dina R, McIndoe GA, et al. Characterization of adnexal masses with MRI. *AJR Am J Roentgenol* 184:1004-1009, 2005.
41. Tanaka YO, Nishida M, Yamaguchi M, et al. MRI of gynaecological solid masses: Pictorial review. *Clin Radiol* 55:899-911, 2000.
42. Jung SE, Rha SE, Lee JM, et al. CT and MRI findings of sex cord-stromal tumor of the ovary. *AJR Am J Roentgenol* 185:207-215, 2005.
43. Szklaruk J, Tamm EP, Choi H, Varavithya V. MR imaging of common and uncommon large pelvic masses. *Radiographics* 23:403-434, 2003.
44. Marin C, Seoane JM, Sanchez M, et al. Magnetic resonance imaging of primary lymphoma of the cervix. *Eur Radiol* 12:1541-1545, 2002.
45. The Rotterdam ESHRE/ASRM-Sponsored PCOS Consensus Workshop Group. Revised 2003 Consensus on Diagnostic Criteria and Long-Term Health Risks Related to Polycystic Ovary Syndrome (PCOS). *Hum Reprod* 19:41-47, 2004.
46. Kuligowska E, Deeds L, Kang L. Pelvic pain: Overlooked and underdiagnosed gynecologic conditions. *Radiographics* 25:3-20, 2005.

Index

Note: Page numbers followed by f refer to figures; page numbers followed by t refer to tables.

A

Abdominal aortic aneurysm, 256–257, 256f–257f

Abscess

- gallbladder, 173, 175f
- hepatic, 64
- amebic, 61t, 64–66
- fungal, 61t, 64
- vs. metastatic disease, 87
- mycobacterial, 61t
- pyogenic, 61t, 64, 64f–65f
- renal, 218–221, 221f, 238–239
- tuboovarian, 338–342, 339t, 341f–343f

Accident prevention, 28–29, 32f

Acinar cell, 129

Acinar cell carcinoma, 160

Acoustic noise, 29–32

Acquired cystic kidney disease, 215, 217t

Acquisition time, 22–23

Adenocarcinoma, pancreatic. *See* Pancreas, adenocarcinoma of

Adenoma

- adrenal, 48f, 246–248, 248f
- gallbladder, 177, 179f
- hepatic, 68–70, 69f
- vs. focal nodular hyperplasia, 70–71
- vs. metastatic disease, 86–87

Adenoma malignum, 305t, 310, 314f

Adenomyoma, 267f–268f, 270f, 290f–291f, 298f

Adenomyomatosis, gallbladder, 176, 178f

Adenomyosis

- cervical, 304, 305t
- myometrial, 294–296, 296t, 297f

Adhesions, intrauterine, 271, 272f

Adnexa, 317–367. *See also* Fallopian tube(s); Ovary (ovaries)

- imaging of, 261–262
- coil placement in, 265, 266f
- dynamic, 261–262, 264t
- interpretation of, 265–268, 265t, 267t
- normal, 317–321

Adrenal glands, 242–249, 244f

- adenoma of, 48f, 246–248, 248f
- carcinoma of, 249, 254f
- cystic lesions of, 244–246, 244f–245f
- echinococcal cysts of, 246
- hemorrhage of, 243, 244f, 246, 247f
- hyperplasia of, 248–249
- imaging of, 199–200, 200f
- indications for, 199, 200t
- interpretation of, 200–201

Adrenal glands (*Continued*)

- lymphoma of, 249
- metastatic disease of, 229f, 249, 252f–253f
- myelolipoma of, 249, 250f
- normal, 203f, 242–243
- pheochromocytoma of, 249, 250f–251f
- solid lesions of, 244f, 246–249, 247f

Amebiasis, 61t, 64–66

Amniotic fluid, 332f

Ampere's Law, 2–3, 4f

Angiomyolipoma

- hepatic, 97–98, 98f
- renal, 216f, 231–232, 233f

Angiomyxoma, 360, 361f

Angular momentum (spin), 1, 3f

Annular pancreas, 130–131, 132f

Aorta, aneurysm of, 52f, 256–257, 256f–257f

Arteriovenous malformation, 363t, 364–365, 366f

Artifact

- India ink, 15f, 17
- motion. *See* Motion artifact
- phase cancellation, 332f
- prohibitive, 36f–37f
- susceptibility. *See* Susceptibility artifact
- wraparound, 23, 25f, 267f–268f

Ascites, 112–113, 114f

Asherman's syndrome, 271, 272f

Autoimmune hepatitis, 115

Autoimmune pancreatitis, 135–144, 143f

B

Bartholin's gland cyst, 289f, 308–310, 310t, 312f–313f

Beaded appearance, in primary sclerosing cholangitis, 42f–43f, 115–116, 116f

Bile duct(s). *See also* Biliary tract

- common, 133f
- calculi of, 185–186, 185f
- stricture of, 186, 187f
- cyst of, 54, 54f
- cystadenocarcinoma of, 61
- cystadenoma of, 61, 62f
- hamartoma of, 54, 56f, 66

Bile salts, 171–172, 179

Biliary tract, 178–186. *See also* Bile duct(s)

- ampullary carcinoma of, 193–196, 194f–195f
- anatomy of, 178–179
- benign strictures of, 186, 187f
- calculi of, 185–186, 185f–186f

Biliary tract (*Continued*)

- carcinoma of, 188–193, 190f–195f
- congenital communicating cavernous ectasia of, 54–56, 184
- congenital dilatation of, 182–184, 182f–185f
- hamartoma of, 54, 56f, 66
- imaging techniques for, 181–182
- infection of, 187–188
- inflammation of, 187–188, 188f–189f
- normal, 178–179
- obstruction of, 186
- benign, 186, 187f
- infectious, 187–188
- inflammatory, 187–188, 188f–189f
- malignant, 188–196, 195f. *See also* Cholangiocarcinoma
- postoperative strictures of, 186
- rupture of, 66–67, 67f, 123

Biloma, 66–67, 67f, 123

Birt-Hogg-Dube syndrome, 225f

Bladder, 268

- fetal, 332f
- metastatic disease of, 320f

Blooming, 17, 18f

Bowel, 18f, 26f, 44f, 47f, 267f–268f, 268

Breast implants, 56f

Brenner's tumor, 350–351, 353t

Budd-Chiari syndrome, 117–120, 118t, 119f

- vs. cirrhosis, 120
- nodules in, 118–120

Burn injury, 29

C

CA 19-9, in pancreatic adenocarcinoma, 150

Calcification

- in chronic pancreatitis, 135, 142f
- in hepatic hemangioma, 58–60
- in hereditary pancreatitis, 144, 146f
- in pancreatic solid-cystic papillary epithelial neoplasm, 171f–172f

Calculi

- biliary, 185–186, 185f–186f
- gallbladder, 47f, 173, 174f
- renal, 218, 220f

Candidiasis, 66

Carcinoma

- adrenal, 249, 254f
- biliary. *See* Cholangiocarcinoma
- cervical. *See* Cervical carcinoma
- endometrial. *See* Endometrial carcinoma
- gallbladder, 177–178, 179f–180f

- Carcinoma (*Continued*)
 hepatic. *See* Hepatocellular carcinoma
 ovarian. *See* Ovarian carcinoma
 pancreatic. *See* Pancreas, adenocarcinoma of
 renal. *See* Renal cell carcinoma
 vaginal, 317
- Caroli's disease, 54-56, 184
- Cerebrospinal fluid (CSF), 21f, 47f
- Cervical carcinoma, 266f, 310-317, 315f
 bladder invasion in, 320f
 differential diagnosis of, 310, 312t
 endometrial metastases from, 280-282, 281f
 fibrous stroma in, 310-317, 316f
 parametrial invasion in, 318f-319f
 rectal invasion in, 318f-320f
 staging of, 310-317, 317t
- Cervicitis, 305t, 308, 308f
- Cervix, 304-317
 adenoma malignum of, 305t, 310, 314f
 adenomyosis of, 304, 305t
 carcinoma of. *See* Cervical carcinoma
 cystic lesions of, 304-310, 305f, 305t
 glandular hyperplasia of, 304, 305t, 306f-307f
 imaging of, 261-262
 interpretation of, 265t, 266
 inflammation of, 305t, 308, 308f
 lymphoma of, 359
 Nabothian cyst of, 304, 305f, 305t
 normal, 304
- Cesarean section defect, 272, 274f
- Chain of lakes appearance, in chronic pancreatitis, 135, 141f
- Chelation, in hemochromatosis, 107
- Chemical shift imaging, 14-15, 15f
- Chemoembolization, hepatic
 complications of, 91, 93f
- Chemotherapy, hepatic complications of, 91
- Cholangiocarcinoma, 188-193, 189f, 191f-192f
 extrahepatic, 91-92, 92t, 188, 193f
 hilar (Klatskin's tumor), 91-92, 92t, 102f, 188, 190f
 peripheral, 91-95, 92t, 188
 capsular retraction in, 92-93, 95f-96f, 97t
 infiltrating, 92-93, 94f
 intraductal papillary, 92-93, 94f
 mass-forming, 92-93, 94f
 staging of, 97t
- Cholangitis, 187-188, 188f-189f
- Cholecystitis, 173-176
 acute, 173, 174f-175f
 chronic, 176, 176f
 gangrenous, 176
- Cholecystoses, hyperplastic, 176-177
- Choledochal cyst, 182-184
 classification of, 182f
 type I, 182-183, 182f-183f
 type II, 183, 184f
 type III, 183, 184f
 type IV, 184, 185f
- Choledocholithiasis, 185-186, 185f
- Cholelithiasis, 47f, 173, 174f
- Cholestasis, intrahepatic, 103-104, 104f
- Cholesterosis, 176-177
- Choriocarcinoma, 282
- Cirrhosis, 110-115
 ascites in, 112-113, 114f
 atrophy-hypertrophy pattern in, 108f, 110-111, 110f, 112f
 vs. Budd-Chiari syndrome, 120
 caudate-to-right lobe ratio in, 111, 111f
 etiology of, 113-115, 113t
 fibrosis in, 111-112
 hepatocellular carcinoma and, 112-113
 imaging signs in, 110-111, 110f
 portal venous thrombus in, 114f
 portosystemic collaterals in, 47f, 108f, 112-113, 112f-114f
 regenerative nodules in, 73, 74f-75f, 111-112, 111f
- Column of Bertin, 207, 208f
- Corpus luteal cyst, 322-324, 323f, 325f-326f, 338, 339f
- Cortical rim sign, 239-240
- Cyst(s)
 of adenoma malignum, 305t, 310, 314f
 adrenal, 244-246, 244f-245f
 cervical, 304-310, 305t
 Nabothian, 304, 305f, 305t
 choledochal, 182-184, 182f-185f
 hepatic, 53, 54f
 echinococcal, 61-63, 61t, 63f
 vs. metastatic disease, 88f, 89
 ovarian, 266-267, 321-346, 321t-322t, 324t. *See also* Dermoid cyst
 complex, 346
 hemorrhagic, 324-328, 328f-329f, 338, 338t-339t
 lipid content in, 324-328, 328f-333f
 water content in, 322, 323f, 325f-327f
 pancreatic, 145, 149f, 161-170, 164f
 parovarian, 324
 renal, 207, 208f, 209
 acquired, 215, 217t
 classification of, 207, 209t, 210, 211f
 complex, 207, 210-212, 212f-213f, 218, 220f
 differential diagnosis of, 209f
 exophytic, 210, 210f-211f
 hemorrhagic, 201, 208f, 209-211, 212f-213f
 infection of, 221
 infectious, 218-221, 220f-221f
 lithium-induced, 214f, 215, 217f, 220f
 neoplastic. *See* Multilocular cystic nephroma; Renal cell carcinoma, cystic
 parapelvic, 210, 211f
 parenchymal, 210, 211f
 septated, 213f
 simple, 207, 208f, 209-212, 210f-211f, 213f
 site of, 210, 211f
- Skene's gland, 308-310, 310t, 313f
- Cyst(s) (*Continued*)
 vaginal
 Bartholin's gland, 289f, 308-310, 310t, 312f-313f
 Gartner's duct, 308, 309f, 310t
 inclusion, 308-310, 310t
 Müllerian duct, 311f
 water in, 21f, 322, 323f, 325f-327f
- Cystadenocarcinoma
 biliary, 61
 ovarian, 347-350, 350f-351f, 354f
- Cystadenofibroma, 266f, 351, 355f
- Cystadenoma
 biliary, 61, 62f
 ovarian, 350, 352f-353f
 pancreatic, 164f, 166, 167f-168f
- Cystic fibrosis, 145, 147f
- D**
- Dermoid cyst, 328-329, 328f-333f, 339t
- Diagmagnetic substances, 16
- Diethylstilbestrol, fetal exposure to, 264f, 303-304
- Diffusion-weighted imaging, 10
- Double duct sign, 150-151, 153f-154f
- Doughnut sign, 85-86, 87f
- Dysgerminoma, 354, 356f
- E**
- Echinococcal cysts
 adrenal, 246
 hepatic, 61-63, 61t, 63f
- Echo, 9
- Edema
 fallopian tube, 342f
 gallbladder, 176, 177f
 ovarian, 338, 341f, 342, 347f
 pancreatic, 134, 137f-138f
- Embryo, 282
- Endodermal sinus tumor, 354
- Endometrial carcinoma, 263f, 273-282, 279t
 classification of, 276, 276t
 invasive, 276-277, 279f-281f, 280
 pedunculated, 276f-277f
 vs. polyps, 272-273
 sessile, 276-277, 278f
 staging of, 279, 280t
- Endometrioma, 19f, 276f-277f, 283f, 329, 338, 338t, 353t
 shading in, 334f, 337f, 340f
 wall thickening in, 335f
- Endometriosis, 329, 336f-337f, 338
- Endometritis, 270
- Endometrium, 270-282, 270f
 carcinoma of. *See* Endometrial carcinoma
 diffuse abnormalities of, 270, 271f
 fluid in, 269-270
 focal abnormalities of, 271, 272f.
See also specific abnormalities
 gas in, 269-270
 hormonal effects on, 270
 hyperplasia of, 270
 metastatic disease of, 280-282, 281f
 polyps of, 263f, 272-273, 275f-277f
 tamoxifen-related changes in, 271, 271f
 thickness of, 269-270

- Endoscopic retrograde
cholangiopancreatography, 181
- Entamoeba histolytica* infection, 61t, 64-66
- F**
- Fallopian tube(s), 269f
blood in, 338, 340f
inflammation of, 338-342, 342f
- Fat, 15-16, 15f-16f
- Fat-water chemical shift imaging, 14-15, 15f
- Femoral vein thrombus, 320f
- Ferromagnetic substances/objects, 28-29
- Fertility treatment, ovarian
hyperstimulation syndrome with, 360, 363f
- Fetus
bladder of, 332f
diethylstilbestrol exposure and, 264f, 303-304
MRI effects on, 33
- Fibroids, uterine. *See* Uterine fibroid(s)
- Fibroma, ovarian, 354-355, 357f
- Field of view (FOV), 22-23, 24f-25f
- Five-gauss line, 28-29, 32f
- Flip angle (FA), 13
- Focal nodular hyperplasia, 52f-53f, 70-71, 70f-72f
vs. adenoma, 69-70
vs. hemangioma, 70-71
vs. hepatocellular carcinoma, 69-71
vs. metastatic disease, 86-87
vs. transient intensity differences, 72
- Fourier transform, 7-8
- Fractional echo sampling, 27-28, 28f
- Fringe field, 28-29, 32f
- Fungal infection, hepatic, 61t, 64, 66
- G**
- Gadolinium
adverse reactions to, 32-33, 33f
formulations of, 32, 33f
pregnancy-related administration of, 33
pulse sequences with, 17, 19f-20f
- Gallbladder, 170-178
abscess of, 173, 175f
accessory, 172
adenoma of, 177, 179f
adenomyomatosis of, 176, 178f
agenesis of, 172
anatomy of, 170-171
calculi of, 47f, 173, 174f
carcinoma of, 177-178, 179f-180f
ectopic, 172, 173f
edema of, 176, 177f
free water in, 21f
imaging technique for, 172
inflammation of, 173-176
acute, 173, 174f-175f
chronic, 176, 176f
gangrenous, 176
metastatic disease of, 178, 181f
normal, 171-172
polyps of, 176-177
- Gallstones, 47f, 173, 174f
- Gartner's duct cyst, 305t, 308, 309f, 310t
- Gas, endometrial, 269-270
- Gastrinoma, 156, 156f
- Gastrointestinal system, free water in, 21f
- Germ cell tumor, 347t, 351-354
- Gerota's fascia, 203
- Gestational trophoblastic disease, 280-282
- Ghosting, 21, 22f. *See also* Motion artifact
- Glucagonoma, 156-158, 156f
- Gradient moment nulling, 27, 27f
- Gradient system, 4-6, 5f
X (frequency-encoding), 4-5, 5f
Y (phase-encoding), 4-5, 5f-6f
Z (slice-select), 4, 5f
- Granulosa cell tumor, 354-358, 358f
- Groove pancreatitis, 144, 144f-145f
- Gyromagnetic ratio, 1
- H**
- Halo sign, 115, 116f
- Hamartoma, biliary, 54, 56f
vs. candidiasis, 66
- Hazards, 28-33, 29f-31f
screening for, 30f-31f
- Helium, risk of, 32
- Hemangioma
free water in, 21f
hepatic, 56-61, 57f-58f
calcification in, 58-60
complex, 58-60, 59f
vs. focal nodular hyperplasia, 70-71
giant, 58, 59f
malignant transformation of, 60
small, 57, 58f
STIR image of, 26f
- Hemangiomas, 60-61, 60f
- Hematoma
hepatic, 66, 67f
intervention-related, 91, 94f
renal, 222-223
- Hematosalpinx, 338, 340f
- Hemochromatosis
hepatic, 106-107, 107f-108f, 109t
pancreatic, 107, 145, 148f
splenic, 108f
- Hemolysis, renal, 241-242, 243f
- Hemorrhage
adrenal, 243, 244f, 246, 247f
hepatic, 86
pancreatic, 134, 136f
precontrast imaging of, 17, 19f
renal, 222-223, 224f, 241-242
retroperitoneal, 253-256
- Hemosiderosis, 48f, 106-107, 107f-108f
- Hepatic adenoma, 68-70, 69f
vs. focal nodular hyperplasia, 70-71
vs. metastatic disease, 86-87
- Hepatic artery thrombosis, 121-122
- Hepatitis
acute, 105f, 105t
autoimmune, 115
chronic, 113-115
- Hepatocellular carcinoma, 42f-43f, 77-83
vs. adenoma, 69-70
- Hepatocellular carcinoma (*Continued*)
cirrhosis and, 112-113
classic imaging features of, 78, 80f-82f
differential diagnosis of, 79-83, 83t-84t
diffuse, 78, 79f
extrahepatic spread of, 79, 83f
fat in, 78, 79f-80f
fibrolamellar, 70-71, 83-84, 85f
vs. focal nodular hyperplasia, 70-71
vs. high-grade dysplastic nodules, 75-76
hyperintensity in, 78, 79f-82f
hypointensity in, 78
lymphadenopathy in, 79, 83f
vs. metastatic disease, 86-87
nodular, 78
nodule-within-nodule appearance in, 76, 77f
pathogenesis of, 72-73, 74f, 76-77
pseudocapsule in, 78, 80f-81f
vs. regenerative nodules, 73-75
screening for, 77-78, 78t
solitary, 78
staging of, 78t
vs. steatosis, 99
thrombus in, 78-79, 79f, 82f
vascular invasion in, 78-79, 81f-82f
washout in, 53f, 68, 68f, 78, 80f-81f, 85f
- Hepatoma. *See* Hepatocellular carcinoma
- Hydatid disease, 61-63, 61t, 63f
- Hydatidiform mole, 282
- Hydrogen, 1, 2f
- Hydronephrosis, 215-218, 218t, 219f, 234f, 240
- I**
- Image blur, 23-24
- In-phase imaging, 14-15, 15f-16f, 17, 18f
- Inclusion cyst
ovarian, 324
peritoneal, 324, 327f
vaginal, 308-310, 310t
- India ink artifact, 15f, 17
- Infarction
hepatic, 101, 102f
intervention-related, 91, 93f
post-transplantation, 122-123, 124f
renal, 239-240, 239f
- Inferior vena cava, anomalies of, 252, 252t
- Inflammatory abdominal aortic aneurysm, 256-257, 256f-257f
- Informed consent, pregnancy and, 282
- Insulinoma, 156, 156f, 158f
- Intraductal papillary mucinous neoplasms, 149f, 153f, 162-166
branch duct, 164f, 166, 166f, 168f
main duct, 162, 164f-165f, 166
- Intrauterine adhesions, 271, 272f
- Intrauterine device (IUD), 271-272, 273f
- Inversion time (TI), 14, 14f

Iron

- hepatic deposition of, 48f, 102, 106-107, 107f-108f, 109t
- pancreatic deposition of, 107, 145, 148f

Islet cell tumors. *See* Pancreas, neuroendocrine tumors of
Islets of Langerhans, 129

J

Johanson-Blizzard syndrome, 145-148

K

K space, 7-8, 7f-8f

Kasabach-Merritt syndrome, 60

Kidney(s), 199-260, 266f

- abscess of, 218-221, 221f, 238-239
- agenesis of, 204-205
- angiomyolipoma of, 216f, 231-232, 233f

“bean” vs. “ball” lesions of, 223, 224f

benign neoplasms of, 229-232, 231f-232f

calculi of, 218, 220f

column of Bertin of, 207, 208f

corticomedullary differentiation of, 201, 201f, 203

cysts of, 207, 208f, 209

- acquired, 215, 217t
- classification of, 207, 209t, 210, 211f

complex, 207, 210-212, 212f-213f, 218, 220f

differential diagnosis of, 209f

exophytic, 210, 210f-211f

hemorrhagic, 19f, 201, 208f,

209-211, 212f-213f

infection of, 221

infectious, 218-221, 220f-221f

lithium-induced, 214f, 215, 217f, 220f

neoplastic. *See* Multilocular cystic nephroma; Renal cell carcinoma

parapelvic, 210, 211f

parenchymal, 210, 211f

septated, 213f

simple, 207, 208f, 209-212,

210f-211f, 213f

site of, 210, 211f

unilateral, 215-218

developmental anomalies of,

204-207, 204t, 205f-207f

diffuse lesions of, 237-242, 237f

bilateral, 241-242, 241t

unilateral, 240, 240t, 241f

faceless, 233-235

fetal lobulation of, 207

focal lesions of, 207-237, 208f

fusion anomalies of, 205-206, 206f

hematoma of, 222-223, 224f

hemolysis of, 241-242, 243f

hemorrhage in, 222-223, 224f,

241-242

spontaneous, 231-232

horseshoe, 205-206, 207f

imaging of, 199-200

indications for, 199, 200t

interpretation of, 200-201, 201f

protocols for, 199-200, 200f

reference standard for, 201

Kidney(s) (Continued)

region of interest measurements

in, 201, 202f-203f

lymphoma of, 232, 236-237, 236f

malrotation of, 206f

mechanical hemolysis of, 241-242,

243f

medullary cystic disease of, 214,

214f, 220f

metastatic disease of, 232, 237

multilocular cystic nephroma of,

220f, 222, 223f

normal, 201f, 203, 203f

oncocytoma of, 225f, 231, 232f

pancake, 205-206

polycystic disease of, 214-218,

214f

autosomal dominant, 214,

214f-215f, 214t, 217t, 220f

autosomal recessive, 214, 214f,

217t, 220f

positional anomalies of, 204-205,

205f-206f

pseudolesions of, 204-207, 204t,

223, 224f

ptotic, 204-205, 205f

segmental lesions of, 237-242, 237f

solid lesions of, 207-209, 209t,

223. *See also* Renal cell

carcinoma

vs. cyst, 208f

squamous cell carcinoma of,

232-236

structural anomalies of, 207

transitional cell carcinoma of, 220f,

232-236, 234f-235f

in tuberous sclerosis, 214, 214f,

216f, 217t, 220f

Klatskin's tumor, 91-92, 92t, 102f,

188, 190f

Krukenberg's tumor, 353t, 359

L

Larmor equation, 3

Leiomyomas. *See* Uterine fibroid(s)

Leiomyosarcoma, 294, 297-298, 299f

Leydig cell tumor, 354, 358

Lightbulb sign, 85-86, 87f

Lipoma, hepatic, 98

Lipomatosis, pancreatic, 133

Lithium, renal cysts with, 214f, 215,

217f, 220f

Liver, 35-128. *See also* Bile duct(s);

Biliary tract

ablated-lesion imaging in, 90-91,

91f-92f, 91t

abscess of, 64

amebic, 61t, 64-66

fungal, 61t, 64, 66

mycobacterial, 61t

pyogenic, 61t, 64, 64f-65f

vs. metastatic disease, 87

adenoma of, 68-70, 69f

vs. focal nodular hyperplasia,

70-71

vs. metastatic disease, 86-87

angiomyolipoma of, 97-98, 98f

candidiasis of, 66

carcinoma of. *See* Hepatocellular

carcinoma

chemoembolization-related lesions

of, 91, 93f

Liver (Continued)

chemotherapy-related lesions of, 91

cholestasis of, 103-104, 104f

cirrhosis of. *See* Cirrhosis

confluent fibrosis of, 103, 103f

cystic lesions of, 53, 54f

infection of, 54

vs. metastatic disease, 88f, 89

developmental lesions of, 54-61

diffuse abnormalities of, 104-125,

104t

occult, 104-105, 105t

echinococcal cysts of, 61-63, 61t,

63f

fatty (steatosis), 38f, 48f, 100f,

105-106, 106f

geographic, 36f-37f, 102, 103f

micro- vs. macrovesicular, 99

nodular, 99

fibrocystic ductal plate diseases of,

54-55, 55t

focal fatty sparing in, 99, 100f

focal lesions of, 51-99. *See also*

specific cystic and solid

lesions

focal nodular hyperplasia of,

52f-53f, 70-71, 70f-72f

vs. adenoma, 69-70

vs. hemangioma, 70-71

vs. hepatocellular carcinoma,

69-71

vs. metastatic disease, 86-87

vs. transient intensity differences,

72

geographic lesions of, 99-104,

101f

hemangioma of, 56-61, 57f-58f

hemangiomatosis of, 60-61, 60f

hematoma of, 66, 67f

intervention-related, 91, 94f

hemorrhagic cysts of, 54

imaging of, 35-45

BolusTrack, 39f, 40

coils in, 35, 40, 41f

dynamic, 35, 39f, 41, 47-51,

49f-50f, 52f-53f

fading on, 68, 68f

field-of-view in, 40, 42f-43f

gadolinium for, 35, 39f, 39t, 41,

51, 52f

heavily T2-weighted, 40-41, 46,

50, 50f

indications for, 35, 37t

interpretation of, 45-50, 45t-46t,

84t

moderately T2-weighted, 41-46,

49-50, 50f

protocol for, 40-45, 40t

signal-to-noise ratio in, 35,

36f-38f

SSFSE (single-shot fast spin-echo),

38f, 40-41, 41f, 44f, 46, 47f,

50f

steady-state, 46, 47f

T1-weighted, 41, 41t, 46-50, 46t,

48f

three-dimensional pulse

sequences in, 45

washout on, 53f, 68, 68f, 78,

80f-81f, 85f

infarction of, 101, 102f

intervention-related, 91, 93f

- Liver (Continued)**
 post-transplantation, 122-123, 124f
 infectious lesions of, 61-66, 61t
 inflammation of, 104-105, 105f, 105t, 115
 iron deposition in, 48f, 102, 106-107, 107f-108f, 109t
 lipid-based lesions of, 97-99
 lipoma of, 98
 lymphoma of, 89-90, 90f
 metastatic disease of, 48f
 hemorrhage and, 86
 vs. hepatocellular carcinoma, 79
 hypervascular, 84-87, 84t, 86f-87f
 hypovascular, 88-89, 88f-89f, 88t
 stratification of, 88, 89t
 neoplastic lesions of, 61. *See also* Hepatocellular carcinoma
 nodules of, 72-76, 74f
 dysplastic, 72-73, 74f, 75-76, 76f-77f
 nodule within a nodule of, 76, 77f
 prehypervascular, 72-73, 75
 regenerative, 72-73, 74f-75f, 111-112, 111f
 siderotic, 72-73
 normal, 50-51, 51f
 passive congestion of, 120, 120f
 PEComa of, 49f
 polycystic disease of, 54, 55f
 primarily enhancement lesions of, 100-102
 schwannoma of, 20f
 segments of, 51f
 simple cysts of, 54, 54f
 solid lesions of, 67-88. *See also specific solid lesions*
 cystic components of, 67
 hypervascular, 68, 68f, 84t
 hypovascular, 87-88, 88f, 88t
 transient intensity differences of, 72, 101, 101f
 vs. focal nodular hyperplasia, 72
 geographic, 73f
 pseudoglobular, 72, 74f
 transplantation of. *See* Liver transplantation
 traumatic lesions of, 66-67
 von Meyenburg complex of, 54, 56f
- Liver transplantation, 120-125, 121f**
 biliary complications of, 123-125
 biloma after, 123
 complications of, 121f
 hepatic artery thrombosis after, 121-122
 infarction after, 122-123, 124f
 inferior vena cava stenosis after, 122, 124f
 lymphoproliferative disorder syndromes after, 125, 125t
 malignancy after, 125
 perihepatic fluid after, 120-121, 121f, 123
 periportal fluid after, 120-121, 122f
 portal venous complications of, 122, 123f
 rejection after, 121-122
 stenosis after, 121-122
- Lumbar spine, 268**
- Lungs, metastatic disease of, 299f**
- Lymphadenopathy**
 in hepatocellular carcinoma, 79, 83f
 periportal, 20f
- Lymphoma**
 adrenal, 249
 cervical, 359
 hepatic, 89-90, 90f
 myometrial, 297-298
 pancreatic, 160-161, 162f-163f
 pelvic, 266f, 359
 periportal lymphadenopathy in, 20f
 renal, 232, 236-237, 236f
 retroperitoneal, 257, 258f
- Lymphoplasmacytic sclerosing pancreatitis, 135-144, 143f**
- M**
- Magnet, 1-3, 4f, 8f**
- Magnetic alignment, 1, 2f**
- Magnetic resonance**
 cholangiopancreatography (MRCP)
 in ampullary carcinoma, 194f-195f
 in biliary hamartoma, 56f
 in biliary stricture, 186, 187f
 in cholangiocarcinoma, 190f, 193f
 in choledocholithiasis, 185f
 in chronic pancreatitis, 141f
 in ectopic gallbladder, 173f
 in groove pancreatitis, 144, 145f
 in hereditary pancreatitis, 146f
 in infectious cholangitis, 187-188
 in intraductal papillary mucinous neoplasm, 164f, 166f
 in lithium nephropathy, 217f
 in Mirizzi's syndrome, 186f
 in mucinous cystic neoplasm, 169f-170f
 in pancreas divisum, 133f
 in pancreatic adenocarcinoma, 154f-155f
 in pancreatic serous cystadenoma, 167f-168f
 in primary sclerosing cholangitis, 42f-43f, 116f-117f, 188f-189f
 in septated renal cyst, 213f
- Magnetic spin, 3, 3f**
- Magnetic susceptibility, 16**
- Magnetically active nuclei, 1, 2f**
- Magnetism, 1, 2f-3f, 16**
- Medullary sponge kidney, 214-215, 220f**
- Melanoma**
 hepatic metastases from, 48f, 86, 86f
 pancreatic metastases from, 160f-161f
 uveal, 19f, 48f, 86f
- Menstrual cycle, 322-324**
- Metastatic disease**
 adrenal, 229f, 249, 252f-253f
 bladder, 320f
 endometrial, 280-282, 281f
 gallbladder, 178, 181f
 hepatic, 48f
 vs. hepatocellular carcinoma, 79
 hypervascular, 84-87, 84t, 86f-87f
- Metastatic disease (Continued)**
 hypovascular, 88-89, 88f-89f, 88t
 stratification of, 88, 89t
 lymph node, 79, 83f
 ovarian, 359, 359f
 pancreatic, 158-160, 160f-162f
 pulmonary, 299f
 rectal, 318f-320f
 renal, 232, 237
 retroperitoneal, 257-259, 258f
 vaginal, 281f, 318f-319f
- Mirizzi's syndrome, 185-186, 186f**
- Motion artifact, 21-27, 22f**
 acceleration factor and, 22-24
 echo train length and, 22-24
 field of view and, 22-23, 24f-25f
 geometry factor in, 24
 gradient moment nulling and, 27, 27f
 in liver imaging, 35, 36f-37f
 minimization of, 22-23, 23f, 26, 26f
 number of excitations and, 22-23, 26
 in pelvic imaging, 267f-268f, 280f-281f
 physiologic monitoring and, 24-26, 26f
 spatial resolution and, 24
 tissue-specific signal intensity and, 26
 view-to-view, 21, 22f
 within-view, 21, 22f, 27
- Mucinous cystic neoplasm, 166, 168f-170f**
- Müllerian duct anomalies, 298-304, 300f**
 class II (unicornate uterus), 298-301, 300f
 class III (didelphys uterus), 298-301, 300f-301f
 class IV (bicornuate uterus), 300f, 301-303, 302f-303f
 class V (septate uterus), 264f, 300f, 301-303, 302f-303f
 class VI (arcuate uterus), 303, 304f
 imaging of, 261, 264f
- Müllerian duct cyst, 311f**
- Myelolipoma, adrenal, 249, 250f**
- Myometrium, 282-304**
 adenomyosis of, 294-296, 296t, 297f
 anatomy of, 262f, 270f, 282
 contractions of, 296
 malignant disease of, 297-298, 299f
- N**
- Nabothian cyst, 304, 305f, 305t**
- Navigatory pulse, 26**
- Necrosis, pancreatic, 134, 139f**
- Nephrogenic fibrosing dermatopathy, 32-33**
- Nephroma, cystic, multilocular, 220f, 222, 223f**
- Nephropathy, contrast-induced, 32**
- Net magnetic vector, 1-4, 3f-4f**
- Neuroendocrine (islet cell) tumors, 151-158, 156f-157f**
 cystic, 157f, 159f, 166
 gastrin-secreting, 156, 156f
 glucagon-secreting, 156-158, 156f
 insulin-secreting, 156, 156f, 158f

- Neuroendocrine (islet cell) tumors
(*Continued*)
nonfunctioning, 156f, 158, 159f
somatostatin-secreting, 156-158,
156f
VIP-secreting, 156-158, 156f
Nonalcoholic fatty liver disease,
105-106, 106f
Notch sign, 110f
Nuclei, 1, 2f
- O**
- Ohmic heating, 29
Oncocalyx, 232-233
Oncocytoma, 225f, 231, 232f
Operator's console, 8, 8f
Ormond's disease, 253
Out-of-phase imaging, 14-15, 15f-16f,
17, 18f
- Ovarian carcinoma, 346-351, 347t,
353t
classification of, 347t, 349t
clear cell, 350-351
endometrioid, 350-351
mucinous, 350, 350f-351f, 353t,
354f
serous, 350, 350f-351f, 353t
staging of, 349t
- Ovarian hyperstimulation syndrome,
360, 363f
- Ovarian vein thrombosis, 363t, 367,
367f
- Ovary (ovaries), 317-367
corpus luteal cyst of, 322-324, 323f,
325f-326f, 338, 338t, 339f
cystadenocarcinoma of, 347-350,
350f-351f, 354f
cystadenofibroma of, 266f, 351,
353t, 355f
cystadenoma of, 350, 352f-353f
cystic lesions of, 266-267,
321-346, 321t-322t, 324t
complex, 346
hemorrhagic, 324-328,
328f-329f, 338, 338t-339t
lipid content in, 324-328,
328f-333f
water content in, 322, 323f,
325f-327f
dermoid cyst of, 328-329,
328f-333f, 339t
dimensions of, 269t
edema of, 338, 341f, 342, 347f
follicle cyst of, 320f, 322-324
functional cysts of, 322-324
globally abnormal, 360
hyperstimulation of, 360, 363f
imaging of, 261-262
interpretation of, 266-267
inclusion cyst of, 324
massive edema of, 342, 347f
multifollicular, 360
neoplasms of, 346-360
classification of, 347t
dysgerminoma, 354, 356f
endodermal sinus, 354
epithelial, 323f, 346-351, 347t
benign, 346-351, 349t,
352f-353f, 353t, 355f
classification of, 346-351
malignant, 346-351, 349t,
350f-351f, 353t, 354f
- Ovary (ovaries) (*Continued*)
fibroblastic, 354-355, 357f
germ cell, 347t, 351-354
granulosa cell, 354-358, 358f
Leydig cell, 354, 358
metastatic, 359, 359f
Sertoli cell, 354, 358
sex cord-stromal, 347t, 351-354,
358-359
thecal cell, 354-355
normal, 269f, 317-321, 320f-322f
polycystic, 360, 362f
postmenopausal cysts of, 322-324
teratoma of, 351-354. *See also*
Dermoid cyst
torsion of, 339t, 342, 344f-347f,
353t
- P**
- Pancreas, 129-170
acinar cell carcinoma of, 160
acinar cell of, 129
adenocarcinoma of, 149f-150f,
150-151
arterial phase imaging in,
150-151, 152f-153f
duct obstruction in, 150-151,
153f-154f
hypointensity in, 151f
vs. metastatic disease, 158-160
vs. pancreatitis, 150f, 151
spread of, 151, 154f-155f
unresectability of, 151, 154f
agenesis of, 132-133
anatomy of, 129, 130f
annular, 130-131, 132f
congenital/developmental
anomalies of, 130-133,
132f-134f
in cystic fibrosis, 145, 147f
cysts of, 145, 149f, 161-170,
164f
edema of, 134, 137f-138f
embryology of, 130, 131f
focal lesions of, 148-170, 149f
cystic, 149f, 161-170, 164f
solid, 148-161, 149f-150f
function of, 129
hemochromatosis of, 107, 145,
148f
imaging of, 129-130
dynamic, 129-130, 131f
fat-suppressed T1-weighted, 129,
130f
fat-suppressed T2-weighted, 129,
134, 137f
T1-weighted, 129, 130f
T2-weighted, 129, 131f
inflammation of. *See* Pancreatitis
intraductal papillary mucinous
neoplasms of, 149f, 153f,
162-166, 164f-166f, 168f
islet cell tumors of. *See* Pancreas,
neuroendocrine tumors of
in Johanson-Blizzard syndrome,
145-148
lipomatosis of, 133
lymphatic of, 160-161, 162f-163f
metastatic disease of, 158-160,
160f-162f
mucinous cystic neoplasm of, 166,
168f-170f
- Pancreas (*Continued*)
neuroendocrine tumors of,
151-158, 157f
cystic, 166
gastrin-secreting, 156, 156f
glucagon-secreting, 156-158,
156f
insulin-secreting, 156, 156f, 158f
nonfunctioning, 156f, 158, 159f
somatostatin-secreting, 156-158,
156f
VIP-secreting, 156-158, 156f
normal, 129, 130f-131f
pseudocysts of, 138f, 161
in Schwachman-Diamond
syndrome, 145
serous cystadenoma of, 164f, 166,
167f-168f
solid-cystic papillary epithelial
neoplasm of, 170, 171f-172f
in von Hippel-Lindau disease, 145,
149f, 161
- Pancreas divisum, 132, 133f-134f
Pancreatic ducts, 130, 131f
anatomic variants of, 132, 134f
failed fusion of, 132, 134f
Pancreatitis, 134-144
acute, 131f, 134-135
fluid collection in, 134,
137f-138f
hemorrhagic, 134, 136f
necrotic, 134, 139f
pseudoaneurysm formation with,
134, 140f
venous thrombosis in, 134-135
autoimmune, 135-144, 143f
chronic, 131f, 135, 141f-142f
vs. intraductal papillary mucinous
neoplasm, 162
etiology of, 134, 135f
groove, 144, 144f-145f
hereditary, 144, 146f
Parallel imaging, 24, 25f
Paramagnetic substances, 16, 16f, 19f
Parovarian cyst, 324
PEComa, 49f
Pelvic arteries/veins, 364f-365f
Pelvic congestion syndrome, 363t,
365
Pelvic inflammatory disease, 338, 341f
Pelvic miscellaneous lesions, 359,
359t
Pelvic vein, 360-364, 364f
Pelvic vein syndrome, 365
Pelvic venous incompetence, 365
Pelvis, female, 261-368. *See also at*
Adnexa; Cervix; Ovary (ovaries);
Uterus; Vagina
imaging of, 261-262, 263t
coil placement in, 265, 266f
dynamic, 261-262, 264t
indications for, 261, 262t
interpretation of, 265-268, 265t
vascular anatomy of, 360-364,
364f-365f
Perineum, angiomyxoma of, 360, 361f
Periportal halo sign, 115, 116f
Peritoneal inclusion cyst, 324, 327f
Phase cancellation artifact, 332f
Pheochromocytoma, 249, 250f-251f
Placental site trophoblastic tumor,
282

- Polycystic kidney disease, 214–218, 214f
 autosomal dominant, 214, 214f–215f, 214t, 217t, 220f
 autosomal recessive, 214, 214f, 217t, 220f
- Polycystic liver disease, 54, 55f
- Polycystic ovary disease, 360, 362f
- Polyps
 endometrial, 263f, 272–273, 275f–277f
 gallbladder, 176–177
- Portal hypertension, 112–113, 114f
- Portal vein thrombus, 102, 102f
 in hepatocellular carcinoma, 78–79, 79f, 82f
- Posttransplant lymphoproliferative disorder syndromes, 125, 125t
- Pregnancy, 282
 dermoid cyst in, 332f
 ectopic, 339t, 346, 348f–349f
 gadolinium administration and, 33
 hydronephrosis and, 219f
 informed consent and, 282
 ovarian torsion in, 347f
- Primary biliary cirrhosis, 115, 115f–116f
- Primary sclerosing cholangitis, 42f–43f, 55–56, 115–117, 116f–117f, 187, 188f–189f
 differential diagnosis of, 117
- Proton density pulse sequence, 12–13, 13f
- Pseudoaneurysm, pancreatic, 134, 140f
- Pseudocyst
 adrenal, 244
 pancreatic, 138f, 161
- Pulsatile vascular flow, 21
- Pulse sequence, 6, 6f, 9–10
 bound water, 17–18, 20f
 chemical-shift, 14–15, 15f
 dynamic, 17, 19f–20f
 susceptibility artifact and, 27–28, 28f
- echo planar (EPD), 10
 fast spin-echo, 16f
 fat-saturation, 14
 fat-suppression, 14
 susceptibility artifact and, 28
- fluid attenuation inversion recovery (FLAIR), 14
- free water, 18–20, 21f
- gradient-echo, 6f, 9–10, 9f–10f
- gradient-recalled echo, 16f
- heavily T2-weighted, 18–20, 21f
- interstitial, 17, 20f
- inversion, 14, 14f
- lesion suppression, 18–20, 21f
- moderately T2-weighted, 17–18, 20f
- paramagnetic, 17, 19f
- proton density, 12–13, 13f
- short tau inversion recovery (STIR), 14, 24–26, 26f
- single-shot fast spin-echo (SSFSE), 16f, 18f–19f
- spectrally selective, 14
- spin-echo, 6f, 9–10, 9f–10f
- steady-state free precession (SSFP), 10
- T1-weighted, 12–21, 12f–13f, 16f
- Pulse sequence (*Continued*)
 T2-weighted, 12, 13f, 14–21, 16f, 19f–21f
 vascular (solid/viable tissue), 17
 water-only, 20–21
- Pyelonephritis, 237–239, 237f–238f
 xanthogranulomatous, 240
- Pyonephrosis, 238–239
- Pyosalpinx, 338–342, 342f
- Q**
 Quenching, 32
- R**
 Receiver system, 6–7, 8f
- Rectangular field of view, 22–23, 24f
- Rectum, metastatic disease of, 318f–320f
- Recurrent pyogenic cholangitis, 55–56
- Renal artery (arteries), 239f
 infarction of, 239–240, 239f
 stenosis of, 237f, 240, 241f
- Renal cell carcinoma, 25f, 220f, 223–231
 acquired cystic kidney disease and, 215, 217t
 adrenal extension of, 229f
 chromophobe, 229, 230f
 clear cell, 225, 225f–227f, 229f
 collecting duct, 236
 cystic, 211–212, 216f, 221–222, 222f, 229
 in hereditary syndromes, 225f
 lymph node assessment in, 228
 medullary, 236
 vs. multilocular cystic nephroma, 222
 pancreatic metastases from, 162f
 papillary, 225f, 228–229, 230f
 solid lesions of, 224f
 staging of, 204f, 225–226, 228f
 subtypes of, 221–222, 221t
 thrombus with, 226, 227f–228f
 vascular invasion of, 227f
- Renal collecting system, 238f
 carcinoma of, 232–236, 234f–235f
 distention of, 218, 218t, 219f
 imaging of, 200, 200t, 203
 infection of, 237–239, 238f
- Renal insufficiency, cystic disease in, 215
- Renal vein thrombosis, 237f, 240–242, 242f
 in renal cell carcinoma, 226, 227f–228f
- Resonance, 1
- Respiratory triggering, 26, 26f
- Retrograde pyelography, 208f
- Retroperitoneum, 249–259, 254f–255f. *See also* Adrenal glands; Kidney(s)
 fibrosis of, 253–256, 255f
 hemorrhage of, 253–256
 lymphoma of, 257, 258f
 metastatic disease of, 257–259, 258f
 neoplasms of, 257, 258f
 sarcoma of, 259
- Rf transmitter system, 3–4
- Rokitansky-Aschoff sinuses, 176, 178f
- Rokitansky's nodule, 331f
- Round ligament, 266–267, 269f, 322f
- S**
 Safety, 28–33, 29f, 32f
- Santorini, duct of, 130, 132, 132f–133f
- Sarcoma, retroperitoneal, 259
- Schwachman-Diamond syndrome, 145
- Schwannoma, hepatic, 20f
- Screening form, 30f–31f
- Sertoli cell tumor, 354, 358
- Sex cord-stromal tumor, 347t, 351–354, 358–359
- Signal-to-noise ratio, 28, 28f
- Skene's gland cyst, 308–310, 310t, 313f
- Solid-cystic papillary epithelial neoplasm, 149f, 170, 171f–172f
- Somatostatinoma, 156–158, 156f
- Spatial resolution, reduction in, 24
- Specific absorption rate, 32
- Spin, 1, 3f
- Spin-spin relaxation, 12
- Spiral valves of Heister, 170–171
- Squamous cell carcinoma, urothelial, 232–236
- Stein-Leventhal syndrome, 360, 362f
- Stenosis, renal artery, 237f, 240, 241f
- Stent, 29
- Stones
 biliary, 185–186, 185f–186f
 gallbladder, 47f, 173, 174f
 renal, 218, 220f
- String of pearls appearance, in chronic pancreatitis, 135, 141f
- Superparamagnetic substances, 16
- Surgical clips, 27
- Susceptibility artifact, 27–28, 28f
 in gastrointestinal tract imaging, 18f
 in liver imaging, 40–41, 44f, 48f, 69f, 108f, 111f
 minimization of, 27–28, 27f–28f, 40–41, 44f, 47f
 in pelvic imaging, 267f–268f, 274f, 278f
 in renal imaging, 220f
- T**
 T2 contrast, 12
 T2* contrast, 12
 T2* decay, 9, 12
 T1 relaxation, 11–12, 11f–12f
- Tamoxifen, 271, 271f
- Tampon, 278f
- TE (time to excitation), 12–13
- Teratoma, ovarian, 351–354
 mature. *See* Dermoid cyst
- Thecal cell tumor, 354–355
- Thumb rule, 2–3, 4f
- Time-varying magnetic fields, 29
- Tissue contrast, 11–15
 T2 decay and, 11–12, 11f
 T1 relaxation and, 11, 11f
- TR (time to repetition), 9
- Transient hepatic intensity differences, 72, 101
 vs. focal nodular hyperplasia, 72
 pseudoglobular, 72
- Transitional cell carcinoma, 220f, 232–236, 234f–235f
- Tuberous sclerosis, 214, 214f, 216f, 217t, 220f, 225f
- Tuboovarian abscess, 338–342, 339t, 341f–343f

- U**
- Ultrasonography, in tuboovarian abscess, 343f
- Urethra, Skene's gland cysts of, 308-310, 310t, 313f
- Uterine artery embolization, 291, 294, 294f-295f, 295t
- Uterine fibroid(s), 282-294
 classification of, 282, 282f
 cystic degeneration of, 289-291, 291t, 292f
 degeneration of, 289-291, 290f-293f, 291t
 differential diagnosis of, 286-289, 290t
 hemorrhagic degeneration of, 289-291, 291t, 293f
 hyaline degeneration of, 289-291, 291t
 identification of, 282-286
 intracavitary, 282, 282f
 intramural, 263f, 282, 282f, 284f-285f, 288f-289f, 293f-295f, 340f
 malignant degeneration of, 294, 296f
 myxoid degeneration of, 289-291, 290f-291f, 291t
 pedunculated, 282, 282f
 postembolization, 291, 294, 294f-295f, 295t
 submucosal, 282, 282f-283f, 289f
 subserosal, 263f, 282, 282f, 285f-287f, 286-289, 320f, 353t
 vascularity of, 286-289, 288f-289f
- Uterus, 268-304
 anatomy of, 262f, 269f-270f, 365f
 antelexion of, 272, 274f
 anteversion of, 274f
 arcuate, 300f, 303, 303f-304f
 arteriovenous malformation of, 364-365
- Uterus (Continued)**
 bicornuate, 300f, 301-303, 302f-303f
 cesarean section defect of, 272, 274f
 didelphys, 298-301, 300f-301f
 endometrial disease of, 270-282.
See also at Endometrial carcinoma; Endometriosis; Endometrium
 fibroids of. *See* Uterine fibroid(s)
 global abnormalities of, 298-304.
See also Müllerian duct anomalies
 gravid, hydronephrosis and, 219f
 imaging of, 261-262
 coil placement in, 265, 266f
 indications for, 262t
 interpretation of, 265-268, 265t
 protocol for, 263t
 myometrial disease of, 282-304.
See also Adenomyosis; Uterine fibroid(s)
 normal, 262f, 268-270, 269t, 270f
 retroversion of, 270f, 274f
 septate, 264f, 300f, 301-303, 302f-303f
 size of, 265, 268-269, 269t, 270f
 T-shaped, 264f, 303-304
 unicornuate, 298-301, 300f
- V**
- Vagina, 304-317
 arteriovenous malformation of, 364-365
 Bartholin's gland cyst of, 289f, 308-310, 310t, 312f-313f
 carcinoma of, 317
 cystic lesions of, 304-310, 310t
 Gartner's duct cyst of, 308-310, 309f, 310t
 inclusion cyst of, 308-310, 310t
- Vagina (Continued)**
 metastatic disease of, 281f, 318f-319f
 Müllerian duct cyst of, 311f
 Varices, pelvic, 360-365, 363t
 Vascular (solid/viable tissue) pulse sequence, 17
- Venous thrombosis
 femoral vein, 320f
 ovarian vein, 363t, 367, 367f
 in pancreatitis, 134-135
 portal vein, 78-79, 79f, 82f, 102, 102f
 renal vein, 226, 227f-228f, 237f, 240-242, 242f
- VIPoma, 156-158, 156f
- Von Hippel-Lindau disease
 pancreatic lesions in, 145, 149f, 161
 renal lesions in, 214, 214f, 216f, 217t, 225f
- Von Meyenburg complex, 54, 56f
- W**
- Water, 15-16, 16f, 20-21
 bound, 17-18, 20f
 free, 18-20, 21f
- Wraparound artifact, 23, 25f, 267f-268f
- Wunderlich's syndrome, 231-232
- X**
- X (frequency-encoding) gradient, 4-5, 5f
- Xanthogranulomatous pyelonephritis, 240
- Y**
- Y (phase-encoding) gradient, 4-5, 5f-6f
- Z**
- Z (slice-select) gradient, 4, 5f
- Zollinger-Ellison syndrome, 156